An Improved Algorithm of Orthogonal Vector Spectral Estimation Method

Dengshan Huang, **Xingzhao Liu**, **and Jie Ren**
School of Electronics and Information, Northwestern Polytechnical University
Xi'an, Shaanxi 710072, China

Abstract— Orthogonal Vector Spectral Estimation method — OVSS method, with high statistical stability, high resolution, is much better than other existing spectral estimation methods (such as the MUSIC method). But while the method is used for dealing with superposition of multiple sinusoidal signals, the pseudo-peaks will often appear. In this paper, the principle of the OVSS is investigated in detailed. A new matrix is formed by using the elements of the primary eigenvectors and the right singular vector corresponding to the zero singular value of the matrix is orthogonal with signal space. Actually, the signal information can be extracted by extending the processing of autocorrelation matrix. However, when there are several signals, pseudo-peaks will appear inevitably because of spurious zeros. From this view, a new method for eliminating the pseudo-peaks should be found. Based on the matrix above, a modified matrix is formed through reusing the specific elements on specific positions, and then following the steps of OVSS method, a modified OVSS method can be gained. A large number of simulation experiments show that, the pseudo-peaks can be eliminated by using the modified OVSS method, with a little loss of resolution in low SNR cases, and without significant loss of statistical stability in high SNR cases.

1. INTRODUCTION

When processing power spectrum estimation problem of the multi-sinusoidal signals (with K) mixed with white noise, the signal correlation matrix eigenvalue decomposition is adopted usually. By eigen-decomposition of the P-dimensional signal correlation matrix, a set of mutually orthogonal eigenvector are obtained to form a vector space. This space can be divided into two sub-spaces(known as orthogonal subspace): the signal subspace and noise subspace. The signal subspace can be made by the eigenvector (primary eigenvector) corresponding to K large eigenvalue (primary eigenvalue) and noise subspace formed by eigenvector corresponding to the (P-K) characteristic values. The power spectrum estimation methods (such as the AR, MA methods, etc.) based on signal subspace have good statistical stability; and the power spectrum estimation methods (such as the MUSIC method, etc.) based on the orthogonal subspace have a higher spectral resolution. A new orthogonal vector spectral estimation method, known as the OVSS method [3] with a higher statistical stability and resolution, is much better than the other common methods in the same conditions. However, because of spurious zeros, pseudo-peaks often appear in the OVSS method and disturbe the estimation. In this paper, the OVSS method is improved. When processing the primary eigenvectors of the self-correlation matrix, it will conduce to extract the signal information by reusing specific vector element. Simulation results show that in any cases, the algorithm has a higher statistical stability and can effectively eliminate the pseudo-peak.

2. THE PRINCIPLE OF OVSS METHOD

Suppose there are K complex sine-waves plus Gaussian white noises. In theory, the $P \times P$-dimensional signal autocorrelation matrix is showed as follows:

$$R = \begin{bmatrix} r(0) & r(-1) & \cdots & r(1-P) \\ r(1) & r(0) & \cdots & r(2-P) \\ \vdots & \vdots & \ddots & \vdots \\ r(P-1) & r(P-2) & \cdots & r(0) \end{bmatrix} = \sum_{i=1}^{K} \rho_i U_P(\omega_i) U_P^H(\omega_i) + \sigma^2 I = R_0 + \sigma^2 I \quad (1)$$

$$U_P(\omega_i) = \begin{bmatrix} 1 & e^{j\omega_i} & \cdots & e^{j(P-1)\omega_i} \end{bmatrix}^T \quad (2)$$

where, ρ_i is the power of the sine-wave signal of No. i ($i = 1, 2 \ldots, K$); σ^2 is the variance of the white noise; $U_P(\omega_i)$ is the complex sine-signal vector of No. i; ω_i is the complex sine frequency of No. i; "T" indicates transpose and "H" indicates complex conjugate transpose.

The eigenvalue/eigenvector decomposition of R is:

$$R = \sum_{i=1}^{K} (\lambda_{0i} + \sigma^2) u_i u_i^H + \sum_{i=K+1}^{P} \sigma^2 u_i u_i^H \tag{3}$$

where λ_{0i} is the K non-zero eigenvalue of R_0; $\lambda_i = \lambda_{0i} + \sigma^2 (i = 1, 2, \ldots, K)$ is the primary eigenvalue of R; $\lambda_{K+1} = \lambda_{K+2} = \cdots = \lambda_P = \sigma^2$ is the primary eigenvalue of noises.

Primary eigenvector corresponding to the primary eigenvalue is:

$$u_i = \sum_{k=1}^{K} b_{iK} U_P(\omega_K), \ (b_{iK} \neq 0) \tag{4}$$

While

$$u_i^H U_P(\omega_k) = 0, \ (i = K+1, K+2, \ldots, P; \ k = 1, 2, \ldots, K) \tag{5}$$

The eigenvector corresponding to the largest eigenvalue can be written to the linear sum:

$$u_1 = [u_{11} \quad u_{12} \quad \cdots \quad u_{1P}]^T = \sum_{k=1}^{K} b_{ik} U_P(f_k) \tag{6}$$

We make it to $L \times M$ orders matrix:

$$V = \begin{bmatrix} \nu(M) & \nu(M-1) & \cdots & \nu(1) \\ \nu(K_s + M) & \nu(K_s + M - 1) & \cdots & \nu(1 + K) \\ \vdots & \vdots & \ddots & \vdots \\ \nu((L-1)K_s + M) & \nu((L-1)K_s + M - 1) & \cdots & \nu((L-1)K_s + 1) \end{bmatrix} \tag{7}$$

where, $\min(L, M) > K, 1 \leq K_s \leq M, M + (L-1)K_s \leq P$.

The literature [1, 2] has proved that V is a singular matrix and its rank is equal to the number of signals, without relation to SNR.

The right singular vector corresponding to the zero singular value of matrix V is orthogonal with M-dimensional signal space. Take advantage of this feature, orthogonal vectors spectral estimation method — OVSS method can be exported:

$$P_{sd}(f) = \frac{1}{\left| w_i^T U_M(f_k) \right|^2} \tag{8}$$

3. THE PROBLEMS AND MODIFIED OVESS METHOD

According to Equation (8), we try to find the zeros of denominator polynomial to form the peaks of signal frequencies. But there are pseudo-peaks in the spectral because of spurious zeros. The accuracy of estimating signal frequency will be interfered. Therefore, an improved algorithm is to be found to eliminate the pseudo-peaks.

By the Equation (7), the eigenvector u_1 corresponding to the largest eigenvalue can be written to a linear sum of the signal-vector. This means u_1 contains a wealth of signal Information. The purpose of OVSS method is to extract the information from u_1. Therefore, when we form the matrix V, the elements of u_1 such as $\nu(K_s+1), \nu(K_s+2), \ldots, \nu((L-2)K_s + M)$ have been reused. In fact the signal processing has been expended. From this point, we try to reuse the other elements $\nu(1), \nu(2), \ldots, \nu(K_s)$ and $\nu((L-2)K_s + M + 1), \nu((L-2)K_s + M + 2), \ldots, \nu((L-1)K_s + M)$. For example, we reuse the element $\nu(1)$ to form a V matrix like:

$$V' = \begin{bmatrix} \nu(M) & \cdots & \nu(1) & \nu(1) \\ \nu(K_s + M) & \nu(K_s + M - 1) & \cdots & \nu(K_s + 1) \\ \vdots & \vdots & \ddots & \vdots \\ \nu((L-1)K_s + M) & \nu((L-1)K_s + M - 1) & \cdots & \nu((L-1)K_s + 1) \end{bmatrix} \tag{9}$$

By the moment, the results of spectral estimation will be optimized.

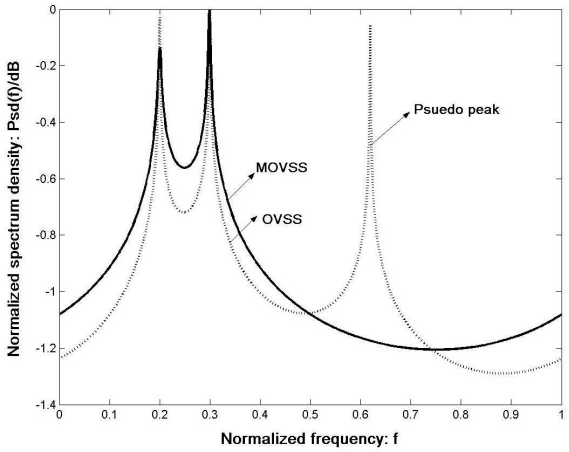

Figure 1: In the short data length, high-SNR case, the comparison of two methods. We take 100 times the average, $N = 25$, SNR $= 20$ dB. As can be seen, the improved method is effective to eliminate the pseudo-peak without significant loss of clarity of spectral lines.

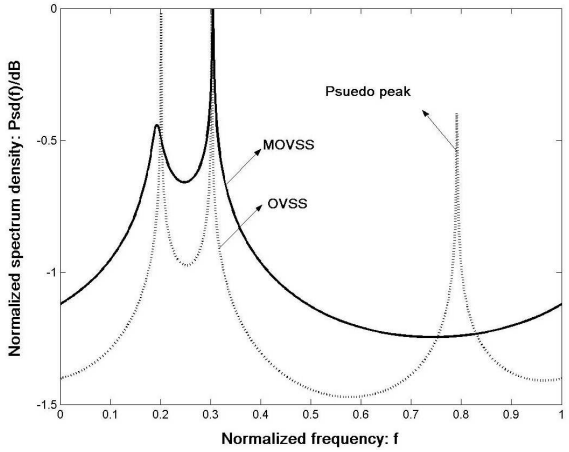

Figure 2: In the short data length, low-SNR case, the comparison of two methods. We take 100 times the average, $N = 25$, SNR $= 10$ dB. With the lower SNR, the MOVSS method can still eliminate pseudo-peak. But the clarity is no longer as good as OVSS.

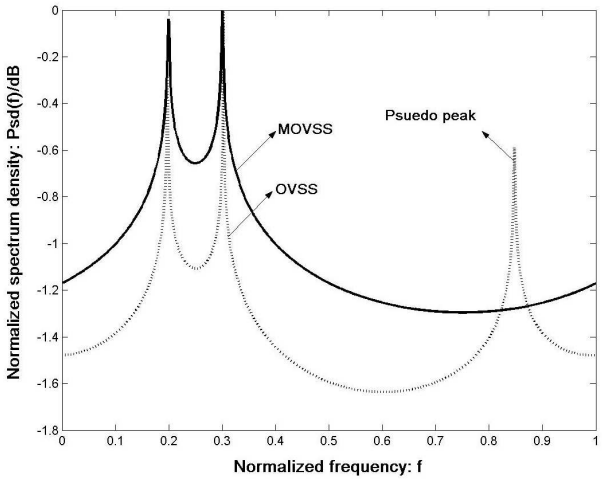

Figure 3: In the long data length, high-SNR case, the comparison of two methods. We also take 100 times the average, $N = 50$, SNR $= 20$ dB. It's obviously that long data is helpful to spectrum estimation. The modified algorithm at this time can still eliminate pseudo-peak.

4. SIMULATION

We assume that the signal model is:

$$x(n) = e^{j2\pi n f_1} + e^{j2\pi n f_2} + W(n) \tag{10}$$

where: $n = 0, 1, \ldots, N-1$, f_1, f_2 are normalized frequency of sine waves. $W(n)$ is complex Gaussian white noise with variance of σ^2 and zero mean. N is the length of sampling data and σ^2 determines the size of the SNR. We take $Ks = 2$, $L = M = 4$, $f_1 = 0.2$, $f_2 = 0.3$, and we call the modified OVSS method MOVSS.

5. CONCLUSION

When we estimate sine wave signals' frequencies using the OVSS method, it's inevitably that the pseudo-peak will appear. From a theoretical point of view, the text tries to find an improved algorithm to eliminate pseudo-peak. A large number of simulation experiments show that in all cases, this improved algorithm can eliminate pseudo-peak. It is a more stable and desirable method of spectral estimation.

REFERENCES

1. Cadzow, J. A., "Spectral estimation: An overdetermined rational model equation approach," *Proc. IEEE*, Vol. 70, 907–939, 1982.
2. Hu, B. and R. G. Gosine, "A new eigenstructure method for sinusoidal retrieval in white noise," *IEEE Signal Processing*, Vol. 45, No. 12, 3073–3083, 1997.
3. Huang, D., "A new approach to sinusoidal frequency estimation," *Journal of Electronics and Information Technology (with Chinese)*, Vol. 24, No. 12, 1857–1862, 2002.
4. Zhang, X., W. Lv, Y. Shi, R. Zhao, and D. Xu, "A novel DOA estimation algorithm based on eigen space," *IEEE 2007 International Symposium on Microwave, Antenna, Propagation and EMC Technologies for Wireless Communications, MAPE*, 551–554, 2006.
5. Liu, Q., H. C. Zhou, and Y. N. Wang, "A new DOA estimate algorithm for coherent sources," *Micro-computer Information*, Vol. 23, No. 7, 290–292, 2007.
6. Kaneko, K. and A. Sano, "Music-like iterative DOA estimation in multipath environments," *IEEE Sensor Array and Multichannel Signal Processing Workshop*, 212–215, 2008.
7. Sansal, M. and M. K. Uner, "Spectrum based covariance estimation for nongaussian multipulse detectors," *IEEE 17th Signal Processing and Communications Applications Conference, SIU 2009*, 117–120, April 9–11, 2009.
8. Guo, L., B. A. Gebre, and K. Pochiraju, "Parameter estimation of acoustic signals using linear microphone arrays," *IEEE Sarnoff Symposium, SARNOFF'09*, 1–6, March 30–April 1, 2009.

Rigorous Computation of Large Radiation Problems by Means of an Iterative Approach

Carlos Delgado, **Felipe Cátedra**, **Iván González**, **Josefa Gómez**, **and Abdelhamid Tayebi**
Computer Science Department, Universidad de Alcalá, Spain

Abstract— In this work, we present a numerical technique for the analysis of the radiation pattern of antennas which interact with complex structures. For this purpose we isolate different parts of the geometry and obtain the primary currents taking into account the external excitations. Next, we compute the interactions between different parts of the geometry and update the total currents. This method is especially well suited for problems that lie beyond the scope of both rigorous and high-frequency conventional techniques, due to computational and/or accuracy requirements.

1. INTRODUCTION

It is well known that, despite the fact that the Moment Method (MM) is usually taken as a reference for the analysis of scattering or radiation problems, its practical implementation suffers from a heavy burden posed by the size and the density of the impedance matrix. Different approaches have been developed in the past years in order to reduce the computational requirements of the conventional MM, among which we can mention the Fast Multipole Method [1] or its multilevel implementation [2], which allows a fast matrix vector product calculation in the iterative solution process, as well as a noticeable reduction in the memory requirements due to the fact that only the near field coupling terms are to be stored. Other methods take advantage of the use of macro-basis functions in order to reduce the total number of unknowns of the linear system that defines the original problem [3, 4]. However, it is important to remark that some realistic problems can still suffer from convergence issues or slow iteration time because of the size of the problem under analysis or the geometrical features of the problem. Moreover, in many realistic problems most of the parts of the geometry are weakly coupled, which allows to make use of high-frequency approaches instead of using rigorous solvers [5]. The aim of the approach we present in this work is to obtain similar results to those given by the MM, highly reducing the computational effort by taking advantage of the MM-MLFMA method combined with an iterative technique used to compute interactions between different parts of the geometry in a totally adaptive fashion.

2. DESCRIPTION OF THE APPROACH

The volume that contains the mesh to be analyzed is divided in a preprocessing step into a set of cubic volumes called *windows*. It can be done following an automatic process, or a user-defined window partitioning scheme. Next, we perform a full-wave analysis of each window, considering the external fields as the excitation. All the unknowns contained inside a given window are considered fully coupled, and the induced currents due to the external sources are computed for each window, considering that it is isolated from the rest of the geometry. By following this procedure we solve several smaller problems instead of a very large one. However, in order to avoid artificial edge behavior of the calculated induced currents at the limits of the windows, it is convenient to define an extended version of each window, calculate the induced currents for the extended version and only retain those unknowns that are confined inside the original window (Fig. 1). The currents calculated in this step will be called *primary currents*. After this step, the iterative process of the approach is performed to take into account the interactions between different windows. It is important to mention that we store the rigorous part of the coupling matrix corresponding to each window so that when we need to compute the far-field interactions between them it can be done very fast.

After computing the primary currents, these are updated by considering different interactions between different parts of the geometry. However a "brute force" approach where every single window interacts with the rest is not desirable. Given a primary current on a window, we can estimate where the radiated field will be stronger by aggregating the primary current to one or several points and determining the radiation pattern from the resulting multipole expansion. It is straightforward to detect the main peaks in this radiation pattern and determine that the windows which will interact with the given one are those will intersect the rays shot in those directions

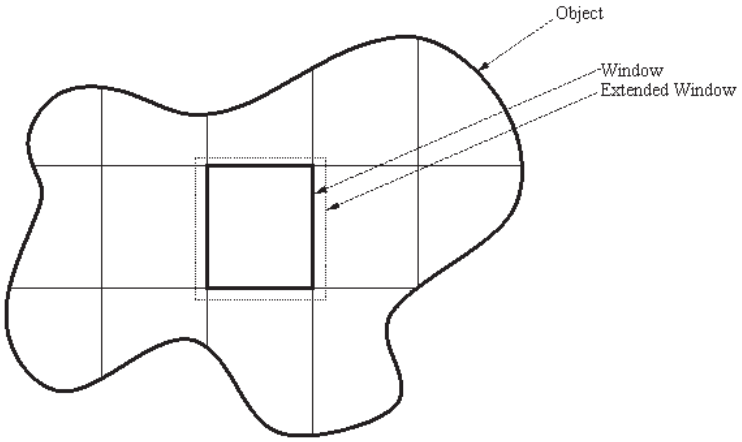

Figure 1: Scheme of the window partitioning and the window extensions.

indicated by the radiation pattern of the active primary currents. This procedure can obviously be performed repeatedly to compute an arbitrary number of interactions between different windows. The stop condition of this procedure can be given by a maximum number of interactions, as well as the computed error for each step, which can be very easily calculated, since we know the tangential fields on the geometry due to external sources and also the updated values of the induced currents for each iteration.

3. NUMERICAL RESULTS

The method outlined above can be applied to the analysis of scattering or radiation problems involving realistic structures like large antennas, arrays, RCS, on-board antennas etc. Also, multi-scale problems can take advantage of this methodology, since only the resulting fields radiated by an active window are required to feed the passive window. We have observed good convergence properties in a wide variety of problems analyzed, and the approach can be parallelized very easily because little communication between processing nodes is required. Different nodes can be solving independent problems and exchange the resulting far fields if an interaction between two different windows is required to be computed. Figs. 2 and 3 show an example where we have considered an offset reflector fed by a conical horn antenna. The partitioning of the geometry in terms of windows can be seen on the right side of Fig. 2. A very good agreement between the conventional MoM-MLFMA and the presented approach is observed in the results. The total CPU time spent by the MoM-MLFMA approach was 12743 s using a 64-bit AMD Opteron Processor with a clock frequency of 2.4 GHz and 16 Mbytes of RAM, while the proposed approach required 4512 s in the same machine. We have also considered a large Cassegrain reflector fed by a horn antenna (Fig. 4). Fig. 5 show the computed gain with and without blockage (blue and red lines, respectively).

Figure 2: Offset reflector fed by a conical horn: Geometry of the problem (left) and scheme of the 7 windows shown in different colours (right).

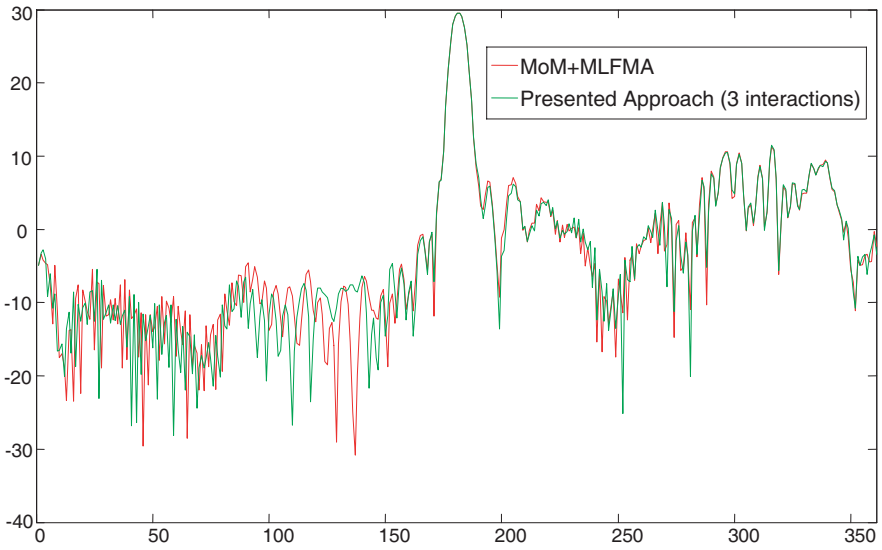

Figure 3: Comparison of MoM-MLFMA results with those obtained with the presented approach for the offset reflector shown above, using 3 interactions between windows ($\Phi = 90°$ cut).

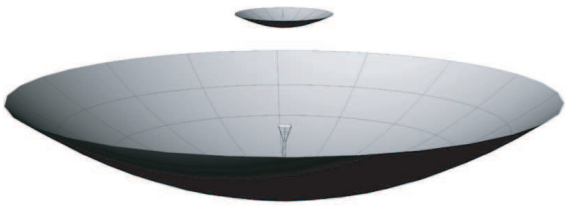

Figure 4: Geometry of a Cassegrain reflector fed by a pyramidal horn.

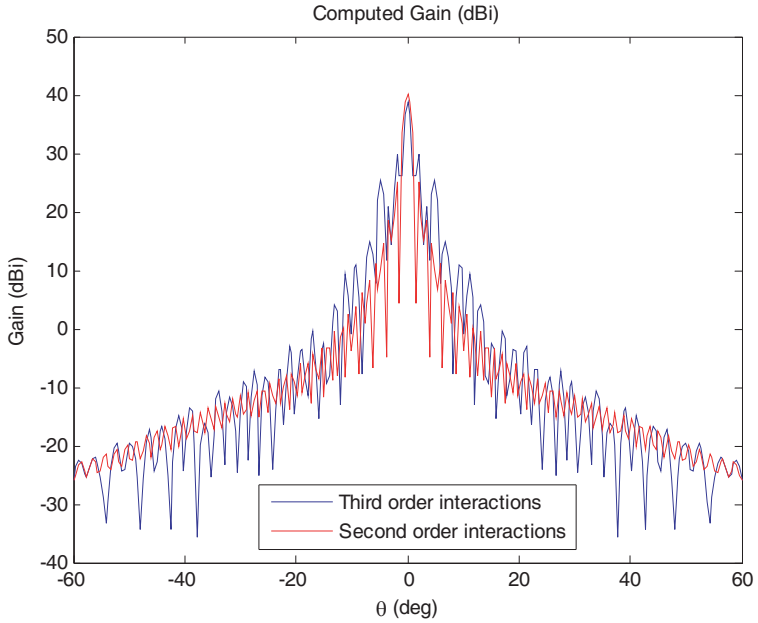

Figure 5: Computed gain for a $\Phi = 0°$ cut considering second and third order interactions for the Cassegrain reflector previously shown (red and blue line, respectively).

4. CONCLUSION

The approach presented in this communication entails a simple way to deal with a good number of realistic problems which due to convergence or size limitations cannot be handled by conventional rigorous solvers, but are not included in the field of application of high-frequency techniques either. These geometries can include structures containing fine details, multiscale problems, interactions with cavities etc. The results obtained with the presented approach are very accurate, and we can even "customize" the degree of accuracy by setting the size of the windows and the number of interactions between them. The scheme proposed in this work is well suited to be parallelized due to the fact that the computational effort is divided into many processes, and little communication between nodes is needed.

ACKNOWLEDGMENT

This work has been supported in part by the Comunidad de Madrid project S-0505/TIC/0255, the Comunidad de Madrid project CCG07-UAH/TIC-2058 and by the Spanish Department of Science, Technology Projects TEC 2007-66164 and CONSOLIDER-INGENIO No. CSD-2008-0068.

REFERENCES

1. Engheta, N., W. D. Murphy, V. Rokhlin, and M. S. Vassiliou, "The fast multipole method (FMM) for electromagnetic scattering problems," *IEEE Trans. Antennas and Propagat.*, Vol. 40, No. 6, 634–641, Jun. 1992.
2. Chew, W. C., J. Jin, E. Michielssen, and J. Song, *Fast and Efficient Algorithms in Computational Electromagnetics*, Artech House Inc., 2001.
3. Prakash, V. V. S. and R. Mittra, "Characteristic basis function method: A new technique for efficient solution of method of moments matrix equation," *Microwave and Optical Technology Letters*, Vol. 36, No. 2, 95–100, Jan. 2003.
4. Delgado, C., F. Cátedra, and R. Mittra, "Application of the characteristic basis function method utilizing a class of basis and testing functions defined on NURBS patches," *IEEE Trans. Antennas and Propagat.*, Vol. 56, No. 3, Mar. 2008.
5. Knott, E. F., "A progression of high-frequency RCS prediction techniques," *Proceedings of the IEEE*, Vol. 73, No. 2, 252–264, Feb. 1985.

Advantages of DOF's Continuous Matching in EIT Inverse Problem

J. Dědková, R. Kubásek, and K. Ostanina
FEEC BUT, UTEE, Kolejní 2906/4, Brno 612 00, Czech Republic

Abstract— This paper proposes new possibilities to solve the electrical impedance tomography inverse problem. Usually, a set of voltage measurements is acquired from the boundaries of an investigated volume, whilst this is subjected to a sequence of low-frequency current patterns. To find unknown material property distribution inside investigated object we can use the deterministic approach only, but there is often problem in such cases to find the stable and accurate solutions. To improve the stability and the accuracy of electrical impedance tomography image reconstructions new algorithm was created. In recent years is very often used the Level Set method to identify regions with different image or material properties and to separate the regions with known and unknown conductivity value. New algorithm is based on both of standard Tikhonov Regularization method and Level Set method. Further are presented also obtained reconstruction results.

1. INTRODUCTION

The image reconstruction problem based on electrical impedance tomography (EIT) is still a widely investigated problem with many applications in physical and biological sciences. Although the back image reconstruction based on EIT is highly ill-posed inverse problem the medical imaging is non-invasive technique and can be used primarily for the detection of pulmonary emboli, non-invasive monitoring of a heart function and a blood flow, or for the breast cancer detection.

The basic theory behind EIT is that by applying current across a material the voltage distribution resulting on the surface will reflect the internal conductivity (or resistivity) distribution. However, intuitively one will understand that multiple conductivity distributions can produce the same voltage distribution at the surface. Therefore the system is stimulated in multiple manners to constrain the possible conductivity distributions.

The EIT system comprises three main areas of development; electrode configuration and connection, data acquisition, and data processing. In this paper we would like to find some new way to improve the quality of the last area. There are two different types of EIT image reconstructions, static and dynamic EIT. In static EIT, only the absolute conductivity in each element is computed and a picture of the internal organs of different conductivity is imaged. In dynamic EIT, temporal variations in conductivity are computed. Both types can be very useful especially in medical applications.

So, the main goal of the high-quality image reconstructions is to find the very accurate distribution of an unknown conductivity (generally impedivity) inside the region of an investigated object from the currents and voltages measured on the electrodes attached to the surface of this object [1, 2]. There is necessary to use an appropriate regularization and some prior information constraint. Various numerical techniques with different advantages have been developed to solve this problem; the main aim is to find such techniques which offer stable, accurate and no too much time-consuming reconstruction process.

2. BASIC THEORY

Usually, a set of voltage measurements is acquired from the boundaries of an investigated volume, whilst this is subjected to a sequence of low-frequency current patterns, for image reconstruction based on EIT. To find the unknown conductivity distribution inside investigated object we can use the deterministic approach based on the Least Squares method. Due to the ill-posed nature of this nonlinear problem, regularization has to be used. For example the standard Tikhonov Regularization method (TRM) with a Newton-Raphson method can be applied to solve the inverse EIT problem. We have to minimize the objective function $\Psi(\sigma)$

$$\Psi(\sigma) = \frac{1}{2}\sum \|U_{\mathrm{M}} - U_{\mathrm{FEM}}(\sigma)\|^2 + \alpha \|L\sigma\|^2 \tag{1}$$

Here σ is the unknown conductivity distribution vector in the object, U_M is the vector of measured voltages on the object boundary, $U_{FEM}(\sigma)$ is the vector of computed peripheral voltages

with respect to σ which can be obtained using the Finite Element method (FEM), α is a regularization parameter and L is a regularization matrix connecting adjacent elements of the different conductivity values. For the solution of (1) was applied a Newton-Raphson method and after the linearization was used the iteration procedure

$$\sigma_{i+1} = \sigma_i + (J_i^T J_i + \alpha L^T L)^{-1} J_i^T (U_{\mathrm{M}} - U_{\mathrm{FEM}}(\sigma_i)) - \alpha L^T L\, \sigma_i) \tag{2}$$

where i is the i-th iteration and J is the Jacobian for forward operator $U_{FEM}(\sigma)$ and it can be calculated very effectively.

This procedure is commonly used in the EIT inverse problem for its fast convergence and good reconstruction quality. However, it is likely to be trapped in local minima and so additional regularization must be taken into account to obtain the demanded solution. The stability of the TRM algorithm is a bit sensitive to the setting of the starting value of searching conductivities; to number of unknown values so called Degrees of Freedom (DOFs) and to an optimal choice of the regularization parameter provides balance between the accuracy and the stability of the solution.

Based on above experience we implemented the Level Set method to reconstruction process to reliably identify regions with different conductivities. The distribution of unknown conductivity σ can be described in terms of level set function F depending on the position of the point r with respect to the boundary Γ between regions with different values of σ

$$\sigma\,(r) = \begin{cases} \sigma_{int}\,\{r : F(r) < 0\} \\ \sigma_{ext}\,\{r : F(r) > 0\} \end{cases} \qquad \Gamma = \{r : F(r) = 0\}\,. \tag{3}$$

To improve the stability and the accuracy of EIT image reconstructions new algorithm was created. This algorithm uses both of mentioned methods TRM and LSM. During iteration process based on minimizing objective function $\Psi(\sigma)$ the boundary Γ is searched in accordance with request that the $\sigma(r)$ minimizes the $\Psi(\sigma)$, too.

It emerged also that it is very useful to match the number of unknown values during the reconstruction process to actual conditions for obtained results; it makes this procedure more stable with very good convergence. New algorithm was applied to the several image reconstructions, with different type of constrains. There are presented some obtained results of new reconstruction process, which can illustrate its advantage.

3. ILUSTRATTIVE EXAMPLES

In this part we restrict a range of tasks to the objects with a biological tissue only. The basic model of the simple 2D arrangement of original conductivity distribution you can see in Fig. 1 (on the left). The conductivity of homogenous region is 0.333 S/m (represents tissue), the conductivity of one region is 0.1 S/m (dark blue color, represents lungs) and finally the conductivity of the second is 0.667 S/m (brown color, represents heart).

During the reconstruction process the TRM was used to identify the locations and to specify exactly the conductivity values of non-homogenous regions. In the case of an unexpected finishing of iteration process because of non-stability was applied the LSM to specify the locations of non-homogenous regions. Finally, the TRM was applied again to specify the conductivity values, but only inside limited regions with non-homogeneity.

Now, let as suppose unknown locations of non-homogeneities, first with unknown values of conductivity. The results after both above mentioned steps are the same, it means after using TRM and after using LSM, you can see them at Fig. 1 (in the middle), final conductivity distribution is in Fig. 1 (on the right).

When we suppose the knowledge of conductivities of all components inside the investigated object (tissue, heart and lungs), the image reconstruction passes to simpler case and it is possible to obtain better results, which are shown in Fig. 2. The conductivity distribution after the first step (using TRM) is shown in this Figure on the left, the conductivity distribution after the second step (using LSM) is shown in the middle of Fig.2, final results of image reconstruction are shown on the right. There is evident, that the algorithm works very well in this case, because we obtained the identical distribution as the original.

The following aim is to find all local non-homogeneities inside the lungs region or inside the heart region. We suppose the lungs, tissue and heart conductivities knowledge, the location and conductivity value of possible non-homogeneity are unknown. First we consider the case of non-homogeneities detection inside lung region. New algorithm has to find the sub regions with con-

ductivity different of the lungs conductivity. The original conductivity is shown in Fig. 3 (on the left), here three sub regions have 80% conductivity of lungs.

The conductivity distribution after using TRM is shown in Fig. 3 (in the middle), the conductivity distribution after using LSM is shown in Fig. 3, and final conductivity distribution is the same as the original distribution.

The last example represents the non-homogeneities detection inside the heart region. Let as consider again the detection of non-homogenous sub regions with conductivity 120% of heart conductivity. The original conductivity distribution is shown in Fig. 4 (on the left).

The advantage of an improved algorithm is evident from the comparison the unknown numbers (the number of DOF's) and values of the objective function $\Psi(\sigma)$ for the previous way and for the new way. These values are shown for the last above described example in the Table 1.

Table 1.

step of iteration		number of DOF's		objective function $\Psi(\sigma)$	
previous	new	previous	new	previous	new
0	0	300	300	1.0e+05	1.0e+05
5	56	300	135	9.8e−02	1.2e−03
6	58	70	31	8.8e−01	3.3e−04
8	60	70	31	1.1e+00	9.3e−10
10	64	70	30	1.7e+01	1.7e−20
15	68	70	15	1.1e+03	2.7e−21

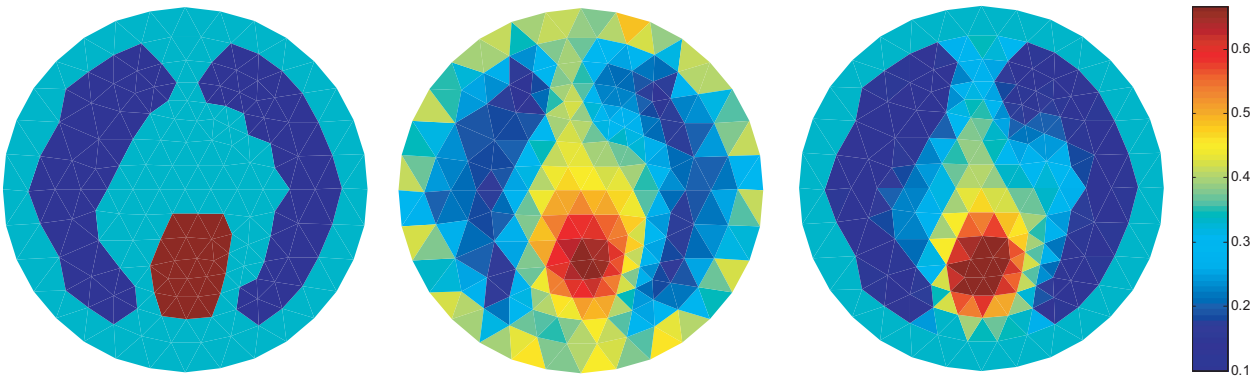

Figure 1: Basic model and $\sigma(r)$ original (left), $\sigma(r)$ after using TRM, LSM (in the middle), $\sigma(r)$ final (right).

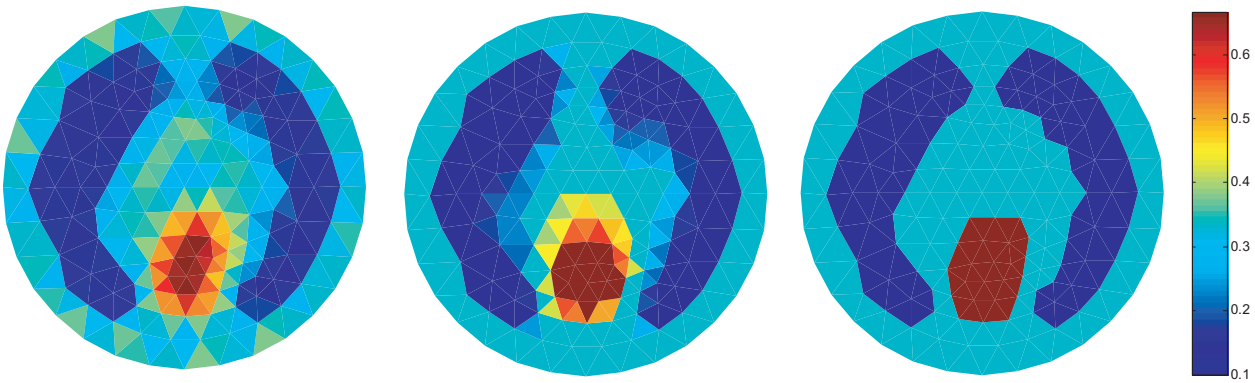

Figure 2: On the left $\sigma(r)$ after using TRM, in the middle $\sigma(r)$ after using LSM, on the right final $\sigma(r)$.

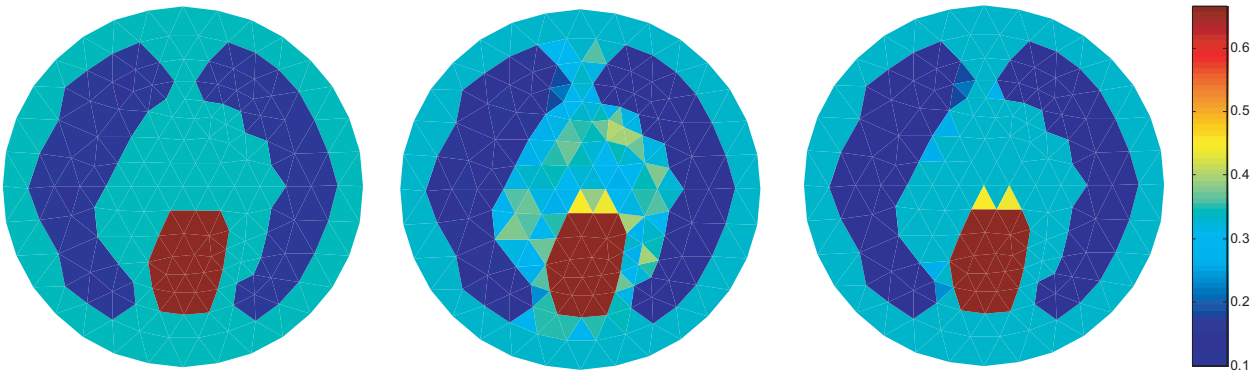

Figure 3: Both $\sigma(r)$ original and final (left), $\sigma(r)$ after using TRM (in the middle), $\sigma(r)$ after using LSM (right).

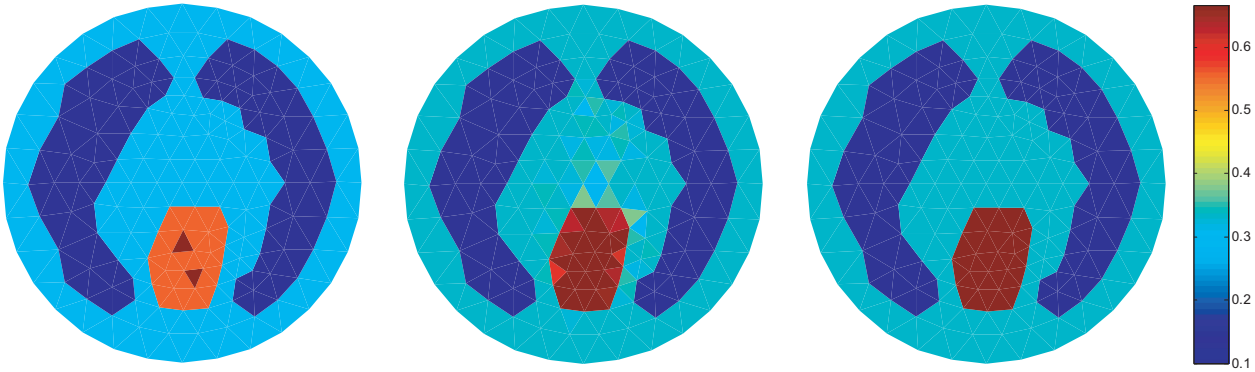

Figure 4: Both $\sigma(r)$ original and final (left), $\sigma(r)$ after using TRM (in the middle), $\sigma(r)$ after using LSM (right).

4. CONCLUSIONS

There is present an improved approach to the EIT image reconstruction, which combines advantages of the level set algorithm, Tikhonov regularization method and the matching the unknown values during reconstructions. This new way of an optimization process was used for the acquirement of more accurate reconstruction results in the specific cases. The new approach was tested on different shapes and sizes of non-homogenous regions. Based on appreciable number of realized numerical tests we can summarize, that the proposed algorithm ensures good stability and very often the highest accuracy of a reconstruction process in comparison with the previous algorithm which was based on the TRM only.

ACKNOWLEDGMENT

The research described in the paper was financially supported by the research program MSM 0021630503.

REFERENCES

1. Cheney, M., D. Isaacson, and J. C. Newell, "Electrical impedance tomography," *SIAM Rev.*, Vol. 41, No. 1, 85–101, 1999.
2. Holder, D. S., *Electrical Impedance Tomography*, IOP Publishing, Philadelphia, 2005.
3. Burger, M., "A level set method for inverse problems," *Inverse Problems*, Vol. 17, 1327–1356, 2001.
4. Sethiah, J. A., *Level Set Methods and Fast Marching Methods*, Cambridge University Press, Cambridge, 1999.
5. Chan, T. and L. Vese, "Active contour without edges," *IEEE Trans. Imag. Proc.*, Vol. 10, 266–277, 2001.
6. Osher, S. and R. Fedkiw, *Level Set Methods and Dynamic Implicit Surfaces*, Springer-Verlag, New York, 2002.

Highly Miniaturized On-chip Impedance Transformer Employing Coplanar Waveguide with Periodic Ground Structure on GaAs MMIC

Young-Bae Park, **Bo-Ra Jung**, **Suk-Youb Kang**, **Jang-Hyeon Jeong**, **Jeong-Gab Ju**, **and Young Yun**
Department of Radio Communication Engineering, Korea Maritime University, Republic of Korea

Abstract— In this study, we propose a highly miniaturized and broadband on-chip impedance transformer on monolithic microwave integrated circuit (MMIC), which was fabricated by a coplanar waveguide employing Periodic Ground Structure (PGS). The novel highly miniaturized impedance transformer was developed for application to low impedance matching in broadband. The size of the impedance transformer employing the coplanar waveguide with PGS is 0.64% of the one fabricated by conventional coplanar waveguide. The transformer showed a good RF performance The above results indicate that the impedance transformer fabricated by a coplanar waveguide structure with PGS is promising candidate for applications to highly miniaturized passive components on MMIC on GaAs substrate, and it will enable to the development of fully integrated MMICs due to the miniaturized size.

1. INTRODUCTION

Recently, demands for broadband and fully integrated MMICs (monolithic microwave integrated circuits) have increased in the broadband wireless communication systems market [1]. To realize fully integrated MMICs, it is so important to development of highly miniaturized passive components. To solve this problem, we already proposed microstrip line employing PGS (Periodic Ground Structure) [2]. According to our previous reports [2], the microstrip line employing PGS showed much shorter wavelength than conventional microstrip line, which enabled a realization of highly miniaturized on-chip passive components on MMIC. For application to various on-chip components on MMIC, basic characteristics of PGS structure should be explored thoroughly. We have published several papers dealing with loss and bandwidth of PGS structure [2, 6, 7], however, an extensive investigation of basic characteristics of coplanar waveguide employing PGS structure has not been performed yet.

In this work, basic characteristics of the coplanar waveguide employing PGS was investigated for application to a development of miniaturized on-chip passive components. For application to miniaturized on-chip component, impedance transformer was developed using coplanar waveguide employing PGS structure. Using the coplanar waveguide employing PGS, the impedance transformer can be highly miniaturized compared with conventional one. So it will allow the development of highly miniaturized and low-impedance passive components on MMICs.

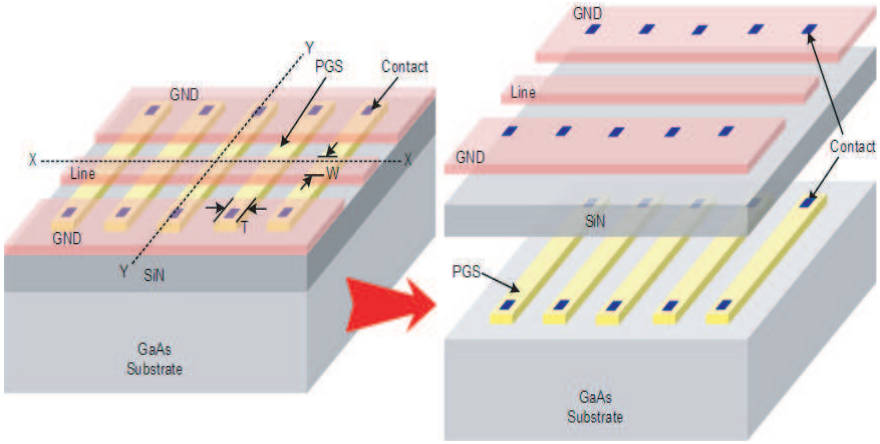

Figure 1: A structure of the coplanar waveguide employing PGS.

2. NOVEL COPLANAR WAVEGUIDE STRUCTURE EMPLOYING PGS WITH LOW CHARACTE-RISTIC IMPEDANCE AND SHORT GUIDED-WAVELENGTH

Figure 1 shows a structure of the coplanar waveguide employing PGS. As shown in Fig. 1, PGS was inserted at the interface between SiN film and GaAs substrate, and it was electrically connected to top-side ground planes (GND planes) through the contacts. Therefore, PGS was grounded through GND planes. As is well known, conventional coplanar waveguide without PGS has only a periodical capacitance C_a (C_a is shown in Fig. 1) per a unit length, while the coplanar waveguide employing PGS has additional capacitance C_b as well as C_b due to PGS. As shown in Fig. 1, C_b is a additional capacitance between line and PGS. In other words, a total capacitance (per unit length) of the coplanar waveguide employing PGS corresponds to $C_a + C_b$, but, it corresponds to C_a for a conventional coplanar waveguide without PGS. Therefore, the coplanar waveguide employing PGS exhibits wavelength (λ_g) much shorter than conventional one, because λ_g is inversely proportional to the periodical capacitance, in other words, $\lambda_g = 1/[f \cdot (LC)^{0.5}]$.

Measured characteristic impedance of the coplanar waveguide employing PGS is shown in Fig. 2, where line length W was fixed to a value of 20 µm. As T becomes larger, characteristic impedance becomes lower, because characteristic impedance is inversely proportional to a periodical capacitance of transmission line, in other words, $Z_0 = (L/C)^{0.5}$, and an increase of T results in an enhancement of periodical capacitance C_b due to an increase of capacitive area. For this reason, as shown Fig. 2, characteristic impedance of the coplanar waveguide employing PGS can be easily controlled by only changing the T. Especially, using PGS, characteristic impedance can be reduced to a value much lower than conventional coplanar waveguide. For example, as shown in Fig. 2, characteristic impedance shows a value of 32–67 Ω by changing T from 0 to 50 µm. This characteristic is very favorable to a reduction of size of passive components on RFIC, because a very low impedance line is required for impedance matching between active devices. In other words, the input/output impedance of FETs are much lower than 50 Ω (10–40 Ω) in RF band [5], and a very low impedance line should be used for impedance matching between FETs. For example, the line width W of conventional coplanar waveguide (having a space of 30 µm between line and ground plane) with a characteristic impedance of 35 Ω is 130 µm, while line width W of coplanar waveguide employing PGS (having a T of 20 µm) with the same characteristic impedance is only 20 µm. Therefore, if coplanar waveguide employing PGS is used for impedance matching between active devices with low impedance, line width W can be highly reduced (by only adjusting T) compared with conventional coplanar waveguide.

3. APPLICATION TTO HIGHLY MINIATURIZED ON-CHIP IMPEDANCE TRANSFORMER

Figure 1 shows the structure of the coplanar waveguide employing PGS. Using the coplanar waveguide employing PGS, we fabricated a highly miniaturized impedance transformer on GaAs MMIC.

Figure 3 shows a photograph of the impedance transformer fabricated on GaAs substrate. GSG pads were connected for on-wafer measurement, and the impedance transformer corresponds to the part surrounded by dotted line. The line width and length of the $\lambda/4$ transformer with a center

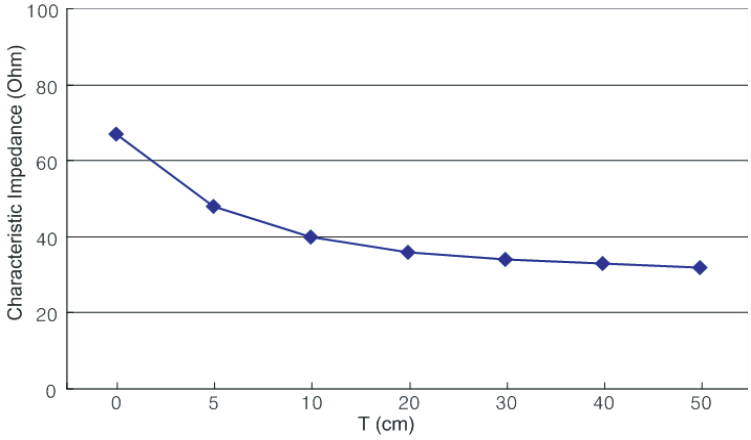

Figure 2: Measured characteristic impedance of the coplanar waveguide employing PGS.

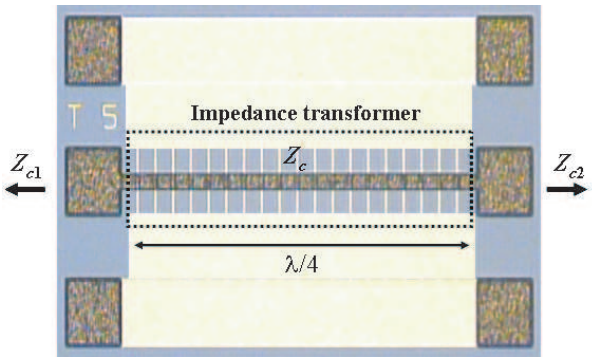

Figure 3: The photograph of impedance transformer employing coplanar waveguide with PGS on GaAs MMIC.

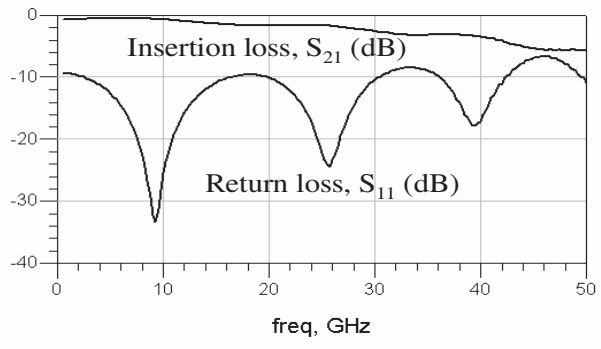

Figure 4: Measured return loss S_{11} and insertion loss S_{21} of impedance transformer employing coplanar waveguide with PGS.

Table 1: Measured RF performance, bandwidth and size of impedance transformer employing coplanar waveguide with PGS.

T [μm]	Transformation impedance (Z_{c1}/Z_{c2})	S_{11}/S_{21} at first center frequency	First and second center freq. and bandwidth	Size comparison at first and second center freq.
5	24 Ω/12 Ω	−31.6 dB/−0.52 dB at 11 GHz	11 ± 8.5 GHz 32 ± 9.1 GHz	1% and 2.91% of conventional transformer
10	20 Ω/10 Ω	−33.5 dB/−0.64 dB at 9 GHz	9.25 ± 7.2 GHz 26 ± 5.3 GHz	0.64% and 1.86% of conventional transformer
20	16 Ω/9 Ω	−44.1 dB/−0.78 dB at 8 GHz	8 ± 7.2 GHz 23 ± 4.3 GHz	0.47% and 1.35% of conventional transformer

frequency of 9.25 GHz are 20 and 500 μm, respectively. The size of the impedance transformer employing the coplanar waveguide with PGS is 0.64% of the one fabricated by conventional microstrip lines. Measured return and insertion loss of the impedance transformer are shown in Fig. 4. As is well known, impedance transformer has first and second center frequency at which its line length corresponds to $\lambda/4$ and $3\lambda/4$, respectively. Therefore, as shown in Fig. 4, we can also observe a good return and insertion loss in the vicinity of 26 GHz as well as 9.25 GHz. Actually, the second center frequency is accurately 27.75 GHz, however, the second frequency shown in Fig. 4 is 26 GHz, because the wavelength of the PGS structure is not linearly proportional to a frequency due to its parasitic elements. If an impedance transformer with a center frequency of 26 GHz is fabricated by conventional microstrip line on GaAs substrate with a thickness of 100 μm, the line width and length are 560 μm and 962 μm, respectively. Therefore, compared with the conventional impedance transformer operating at 26 GHz, the size of the impedance transformer employing PGS is only 1.86% of the conventional one. Measured RF performances, bandwidth and size of the impedance transformer employing the coplanar waveguide with PGS are summarized in Table 1.

4. CONCLUSIONS

In this paper, for application to miniaturized on-chip passive components, we have developed highly miniaturized on-chip impedance transformer fabricated by the coplanar waveguide employing PGS. Using the novel coplanar waveguide structure employing PGS, we can easily transform impedance, due to the much higher impedance changing of PGS. The size of the impedance transformer was 6 and 0.64% of the conventional one. Above all result indicate that the coplanar waveguide employing PGS is a promising candidate for a development of on-chip passive impedance matching components on MMIC.

ACKNOWLEDGMENT

This research was supported by the MKE (The Ministry of Knowledge Economy), Korea, under the ITRC (Information Technology Research Center) support program supervised by the NIPA (National IT Industry Promotion Agency)" (NIPA-2009-C1090-0903-0007). This work was financially supported by the Ministry of Knowledge Economy (MKE) and the Korea Industrial Technology Foundation (KOTEF) through the Human Resource Training Project for Strategic Technology. This work was partly sponsored by KETI (Korea Electronics Technology Institute). This work was also partly supported by ETRI SoC Industry Promotion Center, Human Resource Development Project for IT SoC Architect.

REFERENCES

1. Matsunaga, K., I. Miura, and N. Iwanta, "A CW 4-W Ka-band power amplifier utilizing MMIC multichip technology," *IEEE J. Solid-state Circuits*, Vol. 35, No. 9, 1293–1297, Sep. 2000.
2. Yun, Y., et al., "Basic RF characteristics of the microstrip line employing periodically perforated ground metal and its application to highly miniaturized on-chip passive components on GaAs MMIC," *IEEE Trans. Microwave Theory Tech.*, Vol. 54, No. 10, 3805–3817, Oct. 2006.
3. Ahn, D., J. S. Park, C. S. Kim, J. Kim, Y. Qian, and T. Itoh, "A design of low-pass filter using the novel microstrip defected ground structure," *IEEE Trans. Microwave Theory Tech.*, Vol. 49, 86–93, Jan. 2001.
4. Lai, A. and T. Itoh, "Microwave composite right/left-handed metamaterials and devices," *Proc. Asia-Pacific Microwave Conf.*, 31–34, Suzhou, China, Dec. 2005.
5. Gao, J. and L. Zhu, "Per-unit-length parameters of 1-D CPW metamaterials with simultaneously series-C and shunt-L loading," *Proc. Asia-Pacific Microwave Conf.*, Suzhou, China, 39–42, Dec. 2005.
6. Yun, Y., et al., "Experimental study on isolation characteristics between adjacent microstrip lines employing periodically perforated ground metal for application to highly integrated GaAs MMICs," *IEEE Microwave and Wireless Components Letters*, Vol. 17, No. 10, 703–705, Oct. 2007.
7. Yun, Y., "A novel microstrip line structure employing a periodically perforated ground metal and its application to highly miniaturized and low impedance passive components fabricated on GaAs MMIC," *IEEE Transactions on Microwave Theory and Technique*, Vol. 53, No. 6, 1951–1959, Jun. 2005.

Analysis of Characteristics of Coplanar Waveguide with Finite Ground-planes by the Method of Lines

Min Wang, **Bo Gao**, **Yu Tian**, **and Ling Tong**
College of Automation Engineering, University of Electronic Science and Technology of China
Chengdu 610054, China

Abstract— The method of lines (MoL) has been used to analyze the characteristics of various structures of coplanar waveguide widely. However, a large number of literatures do not study the effects of the ground-plane width on the propagation characteristics, especially characteristic impedance. In this paper, the characteristics (effective dielectric constant and especially characteristic impedance) of shielding coplanar waveguide with finite ground-planes are analyzed by MoL and the computation results are shown.

1. INTRODUCTION

Presently, planar transmission lines have predominantly been used in microwave integrated circuits (MICs) as well as monolithic microwave integrated circuits (MMICs). And coplanar waveguide (CPW) is considered more suitable for MIC and MICC applications than conventional microstrip line because the CPW offer several advantages over conventional microstrip line: First, it simplifies fabrication; second, it facilitates easy shunt as well as series surface mounting of active and passive devices [1]; third, it eliminates the need for wraparound and via holes [1], and fourth, it reduces radiation loss [1]. Since the adoption of CPW in certain MIC and MMIC applications, the need for an in-depth analysis of this structure has increased.

As is well known, the reason for making the lateral ground planes of finite extent is because this more closely models a practical CPW circuit. The finite-difference time-domain (FDTD) method [2] has been used to analyze a given CPW configuration, but it would take lots of time. So the method of line (MoL) [3] is an effective method to analyze the CPW to clarity the impact of the change of ground-plane widths on dispersion and attenuation characteristics.

In this paper, MoL with nonequadistant discretization to analyze the characteristics of CPW with finite ground-planes is presented. The shielding CPW as an example, the propagation constants are calculated with the frequency up to 120 GHz. The influence of finite ground planes is focus to be discussed.

2. ANALYSIS PROCEDURE

Figure 1 illustrates the structure under investigation. Layer II is the lossy substrate,and ground-planes as well as center-strip are assumed to be prefect electric conductors (PECs) on the substrate. Layer I and layer III are the vacuum below and above the substrate. The top, bottom and lateral boundaries are also PECs, so it do not include raditation effects. Thus, the resulting attenuation is only owing to substrate loss. Due to symmetry, only half of the structure needs to be analyzed with a magnetric wall in the center for simplifying calculation.

We use the MoL to analyze this structure, and we start with the independent field components e_z and h_z. From Maxwell's equations, we find that e_z and h_z must fulfill the Helmholtz equation

$$\begin{aligned} \frac{\partial^2\psi}{\partial x^2}+\frac{\partial^2\psi}{\partial y^2}+\frac{\partial^2\psi}{\partial z^2}+k^2\psi = L\psi = 0 \\ k^2=\varepsilon_r k_0^2 \quad k_0=\omega\sqrt{\mu_0\varepsilon_0} \end{aligned} \tag{1}$$

in each separate layer (for ψ we have to substitute either e_z or h_z). Moreover, e_z and h_z must fulfill the following boundary conditions:

$$\begin{aligned} \text{Electric Wall} \quad & e_z = 0(D); \quad \frac{\partial h_z}{\partial n} = 0(N) \\ \text{Magnetic Wall} \quad & h_z = 0(D); \quad \frac{\partial e_z}{\partial n} = 0(N) \end{aligned} \tag{2}$$

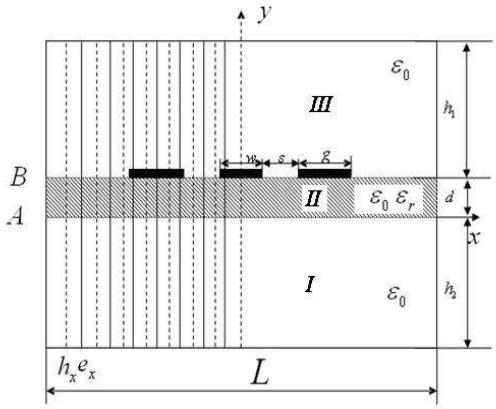

Figure 1: Cross section of shielding coplanar waveguide with finite ground-planes.

The fields, the field equations, and the wave equations (Helmholtz equations for E_z and H_z) of each layer are discretized in one direction (along the x coordinate in Fig. 1). The steps of nonequidistant discretization are studied in detail in [3]. And the discretized differential quotients can be written in the following way:

$$\begin{aligned}
&h\mathbf{r_h^{-1}}\mathrm{diag}\left(\frac{\partial e_z}{\partial x}\Big|_i\right) \rightarrow \mathbf{r_h D E_z} = \mathbf{r_h D r_e E_{nz}} = \bar{\mathbf{D}}\mathbf{E_{nz}} \\
&h\mathbf{r_e^{-1}}\mathrm{diag}\left(\frac{\partial h_z}{\partial x}\Big|_i\right) \rightarrow -\mathbf{r_e D^t H_z} = -\mathbf{r_e D^t r_h H_{nz}} = -\bar{\mathbf{D}}^{\mathbf{t}}\mathbf{H_{nz}} \\
&h^2\mathbf{r_e^{-1}}\mathrm{diag}\left(\frac{\partial^2 e_z}{\partial x^2}\Big|_i\right) \rightarrow -\bar{\mathbf{D}}^{\mathbf{t}}\bar{\mathbf{D}}\mathbf{E_{nz}} = -\bar{\mathbf{P}}_{\mathbf{DN}}\mathbf{E_{nz}} \\
&h^2\mathbf{r_h^{-1}}\mathrm{diag}\left(\frac{\partial^2 h_z}{\partial x^2}\Big|_i\right) \rightarrow -\bar{\mathbf{D}}\bar{\mathbf{D}}^{\mathbf{t}}\mathbf{H_{nz}} = -\bar{\mathbf{P}}_{\mathbf{ND}}\mathbf{H_{nz}}
\end{aligned} \tag{3}$$

with $\mathbf{r_e} = \mathrm{diag}(\sqrt{h/e_i})$ and $\mathbf{r_h} = \mathrm{diag}(\sqrt{h/h_i})$. The difference operators $\bar{\mathbf{P}}_{DN}$ and $\bar{\mathbf{P}}_{ND}$ are real symmetric tridiagonal matrices. Assuming E_z or H_z wave propagation in z direction according to $e^{-jk_z z}$, thus we obtain with Eq. (3) the ordinary differential equation which can be written as

$$\left[\left(\frac{d^2}{dy^2} + k^2 - k_z^2\right)\mathbf{I} - h^{-2}\boldsymbol{\lambda}^{\mathbf{2}}\right]\bar{\boldsymbol{\Psi}}_{\mathbf{n}} = \mathbf{0} \tag{4}$$

with $\boldsymbol{\Psi}_{\mathbf{n}} = \mathbf{T}\bar{\boldsymbol{\Psi}}_{\mathbf{n}}$ and $\mathbf{T'PT} = \boldsymbol{\lambda}^{\mathbf{2}}$, where $\mathbf{T}$ is the transformation matrices for a homogeneous dielectric layer and the eigenvector matrix belonging to $\mathbf{P}$. $\boldsymbol{\lambda}^2$ is the eigenvalue matrix. Let

$$k_{yi}^2 = k_0^2\left(\bar{\lambda}_i^2 - \varepsilon_r + \varepsilon_{re}\right), \quad \left(\varepsilon_{re} = \frac{k_z^2}{k_0^2}, \quad \bar{\lambda}_i^2 = \frac{\lambda_i^2}{(k_0 h)^2}\right) \tag{5}$$

Since in most cases the components and their derivatives are only needed on the layer interfaces, we give the solution for a homogeneous dielectric layer with thickness d (see Fig. 1) also in the following form at the interfaces A and B:

$$\begin{bmatrix} \bar{\boldsymbol{\Psi}}'_A \\ \bar{\boldsymbol{\Psi}}'_B \end{bmatrix} = \mathbf{k}_y^2 \begin{bmatrix} \boldsymbol{\gamma} & \boldsymbol{\alpha} \\ \boldsymbol{\alpha} & \boldsymbol{\gamma} \end{bmatrix} \begin{bmatrix} -\bar{\boldsymbol{\Psi}}_A \\ \bar{\boldsymbol{\Psi}}_B \end{bmatrix} \tag{6}$$

with

$$\begin{aligned}
&\bar{\boldsymbol{\Psi}}' = \frac{1}{k_0}\frac{d}{dy}\bar{\boldsymbol{\Psi}} \qquad \boldsymbol{\alpha} = \mathrm{diag}\left(\frac{k_{yi}}{k_0}\sinh k_{yi}d\right)^{-1} \\
&\mathbf{k_y} = \mathrm{diag}\left(\frac{k_{yi}}{k_0}\right) \qquad \boldsymbol{\gamma} = \mathrm{diag}\left(\frac{k_{yi}}{k_0}\tanh k_{yi}d\right)^{-1}
\end{aligned} \tag{7}$$

After some algebraic manipulations using Eq. (6), the following system equations for the tangential field components is obtained and can be written in a shorter way detailed in [3]:

$$\begin{bmatrix} \bar{\mathbf{H}}_A \\ \bar{\mathbf{H}}_B \end{bmatrix} = \begin{bmatrix} \bar{\mathbf{y}}_1 & \bar{\mathbf{y}}_2 \\ \bar{\mathbf{y}}_2 & \bar{\mathbf{y}}_1 \end{bmatrix} \begin{bmatrix} \bar{\mathbf{E}}_A \\ -\bar{\mathbf{E}}_B \end{bmatrix} \tag{8}$$

where

$$\bar{\mathbf{E}}_{A,B} = \begin{bmatrix} \bar{\mathbf{E}}_{xA,B} \\ -j\bar{\mathbf{E}}_{zA,B} \end{bmatrix} \qquad \bar{\mathrm{H}}_{A,B} = \eta_0 \begin{bmatrix} -j\bar{\mathbf{H}}_{zA,B} \\ \bar{\mathbf{H}}_{xA,B} \end{bmatrix} \tag{9}$$

In layer I and III, the tangential components of the electric field are zero at the interface top and bottom. According to Eq. (8),

$$\bar{\mathbf{H}}_A = -\bar{y}_1^I \bar{\mathbf{E}}_A \qquad \bar{\mathbf{H}}_B = \bar{y}_1^{III} \bar{\mathbf{E}}_B \tag{10}$$

In layer II, according to Eq. (10), we can obtain

$$\bar{\mathbf{H}}_B = \left[\bar{\mathbf{y}}_{\mathbf{2}}^{\mathbf{II}} \left(\bar{\mathbf{y}}_{\mathbf{1}}^{\mathbf{I}} + \bar{\mathbf{y}}_{\mathbf{1}}^{\mathbf{II}}\right)^{-\mathbf{1}} \bar{\mathbf{y}}_{\mathbf{2}}^{\mathbf{II}} - \bar{\mathbf{y}}_{\mathbf{1}}^{\mathbf{II}}\right] \bar{\mathbf{E}}_{\mathbf{B}} \tag{11}$$

In the next step we have to take care of fulfilling the continuity conditions at all the interfaces. At this interface the matching equations hold

$$\bar{\mathbf{E}}_B^{II} = \bar{\mathbf{E}}_B^{III} = \bar{\mathbf{E}}_B \qquad \bar{\mathbf{H}}_B^{II} - \bar{\mathbf{H}}_B^{III} = \bar{\mathbf{J}}_B \tag{12}$$

From Eq. (11) and Eq. (12), we can obtain

$$\begin{bmatrix} \mathbf{T}_h & \mathbf{0} \\ \mathbf{0} & \mathbf{T}_e \end{bmatrix} \begin{bmatrix} \bar{\mathbf{Z}}_{\mathbf{11}} & \bar{\mathbf{Z}}_{\mathbf{12}} \\ \bar{\mathbf{Z}}_{\mathbf{21}} & \bar{\mathbf{Z}}_{\mathbf{22}} \end{bmatrix} \begin{bmatrix} \mathbf{T}_h^t & \mathbf{0} \\ \mathbf{0} & \mathbf{T}_e^t \end{bmatrix} \begin{bmatrix} j\mathbf{J}_{xB} \\ \mathbf{J}_{zB} \end{bmatrix} = \begin{bmatrix} \mathbf{Z}_{\mathbf{11}} & \mathbf{Z}_{\mathbf{12}} \\ \mathbf{Z}_{\mathbf{21}} & \mathbf{Z}_{\mathbf{22}} \end{bmatrix} \begin{bmatrix} j\mathbf{J}_{xB} \\ \mathbf{J}_{zB} \end{bmatrix} = \begin{bmatrix} \mathbf{E}_{xB} \\ -j\mathbf{E}_{zB} \end{bmatrix} \tag{13}$$

For interface B in Fig. 1, the electric field E on the metallization in the slot and the electric current J in the slot are zero. So we rewrite Eq. (13) in a conventient way. In the first step we omit the columns mentioned in each submatrix Z_{ik} $(i,k=1,2)$, yielding the so-called reduced matrix. In the second step we partition each of the rectangular submatrices in an upper (superscript u) and a lower (superscript l) submatrix according to the partition of the vector on right-hand side, and we obtain two system equations

$$\begin{bmatrix} \mathbf{Z}_{\mathbf{11}}^{\mathbf{rl}} & \mathbf{Z}_{\mathbf{12}}^{\mathbf{rl}} \\ \mathbf{Z}_{\mathbf{21}}^{\mathbf{rl}} & \mathbf{Z}_{\mathbf{22}}^{\mathbf{rl}} \end{bmatrix} \begin{bmatrix} j\mathbf{J}_{xm} \\ \mathbf{J}_{zm} \end{bmatrix} = \begin{bmatrix} \mathbf{0} \\ \mathbf{0} \end{bmatrix} \tag{14}$$

and

$$\begin{bmatrix} \mathbf{Z}_{\mathbf{11}}^{\mathbf{ru}} & \mathbf{Z}_{\mathbf{12}}^{\mathbf{ru}} \\ \mathbf{Z}_{\mathbf{21}}^{\mathbf{ru}} & \mathbf{Z}_{\mathbf{22}}^{\mathbf{ru}} \end{bmatrix} \begin{bmatrix} j\mathbf{J}_{xm} \\ \mathbf{J}_{zm} \end{bmatrix} = \begin{bmatrix} \mathbf{E}_{xs} \\ -j\mathbf{E}_{zs} \end{bmatrix} \tag{15}$$

The superscript r means reduced in connection with the first step. The subscript s in E_x and E_z stands for slot and the subscript m in J_x and J_z for metallization.

Because $\mathbf{J}_{xm} \neq \mathbf{0}$ and $\mathbf{J}_{zm} \neq \mathbf{0}$, the nontrivial solution of Eq. (14) requires

$$\begin{vmatrix} \mathbf{Z}_{\mathbf{11}}^{\mathbf{rl}} & \mathbf{Z}_{\mathbf{12}}^{\mathbf{rl}} \\ \mathbf{Z}_{\mathbf{21}}^{\mathbf{rl}} & \mathbf{Z}_{\mathbf{22}}^{\mathbf{rl}} \end{vmatrix} = \mathbf{0} \tag{16}$$

Using the numerical method, such as the Newton iteration method and muller method, the normalized propagation constant ε_{re} and attenuation constant α can be obtained.

In waveguides where hybrid waves can propagate, characteristic impedances Z_0 are defined by means of the power transfer P. For example, in this symmetrical coplanar waveguide it is defined as $Z_0 = U^2/P$ where U is the integral of the electric field from one finite ground-plane edge in the slot to the center strip. P is determined as the integral of the Poynting vector over the waveguide cross section F. And P must be calculated for each layer of the planar structure separately and summed over all layers. For the layer II between y_1 (interface A) and y_2 (interface B) in Fig. 1, we obtain

$$\mathbf{P} = \iint_{(F)} (\mathbf{e}_x \mathbf{h}_y - \mathbf{e}_y \mathbf{h}_x) dx dy \approx h \int_{y_1}^{y_2} \left(\mathbf{E}_x^t \mathbf{H}_y - \mathbf{E}_y^t \mathbf{H}_x\right) dy = h \int_{y_1}^{y_2} \left(\bar{\mathbf{E}}_x^t \bar{\mathbf{H}}_y - \bar{\mathbf{E}}_y^t \bar{\mathbf{H}}_x\right) dy \tag{17}$$

because

$$\mathbf{E}_x^t \mathbf{H}_y = \bar{\mathbf{E}}_x^t \mathbf{T}^t \mathbf{T} \bar{\mathbf{H}}_y = \bar{\mathbf{E}}_x^t \bar{\mathbf{H}}_y \tag{18}$$

When we get the second system Eq. (15), the current vector $[j\mathbf{J}_{xm}^t, \mathbf{J}_{zm}^t]^t$ is determined as an eigenvector afterwards. If ε_{re} and the current vector are evaluated, the field vector $[\mathbf{E}_{xs}^t, -j\mathbf{E}_{zs}^t]^t$ can be calculated with the system Eq. (15) and all the other field components in the various interfaces can be obtained.

Then we can write for the first term in Eq. (17)

$$\int_{y_1}^{y_2} \bar{\mathbf{E}}_x^t \bar{\mathbf{H}}_y dy = \frac{1}{2} \begin{bmatrix} \bar{\mathbf{E}}_{xA} \\ \bar{\mathbf{E}}_{xB} \end{bmatrix}^t \begin{bmatrix} \mathbf{g}_1 & \mathbf{g}_2 \\ \mathbf{g}_2 & \mathbf{g}_1 \end{bmatrix} \begin{bmatrix} \bar{\mathbf{H}}_{yA} \\ \bar{\mathbf{H}}_{yB} \end{bmatrix} \tag{19}$$

where

$$\mathbf{g}_1 = k_0^{-1} \left(\gamma_h - k_0 d \mathbf{k}_{yh}^2 \boldsymbol{\alpha}_h^2 \right) \qquad \mathbf{g}_2 = k_0^{-1} \left(k_0 d \mathbf{k}_h^2 \boldsymbol{\alpha}_h \gamma_h - \boldsymbol{\alpha}_h \right) \tag{20}$$

and $\boldsymbol{\alpha}$, $\boldsymbol{\gamma}$ and $\mathbf{k_y}$ are according to Eq. (7). From these steps, P of the layer II can be obtained, and P of the other layers should be obtained as the same steps. We also get the voltage U from the electric field from either ground-plane to the center conductor and then we obtain Z_0.

3. NUMERICAL RESULTS

In this Section, numerical results will be presented to assess the results of the computations as well as to investigate the effect of finite ground-planes on the propagation characteristics of shielding CPW structure.

To verify the validity of this method, the frequency-dependent ε_{re} and Z_0 computed by MoL are compared with that calculated by HFSS and the results in [4]. Fig. 2 shows that ε_{re} computed by MoL agrees well with that by HFSS and is slightly larger than ε_{re} in [4]. This is because the ground planes in [4] extend to lateral board boundaries. From Fig. 3, it can be observed that the values of $\mathrm{Re}(Z_0)$ and $\mathrm{Im}(Z_0)$ calculated by both MoL and HFSS are close to each other. It is worth mentioning that $\mathrm{Re}(Z_0)$ first increases slowly with frequency, reaches its peak at around 60 GHz, and then decreases rapidly.

Figure 4 shows the values of ε_{re}, α, $\mathrm{Re}(Z_0)$ and $\mathrm{Im}(Z_0)$ calculated separately with different finite ground-planes width g: 0.6 mm, 1 mm and 9 mm. The values of ε_{re} and α increase with the increasing frequency. Three curves of α with different g almost overlap. It's because finite ground planes can hardly influence attenuation when conductors are PECs. When the frequency reaches the high value, the values of ε_{re} approach each other, the values of $\mathrm{Re}(Z_0)$ drop sharply and the values of $\mathrm{Im}(Z_0)$ change obviously. The question arises as to how far g would have an effect on the propagation characteristics. In Fig. 5, the results of ε_{re}, α, $\mathrm{Re}(Z_0)$ and $\mathrm{Im}(Z_0)$ verus g from 0.5 mm to 9.5 mm are given. As can be seen from Fig. 5, the values of ε_{re} and α decrease with increased g. When g reaches about 4 mm or more, the curves keep stable. From Fig. 5, we can see trends of $\mathrm{Re}(Z_0)$ and $\mathrm{Im}(Z_0)$ verus g are different, when calculated frequency is different. For instance, the curves of $\mathrm{Re}(Z_0)$ and $\mathrm{Im}(Z_0)$ are shown in Fig. 5 at a low frequency (3 GHz) and a high one (115 GHz). In general, those characteristic parameters all converge at certain values when the width of ground-planes is up to a high value.

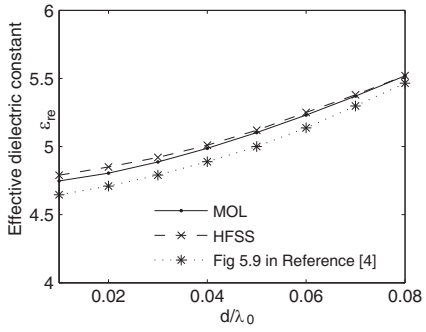

Figure 2: Computed ε_{re} as a function of the reciprocal of the free space wavelength with the conductor thickness as a parameter. $L/d = 40$, $h_1/d = 14.5$, $h_2/d = 14.5$, $w/d = 0.4$, $(w + 2s)/d = 2.4$, $(w + 2s + 2g)/d = 15$, $\varepsilon_r = 9.6$, $f = 3$ GHz.

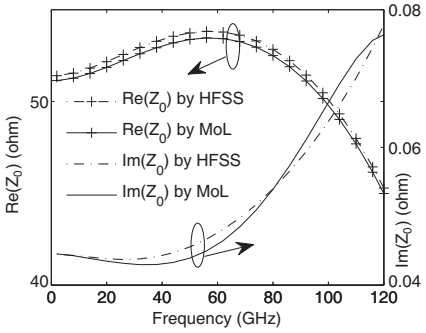

Figure 3: Computed characteristic impedance Z_0 against frequency by MOL compares with HFSS. $L = 20$ mm, $h_1 = 3.746$ mm, $h_2 = 3.746$ mm, $w = 0.35$ mm, $s = 0.14$ mm, $d = 0.254$ mm, $\varepsilon_r = 9.9$, $\tan\delta = 0.002$, $g = 1$ mm.

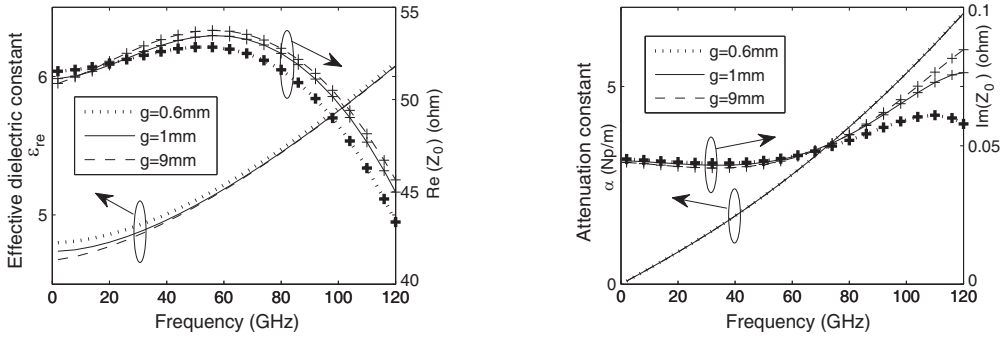

Figure 4: ε_{re}, α, Re(Z_0) and Im(Z_0) against frequency from 1 GHz to 120 GHz, $L = 20$ mm, $h_1 = 3.746$ mm, $h_2 = 3.746$ mm, $w = 0.35$ mm, $s = 0.14$ mm, $d = 0.254$ mm, $\varepsilon_r = 9.9$, $\tan\delta = 0.002$, $g = 0.6$ mm, 1 mm, 9 mm.

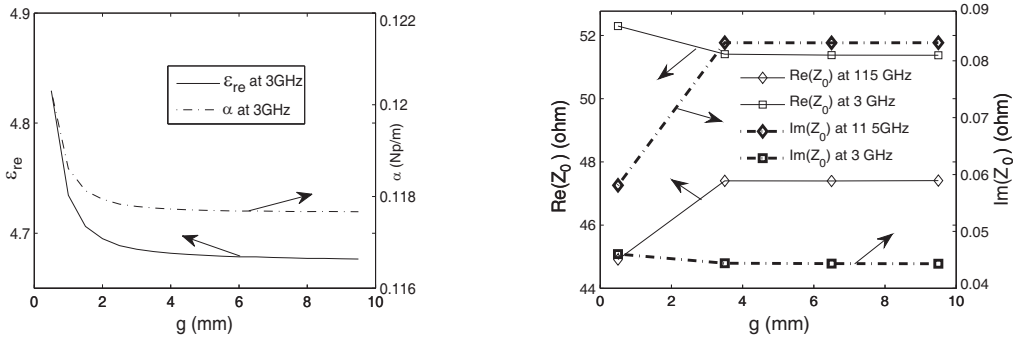

Figure 5: ε_{re} and α against g at the frequency 3 GHz, Re(Z_0) and Im(Z_0) against g at the frequency 3 GHz and 115 GHz, $L = 20$ mm, $h_1 = 3.746$ mm, $h_2 = 3.746$ mm, $w = 0.35$ mm, $s = 0.14$ mm, $d = 0.254$ mm, $\varepsilon_r = 9.9$, $\tan\delta = 0.002$, g varies from 0.5 mm to 9.5 mm, and the step is 0.5 mm.

4. CONCLUSION

In this paper, the method of lines is used for analyzing the propagation characteristics of CPW with finite ground-planes in a large range of frequency. The MoL with nonequidistant discretization provides accurate results with high computational efficiency. The process to calculate some propagation characteristics (especially characteristic impedance) of CPW is introduced and results with frequency from 1 GHz to 120 GHz and finite ground-planes width from 0.5 mm to 9.5 mm are given. The effective dielectric constant, attenuation constant and characteristic impedance with respect to the frequency and finite ground-planes width are discussed and results agree well. The effects of finite ground planes have been investigated and the results may be useful for the design of the circuits.

ACKNOWLEDGMENT

This work was supported by basic research item of National Key Lab of Electronic Measurement Technology of China.

REFERENCES

1. Browne, J., "Broadband amps sport coplanar waveguide," *Microwaves & RF*, Vol. 26, No. 2, 131–134, 1987.
2. Liang, G.-C., Y.-W. Liu, and K. K. Mei, "Full-wave analysis of coplanar waveguide and slotline using the time-domain finite-difference method," *IEEE Trans. on MTT*, Vol. 37, No. 12, 1949–1957, 1989.
3. Pregla, R. and W. Pascher, *Numerical Techniques for Microwave and Millimeter Wave Passive Structures*, John Wiley & Sons, Inc, New York, 1989.
4. Simons, R. N., *Coplanar Waveguide Circuits, Components, and Systems*, John Wiley & Sons, Inc, 2001.

A Study on Equivalent Circuit of Highly Isolated Coupled Microstrip Line Employing PGS on GaAs MMIC

Jang-Hyeon Jung, **Bo-Ra Jung**, **Young-Bae Park**, **Jeong-Gab Ju**, **Suk-Youb Kang**, **and Young Yun**
Department of Radio Sciences and Engineering, Korea Maritime University, Korea

Abstract— In this work, equivalent circuit of highly isolated coupled microstrip line employing periodic ground structure (PGS) were investigated using theoretical analysis. Equivalent circuits for the PGS cell were extracted, and all lumped circuit parameters were expressed by closed-form equation. The high isolation characteristic was originated form a resonance between adjacent microstrip lines employing PGS. According to results, a much better isolation characteristic was observed from the adjacent microstrip lines employing PGS compared with conventional microstrip lines. Microstrip lines employing PGS are very useful for application to compact signal lines of highly integrated MMIC.

1. INTRODUCTION

Recently, with a rapid development of information and communication industry, the focus in the MMIC (Monolithic Microwave Integrated Circuit) are increasing for an improvement of electromagnetic environment. Especially, a reduction of electromagnetic coupling has become an issue in MMIC problem, because it causes a serious trouble in communication system.

In this work, we propose highly isolated coupled microstrip line employing PGS (Periodic Ground Structure), and its equivalent circuit was thoroughly studied for application to circuit design. In addition, the origin of the highly isolation characteristic between microstrip lines employing PGS was theoretically analyzed using an equivalent circuit.

2. STRUCTURE OF MICROSTRIP LINE EMPLOYING PGS

In this work, microstrip line employing PGS was developed for a high isolation characteristic.

Figure 1 shows a coupled microstrip line structure employing PGS. PGS was inserted at the interface between SiN film and GaAs substrate, and the PGS serves as ground plane because it was electrically connected to backside ground metal through the via-holes. We can deduce that the above structure shows high isolation characteristics from equivalent circuit.

3. EQUIVALENT CIRCUIT OF MICROSTRIP LINE EMPLOYING PGS

Figure 2 shows the equivalent circuit of adjacent two lines, which corresponds to the equivalent circuit of the Nth unit section of the periodic structure surrounded by rectangular box in Fig. 1. C_b corresponds to the capacitance between top line and PGS, which is shown in Fig. 1, and it is proportional to the cross area $W \cdot T$ of line of line and PGS (As shown in Fig. 1, W and T are the width of top lines and the periodic strips of PGS, respectively). R_g and L_g are resistance and inductance originating from the loss and current flow of the periodic strip of PGS with width T,

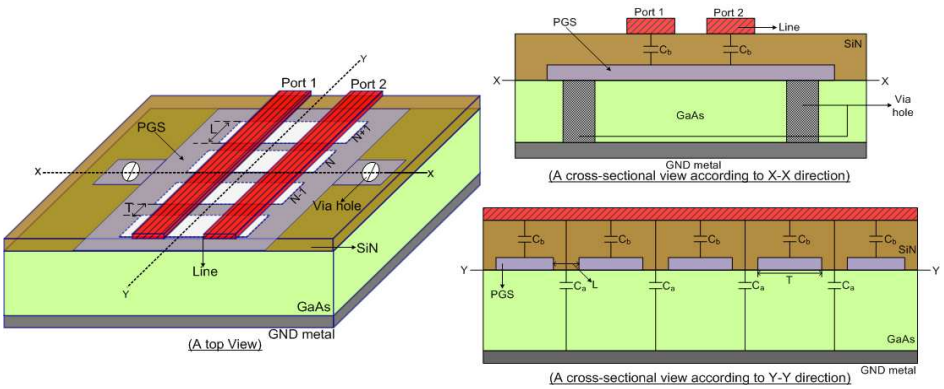

Figure 1: Coupled microstrip line structure employing PGS.

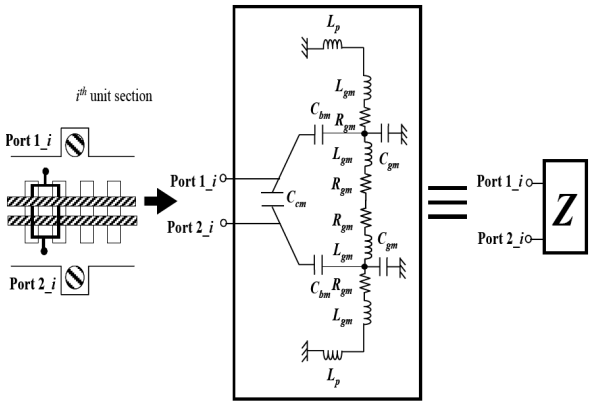

Figure 2: An equivalent circuit for a unit cell of the microstrip line employing PGS.

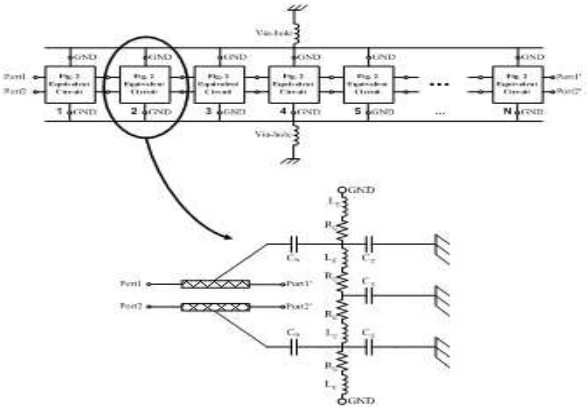

Figure 3: The equivalent circuit for microstrip line employing PGS.

respectively. C_g corresponds to the capacitance between PGS and backside metal of GaAs substrate. L_p is parasitic inductance originating from via-holes. C_c is coupling capacitance between adjacent lines.

Figure 3 shows an equivalent circuit of the coupled microstrip line employing PGS. As shown in this figure, a number of the equivalent circuits of unit section are connected to each other, and via-hole was expressed as lumped inductor. The capacitance and inductance of the equivalent circuit are given by,

$$C_b = \left[0.019 + \left(\frac{T}{d_i}\right) \times 7 \times 10^{-5} - \left(\frac{T}{d_i}\right) \times 2 \times 10^{-7}\right] \text{(pF)} \tag{1}$$

$$C_g = \frac{T}{d_s} \times 10^{-3} \text{(pF)} \tag{2}$$

$$L_g = \frac{l_s}{T} \times 1.875 \times 10^{-3} \text{(nH)} \tag{3}$$

$$R_g = \frac{l_s}{T} \times 3.125 \times 10^{-2} \text{(}\Omega\text{)} \tag{4}$$

where d_i, d_s and l_s are thickness of SiN film, thckness of semiconducting substrate and length of PGS strip, respectively.

4. ISOLATION CHARACTERISTIC OF MICROSTRIP LINE EMPLOYING PGS

Figure 4 shows measured and calculated insertion loss S_{21} for microstrip line employing PGS. For a comparison, measured and calculated isolation characteristics of the microstrip line employing PGS with $T = 5$ and 10 µm are shown in Figs. 4(a) and (b). For the calculation results, equivalent circuit of Fig. 3 and closed-form Equations (1)–(4) were employed. The coupled microstrip line showed much better isolation characteristic than conventional one, because parastic inductance and capacitance comprise RC resonance structure as shown in Fig. 2. Table 1 shows measured isolation characteristic of coupled microstrip line and conventional one.

Table 1: Measured isolation for the coupled microstrip line employing PGS and conventional one at 60 GHz.

Microstrip line employing PGS	−45 dB
Conventional microstrip line	−8 dB

As expected, we can observe the resonance characteristics in the measured results for the PGS structure, which results in much better isolation characteristics than conventional one. Especially, highly improved isolation characteristics are observed in the vicinity of resonance frequency. As shown in this figure, we can observe a fairly good agreement between calculated and measured results.

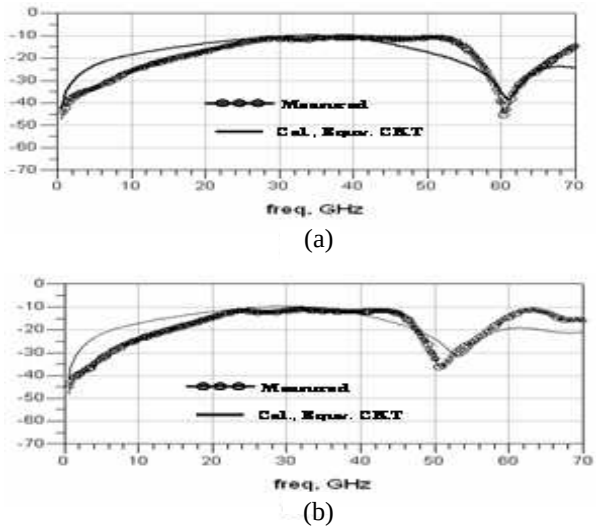

Figure 4: (a) Measured and calculated isolation characteristic of PGS ($T = 5\,\mu m$). (b) Measured and calculated isolation characteristic of PGS ($T = 10\,\mu m$).

5. CONCLUSIONS

In this work, equivalent circuit of highly isolated coupled microstrip line employing PGS were investigated using theoretical analysis. With only a spacing of 10 μm, the coupled microstrip line employing PGS showed an isolation value of −45 dB at 60 GHz. On the other hand, the conventional microstrip line showed an isolation value of −8 dB at 60 GHz. According to the theoretical analysis, it was found that the innate resonance characteristic originating from the parasitic elements of PGS structure enabled a high isolation characteristic. Especially, the isolation characteristic was highly improved in the vicinity of resonance frequency, and the resonance frequency could be easily controlled by only changing T, which made the resonance frequency easily tuned to the signal coupling frequency for a suppression of coupling between lines. Microstrip lines employing PGS are very useful for application to compact signal lines of highly integrated MMIC.

ACKNOWLEDGMENT

This research was supported by the MKE (The Ministry of Knowledge Economy), Korea, under the ITRC (Information Technology Research Center) support program supervised by the NIPA (National IT Industry Promotion Agency) (NIPA-2009-C1090-0903-0007). This work was financially supported by the Ministry of Knowledge Economy (MKE) and the Korea Industrial Technology Foundation (KOTEF) through the Human Resource Training Project for Strategic Technology. This work was partly sponsored by KETI (Korea Electronics Technology Institute). This work was also partly supported by ETRI SoC Industry Promotion Center, Human Resource Development Project for IT SoC Architect.

REFERENCES

1. Uusimaki, M. and A. Renko, "A systematic approach and comparison of different 3-D chip structures for electromagnetic compatibility," *International Symposium on Electromagnetic Compatibility, EMC 2004*, Vol. 2, 734–739, Aug. 9–13, 2004
2. Kim, S. H., Y. B. Park, M. H. Kim, and Y. Yun, "A highly isolated transmission line employing periodic ground structure on MMIC for an EMC solution," *Advance Program of EMC'09*, Kyoto, Jul. 1, 2009.
3. Adan, A. O., M. Fukumi, K. Higashi, T. Suyama, M. Miyamoto, and M. Hayashi, "Electromagnetic coupling effects in RFCMOS circuit," *2002 IEEE MTT-S International Microwave Symposium Digest*, Vol. 1. 39–42, Seattle, WA, USA, Jun. 2–7, 2002.
4. Kurizki, G. and A. Z. Genack, "Suppression of molecular interactions in periodic dielectric structure," *Physics Review Letters*, Vol. 61, No. 19, 2269–2271, Nov. 1988.
5. Lai, A. and T. Itoh, "Microwave composite right/left-handed metamaterials and devices," *Proc. Asia-Pacific Microwave Conf.*, 31–34, Suzhou, China, Dec. 2005.

Design of Suppressing Crosstalk by Vias of Serpentine Guard Trace

W.-T. Huang[1], **C.-H. Lu**[2], **and D.-B. Lin**[2]

[1]Department of Computer Science and Information Engineering
Minghsin University of Science and Technology, Taiwan, R.O.C.
[2]Graduate Institute of Computer and Communication Engineering
National Taipei University of Technology, Taiwan, R.O.C.

Abstract— The design of the serpentine guard trace (SGT) in the literal is to add two terminally matching resistances on the serpentine guard trace. Although this approach can get more layout space and suppress far-end crosstalk, it neglects the interference of near-end crosstalk. Therefore, we propose an approach, namely "vias of serpentine guard trace (VSGT)", which the grounded-vias are added on the guard trace by a proper location and the ratio between the length of the horizontal and vertical on the guard trace can be adjusted in a better state such that the near-end crosstalk (NEXT) and far-end crosstalk (FEXT) coefficient will be minimum and get the better performance. Hence, our proposed approach can simultaneously suppress NEXT and FEXT. Verified in the frequency-domain simulation results, our approach, VSGT, can improve not only NEXT by 3.7 and 0.83 dB but also FEXT by 5.11 and 0.1 dB compared to the three-width rule and SGT, respectively. Moreover, verified in the time-domain, VSGT can reduce not only NEXT by 34.67 and 27.5% but also FEXT by 46.78 and 6.91% than that of the three-width rule and SGT, respectively.

1. INTRODUCTION

As modern technology progress, the design of digital devices and chip packages tends toward high-speed, high-density, and low-voltage operation. This makes the interconnection of multiple traces within a printed circuit board (PCB) and among chips much difficult [1]. Since high-speed operations will cause more noise of the side effect, poor designs of interconnection traces and the coupling effect of multiple traces affect signal integrity (SI) [1, 2]. SI is a critical factor in the design of a high-speed PCB [2]. Crosstalk is one noise source in PCBs and is of particular concern in high-density and high-speed circuits, is one major source of noise to interfere with SI. Moreover, since crosstalk occurs due to the coupling effects of the mutual capacitance and inductance of two adjacent traces when transient signals in one transfer energy to the other, then, this can disrupt normal signal operations [1, 2]. Nowadays, attention has increasingly focused on the SI design and layout within and PCBs [3].

One popular design method for reducing the crosstalk is called the three-width rule (3W) [3]. The other one is to add one extra "serpentine guard trace [SGT]" [4] between two parallel traces that the active trace to which the signal is applied is called the aggressor and the passive trace to which no signal is applied is called the victim. Lee et al. first proposed the SGT approach to reduce the peak FEXT of parallel traces on printed circuit boards (PCB) [4]. The two terminally matching resistances of the SGT structure can get the impendence match of the trace. Moreover, SGT can get the advantage of layout space. In the SGT design, since SGT with the vertical parts can increase the mutual capacitance without changing the mutual inductance between the aggressor and victim, this can lower the amount of inducted energy from the aggressor and then reduce FEXT [4]. Although the SGT approach can get the above 2 advantages, this SGT method neglects the interference of near-end crosstalk. Therefore, extended this study, we propose an approach, namely "vias of serpentine guard trace [VSGT]", whose grounded-vias are added on the guard trace by a proper location and the scale between horizontal and vertical length of the guard trace can be adjusted in a better state such that the near-end crosstalk [NEXT] and far-end crosstalk coefficient will be minimum and get the better performance. Hence, our proposed design can simultaneously suppress NEXT and FEXT.

2. CROSSTALK

Crosstalk occurs due to the coupling effects caused by the mutual capacitance (C_m) and mutual inductance (L_m) of the victim and aggressor, driven by the transient signals in the aggressor. The equivalent model of the two parallel traces is shown in Fig. 1(a), and the typical crosstalk signature of the victim without a guard trace is shown in Fig. 1(b) [2]. The end of the victim closest to

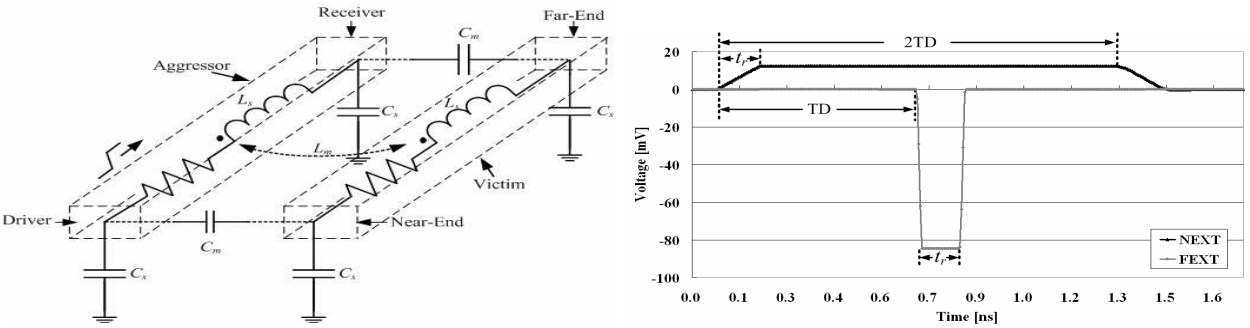

Figure 1: (a) Equivalent model of the two parallel traces [1]. (b) Typical crosstalk signature of the victim without a guard trace [2].

the driver (receiver) of the aggressor is called the near (far) end. When the rise and fall times of the aggressor's transient logic states change continually, the signal operation of the victim will be destroyed, since the coupling effect of C_m and L_m transfer energy from the aggressor [1]. Since modern high-density circuits have high C_m and L_m, crosstalk noise is a major cause of concern in system design.

During the two parallel traces as shown in Fig. 1(a), FEXT and NEXT are the voltage induced at the receiving and driving end of the victim, respectively. The FEXT and NEXT waveform in the lossless case can be represented by (1) and (2), respectively [1]. The coefficients of NEXT and FEXT dominate the crosstalk energy of the victim. Let K_{NE} and K_{FE} be the coefficient of NXET and FEXT as shown in (1) and (2) [5], respectively. Lower coefficient can get lower coupling crosstalk noise of the victim from the aggressor. Let L_S (L_m) and C_S (C_m) be the self- (mutual-) induction and self- (mutual-) capacitance as shown in Fig. 1(a), respectively.

$$K_{NE} = \frac{1}{4} \cdot \left(\frac{C_m}{C_s} + \frac{L_m}{L_s} \right) \tag{1}$$

$$K_{FE} = \frac{1}{2} \left(\frac{C_m}{C_S} - \frac{L_m}{L_S} \right) \tag{2}$$

Hence, how to get lower K_{NE} and K_{FE} is our major subject. K_{NE} is the summation of the capacitive coupling C_m/C_s and inductive coupling L_m/L_s; K_{FE} is that C_m/C_s subtracts from L_m/L_s. However, since L_m/L_s of K_{FE} is more than C_m/C_s in the parallel traces with one side exposed to air, K_{FE} has the negative pulse at the rising edge as shown in Fig. 1(b).

3. THE STRUCTURE OF SERPENTINE GUARD TRACE

One pair of coupled parallel traces without guard trace called 3W as shown in Fig. 2(a) [3], its structure is just placed on FR4 PCB and its layout parameters are as follows. The dielectric thickness, width of each trace, thickness of copper, the spacing between the aggressor and victim, the length of the parallel traces, are 7, 12, 1.4, 36, and 4000 mil, respectively. Fig. 2(b) of the SGT structure [4] and Fig. 2(c) of the VSGT structure show one pair of the parallel traces with a serpentine guard trace added between the aggressor and victim, respectively. For the fair comparison, all of the above layout parameters are the same among these three approaches. Fig. 2(b) shows the structure and layout parameters of the SGT approach, in which the serpentine combination of a horizontal section with a vertical section is always repeated along the parallel traces. The horizontal parts along the parallel traces are located close to the aggressor and the victim. A vertical part connects two horizontal parts close to the aggressor and victim. Since the direction of the current flow in the vertical part is perpendicular to that of the aggressor, there is no magnetic coupling between the aggressor and vertical part of the serpentine guard. Thus, the vertical part of the serpentine guard increases the mutual capacitance without much increasing the mutual inductance between the aggressor and guard trace [4]. Hence, due to the symmetry layout, the mutual capacitance between the aggressor and guard trace is increased. So does the mutual capacitance between the guard trace and victim. Finally, the mutual capacitance is indeed increased between the aggressor and victim.

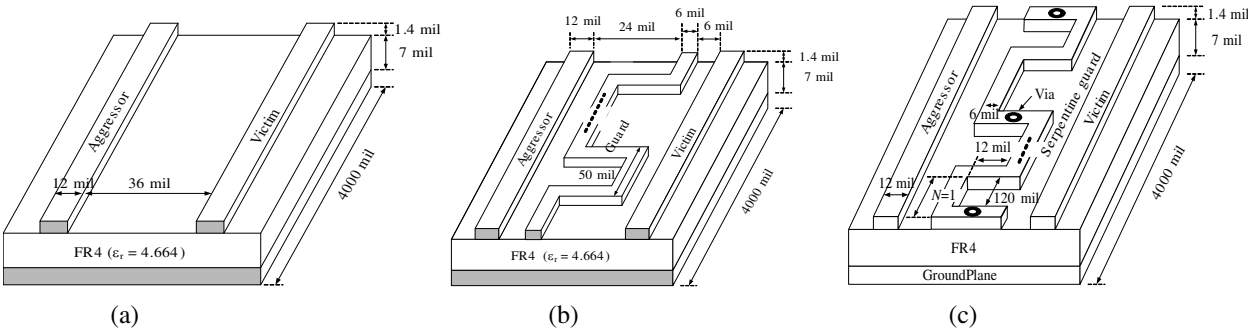

Figure 2: Comparison among three topologies. (a) 3-W rule [3]. (b) SGT [4]. (c) VSGT.

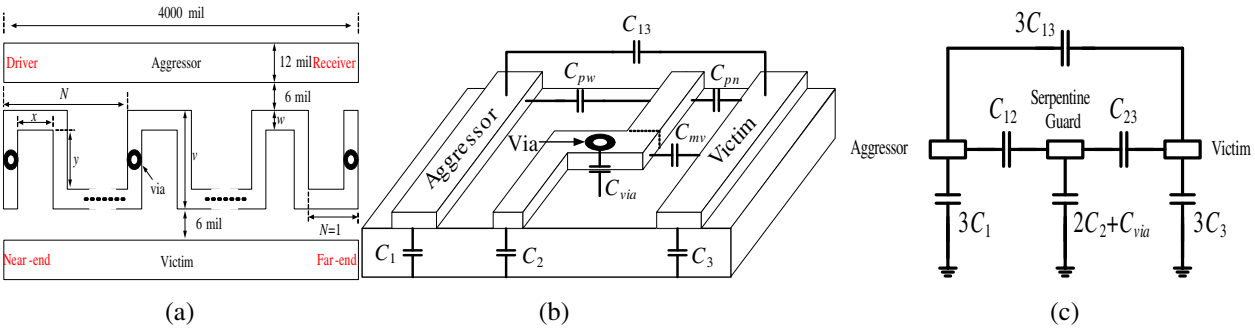

Figure 3: (a) Structure of VSGT. (b) Topology of VSGT with the mutual capacitance effect. (c) Equivalent circuit of VSGT.

Although we extend this study for increasing the mutual capacitance of SGT, our approach VSGT modified the structure of SGT as follows. For getting a better layout and test reasons, the first and last vertical parts are located at the starting and ending perpendicular to the aggressor and victim as shown in Fig. 3(a). Moreover, some grounded-vias are added on the guard trace by a proper location and the scale between horizontal and vertical length of the guard trace can be adjusted in a better state such that the coefficients of NEXT and FEXT can be minimum and get the better performance. Beside them, other layout parameters of VSGT are the same as that of SGT. The topology of VSGT with the mutual capacitance effect is shown in Fig. 3(b) and its equivalent circuit of VSGT is shown in Fig. 3(c).

To prove that the serpentine guard increases the mutual capacitance between the aggressor and victim, a lengthwise unit section of serpentine guard, the notations of the self- and mutual capacitance between the aggressor and victim are shown in Figs. 3(b) and 3(c). There is the mutual effect between one pair trace under the high-speed signal. Let C_1, C_2, C_3, and C_{via}, be the self-capacitance of the aggressor, the serpentine guard trace, victim, and middle part of self-capacitance of the serpentine guard trace, respectively. Also, let C_{12}, C_{23}, and C_{13} be the mutual-capacitance between the aggressor and guard trace, the guard trace and victim, and victim and aggressor, respectively. Moreover, there are three effects, C_{pw}, C_{pn}, and C_{mv}, of C_{12} and C_{23}. That is, $C_{12} = C_{23} = (C_{pw} + C_{pn} + C_{mv})$ [4].

Design the scale among the vertical part, horizontal part, and total length of the guard trace. Since the vertical parts of the serpentine guard increase the mutual capacitance without much changing the mutual inductance between the aggressor and victim, this causes more K_{NE} and less K_{FE}. The layout parameters of the VSGT structure are as follows and shown in Fig. 3(a). The length of aggressor and victim are 4000 mil, the width of each microstrip line is 6 mil, x is 120 mil, y is 12 mil, v is 24 mil, w is 6 mil, N is the amount of the segments, the thickness of copper is 7 mil, ε_r be 4.664, tan δ is 0.035, the width of each microstrip line is 6 mil, the diameter of one via is 9 mil. In our simulation result, let horizontal segments be form 120 to 128 mil and the length of VSGT be 2000 to 4000 mil.

Using the tool [6] to simulate the three approaches, the results are shown in Table 1. Compared with the other two approaches, the mutual capacitance (inductance) $C_m(L_m)$ between the aggressor and victim of VSGT is less than around 17.7% (42.72%) and 43.6% (42.72%) of 3W and SGT,

Table 1: The simulation results among 3 models with various parameters.

	3W [3]	SGT [4]	VSGT	VSGT advantages
C_m (pF/mm)	0.000475	0.000693	0.000391	Reduced
C_S (pF/mm)	0.114245	0.114264	0.114874	
L_m (nH/mm)	0.008552	0.008552	0.004989	Reduced
L_S (nH/mm)	0.342262	0.342237	0.338813	
K_{NE}	0.007286	0.007763	0.004532	Reduced
K_{FE}	−0.01041	−0.00946	−0.00566	Reduced

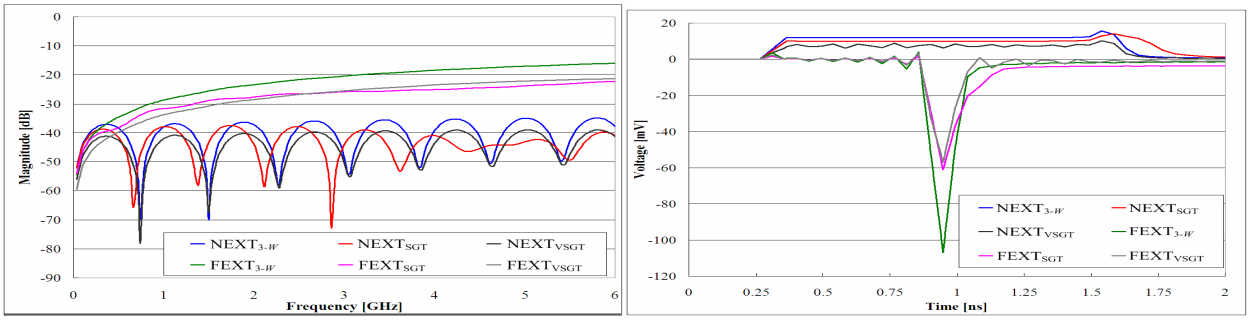

(a) (b)

Figure 4: Comparison of simulation results among NEXT and FEXT of 3-W [3], SGT [4], and VSGT. (a) Example of over frequency-domain. (b) Example of over time-domain.

respectively. Hence, since VSGT can effectively reduce C_m and L_m, these 2 coupling effects can simultaneously dominate the coefficient of K_{NE} and K_{FE}. Moreover, in our results, K_{NE} (K_{FE}) of VGST is less than around 37.8% (45.6%) and 41.6% (40.2%) of 3W and SGT, respectively. Hence, VSGT can indeed reduce K_{NE} and K_{FE}.

4. SIMULATION RESULTS AND DISCUSSION

Let $NEXT_{3\text{-}}W$ ($FEXT_{3\text{-}}$)W, $NEXT_{SGT}$ ($FEXT_{SGT}$), and $NEXT_{VSGT}$ ($FEXT_{VSGT}$) be to represent one simulation result of NEXT (FEXT) of 3-W ruler, SGT, and VSGT, respectively. All parameters of our design structure are shown in Fig. 2. The simulation tool is shown in [7]. The comparison, which one curve is to represent its corresponding result, of simulation results among the NEXT and FEXT of 3-W [3], SGT [4], and VSGT is shown in Figs. 4(a) and 4(b), respectively. The examples of the frequency-domain within 6 GHz range and time-domain with one full cycle time are shown in Figs. 4(a) and 4(b), respectively.

5. CONCLUSIONS

Verified in the frequency-domain simulation results, our approach of the vias of serpentine guard trace can improve not only the near-end crosstalk by 3.7 and 0.83 dB but also the far-end crosstalk by 5.11 and 0.1 dB compared to the three-width rule and the serpentine guard trace, respectively. Moreover, verified in the time-domain, the vias of serpentine guard trace can reduce not only the near-end crosstalk by 34.67 and 27.5% but also the far-end crosstalk by 46.78 and 6.91% than that of the three-width rule and the serpentine guard trace, respectively. All of them indicate that our design in the best performance among these three approaches. Hence, our method can be indeed employed to those products of the high-speed printed circuit board applications to suppress the crosstalk and then increase their reliability.

ACKNOWLEDGMENT

The authors would like to thank the National Science Council of the Republic of China for financially supporting this research under Contract No. NSC 97-3114-E-320 -001- and NSC 98-2221-E-166-008-.

REFERENCES

1. Sharawi, M. S., "Practical issues in high speed PCB design," *IEEE Potentials*, Vol. 23, No. 2, 24–27, Apr./May 2004.
2. Bogatin, E., *Signal Integrity-simplified*, Prentice Hall, 2003.
3. Montrose, M. I., *EMC and the Printed Circuit Board: Design, Theory, and Layout Made Simple*, IEEE Press, 1998.
4. Lee, K., H. B. Lee, H. K. Jung, J. Y. Sim, and H. J. Park, "A serpentine guard trace to reduce the far-end crosstalk voltage and the crosstalk induced timing jitter of parallel microstrip," *IEEE Transactions on Advanced Packaging*, Vol. 31, 809–817, Nov. 2008.
5. Young, B., *Digital Signal Integrity: Modeling and Simulations with Interconnects and Packages*, Prentice-Hall, 2001.
6. IE3D User's Manual, Zeland Software, Inc.
7. Ansoft HFSS user's Guide — High Frequency Structure Simulator, Ansoft Co., 2003.

Model and Performance Analysis of Coplanar Waveguide Based on Different Oxide Structure HR-Si Substrate

Xi Li, **Yanling Shi**, **and Yanfang Ding**
Department of E. E., East China Normal University, Shanghai 200241, China

Abstract— Coplanar waveguides (CPW) are widely used in MMICs as interconnects and matching networks. Through conventional CMOS processing, three kinds of 50 Ω CPWs are designed and fabricated on three different types of substrates, including HR-Si (High-Resistivity Silicon) directly, HR-Si with continuous SiO_2 layer and HR-Si with discontinuous SiO_2 layer where the SiO_2 between signal and ground line is etched. Measurement shows that CPW on HR-Si owes the least transmission loss while the one on HR-Si with continuous SiO_2 owes the most loss. The insertion losses at 20 GHz are −0.88 dB, −2.50 dB and −1.06 dB respectively. Based on the two-port network analysis of the equivalent model of the substrates, it has been proved that the major factors influencing the transmission loss are resistivity of substrate, oxide capacitance and coupling capacitance. With this conclusion, the theoretical analysis is consistent with the measured results.

1. INTRODUCTION

Coplanar waveguide (CPW) has gained wide interest in MMICs as interconnects and matching networks because the grounds in CPW structure are on the same surface as the signal line, which eliminates the need for via holes and substrate thinning, and simplifies the fabrication process [1]. However, the performance of integrated circuits on conventional Si wafers is very poor at microwave frequency due to the high loss coming from the low resistivity of the substrate. The loss is primarily caused by penetration of the electric field of the device into the conductive Si, inducing parasitic substrats currents [2]. Using high-resistivity Si substrate is one of the approaches to reduce transmission loss [3–5], which extends the application of HR-Si in RF circuits.

Usually, CPWs are fabricated on oxided Si because transmission lines and microwave devices are always on wiring layers. Different SiO_2 structures will make different influence on transmission characteristics which changes the substrate model of transmission lines [6]. Different from traditional charge analysis in the oxide layer [7], theoretical study based on the two-port network analysis of the equivalent model of the coplanar waveguide based on different oxide structure HR-Si substrate has been discussed. Characteristic difference of CPWs on different SiO_2 structures has been validated with the theory derivation and the model discussion. It has been proved that the major factors influencing the transmission loss are resistivity of substrate, oxide capacitance and coupling capacitance.

2. EXPERIMENTAL PROCEDURE AND RESULTS

In this research, coplanar waveguides (CPWs) are designed with a length of 2 mm and a characteristic impedance of 50 Ω. CPWs on HR-Si directely (A-type), HR-Si with continuous SiO_2 (B-type) and HR-Si with discontinuous SiO_2 where the SiO_2 between signal and ground line (C-type) is etched were fabricated. The resisitivity and thickness of the HR-Si are about 1000 Ω · cm and 350 µm respectively. The thermal SiO_2 is 1 µm thick. CPWs are made of 1 µm thick aluminum. Fig. 1 shows the profiles of CPWs on HR-Si substrate with three different oxide structures. W is the width of signal, S is the space between signal and grounds. The dimension of the CPW is $W/S = 39/24$ µm.

The CPW characteristics have been measured by Agilent E8363B Network Analyzer and a probe station at frequency up to 40 GHz. Fig. 2 shows S-Parameter comparison of CPWs on three types of substrates. From the figure, it can be found that A-type owes the least transmission loss and B type the most. At 20 GHz, the insert losses of A-type, B-type and C-type are −0.88 dB, −2.50 dB and −1.06 dB respectively.

3. DISCUSIONS

In order to analyze the substrate loss, metal loss is ignored temporarily. Fig. 3 displays the equivalent model of different substrates. C_a is the coupling capacitance of signal and grouds via air. C_i is the coupling capacitance of signal and grouds. C_{ox} is oxide capacitance of metal and substrate

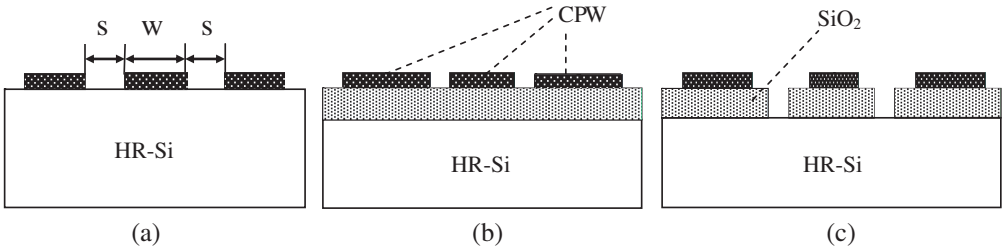

Figure 1: CPWs on substrates with different oxide structures. (a) A-type: CPW on HR-Si with no SiO_2, (b) B-type: CPW on HR-Si with continuous SiO_2, (c) C-type: CPW on HR-Si with discontinuous SiO_2.

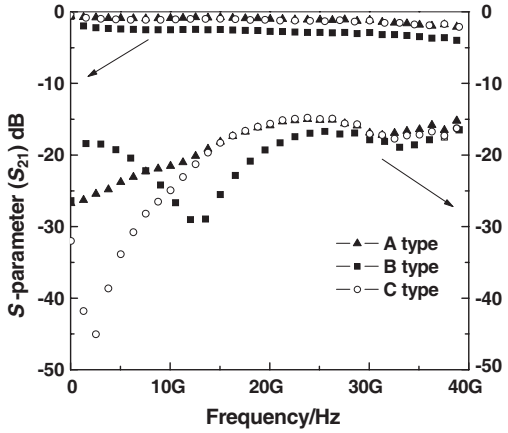

Figure 2: S-Parameter comparison of CPW on three different substrates.

via oxide layer. C_s and R_s are substrate's barrier layer capacitance and resistance respectively. Because of the unpresidence of oxide layer, C_{ox} and C_i are zero in A-type. We could also find that C_i of C-type is less than that of B-type.

Regarding C_a and C_i as C, we could find that

$$C(\text{A-type}) \leq C(\text{C-type}) \leq C(\text{B-type}). \tag{1}$$

The model of different substrates could be unified as one equivalent circuit in Fig. 4. Equal the equivalent circuit to a two port network shown in Fig. 5. Suggest Z_B as equivelent impedence of metal layer, Z_A and Zc as equivelent impedence of substratae in either side. Here, Z_A equals Z_c. Using two port network analysis, the relationship of voltage and current is

$$\begin{pmatrix} V_1 \\ V_2 \end{pmatrix} = \begin{pmatrix} Z_{11} & Z_{12} \\ Z_{21} & Z_{22} \end{pmatrix} \begin{pmatrix} i_1 \\ i_2 \end{pmatrix},$$

where $Z_{11} = \frac{V_1}{i1}|t2 = 0$, $Z_{21} = \frac{V_2}{i1}|t2 = 0$.

Z_{11} is the ratio of V_1 and i_1 when port 2 is open. Thus,

$$Z_{11} = Z_A//(Z_B + Z_C) \tag{2}$$

Z_{21} is the ratio of V_2 and i_1 when port 2 is open, so current flowing in Z_c is the distribution of i_1 into Z_c and Z_B. Therefore,

$$Z_{21} = \frac{V_2}{i_1} = \frac{Z_A Z_C}{Z_A + Z_B + Z_C} = \frac{Z_A^2}{2Z_A + Z_B} = \frac{1}{\frac{2}{Z_A} + \frac{Z_B}{Z_A^2}} = S_{21}. \tag{3}$$

The insertion loss $IL = -20\lg|S_{21}| = \frac{1}{|S_{21}|}$, so Z_A and Z_B are major factors influencing the insertion loss IL of CPW. Z_B is temporarily assumed to be a constant while discussing the substrate loss. From Equation (3), we could make the conclusion that S_{21} increases as Z_A rises, which represents the increase of transmission loss.

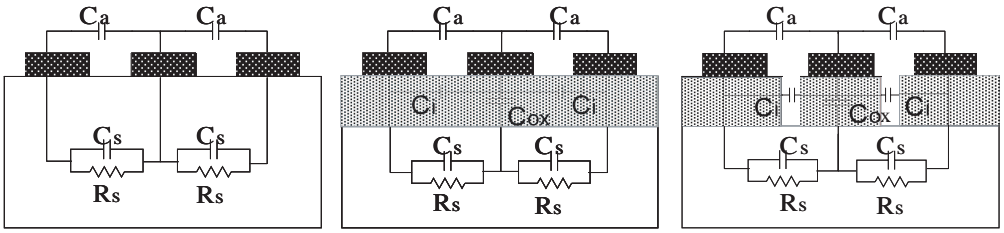

(a) A-type (b) B-type (c) C-type

Figure 3: Equivalent model of different substrates.

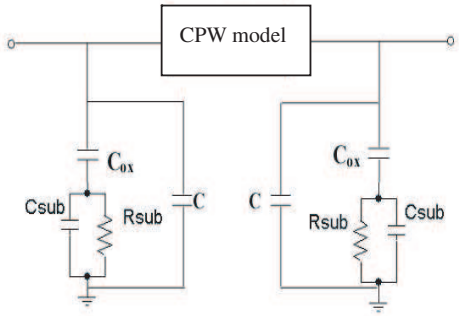

Figure 4: Unified equivalent circuit.

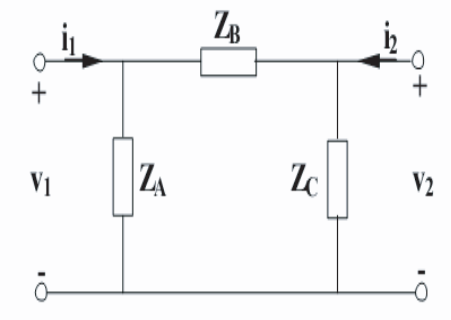

Figure 5: Tow port network of CPW.

In Fig. 4, we suppose $Z_{A1} = -\mathrm{j}\frac{1}{\omega C_{ox}}$,

$$Z_{A2} = R_S // Z_{C_S} = \frac{1}{\mathrm{j}\omega C_S + \frac{1}{R_S}}.$$

Hence,

$$Z'_A = Z_{A1} + Z_{A2} = -\mathrm{j}\frac{1}{\omega C_{ox}} + \frac{R_S}{\mathrm{j}\omega C_S R_S + 1} \tag{4}$$

Suppose $\omega C_{ox} = a$ and $\omega C_S = b$. Therefore,

$$ZA' = -\mathrm{j}\frac{1}{a} + \frac{R_S}{\mathrm{j}bR_S + 1} = \frac{R_S - \mathrm{j}bR_S^2}{1 - b^2R_S^2} - \frac{\mathrm{j}}{a} = \frac{aR_S - \mathrm{j}\left[abR_S^2 + \left(1 - b^2R_S^2\right)\right]}{a\left(1 - b^2R_S^2\right)} \quad . \tag{5}$$

Supposing $1 - b^2R_S^2 = \beta$, the equation $R_S^2b^2 = 1 - \beta$ can be obtained. So,

$$Z'_A = \frac{aR_S - \mathrm{j}\left[a\frac{(1-\beta)}{b} + \beta\right]}{\alpha\beta} = \frac{aR_S - \mathrm{j}\left[\frac{a+(b-a)\beta}{b}\right]}{\alpha\beta} = \frac{abR_S - \mathrm{j}\left[a + (b-a)\beta\right]}{ab\beta} \tag{6}$$

The absolute value

$$\begin{aligned} \left|Z'_A\right| &= \frac{\sqrt{(abR_S)^2 - \left[a + (b-a)\beta\right]^2}}{(ab\beta)^2} = \frac{\sqrt{2a^2 - a(2b-3a)\beta + (b-a)^2\beta^2}}{a^2b^2\beta^2} \\ &= \frac{\sqrt{\frac{2a^2}{\beta^2} - \frac{a(2b-3a)}{\beta} + (b-a)^2}}{a^2b^2}. \end{aligned} \tag{7}$$

From the derivation above, R_s increase makes β decrease, subsequently $|Z'_A|$ increases and IL decreases. Another conclusion can be achieved that C_{ox} decrease makes S_{21} decrease.

Combining the relationship $Z_A = Z'_A//C$ and Equation (1), the following inequality can be obtained,

$$Z_A(\text{A-type}) \geq Z_A(\text{C-type}) \geq Z_A(\text{B-type}).$$

It explains the phenomenon in the experiment that

$$IL(\text{A-type}) \leq IL(\text{C-type}) \leq IL(\text{B-type}).$$

So, the major influencing factors on CPW loss are resistivity of substrate, oxide capacitance and coupling capacitance.

4. CONCLUSION

CPWs with a characteristic impedance of 50 Ω on HR-Si, HR-Si with continuous SiO_2 and HR-Si with discontinuous SiO_2 where the SiO_2 between signal and grounds is etched are fabricated. The tested results have shown that CPW on HR-Si owes the least transmission loss and the one on HR-Si with continuous SiO_2 the most.

With the theory of two port network, the equivalent model of the coplanar waveguide based on different oxide structure HR-Si substrate has been discussed. The major causes of the transmission loss and the characteristic difference of CPWs on different SiO_2 structures has been validated with the theory derivation and the model discussion.

ACKNOWLEDGMENT

This work was supported by Foundation of Shanghai Science & Technology Committee (075007033, 04QMX1419) and Natural Science Foundation of China (No. 60676047, 60606010).

REFERENCES

1. Strohm, K. M., F. J. Schmuckle, B. Schauwecker, W. Heinrich, and J.-F. Luy, "Silicon micromachined CPW transmission lines," *32nd European Microwave Conference*, 1–4, Oct. 2002.
2. Ma, Y., B. Rejaei, et al., "Low-loss on-chip transmission lines with micro-patterned artificial dielectric shields," *Electronics Letters*, Vol. 44, No. 15, 913–914, Jul. 2008.
3. Lakshminarayanan, B. and T. Weller, "Experimental results for parasitic coupling and attenuation of coplanar waveguides on high resistivity silicon," *56th ARFTG Conference Digest-Fall*, Vol. 38, 1–11, Nov. 2000.
4. Kikkawa, T., and A. B. M. H. Rashid, "Effect of silicon substrate on the transmission characteristics of integrated antenna," *IEEE Topical Conference on Wireless Communication Technology*, 144–145, Oct. 2003.
5. Rashid, A. B. M. H., "High transmission gain integrated antenna on extremely high resistivity Si for ULSI wireless interconnect," *IEEE Electron Device Letters*, Vol. 23, No. 12, 731–733, Dec. 2002.
6. Wang, G., W. Woods, H. Ding, and E. Mina, "Novel low-cost on-chip CPW slow-wave structure for compact RF components and mm-wave applications," *ECTC 2008, 58th Electronic Components and Technology Conference*, 186–190, May 2008.
7. Lederer, D. and J.-P. Raskin, "Substrate loss mechanisms for microstrip and CPW transmission lines on lossy silicon wafers," *IEEE MTT-S International Microwave Symposium Digest*, Vol. 2, 685–688, 2002.

Novel Rectangular Coupled Line Bandpass Filter

Souren Shamsinejad[1], **Shila Shamsadini**[2], **and Mohamad Soleimani**[1]

[1]Electrical Engineering Department, Iran University of Science and Technology (IUST), Tehran, Iran
[2]Electrical Engineering Department, South Tehran Branch, Azad University, Tehran, Iran

Abstract— This paper reports a novel band pass filter without any periodic response. The novel filter has been named Rectangular Parallel Coupled Line filter (RPCL) and derived from reforming the conventional parallel coupled line filters. The novel band-pass filter has narrowband response. RPCL filter with center frequency of 475 MHz, 1 dB pass-band of 10 MHz and 25 dB stop-band of 50 MHz has been reported here. The area which has been occupied by this RPCL filter is approximately about 52 cm^2. The RPCL can be tuned for various applications at desired center frequency and bandwidth. The occupied area by the filter reduced related to the center frequency of RPCL. High power transmission capability is another distinguished feature of the RPCL filter. Furthermore, at high frequency applications the filter can be designed due to use in high power MMIC packages. The periodic frequency responses related to approximately all types of Microstrip passive filters has been suppressed in the novel RPCL filter. The novel RPCL filter can be designed for dual band applications such as 3G/GSM in a 3 cm^2 MMIC package.

1. INTRODUCTION

Filters play an important role in the design of microwave circuits and their applications are various. So far, quite a lot of Filter structures with various types such as LPF, BPF and HPF have been proposed. Parallel coupled line filters are one of the most practical and common structures in microwave transceivers. In almost all of the parallel coupled line filter structures, quarter wavelength long transmission lines are used as the basic building section resulting in a significant circuit size. Consequently, continuous efforts were carried on to reduce the device length while increasing the original performances [1, 2].

Periodic response is another feature which is existed in almost all of the microstrip filter structures. The novel filter has suppressed the periodic response. This suppression has been estimated about −25 dB.

Some of the narrowband transceivers require narrowband band-pass filters with high rejection at near frequency offsets. One of the vital requirements of the microwave transmitters is high power elements include filters. The microstrip passive elements can transmit high power signals and because of this feature, microstrip filters [4] are indispensable components of microwave transmitters. The novel proposed filter is one of the modified and enhanced microstrip filters and has a new shape with smaller area on board. However, conventional parallel coupled line filters are quite long especially below C-Band where the quarter-wave transmission lines can be several centimeters long.

The design of proposed filter has been based on theoretical parallel coupled line relationships for a Butterworth filter. The filter employs one stub for suppressing the periodic response. To fully illustrate this approach, the characteristics and the shape of novel Rectangular Coupled Line filter together with related equations are presented and its dimensions and simulation results are compared to the conventional one. The characteristics include 1 dB bandwidth, 3 dB bandwidth, 25 dB rejection, and insertion loss. The new enhanced filter is designed at frequency of 475 MHz which is the operational frequency of a specific telecommunication system.

2. NOVEL BAND PASS FILTER DESIGN

Indeed, the novel filter is a modified version of the conventional parallel coupled line filter. Therefore, at the beginning, the conventional one should be designed at desired center frequency. This one consists of some $\lambda/4$ transmission lines which have been coupled with adjacent lines, as shown in Fig. 1.

2.1. Conventional Filter Design

It is a Butterworth filter and the amplitude-squared transfer function for Butterworth filters with insertion loss $L_{Ar} = 3.01$ dB at the cutoff frequency $\Omega_C = 1$ is given by [4]:

$$|S_{21}(j\Omega)|^2 = \frac{1}{1+\Omega^{2n}} \tag{1}$$

For this filter, the elements values of the low-pass prototype can be derived from the following equations [4]:

$$\begin{aligned} g_0 &= 1.0 \\ g_i &= 2\sin\left(\frac{(2i-1)\pi}{2n}\right) \quad \text{for} \quad i = 1 \text{ to } n \\ g_{n+1} &= 1.0 \end{aligned} \tag{2}$$

The minimum value of n can be calculated from the following equation:

$$n \geq \frac{\log(10^{0.1L_{AS}} - 1)}{2\log\Omega_s} \tag{3}$$

Equation (3) suggests that for $L_{AS} = 25\,\text{dB}$ and $\Omega_s = 3$, $n \geq 2.6$, therefore, a 3-pole ($n = 3$) Butterworth prototype has been chosen and eventually the values of the low-pass prototype elements has been calculated and shown at the following table.

The required frequency transformation of a low-pass prototype response to a band-pass prototype response has been shown at (4); and the center angular frequency ω_0 and the fractional bandwidth FBW can be inferred from (4) [4].

$$\begin{aligned} \Omega &= \frac{\Omega_c}{\text{FBW}}\left(\frac{\omega}{\omega_0} - \frac{\omega_0}{\omega}\right) \\ \text{FBW} &= \frac{\omega_2 - \omega_1}{\omega_0} \\ \omega_0 &= \sqrt{\omega_2\omega_1} \end{aligned} \tag{4}$$

The FBW and ω_0 resulted from (4) together with the upper and lower 3 dB cutoff frequencies, have been listed in Tables 2 and 3. The characteristic admittances of J-inverters can be calculated from (5) where Y_0 is the characteristic admittance of the terminating lines. To realize the J-inverters, the even- and odd-mode characteristic impedances of the coupled microstrip line resonators has been determined by (6) and listed in Table 4 beside their related J-inverters values [3].

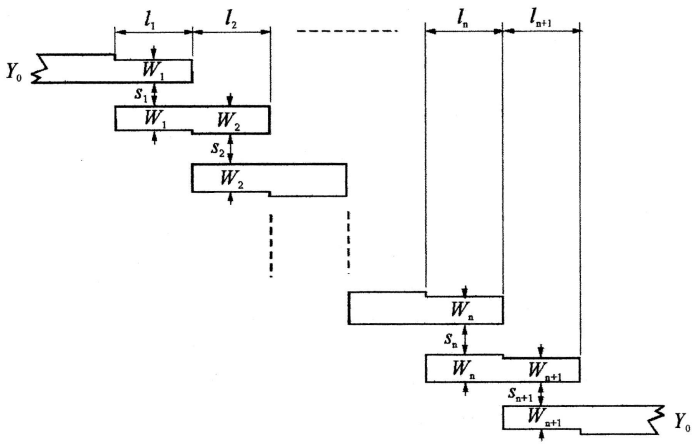

Figure 1: Conventional parallel coupled line filter.

g_0	g_1	g_2	g_3	g_4
1.0	1.0	2.0	1.0	1.0

Table 1: The values of Low pass filter prototype elements.

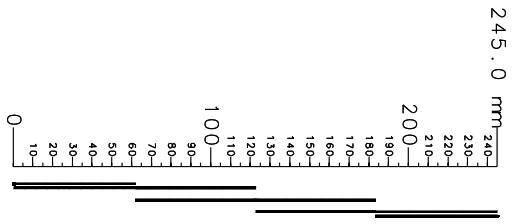

Figure 2: Conventional parallel coupled line filter layout.

Table 2: Pass and Stop frequencies of desired filter.

f_{s1}	f_1 (3 dB cutoff)	f_2 (3 dB cutoff)	f_{s2}
450 MHz	467 MHz	483 MHz	500 MHz

Table 3: Fractional bandwidth and center angular frequency.

FBW	ω_0	ω_1	ω_2
0.02	$2\pi\times475$ MHz	$2\pi\times470$ MHz	$2\pi\times480$ MHz

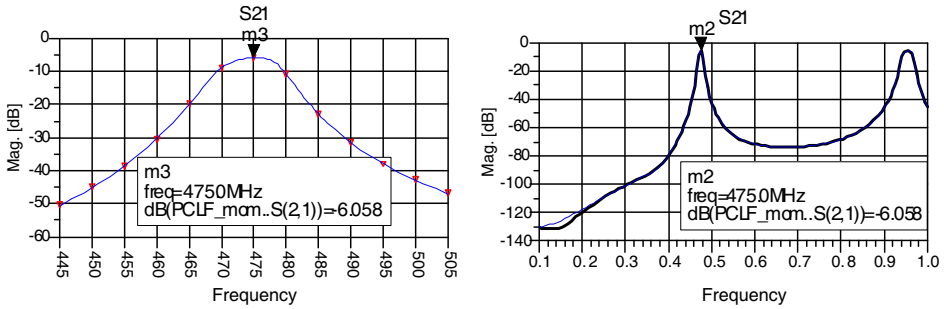

Figure 3: Conventional Parallel coupled line filter frequency response.

The next step of the filter design is finding the dimensions of coupled microstrip lines that exhibit the desired even- and odd-mode impedances. This microstrip filter has been constructed on substrate Cer10 with a relative dielectric constant of 10 and thickness of 1.27 mm. Using the design equations for coupled microstrip lines given in [5], the width and spacing for each pair of quarter-wavelength coupled sections have been derived. The conventional parallel coupled line filter layout and its simulation results have been depicted in Figs. 2 and 3, respectively.

$$\begin{aligned} \frac{J_{01}}{Y_0} &= \sqrt{\frac{\pi}{2}\frac{\text{FBW}}{g_0 g_1}} \\ \frac{J_{j,j+1}}{Y_0} &= \frac{\pi\text{FBW}}{2}\frac{1}{\sqrt{g_j g_{j+1}}} \qquad j = 1 \text{ to } n-1 \\ \frac{J_{n,n+1}}{Y_0} &= \sqrt{\frac{\pi\text{FBW}}{2 g_n g_{n+1}}} \end{aligned} \tag{5}$$

$$\begin{aligned} (Z_{0e})_{j,j+1} &= \frac{1}{Y_0}\left[1 + \frac{J_{j,j+1}}{Y_0} + \left(\frac{J_{j,j+1}}{Y_0}\right)^2\right] \quad j = 0 \text{ to } n \\ (Z_{0o})_{j,j+1} &= \frac{1}{Y_0}\left[1 - \frac{J_{j,j+1}}{Y_0} + \left(\frac{J_{j,j+1}}{Y_0}\right)^2\right] \quad j = 0 \text{ to } n \end{aligned} \tag{6}$$

2.2. Novel Filter Design

The proposed filter which has been named Rectangular Parallel Coupled Line filter or RPCL has been designed by deforming the conventional one in order to fit aptly in the receiver and transmitter circuits. The filter transmission lines have been curved with 90 degrees angle to shape a rectangular which has been depicted in Fig. 4. Additionally, an open ended quarter wavelength stub at frequency of 950 MHz has been used at filter configuration due to suppress the periodic response of filter at double center frequency of 475 MHz. The stub has been deformed too to fit tightly in the filter inner space.

As we see, we have been obliged to choose filter order equal to $n = 3$ in order to shape a rectangular. The filter depicted in Fig. 4 has been optimized to reach the desired responses. The length and width of Transmission lines together with the curves radiuses and spaces between transmission lines have been optimization parameters and their values after optimization has been listed in Table 5.

Table 4: The J-inverters values together with even- and odd-mode impedances.

j	$J_{j,j+1}/Y_0$	$(Z_{0e})_{j,j+1}$	$(Z_{0o})_{j,j+1}$
0	0.231	64.22	41.12
1	0.038	51.97	48.17
2	0.038	51.97	48.17
3	0.231	64.22	41.12

Table 5: Values of Lengths, widths and spaces.

j	W_j	S_j	L_j
0	1.11 mm	0.64 mm	56.9 mm
1	1.20 mm	3.04 mm	55.6 mm
2	1.20 mm	3.54 mm	58 mm
3	1.11 mm	0.81 mm	55 mm

3. RPCL FILTER ANALYSIS

The RPCL filter layout after final optimization and the conventional one layout have been simulated with momentum method by ADS software. The conventional filter simulation results have been illustrated in previous section at Fig. 3 and the simulation results of proposed RPCL filter has been illustrated in Figs. 5 and 6. Improvements in some aspects have been considered in designing the RPCL filter.

First, the conventional filter was very long which could not be appropriate for implementation in transmitters and receivers circuits. Second, the filter can be used in high power transmitters because of its transmission lines widths. This filter can pass about 500 Watt of signal power which can be applicable in the outputs of some high power amplifiers. Third, the parallel coupled line filters have periodic responses like a lot of microwave filters. In the novel RPCL filter, the second periodic response has been suppressed about -25 dB compared with the conventional one. The frequency responses of the novel RPCL filter and conventional one have been compared in Table 6 at some frequency points. The insertion loss of RPCL filter has been improved about 2 dB related to conventional filter. The bandwidth of the novel filter has been increased by optimization due to specific application which required 1 dB bandwidth of 10 MHz. Additionally, the suppression at 950 MHz is an useful enhancement to eliminate interferences.

Table 6: Comparison table for frequency responses.

	Loss at 450 MHz	Loss at 460 MHz	Loss at 467 MHz	Loss at 470 MHz	Insertion Loss	Loss at 480 MHz	Loss at 483 MHz	Loss at 490 MHz	Loss at 500 MHz	Loss at 950 MHz
RPCL	33.1 dB	18.6 dB	7.3 dB	5.3 dB	4.3 dB	5.1 dB	7.6 dB	18.1 dB	29.5 dB	< 30.3 dB
conventional	44.2 dB	29.5 dB	15.7 dB	9.0 dB	6.1 dB	11.4 dB	18 dB	31.6 dB	42.2 dB	6.6 dB

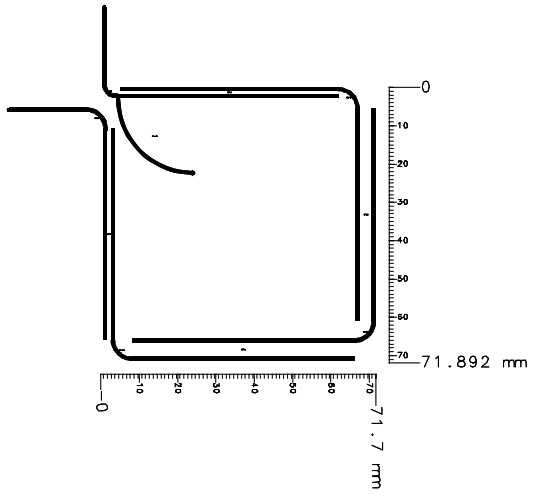

Figure 4: Novel PRCL filter layout.

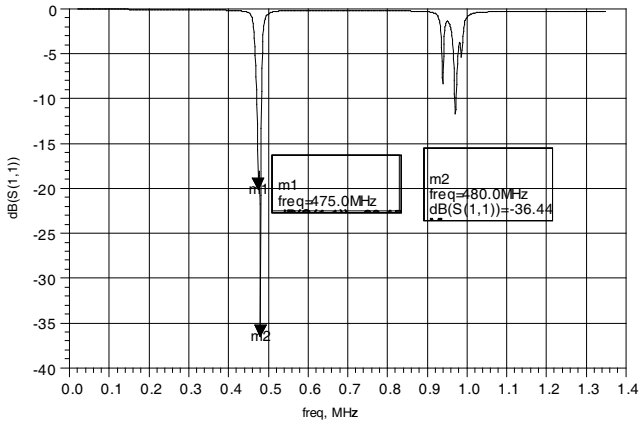

Figure 5: Return loss of novel RPCL filter.

4. DIMENSIONS COMPARISON

The filter shape has been one of the most important motivations in the forming of RPCL. The dimensions of two types of filters have been compared in Table 7. The central area of filter has been left empty. If this filter was designed for GSM systems at 900 MHz together with UMTS systems at 2140 MHz, higher frequency filter could be fitted in central empty area of lower frequency one. On the other hand, it is a good idea to implement some parts of transceiver circuits in this area.

5. APPLICATION OF NOVEL RPCL FILTER

The RPCL filter which has been reported in this paper, has been designed to use in a particular high power transmitter which transmitted the signal at 475 MHz with 1 dB bandwidth of 10 MHz. However, the novel RPCL filter is a general method in band-pass filter designing at desired center frequency with proper bandwidth for so many applications.

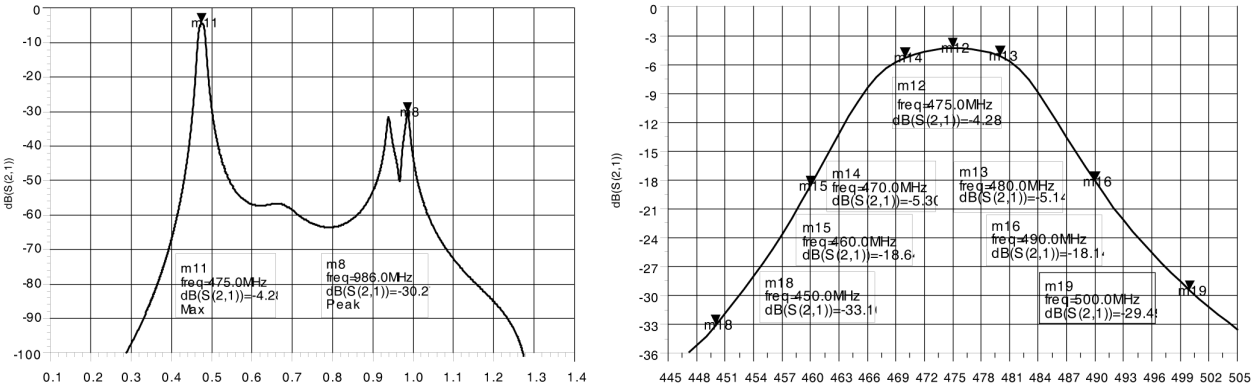

Figure 6: Frequency response of novel RPCL filter.

Table 7: Filters dimensions comparison table.

	RPCL	Conventional
Length	72 mm	245 mm
Width	72 mm	18 mm

6. CONCLUSION

A novel Rectangular Parallel Coupled Line filter has been developed and reported. A shape deforming, insertion loss reducing and periodic response suppression has been achieved. Also the novel filter has extra narrowband response and the area which has been occupied by this RPCL filter is arguably decreased.

ACKNOWLEDGMENT

The authors wish to acknowledge the assistance and support of the PIERS Steering Committee.

REFERENCES

1. Fok, S. W., P. Cheong, K. W. Tam, and R. Martins, "A novel microstrip bandpass filter design using asymmetric parallel coupled-line," *IEEE International Symposium on Circuits and Systems, ISCAS 2005*, Vol. 1, 404–407, 2005.
2. Ahumada, M. C. V., J. Martel, and F. Medina, "Microstrip coupled line filters with spurious band suppression," *PIERS Online*, Vol. 3, No. 6, 948–950, 2007.
3. Matthaei, G. L., L. Young, and E. M. T. Jones, *Microwave Filter, Impedance Matching Networks, and Coupling Structures*, McGraw-Hill, New York, 1964.
4. Hong, J. S. and M. J. Lancaster, *Microstrip Filters for RF/Microwave Applications*, John Wiley & Sons Inc, 2001.
5. Garg, R. and I. J. Bahl, "Characteristics of coupled microstriplines," *IEEE Trans. MTT*, Vol. 27, 700–705, July 1979; Corrections in *IEEE Trans., MTT*, Vol. 28, 272, March 1980.

Optimization of Broadband Withdrawal Weighted SAW Filters

Ying Liu, **Yali Qin**, **and Changming Xie**
Zhejiang Key Research Lab of Fiber-optic Communication Technology
Colleage of Information Engineering, Zhejiang University of Technology, HangZhou, China

Abstract— This paper describes using withdrawal weighted transducer design of bandpass SAW Filter. With a new optimization algorithm design of broadband SAW transversal filter. Design the most simple and compact configuration of surface acoustic wave (SAW) filters in this algorithm with an apodized interdigital transducer (IDT) as input a withdrawal weighted interdigital transducer (IDT) as the output. The algorithm is based on the delta function model to achieve performance requirements of frequency response (FR) with a shape factor of 1.3 or less, bandwidth of more than 15% and stopband rejection of 40 dB or more.

1. INTRODUCTION

A lot of researches have been made on analysis and design of SAW filters to achieve a variety of performance requirements as wide bandwidth, good linearity, low sidelobe level and a shape factor, and so on. Thus, with the SAW filter performance to improve and the mobile communication development the application of SAW filters are widely in communications. Withdrawal weighted SAW transversal filter can achieve these performance requirements with small diffraction by the uniformity of the electrodes, less loading effects, good shape factor, and so on. The withdrawal weighted transducer optimization algorithms are constantly improving. The withdrawal weighted SAW filter was first introduced by Hartmann in 1973 [1], and since then a lot of work has focused on developing the design technique of the withdrawal weighted SAW filter. Smith and Fedler [2], Yamaguchi [3] presented an iterative method to skip and add specific IDT fingers to suppress the sidelobe level of the SAW filter. Recently, Bausk and Yakovkin [4] and Youngjin Lee [5] used the delta function model to optimize the FR of the SAW filter.

2. OPTIMIZATION ALGORITHMS

Withdrawal weighted transducer is developed on the basic of the uniform IDT. Usually, there are two ways design of the withdrawal weighted transducer. Withdrawal weighting (WW) is removing some interdigital electrodes from the uniform IDT then polarity weighting (PW) is to change the polarity individual electrodes (Fig. 1). They all have relative advantages and disadvantages [6]. WW transducer can achieve less than 1 dB of the insertion loss, the sidelobe suppression to achieve 50 dB, and so on. PW transducer can simultaneously take into account the insertion loss, passband ripple, bandwidth as well as sidelobe suppression to meet a variety of requirements for SAW filters [5, 7]. WW and PW of these structures have been proposed in a fixed cycle length of the uniform IDT. Non-fixed periodic interdigital transducer can also be weighted with withdrawal weighted such as: high-selective fan-shaped and quasi-slanted IDT [8].

Withdrawal weighted transducer continuous development and research because the structure of input and output IDT can be weighted separately eliminating the apodized transducer restriction. The apodized transducer design flexible and convenient; however, the input and output transducers can not be simultaneously apodized transducer, if the input and output are apodized transducers then the design are more complex and requires a multistrip coupler to connect two apodized transducers. In this case SAW filter includes only two selective elements input and output IDT, the

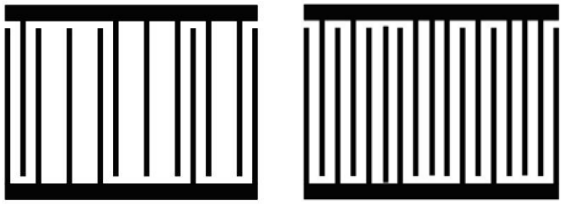

Figure 1: (a) Withdrawal weighting and (b) polarity weighting IDT.

apodized transducer as input a uniform IDT as output the frequency response (FR) of the SAW filter is relatively poor. When using withdrawal weighted transducer replace of uniform IDT to improve the performance of SAW filters such as sidelobe suppression.

Apodized transducer as input to provide a very low FR shape factor, withdrawal weighted transducer with a constant length of electrodes as the receiving transducer can reduce the diffraction effects while improving the sidelobe suppression. The apodized transducer as input not only with the WW transducer but also with PW transducer can constitute of the SAW filters, thus, an apodized transducer as input and the WW transducer as the output of such a structure are more and more extensive study (Fig. 2).

WW transducer divided into symmetric and asymmetric weighted [Figs. 2(b) and (c)], the symmetric WW transducer able to achieve a linear phase. In contrast, the asymmetric weighted transducer is not linear phase restriction removing the electrodes that is relatively independently. Therefore, it is more selective to remove of interdigital electrodes for get a better FR [9, 10].

An apodized transducer as input and a asymmetric WW transducer as output of the broadband SAW filter, with the delta function model to calculate WW transducer FR, WW transducer FR expressions such as (1) shown [11].

$$H_{out}(f) = \sum_{n=1}^{N} (-1)^n A_n \exp(in\pi f/f_0 + \varphi_n) \tag{1}$$

where f_0 is the passband center frequency, N is the number of electrode positions in the IDT, A_n is the SAW source amplitude on the nth electrode, and φ_n is the shift of a source position from the center of this electrode. If the nth electrode is absent, A_n is equal to 0; otherwise, values of A_n and φ_n depend on presence or absence of neighboring electrodes [12, 13]. That is, a disturbance of SAW source distribution in some region of the IDT, caused by removing any electrode, is taken into account.

For symmetric withdrawal weighting transducer expression (1) the calculation of the amount will be reduced by half, when N is even:

$$H_{out}(f) = 2\sum_{n=1}^{N/2} (-1)^n A_n \sin((n-0.5)\pi f/f_0 + \varphi_n) \tag{2}$$

When N is odd:

$$H_{out}(f) = A_1 + 2\sum_{n=2}^{(N+1)/2} (-1)^{n-1} A_n \cos(n\pi f/f_0 + \varphi_n) \tag{3}$$

Dual-channel SAW filter structure is also possible to achieve high frequency selectivity and linear phase, two asymmetrical withdrawal weighted transducer placed on the weighted apodized transducers both sides, asymmetric withdrawal weighted transducer placed without their mirror reflection. It is equivalent to two parallel channels, when two asymmetrical weighted transducer placed on the mirror as the output (Fig. 3). The output transducer FR expressions of dual-channel structure are as follows.

$$H_{out}(f) = \sum_{n=1}^{N} (-1)^n A_n \cos(n\pi f/f_0 + \varphi_n) \tag{4}$$

The main focus of the algorithm is the process of weighted transducer. How to determine the position of weighted electrodes to meet the design requirements. When the output withdrawal

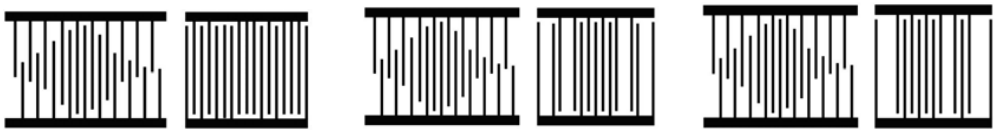

(a) (b) (c)

Figure 2: The output of SAW filter (a) polarity weighting (b) symmetric withdrawal weighting (c) asymmetric withdrawal weighting.

Figure 3: Dual-channel SAW filter structure.

weighted transducer with N electrodes, all the possible combinations of removing electrodes equals 2^N. Optimized combination of symmetric calculation is less than asymmetrical for each additional pair of electrodes that the computing time will increase twice as much.

For long IDT need to find suboptimal is very complex and need to analyze all possible combinations of weighted electrodes. First, in the uniform interdigital transducers to determine a short structure, usually, this structure has 8–15 electrodes, according to the number of IDT to determine the length of the transducer. This is a short structure of the transducer as a "window", the "window" all combination of the weighted electrode interdigital transducer scans step by step through the IDT many times. The process continues until find a better FR. If all combinations have carried out there are no improvement, the process of optimization is complete. By changing the form of the "window" from time to time to avoid the local optimization to replace the global optimization.

The frequency specifications can be applied to a output withdrawal weighted IDT but also to the entire SAW filter, the filter FR equation can be written as follows:

$$H_{fil}(f) = H_{in}(f) \times H_{out}(f) \tag{5}$$

where $H_{in}(f)$ and $H_{out}(f)$ are respectively input and output transducer frequency response, if $H_{in}(f)$ is known, the algorithm can find a withdrawal weighted transducer of the output to optimize the overall FR of SAW filter $H_{fil}(f)$.

3. EXPERIMENTAL RESULTS

Figure 4 shows the normalized FR before optimization (broken line) and after (solid line) with an apodized transducer $109\lambda_0$ as input and a WW transducer $76\lambda_0$ as output, where λ_0 is a transducer period that design the SAW filter to obtain normalized FR characteristics including large sidelobe suppression, the bandwidth can be achieved for more than 15 percent, the shape factor is less than 1.3, and GDT within the passband is very smooth and stopband rejection over 40 dB. Fig. 5 shows the normalized FR and group delay time (GDT) of the optimal FR.

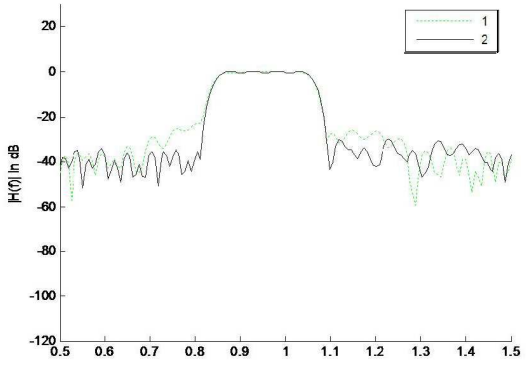

Figure 4: Non-optimized (1) and optimized (2) FR of SAW filter.

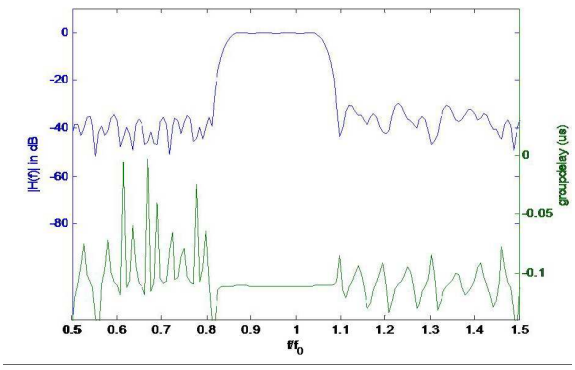

Figure 5: The FR and GDT of SAW filter.

4. CONCLUSIONS

Many of synthesis algorithms have been developed to optimize withdrawal weighted transducer with apodized transducer constitute the SAW filters. This approach can achieve a good FR with

bandwidth of more than 15%, stopband rejection of over 40 dB, a 3 dB–40 dB shape factor is less than 1.3 and group delay within the passband is very smooth.

REFERENCES

1. Hartmann, C. S., "Weighting interdigital surface wave transducers by selective withdrawal of electrodes," *Proc. IEEE Ultrason. Symp.*, 423–426, 1973.
2. Smith, W. R. and W. F. Fedler, "Fundamental and harmonic frequency circuit model analysis of interdigital transducers with arbitrary metallization ratios and polarity sequences," *IEEE Trans. Microwave Theory Tech.*, Vol. 23, No. 11, 853–864, 1975.
3. Yamaguchi, M., K. Hashimoto, and H. Kogo, "A simple method of reducing sidelobes for electrode-withdrawal weighted SAW filters," *IEEE Trans. Sonzcs Ultrason.*, Vol. 26, No. 5, 334–339, 1979.
4. Bausk, E. V. and I. B. Yakovkin, "Synthesis algorithm of broadband withdrawal weighted SAW transducers with specified amplitude and phase responses," *Proc. IEEE Freq. Contr. Symp.*, 831–835, 1997.
5. Lee, Y., S. Lee, and Y. Roh, "Design of the optimal structure of withdrawal weighted SAW transverse filters," *Proc. IEEE Ultrason. Symp.*, Vol. 1, 65–68, October 17–20, 1999.
6. Bausk, E. V., "Two types of uniform-beam-profile IDT's in broadband SAW filters," *Proc. 4th Int. Symp. Surface Waves in Solid and Layered Structures (ISSWAS-4)*, St. Petersburg, Russia, 1998.
7. Lee, Y., S. Lee, and Y. Roh, "Design of withdrawal-weighted SAW filters," *IEEE Transactions on Ultrasonics, Ferroelectrics and Frequency Control*, Vol. 49, No. 3, 337–344, March 2002.
8. Bausk, E. V., R. Taziev, and A. Lee, "Synthesis of slanted and quasi-slanted SAW transducers," *IEEE Transactions on Ultrasonics, Ferroelectrics and Frequency Control*, Vol. 51, No. 8, August 2004.
9. Bausk, E. V. and I. B. Yakovkin, "Design of low-shape-factor saw filters having a single acoustic track," *Proceedings of the 1996 IEEE International Frequency Control Symposium*, 291–295, June 5–7, 1996.
10. Bausk, E. V. and I. B. Yakovkin, "Systhesis algorithm of broadband withdrawal weighting SAW transducers with specified amplitude and phase responses," *Proceedings of the 1997 IEEE International Frequency Control Symposium*, 831–835, May 28–30, 1997.
11. Bausk, E. V., "Optimization of broadband withdrawal weighted interdigital transducers for high selective SAW filters," *IEEE Transactions on Ultrasonics, Ferroelectrics and Frequency Control*, Vol. 46, No. 5, 1276–1282, September 1999.
12. Laker, K. R., E. Cohen, and A. J. Slobodnik, "Electric field interaction within finite arrays and the design of withdrawal weighted SAW filters at fundamental and higher harmonics," *Proc. IEEE Ultrason. Symp.*, 317–321, 1976.
13. Laker, K. R., E. Cohen, T. L. Szabo, and J. A. Pustaver, "Computer-aided design of withdrawal-weighed SAW bandpass filters," *IEEE Trans. Circuits and Systems*, Vol. 25, No. 5, 242–251, 1978.

The Application of the Equal Area Law in Ferroresonance for Distribution Power System

Zheng-Wang Du[1], **Heng-Xu Ha**[2], **Lei Zhai**[3], **Hai-Quan Zhou**[2], **Song-Bo Gou**[1], **and Chong-Shan Zhong**[1]

[1]Shenli Oil Field Power Company, Dong Ying, China
[2]Dept. of Electric & Electronics Engineering, Shandong University of Technology, Zibo, China
[3]School of Electrical Engineering & Automation, Hebei University of Technology, Tianjin, China

Abstract— Ferro-resonance frequently occur and become a serious threat to the safe operation in the power system, in order to effectively suppress the complex phenomena of the system, this paper introduces the time-varying phasor, while, establishes the time-varying phasor mathematical model corresponded it. Based on this, the Equal Area Rule is applied to the ferro-resonance circuit analysis as a innovative way, that makes the analysis of ferro-resonance increased from qualitative analysis to quantitative analysis, while, defines the energy function which gives the calculation method of the system stability margin. This paper verify the actual of the time-varying Equal Area Rule applied in the ferro-resonance analysis through simulating the simple resonant circuit with AT-P, that provide the theoretical basis to effectively prevent the ferro-magnetic resonance.

1. INTRODUCTION

In the power system, there are many capacitive and inductive components, such as transformers, generators, arc-suppression coil, reactor, circuit wire inductor, line wires and alternate with of capacitance, compensation electrical appliances, the stray capacitance of the high-voltage equipment, etc. When operating the system or failure occur, the capacitors and the inductors formed oscillation circuit components which may have resonance phenomenon. Resonance will lead to the system or component over-voltage and thus endanger the equipment or insulation, and to produce over-current caused equipment overheating and even burning [1].

In distribution network, it is a very common phenomenon that nonlinear ferro-resonance caused by the saturation of voltage transformer core. So, over-voltage and over-current caused by ferro-resonance often lead to burning of the voltage transformer [2, 3]. According to statistics, in 2007, the transformer burning occurred 16 times in ShengLi Oilfield, which lead to 36 transformers are burned down, it involved 9 substations and more than 50 lines cut off, and caused huge economic losses.

At present, there are further research based on the ferro-resonance at home and abroad which give a number of criteria and the corresponding analytical methods, such as Peterson's theorem [4], graphical method [5–7], analytical method [8, 9], digital simulation analysis method [10–13], wavelet identification method [14], nonlinear dynamic analysis method [15–20], among which [4] through a large number of tests given the conclusions that the ratio range between the zero-sequence capacitance and the inductive reactance in rated line voltageto determine the resonant type; the literature [5–7] is simple and easy, which analyze the fundamental ferro-resonance through the qualitative graph and roughly give the condition which the resonance occur; literature [8, 9] obtain the system critical conditions of the fundamental ferro-resonance through complex mathematical transform, filter out other frequencies; literature [10–13] analyze the fundamental resonance by using the simulation software to simulate digitally; literature [14] introduce the wavelets to identify the type of resonance; literature [15–20] use the nonlinear dynamics to analyze the nonlinear circuits, which give the method of the resonance or not and the resonant type by the phase-plane characteristics. But the above methods all have limitations, some are not universal and suitable only for the fundamental resonance research, and some are too imprecise and qualitative, and some are too cumbersome to analyze the complex systems, and some give the criterion beside giving how to eliminate the resonance, and so on.

In this paper, it introduces the time-varying phasor to analyze the system parameters timely, while, establishes the time-varying phasor mathematical model corresponded it. Based on this, the Equal Area Rule is applied to the ferro-resonance circuit analysis as a innovative way, that makes the analysis of ferro-resonance increased from qualitative analysis to quantitative analysis, while, defines the energy function which gives the calculation method of the system stability margin. This

paper verify the actual of the time-varying Equal Area Rule applied in the ferro-resonance analysis through simulating the simple resonant circuit with ATP, that provide the theoretical basis to effectively prevent the ferro-resonance.

2. BASIC PRICIPLE

2.1. Time-varying Phasor

Sinusoidal voltage or current generated, from the rotating DC magnetic field, and the projection of the real axis of the rotating phasor is defined sine wave. Steady-state phasor model was not fixed, because the observer have the synchronization with the rotation. At the same time, assuming that the phasor rotation speed is still the power angular velocity, when the system is disturbed, but the phasor magnitude and the initial phase will change over time, then, the changed phasor shall be time-varying, as shown in the next diagram:

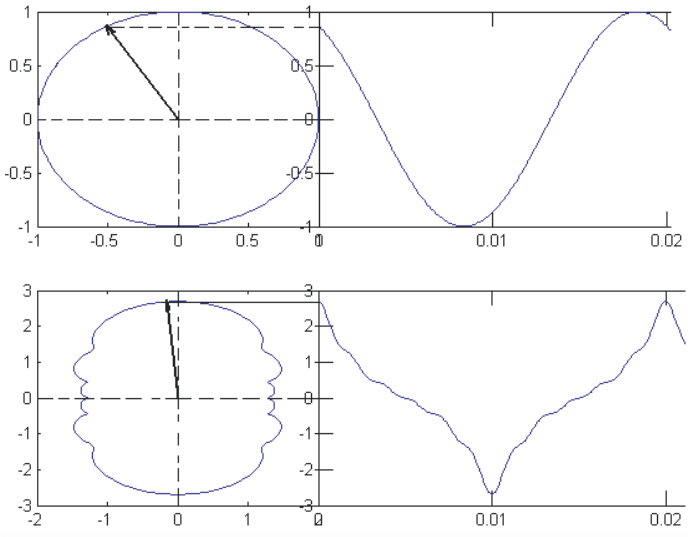

Figure 1: Comparion of the steady phasor and the time-varying phasor.

In the two diagram, the left is the trajectory map which produce by the phasor rotate in space, and the right is the projection on the real axis. Meanwhile, the above shows the steady-state phasor, which rotating trajectory is a round, the below shows the time-varying phasor, which rotating trajectory is irregular.

Assuming the sinusoidal voltage as:

$$u(t) = U_m \cos(\omega_0 t + \varphi_0) = Re\left[U_m(t)e^{j\varphi(t)}e^{j\omega_0 t}\right] = Re\left[\dot{U}(t)e^{j\omega_0 t}\right]$$

which is shown as Figure 2.

Then, for the arbitrary variable $x(t)$, we can express it as follow:

$$x(t) = Re\left[\dot{X}_m(t)e^{j\omega_0 t}\right]$$

the number of its derivation is:

$$\frac{dx\,(t)}{dt} = Re\left[\frac{d\dot{X}_m(t)}{dt}e^{j\omega_0 t} + j\omega_0 \dot{X}_m(t)e^{j\omega_0 t}\right] \tag{1}$$

2.2. The Time-varying Phasor Mathematical Model

A simple series circuit, for example, comparing the steady phasor and buliding the time-varying phasor mathematical model as in Figure 3.

$R(t)$ is the total circuit resistance, L is the equivalent nonlinear inductance of the voltage transformer, $e(t)$ is the line voltage, $U_C(t)$, $U_L(t)$ is, respectively, the equivalent capacitance voltage and the equivalent nonlinear inductance voltage.

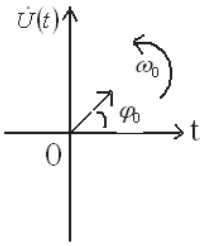

Figure 2: The time-varying phasor.

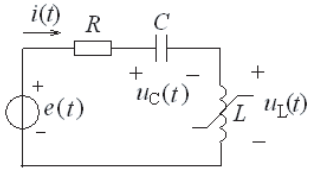

Figure 3: Series ferroresonance circuit model.

According to Figure 2, we establish the series resonance time-domain (steady-state phasor) Mathematical Model:

$$\begin{cases} \dfrac{d\varphi}{dt} = U_L \\ \dfrac{dU_C}{dt} = \dfrac{I}{C} g(\varphi) \\ e(t) = Ri_L + U_L + U_C \\ i_L = g(\varphi) \end{cases}$$

When the introduction of the time-varying phasor concept, the mathematical expression of the system parameters has changed, which is no longer a simple scalar, but the amplitude and phase over time and change.

Required from the formula (1), we have:

$$\begin{cases} \varphi(t) = Re\left[\dot{\Phi}(t)e^{j\omega t}\right] \\ \dfrac{d\varphi(t)}{dt} = Re\left[\dfrac{d\dot{\Phi}(t)}{dt}e^{j\omega t} + j\omega\dot{\Phi}(t)e^{j\omega t}\right] = \dot{U}_L - j\omega\dot{\varphi}(t) \end{cases} \tag{2}$$

Other variables will be derivated such as (2), not go into details here.

By (2) combined with Figure 3, we can establish the time-varying model as follows:

$$\begin{cases} \dfrac{d\dot{\varphi}(t)}{dt} = \dot{E} - \dot{U}_C - j\omega_0\dot{\Phi} - R\dot{I} \\ \dfrac{d\dot{U}_C}{dt} = \dfrac{\dot{I}}{C} - j\omega_0\dot{U}_C \\ \dot{I} = G(\dot{\Phi}) \end{cases} \tag{3}$$

When the system is running at the equilibrium point, that is,

$$\begin{cases} \dfrac{d\dot{\Phi}(t)}{dt} = \dot{E} - \dot{U}_C - j\omega_0\dot{\Phi} - R\dot{I} = \dot{E} - \Delta\dot{U}(\dot{\Phi}) = 0 \\ \dfrac{d\dot{U}_C}{dt} = \dfrac{\dot{I}}{C} - j\omega_0\dot{U}_C = 0 \end{cases} \tag{4}$$

By (3) and (4), we can obtain:

$$\Delta\dot{U}(\dot{\Phi}) = j\omega_0\dot{\Phi} - j\frac{G(\dot{\Phi})}{\omega_0 C} = \dot{U}_L(\dot{\Phi}) - \dot{U}_C(\dot{\Phi}) \tag{5}$$

2.3. The Balance Point

Changing the form of Equation (5), we can get the following equation:

$$\begin{cases} \Delta\dot{U} = \dot{U}_C - \dot{U}_L \\ \dot{U}_C = \dfrac{G(\dot{\Phi})}{j\omega_0 C} \\ \dot{U}_L = j\omega_0\dot{\Phi} \end{cases} \Rightarrow \begin{cases} \Delta U = |U_C - U_L| \\ U_C = \dfrac{G(\dot{\Phi})}{\omega_0 C} \\ U_L = j\omega_0\dot{\Phi} \end{cases} \tag{6}$$

Through the Equation (6), in the system the relationship between parameters and flux linkage can be showed in the picture 4.

In picture, the x-coordinate represents the flux linkage, the y-coordinate represents the voltage, the blue dashed line represents the voltage across the nonlinear inductance, the green dashed line represents the voltage across the capacitor, the red curve represents ΔU, the green solid line represents the system voltage.

From the picture, we conclude that the A, B and C points are three balance points of the system, two points among them are stable balance point (A and C), another is unstable balance point (B), it is impossible for the system to operate at the unstable balance point. of the stable balance points, one is normal operating point (A), and the other is stable resonance point (C).

The transient resonance is caused by the system oscillation at the stable balance point, the oscillation frequency depends on the operating point and the capacitance, the oscillation amplitude is determined by the disturbance quantity, the amplitude and frequency of the flux linkage directly influence the over-voltage size.

Whether the stable resonance happens, network parameters and operation parameters play a decisive role, most important parameters are C and Φ. If C can be adjusted according to the Φ at the normal operation point, to make the ΔU curve monotone, then the system will lack the resonance condition. From the qualitative analysis, we can draw the conclusion that the smaller and bigger C can make the curve monotone, which is also consistent with the Peterson Theorem.

2.4. The Equal Area Rule

Section 2.3 shows the relationship between system resonance and parameters through the static analysis of the system, and also put forward two balance points, one is normal working point, another is stable resonance point. But the qualitative analysis is not enough, only quantitative resonance condition or resonance criterion can put forward methods to solve the resonance problem, to reduce economic losses. So the equal area rule play an essential role in system dynamic analysis.

In following picture, the x-coordinate represents flux linkage (P.U), the y-coordinate represents voltage (P.U), the blue solid curve represents initial voltage E_0, the green solid curve represents post-disturbance voltage E. A, A' and C' respectively represent the normal working point at the initial voltage, the normal working point and resonance point at the post-disturbance voltage point.

In order to better solve resonance problem, we introduce the Eaqual Area Rule, defining the black area to acceleration area (S_2) and red area to deceleration area which is stability margin (S_1). If the acceleration area is larger than the deceleration area, the system can enter the resonance zone, and the system will operate at the C point, which result the happening of stable resonance; on the contrary, the system will operate at the A' point. At the same time, because $\dot{I} = \dot{G}(\Phi)$ is time variant, the Equal Area Rule is time variant, that is to say, if the acceleration area is bigger than the deceleration area, then the system satisfies the resonance condition, and if the time of disturbance is appropriate, the resonance will happen, and the system will operate at the resonance point. So if the time of disturbance is appropriate and the system satisfies the following condition:

When $S_2 > S_1$, the system can enter resonance condition, and operates at resonance balance point C';

When $S_2 > S_1$, the system can not enter resonance condition, and operates at the normal working point;

When $S_2 = S_1$, the system is at the critical resonance state.

If we define the energy function S (calculating area) is as follows:

$$S = \int_a^b |\Delta U - E| d\varphi \tag{7}$$

where a, b are the x-coordinates of balance points (A, A') for acceleration area, and balance points (A', B') for deceleration area, ΔU is the Equation (6).

2.5. Experiment Example and Simulation Verdication

We establish a simple series resonant modethe fault type is the voltage rise, as shown below:

U_1 is the initiative voltage, and U_2 is the risen voltage at last, in the simulation we let $U_2 = 3000\,\mathrm{V}$, the a switch's working time is $-1 \sim$ ts and the b switch's working time is $t \sim 10\,\mathrm{s}$, and $R = 6000\,\Omega$, $C = 0.011\,\mathrm{Uf}$, the excitation characteristic curve of nonlinear inductance is as follows (calculated under p.u):

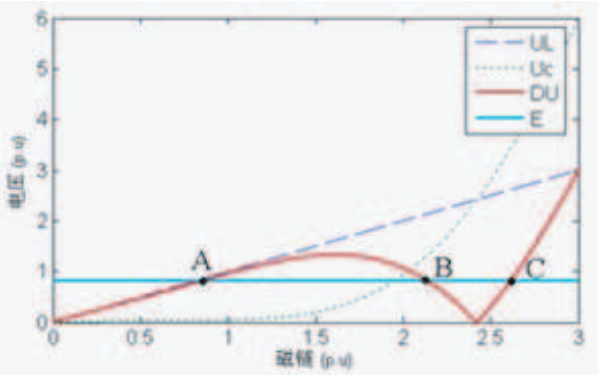

Figure 4: ΔU and the flux.

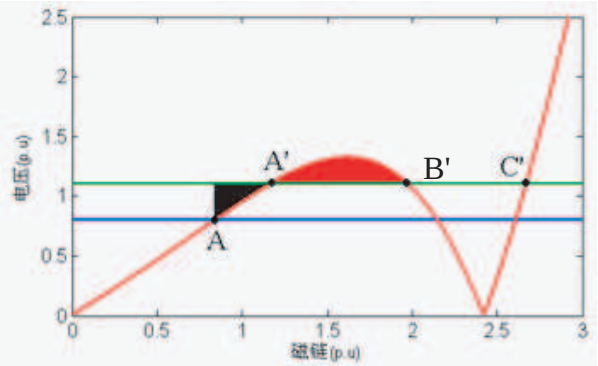

Figure 5: Analysis of the equal area.

From the Equation (8), three balance points can be got:

Where E is the voltage of source.

Through the MATLAB program, we can get $A' = 1.049$ and $B' = 1.434$. According to the Equation (7), we can get $S_1 = 0.0212$, the critical voltage which satisfies $S_2 = S_1$ is $U_1 = 2321.3\,\mathrm{V}$.

According the theory of Equal Area Rule, at the appropriate time, when $U_1 < 2321.3\,\mathrm{V}$, that is $S_2 > S_1$,

$$\Delta U = |U_C - U_L| = E \tag{8}$$

the system can enter resonance condition; when $2321.3\,\mathrm{V} < U_1 < 3000\,\mathrm{V}$, that is $S_2 < S_1$, the system can return to the normal working point A'.

1) when $t = 0.223\,\mathrm{s}$, $U_1 = 1500\,\mathrm{V}$, other conditions don't change, the current is as Figure 8;
2) when $t = 0.222\,\mathrm{s}$, $U_1 = 2000\,\mathrm{V}$, other conditions don't change, the current as Figure 9;
3) when $t = 0.01\,\mathrm{s}$, $U_1 = 2000\,\mathrm{V}$, other conditions don't change, the current is as Figure 10;
4) when $t = 0.012\,\mathrm{s}$, $U_1 = 2500\,\mathrm{V}$, other conditions don't change, the current is as Figure 11.

Contrast to Figure 8, Figure 9 and Figure 11, the Equal Area Rule theory is validated; contrast to Figure 9 and Figure 10, we can validate that the fault time influence the happening of the resonance. Through the four pictures, we find that the time variant Equal Area Rule is applicable in resonance problem, which provide an important theoretical basis for avoiding resonance.

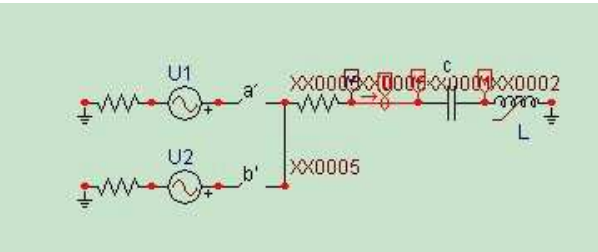

Figure 6: Model of the equal area rule.

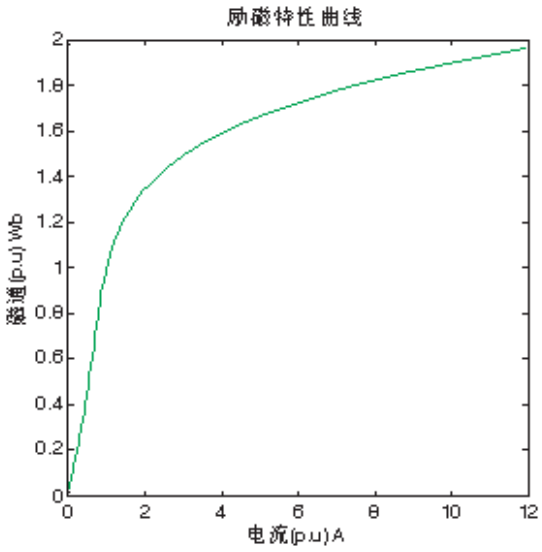

Figure 7: The fitting excitation curve.

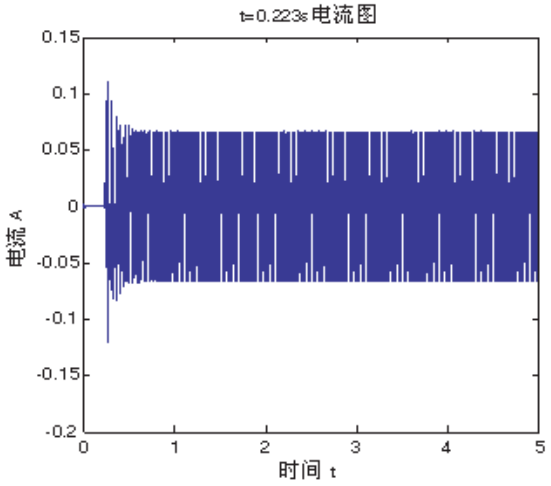

Figure 8: The current waveform at $U_1 = 1500\,\mathrm{V}$.

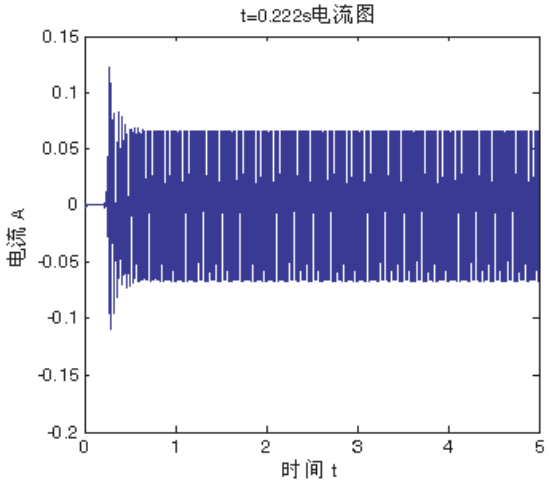

Figure 9: The current waveform at $U_1 = 2000\,\mathrm{V}$.

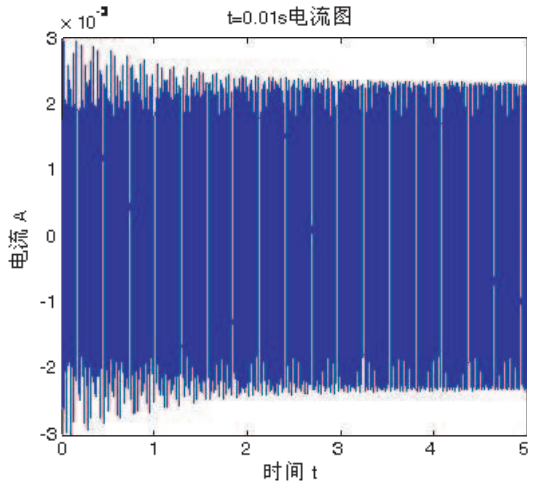

Figure 10: The current waveform at $U_1 = 2000\,\mathrm{V}$.

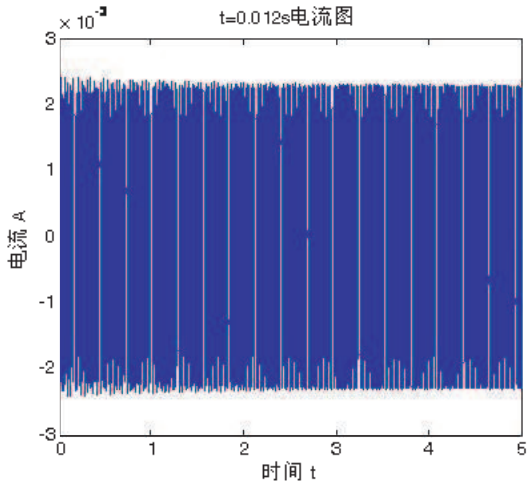

Figure 11: The current waveform at $U_1 = 2500\,\mathrm{V}$.

3. CONCLUSION

The paper first introduce the new conception of time-variant vector, and establish time-variant vector mathematical model of a simple series resonance model, on the basis of it, we put forward the conclusion of three balance points (one is normal working point, one is unstable working point, another is frequency resonance point).

Secondly, on the basis of static analysis, we define the energy function, and make dynamic analysis to the system. We put forward the Equal Area Rule on the Basis of time-variant vector, and we calculate the stability margin S_1 through MATLAB and ATP:

When the acceleration area is larger than S_1, we find the industrial frequency resonance point through simulation.

When the acceleration area is smaller than S_1, the system operates at the normal working point.

In summation, we validate the correctness and practicality of the Equal Area Rule in the analysis of resonance problem, which provides theoretical basis for the future research of restraining resonance.

REFERENCES

1. Yang, Q.-X., "The digital simulation of ferroresona ce in power system and wavelet analysis," *Journal of North China Electric Power University*, Beijing, 2001.
2. Jin, X.-F. and Z.-K. Li, "Research review on ferroresonance in power systerm," *Sichuan Electric Power Technology*, No. 1, 2004.
3. Zhang, X.-D., H.-L. Zhang, and Y. Li, "Danger distinction and prevention and cure treatment

on ferro-re- sonance in electricity system," *Journal of Electric Power*, Vol. 17, No. 4, 283–286, 2002.
4. Marti, J. R., "Soudack AC. Ferro resonance in power system: Fundamental solution," *IEE Proceedings*, Vol. 1–38, No. 4, 321–329, 1991.
5. Marti, J. R. and A. C. Soudack, "Ferroresonance in power system fundamental solution," *IEE Proceedings*, Vol. 1–38, No. 4, 321–329, 1991.
6. Ma, S.-X., "Brief introduction to an accident resulted from ferroresonance at 220 kV Dongshan substation," *Ningxia Electric Power*, No. 1, 56–58, 1995.
7. Shi, F., "Analysis of ferroresonance happening on the deenergized busbars at 110–220 kV substations," *Hunan Electric Power*, Vol. 21, No. 1, 14–16, 2001.
8. Li, Y.-G. and W. Shi, "Novel analytical solution to fundamental ferroresonance in grounded neutral system solution to the power frequency excitat ion characteristic of non-linear inductors," *Proceeding of the CSEE*, Vol. 23, No. 10, 94–98, 2003.
9. Li, Y.-G. and W. Shi, "Study of fundamental ferro-resonance on neutral-grounded systems by using analytical method criterion and elimination," *Proceeding of the CSEE*, Vol. 23, No. 9, 141–145, 2003.
10. Shi, Q.-X. and S.-T. Tan, "Digital simulation analysis of ferroresonance of electromagnetic potential transformer based on matlab," *High Voltage Engineering*, Vol. 30, No. 8, 25–27+49, 2004.
11. Lu, F.-C., X.-W. Du, Y.-P. Liu, and J. Wang, "Simulation and resonance erasing measurement for ferroresonance of neutral grounding system based on ATP-EMTP," *Journal of North China Electric Power University*, Vol. 33, No. 2, 1–4, 2006.
12. Wang, H.-T., C.-X. Dou, N. Wang, H.-U. Xue, and Q.-Q. Jia, "Research on PT ferroresonance and resonance elimination measures based on ATP-EMTP," *Transformer*, Vol. 45, No. 3, 24–28, 2008.
13. Ge, D., T.-C. Lu, and P. Wang, "Study on simulation calculation of ferroresonance elimination in power distribution system," *High Voltage Engineering*, Vol. 29, No. 11, 17–19, 2003.
14. Yang, Q.-X., W. Zong, and B.-Y. Tian, "Detection of ferromagnetic resonanance based on wavelet analysis," *Power System Technology*, Vol. 25, No. 11, 55–61, 2001.
15. Liu, F., C.-X. Sun, and M.-W. Si, "Theoretical analysis of chaotic oscillation of ferroresonance overvoltage in power systems," *Transactions of China Electrotechnical Society*, Vol. 21, No. 2, 103–107, 2006.
16. Zahawi, B. A. T. A., Z. Emin, and Y. K. Tong, "Chaos in Frroresonant wound voltage transformer effect of core losses and universal circuit behavior," *IEE Proc. Sci. Meas. Technol.*, Vol. 145, No. 1, 39–43, 1998.
17. Emin, Z., B. A. T. A. Zahawi, D. W. Auckland, and Y. K. Tong, "Ferroresonance in electromagnetic voltage transformers: A study based on nonlinear dynamics," *IEE Proc. Gener. Transm. Distrib.*, Vol. 144, No. 4, 383–387, 1997.
18. Zhang, B., T.-C. Lu, and X.-L. Du, "Nonlinear dynamic analysis of ferroresonance in neutral-grounded power system," *High Voltage Engineering*, Vol. 33, No. 1, 31–35, 2007.
19. Soudack, A. C., "Ferroresonance in power system and chaos behavior," *IEE Proc. Sci. Technol.*, Vol. 140, No. 3, 62–64, 1993.
20. Jacobson, D. A. N., P. W. Lehn, and R. W. Menzies, "Stability domain calculations of period ferroresonance in a nonlinear resonant circuit," *IEEE Trans. on Power Delivery*, Vol. 17, No. 3, 865–871, 2002.

High Input Impedance Electronically Tunable Voltage-mode Multifunction Filter

Hua-Pin Chen[1], **Wei Chien**[2], **Chi-Hsien Sun**[3], **Chien-Ching Chiu**[3], **and Yi Sun**[4]

[1]Department of Electronic Engineering, Ming Chi University of Technology, Taiwan
[2]Department of Electronic Engineering, De Lin Institute of Technology, Tu-Cheng, Taipei, Taiwan
[3]Department of Electronic Engineering, Tamkang University, Tamsui, Taiwan
[4]School of Electrical Engineering, Beijing Jiaotong University, Beijing, China

Abstract— A new high input impedance electronically tunable voltage-mode multifunction filter with single input and three outputs employing two single-output current-controlled current conveyors, one differential difference current conveyor and two grounded capacitors is proposed. The proposed filter can be realized the second-order highpass, bandpass and lowpass filter functions simultaneously without component matching conditions. The input of the filter exhibits high input impedance so that the synthesized filter can be cascaded without additional buffers. The proposed circuit employing two grounded capacitors which is very suitable to further develop into an integrated circuit implementation. The parameter sensitivities are very low and the structure does not employ external resistors thus is an active-C filter. HSPICE simulation results based on using TSMC 0.35 μm CMOS model are included to verify the theoretical analysis.

1. INTRODUCTION

Voltage-mode filters employing current conveyors have been receiving attention nowadays. Moreover, it is good for a circuit to employ only grounded passive elements especially grounded capacitors and not require passive component-matching conditions thus it is convenient for fully integrated circuit technology. Second generation current controlled conveyors (CCCIIs) have recently become popular for realizing tunable functions as their port-X tunable resistance can be controlled through the bias current of conveyor. Thus several electronic functions using these devices have been reported in the literature [1–9]. On the other hand, the use of differential difference current conveyors (DDCCs) in filters design has received considerable attention because its can utilize the addition and subtraction operators at the port X terminal [10–16]. Of particular interest here is the use of CCCIIs and DDCC for designing an electronically tunable high input impedance voltage-mode multifunction biquadaitic filter. Also, active filters with high input impedance are of great interest because it can be easily cascaded to synthesize high-order filters [17–20].

In 2004, Horng et al. proposed a high input impedance voltage-mode highpass, bandpass and lowpass filters, simultaneously, by using two DDCCs, two grounded capacitors and two grounded resistors. However, it locks of electronic tunability [13]. In this paper, a new high input impedance electronically tunable voltage-mode multifunction filter with single input and three outputs using two single-output current-controlled conveyors and two grounded capacitors is proposed. The proposed configuration does not employ external resistor thus is an active-C filter. Meanwhile, using CCCII to replace resistor, we can reduce the chip area effectively. The circuit can simultaneously obtain second-order highpass, bandpass and lowpass filter responses and still exhibits the following advantage features: (i) the employment two grounded capacitors ideal for integrated circuit implementation, (ii) high input impedance good for cascadability for the voltage-mode circuits, (iii) no need to impose component choice, (iv) no need to employ inverting-type current input signals and (v) low active and passive sensitivity performances.

2. CIRCUIT DESCRIPTION

The CCCII can be characterized by the port relations with $I_Y = 0$, $V_X = V_Y + I_X R_X$ and $I_Z = \pm I_X$, where the parasitic resistance $R_X = V_T/2I_o$, V_T is the thermal voltage, I_o is bias current of CCCII, the sign $\pm$ refers to plus or minus type CCCII, respectively. The plus-type DDCC can be characterized by the port relations with $V_X = V_{Y1} - V_{Y2} + V_{Y3}$ and $I_{Z+} = I_X$ [2]. The proposed circuit, as shown in Figure 1, employs two CCCIIs, one DDCC and two grounded

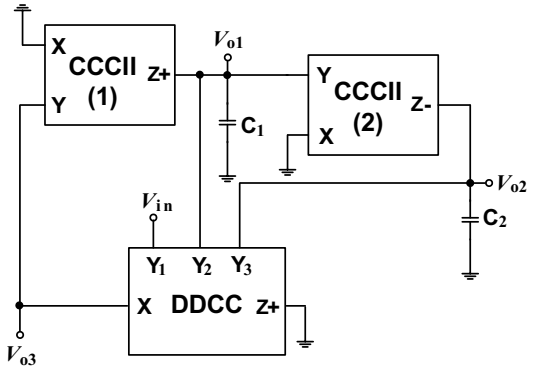

Figure 1: The proposed single-input three-output voltage-mode multifunction filter.

capacitors. Circuit analysis yields the following voltage-mode filter transfer function:

$$\frac{V_{o1}}{V_{in}} = \frac{sC_2G_{X1}}{s^2C_1C_2 + sC_2G_{X1} + G_{X1}G_{X2}} \tag{1}$$

$$\frac{V_{o2}}{V_{in}} = \frac{-G_{X1}G_{X2}}{s^2C_1C_2 + sC_2G_{X1} + G_{X1}G_{X2}} \tag{2}$$

$$\frac{V_{o3}}{V_{in}} = \frac{s^2C_1C_2}{s^2C_1C_2 + sC_2G_{X1} + G_{X1}G_{X2}} \tag{3}$$

Thus, we can obtain a non-inverting bandpass, an inverting lowpass and a non-inverting highpass filter response at the output voltages, V_{o1}, V_{o2} and V_{o3}, respectively.

In all cases the resonance angular frequency ω_o and quality factor Q are given by

$$\omega_o = \sqrt{\frac{G_{X1}G_{X2}}{C_1C_2}} \quad \text{and} \quad Q = \sqrt{\frac{C_1G_{X2}}{C_2G_{X1}}} \tag{4}$$

A sensitivity study forms an important index of the performance of any active network. The formal definition of sensitivity is

$$S_x^F = \frac{x}{F}\frac{\partial F}{\partial x} \tag{5}$$

where F represents one of ω_o, Q and x represents any of the passive elements (G_{X1}–G_{X2}, C_1–C_2). Using the above definition the resonance angular frequency ω_o and quality factor Q sensitivities are given as

$$S_{G_{X1}}^{\omega_o} = S_{G_{X2}}^{\omega_o} = -S_{C_1}^{\omega_o} = -S_{C_2}^{\omega_o} = \frac{1}{2} \tag{6}$$

$$S_{C_1}^{Q} = S_{G_{X2}}^{Q} = -S_{C_2}^{Q} = -S_{G_{X1}}^{Q} = \frac{1}{2} \tag{7}$$

Hence, the filter parameter sensitivities are low and not large than 0.5 in absolute value.

3. SIMULATION RESULTS

Finally, to verify the theoretical prediction of the proposed universal voltage-mode filter, a simulation using HSPICE with TSMC 0.35 µm process was performed. The CMOS implementation of a CCCII is shown in [5]. The aspect ratios (W/L) of the MOS transistors were taken as 20/0.35 for M1, M2; 60/0.35 for M3, M4, 30/2 for M5, M6, M7, 10/2 for M8, M9, 10/1 for M10, M11, M16, M17, 30/1 for M12, M13, M14, M15. The supply voltages are $V_{DD} = -V_{SS} = 1.65\,\text{V}$. The MOS implementation of a DDCC is shown in [11] with the NMOS and PMOS transistor aspect ratios ($W/L = 5\mu\text{m}/1\mu\text{m}$) and ($W/L = 10\mu\text{m}/1\mu\text{m}$), respectively. The supply voltages are $V_{DD} = -V_{SS} = 1.65\,\text{V}$ and the biasing voltages are $V_{B1} = -0.25\,\text{V}$ and $V_{B2} = -0.65\,\text{V}$, respectively. Figure 2 shows the simulated amplitude responses for the highpass (HP), bandpass (BP) and lowpass (LP) filters with $I_{o1} = I_{o2} = 50\,\mu\text{A}$ and $C_1 = C_2 = 500\,\text{pF}$, leading to a center frequency of $f_o = 570\,\text{kHz}$ and quality factor of $Q = 1$. It appears from Figure 2 that the simulation results agree well with theoretical analysis.

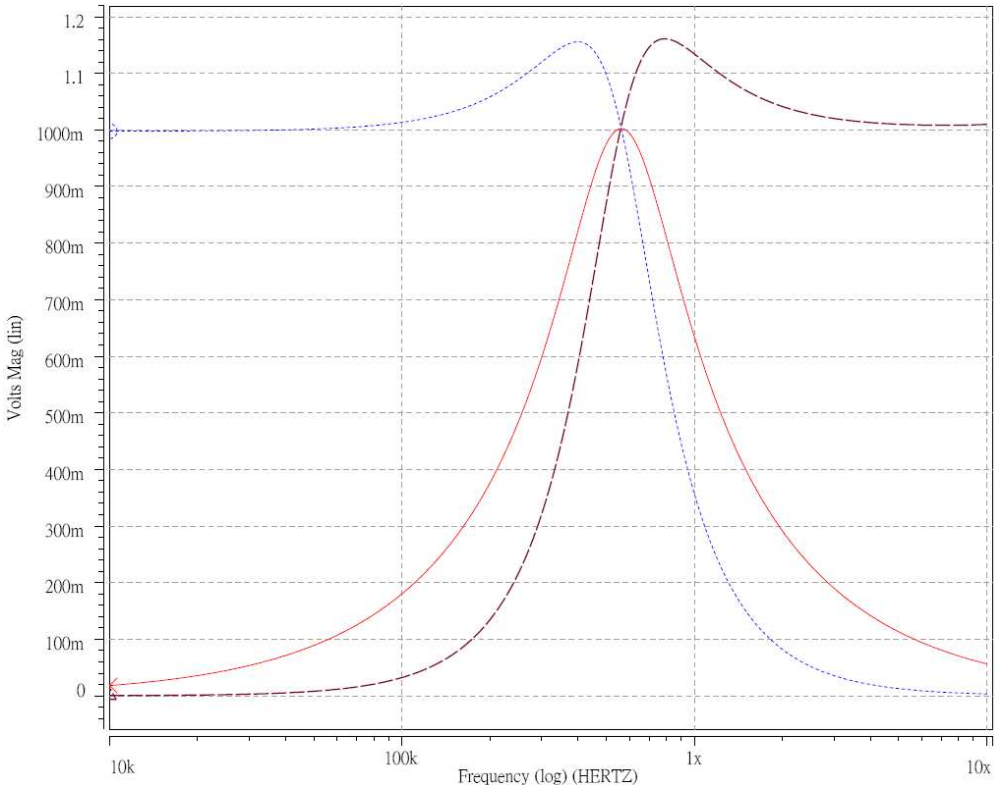

Figure 2: The highpass, bandpass and lowpass amplitude-frequency responses of Figure 1.

4. CONCLUSION

In 2004, Horng et al. presented a good voltage-mode multifunction filter with a single input and three outputs using two DDCCs, two grounded capacitors and two grounded resistors [13]. It can simultaneously obtain highpass, bandpass and lowpass filter responses. In this paper, the author also proposed a high input impedance multifunction voltage-mode biquadratic filter. The proposed configuration can also simultaneously obtain highpass, bandpass and lowpass filtering signals. It offers two more advantages compared with recently proposed by Horng et al. [13]: (i) it requires no external resistor thus is an active-C filter and (ii) the resonance angular frequency ω_o and quality factor Q are electronically adjustable.

ACKNOWLEDGMENT

This work was supported by National Science Council, Republic of China, under Grant NSC-98-2221-E-131-027.

REFERENCES

1. Fabre, A., O. Saaid, F. Wiest, and C. Boucheron, "High frequency applications based on a new current controlled conveyor," *IEEE Trans. Circuits Syst. — I*, Vol. 43, No. 2, 82–91, 1996.
2. Abuelmaatti, M. T. and M. A. Alqahatani, "A new current-controlled multiphase sinusoidal oscillator using translinear current conveyors," *IEEE Trans. Circuits Syst. — II*, Vol. 45, No. 7, 881–885, 1998.
3. Minaei, S. and S. Turkoz, "New current-mode current controlled universal filter with single input and three outputs," *Int. J. Electron.*, Vol. 88, No. 3, 333–337, 2001.
4. Horng, J. W., "A sinusoidal oscillator using current controlled conveyors," *Int. J. Electron.*, Vol. 88, No. 6, 659–664, 2001.
5. Altuntas, E. and A. Toker, "Realization of voltage and current mode KHN biquads using CCCIIs," *Int. J. Electron. Commun. (AEÜ)*, Vol. 56, No. 1, 45–49, 2002.
6. Sagbas, M. and K. Fidanboylu, "Electronically tunable current-mode second-order universal filter using minimum elements," *Electron. Lett.*, Vol. 40, No. 1, 2–4, 2004.

7. Tangsrirat, W., "Current-tunable current-mode multifunction filter based on dual-output current-controlled conveyors," *Int. J. Electron. Commun. (AEÜ)*, Vol. 61, No. 8, 528–533, 2007.
8. Yuce, E. and S. Minaei, "Universal current-mode filters and parasitic impedance effects on the filter performances," *Int. J. Circuit Theory Appl.*, Vol. 36, No. 2, 161–171, 2008.
9. Sedef, H., M. Sagbas, and C. Acar, "Current-controllable fully-integrated inductor simulator using CCCIIs," *International Journal of Electronics*, Vol. 95, No. 5, 425–429, 2008.
10. Chiu, W., S. I. Liu, H. W. Tsao, and J. J. Chen, "CMOS differential difference current conveyors and their applications," *IEE Proc. — Circuits Devices Syst.*, Vol. 143, No. 2, 91–96, 1996.
11. Ibrahim, M. A. and H. Kuntman, "A novel high CMRR high input impedance differential voltage-mode KHN-biquad employing DO-DDCCs," *Int. J. Electron. Commun. (AEÜ)*, Vol. 58, No. 6, 429–433, 2004.
12. Chang, C. M. and H. P. Chen, "Universal capacitor-grounded voltage-mode filter with three inputs and a single output," *Int. J. Electron.*, Vol. 90, No. 6, 401–406, 2003.
13. Horng, J. W., W. Y. Chui, and H. Y. Wei, "Voltage-mode highpass, bandpass and lowpass filters using two DDCCs," *Int. J. Electron.*, Vol. 91, No. 8, 461–464, 2004.
14. Chen, H. P., "Universal voltage-mode filter using only plus-type DDCCs," *Analog Integr. Circuits and Signal Process.*, Vol. 50, No. 2, 137–139, 2007.
15. Chiu, W. Y. and J. W. Horng, "High-input and low-output impedance voltage-mode universal biquadratic filter using DDCCs," *IEEE Trans. Circuits Syst. — II*, Vol. 54, No. 8, 649–652, 2007.
16. Horng, J. W., "High input impedance voltage-mode universal biquadratic filter with three inputs using DDCCs," *Circuits Syst. Signal Process.*, Vol. 27, No. 4, 553–562, 2008.
17. Liu, S. I. and H. W. Tsao, "The single CCII biquads with high-input impedance," *IEEE Trans. Circuits Syst.*, Vol. 38, No. 4, 456–461, 1991.
18. Fabre, A., F. Dayoub, L. Duruisseau, and M. Lamoun, "High input impedance insensitive second-order filters implemented from current conveyors," *IEEE Trans. Circuits Syst. — I: Fundamental Theory Applications*, Vol. 41, No. 12, 918–921, 1994.
19. Horng, J. W., "High-input impedance voltage-mode universal biquadratic filter using three plus-type CCIIs," *IEEE Trans. Circuits Syst. — II: Analog Digital Signal Process.*, Vol. 48, No. 10, 996–997, 2001.
20. Ibrahim, M. A., H. Kuntman, and O. Cicekoglu, "Single DDCC biquads with high input impedance and minimum number of passive elements," *Analog Integr. Circuits and Signal Process.*, Vol. 43, No. 1, 71–79, 2005.

The Loop Ring BSF Design and Its Application in BPF Stopband Enhancement

Min-Hua Ho and Yi-Chao Lin
Graduate Institute of Communications Engineering, National Changhua University of Education, Taiwan

Abstract— The microstrip loop ring structure was investigated for the bandstop filter (BSF) design. This structure alone or together with the traditional quarter-wavelength open stub created a band rejection response. The ring was in a rectangular shape with its circumference dimension being one wavelength or one and half wavelengths. The rectangular loop's each side might have different width. Transmission line model was derived for the loop structure with or without the attached open-stubs. The application of the loop BSF in enhancing the stopband bandwidth (BW) for a BPF of coupled-lines structure was demonstrated. The frequency responses calculated from the transmission line model were compared with those obtained from commercial electromagnetic software. Experiment was conducted to validate the circuit design.

1. INTRODUCTION

Higher harmonics exist in the filters of distributive structures always limit their applications in some modern wireless communication systems. Many solutions have been proposed to deal with the unwanted harmonics or very limited stopband. For example, the stepped-impedance resonator (SIR) proposed by Makimoto and Yamashita [1] pushed resonator's second harmonic to a higher frequency and hence increased the filter's upper stopband limit. Kuo and Shih [2] controlled the feed position of the SIR filter to optimally extend the rejection BW. In [3, 4], shunt-open-stubs of quarter wavelength or half wavelength were employed in the coupled-lines filters to create controllable transmission zeros in the stopband, which expanded the stopband region. To suppress the coupled-lines' second resonance, [5] reformed the straight coupling edge to a periodical one in the coupling zone to compensate the discrepancy of even- and odd-mode phase velocity.

Intuitively, a BSF were used to suppress the signal at the interesting frequency band. As a result of that, a BPF was usually connected with a bandstop structure, which might also guarantee the stopband performance while the latter rejected signal at the former's stopband region. The traditional bandstop structures composed of a few quarter-wavelength spaced open stubs (stubs also in quarter-wavelength dimension) which shunted to a straight line [6]. In [7], the open stub together with the spurline was used to build a compact BSF. However, this structure belonged to narrow band operation. The wide-band structures were commonly seen in defected ground configuration [8]. Recently, two compact end-loaded coupled-lines filter structures, which distinguished by presence or absence of open-stubs [9, 10], could achieve an extremely wide stopband performance. The coupled lines were anti-parallel coupled form with their non-I/O ends shorting to a loading line. In [11], Hsieh and Chang discovered that a loop ring in conjunction with tuning stubs might suppress signals over a wide frequency range. Three of the distinct loop rings cascading in series form a wide-band BPF with sharp band-edge rejection.

In this paper, we proposed a BSF of loop ring structure. The loop ring was in a rectangular shape with its four sides built from lines of two different impedances. The circumference length of the loop was one or one and half wavelengths. Without deteriorating its performance, a tuning stub might attach to the corner of the rectangular loop to slightly increase the signal rejection zone. The transmission line model was developed to design the filter. The effect of varying the lines' impedances was investigated. By changing the impedance of the lines, we could control the BSF's BW. The calculated data from the transmission line model was verified by the HFSS software package [12], and the experiments were conducted to validate the circuit design and its performance. To demonstrate its application in suppressing the unwanted harmonics, the traditional parallel coupled-lines BFP cascaded the developed BSF for eliminating the former's second harmonic. The combined structure successfully enhanced the BPF's stopband performance and dramatically increased the stopband BW.

2. THE TRANSMISSION LINE MODEL

Shown in Fig. 1 is the proposed loop ring BSF structure with its side branches having two different impedances. The branches have the characteristic impedance and electrical length Z_{0i}, and θ_i,

$i = 1, 2$. Each branch route has the $ABCD$ matrix form representing a transmission line as

$$M_i = \begin{bmatrix} \cos\theta_i & jZ_{0i}\sin\theta_i \\ jY_{0i}\sin\theta_i & \cos\theta_i \end{bmatrix},\ i = 1,\ 2 \tag{1}$$

The $ABCD$ matrices corresponding to the upper and lower route between the I/O ports are then taking the forms M_1 and $M_T = M_2M_1M_2$, respectively. The $ABCD$ matrices convert to their corresponding Y matrices and add up to form the Y matrix of the loop ring BSF. The overall S-parameter matrix of the transmission is conformed from transmission line Y. By performing the procedure, we have the transmission line's S_{11} and S_{21} as

$$S_{11} = \frac{(Y_0 - Y_{11})(Y_0 + Y_{11}) + Y_{12}Y_{21}}{(Y_0 + Y_{11})(Y_0 + Y_{22}) - Y_{12}Y_{21}}, \tag{2}$$

$$S_{21} = \frac{-2Y_{21}Y_0}{(Y_0 + Y_{11})(Y_0 + Y_{22}) - Y_{12}Y_{21}} \tag{3}$$

with Y_0 denoting the characteristic admittance of I/O and the elements of Y matrix given as

$$Y_{11} = Y_{22} = -\frac{j\cos\theta_1}{Z_{01}\sin\theta_1} - \frac{j\left\{\cos\theta_1\cos 2\theta_2 - 0.5\sin\theta_1\sin\theta_2(Y_{01}Z_{02} + Z_{01}Y_{02})\right\}}{Z_{02}\cos\theta_1\sin\theta_2 + \sin\theta_1(Z_{01}\cos^2\theta_2 - Y_{01}Z_{02}^2\sin^2\theta_2)} \tag{4}$$

$$\begin{aligned} Y_{12} = {} & \frac{j}{Z_{01}\sin\theta_1} + j\left\{Y_{02}\cos\theta_1\sin 2\theta_2 + \sin\theta_1\left(Y_{01}\cos^2\theta_2 - Z_{01}Y_{02}^2\sin^2\theta_2\right)\right\} \\ & + \frac{j\left\{\cos\theta_1\cos 2\theta_2 - 0.5\sin\theta_1\sin\theta_2(Y_{01}Z_{02} + Z_{01}Y_{02})\right\}^2}{Z_{02}\cos\theta_1\sin\theta_2 + \sin\theta_1\left(Z_{01}\cos^2\theta_2 - Y_{01}Z_{02}^2\sin^2\theta_2\right)} \end{aligned} \tag{5}$$

$$Y_{21} = \frac{j}{Z_{01}\sin\theta_1} + \frac{j}{Z_{02}\cos\theta_1\sin\theta_2 + \sin\theta_1\left(Z_{01}\cos^2\theta_2 - Y_{01}Z_{02}^2\sin^2\theta_2\right)} \tag{6}$$

To investigate the effects of branch impedance variations to the frequency responses, we change the impedance of Z_{01} or Z_{02} in the applied transmission line equations to calculate the proposed BSF's frequency responses. In Fig. 2, we give the calculated frequency responses with varying Z_{01} and Z_{02} for Figs. 2(a) and 2(b), respectively. In Fig. 2(a), the Z_{01} is fixed to $50\,\Omega$ and $Z_{02} = 50\,\Omega$ in Fig. 2(b). The circumference's electrical length of the loop ring is one and half wavelengths with Z_{01} sections half wavelengths of and the one of Z_{02} quarter wavelengths at the frequency of 2 GHz. The proposed BSF possesses three transmission zeros and the effective rejection BW is mainly formed by those zeros. It is evidenced from the figures that the filter's second zero remains fixed and its first and the third zero vary while changing Z_{01} or Z_{02}. In Fig. 2(a), the lower impedance of Z_{01} causes a wider separation between the first and the second zeros, results in a larger rejection BW. The drawback is less signal rejection levels. In Fig. 2(b), a higher Z_{02} arises a wider BW which is contrary to Z_{01}'s effect. It should be concluded from the figures that a larger ratio of Z_{01}/Z_{02} causes a deeper signal rejection levels but comes along with a smaller rejection BW.

Figure 3 shows the transmission line model of the loop ring structure with a corner tapped by an open stub. The electrical length of the loop's circumference is one wavelength which is half wavelength shorter than the one in Fig. 1. Each individual branch of loop ring and the open stub are in quarter-wavelength dimension. The circuit size is slightly reduced and the open stub can be bended to further lessen circuit dimension.

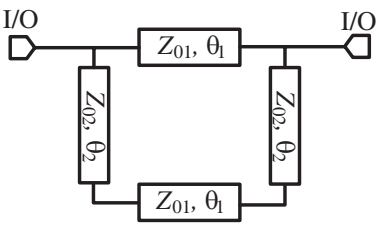

Figure 1: The loop ring BSF's transmission line structure.

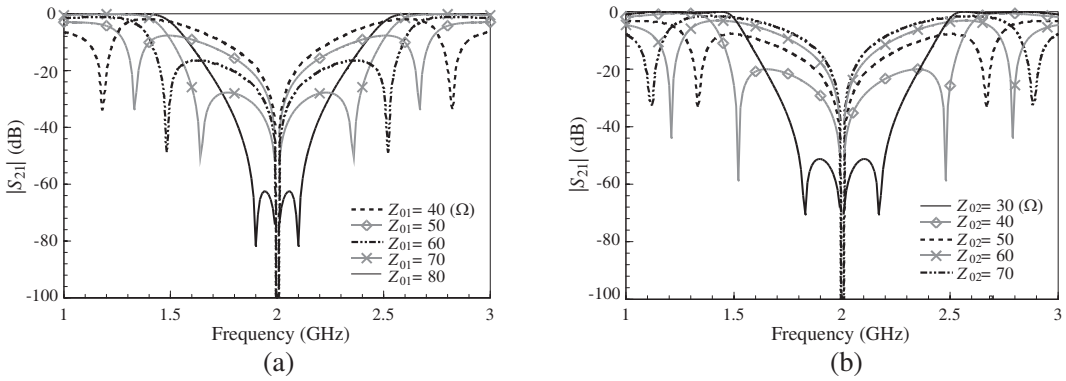

Figure 2: The calculated frequency responses with varying (a) Z_{01} and (b) Z_{02}.

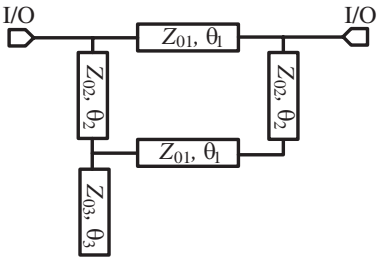

Figure 3: The open-stub attached loop-ring BSF structure.

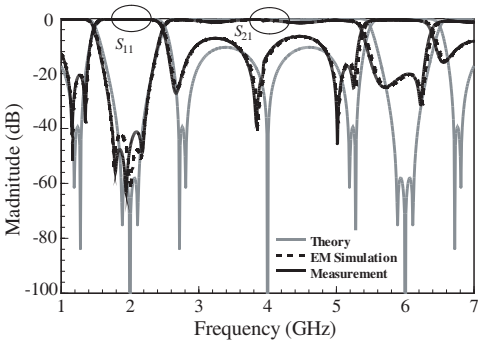

Figure 4: The wide-band scope of the calculated and measured frequency responses for the BSF in Fig. 1.

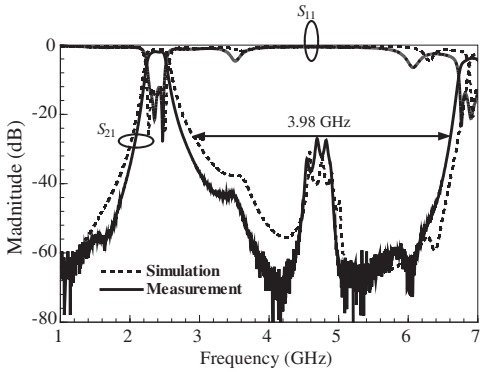

Figure 5: The plots of simulated and measured frequency responses for the BPF and BSF cascaded structure.

3. SAMPLE RESULTS

The experimental circuit of Fig. 1 is built on a 0.635 mm thickness RT/Duroid substrate with a dielectric constant 10.2 and a loss tangent 0.0023. In Fig. 4, we show the wide-band scope of the frequency responses obtained from the transmission line model, HSFF simulation, and the experimental measurement. The impedance values of Z_{01} and Z_{02} are 53 and 83 Ω, respectively. It is observed that the BSF has its operation band repeated every $2f_0$ (here $f_0 = 2$ GHz). The data based on the transmission line model agree quite well with the ones obtained from HFSS and measurement. The filter's first rejection band has most of its measured rejection levels greater than 40 dB which provide a good bandstop effect. As we expected that the second rejection band has its bandstop effect inferior to the first one. The insertion losses of the passband between the two stop-bands are insignificant. Not shown in figure, the frequency response of Fig. 3 is similar to the ones in Fig. 4.

To demonstrate the application of the BSF in the BPF's stopband enhancement, the latter is cascaded to the former for suppressing the undesired harmonic. The traditional parallel-coupled-lines BPF with 2.45 GHz central frequency is built for the WLAN applications. The cascaded BSF has its central operation frequency at 4.8 GHz to suppress the second harmonic suppression of the

coupled-lines structure. In Fig. 5, we show the simulated and measured frequency responses for the filter. Again, the agreement between the simulation and measurement is achieved. The BPF has its measured stopband BW (defined by rejection level larger than 25 dB) increased from 1.49 GHz to 3.98 GHz while adding the BSF.

4. CONCLUSION

The design of loop-ring BSF formed by different impedance lines has been presented in this paper. The equations based on transmission line model for the proposed BSF with or without the open stub was derived to design the circuit and to analyze its performance. The effect of the impedance ratio on the BSF's BW and the rejection levels was investigated. Its application in enhancing the stopband performance of a WLAN BPF is demonstrated. By using the BSF, the demonstrated BPF successfully suppressed the coupled-lines' second harmonic and extended the upper stopband BW from 1.49 to 3.98 GHz.

ACKNOWLEDGMENT

The authors wish to acknowledge the support of National Science Council of R.O.C. under the grand No. NSC 97-2221-E-018-004-MY2. The numerous discussions and valuable comments provided by Prof. C.-H. Lee of National Changhua University of Education and Prof. C.-I G. Hsu of National Yunlin University of Science and Technology are also acknowledged.

REFERENCES

1. Makimoto, M. and S. Yamashita, "Bandpass filters using parallel coupled stripline stepped impedance resonators," *IEEE Trans. Microw. Theory Tech.*, Vol. 28, No. 12, 1413–1417, Dec. 1980.
2. Kuo, J.-T. and E. Shih, "Microstrip stepped impedance resonator bandpass filter with an extended optimal rejection bandwidth," *IEEE Trans. Microw. Theory Tech.*, Vol. 51, No. 5, 1554–1559, May 2003.
3. Tu, W.-H. and K. Chang, "Compact second harmonic-suppressed bandstop and bandpass filters using open stubs," *IEEE Trans. Microw. Theory Tech.*, Vol. 54, No. 6, 2497–2502, Jun. 2006.
4. Zhu, L. and W. Menzel, "Compact microstrip bandpass filter with two transmission zeros using a stub-tapped half-wavelength line resonator," *IEEE Microw. Wireless Compon. Lett.*, Vol. 13, No. 1, 16–18, Jan. 2003.
5. Kuo, J.-T., W.-H. Hsu, and W. T. Huang, "Parallel coupled microstrip filters with suppression of harmonic response," *IEEE Microw. Wireless Compon. Lett.*, Vol. 12, No. 10, 383–385, Oct. 2002.
6. Hong, J.-S. and M. J. Lancaster, *Microstrip Filters for RF/Microwave Applications*, John Wiley & Sons, NY, 2001.
7. Tu, W.-H. and K. Chang, "Compact microstrip bandstop filter using open stub and spurline," *IEEE Microw. Wireless Compon. Lett.*, Vol. 15, No. 4, 268–270, Apr. 2005.
8. Woo, D.-J. and T.-K. Lee, "Suppression of harmonics in Wilkinson power divider using dual-band rejection by asymmetric DGS," *IEEE Trans. Microw. Theory Tech.*, Vol. 53, No. 6, 2139–2144, Jun. 2005.
9. Shaman H. and J.-S. Hong, "Wideband bandstop filter with cross-coupling," *IEEE Trans. Microw. Theory Tech.*, Vol. 55, No. 8, 1780–1785, Aug. 2007.
10. Hsieh, M. and S. Wang, "Compact and wideband microstrip bandstop filter," *IEEE Microw. Wireless Compon. Lett.*, Vol. 15, No. 7, 472–474, Jul. 2005.
11. Hsieh, L.-H. and K. Chang, "Compact, low insertion-loss, sharp-rejection, and wide-band microstrip bandpass filters," *IEEE Trans. Microw. Theory Tech.*, Vol. 51, No. 4, 1241–1246, Apr. 2003.
12. HFSS Ver. 8.5, Ansoft PA, 2000.

Voltage-mode Highpass, Bandpass and Lowpass Filters Using a Single DVCC

Hua-Pin Chen and Tsang-Yen Hsieh
Department of Electronic Engineering, Ming Chi University of Technology, Taishan, Taiwan

Abstract— Despite the extensive literature on current conveyor-based voltage-mode multifunction biquads with single input and three outputs, no filter circuits have been reported to date which simultaneously achieve all of the advantageous features: (i) the employment of only one differential voltage current conveyor (DVCC), (ii) the employment of only two grounded capacitors, (iii) the employment of only three resistors, (iv) simultaneous realization of voltage-mode highpass, bandpass and lowpass filter signals from the three output terminals, respectively, (v) no need to employ inverting type input signals, (vi) no need to impose component choice, (vii) low passive sensitivity performance and (viii) simpler configuration due to the use of single DVCC only. This paper describes a novel voltage-mode multifunction biquadratic filter with single input and three outputs. The proposed configuration employs a single DVCC, two grounded capacitors and three resistors. The use of grounded capacitors makes the circuit suitable for integration because grounded capacitor circuit can compensate for the stay capacitances at their nodes. The proposed circuit has all the above features simultaneously, and without trade-offs. HSPICE simulation results based on using TSMC 0.35 μm CMOS model are included to verify the theoretical analysis.

1. INTRODUCTION

As a current-mode active device , the differential voltage current conveyors (DVCC) has the advantages of both of the second generation current conveyor (CCII) (such as large signal bandwidth, great linearity, wide dynamic range) and the differential difference input amplifier (DDA) (such as high input impedance and arithmetic operation capability) [1]. Also, the design of filter circuits employing current-mode active elements may be used in phase-locked look frequency modulation stereo demodulators, touch-tone telephone tone decoder and cross-over networks in a three-way high fidelity loudspeaker [2, 3]. With the increasing emphasis on the voltage-mode universal biquad filters with single input and multiple outputs [4–7], there is still a need to develop new biquad filters that offer new advantages. In 1997, Horng et al. [4] proposed a voltage-mode multifunction filter with a single input and three outputs, which can realize lowpass, bandpass and highpass filter transfer functions, using four CCII+s, three grounded capacitors and five grounded resistors. In the same year, Chang proposed five voltage-mode multifunction biquadratic filters using four CCIIs, two grounded capacitors and three-five resistors [5]. However, these two proposed configurations required at least four active components. In 1999, Chang and Lee proposed a voltage-mode lowpass, bandpass and highpass biquadratic filters with a single input and three outputs using only two compound current conveyors, two grounded capacitors and three resistors [6]. Then, Horng et al. proposed a voltage-mode highpass, bandpass and lowpass biquadratic filters using two DDCCs, two grounded capacitors and two grounded resistors [7]. However, these two proposed configurations required at least two (not one) active components. From the point view of the advantages of low cost, space saving and power dissipation, the filters using single active element receive more attention at present. Although, the multifunction filter with a single input and four outputs was proposed by Chang et al. [8], which can realize highpass, bandpass and lowpass filters using a single FDCCII, two grounded capacitors and two grounded resistors. However, the use of FDCCII can be divided into two separate DVCCs. It leads to the use of a single DVCC which is simpler than the use of a single FDCCII. Moreover, the CMOS model of DVCC is simpler than FDCCII. In this paper, the authors propose a new voltage-mode lowpass, bandpass and highpass biquad filter with a single input and three outputs. The proposed circuit employs one fewer current conveyor than the recent one [7] in addition to two grounded capacitors and three resistors. The use of grounded capacitors is particularly attractive for integrated circuit implementation [9]. Anyway, the use of only one DVCC and five passive components is a simpler configuration than Horng et al. [7].

2. CIRCUIT DESCRIPTION

The electrical symbol of the DVCC is shown in Figure 1 and its terminal relations are given by $V_X = V_{Y1} - V_{Y2}$, $I_{Z1} = +I_X$ and $I_{Z2} = -I_X$ [1]. The proposed biquad filter, based on the

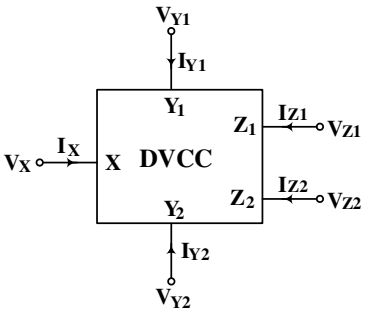

Figure 1: Block diagram of the DVCC.

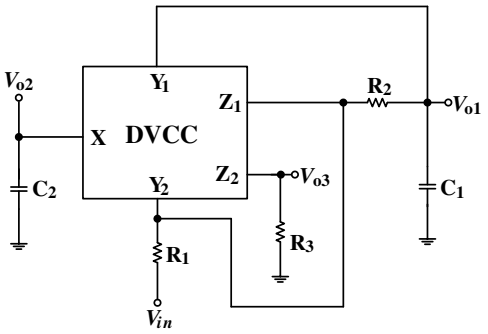

Figure 2: The proposed voltage-mode multifunction biquad.

differential voltage current conveyor, is shown in Figure 2. It is composed of a single DVCC, two grounded capacitors and three resistors. The use of grounded capacitors makes the circuit suitable for integration because grounded capacitor circuit can compensate for the stay capacitances at their nodes [9–11]. Circuit analysis yields the following voltage-mode filter transfer function:

$$\frac{V_{o1}}{V_{in}} = \frac{G_1G_2}{s^2C_1C_2 + sC_1(G_1+G_2) + G_1G_2} \tag{1}$$

$$\frac{V_{o2}}{V_{in}} = \frac{-sC_1G_1}{s^2C_1C_2 + sC_1(G_1+G_2) + G_1G_2} \tag{2}$$

$$\frac{V_{o3}}{V_{in}} = \left(\frac{G_1}{G_3}\right)\frac{s^2C_1C_2}{s^2C_1C_2 + sC_1(G_1+G_2) + G_1G_2} \tag{3}$$

where $R_1 = \frac{1}{G_1}$, $R_2 = \frac{1}{G_2}$ and $R_3 = \frac{1}{G_3}$.

Thus, we can obtain a non-inverting lowpass, an inverting bandpass, and a non-inverting highpass filter response at the output voltages, V_{o1}, V_{o2} and V_{o3}, respectively. Examining (1)–(3) show that the resonance angular frequency ω_o and the quality factor Q of the biquad filter are given by

$$\omega_0 = \sqrt{\frac{G_1G_2}{C_1C_2}} \quad \text{and} \quad Q = \frac{1}{G_1+G_2}\sqrt{\frac{C_2G_1G_2}{C_1}} \tag{4}$$

A sensitivity study forms an important index of the performance of any active network. The formal definition of sensitivity is

$$S_x^F = \frac{x}{F}\frac{\partial F}{\partial x} \tag{5}$$

where F represents one of ω_o, Q and x represents any of the passive elements (G_1–G_3, C_1–C_2). Using the above definition the passive sensitivities of the proposed circuit shown in Figure 2 are given as

$$S_{G_1}^{\omega_0} = S_{G_2}^{\omega_0} = -S_{C_1}^{\omega_0} = -S_{C_2}^{\omega_0} = \frac{1}{2}, \quad -S_{C_1}^{Q} = S_{C_2}^{Q} = \frac{1}{2}, \quad S_{G_1}^{Q} = \frac{1}{2} - \frac{G_1}{G_1+G_2},$$
$$S_{G_2}^{Q} = \frac{1}{2} - \frac{G_2}{G_1+G_2} \quad \text{and} \quad S_{G_3}^{\omega_0} = S_{G_3}^{Q} = 0. \tag{6}$$

Hence, the filter parameter sensitivities are low and not large than 1/2 in absolute value.

3. SIMULATION RESULTS

Finally, to verify the theoretical prediction of the proposed biquad filter, a simulation by using HSPICE simulation with TSMC 035 µm process was performed and the CMOS implementation of a DVCC is shown in Figure 3 [1] with the NMOS and PMOS transistor aspect ratios ($W/L = 5\,\mu m/1\,\mu m$) and ($W/L = 10\,\mu m/1\,\mu m$), respectively. The supply voltages are $V_{DD} = -V_{SS} = 1.65\,V$ and the biasing voltages are $V_{B1} = -0.25\,V$ and $V_{B2} = -0.75\,V$, respectively. The proposed circuit was designed for $f_o = 1\,MHz$ and $Q = 1.58$ by choosing $R_1 = R_2 = R_3 = 10\,k\Omega$, $C_1 = 5\,pF$ and $C_2 = 50\,pF$. Figure 4 shows the simulated and theoretical response of lowpass, bandpass and highpass of Figure 2. As can be seen, there is a good close agreement between the theory and the simulation.

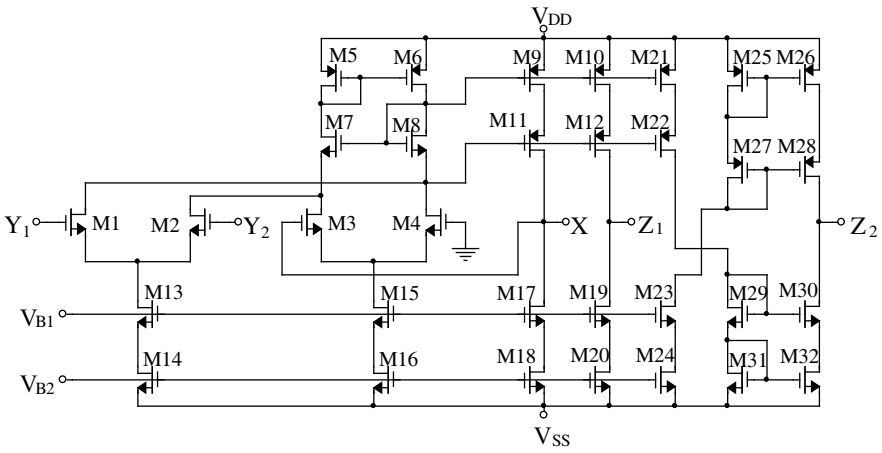

Figure 3: The CMOS implementation of a DVCC.

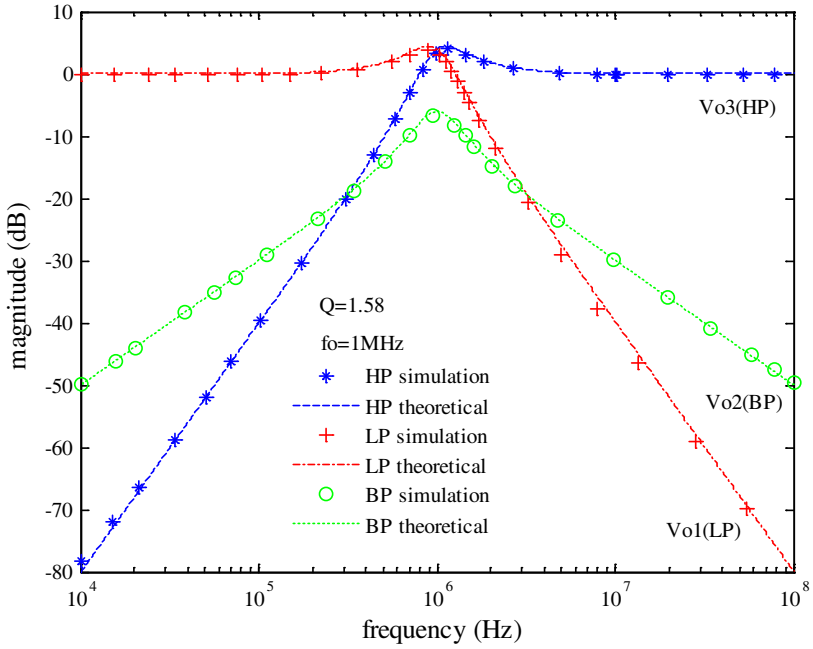

Figure 4: The Amplitude-frequency responses of Figure 2.

4. CONCLUSION

In 2004, Horng et al. presented a voltage-mode multifunction filter with a single input and three outputs employing two DDCCs, two grounded capacitors and two grounded resistors [7]. It can simultaneously obtain highpass, bandpass and lowpass filter responses. In this paper, the authors also proposed a voltage-mode multifunction filter with a single input and three outputs. The new one is simpler in configuration than the old filter [7] due to the use of single DVCC only. Moreover, the proposed circuit still enjoys no requirements for component matching conditions, no need to employ inverting type input signals and employs two grounded capacitors suitable for integrated circuit implementation.

ACKNOWLEDGMENT

This work was supported by National Science Council, Republic of China, under Grant NSC-98-2221-E-131-027.

REFERENCES

1. Elwan, H. O. and A. M. Soliman, "Novel CMOS differential voltage current conveyor and its applications," *IEE Proc. Circuits Devices Syst.*, Vol. 144, No. 3, 195–200, 1997.

2. Fabre, A., O. Saaid, F. Wiest, and C. Boucheron, "Low power current-mode second-order bandpass IF filter," *IEEE Trans. Circuits Syst. — II: Analog Digital Signal Process*, Vol. 44, No. 6, 436–446, 1997.
3. Ibrahim, M. A., S. Minaei, and H. Kuntman, "A 22.5 MHz current-mode KHN-biquad using differential voltage current conveyor and grounded passive elements," *Int. J. Electron. Commun. (AEÜ)*, Vol. 59, No. 5, 311–318, 2005.
4. Horng, J. W., J. R. Lay, C. W. Chang, and M. H. Lee, "High input impedance voltage-mode multifunction filters using plus-type CCIIs," *Electron. Lett.*, Vol. 33, No. 6, 472–473, 1997.
5. Chang, C. M., "Multifunction biquadratic filters using current conveyors," *IEEE Trans. Circuits Syst. — II: Analog Digital Signal Process*, Vol. 44, No. 11, 956–958, 1997.
6. Chang C. M. and M. J. Lee, "Voltage-mode multifunction filter with single input and three outputs using two compound current conveyors," *IEEE Trans. Circuits Syst. — I: Fundamental Theory Applications*, Vol. 46, No. 11, 1364–1365, 1999.
7. Horng, J. W., W. Y. Chui, and H. Y. Wei, "Voltage-mode highpass, bandpass and lowpass filters using two DDCCs," *Int. J. Electron.*, Vol. 91, No. 8, 461–464, 2004.
8. Chang, C. M., B. M. Al-Hashimi, C. L. Wang, and C. W. Hung, "Single fully differential current conveyor biquad filters," *IEE Proc. — Circuits Devices Syst.*, Vol. 150, No. 5, 394–398, 2003.
9. Chang, C. M. and H. P. Chen, "Universal capacitor-grounded voltage-mode filter with three inputs and a single output," *Int. J. Electron.*, Vol. 90, No. 6, 401–406, 2003.
10. Bhushan, M. and R. W. Newcomb, "Grounding of capacitors in the integrated circuits," *Electron. Lett.*, Vol. 3, No. 4, 48–149, 1967.
11. Senani, R., "New universal current mode biquad employing all grounded passive components but only two DOCCs," *Journal of Active and Passive Electronic Devices*, Vol. 1, No. 3–4, 281–288, 2006.

Modified Approximation Types for Lossy Building Blocks

Martin Friedl, **Lubomír Fröhlich**, **and Jiří Sedláček**
Brno, FEEC BUT, UTEE, Kolejní 2906/4, Brno 612 00, Czech Republic

Abstract— In paper here are discussed some possibilities of filter optimization by using of active buildings blocks (simulated inductors and frequency dependent negative resistances — FDNRs) with modern active elements at higher frequencies. In some practical examples there are briefly prescribed new possibilities and resulting parameters of designed and realized ARC low pass, high pass and band pass filter types with different modified approximation functions.

1. INTRODUCTION

Active RC filters designed using non-cascade filter synthesis realized on the base of passive RLC filter prototypes exhibit some advantages — namely low sensitivities. Usage of new modern active elements (operational amplifiers with high GBW) and possibilities of goal-directed lossy RLC ladder prototypes enable to design optimized ARC filter realizations with simple and economic active building blocks to higher frequency range. These simple grounded active selective blocks working only with one active element enable in present time to design active filters of low pass (LP), high pass (HP), as well as band pass (BP) filter types with optimized parameters.

2. NON-CASCADE FILTER SYNTHESIS

By non-cascade filter synthesis there are used many different principles to reach required filter parameters. The one from most often used principles of ARC non-cascade LP filter synthesis where active filters are based on passive LRC ladder prototype is drawn in Fig. 1(a). Using very good known Brutons transformation is in the first step of filter design calculated original of LRC ladder prototype transformed to active RCD structure.

In the active RCD structure (realised using some active elements as operational amplifiers) are all inductors changed by active building FDNR blocks (Frequency depended negative resistor) and load resistor R is changed by load capacitor C. In the HP filter synthesis technique in the original LRC ladder prototype can be inductors realized using coils directly replaced by active synthetic inductors SI realized using active elements [2] (see Fig. 1(b)). Similarly can be realized using synthetic inductors SI filter design of BP filters of capacitive coupled band pass filters (Fig. 1(c)). Second possibility how to realize active BP filter design is using FDNR filter blocks in inductive coupled LCR band pass ladder filter (Fig. 2) [4].

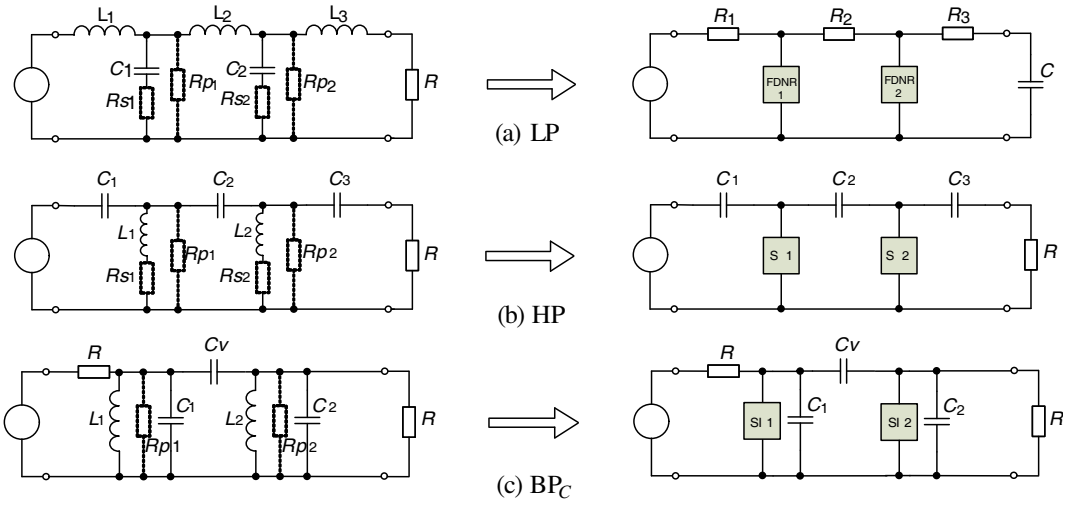

Figure 1: (a) Principle of Active LP filter design, (b) Active HP filter design, (c) BP filter design — capacitive coupled.

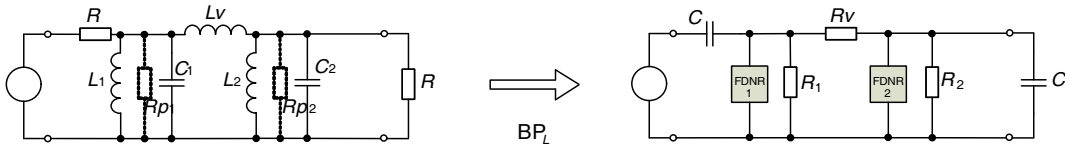

Figure 2: Principle of active BP filter design — inductive coupled filter.

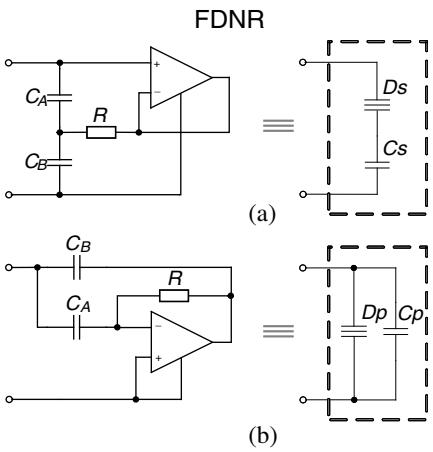

Figure 3: FDNR active block — (a) serial (b) parallel lossy.

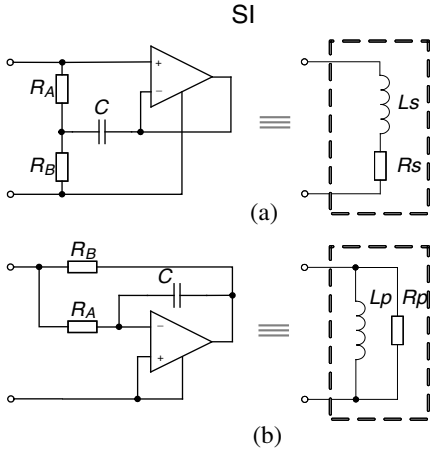

Figure 4: SI active block — (a) serial (b) parallel lossy.

3. ACTIVE BUILDING FILTER BLOCKS

As active FDNR and SI building blocks can be used many active circuits, their connections, frequency behaviour and parameters have been prescribed in many active filter literature [1, 2]. These above mentioned active building blocks are divided to two groups — lossles circuits which required usually higher number of active elements (operational amplifiers) and on the other side- lossy circuits. These lossy FDNR and SI active elements required only minimum number of active elements, are very simple and economic, what is on the other hand paid by some imperfections usually modelled by parasitic lossy elements. The most often used connections of lossy FDNR active building blocks and lossy SI active building blocks are depictured in Fig. 3. All this active structures can be in filter design process in all kinds of filters from Fig. 1 and Fig. 2 used. The possibilities, resulting filter parameters and filter sensitivities of above mentioned filters with active lossy elements have been very widely investigated.

4. MODIFICATION OF APPROXIMATION FUNCTIONS

These above discussed simple and economic lossy active building blocks enable to design ARC filters with minimization of element value spread, optimization of sensitivities and increasing of dynamic range [2]. Their using on the other side requires design witch is based on lossy ladder prototypes with modified approximation functions. To generate modified approximation functions have been developed some numerical iterative methods, which enable using active blocks with parallel as well as serial losses. Advantage of LCR ladder prototypes with parallel losses is in fact, that modified approximation function may be identical to ideal approximation function (without lossy elements), however in the resulting ARC realization can be slope of transfer response rather different due a real properties of operational amplifier (inserted parasitic pole) [2] how it is seen from Fig. 5. Using of LRC ladder with serial losses in parallel filter branches brings higher imperfections — slope of modified transfer magnitude curve is already smaller then ideal , however imperfections can be diminish to in practise negligible values (see Fig. 5). On the other side advantage of these circuit is monotonic filter response in stop-band and usually higher dynamic range of resulting filter.

The comparison between classically designed active filter of 7th order with active real building blocks (Fig. 7(b)) and active filter designed using modified approximations with serial and parallel lossy LRC prototype (Fig. 7(a)) we can see from these figures. How is very clearly seen from figures, optimized filter designed using serial goal-directed lossy synthesis method exhibit the magnitude

response very near to filter with parallel losses, which is very nearly to ideal response. The classically designed low-pass filter starting grown from ideal LCR ladder prototype with real building active elements (with supposed $Q = 10$) exhibit significant degeneracy of magnitude response namely in area of corner frequency of filter, the similar degeneracy is visible also at higher frequencies of stop-band of filter. The resulting influence of real parameters of active block are also very significant by degeneracy of group delay (g_d) curve.

In last year have been developed special programs for calculating goal-directed ladder prototypes with parallel and serial lossy resistors [2, 3] in parallel branches of filter. In [4] was published also a new optimizing method, which can be used very easy to design of the goal-lossy filter structures

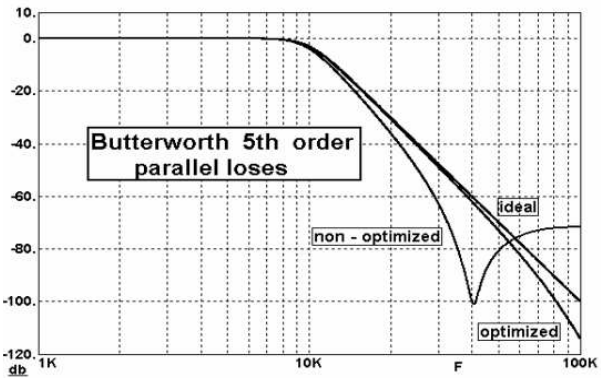

Figure 5: The magnitude response of LP filter (paralel losses).

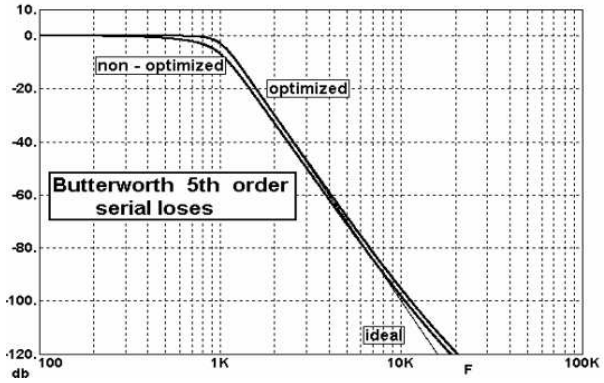

Figure 6: The magnitude response of LP filter (serial losses).

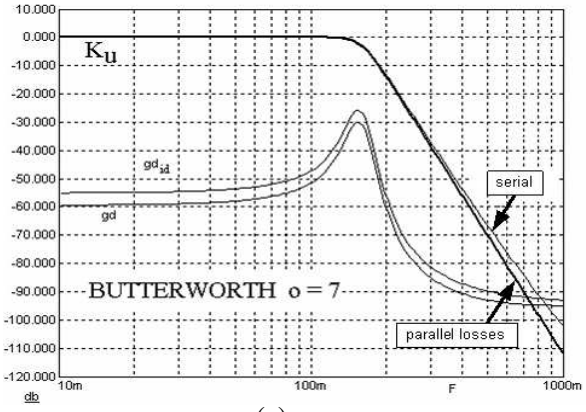

(a)

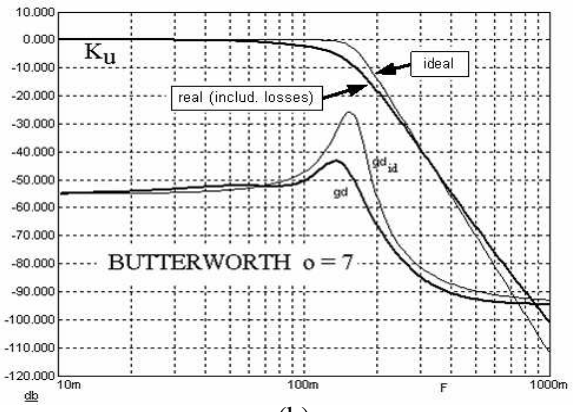

(b)

Figure 7: The normalized filter responses –C filter designed (a) using modified approximation filter type, (b) using classical ideal filter prototype.

Table 1: The normalised LP and modified approximation types — single terminated RLC ladder, normalized to $\omega = 1$, with terminal resistor $r = 1\,\Omega$.

Type	Order	R_s	R_p	l_1	c_1	l_2	c_2	l_3	c_3	l_4	Remark
Butterworth	5	-	1	**1,5443**	**1,6936**	**1,3813**	**0,8940**	**0,3089**	-	-	ideal
		0,05	-	1,3487	1,7132	1,4194	0,9068	0,3355	-	-	serial losses
		0,1	-	1,1284	1,7808	1,4705	0,9247	0,3651	-	-	
		-	4	0,9630	2,3700	1,1590	1,0980	0,3450	-	-	parallel losses
		-	2	0,6928	3,0570	0,9805	1,2820	0,3726	-	-	
	7	-	1	**1,5571**	**1,7982**	**1,6583**	**1,3967**	**1,0546**	**0,6557**	**0,2224**	ideal
		0,05	-	1,2676	1,8322	1,6896	1,4187	1,0953	0,6709	0,2439	serial losses
		0,1	-	0,8987	2,0297	1,76	1,4588	1,1472	0,6915	0,2685	
		-	4	0,8167	2,95	1,14	2,01	0,8876	0,8132	0,2507	parallel losses
		-	2	0,5438	4,12	0,8605	2,61	0,7593	0,9585	0,2725	

using usually accessible analysis software. It enables to calculate all elements of LP, HP and BP filters growing from goal-directed lossy LCR ladder prototypes with modified approximation types. As an example here are presented in Table 1 resulting normalized parameters of Butterworth types LP filters of 5th and 7th filter order with serial and parallel lossy elements which have been calculated using developed programs based on iterative numerical methods. This table enables to fulfil most often solved filter requirements of modified approximation filter function.

5. SOME EXAMPLES OF FILTERS REALISED WITH MODIFIED APPROXIMATION FUNCTIONS

As an examples of filters which have been designed according above mentioned method are here presented some optimized circuits of different filter types (LP, HP and BP) realized with modern operational amplifiers demonstrating their working possibility at higher frequencies. The first

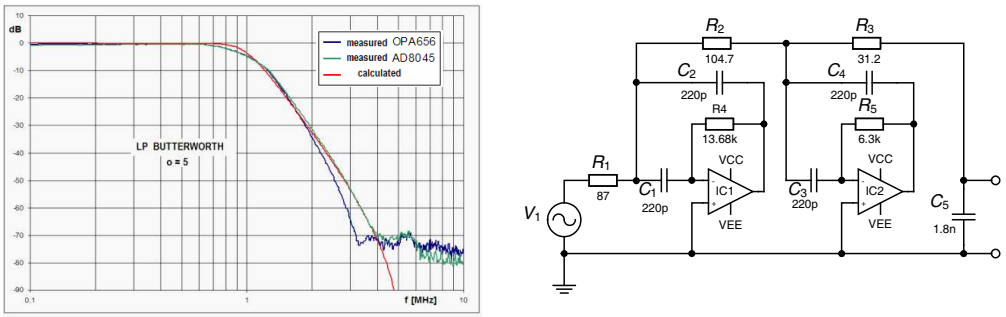

(a) (b)

Figure 8: The example of active LP filter with modified approximation (paralel losses) — (a) magnitudere-sponse, (b) circuit active RC.

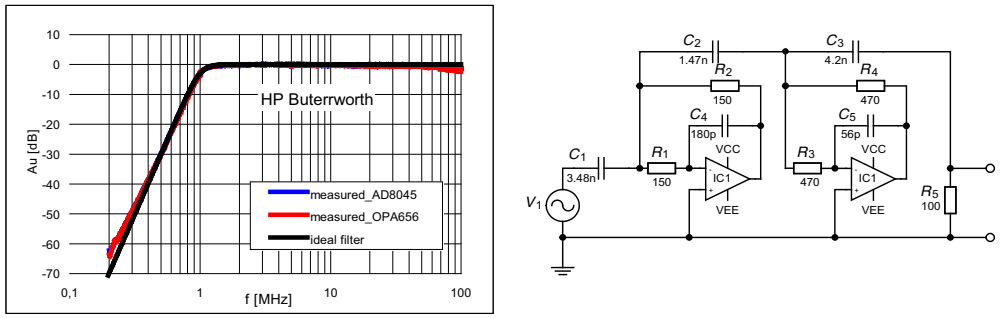

(a) (b)

Figure 9: The active highpass filter ($f_0 = 1\,\mathrm{MHz}$) with lossy SI elements — (a) magnitude response, (b) circuit diagram.

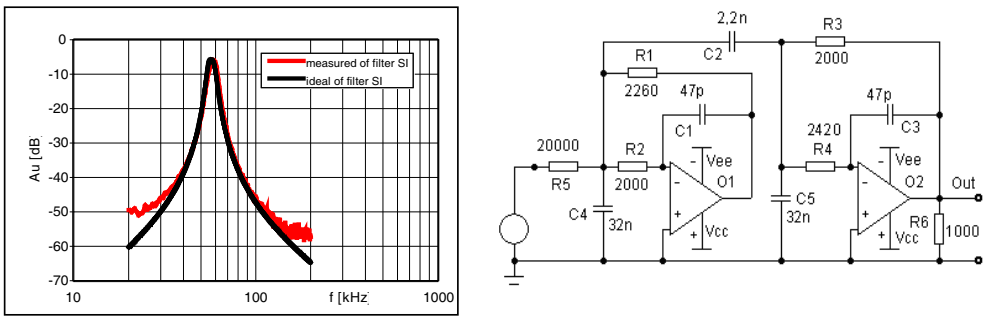

(a) (b)

Figure 10: The active band-pass filter ($f_0 = 57\,\mathrm{kHz}$) with lossy SI elements — (a) magnitude response, (b) circuit diagram.

example (see Fig. 8) demonstrates function of LP filter with corner frequency $f_0 = 1\,\mathrm{MHz}$. From measured magnitude response is seen good equivalence measured and calculated filter response (the higher slope of curve in stop-band for OA with smaller GBW due to parasitic pole good corresponds with theoretic knowledge).

The second example — demonstrate possibility of active filter HP (Fig. 9), which is good working at the same corner frequency — here measured and calculated responses corresponds very closely. Similarly very nearly correspond resulting measured and calculated magnitude responses (see Fig. 10) of BP filter, which demonstrate here as last example resulting parameters and possibility of good function of active (capacitive coupled) BP filter working at resonant frequency $f_0 = 57\,\mathrm{kHz}$.

6. CONCLUSIONS

This contribution deals with design and optimization of ARC filters based on modified approximation filter functions which enable construct filters of LP, HP and BP with simple and economic lossy building blocks. Using a new modern operational amplifier with wide GBW the prescribed method enable to design simple and economic ARC filters working at frequencies about units of MHz. The above discussed method can be used by filter optimization process -very important part of filter design in most higher order filters namely in case of special or stringent filter requirements. The presented optimization process was requested for pre-processing of analogue signals before digitalization in the NMR signal processing area.

ACKNOWLEDGMENT

This work has been supported by the Research Project: MSM 0021630513 of the Czech Republic.

REFERENCES

1. Hajek, K. and J. Sedlacek, *Kmitočtové Filtry*, Vydavatelství BEN Praha, 2002
2. Hajek, K. and J. Sedlacek, "Lossy LC ladder prototypes and their use for ARC filter optimization," *Wseas Transactions on Electronics*, Vol. 2, No. 3, 94–99, July 2005.
3. Martinek, P. and T. Daša, "Evolutionary algorithms by ARC filter synthesis," *ECCTD 05*, 155–159, Cork, 2005.
4. Hajek, K., V. Michal, J. Sedlacek, and M. Steinbauer, "A simple method of goal-directed lossy synthesis and network optimization," *Electrical and Electronic Engineering*, 249–253, Žilina, 2006.

Optimization of ARC Component Filter Sensitivity

Martin Friedl and Jiří Sedláček
FEEC BUT, UTEE, Kolejní 2906/4, Brno 61200, Czech Republic

Abstract— In the presented contribution are discussed some optimization methods leading to improving of resulting parameters of active filters designated using non-cascade method. Here are discussed and compared real parameters of active filters with modern active elements derived from singly or doubly terminated RLC passive prototype networks. In some examples of designated ARC filters there are prescribed some possibilities and optimization methods which enable to design and optimize of component filter sensitivity.

1. INTRODUCTION

A filter design optimization and namely the minimization of filter element sensitivity of resulting active RC filters is very important step in filter design process of each filter types. Their significance is increasing by increasing filter order and steepness of transfer filter response. This part of filter design is necessary for successfully work of each filter and must be solved namely for special filter requirements where filters are working in specific given conditions.

2. MINIMIZATION OF SINGLE AMPLIFIER BLOCK SENSITIVITY

By optimization of single amplifier biquads (SABs) are important two factors — the sensitivity minimization to value element variation of passive elements and minimization of parasitic effects of real active elements (operational amplifier OA). Optimization process is usually starting by proper circuit SAB topology selection, continues by design minimizing passive element sensitivity and proper amplifier gain setting [3].

The first step of filter design and optimization is necessarily proper SABs topology selection. From the point of sensitivity minimization view there are many network topologies that have been in many different modifications published. As main suitable topology from sensitivity point of view are SABs based on bridged T circuits with coupled capacitors respectively resistors and their modifications while networks based on Wien network topology are much greater sensitive. Consequently in the optimization process must be preferable using four basic SABs networks. Low-pass (Fig. 1(a)), high pass (Fig. 1(b)) and two modifications of band-pass circuits (Figs. 1(c), (d)) [1]. The main problem of sensitivity optimization is to optimize sensitivity to Q factor which is dominant problem, because sensitivity of resonant frequency to the component value is in practice negligible.

To sensitivity analysis and filter optimization all ratios of filter components has been defined — the ratio of resistors as $\alpha = R_2/\mathrm{R}_1$, ratio of capacitors as $\beta = C_2/\mathrm{C}_1$ and ratio of resistors which are adjusting the amplifier gain as $\gamma = R_4/\mathrm{R}_3$, then resulting sensitivities are ordered in Table 1. Although many possible alternative choice for the design parameters exist, the topologies

	Networks equal C	Networks equal R
Q	$Q = \frac{\sqrt{\alpha\beta}}{\beta(1-\alpha\gamma)+1}$	$Q = \frac{\sqrt{\alpha\beta}}{\alpha(1-\beta\gamma)+1}$
S_α^Q	$\frac{1}{2} - \frac{Q}{\sqrt{\alpha}}\left(\sqrt{\beta} + \frac{1}{\sqrt{\beta}}\right)$	$\frac{1}{2} - \frac{Q}{\sqrt{\alpha\beta}}$
S_β^Q	$\frac{1}{2} - \frac{Q}{\sqrt{\alpha\beta}}$	$\frac{1}{2} - \frac{Q}{\sqrt{\beta}}\left(\sqrt{\alpha} + \frac{1}{\sqrt{\alpha}}\right)$
S_γ^Q	$\frac{Q}{\sqrt{\alpha}}\left(\sqrt{\beta} + \frac{1}{\sqrt{\beta}}\right) - 1$	$\frac{Q}{\sqrt{\beta}}\left(\sqrt{\alpha} + \frac{1}{\sqrt{\alpha}}\right) - 1$
Opt	$\beta = 1$, $\alpha \to \infty$ $(4Q^2, Q^2)$	$\alpha = 1$, $\beta \to \infty$ $(4Q^2, Q^2)$

Table 1: Important sensitivities of SABs.

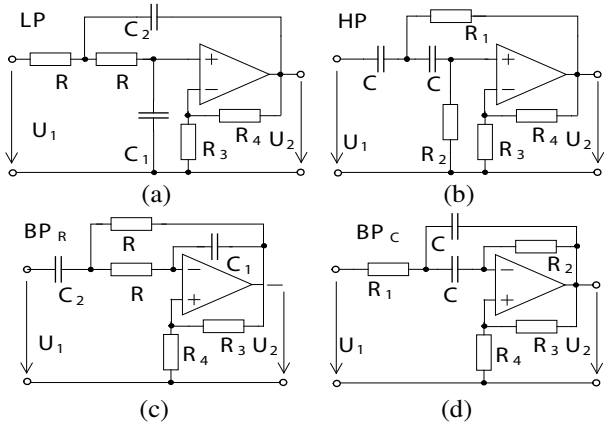

Figure 1: The circuit diagram of derived SABs.

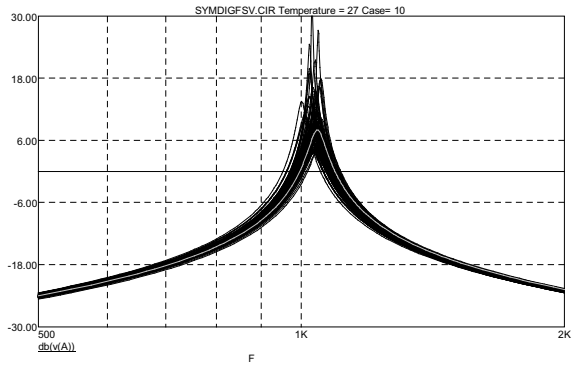

Figure 2: The BP Monte Carlo analysis ($A = 1,3145$).

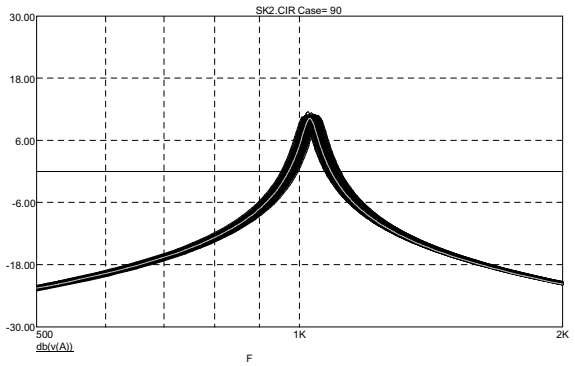

Figure 3: The BP Monte Carlo analysis ($A = 1$).

with equal capacitors when $\beta = 1$ (Figs. 1(b), (d)) and equal resistors when $\alpha = 1$ (Figs. 1(a), (c)) provide a good deal in the sensitivity behaviour of the SABs.

The networks analysis investigation leads to conclusion that optimum value from point of sensitivity view is for parameter γ=0 respectively γ=1/α or γ=1/β. Optimum case for γ=0 is leading for high value of Q factors ($Q > 30$) to extremely high spread of components and consequently to higher parasitic losses what is most important fact limiting Q by design of these SABs. Except finite amplifier gain A_0 as further limiting factor by active elements (OAs) the frequency parameters of amplifier gain (mostly defined using GBW-gainbandwidth parameter) and amplifier output resistance must be by more accurate network analysis realized.

To demonstrate above defined conclusion a sensitivity comparison using Monte Carlo method simulation is here briefly in Fig. 2 and Fig. 3 presented. From the presented pictures sensitivity comparison of the two different network modifications (with different values of amplifier gain A_0 — that means also with different value of γ) of designed SAB (network from the Fig. 1(d)) can be made. Networks have been designed with required Q factor ($Q = 30$) and modified values of resistors R_3 and R_4 (that means also parameter γ) in range 10%. The results of Monte Carlo analysis correspond very well with previously theoretic conclusions.

3. SENSITIVITY MINIMIZATION OF HIGHER FILTER ORDERS

There are two different methods by process of design for higher order filters. The first way — cascade method of filter design is based on decomposition of required transfer filter function to relatively isolated function blocks of second, respectively first order filter functions. This method is in area of ARC filter design very popular, filter design is in many filter literatures good described, all process are relative easy, each from simple blocks may be relative easy adjusted. However, resulting filter sensitivity is due cascade block connection relatively very high and quickly increasing by higher filter order, rapidly increasing by filter approximations with higher slope of filter response in filter transition band.

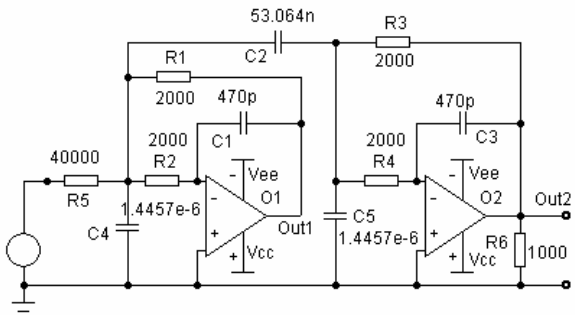

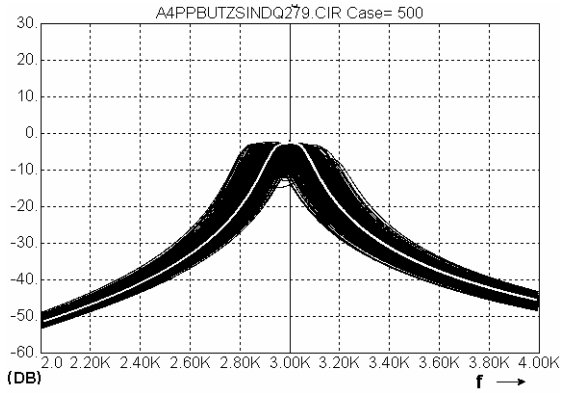

Figure 4: The band-pass filter with active lossy inductors — non cascade method of synthesis.

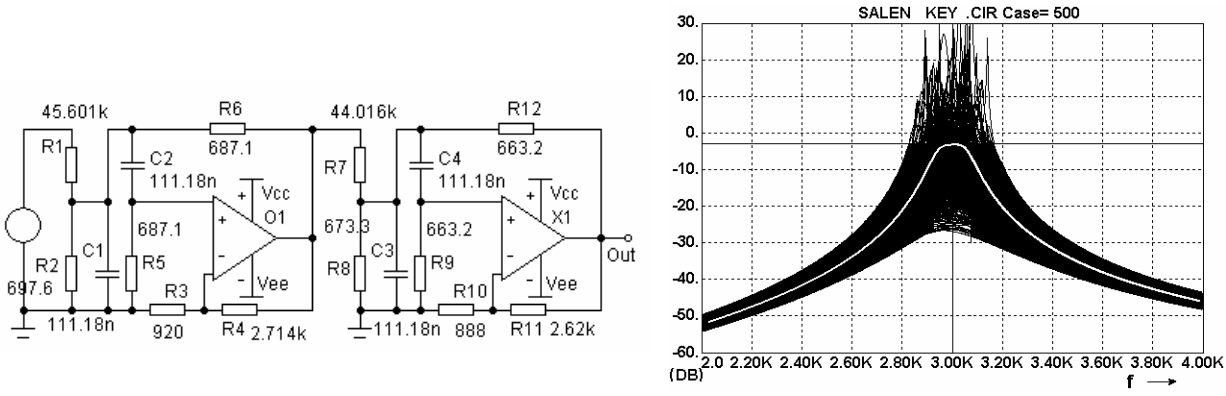

Figure 5: The resulting band-pass filter-cascade method of synthesis.

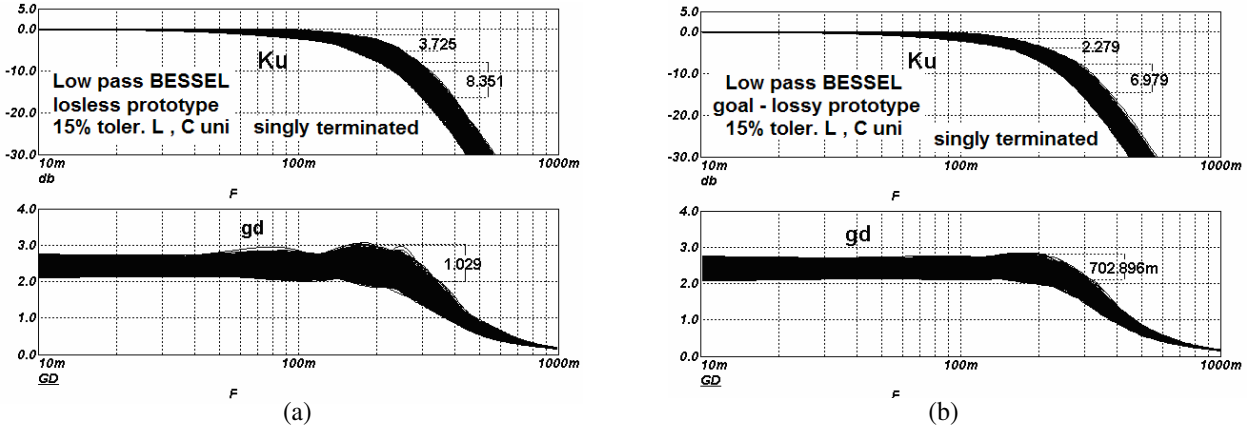

Figure 6: Monte Carlo sensitivity analysis of singly terminated LCR ladder (a) losless prototype, (b) goal-lossy prototype.

The second way leading to higher filter orders (non-cascade method of synthesis) have some different realization processes. One from non-cascade filter design manners results ladder network structure — this method is very good known from area of passive filter design.

The method exhibit two significant advantages in comparison to previously mentioned cascade synthesis method. The first advantage — filter prototype elements for any required filter type approximations as well as filter orders have been calculated and are to disposal to designers in tables in many filter design literature. The second-great advantage of this method is much smaller resulting filter sensitivity in comparison to cascade method synthesis which is paid on the other hand by rather difficult filter realization.

From point of view of minimization of filter element sensitivity this method is preferable also for ARC filter design because enable to reach minimized component sensitivity of resulting filter. To demonstrate this conclusion in the Fig. 4 and Fig. 5 here were presented resulting magnitude responses of two band pass filters designed according both above discussed synthesis method. The comparison is very good visible-filter designed using cascade method exhibits much greater sensitivity then filter designed using non-cascade synthesis method.

4. SENSITIVITY MINIMIZATION USING RLC LADDER PROTOTYPES

During recent years it has become evident that the sensitivity of the required network to its component is intimately related to the structure of the network. Thus from many publications are clear that LCR ladder structures doubly terminated are much less sensitive then singly terminated structures. In the last year has been found and in many practice measuring verified the new aspect — that goal-lossy ladder network structures exhibit smaller sensitivity to filter element variations then standard (lossless) ladder structures [2]. To demonstrate this conclusion which is not till now fully respected in filter technique design here are in next figures (Fig. 6, Fig. 7) presented results of

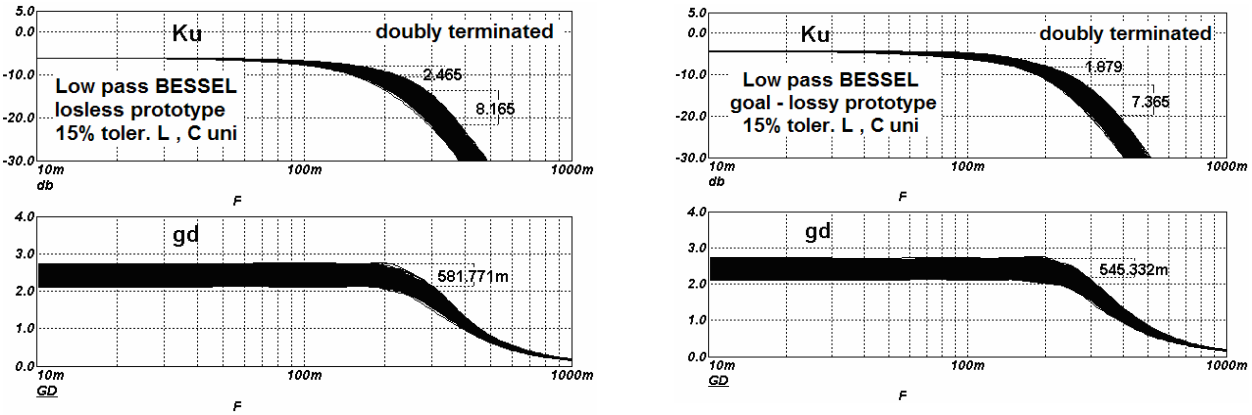

(a) (b)

Figure 7: Monte Carlo sensitivity analysis of singly terminated LCR ladder (a) losless prototype, (b) goal-lossy prototype.

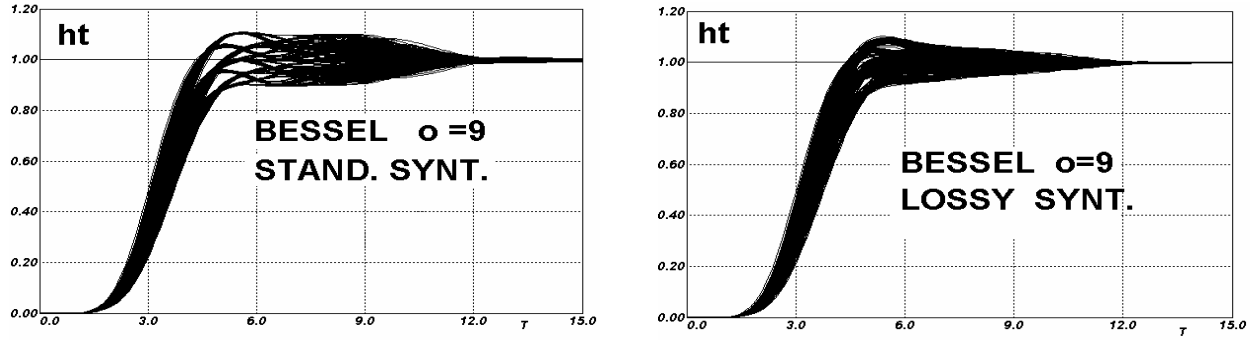

(a) (b)

Figure 8: Monte Carlo sensitivity analysis of $h(t)$ response filter designed on base of LCR ladder (a) ideal (lossles) pototype, (b) goal-directed lossy prototype.

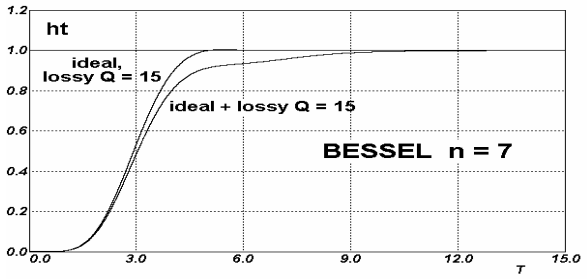

Figure 9: Resulting active band pass BP filter response.

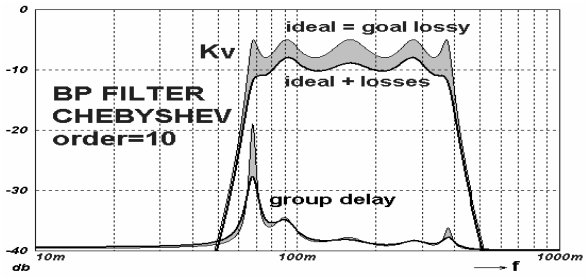

Figure 10: Resulting low pass filter $h(t)$ response.

Monte Carlo sensitivity analysis for different LCR ladder prototypes. How we can see from figures of five order low pass filter goal-lossy prototypes exhibit smaller spread of filter characteristics (are signed by normalized frequency $\omega = 1$, respectively $\omega = 2$) with comparison to standard lossless prototypes, thus consequently exhibit evidently smaller sensitivities in both — frequency and time domain too.

This fact is also clear from Fig. 8, where are presented resulting Monte Carlo sensitivity analysis (worse case) of $h(t)$ filter responses.

Except above discussed advantage of ARC filters grown from lossy ladder prototype there are in practice next great advantage-smaller imperfections caused by real parameters of passive as well as active filter elements. Their real lossy may be encountered into filter design by proper lossy ladder selecting, as can be seen from Fig. 9. Here response of filter designed using lossy ladder respects lossy, consequently response is very closely to ideal, while filter designed on base of ideal lossless ladder (with resulting real elements $Q = 15$) exhibit significant imperfection. All above

given conclusions demonstrated here on low pass filter types are fully valid for other types of filters as demonstrates Fig. 10 [4].

5. CONCLUSIONS

In the presented contribution are discussed some optimization methods leading to improving of resulting parameters passive and namely active filters. Here are very briefly discussed basic methods which enable to optimize active filter elements sensitivity. In some examples of designated ARC filters there are prescribed some possibilities and optimization methods which enable minimization of element value spread, optimization of sensitivities, minimization of number of active elements (OAs) and increasing of dynamic range.

ACKNOWLEDGMENT

This work has been supported by the Research Project: MSM 0021630513 of the Czech Republic .

REFERENCES

1. Hájek, K. and J. Sedláček, *Kmitočové Filtry*, Vydavatelství BEN, Praha, 2002.
2. Hájek, K. and J. Sedláček, "Lossy LC ladder prototypes and their use for ARC filter optimization," *Wseas Transactions on Electronics*, Vol. 2, No. 3, 94–99, ISSN 1109–9445, July 2005,
3. Schmid, H. and G. S. Moschytz, "Minimum sensitivity single-amplifier biquadratic filters," *ECCTD'99*, 1027–1030, Stresa, Italy, September 1999.
4. Hájek, K., V. Michal, J. Sedláček, and M. Swiezeny, "Improving of the active RC filters by use of goal-directed lossy LC ladder prototypes," *Proc. of ECCTD-03*, 381–384, Krakow, 2003.

A Compact Microstrip Power Divider Using Periodic DGS and HIOS

S. A. Mohassieb[1], **I. M. Barseem**[1], **E. A.-F. Abdallah**[2], **and H. M. El-Hennawy**[3]

[1]Akhbar Elyom Academy, 6th October City, Egypt
[2]Electronics Research Institute, Dokki, Giza, Egypt
[3]Faculty of Engineering, Ain Shams University, Cairo, Egypt

Abstract— In this paper, miniaturized branch-line couplers (BLCs) are designed, simulated and fabricated using FR4 substrate at the operating frequency 2.4 GHz. First, high impedance open stubs (HIOS) are used to miniaturize the conventional BLC using the combinational-model (combinational of T and π-model). The proposed design is reduced by more than 57.5% compared to the conventional design. The second step is to use defected ground structure (DGS) underneath the BLC. The proposed design is capable to achieve any dividing ratio without reducing the width of the line, which means that the power handling capability is not reduced. In addition, suppression of higher order modes is achieved and more than 18% reduction in size as compared to the conventional shape is obtained. As a final step, the two techniques are combined together and a third BLC is proposed. Good agreement is found between experimental and simulated results using the software package Zeland IE3D.

1. INTRODUCTION

With the ever-increasing complexity of microwave integrated circuits, layout and routing may pose even more problems for designers. Hence, there is a need to search for novel four-port couplers, the conventional branch-line coupler (BLC) consists of four quarter-wavelength transmission lines of loop structure. It has the property that when all ports are matched, the power entering from one port will be divided into other two ports and the fourth port is isolated. However, the conventional branch-line coupler has many disadvantages such as occupying huge area when it is fabricated on a thin substrate, or under the MIC or MMIC technology. It also suffers narrow bandwidth and the existence of higher order modes. One of the problems that are related to the BLC is that when loose coupling is required for example -10 dB coupling, the width of the microstrip line will be very small which complicates the fabrication process and reduces the power handling capability. Many techniques are used to reduce the size of the hybrid junction and to get rid of other limitation such as using artificial transmission lines [1], using space-filling fractal curves [2], using quasi-lumped element approach [3], using discontinuous microstrip lines [4], using defected ground structures [5] and photonic bandgap structures [6]. In this paper, the method of high impedance open stub and the method of defected ground structure are adopted to miniaturize the branch-line coupler, suppress the higher order modes and to increase the power handling capability as compared to the conventional coupler.

2. COMPACT MICROSTRIP BLC USING OPEN STUBS WITH HIGH IMPEDANCES

As mentioned above, there are three models that describe the shortened quarter-wavelength branch-line coupler as shown in Figure 1, namely the T-model, π-model, and Combinational-model (combinational of T- and π-model) which consists of three open-stubs [7]. The detailed procedures for implementing compact branch-line couplers will be described in as following.

$$Y_b \tan\theta_b = \frac{Z_a \sin 4\theta_a - Z_o}{(Z_a \sin 2\theta_a)^2} \tag{1}$$

$$\therefore \quad Y_c \tan\theta_c = \frac{Z_o \cot 2\theta_a - Z_a}{Z_o Z_a} \tag{2}$$

$$\therefore \quad Z_a = \frac{Z_o\left(\sqrt{\cos^2 2\theta_a + 4} - \cos 2\theta_a\right)}{2\sin 2\theta_a} \tag{3}$$

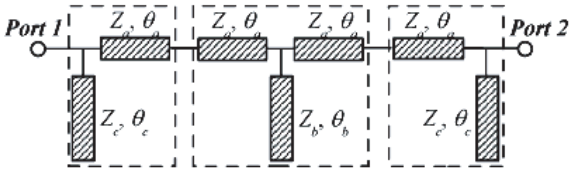

Figure 1: Equivalent quarter-wavelength transmission line of combinational-model.

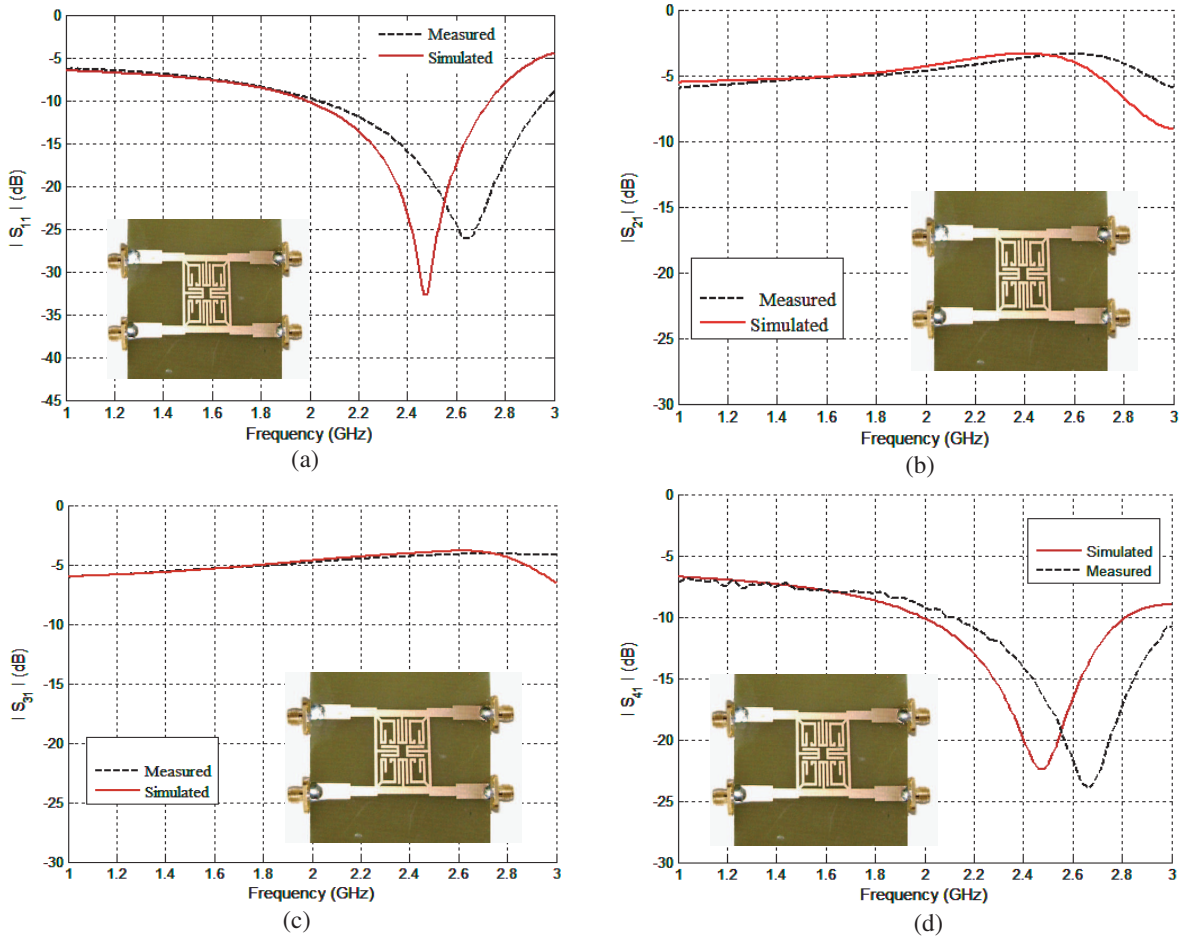

Figure 2: Simulation and measurement results: (a) magnitude of $|S_{11}|$, (b) magnitude of $|S_{21}|$, (c) magnitude of $|S_{31}|$, and (d) magnitude of $|S_{41}|$.

3. FABRICATION AND MEASUREMENTS OF COMPACT −3 dB BLC USING HIOS

The entire area of the fabricated coupler is 12.88 mm × 15.82 mm. The total area is 192.1063 mm^2, this achieves a size reduction of 57.5% compared with that of the conventional branch-line. The bandwidth is 2.1–2.5 GHz, $FBW = 16.13\%$. The amplitude and phase different between S_{21} and S_{31} are within 1 dB and $90° \pm 5°$, respectively. The return loss is better than −15 dB. The simulation results and the measurement results are shown in Figure 2.

4. COMPACT MICROSTRIP −10 dB BLC (9 : 1 UNEQUAL POWER DIVIDER) USING PERIODIC DGS

A U-shape of DGS is one of many shapes that are used to obtain microstrip line having characteristic impedance equal to 150 Ω as shown in Figure 3. Using Zeland software program, S_{11} can be calculated as −1.91 dB [8]. It should be noted that the conductor width of a 150 Ω DGS line is 0.5 mm, whereas 0.5 mm corresponds to a 107 Ω line of a conventional microstrip line. The −15 dB return loss bandwidth extends from 1.55 GHz up to 3 GHz which is an advantage to have a wide bandwidth which reaches 60.42%. However, the size reduction is only 18.75%.

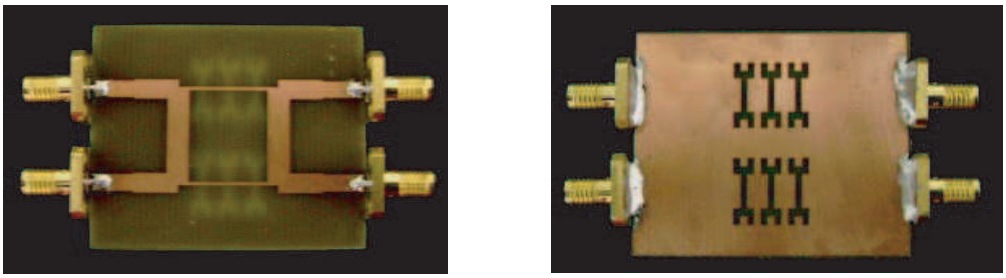

(a) (b)

Figure 3: The photograph of the proposed compact BLC using DGSs (a) top view (b) bottom view.

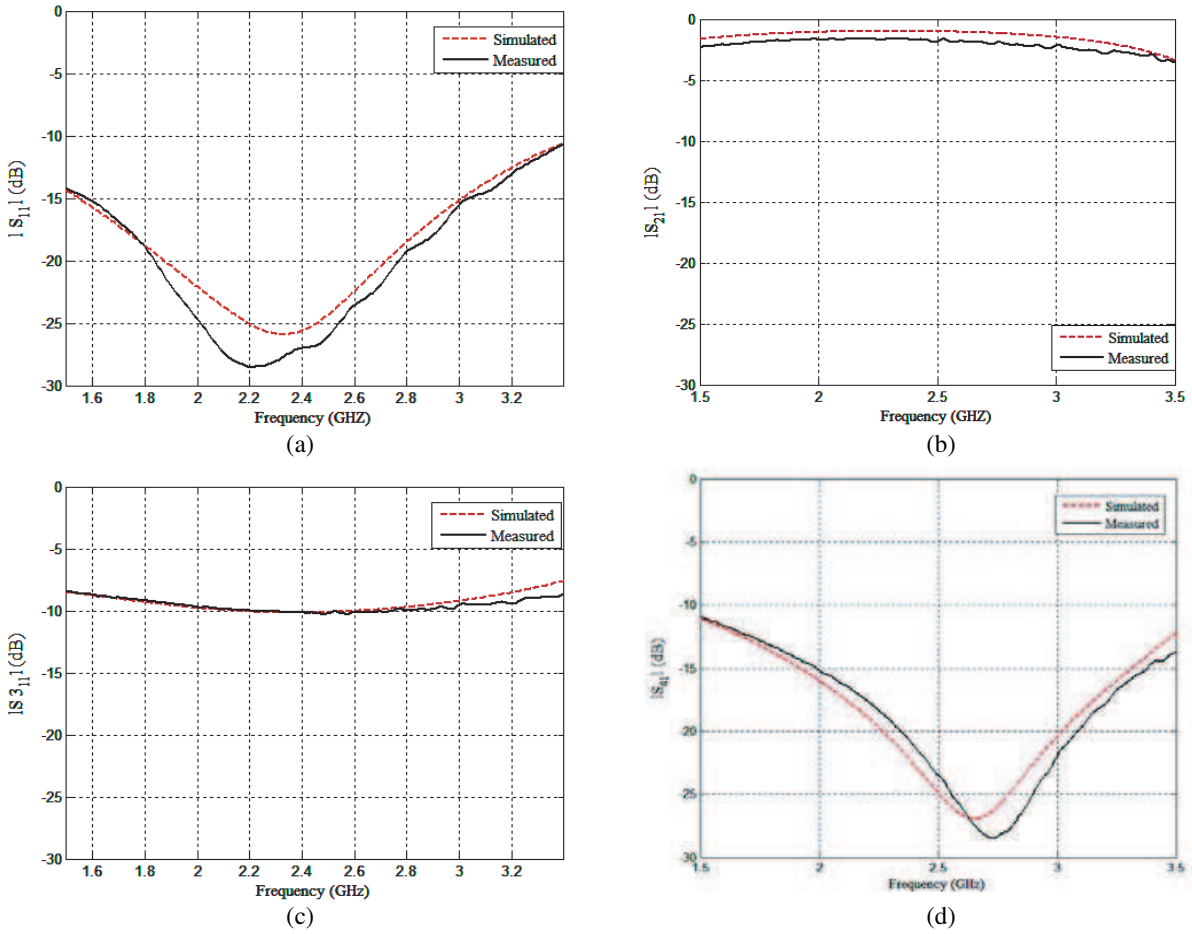

Figure 4: Simulation and measurement results: (a) magnitude of $|S_{11}|$, (b) magnitude of $|S_{21}|$, (c) magnitude of $|S_{31}|$, and (d) magnitude of $|S_{41}|$.

5. FABRICATION AND MEASUREMENTS OF COMPACT −10 dB BLC USING DGS

The microstrip 90° BLC with DGS was fabricated on FR-4 substrate with $\varepsilon_r = 4.6$ and $h = 1.6$ mm. Figures 4 shows comparison between numerical (simulated) and experimental results.

6. THE COMBINED COMPACT −3 dB BLC BY OPEN-STUB WITH PERIODIC DGS

A new microstrip compact branch-line coupler, which combines the compact T-model −3 dB coupler with the defected ground structure (DGS), is presented in [9]. The structure parameters are optimized using Zeland IE3D simulator and the simulation performance is plotted in Figure 5. Nevertheless, the center frequency of the simulation results has a little shift. The bandwidth is enhanced while the size of the coupler becomes smaller. The −15 dB return loss bandwidth is increased by 0.6% from the previous one.

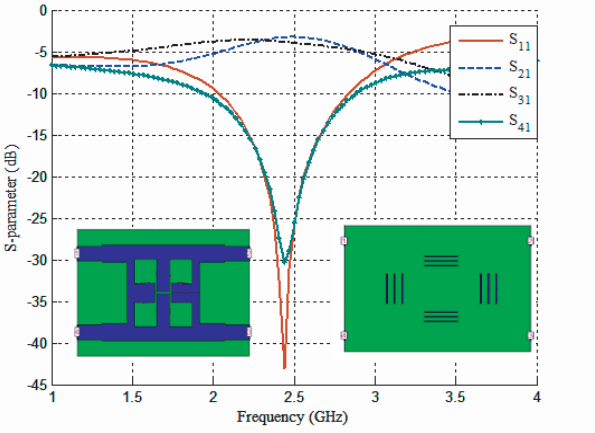

Figure 5: Simulated S-parameters of the compact T-model BLC with DGS.

7. CONCLUSION

Recently, miniaturization of microwave circuits was the goal of many RF engineers in order to reduce the cost of microwave systems. To reduce the circuit size of the branch-line coupler, many compact designs have been introduced. Among these designs, using combinational-model (combinational of T and π model) with high impedance open circuit stub approaches and using DGS underneath the branch-line couplers to achieve the optimum size-reduction. Two branch-line couplers (BLCs) are designed, simulated and fabricated at the Bluetooth frequency, on the same material, which is FR4 of dielectric constant 4.6, dielectric thickness 1.6 mm and loss tangent 0.02. For both designs, excellent agreement was achieved between numerical results using EM simulator Zeland IE3D and measured results.

REFERENCES

1. Wang, C. W., T. G. Ma, and C. F. Yang, "A new planar artificial transmission line and its applications to a miniaturized butler matrix," *IEEE Trans. Microwave Theory Tech.*, Vol. 55, No. 12, 2792–2801, 2007.
2. Chen, W. L. and G. M. Wang, "Design of novel miniaturized fractal-shaped branch-line couplers," *Asia-Pacific Microwave Conference, APMC 2007*, 1–3, December 11–14, 2007.
3. Liao, S. S. and J. T. Peng, "Compact planar microstrip branch-line couplers using the quasi-lumped elements approach with nonsymmetrical and symmetrical T-shaped structure," *IEEE Trans. Microwave Theory Tech.*, Vol. 54, No. 9, 3508–3514, 2006.
4. Sun, K. O., S. J. Ho, C. C. Yen, and D. Weide, "A compact branch-line coupler using discontinuous microstrip lines," *IEEE Microwave and Wireless Components Letters*, Vol. 15, No. 8, 519–520, 2005.
5. Weng, L. H., Y. C. Guo, X. W. Shi, and X. Q. Chen, "An overview on defected ground structures," *Progress In Electromagnetics Research B*, Vol. 7, 173–189, 2008.
6. Shum, K. M., Q. Xue, and C. H. Chan, "A novel microstrip ring hybrid incorporating a PBG cell," *IEEE Microwave and Wireless Components Letters*, Vol. 11, No. 6, 258–260, 2001.
7. Tang, C. W. and M. G. Chen, "Sythesizing microstrip branch-line couplers with predetermined compact size and bandwidth," *IEEE Trans. Microwave Theory Tech.*, Vol. 55, No. 9, 1926–1933, 2007.
8. Lim, J.-S., C.-S. Kim, J.-S. Park, D. Ahn, and S. Nam, "Design of 10 dB 90° branch line coupler using microstrip line with defected ground structure," *IEE Electronics Letters*, Vol. 36, No. 21, 1784–1785, 2000.
9. Wang, H., X. Liu, W. Cai, and H. Cao, "Design and realization of a new compact branch-line coupler using defected ground structure," *9th International Conference on Solid-State and Integrated-Circuit Technology, ICSICT 2008*, 1376–1379, 20–23, 2008.

Mode Conversion at Via Discontinuities in Microwave Circuits

Wenxue Zhu, **Yu Tian**, **and Tong Ling**
University of Electronic Science and Technology of China, Chengdu, China

Abstract— Mode conversion of via discontinuities in multilayer interconnect structures is investigated. Electromagnetic waves travelling along the transmission channels consisting of the horizontal transmission line and vertical via generally excite higher order evanescent modes as well as other propagating modes when encountering discontinuities. Current distributions along the transmission channel are determined by the method of moments and the Galerkin weighting procedure. Matrix pencil method is used to obtain the electromagnetic solutions in frequency domain, the currents along the channels is split into forward and backward multiple mode traveling-wave amplitudes, and dominant modes are extracted for further analysis about radiation mechanism.

1. INTRODUCTION

Vias in microwave and high-speed printed circuit boards (PCBs) and packages are among the components of most concern due to several advantages it offers:

1. provides the shortest approach to connect signal lines in different layers which is crucial as operating frequencies reach to microwave range or even higher.
2. To increase integration density of electronic devices, multilayer structure with vias is indispensable in high-speed electronic systems.

In typical multilayer microwave circuits, a single-ended through via generally penetrates several ground and power planes to connect two microstrips or striplines in different layers, as shown in Figure 1(a). From the cross section view, when the signal travelling along the transmission channels, impedance mismatch or discontinuities including vertical bends and parallel-plates environment will be met. These discontinuities will generally excite new high order wave and reflecting wave. The phenomenon of new mode excitation at discontinuities is called mode conversion. The mode conversion between interior ground-planes has already been investigated in detail in [1] by full-wave and SPICE circuit simulation. In this paper, the focus is set to the transition between microstrip and vertical via, as outlined by dashed rectangle in Figure 1(b), and this transition can be approximated as a junction between microstrip and a coaxial line in nature.

To investigate the mode conversion of junction, under the assumption that the ground plane is finitely large we could simplify the problem by connecting the vertical via to the ground plane. This method enables the simplification of modeling and calculation.

In order to give a clear insight of via behavior due to discontinuities, the transition between microstrip and vertical via is modeled using HFSS as shown in Figure 2(a), and scattering parameters is obtained in Figure 2(c) plotted by solid lines. The filling substrate is Rogers RO4350B, and microstrip characteristic impedance is adjusted to be 50 Ohms.Wave port is employed to let in excitation. The effect of horizontal microstrip portion is also characterized in Figure 2(b), and simulation result is sketched in Figure 2(c) by dotted-lines showing that transition is nearly perfect. Clearly, transition leads to more and more signal reflection as frequencies rise.

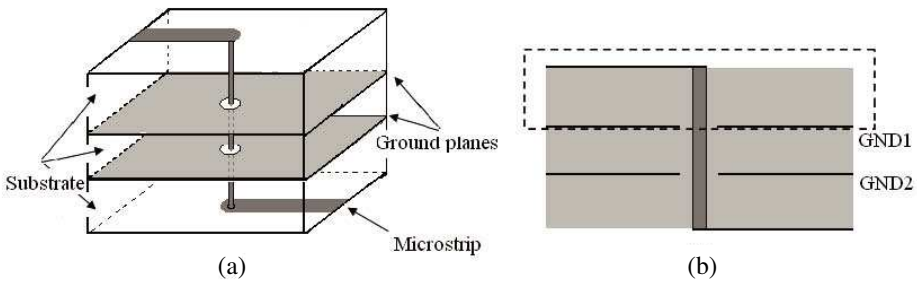

Figure 1: Studied structure: a through via penetrating ground planes to connect two microstrip lines in different layers. (a) 3D view, and (b) cross section under investigation and region of interest.

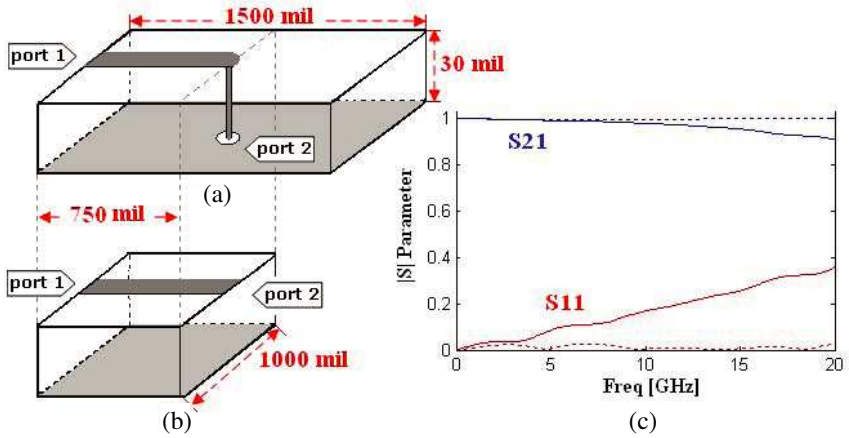

Figure 2: (a) transition between horizontal microstrip and vertical via, (b) microstrip structure with half the length, and (c) scattering parameter comparison between them.

2. FORMULATION

Matrix-Penciled Moment Method [2] is used to analyze structure under investigation. According to [3], the majority of the conduction current is in the propagation direction, and the transverse currents are roughly four orders of magnitude lower than the longitudinal currents. So only the longitudinal current is considered for the sake of simplicity in this paper, and the strips can be alternated by metallic solid cylinder without loss of generality. Under the thin wire approximation, the current is assumed to be placed on the curved wire, and satisfies the following Pocklinton Integral Equation

$$\int I(s')\left(\frac{\partial^2}{\partial s\partial s'}-k^2\right)G(s,s')ds' = jw\varepsilon\hat{s}\cdot\mathbf{E}^i(s) \tag{1}$$

After discretizing, the method of moments (MoM) is used to approximate the current density, the Galerkin weighting procedure is deployed to obtain a set of linear equations in the form:

$$[Z_{mn}]\cdot[\ c_n\ ] = [V] \tag{2}$$

where Z_{mn} is the reaction term between the mth basis function and nth basis function, $[V]$ is the excitation array, and c_n is the to-be-determined current coefficient of the problem.

Matrix pencil post-treatment[4] is then used to extract the propagation constants and modal amplitudes of all the guided modes existing on the wire. If we consider M significant modes, we get

$$c_n = \sum_{i=1}^{M} b_i\cdot\Delta_i^n \quad \text{with} \quad \Delta_i = e^{\Delta\gamma_i} \quad \text{and} \quad n = 0,1,2,\ldots,N_t-1 \tag{3}$$

where γ_i and b_i are, respectively, the complex propagation constant and the modal amplitude of the ith-order mode. N_t is the total number of sampled points, and Δ is the distance between two of the nearby sampling points (length of the cell). Hence, γ_i and b_i can be obtained according to the matrix pencil method. A sufficient N_t of sampled points may be chosen, $[Y_0]$ and $[Y_1]$ are constructed with element values defined by

$$Y_0(i,j) = c_{i+j-2}; \quad Y_1(i,j) = c_{i+j-1}; \tag{4}$$

where $i,j = 1,2,\ldots,N_t-1$, Δ_i corresponds to one of the eigenvalues of the matrix pencil $[Y_0^+]\cdot[Y_1]$, where $[Y_0^+]$ is the pseudoinverse of $[Y_0]$.

To compute the pseudoinverse $[Y_0^+]$, one can use the singular value decomposition (SVD) of $[Y_0]$ as follows:

$$Y_0 = \sum_{i=1}^{M}\left(\sigma_i u_i v_i^H\right) = U\cdot D\cdot V^H \quad Y_0^+ = V\cdot D^{-1}\cdot U^H$$

where $U = [u_1, u_2, \ldots, U_M]$, $V = [v_1, v_2, \ldots, v_M]$ and $D = \mathrm{diag}[\sigma_1, \sigma_2, \ldots, \sigma_M]$. The superscript H denotes the conjugate transpose of a matrix. U and V are matrices of left and right singular vectors, respectively. We choose $[\sigma_1, \sigma_2, \ldots, \sigma_M]$ to be the M largest singular values of Y_0. The number of significant modes is equal to the number of singular values if $N_t/2$ is larger than M. The eigenvalues Δ_i yields γ_i from (8) and can be obtained using the following total-least-squares problem:

$$\begin{bmatrix} c_0 \\ c_1 \\ \vdots \\ c_{N-1} \end{bmatrix} = \begin{bmatrix} 1 & 1 & \cdots & 1 \\ z_1 & z_2 & \cdots & z_M \\ \vdots & \vdots & \ddots & \vdots \\ z_1^{M-1} & z_2^{M-1} & \cdots & z_M^{M-1} \end{bmatrix} \begin{bmatrix} b_0 \\ b_1 \\ \vdots \\ b_{M-1} \end{bmatrix} \tag{5}$$

Note that the incoming and outgoing waves are considered as two different modes in the matrix pencil method.

3. NUMERICAL RESULTS

For computational simplicity, a structure with the physical parameters described in [2] is considered. Due to its high frequency range, when the TEM wave travels along the transmission line, there will be some apparent radiation which can not be neglected. As TEM wave traveling along the wire encounters vertical bend, the bend discontinuity will cause severe wave reflection for impedance mismatching. Incident wave and reflected wave will thus merge to become total wave (corresponding to current distribution) on the transmission line. With given physical parameters and the choice of basis functions shown in Figure 3, the unknown current coefficient c_n along the wire can be solved by (5), and is shown in Figure 3. Note that the magnitudes of both the real and the imaginary parts are calculated at every sampling point in spatial domain. With the imaginary part corresponding to the energy storage and radiation, we can easily draw the conclusion that more energy can be stored or radiated as frequencies increase.

By matrix pencil method, the M significant modes of the electromagnetic field existing on the wire can be extracted. The choice of the parameter M is done after the SVD of $[Y_0]$. One looks at the ratio of the various singular values to the largest one. Typically, the singular values beyond M are set equal to zero. The way M is chosen is as follows. Consider the singular value σ_c such that

$$\frac{\sigma_c}{\sigma_{\max}} \approx 10^{-p} \tag{6}$$

where p is used to filter noise in the data (If the data provided is precise, p is used to obtain existing modes, as is adopted in this paper). For example, if p is chosen to be -3, then the singular values for which the ratio in Equation (11) is below are considered as noise singular values, and should not be used in the reconstruction of the data. In this particular via discontinuities, current distribution is the data to be investigated, but due to the model equivalence and the truncation error of numerical computation, noise is inevitable. All nonzero singular values of Y_0 are listed as follows:

$$\sigma = [4.4141 \quad 3.0608 \quad 0.5394 \quad 0.0260 \quad 0.0081 \quad 0.0004 \quad 0.0001] \tag{7}$$

According to different choices of p values, the number of significant modes M can be calculated, as shown in Tables 1–3.

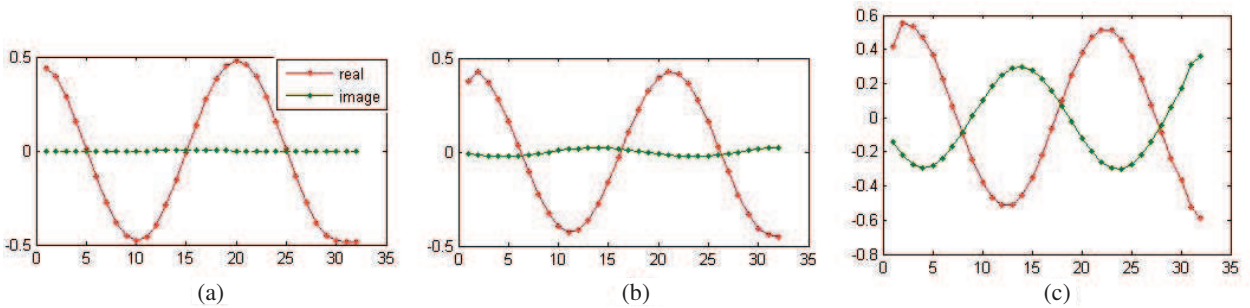

Figure 3: Coefficient of relative current at every sampling point along the wire at different frequencies: (a) 1 GHz, (b) 10 GHz, (c) 20 GHz.

Table 1: Significant modes when $p = -3$.

i	Δ_i	$\ln \Delta_i$	b_i	Propagation Direction
1	$-0.1031 + 0.0136i$	$-2.2634 + 3.0107i$	$0.6050 + 0.0231i$	False
2	$0.9493 - 0.3104i$	$-0.0012 - 0.3160i$	$0.2395 + 0.1261i$	Forward
3	$0.9526 + 0.3092i$	$0.0015 + 0.3138i$	$0.1553 - 0.1493i$	Backward

Table 2: Significant modes when $p = -4$.

i	Δ_i	$\ln \Delta_i$	b_i	Propagation Direction
1	$-0.1202 + 0.0073i$	$-2.1165 + 3.0812i$	$0.5901 + 0.0179i$	False
2	$0.9493 - 0.3101i$	$-0.0014 - 0.3157i$	$0.2410 + 0.1245i$	Forward
3	$0.9540 + 0.3087i$	$0.0027 + 0.3130i$	$0.1540 - 0.1433i$	Backward
4	$0.8643 + 0.0484i$	$-0.1442 + 0.0559i$	$0.0149 + 0.0009i$	False

Table 3: Significant modes when $p = -5$.

i	Δ_i	$\ln \Delta_i$	b_i	Propagation Direction
1	$-0.1183 + 0.0016i$	$-2.1346 + 3.1278i$	$0.5936 + 0.0105i$	False
2	$1.3612 + 0.2930i$	$0.3310 + 0.2120i$	$-0.0000 + 0.0000i$	Backward
3	$0.9519 + 0.3089i$	$0.0008 + 0.3138i$	$0.1556 - 0.1493i$	Backward
4	$0.9506 - 0.3094i$	$-0.0003 - 0.3147i$	$0.2389 + 0.1175i$	Forward
5	$0.7809 - 0.1762i$	$-0.2224 - 0.2220i$	$0.0118 + 0.0213i$	Forward

Note that, in (3) $\Delta = \lambda/20$, and consequently we get attenuation coefficient $\alpha_i = \mathrm{Re}\{\frac{20}{\lambda}\ln[\Delta_i]\}$ and phase coefficient $\beta_i = \mathrm{Im}\{\frac{20}{\lambda}\ln[\Delta_i]\}$. If $\beta_i < 0$, the ith mode is forward mode, it corresponds to the incident wave; if $\beta_i > 0$, it's backward mode and corresponds to the reflected wave. By this procedure, all existing modes are divided into two categories, so incident/reflected waves and their amplitudes can be calculated at the truncated end or elsewhere on the transmission line. It's well known that, for an electromagnetic wave propagating in lossy medium, the amplitude of the wave will damp along the propagating direction, so If $\beta_i < 0$ the attenuation coefficient must satisfy $\alpha_i < 0$, and If $\beta_i > 0$ then $\alpha_i > 0$. Keep this in mind, we can find out false poles in the above three tables (the third mode in Table 1, the first and last mode in Table 2 and the first mode in Table 3), which must be eliminated. In the matter of fact, these false poles mainly represent incident sources. The left modes are all normal ones. And the amplitudes of dominant mode of incident and reflected waves are $A = 0.2713$ and $B = 0.2104$, respectively. In a region far enough from the impressed source port and the discontinuity, higher order modes have negligible amplitudes so that the electric field behavior along the line is of the form

$$V(l) = V^+ e^{-j\beta l} + V^- e^{j\beta l} \tag{8}$$

The propagation constant β of the microstrip being computed in advance, the values of V^+, V^- are defined by voltage magnitudes of incident and reflected waves.

It is also worth mentioning that the incident source having large attenuation coefficient conforms to previous assumption that incident source is only set at the port. The total amplitude of incident source,forward and backward wave summation equals exactly unit amplitude, which indicates conservation of energy.

Radiation is the crucial word in full-wave modeling, and we assume that the structures under study are open, thus we postulate from the very beginning that the surface currents existing on the conducting parts will radiate. The normalized equivalent impedance Z_{sc} of the grounded via is given by $Z_{sc} = (1 + \Gamma_{sc})/(1 - \Gamma_{sc})$.

Figure 4 shows the real and imaginary parts of Z_{sc} versus the frequency for the via structures with the original parameters. It's observed that $\mathrm{Re}\{Z_{sc}\}$ first increases gradually and then more drastically, which reveals the radiation mechanism of via structure. Note that the imaginary part is approximately proportional to frequency when operating frequency is less than ten GegaHz, which confines with quasi-static analysis of short circuit problem implemented in [5] without considering radiation effect shown in Figure 5:

$$Z = jwL_e \propto L_e \tag{9}$$

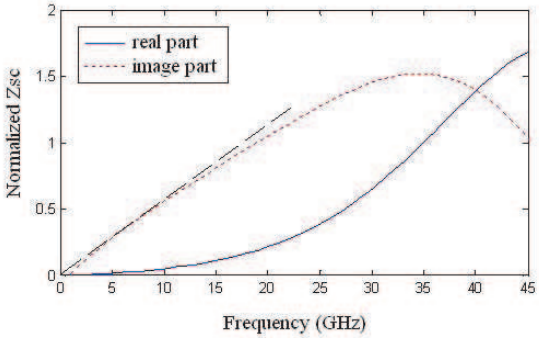

Figure 4: The normalized impedance versus the frequency for default structure and parameters.

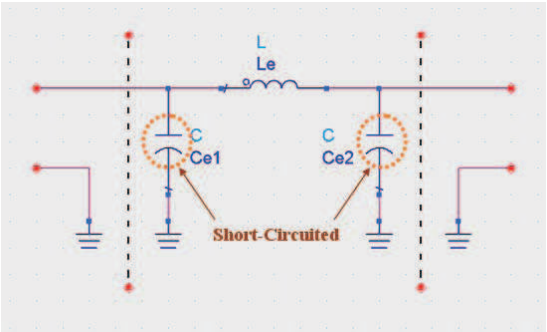

Figure 5: The quasi-static equivalent circuit.

At lower frequencies, the real part tend to be zero, radiation is respected to be very low, and quasi-static method is applicable for successfully predicting the imaginary part of Z_{sc}. But as frequencies go higher, the real part becomes non-negligible compared to its imaginary part, and also the quasi-static model fails to predict the imaginary part since it's no longer proportional to operating frequencies.

4. CONCLUSION

Mode conversion caused by via discontinuities is a critical issue in designing microwave circuits. At lower frequencies, the effects of vias are so negligible that they may be used freely; but as operating frequencies extend to multi-Gigahertz, the concern over via's effect on system performance has become a topic of discussion. Through theoretical analysis, It's generally concluded that:

(1). The via discontinuities may excite many other modes on the trace when an incident TEM mode is imposed on the trace end.
(2). The imaginary part of current coefficient along the wire, which corresponds to energy storage and radiation, increases versus operating frequencies.
(3). Signal attenuation is observed from the propagation constants of all existing modes.
(4). The high order modes decrease rapidly from the source port, only the dominant modes of incident and reflected wave need to be considered in a region far enough from the impressed source port and the discontinuity.
(5). The real part of normalized equivalent impedance growing rapidly with frequency, corresponds to radiation.

ACKNOWLEDGMENT

This work was supported by basic research item of National Key Lab of Electronic Measurement Technology of China.

REFERENCES

1. Liaw, H.-J. and H. Merkelo, "Simulation and modeling of mode conversion at vias in multilayer interconnections," *45th Electronic Components and Technology Conference Proceedings*, 361–367, May 1995.
2. Hsu, S.-G. and R.-B. Wu, "Full wave characterization of a through hole via using the matrix-penciled moment method," *IEEE Trans. Microwave Theory Tech.*, Vol. 42, No. 8, 1540–1547, 1994.
3. Swanson, D. G., Jr. Wolfgang, and J. R. Hoefer, *Microwave Circuit Modeling Using Electromagnetic Field Simulation*, Artech House, Boston, 2003.
4. Sarkar, T. K. and O. Pereira, "Using the matrix pencil method to estimate the parameters of a sum of complex exponentials," *IEEE Antennas and Propagation Mag.*, Vol. 37, No. 1, 48–55, 1995.
5. Wang, T. Y., R. F. Harrington, and J. R. Mautz, "The equivalent circuit of a via," *Trans. SOC. Comput. Simulation*, 97–123, April 1987.

The Feasibility of Numerical Calculations of Vias Using the Matrix-Penciled Moment Method

Hailiang Li, **Yu Tian**, **and Ling Tong**
College of Automation Engineering, UESTC, Chengdu, China

Abstract— The feasibility of numerical calculations of a through hole via using the Matrix-Penciled Moment Method (MP-MM) proposed by Show-Gwo Hsu and Ruey-Beei Wu is investigated. It shows that the MP-MM can't be used to the via which is near the source port, and there is a lower bounded operating wavelength beyond which MP-MM is not applicable. The conclusions are proven by both theory and the simulation results gotten by HFSS.

1. INTRODUCTION

The miniaturization and large scale integration of electronic devices places increasing demand on the multilayer interconnection geometry. Design of high-speed electronic systems requires careful consideration of the high frequency problems due to parasitic effects from these interconnects. In multi-layer structures, there are parallel lines for signal transmission as well as vias to connect the signal lines in different layers. Several studies involving the electrical characterization and design of the signal lines have been reported in previous literature. The equivalent circuits for some basic via structures have been presented by several investigators on the basis of quasi-static analysis [1]. Using the finite-difference time-domain (FD-TD) method [2], presented a full wave analysis for the propagation characteristics of a through hole via. In [3], three-dimensional mode matching technique was used to model the via hole grounds in microstrip. In [4, 5], finite-elment time-domain method was used to analyze through hole.

In the last decade, Show-Gwo Hsu and Ruey-Beei Wu proposed full wave characterization of a through hole via using the Matrix-Penciled Moment Method [6]. Based on the Pocklinton Equation, the method calculates the current distributions on via discontinuities by MoM, extracts poles by using Matrix-penciled method, gets the complex coefficient of every mode by solving Vandermonde equations, and finally, obtains the scattering parameters of via from superposition principle. The analytical and computational process is more complex than any other computational electromagnetic methods, but it has predominance in computational accuracy and speed for using the right basis and testing function and transforming the three dimensional problem to one dimensional by equivalent thin wire approximation.

The MoM is a computational electromagnetic method with high computational accuracy in most scattering and antenna radiation problem, but the method in Show-Gwo Hsu's literature contained two equivalences:

1) The shape of the microstrip/strip lines in horizontal segment (shown in Figure 1 is ignored and treated as circular cylinder. This equivalence is accurate when the length of transmission lines is infinite, but in actual microwave circuits, due to the restriction of trace and the measure of microwave circuit boards, the microstrip/strip line can't extend to infinity. The equivalence theory and its limitation will be presented in Sections 3 and 4, respectively.

2) MP-MM is based on Pocklinton Equation obtained by considering the antenna as thin wire. Section 5 will discuss the condition in which the transmission line can be seen as thin wire and propose a lower bounded operating wavelength of this method.

There is no question about the predominance of this method in computing the electromagnetic characterizations of via, but it is not a general-purposed method for it is not based on the real structure and rigorous equation which has no approximation.

At present, most literatures about this method introduce its principles [6] and/or some particular calculational examples [7], on the contrary, neglecting the investigation about the application spectrum in which the method can be used, that is the emphasis of this paper.

The structure investigated in this paper is a through via with one ground plane. The tool used for simulation is HFSS.

2. PRINCIPLES OF MATRIX-PENCILED MOMENT METHOD

Let us briefly recall the basic principles of MP-MM for investigating the feasibility of this method.

A typical interconnection structure of vertical via in a multi-layered circuit is shown in Figure 1. The upside and downside microstrip/strip lines are connected by a vertical via, and the via penetrates the ground plane through a via hole. The vertical distances between upside, downside transmission lines and the middle ground plane are h_1 and h_2, respectively. The width of upside, downside transmission lines are w_1 and w_2, respectively. The radius of via and the hole in the ground plane is a and b, respectively. The magnitude of incident TEM waves of upside and downside transmission lines are A_1 and A_2, respectively, while the magnitude B_1 and B_2 of reflect waves are need to be calculated for solving the scattering parameters of the via.

For the convenience of calculation, we transform the microstrip/strip lines into circular-cylinders used by the theory of antenna and the equivalent process will be introduced in Section 3. The equivalent radius of the upside and downside transmission lines are ρ_1 and ρ_2, respectively, shown in Figure 2.

Based on equivalent principle, the via hole of ground plane can be substituted by ideal conductor with magnetic current $\overrightarrow{M}$ and $-\overrightarrow{M}$ on its upside and downside plane, thus the problem can be divided into two parts, an antenna radiation problem (shown in Figure 3) and a short-circuit problem (shown in Figure 4).

In the factual calculation, suppose the length of microstrip/strip lines more than one operating wavelength. Using the piecewise sinusoidal basis function $f_n(s)$, the unknown current $I(s')$ on transmission line can be approximated as

$$I\left(s'\right) = \sum_{n=0}^{N} C_n f_n\left(s'\right) \tag{1}$$

Based on the boundary conditions of conductor and some approximations, the integral equation of unknown current can be expressed as [8]

$$\int I\left(s'\right)\left(\frac{\partial^2}{\partial s \partial s'} - k^2\right) G\left(s, s'\right) ds' = jw\varepsilon \hat{s} \cdot \mathbf{E}^i(s) \tag{2}$$

where $G(s, s')$ is Green's function, and $E^i(s)$ is the electric field excited by the magnetic current.

According to image theory, the current coefficient C_n can be obtained using (1) and (2).

Assuming M modes exist in the module, the current coefficient C_n can be expressed as

$$C_n = \sum_{i=1}^{M} b_i e^{\lambda_i n \Delta} = \sum_{i=1}^{M} b_i z_i^n \tag{3}$$

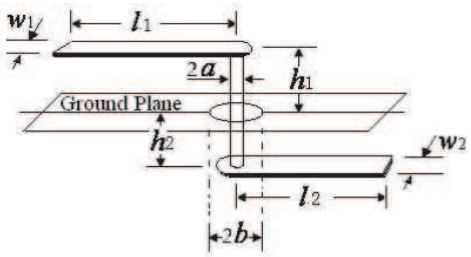

Figure 1: A typical structure of vertical via interconnection.

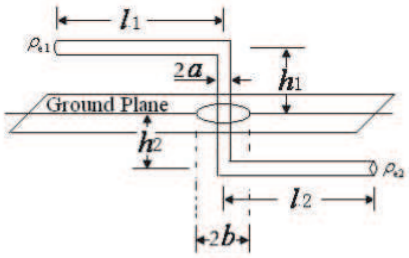

Figure 2: The equivalent structure of vertical via shown in Fig. 1.

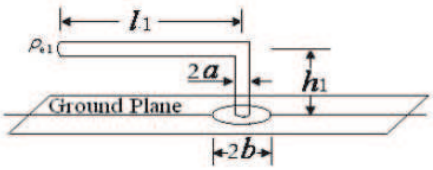

Figure 3: Antenna radiation problem.

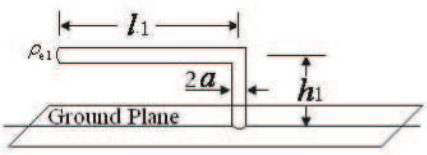

Figure 4: Short-cicuit problem.

where

$$z_i = e^{\lambda_i \Delta} \tag{4}$$

Then, z_i can be obtained by using Matrix-penciled method, and b_i can be gotten by solving Vandermonde equations. Finally, by the superposition principle, the scattering parameters of via can be solved [6].

3. THE EQUIVALENT RADIUS OF UNIFORM ANTENNAS WITH NONCIRCULAR CROSS SECTION

The equivalent radius of uniform antennas with noncircular cross section was suggested by Erik Hallen [9]. Hallen stated that antennas with noncircular cross section could be examined mathematically by considering them to be cylindrical in shape and having an equivalent radius. Once the equivalent radius is known, some very complicated problems, like those of strip antennas in a dielectric slab and slot antennas printed on a dielectric substrate, can be reduced to a much simpler case of equivalent circular-cylindrical antenna with a coaxial dielectric or magnetic. Concretely, in this paper, the equivalent cylinder is used to calculate the current coefficient C_n in the antenna problem (mentioned in Section 2) expediently.

A thin wire antenna with nonregular cross section is shown in Figure 5, as the metallic part of the antenna is assumed to be made of a perfect conductor, the tangential component of the electric-field vector on the metallic surface is zero, and so is the normal component of the magnetic-field vector. If the ratio of l/r is far greater than 1, then the equivalent radius ρ_e of antenna satisfies equation [10]

$$\ln \frac{l}{\rho_e} = \oint_c \varphi\left(s'\right) \ln \frac{l}{d\left(s, s'\right)} ds' \tag{5}$$

where $d(s, s')$ is direct distance between two points s and s' taken on the closed periphery c of the cross section and $\varphi(s')$ is the value of the current density in the periphery c of the cross section.

In the actual antenna, the value of function

$$\psi(s) = \oint_c \ln \frac{l}{d\left(s, s'\right)} ds' \tag{6}$$

changes little with the changing of s. So Equation (5) can be approximated to

$$\ln \rho_e \approx \frac{l}{a^2} \oint_c \oint_c \ln d\left(s, s'\right) ds ds' \tag{7}$$

where a is the length of the closed curve c of the cross section.

For the antenna with flat strip cross section, using (7), we can get

$$\rho_e = \frac{w}{4} \tag{8}$$

where w is the width of the flat strip.

4. FROM MICROSTRIP/STRIP LINE TO CIRCULAR-CYLINDER

In the Section 2, two parts are decomposed for calculating the characterization of a through hole via, and the microstrip/strip lines are transformed into circular-cylinders for the convenience of calculation.

In the short-circuit problem, a partial amount of the energy from source port would radiate into the free space, and the rest would be reflected along the transmission line. And in the antenna problem, a wire antenna is bent into a transmission line shown in Figure 3. Given a unit voltage across the aperture, a partial amount of the energy would radiate into the free space and another partial amount would excite a TEM mode propagating on the transmission line.

So both problems contain electromagnetic radiation, and the electromagnetic radiation relate to frequency and the shape of the antenna. In Section 2, microstrip/strip lines are regarded as circular-cylindrical thin wire, irrespective of the value of l/w. In Section 3, it is deduced that the flat strip antenna can be equivalent to a circular-cylindrical antenna with $\rho_e = w/4$ only if $l/w \gg 1$. It means that the microstrip/strip line can be calculated from its equivalent circular-cylinders only when its shape can be ignored.

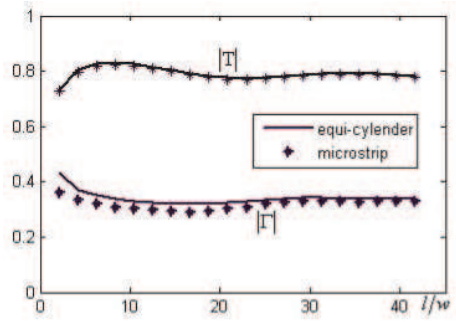

Figure 5: The scattering parameters of two structures changing with l/w.

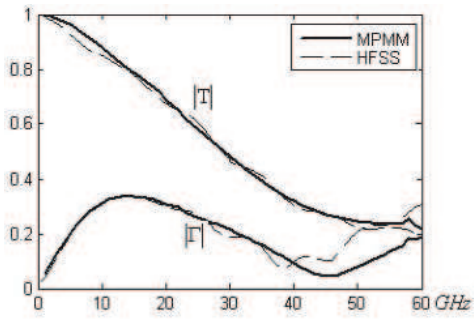

Figure 6: Comparison between the results by present approach and HFSS simulation.

Then the difference of scattering parameters between original and equivalent structure will be simulated with l as sweep-parameter.

Via interconnection structure as shown in Figure 1 and it's equivalent model are selected as research object, assuming $w_1 = w_2 = 4\rho_e = 240\,\mu\text{m}$, $h_1 = h_2 = 1.8\,\text{mm}$, $b = 3a = 180\,\mu\text{m}$, $\varepsilon_{er} = 2$. With the changing of the length of the upper and lower transmission lines, Figure 6 shows the different electromagnetic characterizations between two structures. Note that the scattering parameters of two structures are obtained by HFSS at 15 GHz.

From Figure 5, when $l/w > 25$, the scattering parameters of them are approximately the same. When l/w is less than 25, that's to say the via is very close to the source port, so the shape of transmission line can't be ignored. Thus it can't be simply model as a circular-cylindrical thin wire. So MP-MM couldn't be used in this condition.

5. A LOWER BOUNDED OPERATING WAVELENGTH

The MP-MM is based on Equation (2) which is derived from Pocklinton Equation, so the applicable conditions of Pocklinton Equation also work on it. In the derivation of Pocklinton Equation, it needs the radius of the antenna be far less than the operating wavelength λ_g and the length of antenna. Concretely, in this paper it needs

$$\rho_e \ll \lambda_g, l \tag{9}$$

In Section 4, the relation between l and ρ_e what the antenna should satisfy has been discussed, so in this section, we just investigate the constraint condition $\rho_e \ll \lambda_g$, which implies that there is a lower bounded operating wavelength for the MP-MM to calculate the characterization of vias.

In this section, a through via with real circular-cylinder transmission lines in upper and lower is calculated by MP-MM and simulated by HFSS. The radius of the upper and lower transmission lines are a_1 and a_2, respectively. Assuming $a_1 = a_2 = a = 60\,\mu\text{m}$, $h_1 = h_2 = 1.8\,\text{mm}$, every 1 GHz of 1–60 GHz Frequency band is abstracted as a sample to calculate the scattering parameters of via, and the scattering characteristics including reflect coefficient and transmission coefficient of 1–60 GHz frequency band can be obtained by aggregating all the scattering parameters of samples.

In Figure 6, it can be seen that the difference between HFSS and MP-MM becomes distinct when the operating frequency exceeds 40 GHz, which means that the MP-MM is not applicable in relatively high frequency. From (9) and Figure 6, it is estimated

$$\lambda_{g\,\min} \approx 89\rho_e \tag{10}$$

So if ρ_e is the equivalent radius of microstrip/strip line, from (8) the minimum operating wavelength which MP-MM can be used is

$$\lambda_{g\,\min} \approx 22w \tag{11}$$

To certain through via, the highest frequency solved by MP-MM can be estimated using (11).

6. CONCLUSION

The MP-MM is an approximate approach in essence. It enables the complicated problem of via to be reduced to a simpler thin wire with one dimension, but the application range is deflated at the same time.

The MP-MM can just calculate the via which is far away from the source port and the operating wavelength must exceed 22 times of the width of microstrip/strip line.

ACKNOWLEDGMENT

This work was supported by basic research item of National Key Lab of Electronic Measurement Technology of China.

REFERENCES

1. Wang, T. Y. and R. F. Harrington, "The equivalent circuit of a via," *Trans. Soc. Comput. Simulation*, Vol. 4, No. 1, 97–123, 1987.
2. Maeda, S., T. Kashiwa, and I. Fukai, "Full wave analysis of propagation characteristics of a through hole using the finite-difference time-domain method," *IEEE Trans. Microwave Theory Tech.*, Vol. 40, No. 10, 2154–2159, 1991.
3. Sorretino, R., F. Alessandri, and M. Mongiardo, "Full-wave modeling of via hole grounds in microstip by three-dimensional mode matching technique," *IEEE Trans. Microwave Theory Tech.*, Vol. 40, No. 12, 2228–2234, 1992.
4. Chang, S., R. Coccioli, and Y. Qian, "Finite element time domain based diakoptic method for microwave circuit analysis," *IEEE MTT-S International Microwave Symposium*, Vol. 1, No. 1, 235–238, 2000.
5. Koh, D., H. Lee, and T. Itoh, "A hybrid full-wave analysis of via-hole grounds using finite-difference and finite-elment time-domain methods," *IEEE Trans. Microwave Theory Tech.*, Vol. 45, No. 12, 2217–2222, 1997.
6. Show, G. H. and W. B. Ruey, "Full-wave characterization of a through hole via in multi-layered packaging," *IEEE Trans. Microwave Theory Tech.*, Vol. 43, No. 5, 1073–1081, 1995.
7. Sheng, J., X. Kuang, and X. Jun, "Simulation on vertical via interconnection using matrix-penciled moment method in microwave multi-chip module," *Microwove and Millimeter Wave Technology*, Vol. 1, No. 1, 235–238, 2007.
8. She, J. W. and R. Mittra, "Finite element analysis of MMIC structures and electronic packages using absorbing boundary conditions," *IEEE Trans. Microwave Theory Tech.*, Vol. 42, No. 3, 441–449, 1994.
9. Hallen, E., "Title of the journal paper," *Journal Title Abbreviation*, Vol. 34, No. 10, 1064–1076, 1986.
10. Uda, S., *Yagi-Uda Antenna*, Sasaki Printing and Publ. Co., Japan, 1954.

Microstrip Bandstop Filter Using E-shaped Dual Mode Resonator

X. D. Huang and C. H. Cheng
College of Electronic Science and Engineering, Nanjing University of Posts and Telecommunications
Mailbox 280#, 66 Xinmofan Road, Nanjing 210003, China

Abstract— The proposed bandstop filter (BSF) consists of a dual mode E-shaped resonator and a microstrip feeding line. By adjusting the resonator's central strip, the first two resonant frequencies could be moved together to build the stopband. The gap between the resonator and the feeding line is used as the coupling structure. Two arms of the resonator are bent to realize the balanced coupling, thus two refection zeroes could be observed beside the stopband after adjusting the arms' bend rate carefully. Filter samples are designed, fabricated and measured. As a result, a rejection level of −16.7 dB is achieved at the central frequency 6.01 GHz whereas two reflection zeros (< −45.0 dB) at 5.64 GHz and 6.24 GHz could be observed as predicted. The measured reflection is below −30.0 dB in its passband.

1. INTRODUCTION

Microwave BSF could be used to reject the unwanted signals in a designated frequency band. The miniaturization of a BSF is a hotspot in filter design. In general, the design procedure of a BSF is quite similar to a bandpass filter, thus some techniques used in bandpass filters could be applied directly to BSF applications. For example, planar bandpass filters using dual mode or multi-pole mode resonators have been attracting much attention in recent years, because of the useful features such as miniaturization, sharp rejection, and easy wideband realization [1–3]. Meanwhile, researchers have also applied those concepts to BSF applications for compact use [4, 5]. "Dual mode" here means the first two resonant modes in a physically individual resonator, and the two modes could be either degenerate or not [1, 3–5]. In the case of degenerate, the two modes could be split to resonate at different frequencies after adding some perturbation [1]. In the other case, one can move the first two resonant modes together by designing a specific resonator structure [3]. Then the two modes could be utilized to build the desired working band. The degenerate mode type dual-mode resonator has been applied to the bandstop filter applications in the reported literatures [4, 5]. Their main drawback is the weak passband matching ($|S_{11}| > -20.0$ dB). The non-degenerate type has not been reported for the BSF use so far.

In this research, with the purpose of both miniaturization and good passband matching, we will present a BSF using a non-degenerate E-shaped dual mode resonator. This resonator was originally proposed in 2004 and applied to bandpass application [3]. It is modified here to be E-shaped from T-shaped to obtain good passband matching. The filter structure is shown in Fig. 1. The simulations are all carried on a commercial EM package IE3D, and the substrate is Rogers 5880 with relative dielectric constant 2.2 and height 0.254 mm.

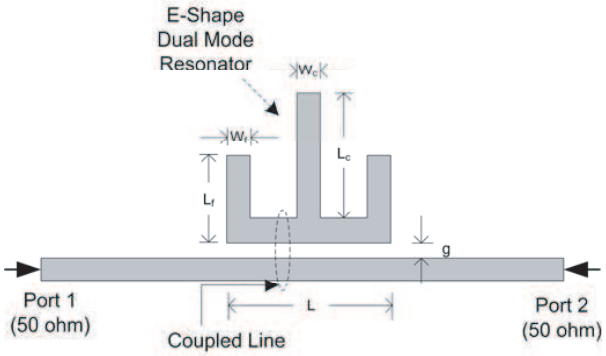

Figure 1: Configuration of the proposed bandstop filter.

2. DESIGN AND DISCUSS

As shown in Fig. 1, an E-shaped resonator is arranged above a piece of microstrip transmission line with length L. The gap between them is used as the coupling structure. The characteristic

impedance of the transmission line is chosen to be 50 Ohm to obtain good passband matching in wideband.

The first two resonant frequencies of the E-shaped resonator could be easily extracted using the odd-even modes analysis. As shown in Fig. 2, in the odd excitation case, an electric wall could be added to the symmetric line of the whole structure. Thus a quasi quarter wavelength resonator could be extracted. In the even case, the electric wall is replaced by a magnetic wall and the resonator can be equivalent to a folded quasi half wavelength resonator. The odd resonant frequency f_o is determined by Z_3, θ_3, Z_2 and θ_2, whereas the even frequency f_e is determined by Z_4, θ_4, Z_3, θ_3, Z_2 and θ_2. Therefore, the central strip length L_c has no influence on f_o, this feature is quite useful for mode tuning. Fig. 3 shows a virtual test circuit with weak coupling for extracting the resonant frequencies. For simplicity, we set $Z_3 = Z_2$, $Z_1 = Z_0$. With the increasing of L_c (θ_4), f_e decreases whereas f_o keeps unmoved as expected. A transmission zero could also be observed which moves with f_e. The results validate the odd-even analysis greatly, and agree well with the former research [3].

Another adjustable parameter is the bend rate of resonator's arm. The BSF will look simpler without bends. However, without bends, the coupling between feeding line and resonator will be weakest in odd mode whereas strongest in even mode according to the coupled line theory [6], as shown in Fig. 2, results in a unbanced coupling or single mode in the working band. Fig. 4 illustrates the relection responses of E-shaped dual mode BSFs with different bend rates. From the curves we could find that two balanced reflection zeros is realized under a proper bend rate. In addtion, the gap between feedline and resonator dominates the coupling in both odd-even cases. As shown in Fig. 5, it is quite sensitive. The coupling is stronger with smaller gap size g. Therefore,

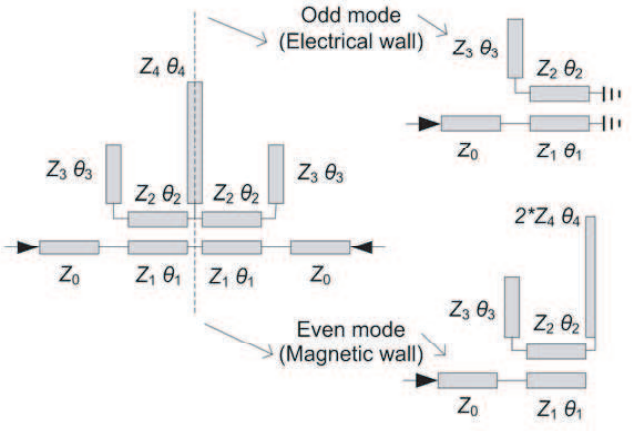

Figure 2: Circuit models of Odd- and Even- modes excitations.

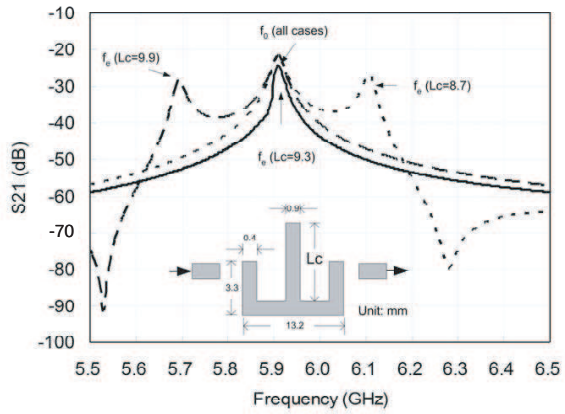

Figure 3: Frequency responses with different lengths of central strip under weak coupling.

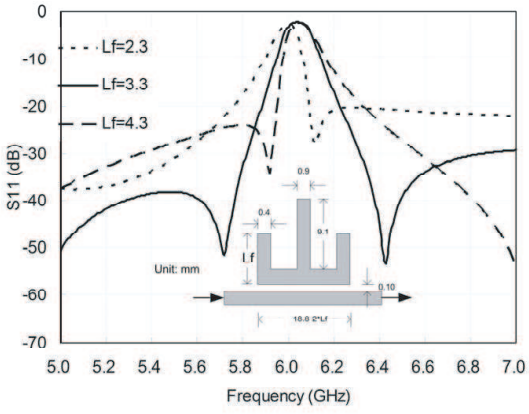

Figure 4: Comparison of S_{11} with different bend rates.

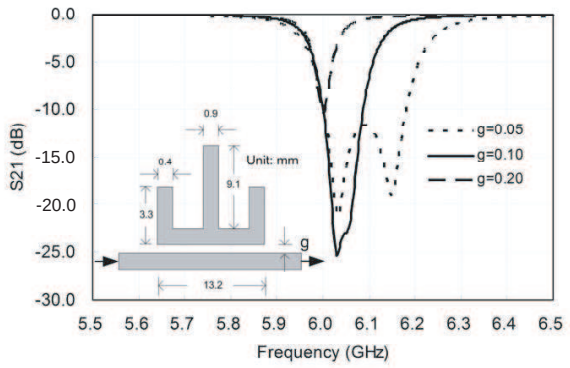

Figure 5: Comparison of S_{21} with different gap sizes.

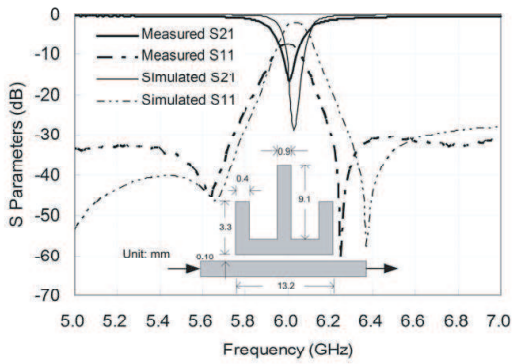

Figure 6: Measured and simulated results of a practical BSF.

the BSF's working frequency is dependent on the odd-mode resonant frequency, which could be modified by $L_f + L/2$. The relative working bandwidth is determined by distance of the odd-even mode frequencies, which could be easily adjusted by L_c. The matching strength is controlled by g while matching balance is controlled by the bend rate L_f/L. The widths of the lines (W_c, W_f) have smaller impact on frequency tuning than the lengths (L_c, L_f).

3. MEASUREMENT

Several BSF samples have been designed and fabricated for measurement. The designated central frequency is around 6.0 GHz for experiment. The circuit dimensions and results are shown in Fig. 6. The measured highest rejection level is −16.7 dB at 6.01 GHz whereas the best simulated rejection is −28.9 dB at 6.03 GHz. The 3 dB bandwidths in measurement and simulation are 3.5% and 2.6%, respectively. Two reflection zeros besides the stopband can be observed at 5.64 GHz and 6.24 GHz, both below −45.0 dB, which offer good passband matching for this BSF. The peak of in-band return loss is about −7.0 dB, much larger than the simulated (−2.0 dB). The reason is that the conducting loss is not considered in the simulations. However, such a high loss in BSF is not as critical as that in a bandpass filter. Because the useful signals will pass through in the passband with good matching; in our case, the passband matching degree achieves −30.0 dB.

4. CONCLUSION

In this study, the authors presented a novel BSF with E-shaped dual mode resonator. Parametric sweeps were performed to investigate the properties of the filter. Filter samples were designed, fabricated and measured. The experimental results agreed with the simulation. It is believed that this filter will be competitive in microwave/RF planar BSF applications.

REFERENCES

1. Wolff, I., "Microstrip bandpass filter using degenerate modes of a microstrip ring resonator," *Electronics Letters*, Vol. 8, No. 12, 302–303, 1972.
2. Zhu, L., S. Sun, and W. Menzel, "Ultra-wideband (UWB) bandpass filters using multiple-mode resonator," *IEEE Microwave and Wireless Components Letters*, Vol. 15, No. 11, 796–798, 2005.
3. Lee, J. R., J. H. Cho, and S. W. Yun, "New compact bandpass filter using microstrip $\lambda/4$ resonators with open stub inverter," *IEEE Microwave and Wireless Components Letters*, Vol. 10 No. 12, 526–527, 2000.
4. Eryilmaz, G. M., E. Gunturkun, A. Gorur, and C. Karpuz, "Microstrip bandstop filter using a dual mode square loop resonator," *Microwave and Optical Technology Letters*, Vol. 51, No. 1, 147–150, 2009.
5. Hong, J. S., "Microstrip dual-mode band reject filter," *IEEE MTT-S International Microwave Symp. Digest*, 3–7, 2005.
6. Pozar, D. M., *Microwave Engineering*, John Wiley, New York, 1997.

Arbitrary Microwave Filters Using Waveguides Filled by Dielectric and Magnetic Layers

M. Khalaj-Amirhosseini and H. Ghorbaninejad-Foumani
College of Electrical Engineering, Iran University of Science and Technology, Iran

Abstract— A new structure was proposed for arbitrary microwave waveguide filters such as bandpass or bandreject filters. This structure utilizes a waveguide filled by several dielectric and magnetic layers and there is no requirement to any inductive elements such as diaphragms. The relative electric permittivity, the relative magnetic permeability and the thickness of the layers are optimally obtained using least mean square method. The usefulness of the proposed structure and its performance are verified by designing an equal ripple X-band waveguide bandpass filter.

1. INTRODUCTION

Microwave filters are an inevitable requirement of microwave circuits and communication circuits. Some various structures have been used for microwave filters such as microstrip filters [1–4], substrate integrated waveguides (SIWs) [5], dielectric resonator (DR) filters [6, 7] and waveguide filters [1–4], [8, 9]. Usually, waveguide filters utilize inductive elements such as irises, rods, diaphragms and posts as impedance inverters between two hollow or dielectric-filled regions of a waveguide [1–4], [8]. Fabrication of these filters has some difficulties because of implementing inductive elements into a waveguide. In this paper, a new structure is proposed to design waveguide filters with arbitrary frequency response and easy fabrication. This structure utilizes a waveguide filled by several dielectric and magnetic layers in a manner that each dielectric layer is followed by a magnetic layer and there is no requirement to any inductive elements such as diaphragms. In fact, the proposed structure is a multi-layer Longitudinally Inhomogeneous Waveguide (LIW) [10–12]. The relative electric permittivity, the relative magnetic permeability and the thickness of the layers are optimally obtained using least mean square approach. Therefore, the proposed structure has the capability to design filters with arbitrary frequency response in addition to the conventional ones such as bandpass and bandstop filters. The usefulness of the proposed structure and its performance is verified by an example.

2. ANALYSIS OF THE PROPOSED FILTERS

Figure 1 shows the proposed waveguide filter which is a waveguide with dimensions a, b and d, filled by K dielectric layers and K magnetic layers, alternately. The relative electric permittivity and the thickness of dielectric layers are $\varepsilon_{r,k}$ and d_{dk}, respectively, and also the relative magnetic permeability and the thickness of magnetics are $\mu_{r,k}$ and d_{fk}, respectively, for $k = 1, 2, \ldots, K$. It is assumed that a TE_{10} mode propagates towards the positive z direction. With this assumption, we have the following transverse electric and magnetic fields

$$E_y(x, z) = \sin(\pi x/a) E_y(z) \tag{1}$$

$$H_x(x, z) = \sin(\pi x/a) H_x(z) \tag{2}$$

The analysis of continuous LIWs has been presented in [10–12]. Here, the frequency domain analysis of the multi-layer LIWs is studied. The differential equations in the k-th dielectric layer at frequency

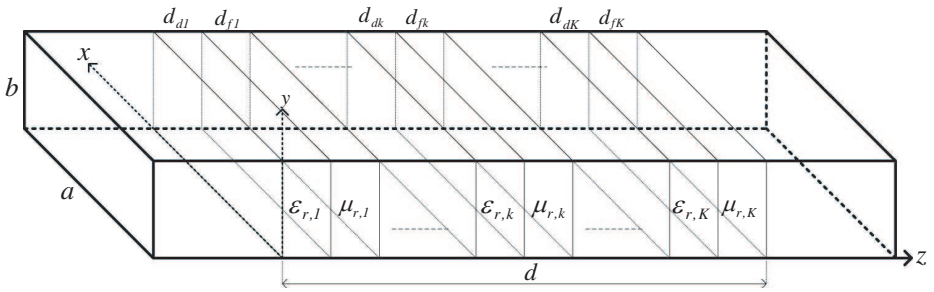

Figure 1: A waveguide filled by several dielectric and magnetic layers.

f are given by

$$\frac{dE_y(z)}{dz} = j\omega\mu_0 H_x(z) \tag{3}$$

$$\frac{dH_x(z)}{dz} = j\omega\varepsilon_0 \left(\varepsilon_{r,k} - (f_c/f)^2\right) E_y(z) \tag{4}$$

where

$$f_c = \frac{c}{2a} \tag{5}$$

in which c is the velocity of the light, is the cutoff frequency of the hollow waveguide, which must be less than f. Also, the differential equations in the k-th magnetic layer at frequency f are given by

$$\frac{dE_y(z)}{dz} = j\omega\mu_0\mu_{r,k} H_x(z) \tag{6}$$

$$\frac{dH_x(z)}{dz} = \frac{j\omega\varepsilon_0}{\mu_{r,k}} \left(\mu_{r,k} - (f_c/f)^2\right) E_y(z) \tag{7}$$

According to similarity of the above differential equations to the differential equations of transmission lines, the chain parameter matrix of the structure can be written as follows

$$\mathbf{T} = \begin{bmatrix} A & B \\ C & D \end{bmatrix} = \prod_{k=K}^{1} (\mathbf{T}_{dk}\mathbf{T}_{fk}) \tag{8}$$

in which $\mathbf{T}_{dk}$ and $\mathbf{T}_{fk}$ are the chain parameter matrices of the k-th dielectric and magnetic layers, respectively as follows

$$\mathbf{T}_d = \begin{bmatrix} \cos(\beta_{dk}d_{dk}) & jZ_{dk}\sin(\beta_{dk}d_{dk}) \\ jZ_{dk}^{-1}\sin(\beta_{dk}d_{dk}) & \cos(\beta_{dk}d_{dk}) \end{bmatrix} \tag{9}$$

$$\mathbf{T}_f = \begin{bmatrix} \cos(\beta_{fk}d_{fk}) & jZ_{fk}\sin(\beta_{fk}d_{fk}) \\ jZ_{fk}^{-1}\sin(\beta_{fk}d_{fk}) & \cos(\beta_{fk}d_{fk}) \end{bmatrix} \tag{10}$$

In (9) and (10), the following propagation coefficients and the characteristic impedances are existed.

$$\beta_{dk} = k_0\sqrt{\varepsilon_{r,k} - (f_c/f)^2} \tag{11}$$

$$\beta_{fk} = k_0\sqrt{\mu_{r,k} - (f_c/f)^2} \tag{12}$$

$$Z_{dk} = \frac{\eta_0}{\sqrt{\varepsilon_{r,k} - (f_c/f)^2}} \tag{13}$$

$$Z_{fk} = \frac{\eta_0\mu_{r,k}}{\sqrt{\mu_{r,k} - (f_c/f)^2}} \tag{14}$$

in which $k_0 = 2\pi f/c$ and $\eta_0 = \sqrt{\mu_0/\varepsilon_0}$ are the wave number wave and the impedance in the free space. After finding the $ABCD$ parameters of the structure, its S parameters can be found as follows

$$S_{11} = \frac{AZ_0 + B - CZ_0^2 - DZ_0}{AZ_0 + B + CZ_0^2 + DZ_0} \tag{15}$$

$$S_{21} = S_{12} = \frac{2Z_0}{AZ_0 + B + CZ_0^2 + DZ_0} \tag{16}$$

$$S_{22} = \frac{-AZ_0 + B - CZ_0^2 + DZ_0}{AZ_0 + B + CZ_0^2 + DZ_0} \tag{17}$$

where Z_0 is the characteristic impedance of the hollow waveguide given by

$$Z_0 = \frac{\eta_0}{\sqrt{1 - (f_c/f)^2}} \tag{18}$$

From (13), (14) and (18), one can see that the reason of using both dielectric and magnetic layers in the proposed filters is to have the characteristic impedances either lower or higher than the characteristic impedance of the hollow waveguide. This property of the proposed structure helps to achieve filters of better performance with respect to waveguide filters using only dielectric layers [9], certainly.

3. DESIGN OF THE PROPOSED FILTERS

In this section a general method is proposed to design optimally the Multi-Layer dielectric and magnetic LIW microwave filters. The method is based on the minimization of a suitable error function along with some constrained conditions to determine optimum values of the permittivity and thickness of dielectrics as well as the permeability and thickness of magnetic layers. One may define the following error function for M frequencies $f_1, f_2, \ldots, f_M$ which are greater than f_c.

$$\text{Error} = \sqrt{\frac{1}{M}\sum_{m=1}^{M}\left|\frac{|S_{21}(f_m)| - |H(f_m)|}{|H(f_m)|}\right|^2} \tag{19}$$

where $H(f)$ is the arbitrary desired transfer function of the filter. Moreover, defined error function has to be restricted by some constraints such as

$$d_{dk} \geq d_{d,\min} \quad \text{and} \quad 1 \leq \varepsilon_{r,k} \leq \varepsilon_{r,\max}; \qquad k = 1, 2, \ldots, K \tag{20}$$

$$d_{fk} \geq d_{f,\min} \quad \text{and} \quad 1 \leq \mu_{r,k} \leq \mu_{r,\max}; \qquad k = 1, 2, \ldots, K \tag{21}$$

to have easy fabrication.

4. EXAMPLE AND RESULTS

In this section, an arbitrary filter is optimally designed using a multi-layer dielectric and magnetic waveguide structure. Consider a WR-90 waveguide ($a = 0.9\,\text{in}$ and $b = 0.4\,\text{in}$) filled by $K = 10$ dielectric and magnetic layers. We would like to design a 3-order chebyshev bandpass filter with the center frequency of 10 GHz, the relative bandwidth of 10% and equal ripples of 1.0 dB. Using the proposed optimization method and considering $d_{d,\min} = d_{f,\min} = 0.4\,\text{mm}$, $\varepsilon_{r,\max} = \mu_{r,\max} = 8$, $f_1 = 8\,\text{GHz}$ and $f_M = 12\,\text{GHz}$ ($M = 200$), the optimum values of the filter parameters were obtained as shown in Table 1. Figure 2 illustrates the relative electric permittivity of dielectric layers as well as the relative magnetic permeability of magnetic layers. Also, Figure 3 shows the thickness of dielectric and magnetic layers. It is seen from Table 1 and Figures 2 and 3 that the designed filter is asymmetric and its total length is $d = 70\,\text{mm}$. Figure 4 compares the magnitude of S_{21} parameter of designed filter with the desired transfer function versus frequency. One sees an excellent agreement between the curves in the range of optimization frequencies. One can see that the frequency response of this designed filter is very closer to the desired transfer function than the frequency response of the conventional waveguide filters consisting of inductive elements, as is seen in [8]. It is evident that, as the number of dielectric and magnetic layers K is increased the agreement increases.

It is obvious that the advantages of the proposed filters could be mentioned as the followings:

1. The fabrication is easy because there is no needing to the elements such as diaphragms, iris, rods and posts and the dielectrics could glue easily to the walls of the waveguide and consequently the waveguide could be made monolithic instead of multi-sectional.
2. The mechanical stability is good because there is a monolithic waveguide filled by dielectrics glued to the walls and each other.
3. It is suitable for high power microwave circuits because the breakdown voltage of dielectrics and magnetics is higher than that of the air.
4. It is applicable to design filters with arbitrary frequency response in addition to the conventional ones such as bandpass and bandstop filters.
5. Their frequency response can be very closer to the desired transfer function than the frequency response of the conventional waveguide filters.

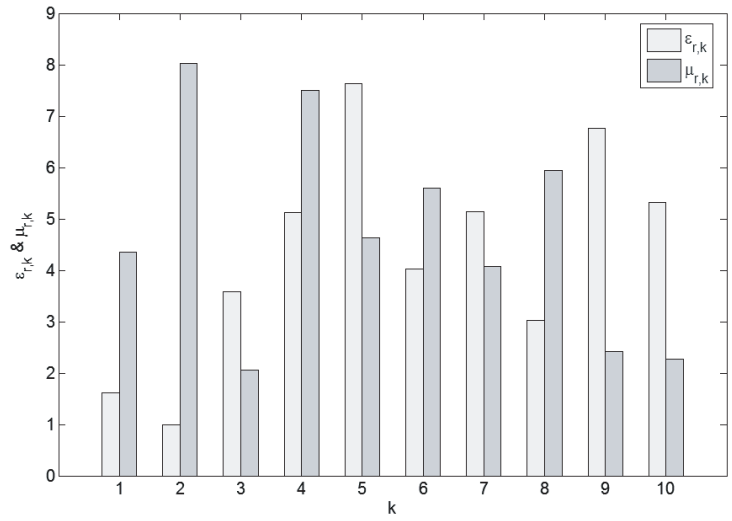

Figure 2: The relative electric permittivity of dielectric layers and the relative magnetic permeability of magnetic layers.

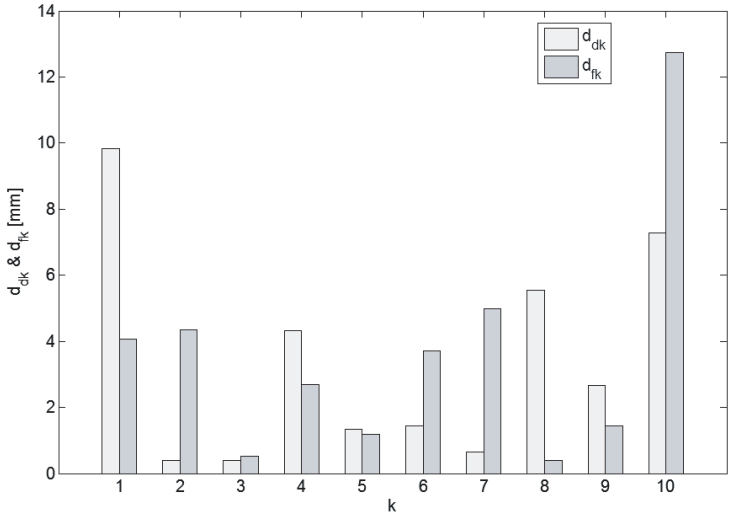

Figure 3: The thickness of dielectric and magnetic layers.

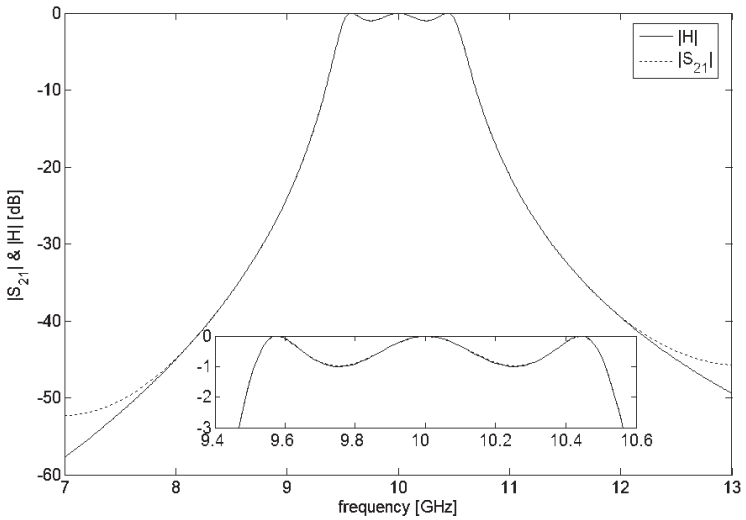

Figure 4: The magnitude of S_{21} parameter of designed bandpass filter and its desired transfer function.

Table 1: The optimum values of the filter parameters.

k	1	2	3	4	5	6	7	8	9	10
$\varepsilon_{r,k}$	1.6158	1.0000	3.5803	5.1193	7.6265	4.0297	5.1377	3.0175	6.7685	5.3221
d_{dk} [mm]	9.8335	0.4000	0.4004	4.3320	1.3312	1.4508	0.6580	5.5441	2.6542	7.2932
$\mu_{r,k}$	4.3452	8.0294	2.0644	7.5010	4.6238	5.6034	4.0700	5.9483	2.4138	2.2711
d_{fk} [mm]	4.0664	4.3563	0.5270	2.6843	1.1874	3.7118	4.9862	0.4000	1.4406	12.7426

5. CONCLUSION

A new structure was proposed for arbitrary microwave waveguide filters such as bandpass filters. The proposed structure utilizes a waveguide filled by several dielectric and magnetic layers. The relative electric permittivity, the relative magnetic permeability and the thickness of the layers are optimally obtained using least mean square method. The usefulness of the proposed structure was confirmed by designing an equal-ripple X-band bandpass filter. It was seen that the proposed filters have some advantages such as easy fabrication, mechanical stability, arbitrary frequency response, more desirable frequency response and capability of using in high power applications.

REFERENCES

1. Matthaei, G. L., L. Young, and E. M. T. Jones, *Microwave Filters, Impedance-Matching Networks and Coupling Structures*, Artech House, Dedham, Mass., 1980.
2. Pozar, D. M., *Microwave Engineering*, Addison-Wesley, 1990.
3. Collin, R. E., *Foundations for Microwave Engineering*, McGraw-Hill, New York, 1996.
4. Levy, R., R. V. Snyder, and G. Mattaei, "Design of microwave filters," *IEEE Trans. Microwave Theory Tech.*, Vol. 50, 783–793, 2002.
5. Sotoodeh, Z., B. Beglarbegian, F. H. Kashani, and H. Ameri, "A novel bandpass waveguide filter structure on SIW technology," *Progress In Electromagnetics Research Letters*, Vol. 2, 141–148, 2008.
6. Kobaysh, Y. and M. Mihegishi, "A band pass filter using high-Q dielectric ring resonators," *IEEE-MTT-S Digest*, 1987.
7. Saliminejad, R. and M. R. Ghafouri Fard, "A novel and accurate method for designing dielectric resonator filter," *Progress In Electromagnetics Research B*, Vol. 8, 293–306, 2008.
8. Ghorbaninejad, H. and M. Khalaj-Amirhosseini, "Compact bandpass filters utilizing dielectric filled waveguides," *Progress In Electromagnetics Research B*, Vol. 7, 105–115, 2008.
9. Khalaj-Amirhosseini, M., "Microwave filters using waveguides filled by multi-layer dielectric," *Progress In Electromagnetics Research*, PIER 66, 105–110, 2006.
10. Khalaj-Amirhosseini, M., "Analysis of longitudinally inhomogeneous waveguides using finite difference method," *International Conference on Information and Communication Technologies: From Theory to Applications (ICTTA 2006)*, 799–800, Damascus, Syria, April 24–28, 2006.
11. Khalaj-Amirhosseini, M., "Analysis of longitudinally inhomogeneous waveguides using Taylor's series expansion," *Journal of Electromagnetic Waves and Applications*, Vol. 20, No. 8, 1093–1100, August 2006.
12. Khalaj-Amirhosseini, M., "Analysis of longitudinally inhomogeneous waveguides using the Fourier series expansion," *Journal of Electromagnetic Waves and Applications*, Vol. 20, No. 10, 1299–1310, October 2006.

Waveguide Bandpass Filters Utilizing Only Dielectric Pieces

Mohammad Khalaj-Amirhosseini and Habib Ghorbaninejad-Foumani
College of Electrical Engineering, Iran University of Science and Technology, Tehran, Iran

Abstract— This paper describes a new procedure to design waveguide bandpass filters and presents analytical and exact formulas for it. The proposed structure consists of a waveguide which has been filled only by dielectric pieces and there is no requirement to any inductive elements such as diaphragms. In the introduced structure, manufacturing complexity is reduced while the performance of the filter is the good. Some analytical relations are obtained for physical and electrical parameters of the filter. Finally, the usefulness of the proposed structures and their performance are verified by designing and simulating an equal ripple X-band waveguide bandpass filter.

1. INTRODUCTION

Bandpass filters have a large variety of applications in microwaves and communication circuits. Some various structures have been used for microwave bandpass filters such as microstrip filters [1–4], substrate integrated waveguides (SIWs) [5], dielectric resonator (DR) filters [6, 7] and waveguide filters [1–4, 8, 9]. Usually, waveguide bandpass filters utilize inductive elements such as irises, rods, diaphragms and posts as impedance inverters between two hollow or two dielectric filled regions of a waveguide [1–4, 8]. Fabrication of these filters has some difficulties because of implementing inductive elements into a waveguide. In this paper, a new method is introduced to design of waveguide bandpass filters, whose fabrication is easy. In this method, a waveguide is filled only by several dielectric pieces and there is no needing to inductive elements such as irises, rods, diaphragms and posts. Moreover, the length of introduced filters may be less than that of filters consisting of hollow waveguides with inductive elements. Also, because there is no discontinuity in the introduced filters, their analysis is easy and accurate and so we do not need to optimization process to design them. The usefulness of the proposed structure and its performance is verified by an example and simulation using a full-wave simulator.

2. THE INTRODUCED WAVEGUIDE FILTERS

Figure 1 shows the proposed dielectric filled waveguide bandpass filter consisting of $2N+1$ dielectric filled regions in a rectangular waveguide. The cross section of the waveguide has dimensions of a and b and the lengths of dielectric filled regions are a quarter- or a half-wavelength alternately. In Fig. 1, λ_{gn} is the waveguide wavelength in the n-th region. The n-th region ($n = 1, 2, \ldots, 2N+1$) has been fully filled by a dielectric with relative electric permittivity ε_{rn}, where $\varepsilon_{r\,0} = \varepsilon_{r,\,2N+2} = 1$. The characteristic impedance and the phase constant of the n-th dielectric filled region are as the followings, respectively.

$$Z_n = \frac{\eta_0}{\sqrt{\varepsilon_{rn} - (f_c/f)^2}} \tag{1}$$

$$\beta_n = \frac{2\pi}{\lambda_{gn}} = \frac{2\pi}{\lambda_0}\sqrt{\varepsilon_{rn} - (f_c/f)^2} \tag{2}$$

where η_0 and λ_0 are the wave impedance and the wavelength of the wave in the free space, respectively. Also, f_c is the cut off frequency of the hollow waveguide. In fact, each quarter wavelength dielectric filled waveguide act as an impedance invertor and each half wavelength dielectric filled waveguide acts as a resonator. We have to choose appropriate values of relative electric permittivity for each section, whose values are determined in the following.

On the other hand, Fig. 2 shows an N-order bandpass filter consisting of N series resonators and $N+1$ impedance invertors. The value of impedance invertors and elements of resonators can be obtained according to the type of filter transfer function, center frequency and the bandwidth of the filter [1–4]. Of course, the values of impedance invertors, K_n, and the values of inductances, L_{0n}, are related to each other. Now we desire to model the proposed waveguide filter shown in Fig. 1 as a bandpass filter shown in Fig. 2 at center frequency f_0. For this purpose, two following modelings are required:

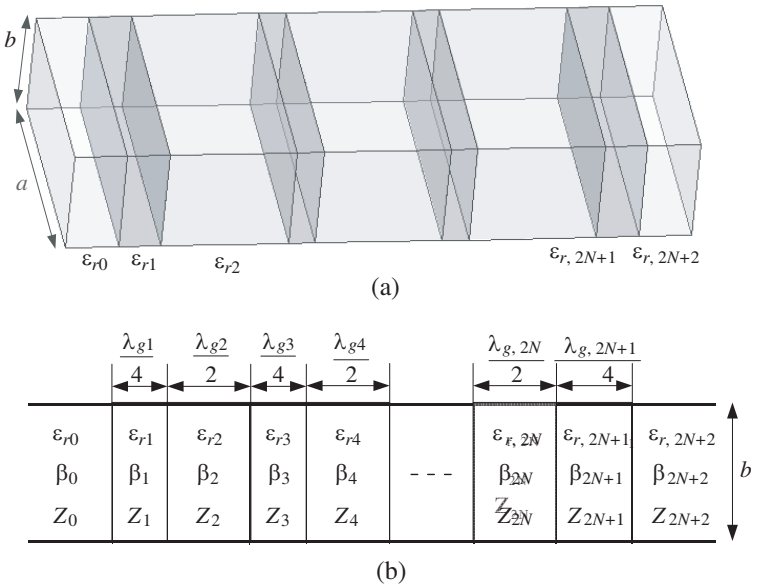

Figure 1: The proposed dielectric filled waveguide bandpass filter. (a) Three dimensional view. (b) Top view.

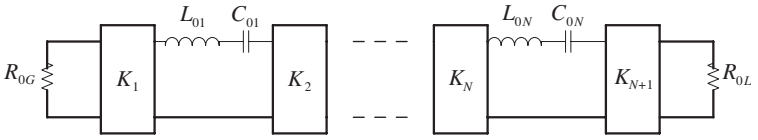

Figure 2: Typical bandpass filter using series resonators and impedance invertors.

M1. Modeling impedance invertors by quarter wavelength transmission lines. From (1) and noting that

$$Z_n = K_{1+(n-1)/2}; \quad n = 1, 3, \ldots, 2N+1 \tag{3}$$

the relative electric permittivities of these transmission lines are obtained as follows.

$$\varepsilon_{rn} = \left(\eta_0/K_{1+(n-1)/2}\right)^2 + (f_c/f_0)^2; \quad n = 1, 3, \ldots, 2N+1 \tag{4}$$

M2. Modeling series resonators by half wavelength transmission lines. Equating the $ABCD$ matrix of a half wavelength waveguide transmission line and its derivative with those of a lumped series resonator gives us the characteristic impedance of the n-th region as follows.

$$Z_n = 4f_0 L_{0(n/2)} \frac{\varepsilon_{rn} - (f_c/f_0)^2}{\varepsilon_{rn}}; \quad n = 2, 4, \ldots, 2N \tag{5}$$

According to the above mentioned modelings, the relative electric permittivities of the regions can be obtained using one of two following approaches:

A1. First, choose the relative electric permittivities of the even regions (resonators) and then determine the values of L_{0n} from (1) and (5) as follows

$$L_{0n} = \frac{\eta_0 \varepsilon_{r\,(2n)}}{4f_0 \left(\varepsilon_{r\,(2n)} - (f_c/f_0)^2\right)^{3/2}}; \quad n = 1, 2, \ldots, N \tag{6}$$

After finding all L_{0n}s the values of all K_ns are obtained. Then the relative electric permittivities of the odd regions (invertors) can be obtained from (4).

A2. First, choose the relative electric permittivities of the odd regions (invertors) and then determine the values of K_n from (4). After finding all K_ns the values of all L_{0n}s are obtained. Then the relative electric permittivities of the even regions (resonators) can be obtained from (1), (3) and (5) as the solution of the following polynomial equation

$$\varepsilon_{rn}^3 - \left[3(f_c/f)^2 + \left(\frac{\eta_0}{4f_0 L_{0(n/2)}}\right)\right]\varepsilon_{rn}^2 + 3(f_c/f)^4 \varepsilon_{rn} - (f_c/f)^6 = 0; \quad n = 2, 4, \ldots, 2N \tag{7}$$

The solution of (7) can be expressed as the following relation

$$\varepsilon_{r\,n} = \sqrt[3]{R + \sqrt{Q^3 + R^2}} + \sqrt[3]{R - \sqrt{Q^3 + R^2}} + T/3; \quad n = 2,\, 4,\, \ldots,\, 2N \tag{8}$$

where R, Q and T have been defined as the following relations

$$R = \frac{1}{54}\left[2\left(3(f_c/f_0)^2 + \left(\frac{\eta_0}{4f_0L_{0(n/2)}}\right)^2\right)^3 - 27(f_c/f_0)^4\left(1 + 3\,(f_c/f_0)^2 + \left(\frac{\eta_0}{4f_0L_{0(n/2)}}\right)^2\right)\right] \tag{9}$$

$$Q = (f_c/f_0)^4 - \left[(f_c/f_0)^2 + \frac{1}{3}\left(\frac{\eta_0}{4f_0L_{0(n/2)}}\right)^2\right]^2 \tag{10}$$

$$T = 3(f_c/f_0)^2 + \left(\frac{\eta_0}{4f_0L_{0n}}\right)^2 \tag{11}$$

After finding the relative electric permittivities of all regions, the length of dielectric regions are obtained as follows

$$d_n = \begin{cases} \frac{\lambda_0}{4\sqrt{\varepsilon_{rn} - (f_c/f)^2}}; & n = 1,\, 3,\, \ldots,\, 2N+1 \\ \frac{\lambda_0}{2\sqrt{\varepsilon_{rn} - (f_c/f)^2}}; & n = 1,\, 2,\, \ldots,\, 2N \end{cases} \tag{12}$$

3. EXAMPLES AND RESULTS

In this section, a bandpass filter is designed utilizing a WR-90 waveguide ($a = 0.9$ inches and $b = 0.4$ inches). We wish to design a 3-order chebyshev type bandpass filter with center frequency 10 GHz, the relative bandwidth 9% and equal ripples 0.5 dB. We use the design approach A1 and choose the relative electric permittivities of the even regions (resonators). It is assumed that all three transmission line resonators have the same relative dielectric permittivity $\varepsilon_{r\,2} = \varepsilon_{r4} = \varepsilon_{r\,6} = 2.1$ (fully dielectric-filled filter) or $\varepsilon_{r\,2} = \varepsilon_{r4} = \varepsilon_{r\,6} = 1$ (partly dielectric-filled filter). Using the relevant relations, the lengths and the relative electric permittivities of the dielectric filled regions for both filters have been calculated and are shown in Tables 1 and 2. Two designed filters are simulated using full-wave software HFSS, which is based on the finite element method FEM. Simulation results of both filters, are illustrated in Figs. 3 and 4. It is seen that the performance of the fully dielectric filled filter is identical to that of the partly dielectric filled filter while the length of former one is 41.43 mm and that of the latter one is 71.14 mm. Therefore the fully dielectric filled filter has about 41.7% compactness compared to the partly dielectric filled filter. Of course, the fully dielectric filled filter requires to higher permittivity dielectrics with respect to the partly filled filter. It is seen that the length of fully dielectric filled filter (41.43 mm) is less than that of waveguide filter consisting of hollow waveguides with inductive diaphragm (50.79 mm) [8]. From the above example one may satisfy regarding to the good performance of the proposed waveguide bandpass filters. Moreover, it is obvious that the advantages of the proposed filters could be mentioned as the followings:

1. The fabrication is easy because there is no needing to the elements such as diaphragms, iris, rods and posts and the dielectrics could glue easily to the walls of the waveguide and consequently the waveguide could be made monolithic instead of multi-sectional.
2. The mechanical stability is good because there is a monolithic waveguide filled by dielectrics glued to the walls and each other.
3. It is suitable for high power microwave circuits because the breakdown voltage of dielectrics is higher than that of the air.
4. The required length may be less than that of filters consisting of hollow waveguides with inductive elements.
5. Their analysis is easy and accurate because there is no discontinuity and so only dominant mode is existed in the waveguide. Therefore, there is no needing to optimization process in design step.

Table 1: The lengths of the dielectric filled regions.

Lengths [mm]	$d_1 = d_7$	$d_3 = d_5$	$d_2 = d_4 = d_6$
Fully dielectric-filled filter	2.5329	0.7795	11.6026
Partly dielectric-filled filter	3.9147	1.8620	19.8618

Table 2: The relative electric permittivities of the dielectric filled regions.

Relative electric permittivity	$\varepsilon_{r1} = \varepsilon_{r7}$	$\varepsilon_{r3} = \varepsilon_{r5}$	$\varepsilon_{r2} = \varepsilon_{r4} = \varepsilon_{r6}$
Fully dielectric-filled filter	9.1901	92.9240	2.1
Partly dielectric-filled filter	4.0947	16.64	1

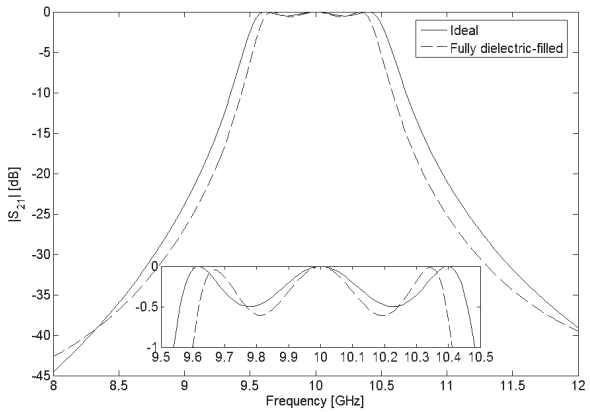

Figure 3: The simulation results of designed fully dielectric-filled bandpass filter.

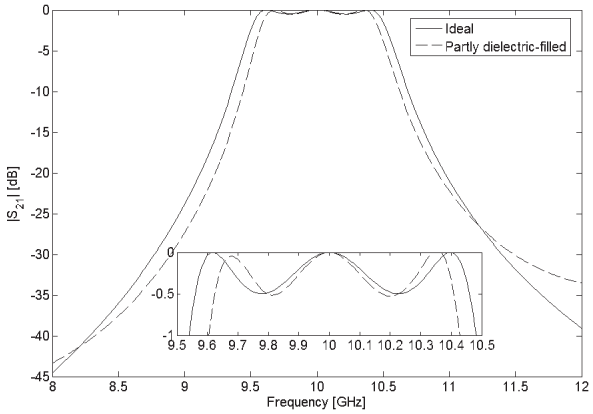

Figure 4: The simulation results of designed partly dielectric-filled bandpass filter.

4. CONCLUSION

A waveguide bandpass filter using fully or partly dielectric-filled waveguides was proposed. The proposed structure consists of several sections as transmission lines in the dominant mode of waveguide. Each section acts as an impedance inverter or a resonator. Some analytical relations are obtained for physical and electrical parameters of the filter. The relation between physical parameters and appropriate relative electric permittivity were obtained. The usefulness of the proposed structures and their performance are verified by designing and simulating an equal ripple X-band waveguide bandpass filter. It was seen that the proposed filters have some advantages such as easy fabrication, mechanical stability, capability of using in high power applications, compactness and having easy and accurate analysis and design relations.

REFERENCES

1. Matthaei, G. L., L. Young, and E. M. T. Jones, *Microwave Filters, Impedance-Matching Networks and Coupling Structures*, Artech House, Dedham, Mass., 1980.
2. Pozar, D. M., *Microwave Engineering*, Addison-Wesley, 1990.
3. Collin, R. E., *Foundations for Microwave Engineering*, McGraw-Hill, New York, 1996.
4. Levy, R., R. V. Snyder, and G. Mattaei, "Design of microwave filters," *IEEE Trans. Microwave Theory Tech.*, Vol. 50, 783–793, 2002.
5. Sotoodeh, Z., B. Beglarbegian, F. Hodjatkashani, and H. Ameri, "A novel bandpass waveguide filter structure on SIW technology," *Progress In Electromagnetics Research Letters*, Vol. 2, 141–148, 2008.
6. Kobaysh, Y. and M. Mihegishi, "A band pass filter using high-Q dielectric ring resonators," *IEEE MTT-S International Microwave Symposium Digest*, Vol. 87, No. 1, 1987.
7. Saliminejad, R. and M. R. Ghafourifard Fard, "A novel and accurate method for designing dielectric resonator filter," *Progress In Electromagnetics Research B*, Vol. 8, 293–306, 2008.

8. Ghorbaninejad, H. and M. Khalaj-Amirhosseini, "Compact bandpass filters utilizing dielectric filled waveguides," *Progress In Electromagnetics Research B*, Vol. 7, 105–115, 2008.
9. Khalaj-Amirhosseini, M., "Microwave filters using waveguides filled by multi-layer dielectric," *Progress In Electromagnetics Research*, PIER 66, 105–110, 2006.

New Antenna Modelling Using Wavelets for Heavy Oil Thermal Recovering Methods

M. D. Santos[1], **A. D. Neto**[2], **J. P. Silva**[3], **and W. Mata**[4]

[1]Departamento de Ciências Exatas e Naturais
Universidade Federal Rural do Semi-Árido — UFERSA, Brazil
[2]Departamento de Engenharia de Computação e Automação
Universidade Federal do Rio Grande do Norte — UFRN, Brazil
[3]Departamento de Ciências Ambientais e Tecnológicas
Universidade Federal Rural do Semi-Árido — UFERSA, Brazil
[4]Departamento de Ciências e Engenharia de Petróleo
Universidade Federal do Rio Grande do Norte Campus Universitário — UFRN, Brazil

Abstract— This paper presents a new computational mathematical model to investigate the use of a cylindrical antenna of the type adapted dipole in the local heating of the dissipative medium, in other words, reservoirs constituted by heavy oil. The thermal methods occupy a prominent position among the improved oil recovery methods due to their applicability in heavy oil reservoirs. These methods consist of supplying heat to the oil reducing in this way its viscosity by injecting a hot fluid, such as steam or hot air, or by the effect of electromagnetic waves on formation fluids. The electromagnetic heating is based on the transformation of electric energy in thermal through the direct interaction between the electromagnetic excitement field and the electrically sensitive particles of the medium. The antenna is implemented using one asymmetrically center-driven dipole with concentric insulated layers, useful local heating in the extraction of heavy petroleum. The utilized antenna exhibits a simple geometry, and has been analyzed through a mathematical model based on Maxwell's equations. Here, the conventional moment method in conjunction with wavelet basis functions were used to obtain the current distribution of the antenna. The results showed that the wavelets can be used to reveal important aspects in different resolution levels to improve the transfer of energy in a dissipative medium. Detailed expressions of the electric field and distribution of power were developed and calculated. The results obtained for the viscous oil reservoir were stable, presenting a good agreement with the models and results found in the literature.

1. INTRODUCTION

Nowadays several recuperation techniques of viscous petroleum reservoirs are used, one of them is the thermal method using electromagnetic heating [1, 2]. The application of the method has been analyzed starting from cylindrical antenna model inserted in a dissipative medium. In this paper we used this technique to study porous mediums in viscous petroleum reservoirs. Here we use the Maxwell's equations to obtain the electromagnetic parameters of interest because the problem involves an electromagnetic phenomenon. Firstly we were interested in obtaining the current distribution starting from the Hallén's equation [3] in conjunction with the moment method (MoM). The application of the classic moment method is developed starting from classis basis functions due to the simplicity for example the application of the pulses functions or functions of the type Dirac Delta [4]. Recently Lashab et al. [6] in their paper used wavelets as basis functions in the moment methods. In the last years the different wavelets have been attracting the researches' attention for the application of them in conjunction with the moment method, this application can produce sparse matrix [7].

In this work, the numeric technique of MoM is formulated considering as basis functions wavelets of the type Haar to obtain the current distribution. Here, we also analyzed the modelling of the electromagnetic field and the power distribution using the continuous wavelets, providing an analysis in different resolution levels.

2. PROBLEM FORMULATION

The model proposed for the antenna used is shown in the Figure 1, the antenna is constituted by two central conductors (region 1) with length (h_1) and (h_2) respectively and radio a, submerged by one dielectric cylinder with one or two layers (regions 2 and 3) constituted by external radios b and c respectively. The cylinder is submerged in an environment with losses (region 4).

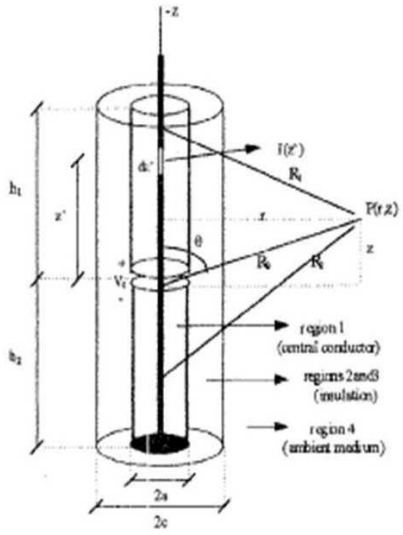

Figure 1: Insulated dipole in ambient medium.

Alternatively to the work proposed in [10], we developed new equations for the axial and radial fields in the region 4:

$$E_{4r}(r,z) = \frac{1}{j\omega\epsilon}\int_{h}^{-h}\left[k^2F + \frac{\partial^2}{\partial z^2}F\right]I\left(z'\right)dz'; \tag{1}$$

$$E_{4z}(r,z) = \frac{1}{j\omega\epsilon}\int_{h}^{-h}\left[\frac{\partial^2}{\partial r\partial z}F\right]I\left(z'\right)dz' \tag{2}$$

where $F(z,z') = \frac{e^{jkR}}{4\pi R}$. From the Equations (1) and (2), we can write the total electrical field in the region 4:

$$|E(r,z)|^2 = |E_{4z}(r,z)|^2 + |E_{4r}(r,z)|^2 \tag{3}$$

The dissipated electromagnetic power (W) in the medium can be written by [1]:

$$W = \frac{(\bar{\sigma} + \omega\varepsilon'')}{2}\vec{E}\cdot\vec{E}^* = \frac{\bar{\sigma}}{2}\left|\vec{E}\right|^2 = \sigma E^2 \tag{4}$$

The current distribution in the antenna is obtained by Hallén's equation [3],

$$\int_{-h}^{h} I_z\frac{e^{-jkR}}{4\pi R}dz' = \frac{j}{2}YV_0^i\text{sen}(k|z|) + C\cos(kz) \tag{5}$$

The solution of the Equation (5) can be obtained through the moment method.

3. MOMENT METHOD WITH WAVELET

In the moment method formulation (MoM) the current distribution I_z is expanded in functions in a domain that involves a linear operator L, i.e.,

$$I_z = \sum_{n=0}^{N}\alpha_n L(I_n) \tag{6}$$

where, α_n represents constants unknown, I_n is the expansion function and L is the linear operator defined by,

$$\begin{aligned} &L : L^2(-z,z) \longrightarrow \mathbb{R} \\ &\qquad I \longmapsto L(I) = \int_{-h}^{h} I(z')\frac{e^{-jkR}}{4\pi R}dz' = \frac{j}{2}YV_0^i\text{sen}(k|z|) + C\cos(kz) \end{aligned} \tag{7}$$

In this case, the moment method can be directly applied and wavelets are used as expansion functions [8]. Through the Multresolution analysis [9] defined by closed subspaces sequence $(V_j)_{j\in\mathbb{Z}} \in L^2(\mathbb{R})$ and a scale function φ, that satisfy the followings conditions:

(1) $V_j \subset V_{j+1} \Longleftrightarrow \ldots \subset V_{-2} \subset V_{-1} \subset V_0 \subset V_1 \subset V_2 \subset \ldots$
(2) $\bigcap_{j\in\mathbb{Z}} V_j = \{0\}$ e $\overline{\bigcup}_{j\in\mathbb{Z}} V_j = L^2(\mathbb{R})$
(3) Se $f(t) \in V_j \Longleftrightarrow f(2t) \in V_{j+1}$
(4) $\exists\, \varphi(t) \in V_0$; $\{\varphi(t-k)\ ;\ k \in \mathbb{Z}\}$ that constitutes an orthonormal basis of V_j.

If $I_z \in L^2(\mathbb{R})$ we can write it as a linear combination:

$$I_z = a_{-n,0}\phi_{-n,0} + \sum_{j=-n}^{N} \sum_{k=0}^{2^{j+n}-1} c_{j,k}\psi_{j,k} \tag{8}$$

where, ϕ is the scalar function, ψ is the Haar wavelet defined by, respectively

$$\varphi_{j,k}(x) = 2^{j/2}\varphi\left(2^j x - k\right), \tag{9}$$

$$\psi_{j,k}(x) = 2^{j/2}\psi\left(2^j x - k\right) \tag{10}$$

Here, j represents translation, $k = 0, 1, \ldots 2^{j+n} - 1$ represents the displacement and the a, c are constants. Through the linearity of the operator (7) we can obtain

$$\sum_{n=0}^{N} \alpha_n \int_{\frac{-h}{2}}^{\frac{-h}{2}} I_n(z') \frac{e^{-jkR_m}}{4\pi R_m} dz' = -\frac{j}{2} Y V_0^i \mathrm{sen}(k|z_m|) + C\cos(kz_m) \tag{11}$$

Defining the test function as Dirac Delta function, we can write

$$w_m = \begin{cases} 1 & se \quad z' \in \Delta z'_m \\ 0 & se \quad z' \notin \Delta z'_m \end{cases} \tag{12}$$

Making the intern product of (11) by (12) we obtain the following equation

$$[Z_{mn}]\,[\alpha_n] = [V_m] \tag{13}$$

where, Z_{mn} is a matrix obtained by:

$$Z_{mn} = \int_{\Delta z'_m} I_n(z') \frac{e^{-jkR_m}}{4\pi R_m} dz' - C\cos(kz),$$

with

$$I_0 = \phi_{0,0}, \qquad I_1 = \psi_{0,0}, \qquad I_2 = \psi_{1,0} \ldots I_n = \psi_{j,k}$$

and

$$V_m = \frac{j}{2} Y V_0^i \mathrm{sen}(k|z|) \ \ e \ \ R_m = \sqrt{a^2 + (z - z'_m)^2}.$$

If the matrix $[Z_{mn}]$ is not singular, the inverse $[Z_{mn}]^{-1}$ exists and the α_n can be written by

$$[\alpha_n] = [Z_{mn}]^{-1}\,[V_m] \tag{14}$$

with α_n, we can obtain the constants C in (11), and the $a_{0,-n}$ and $c_{j,k}$ coefficients. Next, with some algebraic manipulations and defining basis function vectors of the type $\left[\tilde{I_n}\right] = [I_1\ I_2\ \ldots\ I_N]$ we obtain the following expression,

$$\left[\tilde{I_z}\right] = \left[\tilde{I_n}\right][\alpha_n] = \left[\tilde{I_n}\right][Z_{mn}]^{-1}\,[V_m] \tag{15}$$

4. NUMERICAL RESULTS

In order to obtain an optimum configuration, one antenna with $2h = 20\,\text{cm}$ was introduced in a heterogeneous medium, constituted by saturated sand, salt water (0.6 NaC1) and petroleum with high viscosity. The dielectric layer is constituted by one air central layer with extern radio $b = 0.584\,\text{mm}$ with $\varepsilon_{2r} = 2.1$ and other external layer with radio $c = 0.80\,\text{mm}$ with relative permittivity $\varepsilon_{3r} = 2.1$. In the region 4 $\varepsilon_{4r} = 19.9$ and the conductivity $\sigma_4 = 0.257\,\text{S/m}$. In the central conductor $a = 1.79\,\text{mm}$ for the frequency of 1000 MHz.

The current distribution along the isolator symmetric dipole is shown in Figure 2. This simulation was made by using the Equation (5) and comparing with the method proposed in [10]. The Figure 3 shows the current distribution through continuous wavelet transform, here we can observe the boundary conditions [3] and the singularity points generated by gap spacing. The axial and radial distribution field coordinates as shown in 4 and 5 obtained with Equations (1) and (2) using continuous wavelet transform. The total electric field distribution and the dissipated power in the middle is shown in the Figures 6 and 7, in this case, continuous wavelet transform was used too.

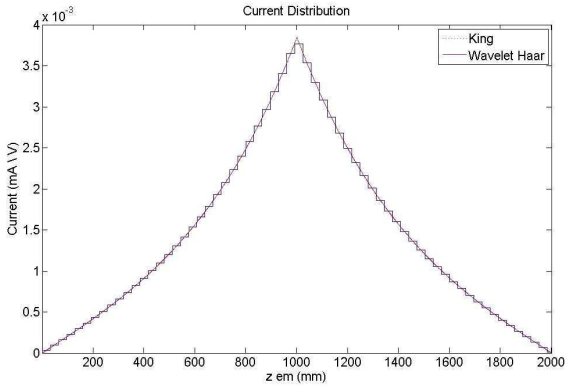

Figure 2: Current distribution: MoM and Haar wavelet.

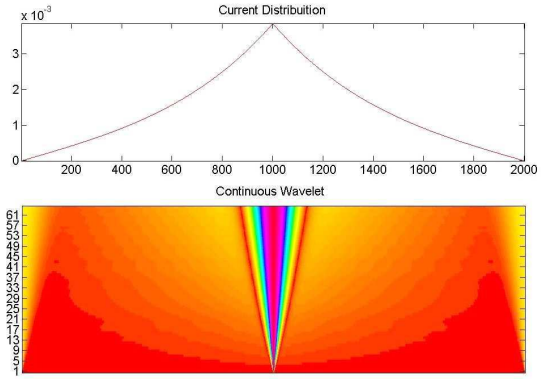

Figure 3: Current distribution: MoM with Haar wavelet and continuous wavelet transform.

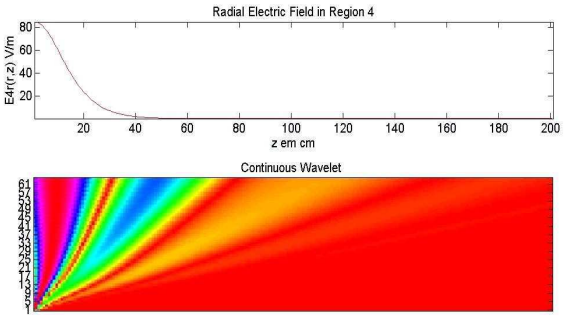

Figure 4: Radial field distribution Equation (2) and continuous wavelet transform (Color Plot).

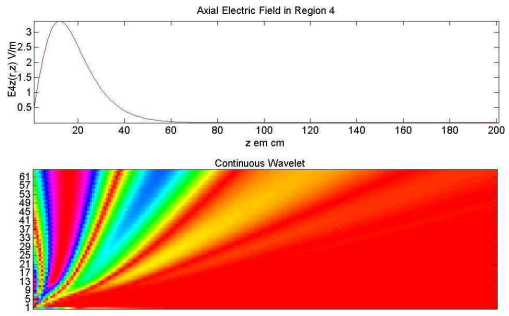

Figure 5: Axial field distribution Equation (1) and continuous wavelet transform (Color plot).

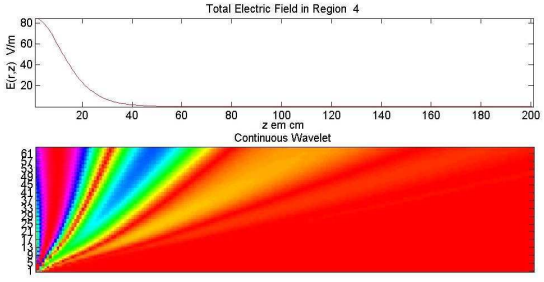

Figure 6: Total electric field in region 4, Equation (3) (porous medium sutured with salt water) and the continuous wavelet transform.

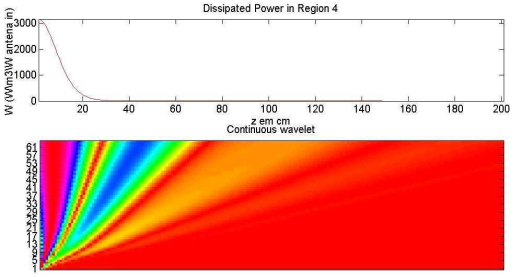

Figure 7: Power distribution in region 4, Equation (4) (porous medium sutured with salt water) and the continuous wavelet transform.

5. CONCLUSION

The validity of the mathematical models and the numeric techniques applied in the analysis of isolated antenna inserted in a dissipative media were verified by the results of many simulations, in particular for the application in heating porous medium saturated with salt water (0.6 NaC1). The models proposed were numeric stable and presented good accordance with others proposed by the literature. Perhaps the isolated dipole antenna is one of the simplest structures found in radiation problems. However, this antenna has great importance for engineering, because it has been very useful for the oil industry.

ACKNOWLEDGMENT

The authors would like to acknowledge the financial support of FAPERN, UFERSA, URFN and CNPq (INCT Fotonicom and Process number 563271/2008-6).

REFERENCES

1. Mata, W., "Recuperation assiste des petroles visqueux par ondes electromagnetiques," D. Sc. Thesis, INPT, France, July 1993.
2. Manichand, R. N., "Análise do desempenho do aquecimento eletromagnético na recuperação de reservatóios de petróeo," Dissertação De Mestrado UFRN/CT/PPGEQ, Natal/RN, Brasil, 2002.
3. Balanis, C. A., *Antenna Theory Analysis and Design*, 3rd Edition Wiley-Interscience, New Jersey, 2004.
4. Harrington, R. F., *Field Computation by Moment Methods*, 1st Edition, 1–38, Macmillan Company, New York, 1968.
5. Belardi, A. A., J. R. Cardoso, and C. A. F. Sartori, "Wavelets application in electrostatic and their computing aspects," *Germany, Electric and Magnetic Fields, EMF*, 43–46, 2003.
6. Lashab, M., C. E. Zebiri, and F. Benabdelaziz, "Wavelet based moment method and wavelet based moment method and physical optics use on large reflector antennas," *Progress In Electromagnetics Research M*, Vol. 2, 189–200, 2008.
7. Pan, G. W., *Wavelet in Electromagnetics and Devices Modelling*, John Wiley & Sons, Inc., New York, 2003.
8. Zunoubi, M. R. and A. A. Kishk, "A combined Bi-CGSTAB and wavelet transform method for EM problems using moment method," *Progress In Electromagnetics Research*, PIER 52, 205–224, 2005.
9. Daubechies, I., *Ten Lectures on Wavelets*, SIAM, Philadelphia, 1992.
10. King, R. W. P., B. S. Trembly, and J. W. Strohbehn, "The electromagnetic field of an insulated antenna in a conducting or dielectric medium," *IEEE Trans. MTT*, Vol. 31, 574, 1983.

A Planar Antenna Array with Separated Feed (PAASF) with Air Gap Technique

M. T. Ali[1], **T. A. Rahman**[1], **M. R. Kamarudin**[1], **R. Sauleau**[2], **M. N. Md Tan**[1], **and M. F. Jamlos**[1]

[1]Wireless Communication Center (WCC), Universiti Teknologi Malaysia
81310 UTM Skudai, Johor, Malaysia
[2]Institut d'Electronique et de Télécommunications de Rennes (IETR)
UMR CNRS 6164, University of Rennes 1, France

Abstract— A novel antenna of Planar Antenna Array with Separated Feed (PAASF) with lower side lobe pattern and higher antenna gain was designed. The unique property of this antenna design is that instead of fabricating all together in the same plane, the antenna's feeding network is separated from the antenna radiating elements (the patches) by an air gap distance. In this paper, the characteristics radiation pattern of two different radiating structures have been studied and compared. The first antenna configuration ("Structure 1") is a 16-element planar antenna array whose feed line is printed on the same plane as the radiating elements. The second ("Structure 2") is a 16-element planar antenna array whose feed network is separated from the radiating elements by an air gap. Both antennas are designed at 5.8 GHz. The PAASF technique is enables to reduce the unwanted spurious effects from the feed line. From the comparison results, it obviously shown that the "Structure 2" is given better sidelobe to mainlobe ration of −11.9 dB while "Structure 1" only −5.35 dB. In this structure, not only improvement is achieved in the sidelobe reduction pattern, but also better performance in term of the antenna gain. The antenna gain generated by "Structure 2" of 11.78 dB is higher compared to 8.539 dB generated by "Structure 1". Since some of the transmission line is placed to another board in PAASF, the size of that antenna become smaller compare to "Structure 1". Finally, in order to proof the validity of the antenna design, the simulated results (CST 2008) have been compared with measurements, and good agreement has been found.

1. INTRODUCTION

Microstrip antennas have been widely used due to their advantages like low profile, light weight, inexpensive and ease of integration with active components and Radio Frequency (RF) devices [1, 2]. When one considers adding new features to existing antennas, the question arises about the uniqueness and versatility of these configurations. The design of microstrip antennas is strongly related to several characteristics, such as complexity, gain, radiation pattern, side lobe level and bandwidth [3, 4]. Etching the antenna array and transmission lines on the same layer enables one to reduce the manufacturing cost. Unfortunately, this may increase the size of the antenna and, at the same time, could degrade the antenna performance [5, 6]. This performance degradation is attributed from the transmission line which indirectly contributes to increase the sidelobe level and decrease the antenna efficiency [7, 8]. Hall [9] estimated that the feed line radiation in a 16-by-16 corporate-fed array could degrade the sidelobe level by 10 dB. Therefore, to overcome this problem, Das [10] proposed multiple-layers printed antennas. In this paper we introduce new structure of planar antenna array where the corporate feed network is separated from radiating element plane in order to avoid spurious radiation from the feed network.

The main objective of this paper is to design, investigate and analyze the concept of separated feed network in planar antenna arrays to reduce the side lobe level and increase the antenna gain. In Section 2.1, an analysis of 16-element arrays including feed network is presented, whilst in Section 2.2, a similar 16-element array with separated feed network is discussed. Both antenna structures are analyzed numerically (using the Computer Simulation Technology (CST) Studio Suite 2008) and experimentally.

2. ANTENNA STRUCTURES

Two 16-element microstrip patch antenna arrays have been designed and compared. In both cases, the antenna prototypes were fabricated on a FR-4 substrate with a dielectric constant of $\varepsilon_r = 4.7$ and thickness $h = 1.6$ mm.

2.1. Single-layer Planar Antenna Array

The antenna layout is represented in Figure 1. The simulated radiation patterns and return loss are given in Figure 2. As can be seen, for such designs, the side lobe level is rather high (around -6 dB).

2.2. Planar Antenna Array with Separated Feed Line

The basic structure of the proposed antenna is constructed using multiple 2×2 sub-array modules, as shown in Figure 2(b). In this structure, the antenna is fed by a 50 Ohm coaxial probe. The size of each patch is 16 mm $\times$ 11.15 mm and their inter-element spacing is approximately $\lambda_o/2$.

The 16-element array comprises four sub-arrays of 4-elements. Figure 2(a) shows the structure of the separated feed antenna was proposed in this paper. The input ports on the antenna board are labeled as P_1 to P_4. The top antennas are fed by a vertical coaxial probe connecting the feed network to each sub-array. The gap height h_1 has been optimized to achieve a good return loss at 5.8 GHz. The best result providing a good impedance matching at 5.8 GHz is obtained for $h_a = 18.5$ mm. Hence, this height has been chosen in the final design.

3. MEASUREMENT AND DISCUSSION

3.1. Fabrication of "Structure 1"

Structure 1 has been manufactured. An open stub of 20 mm length and 1 mm width with 100 Ohm impedance is added at the feed point to improve the input impedance at resonance, as shown in Figure 3. The measured radiation patterns at 5.8 GHz are shown in Figure 4. As mentioned in

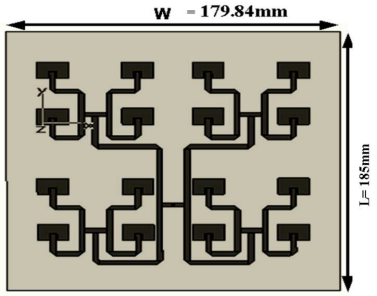

Figure 1: Layout of the single-layer 16-element microstrip antenna ("Structure 1").

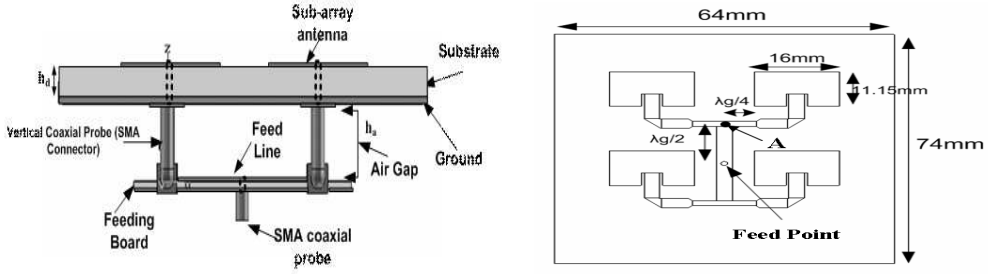

Figure 2: (a) Separated feed antenna structures. (b) The 2×2 sub-array diagram.

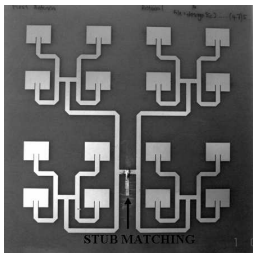

Figure 3: Fabricated prototype antenna.

Section 2, the high side lobe level mainly originates from spurious radiation from the feed network as shown in Figure 5.

3.2. Fabrication of "Structure 2"

Figure 5 shows the final structure after assembly. It is constructed from four sub-array elements. The measured and simulated return loss and radiation pattern is given in Figure 6. The reflection coefficient is smaller than −21 dB at resonance and the experimental and predicted patterns have nearly the same half power bandwidth (HPBW).

3.3. Comparison Between Both Structures

A comparison is made with the radiation pattern and return loss of antenna between "Structure 1" and "Structure 2". The simulation observation has been done in term of the size of the antenna, the sidelobe level, the antenna gain and size of antenna. Figure 7(a), the antenna gain generated by "Structure 2" of 11.78 dB is higher compared to 8.539 dB generated by "Structure 1". It is also noted from Figure 7(b) presents the comparison of simulated radiation pattern for H-cut-plane at 5.8 GHz. It can be seen that the magnitude of the side lobe level for "Structure 1" is clearly higher that "Structure 2", −5.37 dB and −11.9 dB respectively. Since some of the transmission line

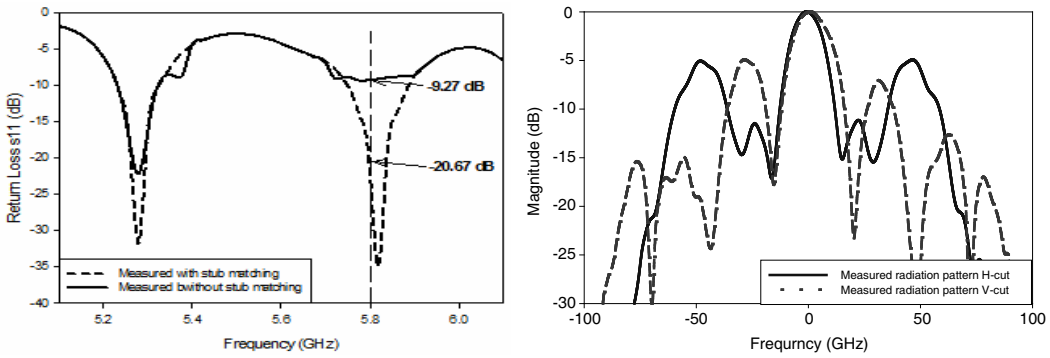

Figure 4: Measured return loss and radiation patterns plotted at 5.8 GHz.

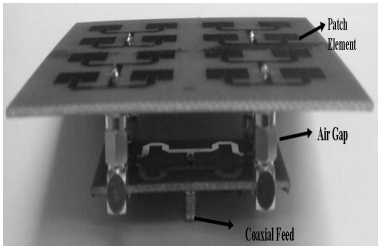

Figure 5: Prototype of the separated feed antenna.

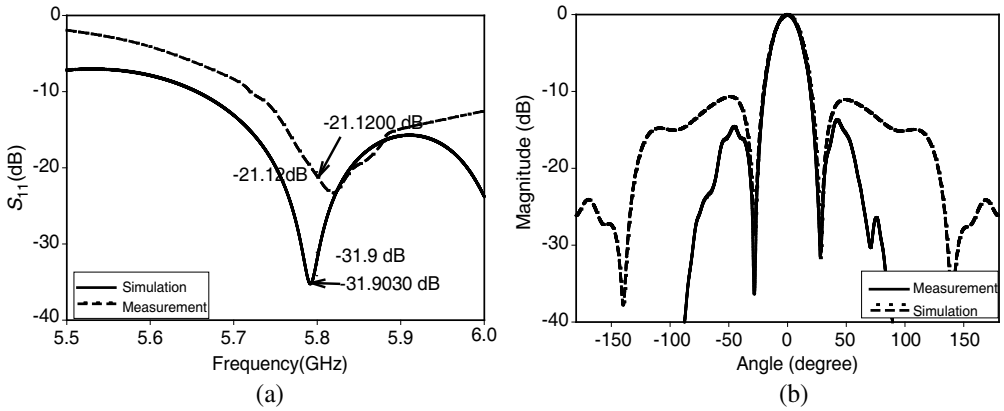

Figure 6: Measured results compare simulated. (a) Return loss. (b) Radiation pattern.

is placed to another board, the size of the antenna become smaller as shown in Table 1. All the comparison parameters are listed in Table 1.

Table 1: The comparison simulated result between two structures.

Specifications	Structure 1	Structure 2
Antenna Gain	8.537 dB	11.7853 dB
Side lobe to main lobe ratio	−5.35 dB	−11.9 dB
Antenna Size, $W \times L$ (mm)	179.84×185	119.2×121.7
Return Loss S_{11}	−29.3782 dB	−31.9 dB

Figure 9 presents the measured radiation pattern results at 5.8 GHz for normalized and non-normalized value of H-cut plane. An important feature that is highly observed of proposed antennas are the sidelobe level produced from the "Structure 1" is clearly higher than the "Structure 2". It is can been seen by comparing these characteristic radiation pattern in normalize format as shown in Figure 8(a). The comparison of measured gain between both structures are obtained by plotted radiation pattern as in Figure 8(b). It is observed from the results, the Structure 2 has 2 dB to 3 dB differents higher gain compared to "Structure 1". Figure 9 shows a photo of the both fabricated antennas. The size of "Structure 2" is smaller than "Structure 1", due to some of feeding line is removed to other board. It is proof that from simulation and measurement result shows the "Structure 2" prototypes antenna given advantages compare to "Structure 1" in term of sidelobe level, antenna gain and size of antenna.

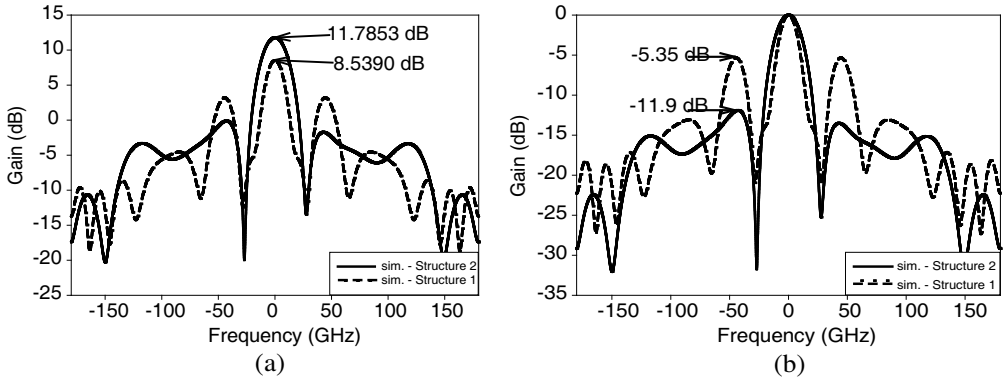

Figure 7: Comparison of simulated radiation pattern between two structures. (a) Non-normalized. (b) Normalized.

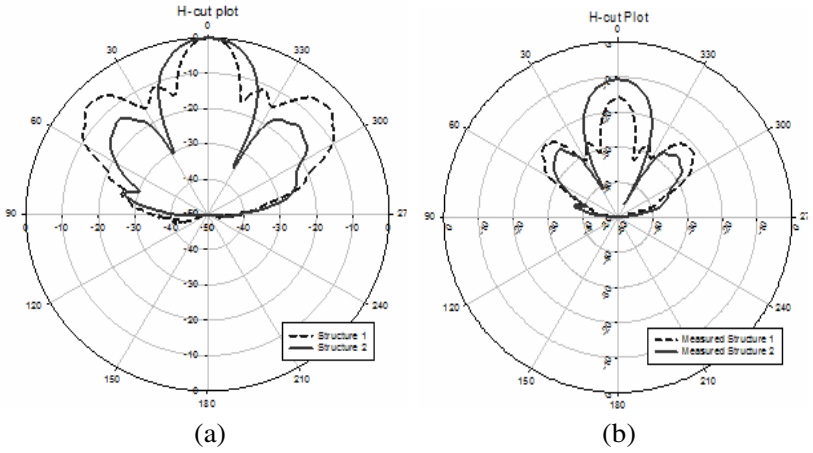

Figure 8: The measured radiation pattern of H-cut plane. (a) Normalized pattern. (b) Non-normalized pattern.

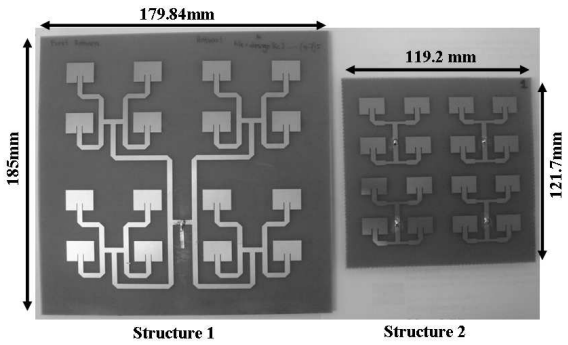

Figure 9: The photo of fabricated antenna for both structures.

4. CONCLUSION

The microstrip planar antenna array with the separated feed line technique concept is studied in this paper with the objective to reduce the sidelobe level and increasing the gain. The unique property of this antenna design is that instead of fabricating all together in the same plane, the antenna's feeding network is separated from the antenna radiating elements (the patches) by an air gap distance. This allows reducing spurious effects from the feed line. The experimental radiation patterns show very good agreement with simulations which the sidelobe level was suppressed. From the comparison results, it obviously shown that the "Structure 2" is given better sidelobe to mainlobe ration of $-11.9\,\mathrm{dB}$ while "Structure 1" only $-5.35\,\mathrm{dB}$. In this structure, not only improvement is achieved in the sidelobe reduction pattern, but also better performance in term of the antenna gain. The advantage of this design is that the radiation arising from the feeding line cannot interfere with the main radiation pattern generated by the antenna.

REFERENCES

1. Medeiros, C. R., A. Castela, J. R. Costa, and C. A. Fernandes, "Evaluation of modelling accuracy of reconfigurable patch antennas," *Proc. Conf. on Telecommunications — ConfTele*, Vol. 1, 13–16, Peniche, Portugal, May 2007.
2. Balanis, C. A., *Antenna Theory, Analysis and Design*, 3rd Edition, 2005.
3. Pozar, D. M., "Microstrip antennas," *Proceedings of the IEEE*, Vol. 80, 79–91, 1992.
4. Bogosanovic, M. and A. G. Williamson, "Microstrip antenna array with a beam focused in the near-field zone for application in noncontact microwave industrial inspection," *IEEE Transactions on Instrumentation and Measurement*, Vol. 56, 2186–2195, 2007.
5. Leon, G., R. R. Boix, M. J. Freire, and F. Medina, "Characteristics of aperture coupled microstrip antennas on magnetized ferrite substrates," *IEEE Transactions on Antennas and Propagation*, Vol. 53, 1957–1966, 2005.
6. Wonkyu, C., K. J. Myoun, B. J. Hoon, and P. Cheolsig, "High gain and broadband microstrip array antenna using combined structure of corporate and series feeding," *Antennas and Propagation Society International Symposium, 2004, IEEE*, Vol. 3, 2484–2487, 2004.
7. Levine, E., G. Malamud, S. Shtrikman, and D. Treves, "A study of microstrip array antennas with the feed network," *AIEEE Transactions on ntennas and Propagation*, Vol. 37, 426–434, 1989.
8. Wenhua, C., F. Mingyan, H. Qing, and F. Zhenghc, "A novel reconfigurable discrete antenna," *Antennas and Propagation Society International Symposium, 2003, IEEE*, Vol. 1, 411–414, 2003.
9. Hall, P. S., "Coplanar corporate feed effects in microstrip patch array design," *IEE Proc. H, Microw. Antennas Propag.*, Vol. 135, No. 3, 180–186, 1988.
10. Das, N. K. and D. M. Pozar, "Printed antennas in multiple layers: general considerations and infinite array analysis by a unified method," *Sixth International Conference on Antennas and Propagation, ICAP 89*, Vol. 1, 364–368, 1989.

Elements Reduction Using Unequal Spacing Technique for Linear Array Antenna

M. N. Md Tan[1], **T. A. Rahman**[2], **S. K. A. Rahim**[2], **M. T. Ali**[1], **and M. F. Jamlos**[2]

[1]Faculty of Electrical Engineering, University Technology Mara (UiTM), Shah Alam, Selangor, Malaysia
[2]Wireless Communication Center (WCC), University Technology Malaysia (UTM), Skudai, Johor, Malaysia

Abstract— The basic idea of this paper is to use unequal spacing technique not only to reduce the side-lobe level but also to reduce the number of element of linear array antenna. The arrangements of the elements followed the arrangement given by R. F. Harrington and Y. T. Lo. Most of the simulation done by previous researches focused on the algorithm, where the mutual coupling effect contributed by the elements was not included. The simulation started with 16 elements rectangular micro-strip patch of linear array antenna with one half wavelength spacing between the elements at an operating frequency of 5.8 GHz, using FR4 substrate with dielectric constant of 4.6, and thickness of 1.6 mm using CST2008 software. The result obtained will be put as a reference and will be compared to the unequal spacing simulation. It will be followed by the simulation of unequal spacing antenna for both symmetrical and asymmetrical arrangement where the amplitude of the excitation is assumed to be constant. Under symmetrical arrangement, another two different arrangements that are space tapered and non-tapered were investigated. The simulation started with 10 elements and was increased until its performance equal or was comparable with the 16 elements equal spacing antenna. The simulations result shows that by using the unequal spacing technique, the linear array antenna has better potential to have fewer numbers of elements but the performance was comparable. In this paper, the number of element reduced from 16 elements to 13 elements with better side-lobe level, same half power beam-width (HPBW) value and produced comparable antenna gain.

1. INTRODUCTION

The capability of the smart antenna system (SAS) to increase the quality of the performance is well recognized. SAS produced higher capacity, extended range, improved coverage, higher quality of services, lower power consumption, increased number of users, reduced interference and etc. [1]. But in contrast, SAS also have some drawback such as expensive, more complicated than traditional antennas and also they are larger in size than traditional systems. In SAS, there are three main parts involved, antenna, RF and Digital Signal Processing (DSP) as shown in Figure 1.

Theoretically, in SAS, each antenna has a RF chain connected to DSP. Meaning, if the system has M number of antenna, it will have M number of RF chain as well. This is one of the main reasons why this system is more expensive than conventional system and indirectly the size becomes larger [2, 3]. Hence, a lot of work conducted by different researchers not only to reduce the side-lobe of the linear array antenna, but also to reduction the number of elements using unequal spacing techniques. The results obtained by previous researchers show that the performance of the system is improved if the spacing of linear array is changed from equal to unequal spacing but all their work was based more on the algorithm part. It is believed that the analysis of unequally spaced antenna arrays on side-lobe reduction was originated by the work of Unz [4]. This work was then continued by different researchers such as Harrington [5] and Ishimaru [6]. Element reduction using unequal spacing techniques was successfully done by [7–9]. In this paper, the concept of unequal spacing focused on the antenna array using rectangular micro-strip path antenna and simulated using CST2008 software is illustrated. The arrangements of the unequal linear array antenna were based on the theory given by [5] and [10]. The main objective is to have an unequal linear array antenna with fewer numbers of elements but the performance is comparable to 16 patches equal spacing. The simulation started with 16 patches equal spacing arrangement and followed by unequal spacing arrangement.

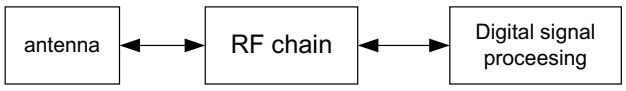

Figure 1: Basic block diagram of smart antenna system.

2. THEORY OF UNEQUAL SPACING LINEAR ARRAY ANTENNA

If the array elements are arranged on the y-axis with a uniform spacing between elements, d, this arrangement is called uniform linear array as shown in Figure 2.

The arrangement of Figure 2 can be re-arranged to form unequal spacing configuration either in symmetrical arrangement or asymmetrical (asym) arrangement. These two arrangements are shown in Figure 3.

There is no specific formula to arrange the elements for unequal spacing; we can have thousands of possible arrangements. According to Y. T. Lo et al. in [10], the unequal spacing for symmetrical arrangement can be categorized into space-tapered (ST) arrays and non-tapered (NT) arrays. The difference between these categories is obvious. Under ST array category, the spacing between the elements becomes wider from the center of the array towards the end. Meanwhile, the spacing between elements becomes smaller from the center of the array towards the end for NT arrangement.

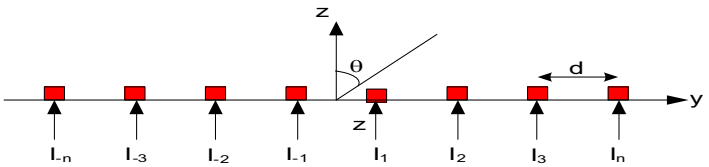

Figure 2: Equal spacing linear array arrangement.

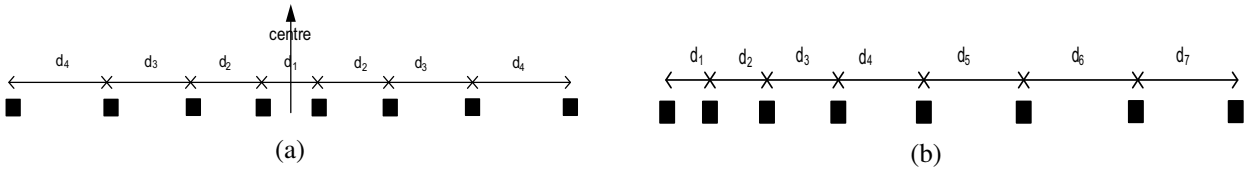

Figure 3: The arrangement of the element for unequal spacing: (a) Symmetrical, (b) Asymmetrical.

3. SIMULATION OF LINEAR ARRAY ANTENNA

The simulation started with 16 patches (16p) linear array antenna with equal spacing and the result obtained will be put as a reference to the rest of the simulation. Since there are no specific rules to design a linear array antenna using unequal spacing concept, a lot of configurations were simulated for all categories but in this paper, only the best result are shown. For each case of arrangement, the simulation will start with 10 patches (10p) and it will be then followed by 12 and 14 patches (12p and 14p). Table 1 shows the table of the detail arrangements for each case.

Table 2 shows the results for 16p equal spacing and 10p, 12p and 14p used unequal spacing technique under different categories. Meanwhile, Figures 4, 5 and 6 show the plotted graphs to show clearer picture of what the results obtained in Table 3. The gain obtained by 10p for each category does not meet the gain produced by 16p equal spacing. This is the main reason the number is increased until the performance is comparable to each other. For unequal spacing under asymmetrical category, does not matters what the total number of elements are, they always produce the highest gain. Since the main target is to have a comparable performance with 16p equal spacing, asymmetrical arrangement is not the best solution. This is due to the asymmetrical arrangement produced bad side-lobe (SL) compared to equal spacing arrangement. As an example, for 14p asymmetrical arrangement having 15.86 dB which is more than what 16p produced but at the same times the SL ratio only 12.3 and the HPBW was 4.5 which is much smaller than the target value. In fact, the total array length of this arrangement is much longer than the rest of the arrangement. As a conclusion, asymmetrical arrangement is not a suitable design in order to reduce the number of element.

NT arrangement produced worse result compared to asymmetrical arrangement. As an example, look at the 10p simulation results. The gain obtained was 13.79 dB which is lower than 10p asymmetrical arrangement and the side-lobe was 11.7 and this value also worse than asymmetrical.

Table 1: The detail spacing for the equal and unequal linear array antenna with different number of element, (a) ST arrangement, (b) NT arrangement, (c) Asymmetrical arrangement.

	Spacing between elements (λ)												
ST	d1	d2	d3	d4	d5	d6	d7	d8	d9	d10	d11	d12	d13
10p	0.70	0.65	0.60	0.55	0.50	0.55	0.60	0.65	0.70				
12p	0.75	0.70	0.65	0.60	0.55	0.50	0.55	0.60	0.65	0.70	0.75		
14p	0.80	0.75	0.70	0.65	0.60	0.55	0.50	0.55	0.60	0.65	0.70	0.75	0.80

(a)

	Spacing between elements (λ)												
NT	d1	d2	d3	d4	d5	d6	d7	d8	d9	d10	d11	d12	d13
10p	0.50	0.55	0.60	0.65	0.70	0.65	0.60	0.55	0.50				
12p	0.50	0.55	0.60	0.65	0.70	0.75	0.70	0.65	0.60	0.55	0.50		
14p	0.50	0.55	0.60	0.65	0.70	0.75	0.80	0.75	0.70	0.65	0.60	0.55	0.50

(b)

	Spacing between elements (λ)												
Asym	d1	d2	d3	d4	d5	d6	d7	d8	d9	d10	d11	d12	d13
10p	0.50	0.55	0.60	0.65	0.70	0.75	0.80	0.85	0.90				
12p	0.50	0.55	0.60	0.65	0.70	0.75	0.80	0.85	0.90	0.95	1.00		
14p	0.50	0.55	0.60	0.65	0.70	0.75	0.80	0.85	0.90	0.95	1.00	1.05	1.10

(c)

Table 2: The simulation result of equal and unequal spacing linear array antenna. (a) 16p equal spacing, (b) 10p, 12p and 14p unequal spacing.

Array	Directivity	Gain, dB	HPBW (°)	SL ratio	Array length (mm)
16p_equal	17.68	15.37	6.3	13.4	422.0

(a)

Array	Directivity	Gain, dB	HPBW (°)	SL ratio	Array length (mm)
10p_ST	16.48	13.93	8.4	14.4	319.4
10p_NT	16.30	13.79	8.4	11.7	309.2
10p_asym	16.90	14.20	7.2	12.6	360.8
12p_ST	17.42	14.82	6.7	14.3	397.0
12p_NT	17.20	14.69	6.6	11.4	384.0
12p_asym	17.90	15.12	5.6	12.4	461.5
14p_ST	18.23	15.60	5.6	14.3	479.8
14p_NT	18.00	15.46	5.4	11.2	464.2
14p_asym	18.70	15.86	4.5	12.3	572.7

(b)

Since the performance of this arrangement is worse than asymmetrical arrangement, it can be concluded that NT arrangement is considered as the worst arrangement for unequal spacing technique. The conclusion made is based on the performance produced by the ST arrangement which is always better than the rest of unequal categories in all parameters.

Referring to the result obtained by space tapered linear array antenna, although the gain produced was not as high as asymmetrical arrangement but the performances produced by this arrangement are almost balance in terms of side-lobe level and also HPBW. The side-lobe level produced by ST was almost consistent and better than the rest of the arrangement. The gain obtained by 12p was 14.82 dB which is a bit lower than the gain produced by 16p equal spacing and at the

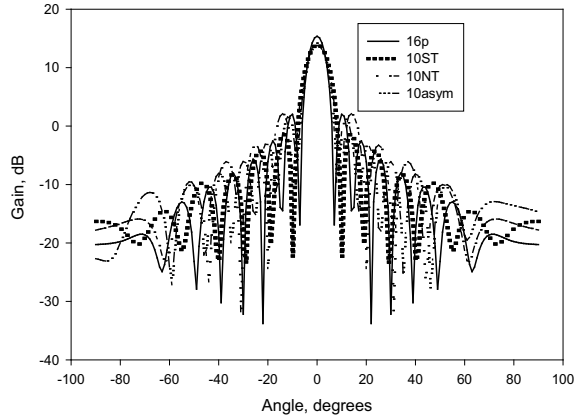

Figure 4: Graph for 10p unequal spacing for ST, NT and Asymmetrical arrangement.

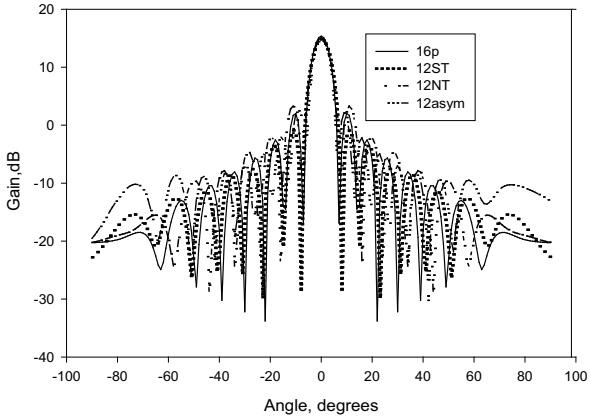

Figure 5: Graph for 12p unequal spacing for ST, NT and Asymmetrical arrangement.

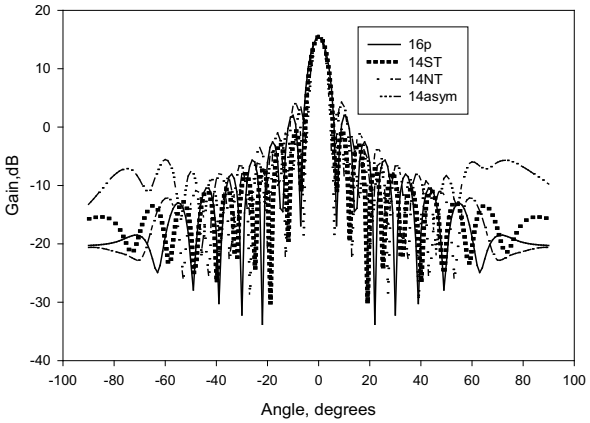

Figure 6: Graph for 14p unequal spacing for ST, NT and Asymmetrical arrangement.

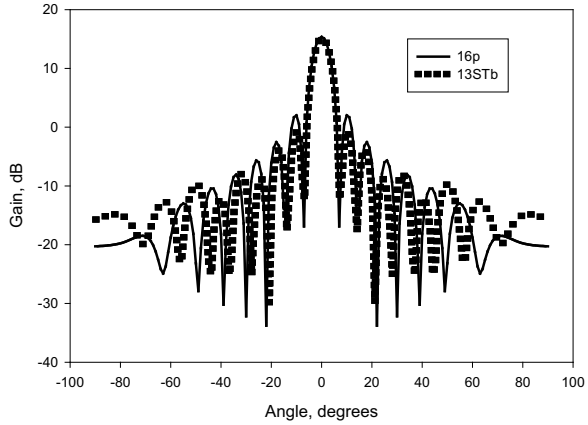

Figure 7: Graph for 16 patches equal spacing and 13STb unequal spacing.

same time the HPBW was also bigger than 6.3 degrees. Meanwhile, the gain obtained by 14p was 15.86 dB which is a bit higher than the 16p equal spacing but the HPBW now is much smaller than 6.3 degrees by 16p. Based on this reason, the 13 patches (13p) unequal array antenna was simulated. Based on Table 3, first simulation started with 13p_ST. It is clearly shown that the performances of the unequal spacing linear array antenna with 13p are almost comparable to the performance of 16 patches equal spacing. The array length increased only 0.8 mm that is about 0.19% increment. The HPBW obtained by 13 elements also shows a slight difference that is about 0.1 degrees; meanwhile the side-lobe level is much better compared to 16p. Only the gain has not met the 16p performance yet. Based on 13p_ST arrangement, another 4 designs for 13p antennas were simulated and labeled as STa, STb, STc and STd. Obviously the side-lobe level are consistent for all designs meanwhile the gain shows some improvements but the HPBW are reduced gradually and of course the array length become longer.

Since the HPBW are lower than 16p and the length also much longer, STc and STd are not the design to be considered. So the last option is between STa and STb. The performances between these two designs are just about the same. The gain produced by STb is a bit higher that STa but both having the same value of HPBW and side-lobe level. The array length of STa is 422.8 mm that is about 1.9% longer than the array length of the 16p equal spacing antenna and the array length of STb is 433 mm that is 2.6% longer than 16p these two designs. That is considerably very small. Since STb has better gain, 13p_STb is taken as the final design that is going to be compared with 16 patches equal spacing antenna.

Figure 7 shows the simulation results between 16p equal spacing and 13p unequal spacing design STb. The graph clearly shows that both designs are having almost comparable performance in terms of HPBW and gain but with better side-lobe level. As for comparison, linear array with

Table 3: The simulation result for 13p and 16p equal spacing and 13p unequal spacing.

Array	Directivity	Gain, dB	HPBW (°)	SL ratio	Array length (mm)
16p_equal	17.68	15.37	6.3	13.4	422.0
13p_ST	17.69	15.11	6.4	14.4	422.8
13p_STa	17.70	15.13	6.3	14.3	428.0
13p_STb	17.78	15.18	6.3	14.3	433.0
13p_STc	17.80	15.20	6.2	14.3	438.2
13p_STd	17.80	15.20	6.2	14.3	443.2
13p_equal	16.80	14.47	7.7	13.4	344.6

equal spacing for 13p also simulated. Only 14.47 dB gain produced by this design with 7.7 degrees of HPBW and worse SL ratio.

4. CONCLUSION

In conclusion, unequal spacing technique capable not only to reduce the side-lobe level, but also to reduce the number of elements. The results obtained also agreed as what was mentioned in [10] that in many cases of arrangement, space tapered always capable to perform good result. Although the reduction of the element was only 3 out of 16 patches, in SAS, this reduction is considerably good enough to reduce the overall size of the SAS and indirectly can reduce the cost of implementing it.

ACKNOWLEDGMENT

The authors would like to thank to everyone for their helps and supports in completing this project especially to University Technology Malaysia (UTM), Wireless Communication Center (WCC) and also to University Technology Mara (UiTM).

REFERENCES

1. Van Rooyen, P. and A. Alexiou, "The wireless world research forum and future smart antenna technology," *Spread Spectrum Techniques and Applications, 2006 IEEE Ninth International Symposium*, 447–451, Aug. 28–31, 2006.
2. Ohira, T., "Adaptive array antenna beam-forming architectures as viewed by a microwave circuit designer," *Pro. Asia Pacific Microwave Conference*, 828–833, Sydney, Australia, Dec. 2000.
3. Sun, C. and N. C. Karmakar, "Direction of arrival estimation with a novel single port smart antenna," *EURASIP Journal on Applied Signal Processing 2004*, 1364–1375, 2004.
4. Unz, H., "Linear arrays with arbitrarily distributed elements," *IRE Trans. on Antenna and Propagation*, Vol. 8, 222–223, Mar. 1960.
5. Harrington, R. F., "Side-lobe reduction by non-uniform elements spacing," *IRE Trans. on Antenna and Propagation*, Vol. 9, 187, Mar. 1961.
6. Ishimaru, A., "Theory of unequally spaced arrays," *IEEE Trans. on Antenna and Propagation*, Vol. 10, 691–702, Nov. 1962.
7. Andreason, M. G., "Linear arrays with variable inter-element spacing," *IRE Trans. on Antenna and Propagation*, Vol. 10, 137–143, Mar. 1962.
8. King, D. D., R. F. Packard, and R. K. Thomas, "Unequall-spaced, broadband antenna arrays," *IRE Trans. on Antennas and Propagation*, Vol. 8, 380–384, Aug. 1997.
9. Kurup, D. G., M. Himdi, and A. Rydberg, "Synthesis of uniform amplitude unequally spaced antenna arrays using the differential evolution algorithm," *IEEE Trans. on Antenna and Propagation*, Vol. 51, 2210–2217, Sep. 2003.
10. Lo, Y. T. and S. W. Lee, "A study of space-tapered arrays," *IEEE Trans. on Antenna and Propagation*, Vol. 14, No. 1, 22–30, Jan. 1966.

Reconfigurable Aperture Coupled Planar Antenna Array at 2.3 GHz

M. F. Jamlos[1], **T. A. Rahman**[2], **M. R. Kamarudin**[2], **M. T. Ali**[2], **M. N. Md Tan**[2], **and P. Saad**[3]

[1]Faculty of Computer and Communication Engineering, University of Malaysia Perlis (Unimap), Malaysia
[2]Wireless Communication Center (WCC), University of Technology Malaysia (UTM), Malaysia
[3]Faculty of Computer Science and Information System (FSKSM)
University of Technology Malaysia (UTM), Malaysia

Abstract— Reconfigurability in an antenna system is a desired characteristic that has been the focus of much interest in recent years. This paper describes the concept of reconfigurable antenna and how advances in switch technology have made these designs realizable. Complete design of the radiating patches, diode switches and biasing circuitry are also discussed. The structure of modified corporate-feed network is used to realize the array antenna consisting of 16 elements of rectangular patches at 2.3 GHz. The antenna patches through deployment of 4 PIN diodes switches at the feeding lines enabled the radiation pattern to be altered with respect to the beam shaping characteristics. While the planar arrays design making it more feasible for other antenna performances to be enhanced. The resistance for OFF and ON states of PIN diodes could strongly affect the performance of antenna. Hence, in order to improve the performance of the antenna, aperture coupled configuration is used to boost the antenna gain and directivity. The slot's geometry of aperture coupled antenna is stressed out as it determines the amount of coupling to the patches from feeding lines of the antenna. It is shown through simulations and measurements that 4 types of radiation pattern of the antenna can be well reconfigured by turning the diode switches on and off. The gain, directivity, beamwidth, efficiency and return loss are also changed. The proposed antenna, aperture coupled microstrip antenna array with quadratic slots, Q-ACMAA strengthen the level of coupling to the patches from feeding line with almost 50% of efficiency. Good agreement between the simulations and measurements were obtained. These results extend the validity of the analysis and will be useful for applications involving this type of reconfigurable antenna.

1. INTRODUCTION

Wireless communication systems have experienced a significant increased in the number of antennas applications. A single reconfigurable antenna could be delivered the same functionality of more than one conventional single purpose systems. Existing microstrip array antenna has been widely used in reconfigurable technology owing to their distinct advantages such as costing and less complexity. However point-to-point, some applications required an antenna that has a better gain (dB) and directivity (dBi).

Efforts have been specialized to the efficiency enhancement of microstrip antennas, and many techniques have been proposed [9]. But with the quadratic slots of ACMAA, the antenna has almost 50% efficiency compared to 30% of traditional microstrip antenna. However, the proposed reconfigurable microstrip antenna, Q-ACMAA makes the isolation between co-polarization and cross-polarization on E plane are at acceptable level (> 20 dB). When the isolation is higher, the gain and directivity is also getting better.

In [5], switching mechanisms are utilized to alter the current paths and provide pattern reconfigurable behavior. Deployment of RF switch technology to actively change the operating beamwidth of an antenna is also investigated. Works presented in this paper analyze a comprehensive investigation of reconfigurable with a primary focus on controlling radiation pattern.

2. ANTENNA DESIGN

An aperture coupled microstrip antenna utilizes three layers of metallization and two dielectric substrates, making it feasible for implementation using multilayer technology. The radiating patch is printed on the top (antenna) substrate, while a microstrip feeding lines is printed on the bottom (feed) substrate. A small non resonant aperture in the ground plane couples the patch to the feeding lines. To form a uniform monolithic structure, both the upper and lower substrates are composed of FR4 (relative permittivity = 4.7, loss tangent = 0.019) dielectric layer. FR4 also have the advantages of low cost and good reproducibility.

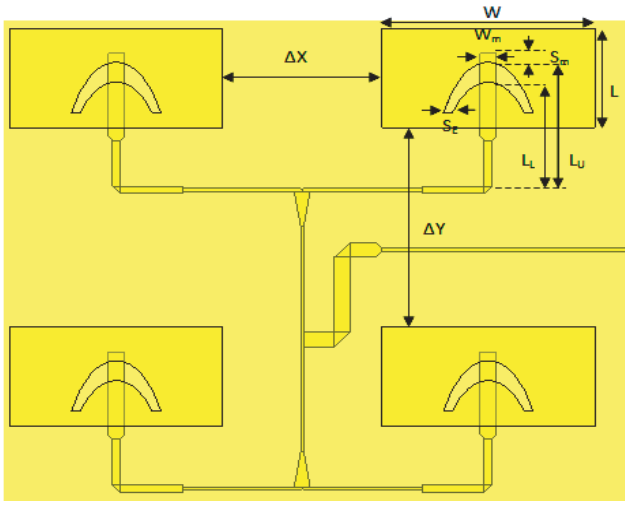

Figure 1: Detail geometry of ACMAA with transparency mode of the feeding line. $S_m = 8.5$, $L_m = 21$, $W_s = 20$, $W = 40$, $W_m = 3$, $L = 22$, $L_s = 1.2, \Delta X = 30, \Delta Y = 38$ all in mm.

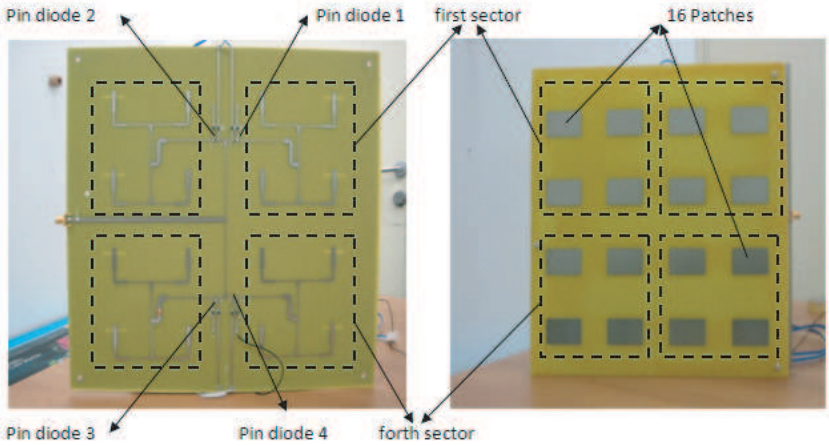

(a) (b)

Figure 2: 16 patches of aperture-coupled antenna array. (a) Back layer. (b) Front layer.

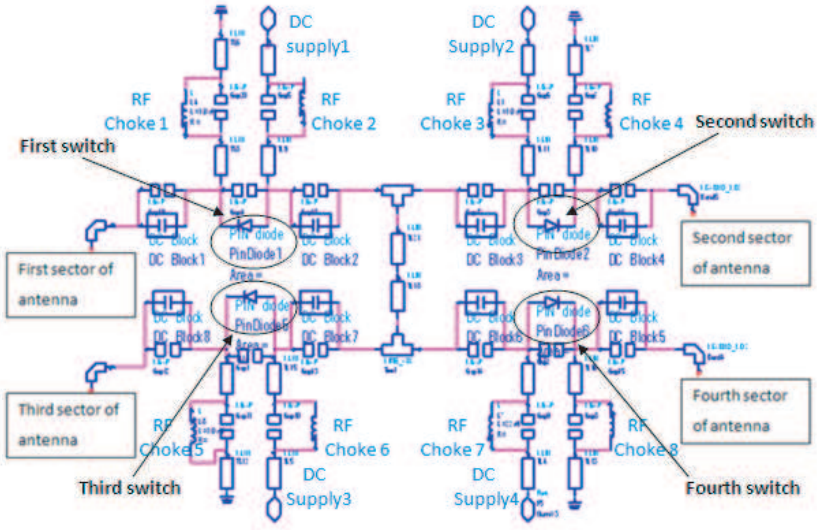

Figure 3: Schematic of RF PIN Diodes biasing circuit.

2.1. Aperture-coupled Planar Antenna Array

The fabricated structure of quadratic ACMA array (Q-ACMAA) is shown in Figure 3. Since all layers adhere to conformal printed circuit technology, fabrication is thus made simple. However, alignment between layers and correct selection of aperture size and position will be critical in controlling the antenna's impedance [8]. The natural existence of small gaps in between the layers of dielectric laminates can significantly alter the input impedance values.

2.2. Quadratic Aperture Design

The aperture is one of the most important parts in the aperture coupled structure. It determines the amount of coupling to the patches from feeding lines of the antenna [5]. The dimensions of the aperture also influence the resonant frequency of the structure and the amount of the undesired radiation in the back direction. The quadratic slot has less surface impedance and higher in term of admittance and conductance as shown in Figure 4. It means almost all of the induced current and power from the source is delivered to the radiating patches.

3. SWITCHING TECHNOLOGY OF RECONFIGURABLE Q-ACMAA

The PIN diode switch is a popular in microwave circuit applications due to its fast switching times and relatively high current handling capabilities. Moreover, The PIN diode can operate at speeds orders of magnitude faster than mechanical switches. Switching speeds of less than 100 ns are typical. Forward biasing the diode introduces electron-hole pairs into the intrinsic region. When this is happen, the pin diode currently acting like a closed switch (ON). Referring to Figure 3, each sector consists of 1 pin diode, 2 capacitors and 2 inductors. Each of pin diodes is placed between 2 capacitors. The inductors are inserted after the DC supply power and before grounding at the output ports.

When DC is supplied through the input ports, the RF choke which is a fixed inductor primarily intended to choke off alternating current (AC) and radio frequency (RF) from flows into the feeding lines. Meanwhile, the capacitors functions as a devices allowing the AC to flow but at the same time blocking the direct current (DC). The DC will stop flowing when the capacitor has fully charged within a seconds. In reconfigurable technology, a biasing circuit is crucial in order to control the ON/OFF stage of PIN diode switches as shown in Figure 3. When the first switch is ON, it means 1 switch has been activated while when the first and second switches are ON simultaneously, it means 2 switches has been activated and so on.

4. RESULT AND DISCUSSION

4.1. *S*-parameter

Figure 4 shows the measured and simulated return losses of the optimized ACMAA and TLAA. As for the reconfigurable purpose, the RL parameter of the same feeding lines with a different number of activated PIN diodes switches are also presented. The *RLs* were better than 10 dB for almost cases, shows that a good impedance matching has been achieved in both designs. The coupling

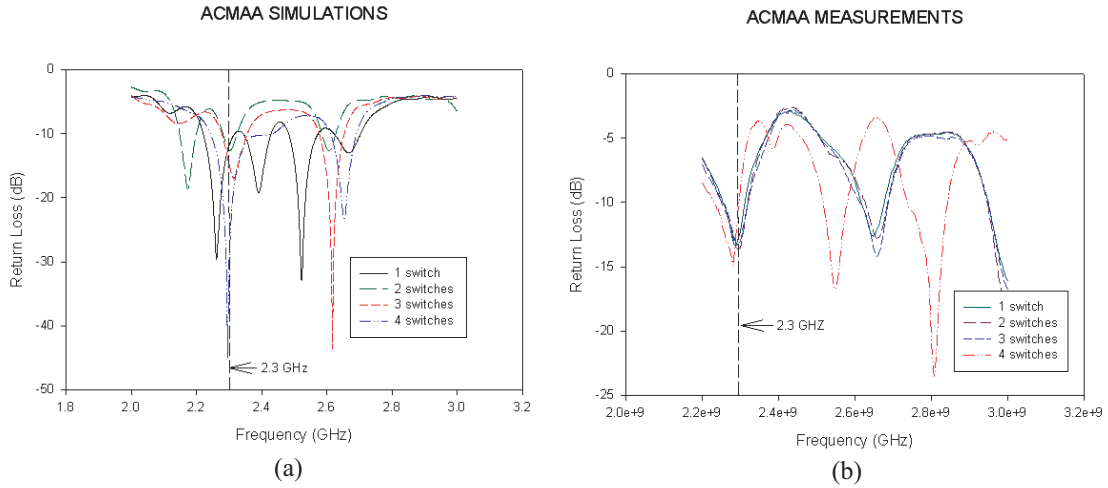

Figure 4: The return loss of reconfigurable ACMAA at 2.3 GHz. (a) Simulations. (b) Measurements.

mechanism in Q-ACMAA is critical and serves as the main mechanism of operation. It is easily affected by external elements, especially when working in a practical environment [3]. Buried lines in Q-ACMAA which has a non-contacting feeds help to minimize spurious radiation.

4.2. Radiation Characteristics

Figure 5 displayed a co-polar and cross-polar of reconfigurable Q-ACMAA on E plane. The higher the isolation is, the better its gain and directivity values produced [8]. It is also shown in Table 1 that the reconfigurable Q-ACMAA has better efficiencies (η) which are in the averaged magnitude of 60%. In terms of gain and directivity, the simulated reconfigurable Q-ACMAA values of each case produced slightly larger value as compared to measured. Figure 6 is a proof of slight losses when the antennas are operated in practice. The measured radiation patterns, in Figure 6(b), show very good agreement with the simulation but slightly lean to the right.

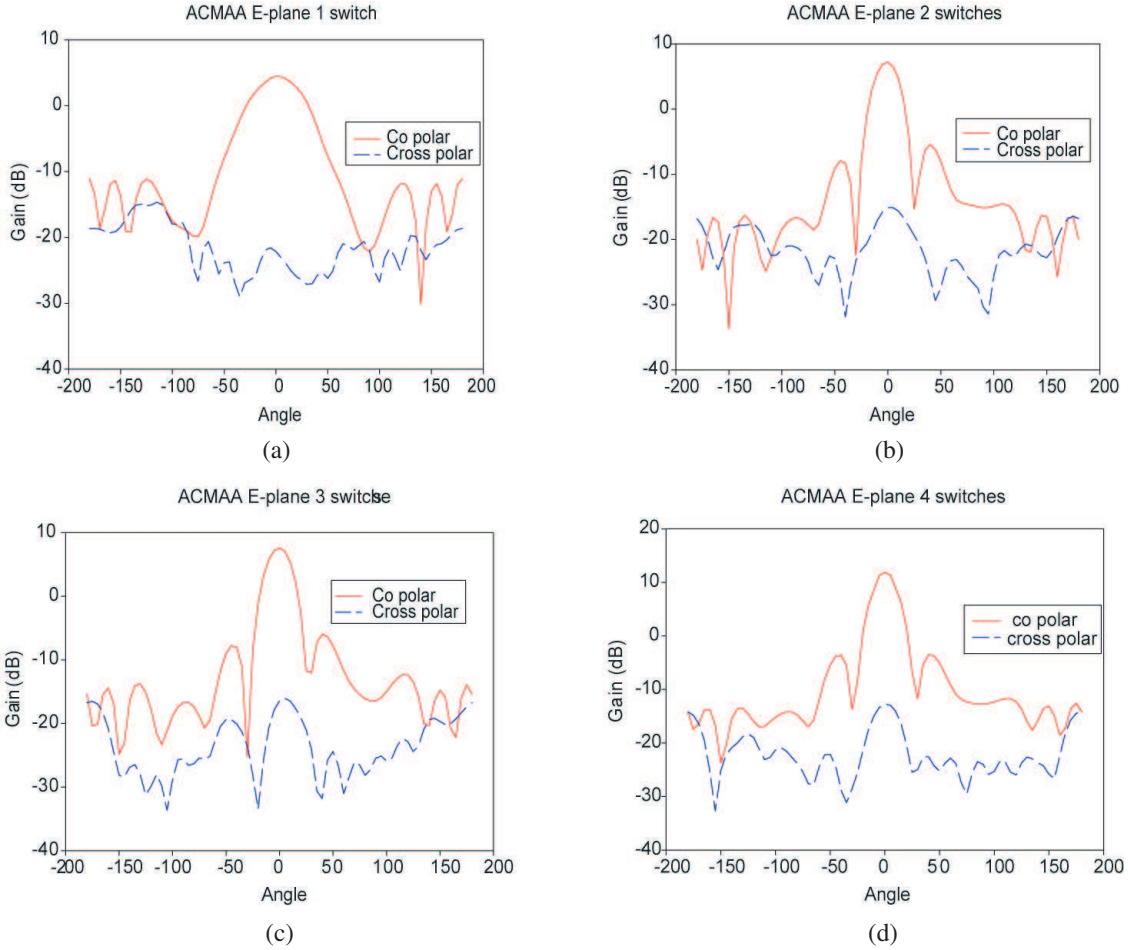

Figure 5: Simulation of reconfigurable Q-ACMAA E-plane polar and cross-polar radiation pattern. (a) 1 switch. (b) 2 switches. (c) 3 switches. (d) 4 switches.

Table 1: The directivity, gain and isolation of reconfigurable of Q-ACMAA.

Feeding technique	Number of activated switch	Directivity (dBi)	Gain (dB)	E plane			Return loss (dB)
				Isolation (dB)	Co polarization (dB)	Cross polarization (dB)	
Q-ACMAA	1	10	4.85	26.36	4.45	−21.91	−12.57
	2	14.3	7.2	23.34	7.2	−16.135	−13.9
	3	14.2	7.68	25.28	7.68	−17.604	−16.87
	4	17.2	11.87	26.59	11.87	−14.718	−30.07

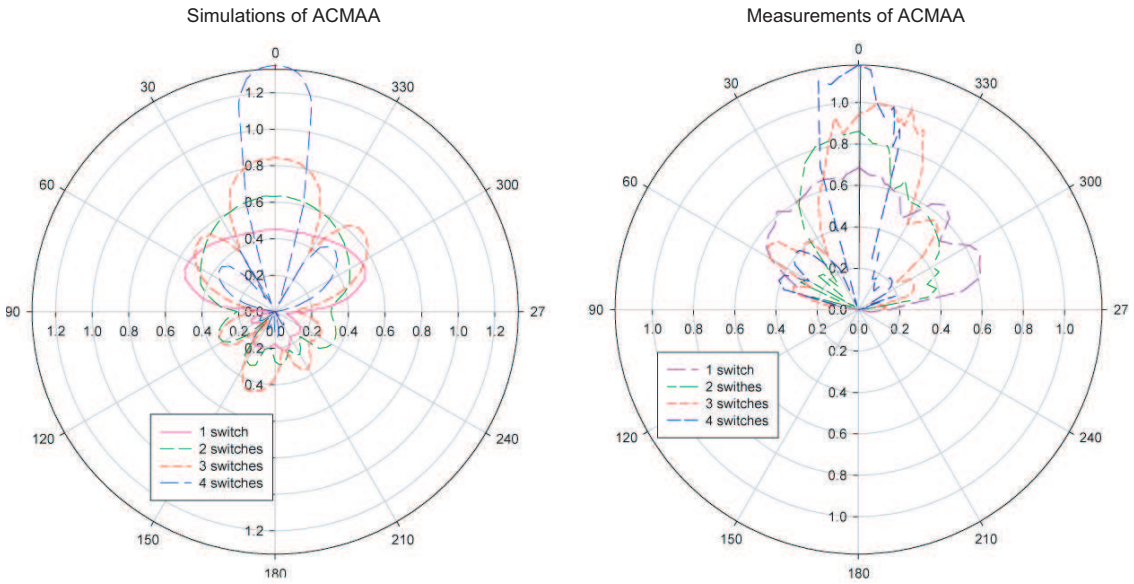

Figure 6: The radiation patterns of reconfigurable Q-ACMAA at 2.3 GHz. (a) Simulations. (b) Measurements.

5. CONCLUSION

The quadratic aperture coupled microstrip antenna array, Q-ACMAA is investigated to be applied in reconfigurable application. Quadratic slots had proven to strengthen the level of coupling between the patches and feeding line.

The gain (dB) becomes higher as isolation makes higher. Indirectly, it has better in term of efficiencies (η) which are in the averaged magnitude of 50%. The experimental show very good agreement with simulations which the radiation patterns are formed successfully with respect to the beam shaped characteristics. With higher gain (dB), it obviously shown that the reconfigurable Q-ACMAA would be greatly suitable for any reconfigurable application.

ACKNOWLEDGMENT

The authors would like to thank to everyone for their helps and supports in completing this project especially to Wireless Communication Center (WCC), University of Technology Malaysia (UTM) and University of Malaysia Perlis (Unimap).

REFERENCES

1. Ouyang, F. Y., S. W. Yang, Z. P. Nie, and Z. Q. Zhao, "A novel radiation pattern and frequency reconfigurable microstrip antenna on a thin substrate for wide-band and wide-angle scanning application," *Progress In Electromagnetics Research*, PIER 4, 167–172, 2008.
2. Fayad, H. and P. Record, "Multi-feed dielectric resonator antenna with reconfigurable radiation pattern," *Progress In Electromagnetics Research*, PIER 76, 341–356, 2007.
3. Wang, Y. J. and C. K. Lee, "Compact and broadband microstrip patch antenna for the 3g Imt-2000 handsets applying Styrofoam and shorting-posts," *Progress In Electromagnetics Research*, PIER 47, 75–85, 2004.
4. Niikura1, K., R. Kokubo, K. Southisombath, H. Matsui, and T. Wakabayashi, "On analysis of planar antennas using FDTD method," *PIERS Online*, Vol. 3, No. 7, 2007.
5. Ali, M. T., M. R. Kamarudin, and T. A. Rahman, "Design of reconfigurable multiple elements microstrip rectangular linear array antenna," *Progress In Electromagnetics Research C*, Vol. 6, 21–35, 2009.
6. Spasos, M., N. Charalampidis, N. Mallios, D. Kampitaki1, K. Tsiakmakis, P. Tsivos Soel, and R. Nilavalan, "On the design of an Ohmic RF MEMS switch for reconfigurable microstrip antenna applications," *Wseas Transactions on Communications*, Vol. 8, No. 1, January 2009.
7. Ramesh, M. and K. B. Yip, "Design formula for inset fed microstrip patch antenna," *Journal of Microwaves and Optoelectronics*, Vol. 3, No. 3, December 2003.

8. Kanamaluru, S., M.-Y. Li, and K. Chang, "Analysis and design of aperture coupled microstrip patch antennas and arrays fed by dielectric image line," *IEEE Trassactions on Antennas and Propagation*, Vol. 44, July 1996.
9. Smith, G. S., "An analysis of the wheeler method for measuring the radiating efficiency," *IEEE Transactions on Antennas and Propagation*, July 1977.
10. Kim, B., B. Pan, S. Nikolaou, Y.-S. Kim, J. Papapolymerou, and M. M. Tentzeris, "A novel single-feed circular microstrip antenna with reconfigurable polarization capability," *IEEE Transactions on Antennas and Propagation*, Vol. 56, No. 3, March 2008.

Comparison of Microwave Waveguide Applicators for Thermotherapy

Jaroslav Vorliček, **Jan Borovka**, **and Jan Vrba**
Dept. of Electromagnetic Field, Czech Technical University, Czech Republic

Abstract— The purpose of this paper is to compare the three most used microwave thermo therapeutic applicators in hyperthermia oncology treatment. In this case we have been focused on the applicator's radiation pattern from the aperture, and the depth of effective penetration of biological tissue. Applicators used in this survey are: TEM wave horn applicator, Lucite horn applicator, and TE_{10} horn applicator. All three of them have the same size of aperture, which makes them easy to compare. Simulations are performed in simulator of electromagnetic field SEMCAD BERNINA 13.4. Effective size of the aperture and the depth of effective penetration are computed in SEMCAD BERNINA 13.4.

1. INTRODUCTION

Nowadays the use of microwave thermotherapy [1] is a usual part of the clinical hyperthermia oncology treatment. Thus, the paper deals with the survey of prospective types of microwave applicators for thermotherapy. The discussed applicators are Strip TEM wave applicator, Lucite horn applicator and TE_{10} wave applicator. We are mostly interested in the shape of radiated power from the aperture and the depth of effective penetration of the biological tissue. These two main parameters have the greater impact on the process of hyperthermia oncology treatment. Thus, we want to irradiate the cancerous tissues with the predictable doze of microwave radiation. For this reason we are running the simulations of these above mentioned microwave thermo therapeutic applicators not only for the impedance matching to the biological tissue, but also for the shape of radiated power from applicators aperture, together with the determining the depth of effective penetration. For the simple comparison, all the applicators have the same size of the aperture 120 mm × 80 mm. Numeric verification of specific absorption rate *(SAR)* distribution is calculated in homogenous plane phantom having electrically the same parameters as the biological tissue.

2. THERMAL EFFECTS ON HUMAN ORGANISM

Hyperthermic effects on living organism are not that simple matter [2] as it can be seen but here comes a variety of factors to deal with. We can divide them into two major groups; effects caused by blood flow in the tissue and effects of the heat shock proteins (HSP). On cellular level we can describe the heat shock proteins as agents which are protecting the cells and the whole organism from lethal hyperthermia expositions.

In mammals the effects of higher temperatures (up to 43°C) cause cellular damage caused by a denaturation of proteins. When this happen the cell protheosynthesis is terminated and apoptosis is induced.

Physiologically the thermal exposition in mammals happens together with fever when heat shock proteins come to action. This supports the hypothesis that the heat shock proteins are protecting the cells against high temperatures. In fact we still know very little about heat shock proteins as the fever sicknesses are as old as the humankind.

The other very important physiological parameter influencing tissue response to heat is the blood flow. At higher temperatures blood perfusion increases in many tumors and this effect is dependent on heating time, temperature and also tumor structure. Blood flow increases to improve tumor oxygenation, but in most cases it is not sufficient because of the increased consumption of oxygen in heated tissue. When heating is terminated, blood perfusion and oxygenation slowly recover [2] and how quickly this occurs appears to be tumor-specific. Similar physiological effects occur in normal tissues, but normal tissue has more sophisticated vascular structures to help the tissue deal with the higher temperatures. Heating tumors to higher temperatures typically causes increase in perfusion during heating which is followed by vascular collapse and if sufficient, this will lead the tumor to necrosis. The speed and degree of vascular collapse depends on heating time, temperature and, of course, on the tumor.

The tumor vascular supply can also be exploited to improve the response to heat. Decreasing blood flow, using physiological modifiers or longer acting vascular disrupting agents prior to the

initiation of heating can both increase the accumulation of physical heat in the tumor, as well as increase the heat sensitivity of the tumor.

3. HYPERTHERMIA ONCOLOGY

Hyperthermia, also called thermotherapy, is a type of cancer treatment [1] in which body tissue is exposed to high temperatures (up to 45°C). It has been shown that high temperatures can damage and kill cancer cells, usually with lower injury to normal tissues. Damaging proteins and structures within cells is causing death of cancer cells by damaging proteins and their inner structures.

Hyperthermia is often used with other forms of cancer therapy, such as chemotherapy and radiation therapy. Hyperthermia may make some cancer cells more sensitive to radiation or harm other cancer cells that radiation cannot damage and it can also enhance [1] the effects of certain cytostatics.

There are two main streams in hyperthermia thermotherapy depending on the area of the human body where the heat was applied. Thus, we have a local hyperthermia application and a whole body application.

In local hyperthermia, heat is applied to a small area, such as a tumor, using techniques that deliver energy to heat the tumor. Different types of energy may be used in this case including radiofrequency, microwave, or ultrasound.

Depending on the tumor location, there are several approaches to local hyperthermia: External approaches are used to treat tumors in superficial area, which means that the tumors are not more than 30 mm below the skin. External applicators are often positioned around or near the appropriate region, and energy is focused on the tumor.

The internal method may be used to treat tumors close or near body cavities, such as the esophagus or rectum. Intracavitary applicators are placed inside the cavity and inserted into the tumor to deliver energy which dissipates into heat in the desired area.

Interstitial techniques are used to treat tumors deep within the body, such as brain tumors. This technique allows the tumor to be heated to higher temperatures than external techniques. Under anesthesia, intracavitary applicators are inserted into the tumor. Imaging techniques, such as ultrasound, may be used to make sure the probe is properly positioned within the tumor.

To ensure that the desired temperature is reached, but not exceeded, the temperature of the tumor and surrounding tissue is monitored throughout hyperthermia treatment. Using local anesthesia, the doctor inserts small needles with tiny thermometers into the treatment area to monitor the temperature. Imaging techniques, such as computer tomography, may be used to make sure the probes are properly positioned.

4. WAVEGUIDE APPLICATORS

There is a variety of thermo therapeutical microwave applicators used in hyperthermia oncology treatment. Depending on their location when heating the patient body we can divide them as the invasive and non invasive. In this study we have been concerned more with the non invasive applicators used in local hyperthermia treatment.

For this purpose the planar and waveguide type applicators are often used, demanding the more focused radiation pattern we choose the waveguide applicators for this comparison. Their main advantage is in the good focusation of microwave energy into the biological tissue, also their power capabilities are outstanding.

For the mutual comparison of two basic parameters of the microwave applicators we choose a TEM wave horn applicator, Lucite horn applicator and TE_{10} wave horn applicator. All the applicators work on the frequency $f = 434\,\mathrm{MHz}$, to achieve the reasonable dimensions, they are filled with the dielectric, in this case distilled water ($\varepsilon_r = 78$). Also by filling the inner cavity of the applicator by water, the propagating electromagnetic wave will be created in very similar environment as the biological tissue of the body. The human body itself contains approximately 70% of the water.

4.1. TEM Wave Applicator

TEM wave applicator used in thermotherapy [3] is the applicator which according to its name allows transversal electromagnetic wave to propagate. Its dimensions are chosen suitably for creating and propagating of transversal electromagnetic wave. Applicator is working on the frequency $f = 434\,\mathrm{MHz}$ and is filled with dielectric, which is distilled water.

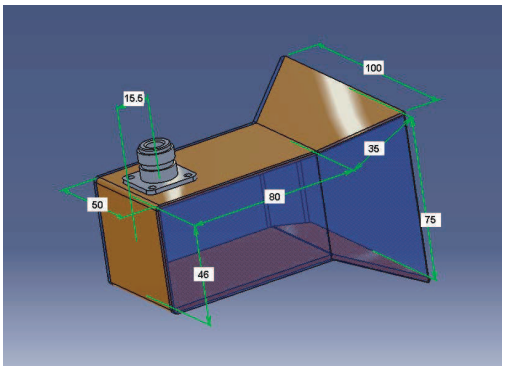

Figure 1: TEM wave applicator.

Applicator coating is from the conductive material and the lateral sides are simulated to be from acrylic glass. For the simple sketch of the TEM mode wave applicator see the Figure 1.

4.2. TE_{10} Mode Wave Applicator

TE_{10} mode wave applicator is a rectangular waveguide with the dimensions chosen suitably to create only the dominant TE_{10} mode. This applicator is working on the frequency $f = 434\,\text{MHz}$ and is filled with dielectric, distilled water. Opposite of the TEM wave applicator all the sides of the applicators body are from the conductive material, forcing the propagating electromagnetic wave to be more focused and enabling it to achieve the deepest penetration to the biological tissues among those three applicators. On the other hand, closed waveguide of this structure is not allowing the propagating electromagnetic wave to expand and create the large area of effective irradiated biological tissue.

4.3. Lucite Horn Applicator

For the combination of the advantages of the previously mentioned applicators we choose the Lucite horn applicator which has a non divergent part of the body created from closed waveguide and the divergent part towards the applicators aperture has the lateral sides from the acrylic glass. This applicator is supposed to have the middle parameters of the effective aperture size and also the depth of the effective penetration.

5. SIMULATIONS

All the simulations for this applicator have been performed using the simulator of electromagnetic field SEMCAD BERNINA 13.4. It uses a finite diferention time domain (FDTD) method to solve the electromagnetic field problems.

The main objective of the simulations was to find a suitable impedance matching of the thermo therapeutic applicator to the biological tissue with the required parameter $S_{11} < -15\,\text{dB}$.

The applicators are simple open cavity resonators filled with the dielectric with the variety means of tuning. The most reasonable tuning can be performed by changing the position of N-connector which also works as the feed of this structure.

After the modeling of the applicator's body shape, and setting the parameters of transient and harmonic analysis, we gain the first results. There is a need to keep attention in setting the cells mesh, and add the sufficient discretization density of cells, when it is needed. Otherwise, the results will not gain the demanded impedance matching. As the lowest discretization with the sufficient outcome, we can assume the density of 16 discretization lines per wavelength.

In the simulations we have been focused on the shape of radiating power from the applicator see Figure 2. Quantification of the SAR distribution simulations for mutual comparison was determined using the MATLAB script we developed [4]. This is very useful information giving us a basis concept of focusing on the microwave thermo therapeutic applicators to biological tissue.

Effective field size of the aperture (EFS) is the area of the aperture where the radiated power from applicator does not go under the attenuation of 3 dB. This area was determined using the MATLAB script we developed [4] and it is 42% for the Lucite horn applicator, 31% for the TE_{10} wave applicator and 57% for the TEM wave applicator.

In hyperthermia treatment planning, we are also interested in the other parameter of microwave thermo therapeutic applicator which is the depth of effective penetration *(DEP)* of the biological

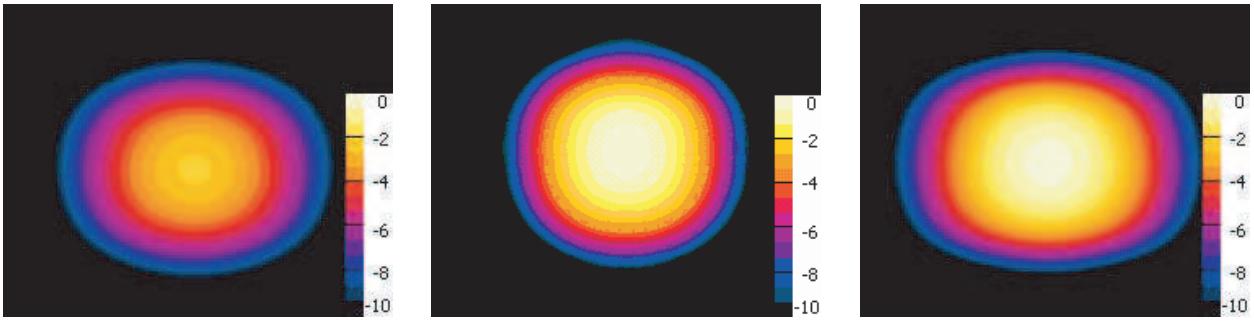

Figure 2: Power radiated from the applicator's aperture. Left: TE_{10} wave horn applicator, Middle: Lucite horn applicator, Right: TEM wave applicator.

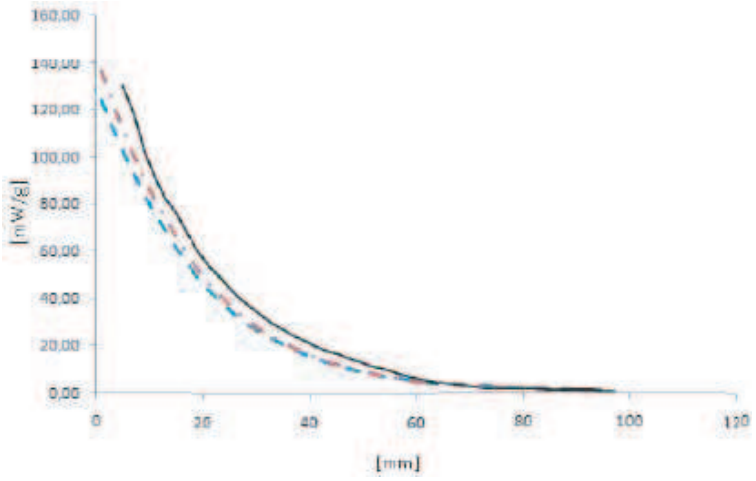

Figure 3: Depth of effective penetration for TEM wave horn applicator (dashed curve), TE_{10} horn applicator (dash-dot curve) and Lucite horn applicator (solid curve).

tissue. The Figure 3 shows depth of the effective penetration for simulated applicators. We can consider that all the mentioned applicators differs in the effective size of the aperture more than in the parameter of the depth of effective penetration.

The depth of effective penetration is the depth at which propagating electromagnetic waves have the attenuation not more than 3 dB. This length was determined using the simulator of electromagnetic field SEMCAD BERNINA 13.4 and it is 23 mm for the Lucite horn applicator, 25 mm for TE_{10} wave applicator and 18 mm for TEM wave applicator.

6. CONCLUSION

Our main aim was to compare the microwave applicators, their effective field size and the depth of effective penetration. As results based on the simulations in simulator of electromagnetic field SEMCAD BERNINA 13.4. We can assume that the most suitable applicator for the superficial thermotherapy covering the largest area of tissue among those three is the strip waveguide with TEM mode wave. Its EFS is 57% and the depth of effective penetration is 18 mm. On the other hand, the waveguide applicator with TE_{10} mode wave applicator has the smallest effective field size ($EFS = 31\%$) but the radiated field is more focused, and the depth of effective penetration is also the highest among those three applicators ($DEP = 25$ mm). TE_{10} applicator is useful for heating small superficial tumors which are located not more than 30 mm under the skin.

ACKNOWLEDGMENT

This research is supported by Grant Agency of the Czech Republic, project: "Non-standard application of physical fields-analogy, modeling, verification and simulation" (102/08/H081).

REFERENCES

1. Falk, H. M. and R. D. Issels, "Hyperthermia in oncology," *International Journal of Hyperthermia*, Vol. 17, No. 1, 1–18, 2001.

2. Horsman, R. M., "Tissue physiology and the response to heat," *International Journal of Hyperthermia*, Vol. 22, No. 3, 197–203, 2006.
3. Vorlícek, J., "Strip microwave applicator for local hyperthermia," Diploma Thesis, Prague, 2008.
4. Vorlicek, J. and J. Rusz, "Useful Matlab tool for radio frequency designer," Technical Computing Prague 2009, Full paper CD-ROM proceedings, (P. Byron Ed.), Humusoft s.r.o. & Institute of Chemical Technology, Prague, 2009.

Off-axis Scattering Particle Holography: A Numerical Study

Xuecheng Wu[1], **Gérard Gréhan**[2], **Siegfried Meunier-Guttin-Cluzel**[2], **Ruiyang Qu**[1], **Minglun Gu**[1], **Jiaping Xu**[1], **Linghong Chen**[1], **Kunzan Qiu**[1], **and Kefa Cen**[1]

[1]State Key Laboratory of Clean Energy Utilization, Institute for Thermal Power Engineering
Zhejiang University, 38#, Zheda road, Hangzhou 310027, China
[2]LESP, UMR 6614 / CORIA, CNRS, Université et INSA de Rouen, Site du Madrillet
Avenue de l'Université, BP12 76801 Saint Etienne du Rouvray, France

Abstract— Particle holograms at off-axis scattering in-line recording are investigated. A code based on the near field Lorenz-Mie framework capable of calculating particle hologram with arbitrary size, location and refractive index at arbitrary off-axis scattering angle has been developed. Characteristics of off-axis particle holograms are analyzed. The advantages, limitations and potential of particle characterization (refractive index, location, size, etc.) using off-axis scattering in-line recording are discussed.

1. INTRODUCTION

In recent years, the digital holographic imaging technique has been developed and demonstrated to be a powerful three-dimensional (3D) diagnostic in a variety of applications. Due to the poor recording resolution of CCD, however, forward scattering in-line hologram recording is normally adopted, which causes severe speckle noise and large depth of focus in the hologram reconstruction. Recently, we have shown that accurate measurement (both in position, size and refractive index) of particle smaller than 5 μm can be performed by processing simulated classical in line holograms using Lorenz-Mie theory and genetic algorithm [1, 2], which can be view as an extension of Griet's group work on very small particles. A recent work of Meng's group showed the possibility of dense particle field measurement by using in-line holograms with 90° scattering light [3].

In this paper, Particle holograms at off-axis scattering in-line recording are numerically investigated. The advantages, limitations and potential of particle characterization (refractive index, location, size, etc.) using off-axis scattering in-line recording are discussed.

2. GEOMETRY UNDER STUDY

A code based on the near field Lorenz-Mie framework capable of calculating particle hologram with arbitrary size, location and refractive index at arbitrary off-axis scattering angle has been developed. The configuration of off-axis scattering hologram calculation is schematized in Figure 1. A perfectly spherical, homogeneous and isotropic particle, characterized by its diameter d_p and its complex refractive index n, is arbitrary located in space. Its center is at coordinates (x_p, y_p, z_p). The particle is illuminated by a plane wave with a wavelength of λ which travels from the negative toward the positive Z. A CCD detector is located with an off-axis angle of θ and at a distance of R from the origin O, which is assumed to be perfectly perpendicular to the radius going from O to the detector center. The detector records the fringe pattern coming from the light scattered

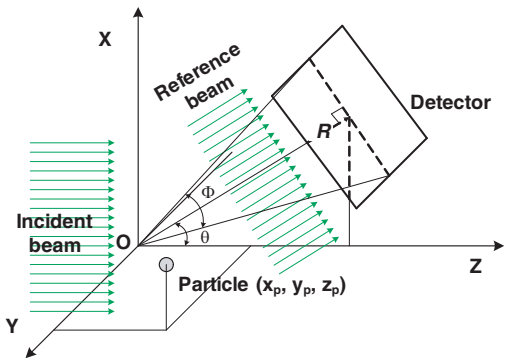

Figure 1: The optical layout of off-axis particle hologram calculation system. r: the distance between coordinate origin and the detector center; θ: off-axis angle; Φ: solid collection angle.

by the particles and a reference light with the same wavelength λ but adjustable amplitude and a direction perpendicular to the detector.

The light scattered by the particle is computed in the framework of the near-field Generalized Lorenz-Mie theory [4]. A particularities of the code, is that for each pixel of the detector, the 6 values of the field are recorded, starting with the incident field, and then adding fields scattered by the particles, one after one. This approach neglects the multiple scattering effects but permits to take into account the interferences between the light scattered by different particles. The code is capable of calculation of multi-particles holograms, but in this paper, only single particle located at the origin O is investigated.

3. EXAMPLE OF COMPUTED HOLOGRAMS

Figures 2 and 3 are examples of such holograms (with a resolution of 512×512) computed for a $60\,\mu m$ glass particle with $n = 1.5 - 0.0i$ at different off-axis angles. The recording distances R and collection angle Φ are equal to 1 mm and 20° in Figure 2 and 100 mm and 6° in Figure 3, respectively. Several recording angles 20°, 55°, 90° and 157° are considered, among which the last one is the first order rainbow angle. As can be seen, in Figure 2, the main characteristic is the dual aspect of the image (very visible for image (a), (b) and (c)) while in Figure 3 the four images are essentially identical and the main characteristic is the ghost images due to moiré effect.

The holograms behavior displayed in Figures 2 and 3 must be discussed and compared to the more classical in line Gabor holograms. It is the aim of the next section.

4. DISCUSSION AND COMPARISON WITH IN LINE GABOR HOLOGRAMS

4.1. Origin of the Strong Moiré Effect

Figures 4(a) and 4(b) display two holograms computed for the same parameters except the recording angle θ. In Figure 4(a), the recording angle is equal to 0° (in line Gabor configuration) while in Figure 4(b), the recording angle is equal to 90°. It is shown that Figure 4(b) is characterized by a very strong moiré effect. This difference of behavior can be easily explained by observing the scattered light angular distribution. Such scattered light angular distributions are plotted in Figures 4(c) and 4(d), corresponding to the holograms 4(a) and 4(b), respectively. In Figure 4(c),

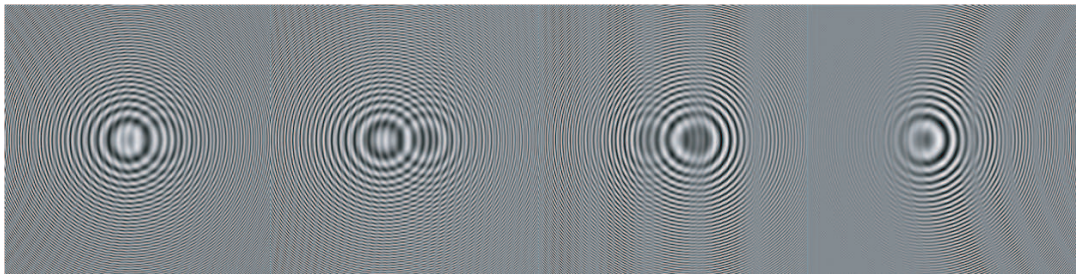

(a) (b) (c) (d)

Figure 2: Holograms of a $60\,\mu m$ glass particle ($n = 1.5 - 0.0i$) at different off axis angle ((a) $\theta = 20°$; (b) $\theta = 55°$; (c) $\theta = 90°$; (d) $\theta = 157°$) with a recording distance $R = 1\,mm$ and a collection angle $\Phi = 20°$ with a 512×512 CCD camera.

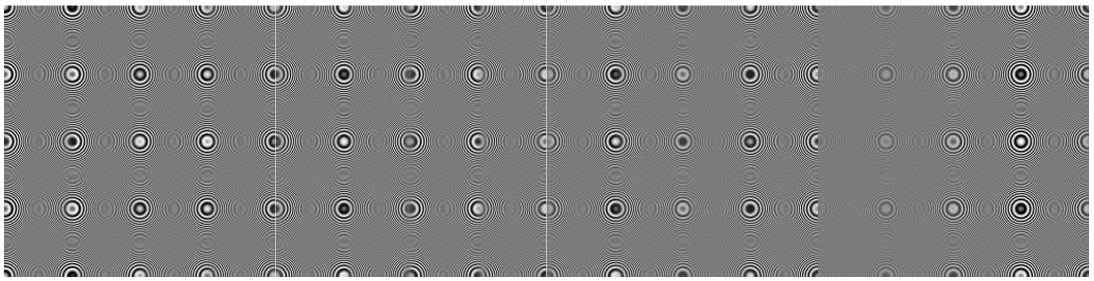

(a) (b) (c) (d)

Figure 3: Holograms of a $60\,\mu m$ glass particle ($n = 1.5 - 0.0i$) at different off axis angle ((a) $\theta = 20°$; (b) $\theta = 55°$; (c) $\theta = 90°$; (d) $\theta = 157°$) with $R = 100\,mm$ and $\Phi = 6°$ with a 512×512 CCD camera.

corresponding to forward scattering, the scattered light is dominated by diffraction which is much stronger than reflected or refracted lights. Then the amplitude of the interferences with the reference beam will rapidly decreases as the distance from the maximum of scattered light increases. On the contrary, for detection at 90°, the scattered light is relatively uniform on the detector surface. The amplitude of the interferences with the reference beam will be essentially constant, only modulated by the fringes created by the interference between the different orders of scattering. Then the visibility of the fringes in the hologram will be essentially constant on the detector surface, creating strong moiré effects.

The moiré effect can be, at least partially, removed by reducing the solid collecting angle or increasing the resolution of the detector. The experimental research of Meng's group using in-line holograms with 90° scattering light [3] did not show the moiré effect on the particle hologram, due to the fact that the collection angle is very small (less than 1°).

4.2. Origin of the Dual Fringe Pattern

Figure 6(a) corresponds to the 90° hologram of a 60 µm transparent particle located at 1 mm from the detector. The dual aspect of the image is clearly visible. When recorded in forward scattering the dual aspect is not present. The dual aspect is due to the creation of one image by the refracted light and one image by the refracted light. These two kinds of light leave the particle at two different locations, then, in the near field, a pixel of the detector is view at two different angles by the two kinds of light. That fact can be illustrated by computing the holograms for an opaque particle ($n = 1.5 - 1.0i$), shown in figures. It can be found that the dual aspect has been completely removed. Note that the low frequency vertical lines (visible in Figure 6(a)) also disappear as these fringes correspond to interference between refracted and reflected light. The differences between Figures 5(a) and 5(c) are large, however, in forward scattering the fringe patterns are nearly the same, as shown in Figures 5(b) and 5(d).

5. RECONSTRUCTION

The particle holograms under various cases were numerically reconstructed using a wavelet transform based approach [5]. Figure 6(a) is a reconstructed image at a distance of 0.99 mm of the 55°

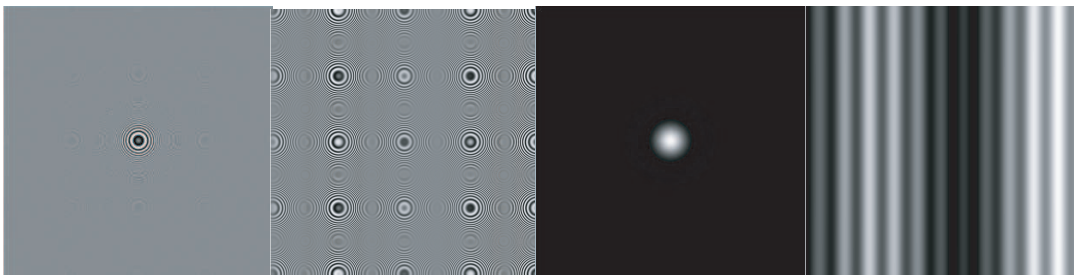

(a) (b) (c) (d)

Figure 4: Comparison of particle ($d_p = 60\,\mu m$, $n = 1.5 - 0.0i$) holograms ((a) in-line; (b) 90° scattering) and scattering maps ((c) in-line; (d) 90° scattering) with $R = 100$ mm, $\Phi = 6°$) with a 512×512 CCD camera.

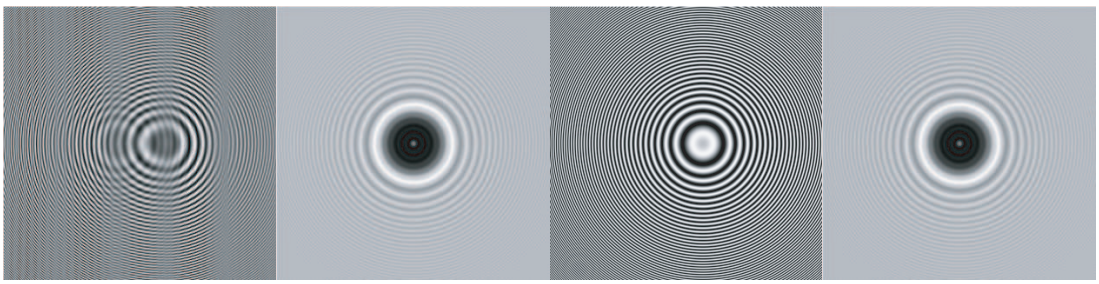

(a) (b) (c) (d)

Figure 5: Comparison of holograms of transparent and opaque particles in in-line and off-axis scattering ($d_p = 60\,\mu m$, $R = 1$ mm, $\Phi = 20°$, 512×512). (a) $n = 1.5 - 0.0i$, $\theta = 90°$; (b) $n = 1.5 - 0.0i$, $\theta = 0°$; (c) $n = 1.5 - 1.0i$, $\theta = 90°$; (d) $n = 1.5 - 1.0i$, $\theta = 0°$.

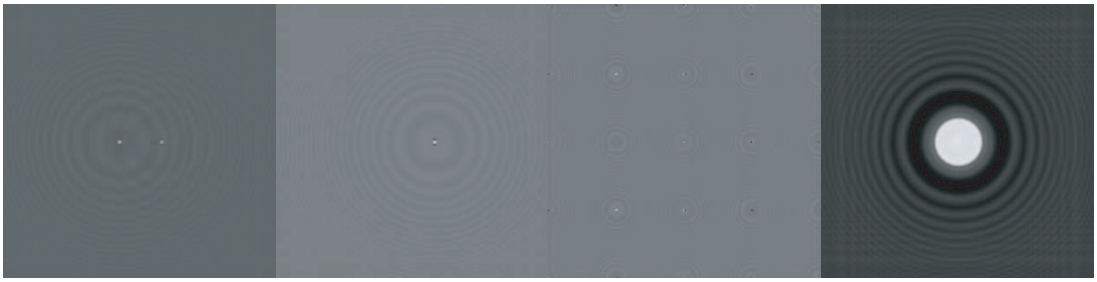

Figure 6: Comparison of reconstructed particle images for different studying cases. (a) computation distance $R_c = 0.99\,\text{mm}$, hologram Figure 2(b); (b) $R_c = 0.99\,\text{mm}$, hologram Figure 5(c); (c) $R_c = 100\,\text{mm}$, hologram Figure 3(b); (d) $R_c = 1\,\text{mm}$, hologram Figure 5(b).

off-axis hologram shown in Figure 2(b). As can be seen, normally two glare spots can be found for transparent particle due to the reflected and refracted lights coming from the particle. This can be further validated by calculating an opaque particle for the same condition, where only one glare spot due to reflected light is found, as shown in Figure 6(b). The position and distance of the two glare spots contain the information of both the particle 3D position and particle size. Meanwhile, a possible application of such off-axis holography is the measurement of refractive index since the intensity ratio of the two glare spots can be easily obtained. Figure 6(c) is a reconstructed image of the particle hologram with moiré effect, which shows that in such cases the particle image cannot be reconstructed successfully. In compassion, Figure 6(d) is a reconstructed image of typical in-line particle hologram where a whole particle image can be obtained with a size indicating the particle size.

6. CONCLUSION

With a code based on the near field Lorenz-Mie framework, off-axis scattering in-line recording particle holograms were analyzed. It is shown that for transparent particles, the off-axis scattering hologram is characterized by dual fringe patterns due to the reflected and refracted lights. Rather than an particle image obtained in forward scattering, two glare spots may be obtained in off-axis scattering by reconstruction of the hologram, which contain the information of particle size and location, and also shows the possibility of refractive index measurement by using the intensity ratio of the two glare spots. The second conclusion is that the moiré effect in off-axis hologram is much more serious than in in-line case, which should be concerned.

ACKNOWLEDGMENT

The authors gratefully acknowledge the financial supports from the National Natural Science Foundation of China (NSFC) projects (grants 50576086), the National Basic Research Program of China (grants 2009CB219802) and the Program of Introducing Talents of Discipline to University (B08026).

REFERENCES

1. Wu, X. C., G. Gréhan, S. Meunier-Guttin-Cluzel, et al., "Sizing of particles smaller than 5 μm in digital holographic microscopy," *Optics Letters*, Vol. 34, 857–859, 2009.
2. Meunier-Guttin-Cluzel, S., G. Gréhan, X. C. Wu, et al., "Measurement of position, size and refractive index of particles by digital microhologaphy in micro-channel," *Asian Aerosol Conference*, Bangkok, Thailand, 2009.
3. Cao, L., G. Pan, J. de Jong, et al., "Hybrid digital holographic imaging system for three-dimensional dense particle field measurement," *Applied Optics*, Vol. 47, 4501–4508, 2008.
4. Slimani, F., G. Grehan, G. Gouesbet, et al., "Near-field Lorenz-Mie theory and its application to microholography," *Applied Optics*, Vol. 23, 4140–4148, 1984.
5. Lebrun D., A. M. Benkouider, and S. Coëtmellec, "Particle field digital holographic reconstruction in arbitrary tilted planes," *Optics Express*, Vol. 11, 224–229, 2003.

A RCS Reduction Design of Object with Anisotropic Impedance Surface Using Genetic Algorithm

Jing-Jing Yao, **Si-Yuan He**, **Hai-Tao Chen**, **and Guo-Qiang Zhu**
School of Electronic Information, Wuhan University, Wuhan 430079, China

Abstract— In this paper, a universal radar cross section (RCS) reduction design method for the object with anisotropic impedance surface is proposed. It is effective to reduce RCS of the target with anisotropic impedance surface, because the anisotropic material can not only absorb the incident radar wave, but also redistribute the scattering energy in the whole space, by controlling the principal axis of the anisotropic material. The whole procedure of the proposed method is composed of three parts: universal geometry modelling, high-frequency method and standard genetic algorithm. First, the universal geometry modelling based on triangular meshing can exactly describe the geometry features of the object. Then the high-frequency method Physical optics (PO) is adopted as the forward algorithm to calculate the RCS of the target in desired angle range. Finally, in the standard genetic algorithm, the surface impedances of the target and the direction of the principal axis are considered as the optimized parameters. A reduction example of a square plate which is first illustrated in the paper demonstrates that the method is effective for the RCS reduction. In the following, the study focuses on how to reduce the RCS of a figure-complicated target in desired angle range and the DF31 missile's is taken as the example. As a comparison, the optimization of RCS for the isotropic impedance object is also presented at the same time. The simulation results demonstrate that the RCS of the object with the anisotropic impedance surface can be reduced evidently. It is found that the RCS reduction of the target coated by anisotropic material is better than the object with isotropic material coating in our research.

1. INTRODUCTION

Anisotropic material coating on some object's surface is a common method of Radar cross section reduction which is a very important technology in military fields. It can not only absorb the incident wave, but also redistribute the scattering energy by controlling the principal axis of the anisotropic material.

The paper proposes a universal RCS reduction method using physical optics (PO) and genetic algorithm (GA) which will be introduced in Section 2 and Section 3. The method proves to be effective via two numerical examples given in Section 4.

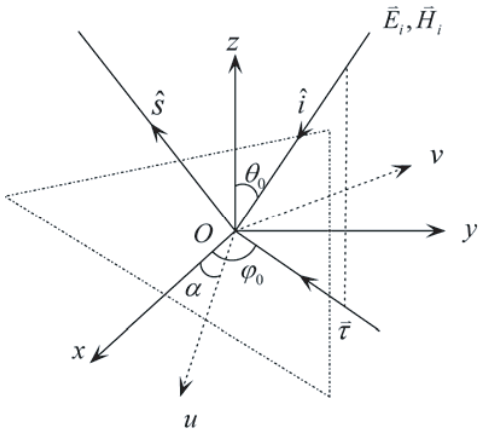

Figure 1: The EM model of an anisotropic impedance triangle facet.

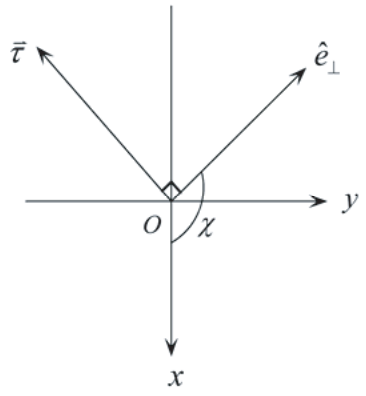

Figure 2: The local referenced coordinates x, y on the surface of the triangle facet and the principal directions u, v of the anisotropic surface impedance.

2. PHYSICAL OPTICS OF ANISOTROPIC IMPEDANCE TRIANGLE FACET

The surface of an object can be described as a composition of many triangle facets, so the scatter field of the target can also be computed as a sum of scatter field due to the contribution of each

triangle facet shown in Figure 1. Figure 2 illustrates the relationship of the anisotropic impedance axis u, v and the local referenced coordinates x, y on the surface which are selected as the tangent vectors of the surface.

Within the local referenced frame xoy, the surface impedance can be defined as

$$\begin{bmatrix} E_x \\ E_y \end{bmatrix} = \begin{bmatrix} Z_{xx} & Z_{xy} \\ Z_{yx} & Z_{yy} \end{bmatrix} \begin{bmatrix} -H_y \\ H_x \end{bmatrix} \tag{1}$$

And the impedance can also be described within the anisotropic principle axis coordinates uov as

$$\begin{bmatrix} E_u \\ E_v \end{bmatrix} = \begin{bmatrix} Z_{uu} & 0 \\ 0 & Z_{vv} \end{bmatrix} \begin{bmatrix} -H_v \\ H_u \end{bmatrix} \tag{2}$$

So the relationship of the two coordinates can be shown as

$$\begin{bmatrix} Z_{xx} & Z_{xy} \\ Z_{yx} & Z_{yy} \end{bmatrix} = \begin{bmatrix} \cos^2\alpha Z_{uu} + \sin^2\alpha Z_{vv} & \cos\alpha\sin\alpha\left(Z_{uu} - Z_{vv}\right) \\ \cos\alpha\sin\alpha\left(Z_{uu} - Z_{vv}\right) & \cos^2\alpha Z_{vv} + \sin^2\alpha Z_{uu} \end{bmatrix} \tag{3}$$

In Pelosi's work [3], the PO currents in the illuminated region of the target's surface can be formulated as following

$$\vec{J}_s^{PO} = \frac{1}{Z_0}\left[\left(1 - R_{22}\right)E_\perp^i - R_{21}E_{//}^i\right]\cos\theta_0\hat{e}_\perp + \frac{1}{Z_0}\left[R_{12}E_\perp^i + \left(1 + R_{11}\right)E_{//}^i\right](\hat{n}\times\hat{e}_\perp) \tag{4}$$

$$\vec{J}_{ms}^{PO} = \left[\left(1 - R_{11}\right)E_{//}^i - R_{12}E_\perp^i\right]\cos\theta_0\hat{e}_\perp - \left[R_{21}E_{//}^i + \left(1 + R_{22}\right)E_\perp^i\right](\hat{n}\times\hat{e}_\perp) \tag{5}$$

where Z_0 is the free-space intrinsic impedance, $[R_{11}, R_{12}, R_{21}, R_{22}]$ is the tensor reflect coefficient of the anisotropic surface. By using the Gordon's method [3, 4], the PO approximation of the scattered electric field of each triangle facet can be expressed as

$$\vec{E}^s\left(\vec{r}\right) = \frac{1}{4\pi r}e^{-jkr}\left[\hat{s}\times\left(\vec{J}_{ms}^{PO} + Z_0\hat{s}\times\vec{J}_s^{PO}\right)\right]\cdot\sum_{n=1}^{3}\frac{\hat{p}\times\hat{z}}{\left|\hat{p}\times\hat{z}\right|^2}\cdot\Delta\vec{a}_n e^{-jk\frac{\vec{a}_n + \vec{a}_{n+1}}{2}\cdot\vec{w}}\sin c\left(\frac{k\vec{w}\cdot\Delta\vec{a}_n}{2}\right) \tag{6}$$

where $\hat{w} = \hat{i} - \hat{s}$, $\hat{p} = \hat{w} - (\hat{w}\cdot\hat{n})\hat{n}$, $\Delta\vec{a}_n = \vec{a}_{n+1} - \vec{a}_n$, $\vec{a}_n$ $(n = 1, 2, 3, 4)$ is the vector of nth top point and $\vec{a}_4 = \vec{a}_1$.

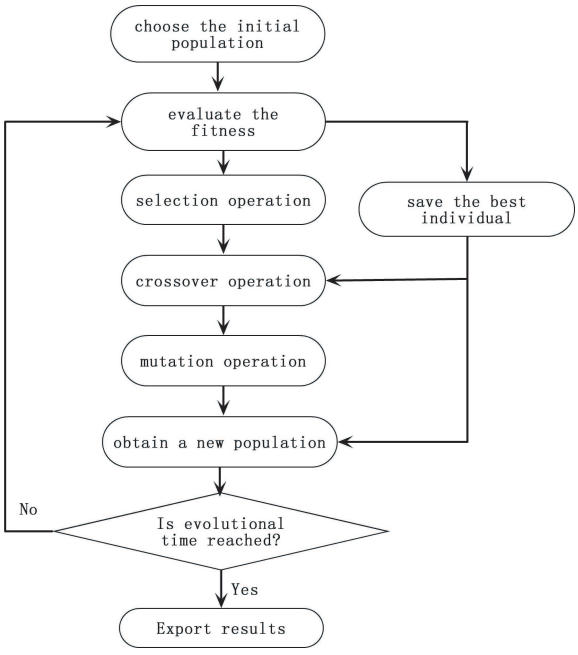

Figure 3: Flow chart of the genetic algorithm.

3. GENETIC ALGORITHM FOR OPTIMIZATION

The RCS of the target within some special angles is expected to be reduced for avoiding the enemy radar, so the fitness function of the optimization method can be expressed as

$$F\left(Z_{uu}, Z_{vv}, \alpha\right) = \frac{1}{\sum_{n=1}^{N} a_n \cdot \left[\sigma\left(\theta_n, \varphi_n\right)\right]^2} \tag{7}$$

where N is the number of samples in concerned angle region, $\sigma\left(\theta_n, \varphi_n\right)$ is the RCS of nth angle, Z_{uu}, Z_{vv}, α are the surface impedance and the principal angle, a_n is the calculation weight of the RCS of nth angle ($a_n = 1$ in all cases of this paper). The GA optimization process is used to search the maximum value of (7). Because the optimized parameters in the GA should be real number, they can be set as: $\mathrm{Real}(Z_{\mathrm{uu}}), \mathrm{Imag}(Z_{uu}), \mathrm{Real}(Z_{vv}), \mathrm{Imag}(Z_{\mathrm{vv}}), \alpha$. If the target's surface is divided into M regions and coated with different anisotropic impedance material in each region, the number of optimized parameters will be $M \times 5$.

The flowchart of GA for optimization is shown in Figure 3. Step 1, the initial population of individuals is chosen. Step 2, the fitness of each individual of the population is evaluated. Step 3, the best individual which has the highest fitness is saved as one part of the new population, and the others are changed to be the other part of the new population by selection, crossover and mutation operation. The process repeats Step 2∼3 until reaching the evolutional time, and Step 4, the final results are exported.

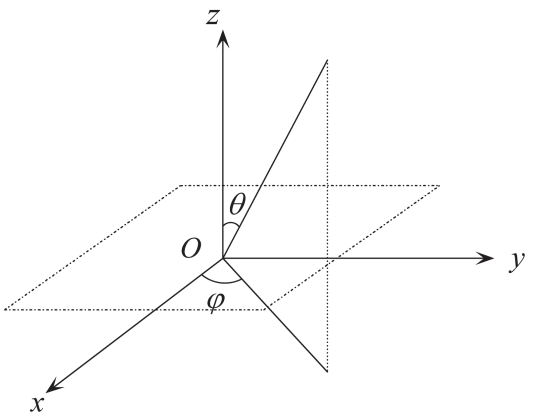

Figure 4: The plate model.

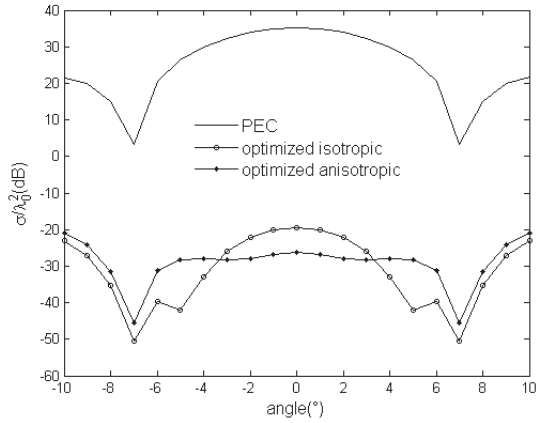

Figure 5: The optimized RCS of plate model.

Table 1: The results of plate's optimization.

The plate's optimization results				
Regions' num.	Isotropic impedance		Anisotropic impedance	
	Fitness	$\sum \sigma^2$	Fitness	$\sum \sigma^2$
1	2164.98	0.000461898	5189.97	0.000192679

Table 2: The results of missile's optimization.

The missile's optimization results					
No.	Regions' num.	Isotropic impedance		Anisotropic impedance	
		Fitness	$\sum \sigma^2$	Fitness	$\sum \sigma^2$
1	1	489.682	0.00204214	671.444	0.00148933
2	2	559.206	0.00178825	701.639	0.00142523
3	8	802.3	0.00124642	918.707	0.00108849

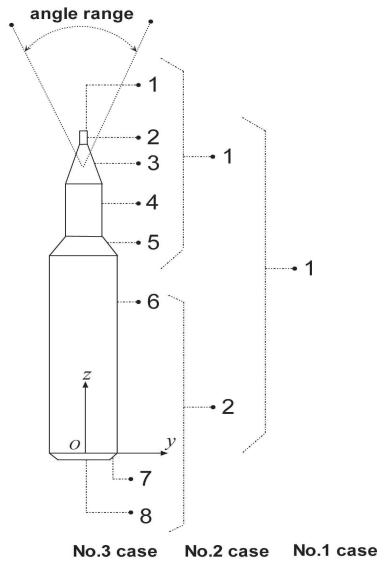

Figure 6: The missile model.

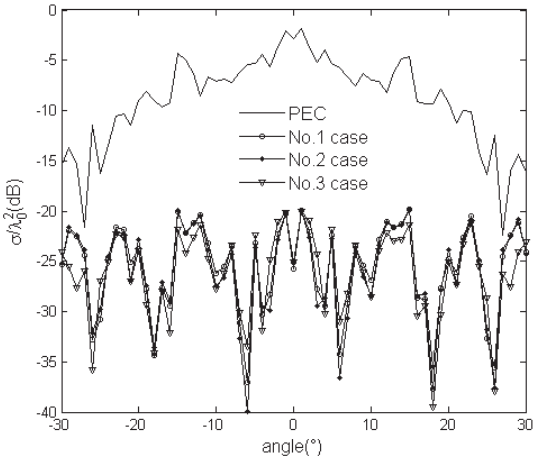

Figure 7: The optimized RCS of the missile with isotropic impedance surface in Nos. 1, 2 and 3 case.

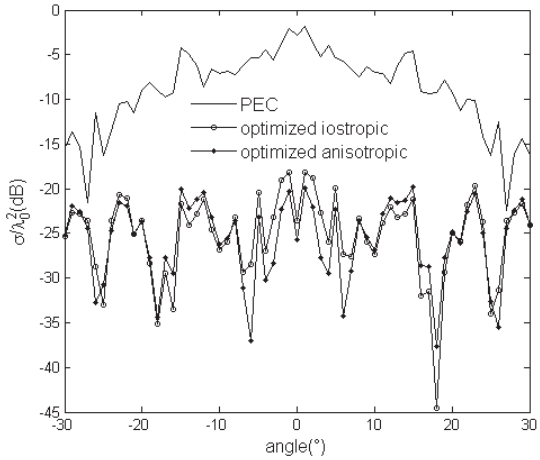

Figure 8: The optimized RCS of the missile in No. 3 case.

4. NUMERICAL RESULTS AND CONCLUSIONS

As shown in Figure 4, a square plate is illuminated by a plane incident wave with vertical polarization. Its edge length is $4\lambda_0$. The aim of the optimization is to reduce the RCS within $\pm 10^\circ$ around the mirror direction. The optimization results of the isotropic and anisotropic impedance surface are list in Table 1 and given in Figure 5. Comparing to PEC surface's situation, it is effective to reduce the RCS of the plate in some special angles by coating isotropic and anisotropic impedance material.

A missile's geometric surface is so complicated that it can be divided to 8 regions. According the different impedance value chosen for each region, 3 kinds of optimizations are presented to reduce the RCS of the missile within $\pm 30^\circ$ around the nose direction. As stated in Figures 6, 8 surface regions have different impedance values on the missile's surface in case 3, but in case 2 and case 1 the numbers of different impedance regions are 2 and 1 separately. The incident wave is a plane wave with vertical polarization. Optimization results are recorded in Table 2, and a part of them are shown in Figures 7 and 8. It is clearly that anisotropic impedance optimization can obtain lower RCS in each case than isotropic impedance optimization. And it is possible to get a better result if the surface is divided to more regions with different impedance values.

ACKNOWLEDGMENT

This work is supported by the National Natural Science Foundation of China under Grant No. 60671-040 and the Chinese National High Technology Research Plan (863 Plan) under Grant No. 2007AA1-2Z172.

REFERENCES

1. Mosallaei, H. and Y. Rahmat-Samii, "RCS reduction of canonical targets using genetic algorithm synthesized RAM," *IEEE Trans. Antennas Propagat.*, Vol. 48, No. 10, 1594–1606, Oct. 2000.
2. Chen, H. T., G. Q. Zhu, and S. Y. He, "Using genetic algorithm to reduce the radar cross section of three-dimensional anisotropic impedance object," *Progress In Electromagnetic Reasearch B*, Vol. 9, 231–248, 2008.
3. Pelosi, G., G. Manara, and M. Fallai, "Physical optics expressions for the fields scattered from anisotropic impedance flat plates," *Microwave and Optical Technology Letters*, Vol. 14, No. 6, 316–318, 1997.
4. Gordon, W. B., "Far-field approximations to the Kirchhoff-Helmholtz representations of scattered fields," *IEEE Trans. Antennas Propagat.*, Vol. 23, No. 5, 590–592, July, 1975.
5. Tezel, N. S., "Electromagnetic scattering from cylinder with generalized impedance boundary condition," *Microw. Opt. Technol. Lett.*, Vol. 49, No. 12, 3090–3093, Dec. 2007.

Asymptotic Waveform Evaluation in Anisotropic Impedance Wedge's Scattering Problem Including the Diffraction of Surface Waves

Ji Li, **Jing-Jing Yao**, **Si-Yuan He**, **and Guo-Qiang Zhu**
School of Electronic Information, Wuhan University, Wuhan 430079, China

Abstract— In this paper the asymptotic waveform evaluation (AWE) technique is introduced to solve the anisotropic impedance wedge's scattering problem When a plane wave obliquely incident on an anisotropic impedance wedge, considering the coupling of the electric field and the magnetic field, we can't get the result of the diffraction field by using the classical uniform geometrical theory of diffraction (UTD). Due to the limitation of the perturbation approach, there is no satisfactory UTD solution for the case of large deviations from normal incidence or the grazing to the edge incidence. The numerical result proved the method can effectively resolve the general scattering problem of anisotropic impedance wedge.

1. INTRODUCTION

The computation of the field diffracted from a wedge with anisotropic impedance is of relevant importance in the solution of high-frequency radiation and scattering problems. Anisotropic impedance boundary conditions (IBC's) are the most effective way to solve these problems. In recent years, many works have been carried out based on numerical [1, 2] or analytical approaches [3–10]. Most works used high-frequency asymptotic methods like UTD and physical theory of diffraction(PTD) and studied on the diffraction of the GO field by right-angled wedge [6, 10]. R. Tiberio [9] had researched the diffraction of the SW of dielectric screen at normal incidence. While in the case of oblique incidence, there are not good solutions to the coupled difference equations generated by the boundary conditions yet, so the researches are limited to specific configurations [5–9]. It is also noted that the AWE technique has already been successfully used in various electromagnetic problems [11].

In this paper we mainly research the scattering of a plane wave obliquely incident on an anisotropic impedance wedge, in which the impedance tensor has its principal anisotropy axes along directions parallel and perpendicular to the edge. This paper divides the total field into the GO field, the SW field, the diffraction fields of the GO and SW field, starting from the anisotropic IBC's, and based on the Sommerfeld-Maliuzhinets Method [5]. With the AWE technique, the spectral function is expanded by a product of Maliuzhinets special function, meromorphic function and a rational function achieved from the series expression via Pade approximation. Through the Van der Waerden method [9], the diffraction fields of the SW field are given. The space wave and surface wave diffractions contribution is represented by uniform high-frequency expressions.

2. FORMULATION OF THE PROBLEM

The three-dimensional (3-D) geometry of wedge scattering problem is shown in Fig. 1. An arbitrary polarization harmonic plane wave impinges on the edge from the direction determined by the two angles: β_0 and ϕ_0. β_0 is a measure of the incident skewness with respect to the edge of the wedge. Suppressing the time dependence $\exp(j\omega t)$, the longitudinal components of the incident field can be expressed as

$$\begin{bmatrix} E_z^i \\ \eta_0 H_z^i \end{bmatrix} = \begin{bmatrix} U_e^i \\ U_h^i \end{bmatrix} e^{jk\rho \sin\beta_0 \cos(\phi-\phi_0)} e^{-jkz\cos\beta_0} \tag{1}$$

where k and η_0 are the wavenumber and the intrinsic impedance of free-space, respectively. $U_{e,h}^i$ are the amplitudes of incident electric field and magnetic field.

The observation point is P and $n\pi$ refers to the exterior wedge angle. We consider the impedance tensors of the wedge surface have their principal anisotropy axes along directions parallel or perpendicular to the edge. According to the Maxwell equations, all the field components transverse to the z-axis can be represented in terms of E_z and $\eta_0 H_z$, two groups of boundary conditions for

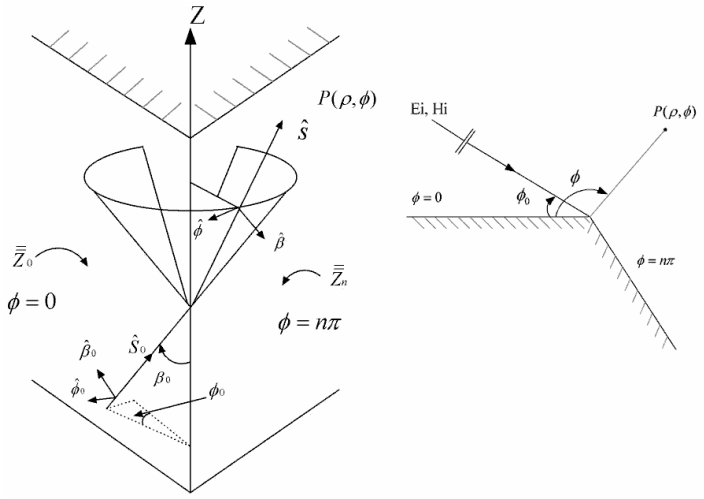

Figure 1: Geometry for the diffraction by a wedge with an anisotropic impedance face.

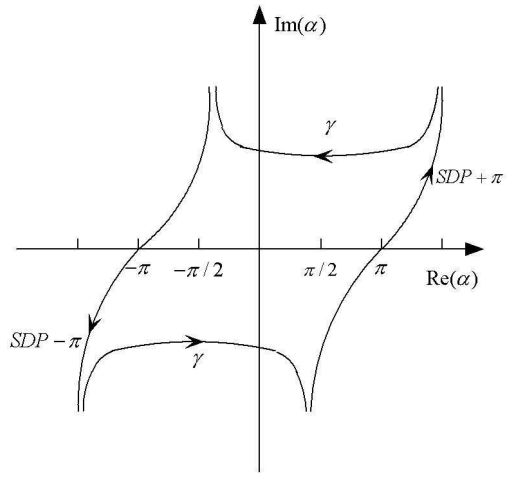

Figure 2: Integration paths in the α-complex plane

corresponding faces of the third kind are obtained

$$\frac{1}{\rho}\frac{\partial(\eta_0 H_z)}{\partial\phi} \mp jk_t \sin\theta_h^{0,n}(\eta_0 H_z) + \cos\beta_0 \frac{\partial E_z}{\partial\rho} = 0 \qquad \phi = 0, n\pi \tag{2a}$$

$$\frac{1}{\rho}\frac{\partial E_z}{\partial\phi} \mp jk_t \sin\theta_h^{0,n} E_z - \cos\beta_0 \frac{\partial(\eta_0 H_z)}{\partial\rho} = 0 \qquad \phi = 0, n\pi \tag{2b}$$

where $kt = k\sin\beta_0$, $\sin\theta_h^{0,n} = \sin\beta_0(Z_\rho^{0,n}/\eta_0)$ and $\sin\theta_e^{0,n} = \sin\beta_0(\eta_0/Z_z^{0,n})$.

An appropriate representation of the total field longitudinal components solution is expressed as the form of Sommerfeld integrals:

$$\begin{bmatrix} E_z \\ \eta_0 H_z \end{bmatrix} = \frac{e^{-jkz\cos\beta_0}}{2\pi j} \int_\gamma S_{e,h}\left(\alpha - \phi + \frac{n\pi}{2}\right) e^{jk_t\rho\cos\alpha} d\alpha \tag{3}$$

where γ is the Sommerfeld double integral path (Fig. 2).

The spectral functions $S_e(\alpha)$ and $S_h(\alpha)$ are analytical inside the strip $|\mathrm{Re}[\alpha]| \le \pi/2$ in order to satisfy the radiation condition, except for a fist-order pole at $\alpha = n\pi/2 - \phi_0$, whose residue just reproduces the incident field.

Using AWE, the spectral functions are set as

$$S_{e,h}(\alpha) = \sigma_{\phi_0}(\alpha)\Psi_{e,h}(\alpha)\Pi_{e,h}(\alpha) \tag{4}$$

where $\Pi_{e,h}(\alpha) = \frac{a_0+a_1\cos\beta 0}{1+b_1\cos\beta 0+b_2\cos^2\beta 0}$. $\Psi_{e,h}(\alpha) = \Psi_{e,h}(\alpha, \theta^0_{e,h}, \theta^n_{e,h})$ contain the Maliuzhinets special function, and $\sigma_{\phi_0}(\alpha) = \frac{1}{n}\sin\frac{\phi_0}{n}/\left(\sin\frac{\alpha}{n} - \cos\frac{\phi_0}{n}\right)$ is a meromorphic function with first-order poles, whose residues just provide the GO field.

$a_{e,h}, b_{e,h}$in (4) are set by

$$\begin{bmatrix} \xi^1_{e,h} & \xi^0_{e,h} \\ \xi^0_{e,h} & \xi^1_{e,h} \end{bmatrix} \cdot \begin{bmatrix} b^1_{e,h} \\ b^1_{e,h} \end{bmatrix} = - \begin{bmatrix} \xi^2_{e,h} \\ \xi^3_{e,h} \end{bmatrix}$$
$$\begin{bmatrix} a^0_{e,h} \\ a^1_{e,h} \end{bmatrix} = \begin{bmatrix} \xi^0_{e,h} & 0 \\ \xi^1_{e,h} & \xi^0_{e,h} \end{bmatrix} \cdot \begin{bmatrix} 1 \\ b^1_{e,h} \end{bmatrix} \tag{5}$$

3. UTD SOLUTION

By applying the residue theorem, the Sommerfeld integration can be deformed into the collective contribution of: the residues of the poles of $S_{e,h}(\alpha)$ and the two steepest descent path (SDP) integrals through the saddle points $(\pm\pi)$ (Fig. 2). So the high frequency field is represented as$U^t = U^{GO} + U^{SW} + U^d$, where $U^d = U^{dGO} + U^{dSW}$. U^{dGO} is the diffraction of the GO field, and U^{dSW} is an additional term to compensate the discontinuities of the SW field.

The meromorphic functions $\sigma_{\phi_0}(\alpha + n\pi/2 - \phi)$ have three real poles when $\phi \in (0, n\pi)$, $\alpha^{GO} = \phi - \phi_0$, $\phi + \phi_0, \phi + \phi_0 - 2n\pi$, whose residues just reproduce the incident field, the reflected field by $\phi = 0$ face, and the reflected field by $\phi = n$ face respectively.

The SW field is expressed as

$$\begin{bmatrix} E^{SW}_z \\ \eta_0 H^{SW}_z \end{bmatrix} = \left\{ \begin{bmatrix} L_e(\alpha^{SW}_0) \\ L_h(\alpha^{SW}_0) \end{bmatrix} \sigma_{\phi_0}(\alpha^{SW}_0) e^{jk\rho\cos\alpha^{SW}_0} + \begin{bmatrix} L_e(\alpha^{sw}_n) \\ L_h(\alpha^{sw}_n) \end{bmatrix} \sigma_{\phi_0}(\alpha^{sw}_n) e^{jk\rho\cos\alpha^{SW}_n} \right\} h(\phi) \tag{6}$$

where $\begin{bmatrix} L_e(\alpha^{SW}_{0,n}) \\ L_h(\alpha^{SW}_{0,n}) \end{bmatrix} = \mathrm{Res}\left\{ \begin{bmatrix} \Psi_e(\alpha) \\ \Psi_h(\alpha) \end{bmatrix}, \alpha = \alpha^{SW}_{0,n} \right\} \cdot \begin{bmatrix} \Pi_e(\alpha^{SW}_{0,n}) \\ \Pi_h(\alpha^{SW}_{0,n}) \end{bmatrix}$.

In (7), $\alpha^{SW}_{0,n}$ is the SW pole, and $\alpha^{SW}_{0,n} = -\phi + n\pi/2 \mp (\pi + \theta_{0,n} + n\pi/2)$. $h(\phi) = 1$ account for SW field occurs, when $0 < \phi < gd[\mathrm{Im}(\theta_0)] - \mathrm{Re}(\theta_0)$ near the $\phi = 0$ face and $\phi > n\pi + \mathrm{Re}(\theta_n) - gd[\mathrm{Im}(\theta_n)]$ near the $\phi = n$ face, where $gd[x] = 2\arctan[e^x] - \frac{1}{2}\pi$ denotes the Gudermann function, $h(\phi) = 0$ elsewhere.

The shadow boundaries (SB) appear at $\phi = \pi \pm \phi_0$. Applying the modified Pauli-Clemmow's SDP method, the asymptotic solution of the GO diffraction fields can be finally obtained.

$$\begin{aligned} \begin{bmatrix} E^{dGO}_z \\ \eta_0 H^{dGO}_z \end{bmatrix} &= \frac{e^{-jk\rho}e^{-jkz\cos\beta_0}e^{-j\frac{\pi}{4}}}{2n\sqrt{2\pi k_t\rho}} \left\{ \begin{bmatrix} \Pi_e(\pi + n\pi/2 - \phi) \\ \Pi_h(\pi + n\pi/2 - \phi) \end{bmatrix} \right. \\ &\cdot \left(\cot\frac{\pi - (\phi - \phi_0)}{2n} F\{k_t\rho[1 + \cos(\phi - \phi_0)]\} - \cot\frac{\pi - (\phi + \phi_0)}{2n} F\{k_t\rho[1 + \cos(\phi + \phi_0)]\} \right) \\ &\left. + \begin{bmatrix} \Pi_e(-\pi + n\pi/2 - \phi) \\ \Pi_h(-\pi + n\pi/2 - \phi) \end{bmatrix} \left(\cot\frac{\pi + (\phi - \phi_0)}{2n} - \cot\frac{\pi + (\phi + \phi_0)}{2n} \right) \right\} \end{aligned} \tag{7}$$

where $F(x) = j2\sqrt{x}\exp(jx)\int\limits_{\sqrt{x}}^{\infty} e^{-jt^2}dt$ is the UTD transition function.

Applying the Van der Waerden method [9], the SW diffraction fields can be expressed as

$$\begin{bmatrix} E^{dSW}_z \\ \eta_0 H^{dSW}_z \end{bmatrix} = \frac{-e^{-jk_t\rho}e^{-jkz\cos\beta_0}e^{-j\frac{\pi}{4}}}{2n\sqrt{2\pi k_t\rho}} \begin{bmatrix} L_e(\alpha^{SW}_{0,n}) \\ L_h(\alpha^{SW}_{0,n}) \end{bmatrix} \frac{1}{2\sin\left(\frac{\phi - \alpha^{SW}_{0,n}}{2}\right)} \left\{ 1 - F\left[2k\rho\sin^2\left(\frac{\phi - \alpha^{SW}_{0,n}}{2} \right) \right] \right\} h(\phi) \tag{8}$$

4. NUMERICAL EXAMPLES AND CONCLUSION

We choose a right-angled wedge $(n = 3/2)$, due to the fact that in this configuration, the Maliuzhinets function is known in a closed form. Meanwhile, in all the numerical examples below, the independent factor $\exp(-jkz\cos\beta_0)$ is suppressed, and all the fields are evaluated at a normalized distance $k_t\rho = 10$.

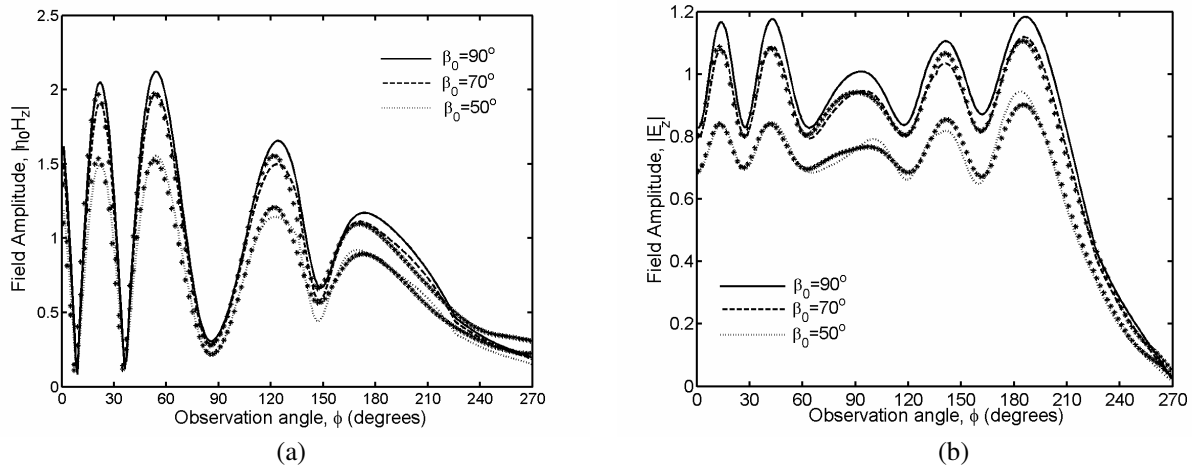

Figure 3: Amplitude of the copolar longitudinal components of the total fields.

The amplitude of the total field in the presence of isotropic impedance wedge with $Z^0_{zz}/\eta_0 = Z^0_{\rho\rho}/\eta_0 = 0.5j$, $Z^n_{zz}/\eta_0 = Z^n_{\rho\rho}/\eta_0 = 0$ is shown in Fig. 3(a). The incident plane wave is TE polarized ($E^i_{\beta_0} = 0$, $E^i_{\phi_0} = 1$), and the geometrical parameters: $\phi_0 = 45°$ and$\beta_0 = 50°, 70°, 90°$. The amplitude of total field's variation agrees well with the fig.6 given by Pelosi (marked by *) [10].

Figure 3(b) shows the amplitude of the total field in TM case ($E^i_{\beta_0} = 1$, $E^i_{\phi_0} = 0$). The anisotropic impedance wedge is characterized by a vanishing impedance: $Z^0_{zz}/\eta_0 = Z^0_{\rho\rho}/\eta_0$=1, $Z^n_{zz}/\eta_0 = Z^n_{\rho\rho}/\eta_0 = 2$. The Geometrical parameters: $\phi_0 = 45°$ and $\beta_0 = 50°, 70°, 90°$. The amplitude of total field's variation agrees well with the Fig. 5(a) given by Pelosi (marked by *) [10].

From the whole solution, we can get the integrated physical signification of anisotropic impedance wedge scattering. The SW filed and the diffraction fields of the SW field don't contribute much in the total field, but in the special area (near the wedge face) these contributions can't be ignored.

ACKNOWLEDGMENT

This work is supported by the National Natural Science Foundation of China under Grant No. 60671-040 and the Chinese National High Technology Research Plan (863 Plan) under Grant No. 2007AA1-2Z172.

REFERENCES

1. Zhu, N. Y. and F. M. Landstofer, "Numerical study of diffraction and slope-diffraction at anisotropic impedance wedges by the method of parabolic equation: Space waves," *IEEE Trans. Antennas Propagat.*, Vol. 45, No. 5, 822-828, 1997.
2. Pelosi, G., S. Selleri, and R. D. Graglia, "The parabolic equation model for the numerical analysis of the diffraction at an anisotropic impedance wedge," *IEEE Trans. Antennas Propagat.*, Vol. 45, No. 5, 767–771, 1997.
3. Manara, G., P. Nepa, G. Pelosi, and A. Vallecchi, "An approximate solution for skew incidence diffraction by an interior right-angled anisotropic impedance wedge," *Progress In Electromagnetics Research*, PIER 45, 45–75, 2004.
4. Maliuzhinets, G. D., "Excitation, reflection and emission of surface waves from a wedge with given face impedances," *Mathematical Physics*, Vol. 3, Apr. 10, 1958.
5. Lyalinov, M. A., "Perturbation method in the problem of diffraction of an obliquely incident electromagnetic plane wave by an impedance wedge and diffraction coefficients," *Day on Diffraction*, 180–186, 2001.
6. Yuan, F. and G. Q. Zhu, "Electromagnetic diffraction at skew incidence by a wedge with anisotropic impedance faces," *Radio Sci.*, Vol. 40, No. 6, Art. No. RS6014, Dec. 2005.
7. Van der Waerden, B. L., "On the method of saddle points," *Appl. Sci. Res.*, Vol. B2, 33–45, 1951.

8. Manara, G. and P. Nepa, "Electromagnetic scattering from a right-angled anisotropic impedance wedge with a perfectly conducting face," *Nat. Radio Sci. Meet.*, Boulder, Co, Jan. 1998.
9. Tiberio, R., A. Polemi, and A. Toccafondi, "UTD-based formulation for the diffraction at the edge of a truncated dielectric screens: Surface wave phenomenology," *IEEE Antennas and Propagation Society International Symposium*, Vol. 4B, 255–258, Jul. 2005.
10. Pelosi, G., G. Manara, and P. Nepa, "A UTD solution for the scattering by a wedge with anisotropic impedance faces: Skew incidence case," *IEEE Trans. Antennas Propagat.*, Vol. 46, No. 4, Apr. 1998.
11. Erdemli, Y. E., J. Gong, C. J. Reddy, and J. L. Volakis, "Fast RCS pattern fill using AWE technique," *IEEE Trans. Antennas Propagat.*, Vol. 46, No. 11, 1752–1753, Nov. 1998.

Electromagnetic Scattering from Anisotropic Inhomogeneous Impedance Cylinder of Arbitrary Shape with Generalized Impedance Boundary Condition

Ding-Feng Yu[1], **Ke Li**[2], **Jing-Jing Yao**[1], **and Guo-Qiang Zhu**[1]

[1]School of Electronic Information, Wuhan University, Wuhan 430079, China
[2]Shanghai Institute of Satellite Engineering, Shanghai 200240, China

Abstract— In this paper, the electromagnetic scattering from inhomogeneous anisotropic impedance cylinder of arbitrary shape, whose surface satisfies most general impedance boundary, is investigated by Method of Moments (MoM). Cylinder is illuminated by monochromatic plane wave polarized in the cylinder axis (z-axis). The scattered field is calculated using the electric field integral equation of Stratton-Chu, current continuity equation and two-dimensional Green's function. In consideration of the difficulty in solving the vector integral equation, transformation from cylindrical coordinates to Cartesian coordinates is adopted to simplify the electric field integral equation using impedance boundary condition. For simplicity and high efficiency, pulse basis expansion functions are chosen for MoM. It is noteworthy that not only the induced electric current, but also the induced magnetic current and electric charge make contribution to the scattered field, so the derivative of pulse function will appear in the equation. Differential is replaced by difference to cope with the derivative of pulse function as an approximation. When the integral terms appear in the expression of impedance matrix elements, QDAGS function in the IMSL Libraries is used to ensure the accuracy of the calculation. Once the radius of the cylinder is equal to a constant value, the proposed method in this paper is still valid. Obtained scattering width results are compared with those obtained by analytical method or physical optics (PO) method, and good agreements are observed.

1. INTRODUCTION

Scattering from anisotropic inhomogeneous cylinder has been explored analytically in [1]. Scattering from inhomogeneous anisotropic impedance cylinder of arbitrary shape has been investigated by physical optics (PO) method in [2]. In this paper, well-known Method of Moments (MoM) has been applied to the scattering problems of arbitrary-shaped anisotropic inhomogeneous impedance objects.

In Section 2, the scattering problem is formulated and solved. In Section 3, some examples are given. The results are compared with those obtained by PO method and analytical method. Both results match well. Finally, conclusions are given in Section 4. A time factor exp (-iwt) is assumed and omitted throughout this paper.

2. FORMULATION AND SOLUTION OF THE PROBLEM

The geometry of the considered scattering problem and parameters employed in the formulation are shown in Figure 1. The cylinder's radius is arbitrary and inhomogeneous anisotropic complex surface impedance $\overline{\overline{Z}}(\vec{\rho})$ is defined as

$$\overline{\overline{Z}}(\vec{\rho}) = Z_{tt}(\vec{\rho})\hat{t}\hat{t} + Z_{tz}(\vec{\rho})\hat{t}\hat{u}_z + Z_{zt}(\vec{\rho})\hat{u}_z\hat{t} + Z_{zz}(\vec{\rho})\hat{u}_z\hat{u}_z \tag{1}$$

where (ρ, ϕ) denotes the cylindrical polar coordinates, $\hat{t}$ is tangential unit vector on C.

Cylinder is illuminated by monochromatic plane wave polarized in the cylinder axis (z-axis). The z-component of the incident wave is given by

$$E_z^i(\vec{\rho}) = \exp(i\vec{k_i} \cdot \vec{\rho}) \tag{2}$$

The total electric field satisfies the Stratton-Chu's formula [3] and the inhomogeneous anisotropic IBC [4]. For simplicity and high efficiency, pulse basis expansion functions are chosen for MoM.

The resulting equation can be enforced at the center of each of the N cells in the cylinder model (point matching) to produce the $N \times N$ system

$$\begin{bmatrix} E_z^i(t_m)_{N\times 1} \\ 0_{N\times 1} \end{bmatrix} = \begin{bmatrix} A_{N\times N} & B_{N\times N} \\ C_{N\times N} & D_{N\times N} \end{bmatrix} \cdot \begin{bmatrix} Jz_{N\times 1} \\ Jt_{N\times 1} \end{bmatrix} \qquad (m = 1, 2, \ldots, N) \tag{3}$$

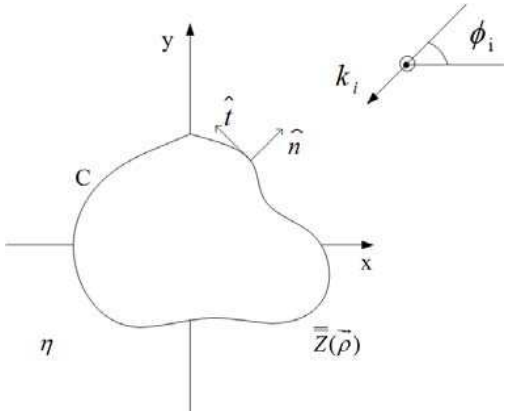

Figure 1: Geometry of the problem.

Take the A_{mn} as an example, the off-diagonal matrix elements are given by

$$A_{mn}=\frac{k\eta}{4}\int_{\text{cell}} H_0^{(1)}(kR_m)\,dt' - \frac{jk}{4}\int_{\text{cell}} H_1^{(1)}(kR_m)\frac{[x_m - x(t')]\sin\Omega(t') - [y_m - y(t')]\cos\Omega(t')}{R_m} Z_{zz}\,dt' \quad (4)$$

where

$$R_m = \sqrt{[x_m - x(t')]^2 + [y_m - y(t')]^2} \quad (5)$$

$\eta = 120\pi$. In order to obtain the diagonal matrix entries, the limit of the integral of Hankel function has to be considered. Take the A_{mn} as an example, it can be expressed as

$$A_{mn} = \frac{1}{2}Z_{zz} + \frac{k\eta}{4}\left(\int_{t_{n-1}}^{t1_m-\varepsilon} + \int_{t1_m+\varepsilon}^{t_n}\right) H_0^{(1)}(kR_m)\,dt' + \varepsilon - \frac{k^2}{4}\cdot\frac{\varepsilon^3}{3} + i\frac{2\varepsilon}{\pi}\cdot\ln\left(\frac{\gamma k\varepsilon}{2e}\right)$$
$$-\frac{jk}{4}\left(\int_{t_{n-1}}^{t1_m-\varepsilon} + \int_{t1_m+\varepsilon}^{t_n}\right) H_1^{(1)}(kR_m)\frac{[x(t)-x(t')]\sin\Omega(t')-[y(t)-y(t')]\cos\Omega(t')}{R_m} Z_{zz}dt' \quad (6)$$

where $t1_m$ denotes the length of arc from the starting point to marched point defined on the cell m. $\gamma = 1.781072418$ is the Euler's constant. ε is an arbitrary constant that approximate zero. The other diagonal matrix elements can be obtained similarly. To simplify the matrix operations, (3) is transformed as

$$G_{2N\times 1} = ABCD_{2N\times 2N}\cdot Jzt_{2N\times 1} \quad (7)$$

Then two scalar equations are simplified to one matrix equation, the current coefficients $\{Jz_n\}$ and $\{Jt_n\}$ will be obtained easily by it.

After the induced electric current is obtained, we can solve the scattered TM or TE field. The bistatic normalized scattering width (NSW) and scattering width (SW) is defined respectively in [1] and [2].

3. NUMERICAL RESULTS

The proposed procedure has been applied to three examples. In case 1, isotropic ($Z_{zt} = Z_{tz} = 0$) inhomogeneous impedance object is investigated for frequency 1 GHz, incident angle $\phi_i = 0$. Contour of the object and its surface impedance are defined as $\rho = 2\lambda + \frac{\lambda}{2}\cos\phi + \frac{\lambda}{4}\sin(2\phi)$, $Z_{zz} = Z_{tt} = \eta(0.3 + i0.5)\sin\phi$ respectively. The bistatic scattering width (SW) result is shown in Figure 2.

In case 2, $f = 390$ MHz, $\phi_i = \pi/2$, $\rho = 1.3\lambda\sqrt{\cos^2(\phi) + 0.25\sin^2(\phi)}$, $Z_{zz} = Z_{tt} = 0.27\eta(1 + i)\sin\phi$, $Z_{zt} = Z_{tz} = 0.27\eta(1 + i)\cos\phi$. Co polarized bistatic SW result is given in Figure 3.

In case 3, $f = 33$ MHz, $\phi_i = 0$, $\rho = \lambda$, $Z_{zz} = Z_{tt} = 40(\phi + i\phi^2)$, $Z_{zt} = Z_{tz} = 0$. The contour becomes a circle in this condition. Obtained bistatic NSW result is depicted in Figure 4.

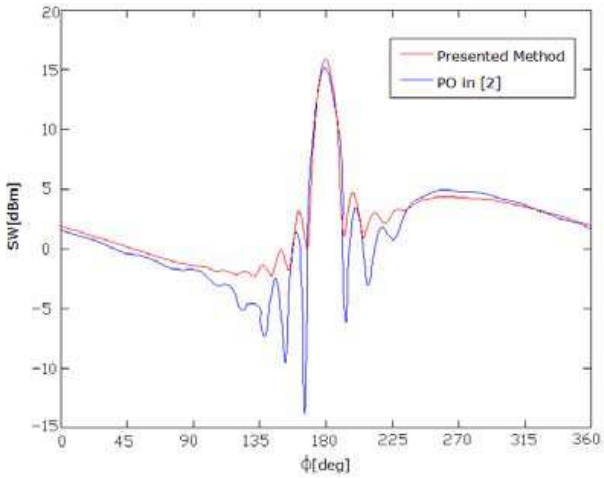

Figure 2: SW in case 1.

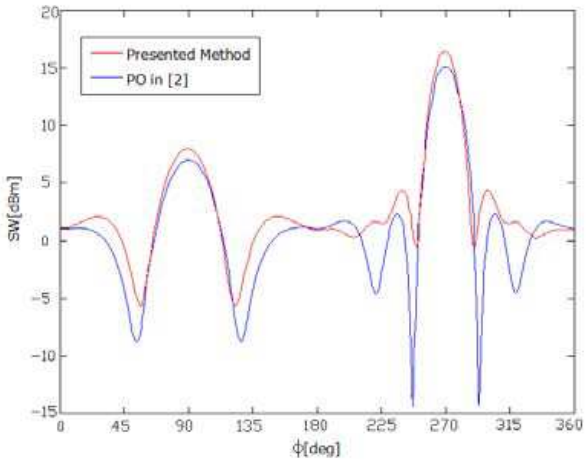

Figure 3: SW in case 2.

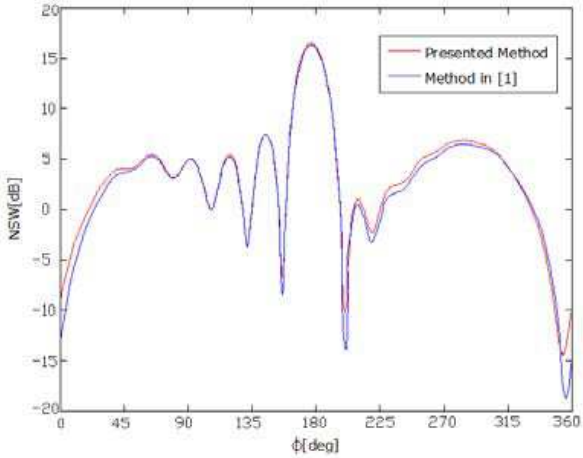

Figure 4: NSW in case 3.

4. CONCLUSIONS

In this paper, scattering from inhomogeneous anisotropic impedance cylinder of arbitrary shape for TM incidence is investigated by MoM. Once the radius of the cylinder is equal to a constant value, the proposed method in this paper is still valid. Similar procedure can be applied for TE incidence case too. Obtained scattering width results are compared with those obtained by analytical method or physical optics (PO) method, and good agreements are observed.

ACKNOWLEDGMENT

This work is supported by the National Natural Science Foundation of China under Grant No. 60671-040 and the Chinese National High Technology Research Plan (863 Plan) under Grant No. 2007AA1-2Z172.

REFERENCES

1. Tezel, N. S., "Electromagnetic scattering from cylinder with generalized impedance boundary condition," *Microw. Opt. Technol. Lett.*, Vol. 49, No. 12, 3090–3093, Dec. 2007.
2. Tezel, N. S., "Electromagnetic scattering by anisotropic inhomogeneous impedance cylinder of arbitrary shape using physical optics," *IEEE Geosci. Remote Sens. Letters*, Vol. 5, No. 4, Oct. 2008.
3. Stratton, J. A., *Electromagnetic Theory*, Macgraw-Hill, New York, 1941.
4. Cheng, D., W. Lin, and Y. Zhao, "Anisotropic impedance boundary condition for a cylindrical conductor coated with a bi-isotropic medium," *J. Phys. D, Appl. Phys.*, Vol. 26, No. 4, 517–521, Apr. 1993.
5. Peterson, A. F., *Computational Methods for Electromagnetics*, Oxford University Press, 1997.

Scintillations in Weak Turbulence of Annular Beams Whose Individual Components Are Incoherent

Y. Baykal[1], **H. T. Eyyuboğlu**[1], **and Y. Cai**[2]

[1]Electronic and Communication Engineering Department, Çankaya University
Öğretmenler Cad. No. 14, Yüzüncüyıl, Balgat 06530, Ankara, Turkey
[2]School of Physical Science and Technology, Soochow University, Suzhou 215006, China

Abstract— The scintillation index, arising from the intensity fluctuations in weak atmospheric turbulence of annular beams whose individual components are incoherent, is formulated. For such beams whose annularities are obtained by varying the source sizes and magnitudes of the individual beams, evaluations show that at very small sized beam structures, thinner beams possess smaller scintillations. As the sizes increase, the scintillation index values of thick and thin beams approach each other, eventually exhibiting the same scintillation behavior at large sized beam structures. Examination of the intensity fluctuations of the annular beams, whose individual incoherent components are at the same size but at different magnitudes, yield reverse behavior such that at very small sized beam structures, thicker beams possess smaller scintillations, however the scintillation values are very close to each other. Again, for large sized beams, the scintillation index values of thick and thin beams approach each other, eventually exhibiting the same scintillation behavior at large sized beam structures. Comparing the scintillation indices of annular beams whose individual components are incoherent to those of traditional annular beams of coherent components, it seems that for large sized beams, incoherently subtracted beams are advantageous, however the reverse is valid for very small sized beam structures.

1. INTRODUCTION

Many beams are composed of sub beams which are added to or subtracted from each other. Examples of such beams are annular [1, 2], flat-topped [3–6], sinusoidal Gaussian [7] and many others. Common property of these beams is that the addition or subtraction of the sub beams are made coherently. Recently, there is interest in the incoherently superposed beams [8–12]. Annular beams whose individual components are coherent are introduced to atmospheric turbulence through correlation functions [13], scintillations [14, 15], incoherent [16] and partially coherent [17] incidences. In this paper, we investigate the intensity fluctuations in weak atmospheric turbulence of annular beams whose individual components are incoherent. Comparing our results with the scintillations of annular beams with coherent components, we scrutinize whether incoherently subtracted annular beam structures will have advantage over their coherently subtracted classical annular beam counterparts in short optical links.

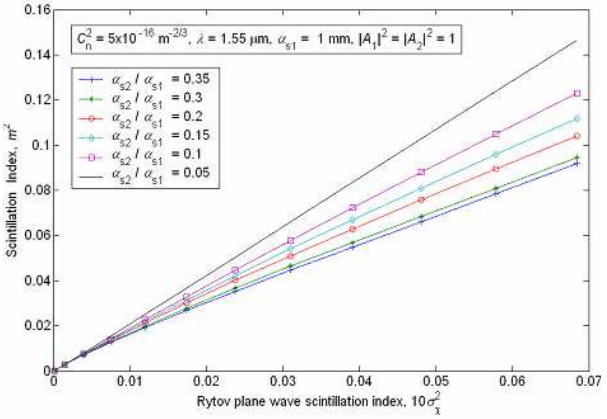

Figure 1: Scintillation index of annular beams whose individual beams are incoherent with a primary beam size of 1 mm.

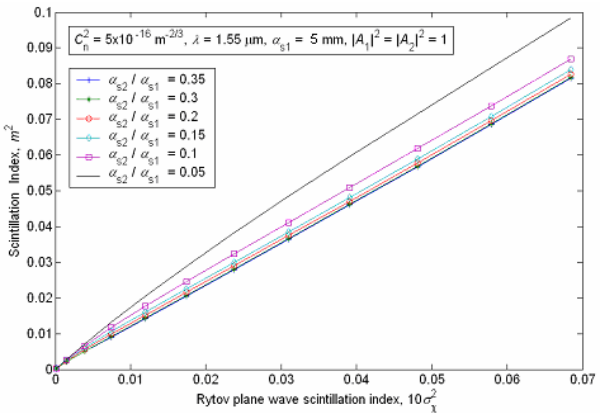

Figure 2: Scintillation index of annular beams whose individual beams are incoherent with a primary beam size of 5 mm.

2. FORMULATION

Using the extended Huygens Fresnel principle, intensity of the nth Gaussian beam in turbulence is [18]

$$I_n(L) = \frac{1}{(\lambda L)^2}\int_{-\infty}^{\infty}\int_{-\infty}^{\infty} d^2s_1 \int_{-\infty}^{\infty}\int_{-\infty}^{\infty} d^2s_2 \left|A_n\right|^2 \exp\left[-\frac{1}{2\alpha_{sn}^2}\left(|s_1|^2+|s_2|^2\right)\right] \exp\left[\frac{ik}{2L}\left(|s_1|^2-|s_2|^2\right)\right]\exp\left[\psi(s_1)+\psi^*(s_2)\right], \quad (1)$$

where * is the complex conjugate, L is the path length, λ is the wave length, A_n and α_{sn} are the amplitude and the source size of the nth beam, $\psi(s)$ is the Rytov method solution representing the random part of the complex phase of a spherical wave propagating from the source point $\mathbf{s}=(s_x,s_y)$ to the receiver origin. The instantaneous received intensity of annular beams with incoherent components is $I(L)=I_1-I_2$. Employing $\langle\exp[\psi(\mathbf{s}_1,\mathbf{p})]\exp[\psi^*(\mathbf{s}_2,\mathbf{p})]\rangle = \exp(-|\mathbf{s}_1-\mathbf{s}_2|^2\rho_0^{-2})$ where $\langle\rangle$ is the ensemble average over the medium statistics, D_ψ is the wave structure function, $\rho_0=(0.545C_n^2k^2L)^{-3/5}$ is the coherence length of a spherical wave propagating in the turbulent medium, C_n^2 is the structure constant, and performing the integrations, the average received intensity of an annular beam whose individual components are incoherent is found to be

$$\langle I(L)\rangle = \frac{\pi^2}{(\lambda L)^2}\left\{|A_1|^2\left[\left|\left(\frac{1}{2\alpha_{s1}^2}+\frac{1}{\rho_0^2}-\frac{ik}{2L}\right)\right|^2-\frac{1}{\rho_0^4}\right]^{-1} - |A_2|^2\left[\left|\left(\frac{1}{2\alpha_{s2}^2}+\frac{1}{\rho_0^2}-\frac{ik}{2L}\right)\right|^2-\frac{1}{\rho_0^4}\right]^{-1}\right\}, \quad (2)$$

Employing $I(L)=I_1-I_2$ together with Eq. (1), using the fourth order coherence function provided in [17] and performing the resultant 8-fold integral, $\langle I^2(L)\rangle$ is found as

$$\langle I^2(L)\rangle = \sum_{j=1}^{3} G_j\pi^4(\lambda L)^{-4} \left[|A_1|^4B|_{n=m=1} - |A_1|^2|A_2|^2B|_{n=1,m=2} - |A_1|^2|A_2|^2B|_{n=2,m=1} + |A_2|^4B|_{n=m=2}\right], \quad (3)$$

where $B=\xi_{j1n}^2\xi_{j2n}^2\xi_{j3nm}^2\xi_{j4nm}^2$, and $B|_{n=a,m=b}$ indicates that B is evaluated at $n=a$ and $m=b$, and

$$\xi_{j1n}^2 = \frac{1}{2\alpha_{sn}^2}-\frac{ik}{2L}+\frac{2}{\rho_0^2}+T_j, \qquad \xi_{j2n}^2 = -\frac{1}{\xi_{j1}^2\rho_0^4}+\frac{1}{2\alpha_{sn}^2}+\frac{ik}{2L}+\frac{2}{\rho_0^2}-R_j,$$

$$R_j = \begin{cases} \rho_0^{-2}+i\rho_{\chi S}^{-2}, & \text{for} \quad j=1,2 \\ i\rho_{\chi S}^{-2}, & \text{for} \quad j=3 \end{cases}$$

$$\xi_{j3nm}^2 = \frac{1}{2\alpha_{sm}^2}-\frac{ik}{2L}+\frac{2}{\rho_0^2}+T_j-\frac{T_j^2}{\xi_{j1n}^2}-\frac{1}{\xi_{j2n}^2}\left[\frac{T_j\rho_0^{-2}}{\xi_{j1n}^2}+\frac{1}{\rho_0^2}\right]^2,$$

$$G_j = \begin{cases} 1 & \text{for} \quad j=1 \\ 2\sigma_\chi^2 & \text{for} \quad j=2,3 \end{cases}, \quad T_j = \begin{cases} i\rho_{\chi S}^{-2}-\rho_0^{-2}, & \text{for} \quad j=1,3 \\ i\rho_{\chi S}^{-2}, & \text{for} \quad j=2 \end{cases},$$

$$\xi_{j4nm}^2 = -\frac{1}{\xi_{j3nm}^2}\left\{\left[\frac{1}{\xi_{j2n}^2}\left(\frac{\rho_0^{-4}}{\xi_{j1n}^2}-R_j\right)\right]\left[\left(\frac{T_j\rho_0^{-2}}{\xi_{j1n}^2}+\frac{1}{\rho_0^2}\right)\right]+\frac{T_j\rho_0^{-2}}{\xi_{j1n}^2}+\frac{1}{\rho_0^2}\right\}^2 + \frac{1}{2\alpha_{sm}^2}+\frac{ik}{2L}+\frac{2}{\rho_0^2}-R_j-\frac{1}{\xi_{j2n}^2}\left[\frac{\rho_0^{-4}}{\xi_{j1n}^2}-R_j\right]^2-\frac{\rho_0^{-4}}{\xi_{j1n}^2},$$

$\sigma_\chi^2=0.124C_n^2k^{7/6}L^{11/6}$, $\rho_{\chi S}=(0.114k^{13/6}C_n^2L^{5/6})^{-1/2}$. Scintillation index is $m^2=\langle I^2(L)\rangle/\langle I(L)\rangle^2-1$.

3. RESULTS AND COMPARISONS

In all the figures, scintillation indices in weak turbulence of annular beams with incoherent components are examined versus Rytov plane wave scintillation index at $\lambda = 1.55\,\mu\text{m}$ and $C_n^2 =$

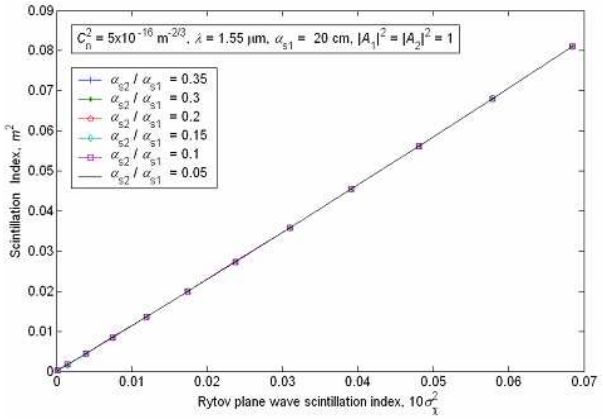

Figure 3: Scintillation index of annular beams whose individual beams are incoherent with a primary beam size of 20 cm.

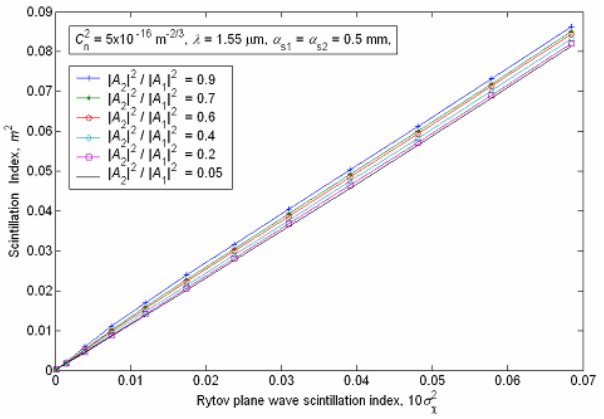

Figure 4: Scintillation index of annular beams whose individual beams are incoherent with equal beam sizes of 0.5 mm and with different magnitudes.

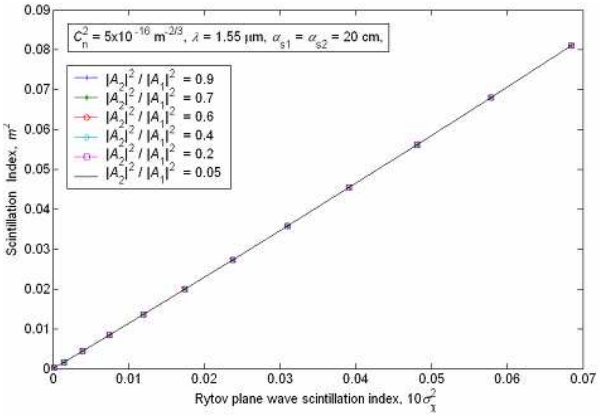

Figure 5: Scintillation index of annular beams whose individual beams are incoherent with equal beam sizes of 20 cm and with different magnitudes.

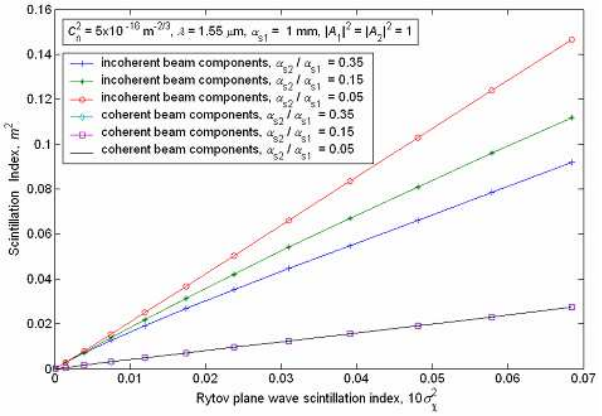

Figure 6: Comparison of the scintillation indices of annular beams with incoherent and coherent beam components with a primary beam size of 1 mm.

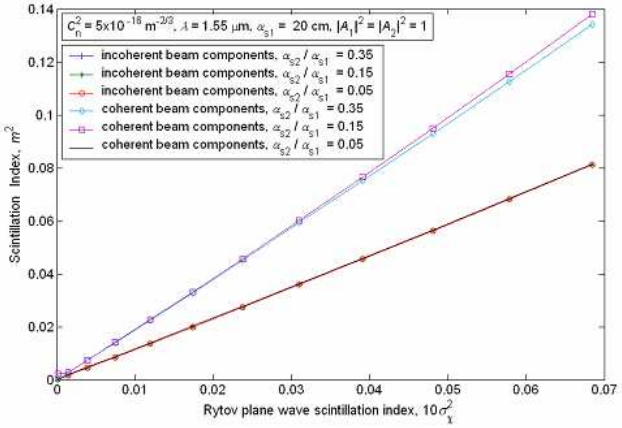

Figure 7: Comparison of the scintillation indices of annular beams with incoherent and coherent beam components with a primary beam size of 20 cm.

$5 \times 10^{-16}\,\mathrm{m}^{-2/3}$. In Figures 1–3, the effects of the primary beam source size on the scintillations are investigated. For very small primary beam sized beams, the scintillations are smaller as the beam becomes thinner, increasing the primary beam size causes the scintillations of thick and thin beams approach each other and when the primary beam size is increased further, the scintillation indices of thick and thin annular beams possessing incoherent components merge. Figures 4 and 5 show that annular beams generated by the same source sized incoherent components but with different magnitudes, have smaller intensity fluctuations for thicker beams when the source size is very small. For large source sizes of these beam structures, the scintillation indices of thick and thin beams merge. Comparisons of the scintillation indices of annular beams with incoherent and coherent beam components are made in Figures 6 and 7 which indicate that smaller scintillations are exhibited by incoherently subtracted annular beams of large sizes, and by coherently subtracted annular beams of very small sizes.

4. CONCLUSIONS

Intensity fluctuations in weak atmospheric turbulence of annular beams whose individual components are incoherent are evaluated. Thinner beams of very small primary beam sizes exhibit smaller scintillations, when the primary beam size increases, the scintillation index values for thick and thin beams attain closer values, eventually becoming the same at very large primary beam sizes. Annular beams whose incoherent components have the same size but different magnitudes, seem to have smaller scintillations for thick and very small sized sources, when the source size increase, the intensity fluctuations of thick and thin annular beams tend to approach each other. Annular beams with incoherent components seem to be advantageous over the annular beams with coherent components for beams of large sizes, however this behavior is reversed for very small sized annular beams.

ACKNOWLEDGMENT

This study was performed within the framework of the Scientific and Technological Research Council of Turkey (Tübitak) grant No. 108E130. Y. Baykal and H. T. Eyyuboglu gratefully acknowledge the support provided by Çankaya University and Tübitak. Y. Cai acknowledges the support by the National Natural Science Foundation of China under Grant No. 10904102, the Foundation for the Author of National Excellent Doctoral Dissertation of PR China under Grant No. 200928 and the Natural Science of Jiangsu Province under Grant No. BK2009114.

REFERENCES

1. Ciofini, M. and A. Lapucci, "Guided talbot resonators for annular laser sources," *J. Opt. A*, Vol. 2, No. 3, 223–227, 2000.
2. Masamori, E., "Numerical simulator of an optical resonator for generation of a doughnut-like laser beam," *Opt. Express*, Vol. 12, No. 9, 2004.
3. Tovar, A. A., "Propagation of flat-topped multi-Gaussian beams," *J. Opt. Soc. Am. A*, Vol. 18, No. 8, 1897–1904, 2001.
4. Li, Y., "Light beams with flat-topped profiles," *Opt. Lett.*, Vol. 27, No. 12, 1007–1009, 2002.
5. Li, Y. "New expressions for flat-topped light beams," *Opt. Commun.*, Vol. 206, No. 4–6, 225–234, 2002.
6. Gori, F., "Flattened Gaussian beams," *Opt. Commun.*, Vol. 107, No. 5–6, 335–341, 1994.
7. Tovar, A. A. and L. W. Casperson, "Production and propagation of Hermite-sinusoidal-Gaussian laser beams," *J. Opt. Soc. Am. A*, Vol. 15, No. 9, 2425–2432, 1998.
8. Ji, X., E. Zhang, and B. Lv, "Propagation of multi-Gaussian beams in incoherent combination through turbulent atmosphere and their beam quality," *J. Mod. Opt.*, Vol. 53, No. 15, 2111–2127, 2006.
9. Zhang, E., X. Ji, D. Yang, and B. Lv, "Propagation and far-field beam quality of $M \times N$ Hermite-Gaussian beams propagating through atmospheric turbulence," *J. Mod. Opt.*, Vol. 55, No. 3, 387–400, 2008.
10. Cheng, K. and B. Lv, "Composite coherence vortices in coherent and incoherent superpositions of two off-axis partially coherent vortex beams," *J. Mod. Opt.*, Vol. 55, No. 17, 2751–2764, 2008.
11. Zhou, P., Z. Liu, X. Xu, and X. Chu, "Comparative study on the propagation performance of coherently combined and incoherently combined beams," *Opt. Commun.*, Vol. 282, No. 8, 1640–1647, 2009.

12. Sprangle, P., A. Ting, J. Peñano, R. Fischer, and B. Hafizi, "Incoherent combining and atmospheric propagation of high-power fiber lasers for directed-energy applications," *IEEE J. Quantum Electron.*, Vol. 45, No. 2, 138–148, 2009.
13. Baykal, Y., "Log-amplitude and phase fluctuations of higher-order annular beams in a turbulent medium," *J. Opt. Soc. Am. A*, Vol. 22, No. 4, 672–679, 2005.
14. Eyyuboglu, H. T. and Y. Baykal, "Scintillations of cos-Gaussian and annular beams," *J. Opt. Soc. Am. A*, Vol. 24, No. 1, 156–162, 2007.
15. Vetelino, F. S. and L. C. Andrews, "Annular Gaussian beams in turbulent media," *Proceedings of SPIE*, Vol. 5160, 86–97, San Diego, CA, USA, January 2004.
16. Baykal, Y., H. T. Eyyuboglu, and Y. Cai, "Incoherent sinusoidal-Gaussian and annular beam scintillations," *Proceedings of SPIE*, Vol. 6936B, Baikal Lake, Ulan Ude, Russia, February 2008.
17. Baykal, Y., H. T. Eyyuboglu, and Y. Cai, "Scintillations of partially coherent multiple Gaussian beams in turbulence," *Appl. Opt.*, Vol. 48, No. 9, 1943–1954, 2009.
18. Andrews, L. C. and R. L. Phillips, *Laser Beam Propagation through Random Media*, SPIE, Bellingham, Washington, 2005.

An Application of a Fixed Point Iteration Method to Object Reconstruction

F. S. V. Bazán[1], **K. H. Leem**[2], **and G. Pelekanos**[2]

[1]Federal University of Santa Catarina, Brazil
[2]Southern Illinois University, Edwardsville, USA

Abstract— Kirsch's factorization method is a fast inversion technique for visualizing the profile of a scatterer from measurements of the far-field pattern. The mathematical basis of this method is given by the far-field equation, which is a Fredholm integral equation of the first kind in which the data function is a known analytic function and the integral kernel is the measured (and therefore noisy) far field pattern. We present a Tikhonov parameter choice approach based on a fast fixed point iteration method which constructs a regularization parameter associated with the corner of the L-curve in log-log scale. The performance of the method is evaluated by comparing our reconstructions with those obtained via the L-curve and we conclude that our method yields reliable reconstructions at a lower computational cost than the L-curve.

1. INTRODUCTION

For inverse acoustic scattering the original linear sampling method was introduced by Colton and Kirsch [5], and mathematically clarified in [6]. Kirsch improved the original version of the linear sampling method, leading to the so-called $(F^{\star}F)^{1/4}$-method shown in [9]. Recently, Arens presented a proof of convergence for this method for the case of acoustic scattering by sound soft obstacles in [1]. In most numerical applications of the linear sampling method, Tikhonov regularization has been employed and the regularization constant was computed via Morozov's discrepancy principle [6], which involved the computation of the zeros of the discrepancy function at each point of the grid, a process that is time-consuming. In addition, the noise level in the data should be known *a priori*, something that in real life applications is not the case in general. Several other strategies for selecting the regularization parameter have been proposed, one of them being the L-curve method [8], see also [10] for an application of the L-curve method in inverse elastic scattering. The L-curve method is a log-log plot of the norm of a regularized solution versus the norm of the corresponding residual norm. The L-curve method selects the parameter which maximizes the curvature of the L-curve. However, computing the point of maximum curvature in a robust way is not an easy task [7, 8, 11].

In this work we propose a fixed-point (FP) algorithm for selecting the regularization parameter based on an earlier work of Reginska [11] and Bazán [2, 3], which we use for the characterization of an object via Kirsch's $(F^{\star}F)^{1/4}$ -method. The FP algorithm only needs computation of the solution norm(or solution seminorm) and the residual norm, while the L-curve requires either the SVD (or GSVD) or the computation of the derivative of the solution norm with respect to the regularization parameter. Hence the FP algorithm is simpler and better suited for large-scale problems.

In what follows the method will be denoted by MKM-FP which stands for modified Kirsch's method coupled with the FP-algorithm.

2. A DESCRIPTION OF THE FACTORIZATION METHOD

It is well known that the propagation of time-harmonic acoustic fields in a homogeneous medium, in the presence of a sound soft obstacle D, is modeled by the exterior boundary value problem (direct obstacle scattering problem)

$$\triangle_2 u(x) + k^2 u(x) = 0, \quad x \in \mathbb{R}^2 \setminus \bar{D} \tag{1}$$

$$u(x) + u^i(x) = 0, \quad x \in \partial D \tag{2}$$

where k is a real positive wavenumber and u^i is a given incident field, that in the presence of D will generate the scattered field u.
In addition, the scattered field u will satisfy the Sommerfeld radiation condition. The Green formula

implies that the solution u of the direct obstacle scattering problem above has the asymptotic behaviour

$$u(x) = u_\infty(\hat{x})\frac{e^{ikr}}{\sqrt{r}} + O(r^{-3/2}) \tag{3}$$

for some analytic function u_∞, called the far field-pattern of u, and defined on the unit sphere Ω. In the case of the inverse problem, it represents the measured data. In particular, the inverse problem that will be considered here, is the problem of finding the shape of D from a complete knowledge of the far-field pattern.

We now define the far-field equation

$$(Fg_z)(\hat{x}) = \frac{e^{i\pi/4}}{\sqrt{8\pi k}}e^{-ik\hat{x}\cdot z} \tag{4}$$

where the right hand side is the far-field pattern of the fundamental solution of the Helmholtz equation, $z \in \mathbb{R}^2$ and $F : L^2(\Omega) \to L^2(\Omega)$ is given by

$$(Fg)(\hat{x}) = \int_\Omega u_\infty(\hat{x};\hat{d})\, g(\hat{d})\; ds(\hat{d}), \quad d \in \Omega \tag{5}$$

It is well known that the first version of the linear sampling method [5] solves the linear operator Equation (4) based on the numerical observation that its solution will have a large norm outside and close to ∂D. Hence, reconstructions are obtained by plotting the norm of the solution. However, the problem is that the right-hand side does not in general belong to the range of the operator F. Kirsch [9] was able to overcome this difficulty with the introduction of a new version of the linear sampling method based on appropriate factorization of the far-field operator F. In this method, Kirsch is elegantly using the spectral properties of the operator F to characterize the obstacle. In particular, the following far-field equation is now used in place of Equation (4)

$$(F^\star F)^{1/4} g_z = \frac{e^{i\pi/4}}{\sqrt{8\pi k}}e^{-ik\hat{x}\cdot z} \tag{6}$$

and the spectral properties of F are used for the reconstructions. However, due to noisy data, the discretized version of the far field operator F is characterized by numerical instability which may result to false information about its singular system. In the next section, we will show that we can overcome this difficulty via the a priory determination of a Tikhonov regularization constant.

3. THE FIXED-POINT METHOD FOR THE SELECTION OF THE TIKHONOV PARAMETER

We start by describing some notation concerning Tikhonov method for problems of the form

$$\min_{f\in\mathbb{R}^n} \|g - Af\|_2, \quad A \in \mathbb{R}^{m\times n}\ (m \geq n), \quad g \in \mathbb{R}^m, \tag{7}$$

where A is ill-conditioned and has singular values decaying to zero without particular gap in the singular value spectrum. In its simplest form, Tikhonov's method amounts to replacing the least squares problem (7) by

$$\min_{f\in\mathbb{R}^n} \{\|g - Af\|_2^2 + \lambda^2\|f\|_2^2\} \tag{8}$$

where $\lambda > 0$ is the regularization parameter. Solving (7) is equivalent to solving the *regularized* normal equations

$$(A^TA + \lambda^2 I_n)f = A^Tg, \tag{9}$$

whose solution is $f_\lambda = (A^TA + \lambda^2 I_n)^{-1}A^Tg$, where I_n is the $n \times n$ identity matrix.

Let the SVD of A be

$$A = U\Sigma V^*$$

where U and V are square orthonormal matrices, and $\Sigma = \mathrm{diag}(\sigma_1, \ldots, \sigma_n)$, with $\sigma_1 \geq \sigma_2 \cdots \geq \sigma_p > \sigma_{p+1} = \cdots = 0$, $p = \mathrm{rank}(A) \leq n$.

Define $\alpha_i = |u_i^T g|^2$ (the squared Fourier coefficient of g), and $\delta_0 = \|(I - UU^T)g\|_2$ (the size of the incompatible component of g that lies outside the column space of A).

Define also $y(\lambda) = \|f_\lambda\|_2^2$, and $x(\lambda) = \|g - Af_\lambda\|_2^2$. Then it is easy to see that

$$x(\lambda) = \sum_{i=1}^{p} \frac{\lambda^4 \alpha_i}{(\sigma_i^2 + \lambda^2)^2} + \delta_0^2, \qquad y(\lambda) = \sum_{i=1}^{p} \frac{\sigma_i^2 \alpha_i}{(\sigma_i^2 + \lambda^2)^2}. \tag{10}$$

The fixed-point method can be regarded as a realization of a parameter choice rule devised by Regińska [11], who proposed as regularization parameter a local minimum of the function

$$\Psi_\mu(\lambda) = x(\lambda) y^\mu(\lambda), \tag{11}$$

for proper $\mu > 0$. The motivation for using this rule can be supported heuristically noting that when λ is small, the squared solution norm $y(\lambda)$ gets large while $x(\lambda)$ gets small, and $\Psi_1(\lambda)$ is not minimized. Conversely, when λ is large, $y(\lambda)$ gets small while $x(\lambda)$ gets large, and once again $\Psi_1(\lambda)$ is not minimized. This suggests that the minimizer of $\Psi_1(\lambda)$ corresponds to a good balance between the size of the solution norm and the size of the corresponding residual norm. Regińska proved that if the curvature of the L-curve is maximized at $\lambda = \lambda^*$, and if the tangent to the L-curve at $(\log x(\lambda^*), \log y(\lambda^*))$ has slope $-1/\mu$, then $\Psi_\mu(\lambda)$ is minimized at $\lambda = \lambda^*$.

Bazán in [2] investigated the properties of $\Psi_\mu(\lambda)$ and concluded that its minimizers are converging values of a sequence defined by

$$\lambda_{j+1} = \phi_\mu(\lambda_j), \;\; j \geq 0, \;\; \phi_\mu(\lambda) = \sqrt{\mu} \frac{\|g - Af_\lambda\|_2}{\|f_\lambda\|_2}, \;\; \lambda > 0, \tag{12}$$

which gave rise to the fixed-point (FP) algorithm. One of the main advantages of the FP method is that it does not exploit any knowledge of the norm of the error in g. The main steps of FP can be described as follows.

- Given a proper initial guess, FP starts with $\mu = 1$ as a default value, and then proceeds with the iterates (12) until the largest-fixed point of ϕ_1 is reached. The choice $\mu = 1$ is because in most problems this value yields a regularization parameter that leads to a point on the L-curve near the corner of maximum curvature (geometrically, $\mu = 1$ means that the tangent line to the L-curve at the L-corner forms an angle of 135 degrees with the horizontal axis).
- If $\mu = 1$ does not work (wich means $\phi_1(\lambda > \lambda)$ for all $\lambda > 0$), μ is adjusted and the iterations restart; see [2, 3] for details.

Numerical experiments have shown that FP performs well when the L-curve is well-behaved (i.e., when there is a unique and sharp convex L-corner), and when the convexity regions of the L-curve are well-defined, as often seen in most practical problems.

However, due to the fact that minimizers of Ψ_μ (when they exist) are points where the L-curve is convex, it results intuitively clear that the FP-method can fail when the curve is concave for all $\lambda > 0$. We conclude by pointing out the following convexity result due to Regińska [11]: "When $\delta_0 \neq 0$ the curve is always convex on $(0, \epsilon)$ for ϵ sufficiently small and concave on (σ_1, ∞)". More informative results on convexity properties of the L-curve can be found in [3].

4. NUMERICAL APPLICATIONS

In this section we shall describe a method for selecting the Tikhonov regularization parameter in connection with the $(F^*F)^{1/4}$ method by Kirsch [9]. Recall that the goal of Kirsh's method is to solve the linear equation

$$(F^*F)^{1/4} g = r_z,$$

for each z in a grid, with F replaced by a discrete counterpart that is corrupted by noise: $\widetilde{F}_d = F_d + E \in \mathbb{C}^{n \times n}$, where n denotes the number of observed incident fields. We also observe that because the far-field operator is compact, the singular values of F_d decay quickly to zero and in general there is no particular gap in the singular spectrum. Taking all these under consideration, the problem we are interested in is to select the Tikhonov regularization parameter for

$$\min_{g \in \mathbb{R}^n} \{\|r_z - \widetilde{A}_d\|_2^2 + \lambda^2 \|g\|_2^2\}, \tag{13}$$

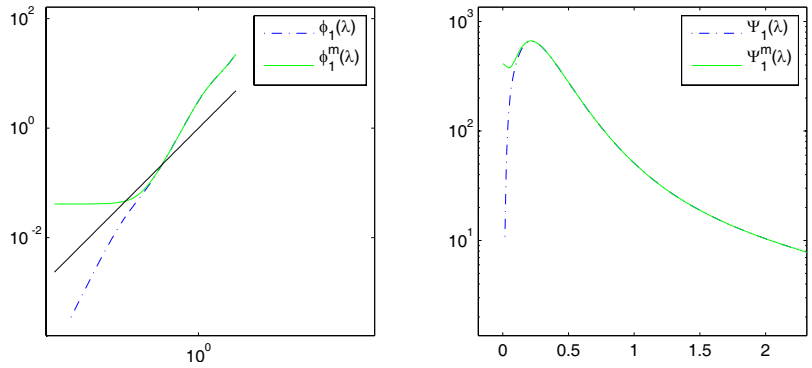

Figure 1: Functions ϕ_1 and Ψ_1 for the problem (13) and functions $\phi_1^{(m)}$ and $\Psi_1^{(m)}$ associated with MKM-FP.

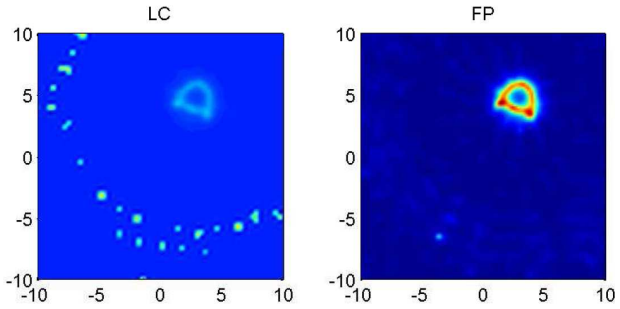

Figure 2: Reconstruction results of L-curve and FP methods for a kite shown on a grid of 64×64 obtained by interpolating the g_z values.

where for simplicity we denote $\widetilde{A}_d = (\widetilde{F}_d^* \widetilde{F}_d^*)^{1/4}$. The choice of λ for the above problem has been done via Morozov's discrepancy principle [5, 6, 9], adapted to the case when the data matrix is corrupted by noise. The strategy is reliable but the noise level (or some estimate) must be known in advance. However, the norm of the error $A_d - \widetilde{A}_d$ is rarely available in practice (making the discrepancy principle of little use), and rules that do not exploit this information are highly desirable.

In what follows we will discuss how to choose the Tikhonov regularization parameter by using the FP-method.

We start with the crucial observation that due to the fact that $\widetilde{F}_d$ is square and nonsingular (since A_d so is), the linear system

$$\widetilde{A}_d g = r_z \tag{14}$$

is always compatible and hence the important constant δ_0 introduced in the previous section satisfies $\delta_0 = 0$. To make matters worse, numerical examples with several reconstruction problems showed that the iteration function ϕ_1 has a unique fixed point that is a maximizer of Ψ_1, making the FP-method unpractical for solving the reconstruction problem. In order to overcome this difficulty we propose to replace $\widetilde{A}_d$ by another matrix, say $\widetilde{B}_d$, with $\widetilde{B}_d$ close to A_d in some sense and such that $\delta_0 \neq 0$.

To be precise, let the SVD of $\widetilde{F}_d$ be

$$\widetilde{F}_d = \widetilde{U}\widetilde{\Sigma}\widetilde{V}^* = \sum_{i=1}^{n} \widetilde{\sigma}_i \widetilde{u}_i \widetilde{v}_i^*$$

such that $\widetilde{A}_d = \sum_{i=1}^{n} \sqrt{\widetilde{\sigma}_i} \widetilde{v}_i \widetilde{v}_i^*$. Then if we take $\widetilde{B}_d$ to be

$$\widetilde{B}_d = \sum_{i=1}^{m} \sqrt{\widetilde{\sigma}_i} \widetilde{v}_i \widetilde{v}_i^*,$$

with a chosen cut-off index $m < p$, our proposal is to reconstruct the object by solving (13) with $\widetilde{B}_d$ in place of $\widetilde{A}_d$ with the Tikhonov parameter being chosen by the FP-method. In what follows this method will be denoted by MKM-FP which stands for modified Kirsch's method coupled with the FP-algorithm.

In order to explain why MKM-FP is expected to work, we first observe that the constant δ_0 for the new problem is given by $\delta_0 = \sum_{k=m+1}^{p} |v_k^* r_z|^2$ and that this value is expected to be very small but nonzero. This is an important observation since when this is so the L-curve is convex in a vicinity of the origin, in which case at least one minimizer of Ψ_1 is always guaranteed to exist [1]. In order to illustrate the fundamental difference of using $\widetilde{B}_d$ instead of $\widetilde{A}_d$, we have computed the functions ϕ_1 and Ψ_1 associated with (13) as well as the corresponding functions associated with MKM-FP which we denote by $\phi_1^{(m)}$ and $\Psi_1^{(m)}$ respectively. The problem considered in this illustration is that of reconstructing the profile of a kite. All these functions are depicted in Figure 1. Observe from this figure that while ϕ_1 has a unique fixed point that maximizes Ψ_1, the function $\phi_1^{(m)}$ has two fixed-points, the smallest one being a minimizer of $\Psi_1^{(m)}$ and the largest one being a maximizer of $\Psi_1^{(m)}$. Note that the cut-off index m is chosen to be the largest index in which the quantity $\sum_{k=m+1}^{p} |v_k^* r_z|^2 < \epsilon$ for a given tolerance ϵ. In our image reconstruction experiment, tolerance ϵ of 1.0e-12 is used.

The image reconstructions of a kite via L-curve and MKM-FP are displayed in Figure 2. In this example the far-field matrix $\widetilde{F}_d$ is 21×21 (i.e., we use 21 incident observed directions), the noise level (in a relative sense) is 3% and the object is located in a grid of 64×64 points. For MKM-FP, the cut-off index m is 20, meaning that MKM-FP uses only the first 20 singular values and corresponding singular vectors for the image reconstruction.

REFERENCES

1. Arens, T., "Why linear sampling works," *Inverse Problems*, Vol. 20, 163–173, 2002.
2. Bazán, F. S., "Fixed-point iterations in determining the Tikhonov regularization parameter," *Inverse Problems*, Vol. 24, 1–15, 2008.
3. Bazán, F. S. and J. B. Francisco, "An improved fixed-point algorithm for determining a Tikhonov regularization parameter," *Inverse Problems*, Vol. 25, 2009.
4. Colton, D. and R. Kress, *Inverse Acoustic and Electromagnetic Scattering Theory*, Springer-Verlag, New York, 1992.
5. Colton, D. and A. Kirsch, "A simple method for solving the inverse scattering problems in the resonance region," *Inverse Problems*, Vol. 12, 383–393, 1996.
6. Colton, D., M. Piana, and R. Potthast, "A simple method using Morozov's discrepancy principle for solving inverse scattering problems," *Inverse Problems*, Vol. 13 1477–1493, 1999.
7. Hanke, M., "Limitations of the L-curve method in ill-possed problems," *BIT*, Vol. 36, 287–301, 1996.
8. Hansen, P. C., "Rank-deficient and discrete ill-posed problems," *SIAM*, Philadelphia, 1998.
9. Kirsch, A., "Characterization of the shape of a scattering obstacle using the spectral data of the far field operator," *Inverse Problems*, Vol. 14, 1489–1512, 1998.
10. Pelekanos, G. and V. Sevroglou, "Shape reconstruction of a 2D-elastic penetrable object via the L-curve method," *J. Inv. Ill-Posed Problems*, Vol. 14, No. 4, 1–16, 2006.
11. Regińska, T., "A regularization parameter in discrete ill-posed problems," *SIAM J. Sci. Comput.*, Vol. 3, 740–749, May 1996.

Frequency Dependence of Image Reconstruction of Linear Sampling Method in Electromagnetic Inverse Scattering

G. H. Li, X. Zhao, and K. M. Huang
College of Electronics and Information Engineering, Sichuan University, Chengdu 610064, China

Abstract— An inverse electromagnetic scattering problem is to determine the support of a scattering object from scattered field or its far-field pattern. This problem, characterized by ill-posedness and non-linearity, leads to difficulties in theoretical research and numerical implementation. In this study, by employing Linear Sampling Method, we performed reconstructions of two- and three-dimensional scatterers. In particular, under a specified set of incident and observation angles, shape reconstruction is mainly discussed when scatterer is irradiated at different frequencies within a range. Results indicate frequency-dependence aspect of Linear Sampling Method. For a given scatterer with particular dimension and of specified shape, an optimum frequency range exists in which reconstruction resolution would be better than that of others. A further understanding of Linear Sampling Method can be obtained. Meanwhile, a guide is provided as for how to choose a sensible frequency range.

1. INTRODUCTION

An inverse electromagnetic scattering problem, one of classical inverse problems, is to determine the geometrical and/or physical properties (such as position, size, shape, permittivity, conductivity, and permeability) of a scatterer from the knowledge of scattered field or its far-field pattern, as shown in Figure 1. Classical electromagnetic inverse scattering theory faces the ill-posed problems in the sense of Hadamard [1]. At the same time, it also suffers from strong non-linearity. These two aspects mutually make each other in a worse condition. Consequently, it is difficult to do a theoretical research and to implement numerical experiment. Two kinds of traditional algorithms came into being to solve the problem. One is linearizing approximation at a fast speed but with low accuracy. The other is non-linear optimization scheme, requiring a great deal of computation time [2].

Linear Sampling Method (LSM), proposed by Colton and Kirsch in 1996 [2], involves the solution of linear integral equations. It avoids the use of linearizing algorithms as well as expensive computational iteration. As a result, alleviation of the contradiction between computational speed and reconstruction resolution is made possible. In 1996, in a paper by Colton and Kirsch [3], LSM was developed in the resonance region for the first time, in the case of two-dimensional obstacles: unit circle, 'single kite', and 'double kite'. Then, in 1997, a comparison of effect on reconstruction quality for two different frequencies of incident waves was made, in the case of 'double kite' [4]. An open problem is still unresolved that whether LSM largely depends upon frequency or not. And if so, what is the reason for the impact of frequency? In 1998, in a paper by Colton et al. [5], Colton expected reconstructions to deteriorate for lower frequencies and to improve for higher ones. It has not yet been demonstrated up till now.

This paper presents a discussion about frequency dependence of LSM. For several scatterers, we consider what happens for different frequencies, particularly in the case of such obstacle as 'double rectangle'. An interpretation for LSM's frequency dependence is also given briefly. Moreover, there is a relationship between frequency of incident waves and the number of incident wave and observation angles.

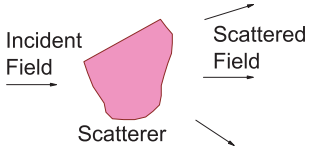

Figure 1: Schematic of the model inverse scattering problem.

2. FUNDAMENTALS AND IMPLEMENTATION OF LSM

Define the far-field operator F [2]:

$$(Fg)(\hat{\mathbf{R}}') := \int_{\Omega} u_{\infty}(\hat{\mathbf{R}}', \hat{\mathbf{k}}_i) g(\hat{\mathbf{k}}_i, R) ds(\hat{\mathbf{k}}_i) = \frac{\mathrm{e}^{-\mathrm{j}\pi/4}}{\sqrt{8\pi k}} \mathrm{e}^{-\mathrm{j}k\hat{\mathbf{R}}'\cdot R}, \ \hat{\mathbf{R}}' \in \Omega \tag{1}$$

where $\hat{\mathbf{R}}'$ is the unit vector pointed in the direction of an observation point, $\hat{\mathbf{k}}_i$ is the unit vector of an incident plane wave with frequency $f = kc/2\pi$, $u_{\infty}(\hat{\mathbf{R}}', \hat{\mathbf{k}}_i)$ is the far field pattern of scattered field, Ω is the unit circle along which $\hat{\mathbf{R}}'$ and $\hat{\mathbf{k}}_i$ are uniformly distributed, R is the coordinate for a sampling point in the reconstruction domain.

Equation (1), a linear integral equation, is the two-dimensional mathematical model for LSM. The Euclidean norm of the solution $g(R)$ becomes unbounded as R approaches the boundary of the scatterer [6]. Consequently, shape can be reconstructed by plotting gray values transformed from the norms.

In numerical implementation, Equation (1) is discretized as

$$Fg = f(R), \tag{2}$$

where

$$F = \begin{bmatrix} u_{\infty}(\hat{\mathbf{R}}'_1, \hat{\mathbf{k}}_{i;1}) & u_{\infty}(\hat{\mathbf{R}}'_1, \hat{\mathbf{k}}_{i;2}) & \cdots & u_{\infty}(\hat{\mathbf{R}}'_1, \hat{\mathbf{k}}_{i;N}) \\ u_{\infty}(\hat{\mathbf{R}}'_2, \hat{\mathbf{k}}_{i;1}) & u_{\infty}(\hat{\mathbf{R}}'_2, \hat{\mathbf{k}}_{i;2}) & \cdots & u_{\infty}(\hat{\mathbf{R}}'_2, \hat{\mathbf{k}}_{i;N}) \\ & & \vdots & \\ u_{\infty}(\hat{\mathbf{R}}'_N, \hat{\mathbf{k}}_{i;1}) & u_{\infty}(\hat{\mathbf{R}}'_N, \hat{\mathbf{k}}_{i;2}) & \cdots & u_{\infty}(\hat{\mathbf{R}}'_N, \hat{\mathbf{k}}_{i;N}) \end{bmatrix},$$

$$g(R) = \left[g(\hat{\mathbf{k}}_{i;1}, R), \ g(\hat{\mathbf{k}}_{i;2}, R) \cdots g(\hat{\mathbf{k}}_{i;N}, R) \right]^{\mathrm{T}},$$

and

$$f_n(R) = \frac{\mathrm{e}^{-\mathrm{j}\pi/4}}{\sqrt{8\pi k}} \mathrm{e}^{-\mathrm{j}k\hat{\mathbf{R}}'_n\cdot R}, \quad n = 1, 2, \ldots, N.$$

We used full aperture data based on 45 incident plane waves and 45 observation angles. The images in Figure 3 in the following section are 150 by 150 pixels, with a spacing of 0.056 m between pixels.

3. RESULTS AND DISCUSSION

Numerical experiments were conducted to reconstruct two- and three-dimensional scatterers. Figure 2 depicts several reconstructions.

In the case of 'double rectangle', we considered the impact of frequency on reconstruction resolution. Figure 3 presents reconstructions for different frequencies. A comparison of these reconstructions indicates that shape restorations at frequencies near 550 MHz are closer to the exact geometry. Deterioration happens when frequency becomes larger or smaller than this specific range. The same is true when restoring support of scatterers depicted in Figure 2. In other words, the behavior of LSM varies with frequency.

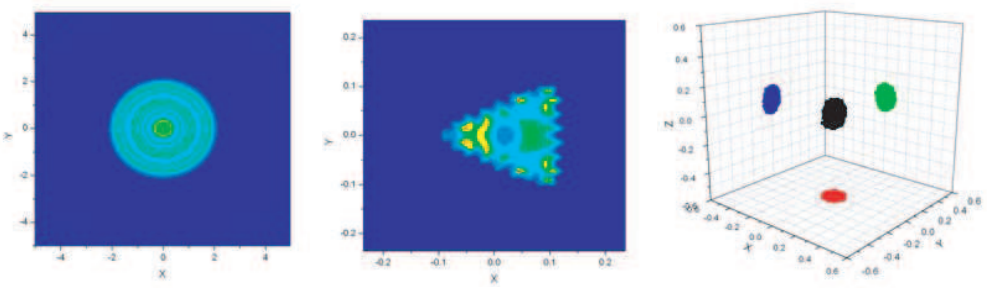

(a) (b) (c)

Figure 2: Reconstruction of different scatterers using LSM: (a) perfectly conducting cylinder with circular section, (b) medium cylinder with triangular section, and (c) perfectly conducting sphere.

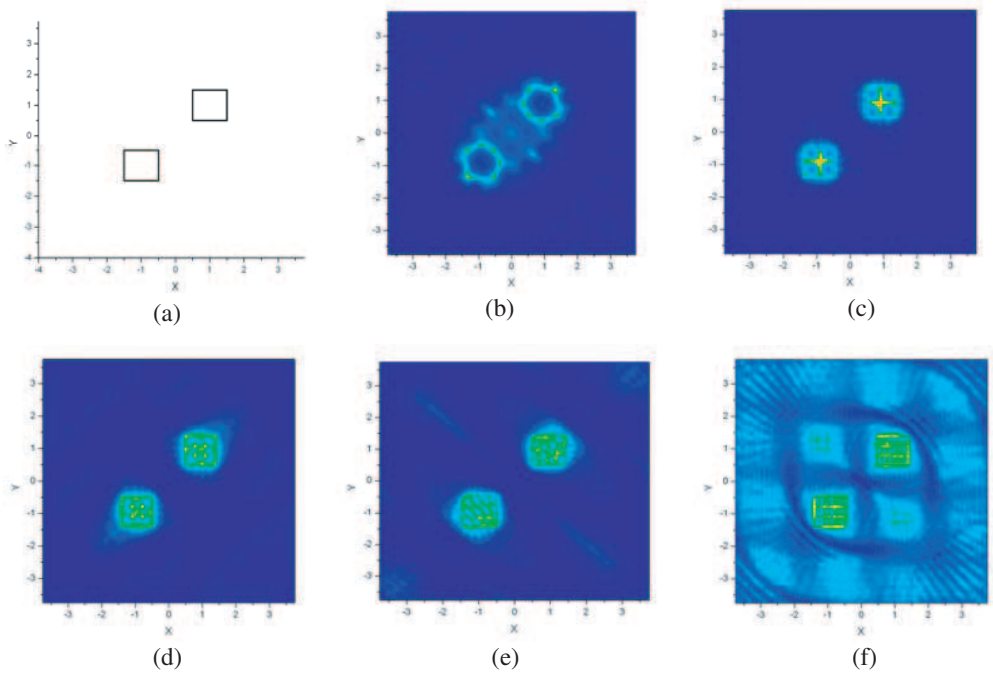

Figure 3: A series of reconstructions of 'double rectangle' for different frequencies of incident plane waves: (a) the exact geometry, (b) *frequency* = 200 MHz, (c) *frequency* = 400 MHz, (d) *frequency* = 550 MHz, (e) *frequency* = 700 MHz, and (f) *frequency* = 1 GHz.

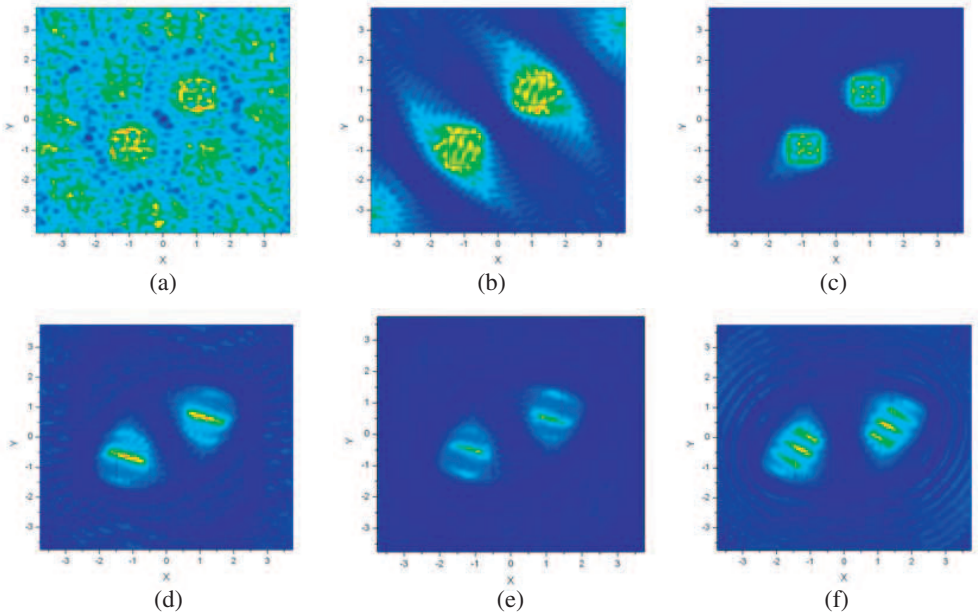

Figure 4: Reconstruction of two cylinders with rectangular cross section when frequency is 550 MHz and the number (N) of incident and observation angle goes from 25 to 75 with a step of 10.

On one hand, a decrease in frequency results in strong diffraction, strengthening the correlations among far-field patterns of different incident and observation angles. As a result, Equation (2) becomes more ill-posed, which can be demonstrated by analyzing the condition number of coefficient matrix. On the other hand, this ill-posedness becomes weaker with an increase. Yet on the right-hand side of Equation (2), each component of vector f attenuates at the level of $1\Big/\sqrt{k}$. The Euclidean norm of vector f decays correspondingly. At the same time, that of coefficient matrix F changes only within a small range. Thus, we can expect that $\|g\|$ would decrease due to an increase in frequency. This expectation is in accordance with numerical experiments. Deterioration of reconstruction occurs because of an over-small $\|g\|$ in high frequency range.

Numerical experiments show that, for a given scatterer with particular dimension and of specified shape, an optimum frequency range exists in which reconstruction resolution would be better than that of other frequencies. And within this frequency range, the electrical length of the scatterer is from 1.5 to 2. What is also interesting is that there exists a specific number of incident and observation angle for a particular frequency. Under the condition of this number, the LSM approach works better, as shown in Figure 4.

4. CONCLUSIONS

In this study, we implemented the LSM approach in the case of two- and three-dimensional scatterers. Emphasis is placed on the frequency dependence of image reconstruction of LSM approach. Results indicate that no matter whether scatterer is penetrable or not, LSM highly depends on frequency. For a given scatterer with particular dimension and of specified shape, reconstruction results visually look significantly better when frequency belongs to an optimum frequency range. The analysis of results is proposed in details. A further understanding of the frequency behavior of LSM can be obtained.

ACKNOWLEDGMENT

This research was supported in part by grant 60801035 from the National Science Foundation China.

REFERENCES

1. Hadamard, J., *Lectures on Cauchy's Problem in Linear Partial Differential Equations*, Dover Publications, New York, 2003.
2. Brandfass, M., A. D. Lanterman, and K. F. Warnick, "A comparison of the Colton-Kirsch inverse scattering methods with linearized tomographic inverse scattering," *Inverse Problems*, Vol. 17, No. 6, 1797–1816, 2001.
3. Colton, D. and A. Kirsch, "A simple method for solving inverse scattering problems in the resonance region," *Inverse Problems*, Vol. 12, No. 4, 383–393, 1996.
4. Colton, D., M. Piana, and R. Potthast, "A simple method using Morozov's discrepancy principle for solving inverse scattering problems," *Inverse Problems*, Vol. 13, No. 6, 1477–1493, 1997.
5. Colton, D. and M. Piana, "The simple method for solving the electromagnetic inverse scattering problem: the case of TE polarized waves," *Inverse Problems*, Vol. 14, No. 3, 597–614, 1998.
6. Colton, D., H. Haddar, and M. Piana, "The linear sampling method in inverse electromagnetic scattering theory," *Inverse Problems*, Vol. 19, No. 1, S105–S137, 2003.

Diffraction Properties of Partially Coherent Elegant High-order Beam

Fei Wang[1], **Yangjian Cai**[1], **Halil T. Eyyuboğlu**[2], **and Yahya Baykal**[2]

[1]School of Physical Science and Technology, Soochow University, Suzhou 215006, China
[2]Department of Electronic and Communication Engineering, Çankaya University
Öğretmenler Cad. 14, Yüzüncüyıl Balgat Ankara 06530, Turkey

Abstract— The diffraction properties of a partially coherent elegant higher-order beam in free space are investigated in detail. It is found that the diffraction properties of a partially coherent elegant higher-order beam upon propagation are closely related to its initial coherence. A partially coherent elegant higher-order beam spreads more slowly than a partially coherent standard higher-order beam, which has potential application in free-space optical communications.

1. INTRODUCTION

In 1973, Siegman introduced new Hermite-Gaussian (HG) solutions named elegant HG modes that satisfy the paraxial wave equation but have a more symmetrical form [1]. The diffraction properties of elegant HG and standard HG beams in free space and through paraxial ABCD optical system have been studied extensively [2–4]. Takenaka et al. proposed the elegant Laguerre-Gaussian (LG) beam as an extension of standard LG beam [5, 6]. Paraxial and non-paraxial propagation of elegant LG beams have been examined in [7–9]. In this paper, we investigate the diffraction properties of partially coherent elegant high-order beams (including elegant LG and HG beams). Analytical propagation formulae are derived. Some interesting numerical examples are illustrated.

2. THEORY

The cross-spectral density of partially coherent elegant HG beams generated by a Schell model source at $z = 0$ can be expressed as follows:

$$W(x_1, x_2; 0) = H_n\left(\frac{x_1}{\omega_0}\right) H_n\left(\frac{x_2}{\omega_0}\right) \exp\left[-\frac{x_1^2 + x_2^2}{\omega_0^2} - \frac{(x_1 - x_2)^2}{2\sigma_g^2}\right] \tag{1}$$

where H_n is the Hermite polynomial of order n, ω_0 is the beam waist width of the fundamental Gausian mode.

Within the validity of the paraxial approximation, the propagation of the cross-spectral density of a partially coherent beam through an aligned ABCD optical system in free space can be studied with the help of the following generalized Collins formula [10]

$$\begin{aligned} W(\xi_1, \xi_2; z) \;=\; & \frac{1}{\lambda |B|} \int_{-\infty}^{-\infty} \int_{-\infty}^{\infty} W(x_1, x_2; 0) \exp\left[-\frac{ik}{2B}\left(Ax_1^2 - 2x_1\xi_1 + D\xi_1^2\right)\right] \\ & \times \exp\left[\frac{ik}{2B}\left(Ax_2^2 - 2x_2\xi_2 + D\xi_2^2\right)\right] dx_1 dx_2 \end{aligned} \tag{2}$$

A, B, C and D are the transfer matrix elements of optical system, $k = 2\pi/\lambda$ is the wave number with λ being the wavelength. Substituting Eq. (1) into Eq. (2), after integration, we obtain the cross-spectral density of a partially coherent elegant HG beam passing through an aligned ABCD optical system as follows

$$\begin{aligned} W(\xi_1, \xi_2, z) = & \frac{\pi}{\lambda B}\sqrt{\frac{1}{M_1 M_2}}\left(1 - \frac{1}{\omega_0^2 M_1}\right)^{n/2} \exp\left[-\frac{ikD}{2B}(\xi_1^2 - \xi_2^2)\right] \exp\left(-\frac{k^2\xi_2^2}{4M_1 B^2}\right) \\ & \times \exp\left[-\frac{k^2}{4M_2 B^2}\left(\xi_1 - \frac{\xi_2}{2M_1\sigma_g^2}\right)^2\right] \frac{1}{2^{n/2}} \sum_{m=0}^{[n/2]} \sum_{k_1=0}^{n} \sum_{j=0}^{[k_1/2]} \binom{n}{k_1} (-1)^{m+j} \frac{n!}{m!(n-2m)!} \end{aligned}$$

$$\times\frac{k_1!}{j!(k_1-2j)!}\left(\frac{1}{\sqrt{M_2}}\right)^{n+k_1-2m-2j}(2i)^{2m+2j-n-k_1}\left(\frac{2}{\omega_0}\right)^{n-2m}\left(\frac{2}{\sqrt{2}\sigma_g^2\sqrt{\omega_0^2M_1^2-M_1}}\right)^{k_1-2j}$$
$$\times H_{n-k_1}\left(-\frac{ik\xi_2}{\sqrt{2}B\sqrt{\omega_0^2M_1^2-M_1}}\right)H_{n+k_1-2m-2j}\left(\frac{k\xi_2}{4M_1\sqrt{M_2}\sigma_g^2B}-\frac{k\xi_1}{2\sqrt{M_2}B}\right), \quad (3)$$

where $M_1=1/\omega_0^2+1/2\sigma_g^2-ikA/2B$, $M_2=1/\omega_0^2+1/2\sigma_g^2+ikA/2B-1/(4M_1\sigma_g^4)$. Then intensity of a partially coherent elegant HG beam at the output plane is give by $I(\xi_1,z)=W(\xi_1,\xi_1,z)$.

The cross-spectral density of a partially coherent elegant LG beam generated by a Schell-model source at $z=0$ can be expressed as follows

$$\begin{aligned}W(x_1,y_1,x_2,y_2;0) &= \frac{1}{2^{4p+2l}(p!)^2}\sum_{m=0}^{p}\sum_{n=0}^{l}\sum_{h=0}^{p}\sum_{s=0}^{l}(i^n)^*i^s\binom{p}{m}\binom{l}{n}\binom{p}{h}\binom{l}{s}\\ &\times H_{2m+l-n}\left(\frac{x_1}{\omega_0}\right)H_{2h+l-s}\left(\frac{x_2}{\omega_0}\right)H_{2p-2m+n}\left(\frac{y_1}{\omega_0}\right)H_{2p-2h+s}\left(\frac{y_2}{\omega_0}\right)\\ &\times\exp\left(-\frac{x_1^2+y_1^2+x_2^2+y_2^2}{\omega_0^2}\right)\exp\left(-\frac{(x_1-x_2)^2+(y_1-y_2)^2}{2\sigma_g^2}\right). \quad (4)\end{aligned}$$

In derivation of Eq. (4), we have used following relation between an LG mode and an HG mode [21]

$$e^{il\varphi}\rho^lL_p^l(\rho^2)=\frac{(-1)^p}{2^{2p+l}p!}\sum_{m=0}^{p}\sum_{n=0}^{l}i^n\binom{p}{m}\binom{l}{n}H_{2m+l-n}(x)H_{2p-2m+n}(y), \quad (5)$$

Substituting Eq. (5) into Eq. (2) (first, we need to extend the generalized Collins formula to three dimensional), after tedious calculating, we obtain the analytical formulae for the cross-spectral density of a partially coherent elegant LG beam passing a paraxial ABCD optical system:

$$\begin{aligned}&W(u_1,u_2,v_1,v_2,z)\\ =&\left(\frac{1}{\lambda|B|}\right)^2\frac{1}{2^{4p+2l}(p!)^2}\frac{\pi^2}{M_1M_2}\left(\frac{1}{2M_2}-\frac{1}{2M_1M_2\omega_0^2}\right)^{(2p+l)/2}\left(\frac{2q}{\omega_0}\right)^{2p+l}\\ &\times\exp\left[-\frac{ikD}{2B}u_1^2+\frac{ikD}{2B}u_2^2)\right]\exp\left(-\frac{k^2u_2^2}{4M_1B^2}\right)\exp\left[-\frac{k^2}{4M_2}\left(\frac{u_1}{B}-\frac{u_2}{2M_1\sigma_g^2B}\right)^2\right]\\ &\times\exp\left[-\frac{ikD}{2B}v_1^2+\frac{ikD}{2B}v_2^2)\right]\exp\left(-\frac{k^2v_2^2}{4M_1B^2}\right)\exp\left[-\frac{k^2}{4M_2}\left(\frac{v_1}{B}-\frac{v_2}{2M_1\sigma_g^2B}\right)^2\right]\\ &\times\sum_{m=0}^{p}\sum_{n=0}^{l}\sum_{c_1=0}^{[(2m+l-n)/2]}\sum_{e_1=0}^{[(2p-2m+n)/2]}\sum_{h=0}^{p}\sum_{s=0}^{l}\sum_{d=0}^{2h+l-s}\sum_{c_2=0}^{[d/2]}\sum_{d_1=0}^{p-2h+s}\sum_{e_2=0}^{[d_1/2]}(i^n)^*i^s\binom{p}{m}\binom{l}{n}\\ &\times\binom{p}{h}\binom{l}{s}\binom{2h+l-s}{d}\binom{2p-2h+s}{d_1}(-1)^{c_1+c_2+e_1+e_2}\frac{(2m+l-n)!}{c_1!(2m+l-n-2c_1)!}\\ &\times\frac{d!}{c_2!(d-2c_2)!}\frac{(2p-2m+n)!}{e_1!(2p-2m+n-2e_1)!}\frac{d_1!}{e_2!(d_1-2e_2)!}(2i)^{2c_1+2c_2+2e_1+2e_2-d-d_1-2p-l}\\ &\times\left(\frac{1}{\sqrt{M_2}}\right)^{d+d_1-2c_1-2c_2-2e_1-2e_2}\left(\frac{2}{\omega_0}\right)^{-2c_1-2e_1}\left(\frac{2}{\sqrt{2}\sigma_g^2\sqrt{M_1^2\omega_0^2-q^2M_1}}\right)^{d+d_1-2c_2-2e_2}\\ &\times H_{2h+l-s-d}\left(-\frac{iku_2}{\sqrt{2}B\sqrt{M_1^2\omega_0^2-M_1}}\right)H_{2m+l-n+d-2c_1-2c_2}\left(\frac{ku_2}{4M_1\sqrt{M_2}\sigma_g^2B}-\frac{ku_1}{2\sqrt{M_2}B}\right)\\ &\times H_{2p-2h+s-d_1}\left(-\frac{ikv_2}{\sqrt{2}B\sqrt{M_1^2\omega_0^2-M_1}}\right)H_{2p-2m+n+d_1-2e_1-2e_2}\left(\frac{kv_2}{4M_1\sqrt{M_2}\sigma_g^2B}-\frac{kv_1}{2\sqrt{M_2}B}\right). \quad (6)\end{aligned}$$

The intensity of a partially coherent elegant LG beam at the output plane can be obtained by setting $u_1=u_2$ and $v_1=v_2$ in Eq. (6).

3. NUMERICAL RESULTS

In this section, as numerical examples, we study the propagation properties of partially coherent elegant HG and LG beams in free space using the formulae derived in Section 2. The intensity in following figures at propagation distance z is normalized with respect to its maximum value at z. we calculate in Figs. 1 and 2 the normalized intensity distribution of a partially coherent elegant HG beam ($n = 5$, $\omega_0 = 1\,\mathrm{mm}$ in Fig. 1) and partiallly coherent elegant LG beam (p, $l = 1$, $\omega_0 = 2\,\mathrm{mm}$ in Fig. 2) for different initial coherence width at several propagation distances in free space. As shown in Fig. 1 and Fig. 2, as the initial coherence width decreases, the spot of partially coherent elegant HG or LG beam spreads more rapidly, and its beam profile converse into a Gaussian beam in the far field.

To learn about the spreading properties of partially coherent elegant higher-order beam up propagation, we study the evolution of its effective beam size on propagation. The effective beam

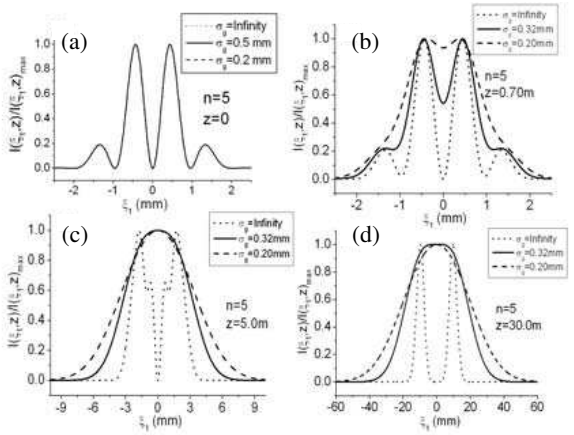

Figure 1: Normalized intensity distribution of a partially coherent EHGB ($n = 5$) for different initial coherence width at several propagation distances in free space.

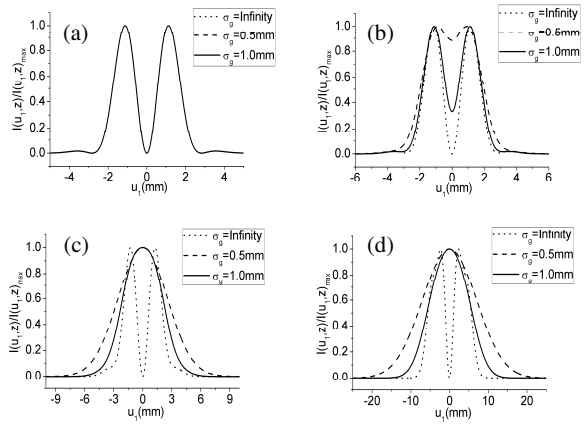

Figure 2: Normalized intensity distribution of a partially coherent elegant LG beam for different values of the initial coherence width with $p = 1$, $l = 1$ at several propagation distances in free space. (a) $z = 0$, (b) $z = 3\,\mathrm{m}$, (c) $z = 10\,\mathrm{m}$, (d) $z = 30\,\mathrm{m}$.

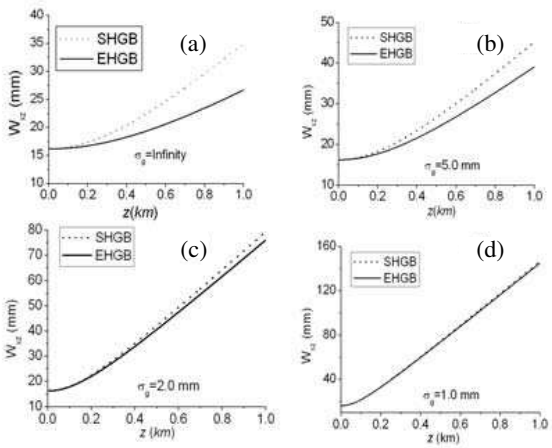

Figure 3: Effective beam sizes of a partially coherent EHGB and a partially coherent SHGB with $n = 2$ versus the propagation distance z in free space for different initial coherence width.

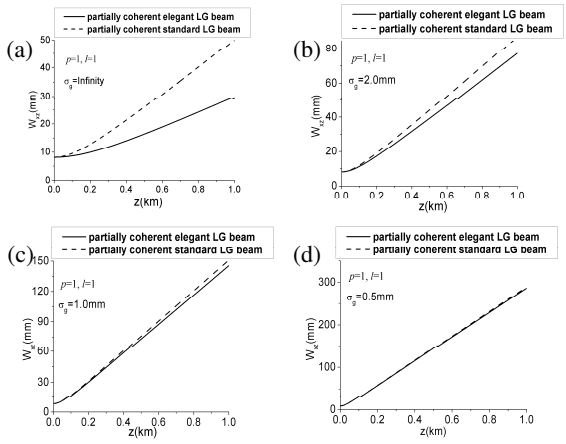

Figure 4: Effective beam sizes of partially coherent standard LG beam and elegant LG beam versus the propagation distance z in free space for different values of the initial coherence width.

size of a partially coherent EHGB in ξ direction at plane z is defined as [12]

$$W_{\xi_1 z} = \sqrt{2\int_{-\infty}^{\infty} \xi_1^2 I(\xi_1, z) d\xi_1} \Big/ \sqrt{\int_{-\infty}^{\infty} I(\xi_1, z) d\xi_1}. \tag{7}$$

Figures 3 and 4 the effective beam sizes of partially coherent standard and elegant HG and LG beams versus the propagation distance z in free space for different values of the initial coherence width, respectively. For the convenience of comparison, we have set $\omega_0 = 10\,\text{mm}$ for a partially coherent elegant LG beam, $\omega_0 = 5.773\,\text{mm}$ for a partially coherent standard LG beam, $\omega_0 = 15\,\text{mm}$ for the partially coherent elegant HG beam and $\omega_0 = 10.25\,\text{mm}$ for the partially coherent standard HG beams, so that partially coherent standard and elegant HG or LG beams have the same effective beam sizes at the source plane ($z = 0$). One finds from Figs. 3 and 4 that a coherent standard HG or LG beam spreads more rapidly than a partially coherent elegant HG or LG beam. As the initial coherence width decrease, its advantage disappears.

4. CONCLUSIONS

We have proposed theoretical model to describe partially coherent elegant HG and LG beams, and have derived the analytical formulae for the cross-spectral densities of such beams propagating through paraxial ABCD optical systems. By numerical examples, we have studied the intensity and spreading properties of partially coherent elegant HG and LG beams in free space, comparatively. We have found that partially coherent elegant HG and LG beams have some advantages over the corresponding standard HG and LG beams, the result which can be employed in applications, such as free-space optical communications and remote sensing.

ACKNOWLEDGMENT

Y. Cai acknowledges the support by the Foundation for the Author of National Excellent Doctoral Dissertation of PR China under Grant No. 200928, the Natural Science of Jiangsu Province under Grant No. BK2009114 and the National Natural Science Foundation of China under Grant No. 10904102.

REFERENCES

1. Siegman, A. E., "Hermite-Gaussian functions of complex argument as optical-beam eigenfunctions," *J. Opt. Soc. Am.*, Vol. 63, 1093–1094, 1973.
2. Saghafi, S., C. J. R. Sheppard, and J. A. Piper, "Characterising elegant and standard Hermite-Gaussian beam modes," *Opt. Commun.*, Vol. 191, 173–179, 2001.
3. Lu, B. and H. Ma, "A comparative study of elegant and standard Hermite-Gaussian beams," *Opt. Commun.*, Vol. 174, 99–104, 2000.
4. Yuan, Y., Y. Cai, J. Qu, H. T. Eyyuboğlu, and Y. Baykal, "Average intensity and spreading of elegant Hermite-Gaussian beam in turbulent atmosphere," *Opt. Express*, Vol. 17, 11130–11139, 2009.
5. Takenaka, T., M. Yokota, and O. Fukumitsu, "Propagation of light beams beyond the paraxial approximate," *J. Opt. Soc. Am. A*, Vol. 2, 826–829, 1985.
6. Zauderer, E., "Complex argument Hermite-Gaussian and Laguerre-Gaussian beams," *J. Opt. Soc. Am. A*, Vol. 3, 465–469, 1986.
7. Bandres, M. A. and J. C. Gutiérrez-Vega, "Higher-order complex source for elegant Laguerre-Gaussian waves," *Opt. Lett.*, Vol. 29, 2213–2215, 2004.
8. Mei, Z. and D. Zhao, "The generalized beam propagation factor of truncated standard and elegant Laguerre-Gaussian beams," *J. Opt. A*, Vol. 6, 1005–1011, 2004.
9. April, A., "Nonparaxial elegant Laguerre-Gaussian beams," *Opt. Lett.*, Vol. 33, 1392–1394, 2008.
10. Cai, Y. and C. Chen, "Paraxial propagation of a partially coherent Hermite-Gaussian beam through aligned and misaligned ABCD optical systems," *J. Opt. Soc. Am. A*, Vol. 24, 2394–2401, 2007.
11. Sidoro, K. and R. E. Luis, "Relations between Hermite and Laguerre Gaussian modes," *IEEE J. Quantum. Electron.*, Vol. 29, 2563–2567, 1993.
12. Carter, W. H., "Spot size and divergence for Hermite-Gaussian beams of any order," *Appl. Opt.*, Vol. 19, 1027–1029, 1980.

Radar Cross Section of a Cavity in a Finite Elliptic Cylinder

N. Altın[1] and E. Yazgan[2]

[1]Turkish Aerospace Industries, Inc., Ankara, Turkey
[2]Electrical & Electronics Engineering Department, Hacettepe University, Turkey

Abstract— In this paper, the part of the cockpit of the air vehicle in a far field with a plane wave of warning, scattering fields from cockpit part is assumed to be radiate in free space. Fuselage of the air vehicle is modeled finite elliptical cylinder and a large cavity is mounted in the sidewall of a finite elliptical cylinder. The part of the cockpit of the air vehicle is modeled close to the real model. A Radar Cross Section (RCS) analysis of cockpit part is calculated using together Shooting and Bouncing Ray (SBR) and Geometrical Optics (GO) methods and RCS analysis of elliptical cylinder is calculated Uniform Geometrical Theory of Diffraction (UTD) and Physical Optics (PO) method. Shooting and Bouncing Ray (SBR) using for analyses does not limit the form of model. By using of proposed method, outputs for cockpit part and fuselage RKA analyses were provided.

1. INTRODUCTION

In computational electromagnetic, the scattering of EM waves of very large objects from wavelength to examine the geometrical and physical optics-based techniques are known for a long time. However, in practice, widespread use of geometrical optics-based approach is by means of the shooting and bouncing rays (SBR) technique. SBR method is developed recently by the authors [7–9].

Two very different approaches have been proposed thus far for obtaining the RCS due to the interior irradiation of open cavities in the high frequency regime. First of these approaches is the waveguide modal method. Typically, the cavity under consideration is assumed to be elongated in a preferred direction and have a uniform cross section along that direction. The field inside the cavity is then expressed in terms of the known waveguide modes. The unknown modal coefficients are found via application of the reciprocity relationship and Kirchoff's approximation [2, 3].

Second of these approaches is the shooting and bouncing ray method. Scattering fields of large and complex objects are calculated with ray tracing technique which is one of the high frequency techniques. In this technique involves tracing a dense grid of geometrical optics rays originating from the incident wave into the cavity through its opening. After multiple bounces from the interior walls of the cavity, the rays eventually exit the cavity through the opening. The scattered field associated with each exit ray is then determined by a physical optics scheme. The total scattered field results from summing the scattered field due to individual rays. This approach has the feature that a real physical problem can be modeled closely, taking into account the noncircular opening of the cavity, the wall coating and the longitudinal bending or twisting of the cavity. It is so simple in concept that there is virtually no restriction on the shape or material loading of the cavity [4].

In the literature, rectangular cavity was used to represent a structure such as a cockpit in an air vehicle and has been flush mounted in the sidewall of a finite circular cylinder [2, 3]. In this study, fuselage of the air vehicle is modeled finite elliptical cylinder and a large cavity is mounted in the sidewall of a finite elliptical cylinder. The part of the cockpit of the air vehicle is modeled close to the real model. Shooting and bouncing ray method was used for the cavity, and finite elliptical cylinder effects were accounted for via the Uniform Geometrical Theory of Diffraction (UTD) and Physical Optics (PO). To resolve discontinuity in the RCS analysis of elliptical cylinder PO method is used. Many numerical methods have been developed for the purpose of solving complex structure of an object from the effects of electromagnetic wave scattering problem.

2. DIFFRACTION MECHANISM AND MODEL

Fuselage of the air vehicle is modeled finite elliptical cylinder and a large cavity is mounted in the sidewall of a finite elliptical cylinder as shown in Fig. 1.

2.1. Analysis and Calculation

For RCS, there are four scattering sources as shown Fig. 1. They are mirror reflection field of ellipse, diffraction field in the ellipse, cavity, creeping wave interactions of the cavity and ellipse. This is shown in Figs. 2 and 3. The cavity contribution is found by using ray tracing method. In

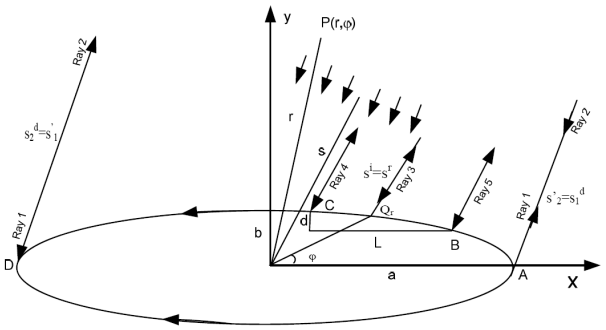

Figure 1: Finite elliptical cylinder and cockpit illuminated by a plane wave.

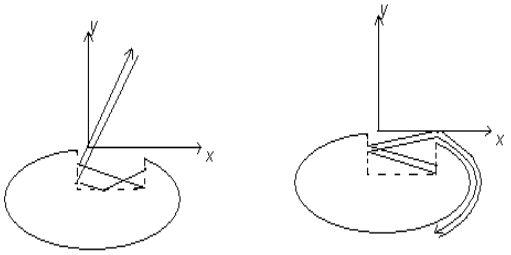

Figure 2: Intuitive ray path tracing inside the cockpit.

the SBR method, a large number of parallel rays from the direction of the incident plane wave are "shot" into the cavity. Each ray that enters the cavity bounces off the walls and eventually exits the structure via the aperture opening. The exiting rays contribute to the backscattering field and then calculate the RCS. Below the scattering mechanism of each source and computing method will be analyzed.

2.2. Incidence Field of Ellipse

At $P(r,\phi)$ position in the Fig. 1, a unit amplitude plane wave incident at angle ϕ_i is described as follows.

$$E^i(r,\phi) = A \cdot e^{jkr\cos(\phi-\phi_i)} \tag{1}$$

where A is the amplitude and value is one.

2.3. Mirror Reflection Field of Ellipse

As shown in Fig. 1, the plane wave is incident on the elipse from a direction φ, the incident ray at the point of reflection Q_r is reflected. Reflected field formula is as follows.

$$E_r(s,\phi_i) = E_i(Q_r)\sqrt{a_o(\gamma_r)/2}R_{s,h}(\xi_p, X_p)\frac{e^{-jks^r}}{\sqrt{s^r}} \tag{2}$$

where $E_i(Q_r)$ is incident field to reflection point on the ellipse surface, $R_{s,h}(\xi_p, X_p)$ is the uniform theory of diffraction reflection coefficient [1, 8, 13], $a_0(\gamma_r)$ is the radius of curvature at any point γ on the elliptical surface [1,8,13]. s and h are respectively soft and hard boundary condition.

2.4. Diffraction Field on the Ellipse

The surface diffracted field at any observation point is given by

$$E_1^d\left(s_1^d,\phi_i\right) = E^i\left(Q_1'\right)T_{s,h}(\xi_{d1}, X_{d1}, t_1)\frac{e^{jks_1^d}}{\sqrt{s_1^d}} \tag{3}$$

where $E_i(Q_1')$ is an incident field at attachment point Q_1', $T_{s,h}(\xi_d, X_d, t)$ is the uniform theory of diffraction surface diffraction coefficient [1, 8, 13].

2.5. Cavity RCS

The cavity contribution is found by using ray tracing method. In the SBR method, a large number of parallel rays from the direction of the incident plane wave are "shot" into the cavity. Each ray that enters the cavity bounces off the walls and eventually exits the structure via the aperture opening. Exit rays involve calculating the ray tube divergence factors and the reflection coefficients. The exiting rays contribute to the backscattering field and then calculate the RCS [4].

By summing over each ray tube, expressions for A_θ and A_ϕ due to each exit ray tube are obtained as follows.

$$\begin{bmatrix} A_\theta \\ A_\phi \end{bmatrix} = \frac{jk_0}{2\pi}\sum_{i\,all\,rays}\begin{bmatrix} E_x(x_i,y_i)\cos\phi^i + E_y(x_i,y_i)\sin\phi^i \\ \left(-E_x\sin\phi^i + E_y\cos\phi^i\right)\cos\theta^i \end{bmatrix}\cdot e^{jk_0(s_x x_i + s_y y_i)}(\Delta x_i \Delta y_i) I_i \tag{4}$$

where

$$I_i = \frac{1}{(\Delta x_i \Delta y_i)} \int_{ith\,exit} \int_{ray\,tube} dxdy e^{jk_0[(u-s_x)x+(v-s_y)y]} \tag{5}$$

And $(\Delta x_i \Delta y_i)$ = area of the exit ray tube, $E_x(x_i, y_i)$ and $E_y(x_i, y_i)$ are respectively x and y components of the outgoing field on the exit ray tube [4].

2.6. Total RCS

Fuselage of the air vehicle is modeled finite elliptical cylinder and a large cavity is mounted in the sidewall of a finite elliptical cylinder as shown in Fig. 1. Total radar cross section of fuselage and cockpit is given as below.

RCS of elliptical surface is obtained as follows.

$$RCS_{ellipticalsurface} = \lim_{s\to\infty} 2\pi s \left[\frac{\left|E^r(s,\phi_i) + E^d(s,\phi_i)\right|^2}{\left|E^i(s,\phi_i)\right|^2}\right] \tag{6}$$

RCS of cockpit is given as below.

$$RCS_{\phi\phi} = 4\pi \left|A_\phi\right|^2 \tag{7}$$

$$RCS_{\theta\theta} = 4\pi \left|A_\theta\right|^2 \tag{8}$$

Field arises from cockpit is calculated only when incidence angle ϕ is at the range of 0°–55° by formula (7 or 8)

To eliminate discontinuity in the RCS analysis of elliptical surface, physical optic (PO) method is used [12]. When PO method added to UTD, provide an improvement to discontinuity near the $\theta = 90°$ direction.

Consequently, RCS analysis of Fig. 1, combination of UTD, PO and SBR method are used. In the following, RCS value is examined for hard and soft polarization.

3. NUMERICAL RESULT

The UTD/SBR methods were used to compute monostatic RCS in $\theta = 0°$ plane. The cockpit depth is $d = 1.2983$ m and length is $L = 3.4457$ m. Operating frequency is 5 GHz. The elliptical cylinder is $a = 4.5$ m and $b = 1.55$ m as shown in Fig. 1. RCS value is examined for hard and soft polarization.

In Fig. 3, It is shown RCS of finite elliptical cylinder for soft and hard polarization at 5 GHz. RCS of finite elliptical cylinder is calculated UTD method but it was observed discontinuity in the $\phi = 90°$. To remove the discontinuity, Physical Optics method is used. The RCS pattern with an $\Delta\phi = 0.8°$ aspect increment is sketched in Fig. 3.

As shown in Fig. 4, RCS of cockpit is calculated SBR method for soft and hard polarization at 5 GHz. The result is shown in Fig. 4 between $0° \leq \phi \leq 55°$.

The RCS of air vehicle fuselage and cockpit is sketched in Fig. 5 for hard and soft polarization at 5 GHz.

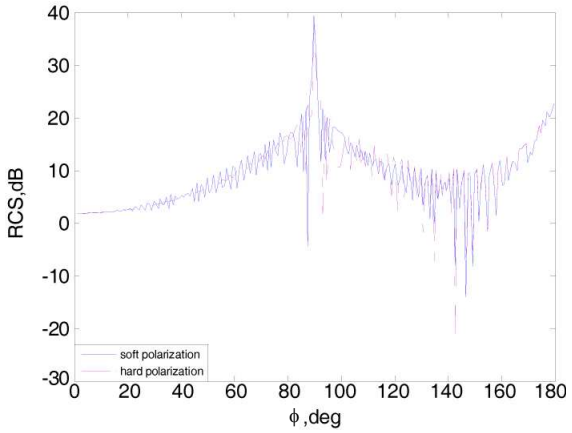

Figure 3: Only RCS of finite elliptical cylinder at 5 GHz.

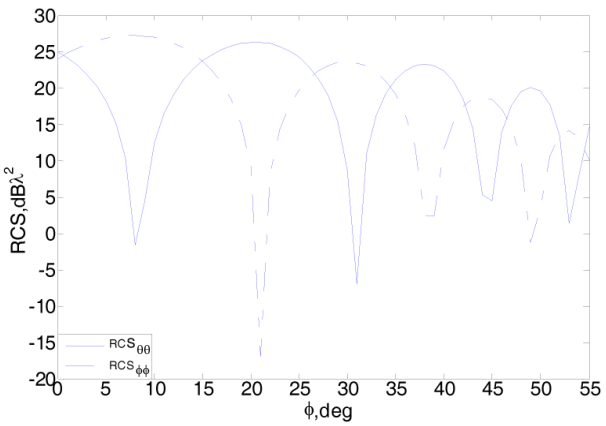

Figure 4: Only RCS of cockpit at 5 GHz.

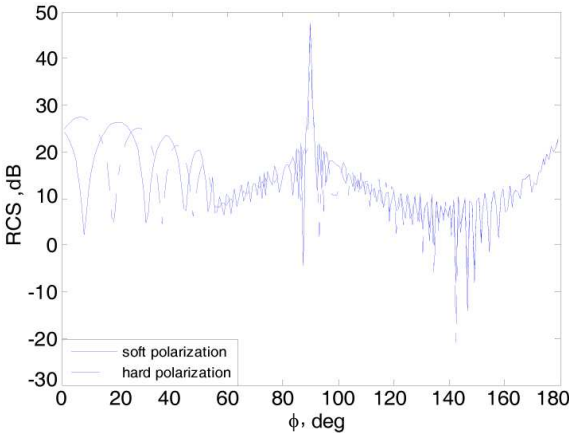

Figure 5: RCS for cockpit in a finite elliptical cylinder at 5 GHz.

4. CONCLUSIONS

The RCS of a cockpit of the air vehicle was calculated by using SBR method, and the RCS of the finite elliptical cylinder was calculated by using UTD/PO method. In this paper, the calculated result is at 5 GHz for hard and soft polarization. It was found that exterior scattering and cockpit effects dominate the RCS.

REFERENCES

1. McNamara, D. A., C. W. I. Pistorius, and J. A. G. Malherbe, *Introduction to the Uniform Geometrical Theory of Diffraction*, Artech House, Boston, 1990.
2. Paknys, R., S. Kashyap, and A. Louie, "Radar cross section of a rectangular cavity in a finite cylinder," *IEEE AP-S International Symposium*, 718–721, Orlando, FL, 2001.
3. Paknys, R., F. Hyjazie, S. Kashyap, and A. Louie, "Radar cross section of a rectangular cavity in a finite ground plane," *IEEE AP-S International Symposium*, 2842–2845, Orlando, FL, July 11–16, 1999.
4. Ling, H., R. Chou, and S. W. Lee, "Shooting and bouncing rays: Calculating the RCS of an arbitrarily shaped cavity," *IEEE Trans. on Antennas and Propagat.*, Vol. 37, No. 2, 194–205, 1989.
5. Glassner, A. S., *An Introduction to Ray Tracing*, Academic Press, London, 1989.
6. Jenn, D. C., *Radar and Laser Cross Section Engineering,* AIAA Education Series, California, ABD, 1995.
7. Ling, H., S. W. Lee, and R. C. Chou, "High frequency RCS of open cavities with rectangular and circular cross section," *IEEE Trans. AP-S*, 648–654, 1989.
8. Pathak, P. H., W. D. Burnside, and R. J. Marhefka, "A uniform GTD analysis of the diffraction of electromagnetic waves by a smooth convex surface," *IEEE Trans. on Antennas and Propagat.*, Vol. 28, No. 5, 631–642, September 1980.
9. Pearson, L. W., "A Scheme for automatic computation of fock-type integrals," *IEEE Trans. on Antennas and Propagat.*, Vol. 35, No. 10, 1111–1118, October 1987.
10. Michaeli, A., "Asymptotic analysis of edge-excited currents on a convex face of a perfectly conducting wedge under overlapping penumbra region conditions," *IEEE Trans. on Antennas and Propagat.*, Vol. 44, No. 1, January 1996.
11. Weinmann, F., "Ray Tracing with PO/PTD for RCS modeling of large complex objects," *IEEE Trans. on Antennas and Propagat.*, Vol.54, No.6, June 2006.
12. Mahafza, R. B., *Radar Systems Analysis and Design Using Matlab*, Chapman&Hall CRC, 2000.
13. Casciato, M. D. and K. Sarabandi, "High-frequency radio wave diffraction from singly curved, convex surfaces — A heuristic approach," *IEE Proc. — Microw. Antennas Propag.*, Vol. 151, No. 1, 43–53, February 2004.

A Novel GL Double Layer Electromagnetic Cloaks in Broad Frequency Band and Reciprocal Law

Ganquan Xie, Jianhua Li, Feng Xie, and Lee Xie
GL Geophysical Laboratory, USA

Abstract— In this paper, we propose a novel GL double layer EM cloak in the broad frequency band. In short, we call it as GLWF double EM cloak. The GLWF double layer cloak (GLWF cloak) consists of two sphere annular layers, $R_1 \le r \le R_2$ and $R_2 \le r \le R_3$. Two type cloak materials are proposed and installed in its each layer, respectively. The outer layer of the GL cloak has the invisible function in broad frequency band, while its inner layer has the fully absorption function. The outer layer cloaks the Local concealment from the Global exterior EM field; The inner layer cloaks the Global free space region from the Local field excited inside the concealment. The GLWF double layer cloak overcomes the following difficulties of the single layer PS cloak. (1) The PS cloak damaged the EM environment of its concealment, such that there exists no EM wave field can be excited inside the concealment of the PS cloak, the concealment of the PS cloak is blind. Our GL double layer cloak recovered the normal EM environment in its concealment, such that the EM wave field can be excited inside the concealment of the GL double layer cloak. (2) The PS cloak is very strong dispersive and strong degenerative cloak material. The PS cloak has invisibility only in very narrow frequency band. There is exceeding light speed physical violation in PS cloak. Our GLWF double layer cloak corrects the violation. (3) The two sources reciprocal law is very important principle in the electromagnetic theory and application. The reciprocal law is satisfied in our GL double cloak media. However, the PS cloak damaged the reciprocal law. The following physical statements are described: (1) In the domain consist of free space, single layer PS cloak and its cloaked concealment with normal material, the two sources reciprocal law is damaged. (2) In the domain consist of free space, single layer cloak and its cloaked concealment with some special double negative refractive index metamaterial, the two sources reciprocal law is recovered, but the cloak invisibility function is lose. (3) In the domain consist of free space, GLWF double layer cloak and its cloaked concealment with any material, the two sources reciprocal law is satisfied, and the cloak invisibility function is complete, sufficient and in broad frequency band. The simulations and comparisons of the EM wave field propagation through the GLWF double cloak, GL double cloak and GL double layer with PS outer layer are presented to show the advantages of the GLWF double layer EM cloak. The GL double layer cloaks are proposed by our GL EM modeling and inversion. The GL modeling combines analytical and numerical approaches. There are no large matrices to solve in the GL method. Moreover, the GL method does no need artificial boundary and absorption boundary condition on it to truncate infinite domain. The 3D GL EM modeling simulations for the double layer cloak are presented. The GL method is different from the conventional methods. It has dual capabilities of the theoretical analysis and numerical simulations to study the cloak meta-materials, and field scattering problem in physical sciences.

1. INTRODUCTION

We have proved that there exists no Maxwell wavefield can be excited by sources inside the single layer cloaked concealment with normal materials [1]. For covering this difficulty, we proposed a GL double layer cloak [2]. Its outer layer has invisibility from the exterior light and EM wave field, never disturb the exterior field, and cloak the Local inner layer and concealment from the Global exterior wavefield. Its inner layer cloak absorbs the internal wave field, such that the internal wave field, which is excited from the sources inside the concealment, can not propagate outside of the inner layer. Our GL double layer cloak is proposed by the GL EM modeling and inversion [3]. The GL double layer cloak overcomes the following difficulties of the single layer PS cloak by Pendry [4]. (1) The PS cloak damaged the EM environment of its concealment, such that there exists no EM wavefield can be excited inside the concealment of the PS cloak, the concealment of the PS cloak is blind. Our GL double layer cloak recovered the normal EM environment in its concealment, such that the EM wave field can be excited inside the concealment of the GL double layer cloak. (2) The two sources reciprocal law is very important principle in the electromagnetic theory and application. The reciprocal law is satisfied in our GL double cloak media. However, the reciprocal law is damaged by the PS cloak. The PS cloak is strong dispersive cloak material, in which the $\varepsilon_r\varepsilon_\theta = R_3^2(r-R_2)^2/r^2/(R_3-R_2)^2$, when $r \to R_2 \varepsilon_r\varepsilon_\theta \approx (r-R_2)^2 \to 0$. such that the EM

wave velocity exceed the light speed in some part of the PS cloak that is violated to the physical principle. The PS cloak has invisibility only in very narrow frequency band. In the GL outer layer cloak [2, 5, 6], the weak dispersion is obtained, when $r \to R_2\varepsilon_r\varepsilon_\theta \approx (r-R_2)^{1.5} \to 0$. In this paper, we obtain very significant progress to overcome the difficulty. very pefect weak dispersive and degenerative rate, $\varepsilon_r\varepsilon_\theta \approx 1/\log(r-R_2) \to 0$, is obtained. Chen et al. proposed an analytical method for analysis of the PS cloak [7].

Finding and exploration is inverse problem; Hiding and cloaking is other inverse problem. They have close relationship. Based on the 3D GL EM modeling simulations [3] and GL Metre Carlo inversion [5], We propose a novel GL double layer cloak in the broad frequency band.

The President Professor Yuesheng Li in Sun Yat-Sen University very concerns and encourages our research works on the GL EM modeling method and the GL double cloak. Our paper is for celebrating his great scientific computational carrier in 60 years and his 80 birthday.

The description order of this paper is as follows. We have introduced single layer cloak and our GL double layer cloak and main content and research cue path in Section 1. In Section 2, we propose a novel GL double layer cloak in the broad frequency band. The EM wave propagation simulations in our wide frequency band GL double layer cloak are presented in Section 3. The important reciprocal law in the cloak media is presented in Section 4. In Section 5, we will conclude our paper.

2. THE GL DOUBLE LAYER CLOAK MATERIALS IN BROAD FREQUENCY BAND

For overcoming the weakness of the single layer cloak, we proposed the GL double layer cloak in broad frequency band, in short it is called GLWF, which consists of the inner layer cloak and outer layer cloak.

2.1. GLWF Inner Layer Cloak Anisotropic Material

On the inner sphere annular layer domain, $\Omega_{\mathrm{GLI}} = \{r : R_1 \le r \le R_2\}$, by the GL EM modeling and inversion [3, 5], we propose an anisotropic metamaterial as follows,

$$\begin{aligned}
[D]_{\mathrm{GLI}} &= \mathrm{diag}\left[\bar{\varepsilon}_i, \bar{\mu}_i\right], \\
\bar{\varepsilon}_i &= \mathrm{diag}\left[\varepsilon_{r,i}, \varepsilon_{\theta,i}, \varepsilon_{\phi,i}\right]\varepsilon_b, \\
\bar{\mu}_i &= \mathrm{diag}\left[\mu_{r,i}, \mu_{\theta,i}, \mu_{\phi,i}\right]\mu_b, \\
\varepsilon_{r,i} &= \mu_{r,i} = \left(\frac{R_2^2 - R_1^2}{R_2^2}\right)\sqrt{\frac{R_2^2 - r^2}{R_2^2 - R_1^2}}, \\
\varepsilon_{\theta,i} &= \varepsilon_{\phi,i} = \mu_{\theta,i} = \mu_{\phi,i} = \sqrt{\frac{R_2^2 - R_1^2}{R_2^2 - r^2}}\frac{R_2^2}{R_2^2 - r^2}.
\end{aligned} \tag{1}$$

The Ω_{GLI} is called as GL inner layer cloak, the materials, $[D]_{\mathrm{GLI}} = \mathrm{diag}[\bar{\varepsilon}_i, \bar{\mu}_i]$ in (1), are the anisotropic GL inner layer cloak metamaterials. Where the subscript GLI means the GL inner layer, the symbol diag denotes the diagonal matrix, $[D]_{\mathrm{GLI}}$ is 6×6 diagonal matrix, $\bar{\varepsilon}_i$ is 3×3 dielectric diagonal matrix in the inner layer, the subscript i denotes the inner layer, $\bar{\mu}_i$ is 3×3 magnetic permeability diagonal matrix in the inner layer, $\varepsilon_{r,i}$ is the relative dielectric cloak metamaterial which is formulated by the fourth sub equation in (1), the subscript index r, i denotes the dielectric is in r direction and in the inner layer, $\varepsilon_{\theta,i}$ is the relative dielectric cloak metamaterial in θ direction and in the inner layer which is formulated by the fifth sub equation in (1), The $\mu_{r,i}$ is the relative permeability cloak metamaterial which is formulated by the fourth sub equation in (1), ε_b is the basic dielectric in free space, $\varepsilon_b = 0.88541878176\ldots \times 10^{-11}$ F/m, μ_b is the basic magnetic permeability in free space, $\mu_b = 1.25663706 \times 10^{-6}$ m kg s^{-2}A^{-2}, other symbols in (1) have similar explanation.

The EM wavefield of sources located inside inner layer or the cloaked concealment is completely absorbed by the inner layer and never reaches the outside boundary of the inner layer, also, the EM wavefield excited in concealment is not disrupted by the cloak. The inner layer metamaterial, in Equation (1), cloaks outer space from the local field excited in the inner layer and concealment, which can also be useful for making a complete absorption boundary condition to truncate infinite domain in numerical simulation.

2.2. GLWF Outer Layer Cloak Anisotropic Material

We proposal a new novel GLWF outer layer cloak in this section. Let the outer sphere annular layer domain $\Omega_{\mathrm{GLO}} = \{r : \ R_2 \le r \le R_3\}$ be the GL outer layer cloak with the following anisotropic

GLWF outer layer cloak metamaterials,

$$\begin{aligned}
[D]_{\mathrm{GLWFO}} &= \mathrm{diag}\left[\bar{\varepsilon}_{\mathrm{glwfo}}, \bar{\mu}_{\mathrm{glwfo}}\right], \\
\bar{\varepsilon}_{\mathrm{glwfo}} &= \mathrm{diag}\left[\varepsilon_{r,\mathrm{glwfo}}, \varepsilon_{\theta,\mathrm{glwfo}}, \varepsilon_{\phi,\mathrm{glwfo}}\right]\varepsilon_b, \\
\bar{\mu}_{\mathrm{glwfo}} &= \mathrm{diag}\left[\mu_{r,\mathrm{glwfo}}, \mu_{\theta,\mathrm{glwfo}}, \mu_{\phi,\mathrm{glwfo}}\right]\mu_b, \\
\varepsilon_{r,\mathrm{glwfo}} &= \mu_{r,\mathrm{glwfo}} = 2\left(r - R_2\right)\sqrt{\log\left(e^{1/R_3^2} r\sqrt{\left(R_3^2 - R_2^2\right)/\left(r^2 - R_2^2\right)}/R_3\right)}/R_2/r \\
\varepsilon_{\theta,\mathrm{glwfo}} &= \mu_{\theta,\mathrm{glwfo}} = \varepsilon_{\phi,\mathrm{glwfo}} = \mu_{\phi,\mathrm{glwfo}} \approx 1/(r-R_2)/\log^{1.5}\left(e^{1/R_3^2} r\sqrt{\left(R_3^2-R_2^2\right)/\left(r^2-R_2^2\right)}/R_3\right)/r
\end{aligned} \tag{2}$$

The GL outer layer clok [2] is presented as follows

$$\begin{aligned}
[D]_{\mathrm{GLO}} &= \mathrm{diag}\left[\bar{\varepsilon}_{\mathrm{glo}}, \bar{\mu}_{\mathrm{glo}}\right], \\
\bar{\varepsilon}_{\mathrm{glo}} &= \mathrm{diag}\left[\varepsilon_{r,\mathrm{glo}}, \varepsilon_{\theta,\mathrm{glo}}, \varepsilon_{\phi,\mathrm{glo}}\right]\varepsilon_b, \\
\bar{\mu}_{\mathrm{glo}} &= \mathrm{diag}\left[\mu_{r,\mathrm{glo}}, \mu_{\theta,\mathrm{glo}}, \mu_{\phi,\mathrm{glo}}\right]\mu_b, \\
\varepsilon_{r,\mathrm{glo}} &= \mu_{r,\mathrm{glo}} = \frac{R_3}{r}\frac{r^2 - R_2^2}{r^2}\frac{\sqrt{r^2 - R_2^2}}{\sqrt{R_3^2 - R_2^2}}, \\
\varepsilon_{\theta,\mathrm{glo}} &= \mu_{\theta,\mathrm{glo}} = \varepsilon_{\phi,\mathrm{glo}} = \mu_{\phi,\mathrm{glo}} = \frac{R_3}{\sqrt{R_3^2 - R_2^2}}\frac{r}{\sqrt{r^2 - R_2^2}}.
\end{aligned} \tag{3}$$

We chose the PS cloak [4] as outer layer cloak

$$\begin{aligned}
[D]_{\mathrm{PSO}} &= \mathrm{diag}\left[\bar{\varepsilon}_{\mathrm{pso}}, \bar{\mu}_{\mathrm{pso}}\right], \\
\bar{\varepsilon}_{\mathrm{pso}} &= \mathrm{diag}\left[\varepsilon_{r,\mathrm{pso}}, \varepsilon_{\theta,\mathrm{pso}}, \varepsilon_{\phi,\mathrm{pso}}\right]\varepsilon_b, \\
\bar{\mu}_{\mathrm{pso}} &= \mathrm{diag}\left[\mu_{r,\mathrm{pso}}, \mu_{\theta,\mathrm{pso}}, \mu_{\phi,\mathrm{pso}}\right]\mu_b, \\
\varepsilon_{r,\mathrm{pso}} &= \mu_{r,\mathrm{pso}} = R_3(r - R_2)^2/r^2/(R_3 - R_2) \\
\varepsilon_{\theta,\mathrm{pso}} &= \mu_{\theta,\mathrm{pso}} = \varepsilon_{\phi,\mathrm{pso}} = \mu_{\phi,\mathrm{pso}} = R_3/(R_3 - R_2)
\end{aligned} \tag{4}$$

where the subscript GLWFO means the GLWF outer layer, $[D]_{\mathrm{GLWFO}}$ is 6×6 diagonal matrix, $\bar{\varepsilon}_{\mathrm{glwfo}}$ is 3×3 dielectric diagonal matrix in the outer layer, the subscript o denotes the outer layer, $\bar{\mu}_{\mathrm{glwfo}}$ is 3×3 magnetic permeability diagonal matrix in the outer layer, $\varepsilon_{r,\mathrm{glwfo}}$ is the relative dielectric cloak metamaterial which is formulated by the fourth sub equation in (2), the subscript index r, glwfo denotes the dielectric is in r direction and in the outer layer, $\varepsilon_{\phi,\mathrm{glwfo}}$ is the relative dielectric cloak metamaterial in ϕ direction and in the outer layer which is formulated by the fifth sub equation in (2), The $\mu_{r,\mathrm{glwfo}}$ is the relative permeability cloak in outer layer and in r direction which is formulated by the fourth sub equation in (2), Similar explanation for GL outer layer cloak GLO and PS cloak as outer layer PSO, The outer layer cloak provides invisibility, does not disturb exterior EM wave field, and cloaks the local concealment from the global exterior EM wavefield.

2.3. GLWF Double Layer Cloak

The GL inner cloak Ω_{GLI} domain and GL outer cloak Ω_{GLWFO} domain are bordering on the sphere annular surface $r = R_2$. We assemble the Ω_{GLI} as the inner sphere annular domain and Ω_{GLWFO} as the outer sphere annular domain and make them coupling on their interface boundary annular surface $r = R_2$ as follows,

$$\begin{aligned}
\Omega_{\mathrm{GLWF}} &= \Omega_{\mathrm{GLI}} \bigcup \Omega_{\mathrm{GLWFO}} \\
&= \{r : R_1 \le r \le R_2\} \bigcup \{r : R_2 \le r \le R_3\} \\
&= \{r : R_1 \le r \le R_3\},
\end{aligned} \tag{5}$$

and situate the double layer anisotropic dielectric and magnetic permeability susceptibility tensors $[D]_{\mathrm{GLWF}}$ on the Ω_{GLWF} as follows,

$$[D]_{\mathrm{GLWF}} = \begin{cases} [D]_{\mathrm{GLI}}, & r \in \Omega_{\mathrm{GLI}} \\ [D]_{\mathrm{GLWFO}}, & r \in \Omega_{\mathrm{GLWFO}}. \end{cases} \tag{6}$$

The GL cloak material $[D]_{\mathrm{GLI}} = \mathrm{diag}[\bar{\varepsilon}_i, \bar{\mu}_i]$ in (1) on the inner layer domain Ω_{GLI} and GL outer layer cloak material $[D]_{\mathrm{GLWFO}} = \mathrm{diag}[\bar{\varepsilon}_{\mathrm{glwfo}}, \bar{\mu}_{\mathrm{glwfo}}]$ in (2) on outer layer domain Ω_{GLWFO} are assembled into the GL anisotropic doubled layer cloak material on the domain Ω_{GLWF}. The domain Ω_{GLWF} with the metamaterial $[D]_{\mathrm{GLWF}}$ in (6) is called as the GL double layer cloak in broad frequency band, say GLWF double cloak. Similar explanations are for GL double layer cloak coupled by GLI in (1) and GLO in (3), and GLI-PSO double layer cloak coupled by GLI in (1) and PSO in (4).

The GL cloak means that the outer layer has invisibility, never disturb exterior wavefield and cloaks the Local concealment from the exterior Global field, while the inner layer cloaks outer Global space from interior wavefield excited in the Local concealment. The properties of the double layer material are studied by GL method simulations and analysis in next sections.

3. THE GL EM MODELING SIMULATIONS AND COMPARISON OF THE EM WAVE FIELD THROUGH THE GLWF DOUBLE, GL DOUBLE, AND OUTER LAYER PS CLOAKS

3.1. The Simulation Model of the GLIWFO, GLIO, GLI-PSO Double Layer Cloak

The simulation model: the 3D domain is $[-0.5\,\mathrm{m}, 0.5\,\mathrm{m}] \times [-0.5\,\mathrm{m}, 0.5\,\mathrm{m}] \times [-0.5\,\mathrm{m}, 0.5\,\mathrm{m}]$, the mesh number is $201 \times 201 \times 201$, the mesh size is 0.005 m. The electric current point source is defined as

$$\delta(r - r_s)\delta(t)\vec{e}, \tag{7}$$

where the r_s denotes the location of the point source, the unit vector $\vec{e}$ is the polarization direction, the time step $dt = 0.3333 \times 10^{-10}$ second, the frequency band is from 0.05 GHz to 15 GHz, the largest frequency $f = 15\,\mathrm{GHz}$, the shortest wave length is 0.02 m. The inner layer Ω_{GLI} is denoted by (1). The EM GL double layer cloak $\Omega_{\mathrm{GLWF}} = \Omega_{\mathrm{GLI}} \bigcup \Omega_{\mathrm{GLWFO}}$ in (2), $\Omega_{\mathrm{GLIO}} = \Omega_{\mathrm{GLI}} \bigcup \Omega_{\mathrm{GLO}}$ in (3), and $\Omega_{\text{GLI-PSO}} = \Omega_{\mathrm{GLI}} \bigcup \Omega_{\mathrm{PSO}}$ in (4) are consist of the double spherical annular with the center in the origin and interir radius $R_1 = 0.21\,\mathrm{m}$, meddle radius $R_2 = 0.31\,\mathrm{m}$. and exterior radius $R_3 = 0.45\,\mathrm{m}$. The cloak is divided into $90 \times 180 \times 90$ cells. The spherical coordinate is used in the sphere $r \le R_3$, the Cartesian rectangular coordinate is used in outside Ω_{GL} to mesh the domain.

3.2. Point Source S_1 in the Concealment and Other Point Source S_2 in the Free Space

The two point sources S_1 and S_2 are used to excite the EM wave propagation through the GLWF, GLO, and GLI-PSO double layer cloaks. The first point current source S_1 is located inside of the center sphere concealment at $(-0.18\,\mathrm{m}, 0.0, 0.0)$, the excited EM wave excited by S_1 is named as *First electric wave*, $E_{xx,1}$. The second current point source S_2 is located in free space at

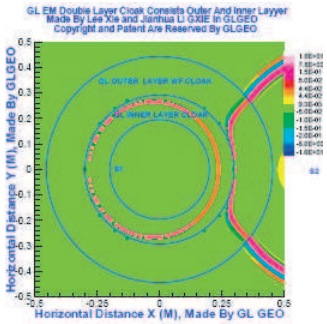

Figure 1: (color online) At time step $48dt$, front of *Second EM wave*, $E_{xx,2}$ inside of the outer layer of GLWF cloak $R_2 \le r \le R_3$ propagates no faster than light speed, it is faster than the wave speed in Figure 2 and in Figure 3. The wave front of the *First electric wave*, $E_{xx,1}$, propagates inside the inner layer, $R_1 \le r \le R_2$.

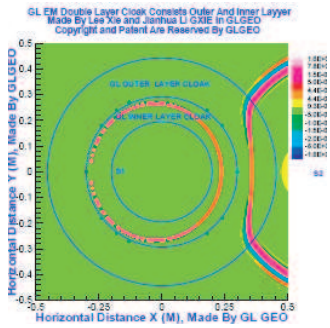

Figure 2: (color online) At time step $48dt$, front of *Second EM wave*, $E_{xx,2}$ inside of the outer layer of GL outer layer cloak $R_2 \le r \le R_3$ propagates no faster than light speed. It is slower than $E_{xx,2}$ in Figure 1 and faster than $E_{xx,2}$ in Figure 3 The wave front of the $E_{xx,1}$, propagates inside the inner layer, $R_1 \le r \le R_2$.

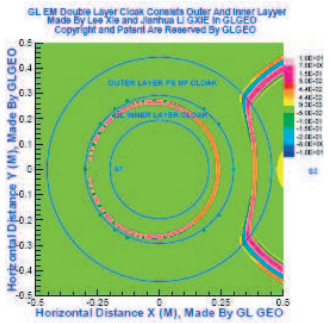

Figure 3: (color online) At time step $48dt$, front of *Second EM wave*, $E_{xx,2}$ inside of the outer layer of PS outer layer cloak $R_2 \le r \le R_3$ propagates no faster than light speed. It is slower than $E_{xx,2}$ in Figure 1 and Figure 2. The wave front of the $E_{xx,1}$, propagates inside the inner layer, $R_1 \le r \le R_2$.

(0.73 m, 0.0, 0.0) where is located the right side outside of the whole GL double layer cloaks. The EM wave excited by the S_2 is named as *Second electric wave*, $E_{xx,2}$.

3.3. Comparison Between EM Wave Propagation through the GLWF, GLO, and GLI-PSO Double Layer Cloaks

The GL modeling simulations of the EM wave excited by above two point sources S_1 and S_2 propagation through the GLWF, GLO, and GLI-PSO double layer cloaks are presented in the Figures 1–3 at 48th time step, in Figures 4–6 at 74th time step. in Figures 7–9 at 128th time step, respectively. For comparison, we arrange Figures 1–3, Figures 4–6, and Figures 7–9 as four figure group rows. At time step $48dt$, front of electric wave $E_{xx,2}$ inside of the outer layer of GLWF, GLO outer layer cloak, and PS outer layer, $R_2 \le r \le R_3$ are presented in Figures 1–3 respectively. In Figure 1, $E_{xx,2}$ inside of the outer layer of GLWF, $R_2 \le r \le R_3$, propagates no faster than light speed, it is faster than the wave speed in Figure 2 and in Figure 3. In Figure 2 electric wave $E_{xx,2}$ inside of the outer layer of GL outer layer cloak $R_2 \le r \le R_3$ propagates no faster than light speed.

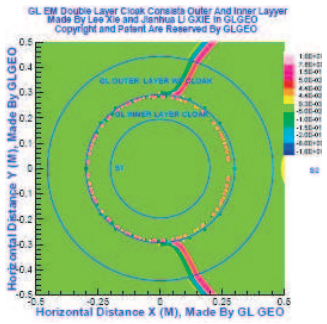

Figure 4: (color online) At time step $74dt$, front of $E_{xx,2}$ inside of GLWF outer layer cloak $R_2 \le r \le R_3$ propagates no faster than light speed, it is slower than the wave speed in Figure 5 and in Figure 6. The wave front of the *First electric wave*, $E_{xx,1}$, propagates inside the inner layer, $R_1 \le r \le R_2$.

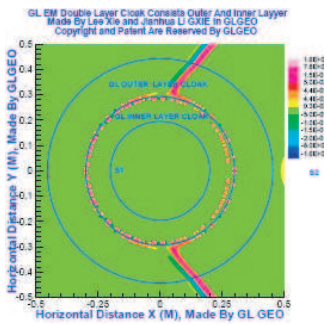

Figure 5: (color online) At time step $74dt$, front of $E_{xx,2}$ inside of GL outer layer cloak $R_2 \le r \le R_3$ propagates a little faster than light speed. It is faster than $E_{xx,2}$ in GLWF in Figure 4 and slower than $E_{xx,2}$ in PS in Figure 6. The wave front of the $E_{xx,1}$, propagates inside the inner layer, $R_1 \le r \le R_2$.

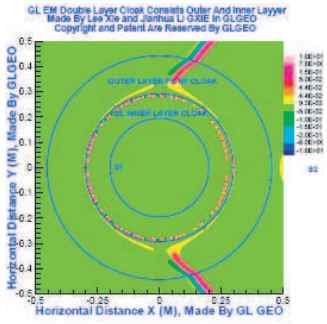

Figure 6: (color online)At time step $74dt$, front of $E_{xx,2}$ inside of PS outer layer cloak $R_2 \le r \le R_3$ propagates faster than light speed. It is faster than $E_{xx,2}$ in GLWF in Figure 4 and GLO in Figure 5. The wave front of the $E_{xx,1}$, propagates inside the inner layer, $R_1 \le r \le R_2$.

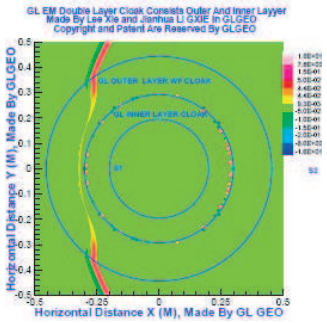

Figure 7: (color online) At time step $128dt$, front of $E_{xx,2}$ inside of GLWF outer layer cloak $R_2 \le r \le R_3$ propagates slower than light speed, it is slower than the wave speed in Figure 8 and in Figure 9. The wave front of the *First electric wave*, $E_{xx,1}$, propagates inside the inner layer, $R_1 \le r \le R_2$.

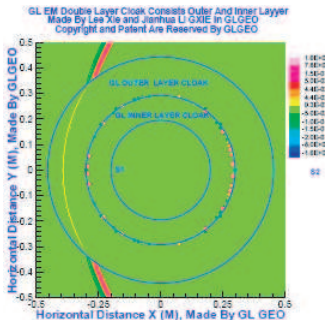

Figure 8: (color online) At time step $128dt$, front of $E_{xx,2}$ inside of GL outer layer cloak $R_2 \le r \le R_3$ propagates faster than light speed. It is faster than $E_{xx,2}$ in GLWF in Figure 7 and slower than $E_{xx,2}$ in PS in Figure 9. The wave front of the $E_{xx,1}$, propagates inside the inner layer, $R_1 \le r \le R_2$.

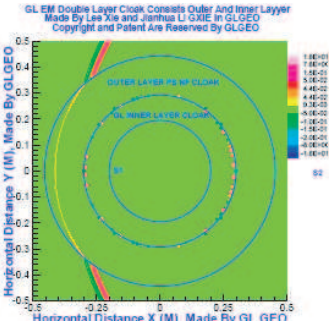

Figure 9: (color online) At time step $128dt$, front of $E_{xx,2}$ inside of PS outer layer cloak $R_2 \le r \le R_3$ propagates more faster than light speed. It is faster than $E_{xx,2}$ in GLWF in Figure 7 and GLO in Figure 8. The wave front of the $E_{xx,1}$, propagates inside the inner layer, $R_1 \le r \le R_2$.

It is slower than $E_{xx,2}$ in Figure 1 and faster than $E_{xx,2}$ in Figure 3. In Figure 3, front of $E_{xx,2}$ inside of the outer layer of PS outer layer cloak, $R_2 \leq r \leq R_3$, propagates no faster than light speed. It is slower than $E_{xx,2}$ in Figure 1 and Figure 2. The wave front of the $E_{xx,1}$, propagates inside the inner layer, $R_1 \leq r \leq R_2$. At time step $74dt$, front of electric wave $E_{xx,2}$ inside of the outer layer of GLWF, GLO outer layer cloak, and PS outer layer, $R_2 \leq r \leq R_3$ are presented in Figures 4–6 respectively. In Figure 4, front of $E_{xx,2}$ inside of GLWF outer layer cloak $R_2 \leq r \leq R_3$ propagates no faster than light speed, it is slower than the wave speed in Figure 5 and in Figure 6. In Figure 5, front of $E_{xx,2}$ inside of GL outer layer cloak $R_2 \leq r \leq R_3$ propagates little faster than light speed. It is faster than $E_{xx,2}$ in GLWF in Figure 4 and slower than $E_{xx,2}$ in PS in Figure 6. In Figure 6, front of $E_{xx,2}$ inside of PS outer layer cloak $R_2 \leq r \leq R_3$ propagates faster than light speed. It is faster than $E_{xx,2}$ in GLWF in Figure 4 and GLO in Figure 5. At time step $128dt$, front of electric wave $E_{xx,2}$ inside of the outer layer of GLWF, GLO outer layer cloak, and PS outer layer, $R_2 \leq r \leq R_3$ are presented in Figures 7–9 respectively. In Figure 7, front of $E_{xx,2}$ inside of GLWF outer layer cloak $R_2 \leq r \leq R_3$ propagates slower than light speed, it is slower than the wave speed in Figure 8 and in Figure 9. In Figure 8, front of $E_{xx,2}$ inside of GL outer layer cloak $R_2 \leq r \leq R_3$ propagates little faster than light speed. It is faster than $E_{xx,2}$ in GLWF in Figure 7 and slower than $E_{xx,2}$ in PS in Figure 9. In Figure 9, front of $E_{xx,2}$ inside of PS outer layer cloak $R_2 \leq r \leq R_3$ propagates more faster than light speed. It is faster than $E_{xx,2}$ in GLWF in Figure 7 and GLO in Figure 8. The wave front of the $E_{xx,1}$, propagates inside the inner layer, $R_1 \leq r \leq R_2$.

4. THEORY OF RECIPROCAL LAW OF THE EM WAVE FIELD THROUGH THE CLOAKS

4.1. Theory of the EM Wave Field through the GL Double Layer Cloaks

We propose the theoretical analysis of the interaction between the EM wave and GL cloaks in this section.

Statement 1: Let domain Ω_{GL} in (3) and the metamaterial D_{GL} in (4) be GL double layer cloak, and $\varepsilon = \varepsilon_b$, $\mu = \mu_b$ be basic permittivity and permeability, respectively, inside of the central sphere concealment $|\vec{r'}| < R_1$ and outside of the GL cloak $|\vec{r'}| > R_3$, we have the following statements: (1) Provide the local source is located inside of the concealment of GL double layer cloak, $|\vec{r}_s| < R_1$, the excited EM wave field inside of the concealment never be disturbed by the cloak; (2) Provide the local source is located inside of concealment or inside of the inner layer of the GL double layer cloak, $|\vec{r}_s| < R_2$, the EM wave field is vanished outside of the inner layer of GL cloak and is always propagating and going to the boundary $r = R_2$ and before $r = R_2$. (3) Provide the source is located outside of the GL double layer cloak, $|\vec{r}_s| > R_3$, the excited EM wave field propagation outside of the double layer cloak as same as in free space and never be disturbed by the double layer cloak; (4) Provide the local source is located outside of double layer cloak or located inside of the outer layer of GL cloak, $|\vec{r}_s| > R_2$, the excited EM wave field never propagate into the inner layer of GL cloak and the concealment.

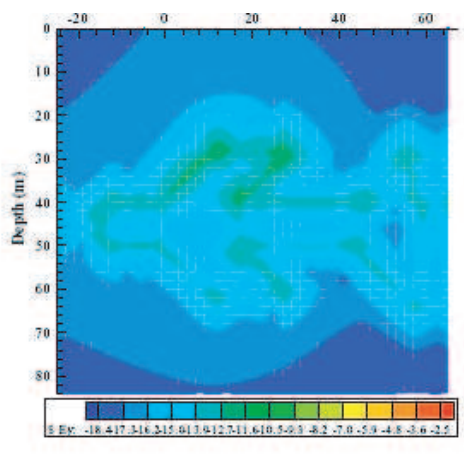

Figure 10: (color online) A double cloth anti detection is around the fly model, The Figure 5 is from the Figure 11 in paper [8] in 2001.

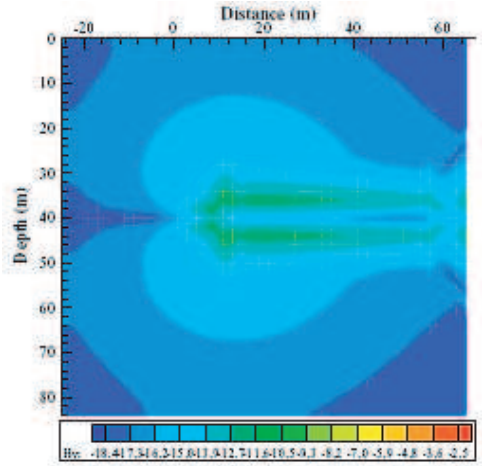

Figure 11: (color online) A double cloth anti detection is around the bar model. The Figure 6 is from the Figure 2 in paper [8] in 2001.

4.2. Theory of Reciprocal Law of the EM Wave Field through the Cloaks

Statement 2: (1) In the domain consist of free space, single layer cloak and its cloaked concealment with normal material, the two sources reciprocal law is damaged. (2) In the domain consist of free space, single layer cloak and its cloaked concealment with some special double negative refractive index metamaterial, the two sources reciprocal law is recovered, but the cloak invisibility function is lose. (3) In the domain consist of free space, GL double layer cloak and its cloaked concealment with normal material, the two sources reciprocal law is satisfied, and the cloak invisibility function is complete and sufficient in wide frequency band.

4.3. There Exists No Maxwell EM Wavefield Can Be Excited by Nonzero Local Sources inside of the Single Layer Cloaked Concealment with Normal Materials

Statement 3: Suppose that a 3D anisotropic inhomogeneous single layer cloak domain separates the whole 3D space into three sub domains, one is the single layer cloak domain Ω_{clk} with the cloak material; the second one is the cloaked concealment domain Ω_{conl} with normal EM materials; other one is the free space outside of the cloak. If the Maxwell EM wavefield excited by a point source or local sources outside of the concealment Ω_{conl} is vanished inside of the concealment Ω_{conl}, then there exists no Maxwell EM wave field can be excited by the local sources inside the cloaked concealment Ω_{conl} with normal materials.

The statement 2 is proved by the GL method in author's paper [12].

5. HISTORY AND DISCUSSIONS

5.1. History

A double layer cloth phenomenon to prevent the GILD inversion [6, 8] detection has been observed in paper [9] in 2001 which is published in SEG online *http://segdl.org/journals/doc/SEGLIB-home/dci/searchDCI.jsp.* The double layer cloth to cloak fly from the exterior wave GILD detection is obvious around the fly which is shown in Figure 10; the double cloth around the bar is shown in Figure 11. We developed a novel and effective Global and Local field (GL) modeling and inversion [2, 3, 5] to study the meta materials, periodic photonic crystals and condense physics etc. wide physical sciences. 3D GL EM modeling and inversion [3, 5] and computational mirage have been presented in PIERS 2005 and published in proceeding of PIERS 2005 in Hangzhou, which can be downloaded from *http://piers.mit.edu/piersproceedings/piers2k5Proc.php*, please see the references of [2]. We developed 3D FEM for the elastic mechanics first in China in 1972 [10] and discovered the superconvergence of the 3D cubic curve isoparameter element first in the world [11]. The 3D isoparameter element can be used for making arbitrary curve cloak [10]. We deeply to know the merits and drawbacks of FEM. The GL method overcomes the drawbacks of FEM and FD methods. The history of development of FEM and GILD and GL method has been described in [11] and reference of [2]. The 3D and 2D GL parallel software is made and patented by GLGEO. The GL modeling and its inversion [3, 5] and GL EM quantum field modeling are suitable to solve quantization scattering problem of the electromagnetic field in the dispersive and loss metamaterials, cloaks and more wide anisotropic materials.

5.2. Advantages of the GL Method

The GL EM modeling is fully different from FEM and FD and Born approximation methods and overcome their difficulties. There is no big matrix equation to solve in GL method. Moreover, it does not need artificial boundary and absorption condition to truncate the infinite domain. Born Approximation is a conventional method in the quantum mechanics and solid physics However, it is one iteration only in whole domain which is not accurate for high frequency and for high contrast materials. The GL method divides the domain as a set of small sub domains or sub lattices. The Global field is updated by the local field from the interaction between the global field and local subdomain materials successively. Once all subdomain materials are scattered, the GL field solution is obtained which is much more accurate than the Born approximation. GL method is suitable for all frequency and high contrast materials. When the size of the sub domain is going to zero, the GL method is convergent and has $O(h^2)$ if the trapezoidal integral formula is used, moreover, is has super convergence $O(h^4)$ if the Gaussian integral formula is used [10]. Chen et al. proposed an analytical method for analysis of the PS cloak [7]. The GL method has double capabilities of the theoretical analysis and numerical simulations that has been shown in this paper.

6. CONCLUSION

The simulations of the EM wave propagation through the GLWF. GLO, and GLI-PSO double layer cloaks and comparison between them show that the GLWF and GLO double layer cloak overcomes the following difficulties of the single layer PS cloak. (1) The PS cloak damaged the EM environment of its concealment, such that there exists no EM wavefield can be excited inside the concealment of the PS cloak, the concealment of the PS cloak is blind. Our GL double layer cloak recovered the normal EM environment in its concealment, such that the EM wave field can be excited inside the concealment of the GL double layer cloak. (2) The PS cloak is very strong dispersive and strong degenerative cloak material. The PS cloak has invisibility only in very narrow frequency band. There is exceeding light speed physical violation in PS cloak. Our GLWF double layer cloak corrects the violation. (3) The two sources reciprocal law is very important principle in the electromagnetic theory and application. The reciprocal law is satisfied in our GLWF and GLO double cloak media. However, the PS cloak damaged the reciprocal law. The following physical statements are described: (1) In the domain consist of free space, single layer PS cloak and its cloaked concealment with normal material, the two sources reciprocal law is damaged. (2) In the domain consist of free space, single layer cloak and its cloaked concealment with some special double negative refractive index metamaterial, the two sources reciprocal law is recovered, but the cloak invisibility function is lose. (3) In the domain consist of free space, GLWF and GLO double layer cloak and its cloaked concealment with any material, the two sources reciprocal law is satisfied, and the cloak invisibility function is complete, sufficient, moreover the GLWF has all advantages of the GL double layer cloak in broad frequency band. The GLWF and GLO double layer cloak materials and the 3D and 2D GL parallel algorithms and software are made by authors in GL Geophysical Laboratory and are patented by GLGEO and all rights are reserved in GLGEO.

ACKNOWLEDGMENT

We wish to acknowledge the support of the GL Geophysical Laboratory and thank the GLGEO Laboratory to approve the paper publication. Authors thank to Professor P. D. Lax for his concern and encouragements Authors thank to Dr. Michael Oristaglio for his encouragements.

REFERENCES

1. Li, J. H., G. Xie, L. Xie, and F. Xie, "No Maxwell electromagnetic wavefield excited inside cloaked concealment and broadband GL cloaks," *PIERS Proceedings*, 66–72, Moscow, Russia, August 18–21, 2009.
2. Xie, G., J. Li, F. Xie, and L. Xie, "Global and local field EM modeling and novel GL double layered electromagnetic cloaks," *PIERS Proceedings*, 335–343, Moscow, Russia, August 18–21, 2009.
3. Xie, G., F. Xie, L. Xie, and J. Li, "New GL method and its advantages for resolving historical diffculties," *Progress In Electromagnetics Research*, PIER 63, 141–152, 2006.
4. Pendry, J. B., D. Schurig, and D. R. Smith, "Controlling electromagnetic field," *Science Express*, Vol. 312, 1780, 2006.
5. Xie, G., J. Li, L. Xie, and F. Xie, "A GL metro carlo EM inversion," *Journal of Electromagnetic Waves and Applications*, Vol. 20, No. 14, 1991–2000, 2006.
6. Xie, G. and J. Li, "New parallel SGILD modeling and inversion," *Physics D*, Vol. 133, 477–487, 1999.
7. Chen, H., B. Wu, B. Zhang, and J. A. Kong, "Electromagnetic wave interactions with a metamaterial cloak," *Physical Review Letters*, Vol. 99, 063903, 2007.
8. Xie, G., "A new iterative method for solving the coefficient inverse problem of wave equation," *Comm. on Pure and Applied Math.*, Vol. 39, 307–322, 1986.
9. Li, J., G. Xie, C. Lin, and J. Liu, "2.5 dimensional GILD electromagnetic modeling and application," *SEG, Expanded Abstracts*, Vol. 21, No. 1, 692–695, 2002, http://www.segdl.org/journals/doc/SEGLIBhome/dci/searchDCI.jsp.
10. Xie, G., "The 3-D finite element method in the elastic structure," *Mathematical Practice and Knowledge,* Vol. 1, 28–41, 1975 (Chinese).
11. Brandts, J. and M. Krizek, "History and futures of superconvergence in three dimensional finite element method," *Mathematical Sciences and Applications*, Vol. 15, 24–35, 2001.

High Transmission Y-shaped Waveguides in 2D Photonic Crystals with Square Lattice

Wu Yang[1, 2], **Xiaoshuang Chen**[1], **Xiaoyan Shi**[2], **and Wei Lu**[1]

[1]National Laboratory for Infrared Physics
Shanghai Institute of Technical Physics, Chinese Academy of Sciences
500 Yutian Road, Shanghai 200083, China
[2]College of Science, Henan University of Technology, Zhengzhou 450001, China
[3]College of Science, Information Engineering University of PLA, Zhengzhou 450001, China

Abstract— We design a Y-shaped photonic crystal waveguide of high transmission based on 2D photonic crystal of square lattice. We create an input waveguide by removing a single row of rods and an 135° output waveguide by removing two row of rods. We add additional rods in 135° output waveguide edge for increasing transmission coefficient. And based on the coupled mode theory, two additional rods are placed between the input waveguide and the 135° output waveguide to improve transmission coefficient. The numerical simulation results by the finite-difference time-domain method show that total transmission is obtained up to 99%.

1. INTRODUCTION

Photonic crystal waveguides, line defects formed in photonic crystal, are expected to provide low loss transmission and well-confined branches when being operated at wavelengths within the photonic band gap [1]. They can play an important role in future optical circuits. Waveguide branches split the input power into the output waveguides without significant reflection or radiation losses. Many efforts have been devoted to get highly efficient transmission for photonic crystal waveguides, such as T-shaped and Y-shaped photonic crystal waveguide [2–5]. However, a typical Y-junction structure has poor transmittance for non-zero reflection [2, 4]. A power-splitting based on directional coupling consisting of an array of air holes with a triangular lattice structure has been proposed by Park et al, in which the transmission coefficients is up to 47.6% for each output [5].

Ordinary, T-shaped photonic crystal waveguide is based on the square lattice and Y-shaped photonic crystal waveguide is based on the triangular lattice [2–5]. Heterostructure is also applied to improve transmission coefficients in photonic crystal waveguide [6]. In this paper, we design a Y-shaped photonic crystal waveguide of high transmission based on square lattice. We add additional rods in 135° output waveguide edge for increasing transmission coefficient. Based on the coupled mode theory, two additional rods are placed between the input waveguide and the 135° output waveguide to improve transmission coefficient. The numerical simulation results by the finite-difference time-domain method shows that total transmission up to 99% is obtained.

2. Y-SHAPED PHOTONIC CRYSTAL WAVEGUIDE OF SQUARE LATTICE

We create input and output waveguides by removing a single row of rods, and a 135° waveguide by removing two row of rods between input and output waveguide, see the inset of Fig. 1. The rods have a dielectric constant of 11.56 and a radius of $0.2a$. A broadband bandgap is formed with the guided single mode spanning from $0.32 < \omega a/2\pi c < 0.43$. The transmission of the structure is calculated by the FDTD method with perfectly-matched-layer boundary conditions [7, 8]. To calculate the transmission efficiency from the input waveguide into the output waveguides, a large structure, 120×20 lattice constants, with long input and output waveguides is simulated. A dipole located at the entrance of the input waveguide creates a pulse with a Gaussian envelope in time. The field amplitude is monitored inside the guide at two points, one before the Y-junctions and another after Y-junctions, respectively. Although most of the light reaching the edge of the computational cell is absorbed by the boundaries, some light is reflected back from the ends of the waveguide. By positioning each monitor point appropriately, we can distinguish and separate all the different pulses propagating in the cell [2]. Four pulses are sent down the waveguide, and each covers different ranges of frequencies. By the Fourier transforms, the transmission coefficient is obtained for each frequency of the pulses, as shown in Fig. 1. The transmission coefficient is lower than 40% for a wide range of frequency. The combined transmission and the reflection coefficients add up to unity within an accuracy of 0.1%. It indicates that our calculation gives an accurate description to the response function of the waveguide.

To improve the transmission coefficient, we add additional rods in 135° waveguide edge, as shown in the inset of Fig. 2. The additional rods can decrease the reflection in 135° waveguide. The transmission coefficient is obtained by the before-mentioned method, as shown in Fig. 2. The transmission coefficient is higher than 40% for a wide range of frequency compared with Fig. 1.

3. COUPLED MODE THEORY

The coupled mode theory is used to analyze the transmission properties [2, 3]. The Y-junction is treated as a cavity that couples to the input and output waveguides, as shown in Fig. 3. The resonance in the cavity determines the transmission properties of Y-junction, which can be calculated by using the coupled-mode theory [2].

$$\frac{da}{dt} = j\omega_0 a - a\left(\sum_i \frac{1}{\tau_i}\right) + \sum_i \left(S_{+i}\sqrt{\frac{2}{\tau_i}}\right) \tag{1}$$

$$S_{-i} = -S_{+i} + \sqrt{\frac{2}{\tau_i}}a \tag{2}$$

Here, S_{+i} and S_{-i} are the incoming and outgoing wave amplitudes of waveguides, a is the amplitude of the resonance, ω_0 is the resonant frequency, τ_i is the amplitude decay rate of the resonance into the ith port. When the electromagnetic wave is incident from port 1, the reflection and the transmission coefficients can be obtained basing on the equations of Ref. [2]. Zero reflection can be

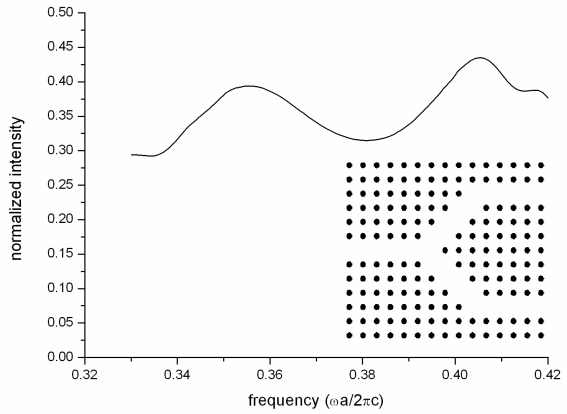

Figure 1: The transmission coefficient of Y-shaped photonic crystal waveguide of square lattice.

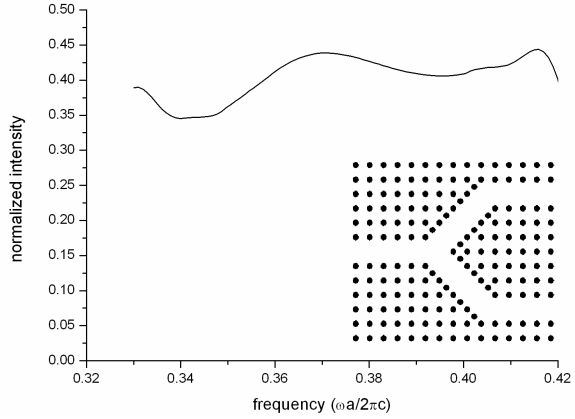

Figure 2: The transmission coefficient of additional rods in the edge of 135° waveguide.

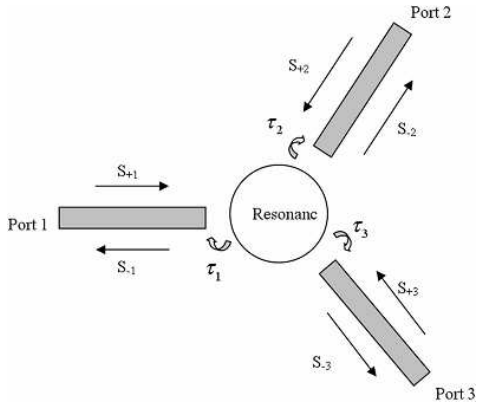

Figure 3: Scheme of the coupled mode model.

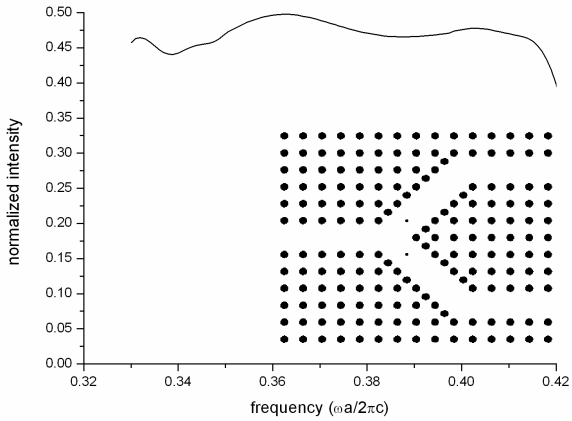

Figure 4: The transmission coefficient for the Y-shaped waveguide with two additional rods between the input waveguide and the 135° waveguide.

achieved at the resonant frequency ω_0, if following conditions:

$$\frac{1}{\tau_1} = \frac{1}{\tau_2} + \frac{1}{\tau_3} \tag{3}$$

is satisfied [2].

Based on the coupled mode theory, two additional rods are placed between the input waveguide and the 135° waveguide to improve transmission coefficient, as shown in the inset of Fig. 3. The radius of the placed additional rods is varied in order to obtain the optimization performance. In the case where the radius is 0.07 lattice constant, the transmission coefficient is optimum. As shown in Fig. 4. The transmission coefficient is higher than 46% for a wide range of frequency. And a peak transmission of 49.5% (99% for two outputs) is obtained about $0.36(2\pi c/a)$.

4. CONCLUSIONS

We design a Y-shaped photonic crystal waveguide based on square lattice. The high transmission is obtained in the optimized waveguide. Two schemes are used to improve the transmission coefficient, One is to add the additional rods in the edge of 135° output waveguide, another is to place two additional rods between the input waveguide and the 135° output waveguide based on the coupled mode theory. The transmission coefficient is higher than 46% for each output port for a wide range of frequency. The total transmission of 99% for two outputs is obtained about $0.36(2\pi c/a)$.

ACKNOWLEDGMENT

This work is partially supported by multiple grants from the State Key Program for Basic Research of China (2007CB613206, 2006CB921704), National Natural Science Foundation of China (10725418, 10734090, 10474108 and 60576068), Key Fund of Shanghai Science and Technology Foundation (08JC14 21100 and 09DJ1400203), and Knowledge Innovation Program of the Chinese Academy of Sciences.

REFERENCES

1. Joannopoulos, J. D., S. G. Johnson, J. N. Winn, and R. D. Meade, *Photonic Crystal: Molding the Flow of Light*, Princeton University Press, Princeton, 2008.
2. Fan, S., S. G. Johnson, J. D. Joannopoulos, C. Manolatou, and H. A. Haus, "Waveguide branches in photonic crystals," *J. Opt. Soc. Am. B*, Vol. 18, 162–165, 2001.
3. Monifi, F., M. Djavid, A. Ghaffari, and M. S. Abrishamian, "Design of efficient photonic crystal bend and power splitter using super defects," *J. Opt. Soc. Am. B*, Vol. 25, 1805–1810, 2008.
4. Boscolo, S., M. Midrio, and T. F. Krauss, "Y junctions in photonic crystal channel waveguides: Hightransmission and impedance matching," *Opt. Lett.*, Vol. 27, 1001–1003, 2002.
5. Park, I., H.-S. Lee, H.-J. Kim, K.-M. Moon, S.-G. Lee, B.-H. O, S.-G. Park, and E.-H. Lee, "Photonic crystal power-splitter based on directional coupling," *Opt. Express*, Vol. 12, 3599–3604, 2004.
6. Sharkawy, A., S.-Y. Shi, and D. W. Prather, "Heterostructure photonic crystal: Theory and applications," *Applied Optics*, Vol. 41, No. 34, 7245–7253, 2002.
7. Taflove, A., *Computational Electrodynamics: The Finite-Difference Time-Domain Method*, Artech House, Norwood, Mass., 1995.
8. Chen, J. C. and K. Li, "Quartic perfectly matched layers for dielectric waveguides and gratings," *Microwave Opt. Technol. Lett.*, Vol. 10, 319–323, 1995.

Surface Plasmon Resonance Electro-optic Light Modulator Based on Polymer Grating Coupler

Wen-Kai Kuo and Meng-Ting Chen
Department of Electro-Optics Engineering, National Formosa University
64 Wenhua Rd., Huwei, Yunlin 63208, Taiwan, R.O.C.

Abstract— In this study, an electro-optic light modulator based on grating-coupled surface plasmon resonance is numerically investigated using finite-difference time-domain (FDTD) simulation. A new grating coupler structure is proposed and compared with the conventional one. The numerical simulation results show that the new structure has higher modulation efficiency.

1. INTRODUCTION

A surface plasmon is an electromagnetic wave propagating along the surface of a metal and dielectric interface. Under phase-matching or resonance conditions, the energy of the incident light wave can be coupled to the collective oscillation of free electrons on the metal surface. This energy transfer phenomenon can be achieved with p-polarized light by using either a prism or a grating coupler [1]. The energy transferred for excitation of the surface plasmon resonance (SPR) is observed as a rapid decrease in reflectivity. Since the SPR is highly sensitive to changes in the refractive index on the metal surface, this technique has been extensively applied to bio-chemical sensing [2]; moreover, it has also played an important role in optical modulators. Further, the SPR technique can be combined with an electro-optic (EO) polymer in order to implement a simple and high-speed optical modulator. The principle of the modulator is based on electrically varying the refractive index of the EO polymer and hence controlling the efficiency of coupling the incident TM light beam onto the surface plasmons. This type of device has been theoretically described first [3] and experimentally demonstrated later with different advancements [4–6]. Recently, a new type of a modulator that uses a resonant metal grating to greatly improve the modulation index has been proposed and numerically studied [7]. For the above modulators, prism coupling or the Kretschmann (KR) configuration is used for exciting SPR. However, this configuration requires a prism with high refractive index and therefore results in a noncompact and high-cost modulator.

2. GRATING-COUPLED SPR MODULATOR STRUCTURE

A conventional grating coupler adapted for EO polymer modulation purpose is shown in Fig. 1. In this structure, a polymer layer with a thickness of 300 nm covers a gold grating with a modulation height of 70 nm and a pitch of 710 nm. For the grating-coupled SPR calculation, a rigorous coupled-wave analysis (RCWA) [8], a frequency-domain method, or finite-difference time-domain (FDTD) algorithm [9] are usually used. Here, a commercialized 3D electromagnetic solver based on the FDTD method is used. This simulation tool is specially designed for scattering problems of periodic structures illuminated by arbitrary incident fields. By this simulation tool, for the structure shown in Fig. 1, the reflectivity curves are calculated as a function of the angle of incidence for incident laser light with a wavelength of 632.8 nm and polymer refractive indexes of 1.489 and 1.490. The results, shown in Fig. 2, reveal that the full width at half maximum (FWHM) of the reflectivity curve exceeds 3°, and a nonsignificant resonance angle shift is observed on increasing the refractive index of the polymer layer by 0.001. Hence, this structure can achieve only a very low modulation depth. A similar structure using a nanopolymer dispersed liquid crystal (LC) electro-optic material with high EO coefficients has been proposed [10]. They demonstrated SPR displacement by electrically varying the refractive index of the LC material deposited on the metal grating surface. Though the LC material has a large EO coefficient, its slow response time prevents it from being applied to a high-speed optical modulator. In contrast to this structure, our proposed grating coupler structure is shown in Fig. 3. Instead of a metal grating, a dielectric grating formed on a flat metal film is utilized. A similar structure has been previously described [11], and a novel implementation of such a structure has been demonstrated [12]. In [11], a grating structure is directly formed on a flat metal film; in [12], an elastomeric grating fabricated by the replica molding method is placed on the surface of a metal film. The conformal contact between the elastomeric grating and the metal surface periodically alters the refractive index of the dielectric material near the interface so as to

match the momentum of the incident light with that of the surface plasmons. In the present study, the above structure is further modified by depositing a thin dielectric layer on the metal surface to improve the performance and protect the thin gold surface from potential damage caused by direct contact with the dielectric grating.

3. SIMULATION RESULTS

The new structure can be divided into two parts: The top glass substrate with an indium-tin-oxide (ITO) layer and the grating structure on the downside, and the bottom glass substrate coated with dielectric, gold, and silver films on the upside. The refractive indexes of all materials in this structure for simulation are as follow: (from bottom to top): $n_0 = 1.515$ (glass), $n_1 = 0.14 + 4.15i$ (silver), $n_2 = 0.166 + 3.15i$ (gold), $n_3 = 1.457$ (dielectric passivation, SiO_2), $n_4 = 1.489$ (polymer), and $n_5 = 1.72$ (ITO). The thicknesses of silver, gold, SiO_2, polymer, and ITO are 100 nm, 5 nm, 125 nm, 1 μm and 100 nm, respectively. The thicknesses of silver and gold are following the suggestion in [11]. The modulation height and pitch of the grating structure are the same as those in Fig. 1. In contrast to a high-refractive-index prism in the KR configuration, a glass substrate with a low refractive index of 1.515 is used here. Fig. 4 presents FDTD-calculated reflectivity as a function of the angle of incidence for different thicknesses of the passivation dielectric layer from 0 nm to 150 nm in steps of 25 nm. The results indicate that structures with a passivation dielectric layer have a narrower FWHM than that without this layer and hence, they will have better sensitivity to changes in the refractive index and better modulation performance. Basically, the FWHM of the reflectivity curves with a thicker dielectric layer achieves a narrower resonance and hence better modulation performance. However, a too-thick dielectric layer decreases the coupling efficiency and results in a high reflectivity at the resonance angle. The above observations imply that thickness control of the dielectric layer is very important for this high-performance grating-coupled SPR EO modulator. In this configuration, the dielectric layer and the grating structure are separated; therefore, the dielectric layer can be fabricated by the chemical vapor deposition (CVD) method and its thickness can be controlled well by a known deposition rate. In contrast to the structure described in [11], the dielectric layer and the grating structure are same material and formed together by an interference method; therefore, it's difficult to control the thickness of the dielectric layer separately.

From the simulation results shown in Fig. 4, we choose the structure with a 125-nm thick dielectric layer for further investigating its application to an EO polymer modulator. This case has the narrowest resonance and still maintains a high plasmon coupling efficiency of about 80%. In order to study the effect of the gold thickness, results of different gold thickness of 0 nm, 5 nm, and 10 nm for the case of 125 nm-thick dielectric layer are shown in Fig. 5. The results show that the gold thickness of 5 nm provides the highest coupling efficiency. Furthermore, simulation is also performed for investigating the effect of the silver thickness and it is found that the silver thickness has no significant effect on the reflective curve. Next, for the structures with a 125-nm-thick dielectric layer and a 5-nm-thick gold film, two simulation curves with different EO polymer

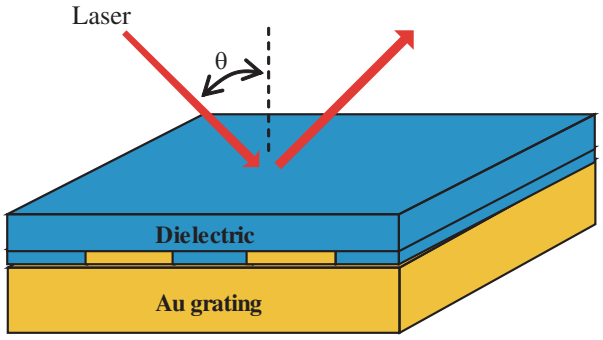

Figure 1: Schematic of the SPR EO modulator based on a conventional grating coupler structure.

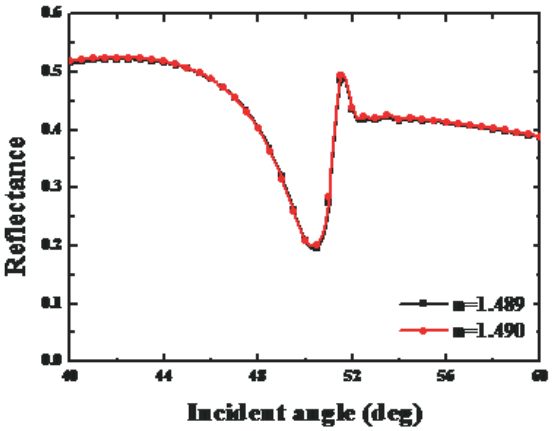

Figure 2: Reflectivity curves of the structure shown in Fig. 1 calculated as a function of the angle of incidence for incident laser light.

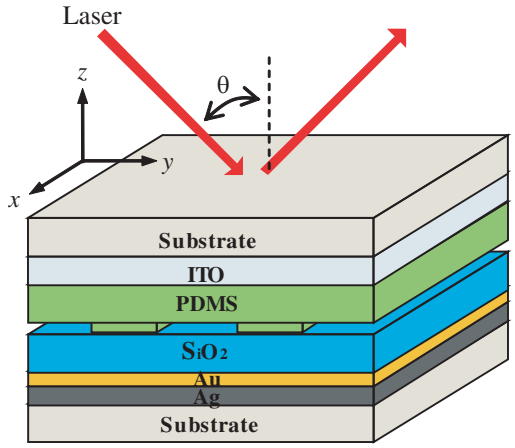

Figure 3: Schematic diagram of the grating coupler EO modulator with a passivation layer SiO_2 on.

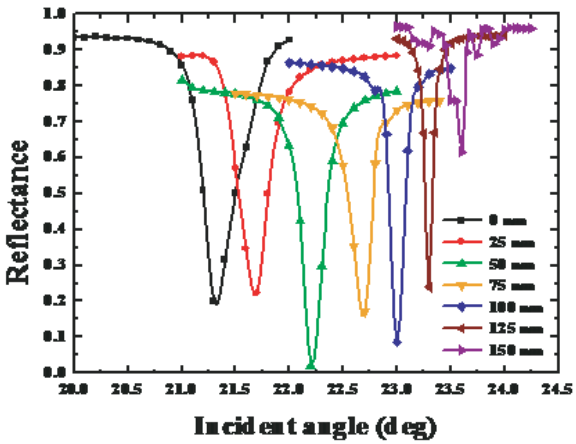

Figure 4: Reflectivity curves of the structure shown in Fig. 2 as a function of the angle of incidence for different thicknesses of the passivation dielectric layer.

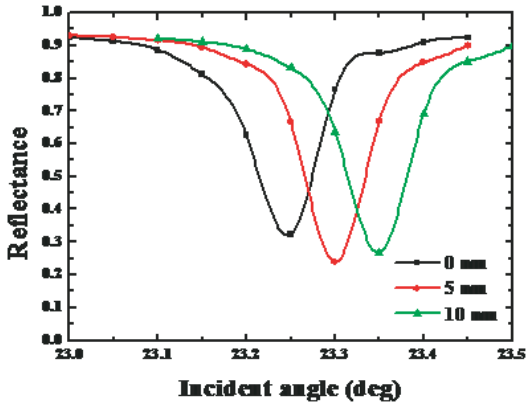

Figure 5: Reflectivity curves of different gold thickness of 0 nm, 5 nm, and 10 nm for the case of 125 nm-thick dielectric layer.

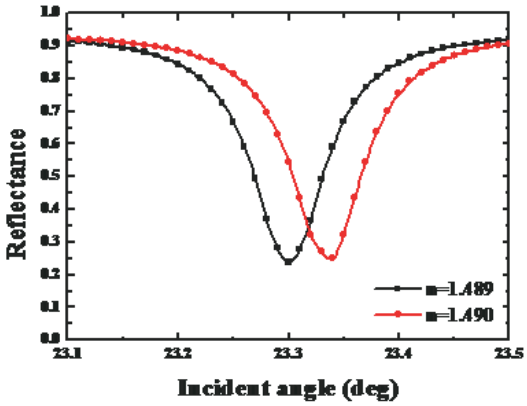

Figure 6: Reflectivity curves of the structure shown in Fig. 2 with different EO polymer indexes of 1.489 and 1.490.

indexes of 1.489 and 1.490 are shown in Fig. 6. As compared with Fig. 2, a significant resonance angle shift is observed when the same small increment is made in the refractive index of the polymer layer. If the incident angle is set to 23.27°, the index increment of 0.001 causes the reflectivity to increase from 50% to 75%. This result is much better than that obtained from the conventional structure shown in Fig. 2. For the EO polymer layer, if the poling field is applied along the z-axis as the reference principal axes as shown in Fig. 3, after the poling process, the EO tensor for the polymer is [13]

$$[r] = \begin{bmatrix} 0 & 0 & r_{13} \\ 0 & 0 & r_{13} \\ 0 & 0 & r_{33} \\ 0 & r_{13} & 0 \\ r_{33} & 0 & 0 \\ 0 & 0 & 0 \end{bmatrix} \tag{1}$$

In the presence of a modulation electrical field $\mathbf{E}= (E_x, E_y, E_z)$, the index ellipsoid of the poled polymer becomes:

$$\left(\frac{1}{n_o^2} + r_{13}E_z\right)(x^2 + y^2) + \left(\frac{1}{n_e^2} + r_{33}E_z\right)z^2 + 2r_{13}E_y yz + 2r_{13}E_x xz = 1 \tag{2}$$

where n_o and n_e are refractive indices of the poled polymer for ordinary and extra-ordinary rays, respectively. If the optical wave propagates along the y-direction and only z-axis electric-field E_z

is applied, the index ellipsoid in Eq. (2) can be simplified as an index ellipse equation as

$$\left(\frac{1}{n_o^2} + r_{13}E_z\right)x^2 + \left(\frac{1}{n_e^2} + r_{33}E_z\right)z^2 = 1 \tag{3}$$

For the optical wave to excite the SPR, its polarization direction is along z-axis and hence the corresponding refractive index change Δn of the EO polymer induced by the voltage V applied across the polymer is

$$\Delta n = \frac{1}{2}n_e^3 r_{33}\frac{V}{d} \tag{4}$$

where d is the thickness of the EO polymer and V/d is corresponding to the electric-field E_z. Assume that a polymer material with a high EO coefficient r_{33} of 200 pm/V is used, an applied voltage less than 5 V can achieve a Δn of 0.001.

4. CONCLUSION

In conclusion, a new structure of a grating-coupled SPR EO modulator with good modulation performance has been numerically demonstrated using the FDTD simulation. In this new configuration, the dielectric passivation layer formed between the grating structure and the metal surface not only protects the thin gold film but also improve the sensitivity to changes in the index change. The simulation results show that the resonance angle of this new configuration shifts significantly for a small index increment of 0.001 in the EO polymer grating structure.

ACKNOWLEDGMENT

The authors gratefully acknowledge the financial support provided by the National Science Council, Taiwan, R.O.C., under Grant No. NSC97-2221-E-150-020-MY3.

REFERENCES

1. Raether, H., *Surface Plasmons on Smooth and Rough Surfaces and on Gratings*, Springer-Verlag, Berlin, 1988.
2. Homola, J., S. S. Yee, and G. Gauglitz, "Surface plasmon resonance sensors: Review," *Sensor and Actuators B*, Vol. 56, No. 3, 1999.
3. Schildkraut, J. S., "Long-range surface plasmon electrooptic modulator," *Appl. Opt.*, Vol. 27, 4587, 1988.
4. Solgaard, O., F. Ho, J. I. Thackara, and D. M. Bloom, "High frequency attenuated total internal reflection light modulator," *Appl. Phys. Lett.*, Vol. 61, 2500, 1992.
5. Jung, C., S. Yee, and K. Kuhn, "Electro-optic polymer light modulator based on surface plasmon resonance," *Appl. Opt.*, Vol. 34, 946, 1995.
6. Deng, X., X. Zheng, Z. Cao, Q. Shen, and H. Li, "Fast speed electro-optic polymer variable optical attenuator based on cascaded attenuated-total-reflection technique," *Appl. Phys. Lett.*, Vol. 90, 151124, 2007.
7. Wu, Z., R. L. Nelson, J. W. Haus, and Q. Zhan, "Plasmonic electro-optic modulator design using a resonant metal grating," *Opt. Lett.*, Vol. 33, 55, 2008.
8. Moharam, M. G. and T. K. Gaylord, "Rigorous coupled-wave analysis of metallic surface-relief gratings," *J. Opt. Soc. Am. A*, Vol. 3, 1780, 1986.
9. Taflove, A. and S. C. Hagness, *Computational Electrodynamics: The Finite-Difference Time-Domain Method*, 3rd Edition, Artech House, Boston, London, 2005.
10. Massenot, S., R. Chevallier, J.-L. De Bougrenet de la Tocnaye, and O. Parriaux, "Tunable grating-assisted surface plasmon resonance by use of a nano-polymer dispersed liquid crystal electro-optical material," *Optics Comm.*, Vol. 275, 318, 2007.
11. Muller, K. G., M. Veith, S. Mittler-Neher, and W. Knoll, "Plasmon surface polariton coupling with dielectric gratings and the thermal decomposition of these dielectric gratings," *J. Appl. Phys.*, Vol. 82, 4172, 1997.
12. Kocabas, A., A. Dana, and A. Aydinli, "Excitation of a surface plasmon with an elastomeric grating," *Appl. Phys. Lett.*, Vol. 89, 041123, 2006.
13. Yariv, A. and P. Yeh, *Optical Waves in Crystals*, Wiley, New York, 1983.

Theoritical Analysis of Some Homogenized Metamaterials and Application of PML to Perform Cloaking and Back-scattering Invisibility

P. H. Cocquet, V. Mouysset, and P. A. Mazet
Department of Information Treatment and Modelization (DTIM), ONERA Toulouse, France

Abstract— A general Drude-Born-Fedorov (DBF) system, with materials like metamaterials, on a bounded domain is studied. Due to the presence, for some pulsation, of negative permittivity and permeability, the well-posedness of this kind of system remains a steady point. In this paper, we treat examples dealing with homogenized metamaterials like a periodic array of Split-Ring-Resonators (SRR), homogenized dielectric-chiral photonic crystals and convex absorbing boundary conditions of PML type have been treated. At last, we show both theoretically and numerically that PML can perform electromagnetic cloaking and back-scattering invisibility.

1. INTRODUCTION

In 1968, V. G. Veselago [11] theoretically studied electromagnetic phenomenons in materials with simultaneous negative permittivity [ε] and permeability [μ]. Due to the reversed Poynting vector, he named these materials "Left-Handed-Materials" (LHM). He also remarks that these materials had exotics properties (reversed Doppler effect for example).

The keen interest for the LHM was initiated by J. B. Pendry's in 2000 [6]. He managed to build LHM using a periodic array of Split-Ring-Resonators (SRR) and suggested making a perfect lens with these structures. Futhermore, these exotic building were named "metamaterials".

However, as metamaterials can't be found in nature as negative indexes materials, they are usually the result of an homogenization (see for example [3, 4, 6, 7, 9]). The problem arises from the choice for homogenization's method. Every method can lead to a different homogenized material and by the way to a new partial diffential equation. The question is then to know, in a first step, which of these homogenized problems are well-posed. A second step will be linked with a suitable approximation of the solution of these homogenized systems. Unfortunatly, the well-posedness of these homogenized problems remains a steady point. In fact, homogenized metamaterials have their permitivitty and permeability depending on the pulsation w and start to be negative definite for some w. This implies that the well-posedness of the DBF system, which establishes electromagnetic phenomenons in chiral materials, can't be a priori issued.

So, we are going to study a generalized DBF system including some negative index phenomenons. A well-posedness result for this generalised DBF system is given in the first section. Next, homogenized dielectric-chiral photonic crystals [4], periodical arrangement of Split-Ring-Resonator (SRR) [7] and convex absorbing boundary conditions of PML type for Maxwell's equations [5], seen as "ideal metamaterial", are studied. At last, we show theoretically and check numerically that convex PML for Maxwell's equations can perform electromagnetic cloaking and back-scattering invisibility.

2. MATHEMATICAL FRAMEWORK

Lots of electromagnetic phenomenons in homogenized chiral photonic crystals can be modelized by the following Drude-Born-Fedorov (DBF) system (1), (2) (e.g., [3]):

$$\begin{cases} \text{Find } (e,h) \in H(curl,\Omega)^2 \text{ such that :} \\ (K_0(p,x) + K_1(p,x)\mathbb{M}) \begin{pmatrix} e \\ h \end{pmatrix} = f, \quad x \in \Omega \\ \mathbf{n}(x) \times (e + \Lambda(x)\mathbf{n}(x) \times h) = 0, \quad x \in \partial\Omega \quad , \end{cases} \tag{1}$$

$$\begin{aligned} \mathbb{M} &= \begin{pmatrix} 0 & -\nabla\times \\ \nabla\times & 0 \end{pmatrix}, \quad K_0(p,x) = \begin{pmatrix} p[\varepsilon(p,x)] & 0 \\ 0 & p[\mu(p,x)] \end{pmatrix}, \\ K_1(p,x) &= \begin{pmatrix} \mathbb{I}_3 & p[\beta(p,x)][\varepsilon(p,x)] \\ -p[\beta(p,x)][\mu(p,x)] & \mathbb{I}_3 \end{pmatrix}. \end{aligned} \tag{2}$$

where e and h are the electric and the magnetic fields. The permitivity $[\varepsilon]$, the permeability $[\mu]$ and the chirality $[\beta]$ are the homogenized parameters of the media which are smoothly depending both on $p = iw$, w is the pulsation, and x, $f \in L^2(\Omega)^6$. At last Ω is a simply connected bounded domain in $\mathbb{R}^3$ with C^1 boundary whose outward unitary normal is denoted $\mathbf{n}$ and $\Lambda \in Lip(\Omega, \mathcal{L}(\mathbb{C}^6))$ such that $\mathrm{Re}(\Lambda(x)+\Lambda^*(x))$ is nonnegative. We also set $\mathbf{H} = \{(e,h)^T \in (L^2(\Omega)^3)^2,\ (\nabla\times e, \nabla\times h)^T \in (L^2(\Omega)^3)^2$ and $\mathbf{n}(x)\times(E+\Lambda(x)\mathbf{n}(x)\times H) = 0,\ x \in \partial\Omega\}$ for the functional space to look solution wherein.

In "usual" materials, $[\varepsilon]$ and $[\mu]$ are bounded and positively definite so the multiplication operators $K_0(p)$ and $K_1(p)$, in Laplace transform, are bounded and uniformly coercive (with respect to $x \in \Omega$) for all $p = iw + \gamma \in \mathbb{C}$ such that $\gamma > 0$. As the operator $(\mathbb{M}, \mathbf{H})$ is closed maximal dissiptive [8], taking the limit $\gamma \to 0$ leads to the well-posedness of the system (1), (2) for all $p = iw$.

In some examples linked with the metamaterials, the permitivity and/or the permeability, which are functions of the pulsation w, become negative definite for some w thus the well-posedness of the system (1), (2) can't be, a priori, issued. Note that system (1) can both modelize photonic crystals with DBF equations, and electromagnetic phenomenons with Maxwell's equations by setting $K_1 = \mathbb{I}_6$.

But, we have the following result [2]:

Theorem 1. *Let D be a domain of $\mathbb{C}$ such that $D \cap i\mathbb{R} \neq \emptyset$ and let's assume:*

- *$(H1)$: $K_j(p,.) \in L^\infty(\Omega),\ j = 0,1$ and $K_1(p,x)$ is invertible $\forall (p,x) \in D \times \Omega$,*
- *$(H2)$: $K_j(.,x)$ is holomorphic for $p \in D$.*
- *$(H3)$: There exists $p_0 \in D$ such that $K_j(p_0)$ for $j = 0,1$ is coercive.*

Then, under assumptions $(H1)-(H2)-(H3)$, the problem (1) is well-posed with compact resolvant for all p in D except for a discrete set of values in D.

Theorem 1 gives an existence and uniqueness result for the generalized DBF system (1). $(H1)-(H2)$ are the descriptive and phenomenological hypotheses which describe the considered media. They ask for piecewise bounded indexes depending smoothly on the Laplace variable p. Note that meromorphic $K_j(p)$ can be taken into account by removing their poles from D. Hence, for example, Debye's and Lorentz's materials satisfy $(H1)-(H2)$. The hypothesis $(H3)$ have been stated in [11] and can be checked experimentally (see Figure 1 in [7]). It means that the considered media behaves as an "usual" one for some p_0. Then, for this p_0, the generalized DBF system is well-posed. And finally, theorem 1 extends the well-posedness of this system to almost all p in the domain of study D.

3. STUDY OF A PERIODIC ARRAY OF SPLIT-RING-RESONATORS

The Split-Ring-Resonators (SRR) have been introduced by J. B. Pendry in 2000 suggesting to make a perfect lens using negative index materials [4]. Some studies dealing with homogenization using a periodic array of SRR follow [6, 9] but the well-posedness of this system remains unanswered at the best of our knowledge.

The effective parameters of a periodical array of interspaced conducting nonmagnetic split-ring-resonators and continuous wires calculated in [9] has the following expressions:

$$[\varepsilon(p,x)] = \left(1 + \frac{w_p^2}{p^2}\right)\mathbb{I}_3,\ [\mu(p,x)] = \left(1 + \frac{\delta p^2}{-p^2 - w_0^2 + p\Gamma}\right)\mathbb{I}_3,\ [\beta(p,x)] = 0, \tag{3}$$

where $w_p > 0$ is the plasma pulsation of gold, $w_0 = \sqrt{\frac{3l}{\pi^2\mu_0 C r^3}}$ and $\Gamma = \frac{2l\rho}{r\mu_0} > 0$ are constants. Here ρ is the resistance per unit length of the rings measured around the circumference, l is the distance between layers, a is the lattice parameter, r is defined on Figure 1 in [9] and C is the capacitance associated with the gaps between the rings.

First, remark that $[\varepsilon]$ and $[\mu]$ defined by (3) are free from x. Futhermore, they depend on p as rational fractions thus $K_0(p)$ and $K_1(p)$ defined by (2), (3) are holomorphic on $D = \mathbb{C}\backslash Z$ where Z is the set of zeros of their denominators. Namely $Z = \left\{\frac{\Gamma-\sqrt{\Gamma^2-4w_0^2}}{2}, 0, \frac{\Gamma+\sqrt{\Gamma^2-4w_0^2}}{2}\right\}$ where $\sqrt{y}$ is equal to $i\sqrt{-y}$ if $y < 0$. Hypothese $(H1)-(H2)$ are then satisfied on $D \times \Omega$. Now, let

$$f : p \in \mathbb{R}\backslash\{0\} \longrightarrow -p^2 - w_0^2 + p\Gamma \in \mathbb{R}.$$

The maximum of f is reached for $p_0 = \frac{\Gamma}{2}$. As $f(p_0) > 0$, $K_0(p_0)$ and $K_1(p_0)$ defined by (2), (3) are coercive thus $(H3)$ is verified. Hence, homogenized parameters $[\varepsilon]$, $[\mu]$ in (3) define an admissible problem in the sence of theorem 1 which can be lately mathematically and numerically investigated.

4. STUDY OF A HOMOGENIZED DIELECTRIC-CHIRAL PHOTONIC CRYSTALS

Let ε_c, μ_c, β_c be the parameters of a chiral media. The photonic crystal, hosted in the vacuum, formed by a periodic array of chiral spheres can be described as a homogenised chiral medium (noted Ω) whose coefficients can be written as follow [7]:

$$\begin{aligned}
[\varepsilon(p,x)] &= \frac{\{(2+\varepsilon_c-2\delta(1-\varepsilon_c))\}\{2+\mu_c-2\delta(1-\mu_c)\}+4(\delta-1)^2\varepsilon_c\mu_c p^2\beta_c^2}{\{(2+\varepsilon_c+\delta(1-\varepsilon_c))\}\{2+\mu_c-2\delta(1-\mu_c)\}-2(\delta-1)(\delta+2)\varepsilon_c\mu_c p^2\beta_c^2}\mathbb{I}_3,\\
[\mu(p,x)] &= \frac{\{(2+\varepsilon_c-2\delta(1-\varepsilon_c))\}\{2+\mu_c-2\delta(1-\mu_c)\}+4(\delta-1)^2\varepsilon_c\mu_c p^2\beta_c^2}{\{(2+\varepsilon_c-2\delta(1-\varepsilon_c))\}\{2+\mu_c+\delta(1-\mu_c)\}-2(\delta-1)(\delta+2)\varepsilon_c\mu_c p^2\beta_c^2}\mathbb{I}_3,\\
[\beta(p,x)] &= \frac{9\delta\varepsilon_c\mu_c\beta_c}{\{(2+\varepsilon_c-2\delta(1-\varepsilon_c))\}\{2+\mu_c-2\delta(1-\mu_c)\}+4(\delta-1)^2\varepsilon_c\mu_c p^2\beta_c^2}\mathbb{I}_3,
\end{aligned} \tag{4}$$

where $0 < \delta < 1$ is the fraction of the total volume occupied by the spheres.

Notice first that $[\varepsilon]$, $[\mu]$ and $[\beta]$ defined by (4) are free from x. Thus coefficients K_0 and K_1 defined by (2)–(4) are bounded with respect to $x \in \Omega$. Futhermore $[\varepsilon(p)]$, $[\mu(p)]$, $[\mu(p)][\beta(p)]$ and $[\varepsilon(p,x)][\beta(p,x)]$ depend on p as rational fraction. Thus the holomorphy of K_0 and K_1 holds on $D = \mathbb{C}\backslash Z$ where Z is the set of zeros of their denominators. This implies that:

$$Z=\left\{\pm\sqrt{\frac{\{2+\varepsilon_c+\delta(1-\varepsilon_c)\}\{2+\mu_c-2\delta(1-\mu_c)\}}{2(\delta-1)(\delta+2)\varepsilon_c\mu_c\beta_c^2}},\pm\sqrt{\frac{\{2+\varepsilon_c-2\delta(1-\varepsilon_c)\}\{2+\mu_c+\delta(1-\mu_c)\}}{2(\delta-1)(\delta+2)\varepsilon_c\mu_c\beta_c^2}}\right\}, \tag{5}$$

with the same notation of $\sqrt{.}$ as previously. So hypotheses $(H1)-(H2)$ are satisfied on $D\times\Omega$ where $D = \mathbb{C}\backslash Z$. We remark that $K_0(1)$ and $K_1(1)$ defined by (2)–(4) are coercive. Hence, the physical modelling which gives the parameters defined by (4) leads to an admissible DBF system in the sence of theorem 1. This problem can be lately numerically and mathematically studied.

Remark 1. *The fraction of the total volume occupied by the spheres, noted δ, can depend on $x \in \Omega$. So $[\varepsilon]$, $[\mu]$ and $[\beta]$ defined in (4) will be able to depend on x too. The study of the well-posedness of the system (1), (2), (4) with $\delta = \delta(x)$ is not slighty different from the previous case. The main modification occurs on the definition of the set Z (5), now noted Z': $p \in Z' \Longleftrightarrow \forall x \in \Omega$,*

$$\left\{\begin{array}{l}
\{2+\varepsilon_c-2\delta(x)(1-\varepsilon_c)\}\{2+\mu_c+\delta(x)(1-\mu_c)\}-2(\delta(x)-1)(\delta(x)+2)\varepsilon_c\mu_c p^2\beta_c^2=0,\\
\{2+\varepsilon_c+\delta(x)(1-\varepsilon_c)\}\{2+\mu_c-2\delta(x)(1-\mu_c)\}-2(\delta(x)-1)(\delta(x)+2)\varepsilon_c\mu_c p^2\beta_c^2=0.
\end{array}\right.$$

Remark that Z' is the disjoint union of four intervals located on the imaginary axis. Moreover, $Z'\cap\{0\}=\emptyset$ and, if δ is free from x, $Z = Z'$. As for all x in Ω, $0 < \delta(x) < 1$, hypotheses $(H1)-(H2)$ are satisfied on $D\times\Omega$ where $D = \mathbb{C}\backslash Z'$. $K_0(1)$ and $K_1(1)$ still define coercive multiplication operators. Thus $(H3)$ is checked. Hence the same conclusion as previously (with δ free from x) holds.

5. CLOAKING AND BACK-SCATTERING INVISIBILITY WITH PML

At last we study some absorbing boundary conditions of PML type. Using the result of the Section 2, we show that Maxwell's equations with convex PML are well-posed. We also show theoretically that PML can perform cloaking and back-scattering invisibility. Moreover we give some numerical results showing these properties using finite volumes method for T. M. Maxwell's equations.

Let $x = (x_1, x_2) \in \Omega \subset \mathbb{R}^2$ and consider the following T.M Maxwell's system:

$$\left\{B(p)\begin{pmatrix} e_1\\ e_2\\ h_3\end{pmatrix}+\begin{pmatrix} 0 & 0 & -\partial_y\\ 0 & 0 & \partial_x\\ -\partial_y & \partial_x & 0\end{pmatrix}\begin{pmatrix} e_1\\ e_2\\ h_3\end{pmatrix}=f, \right. \tag{6}$$

where

$$B(p)=\begin{pmatrix} \frac{\widetilde{\gamma}(p,x)}{\gamma(p,x)} & 0 & 0\\ 0 & \frac{\gamma(p,x)}{\widetilde{\gamma}(p,x)} & 0\\ 0 & 0 & \gamma(p,x)\widetilde{\gamma}(p,x)\end{pmatrix}, \tag{7}$$

acts as absorbing boundary condition of convex PML type on a subset Θ of Ω. Two different types of PML will be used according to the geometry studied: circular PML and cartesian PML.

Circular PML are defined on an annulus $\Gamma \subset \Omega$ of radius r_1 and r_2 by (7) with:

$$\left\{ \begin{array}{l} \gamma(p,x) = 1 - \frac{\sigma_\rho(\rho)}{p}, \\ \widetilde{\gamma}(p,x) = 1 - \frac{\int_{\rho_1}^{\rho} \sigma_\rho(s)ds}{p\rho}, \end{array} \right. \tag{8}$$

where $\rho = |x|$, $\sigma_\rho(\rho) \geq 0$ for x in Γ and $\sigma_\rho(\rho) = 0$ for x in $\Omega \backslash \overline{\Gamma}$.

Cartesian PML are defined on $]-a,+a[\times]-b,+b[\subset \Omega$, by (7) with:

$$\left\{ \begin{array}{l} \widetilde{\gamma}(p,x) = \frac{\sigma_2(x_2)+p}{p}, \\ \gamma(p,x) = \frac{\sigma_1(x_1)+p}{p}, \end{array} \right. \tag{9}$$

where $\sigma_{x_1}(x_1) = 0$ for x_1 in $]-a,+a[$ and $\sigma_{x_1}(x_1) > 0$ for x_1 in $\mathbb{R}\backslash]-a,+a[$, $\sigma_{x_2}(x_2) = 0$ for x_2 in $]-b,+b[$ and $\sigma_{x_2}(x_2) > 0$ for x in $\mathbb{R}\backslash]-b,+b[$.

We use Finite Volume method for T.M Maxwell's equation (6), (7) to investigate numerically the cloaking and back-scattering invisibility properties. The cloaking effect is numerically shown on an annulus with circular PML (8). The back-scattering abilities has been computed with cartesian PML (9) on a square. A point source is introduced. It is described in Equation (6) with $f = \widetilde{f}[0,0,1]^T$ where $\widetilde{f}$ is a mollification of δ_{x_0} supported by the open disk of radius $\eta = \frac{\pi}{1.4}$:

$$\widetilde{f}(x) = \left\{ \begin{array}{l} 0, |x - x_0| \geq \eta, \\ \exp(\eta) \exp\left(\frac{-\eta}{|x-x_0|^2}\right), |x - x_0| < \eta. \end{array} \right. \tag{10}$$

Figure 1(a) represents the approximation of the field $\mathrm{Re}(h_3)$ solution of T. M. Maxwell's equations (6)–(8), (10) with $x_0 = (0,0)$ and $\sigma_\rho(\rho) = 5,617 \exp(-(\rho - \frac{r_1+r_2}{2})^2)$. We can see that PML absorbs strongly the field $\mathrm{Re}(h_3)$. Moreover it is reflectionless thus electromagnetic cloaking can be performed with PML. The field outside the annulus, the concentric circles, is closed to zero ($\approx \pm 0.2$). Inside the annulus, we have exactly the restriction of the solution of (6)–(8), (10) propagating on unbounded space.

Figure 1(b) represents the approximation of the field $\mathrm{Re}(h_3)$ solution of T. M. Maxwell's equations (6), (7), (10), (9) with $x_0 = (-5,0)$, $\sigma_j^k(x_j) = (x_j \pm d_k)^2$. There are two layers of PML. One on the boundary of our computational domain, for numerical purpose, defined by (9) with $\sigma^1(x_j) = (x_j \pm 12)^2$. The other, which is lying in the middle of the aera, for invisibility aim, is (9) with $\sigma^2(x_j) = (x_j \pm 3)^2$. We can see that a measurement of the field at $x = (x_1^m, x_2^m)$ with $x_1^m \leq -5$ and $x_2^m = 0$ is not modified by the presence of the internal PML box. Hence back scattering invisibility is performed.

The electromagnetic wave propagation in vacuum is approached by the system (6), (7). The matrix $B(p,x)$ is bounded and holomophic on $(\mathbb{C}\backslash\{0\}) \times \Omega$ thus satisfy $(H1) - (H2)$. As the multiplication operator $B(1)$ is coercive, $(H3)$ is checked with $p_0 = 1$. Again, the parameters in (7), (8) and (7), (9) define an admissible system in the sence of theorem 1.

This result and the numerical simulations (see Figures 1(a) and (b)) lead us to investigate some properties of the PML. Even if PML are not by nature, we investigate their properties to propose

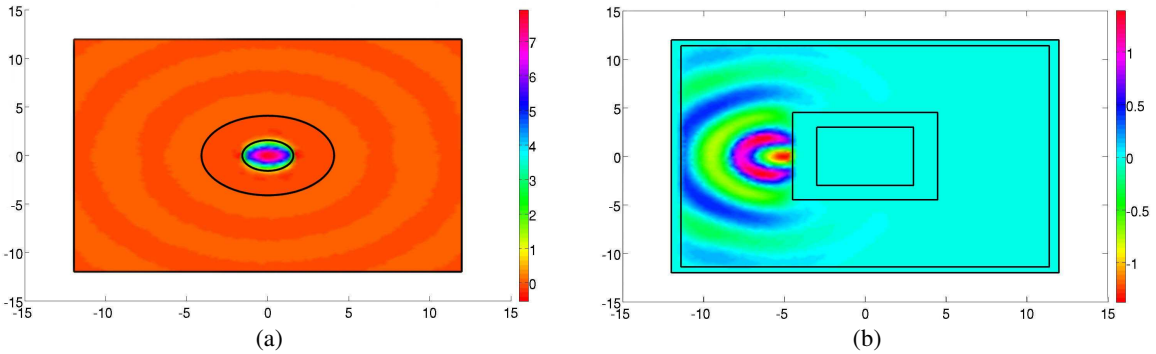

Figure 1: (a) Cloaking. (b) Back-scattering invisibility.

a distribution of indexes performing cloaking and back-scattering invisibility. It is well known that PML is reflectionless and absorbs strongly the scattered waves. Then, PML can performs electromagnetic cloaking. To show that PML can perform back scattering invisibility, we assume, for simplicity, that $\Theta \subset \Omega$ is a circle. We use the following complex formulation of PML [5]:

$$\widetilde{x} : \mathbb{R}^3 \longrightarrow \mathbb{C}^3, x \longrightarrow \widetilde{x}(x) = \widetilde{\rho}(\cos(\theta), \sin(\theta)),$$

where $\widetilde{\rho_x} = \rho_x + \frac{K(\rho)}{p}$, $\theta \in [0, 2\pi]$ and $K \geq 0$.

Let $y \in \mathbb{R}^2$, from [5], the solution of the Maxwell's equations (6), (7) with $f(x) = \delta_y(x)$ is a radial function $\widetilde{G}(|\widetilde{x} - \widetilde{y}|)$. Let $f \in L^2(\Omega)$ be compactly supported in Ω. The solution of (6), (7) is given by $\widetilde{u}(x) = \displaystyle\int_\Omega \widetilde{G}(|\widetilde{x}(x) - \widetilde{y}(y)|) f(\widetilde{y}(y)) dy$. Let $G(|x - y|)$ be the Green's function of the T. M. Maxwell's equations (6) in the vacuum ($B(p) = \mathbb{I}_3$) thus the solution of (6) is given by $u(x) = \displaystyle\int_\Omega G(|x - y|) f(y) dy$. A straightforward calculation of $|\widetilde{x} - \widetilde{y}|$ leads to:

$$|\widetilde{x} - \widetilde{y}|^2 = \widetilde{\rho_x}^2 + \widetilde{\rho_y}^2 - 2\{\cos(\theta_x)\cos(\theta_y) + \sin(\theta_x)\sin(\theta_y)\}.$$

Thus $|\widetilde{x} - \widetilde{y}|^2 = \widetilde{\rho_x}^2 + \widetilde{\rho_y}^2 - 2\{\cos(\theta_x - \theta_y)\}$, and, developing $\widetilde{\rho_x}$, $\widetilde{\rho_y}$, and assuming $\theta_x = \theta_y[2\pi]$, it follows:

$$|\widetilde{x} - \widetilde{y}|^2 = (\rho_x - \rho_y)^2.$$

Then, for all x such that $\theta_x = \theta_y[2\pi]$, we have $\widetilde{u}(x) = u(x)$ so the solution of (6), (7) and the solution of (6) in the vaccum match and we can conclude that PML performs back-scattering invisibility.

Remark that the proof of back-scattering invisibility performed by PML can be done in $\mathbb{R}^3$ with spherical PML for Maxwell's equations.

6. CONCLUSION

In this paper we were interested in analyzing scattering by complex materials either for Drude-Born-Fedorov system or Maxwell's equations. Using a general mathematical framework, we studied a Maxwell's equations with a periodical array of interspaced Split-Ring-Resonators. A DBF system in presence of homogenized dielectric-chiral photonic crystals have been studied. The Maxwell's system with some absorbing boundary condition of PML type, seen as "ideal" metamaterial, have also been considered. At last, we checked both numerically (using Finite Volume method for T.M Maxwell's system) and theoretically the cloaking and back-scattering invisibility abilities of the PML. The homogenized systems treated in this paper have been analyzed with a general mathematical framework. Futhermore, this tool works under compatible assumptions relevant for the physical modelling thus more homogenized systems can be studied using it.

It remains to find how we can approximate the solution of these homogenized systems. The classical numerical methods (Finite Volumes, Finite Elements, Finite Difference, ...) used for the approximation of Maxwell's equations or DBF system in presence of "usual" materials are convergent mainly due to the positiveness of the parameters $[\varepsilon]$ and $[\mu]$. The question is then to know if these numerical schemes are still convergent in presence of materials whose parameters can become negative definite for some pulsation w. An answer can be found in some works dealing with finite element methods for wave propagation in metamaterials which have been made in [1, 10] modifying the Finite Element scheme. However, these result can't be, at the best of our knowledge, straightforwardly used for systems like Maxwell's equations with a periodical arrangement of split-ring-resonators or for the DBF system with chiral photonic crystals.

REFERENCES

1. Bonnet-Bendhia, A. S., P. Ciarlet, and C. M. Zwölf, "Time harmonique wave diffration problems in materials with sign-shifting coefficients," *J. Comput. Appl. Math.*, 2009.
2. Cocquet, P. H., P. A. Mazet, and V. Mouysset, "On well-posedness of some homogenized Drude-Born-Fedorov systems on a bounded domain and applications to metamaterials," submitted.
3. Guenneau, S. and F. Zolla, "Homogenization of 3D finite chiral photonic crystals," *Science Direct, Physica B*, Vol. 394, 145–147, 2007.

4. Kanté, B., S. N. Burokur, F. Gadot, and A. De Lustrac, "Métamatriaux indices de rfraction ngatif en infrarouge," UMR 8622, 91405 Orsay, F-91405.
5. Lassas, M., J. Liukkonen, and E. Somersalo, "Complex riemanninan metric and absorbing boundary conditions," *J. Math. Pures Appl.*, Vol. 80, No. 7, 739–768, 2001.
6. Pendry, J. B., *Intense Focusing Of Light Using Metals*, NATO ASI Series, Ed. C. M. Soukoulis, 2000.
7. Psarobas, I. E., "Effective-medium description of dielectric-chiral photonic crystals," *Optics Communications*, Vol. 162, 21–25, April 1, 1999.
8. Rauch, J., "Symmetric positive systems with boundary characteristic of constant multiplicity," *Transaction of the American Mathematical Society*, Vol. 291, No. 1, September 1985.
9. Smith, D. R., W. J. Padilla, D. C. Vier, S. C. Nemat-Nasser, and S. Schultz, "Composite medium with simultaneously negative permeability and permittivity," *Physical Review Letters*, Vol. 84, No. 18, May 1, 2000.
10. Sukhorukovn, A. A., I. V. Shadrivov, and Y. S. Kivshar, "Wave scattering by metamaterial wedges and interfaces," *Int. J. Numer. Model.*, Vol. 19, 105–117, 2006.
11. Veselago, V. G., "The electrodynamics of substance with simultaneously negative values of ε and μ," *Soviet Physics Uspekhi*, Vol. 10, No. 4, 1968.

Self-field Theory-new Photonic Insights

A. H. J. Fleming
Biophotonics Research Institute, Melbourne, Australia

Abstract— Self-Field Theory is a new description of electromagnetic interactions. At its heart are bispinorial motions for both the electromagnetic fields and the interacting particles. Among its recent successes it has solved a simple model of the hydrogen atom, obtained an analytic estimate for the mass of the photon, and provided the first glimpses of structure within the photon. This may yield an organizational structure for bosons reminiscent in some ways to the chemical table that was glimpsed by Mendeleev in 1860 via a two-dimensional array of elemental properties. The self-field formulation obtains an analytic expression for Planck's number providing a basis for its understanding as a variable of motion applying equally to the electron, the proton and the photon. While there are many differences, this report shows how the fields of Self-Field Theory vary from classical electromagnetics and quantum field theory. In classical electromagnetics the field covers all solid angles around a charge and is defined as a vector. Quantum Field Theory models the field as quanta shown as small wavy lines within Feynman diagrams; the mathematics does not specify an actual path, only the start and the finish points where a Dirac-delta function is used to insert a propagator kernel or Greens function. Basically Quantum Field Theory models the field as an impulse specified at space points. The uncertainty within Quantum Field Theory is related to the lack of a complete electromagnetic bispinorial field form. The fields in Self-Field Theory are discrete streams of photons, rather than the continuous fields of Maxwell's classical electromagnetics. The photons are specified via a bispinorial function as spatially and time-varying motions including spiral-helices between the electron and proton of the hydrogen atom. Thus two distances are involved in the bispinorial motions not one, fundamentally different to CEM and QFT.

1. THE EQUATIONS OF CEM, QFT AND SFT

The history of classical electromagnetics (CEM) can be summarized by the equations of electro- and magnetostatics derived by Coulomb and Ampere (1a), (1b) and their evolution over nearly a century to the Maxwell equations shown below as (3a)–(3d). The static equations describe uncoupled E- and B-fields while Maxwell's equations are coupled E- and H-fields and are first order partial differential equations. Maxwell's original equations were 20 in number and the variables were potentials. Maxwell understood these equations as having an underlying wave basis and he succeeded in deriving wave equations showing the EM phenomenon was a plane-wave propagating in free-space at the speed of light. The Liėard-Wiechert potentials are taken directly between charge points and give the relativistic time-varying EM fields for point charges in arbitrary motion.

$$F_E = \frac{q_1 q_1}{4\pi\varepsilon_0 r^2} \tag{1a}$$

$$\oint_C B \cdot dl = \mu_0 I_{enc} \tag{1b}$$

The history of quantum field theory (QFT) began with the evolution of Schrödinger's non-relativistic equation to Dirac's relativistic equation. Schrödinger expressed the phase of a plane wave as a complex factor (2a). The Klein-Gordon Equation (2b) is a relativistic version of Schrödinger's equation. Using Feynman notation (2c) we see how the Klein-Gordon equation can be analytically factorized to yield the positive and negative energy versions of the Dirac Equation (2d) where the γ_μ are 4×4 bispinors. Dirac thus predicted the electron's anti-particle the positron via these equations. Although Dirac's equation is first-order it is derived from a second order wave equation and it is this that demands gauge symmetry and invariance under conformal transformations.

$$i\hbar \frac{\partial}{\partial t}(x,t) = \widehat{\mathrm{H}}\Psi(x,t) \tag{2a}$$

$$\left[\nabla^2 + \frac{m^2 c^2}{\hbar^2}\right]\psi(r) = 0 \tag{2b}$$

$$\left(\partial^2 + m^2\right)\psi = 0 \rightarrow (i\partial + m)(i\partial - m)\psi = 0 \tag{2c}$$

$$(\gamma_\mu \partial_\mu + im)(\gamma_\mu \partial_\mu - im)\psi = 0 \tag{2d}$$

In SFT the particles and EM fields that control the motions of charged particles satisfy the Maxwell-Lorentz (ML) equations. For application to atomic physics, regions where particle-field interactions occur are assumed isotropic and homogeneous and the constitutive parameters, ε_0 and μ_0 the permittivity and permeability of free-space, are scalars. Where discrete particles carrying units of elementary charge q of opposite polarity are studied, in the absence of nebular regions of charge and current density, the ML equations are written

$$\nabla \cdot \vec{E} = \frac{q}{v_q} \tag{3a}$$

$$\nabla \cdot \vec{H} = 0 \tag{3b}$$

$$\nabla \times \vec{E} + \mu_0 \frac{\partial \vec{H}}{dt} = 0 \tag{3c}$$

$$\nabla \times \vec{H} - \varepsilon_0 \frac{\partial \vec{E}}{dt} = \frac{\pi}{s_q} q\vec{v} \tag{3d}$$

The Lorentz equation for the field-forces acting on the particles is written

$$\vec{F} = q\vec{E} + q\vec{v} \times \vec{B} \tag{3e}$$

The constitutive equations in free-space are

$$\vec{B} = \mu_0 \vec{H} \tag{3f}$$

$$\vec{D} = \varepsilon_0 \vec{E}. \tag{3g}$$

The relationship between the speed of light and the ratio of the fields

$$c = (\varepsilon_0 \mu_0)^{-1/2} \tag{3h}$$

$$dU = \rho dV = \frac{1}{2}\left(\varepsilon_0 \tilde{E} \cdot \tilde{E} + \mu_0 \tilde{H} \cdot \tilde{H}\right) dV \tag{3i}$$

The atomic energy density per volume (3i) depends upon the E- and H-fields in the atomic region. (3a)–(3d) are termed the EM field equations. In these equations, v is the particle velocity, m is its mass. The motion of the electron forms an EM self-field solution, its position is a sum of two spinors $\sigma_o(r_o, \omega_o)$ and $\sigma_c(r_c, \omega_c)$ where r_o and r_c are orbital and cyclotron radii and ω_o and ω_c are orbital and cyclotron angular velocities.

$$r\left(r_o, \omega_o, r_c, \omega_c\right) = r_o e^{j\omega_o t} + r_c e^{j\omega_c t} \tag{4}$$

In Equation (4) only discrete eigenvalues of r_o, r_c, ω_o and ω_c are allowed. After suitable algebraic manipulation, the system may be recast in terms of the energies in matrix form. The Principal mode can be written

$$\begin{bmatrix} 1 & 0 \\ 0 & 1 \end{bmatrix} \begin{bmatrix} V \\ T \end{bmatrix} = \begin{bmatrix} \hbar\omega \\ \hbar\omega \end{bmatrix} \tag{5}$$

In (5) $V = V_o = \frac{1}{4\pi\varepsilon_0}\frac{q}{r_o} = V_c = \frac{1}{4\pi\varepsilon_0}\frac{q}{r_c}$, and $T = T_o$ $T_c = \frac{1}{2}m_e v_o^2 = T_c = \frac{1}{2}m_e v_c^2$ are orbital and cyclotron components of the potential and kinetic energies. In the principal mode $\omega = |\omega_o| = |\omega_c|$ and $r = |r_o| = |r_c|$ where the orbital and cyclotron velocities are also equal $v_o = \omega_o r_o = v_c = \omega_c r_c$. The right hand side of (5) contains a variable termed Planck's 'number' that empirically agrees with the known value of Planck's constant to an accuracy of 7 significant figures. The solution of (5) agrees with similar accuracy to the Bohr radius and the known resonant frequency of the hydrogen atom. By involving the effect of the magnetic field upon the electron this solution forms an extension of Bohr's theory. As it stands (5) contains four variables yielding the deterministic motion of the electron given by (4). This agrees with the four quantum numbers known via quantum mechanics.

If the intrinsic energy of the system changes from that of free-space ε_o and μ_o ((3f), (3g), and (3i)) the EM fields within the atom can adjust altering the atomic and molecular binding structures. In effect this means that the radial and spin states of the two photons involved in the binding energy can adapt to the energy change where the photons themselves are assumed to have a composite

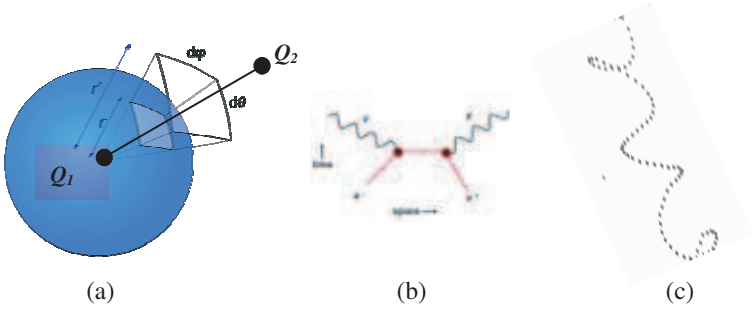

(a) (b) (c)

Figure 1: Field forms. (a) CEM, (b) QFT, (c) SFT.

structure. Now the system has six degrees of freedom including the E- and H-fields in response to the change in ambient energy. The two extra variables give a range of variation orthogonal to the phase diagrams of atoms. A typical phase diagram shows only a solid line separating the various phases. SFT indicates a small range of binding structures that depend on the intrinsic energy of the system.

2. THE ELECTRIC AND MAGNETIC FIELDS OF CEM, QFT AND SFT

The photon streams of SFT are taken between centres of rotation, not between charges as in CEM and QFT. Thus two distances are involved in the bispinorial motion and not one. The fields in SFT are discrete quanta, photons, rather than the continuous vector fields of CEM. QFT also models the fields as discrete quanta. However each individual field in QFT may be taken over the entire range of solid angles connecting any number of particles depending on the geometry and the number of interacting atomic particles. The field can be shown as a small wavy line within Feynman diagrams but the QFT mathematics does not specify any actual path, only the start and end points where Dirac-delta functions are used to insert propagator kernels and Greens functions depending on the field and its geometry. In QFT the field is actually a potential, not the E- and H-fields of SFT. In QFT the fields (potentials) are modeled as impulse functions specified at charge-points. Within SFT, a pair of particles defines the bispinorial field and its motion, this pair of particles and its bispinorial field form a unique couple. Due to orthogonality the fields of this couple do not influence any other charges apart from the couple. The transit of the SFT field is specified via the bispinorial function and assumes various motions including spiral-helices as it transits between the electron and proton within the hydrogen atom. Certainly there is a vast difference between this SFT time-variant field motion and the time-invariant CEM where the field ubiquitously covers all solid angles with no definition other than its vector nature as to the actual field motion, field flux being the only indicator of field motion. Similarly the uncertainty of the field within QFT is related to its lack of a complete and coupled EM bispinorial field form.

There are other major differences including an absence of HUP within SFT. As the photon is modeled via bi-spinors uncertainty is obviated. In SFT the electron's self-fields are modeled via a complete EM function that explicitly includes both E- and H-fields, enabling the complete analysis of the mutual self-field effect between two particles. Unlike the quantum potentials that are expectations yielding probabilistic solutions, the bi-spinorial field variables of SFT allow completely deterministic solutions. This results in a clearer picture of the physics that includes the particle-photon interactions and the binding mechanism. The solution is complete (coupled) and based on the first-order ML equations, hence neither special relativity nor gauge symmetry is problematic. The bi-spinor field variables of SFT are a priori relativistic and its solutions analytic rather than numerical. In EM applications gauge symmetry is maintained by analyzing pairs of particles and not just single particles. Similarly a pair of conjugate photons of finite mass do not constitute '*symmetry breaking*' of the Lagrangian as in QFT.

REFERENCES

1. Jackson, J. D., *Classical Electrodynamics*, 3rd Edition, John Wiley & Sons, New York, 1999.
2. Miller, A. I., *Early Quantum Electrodynamics, A Source Book,* Cambridge U. Press, Cambridge, U.K., 1995.
3. Fleming, A. H. J., "Electromagnetic self-field theory and its application to the hydrogen atom," *Physics Essays*, Vol. 18, No. 3, 265–285, 2005.

4. Fleming, A. H. J., "Self-field theory, analytic spectroscopy of the ordinary photon," *2nd Inter. Conf. on EHE*, Wroclaw, Poland, 18–23, 2007.
5. Fleming, A. H. J., "Analytic estimate for the mass of the photon," *PIERS Proceedings*, 1604–1607, Moscow, Russian, August 18–21, 2009.

Impact of Network Topology on the Matched-pulse-based Fault Detection

L. Abboud[1], **A. Cozza**[1], **and L. Pichon**[2]

[1]Département de Recherche en Électromagnétisme, SUPELEC
3 rue Joliot-Curie, Gif-sur-Yvette 91192, France
[2]Laboratoire de Génie Électrique de Paris (LGEP) — CNRS/SUPELEC
11 rue Joliot-Curie, Gif-sur-Yvette 91192, France

Abstract— An evaluation of the performance of the Matched-Pulse approach and the standard Time Domain Reflectometry is presented. The effect of the network topology on their effectiveness is studied, first through physical interpretation, then by means of a mathematical analysis. All the discussed ideas are finally illustrated through simulation results.

1. INTRODUCTION

The problem of fault detection and location in wire networks has gained an increasing importance in the last few years [1]. Wired networks are found in all modern systems, and are used to transmit different signals (control, alarm, etc.). That is why the issue of safe and reliable wiring systems is among the primary concerns of researchers and government agencies today [2].

There are several methods for wire testing, such as visual inspection, impedance testing [1], and reflectometry methods which are widely used today to help detecting and locating wire faults. These methods send a predefined testing signal down the wire network to be examined. They include Time Domain Reflectometry (TDR), which uses a fast rise time step or pulsed signal as the testing signal, Frequency Domain Reflectometry [3] which uses multiple sinusoidal signals, sequence TDR [4] which uses pseudo noise, etc. Generally, hard faults (open and short circuits) are detectable through standard reflectometry, while soft faults (damaged insulation, etc.) are more critical to detect, especially when dealing with complex wire networks configurations.

In [5], we introduced the Matched Pulse approach, based on the properties of Time Reversal [6], as an improvement of the existing standard TDR. The MP method proposes to adapt the testing signal to the network under test, instead of using a predefined testing signal, as for reflectometry methods. We have shown that this method results in a higher echo energy from the fault to be detected, when compared to TDR.

In this paper, we propose to study the impact of the network topology on the performances of the TDR and MP approaches. That is, to analyze the effect of the network elements (discontinuities, loads, etc.) on the effectiveness of these two methods, in order to have a tool which will allow us to predict, for any system, to which extent the MP might present an advantage over the TDR concerning the detectability of an eventual fault, and which are the elements governing directly those performances.

We first propose to establish the general assumptions under which we will be working in this paper, and then begin our study with a physical interpretation to analyze the impact of the wire network elements on the performances of the TDR. Then, in order to be able to compare our two approaches, we consider a mathematical study based on the definition of a detection gain. A validation of the discussed points is finally presented through simulation results.

2. GENERAL ASSUMPTIONS

We consider uniform lossless single-conductor transmission lines. Here we point out that, in this paper, we are not interested in studying the effect of the length of these lines, provided that they will only introduce time delays. So, as long as any branch in the network is longer than the spatial support of the injected pulse, the time resolution will not be affected and the separation of the first echoes propagating in the system is insured.

We also consider that the testing signal (i.e., the injected signal) is the input to our system, and the reflected signal is the output; the transfer function of such a linear system in the absence of the fault is denoted as $H_0(f)$ and in the presence of the fault as $H_F(f)$. Generally, we can either analyze the reflected signal directly [7], or take the difference of the two reflected signals (with and without the fault), especially when considering soft faults [8], so that the echo from the fault is more

easily detected. This latter method is the one we will be using, assuming that our system is linear time invariant. Analyzing the difference of the two reflected signals is consequently equivalent to analyzing the output of an equivalent system whose transfer function $H(f)$ is defined as follows

$$H(f) = H_F(f) - H_0(f) \tag{1}$$

This equivalent system will be referred to as the difference system. We also note that the reference pulse we will be using is denoted as $I_0(f)$ in the frequency domain (and $i_0(t)$ in the time domain). This pulse is the same as the injected signal in the standard TDR.

3. PHYSICAL STUDY

We evaluate the impact of different elements in the network on the performance of the standard TDR. But first we propose an equivalent representation of the wire network to better illustrate the discussed ideas.

3.1. Equivalent Representation of the Wire Network

We propose to represent any wire network as illustrated in Figure 1(a), where uniform scalar transmission lines are represented with lines (here the transmission lines are not physical objects, they only introduce delays, based on the general assumptions), junctions and terminal loads with circles, and the source is represented with a square. Two parallel lines indicate the position of the fault. We remind that the input to our system (the injection point) and the output (where we analyze the reflected signal) are the same.

3.2. Impact of the Position of the Network Elements

Based on this representation, we notice that the system can be divided into two main parts: the one in front of the fault (i.e., from the source side or upstream of the fault), and the other downstream of the fault. When we use the difference system, the first peak obtained when examining the TDR echo would correspond to the first interaction with the fault. Furthermore, this first reflection on the fault does not depend on the elements behind it, so any change in the elements upstream of the fault would affect all the echoes propagating in the system, including this first peak, whilst any change in the elements downstream of the fault will not affect this first peak.

3.3. Equivalent Reflection Coefficient of the Fault at the Source Position

We denote by Γ_F the reflection coefficient at the fault position (see Figure 1(b)). Here we point out that this coefficient is observed in the time domain; it describes the first interaction with the fault. Consequently, in the difference system, and if the fault is in front of the source (i.e., not separated from the source by any other discontinuity), the first peak we will be observing when examining the reflected signal would correspond to this first interaction; but if the fault is masked from the source by one or more discontinuities, then this first peak would undergo several reflections before arriving to the source position. Consequently, the equivalent reflection coefficient at the source position, denoted as Γ'_F, would change according to the network topology; more precisely, and based on the analysis in the previous paragraph, according to the discontinuities separating the fault from the source.

So why should we be interested in this first peak? because in standard TDR, when determining the presence of an eventual fault, we are also interested in locating this fault. The first peak we observe will help us determine the time delay required to reach the fault from the source, and eventually the position of this fault. We also note that this first peak might or not have the highest amplitude, depending on the system's configuration, along with the nature and position of the fault.

Consequently, we will now determine an expression of Γ'_F, in terms of the network topology. We consider the example illustrated in Figure 1(b), where τ is the transmission coefficient from the first junction. We are interested in finding the amplitude of the first peak arriving to the source position and corresponding to the first interaction with the fault. The amplitude of the voltage wave passing through the first junction of the network is modified by a factor of τ. This wave arrives to the fault and then a part is reflected; its amplitude is modified by a factor of $\tau\Gamma_F$. This wave will next follow the reverse path, and when arriving to the source, the modification in the amplitude will be $\tau^2\Gamma_F$. This whole path is the shortest one to the fault, and since we are considering the difference system, any other echoes which may interact with the first peak or arrive to the source position before it will not be observed in the TDR echo (they are the same with and without the fault, thus the subtraction of the reflected signals in both cases eliminate them).

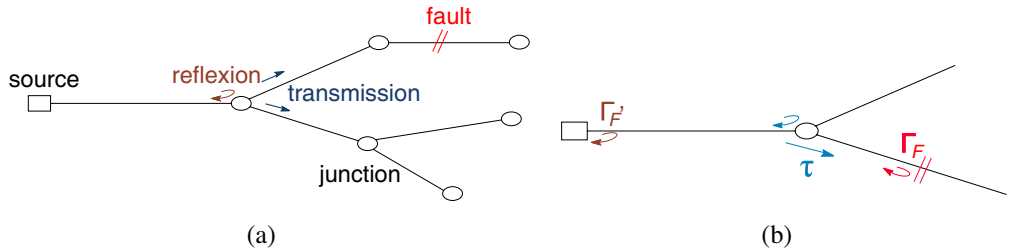

Figure 1: (a) Equivalent topological representation of a wire network; (b) An example illustrating the reflection coefficients $\Gamma_F^{'}$ and Γ_F.

So, in the general case, where N denotes the number of discontinuities separating the source from the fault, τ_i the transmission coefficient associated with the discontinuity number i, α_i the amplitude of the peak number i, and A the amplitude of the injected pulse, then we can say that, in the TDR case, when analyzing the echo, the amplitude α_1 of the peak corresponding to the first interaction with the fault, as seen from the source would be:

$$\alpha_1 = A\Gamma_F' = A\Gamma_F \prod_{i=1}^{N} \tau_i^2 \tag{2}$$

One important point is that, while we have till now seen that the highest peak in the standard TDR case does not necessarily correspond to the position of the fault, we did not examine the problem in the MP case. Here, it is difficult to try to follow the path of the dominant echo. Nevertheless, by analyzing the problem mathematically, let us inject our reference pulse into the network. The obtained TDR echo contains several peaks. If t_i denotes the instant when the peak number i appears, then the first peak will be situated at a time delay t_1 from the source. Before time reversing this echo, let us define a time reference by shifting this echo of t_1. The first peak is now the one situated at the origin. Also, the testing signal is now a time-reversed shifted version of the impulse response of the system $h(t)$. By injecting it into the system, we are convoluting it again with $h(t)$, thus effectively autocorrelating $h(t)$. By calculus, one can easily verify that this autocorrelation has a maximum at the position t_1, which amplitude is $A\sum_i \alpha_i^2$, actually corresponding to the position of the first peak in the TDR case. Thus, in the MP case, we know (by construction) that the peak with the highest amplitude corresponds to the fault.

So far we have analyzed some of the factors influencing the MP and TDR performances, but not yet compared the two approaches. In the next section, we propose a mathematical tool which will allow us to do that.

4. DETECTION GAIN

To be able to evaluate the advantages of the MP method, we need to find a criterion that enables us to compare it with other methods, such as standard TDR.

In [5], we defined a gain based on the normalized energies of the echoes in both cases. But in the detection process, we know that we are interested only in the peak corresponding to the fault. That is why we propose to define a new gain, referred to as the detection gain G.

Let $\mathcal{E}_{\mathrm{TDR}}^1$ denote the energy of the first peak in the TDR case, and $\mathcal{E}_{\mathrm{MP}}^1$ the energy of the peak corresponding to the fault in the MP case. We consider that the energy of the template $I_0(f)$ is normalized, so $\mathcal{E}_{\mathrm{TDR}}^1$ is the square of the cross correlation function of the TDR echo with $i_0(t)$ at time t_1. The same definition applies in the MP case, at the instant t_1' corresponding to the fault. We have

$$\mathcal{E}_{\mathrm{TDR}}^1 = \left| \int H(f)|I_0(f)|^2 e^{-j2\pi f t_1} df \right|^2 \tag{3}$$

and

$$\mathcal{E}_{\mathrm{MP}}^1 = \left| \int |H(f)|^2 (I_0^*(f))^2 e^{-j2\pi f t_1'} df \right|^2 \tag{4}$$

If $\mathcal{E}_{\mathrm{TDR}}$ and $\mathcal{E}_{\mathrm{MP}}$ are respectively the energies of the testing signals in the TDR and MP cases, then

G is defined as

$$G = \frac{\mathcal{E}^1_{\mathrm{MP}}/\mathcal{E}_{\mathrm{MP}}}{\mathcal{E}^1_{\mathrm{TDR}}/\mathcal{E}_{\mathrm{TDR}}} \tag{5}$$

We will now determine a simplified expression of this gain based on the previously discussed ideas.

In general, we know that any spectrum can be represented by a sum of sub spectrums where the spectrum is a constant. So let us consider the case where $|I_0(f)|$ is constant. Under the hypothesis that the coefficients α_i and α_j are uncorrelated, we have:

$$\mathcal{E}^1_{\mathrm{TDR}} = \alpha_1^2 \tag{6}$$

and

$$\mathcal{E}^1_{\mathrm{MP}} = \left| \sum_{i=1}^{N} \alpha_i^2 \right|^2 \tag{7}$$

The detection gain in this case is

$$G = \frac{\sum_{i=1}^{N} \alpha_i^2}{\alpha_1^2} \tag{8}$$

We notice that $G \geq 1$. This result is very interesting; first it proves that the MP is always beneficial compared to standard TDR, when it comes to detecting an eventual fault. We also notice that, the more we have peaks in the TDR echo (which is the testing signal in the MP case), the more the MP is effective compared to standard TDR, where the different peaks (besides the one corresponding to the fault) are considered to be a nuisance in the detection process.

In the next section, we consider numerical examples in order to validate all the previously discussed ideas.

5. SIMULATION RESULTS

5.1. Analyzed Configurations

We consider the configurations illustrated in Figure 2, where the fault is in front of the source (Figure 2(a)) in the first case, then masked from the source by several discontinuities (Figure 2(b)) in the second case.

5.2. Numerical Results

We simulated the voltage propagation in the configurations of Figure 2 using the transmission line theory as presented in [9]. The characteristic impedance of the lines is chosen to be 75 Ω (such as for some coaxial cables). We will verify the obtained values of the detection gain according to the general formula (Equation (5)) and the simplified formula (Equation (8)). In this last case, we will be examining a certain number of peaks, thus specifying an inferior limit to the gain (referred to as a threshold in Table 1).

In the first case (Figure 2(a)), we chose a value of the fault equal to 600 Ω, corresponding to a soft fault. The inferior limit of G in this case is 1.55. When we calculate its exact value, we find $G = 1.73$. In the second case (Figure 2(b)) when the fault is masked from the source by several discontinuities, we chose several values of the fault, illustrated in Table 1. In this configuration, the fault is separated from the source by a discontinuity at 5 m and a junction at 14 m. The numerical values obtained when calculating the inferior limit of the detection gain, along with its exact values are illustrated in Table 1. When examining those results, we notice that the more the fault is soft (i.e., the reflection coefficient at the source position is small), the more the MP becomes effective when compared to standard TDR. If we also compared the two configurations of Figure 2 when the fault's value is 600 Ω, we notice that when the fault is embedded in the system, the gain's value is

Table 1: Numerical results.

Fault value (Ω)	Predicted gain (threshold)	Calculated gain
Short	2.33	2.6
30	3.4	4
600	7.7	9.22

greater than the case where the fault is directly in front of the source. In fact, in the first case we have a greater number of peaks than in the second case; so as predicted by the Equation (8), we have a greater value of the detection gain.

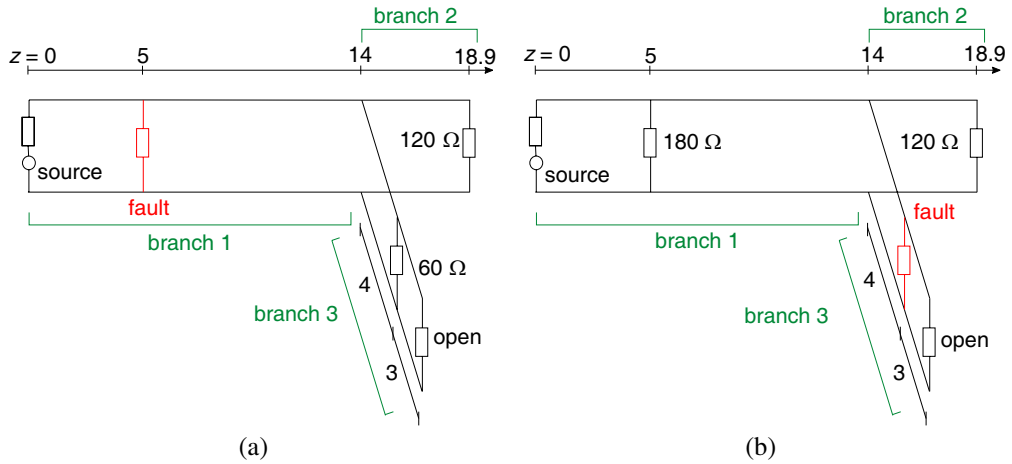

Figure 2: The analyzed networks, showing the positions of the faults in the two studied cases. All lengths are in meters.

6. CONCLUSION

In this paper, we evaluated the impact of the network topology on the performance of the TDR and MP approaches. A physical study allowed us first to state what are the most influencing factors on the effectiveness of the TDR, then a mathematical analysis proved the advantage of the MP method over the standard TDR. The discussed ideas were finally verified through simulation results. This whole study allowed a better understanding of the factors influencing the TDR performance, thus enabling us, for any configuration, to predict the effectiveness of the MP approach compared to standard TDR.

REFERENCES

1. Furse, C. and R. Haupt, "Down to the wire," *IEEE Spectrum*, Vol. 38, No. 2, 34–39, 2001.
2. "Review of federal programs for wire system safety," National Science and Technology Council, White House, Final Report, Nov. 2000.
3. Furse, C., Y. C. Chung, R. Dangol, M. N. G. Mabey, and R. Woodward, "Frequency-domain reflectometery for on-board testing of aging aircraft wiring," *IEEE Transactions on Electromagnetic Compatibility*, Vol. 45, No. 2, 306–315, May 2003.
4. Smith, P., C. Furse, and J. Gunther, "Analysis of spread spectrum time domain reflectometry for wire fault location," *IEEE Sensors Journal*, Vol. 5, No. 6, 1469–1478, Dec. 2005.
5. Abboud, L., A. Cozza, and L. Pichon, "Utilization of matched pulses to improve fault detection in wire networks," *The 9th International Conference on ITS Telecommunications*, Oct. 2009.
6. Fink, M., "Time reversal of ultrasonic fields — Part 1: basic principles," *IEEE Transactions on Ultrasonics, Ferroelectrics, and Frequency Control*, Vol. 39, No. 5, 555–566, Sep. 1992.
7. Furse, C., Y. C. Chung, C. Lo, and P. Pendayala, "A critical comparison of reflectometry methods for location of wiring faults," *Smart Structures and Systems*, Vol. 2, No. 1, 25–46, 2006.
8. Griffiths, L., R. Parakh, C. Furse, and B. Baker, "The invisible fray: A critical analysis of the use of reflectometry for fray location," *IEEE Sensors Journal*, Vol. 6, No. 3, 697–706, Jun. 2006.
9. Paul, C. R., *Analysis of Multiconductor Transmission Lines*, K. Chang, Ed., Wiley-Interscience, 1994.

Modelling and Validating Ferrite-core Probes for GMR-eddy Current Testing in Metallic Plates

M. Cacciola, **G. Megali**, **D. Pellicanò**, **S. Calcagno**, **M. Versaci**, **and F. C. Morabito**
DIMET Department, University "Mediterranea" of Reggio Calabria
Via Graziella Feo di Vito, I-89100 Reggio Calabria, Italy

Abstract— Non Destructive Testing techniques are more and more exploited in order to quickly and cheaply recognize flaws into the inspected materials. Within this framework, modelling is a powerful tool for inspection improvements. It helps probe-coil designers to optimize sensors for each examination requirement, providing better understanding of the involved physics, supporting operator training and increasing defect analysis reliability. The effect of the ferrite core is analyzed in order to optimize the design of probe-coils and study various configurations of inspection. Particularly, Finite Element based analyzes will be carried out into this path. Direct problem will be assessed, and direct model will be formulated, dependent by different parameters, e.g., coil shape, working frequencies and so forth. The model will be subsequently validated by in-lab experimentations.

1. INTRODUCTION

Non Destructive Testing and Evaluation (NDT/E) of metallic materials offers an exciting and interesting challenge to both researchers and applied technologists. For this kind of materials, the major problem of interest is the detection, location, orienting and sizing of single cracks, nondestructive evaluation of homogenous materials is presently in a state of detecting a variety of damage modes. In plane words, the present state of knowledge concerning what damage mode in metallic materials is responsible for the final failure process is still unclear. Hence, it is still not possible to suggest to NDT/E personnel exactly what type of damage, size, orientation, etc. needs to be found in an inspection process. Hence, the challenge. The excitement for researchers in the area of NDT/E of metallic plates is in the fact that NDT/E is presently playing an important role in helping to identify damage mechanisms in homogenous materials and to characterize the role played by these damage mechanisms in the final failure process. A variety of NDT/E techniques has been applied extensively to the investigation and characterization of metallic materials. Generally, one finds that a combination of complementary NDT/E techniques are appropriate, and often required, to obtain as complete information as possible on the damage state of the specimen. Eddy-current (EC) methods are commonly applied because of their relative ease of their use, and the relative amount of information that can be obtained from them. As far as metals are concerned, the EC techniques has been used for quite some time for varied applications such as the detection of cracks, porosities and inclusions; metal sorting, evaluation of plate or tubing thickness, measurement of coating thickness and the thickness of non-conducting films on metallic bases and so forth 1 When a coil carrying alternating current is brought near an electrically conducting material, eddy-currents are induced in the materials by electromagnetic induction. The magnitude of the induced eddy currents depends upon the magnitude and frequency of alternating current; the distance between the current-carrying coil and the material under test; the presence of defects or inhomogeneities in the material and the physical properties of the material. The induced eddy-currents modulate the impedance of the exciting coil or any secondary coil situated in the vicinity of the test material. The difference between the original coil impedance and the modulated coil impedance (due to the presence of eddy currents) is monitored to obtain meaningful information regarding the presence of defects or changes in physical, chemical or microstructural properties. Typical testing configurations may consist of ferrite core coil probes, placed above a planar (or at least locally planar) conductive specimen and operating in the time-harmonic domain, at frequency depending on the problem (typically between a few [Hz] to a few [MHz]) [2]. The aim of ferrite core is to focus the magnetic fields into the specimen, in order to increase the probe sensitivity to the defect. For each application, the coil model as well as the operating frequencies are set according to the task. This work proposes an integrated approach starting from the design and implementation of a novel probe in order to optimize the sensor effect and the drop-in suppression, the operating parameters of the frequency and field strength. For our purposes, a Finite Element Analysis (FEA) code will be exploited for geometrical and physical modelling. In order to deepen the electromagnetic direct problems,

in fact, scientists implement suitable models, able to describe as better as possible the physical behavior of the matter. This paper, dealing with the detection of defects in stainless steel plates, proposes an integrated approach starting from the design and implementation of a novel ferrite-core probe. Subsequently, inspecting performances will be tested by experimentations carried out at our NDT/E Lab. Exploited sensing will be based on a Giant MagnetoRestistance (GMR) device, i.e., a system composed by a GMR sensor [3] and a board able to transmit the electromagnetic response to a general purpose Personal Computer. It has been tested by experimentations carried out at the NDT/E Lab, Faculty of Engineering, University "Mediterranea" of Reggio Calabria, Italy. For our purposes, a FEA code has been exploited for geometrical and physical modelling. Subsequently, experimental measurements have been carried out in order to validate results of simulations.

2. PROPERTY OF THE FERRITE-CORE

Magnetic lines of force are needed to create eddy currents in the material to be investigated. Analyzing metallic materials by ferromagnetic coils, the closer the coil, the narrower the flux lines. Ferrite is rigid and brittle. Like other ceramics, ferrite can chip and break if handled roughly. Luckily it is not as fragile as porcelain and often such chips and cracks will be merely cosmetic. Ferrite varies from silver gray to black in color. The electromagnetic properties of ferrite materials can be affected by operating conditions such as temperature, pressure, field strength, frequency and time. There are basically two varieties of ferrite: soft and hard. This is not a tactile quality but rather a magnetic characteristic. Soft ferrite does not retain significant magnetization whereas hard ferrite magnetization is considered permanent. For our applications, we have exploited a ferrite RM6-N48 produced by Epcos (see Fig. 1 for details).

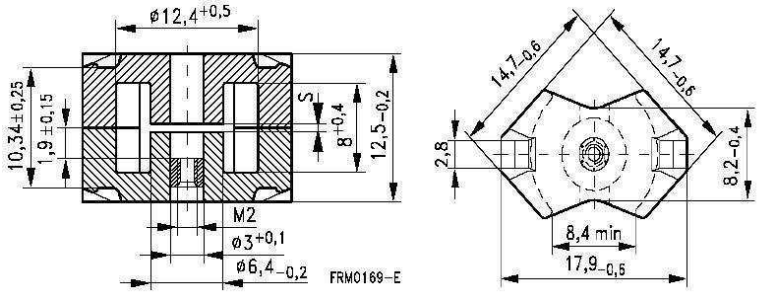

Figure 1: RM6-N48-Epcos ferrite-core without the air gap and with a hole in the middle.

3. FEA APPROACH

In order to simulate the response of a probe to the presence of defects, it is necessary to study how a probe excites the specimen to be tested. Usually, the goal is the optimization of probe and the assessment of such perturbation as lift-off (from 0.3 [mm] to 1 [mm] with a step of 0.1 [mm]) and tilting (from 0 [deg]to 1.5 [deg]with a step of 0.1 deg). A FEA approach will be exploited for this purpose. A probe is placed above and parallel to a metal block. It is made of an E-profiled ferrite core, excited by a coaxial coil. In our simulations, the probe moves along the specimen at a specified speed. We verify the distortion of EC's flux lines caused by the presence of defect and the magnetic field's density while the probe moves over the surface. In our FEAs, since we use $\mathbf{A}$-Ψ formulation [4], just the z-component of magnetic potential $\mathbf{A}$ is non null. Geometrical dimensions of our model are listed in Table 1. For our purpose we verified the distortion of the magnetic field density [T] [5, 6] to detect the defect presence in the specimen. In the case of quasi-static magnetic fields, Ampère-Maxwell's equation can be written as:

$$\nabla \times \mathbf{H} = \mathbf{J} \tag{1}$$

where $\mathbf{H}$ represents the magnetic field and $\mathbf{J}$ the current density, respectively. If we consider a moving object with velocity $\mathbf{v}$ relative to the reference system, the Lorentz force equation establishes that the force $\mathbf{F}$ per charge q is then given by:

$$\frac{\mathbf{F}}{q} = \mathbf{E} + \mathbf{v} \times \mathbf{B} \tag{2}$$

where $\mathbf{E}$ represents the electric field; $\mathbf{v}$ the instantaneous velocity of the object derived from the expression of the Lorentz force and $\mathbf{B}$ the magnetic induction. In a conductive medium, an observer travelling with the geometry sees the current density (considering that σ is the electric conductivity) $\mathbf{J} = \sigma(\mathbf{E} + \mathbf{v} \times \mathbf{B}) + \mathbf{J^e}$; therefore, we can rewrite (1) as follows:

$$\nabla \times \mathbf{H} = \sigma(\mathbf{E} + \mathbf{v} \times \mathbf{B}) + \mathbf{J^e} \tag{3}$$

where $\mathbf{J^e}$ [A/m^2] is an externally generated current density. Considering, for a transient analysis, the definitions of magnetic vector potential $\mathbf{A}$ and electric scalar potential V:

$$\begin{aligned} \mathbf{B} &= \nabla \times \mathbf{A} \\ \mathbf{E} &= -\nabla V - \frac{\partial \mathbf{A}}{\partial t} \end{aligned} \tag{4}$$

and the constitutive relationships:

$$\mathbf{B} = \mu_0 \mu_r \mathbf{H} + \mathbf{B_r} \Leftrightarrow \mathbf{H} = \mu_0^{-1} \mu_r^{-1} \times (\mathbf{B} - \mathbf{B_r}) \tag{5}$$

where μ_0 and μ_r are free space and relative magnetic permeability and $\mathbf{B_r}$ is the residual magnetization. We may rewrite (3), by substituting (4) and (5) in it, as:

$$\sigma \frac{\partial \mathbf{A}}{\partial t} + \nabla \times \left(\mu_0^{-1} \mu_r^{-1} \nabla \times (\mathbf{A} - \mathbf{B_r})\right) - \sigma \mathbf{v} \times (\nabla \times \mathbf{A}) + \sigma \nabla V = \mathbf{J^e} \tag{6}$$

Since we are interested in perpendicular induction current, only the z-component of $\mathbf{A}$ is non null. Therefore, the formulation of the 3D Equation (5) is simplified to:

$$\sigma \frac{\partial \mathbf{A}_z}{\partial t} + \nabla \times \left(\mu_0^{-1} \mu_r^{-1} \nabla \times (\mathbf{A}_z - \mathbf{B_r})\right) - \sigma \mathbf{v} \times (\nabla \times \mathbf{A}_z) = \mathbf{J}_z^{\mathbf{e}} \tag{7}$$

where ΔV is the difference of electric potential and L is the thickness along the z-axis. The Partial Difference Equation (PDE) formulation of Equation (7) can be written as:

$$\sigma \frac{\partial A_z}{\partial t} + \nabla \cdot \left(\mu_0^{-1} \mu_r^{-1} \nabla \times (A_z - \mathbf{B_r})\right) - \sigma \mathbf{v} \cdot \nabla A_z = J_z^e \tag{8}$$

In this way we calculated the magnetic vector potential $\mathbf{A}$ in a generic subdomain Ω. For our aim, it is necessary to impose the boundary conditions as follows. Magnetic field ($\mathbf{n} \times \mathbf{H} = \mathbf{n} \times \mathbf{H_0}$) for boundary of air where acting the rotating magnetic field; for remaining boundaries, included the defect, the continuity is assured by the expression $\mathbf{n} \times (\mathbf{H_1} - \mathbf{H_2}) = 0$ [7, 8]. Table 2 resumes the values of electrical parameters.

4. IN-LAB EQUIPMENT AND RESULTS ABOUT CRACK DETECTION

Simulations carried out by FEA approach have been exploited to build a new exciting ferrite-core probe for detecting cylindrical defects in stainless steel plates by means of GMR sensor [9]. According to the FEA simulations, the coil is able to sense defect presence in superficial analysis, until a depth of 4 [mm]. The best arrangement, according to FEA simulations, has been applied: lift-off 0.3 [mm] and tilting 0 [deg]. The exciting coil forms a part of a ferrite-core-ECT probe. The probe has been designed and built based upon the proposed exciting system to evaluate its efficiency and benefits. During our in-lab measurements, frequency f_{exc} and current I_{eff} have been

Table 1: General settings of numerical models.

Property	Setting
Material used for the specimen	Stainless steel, not-magnetic, isotropic
Dimension of specimen	100 [mm] × 40 [mm]
Electric conductivity	$4.032 * 10^6$ [S/m]
Diameter of the defect	2 [mm]
Height	4 [mm]

Table 2: Electrical parameters.

Parameter	Dimension
f_{exc}	60 [kHz]
$\mathbf{B_r}$	0.150 [mT]
I_{eff}	100 [mA]
$\mathbf{v}$	0.5 [m/s]

varied according to the simulations. The performances of our new ferrite-core probe have been evaluated using experimental inspection of notches in a thick stainless steel. The plate specimen inspected has a length of 100 [mm], width of 100 [mm]. The sensor has been moved over the block by means of a 0.5 [mm] step-by-step automatic scanning, along axes, in order to map the interesting area. The design of new exciting system is represented in Fig. 3. Fig. 4 shows the final result of our in-lab measurement, according to FEA simulations. Applied quantities are $I_{exc} \simeq 100$ [mA] with a $f_{exc} \simeq 60$ [kHz]. The actually used sensor is a GMR device; it is equipped with a particular board able to convert magnetic measurements into voltages, in fact phase demodulation of the measured voltage gives a measurement proportional to the magnetic field parallel to the plane of the sample [10]. Figure 3: General schematic representation of the detection system.

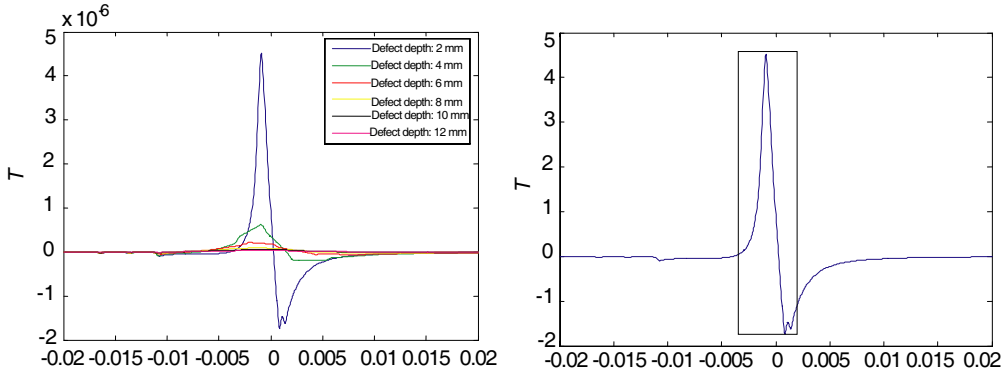

Figure 2: Numerical results obtained by FEA approach.

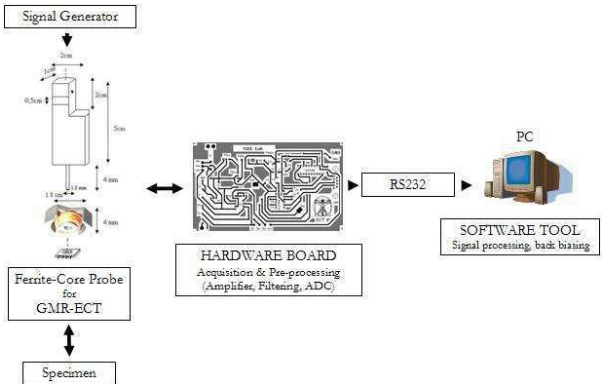

Figure 3: General schematic representation of the detection system.

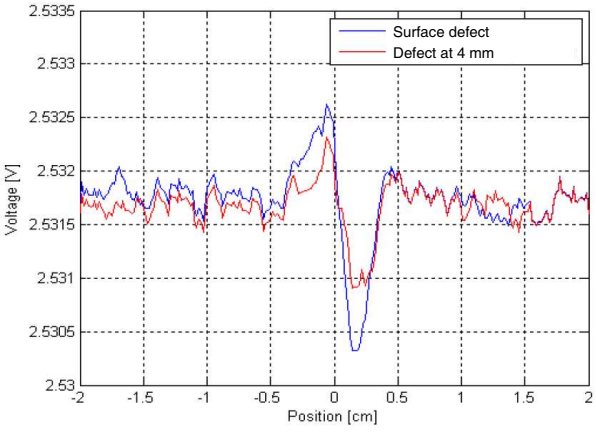

Figure 4: In-lab defect detection by GMR system.

5. CONCLUSION

In this paper, an implementation of ferrite-core-EC with GMR sensor for detection of defect in metallic plate is presented. For this problem, exploiting GMR sensor, a self-implemented time-dependent FEA code with 2D geometries has been studied to evaluate the investigation the variation of magnetic flux density (in modulus). The in-lab measurements confirmed the results obtained by FEA simulations, i.e., our exciting coil is able to detect defect presence for superficial analysis until 4 [mm]. FEA procedure should be validated for defect with higher depth or different shape. Results can be exploited in order to carry out the defect reconstruction in metallic plate from in-lab experimentations. In this case, an Artificial Neural Network approach could be validate to provide a good overall accuracy in reconstructing the extension of the defect. The authors are actually engaged in this direction.

REFERENCES

1. Yamada, S., M. Katou, M. Iwahara, F. P. Dawson, and S. M. Yamada, "Eddy-current testing," *IEEE Trans. Magn.*, Vol. 31, No. 6, 3185–3187, 1995.
2. Theodoulidis, T. P., "Model of ferrite-cored probes for eddy-current nondestructive evaluation," *J. Appl. Phys.*, Vol. 93, 3071–3078, 2003.
3. Fert, A., P. Grnberg, A. Barthlmy, F. Petroff, and W. Zinn, "Layered magnetic structures: Interlayer exchange coupling and giantmagnetoresistance," *J. Magn. Mater.*, Vol. 140, 1–8,1995.
4. Rodger, D., P. J. Leonard, and P. J. Lai, "Interfacing the general 3D A-ψ method with a thin sheet conductor," *IEEE Trans. Magn.*, Vol. 28, 1115–1117, 1992.
5. Koavi, R., "A study of cross-validation and bootstrap for accuracy estimation and model selection," *Proceedings of the 14th International Joint Conference on Artificial Intelligence*, 1137–1143, 1995.
6. Lewis, A. M., "A theoretical model of the response of an eddy-current probe to a surface-breaking metal fatigue crack in a flat test piece," *J. Appl. Phys.*, Vol. 25, 319–326, 1992.
7. Trevisan, F. and L. Kettunen, "Geometric interpretation of discrete approaches to solving magnetostatics," *IEEE Trans. Magn.*, Vol. 40, 361–365, 2004.
8. Tsuboi, H. and T. Misaki, "Three dimensional analysis of eddy current distribution by the boundary element method using vector variables," *IEEE Trans. Magn.*, Vol. 23, 3044–3046, 1997.
9. Megali, G., M. Cacciola, D. Pellicanó, and F. C. Morabito, "Recent patents on integrated software/hardware GMR-based systems and applications for PCB inspection," *Recent Patent on Electrical Engineering*, Vol. 2, 82–91, 2009.
10. Buonsanti, M., S. Cacagno, F. C. Morabito, and M. Versaci, "Eddy current and fuzzy inference to control defect growth in reinforced concrete," *Trans. Tech. Publications*, Vol. 345, 1291–1294, 2007.

Rotating Electromagnetic Field for Crack Detection in Railway Tracks

M. Cacciola, **G. Megali**, **D. Pellicanò**, **S. Calcagno**, **M. Versaci**, **and F. C. Morabito**
DIMET Department, University "Mediterranea" of Reggio Calabria
Via Graziella Feo di Vito, Reggio Calabria I-89100, Italy

Abstract— The main problem about a railway analysis is detection of cracks in the structure. If these deficiencies are not controlled at early stages they might cause huge economical problems affecting the rail network (unexpected requisition of spare parts, handling of incident and/or accidents). Within this framework, the early and continuous use of Non Destructive Tests can be useful. In this context, Eddy Current Testing is increasing in importance and popularity. Particularly, in this paper we exploit the measure of normal component, with respect to the scanned surface, of magnetic field. Whilst the scientific literature proposes a lot of solutions for detecting sub-superficial defects, an open problem is related to the geometrical complexity of the structure and the relevant difficulty of crack detection. In this paper, we propose a Finite Element Method based approach for modelling a fast and accurate evaluation of the defect in railways tracks. The modelled system is strongly versatile and the choice of electrical parameters affect the design of new probes for this kind of inspection. In particular, we propose a solution exploiting a rotating electromagnetic field with very encouraging results: The proposed model is able to recognize deep and surface cracks even if their orientations is vertical to the longitudinal direction of the sensor.

1. INTRODUCTION

In order to improve manufacturing quality and ensure public safety, components and structures are commonly inspected for early detection of defects or faults which may reduce their structural integrity. Non Destructive Testing and Evaluation (NDT/E) techniques present the advantage of leaving the specimens undamaged after inspection. NDT/E involves treating defect detection and characterization as inverse problems. In experimental NDT/E, the available measurement data are exploited in order so some clues may emerge in the inspection signal that are possibly representative of structural modification of specimens, like cracks, flaws and phase transformations that develop to discontinuous deformations. NDT/E in the field of defects identification in metallic elements plays a remarkable role with special regard to those sectors where the material integrity is strictly required. As a consequence, the detection of defects in metallic materials, together with the relevant shape classification, provides the operator with useful information on the actual mechanical integrity of the specimen. It is presently possible to perform forward numerical simulations [1–3] very precisely and rapidly and concerning different applications of the NDT/E. With the evolution of computer systems and numerical methods, the interest in NDT/E has grown so much as problems that a few years ago appeared very difficult to be practically solved, can now be approached by numerical simulations. Cracks or other in-service expected discontinuities occurring in railway may lead to fracture and thus to operational danger. Where necessary, operational safety is guaranteed by the periodic non-destructive inspection of these components. Irregularities may not exceed a specified and limited extension. Moreover, irregularities are closely related to operating speed, covering distance, quality of the track, acceleration, profile wear, rail wear, stiffness bogey, and so on. For this reason, the initial inspection shall be exploited in order to observe all discontinuities or damages. Our numerical simulations were carried out according to the requirements and advices of international standards: European standard (EN), International Standard (ISO) and Unit Identification Code (UIC). As the EN or ISO standards approach the acceptance of rolling stock components in manufacturing stage and not directly in-service inspections, a study of UIC documents and experience achieved after 4 years inspections, in railway networks, focus the inspection requirements. The available rolling stock standards concerning NDT/E are:

- **ISO 1005-1:1994**: Railway rolling stock material — Part 1: Rough-rolled tyres for tractive and trailing stock — Technical delivery conditions;
- **ISO 1005-3:1982**: Railway rolling stock material — Part 3: Axles for tractive and trailing stock — Quality requirements;

- **ISO 1005-6:1994**: Railway rolling stock material — Part 6: Solid wheels for tractive and trailing stock — Technical delivery conditions.

The most common defects in railway are Rolling Contact Fatigue (RCF) cracks, flats and internal cracks initiated from manufacturing defects with diameter less than 1 [mm]. Thus, we assumed all these indications in our simulations. For track inspection, ECTs are generally utilized. Usually, exploiting ECTs, the variation of magnetic field $\mathbf{H}$, induced by the variation of eddy currents, is considered to detect the presence of cracks; particularly, the normal component of $\mathbf{H}$, i.e., $\mathbf{H}_{\perp}$, is measured by suitable sensors, since it is not influenced by the exciting coils. But, if the crack orientation is vertical to the longitudinal direction of the sensor, it could be insensitive to the crack presence itself. Therefore, an insensitive way of inspection could be very useful in order to improve the quality of the analysis. It can be represented by a magnetic rotating field, generated by a multi-transmitter exciting coil, inducing variation of the eddy current density without a mechanical movement. For our purposes, a Finite Element Analysis (FEA) code has been exploited for physical modelling [4]. It requires the geometrical and physical definition of the railway [5]. We verified the magnetic field density [6, 7] caused by the presence of defect. A suitable database of results has been generated in correlation with the rail and track inspection data. It gives the necessary information about discontinuities created in rail components during specific rail and track conditions. The paper is organized as follows: Firstly, a brief description of the principle of the rotating magnetic field is treated; than, the exploited approach and some important results are displayed and, finally, some conclusions are drawn.

2. THE FEA APPROACH

The proposed approach has been carried out by means of Finite Element Method code and the 2D $\mathbf{A}-\Psi$ formulation [9]. In the time-harmonic quasi-static case, Ampère-Maxwell's equation includes the displacement current:

$$\nabla \times \mathbf{H} = \mathbf{J} \tag{1}$$

where $\mathbf{H}$ represents the magnetic field and $\mathbf{J}$ the current density, respectively. If we consider a moving object with velocity $\mathbf{v}$ relative to the reference system, the Lorentz force equation establishes that the force $\mathbf{F}$ per charge q is then given by:

$$\frac{\mathbf{F}}{q} = \mathbf{E} + \mathbf{v} \times \mathbf{B} \tag{2}$$

where $\mathbf{E}$ represents the electric field; $\mathbf{v}$ the instantaneous velocity of the object derived from the expression of the Lorentz force and $\mathbf{B}$ the magnetic induction. In a conductive medium, an observer travelling with the geometry sees the current density (considering that σ is the electric conductivity) $\mathbf{J} = \sigma\left(\mathbf{E} + \mathbf{v} \times \mathbf{B}\right) + \mathbf{J^e}$; therefore, we can rewrite (1) as follows:

$$\nabla \times \mathbf{H} = \sigma\left(\mathbf{E} + \mathbf{v} \times \mathbf{B}\right) + \mathbf{J^e} \tag{3}$$

where $\mathbf{J^e}$ [A/m^2] is an externally generated current density. Considering, for a transient analysis, the definitions of magnetic vector potential $\mathbf{A}$ and electric scalar potential V, and the constitutive relationship for magnetic field and induction:

$$\begin{aligned} \mathbf{B} &= \nabla \times \mathbf{A} \\ \mathbf{E} &= -\nabla V - \frac{\partial \mathbf{A}}{\partial t} \\ \mathbf{B} &= \mu_0 \mu_r \mathbf{H} \Leftrightarrow \mathbf{H} = \mu_0^{-1} \mu_r^{-1} \mathbf{B} \end{aligned} \tag{4}$$

where μ_0 and μ_r are free space and relative magnetic permeability; we may rewrite (3), by substituting (4) in it, as:

$$\sigma \frac{\partial \mathbf{A}}{\partial t} + \nabla \times \left(\mu_0^{-1} \mu_r^{-1} \nabla \times \mathbf{A}\right) - \sigma \mathbf{v} \times (\nabla \times \mathbf{A}) + \sigma \nabla V = \mathbf{J^e} \tag{5}$$

Since we are interested in perpendicular induction current, only the z-component of $\mathbf{A}$ is non null. Therefore, the formulation of the 3D Equation (5) is simplified to:

$$\sigma \frac{\partial \mathbf{A}_z}{\partial t} + \nabla \times \left(\mu_0^{-1} \mu_r^{-1} \nabla \times \mathbf{A}_z\right) - \sigma \mathbf{v} \times (\nabla \times \mathbf{A}_z) = \sigma \frac{\Delta V}{L} + \mathbf{J^e}_z \tag{6}$$

where ΔV is the difference of electric potential and L is the thickness along the z-axis. The Partial Difference Equation (PDE) formulation of Equation (6) can be written as:

$$\sigma\frac{\partial A_z}{\partial t}+\nabla\cdot\left(\mu_0^{-1}\mu_r^{-1}\nabla A_z\right)-\sigma\mathbf{v}\cdot\nabla A_z=\sigma\frac{\Delta V}{L}+J_z^e \tag{7}$$

In this way, we calculated the magnetic vector potential $\mathbf{A}$ in a generic subdomain Ω. For our aim, it is necessary to impose the boundary conditions as follows. Magnetic field ($\mathbf{n}\times\mathbf{H}=\mathbf{n}\times\mathbf{H_0}$) for boundary of air where acting the rotating magnetic field; for remaining boundaries, included the defect, the continuity is assured by the expression $\mathbf{n}\times(\mathbf{H_1}-\mathbf{H_2})=0$ [10, 11]. The rotation effect of the magnetic field vector has been simulated by applying a uniform $\mathbf{B}$ vector, timely rotated according to the following Euler rotation formulation [12]:

$$\begin{bmatrix}\mathbf{x}(t+\tau)\\ \mathbf{y}(t+\tau)\end{bmatrix}=\begin{bmatrix}\cos(\omega t) & \sin(\omega t)\\ -\sin(\omega t) & \cos(\omega t)\end{bmatrix}\begin{bmatrix}\mathbf{x}(t)\\ \mathbf{y}(t)\end{bmatrix} \tag{8}$$

The simulations exploit the Finite Element Method (FEM) and require the geometrical and physical definition of the structure. Table 1 resumes these settings. For our purpose we verified the variation of the magnetic field's density (T) caused by the presence of the defect [6, 7]. For our aims we had imposed the choice of the magnitude of electrical parameters, according Table 2. The performances shown by the proposed solutions are very encouraging: The use of a rotating magnetic field allows not only to detect defects despite of their orientations, but also increases the ability of detecting very small cracks in railways. In Fig. 1, we depict typical defects (called "A": bottom defect; "B": middle defect and "C": top defect) and their representation of preferential direction for crack evolution.

3. SIMULATIONS AND RESULTS

In this section of the paper, we present the simulations carried out by our FEA approach, in order to detect the crack presence in railway. The cracks evolutions under consideration are inspected with

Table 1: Geometrical and physical parameters for simulation step.

Property	Setting
Railway dimensions	0.14×0.2 (m)
Electric conductivity	4.032×10^6 (S/m)

Table 2: Electrical parameters.

Parameter	Dimension
Frequency	50 [Hz]
Pulse	$2\pi f$ [rad/sec]
Magnetic Field	1×10^{-3} [T] in magnitude

Table 3: Geometrical parameters imposed in FEA analysis with a frequency of 50 (Hz) and a Magnetic Field applied of 1 (mT) in modulus.

Crack type	Height defect	Length defect
A	from 1 to 4 (mm)	1 (mm)
B	1 (mm)	from 1 to 5 (mm)
C	1 (mm)	20–60–100 (mm)

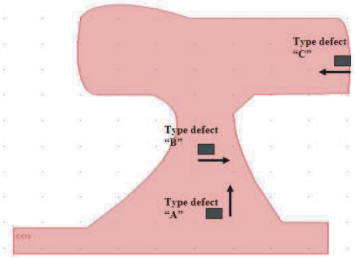

Figure 1: Geometrical representation of the problem and representation of preferential direction for crack evolution.

the main electrical parameters presented in the previous subsection. The dimensional evolution of cracks, according to the frequency analysis, is summarized in Table 3. Results have been compared with numerical output of a railway section without defects, inspected with the same electrical parameters. Fig. 2 depicts a comparison between the numerical simulations without effect and

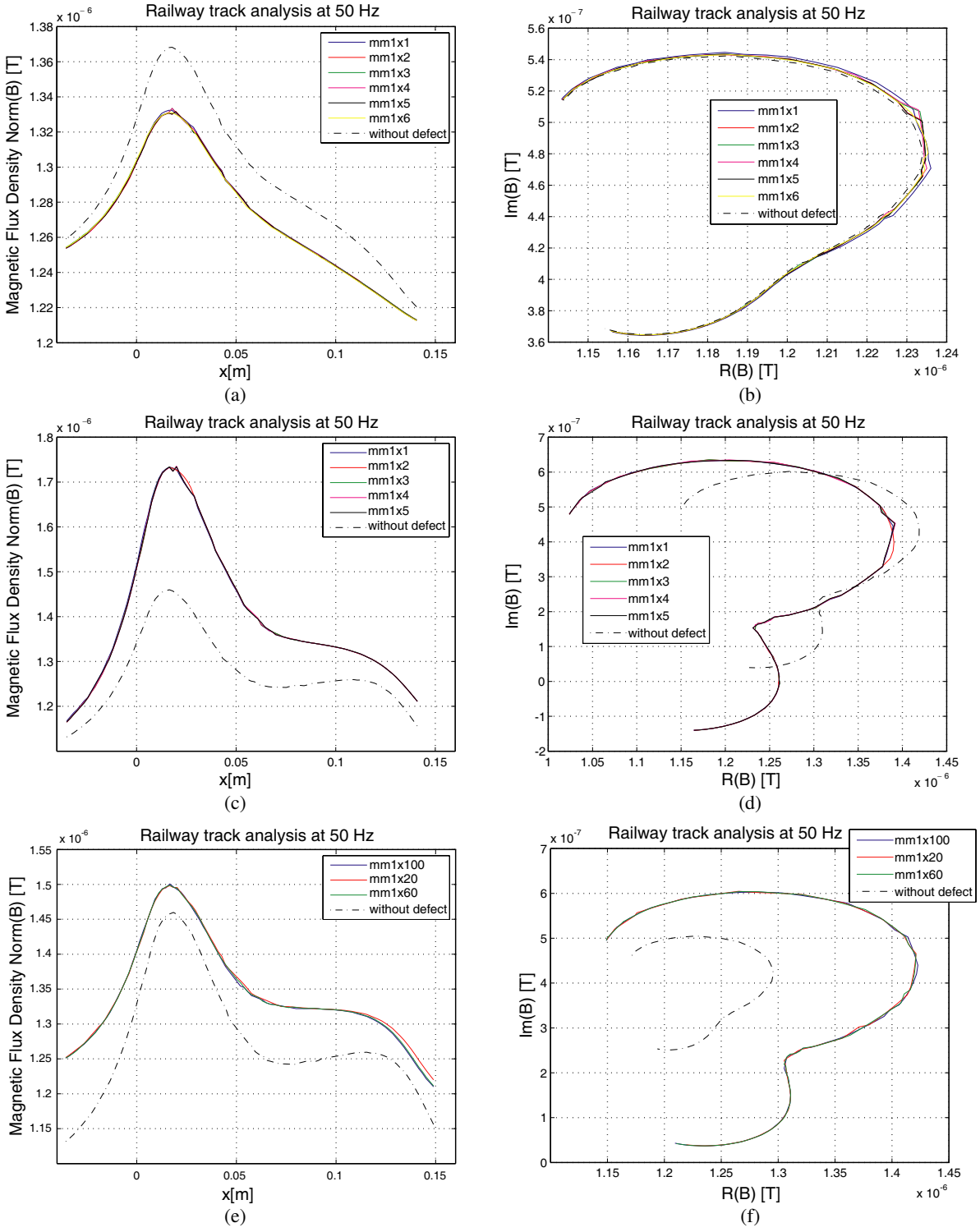

Figure 2: Variation of magnetic field's density module and Phase in presence of crack respect the railway without defect. (a) Modulus of magnetic flux density "A" type crack, (b) phase of magnetic flux density "A" type crack, (c) modulus of magnetic flux density "B" type crack, (d) phase of magnetic flux density "B" type crack, (e) modulus of magnetic flux density "C" type crack, (f) phase of magnetic flux density "C" type crack.

with the increase of the different kind of defects. For a complete investigation, we have obtained final graphs of the evolution of magnitude and phase of **B** for a frequency value of 50 [Hz]. For our aims, final graphs show the difference of information obtained on crack's presence or absence. Results demonstrate the accuracy of the developed simulations with the FEM model and its efficacy in the proposed problem.

4. REMARKS AND CONCLUSIONS

On the basis of the numerical method presented in this paper, we developed a finite element procedure for the analysis of the rotating magnetic field for the detection of railway tracks. For our analysis, we used a 2D section of the railway and simulated different sizes of defects according to the ISO rules. Specifically, exploiting the Ferraris effect, a 2D time dependent model has been studied to evaluate the distortion of the magnetic field density due to the defect presence: Rotating Magnetic Field provides a good overall accuracy in discriminating defect presence, as our experimentations demonstrate. At the same time, the procedure should be validate for other kind of defects, with different geometries or orientations. The same approach should find useful applications like: Detection of third-layer cracks, above all concerning alodine rivets within the framework of aging aircrafts' inspection, or micro-crack and micro-voids detection in welding process. Anyway, the presented results, which also can be considered as preliminary results, are very encouraging and they suggest the possibility of increasing and generalizing the performance model with a physical realization of a rotating field eddy current sensor. The authors are actually engaged in this direction.

REFERENCES

1. Bowler, J. R., "Eddy current interaction with an ideal crack: I. The forward problem," *J. Appl. Phys.*, Vol. 75, 8128–8137, 1994.
2. Tagaki, T., M. Hashimoto, H. Fukutomi, M. Kurokawa, K. Miya, and H. Tsuboi, "Benchmark models of eddy current testing for steam generator tube: Experiment and numerical analysis," *Int. J. Appl. Electrom.*, Vol. 4, 149–162, 1994.
3. Tagaki, T., H. Huang, H. Fukutomi, and J. Tani, "Numerical evaluation of correlation between crack size and eddy current testing signals by a very fast simulator," *IEEE Trans. Magn.*, Vol. 34, 2582–2584, 1998.
4. Specogna, S. and F. Trevisan, "Voltage driven coils within a discrete geometric approach to 3d eddy-currents," *Proceedings of the 11th International IGTE Symposium on Numerical Fields Calculation*, 81–84, 2004.
5. Tonti, E., "Algebric topology and computational electromagnetism," *Proceedings of the 4th Int. Workshop on Electric and Magnetic Fields*, 284–294, 1998.
6. Dodd, C. V. and W. E. Deeds, "Analytical solutions to eddy-current probe-coil problems," *J. Appl. Phys.*, Vol. 39, 2829–2838, 1968.
7. Lewis, A. M., "A theoretical model of the response of an eddy-current probe to a surface-breaking metal fatigue crack in a flat test piece," *J. Phys. D.: Appl. Phys.*, Vol. 25, 319–326, 1992.
8. Ferraris, G., "Rotazioni elettrodinamiche prodotte per mezzo di correnti alternate," *Atti dell'Accademia delle Scienze di Torino*, Vol. 23, 360, 1888 (in Italian Language).
9. Rodger, D., P. J. Leonard, and H. C. Lai, "Interfacing the general 3D A-ψ method with a thin sheet conductor model," *IEEE Trans. Magn.*, Vol. 28, No. 2, 1115–1117, 1992.
10. Tsuboi, H. and T. Misaki, "Three dimensional analysis of eddy current distribution by the boundary element method using vector variables," *IEEE Trans. Magn.*, Vol. 23, 3044–3046, 1987.
11. Weissenburger, W. D. and U. R. Christensen, "A network mesh method to calculate eddy currents on conducting surfaces," *IEEE Trans. Magn.*, Vol. 18, No. 2, 422–425, 1982.
12. Weisteinn, W., "Euler angles," MathWorld, a wolfram web resource, available online: http://mathworld.wolfram.com/EulerAngles.html.

High Resolution, Wide Coverage Termite Imager

N. W. D. Le Marshall[1], **G. A. Rankin**[2], **and A. Z. Tirkel**[3]

[1]School of ITEE, University of NSW@ADFA, Canberra, ACT 2600, Australia
[2]EWA Australia, Innovation House, Mawson Lakes Boulevard, Mawson Lakes, SA 5095, Australia
[3]Scientific Technology, 8 Cecil Street, East Brighton, VIC 3187, Australia

Abstract— This paper describes a 24 GHz radar sensor array, designed to detect and image termite activity, behind a wall, floor or ceiling. This sensor array employs a Matrix Enhanced Matrix Pencil (MEMP) algorithm for Direction of Arrival (DOA) estimation, and receiver focusing for 3D high resolution imaging. Here, we introduce transmitter beamforming, using MIMO techniques employing orthogonal codes, to significantly enhance the performance of the array.

1. INTRODUCTION

Termite detection is a challenging problem. A device which solves this problem has been developed by our group, and commercialized by Termatrac®. Termatrac® is a 24 GHz radar sensor, which can detect termite activity behind a wall, floor or ceiling, but its area of coverage is limited. In practice, this precludes the scanning of a room in a reasonable amount of time. Ideally, a device which could cover an entire wall or floor, and deliver high resolution images is preferable. Wide coverage requires long range, resulting in low Signal to Noise Ratio (SNR). High resolution requires short range, which results in high SNR, but significant wavefront curvature (near field effects). These requirements appear incompatible, and are unlikely to be achieved by a single array. Therefore, a hybrid array has been designed for that purpose [1]. It uses a compact 5×5 sub-array to cover a wide area, from a long range (1000 mm or greater), and provides direction of arrival (DOA) information about any insect activity. The Array Geometry is shown in Figure 1 and the instrument concept is shown in Figure 2.

The method employed for DOA determination is the Matrix Enhanced Matrix Pencil (MEMP) [2]. The detection of activity and its DOA directs the user towards an area of interest. At a range of 100 mm, a high resolution image of the insect movement is obtained from a random geometry beamforming sub-array, which is deployed specifically for this purpose. The reason for splitting the sensor into sub-arrays is that the MEMP (and other methods of determining DOA) performs poorly in the near-field, whilst classical beamforming copes well with wavefront curvature and the associated effects of near-field sensing.

The MEMP DOA estimation accuracy depends critically on the SNR, the presence of distant targets, and targets with vastly different bearings. Distant targets can be rejected by using a chirp,

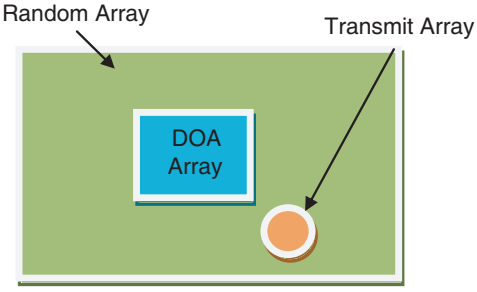

Figure 1: Array geometry.

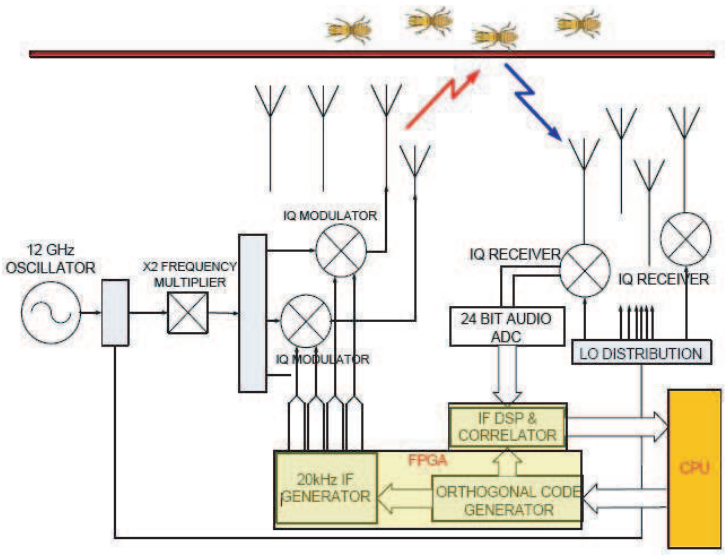

Figure 2: MIMO array block diagram.

and low-pass filtering in the receiver (FMCW range gating). A method of dealing with targets with bearings outside the sector of interest has been presented in [1]. An enhancement, which improves the SNR and rejection of out of sector targets, is transmitter beamforming, which concentrates more power on the target of interest, and less power on spurious targets, thus improving the SNR. Traditionally, this has been accomplished by controlling the magnitudes and phases the signals fed to transmit elements to produce the desired pattern. A major drawback of this approach is that only one beam can be formed at a time, and therefore sequential beamforming is required to complete a scan of a wide region of interest. Also, controlling the signals from individual transmitter elements to produce patterns is difficult and inaccurate. By contrast, processing the digitized signals from the receiver elements is precise, and can be performed in parallel in a FPGA. Therefore, Multiple Input Multiple Output (MIMO) processing, which allows transmitter beamforming after digitization at the receiver, is an attractive solution. In our implementation, the transmitter elements are fed signals which are modulated by a set of orthogonal codes. At each receiver element, the signals from each transmitter element are able to be processed separately, allowing transmitter beamforming to be implemented before the DOA processing.

This paper is organized as follows: Section 2 introduces the hybrid array and explains the method of operation of the two sub-arrays, using MEMP DOA, and high resolution imaging (receiver beamforming). Section 3 introduces the concept of transmitter beamforming via MIMO and describes the method of optimizing the array pattern and null steering. Section 4 presents simulation results of a MEMP with MIMO pre-processing. Section 5 demonstrates the feasibility of construction of such an array by describing our preliminary design.

2. SENSOR ARRAY

Our sensor array is composed of three sub-arrays, Figure 1. A DOA sub-array, for wide area detection of targets at long range (1000–1500 mm), a random 3D imaging sub-array, for high resolution imaging of individual target activity at short range (100–150 mm) and a transmitter sub-array. This section discusses the two receiver sub-arrays.

2.1. MEMP Sub-array

Signals received by a regular rectangular array with element spacing (Δ_x, Δ_y) can be modelled using Equation (1):

$$x(m;n) = \sum_{i=1}^{l} A_i \exp 1 \left(j\gamma_i + 2\pi m \Delta_x \sin\theta_i \cos\varphi_i + j2\pi n \Delta_y \sin\theta_i \sin\varphi_i\right) \tag{1}$$

where i is the signal from array elements 1 to I, A_i is the amplitude, γ_i is the phase, φ_i is the elevation and θ_i is azimuth. The signal sample values are assembled into an enhanced matrix using a partition and stack process [2]. A Singular Value Decomposition (SVD) is used to estimate the number of targets present. This establishes the signal and noise subspaces within the data matrix. The signal subspace eigenvalues are determined by matrix inversion, and are used to estimate the azimuths and elevations of all the targets in the signal subspace via a pairing algorithm [3]. Amplitude and phase information can also be estimated by this process.

2.2. MEMP Array Transformation

MEMP performs best with an ideal, uniform rectangular array. Limitations in physical element placement, phase and amplitude balance, manufacturing tolerances, and mutual coupling can result in non-ideal performance. To apply MEMP to an imperfect real array, a transformation can be applied to the data received from the array. This transformation takes the received data from a real array as an input, and computes the response of an ideal virtual array. The transformation matrix, T, is calculated [4] as the least mean squared solution to:

$$T = \arg\min_T \|TA_R(\phi_i, \theta_i) - A_V(\phi_i, \theta_i)\|_F^2 \tag{2}$$

where A_R and A_V are the array manifolds from a set of angles generated from simulation or calibration data for the real and virtual array respectively. The transformation works well within an angular sector. We use azimuthal sectors of $\pi/2$ and elevation sectors of $\pi/4$. Since the MEMP relies on phase and amplitude information, traditional filtering techniques using multiply and add cannot be used. Hence, we use signal cancellation [1]. We isolate the out-of-sector targets, and suppress them by injecting signals of equal amplitude and opposite phase. A narrow beam Chebyshev spatial

filter is steered towards an unwanted target. The magnitude and phase of the target is computed and then an equal but opposite phase signal is added to the signal data vector. 20 dB suppression has been achieved using this method and is sufficient for our purposes.

2.3. Receiver Beamforming Sub-array

An established method for near field receiver DOA estimation is focusing. Focusing is a special case of beamforming [5]. Recent advances in the processing power of DSP and FPGA devices has brought beamforming over millions of volumetric pixels (voxels) within the reach of portable, low power devices [6]. Receiver beamforming relies on phase shifting the signals from the receiver array elements, and summing the results. This yields the amplitude and phase of any signal originating at the focus of the array. Its performance does not depend on a plane wave assumption, and hence does not degrade in the near field. However, it needs a large amount of computation to scan over the number of voxels required for acceptable resolution (less than 10 mm in 3 dimensions for our application). For a range of 0 to 50 wavelengths, the scan volume is 5.11×10^4 mm^3. With a voxel size of 3 mm $\times$ 3 mm $\times$ 3 mm (i.e., 27 mm^3), a scan contains 18.9×10^6 voxels. By pre-computing phase shifts, only one multiply accumulate (MAC) operation is required for each sub-array element for focusing on each voxel. Termites move relatively slowly, so a 10 Hz frame rate is adequate for detection. We have determined that adequate alias suppression is achieved with between 64 and 128 array elements, hence calculation of several GigaMACs per second is necessary to achieve adequate beamforming performance. This rate is achievable with currently available low cost FPGA's and DSP's [6].

3. TRANSMITTER BEAMFORMING USING MIMO

This section introduces the transmitter array, and a means of controlling it from the receiver back-end by using MIMO techniques. Figure 2 is a block diagram of the MIMO array.

3.1. Principle of Operation

Each transmitter element is encoded with a unique code, with all codes being mutually orthogonal. At each receiver element, the received signal is correlated with each of the orthogonal codes, to determine the magnitude and phase of the signal received from a particular transmitter element. The results of those correlations are multiplied by complex weights and added to form a transmitter beam. The resultant signals are then analyzed by the receiver MEMP method for the Matrix Pencil array, and by receiver element beamforming for the beamforming array. This process can be performed multiple times in parallel with different transmitter beams for each.

Our design has 33 dual polarization transmitter patches with the two polarizations used alternately (Time Division Multiple Access) and hence requires 33 orthogonal codes. Our preferred set of codes is obtained from the cyclic shifts of a pseudonoise quadratic residue sequence (Legendre sequence) of length 36. This results in a 37×37 Hadamard Matrix (after the addition of a row and column of 1's, required for zero cross-correlation and set completion). Any 33 of the 36 non-constant codes are suitable for our application. The IF frequency is chosen to be 20 kHz, which is high enough to avoid $1/f$ noise problems, and low enough to be adequately sampled by a commercial audio ADC with 24 bit resolution. The chip rate is 5 kHz. The data throughput is inversely proportional to the code length. Because the round trip time of our signal is much less than the chip period, our system is effectively synchronous.

3.2. Null Steering

We can also form nulls in the transmit pattern. This allows us to exclude specific regions in order to enhance our dynamic range or to confirm the location of features by their absence when the nulls are present. The selection of filter weights can be stated as an optimisation problem with the following constraints:

$$\begin{aligned} &\text{Minimiz } \max(\text{abs}(A_s\ W)) \\ &\text{Subject to :} \\ &\qquad A_{tar}W = 1 \\ &\qquad A_{null}W = 0 \end{aligned} \tag{3}$$

where W are the array weights, A_{tar} is an array steering vector in the desired beam direction, A_{null} is a set of array steering vectors in the direction of the nulls, and A_s is a set of array steering vectors that span angles not in the direction of the beam nor in the direction of the nulls.

This problem is convex [7] and is also suitable for analysis using the disciplined convex programming which is used by the cvx package [8] and the SDPT3 solver [9]. Convex optimization was chosen as a valid and rapid method of finding an optimum set of weights producing either a desired beam, desired nulls or both in the transmit pattern.

4. RESULTS

MIMO methods enable us to utilise a beamformed transmitter with the actual beamforming process performed after the data is received. With the MEMP, we cannot use receiver beamforming, and hence transmitter beamforming is a valuable method for spatially pre-filtering a sector of interest before the array transformation is applied to compensate an imperfect real array.

As mentioned previously we use convex optimisation to achieve the desired MIMO transmit pattern. Figures 3, 4 and 5 show details from beam patterns produced for our array.

Figure 3 demonstrates the beamforming performance of our array using convex optimization

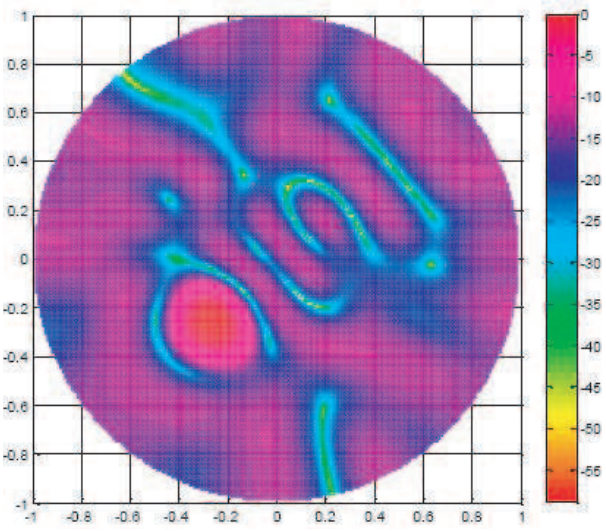

Figure 3: 2D transmit pattern projected onto unit circle. Power in dB. Negative range has been truncated to enhance beam visibillity. Beam is clearly visible.

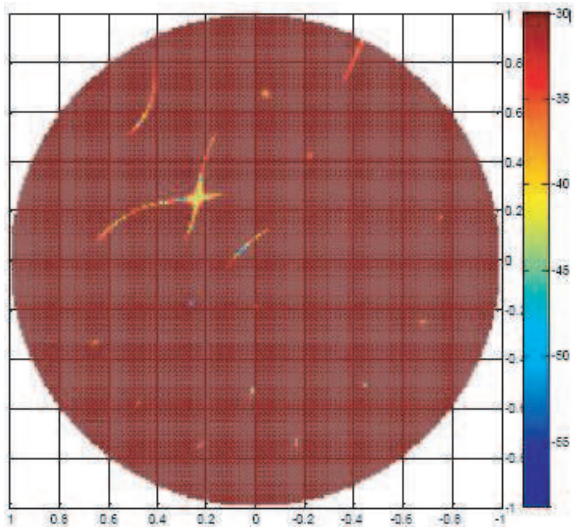

Figure 4: 2D transmit pattern projected onto unit circle. Power in dB. Maximum power has been truncated in plot to highlight position of nulls. The nulls were constrained to 4 points (226 : 30, 226 : 29, 227 : 30, 227 : 29) in order to produce an 'X' shape. Beam is not visible, but is similar to that shown in Figure 3.

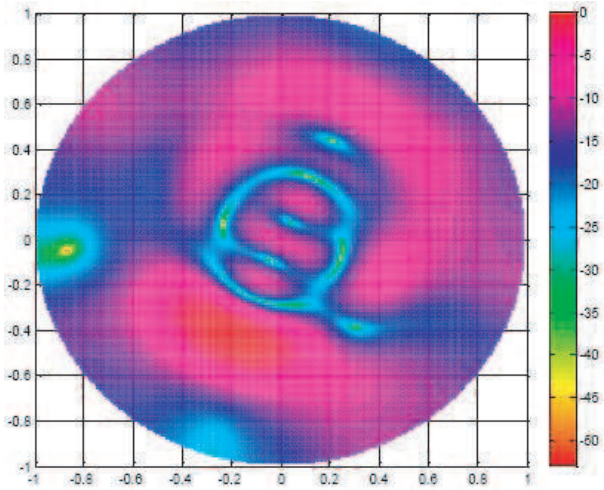

Figure 5: 2D transmit pattern projected onto unit circle. Power in dB. Shows elevation null at 20° as well as beam at 45° elevation and azimuth.

with the resulting beam at least 10 dB above the sidelobes. In Figure 4, we can see an arbitrary null being formed from four point nulls, in this case an 'X' shaped null is formed. Figure 5 shows an elevation null formed at 20 degrees of elevation in combination with a beam at 45 degrees of elevation. Although the beam shape can be distorted by the presence of nearby nulls and the limited number of elements as in Figure 5, placement is accurate to within a few degreeds and shaping of nulls is sufficient for our purposes. Also, we can calculate the array pattern as we form it, allowing us to reject any pattern that has distortions or unintended nulls in problematic positions. In addition multiple array patterns can be combined to form a more complex patterns of nulls.

5. ARRAY DESIGN

Our design is shown in Figure 1. The central 5×5 array is used for the MEMP DOA, and has a dedicated receiver for each patch and each orthogonal polarization i.e., 50 receivers. The beamforming receiver array has 112 dual polarization elements, which are multiplexed using $16:1$ RF multiplexers to 14 receivers. This array is operated at short range (100 mm) where the SNR degradation of a factor of 16 plus the multiplexing losses is tolerable. The 33 dual polarization element transmitter array is slightly to the right and below the central MEMP array.

6. CONCLUSION

We present a hybrid array for detecting and imaging termite activity behind a wall or floor. Adding MIMO processing improves SNR and the discrimination of targets, as shown in our simulations.

ACKNOWLEDGMENT

The authors acknowledge the Australian Research Council for their financial support, under Linkage Grant LP0669638, the University of NSW@ADFA for infrastructure support, Termatrac Pty Ltd and Scientific Technology Pty Ltd (industrial partners) for their facilities and equipment for this project. The authors further acknowledge Dr. Donald Fraser, Prof. Joseph Lai and Prof. Charles Osborne for helpful suggestions in preparing this manuscript.

REFERENCES

1. Le Marshall, N. W. D. and A. Z. Tirkel, "The Application of the MEMP and beamforming to determine the presence of termites in situ," *IEEE EUROCON 2009 Proceedings*, 1568–1572, 2009.
2. Hua, Y., "Estimating two-dimensional frequencies by matrix enhancement and matrix pencil," *IEEE Trans. on Signal Processing*, Vol. 40, No. 9, 2267–2280, 1992.
3. Burintramart, S. and T. Sarkar, "Target localization in three dimensions," *Advances in Direction of Arrival Estimation*, S. Chandran, Editor, Artech House, 2005.
4. Hyberg, P., "Antenna array mapping for doa estimation in radio signal reconnaissance," Ph.D. Thesis, Kungliga Tekniska Högskolan, 2005.
5. Van Trees, H. L., *Detection, Estimation, and Modulation Theory, Part IV, Optimum Array Processing*, Wiley, NY, 2002.
6. Brown, G., "Spartan-DSP takes aim at affordable DSP performance," *Xcell Journal*, Xilinx Inc., 2007.
7. Boyd, S. and L. Vandenberghe, *Convex Optimization*, Cambridge University Press, 2009.
8. Grant, M. and S. Boyd, *CVX User's Guide for cvx V1.2*, http://www.stanford.edu/∼boyd/c-vx/cvx_usrguide.pdf.
9. SPDT3 V4.0, http://www.math.nus.edu.sg/∼mattohkc/sdpt3.html.

Semi-Analytical Mode Match Approach for Scattering Computation of Randomly Densely-distributed Conductive Targets

Hongxia Ye and Ya-Qiu Jin
Key Laboratory of Wave Scattering and Remote Sensing Information (MoE), Fudan University
Shanghai 200433, China

Abstract— A Semi-Analytical Mode Match method (SAMM) is developed to fast compute electromagnetic (EM) scattering from multiple densely-distributed conductive cylinders. First, the scattering field of each target is expanded as a series summation of Hankel functions in its own local coordinate. Then a finite number of sample points are chosen on the target surface to numerically match the boundary condition, and it yields a matrix equation about the expansion coefficients. In order to well restrict the boundary conduction on all targets surface, the sample point number should be more than the unknown expansion coefficients, and the matrix equation is over-determined. Finally the singular value decomposition (SVD) or the least squares method can be used to solve the matrix equation and obtain the optimal solution. This paper also analyzes the problem of series truncation, and obtains the relation of series number and target size for different shapes. Moreover, numerical simulation is made for scattering analysis of multiple random shapes 2D conductive targets, and comparison is made with MoM (Method of Moment) computation to validate the new method.

1. INTRODUCTION

The Inverse synthetic aperture radar (ISAR) technique is of great importance for target surveillance, non-invasive detection of concealed objects, radar guidance and navigation, etc. However, to generate the synthetic range profiles for ISAR image is always a highly time-intensive work, which is a bottleneck to be solved.

Since the classical numerical methods always need large CPU time and computer memory, which restrain scattering computations of wide-band frequencies and multi-angle incidences. New fast EM computation approaches need to be developed. The wave function expansion method was firstly used for scattering analysis of single cylinder, sphere, and ellipse particle [1, 2], and recently be expanded to analyze the multiple objects model of electric-small and sparse particles [3, 4]. Other approaches, such as the reciprocity-equivalent principle [5], the T-matrix method [6], etc., have also been developed for EM scattering computation of multiple cylinders. When the targets are distributed closely, the scattering coupling or mutual interactions should be taken into account. Recently much attention has been paid on the analytical methods which are based on basis wave function expansion. For example, a recursive eigen-function theory is presented to analyze oblique plane-wave scattering from multilayered cylindrical shell [7], and the spectral-domain cylindrical-wave approach is presented to analyze the EM scattering from a set of buried cylinders [8].

In the conventional wave function expansion method, the boundary conductions are analytically matched to obtain the expansion coefficients. So it can only be used for a single regular target, such as a cylinder or a sphere [9]. Based on the wave functions expansion theory, the Semi-Analytical Mode Match method (SAMM) is developed, which chooses some discrete points on target surface to numerically match the boundary conduction. So it can be used for any object shape theoretically. For example, Morgenthaler had used it for scattering analysis ofsingle object buried in a half-space [10, 11].

In this paper, the SAMM is used for scattering computation of multiple random cylinders, which are very closely positioned. First, the scattering field of each cylinder is expanded as a finite series of Hankel wave functions in its local coordinate. Secondly an appropriate number of discrete points are chosen to numerically match the boundary condition, and it yields an over-determined matrix equation with expansion coefficients as the unknowns. Then the singular value decomposition (SVD) or least squares method is used for matrix equation solution. Finally the SAMM is used to compute the EM scattering from composite model of multiple cylindrical objects with different size, and is compared with the numerical MoM computation.

2. SEMI-ANALYTICAL MODE MATCH

As shown in Figure 1, the z-polarized electromagnetic (EM) wave illustrates the composite model of multiple random conductive cylinders. The incident wave can be expressed as

$$E_{zi}(x,y) = e^{-jk\mathbf{k}_i\cdot\mathbf{r}} = e^{-jk(x\cos\varphi+y\sin\varphi)} \tag{1}$$

where $k=\omega\sqrt{\mu\varepsilon}$ is the propagation constant. Under the illumination of E_{zi}, the induced currents on the target surfaces yield the second radiation in the outside space, which is often named scattering field.

Now we consider each object in the composite model respectively. For example, the scattering field from m-th cylinder can be expanded as cylindrical wave functions series in its local coordinate, as in the following form [9]. For the conductive cylinder, only outward wave need be included, and the Hankel function is used for expansion, expressed as

$$E_{zs}^m(P(x,y)) = \sum_{l=-N_m}^{+N_m} A_l^m j^{-l} H_l^2(k\rho^m) e^{-jl\varphi^m} \tag{2}$$

where A_l^m are the expansion coefficients of scattering field, H_l^2 is the second order l-order Hankel function, (ρ^m,φ^m) is the local cylindrical coordinate of field point P. Note that for the conductive cylinder, only outward wave need be included, and the Hankel function is used for expansion. For finite size of cylinders, the series expansion in formula (2) can be truncated at N_m. How to choose N_m will be discussed in Section 3.

On each cylinder surface, the tangential component of total electric field should be zero. In the SAMM method, a finite number of discrete points are chosen on each cylinder surface (such as the solid points as shown in Figure 1) to match the boundary condition. And the following equation is obtained.

$$\sum_{m=1}^{M}\left[\sum_{l=-N_m}^{N_m} A_l^m j^{-l} H_l^2(k\rho^m) e^{-jl\varphi^m}\right] = -E_{zi}(x_p,\, y_p) \tag{3}$$

where the expansion coefficients A_l^m are the unknowns for solution. In order to obtain the unique optimal solution of expansion coefficients, the number of matching points should be larger than the number of expansion terms, and it yields an over-determined matrix equation, which can be solved with the SVD method.

3. DISCUSSION ON EXPANSION ITEMS N_m

Theoretically, the more expansion items is included, the more exact scattering field is computed for the cylinder, but it yields more requirements for memory and CPU time. Define the relative error between the SAMM and MoM computation [12] as follows.

$$\mathrm{Err} \triangleq \left|E_s^A - E_s^N\right|^2 \Big/ \left|E_s^N\right|^2 \tag{4}$$

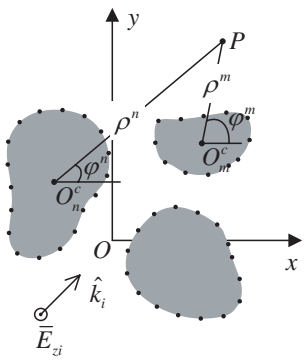

Figure 1: The composite scattering model of multiple cylindrical conductive targets.

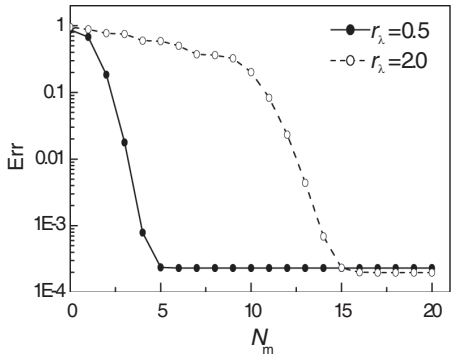

Figure 2: The relationship of relative error and expansion coefficients.

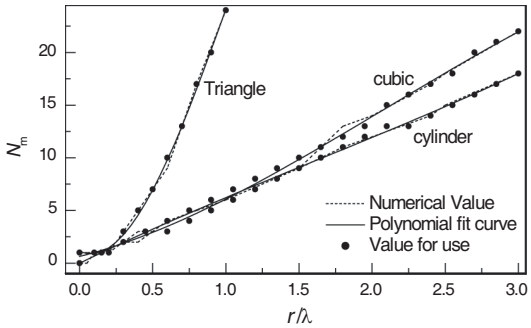

Figure 3: The function relationship of expansion term number vs. relative radius.

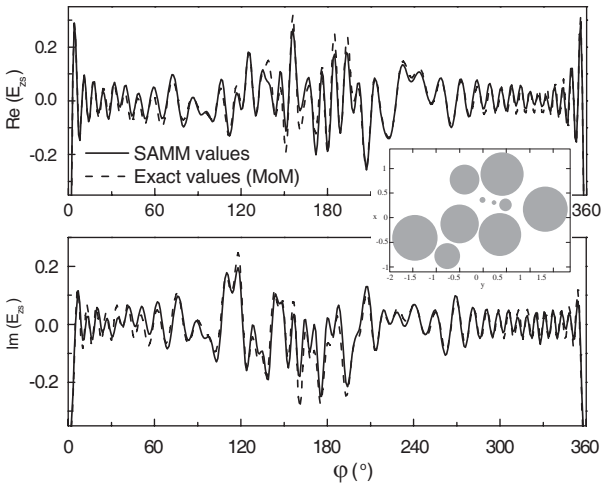

Figure 4: The bi-static scattering fields computed with SAMM and MoM algorithms.

where E_s^A is scattering field computed with the SAMM method, and E_s^N with the numerical MoM method. Note that here we take the numerical MoM computation as a criterion to judge the SAMM method, because the MoM is based on the strict integral equation of EM field.

Figure 2 gives the relative error item vs. expansion items for a single cylinder with the relative radius $r/\lambda = 0.5$, 2.0. It can be seen that the error decrease with expansion term number rapidly. If limit Err $< 10^{-2}$, it yields the relationship of expansion term number N_m vs. the relative radius r/λ, shown as the dot lines in Figure 3 for different shapes. It can be seen that more expansion terms are needed for larger size cylinder. The square column target needs more expansion terms than the cylinder, and the triple column needs the most.

In order to facilitate the usage, a functional expression of N_m and r/λ is fitted as the following polynomial form.

$$N_m = \left[A_3 \left(\frac{r}{\lambda}\right)^3 + A_2 \left(\frac{r}{\lambda}\right)^2 + A_1 \left(\frac{r}{\lambda}\right) + A_0 \right] \tag{5}$$

With the numerical values on the dot line of Figure 3, the polynomial coefficients $A_0 \sim A_3$ can be easily obtained by using the least-squares method. For example, parameters $A_0 = -0.008$, $A_1 = 6.791$, $A_2 = -0.708$, $A_3 = 0.148$ are valued for the cylindrical column. The fitted polynomial curves for different shapes are shown in Figure 3 as the solid line. Moreover, the symbol $[\cdot]$ in Eq. (5) denotes the round operation, in order to obtain an integer for the expansion item number.

4. NUMERICAL RESULTS

Take a composite model of 10 random cylinders for numerical simulation. The radius is valued as the uniformly distributed random numbers at interval $(0 \sim 0.5)$, and the position of x and y coordinates is normally distributed with zero mean and 0.3 variance. The incident electric field polarized in z direction is incident along x direction, expressed as $E_{zi} = e^{-jkx}$. The frequency of EM wave is 1.5 GHz.

One realization is shown in the subfigure in Figure 4, with center coordinates are $(-0.1298, -0.4997)$, $(-0.3439, 0.3573)$, $(0.3567, -0.0113)$, $(0.8849, 0.4068)$, $(0.7742, -0.3919)$, $(0.3071, 0.2333)$, $(0.2569, 0.4781)$, $(-0.7861, -0.7657)$, $(0.1739, 1.3287)$, $(-0.4177, -1.4556)$, and radius are 0.4074, 0.4529, 0.0635, 0.4567, 0.3162, 0.0488, 0.1328, 0.2734, 0.4788, 0.4824, respectively. The SAMM method and numerical MoM are both used to compute the scattering field from the composite model. For the MoM computation, the cylinder surface are discretized into 977 units with the equal interval $\lambda/10$, and it leads to 188.6 s for Matrix equation solution. The bi-static scattering field at $\rho = 50$ m circle is plotted as the solid line in Figure 4.

For SAMM computation, the expansion item number N_m for each cylinder is valued according to Eq. (5), respectively, as 12, 13, 2, 14, 10, 2, 4, 8, 14, 14. It yields totally 196 unknown expansion coefficient to be solved. Appropriate matching points are chosen on each cylinder according to its size, and it yields a matrix equation of 299 rows and 196 columns. Then the SVD method is used to solve the matrix equation. The total CPU time for SAMM is 3.97 s, which is much less than

MoM computation. The bi-static scattering field computed with the SAMM method is plot as the dash line in Figure 4, which is well coincident with the solid line. So the SAMM is an effective and efficient algorithm for composite model of multiple objects, even if the distance is very close.

5. CONCLUSION

This paper presents a new approach named Semi-Analytical Mode Match (SAMM) method to fast compute the composite scattering from multiple densely-distributed random cylinders. The scattering field of cylinder target is expanded as the Hankel function expansion series in its local coordinate. The boundary condition is numerically matched at a finite number of sampled points on the target surface. And it yields a matrix equation with the finite expansion coefficients as unknowns, which are solved with the SVD method. In order to well restrict the boundary condition, the more sample points should be chosen to create a over-determined matrix equation. The truncation for expansion series is also discussed in this paper, and a simple polynomial relationship is fitted for easy use. Finally the SAMM algorithm is experimentally validated by comparison with the MoM computation.

REFERENCES

1. Doicu, A. and T. Wriedt, "Computation of the beam-shape coefficients in the generalized Lorenz-Mie theory by using the translational addition theorem for spherical vector wave functions," *Applied Optics*, Vol. 36, No. 13, 2971–2978, 1997.
2. Xu, Y. L., "Scattering Mueller matrix of an ensemble of variously shaped small particles," *Journal of the Optical Society of America A*, Vol. 20, No. 11, 2093–2112, 2003.
3. Lee, S. C., "Scattering of polarizeds radiation by an arbitrary collection of closely spaced parallel nonhomogeneous tilted cylinders," *Journal of the Optical Society of America A*, Vol. 13, No. 11, 2256–2265, 1996.
4. Ye, H. X., J. W. Dai, and Y. Q. Jin, "Analytical iterative algorithm for fast computation of scattering from multiple conductive cylinders and the image reconstruction," *The European Physical Journal Applied Physics*, Vol. 48, 20903, 2009, doi: 10.1051/epjap/2009145.
5. Chiu, T. and K. Sarabandi, "Electromagnetic scattering interaction between a dielectric cylinder and a slightly rough surface," *IEEE Transactions on Antennas and Propagation*, Vol. 47, No. 5, 902–913, 1999.
6. Wang, Y. M. and W. C. Chew, "A recursive T-matrix approach for the solution of electromagnetic scattering by many spheres," *IEEE Transaction on Antennas and Propagation*, Vol. 41, No. 12, 1633–1639, 1993.
7. Hsu, C. G. and C. N. Chiu, "Oblique plane-wave scattering from a general bi-isotropic cylindrical shell with an interior advanced composite-material backing," *IEEE Transactions on Electromagnetic Compatibility*, Vol. 48, No. 4, 614–620, 2006.
8. Pajewski, L., G. Schettini, and F. Frezza, "Cylindrical-wave approach for the electromagnetic scattering problem by buried two-dimensional objects," *Journal of Applied Geophysics*, Vol. 67, No. 4, 318–326, 2009.
9. Ishimaru, A., *Electromagnetic Wave Propagation, Radiation, and Scattering*, Prentice Hall, New Jersey, 1991.
10. Morgenthaler, A. W. and C. M. Rappaport, "Detecting nonmetallic mines under rough ground using semi-analytic mode matching," *Subsurface Sensing Technologies and Applications*, Vol. 2, No. 3, 231–247, FL, 2001.
11. Firoozabadi, R., E. L. Miller, C. M. Rappaport, and A. W. Morgenthaler, "Subsurface sensing of buried objects under a randomly rough surface using scattered electromagnetic field data," *IEEE Transactions on Geoscience and Remote Sensing*, Vol. 45, No. 1, 104–117, 2007.
12. Jin, Y. Q., P. Liu, and H. X. Ye, *Theory and Method of Numerical Simulation of Composite Scattering from the Object and Randomly Rough Surface*, Science Press, Beijing, 2008.

The Decomposition of the Angular Spectrum Domain in the Parallel Multilevel Fast Multipole Algorithm

Xingang Wang[1, 2], **Bin Cheng**[1], **Hongxia Zhang**[3], **and Weiqin Tong**[1]

[1]School of Computer Engineering and Science, Shanghai University, Shanghai 200072, China
[2]College of Information Engineering, Zhejiang University of Technology, Hangzhou 310014, China
[3]Aviation Industry Development Research Center of China, Beijing 100012, China

Abstract— This paper discusses the decomposition of the angular spectrum domain in the parallel Multilevel Fast Multipole Algorithm (MLFMA), including the equational scheme, the strip scheme and the block scheme. The characteristics and the applicable principles of three methods are analyzed theoretically and numerically. The experiment results show that the block scheme is very efficient for enlarging the parallel scale, and can significantly improve the parallel efficiency.

1. INTRODUCTION

Fast Multipole Method (FMM) [1] and Multilevel Fast Multipole Algorithm (MLFMA) [2] are effective methods in solving the electromagnetic scattering from electrically large objects. It has been shown that FMM can reduce the complexity of a matrix vector multiply (MVM) from $O(N^2)$ to $O(N^{1.5})$, where N is the number of unknowns. The MLFMA can further reduce this complexity to $O(N \log N)$. But it is difficult for the serial methods to solve large-scale electromagnetic scattering from problems whether using FMM or MLFMA. This motivated numerous parallel versions of MLFMA as shown in [3–7] and they had been proved to be effective for solving large-scale electromagnetic scattering problems, some of which involves millions of unknowns [8].

The geometric data calculated by MLFMA can be translated into two domains: the data domain and the angular spectrum domain. The data domain is constituted by the grouping of the geometric data and the angular spectrum domain is constituted by the stratification of the geometric data. The parallelization of MLFMA is essentially parallel processing of the above two domains. As the computation of the two domains will influence each other, this, therefore, increases the difficulty of parallel computing. For different domains, parallel methods have been proposed, e.g., the hierarchical parallel approach is proposed by W. C. Chew et al. [4], where the data domain is partitioned at the distributed levels and the angular spectrum domain is partitioned at the shared levels. O. Ergül et al. [5, 6] proposed the hybrid partitioning scheme to partition the data domain and the angular spectrum domain simultaneously at some levels. Although there is a debate among some researchers on this issue, there is very little in-depth discussion to explore the domain nature, or the efficiency of their solutions.

This paper proposes a better solution for the decomposition of the angular spectrum domain in parallel MLFMA, such as the equational scheme, the strip scheme and the block scheme. Some typical numerical results demonstrate the characteristics and the applicable principles of the three methods. The block scheme is shown to be useful for enlarging the parallel scale and can significantly improve the parallel efficiency.

2. A BRIEF REVIEW OF THE INTERPOLATION OPERATION

During the aggregation phase in MLFMA, the radiation patterns of boxes in the lower levels are sampled coarsely, while finer sampling is required in the higher levels. By the stratification of the geometric data, the interpolation operations are needed in the transformation of the radiation patterns at the finer level to the parent level. This operation can be expressed as

$$F_{parent} = \bar{E}_l \cdot \bar{I}_l \cdot F_{child} \tag{1}$$

where $\bar{E}_l \in C^{M_{l-1} \times M_{l-1}}$ is the diagonal translation matrix, and $\bar{I}_l \in C^{M_{l-1} \times M_l}$ is the interpolation matrix. The best form of the decomposition of the angular spectrum domain depends on the characteristic of the interpolation or anterpolation operation. In this paper, the interpolation algorithm which uses the classical two-dimensional (2-D) local Lagrange interpolation [9] is described

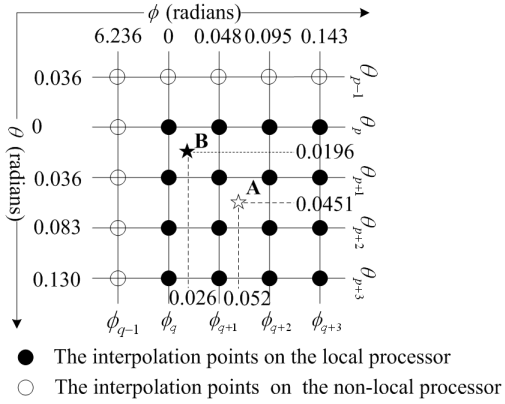

Figure 1: The theory of the interpolation operation.

as follows:

$$A(\theta,\phi)=\sum_{j=q}^{q+3}\sum_{i=p}^{p+3}\left[\prod_{\substack{k=p\\k\neq i}}^{p+3}\left(\frac{\theta-\theta_k}{\theta_i-\theta_k}\right)\prod_{\substack{l=q\\l\neq j}}^{q+3}\left(\frac{\phi-\phi_l}{\phi_j-\phi_l}\right)A(\theta_i,\phi_j)\right] \tag{2}$$

Usually, a Gaussian quadrature rule is used along the θ direction and a trapezoidal quadrature is used along the ϕ direction, where $0\leq\phi\leq 2\pi$, $0\leq\theta\leq\pi$. If a local-point local interpolation method is used, each output value depends on 16 input values, which is "geometrically" close to the evaluation point in Fig. 1.

The point A at the parent level relies on the interpolation points of $\phi_q-\phi_{q+3}$ and $\theta_p-\theta_{p+3}$ at the child level which are all in the local. But the interpolation points of $\phi_{q-1}-\phi_{q+2}$ and $\theta_{p-1}-\theta_{p+2}$ at the child level are not entirely in the local, which are needed by the point B at the parent level. The communications are necessary to get those points from other processors. It is also the key problem to be dealt with in the decomposition of the angular spectrum domain.

3. THE ANGULAR SPECTRUM DOMAIN DECOMPOSITION IN PARALLEL MLFMA

For the parallelization of MLFMA, the angular spectrum domain is partitioned at the higher levels of the distributed tree. Let $N_{\theta,l}$ be the order of the Gaussian quadrature and $N_{\phi,l}$ be the order of the trapezoidal rule at the lth level. In the spherical coordinates, there are $N_{\phi,l}\phi$ samples for each θ sample at the lth level. The samples on the unit sphere may be arranged in a matrix form with $N_{\theta,l}$ rows and $N_{\phi,l}$ columns. We shall refer to this arrangement as the sample matrix. The number of samplings (K_l) in the radiation pattern at the lth level is given by

$$K_l=2L_l(L_l+2) \tag{3}$$

where L_l is the truncation factor at the lth level. $N_{\phi,l}=2L_l$, $N_{\theta,l}=L_\iota+2$. The decomposition of the angular spectrum domain is in essence the partition of K_l or the sample matrix. According to (3), K_l/P can be changed into the following forms:

$$2L_l\left(L_l+2\right)/P \tag{3a}$$

$$\frac{2L_l}{P}\cdot(L_l+2)\quad\text{or}\quad 2L_l\cdot\frac{(L_l+2)}{P} \tag{3b}$$

$$\frac{2L_l}{P_y}\cdot\frac{(L_l+2)}{P_x},\quad P_x\cdot P_y=P \tag{3c}$$

where P is the number of processors. P_x or P_y is the number of processors along the θ direction or the ϕ direction. Eq. (3a) is the equational scheme. Eq. (3b) is the strip scheme by means of partitioning $N_{\phi,l}$ or $N_{\theta,l}$. If $N_{\phi,l}$ and $N_{\theta,l}$ are partitioned at the same time, Eq. (3c) is namely the block scheme. Consequently, the decomposition of the angular spectrum domain is nothing more than the combination of partitioning $N_{\phi,l}$ and $N_{\theta,l}$. The key problem of this partition is

L / P	SLev				
				DLev	
	1	2	3	4	5
0		0	0	0	
1		4	4	4	
2		12	7	5	
3		2	3	2	
4		0	0	0	
5		50	37	24	
6		160	63	30	
7		40	25	21	

Table 1: The communication between the processor 6 and the other processors.

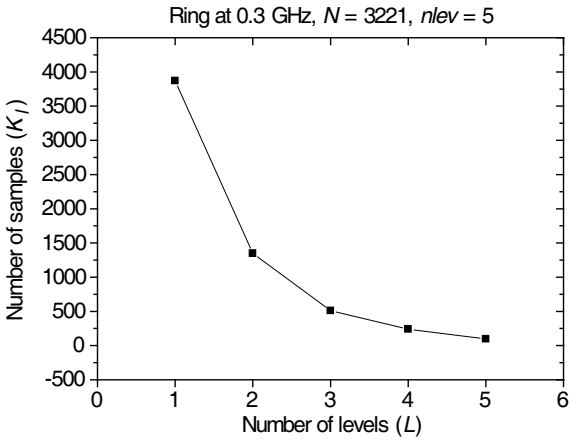

Figure 2: The angular spectrum domain of Ring 4.

how to reduce the communication between the different processors by using the interpolation or anterprolation relationship.

3.1. Equational Scheme

As the sample matrix is two-dimensional, the sample matrix should be changed into one-dimensional arrays [see Eq. (3)] in order to implement the equational scheme. As a consequence, K_l is distributed equally among each processor in Eq. (3a). The parallelization is simple because the equational scheme neglects the interpolation relationship between the angular spectrums. Furthermore, the dense communications which occur among all processors will greatly reduce the parallel efficiency. In the following figures, we denote the number of levels by the symbol *nlev,* the number of shared levels by the symbol *SLev*, the number of distributed levels by the symbol *DLev.* In Fig. 2, the ring with four shared levels and two distributed levels has been paralleled on 8 processors. For the equipartition of the angular spectrums at the shared levels, there is no significant correlation at the consecutive level. See Table 1 for an illustration of the amounts of the data transferred between processor 6 and the other processors. As a result, processor 6 will communicate with five processors at least. For the arbitrary objective, one processor needs to communicate with the others. Obviously, the decomposition of the angular spectrum domain is unreasonable.

In order to obtain good parallel performance, the decomposition of the angular spectrum domain is transformed to minimize the communication volume among the processors and reduce the number of communicant processors.

3.2. Strip Scheme

In Eq. (3b), $\frac{2L_l}{P}\cdot(L_l+2)$ and $2L_l\cdot\frac{(L_l+2)}{P}$ describes the partition along the ϕ direction and θ direction, respectively. The basic idea of this partition lies in the fact that the communications only occur between the adjacent processors, which is done by exploiting the characteristic of the interpolation and anterpolation operations.

Without loss of generality, we assume that $N_{\phi,l}$ is divided by P. When the samples are split into P processors, each processor gets a fixed number of columns of the sample matrix. If a local 16-point local interpolation method is chosen, some processors need at most 2 columns of samples from its left and right processors during the interpolation operation [4]. In order to ensure the communication between its left and right processors, the following equation should be satisfied

$$N_{\phi,l} \geq 2P \tag{4}$$

However, it is not the case for the anterpolation operation. As the anterpolation operation is the inverse operation of the interpolation operation, each output value depends on far more than 16 input values. Therefore, the number of the samples which will be transported from its left and right processors depends on the anterpolation operation. According to the theory of the interpolation or anterpolation operation [4], the following relations are derived:

If P divides $N_{\theta,l}$,

$$N_{\theta,l} \geq 4P, \quad K_l \geq 32P^2, \quad \Lambda_l \approx O(\sqrt{K_l}) \tag{4a}$$

If P divides $N_{\phi,l}$,

$$N_{\phi,l} \geq 3P, \quad K_l \geq \frac{9}{2}P^2, \quad \Lambda_l \approx O(\sqrt{K_l}) \tag{4b}$$

where Λ_l is the maximum length of the message.

Generally, the parallel MLFMA is often used to solve large-scale electromagnetic scattering from problems. On distributed memory computers, the parallelization of MLFMA requires more processors in order to get more memory and reduce the solution time. It is obvious that in (4a) and (4b), the decomposition along the ϕ direction can get more processors than that along the θ direction. Furthermore, under the same condition with P, the decomposition along the ϕ direction can obtain more shared levels than along the θ direction.

3.3. Block Scheme

In the strip scheme, Λ_l has nothing to do with P. In fact, for large scattering from problems, K_l and Λ_l is very large at the top levels. This will result in the very expensive communication cost. For this reason, we proposed the block scheme [10]. The angular spectrums along the θ direction and the ϕ direction are partitioned at the same time, which constructs the block structure. According to (3c), (4a) and (4b), the following relations are obtained:

$$N_{\theta,l} \geq 4P_x, \quad N_{\phi,l} \geq 3P_y, \quad P_x \cdot P_y = P \tag{4c}$$

$$K_l = N_{\theta,l}N_{\phi,l} \geq 12P_xP_y = 12P \tag{4d}$$

The maximum length of the message along the ϕ direction is

$$\Lambda_l = 3\frac{N_{\theta,l}}{P_x} \approx O\left(\sqrt{\frac{K_l}{P}}\right) \tag{4e}$$

The maximum length of the message along the θ direction is

$$\Lambda_l = 4\frac{N_{\phi,l}}{P_y} \approx O\left(\sqrt{\frac{K_l}{P}}\right) \tag{4f}$$

If we compare Λ_l of the strip scheme with of the block scheme, the maximum length of the message can be reduced from $O(\sqrt{K_l})$ to $O(\sqrt{\frac{K_l}{P}})$.

4. NUMERICAL RESULTS

To solve a very-large-scale electromagnetic scattering from problem, it is helpful to increase computational resources by assembling parallel computing platforms. With the decomposition of the angular spectrum domain, the parallel MLFMA can be computed on more processors. This will improve both communications and load-balancing significantly. However, the different parallization in the angular spectrum domain will limit the usable number of processors. For this reason, numerical results are tested for the scaling with the decomposition of the angular spectrum domain and the parallel efficiency. All the computations reported in this paper were done on a Dawning 5000 A supercomputer at Shanghai Supercomputer Center (SSC).

4.1. Scaling with the Decomposition of the Angular Spectrum Domain

For the same size of a scattering from problem (e.g., in Fig. 3), the number of shared levels partitioned by the three schemes on the different number of processors is shown in Fig. 4. Although the equational scheme can maximize the number of the shared levels, the dense communications become significant for shared levels since there are uncertain communication relationships among different processors during the interpolation and anterpolation operations. Moreover, MLFMA is often paralleled with the distributed levels at the finer levels of the distributed tree. Conversely, the number of shared levels with the strip scheme is far less than that with the equational scheme. Using the block scheme, the communications will be limited on the nearby processors, and the communication volume is greatly reduced compared with the strip scheme.

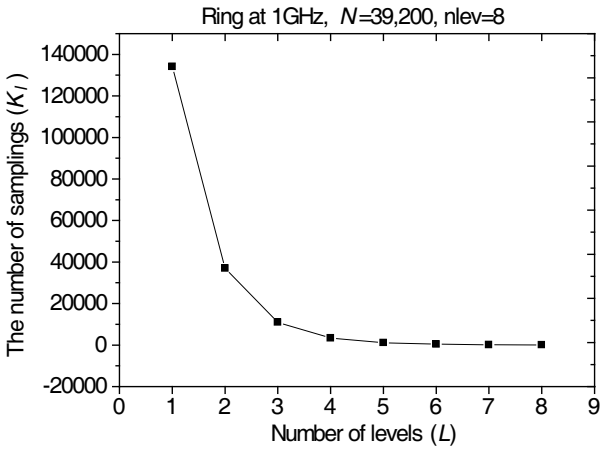

Figure 3: The angular spectrum domain of Ring 8.

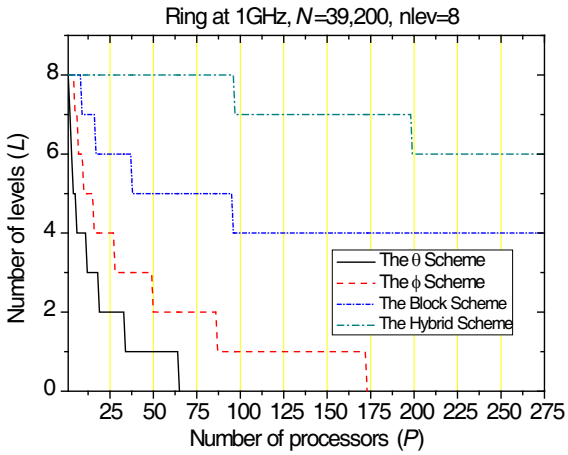

Figure 4: The angular spectrum domain decomposition of Ring 8.

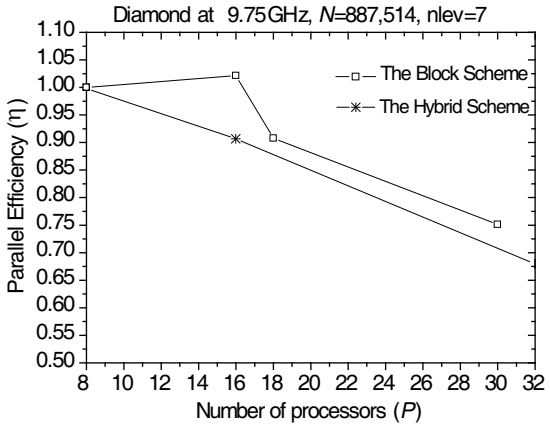

Figure 5: Parellel efficiency for diamond.

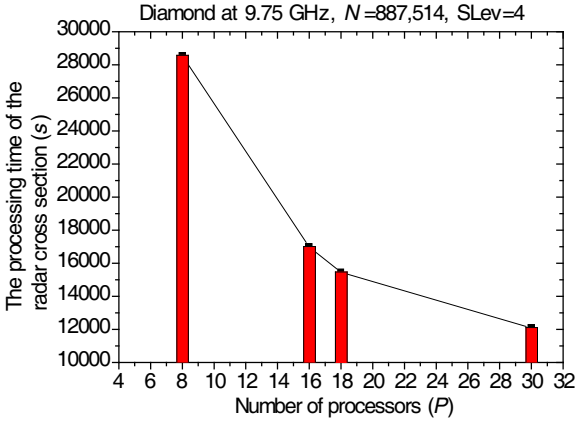

Figure 6: The processing time of diamond using the block scheme.

4.2. Parallel Efficiency

To demonstrate the improved efficiency of the angular spectrum domain decomposition, we present the solution of a scattering problem involving a diamond with 887,514 unknowns. The parallel efficiency η is defined as $\eta = \frac{8T_s}{PT_P}$, where T_p is the time for computing a MVM on P processors.

The parallel efficiency of the single MVM is shown in Fig. 5. Obviously, the block scheme is more efficient compared to the equational scheme. At last, the monostatic radar cross section of the diamond on eleven directions has been computed with the combined field integral equation (CFIE), which is operated under the vertical and horizontal polarization. For the block scheme, the total processing time, including the setup and the iterative solution with conjugate gradient squared method (CGS) is shown in Fig. 6.

5. CONCLUSION

In this paper, we study three domain decomposition algorithms for the parallel MLFMA. On the distributed memory computers, the different scaling with the decomposition of the angular spectrum domain is analyzed using the three methods. The block scheme can run the parallel MLFMA on more processors with many advantages. Compared with the other scheme, the block scheme will limit the communication between nearby processors, and also effectively reduce the length of messages from $O(\sqrt{K_l})$ to $O(\sqrt{\frac{K_l}{P}})$. The numerical results demonstrates that the parallel efficiency of the block scheme raises nearly 10% than that of the equational scheme, and also obtain nearly 75% parallel efficiency on 30 processors.

ACKNOWLEDGMENT

This work is supported in part by Aviation Industry Development Research Center of China, Shanghai Leading Academic Discipline Project (J50103), Shanghai Supercomputer Center (SSC) and the High performance Computing Center of Shanghai University.

REFERENCES

1. Rokhlin, V., "Diagonal forms of translation operators for the Helmholtz equation in three dimensions," *Appl. Comp. Harmon. Anal.*, Vol. 1, 82–93, 1993.
2. Song, J. M., C. C. Lu, and W. C. Chew, "MLFMA for electromagnetic scattering from large complex objects," *IEEE Trans. Ant. Propag.*, Vol. 45, No. 10, 1488–1493, October 1997.
3. Chew, W. C., J.-M. Jin, E. Michielssen, and J. M. Song, Eds., *Fast and Efficient Algorithms in Computational Electromagnetics*, Boston Artech House, 2001.
4. Velamparambil, S. and W. C. Chew, "Analysis and performance of a distributed memory multilevel fast multipole algorithm," *IEEE Trans. Antennas Propag.*, Vol. 53, No. 8, 2719–2727, August 2005.
5. Ergül, O. and L. Gürel, "Hierarchical parallelisation strategy for multilevel fast multipole algorithm in computational electromagnetics," *Electronics Letters*, Vol. 44, No. 1, 3–5, January 2008.
6. Ergül, O. and L. Gürel, "Efficient parallelization of multilevel fast multipole algorithm," *The European Conf. on Antennas and Propagation*, 6–10, France, 2006.
7. Lin, Y., J. Hu, Z. P. Nie, and Y. P. Chen, "A new form of parallel MLFMA: iterative PMLFMA," *IEEE Trans. on Antennas and Propagation Society International Symposium*, Vol. 3B, 200–203, July 2005.
8. Velamparambil, S., W. C. Chew, and J. M. Song, "10 million unknowns: Is it that big?" *IEEE Trans. Antennas Propag.*, Vol. 45, No. 2, 43–58, April 2003.
9. Bucci, O. M., C. Gennarelli, and C. Savarese, "Optimal interpolation of radiated fields over a sphere," *IEEE Trans. on Antennas Propag.*, Vol. 39, No. 11, 1633–1642, November 1991.
10. Wang, X. G., B. Cheng, and W. Q. Tong, "A new parallel strategy for MLFMA based on the partitioned blocks," *IEEE Conf. The International Conference on Information Science and Engineering, ICISE 2009*, Nanjing, China, December 2009, (In press).

Lanczos Biconjugate A-Orthonormalization Methods for Surface Integral Equations in Electromagnetism

B. Carpentieri[1], **Y.-F. Jing**[2], **and T.-Z. Huang**[2]

[1]CRS4 Bioinformatics Laboratory, Italy
[2]University of Electronic Science and Technology of China, China

Abstract— We present a novel class of Krylov projection methods computed from the Lanczos biconjugate A-Orthonormalization algorithm for the solution of dense complex non-Hermitian linear systems arising from the Method of Moments discretization of electromagnetic scattering problems expressed in an integral formulation. Their competitiveness with other popular Krylov solvers, especially when memory is a concern, is illustrated on a set of model problems representative of realistic radar-cross section calculations. The results presented in this study will contribute to assess the potential of iterative Krylov methods for solving electromagnetic scattering problems from large structures and to enrich the database of this technology.

1. INTRODUCTION

In the last decades, the development of boundary element methods (BEM) for solving electromagnetic (EM) scattering problems in two and three dimensions is receiving a vigorous impulse. BEM solvers are computationally attractive because they require a simple description of the surface of the target by means of triangular facets simplifying considerably the mesh generation especially in the case of moving objects. The Method of Moments (MoM) discretization of integral equations leads to the solution of large dense linear systems of equations that are often ill-conditioned. For solving such systems, iterative Krylov algorithms can be a valid alternative to dense direct methods, provided they are combined with the Multilevel Fast Multipole Algorithm (MLFMA) [6, 11] to carry out approximate matrix by vector products (M-V), and with suitable preconditioners. Many integral formulations for surface scattering and hybrid surface/volume discretizations yield non-Hermitian linear systems that cannot be solved using the Conjugate Gradient (CG) algorithm. The Generalized Minimal Residual method (GMRES) [9] and its variant Flexible GMRES (FGMRES) [8] are broadly used in application codes due to their proved robustness and smooth convergence, see e.g., experiments reported in [1, 6] for solving very large boundary element equations involving million discretization points. On the other hand, iterative methods based on Lanczos biconjugation, such as the BiConjugate Gradient Stabilized method (BiCGSTAB) [11] and the Quasi-Minimal Residual method (QMR) [2] can be cheaper in terms of memory demands but they may require many more iterations to converge especially on realistic geometries [1, 7]. In this paper we present a novel class of Krylov projection methods based on the recently developed Lanczos A-orthonormalization procedure for solving dense complex non-Hermitian linear systems arising from the MoM discretization of EM scattering problems expressed in an integral formulation. The first solver is named Biconjugate A-Orthogonal Residual (BiCOR). Two variants of BiCOR are also considered, which do not require multiplication by the Hermitian of A and therefore may be well suited for some implementation of MLFMA. They are the Conjugate A-Orthogonal Residual Squared (CORS) method and the Biconjugate A-Orthogonal Residual Stabilized (BiCORSTAB) method, see [5]. We illustrate numerical experiments on a set of model problems arising in radar cross section (RCS) calculation from complex structures and analyse their performance in comparison with other popular Krylov algorithms.

2. SECTION 1

Krylov subspace methods search for approximate solutions of the linear system

$$Ax = b,\ A \in \mathbb{C}^{n\times n} \text{ non-Hermitian},\ x, b \in \mathbb{C}^n, \tag{1}$$

in Krylov subspaces of increasing dimension $\mathcal{K}_m(A; v) \equiv \text{span}\{v, Av, \ldots, A^{m-1}v\}$. The techniques developed in this study select approximations belonging to $K_m(A, r_0)$ by applying a Petrov-Galerkin approach and imposing the residual be orthogonal to the constraints subspace $A^H K_m\ (A^H, r_0^*)$, where the shadow residual r_0^* is chosen to be equal to $P(A)r_0$ with $P(t)$ an arbitrary polynomial of certain degree with respect to the variable t (a default choice of $r_0^* = Ar_0$ will be adopted in this

study). The basis vectors for the subspaces $K_m(A, r_0)$ and $A^H K_m(A^H, r_0^*)$ are computed by means of the Biconjugate A-Orthonormalization procedure. Starting from two vectors v_1 and w_1 chosen to satisfy certain conditions, the method ideally builds up a pair of biconjugate A-orthonormal basis for the dual Krylov subspaces $K_m(A; v_1)$ and $K_m(A^H; w_1)$; we summarize the pseudocode in Algorithm 1.

Algorithm 1 *Biconjugate A-Orthonormalization Procedure.*

1: Choose v_1, ω_1, such that $\langle \omega_1, Av_1 \rangle = 1$
2: Set $\beta_1 = \delta_1 \equiv 0$, $\omega_0 = v_0 = \mathbf{0} \in C^n$
3: **for** $j = 1, 2, \ldots$ **do**
4: $\alpha_j = \langle \omega_j, A(Av_j) \rangle$
5: $\hat{v}_{j+1} = Av_j - \alpha_j v_j - \beta_j v_{j-1}$
6: $\hat{\omega}_{j+1} = A^H \omega_j - \bar{\alpha}_j \omega_j - \delta_j \omega_{j-1}$
7: $\delta_{j+1} = |\langle \hat{\omega}_{j+1}, A\hat{v}_{j+1} \rangle|^{\frac{1}{2}}$
8: $\beta_{j+1} = \dfrac{\langle \hat{\omega}_{j+1}, A\hat{v}_{j+1} \rangle}{\delta_{j+1}}$
9: $v_{j+1} = \dfrac{\hat{v}_{j+1}}{\delta_{j+1}}$
10: $\omega_{j+1} = \dfrac{\hat{\omega}_{j+1}}{\bar{\beta}_{j+1}}$
11: **end for**

The following proposition states some useful properties of Algorithm 1. For a proof, see [5].

2.1. Proposition 1

If Algorithm 1 proceeds m steps, then the right and left Lanczos-type vectors v_j, $j = 1, 2, \ldots, m$ and w_i, $i = 1, 2, \ldots, m$ form a biconjugate A-orthonormal system in exact arithmetic, i.e.,

$$\langle \omega_i, Av_j \rangle = \delta_{i,j}, \quad 1 \le i,\ j \le m.$$

Furthermore, denote by $V_m = [v_1, v_2, \ldots, v_m]$ and $W_m = [w_1, w_2, \ldots, w_m]$ the $n \times m$ matrices and by T_m the extended tridiagonal matrix of the form

$$T_m = \begin{bmatrix} T_m \\ \delta_{m+1} e_m^T \end{bmatrix},$$

where

$$T_m = \begin{bmatrix} \alpha_1 & \beta_2 & & & \\ \delta_2 & \alpha_2 & \beta_3 & & \\ & \ddots & \ddots & \ddots & \\ & & \delta_{m-1} & \alpha_{m-1} & \beta_m \\ & & & \delta_m & \alpha_m \end{bmatrix},$$

whose entries are the coefficients generated during the algorithm implementation, and in which $\alpha_1, \ldots, \alpha_m$, $\beta_2, \ldots, \beta_m$ are complex while $\delta_2, \ldots, \delta_m$ positive. Then with the Biconjugate A-Orthonormalization Procedure, the following four relations hold

$$AV_m = V_m T_m + \delta_{m+1} v_{m+1} e_m^T \tag{2}$$

$$A^H W_m = W_m T_m^H + \bar{\beta}_{m+1} \omega_{m+1} e_m^T \tag{3}$$

$$W_m^H A V_m = I_m \tag{4}$$

$$W_m^H A^2 V_m = T_m \tag{5}$$

From Proposition 1, a family of Krylov methods for linear systems can be developed based on Algorithm 1 along the following lines. Recall that we consider an oblique projection method onto $K_m(A, v_1)$ and orthogonally to $L_m = A^H K_m(A^H, \omega_1)$ where $v_1 = \frac{r_0}{\|r_0\|_2}$ and ω_1 is chosen arbitrarily such that $\langle \omega_1, Av_1 \rangle \neq 0$. But ω_1 is often chosen to be equal to $\frac{Av_1}{\|Av_1\|_2^2}$ subjecting to

$\langle \omega_1, Av_1 \rangle = 1$. Run Algorithm 1 m steps and seek an mth approximate solution from the affine subspace $x_0 + K_m(A, v_1)$ of dimension m, by imposing the Petrov-Galerkin condition

$$b - Ax_m \perp L_m,$$

which can be mathematically written in matrix formulation as

$$\left(A^H W_m\right)^H (b - Ax_m) = 0, \tag{6}$$

where W_m is defined in Proposition 1. Since the approximate solution can be represented as

$$x_m = x_0 + V_m y_m, \tag{7}$$

where V_m is defined in Proposition 1 and $y_m \in \mathbb{C}^m$ contains the coefficients of the linear combination, by simple substitution and computation with Eqs. (5) and (6), a tridiagonal system for solving y_m is resulted as

$$T_m y_m = \beta e_1,$$

where T_m is formed in Proposition 1, and $\beta = \|r_0\|_2$.

Applying this framework, in [5] the BiCOR algorithm and two hermitian free variants namely CORS and BiCORSTAB are developed. The BiCOR method consists of less than thirty lines of codes and is sketched in Algorithm 2.

Algorithm 2 *Left preconditioned BiCOR method.*

1: Compute $r_0 = b - Ax_0$ for some initial guess x_0.
2: Choose $r_0^* = P(A)r_0$ such that $\langle r_0^*, Ar_0 \rangle \neq 0$,
where $P(t)$ is a polynomial in t. (For example, $r_0^* = Ar_0$).
3: **for** $j = 1, 2, \ldots$ **do**
4: **solve** $Mz_{j-1} = r_{j-1}$
5: **if** $j = 1$ **then**
6: **solve** $M^H z_0^* = r_0^*$
7: **end if**
8: $\hat{z} = Az_{j-1}$
9: $\rho_{j-1} = \langle z_{j-1}^*, \hat{z} \rangle$
10: **if** $\rho_{j-1} = 0$, **method fails**
11: **if** $j = 1$ **then**
12: $p = z_0$
13: $p_0^* = z_0^*$
14: $q_0 = \hat{z}$
15: **else**
16: $\beta_{j-2} = \rho_{j-1}/\rho_{j-2}$
17: $p_{j-1} = z_{j-1} + \beta_{j-2} p_{j-2}$
18: $p_{j-1}^* = z_{j-1}^* + \bar{\beta}_{j-2} p_{j-2}^*$
19: $q_{j-1} = \hat{z} + \beta_{j-2} q_{j-2}$
20: **end if**
21: $q_{j-1}^* = A^H p_{j-1}^*$
22: **solve** $M^H u_{j-1}^* = q_{j-1}^*$
23: $\alpha_{j-1} = \rho_{j-1} / \langle u_{j-1}^*, q_{j-1} \rangle$
24: $x_j = x_{j-1} + \alpha_{j-1} p_{j-1}$
25: $r_j = r_{j-1} - \alpha_{j-1} q_{j-1}$
26: $z_j^* = z_{j-1}^* - \bar{\alpha}_{j-1} u_{j-1}^*$
27: check convergence; continue if necessary
28: **end for**

3. NUMERICAL EXPERIMENTS

We consider the standard electromagnetic scattering problem expressed in an integral formulation as follows:

Find the surface current $\vec{j}$ such that for all tangential test functions $\vec{j}^t$, we have

$$\int_\Gamma \int_\Gamma G(|\vec{r} - \vec{r'}|) \left(\vec{j}(\vec{r'}) \cdot \vec{j}^{\,t}(\vec{r}) - \frac{1}{k^2} \mathrm{div}_\Gamma \vec{j}(\vec{r'}) \cdot \mathrm{div}_\Gamma \vec{j}^{\,t}(\vec{r}) \right) d\vec{S} = \frac{i}{kZ_0} \int_\Gamma \vec{E}_{inc}(\vec{r'}) \cdot \vec{j}^{\,t}(\vec{r'}) d\vec{r'}. \tag{8}$$

We denote by $G(|\vec{r} - \vec{r'}|) = \dfrac{e^{ik|\vec{r} - \vec{r'}|}}{4\pi |\vec{r} - \vec{r'}|}$ the Green's function of Helmholtz equation, Γ the boundary of the object, $\vec{S}$ the surface the wave number and $Z_0 = \sqrt{\mu_0/\varepsilon_0}$ the characteristic impedance of vacuum (ϵ is the electric permittivity and μ the magnetic permeability). Eq. (8) expresses the electric currents in terms of the electric field and is called Electric Field Integral Equation (EFIE). On discretizing Eq. (8) in space by the MoM over a surface mesh and using the Rao-Wilton-Glisson basis functions for the surface expansion, we obtain a dense complex non-Hermitian linear system

to solve which is often ill-conditioned. The set of unknowns are associated with the vectorial flux across an edge in the mesh. The right-hand side varies with the frequency and the direction of the illuminating wave. When the number of unknowns n is related to the wavenumber the iteration count of iterative solvers on EFIE may increase as $\mathcal{O}(n^{0.5})$.

In Table 1, we show the characteristics of the model problems and the complete list of solvers used in our experiments. All the runs are done on a PC cluster facility featuring quad core Intel CPUs at 2.8 GHz and 16 GB of physical RAM.

Description	n	Freq. (MHz)
1. Cylinder	6268	362
2. Sphere	12000	535
3. Satellite	1699	57
4. Jet	7924	615
5. Airbus A318	23676	800

Solver	M-V by A/A^H	Memory	Ref.
BiCOR	1 / 1	n^2+10n	[5]
CORS	2 / 0	n^2+14n	[5]
BiCORSTAB	2 / 0	n^2+13n	[5]
GMRES	1 / 0	$n^2+(i+5)n$	[9]
QMR	2 / 1	n^2+11n	[3]
BiCGSTAB	2 / 0	n^2+7n	[11]

Table 1: Characteristics of model problems (on the left) and of algorithms (on the right) used in the experiments. We denote by n the number of unknowns and by i the iteration count.

In Table 2, we show the number of iterations required by Krylov methods to reduce the initial residual to $\mathcal{O}(10^{-5})$ starting from the zero vector. The right-hand side of the linear system is set up so that the initial solution is the vector of all ones. We observe the effectiveness of the CORS method, that is the fastest non-Hermitian solver with respect to CPU time on most selected examples. Indeed, unrestarted GMRES may outperform all other Krylov methods and should be used when memory is not a concern. However reorthogonalization costs may penalize the GMRES convergence in large-scale applications as shown in earlier studies [1]. The good efficiency of CORS is even more evident on the two realistic aircraft problems, i.e., Examples 4 and 5, which are very difficult to solve by iterative methods as no convergence is obtained to $\mathcal{O}(10^{-5})$ without preconditioning in 3000 iterates. In Table 2, we report on the number of iterations and on the CPU time to reduce the initial residual to $\mathcal{O}(10^{-3})$. Again, CORS is more efficient than restarted GMRES on these two tough problems. The level of tolerance used may enable a correct reconstruction of the RCS of the object as shown in Figure 1.

Therefore, it may be considered accurate enough for engineering purposes.

In our experiments, methods based on Lanczos biconjugation, e.g., BiCGSTAB and TFQMR are less efficient than BiCOR and CORS. In particular, BiCGSTAB often requires more iterations to converge than BiCORSTAB although each iteration is slightly less expensive.

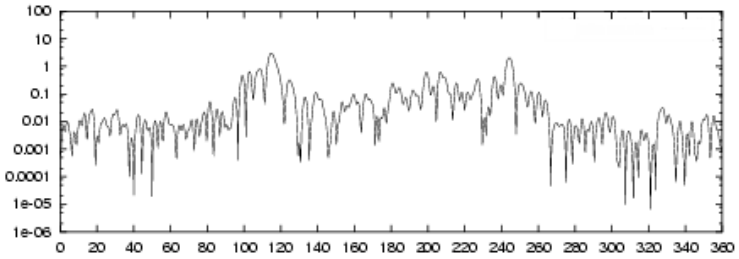

Figure 1: RCS curve computed after the iterative solution for the Airbus aircraft problem.

Table 2: Iterations and CPU time (in seconds) for various Krylov solvers to converge on the selected model problems.

Solver/Example	1	2	3
CORS	601 (253)	294 (451)	371 (11)
BiCOR	785 (334)	338 (525)	431 (15)
BiCORSTAB	941 (614)	423 (1099)	775 (37)
GMRES(50)	2191 (469)	1803 (1397)	871 (17)
TFQMR	482 (398)	281 (863)	373 (27)
BiCGSTAB	1065 (444)	680 (1031)	566 (18)

Example/Solver	CORS	GMRES50
4	1286 (981)	>3000 (>1147)
5	924 (5493)	2792 (8645)

4. CONCLUSION

We have analyzed the performance of a novel class of orthogonal projection Krylov methods computed from the Lanczos biconjugate A-orthonormalization method for solving dense complex non-Hermitian linear systems in realistic RCS calculation. This family of solvers proves to be very competitive with other popular methods showing good convergence properties at cheap memory cost as it is derived from short-term recurrences. Additionally it is parameter-free, does not suffer from the restriction to require a symmetric preconditioner and may not necessitate of matrix multiplication by A^H that might be tricky to implement with MLFMA. The results presented in this study will contribute to enhance the growing body of evidence of iterative Krylov methods for solving realistic electromagnetic scattering problems from large structures.

ACKNOWLEDGMENT

We gratefully thank the EMC Team at CERFACS in Toulouse and EADS-CCR (European Aeronautic Defence and Space — Company Corporate Research Center) in Toulouse, for providing us with some test examples used in the numerical experiments.

REFERENCES

1. Carpentieri, B., I. S. Duff, L. Giraud, and G. Sylvand, "Combining fast multipole techniques and an approximate inverse preconditioner for large electromagnetism calculations," *SIAM J. Scientific Computing*, Vol. 27, No. 3, 774–792, 2005.
2. Freund, R. W. and N. M. Nachtigal, "QMR: A quasi-minimal residual method for non-Hermitian linear systems," *Numerische Mathematik*, Vol. 60, No. 3, 315–339, 1991.
3. Freund, R. W. and N. M. Nachtigal, "An implementation of the QMR method based on coupled two-term recurrences," *SIAM J. Scientific Computing*, Vol. 15, No. 2, 313–337, 1994.
4. Greengard, L. and V. Rokhlin, "A fast algorithm for particle simulations," *Journal of Computational Physics*, Vol. 73, 325–348, 1987.
5. Y.-F. Jing, T.-Z. Huang, Y. Zhang, L. Li, G.-H. Cheng, Z.-G. Ren, Y. Duan, T. Sogabe, and B. Carpentieri, "Lanczos-type variants of the COCR method for complex nonsymmetric linear systems," *Journal of Computational Physics*, Vol. 228, No. 17, 6376–6394, 2009.
6. Malas, T., Ö. Ergül, and L. Gürel, "Sequential and parallel preconditioners for large-scale integral-equation problems," *Computational Electromagnetics Workshop*, 35–43, Izmir, Turkey, August 30–31, 2007.
7. Malas, T. and L. Gürel, "Incomplete LU preconditioning with multilevel fast multipole algorithm for electromagnetic scattering," *SIAM J. Scientific Computing*, Vol. 29, No. 4, 1476–1494, 2007.
8. Saad, Y., "A flexible inner-outer preconditioned GMRES algorithm," *SIAM J. Scientific and Statistical Computing*, Vol. 14, 461–469, 1993.
9. Saad, Y. and M. H. Schultz, "GMRES: A generalized minimal residual algorithm for solving nonsymmetric linear systems," *SIAM J. Scientific and Statistical Computing*, Vol. 7, 856–869, 1986.
10. Song, J. M., C.-C. Lu, and W. C. Chew, "Multilevel fast multipole algorithm for electromagnetic scattering by large complex objects," *IEEE Transactions on Antennas and Propagation*, Vol. 45, No. 10, 1488–1493, 1997.
11. Van der Vorst, H. A., "Bi-CGSTAB: A fast and smoothly converging variant of Bi-CG for the solution of nonsymmetric linear systems," *SIAM J. Scientific and Statistical Computing*, Vol. 13, 631–644, 1992.

Analysis of Polynomial and Geometric Conductivity Profiles in PML Layers: A Comparison

M. Benavides-Cruz[1,3], **M. Álvarez-Cabanillas**[2], **M. Enciso-Aguilar**[1], **and J. Sosa-Pedroza**[1]

[1]ESIME-SEPI, Posgrado en Telecomunicaciones, Instituto Politécnico Nacional
UPALM Edif. Z-4, 3er. piso, Zacatenco 07738, México, D.F., México
[2]Centro de Investigación y Desarrollo de Tecnología Digital, Instituto Politécnico Nacional
Av. Del Parque 1310, Mesa de Otay, Tijuana, Baja California, México
[3]Facultad de Ingeniería Electrónica y Comunicaciones, Universidad Veracruzana
Prolong. Av Venustiano Carranza s/n, Poza Rica, Veracruz, México

Abstract— This paper reports on a new way to measure reflections for several incidence angles of a TM propagating mode in the FDTD Perfect Matched Layer (PML), employing a Gaussian pulse as a source. Experiment is developed using Polynomial and Geometrical conductivity distributions.

1. INTRODUCTION

Since the beginning of FDTD, absorbing boundary conditions (ABC) have been subject of intensive research, due its strong importance in the numeric solution of electromagnetic modeling problems. The (PML) is the best technique so far and has been widely used, due its absorption characteristics independently of the incidence angle over the boundary [1]. The PML ABC is determined by the conductivity profile in such a layer, this profile can be polynomial or geometric. Several efforts have been made by scientific comunity to determinate the optimal conductivity profile values for PML. In [2] the optimal values for a polynomial conductivity profile have been obtained by an analysis in a frequency domain. In order to improve the performance of the conductivity profile, sublayers have been defined by [3]. On the other hand, [4] has defined a conductivity profile that is independent of the problem. This work presents an analysis on the conductivity profile performance by using both polynomial and geometric distributions, under the same matching conditions for the first layer as well as for the same layer numbers that configure the PML region. This enables the user to determinate the accuracy level than can be achieved by the solutions provided by FDTD method as a function of each profile. To this end, the boundary equations are obtained and discretized to be implemented in a FDTD mesh, that models the TM propagation of a Gaussian pulse of finite duration. The reflexion caused by the PML is measured for several incidence angles by an ensemble of sensors strategically located for this purpose.

2. TM PROPAGATION EQUATIONS FOR A PML MEDIUM

The application of a PML boundary condition to a FDTD simulation implies to extend the computation region into a predetermined number of cells. For a TM mode, such cells are confectionated by the same well known field components but with the particularity that the transversal magnetic field component H_z is splitted in two sub components H_{zx} and H_{zy}, in addition the equivalent magnetic conductivity is composed by σ_x^* and σ_x^* depending on the projection axis. To achieve consistence for the electric field equations, the electric conductivity component is associated with the correspondig projection σ_x or σ_y. This is an artifical consideration associated with the PML technique, allowing to the field variations on each direction to be independent on the complementary coordinate. This aasumption leads to reformulate the field equations for a TM mode in a PML [1].

3. CONDUCTIVITY PROFILE IN A PML MEDIUM.

Condition for an optimal performance of a PML ABC requires a smooth transition in the conductivity value for each PML cell, but it must be also intense enough in order to absorb outgoing EM waves, since abrupt changes lead to field uncoupling and reflections, producing a poor performance of the ABC. The smooth change of conductivities between cells is achieved by the conductivity profile. In this paper we compare both, geometrical and polynomial distribution functions, a conductivity σ is assigned to each cell of $\Delta\rho$ length, located at a distance ρ from the interface. The Geometrical distribution function is written as:

$$\sigma(\rho) = \sigma_0 \left(g^{\frac{1}{\Delta\rho}} \right)^{\rho} \tag{1}$$

where σ_0 is the initial conductivity value at the interface, between free space and PML medium, g is a multiplicative factor that commonly takes values between 2 and 4 [1]. For a given value of g, conductivity changes gradually from interface to outer PML cells, conductivity at the PML depends on the conductivity at interface, the factor g and the number of PML cells. Fig. 1 depicts conductivity profiles for g ranging between 3 to 4.

The polynomial distribution function of conductivity is then written as:

$$\sigma(\rho) = \sigma_{\max} \left(\frac{\rho}{c_1 \Delta\rho} \right)^m \tag{2}$$

where $\sigma_{\max}$ is the conductivity value at the outer PML cell, $c_1\Delta\rho$ is the PML width. m is the polinom degree which lies between 1 to 4 [1]. Fig. 2 depicts some normal conductivity profiles for m ranging between 1 and 4.

It can be seen in Fig. 2 that m defines the behavior of the polynomial distribution profile. For example, when $m = 1$ the polynomial distribution profile becomes linear. Moreover, conductivity at the outer PML cell is inversely proportional to m.

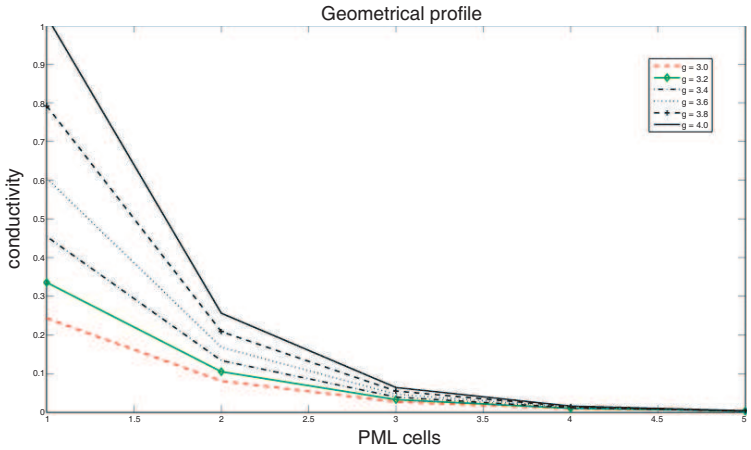

Figure 1: Normalized geometric conductivity profile for a PML layer of 5 cells.

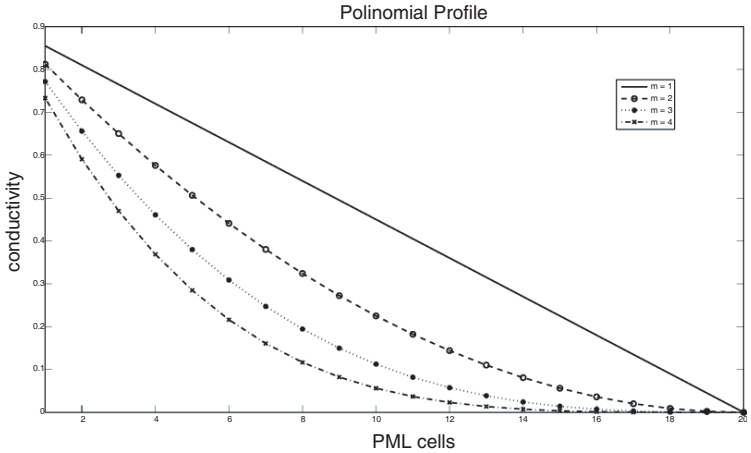

Figure 2: Normalized polynomial conductivity profile for m values between 3 and 4.

4. CONDUCTIVITY PROFILE IMPLEMENTATION IN THE FDTF GRID

Figure 3 schematically represents the Implementation of conductivity profile in the FDTD grid. The inner region is the analysis zone, the interfase states the onset of the PML region; arrows indicate the electric field components and the solid dots the corresponding magnetic field components. The Index L denotes a point into the PML layer, in order to achieve an optimal implementation of the

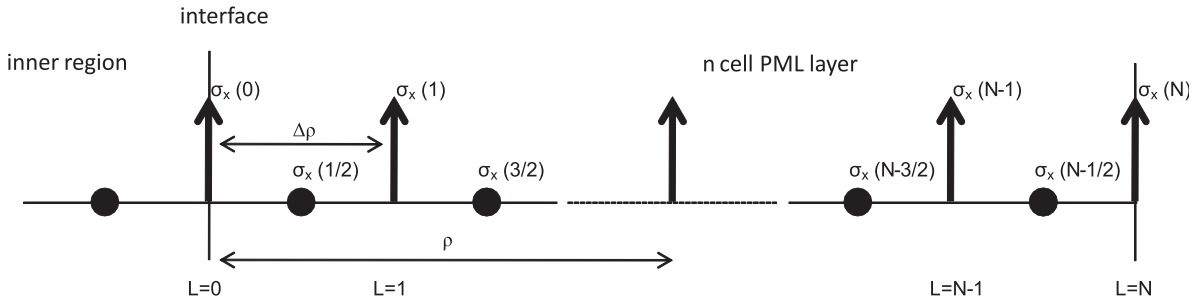

Figure 3: Conductivity distribution in one PML layer composited by N cells.

conductivity profiles (1) and (2), the average conductivity around the point of interest is computed by:

$$\sigma_\rho(L) = \frac{1}{\Delta\rho}\int_{\rho(L)-\frac{\Delta\rho}{2}}^{\rho(L)+\frac{\Delta\rho}{2}} \sigma_p(u)du \tag{3}$$

Leading to build an L-based algorithm to assign a conductivity value to each cell. For a geometrical profile the algorithm is obtained as follows. At the interface $L = 0$:

$$\sigma_{G\rho}(0) = \frac{1}{\Delta\rho}\int_0^{\frac{\Delta\rho}{2}} \sigma_0\left(g^{\frac{1}{\Delta\rho}}\right)^u du = \frac{\sigma_0(\sqrt{g}-1)}{\ln(g)} \tag{4}$$

when $L \neq 0$:

$$\sigma_{G\rho}(L>0) = \frac{1}{\Delta\rho}\int_{\rho(L)-\frac{\Delta\rho}{2}}^{\rho(L)+\frac{\Delta\rho}{2}} \sigma_0\left(g^{\frac{1}{\Delta\rho}}\right)^u du = \frac{\sigma_0 g^L(g-1)}{\ln(g)\sqrt{g}} \tag{5}$$

On the other hand for a polynomial distribution function an algorithm is built as follows: At the interface when $L = 0$:

$$\sigma_{P\rho}(0) = \frac{1}{\Delta\rho}\int_0^{\frac{\Delta\rho}{2}} \sigma_{\max}\left(\frac{u}{N\Delta\rho}\right)^u du = \frac{\sigma_{\max}}{(m+1)2^{m+1}N^m} \tag{6}$$

when $L \neq 0$:

$$\sigma_{P\rho}(L>0) = \frac{1}{\Delta\rho}\int_{\rho(L)-\frac{\Delta\rho}{2}}^{\rho(L)+\frac{\Delta\rho}{2}} \sigma_{\max}\left(\frac{u}{N\Delta\rho}\right)^u du = \frac{\sigma_{\max}}{(m+1)2^{m+1}N^m}\left[(2L+1)^{m+1}-(2L-1)^{m+1}\right] \tag{7}$$

In order to get a comparative analysis between polynomial and geometrical profiles, let us consider the polynomial profile algorithm to have a conductivity σ_0 at the interface, which is calculated as:

$$\sigma_{P\rho}(0) = \sigma_0 \tag{8}$$

then (7) becomes:

$$\sigma_{P\rho}(L>0) = \sigma_0(m+1)2^{m+1}N^m\left[(2L+1)^{m+1}-(2L-1)^{m+1}\right] \tag{9}$$

5. MEASURE OF REFLECTIONS AT THE PML BOUNDARY

As is known, Berenger has established the reflection coefficient for the PML as:

$$R(\Theta) = e^{-(\frac{2}{n+1})(\frac{\sigma_m\delta}{\epsilon_0 c})\cos\theta} \tag{10}$$

Being Θ the incidence angle over the PML. Procedure defines a test domain centered inside a benchmark domain, simulating an almost infinite domain for the reflection layer. The difference between measures inside the test domain and the benchmark domain is a measure of the spurious reflection caused by PML (see Fig. 4).

A different way of reflection measurement is proposed in this paper. We assume a Gaussian pulse propagating over the domain, the incident and reflected waves over the PML boundary are

measured at test points (probes), located inside the domain as shows Fig. 5, then we calculate reflection coefficient to estimate PML absorption as:

$$\Gamma = 20 \log H_r / H_i \tag{11}$$

To avoid both waves impinge the probes at the same time, the incident pulse should disappear when the reflected wave reaches the probe, then do we define the pulse as:

$$Hz(t) = e^{\frac{1}{2s^2}(\Delta t(n_0 - n))} \tag{12}$$

where s is a wave scattering parameter, n is the time step, n_0 is a reference. s can be defined as the number of wavelengths contained in the pulse.

The smaller the s parameter is, the smaller of number of wavelengths in the pulse. The bigger the s parameter is, the bigger the pulse time to get back to zero at any point. The proper selection of s avoids incident and reflected waves interfere each other. For a frequency of 3 GHz in our experiment we choose s as 2×10^{-10} and locate a set of sensors in the domain at different angles of incidence in order to know PML absorption effectiveness at 0, 10, 20, 30, 40 and 45 degrees.

6. RESULTS AND DISCUSSION

We show results for a 3 GHz TM wave propagating in vacuum with a magnitude of $H = 0.2982$ A/m; the 2D domain dimensions are 1350×900 cells, considering stability conditions, meaning $\Delta = 0.5$ cm and $\Delta t = 8.33$ ps respectively. The PML medium is a 12 cell region, surrounding the principal domain, initial conductivity at interface is chosen to be 2×10^{-6} Sm for both, geometrical and polynomial profiles. To measure reflections in PML boundary we locate probes for 6 different incidence angles. The source is a 3 GHz Gaussian pulse with $s = 0.2 \times 10^{-9}$, located at the domain center. The complete setup is already shown in Fig. 5, and Table 1 shows domain dimensions and probe location. As the field moves in the 2D vacuum region, it spreads uniformly over a

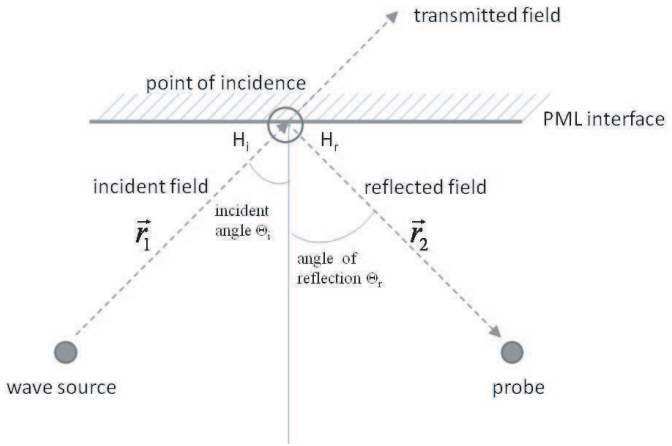

Figure 4: Schematic setup for the calculation of the reflection coefficient.

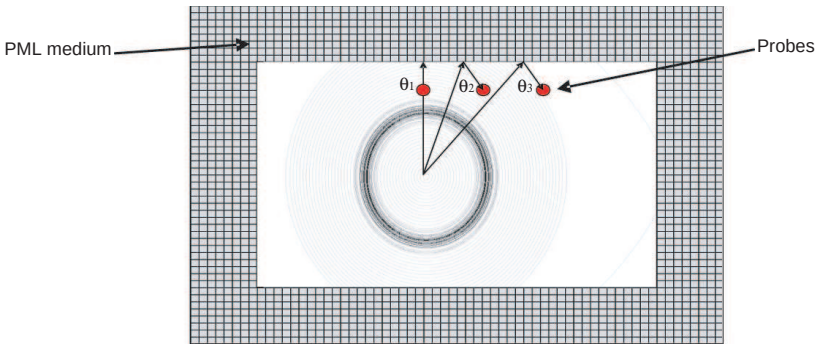

Figure 5: Schematic representation of the measurement setup for several incidence angles.

Table 1: Allocation of wave source, probes and interfaces inside the 1374×924 FDTD grid.

Elements	Coordinates (x, y)	Reflection Coefficient (dB)
Wave Source/Incidence angle	-	-
Probe 1/0°	(887, 737)	−127.11
Probe 2/10°	(803, 737)	−127.22
Probe 3/20°	(665, 737)	−127.70
Probe 4/30°	(554, 737)	−129.28
Probe 5/40°	(455, 737)	−132.69
Probe 4/45°	(362, 737)	−133.04
Left boundary	$x = 12$	-
Right boundary	$x = 1362$	-
Bottom boundary	$y = 12$	-
Top boundary	$y = 912$	-

circumference area πr^2 and is possible to calculate incident and reflected field values in any point at any time in the domain; we measure incident field at each probe and calculate it at the PML boundary, the reflected field is measured at each probe and then using that value calculate the reflected field at the boundary, on the other hand we define the normal to the wave impinging point in PML boundary to calculate the exact reflection angle for each probe, considering it is the same for the incidence angle (Table 1).

7. CONCLUSION

A comparison regarding reflection coefficients for geometrical and polynomial profiles for a PML boundary is presented using an original method of measuring reflection in the principal domain. For the same initial conductivity, we obtain reflection coefficient values varying the m and g parameters for geometrical and polynomial profiles respectively. Best results were presented in Figs. 1, 2 and Table 1, showing attenuation in the PML boundary; as expected, attenuation is larger for the 0° incidence angle and it increases for higher incidence angles. Different experiments were developed varying m between 3 and 4 for the polynomial profile, the best result was obtained for $m = 4$, in this case the reflection coefficient is about −127 dB for 0° and a maximum of 5 dB change when the angle is 45°. For the geometrical profile g varies from 3 to 4, the best result is achieved for $g = 3$, with a reflection coefficient about −129 dB (it will be discussed at talk) and a maximum variation of 20 dB for an incidence angle of 45°.

ACKNOWLEDGMENT

Financial support by the SIP-IPN, COFAA-IPN and CONACyT 106698 project is gratefully acknowledged.

REFERENCES

1. Berenguer, J. P., "A perfectly matched layer for the absorbtion of electromagnetic waves," *J. of Comp. Phys.*, Vol. 114, No. 10, 185–200, 1994.
2. Marengo, E. A., C. M. Rappaport, and E. L. Miller, "Optimum PML ABC conductivity profile in FDTD," *IEEE Trans. on Magetics*, Vol. 35, No. 3, 1986.
3. Winton, S. C. and C. M. Rappaport, "Specifying PML conductivities by considering numerical reflections dependencies," *IEEE Trans. on Ant. and Prop.*, Vol. 48, No. 7, 1055–1063, 2000.
4. Taflove, A. and S. Hagnes, *Computational Electrodynamics, the Finite-difference Time-domain Method*, Artech House, 1986.

Reflection Coefficient of the Isotropic-Dispersion Finite-Difference Time-Domain (ID-FDTD) Method at Planar Dielectric Interfaces

Pingping Deng and Il-Suek Koh
Graduate School of Information Technology & Telecommunications
Inha Unvierstiy, South Korea

Abstract— This paper presents an analytical formulation of the numerical reflection coefficient of the ID-FDTD algorithm at planar dielectric boundaries for a TE wave incidence. The formulation is numerically verified.

1. INTRODUCTION

The standard FDTD method (the Yee scheme) undergoes "numerical dispersion" that makes waves at different phase velocities, which prevents the Yee method from applied to large scale or phase-sensitive problems. Hence, several schemes have been proposed to rectify the numerical dispersion problem, one of which is the isotropic dispersion FDTD (ID-FDTD) scheme to drastically reduce the dispersion [1]. However, at the material interface, the behavior of the ID-FDTD scheme is not clearly characterized. Hence, this paper analytically obtains the numerical reflection coefficient of the ID-FDTD scheme for a TE polarized wave.

2. NUMERICAL REFLECTION COEFFICIENT

Figure 1(a) shows two dielectric half-spaces in an FDTD grid for a TE mode with the numerical wave vector k_i and the frequency ω_0. The wave vectors of the reflected and the transmitted waves are given by k_r and k_t, respectively. In Figure 1(a), Δ and Δt are the grid size and the time step, respectively. μ_0 is the free-space permittivity, and ε_i is the relative permittivity in the material with the index i.

In the two media, the electromagnetic fields are denoted as E_{z1}, H_{x1}, H_{y1} and E_{z2}, H_{x2}, H_{y2} respectively. For example, the numerical waves in the media 1 can be expressed as

$$\begin{aligned} E_{z1}(x,y,t) &= E^i_{z1} + E^r_{z1} = A\cdot e^{j(\omega t - k_{1x}\cdot x - k_y\cdot y)} + B\cdot e^{j(\omega t + k_{1x}\cdot x - k_y\cdot y)} \\ H_{x1}(x,y,t) &= H^i_{x1} + H^r_{x1} = C\cdot e^{j(\omega t - k_{1x}\cdot x - k_y\cdot y)} + D\cdot e^{j(\omega t + k_{1x}\cdot x - k_y\cdot y)} \\ H_{y1}(x,y,t) &= H^i_{y1} + H^r_{y1} = E\cdot e^{j(\omega t - k_{1x}\cdot x - k_y\cdot y)} + F\cdot e^{j(\omega t + k_{1x}\cdot x - k_y\cdot y)}_i \end{aligned} \tag{1}$$

where $A, B, \ldots, F$ are arbitrary constants. The numerical reflection coefficient is defined as $\tilde{r}_{\mathrm{TE}} = B/A = D/C$. At the interface, the tangential field should be continuous, $Ez_1(0,y,t) = Ez_2(0,y,t)$, $Hx_1(0,y,t) = Hx_2(0,y,t)$. From [2], it can be assumed for the ID-FDTD scheme that

$$E_{z0}(0,y,t) = \frac{1}{2}\left[E_{z1}(0,y,t) + E_{z2}(0,y,t)\right], \quad H_{x0}(0,y,t) = \frac{1}{2}\left[H_{x1}(0,y,t) + H_{x2}(0,y,t)\right] \tag{2}$$

Hence, it can be concluded that $Ez_1(0,y,t) = Ez_2(0,y,t) = Ez_0(0,y,t)$ and $Hx_1(0,y,t) = Hx_2(0,y,t) = Hx_0(0,y,t)$ as expected. Based on three steps procedure, the reflection coefficient is analytically formulated. First, we assume Ez_1 and Hx_1 on the dielectric interface, and then Ez_2 and Hx_2 to calculate the other field components. Then, the two results are averaged.

2.1. First Step

The update equations for the grid components at the boundary (Figure 1(b)) are written [1] as

$$\begin{aligned} E_{z1}\Big|^{n+1}_{0,0} \;=\; & E_{z1}\Big|^{n}_{0,0} + C1\cdot\left(H_{x0}\Big|^{n+\frac{1}{2}}_{0,-\frac{1}{2}} - H_{x0}\Big|^{n+\frac{1}{2}}_{0,\frac{1}{2}} + H_{y2}\Big|^{n+\frac{1}{2}}_{\frac{1}{2},0} - H_{y1}\Big|^{n+\frac{1}{2}}_{-\frac{1}{2},0}\right) \\ & + C2\cdot\left(H_{x1}\Big|^{n+\frac{1}{2}}_{-1,-\frac{1}{2}} - H_{x1}\Big|^{n+\frac{1}{2}}_{-1,\frac{1}{2}} + H_{x2}\Big|^{n+\frac{1}{2}}_{1,-\frac{1}{2}} - H_{x2}\Big|^{n+\frac{1}{2}}_{1,\frac{1}{2}}\right. \\ & \left. + H_{y2}\Big|^{n+\frac{1}{2}}_{\frac{1}{2},-1} - H_{y1}\Big|^{n+\frac{1}{2}}_{-\frac{1}{2},-1} + H_{y2}\Big|^{n+\frac{1}{2}}_{\frac{1}{2},1} - H_{y1}\Big|^{n+\frac{1}{2}}_{-\frac{1}{2},1}\right) \end{aligned}$$

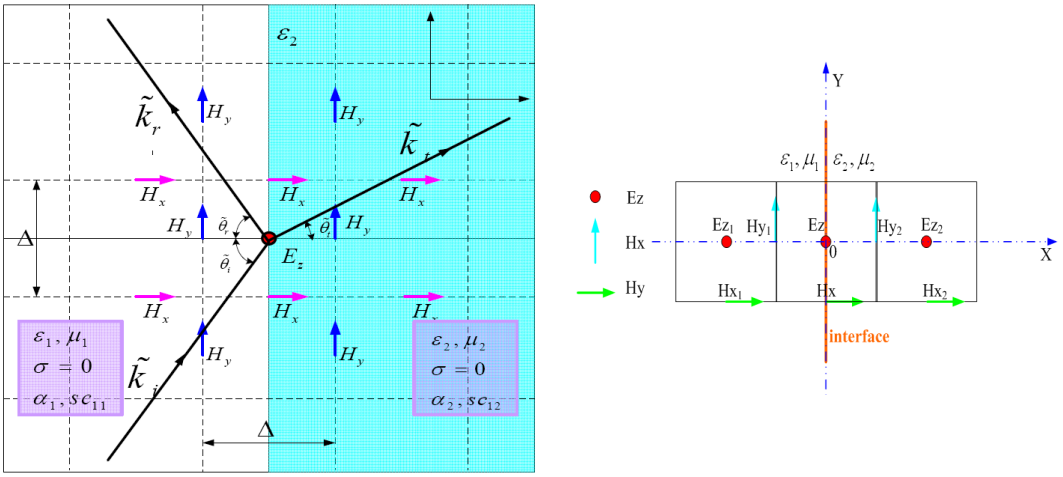

(a) (b)

Figure 1: (a) Two-dimensional FDTD grid for TE modes with planar dielectric boundary. (b) Two-dimensional FDTD grid for TE modes for formulation.

$$
\begin{aligned}
H_{x1}\Big|_{0,-\frac{1}{2}}^{n+\frac{1}{2}} &= H_{x1}\Big|_{0,-\frac{1}{2}}^{n-\frac{1}{2}} + C3\cdot\left(E_{z0}\Big|_{0,-1}^{n+1} - E_{z0}\Big|_{0,0}^{n+1}\right) \\
&\quad + C4\cdot\left(E_{z1}\Big|_{-1,-1}^{n+1} - E_{z1}\Big|_{-1,0}^{n+1} + E_{z2}\Big|_{1,-1}^{n+1} - E_{z2}\Big|_{1,0}^{n+1}\right) \\
H_{x1}\Big|_{-1,-\frac{1}{2}}^{n+\frac{1}{2}} &= H_{x1}\Big|_{-1,-\frac{1}{2}}^{n-\frac{1}{2}} + C3\cdot\left(E_{z1}\Big|_{-1,-1}^{n+1} - E_{z1}\Big|_{-1,0}^{n+1}\right) \\
&\quad + C4\cdot\left(E_{z1}\Big|_{-2,-1}^{n+1} - E_{z1}\Big|_{-2,0}^{n+1} + E_{z1}\Big|_{0,-1}^{n+1} - E_{z1}\Big|_{0,0}^{n+1}\right) \\
H_{x2}\Big|_{1,-\frac{1}{2}}^{n+\frac{1}{2}} &= H_{x2}\Big|_{1,-\frac{1}{2}}^{n-\frac{1}{2}} + C3\cdot\left(E_{z2}\Big|_{1,-1}^{n+1} - E_{z2}\Big|_{1,0}^{n+1}\right) \\
&\quad + C4\cdot\left(E_{z2}\Big|_{0,-1}^{n+1} - E_{z2}\Big|_{0,0}^{n+1} + E_{z2}\Big|_{2,-1}^{n+1} - E_{z2}\Big|_{2,0}^{n+1}\right) \\
H_{y1}\Big|_{-\frac{1}{2},0}^{n+\frac{1}{2}} &= H_{y1}\Big|_{-\frac{1}{2},0}^{n-\frac{1}{2}} + C3\cdot\left(E_{z1}\Big|_{0,0}^{n+1} - E_{z1}\Big|_{-1,0}^{n+1}\right) \\
&\quad + C4\cdot\left(E_{z1}\Big|_{0,-1}^{n+1} - E_{z1}\Big|_{-1,-1}^{n+1} + E_{z1}\Big|_{0,1}^{n+1} - E_{z1}\Big|_{-1,1}^{n+1}\right) \\
H_{y2}\Big|_{\frac{1}{2},0}^{n+\frac{1}{2}} &= H_{y2}\Big|_{\frac{1}{2},0}^{n-\frac{1}{2}} + C3\cdot\left(E_{z2}\Big|_{1,0}^{n+1} - E_{z2}\Big|_{0,0}^{n+1}\right) \\
&\quad + C4\cdot\left(E_{z2}\Big|_{1,-1}^{n+1} - E_{z2}\Big|_{0,-1}^{n+1} + E_{z2}\Big|_{1,1}^{n+1} - E_{z2}\Big|_{0,1}^{n+1}\right)
\end{aligned}
\tag{3}
$$

where $C1 = \frac{(1-0.5\alpha)\Delta t}{\varepsilon\cdot\Delta\cdot sc}$, $C2 = \frac{0.25\alpha\cdot\Delta t}{\varepsilon\cdot\Delta\cdot sc}$, $C3 = \frac{(1-0.5\alpha)\Delta t}{\mu\cdot\Delta\cdot sc}$, and $C4 = \frac{0.25\alpha\cdot\Delta t}{\mu\cdot\Delta\cdot sc}$. The superscript $|_n$ and the subscript $|_{i,j}$ of the field components are the time-step index and the x and y positions of the field component, respectively. Here, $i = 0$ is the index of the material boundary.

Inserting (1) and (2) into the update Equation (3) yields an eigen-value problem [2], whose characteristic equation is given by

$$
\begin{vmatrix}
a_{11} & 0 & a_{13} & a_{14} & a_{15} & a_{16} \\
a_{21} & a_{22} & a_{23} & 0 & 0 & 0 \\
a_{31} & 0 & a_{33} & 0 & 0 & 0 \\
0 & a_{42} & 0 & a_{44} & 0 & 0 \\
a_{51} & 0 & 0 & 0 & a_{55} & 0 \\
0 & a_{62} & 0 & 0 & 0 & a_{66}
\end{vmatrix} = 0 \tag{4}
$$

where the first few constants can be explicitly expressed as

$$a_{11} = (1+\tilde{r}_{\mathrm{TE}})\left(e^{-\frac{j\omega_0\Delta t}{2}} - e^{\frac{j\omega_0\Delta t}{2}}\right),$$
$$a_{13} = \left(e^{\frac{j\tilde{k}_y\Delta}{2}} - e^{-\frac{j\tilde{k}_y\Delta}{2}}\right)\left[\frac{C1\,(1+\tilde{r}_{\mathrm{TE}})}{2} + C2\left(e^{j\tilde{k}_{1x}\Delta} + \tilde{r}_{\mathrm{TE}}e^{-j\tilde{k}_{1x}\Delta}\right)\right].$$

The solution of (4) can be simply written as $P1 + Q1\cdot\tilde{r}_{\mathrm{TE}} = 0$, where

$$P_1 = -4\sin^2\frac{\omega_0\Delta t}{2}\cdot\Lambda\left(2, e^{-j\tilde{k}_{2x}\Delta}\right) + \frac{\Delta t^2}{\varepsilon_{\mathrm{interface}}\cdot\mu_{\mathrm{interface}}\cdot\Delta^2}\left\{\begin{array}{l} 2\sin^2\frac{\tilde{k}_y\Delta}{2}\cdot\Lambda\left(2, e^{-j\tilde{k}_{2x}\Delta}\right)\cdot\left[\Lambda\left(1, e^{j\tilde{k}_{1x}\Delta}\right)\cdot\Lambda\left(1, \cos\tilde{k}_{1x}\Delta\right)\right. \\ \left.+\Lambda\left(1, e^{-j\tilde{k}_{1x}\Delta}\right)\cdot\Lambda\left(2, \cos\tilde{k}_{2x}\Delta\right)\right] + \left(1 - e^{j\tilde{k}_{1x}\Delta}\right) \\ .\frac{\mu_{\mathrm{interface}}}{\mu_1}\Lambda\left(2, e^{-j\tilde{k}_{2x}\Delta}\right)\cdot\Lambda^2\left(1, \cos\tilde{k}_y\Delta\right) + \left(1 - e^{-j\tilde{k}_{2x}\Delta}\right) \\ .\frac{\mu_{\mathrm{interface}}}{\mu_2}\Lambda\left(1, e^{-j\tilde{k}_{1x}\Delta}\right)\cdot\Lambda^2\left(2, \cos\tilde{k}_y\Delta\right) \end{array}\right\}$$

$$Q_1 = -4\sin^2\frac{\omega_0\Delta t}{2}\cdot\Lambda\left(e^{-j\tilde{k}_{2x}\Delta}\right) + \frac{(\Delta t)^2}{\varepsilon_{\mathrm{interface}}\cdot\mu_{\mathrm{interface}}\cdot\Delta^2}\left\{\begin{array}{l} 2\sin^2\frac{\tilde{k}_y\Delta}{2}\cdot\Lambda\left(2, e^{-j\tilde{k}_{2x}\Delta}\right)\left[\Lambda\left(1, e^{-j\tilde{k}_{1x}\Delta}\right)\cdot\Lambda\left(1, \cos\tilde{k}_{1x}\Delta\right)\right. \\ \left.+\Lambda\left(1, e^{j\tilde{k}_{1x}\Delta}\right)\cdot\Lambda\left(2, \cos\tilde{k}_{2x}\Delta\right)\right] + \left(1 - e^{-j\tilde{k}_{1x}\Delta}\right) \\ .\frac{\mu_{\mathrm{interface}}}{\mu_1}\Lambda\left(2, e^{-j\tilde{k}_{2x}\Delta}\right)\cdot\Lambda^2\left(1, \cos\tilde{k}_y\Delta\right) + \left(1 - e^{-j\tilde{k}_{2x}\Delta}\right) \\ .\frac{\mu_{\mathrm{interface}}}{\mu_2}\Lambda\left(1, e^{j\tilde{k}_{1x}\Delta}\right)\cdot\Lambda^2\left(2, \cos\tilde{k}_y\Delta\right) \end{array}\right\}$$

with $\Lambda(i,x) = (1 - 0.5\alpha_i + 0.5\alpha_i\cdot x)$, and $\varepsilon_{\mathrm{interface}}$ and $\mu_{\mathrm{interface}}$ are the relative permittivity and permeability at the interface cell, respectively.

2.2. Second Step

By using the same procedure as before, we can obtain a solution as $P2 + Q2\cdot\tilde{r}_{\mathrm{TE}} = 0$, where

$$P_2 = -4\sin^2\frac{\omega_0\Delta t}{2}\cdot\Lambda\left(1, e^{j\tilde{k}_{1x}\Delta}\right) + \frac{(\Delta t)^2}{\varepsilon_{\mathrm{interface}}\cdot\mu_{\mathrm{interface}}\cdot\Delta^2}\left\{\begin{array}{l} 2\sin^2\frac{\tilde{k}_y\Delta}{2}\cdot\Lambda\left(1, e^{j\tilde{k}_{1x}\Delta}\right)\left[\Lambda\left(2, e^{j\tilde{k}_{2x}\Delta}\right)\cdot\Lambda\left(1, \cos\tilde{k}_{1x}\Delta\right)\right. \\ \left.+\Lambda\left(2, e^{-j\tilde{k}_{2x}\Delta}\right)\cdot\Lambda\left(2, \cos\tilde{k}_{2x}\Delta\right)\right] + \left(1 - e^{j\tilde{k}_{1x}\Delta}\right) \\ .\frac{\mu_{\mathrm{interface}}}{\mu_1}\Lambda\left(2, e^{j\tilde{k}_{2x}\Delta}\right)\cdot\Lambda^2\left(1, \cos\tilde{k}_y\Delta\right) + \left(1 - e^{-j\tilde{k}_{2x}\Delta}\right) \\ .\frac{\mu_{\mathrm{interface}}}{\mu_2}\Lambda\left(1, e^{j\tilde{k}_{1x}\Delta}\right)\cdot\Lambda^2\left(2, \cos\tilde{k}_y\Delta\right) \end{array}\right\}$$

$$Q_2 = -4\sin^2\frac{\omega_0\Delta t}{2}\cdot\Lambda\left(e^{-j\tilde{k}_{1x}\Delta}\right) + \frac{(\Delta t)^2}{\varepsilon_{\mathrm{interface}}\cdot\mu_{\mathrm{interface}}\cdot\Delta^2}\left\{\begin{array}{l} 2\sin^2\frac{\tilde{k}_y\Delta}{2}\cdot\Lambda\left(1, e^{-j\tilde{k}_{1x}\Delta}\right)\left[\Lambda\left(2, e^{j\tilde{k}_{2x}\Delta}\right)\cdot\Lambda\left(1, \cos\tilde{k}_{1x}\Delta\right)\right. \\ \left.+\Lambda\left(2, e^{-j\tilde{k}_{2x}\Delta}\right)\cdot\Lambda\left(2, \cos\tilde{k}_{2x}\Delta\right)\right] + \left(1 - e^{-j\tilde{k}_{1x}\Delta}\right) \\ .\frac{\mu_{\mathrm{interface}}}{\mu_1}\Lambda\left(2, e^{j\tilde{k}_{2x}\Delta}\right)\cdot\Lambda^2\left(1, \cos\tilde{k}_y\Delta\right) + \left(1 - e^{-j\tilde{k}_{2x}\Delta}\right) \\ .\frac{\mu_{\mathrm{interface}}}{\mu_2}\Lambda\left(1, e^{-j\tilde{k}_{1x}\Delta}\right)\cdot\Lambda^2\left(2, \cos\tilde{k}_y\Delta\right) \end{array}\right\}$$

2.3. Third Step

Finally, the reflection coefficient is obtained as

$$\tilde{r}_{\mathrm{TE}} = -\frac{P_1 + P_2}{Q_1 + Q_2} = \frac{X + jZ}{Y - jZ}, \tag{5}$$

For real dielectric constants, the imaginary part of the reflection coefficient should be zero [2]. Hence, $\varepsilon_{\mathrm{interface}}$ and $\mu_{\mathrm{interface}}$ can be determined as

$$\begin{aligned} \varepsilon_{\mathrm{interface\_ID}} &= \frac{\varepsilon_1 f_2 + \varepsilon_2 f_1}{f_1 + f_2} = \frac{\varepsilon_1 + \varepsilon_2}{2} + \frac{\varepsilon_2 - \varepsilon_1}{2} \cdot \frac{f_1 - f_2}{f_1 + f_2}, \\ \mu_{\mathrm{interface\_ID}} &= \frac{(f_1 + f_2)\mu_1\mu_2}{\mu_2 f_1 + \mu_1 f_2} = \frac{2\mu_1\mu_2}{\mu_1 + \mu_2 + \frac{\mu_2 - \mu_1}{2} \cdot \frac{f_1 - f_2}{f_1 + f_2}}. \end{aligned} \tag{6}$$

For this case, the real reflection coefficient is reduced to

$$\tilde{r}_{TE\_ID} = \frac{\sin k_{1x}\Delta \cdot \left[\mu_2 \frac{f_2 f_3}{f_4} + \alpha_1 \cdot H\right] - \sin k_{2x}\Delta \cdot \left[\mu_1 \frac{f_1 f_4}{f_3} + \alpha_2 \cdot H\right]}{\sin k_{1x}\Delta \cdot \left[\mu_2 \frac{f_2 f_3}{f_4} + \alpha_1 \cdot H\right] + \sin k_{2x}\Delta \cdot \left[\mu_1 \frac{f_1 f_4}{f_3} + \alpha_2 \cdot H\right]} \tag{7}$$

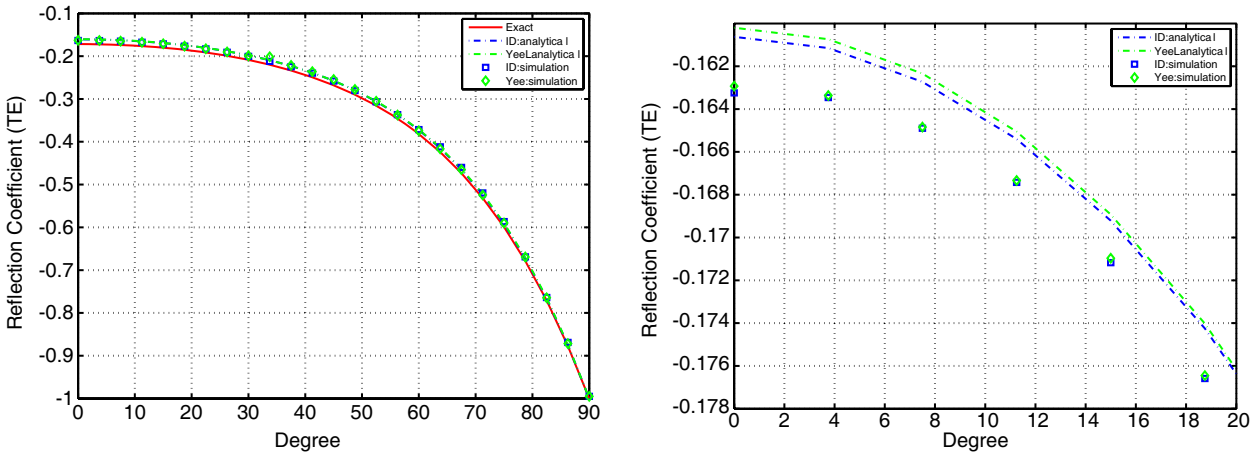

Figure 2: Comparison of the reflection coefficients for CPW = 15 and $\varepsilon_r = 2$. (a) for whole θ, (b) for small interval of θ.

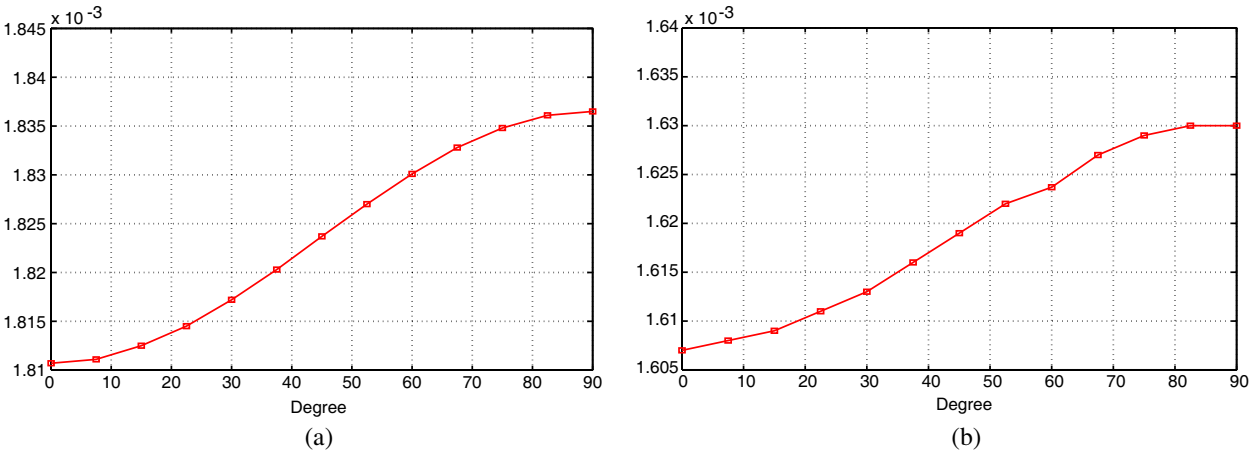

Figure 3: Comparison of the effective dielectric constant for a TE mode. (a) $\varepsilon_1 = 1$, $\varepsilon_2 = 2$, $\mu_1 = \mu_2 = 1$ for $\varepsilon_{\mathrm{interface\_ID}} - (\varepsilon_1 + \varepsilon_2)/2$. (b) $\varepsilon_1 = \varepsilon_2 = 1$, $\mu_1 = 1$, $\mu_2 = 2$ for $\mu_{\mathrm{interface\_ID}} - 2\mu_1\mu_2/(\mu_1 + \mu_2)$.

where $f_1 = (1-\alpha_1 \cdot \sin^2 \frac{k_{1x}\Delta}{2})$, $f_2 = (1-\alpha_2 \cdot \sin^2 \frac{k_{2x}\Delta}{2})$, $f_3 = (1-\alpha_1 \cdot \sin^2 \frac{k_y\Delta}{2})$, $f_4 = (1-\alpha_2 \cdot \sin^2 \frac{k_y\Delta}{2})$, $H = \frac{\mu_2 \frac{f_2 f_3}{f_4} \cdot \sin^2 \frac{k_{1x}\Delta}{2} + \mu_1 \frac{f_1 f_4}{f_3} \cdot \sin^2 \frac{k_{2x}\Delta}{2}}{f_1+f_2}$. For $\alpha = 0$, the effective dielectric constant (5) and the reflection coefficient (6) will be reduced to those of the Yee scheme [2] as $\varepsilon = \frac{\varepsilon_1+\varepsilon_2}{2}$, $\tilde{r}_{\mathrm{TE}} = \frac{\sin \tilde{k}_{1x}\Delta - \sin \tilde{k}_{2x}\Delta}{\sin \tilde{k}_{1x}\Delta - \sin \tilde{k}_{2x}\Delta}$.

3. VERIFICATION

Figure 2 shows a comparison of the reflection coefficients calculated by two formulations of the ID-FDTD and Yee schemes for a TE wave incidence. From the figures, we can observe that the coefficient (6) for the ID-FDTD scheme is more accurate than that for the Yee method. Figure 3 give a comparison of the absolute error of $\varepsilon_{\mathrm{interface}}$ and $\mu_{\mathrm{interface}}$ calculated by (5) and that for the Yee scheme. From the figures, we can observe the difference between the ID-FDTD and the Yee schemes are very small.

4. CONCLUSION

In this paper, we formulate the numerical reflection coefficient of the ID-FDTD scheme for the dielectric interface. The formulation is reduced to those for the Yee scheme and the exact one for $\alpha = 0$ and $\Delta \to 0$, respectively. It's numerically shown that the obtained equations are more accurate than that of the Yee scheme. Therefore, the ID-FDTD scheme can provide accurate results for inhomogeneous problems.

REFERENCES

1. Koh, I., H. Kim, J. Lee, J. Yook, and C. Pil, "Novel explicit 2-D FDTD scheme with isotropic dispersion and enhanced stability," *IEEE Trans. Antennas Propag.*, Vol. 54, No. 11, 3505–3510, Nov. 2006.
2. Christ, A., S. Benkler, J. Fröhlich, and N. Kuster, "Analysis of the accuracy of the numerical reflection coefficient of the finite-difference time-domain method at planar material interfaces," *IEEE Trans. Electromagn. Compat.*, Vol. 48, No. 2, 264–272, May 2006.

Analyzed of Yagi Antenna by the Theory of Maxwellian Circuits

Wenhui Shen[1], **Yanzhong Ma**[1], **Mingliang Wu**[1], **and K. K. Mei**[2]

[1]School of Communication and Information Engineering, Shanghai University, Shanghai 200072, China
[2]Department of Electrical Engineering and Computer Science, University of California, Berkely, USA

Abstract— In this paper, the theory of Maxwellian Circuits(MC) is applied to compute the Yagi antennas, the geometry of the Yagi antennas are formulated by MC in detail. Combining with Hallen's Equation and Lorenz Gauge, the voltage cancellation technique is used to transform the expression of voltage into analytic form. The technique is verified by calculating the current distributions and the radiation patterns of a 3-element Yagi antenna. The same antennas are also computed by the Method of Moments(MoM). The good agreements of the two results show that the theory of Maxwellian circuits is valid and it is as accurate as MoM in investigating disconnected antennas or multibody scattering.

1. INTRODUCTION

Numerical solutions of antenna and scattering problems have replaced the classisical analyses since the development of high speed digital computers. Commercial softwares are now available to solve antennas of arbitrary shapes and help the engineers in their design processes. The mission of computation is completed after providing the current distributions and other related data to the software users. If the results do not satisfy the users, they would change the parameters and start the computations all over again. The theory of Maxwellian circuits [1] shows that the numerical results of the current densities can be used to find the equivalent circuits whose solutions of the voltages and current densities are identical to the solutions of Maxwell's equations. Circuits may provide more insights to design engineers than just current distributions alone, and thus provide guides to fine tune in the design. With the use of metrons the Maxwellian circuits may be found without the solutions of MoM, so it is a computational method as well. In this paper we shall show how Yagi antennas can be represented in terms of MC. MC has been applied to calculate linear antennas and scatterers [1–5], discontinuity of microstrip and the printed spiral antennas [1–5]. The Yagi antennas are different from prior investigations on MC, because they involve several disconnected wires. How disconnected differential equations of the currents are coupled is discussed in this paper.

2. ANALYZING THE YAGI ANTENNAS BY MAXWELLIAN CIRCUITS

As shown in Fig. 1, the diameter of the wire of Yagi antennas is $2a$, length of the three antenna elements are L_1, L_2, L_3, respectively. Array spacing between element L_1-L_2 and L_2-L_3 is d_{12} and d_{23}, respectively. A voltage source V_0 is fed at the center of element L_2. The coupled Hallen's equation of an antenna is

$$\sum_{j=1}^{3}\int_{l_j} G\left(l_i, l'_j\right) I_j\left(l'_j\right) dl'_j = A_i \sin(kl_i) + B_i \cos(kl_i) + \frac{V_0(l_i)}{j2z_0}\sin(k\,|l_i|), \quad (i = 1,\, 2,\, 3) \tag{1}$$

where, $G(l_i, l'_j)$ is free space Green's function, z_0 is wave impedance, k is wave number, $I_j(l'_j)$ is currents distribution of element L_j. Equation (1) represents three coupled integral equations. When the integral equations are converted into matrices, we may use inverses of the matrices to find three antenna type integral equations on each wire, having driving functions related to the boundary conditions of the other wires.

According to the existence theorem of MC, there exists equivalent differential equations for each integral equation with driving functins related to the boundary conditions of other wires. Those differential equations can be represented by the fillowing coupled equations of the Maxwellian circuits:

$$\begin{cases} \frac{dV_i}{dl_i} = -j\omega L_{ii} I_i + \alpha_{ii} V_i - \sum\limits_{j=1, i\neq j}^{3} [j\omega L_{ij} I_j(L_j) + \alpha_{ij} V_j(L_j)] \\ \frac{dI_i}{dl_i} = -j\omega C_{ii} V_i + \beta_{ii} I_i - \sum\limits_{j=1, i\neq j}^{3} [j\omega C_{ij} V_j(L_j) + \beta_i I_j(L_j)], \quad (i = 1,\, 2,\, 3) \end{cases} \tag{2}$$

where L_{ij}, C_{ij} is distributed inductance, distributed capacitance, α_{ij} and β_{ij} are coefficients related to environments, coupling effects, etc.

It noticed that Equation (2) is determined when the unknown coefficients L_{ij}, C_{ij}, α_{ij} and β_{ij} are found. To find L_{ij}, C_{ij}, α_{ij} and β_{ij}, we need three linearly independent current/ incident field pairs. These may be obtained either by solving MoM equations with a incident field of three set of boundary conditions, or use matrons to find incident fields.

We have also take advantage of the fact that,

$$V_i = -\frac{1}{j\omega\varepsilon}\frac{d}{dl_i}\sum_{j=1}^{3}\int_{l_j} G\left(l_i, l'_j\right) I_j\left(l'_j\right) dl'_j \tag{3}$$

And noticed that the left part of Equation (1) and the left part of Equation (2) are the same, so

$$V_i = -\frac{k}{j\omega\varepsilon}\left[A_i\cos(kl_i) - B_i\sin(kl_i)\right] + \frac{V_0(l_i)}{j2z_0}\sin(k\,|l_i|), \quad (i = 1,\ 2,\ 3) \tag{4}$$

It is obvious that the technique of canceling the voltage make the calculation procedure simpler and more accurate.

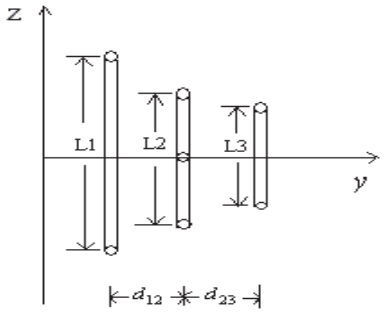

Figure 1: Geometry of Yagi antennas.

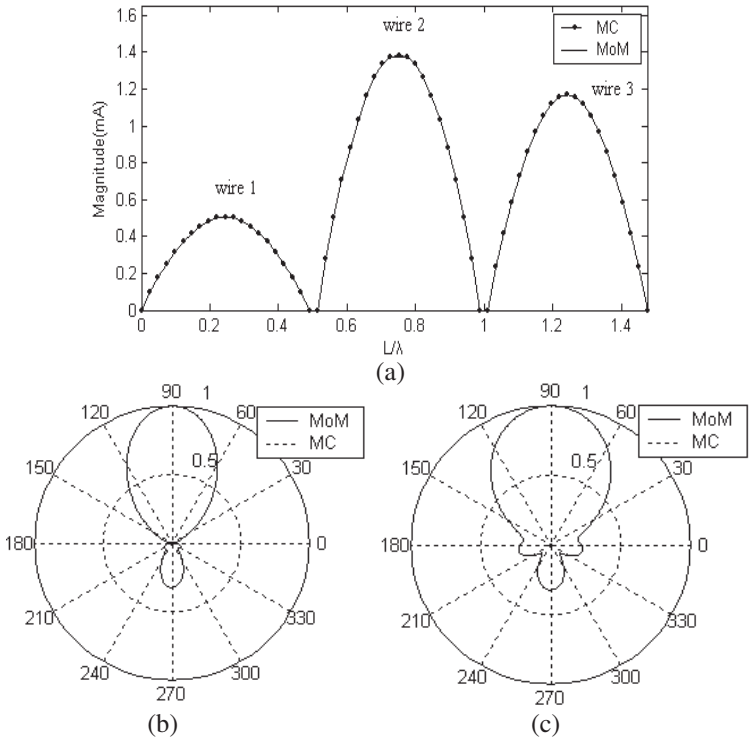

Figure 2: Currents distribution and radiation pattern of a Yagi antenna with array spacing $d_{12}/la = 0.225$ and $d_{23}/la = 0.15$. (a) Amplitude of the currents distribution on each element of Yagi antennas. (b) E-pattern. (c) H-pattern.

Put the pairs of V_i and I_i into Equation (2), then L_{ij}, C_{ij}, α_{ij} and β_{ij} are worked out. After that, the currents distribution of Yagi antennas can be solved.

3. NUMERICAL RESULTS

A three element Yagi antennas as shown in Fig. 1 is calculated by MC and MoM, respectively. The diameter of the wire is $2a/\lambda = 0.005$, length of the element is $L_1/\lambda = 0.49$, $L_2/\lambda = 0.475$, $L_3/\lambda = 0.463$.

Figure 2 depicted the currents distribution and radiation pattern of a three element Yagi antenna, the array spacing is $d_{12}/\lambda = 0.225$ and $d_{23}/\lambda = 0.15$. Results calculated by MC are in high quality agreement with results calculated by MoM shows the correctness and efficiency of MC.

4. CONCLUSION

Investigation of the Yagi antennas by the theory of MC is presented. A three element Yagi antennas is investigated. It shows how the differential equations on separated elements are coupled to one another. The solutions of the coupled differential equations are almost identical to those of the MoM. We have successfully demonstrated that the theory of Maxwellian circuits can be extended to disconnected elements such as multibody scattering.

REFERENCES

1. Mei, K. K., "Theory of Maxwellian circuits," *Radio Sci. Bull.*, Vol. 305, No. 9, 6–13, 2003.
2. Li. Li., Y.-W. Liu, K. K. Mei, and K.-W. Leung, "Applications of the maxwellian circuits to linear wire antennas and scatterers," *IEEE Trans. Antennas. Propag.*, Vol. 54, No. 10, 2725–2730, 2006.
3. Wu, M., W. Shen, G. Zhao, and K. K. Mei, "Comprehensive analysis of linear wire antennas with Maxwellian circuits," *Microwave Conference, 2008 China-Japan Joint*, 327–329, Sep. 2008.
4. Liu, Y. W., J. S. Hong, and K. K. Mei, "Analysis of a double microstrip discontinuity using generalized transmission line equations," *IEEE Trans. Adv. Packag.*, Vol. 26, No. 11, 368–374, 2003.
5. He, M. and X. W. Xu, "Maxwellian circuit models for analysis of printed spiral antennas," *IEEE Trans. Microw. Wireless Compon. Lett.*, Vol. 15, No. 11, 769–771, 2005.

Modelling of Coil-loaded Wire Antenna Using Composite Multiple Domain Basis Functions

A. A. Lysko
Meraka Institute, Council for Scientific and Industrial Research (CSIR), South Africa

Abstract— The paper discusses aspects of a novel impedance matrix compressing technique and applies the technique to a coil-loaded monopole. The technique can reduce the number of variables required for modeling of structures with curvatures and structures with electrically small features. The reduction in the number of unknowns is accomplished by a logical aggregation/grouping of the individual wire segments into equivalent continuous wires. A single composite basis function is applied over several wire segments. This decouples the number of unknowns from the number of geometrical segments. Aggregation of small features aims a reduction in the impedance matrix's condition number. The example of coil-loaded antenna has shown that the proposed novel algorithm achieves better accuracy with fewer unknowns than the traditional formulation of the method of moments.

1. INTRODUCTION

This work discusses aspects of and applies a novel impedance matrix compressing technique [1] to model a coil-loaded monopole antenna. The technique helps to reduce the number of variables required for modeling of structures with curvatures and structures with electrically small features. The presented realization of the technique assumes usage of piece-wise linear approximation of geometry. This approximation is seen as the core to inefficiency in modeling of the above-mentioned types of geometrical structures with a traditional method of moments (MoM). The reduction in the number of variables is accomplished by a logical aggregation/grouping of the individual straight wire segments into equivalent continuous wires with bends. This permits to apply a single basis function over several wire segments, and to decouple the number of unknowns from the number of geometrical segments. Aggregation of individual electrically small features also aims a reduction in the impedance matrix condition number [2]. Following the idea of aggregating domains of multiple segments, the basis functions used in the technique are herein referred to as multiple domain basis functions (MDBF). This name is also consistent with the terminology used in [11], and is an extension to it.

The technique is applied to the method of moments, under the thin wire approximation. The method used in this paper borrows the matrix form of expressions from [3] and develops it further, as to use a Galerkin approach [1, 10]. The method has many similarities with the macro and characteristic basis functions and related methods [4–6]. However, unlike this work, none of the references uses piecewise-linearly interpolated piecewise sinusoidal basis functions as the macro basis functions. In addition, in the main proposed domain of application, i.e., for smoothly bent structures, the technique proposed here requires fewer computations in comparison to the characteristic basis function, as the maximum electrical size covered by a single MDBF can usually be predicted and no solution of the localized systems is required to compose the set of new basis functions.

Section 2 of the paper describes the theoretical basis for the method. In the next section, the model of the coil-loaded monopole is analyzed. The validation of this numerical model is also presented there. Section 4 compares the developed approach to the traditional method of moments and provides a discussion on the results.

2. THEORY OF THE MULTIPLE-DOMAIN BASIS FUNCTIONS

The approach discussed in this paper involves the multiple domain basis functions (MDBF) [1], where a composite basis function aggregates one to several traditional basis functions. The technique is applied under the Galerkin procedure of the method of moments (MoM) as per [1]. This enhances robustness compared to the procedure derived in [3], where rooftop and pulse functions were used for both expansion and testing. The thin wire approximation [11] is used in the modeling. It may however be noted that the method is seen as equally applicable to the flat triangles [8], quadrilaterals or volumetric elements.

Mathematically, the procedure of obtaining the solution is as follows. It is assumed that the MoM procedure results in the set of linear algebraic equations $\mathbf{Z} \cdot \mathbf{I} = \mathbf{V}$, where $\mathbf{Z}$ is the square impedance matrix, $\mathbf{I}$ is the column vector of unknowns, and $\mathbf{V}$ is the column vector describing excitations.

In applying the MDBFs, it is assumed that a relationship between a longer vector of original (old) unknowns $\mathbf{I}$ and the shorter vector with new unknowns $\tilde{\mathbf{I}}$ exists, and may be written in a matrix form as $\mathbf{I} = \mathbf{M}\tilde{\mathbf{I}}$. Herein, $\mathbf{M}$ denotes a matrix grouping/aggregating basis functions. Each row of this matrix contains weights defining which new basis functions are involved in the formation of the respective old basis functions, and with what weights.

The expression relating the old unknowns to the new ones may be substituted into the original system of linear equations $\mathbf{ZI} = \mathbf{V}$. The resultant system $\mathbf{ZM}\tilde{\mathbf{I}} = \mathbf{V}$ is then left-multiplied by the transposed transformation matrix $\mathbf{M}$ to obtain the new system of linear equations: $\underbrace{\mathbf{M}^T\mathbf{ZM}}_{\tilde{\mathbf{Z}}}\tilde{\mathbf{I}} = \underbrace{\mathbf{M}^T\mathbf{V}}_{\tilde{\mathbf{V}}}$. This system may be rewritten in a short form as $\tilde{\mathbf{Z}}\tilde{\mathbf{I}} = \tilde{\mathbf{V}}$. Once this new system is solved and the new unknowns $\tilde{\mathbf{I}}$ obtained, the original unknowns may be computed from $\mathbf{I} = \mathbf{M}\tilde{\mathbf{I}}$.

The results of a MDBF based approach may be made equal to the results of a traditional MoM with the same original expansion functions, if the matrix $\mathbf{M}$ is an identity matrix.

The validity of the technique may be limited when there is a strong feature present in a nearby current distribution which cannot be modeled with the chosen shape of the aggregating basis functions (such as piecewise linear or sinusoidal), like in [7]. This restriction is also characteristic for the global basis functions, where it leads to a poor convergence rate. A possible remedy to this problem within the proposed technique is to estimate the strength of the interactions from the values of the elements of the original impedance matrix in advance, and use this information to form/adjust the boundaries of the new MDBF basis functions. Such a solution can also apply to the macro and characteristic basis functions.

3. NUMERICAL MODEL DESCRIPTION

This paper discusses one of the examples considered in [9]. The choice was based on the complexity of the structure, and availability of measured reference data.

The geometry of the antenna is shown in Figure 1. The drawing shows the two straight wire segments joined by a helical coil. Both straight segments as well as the coil are modeled by straight thin wire sub-segments. The monopole is fed with a 1-Volt delta gap generator described in detail in [10, 11]. The generator was attached to the zero-radius end of a short wire, as seen in Figure 1. This aims to reduce the fringe capacitance problem [11] and improves accuracy of modeling.

The geometrical parameters for this example are as follows: number of turns = 8, length of the lower straight segment $L_{a1} = 15.02\,\text{cm}$, length of the upper straight segment $L_{a2} = 6.68\,\text{cm}$, length of the coil $L_c = 3.3\,\text{cm}$, wire radius for all wires $a = 0.15\,\text{cm}$, inner radius of the coil $a_c = 0.8\,\text{cm}$. Unless stated otherwise, the frequency is 300 MHz. The modeled antenna includes two straight wire segments and a coil placed between them. The coil was modeled using from 3 up to 128 piecewise linear straight wire segments per turn.

Figure 1(b) shows a loaded dipole that was used to investigate some of the properties of the method. This dipole is equivalent to the monopole shown in Figure 1(a) and is made up of two such monopoles. It must be noted that the reason for using the dipole instead of monopole was of purely practical manner related to the easiest and quickest way of obtaining the impedance matrix's elements.

The numerical model was first verified using a traditional MoM with low and higher-order polynomial basis functions [10], where the low order functions are piecewise linear basis functions. This stage included a comparison of the frequency dependence and current distribution profiles against the experimental data from [9]. Figure 2 illustrates a part of the validation and displays and an excellent match between the measurements and the numerical model built. The model validation procedures have confirmed quality of the numerical meshes and resultant models. The validation has also indicated the correctness of the original impedance matrix, critical for applying the method used in this paper.

The original fine mesh was aggregated using three different high level meshing approaches, namely algorithms A, B, and C, first published in [12]. The algorithm A iteratively, segment by segment, tries to aggregate the wire segments into new larger domains. This algorithm maximizes the size of each new domain, which sometimes may lead to undesirably small non-aggregated

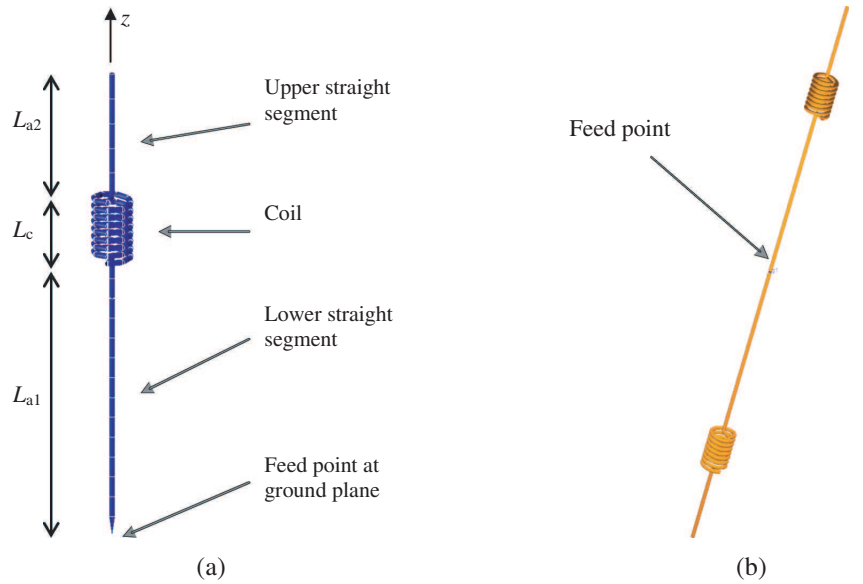

Figure 1: Geometry of the monopole loaded with coil (a), and (b) an equivalent dipole-like structure. Note: (i) The scales for the drawings in (a) and (b) are not the same. (ii) The radius of wire ends touching the feed point is zero for both monopole and dipole (may be especially difficult to see in Figure 1(b) due to the scale).

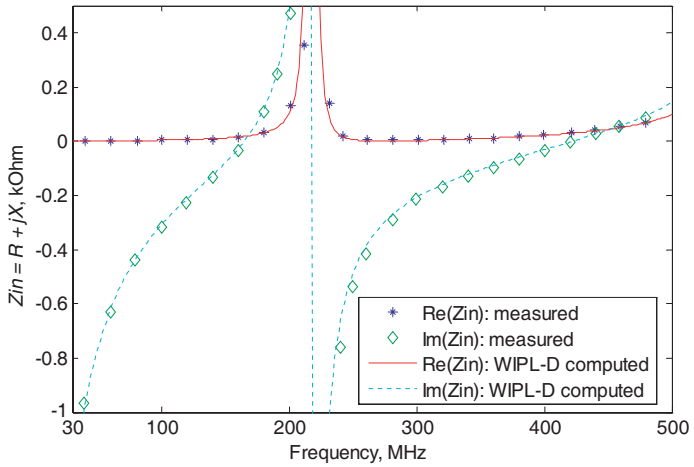

Figure 2: Input impedance of the coil loaded monopole antenna versus frequency, as computed by WIPL-D and measured in [9]. WIPL-D simulation was set to have a basis function based on a 2nd degree polynomial applied to each individual segment. WIPL-D model used eight straight wire segments per one turn of the coil.

segments. The algorithm B improves on this by considering two segments at a time. It reduces the probability of generating small non-aggregated segments but does not eliminate it fully. The algorithm C uses the global knowledge and tries to generate maximally equal new domains. The results are shown in the next section.

4. RESULTS

A set of simulations with various values of the meshing parameters and meshing algorithms were performed in order to generate the convergence curves (of error versus the total number of unknowns).

An example is shown in Figure 3. Each curve denoted with PWL or PWS was obtained by repeating the same simulation scenario, and permitting a different number of unknowns at each simulation. The error in the current at the feed point was taken as the measure of accuracy. The results of a direct MoM solution at the finest mesh were used as the reference. The convergence plots

show that the proposed novel algorithm converges quicker than the traditional MoM based on the piecewise linear basis functions (denoted with δ (Ymono) and δ (Ydip) for monopole and dipole models, respectively), especially if only few unknowns are available or permitted for modeling. When the number of unknowns is small, an order of magnitude improvement in the accuracy of the solution has been observed.

The plot shown in Figure 3 corresponds to a mesh obtained by the chain-splitting algorithm propagating its solution from the feed point towards the free ends. The curves (especially ones marked with dots) experience multiple dips as the number of unknowns is increased, in the region with the number of unknowns greater than 10. This phenomenon is not present (the curve is much smoother) for the chain-splitting algorithm propagating its solution from the free ends towards the feed point (this plot is not shown but may be found in [13]).

In addition, it was observed from Figure 4 that the condition number of the compressed solution for a dipole are ten-fold lower than that of the traditional solution "d1" for the same dipole, although it closely matches the condition number observed for a monopole model (except for the very high number of unknowns).

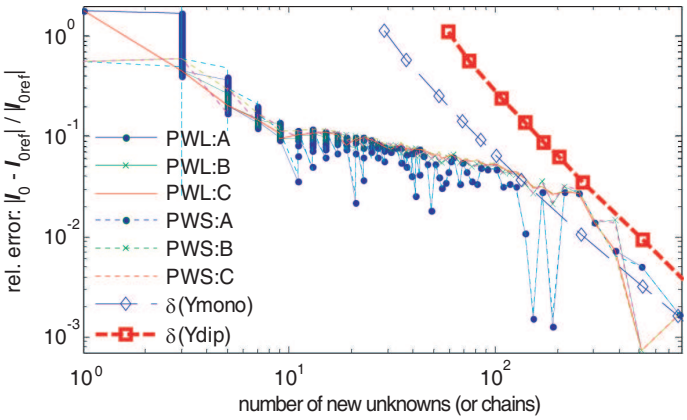

Figure 3: Convergence of error with growth in the total number of used variables (defined by the maximum permitted electrical length of a grouped chain of wire segments). The plot corresponds to the chain-splitting algorithm propagating its solution from the feed point towards the free ends. The notations PWL and PWS stand for piecewise linear and sinusoidal basis functions. The letters A, B or C following, denote the type of splitting algorithm applied [12]. The legend entries "δ" denote the convergence rate for the antennas modeled with a traditional direct MoM [10].

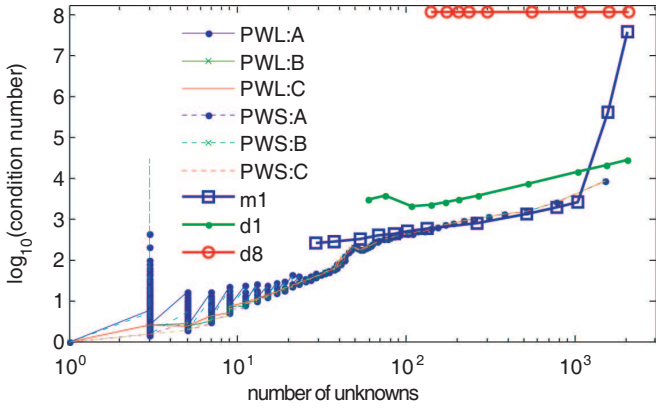

Figure 4: Condition number of the impedance matrix versus the number of unknowns when modeling a coil-loaded monopole and dipole. The notations PWL and PWS stand for piecewise linear and sinusoidal (basis functions used). The letters A, B and C denote the chain-splitting algorithm applied. The first six entries in the legend describe condition number of the new compressed impedance matrix for the respective meshing scenarios. The last three entries in the legend describe the condition number for direct solutions by the MoM. The first symbol in the notations mN or dN stand for monopole/dipole and the second symbol (digit) stands for the WIPL-D's "current expansion" option. There is a slight monotonic increase in the condition number for d8, which is not readily visible due to the scale of the plot.

5. CONCLUSION

A novel method for effective modeling of curved structures and structures with electrically small features has been described. The method aggregates several basis functions into a composite basis function based on a linear interpolation between the original basis functions, and can thus permit a reduction in the number of unknowns with no sacrifice in accuracy. The method has been implemented over the framework of the method of moments

The method has been applied to an example of a coil-loaded antenna. Both piecewise-linear and piecewise-sinusoidal linearly-interpolated profiles of composite basis functions have been applied. The results confirm that the proposed method achieves better accuracy with fewer unknowns than the traditional method of moments.

ACKNOWLEDGMENT

This work was funded in part by the Department of Electronics and Telecommunications, Norwegian University of Science and Technology (NTNU), Norway.

REFERENCES

1. Lysko, A. A., "Using piecewise sinusoidal basis functions to blanket multiple wire segments," *Proc. of IEEE Int'l Symp. on Ant. & Propag. and USNC/URSI Nat. Radio Science Meeting*, 4, USA, Jun. 2009.
2. Chew, W. C., J. Jin, E. Michielssen, and J. Song, *Fast and Efficient Algorithms in Computational Electromagnetics*, Artech House, 2001.
3. Rogers, S. D. and C. M. Butler, "An efficient curved-wire integral equation solution technique," *IEEE Trans. Ant. and Propag.*, 70–79, Vol. 49, Jan. 2001.
4. Mosig, J. and E. Suter, "A multilevel divide and conquer approach to moment method computations," *Proc. of Int'l Symp. on Recent Advances in Microw Tech., ISRAMT'99*, 13–17, Malaga, Spain, Dec. 1999.
5. Suter, E. and J. R. Mosig, "A subdomain multilevel approach for the efficient mom analysis of large planar antennas," *Microw. Opt. Technol. Lett.*, Vol. 26, No. 4, 270–277, Aug. 2000.
6. Yeo, J., V. V. S. Prakash, and R. Mittra, "Efficient analysis of a class of microstrip antennas using the characteristic basis function method (CBFM)," *Microw. Opt. Technol. Lett.*, Vol. 39, 456–464, Dec. 2003.
7. Gvozdev, V. I., G. A. Kouzaev, and E. I. Nefedov, "Balanced slotted line. Theory and experiment." *Radio Engineering and Electronics Physics (Radiotekhnika i Elektronika)*, Vol. 30, No. 6, 1050–1057, 1985.
8. Wan, J. X., J. Lei, and C.-H. Liang, "An efficient analysis of large-scale periodic microstrip antenna arrays using the characteristic basis function method," *Progress In Electromagnetics Research*, PIER 50, 61–81, 2005.
9. Taguchi, M., K. Yamashita, K. Tanaka, and T. Tanaka, "Analysis of coil-loaded thin-wire antenna," *IEEE AP-S Intl. Symp.*, Vol. 3, 273–276, 1990.
10. Kolundzija, B. M. and A. R. Djordjević, *WIPL-D: Electromagnetic Modeling of Composite Metallic and Dielectric Structures. Software and User's Manual*, Artech House, Boston, 2000.
11. Kolundzija, B. M. and A. R. Djordjević, *Electromagnetic Modeling of Composite Metallic and Dielectric Structures*, Artech House, 2002.
12. Lysko, A. A., "On grouping individual wire segments into equivalent wires or chains, and multiple domain basis functions," *Proc. of IEEE Int'l Symp. on Ant. & Propag. and USNC/URSI Nat. Radio Science Meeting*, 4, North Charleston, USA, Jun. 2009.
13. Lysko, A. A., "On multiple domain basis functions and their application to wire radiators," Doctoral (Ph.D.) Thesis, 304, submitted for evaluation at the Norwegian University of Science and Technology (NTNU), Norway, Dec. 2009.

A Method of Applying Single Higher Order Polynomial Basis Function over Multiple Domains

A. A. Lysko
Meraka Institute, Council for Scientific and Industrial Research (CSIR), South Africa

Abstract— A novel method has been devised where one set of higher order polynomial-based basis functions can be applied over several wire segments, thus permitting to decouple the number of unknowns from the number of segments, and so from the geometrical approximation accuracy. The method extends the current state of art from using the composite piecewise uniform, linear and sinusoidal basis and testing functions onto polynomials. The method has been derived within the framework of a method of moments (MoM) with higher-order polynomial basis functions, and applied to a surface form of the electrical field integral equation, under thin wire approximation. The main advantage of the proposed method is in permitting to reduce the required number of unknowns when modeling curved structures and structures including electrically small features. Derivation of the computational complexity in terms of floating point operations (FLOP) showed a possible speed gain nearly an order of the number of unknowns of direct MoM.

1. INTRODUCTION

The process of numerical electromagnetic modeling may be split into several stages [1], including geometry representation/modeling, representation/modeling of the current distribution, solution of the equations, and computation of the radiation and other parameters. A dominant majority of existing theoretical frameworks and available codes are based on approximating the geometry in a piecewise linear manner. This is sufficient for many practical geometrical structures having small localized curvatures but may be inefficient for structures with a large quantity of curved surfaces, like reflector antennas, fuselage of aircrafts and cars etc. The inefficiency usually manifests itself in the number of unknowns used by a method per unit of length or area. If the number of unknowns per unit of length/area is much higher than would have been otherwise required for a straight/flat surface, this is usually because an accurate geometrical approximation demanded a higher number of geometrical segments and associated basis functions than it is necessary to approximate the current distribution.

One possible way to improve efficiency is to use curved geometrical segments [2–4, 10]. This is still a rarely used technique and requires a substantial investment in analytical work. In addition, it cannot be used with or on top of existing codes directly or easily.

This paper presents a new higher-order method permitting to decouple the number of unknowns (i.e., current approximation accuracy) from the number of geometrical segments, and thus also from the geometrical approximation accuracy for curved structures. The method enables aggregation of multiple geometrical segments under the same set of basis/expansion functions. This permits to decouple the number of unknowns and current approximation accuracy from the number of geometrical segments and from the required accuracy of geometrical approximation accuracy. Aggregation of individual electrically small features also aims a reduction in the impedance matrix condition number discussed in [5, 6]. The grounds for this assumption are given in [7].

The method proposed extends the prior art based on the piecewise uniform [8], linear [5] and sinusoidal [9] basis and testing functions onto usage of polynomial basis functions [1]. The idea of aggregating and/or re-arranging the basis functions has been reflected in several different types of basis functions ranging from the use of splines [10], composite basis functions [8], macro basis functions and characteristic basis functions [11–13], to the initial steps into multiple domain basis functions [5, 6, 9].

The work introduces a method permitting to apply higher order basis functions [1] over multiple geometrical segments. The reason to develop this approach is to increase the efficiency of numerical modeling by reducing the number of basis functions required per unit of length or area. This follows an accepted understanding of higher efficiency of higher order polynomial basis functions [1, 10] compared to more traditional pulse and piecewise linear (low order) basis functions.

A special note needs to be made with regards to a comparison of the method proposed, to the characteristic basis functions [13]. The characteristic basis functions require to solve a set of subdomain/local problems, thus permitting to find the problem-specific shape of basis functions

first. This is then followed by using the obtained profiles of basis functions to obtain the global solution under the usual MoM framework. This technique shows high degree of efficiency and accuracy in solving problems. However, it is assumed that on simply-shaped geometries like large smoothly bent structures, the need to apply full MoM solution to each local problem will exceed the amount of resources required to aggregate the basis functions and determine the higher order solution. In addition, the characteristic basis functions are expected to require more work in integrating them with existing numerical MoM codes, compared to the approach proposed in this paper.

Another note needs to be made concerning the applicability of any "macro" type of techniques, including MDBF. Presence of geometrical elements near the domain of an MDBF which can couple to the elements described by this domain, may disturb the current distribution and fields described by the assumed shape of basis function and lead to incorrect results [14]. This is a task of setting a correct mesh and needs to be taken into account during the geometrical modeling stage, when traditional basis functions and/or MDBF are applied.

This paper is organized as follows. Section 2 of this paper provides the theoretical basis for the method proposed. It also includes some suggestions regarding optimizing the computations. The next section offers a discussion on the computational complexity of the method and gives a measure for selecting between the method proposed and a direct MoM solution.

2. THEORY OF THE MULTIPLE-DOMAIN BASIS FUNCTIONS

The technique is based on the following approximating equation [5, 6, 8]

$$\mathbf{I}_1 = \mathbf{M} \cdot \mathbf{I}_2$$

relating the unknowns in a traditional (original) formulation of the MoM to the unknowns in the new formulation [5, 6, 9]. In this equation, $\mathbf{I}_1$ is the column vector with N_1 original unknowns, which are the unknowns used in the direct solution with the traditional method of moments. The column vector $\mathbf{I}_2$ is the vector with N_2 new unknowns. The compression of the impedance matrix is based on N_2 being smaller than N_1. The matrix $\mathbf{M}$ of size N_1 by N_2, relates the two sets of unknowns, and is herein referred to as a *compression matrix*.

The method discussed in this work focuses on establishing the matrix $\mathbf{M}$, when both the original (sub-domain) and new (composite) sets of basis functions are hierarchical polynomials. For simplicity, the derivations are done for a single continuous wire represented by a multiplicity of shorter wire segments. The derivations can be readily expanded onto an arbitrary combination of the wires or quadrilaterals.

It is assumed that each original basis function is written as $a_k \cdot (x - x_{c1})^k$, where x_c and x_{c1} are in a coordinate system common for all the wire segments composing the wire. A composite basis function (MDBF) is supposed to cover several wire segments. It is also assumed that each MDBF covers K wire segments (which is also the ratio of the number of wires to the number of chains). A similar form of $A_k \cdot (x - x_c)^k$ is assumed for the new compressed set of basis functions over the wire. The new co-ordinate system can be related to the original local co-ordinate systems by a simple shift in the coordinate.

The work shows that the matrix $\mathbf{M}$ can be written in the form

$$\mathbf{M} \equiv \mathbf{X} \cdot \mathbf{G} \cdot \mathbf{X}^{-1}.$$

Here, the matrix $\mathbf{X}$ relates the set of original basis functions, $\mathbf{BF}_{\text{old}}$, and their decomposition into terms of a polynomial, $\mathbf{P}_{\text{old}}$ as

$$\mathbf{BF}_{\text{old}} = \mathbf{X} \cdot \mathbf{P}_{\text{old}},$$

while the matrix $\mathbf{G}$ defines a conversion from the hierarchical polynomials defined in the original local coordinate system, $\mathbf{P}_{\text{old}}$, into the new local co-ordinate system, $\mathbf{P}_{\text{new}}$ (i.e., the relationship between the coefficients a_k and A_k):

$$\mathbf{P}_{\text{old}} = \mathbf{G} \cdot \mathbf{P}_{\text{new}}.$$

The elements of the matrices have been derived in the following manner described in detail in [6]. Assuming the relationship $[a_k] = \mathbf{G} \cdot [A_k]$, the elements of the matrix G can be found as $G_{ij} = C_{i-1}^{j-1} \Delta^{k-i}$, where the factor C_n^k is the binomial coefficient defined [15] as $C_n^k \equiv \binom{k}{n} \equiv \frac{k!}{n!(k-n)!}$. The matrix $\mathbf{G}$ is lower triangular.

The transformation between a basis polynomial set $\{x^i\}_i = 1, 2, \ldots, N$ represented as a column vector $[P]_{N\times 1}$, and the set of polynomial basis function represented as a column vector $[\mathrm{BF}]_{N\times 1}$ may be written in a matrix form as

$$[\mathrm{BF}] = [X] \cdot [P].$$

Specific entries of the matrix $\mathbf{X}$ depend on the choice of basis functions. Expanding this notation for nodal and singleton basis functions $\{N_i, S_j\}_{i=1,2;\, j=3,4,\ldots,N}$ defined in [1, 6], the above expression is written as

$$\underbrace{\begin{bmatrix} \frac{1}{2}(1-x) \\ \frac{1}{2}(1+x) \\ x^2-1 \\ x^3-x \\ x^4-1 \\ x^5-x \\ \vdots \end{bmatrix}}_{\mathbf{BF}} = \underbrace{\left[\begin{array}{c|c|cccc|c} \frac{1}{2} & -\frac{1}{2} & 0 & 0 & 0 & 0 & \\ \frac{1}{2} & \frac{1}{2} & 0 & 0 & 0 & 0 & \\ -1 & 0 & 1 & 0 & 0 & 0 & \cdots \\ 0 & -1 & 0 & 1 & 0 & 0 & \\ -1 & 0 & 0 & 0 & 1 & 0 & \\ 0 & -1 & 0 & 0 & 0 & 1 & \\ \vdots & \vdots & & \vdots & & & \ddots \end{array}\right]}_{\mathbf{X}} \cdot \underbrace{\begin{bmatrix} x^0 \\ x^1 \\ x^2 \\ x^3 \\ x^4 \\ x^5 \\ \vdots \end{bmatrix}}_{\mathbf{P}}.$$

The matrixes $\mathbf{X}$ and $\mathbf{X}^{-1}$ do not need to be computed and can be stored to accelerate computations.

3. COMPUTATIONAL COMPLEXITY

The computational cost of the process has been estimated in terms of the floating point operations (FLOPs). This was done by adding up all the FLOPs required to establish the compression matrix, compress the system, solve it, and compute the original unknowns. The result was divided by the number of FLOPs required to obtain a solution via a direct MoM (assuming that the impedance matrix for the direct MoM had been filled in). Considering optimizations like storing the precomputed matrices $\mathbf{X}$ and $\mathbf{X}^{-1}$, the method proposed may provide a relative performance gain (speed up) of up to

$$K^3 \cdot (1 - 3/n_b) - 4K^7/N, \quad N \to \infty,$$

that is relative to the traditional MoM. Here the symbol n_b stands for the number of polynomial basis functions assigned per each geometrical segment, and N is the number of unknowns in the original uncompressed system due to the direct MoM.

From the last expression, it is clear that the number of basis functions assigned per each segment should be maximized in order to improve the efficiency of the method (i.e., use the highest possible order of basis functions).

Also, assuming that n_b and N are large, and analyzing the performance gain expression for a maximum gain, it is possible to show that the maximum relative performance gain with respect to a direct MoM is

$$0.107N^{3/4}(1 - 3/n_b)^{7/4} \tag{1}$$

This means that the method proposed can offer nearly an order of magnitude, $O(N^{3/4})$, advantage in performance, when large problems needs to be solved. A set of curves for the performance gain is shown in Figure 1. The figure indicates that the performance gain can be less than unity, making the method slower than the direct MoM is.

By setting the expression (1) to unity and expressing N via the remaining coefficients and parameter n_b, it is possible to show that the number of unknowns corresponding to the unity gain, N_1, is

$$N_1 = 19.7/(1 - 3/n_b)^{7/3}.$$

This expression can be used to determine whether it is better to use a direct MoM or the method proposed in this paper (if N_1 is smaller than N, then it is advantageous to apply the proposed method).

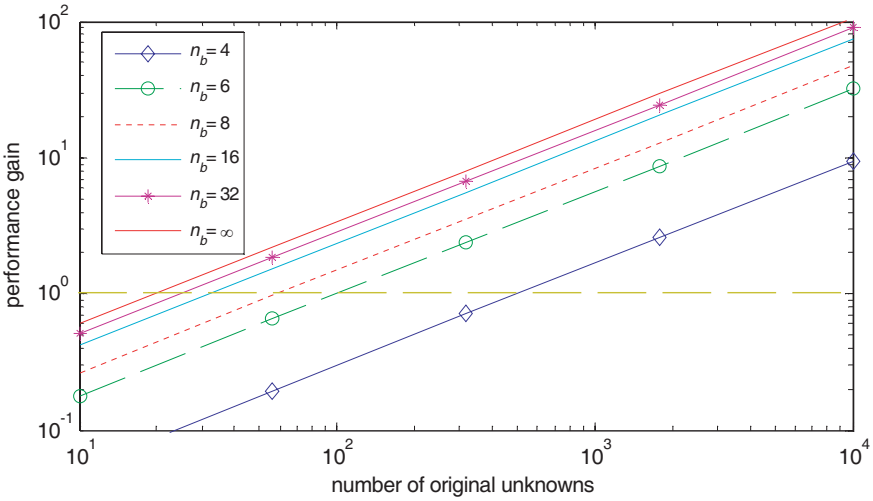

Figure 1. Maximum performance (relative acceleration with respect to the direct MoM) gain versus number of unknowns in the direct MoM; n_b stands for the number of basis functions assigned per geometrical segment.

4. CONCLUSION

A new higher-order method devised for efficient modeling of curved structures has been introduced. Some practical considerations for acceleration of computations related to the method are discussed. An estimate for the computational complexity of the method in terms of the count of floating-point operations (FLOP) has been given. It has been shown that the speed up of up to $O(N^{3/4})$ is possible.

ACKNOWLEDGMENT

This work was funded in part by the Department of Electronics and Telecommunications, Norwegian University of Science and Technology (NTNU), Norway.

REFERENCES

1. Kolundzija, B. M. and A. R. Djordjević, *Electromagnetic Modeling of Composite Metallic and Dielectric Structures*, Artech House, 2002.
2. Champagne, N. J., J. T. Williams, and D. R. Wilton, "The use of curved segments for numerically modeling thin wire antennas and scatterers," *IEEE Transactions on Antennas and Propagation*, Vol. 40, No. 6, 682–689, 1992.
3. Khamas, S. K. and G. G. Cook, "Moment method analysis of printed eccentric spiral antennas using curved segmentation," *IEE Proceedings on Microwaves, Antennas and Propagation*, Vol. 146, No. 6, 407–410, Dec. 1999,
4. Papakanellos P. J., "Alternative sub-domain moment methods for analyzing thin-wire circular loops," *Progress In Electromagnetics Research*, PIER 71, 1–18, 2007.
5. Lysko, A. A., "On grouping individual wire segments into equivalent wires or chains, and multiple domain basis functions," *Proc. of IEEE Int'l Symp. on Ant. & Propag. and USNC/URSI Nat. Radio Sci. Meeting*, 4, North Charleston, USA, Jun. 2009.
6. Lysko, A. A., "On multiple domain basis functions and their application to wire radiators," Ph.D. Thesis, 304, subm. for eval. at the Norwegian University of Science and Technology (NTNU), Norway, Dec. 2009.
7. Chew, W. C., J. Jin, E. Michielssen, and J. Song, *Fast and Efficient Algorithms in Computational Electromagnetics*, Artech House, 2001.
8. Rogers, S. D. and C. M. Butler, "An efficient curved-wire integral equation solution technique," *IEEE Trans. Ant. and Propag.*, Vol. 49, 70–79, Jan. 2001,
9. Lysko, A. A., "Using piecewise sinusoidal basis functions to blanket multiple wire segments," *Proc. of IEEE Int'l Symp. on Ant. & Propag. and USNC/URSI Nat. Radio Sci. Meeting*, North Charleston, USA, Jun. 2009.
10. Liu, Z.-L. and J. Yang, "Analysis of electromagnetic scattering with higher-order moment method and nurbs model," *Progress In Electromagnetics Research*, PIER 96, 83–100, 2009.

11. Mosig, J. and E. Suter, "A multilevel divide and conquer approach to moment method computations," *Proc. of Int'l Symp. on Recent Advances in Microw. Tech., ISRAMT'99*, 13–17, Malaga, Spain, Dec. 1999.
12. Suter, E. and J. R. Mosig, "A subdomain multilevel approach for the efficient mom analysis of large planar antennas," *Microw. Opt. Technol. Lett.*, Vol. 26, No. 4, 270–277, Aug. 2000.
13. Yeo, J., V. V. S. Prakash, and R. Mittra, "Efficient analysis of a class of microstrip antennas using the characteristic basis function method (CBFM)," *Microw. Opt. Technol. Lett.*, Vol. 39, 456–464, Dec. 2003.
14. Gvozdev, V. I., G. A. Kouzaev, and E. I. Nefedov, "Balanced slotted line. Theory and experiment," *Radio Engineering and Electronics Physics (Radiotekhnika i Elektronika)*, Vol. 30, No. 6, 1050–1057, 1985.
15. Rade, L. and B. Westergren, *Mathematics Handbook for Science and Engineering*, 539, Birkhauser Boston, Inc., Secaucus, NJ, 1995.

The Study on the Antenna Optimization

Junping Geng, **Ronghong Jin**, **Xianling Liang**, **Hao Wu**, **Ye Sheng**, **and Bangda Zhou**
E. E. Dept., Shanghai Jiao Tong University, Shanghai 200240, China

Abstract— What is the optimal antenna? No one give a precise answer. In fact, some one optimize the antenna's parameters to get some best performance in some limited range based on experience model. In the further, some others divides a 2-D rectangular area into some grids, then the initial 2-D chromosome population is produced randomly. The size of population is the number of grids, "1" represents the metallized areas and "0" represents the areas without metal. But the fatal problem is that two diagonally metal grid connected at one point in simulation, and it maybe unclear in manufacturing, joint or not?

Here a continuing method is presented to optimize microstrip antenna to try to overcome the shortcoming of those two method — experience model and random grids. Firstly, the procedure is divide into 2 steps: 1) Crude model is constructed based on the continuing rule — the second metal grid always connects the former one with one edge, so that the whole metal area is continuous. 2) Precise model optimization: The crude model is regularized by the surface currency, then it is described by some parameters, and optimize these main parameters to get the best performance of antenna in some range. A multiband antenna is optimized by this method, and the measured results is good.

1. INTRODUCTION

Antenna is always designed upon the experience of the designer, which is an onerous and time-consuming work. Some parameters of the antenna, such as directivity and S-parameter of monopole antenna, are not harmony, which leads great difficulty for the designer to modify the structure for proper working conditions. Till now, most patch antenna structure inherits previous successful case. Some kind of unknown structure may perform better or even be extrapolated as a pattern for antenna design.

Recently, as the huge advancement of computer speed, some kinds of antenna optimization methods have been presented. But the optimized structure is often discontinuous. There are some flaws that grid meshing optimization cannot overcome in antenna optimization [1]. The electric characteristic of two diagonal-connected blocks is unknown and also leads to great difficulty in fabricating [2].

Therefore, a novel way is proposed in this paper to implement computer-aided antenna design with continued border, which contains two steps: rough design and precise design. A small multi-band monopole antenna covering the TD-SCDMA (1.88–2.025 GHz), IEEE 802.11b/g (2.4–2.484 GHz), the Wimax application (3.4–3.6 GHz) and IEEE 802.11a (5.15–5.85 GHz) is achieved finally, by which the effective of this semi-automatic design model is illustrated.

2. METHOD

The proceeding of the design contains two steps: rough design and precise design. In the first step called rough step, a prototype of the desired antenna is created. Unlike the traditional methods that simply set the grids separately, the grids are set one by one in a certain order to avoid discontinuity. In the second step called precise design, smoothness is made for the antenna prototype built in first design so that a more reasonable structure can be obtained. Then some crucial dimensions which have main influences on the performances of the antenna are optimized.

2.1. Grid Setting in Rough Design

Here, a new method that set the grids one by one according to a certain order is presented to guarantee a continuous structure. Assuming that the area is divided into 10×10 grids and use 10-dimensional A-CLPSO [3] for optimization. A serial of 90 binary digits is invited to guide the grids setting (why only use 90 digits to guide 100 grids is discussed later after the whole process is instructed). To gain this serial, the search range on each dimension is set as [0, 512) and the value on every dimension can be changed into a 9-digit binary number. After the values on the 1st dimension to the 10th dimension are changed one by one, a serial of 90 binary digits is got. Then the grids are set as "0" or "1" as following:

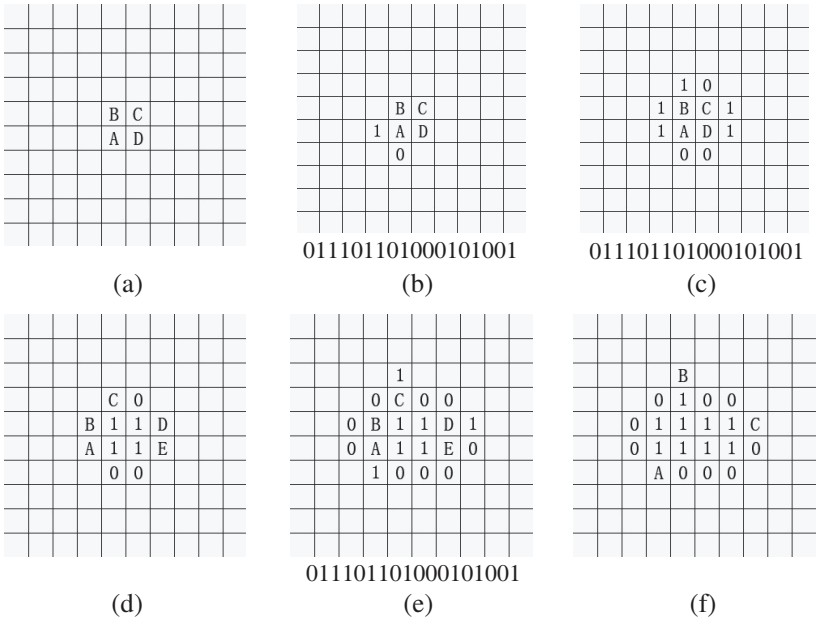

Figure 1: The structure construction process.

Step 1 (Fig. 1(a)), the design area is initialized with the four grids in the center of the area set as "1" while other grids set as "NULL". These four grids of "1" are named A, B, C and D and it is defined that A is B's father grid, B is C's father grid, C is D's father grid and D is A's father grid.

Step 2 (Fig. 1(b)), beginning from A, the direction that point from A to its father grid is defined as "north". Then the grid in the "east", "south" and "west" is set as the value of the digit in the binary serial one by one from the first digit if the grid is still "NULL". If a grid that will be set is already not "NULL", the corresponding digit in the binary serial is reserved to guide the next grid's setting.

Step 3 (Fig. 1(c)), all the grids around other "letter" grids are set by the same method in Step 2. Then the father of every new generated grid of "1" is defined as the corresponding "letter" grid that generates it.

Step 4 (Fig. 1(d)), the new generated grids of "1" are named A, B, C... according to the order that they are generated in the precious turn. Then, the situation is back to Step 1 that every new "letter" grid has its own father grid. So it turns to Step 1 again.

This operation repeats the four steps until either of the following conditions:

(1) all the binary serial is read over

(2) no new grid "1" is created.

The example is shown in Fig. 1 which illustrates how the grids are set when an particle's position in the corresponding 10-D A-CLPSO is at (237, 41, ...) and thus the transformed binary serial is 011101101000101001....

2.2. Fitness Function

It is very important to select a proper fitness function for the optimization algorithm to perform efficiently on a real-world problem. Here, a new fitness function for multi-band antenna which concerns about the bandwidths and frequency offset is proposed:

$$f = \sum_{i=1}^{N} F(i) \tag{1}$$

$$F(i) = \begin{cases} \frac{|f_{mid}(i) - f_0(i)|}{bandwidth(i)} & \text{can find a below } -10\,\text{dB band in } [f_{\inf}(i), f_{\sup}(i)] \\ S & \text{cannot find a below } -10\,\text{dB band in } [f_{\inf}(i), f_{\sup}(i)] \end{cases} \tag{2}$$

N is the number of bands we need, $f_{mid}(i)$ is the medium frequency of the ith found band in $[f_{\inf}(i), f_{\sup}(i)]$, $f_0(i)$ is the medium frequency of the ith desired band, $bandwidth(i)$ is the bandwidth of the found band, $[f_{\inf}(i), f_{\sup}(i)]$ is the ith search range set as a little larger than the ith desired bandwidth, S is a const with a relatively great value to give a bad evaluation if the antenna does not have certain band.

3. RESULT ANALYSIS

3.1. Designed Results

In rough design, the design area (17 mm × 26 mm) is divided into 10 × 10 grids and the width of feed line is set at 2.8 mm to gain 50 Ω impedance since the substrate with $\varepsilon_r = 2.65$ is 1 mm thick. The feed line is 32 mm long and the ground was 29.6 mm × 26 mm. To show the difference between the optimization using the two different kinds of fit function discussed above, we use A-CLPSO with 30 particles and 30000 FEs to solve each fitness function and the two optimized structures. We can easily see that the structure optimized with traditional fitness function is more like an ultra-band antenna that cannot cover the lowest band, but the one optimized using new fitness function has several bands clearly and each band is close to the needed band. Since the structure's characteristic is very crucial for further optimization, especially in the lower frequencies, we choose the new fitness function.

3.2. Optimized Result

Through further adjustments over the raw structure from Fig. 2 (called adusted raw structure), it can be seen that some crucial parts have significant effect on characteristics of antenna. But, modification on just one of them for improving certain characteristic often brings drawbacks on another. So, the optimization algorithm is needed to make an overall optimization on all these parts. In this section, the structure is changed into a more complicated final structure with 12 parameters (X_1 to X_{12}) in Fig. 3. This final structure has some slight modifications on the shapes of the adjusted raw structure's four "crucial" parts to improve the return loss further. Then the 12 parameters are optimized by A-CLPSO with 30 particles again. The final photograph of this proposed multi-band antenna is shown in Fig. 4. The measured and simulated return loss curves of the final structure are shown in Fig. 5, which indicate that the return loss of this final structure fits the desires well.

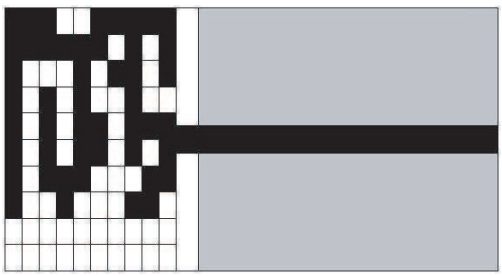

Figure 2: Structure of the optimized multi-band monopole antenna after rough design using the new fitness function (black: copper, white: substrate, grey: ground).

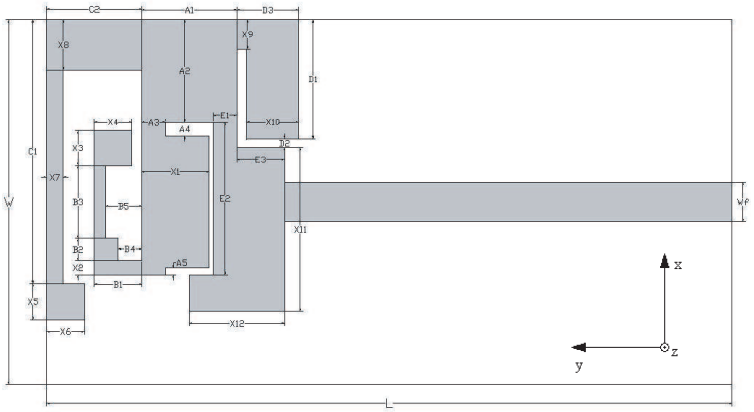

Figure 3: Final structure of the multi-band monopole antenna.

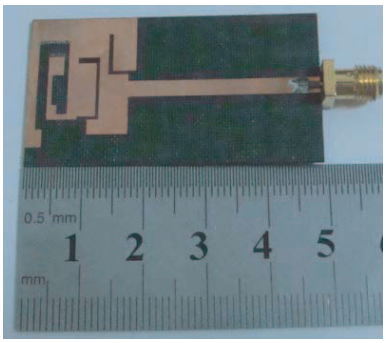

Figure 4: Photograph of the proposed antenna.

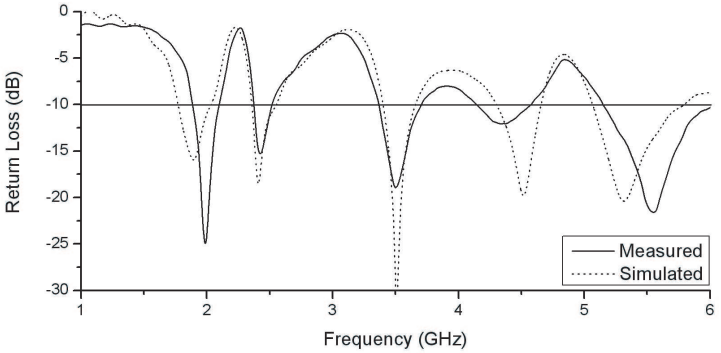

Figure 5: The measured and simulated return loss curves of the final structure.

4. CONCLUSION

A semi-automatic antenna design method based on A-CLPSO is proposed to design a multi-band monopole antenna. In the antenna optimization, a new method of grid setting and a new fitness function are presented. The antenna is produced after rough design and precise design and its measured bands successfully cover the desired TD-SCDMA, WLAN, and WiMax operation. The final antenna indicates that the A-CLPSO performs successfully in antenna designs.

REFERENCES

1. Kennedy, J. and R. Eberhart, "Particle swarm optimization," *IEEE Int. Conf. Neural Networks*, Vol. 4, 1942–1948, Perth, Australia, Dec. 1995.
2. Ding, M., "Optimal design of ultra wideband antennas using a mixed model of 2-D genetic algorithm and finite-difference time-domain," *Microw. Opt. Technol. Lett.*, Vol. 49, No. 12, 3177–3180, Dec. 2007.
3. Wu, H., J. Geng, R. Jin, J. Qiu, W. Liu, J. Chen, and S. Liu, "An improved comprehensive learning particle swarm optimization and its application to the semi-automatic design of antennas," *IEEE Transactions on Antennas and Propagation*, Vol. 57, No. 10, 3018–3028, 2009.

High Performance Antenna Array with Patch Antenna Elements

Dau-Chyrh Chang[1, 2], **Bing-Hao Zeng**[2], **and Ji-Chyun Liu**[3]

[1]Department of Communication Engineering, Oriental Institute of Technology
Banciao, Taipei 220, Taiwan
[2]Department of Communication Engineering, Yuan Ze University
Chung-li, Tao-yuan 32003, Taiwan
[3]Department of Electronics Engineering, Ching Yun University
Chung-li, Tao-yuan 32097, Taiwan

Abstract— In this paper, a high-gain multilayer 2×2 antenna array for the application of WLAN (wireless local area network) AP (access point) is presented. The antenna array consists of four square patch antenna elements fabricated on FR4 substrate. The FR4 substrate is with air gap to the ground plane. By adjusting the thickness of FR4 substrate and geometry of antenna array the maximum gain of array can be achieved. The proposed antenna is designed, fabricated and tested. The measured 10 dB return loss impedance bandwidth is around 14.2% ($2.30 \sim 2.65$ GHz). The gain of simulated and tested antenna array is about 13 dBi. The radiation efficiency for 2.4, 2.5 and 2.6 GHz are all larger than 65% at 2.4 GHz band. The 3 dB beamwidth for E-plane and H-plane is about 30°. The test results of power gain and return loss are agreed with that of simulation.

1. INTRODUCTION

Proposed firstly by G. A. Deschamps early in 1953 that the microstrip antenna has been widely applied because of its several advantages over conventional microwave antennas [1]. Microstrip antenna array is widely used due to its several advantages, such as low profile, light weight, and low cost, etc. [1, 2]. However, microstrip antenna suffers from low gain, low efficiency, and low power handling capability [3]. Various broadband techniques have been reported using multilayer or stacking the patches [3, 4]. High-gain antenna is usually realized by using either parabolic reflectors or line-fed antenna arrays or reflectarrays [5]. In this paper, the high gain antenna array using 2×2 elements and excited with probe-feeding is proposed and applied for IEEE 802.11b/g WLAN AP systems [6–10].

In nowadays microstrip print circuit board (PCB) antenna is widely used for communication systems which include WLAN, global system for mobile communications (GSM), radio-frequency identification (RFID)... etc. Recently, various types of antenna with WLAN systems are also widely used [11–16]. In general, both the requirements of electrical performances and environment conditions of outdoor wireless AP are very critical. For special point to point communication outdoor AP antenna, compact, high gain, and narrower beamwidths at both planes are required [15, 16].

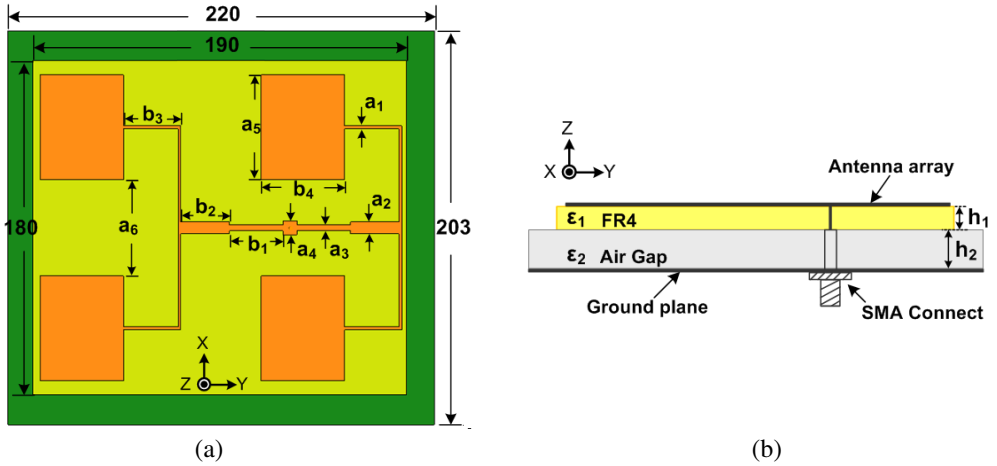

(a) (b)

Figure 1: Simulated structure of array antenna. (a) Top view, (b) side view.

2. DESIGN AND SIMULATION OF ANTENNA ARRAY WITH 2×2 ELEMENTS

Based on the requirements of outdoor AP antenna the compact size, high gain, and narrower beamwidth antenna array is designed as shown in Fig. 1. The antenna array is composed of four patch antenna elements.

The physical dimension of the radiating array is $203 \times 220\,\text{mm}^2$. The radiating patch antenna array with 2×2 elements distribute on the FR4 substrate ($190 \times 180\,\text{mm}^2$) and the size of each patch is $a_5 \times b_4\,\text{mm}^2$. The dimensions are $a_1 = 1.5\,\text{mm}$, $a_2 = 6.5\,\text{mm}$, $a_3 = 3.0\,\text{mm}$, $a_4 = 7.5\,\text{mm}$, $a_5 = a_6 = 54\,\text{mm}$, $b_1 = 27.5\,\text{mm}$, $b_2 = 25\,\text{mm}$, $b_3 = 29.5\,\text{mm}$, and $b_4 = 43\,\text{mm}$. The substrates dielectric constant of FR4 and air are 4.4 (ε_1) and 1 (ε_2), and the thickness are 1.6 mm (h_1) and 5 mm (h_2). The simulated tool is using Ansoft HFSS. The simulation return loss with various heights of air substrate (h_2) of patch antenna element is compared as shown in Fig. 2. Results of the air substrate (h_2) varied from 5 to 8 mm are presented. While result of return loss is smaller than 10 dB at the 2.4 GHz band, the best return loss is with air substrate height $h_2 = 5\,\text{mm}$.

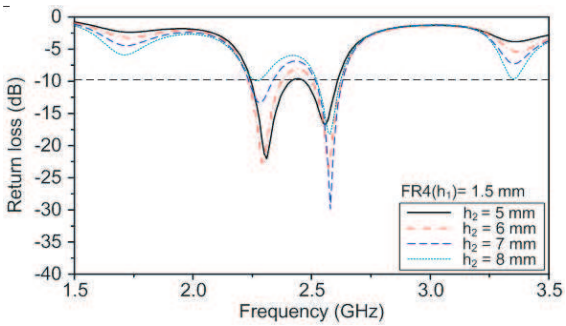

Figure 2: Simulation of return loss for various heights of air substrate.

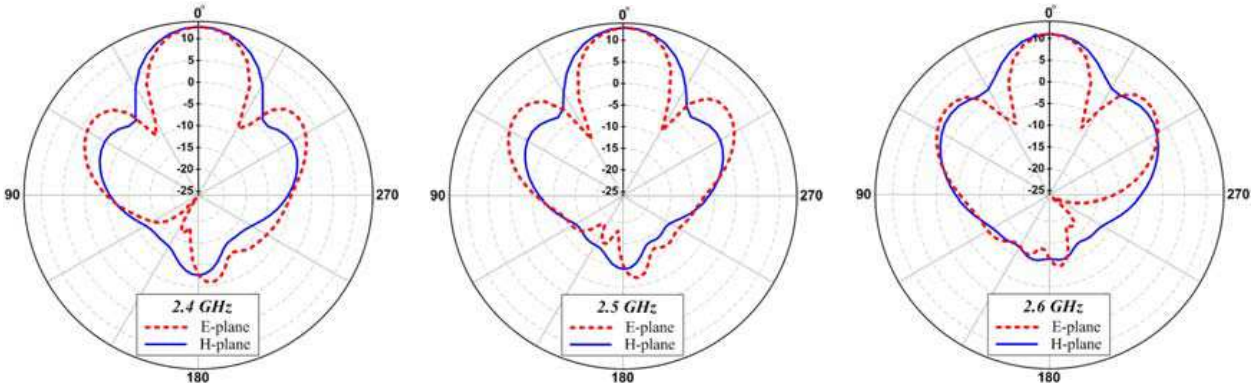

Figure 3: Simulated of antenna radiation patterns. (a) 2.4 GHz, (b) 2.5 GHz, (c) 2.6 GHz.

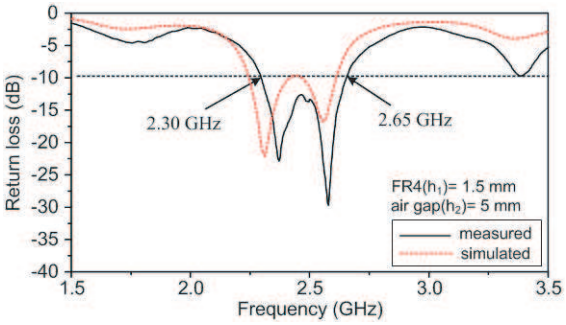

Figure 4: Simulated and measured results of the return loss.

The simulated radiation patterns for frequency at 2.4 GHz 2.5 GHz and 2.6 GHz are also obtained. Fig. 3 shows the result of E-planes (Y-Z plane) and H-planes (X-Z plane) with air substrate height 5 mm. The simulated gains are above 13.6 dBi ∼ 14 dBi for various height (5 ∼ 8 mm) at 2.4 GHz, 2.5 GHz and 2.6 GHz. The thickness of FR4, either 1.2 mm or 1.5 mm, is not so sensitive to the gain of patch array antenna. The simulated gain with various air substrate heights is shown in Table 1.

Table 1: Gains with parameters of air substrate height and substrate thickness.

Frequency		2.4 GHz		2.5 GHz		2.6 GHz	
Gain (dBi)	Air\FR4(h_1)	1.2 mm	1.5 mm	1.2 mm	1.5 mm	1.2 mm	1.5 mm
	h_2 = 5 mm	14.2	13.7	14.2	13.1	14.1	13.1
	h_2 = 6 mm	13.7	13.8	13.8	12.9	13.8	12.8
	h_2 = 7 mm	13.9	14.0	13.6	13.0	13.4	12.9
	h_2 = 8 mm	13.7	13.7	13.3	12.7	13.1	12.5

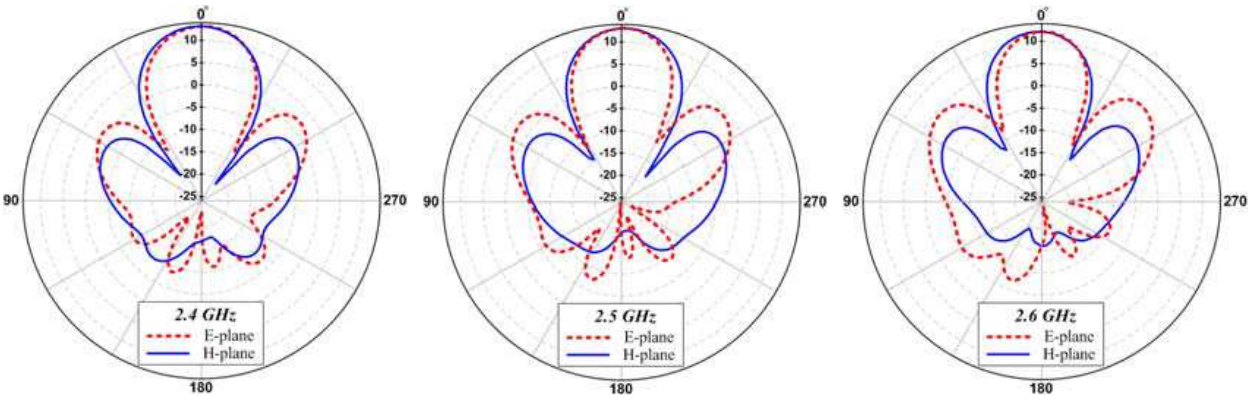

(a) (b) (c)

Figure 5: Measured of antenna radiation patterns. (a) 2.4 GHz, (b) 2.5 GHz, (c) 2.6 GHz.

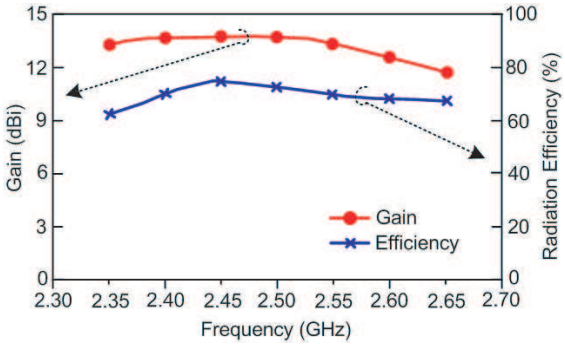

Figure 6: Measured peak gain and radiation efficiency.

3. MEASUREMENT RESULTS

The antenna is measured using the Anritsu 37369C network analyzer. The measured return loss of the proposed array antenna is shown in Fig. 4. Concerning the 10 dB return loss at the 2.4 GHz band, the impedance bandwidth of the antenna ranges from 2.30 GHz to 2.65 GHz with the fractional bandwidth ($FBW = (f_H - f_L)/f_0 = 14.2\%$). The simulated and measured results of the return loss and are in good agreement.

The measured radiation patterns of the proposed antennas at 2.4, 2.5 and 2.6 GHz for both E-plane (Y-Z plane) and H-plane (X-Z plane) are shown in Fig. 5 which are in good agreement

with simulations as shown in Fig. 3. From Fig. 5, the beam pattern is a like a pencil beam. Fig. 6 shows measured antenna gain and radiation efficiency for the proposed antenna array. The peak gains for 2.4, 2.5 and 2.6 GHz are 13.1, 13.08 and 12.6 dBi respectively. The radiation efficiency for 2.4, 2.5 and 2.6 GHz are all larger than 65%.

4. CONCLUSIONS

In this paper, a high-gain multilayer 2×2 antenna array for WLAN AP application is presented. The measured 10 dB return loss impedance bandwidth is around 14.2% ($2.30 \sim 2.65$ GHz). The gain of simulated and measured antenna array is about 13 dBi. The radiation efficiency for 2.4, 2.5 and 2.6 GHz are all larger than 65%. The 3 dB beamwidths are 30° for both E-plane and H-plane The results from both simulated and measured are quite agreed. The high gain antenna array is proposed and applied for IEEE 802.11b/g WLAN AP systems.

ACKNOWLEDGMENT

The authors will thank to National Science Council and Loopcomm Technology Inc. for funding support.

REFERENCES

1. Deschamps, G. A., "Microstrip microwave antennas," *Proceedings of Third USAF Symposium on Antennas*, 1953.
2. James, J. R. and P. S. Hall, *Handbook of Microstrip Antennas*, Peter Peregronic Ltd., London, 1989.
3. Kumar, G. and K. P. Ray, *Broadband Microstrip Antennas*, Artech House, Norwood, MA, 2003.
4. Waterhouse, R. B., "Design of probe-fed stack patches," *IEEE Trans. Antennas Propag.*, Vol. 47, No. 12, 1780–1784, 1999.
5. Pozar, D. M., S. D. Targonski, and H. Syrigos "Design of millimeter wave microstrip reflectarrays," *IEEE Trans. Antennas Propag.*, Vol. 45, No. 2, 287–295, 1997.
6. Ali, M. T., T. B. A Rahman, M. R. B. Kamarudin, M. N. M. Tan, and R. Sauleau, "Planar array antenna with parasitic elements for beam steering control," *PIERS Proceedings*, 181–185, Moscow, Russia, August 18–21, 2009.
7. Soliman, E. A., A. M. Affandi, and K. H. Badr, "Novel microstrip antenna element and 2-by-2 array for satellite TV receivers," *Microw. Opt. Technol. Lett.*, Vol. 51, No. 2, 458–463, 2009.
8. Gupta, R. K. and J. Mukherjee, "Low cost efficient high gain antenna using array of parasitic patches on a superstrate layer," *Microw. Opt. Technol. Lett.*, Vol. 51, No. 3, 733–739, 2009.
9. Gupta, R. K. and J. Mukherjee, "2×2 array with UC-EBG ground for low RCS and high gain," *Microw. Opt. Technol. Lett.*, Vol. 49, No. 6, 1418–1422, 2007.
10. Wang, H., X. B. Huang, and D. G. Fang, "Experimental design of serial feed sequentially rotated 2×2 truncated corner patch antenna array," *Proceedings of IEEE Antennas and Propag. Soc. Inter. Symp.*, 3–8, July 2005.
11. Wong, K. L., *Planar Antennas for Wireless Communications*, Chap. 5, Wiley, New York, 2003.
12. Wang, H., X. B. Huang, and D. G. Fang, "A single layer wideband U-Slot microstrip patch antenna array," *IEEE Antennas Wireless Propag. Lett.*, Vol. 7, 9–12, 2008.
13. Gupta, R. K. and G. Kumar, "High-gain multilayered antenna for wireless applications," *Microw. Opt. Technol. Lett.*, Vol. 5, No. 7, 1923–1929, 2008
14. Gupta, R. K. and G. Kumar, "High-gain multilayer 2×2 antenna array for wireless applications," *Microw. Opt. Technol. Lett.*, Vol. 5, No. 11, 458–463, 2008.
15. Nakamura, Y. and T. Maeda, "Wide-band design of balanced-fed dual-band built-in antennas for high-speed wireless LAN systems," *IEICE Trans. Commun.* (*Japanese Edition*), Vol. J89-B, No. 8, 1476–1485, 2006.
16. Hwang, R. B. and T. C. Pu, "A planar shaped-beam antenna for indoor wireless LAN access points," *IEEE Trans. Antennas Propag.*, Vol. 55, No. 6, 1871–1879, 2007.

A Multiple Antenna System for RFID Access Control Management

Yinlong Huang, **Wei He**, **Weihua Sun**, **and Jiang Xu**
Anti-counterfeit Information Department, The Third Research Institute of MPS, China

Abstract— In this paper, A multiple antenna system for RFID access control management is presented. This multiple antenna system is at UHF (ultra high frequency) band operation and consists of two circular polarization antenna arrays. Two antenna arrays with UHF reader, exploiting antenna diversity selection by radio frequency (RF) chain switches, are used for compensating deficiencies in reading ability of single antenna. In application, a human being with RFID card must be read by both antenna arrays can be permitted to enter the control guard. Designing this system make it a suitable candidate for RFID application in access control for some importance meetings and sporting contests etc.

1. INTRODUCTION

Now RFID (Radio Frequency Identification) system is becoming increasingly popular in the fields [1–4] such as electronic toll collection, tracking containers, asset identification, retail item management, access control, remote monitoring, vehicle security and etc. Especially, the demands for long range identification by retail item management, vehicle management and manufacturers supply chain management have raised the frequency for RFID into UHF (ultra high frequency) and microwave frequency.

A typical UHF RFID system includes a base station (usually called reader) with transmitting/receiving antenna and a transponder (also called tag or label), which is placed on the object to be identified. Most RFID system requires the reader being reliably readable. Since an unread tag may cause significant economic loss or security threat. Robust readability is required for wide practical applications. Thus, the reader antennas sensitivity of a tag is of crucial importance. From this point of view, in this study, antennas with circular polarization (CP), hemispherical coverage and antenna diversity selection by radio frequency (RF) chain switches are proposed for RFID application in access control management

2. ANTENNAS SYSTEM MODELING

In this study, a multiple antenna system for RFID access control management is proposed. The antenna system is consisted of two circular polarization antenna arrays. One array is used for controlling entering gateway. Another array is used for controlling leaving from gateway. Two arrays are arranged back to back. Each array of antennas is oriented 45 angle degree to plumb line. Fig. 1 is schematics of the multiple antenna system. In Fig. 1, No. 1 is a cover gateway which contains all the antennas. The array of $a1$, $a2$, $a3$, $a4$ is used for controlling entering gateway management and the array of $b1$, $b2$, $b3$, $b4$ is used for controlling leaving from gateway management. In designing, all antenna elements not only are circularly polarized but exploit antenna diversity selection by RF chain switches supported by RFID reader chip sets. This multiple antenna system can have larger antenna beam coverage area and get good polarization matching between reader antenna elements and tags. In addition, this multiple antenna system exploiting multiple path effect of transmitting and receiving of antennas can well make the tag (RFID identification card) hung on the chest of human being to be readable with respect to reader antennas. This design is a suitable candidate for UHF RFID application in access control management.

Figure 2 is a CP antenna element. In combination with the technique of air gap, approximately diagonal feeding of square patch and phase modulating, the antenna element exhibits a broad-band characteristic and circular polarization. In Fig. 2, $a = 128\,\text{mm}$, $b = 200\,\text{mm}$, $l = 36\,\text{mm}$, $w = 21.5\,\text{mm}$. The l is phase modulating line. The air gap substrate is used to obtain a particular broad-band characteristic. Approximately diagonal feeding in combination with phase modulating l make the fundamental resonant frequency of the square patch to be split into two resonant modes with 90 phase difference. With such an arrangement, CP operation of antenna can be obtained. In Fig. 2, phase modulating l design can make the antenna to operate on left-hand CP (LHCP) mode. On the other hand, when phase modulating l is on the other side of diagonal line of the square patch, a right-hand CP (RHCP) operation can be achieved.

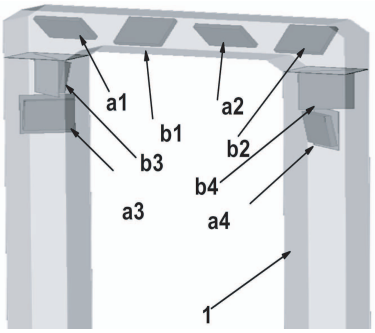

Figure 1. Schematics of the multiple antenna system.

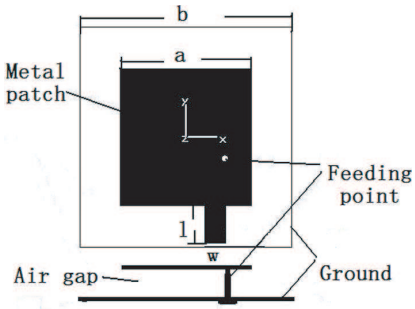

Figure 2. The schematics of the CP antenna element.

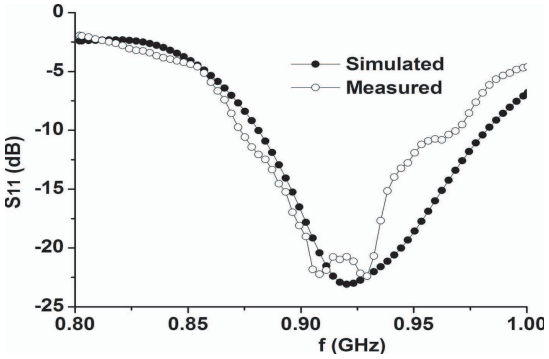

Figure 3. The measured and simulated return loss for the CP antenna element.

In this study, Finite difference time domain (FDTD) method has been used to calculate impedance bandwidth, radiation pattern, axial ratio (AR) and gains, and an Agilent 8722ES Vector Network Analyzer has been applied to measure impedance bandwidth.

Figure 3 shows the simulated and the measured return loss of the CP antenna element. The measured results show satisfactory agreement with the simulation data. It can be seen that distinct resonance modes at 873–968 MHz are excited with good impedance matching. The simulated impedance bandwidths, assuming a limit of −10 dB return loss, are about 881–980 MHz (about 10.6%) and assuming a limit of −15 dB return loss, are about 895–962 MHz (about 7.2%). The measured impedance bandwidths, assuming a limit of −10 dB return loss, are about 873–968 MHz (about 10.3%) and assuming a limit of −15 dB return loss, are about 891–939 MHz (about 5.2%). These can well meet the bandwidths of our native UHF RFID 920–925 MHz band.

Figure 4 shows the simulated radiation patterns of the CP antenna element in E-plane (x-z plane) and H-plane (y-z plane) at 920 MHz respectively. The antenna has good characteristic of directional beam in the x-z plane and in the y-z plane. The simulated 3-dB beam width in the x-z and y-z planes are 68.7° and 66° respectively as shown in Fig. 4. Modeling of such antennas, with simplicity in designing and feeding, can well achieve an approximately semi-spherical coverage area. Peak antenna gains for two operating bands have been determined by simulated as 8.45 dBi at 920 MHz and 8.5 dBi at 925 MHz respectively.

Figure 5 is the simulated axial ratios (AR) for LHCP at broadside and the gains of the antenna element. It can be seen that the AR at 920–925 MHz bands are all less than 1 dB, which have satisfactory characteristic of circular polarization.

3. ANALYSIS OF RFID APPLICATION FOR ACCESS CONTROL MANAGEMENT

In the multiple antenna system for RFID access control management, the antennas are designed for operation at 900 MHz–930 MHz which can well meet the UHF RFID band 920–925 MHz of China. When there is importance conference or meeting, this multiple antenna system, being equipped with RFID reader and computer monitor, is used for access control. In application, all presenters at meeting are required have RFID tag which has permit and service information of meeting. When presenters enter meeting room, only those people having RFID tag being read by two arrays of RFID reader will be permitted to enter meeting room. Otherwise, computer monitor will give

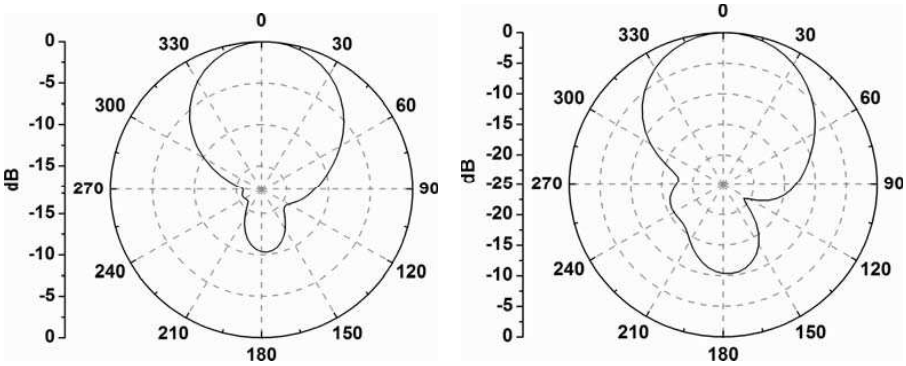

(a) *E*-plane (*x*-*z* plane) (b) *H*-plane (*y*-*z* plane)

Figure 4. The radiation patterns at 920 MHz for the CP antenna element.

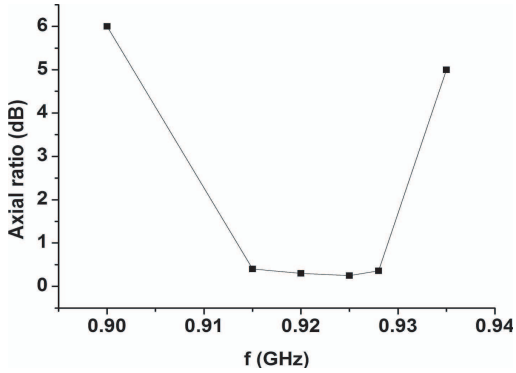

Figure 5. The simulated axial ratios (AR) for LHCP.

Figure 6. The photograph of the multiple antenna system for RFID access control management.

a warning message and prevent people from entering meeting room. At the same time, when attendants leave from meeting room, it is the same to that of entering control.

4. CONCLUSIONS

In this study, a multiple antenna system for RFID access control management being capable of UHF band operation is proposed. In multiple antenna system, the antenna system can have larger antenna beam coverage area and get good polarization matching between reader antenna elements and tags, which can well make the tag (RFID identification card) hung on the chest of human being to be readable with respect to reader antennas. This design is a suitable candidate for UHF RFID application in access control management.

REFERENCES

1. Tuttle, J. R., "Traditional and emerging technologies and applications in the radio frequency identification (RFID) industry," *Radio Frequency Integrated Circuits (RFIC) Symposium, IEEE,* 5–8, Jun. 8–11, 1997.
2. Pala, Z. and N. Inanc, "Smart parking applications using RFID technology," *RFID Eurasia*, 1–3, Sept. 5–6, 2007.
3. Qiu, J., B. Sun, and Q. You, "Study on RFID antenna for railway vehicle identification," *IEEE 6th International Conference on ITS Telecommunications Proceedings*, 237–240, 2006.
4. Marrocco, G., "RFID antennas for the UHF remote monitoring of human subjects," *IEEE Transactions on Antennas and Propagation*, Vol. 55, No. 6, 1862–1870, Jun. 2007.

60 GHz Meta-material Wideband Antenna for FPGA Giga Bit Data Transmission

Ying Peng and Zhirun Hu
School of Electrical and Electronic Engineering, The University of Manchester
Manchester, UK

Abstract— A 60 GHz ultra thin folded dipole antenna on a meta-material structured surface cavity for 3D FPGA high data transmission was proposed. In order to increase the radiation efficiency, meta-material resonant cavity was constructed to act as a reflector. Full wave electromagnetic simulation results reveal that a 4.6 dB gain and 7 GHz bandwidth were obtained at the center frequency of 60 GHz for the novel antenna. The antenna has only 10 μm thick, which is 98% reduction in substrate thickness in comparison with conventional conducting metal cavity antenna having the same gain and bandwidth. The significance of this work is that such low profile antenna can be integrated with standard silicon CMOS technology to make loss cost wireless data transmission possible between FPGA layers or chips.

1. INTRODUCTION

Three-dimensional (3D) FPGA is a new technology that can increase the circuit functionality and scale of integration [1]. The increase of the scale of integration is particularly attractive given that current optical lithography is approaching its natural limits.

In 3D FPGA, multiple layers are integrated and interconnected with through-silicon vias (TSVs). While three-dimensional integration can lead to significant reduction in wire length and interconnect delay through such TSVs, there are also parasitic effects associated with these vias, severely degrading the data transmission rate.

The feasibility of wireless interconnects on 60 GHz band with bandwidth of 7 GHz are proposed in this paper. The wireless data transmission can be envisaged to be applied not only between layers, but also between the chips. However, there is a critical obstacle in realizing such high frequency band antennas on standard CMOS technology due to the high conductor loss of low resistivity Si wafers. Chip antennas on standard silicon wafer (resistivity 1–10 Ω cm) reported to date suffered from low efficiency and narrow bandwidth due to the inherent conductor loss of the wafer.

The work presented here is to demonstrate the feasibility of reducing the effects of the substrate loss by using newly emerged meta-material structured surface.

2. ANTENNA DESIGN

Challenges of making 60 GHz for 3D FPAG applications is obtaining a wide antenna bandwidth and high efficiency that also can be manufacturable in today's low-cost mass production standard silicon CMOS process. It has been shown that based on the simple dipole antenna, a wide bandwidth and well compatible performance can be obtained on folded dipole antenna with meta-material structured surface on dielectric substrates [2]. However, antenna structure in [2] can't be applied to a standard silicon CMOS substrate due to its high conductor loss and restriction of its thin silicon dioxide layer. To overcome these, a low profile folded dipole antenna on a standard CMOS silicon wafer with meta-material structured surface was proposed here. The antenna was designed to have 100 Ω characteristic impedance and fed by a pair of 100 Ω coplanar strip lines. The folded dipole has a length of 1.5 mm.

Cavity resonator is widely used as electromagnetic resonators, inside which waves keep vibrating and bounced back. Low profile antennas can obtain better performance with the effect of a cavity. Fig. 1 shows the presented folded dipole antenna in the cavity built with conducting metal of an inner size of 3 mm × 4.2 mm and a height of 500 μm. Fig. 2 illustrates the meta-material structured surface cavity applied to the proposed antenna. This meta-material structured surface cavity has the same size as the conducting metal cavity but has only 10 μm thick, which is a significant reduction in antenna substrate thickness. The cavity is enclosed with two kinds of meta-material structures, hexagonal surfaces with conducting via and a corrugated metal slab structure. These two structures form high impedance on the metal surface without occurring surface wave loss.

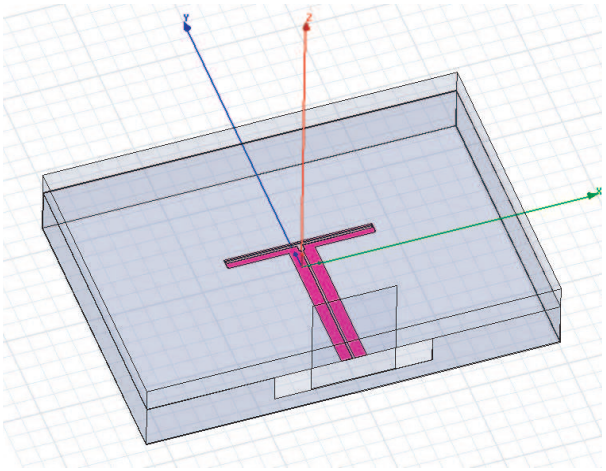

Figure 1: Folded dipole antenna in metallic cavity.

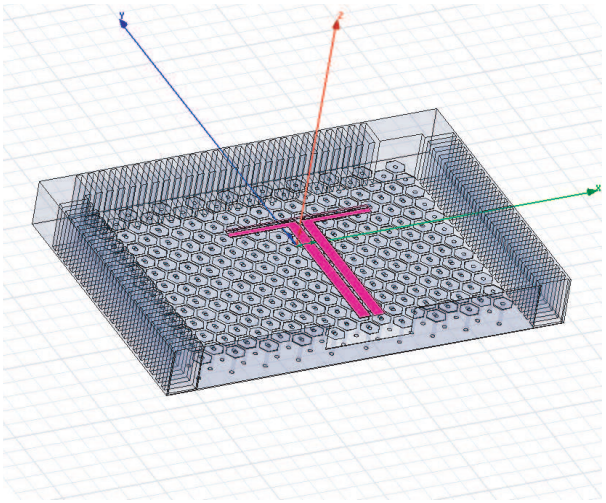

Figure 2: Folded dipole antenna in meta-material structured surface cavity.

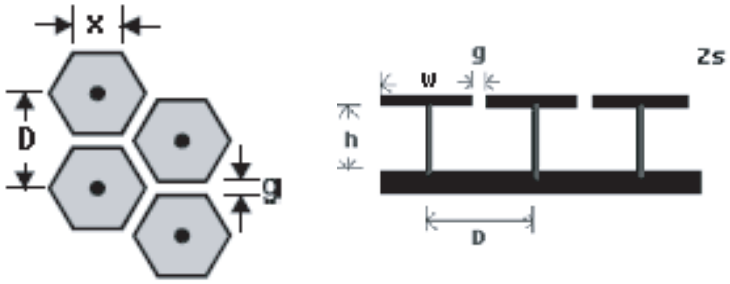

(a) (b)

Figure 3: (a) Top view and (b) side view.

3. META-MATERIAL STRUCTURED SURFACE CAVITY DESIGN

The meta-material structured surface that applied to the cavity has two basic structures: hexagonal metallic 'mushroom' plates and corrugated metal slab. Following to the early work in [2], the equivalent LC circuit has a sheet capacitance and inductance related to the resonant angular frequency, ω, given as

$$\omega = \frac{1}{\sqrt{LC}} = \frac{1}{\sqrt{L_{sheet} \cdot NC_{square}}} \tag{1}$$

$$L_{sheet} = h \cdot \mu_0 \mu_r \tag{2}$$

$$C = \frac{flux}{V} = \frac{x(\varepsilon_1 + \varepsilon_2)}{\pi} \text{Cosh}^{-1}\left(\frac{D}{g}\right) \tag{3}$$

where h is the metal element plate height, x is the period of metal element, D is the center distance of each neighbor elements and g is the gap between each period. The top and side view of the structure is shown in Fig. 3.

Different from the 'mushroom' structure, a corrugated metal slab can be seen as a series of slots cutting vertically. Each slot is very narrow and has a length of one quarter-wavelength deep. When wave propagates to the surface, it travels down to the bottom along the slab [3]. The structure can be regards as a parallel plate transmission line which is shorted at one end and open at the other. Thus impedance in the top is quite high. In the antenna structure, corrugated metal slab is built around four vertical walls as it can be seen in Fig. 2. The walls help to modify the radiation pattern to increase the gain of the antenna.

4. RESULTS

Simulations were carried out using full electromagnetic wave simulator, Ansoft HFSS v11. The simulation was taken for three different structures, a simple folded dipole antenna without cavity, folded dipole antennas shown in Fig. 2 and Fig. 3, respectively. It can be clearly seen from Fig. 4, which is the return loss of the antenna with metal cavity of 500 µm thick, the bandwidth is 6 GHz from 59 GHz to 65 GHz. Fig. 5 shows that the bandwidth of the antenna on meta-material structured suarface cavity with only 10 µm thick has achieved to 7 GHz from 55 GHz to 62 GHz. Furthermore the gain is enhanced from 2.2 dB to 6.9 dB as shown in Fig. 6. Fig. 6(b) also illustrates that radiation pattern back lobe of the metal cavity is removed by the meta-material surface,

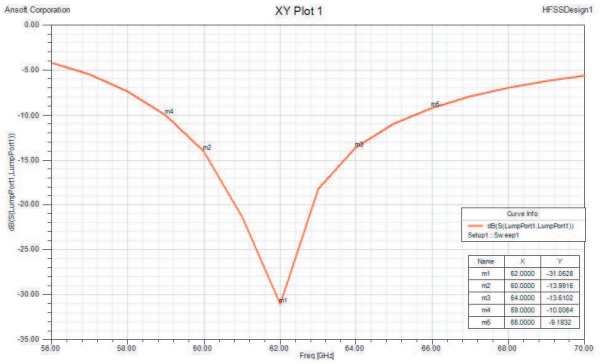

Figure 4: Return loss of the presented antenna with metal cavity.

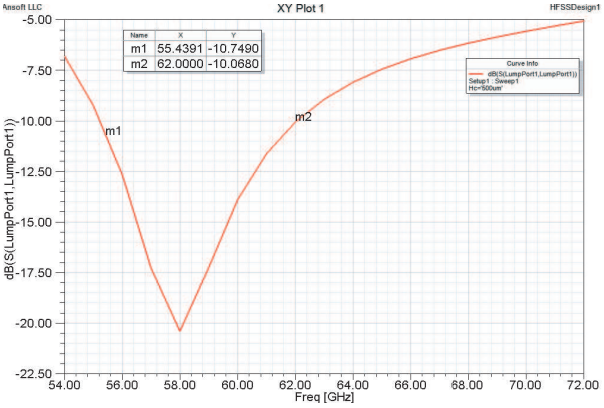

Figure 5: Return loss of the presented antenna with meta-matrial structured surface cavity.

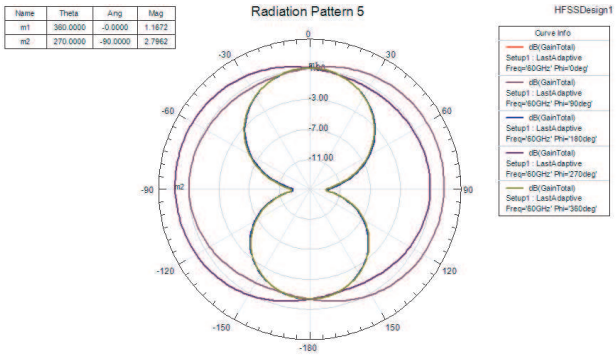

(a)

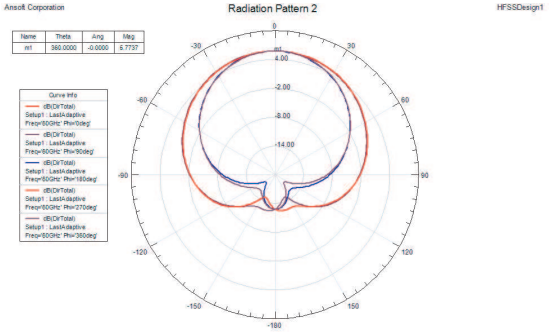

(b)

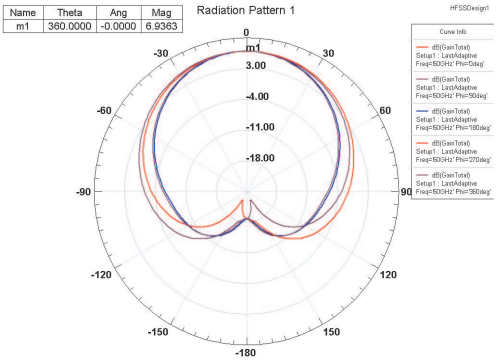

(c)

Figure 6: (a) Antenna gain of the simple folded dipole antenna. (b) Antenna gain of folded dipole antenna with metal cavity backed and (c) Antenna gain of folded dipole antenna with meta-material structured surface cavity.

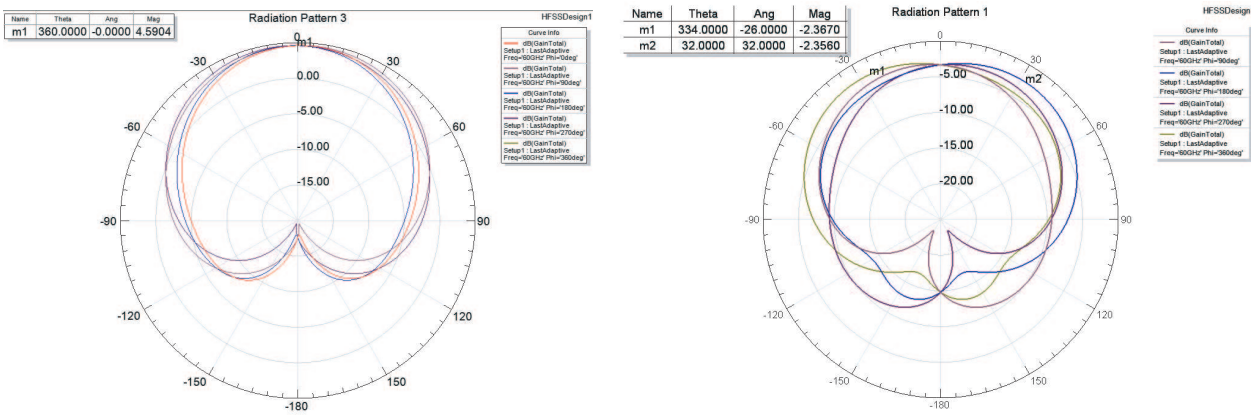

(a) (b)

Figure 7: (a) Gain of the antenna with 10 µm height HIS structure cavity. (b) Gain of the antenna with 10 µm distanced metal reflector.

resulting in a high gain.

Figure 7 shows the antenna gain comparison between the antenna in meta-material structured surface cavity and that with a flat metal one with the same cavity height. It indicates that a gain of 4.59 dB was obtained in the proposed antenna whereas only −2.38 dB could be obtained by using the conventional conducting metal cavity.

5. CONCLUSION

This paper proposes a novel 60 GHz antenna using meta-material structured surface cavity. The antenna has low profile (thin substrate layer), making it suitable for monolithically integrated with 3D FPGA architecture. The simulated results show that the antenna has a bandwidth of 7 GHz around 60 GHz with a gain of 4.6 dB. Mask design of the antenna is currently under way. Fabrication and characterization is expected in early next year.

REFERENCES

1. Banerjee, K., et al., "3-D ICs: A novel chip design for deep-submicrometer interconnect performance and systems-on-chip integration," *Proc. of the IEEE*, Vol. 89, No. 5, 602–633, 2001.
2. Sievenpiper, D., L. Zhang, R. F. J. Broas, N. G. Alexopoulos, and E. Yablonovitch, "High-impedance electromagnetic surface with a forbidden frequency band," *IEEE Trans. Microwave Theory Tech.*, Vol. 47, 2059, 1999.
3. Lee, S. and W. Jones, "Surface waves on two-dimensional corrugated surfaces," *Radio Sci.*, Vol. 6, 811–818, 1971.

A Miniature Coupled Loop Antenna to be Embedded in a Mobile Phone for Penta-band Applications

Sheng-Yu Lin, **Hsien-Wen Liu**, **Chung-Hsun Weng**, **and Chang-Fa Yang**
Department of Electrical Engineering, National Taiwan University of Science and Technology
Taipei, Taiwan

Abstract— A planar compact coupled loop antenna of the mobile phone for GSM850/GSM900/DCS/PCS/UMTS penta-band applications is presented. This antenna comprises folded loop strips and a coupled gap to be embedded inside the mobile phone. By adding a gap between two loop elements for coupling, a resonant mode in the GSM850/900 band can be excited. Simulated and measured results are compared, which show good agreements. Also, good radiation efficiency and return loss are obtained. This antenna can be fabricated with a low cost and can be built in the mobile phone for penta-band applications.

1. INTRODUCTION

In recent years, loop-type antennas with multiband operations have been demonstrated for applications in the portable devices as internal antennas suitable for GSM850/GSM900/DCS/PCS/UMTS communication systems [1–4]. Unlike the conventional planar inverted-F antennas (PIFAs) with a large size, the loop antenna can be designed and printed with a compact size to be embedded inside a mobile phone. Furthermore, due to the planar configuration of the loop antenna, significant reduction in thickness of the mobile phone may be easily achieved. Such loop antenna is also capable of resonating in a balance mode to avoid the interference from the user's hand. In this paper, we propose a novel and miniature coupled loop antenna suitable for penta-band operation. Printed on an FR4 substrate and fed by using a $50\,\Omega$ microstrip line, a low-profile and simple loop antenna configuration with a small size of $10 \times 50\,\text{mm}^2$ is achieved. By properly adjusting the gap and width of the folded loop strips, fairly good impedance matching throughout the interesting bands can be obtained. Omni directional radiation patterns are also observed. Thus, the proposed antenna is suitable for penta-band applications.

2. ANTENNA DESIGN

Figure 1 illustrates the geometry of the proposed panta-band coupled loop antenna. The antenna with an overall size of $10 \times 50\,\text{mm}^2$ is printed on an FR4 substrate with a thickness of 0.8 mm and a relative permittivity of 4.4, and fed by a $50\,\Omega$ microstrip line. To have the multiband operation, the antenna consists of a pair of symmetric folded loop strips, where points A and B are the RF signal feed and shorting structure respectively. In this design, the desired frequency of the first resonant mode is about one-wavelength at 900 MHz, and then a higher order mode based on the first one can be generated through the proposed coupled structure. Thus, the antenna has a second resonant mode at about 1.8 GHz. For better impedance matching over the bands, a parasitic patch was added into the left and bottom of the folded structure to provide the capacitive coupling. Moreover, the gap and width of the folded loop strips can be properly adjusted to broaden the operating bandwidth for penta-band applications. Note that a central gap between the folded strips is optimized to be 3.4 mm, as shown in Fig. 1(b). To study the electrical characteristics and radiation performance of the antenna, a full-wave electromagnetic solver, Ansoft HFSSTM has been employed throughout this work.

3. RESULTS

The prototype of the proposed coupled loop antenna with optimal parameters has been implemented and measured. The antenna was mounted on a test board of $50 \times 100\,\text{mm}^2$ to model a system for the mobile phone. The measured return losses of the antenna have been performed by using an Agilent E8362B network analyzer and compared with the simulations, as shown in Fig. 2. Good agreements are achieved. Two impedance bandwidths with less than 6 dB return loss are $0.824 \sim 0.96$ GHz and $1.71 \sim 2.17$ GHz, corresponding to 15.2% and 23.7%, respectively. Those bandwidths not only cover the GSM850 and GSM900 systems, but also the licensed DCS, PCS and UMTS systems. Fig. 3 simulates the surface current distribution of the antenna for the frequencies at 840 MHz, 900 MHz, 1.8 GHz and 2 GHz, respectively. Uniform surface currents can be observed at 840 MHz

and 900 MHz, which correspond to the first resonant mode. As expected, for the higher order mode resonance, the simulated currents flowing in two opposite directions for both sides were at 1.8 GHz and 2 GHz. Fig. 4 plots the simulated far-field radiation patterns in xz-, yz- and xy-planes for the frequencies at 900 MHz, 1.8 GHz and 2 GHz. Good omni-directional radiation patterns are obtained in the xy-plane (or H-plane). Those patterns demonstrate that the proposed antenna is suitable for penta-band applications.

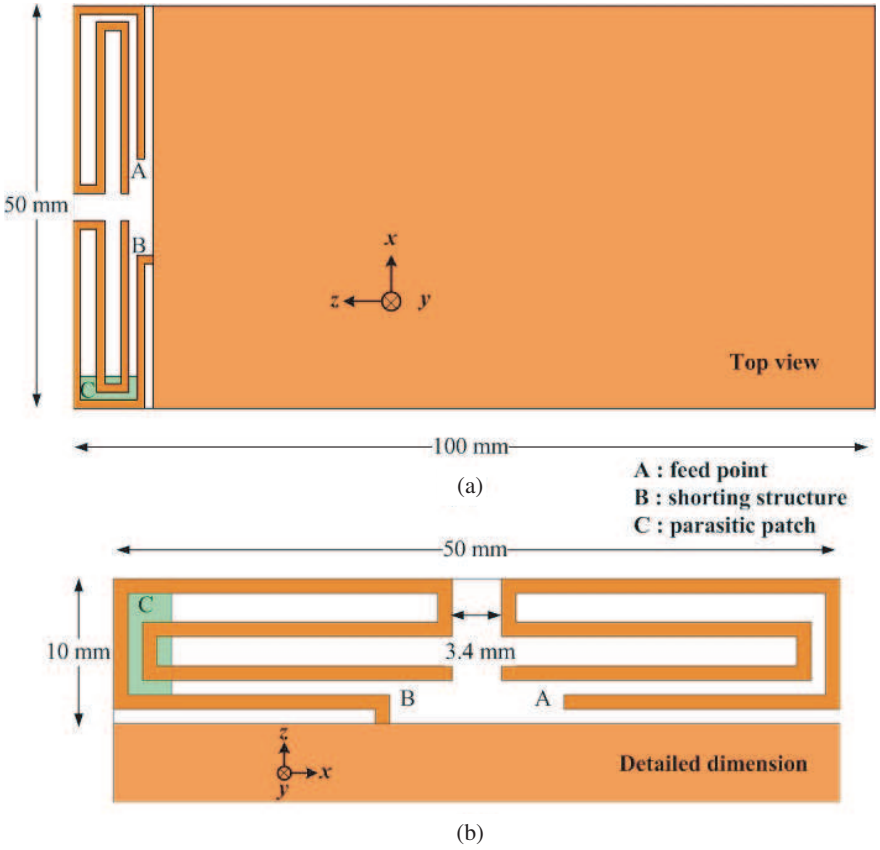

Figure 1: The geometry of the proposed coupled loop antenna.

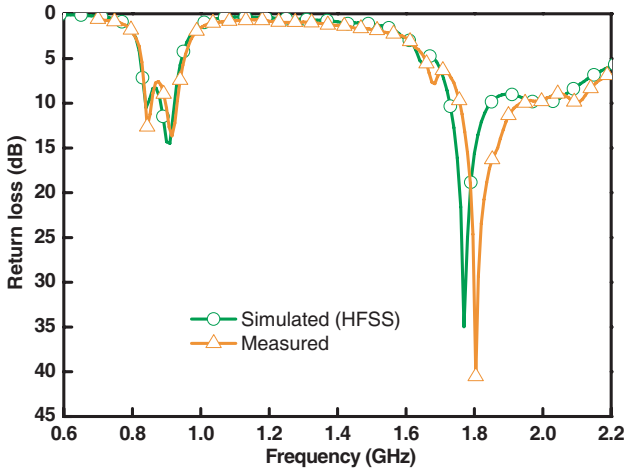

Figure 2: Measured and simulated return loss of proposed antenna.

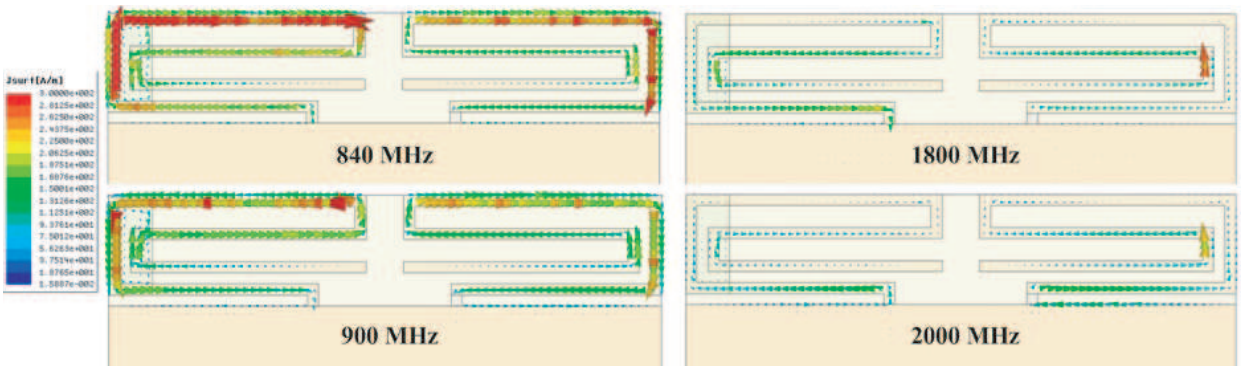

Figure 3: Simulated surface currents at 840, 900, 1800 and 2000 MHz.

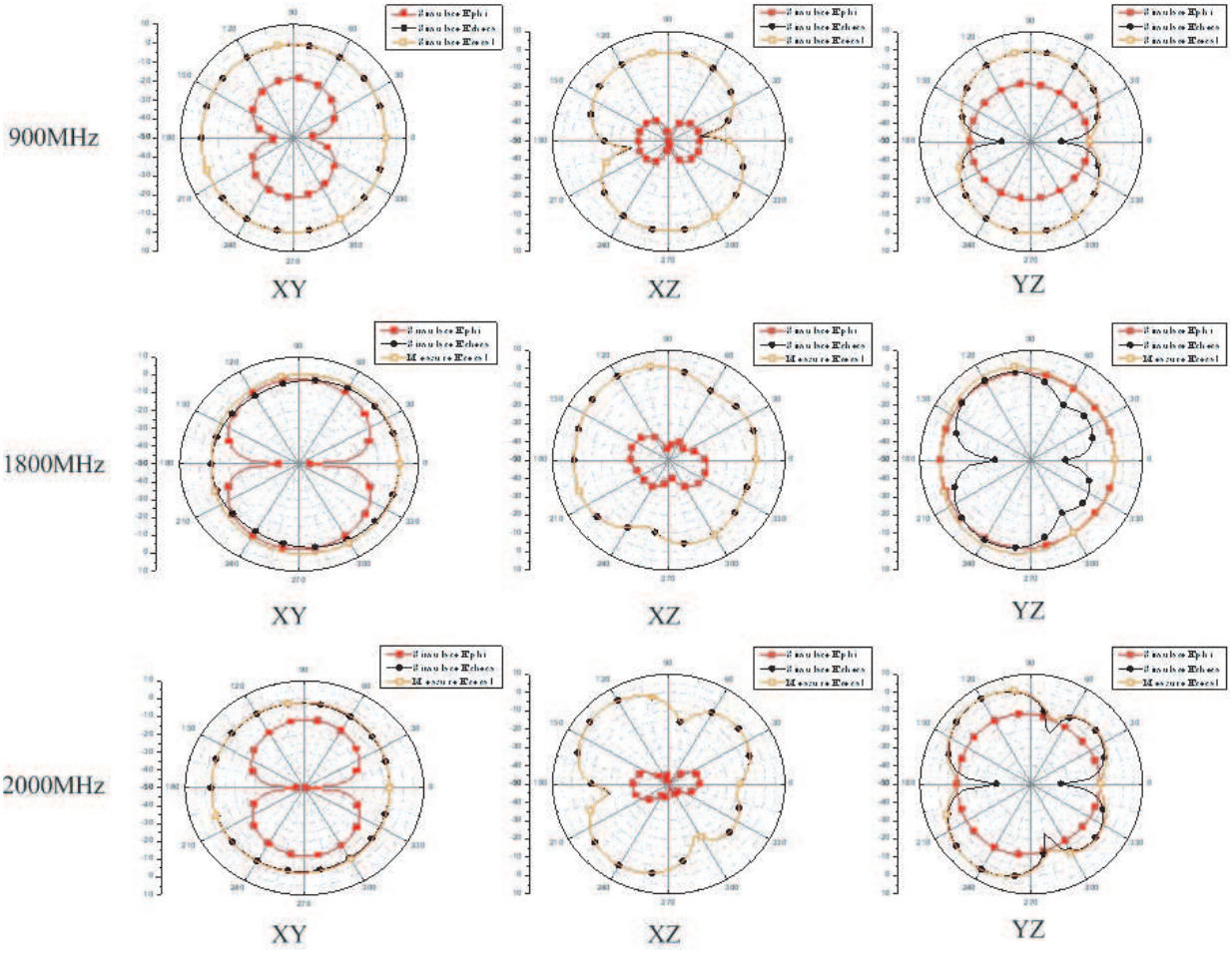

Figure 4: Simulated radiation patterns at 900, 1800 and 2000 MHz.

4. CONCLUSION

A planar coupled loop antenna for GSM850/GSM900/DCS/PCS/UMTS applications has been presented. By using the folded loop strips and a parasitic patch, the antenna achieves quite good impedance matching across the operating bands. Omni-directional radiation patterns have been obtained over the operating bands. Furthermore, the compact design allows the proposed antenna to be easily embedded inside a mobile phone as an internal antenna suitable for penta-band applications.

REFERENCES

1. Yu, B.-K., B. Jung, and H.-J. Lee, "A folded and bent internal loop antenna for GSM/DCS/PCS operation of mobile handset application," *Microw. Opt. Technol. Lett.*, Vol. 48, 463–467, Mar. 2006.
2. Jung, B., H. Rhyu, H.-J. Lee, F. J. Harackiewicz, M.-J. Park, and B. Lee, "Internal folded loop antenna with tuning notches for GSM/GPS/DCS/PCS mobile handset application," *Microw. Opt. Technol. Lett.*, Vol. 48, 1501–1504, Aug. 2006.
3. Wong, K.-L. and C.-H. Huang, "Printed loop antenna with a perpendicular feed for penta-band mobile phone application," *IEEE Trans. Antenna Propag.*, Vol. 56, 2138–2141, Jul. 2008.
4. Chi, Y.-W. and K.-L. Wong, "Compact multiband folded loop chip antenna for small-size mobile phone," *IEEE Trans. Antenna Propag.*, Vol. 57, 3797–3808, Dec. 2008.

A Novel Design of Planar Spiral Antenna with Metamaterial

Nakun Jing, **Huiling Zhao**, **and Lihao Huang**
Northwestern Polytechnical University, Xi'an, Shaanxi 710072, China

Abstract— This paper presents the design of the spiral antennas with metamaterial. It is a new way of producing a low-profile and wide-band antenna. According to the relationship of spiral antenna's active region and frequency, a circumferential multilayer substrate is designed with a reduced antenna total height. Based on effective media theory, circumferential multilayer substrate is implemented with aligned disk lattice. Simulation results demonstrated that the novel spiral antenna has relatively high gain, while S_{11} of the spiral antenna with metamaterial is not as good as expected.

1. INTRODUCTION

With the development of novel wireless communication, low-profile, high gain and wideband antenna designs are becoming increasingly attractive in many applications, ranging from space to voyage, from military to commercial applications. Spiral antennas have characteristics of wideband, circular polarization and low cost, which make them prime candidates in such applications.

In order to obtain an unidirectional beam, reflecting cavity is always introduced. Traditional implementation of spiral antennas entails using a perfect electric conducting (PEC) ground plane placed at a distance of $\lambda/4$ of the operating center frequency below the antenna [1]. However, it limits its bandwidth. The cavity-backed spiral antenna with absorbing material can increase the bandwidth, but it reduces the gain of the antenna. A conical cavity is designed to keep both characteristics of relatively high gain and broad bandwidth. But the thickness of the cavity is too large for many applications. So it is not applicable for conformal and miniature case.

In this paper, we present a new implementation of an Archimedean spiral antenna, which is a low-profile, relatively high gain and wideband antenna with metamaterial. Antenna substrate is substituted by metamaterial with spatial variation of permittivity, which is designed circumferentially to form zones from center to periphery. The metamaterial can equivalently change the electrical space between the spiral antenna and the ground plane, to make sure that the wave reflecting back to the surface and the forward wave are almost in-phase on the spiral surface, so the radiation will increase.

2. SPIRAL ANTENNA WITH CIRCUMFERENTIAL MULTILAYER MEDIUM

It is well known that spiral antenna has the characteristic of effective area, where the diameter $d = \lambda/\pi$ is called 'active region' for wavelength λ. The radiation energy concentrate in the area, and the current on the arms will decrease quickly out of the 'active region'. The 'active region' will move with the frequency changing. In order to meet the requirement that the electrical thickness of substrate below the active region is $\lambda g/4$ (λg is the wavelength in the medium), the substrate is discretized circumferentially into seven regions. Each region has a different dielectric material with appropriate permittivity. The value of permittivity in each region is determined by the substrate thickness and corresponding wavelength. This kind of substrate is depicted in Figure 1 for its top view.

A self-complimentary Archimedean spiral antenna [2] is designed to be working between 6 GHz and 12 GHz. The parameters of the antenna are shown as follows: The inner radius is 1.8 mm, spiral growth rate is 0.6366/rad, thickness of the substrate is 3.4 mm, the spiral outer radius is 15.4 mm, the width of spiral arm and the distance of the two arms are both 1 mm.

To view the characteristic of the spiral antenna with multilayer medium, we compare it with the antenna with conical cavity. Figure 2 shows comparison of S_{11} of the two spiral antennas. As we can see, the S_{11} of the spiral antenna with multilayer medium is almost below -15 dB during the whole bandwidth (6–12 G). And the total height is 3.4 mm, reduced 72% comparing to conical cavity spiral antenna, and 59% comparing to the traditional $\lambda/4$ spiral antenna. The gain of the two antennas at 9 GHz is depicted in Figure 3. The spiral antenna with multilayer medium has higher gain than conical cavity spiral antenna in the axial direction, which can achieve 5.3 dB.

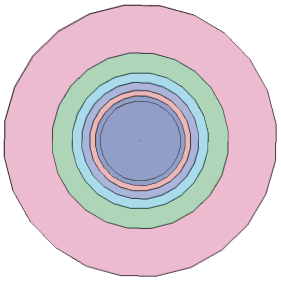

Figure 1: Top view of circumferential multilayer medium.

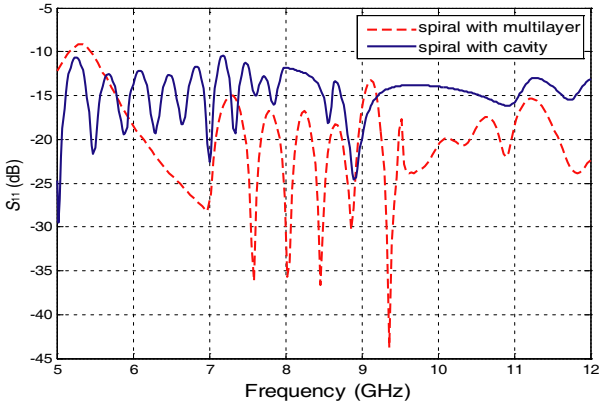

Figure 2: Comparison of S_{11} of the spiral antenna with multilayer medium and conical cavity.

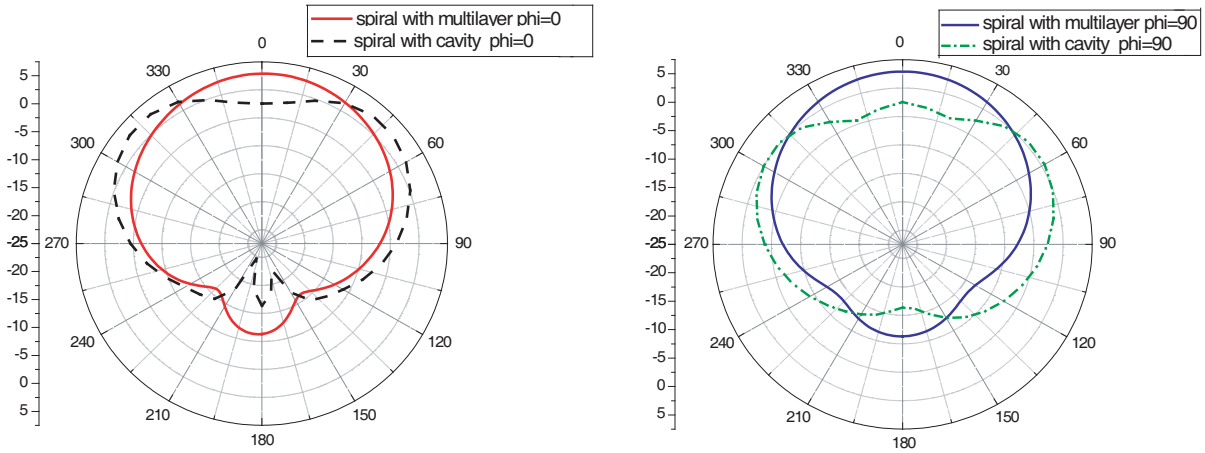

Figure 3: Comparison of gain of the spiral antenna with multilayer medium and conical cavity.

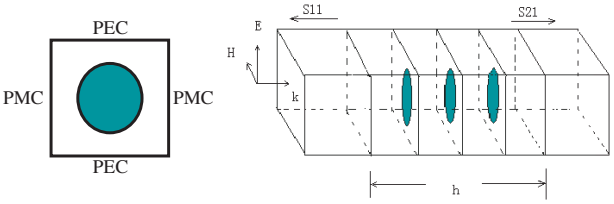

Figure 4: Structure of unit element of three disks aligned in longitudinal.

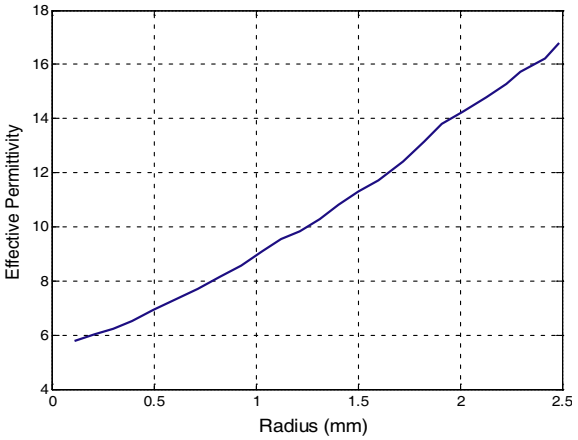

Figure 5: Effective permittivity versus radius of disks.

3. IMPLEMENTATION OF CIRCUMFERENTIAL MULTILAYER MEDIUM

Circumferential multilayer medium is implemented with artificial dielectric medium, which is a collection of metal disks aligned periodically. Effective permittivity of the artificial medium can be retrieved by the S parameters of the structure [3]. The special variation of permittivity can be obtained by controlling the size of unit particles [4]. For a structure illustrated in Figure 4, its

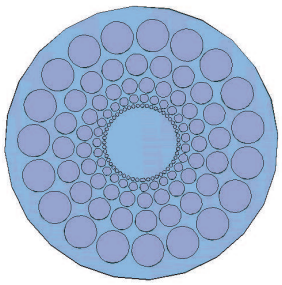

Figure 6: Top view of the metamaterial substrate with metal disks.

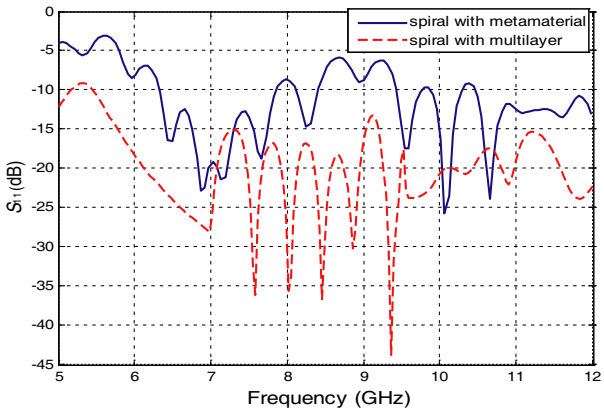

Figure 7: Comparison of S_{11} of the spiral antenna with metamaterial and multilayer medium.

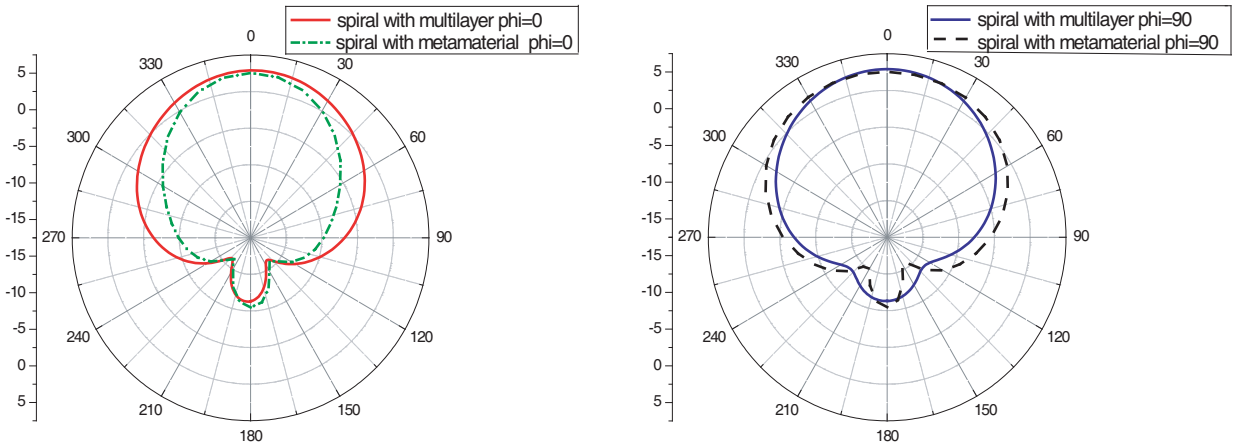

Figure 8: Comparison of gain of the spiral antenna with multilayer medium and metamaterial.

retrieved effective permittivity as a function of radius of disk at 9 GHz is shown in Figure 5. The disks are printed on Rogers TMM3 (tm). The total thickness h is 3.4 mm.

The effective permeability of this structure is nearly 1 for different radius of disks. So it is not mentioned here.

After permittivity of each zone is calculated with changing frequency, then we will know the distribution of the permittivity versus the distance from center to periphery. Based on Figure 5, the circumferential multilayer substrate of spiral antenna is designed by arranging the different radius of disks as shown in Figure 6.

Figure 7 illustrates the spiral antenna with substrate shown in Figure 1, multilayer case, and Figure 6, metamaterial case. As it may be seen, the S_{11} of the spiral antenna with metameterial deteriorates in some frequency band. One reason may be we use one size of the disks in two zones for 8 G and 9 G. (because there is a space limitation for the 'active region'). Another is that the metal disks are not well-distributed periodic structure, the real effective permittivity of the artificial dielectric have shifted from the curve of Figure 5. Although the S_{11} is not as good as the spiral antenna with multilayer medium, the gain at 9 GHz is high, just as Figure 8 shown.

4. CONCLUSION

The design of the Spiral antennas with metalmaterial was introduced. It is a new way of produceing a low-profile and wide-band antenna. Utilization of metamaterial structure offers an antenna height reduction of more than 72% and 59%, comparing with spiral antenna with conical cavity and traditional $\lambda/4$ cavity, respectively. Specially, the novel spiral antenna has a characteristic of relatively wide band and high gain, which can achieve 5 dB. Although S_{11} of the spiral antenna with metamaterial is not as good as expected, the gain is still high. It is a new way for reducing the size of spiral antenna.

REFERENCES

1. Stutzman, W. L. and G. A. Thiele, *Antenna Theory and Design*, 2nd Edition, Wiley, New York, 1998.
2. Werntz, P. C. and W. L. Stutzman, "Design, analysis and construction of an archimedean spiral antenna and feed structure," *Proc. IEEE Souteastcon*, Vol. 1, 308–313, Apr. 1989.
3. Smith, D. R., D. C. Vier, T. Koschny, and C. M. Souloulis, "Electromagnetic parameter retrieval from inhomogeneous metamaterials," *Phys. Rev. E*, Vol. 71, 036617, Mar. 2005.
4. Awai, T. Y., S. Yasui, and Y. J. Zhang, "Very thin artificial dielectric lens antenna made of printed circuit board," *Proc. ISAP 2007*, 390–393, Aug. 2007.

Compact Multi-band Antenna for Global Navigation Satellite Systems

Steven Gao and Li Zheng
Surrey Space Centre, University of Surrey, Guildford GU2 7XH, UK

Abstract— A compact multi-band antenna suitable for Global Navigation Satellite Systems (GNSS) will be presented. The antenna is useful for GNSS receivers onboard small satellites, aircrafts and ground terminal. The antenna operates at two frequency bands which are L1 (1.575 GHz) and L2 band (1.227 GHz). It achieved good circular polarization performance within a broad 3-dB beamwidth, which will enable the small satellite to receive signals from several GNSS satellites. Both the antenna and its feed network are designed. The antenna (without the feed network) has very small size of 1 cm × 1 cm × 1 cm only, and is very light weight. The feed network for the antenna is also designed. To prove the concept, a prototype is developed. The measured results are presented and discussed.

1. INTRODUCTION

GNSS is the generic term for satellite navigation systems that provide autonomous geo-spatial positioning with global coverage. Nowadays, GNSS includes Global Positioning Systems (GPS, USA), Beidou or Compass (China), GLObal NAvigation Satellite System (GLONASS, Russia), and Galileo (Europe), etc. It has been widely used in the precise positioning of spacecrafts, air plane, boats, ships and mobile vehicles on the ground. Space-borne GNSS receiver is also useful for other applications such as remote sensing, occulation measurement and ocean reflectometry. Antenna is a critical component in GNSS receivers. A high-performance GNSS antenna is required for precise positioning.

Several frequency bands have been used in GNSS, such as L1, L2, L5, E5 bands, etc. This requires the design of multi-band antennas or multiple single-band antennas covering each band individually. For space-borne GNSS receivers, the use of multi-band antenna instead of multiple antennas can minimize the number of antennas used onboard, leading to smaller size and lower cost of spacecrafts. It is important to design an antenna which can satisfy the multi-band performance while occupying a very small size.

Many types of antennas have been proposed for GNSS applications, including Quadrifilar helix antenna (QHA), microstrip patch antennas, dielectric antennas, etc [1–5]. The QHA is one of the most popular types of antennas used for GNSS, due to its excellent circular polarization property, broad beamwidth, flexibility in designs and relatively compact size [1]. Most of GNSS antennas developed cover only a single band at 1.575 GHz (L1) [2, 5]. Various manufacturers of GPS equipment use volutes of different size and construction to cover either of the two GPS frequencies of 1.575 GHz (L1) or 1.227 GHz (L2). Some dual-band and tri-band GNSS antennas have been proposed recently [1, 3, 4], however, their sizes and/or weight are rather large for some applications where a very compact size and low mass of antenna is required. Recently, it has been shown that the QHA can achieve a broad bandwidth by using variable pitch angles [6].

It is easy to reduce the size of GNSS antennas by using dielectric loading. For example, the antenna size can be shrinked by using high-permittivity materials loading such as ceramics. However, the use of high-permittivity materials loading would lead to additional cost and fabrication issues as well as low radiation efficiency. In [7], a very compact QHA antenna is presented, which, however, works at L1 band only.

The purpose of this work is to develop a very small, low-mass, dual-band printed square QHA antenna for GNSS receivers onboard micro-satellites. The antenna is required to cover both L1 and L2 bands, and achieve excellent circular polarization properties. Due to the limited space available on a micro-satellite, the antenna size has to be minimised. The configuration of antenna will be explained first, followed by the antenna designs and the feed networks. To prove the concept, a prototype is developed. The measured results will be presented and discussed.

2. ANTENNA AND FEEDNETWORK DESIGNS

The configuration of the dual-band antenna is given in Figure 1. It is based on the single-band antenna work in [7]. The antenna is mounted above a feed substrate board using FR4. The antenna

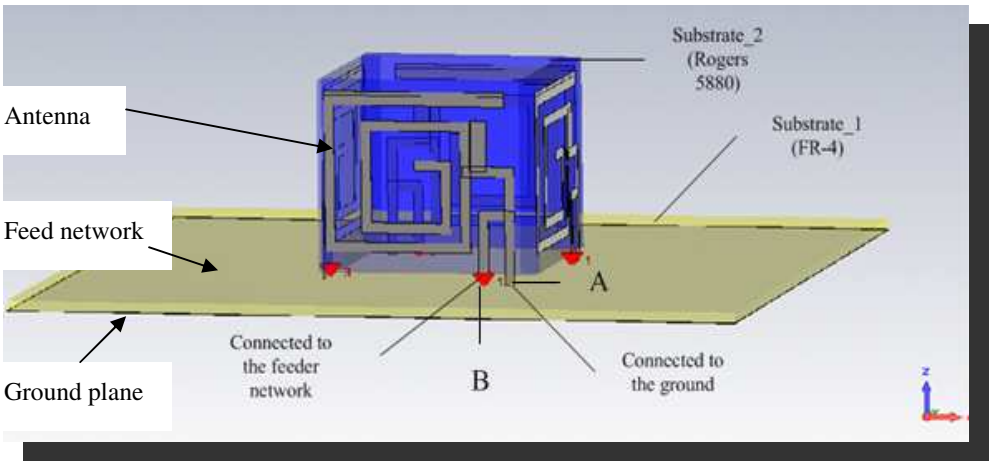

Figure 1: Configuration of the dual-band printed square QHA and its feed network.

has a shape of a cube, formed by four vertical substrate boards. Each vertical board consists of a printed helix on one side of the board. Here Rogers 5880 substrate board is used for the vertical boards. To achieve a dual-band performance, the printed helix on each vertical board consists of two loops having different lengths. The shorter loop corresponds to antenna resonance at L1 band while the longer loop is for L2 band.

To increase the input impedance and improve the matching, the metal strip at point A (in Figure 1) is shorted to ground plane through a via. The metal strip at point B (in Figure 1) is connected to the feed network, which is on the top of FR4 feed substrate. The ground plane is at the bottom of the FR4 feed substrate.

Design and simulation of the antenna were carried out by using the commercial software "CST Microwave Studio" from Computer Simulation Technology. To design the antenna, the total length of the shorter loop is chosen to be about one quarter of wavelength at 1.575 GHz, and that of the longer loop is about one quarter of wavelength at 1.227 GHz. The feed network is to produce four equal amplitude RF signals with relative phases of 0°, 90°, 180°, and 270°, respectively, which, combined with the antenna, can generate circular polarization. The FR4 substrate has permittivity of 4.6 and thickness of 1.6 mm. The Rogers 5880 substrate has permittivity of 2.33 and thickness of 1.6 mm. The size of the antenna (without the feed network) is 1 cm × 1 cm × 1 cm only.

A feed network is designed and implemented by using microstrip lines on a FR4 substrate board. To form the four ports with quadrature phases, it uses three Wilkinson power dividers and different lengths of microstrip lines are used to achieve relative phases of 0°, 90°, 180°, and 270°, respectively. As the feed network (and the antenna) needs to operate at both L1 and L2 bands, the feed network is designed at the center frequency of 1.401 GHz. Four ports from the feed network are to be connected to the four helices. The feed network is of low cost, due to its use of inexpensive FR4 substrate.

It is noted that this antenna achieved a significant reduction of size, without the use of ceramic materials, which can lead to higher cost and lower efficiency.

3. ANTENNA PERFORMANCE

Figure 2 shows the measured return loss results of the dual band antenna [8]. The measured return loss is below −10 dB at both L1 and L2 bands. The impedance matching is achieved by optimizing the lengths of two loops of printed helix, the position and length of the shorted line, etc.

Figure 3 shows the measured results of radiation patterns at 1.227 GHz and 1.575 GHz. The antenna radiates right-hand circularly polarized (RHCP) waves. Both co-polar (RHCP) and cross-polar (LHCP) patterns are measured. It can be seen that the cross-polar results are below −10 dB compared to co-polar radiation pattern levels. This demonstrates the antenna has achieved good circular polarization properties.

Figure 4 shows a photo of the dual band QHA antenna together with its feed network. The antenna (without the feed network) has a very small size of 1 cm × 1 cm × 1 cm, and is light weight. The feed network is, however, rather big. Future work at Surrey is to reduce the size of the feed

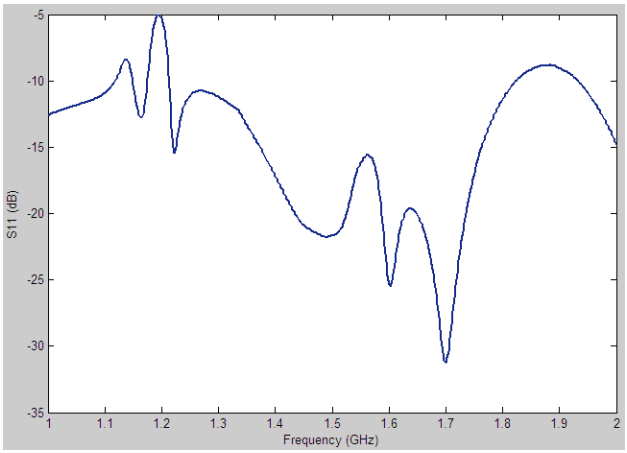

Figure 2: Measured return loss results of the antenna.

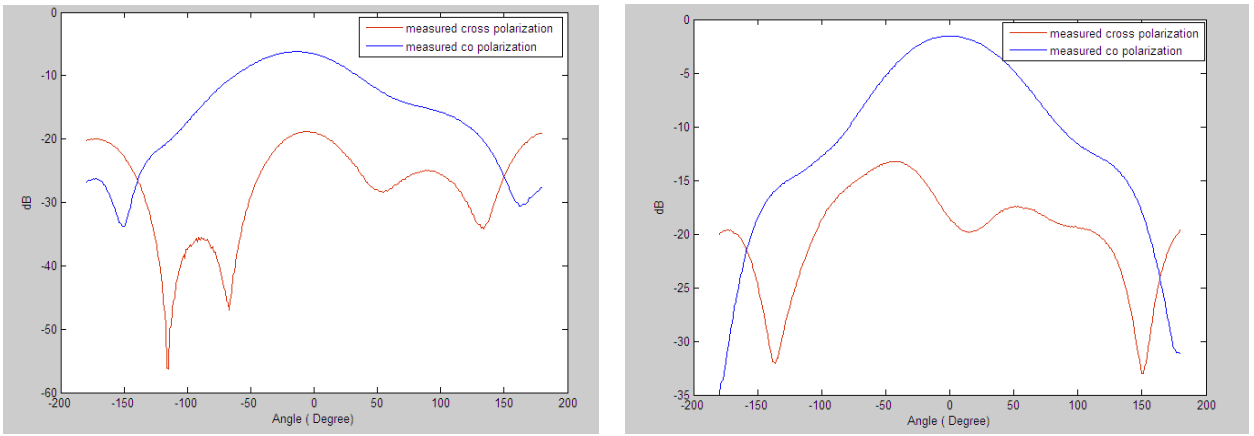

Figure 3: Measured radiation patterns at (a) 1.227 GHz; (b) 1.575 GHz.

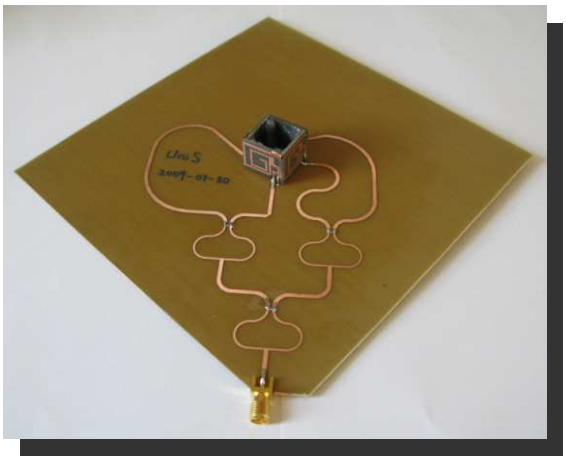

Figure 4: Photo of the dual-band QHA antenna with the feed network.

network.

4. CONCLUSIONS

A novel dual-band printed square QHA antenna is presented. It can achieve good impedance matching performance and right-hand circularly polarized radiation patterns within both L1 and

L2 bands. The antenna (without the feed network) has a very small size of 1 cm × 1 cm × 1 cm, and is light weight. A proof-of-concept prototype has been developed. Both measured and simulated results are presented and discussed. The measured results demonstrated good performance of the antenna. The antenna has very low cost, as it does not need ceramic materials, etc. It could be useful for GNSS receivers onboard small satellites, air planes and mobile vehicles on the ground.

ACKNOWLEDGMENT

The work is a part of the project "Compact multi-band antennas for space-borne GNSS receivers", funded by National Environment Research Council, UK.

REFERENCES

1. Tranquilla, J. M. and S. R. Best, "A study of the quadrifilar helix antenna for Global Positioning System (GPS) applications," *IEEE Trans. Antennas Propagat.*, Vol. 38, No. 10, 1545–1550, Oct. 1990.
2. Boccia, L., G. Amendola, and G. Di Massa, "A shorted elliptical patch antenna for GPS applications," *IEEE Antennas and Wireless Propagation Letters*, Vol. 2, 6–8, 2003.
3. Basilio, L. I., L. Chen, J. T. Williams, and D. R. Jackson, "A new planar dual-band GPS antenna designed for reduced susceptibility to low-angle multipath," *IEEE Trans. Antennas Propagat.*, Vol. 55, No. 8, 2358–2366, Aug. 2007.
4. Zhou, Y., C. C. Chen, and J. L. Volakis, "Dual band proximity-fed stacked patch antenna for triband GPS applications," *IEEE Trans. Antennas Propagat.*, Vol. 55, No. 1, 220–223, Jan. 2007.
5. Leisten, O., J. C. Vardaxoglou, P. McEvoy, R. Seager, and A. Wignfield, "Miniturized dielectrically-loaded quadrifilar antenna for Global Positioning System (GPS)," *Electronics Letters*, Vol. 37, No. 22, Oct. 2001.
6. Bhandari, B. and S. Gao, "Meandered variable pitch angle printed quadrifilar helix antenna," accepted by *2009 Loughborough Antennas and Propagation Conference*, Loughborough, UK, Nov. 2009.
7. Son, W.-I., W.-G. Lim, M.-Q. Lee, S.-B. Min, and J.-W. Yu, "Printed square quadrifilrlar helix antenna (QHA) for GPS receiver," *Proc. of 38th European Microwave Conference*, 1292–1295, Amsterdam, Netherlands, Oct. 27–31, 2008.
8. Zheng, L., "Compact multiband antennas for space-borne Global Navigation Satellite Systems," MSc thesis, University of Surrey, Sept. 2009.

A Numerical Study of the Interaction between Handset Antennas and Human Head/Hand in GSM 900, DCS, PCS and UMTS Frequency Bands

Danoosh Davoodi and Shahin Sharifzad
Sadjad Institute of Higher Education, Mashhad, Iran

Abstract— The interaction between human head/hand tissues and handset antennas is a crucial concept in mobile communications. Mobile handsets are used in proximity to user's body and this affect the transmitted or received power of the handset and some other characteristics e.g., VSWR, radiation pattern. This paper presents a comprehensive study on the performance of various types of handset antennas (two internal, two external) next to human head and hand. The investigated frequency range covers GSM 900, DCS, PCS and UMTS frequency bands. Simulations are performed on antennas next to a simplified two layer cubical hand model and a six layer spherical head model. Radiation patterns and VSWR of these antennas are computed in free space as well as in the presence of head and hand. In addition, radiation efficiencies of these handset antennas are computed in the presence of head and hand.

1. INTRODUCTION

In cellular and wireless mobile communications systems, the quality of the RF link between base station and mobile terminal depends strongly on the amount of power transmitted and received by the mobile handset. The user's body, especially head and hand, influence on the antenna's characteristics such as the voltage standing wave ratio (VSWR), radiation efficiency and radiation patterns. Consequently, interaction of handset antennas with human body is a great consideration in cellular communications.

This paper aims to evaluate the performance of various handset antennas next to human head and hand. Two internal and two external antennas are investigated in free space as well as in presence of human head and hand models. In this study, all radiation characteristics including radiation patterns, radiation efficiency and VSWR of each antenna are examined. All numerical simulations are performed using the Ansoft HFSS v10.

2. MODELING HEAD/HAND

Experimental studies indicate that more than half of the antenna's radiated power is absorbed in the head or hand tissues [1]. Therefore, it is desirable to design antennas for mobile terminals by taking the influence of the human hand and head into account, so as to realize efficient antennas. For this purpose, it is important to develop a human model suitable for handset antenna design.

Biological tissues are modeled by their permittivity and conductivity. The complex permittivity (ε) of a biological tissue is given by:

$$\varepsilon = \varepsilon_0 \varepsilon_r + |j| \frac{\sigma}{\omega}$$

where, σ (S/m) is the conductivity of tissue in siemens per meter and $\varepsilon_0 = 8.854 \times 10^{-12}$ F/m.

In order to demonstrate the effect of hand on the handset antenna's performance, a simplified two layer hand model consisting of a layer of bone surrounded by a layer of muscle is applied. As illustrated in Fig. 1(a), this model covers three sides of the handset. For more realistic position the antenna's box (case) is situated 20 mm from the bottom of the hand model [2].

To avoid the influence of the tilt angle between antenna and head model a six layer head model consisting of skin, fat, bone, dura, CSF and brain is used for modeling the head [3]. Electric properties (ε_r, σ) of the model tissues at investigated frequency bands are available at [4].

Figure 1(b) demonstrates the position of the handset antenna in respect to the head and hand models.

As shown in Fig. 1(b), a 10 mm distance is considered between the head model and antenna. Furthermore due to the spherical shape of the head model, the hand position angle is neglected.

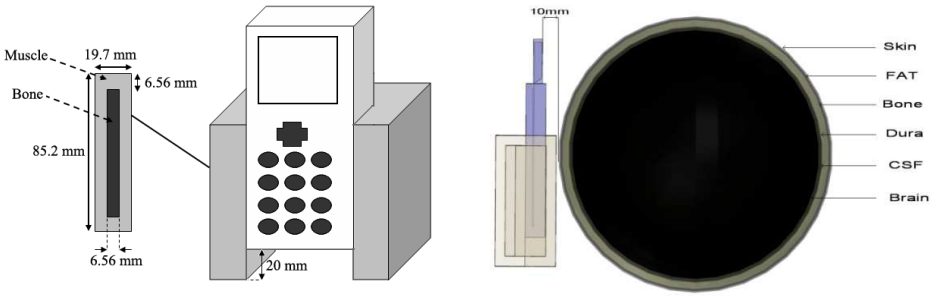

(a) (b)

Figure 1: Position of the handset in respect to head and hand models [2, 3].

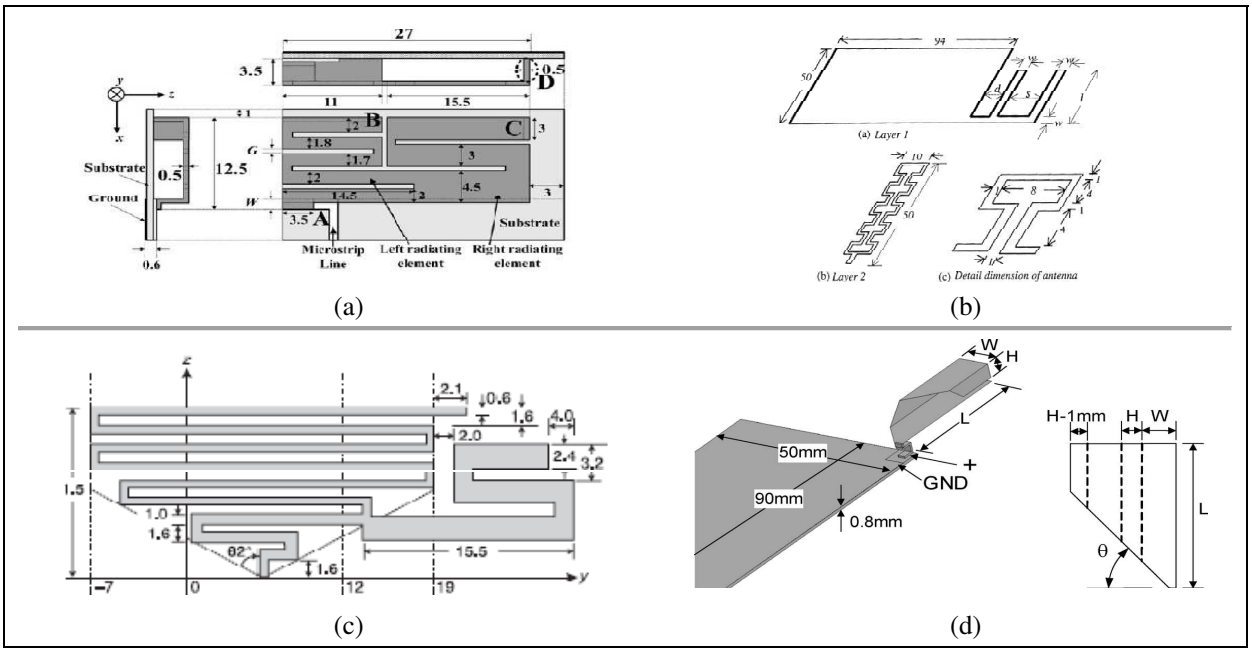

Figure 2: Geometry of the simulated antennas.

3. SIMULATED EXTERNAL/INTERNAL ANTENNAS

Antennas implemented in handset devices, aside from their architecture schemes, are divided into two categories: External antennas and internal antennas. However now a days with modern antenna design methods, using external antennas for commercial handset phones is not a conventional option. Nevertheless for some particular applications, yet they are the best choice.

3.1. Antenna 1: Internal

This is an internal triple band PIFA antenna covering DCS 1800, PCS 1900 and UMTS 2100 frequency bands (1.71–2.17 GHz) [5]. It is fed with a 50 Ω bent microstrip feed line. The simulated PCB substance is FR-4 ($\varepsilon_r = 4.6$). Fig. 2(a), depicts the geometry of the radiating element and microstrip feed line.

3.2. Antenna 2: Internal

This is an internal multiband antenna mounted on a printed circuit board (PCB) covering GSM 900 and DCS 1800 frequency bands (0.85–0.95, 1.71–1.89 GHz) [6]. The geometry of the antenna and its associated PCB is shown in Fig. 2(b), In simulations the antenna is fed with a 50 Ω coaxial feed line and the PCB is FR-4 ($\varepsilon_r = 4.4$).

3.3. Antenna 3: External

This is a dual band meander antenna applicable for GSM 900 and DCS 1800 frequency bands [7]. The required power is fed to the antenna through a 50 Ω coaxial feed line. Fig. 2(c), illustrates the geometry of the antenna.

3.4. Antenna 4: External

This is an ultra wideband stubby antenna that covers all frequency bands between 824 MHz and 6 GHz, which include GSM 850 and 900, GPS, DVB-H US, DCS, PCS, UMTS, BT, WLAN 802.11b/g and WLAN 802.11a [8]. The design technical points and dimensions are introduced in Fig. 2(d), Feed line is a 50 Ω bent microstrip and the simulated PCB material is FR-4 ($\varepsilon_r = 4.4$). In this paper only DCS, PCS and UMTS bands of this antenna are investigated.

4. SIMULATION RESULTS

In this paper all the simulations performed using Finite Element Method based on Ansoft HFSS v10. In this section antenna properties mentioned earlier are discussed under various situations.

4.1. VSWR

Figure 3 illustrates the computed VSWR of the internal antennas in their corresponding frequency ranges. All VSWR curves are computed in free space, in presence of hand and in presence of head and hand. Position of handset in presence of head and hand has been previously shown in Fig. 1(b).

As shown in Fig. 3(a), in GSM band, presence of hand increases VSWR, while in presence of head and hand a decrement of VSWR is observed, especially in the lower GSM. In DCS band a shift to left can be seen in the resonant frequency. Nevertheless in the middle DCS band the simulated VSWR values show an increment. For the PIFA antenna simulated VSWR in presence of hand/presence of hand and head shows greater values in DCS and PCS bands followed by lower values in the UMTS band.

The simulated VSWR for two external antennas are illustrated in Fig. 4. Presence of hand/hand and head next to antenna 3 decreases VSWR in GSM. However in DCS the effect was entirely opposite. Antenna 4 demonstrated appealing changes of VSWR in PCS and UMTS comparing to that of antenna 2.

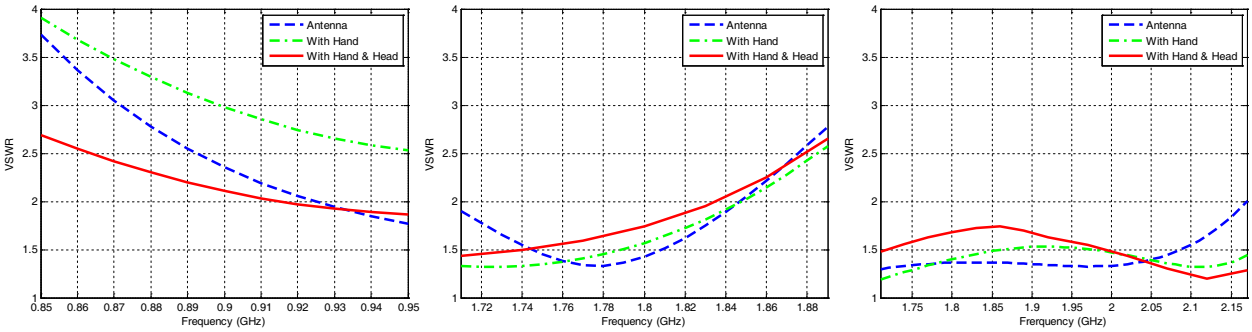

Figure 3: Computed VSWR of the internal antennas, (a) ant 2 GSM, (b) ant 2 DCS, (c) ant 1.

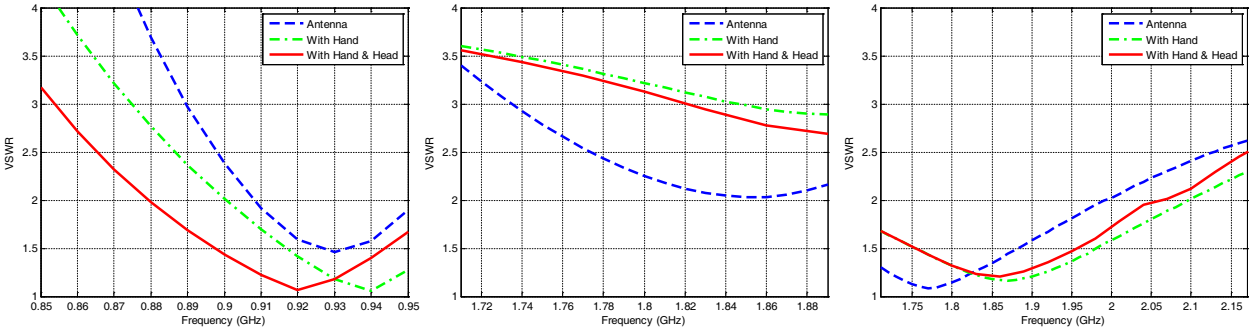

Figure 4: Computed VSWR of the external antennas, (a) ant 3 GSM, (b) ant 3 DCS, (c) ant 4.

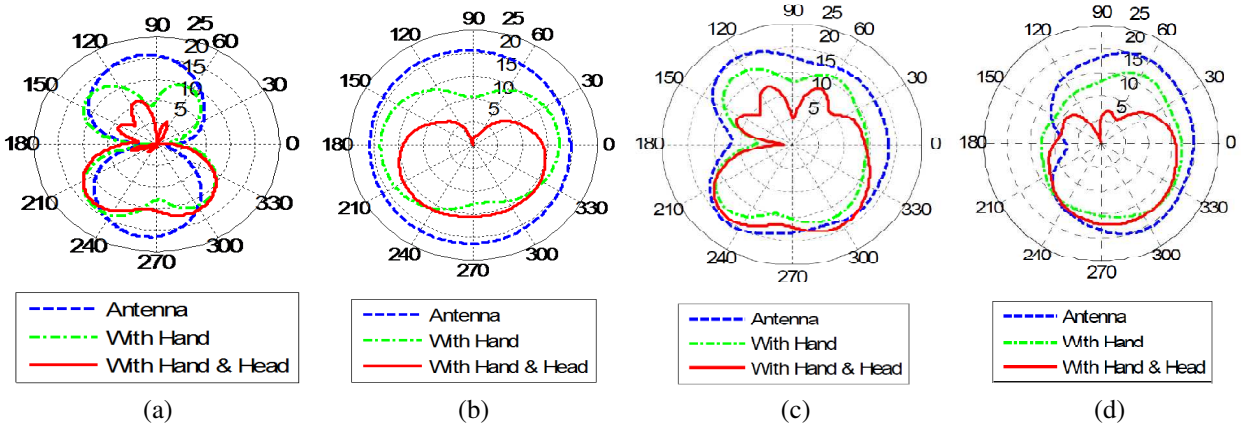

Figure 5: Radiation patterns, (a) ant 1 ($\varphi = 90°$), (b) ant 1 ($\theta = 90°$), (c) ant 2 ($\varphi = 90°$), (d) ant 2 ($\theta = 90°$).

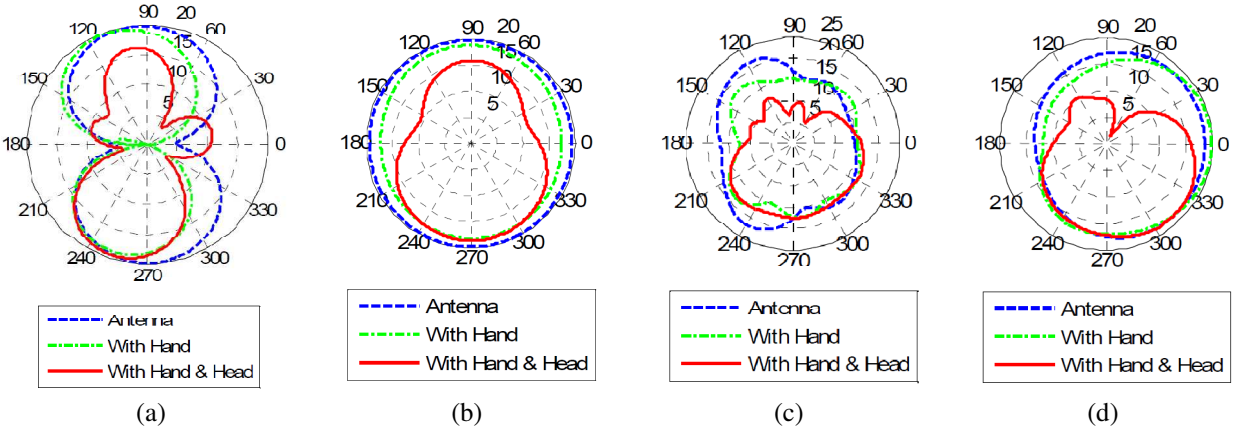

Figure 6: Radiation patterns, (a) ant 3 ($\varphi = 90°$), (b) ant 3 ($\theta = 90°$), (c) ant 4 ($\varphi = 90°$), (d) ant 4 ($\theta = 90°$).

4.2. Radiation Pattern

Figure 5 shows the total-power radiation patterns of internal antennas. Radiation patterns are computed in free space as well as in presence of hand/hand and head models at 1800 MHz. Figs. 5(a) and (c) are the radiating power patterns for antenna 1 and antenna 2 plotted in the zenith plane ($\varphi = 90°$) respectively. Figs. 5(b) and (d) are plotted in the azimuth plane ($\theta = 90°$).

Figure 6 depicts radiation patterns of external antennas. Figs. 6(a) and (c) corresponds to radiated power of antenna 3 and antenna 4 in the zenith plane ($\varphi = 90°$) respectively. Figs. 6(b) and (d) are plotted in the azimuth plane ($\theta = 90°$). The incident power delivered to the input of every antenna (before the effect of return losses) is 1 W.

As it can be seen in the figures, not only the amount of radiated power in presence of both hand and head is lower than that of hand, but also the radiating manner of the antenna, especially in head direction, undergone a whole lots of changes.

In order to better understand effect of presence of hand and head on the radiating power, Table 1, shows the value of power reduction in a specific direction due to the presence of hand and head in respect to the free space radiation. The variations are computed in the zenith plane ($\varphi = 90°$).

4.3. Radiation Efficiency

Due to energy absorption in human body, radiated power of a handset antenna is decreased. This decrement of radiated power is characterized by radiation efficiency (η).

$$\eta = \frac{P_{rad}}{P_{in}} = \frac{P_{rad}}{P_{loss} + P_{rad}}$$

where, P_{loss} is the power absorbed within lossy tissues, P_{rad} is the power radiated to the far field.

Table 2 presents the radiation efficiencies for all antennas in their corresponding frequency bands.

Table 1: Variations in the radiating power due to presence of hand ($\theta = -90°$) and head $\theta = 90°$).

		Antenna 1	Antenna 2	Antenna 3	Antenna 4
GSM 900	$\theta = -90°$	-	−3.1 dB	−9.3 dB	-
	$\theta = 90°$	-	−5.7 dB	−9.1 dB	-
DCS 1800	$\theta = -90°$	−5.9 dB	−1.3 dB	−1.2 dB	−0.25 dB
	$\theta = 90°$	−19.4 dB	−12.5 dB	−4 dB	−8.7 dB
PCS 1900	$\theta = -90°$	−5.4 dB	-	-	−1.9 dB
	$\theta = 90°$	−13.7 dB	-	-	−9.3 dB
UMTS	$\theta = -90°$	−5 dB	-	-	−2.7 dB
	$\theta = 90°$	−20.8 dB	-	-	−7.6 dB

Table 2: Radiation efficiencies in presence of hand and head.

		Antenna 1	Antenna 2	Antenna 3	Antenna 4
GSM 900	Hand	-	50.97	71.55	-
	Hand & Head	-	25.44	39.45	-
DCS 1800	Hand	65.61	71.53	47.93	65.03
	Hand & Head	50.67	56.29	36.09	51.71
PCS 1900	Hand	65.55	-	-	68.45
	Hand & Head	42.89	-	-	47.56
UMTS	Hand	63.74	-	-	74.88
	Hand & Head	41.78	-	-	52.29

REFERENCES

1. IEEE standards for safety levels with respect to human exposure to radio frequency electromagnetic fields, 3 kHz to 300 GHz," IEEE Standard C95.1^{TM}, 2005.
2. Jensen, M. A. and Y. Rahmat-Samii, "EM interaction of handset antennas and a human in a personal communication," *Perceeding of IEEE*, Vol. 83, No. 1, June 7–17, 1995.
3. Kim, J. and Y. Rahmat-Samii, "Implanted antenna inside a human body: Simulation, design and characterization," *IEEE Trans. MIT*, Vol. 52, No. 8, 1934–1943, 2004.
4. Anderuccatti, D., R. Fossi, and C. Gabriel, "Calculation of the dielectric properties of body tissues," 2002, Available: http://www.niremf.ifac.cnr.it/tissprop/htmlclie/htmlclie.htm.
5. Sim, D. U. and S. O. Park, "A triple-band internal antenna: design and performance in presence of the handset case, battery, and human head," *IEEE Trans. on Electromagnetic Compatibility*, Vol. 47, No. 3, August 2005.
6. Ali, M., G. J. Hayes, H.-S. Hwang, and R. A. Sadler, "Design of a multiband internal antenna for third generation mobile phone handsets, *IEEE Trans. on Antennas and Propagation*, Vol. 51, No. 7, July 2003.
7. Sun, B., Q. Liu, and H. Xie, "Compact monopole antenna for GSM=DCS operation of mobile handsets," *Electronics Letters*, Vol. 39, No. 22, October 30, 2003.
8. Zhang, Z., J. C. Langer, K. Li, and M. F. Iskander, "Design of ultrawideband mobile phone stubby antenna (824 MHz–6 GHz)," *IEEE Trans. on Antennas and Propagation*, Vol. 56, No. 7, July 2008.

A Radar Eye on the Moon: Potentials and Limitations for Earth Imaging

M. Calamia[1], **G. Fornaro**[2], **G. Franceschetti**[3], **F. Lombardini**[4], **and A. Mori**[1]

[1]Dipartimento di Ingegneria Elettronica e Telecomunicazioni (DET), Università di Firenze, Italy
[2]Istituto per il Rilevamento Elettromagnetico dell'Ambiente (IREA), Italy
[3]Dipartimento di Ingegneria Biomedica Elettronica e delle Telecomunicazioni
Università di Napoli Federico II, Italy
[4]Dipartimento di Ingegneria della Informazione, Università di Pisa, Italy

Abstract— Among the next space missions goals the exploitation of the Moon, the natural Earth satellite, is gaining an increasing interest. Colonization of the Moon is along the usual track of human civilization and economic expansion; it is also related to a large number of scientific issues, including Earth Observation (EO). With respect to standard LEO satellite commonly used in remote sensing, Moon has specific features. In this work we analyze the potentials as well as the limitations related to active microwave remote sensing with Synthetic Aperture Radar in terms of imaging characteristics and potential applications.

1. INTRODUCTION

The exploitation of the Moon, the natural Earth satellite, is gaining an increasing interest. Calls for ideas are being recently coordinated by several international space agencies, in order to evaluate themes and objectives related to lunar missions. Colonization of the Moon is along the usual track of human civilization and economic expansion; it is also related to a large number of scientific issues, including Earth Observation (EO).

EO is traditionally carried out by means of sensors mounted on artificial satellites mainly orbiting on sun-synchronous Low Earth Orbits (LEO). With respect to standard LEO satellites, Moon has specific features: a longer distance between the sensor and the imaged area, non sun-synchronous orbits, a large surface for the installation of sensors and equipments, etc. In this work we analyze the potentials as well as the limitations related to active microwave remote sensing with Synthetic Aperture Radar (SAR), giving particular emphasis to its distinguished characteristic from LEO satellites in terms of imaging characteristics and potential applications.

One of the major expected problems of Lunar EO with respect to standard LEO satellites is associated with the considerable increasing distance between the scene and the sensor. For a passive system the increasing distance leads to an unavoidable resolution loss. On the contrary, for a SAR system the increase of the distance could, in principle, drastically impact the power budget [1] leading to a transmitted power level demand that could be hardly provided with standard technology. Nonetheless, there are many expected advantages related to the use of a lunar SAR system that make worth further investigations. First of all, the system would be characterized by a large ground swath, thus allowing the imaging of large portions of the Earth surface as well as a reduction of the revisiting time, down to one day. Secondly, a steering of antenna in elevation would lead to quasi-global scene accessibility.

Differently from standard stripmap SAR sensors, a Moon-borne SAR can overcome the limit of half antenna length azimuth resolution [2] due to a peculiar imaging effect associated with the Earth rotation, leading to very high resolution imaging capabilities and hence small pixel size. This feature allows the use of large antennas to partially compensate for power limitations, without to lower the resolution to values unacceptable for some applications; and allows to avoid the need to implement any electronic or mechanical steering of the beam along the azimuth direction typical of more complex acquisition modes aimed at increasing the integration time to achieve very high resolutions. Finally, for a Moon-borne SAR system, the synthetic aperture integration time for full focusing is rather large: this on one side can prevent the possibility to effectively image "fast" moving scenes, such as the sea surface, but on the other side it can allow implementation of "fast" moving target detection, even starting from single antenna data [3].

Moon orbits may in principle allow the implementation of one day repeat pass differential interferometry [4]: due the large variation of the elevation angle from day to day, the number of usable coherent interfering images is rather limited. However, lunar surface allows the installation of multiple SAR sensors (only one transmitting) partially compensating the above mentioned drawback

and also implementing single pass interferometry [4] on a systematic basis, as well as along-track interferometry and advanced 3D imaging [5, 6].

2. THE MOON AND ITS ORBIT

The main orbital and the physical characteristics of the Moon are summarized in Table I. The Moon is in synchronous rotation around the Earth with a sidereal period T_M of about 27 days (sidereal month), resulting in an average angular velocity of $\Omega_M = 2\pi/T_M = 2.664 \cdot 10^{-6}$ rad/s. The Moon also rotates around its axis with a period equal to T_M. As a consequence the same side of the Moon is always facing the Earth (tidal locking), so that an antenna pointed towards the Earth center approximately maintains its orientation, but for higher order effects such as lunar libration.

The Moon orbits around the Earth in a plane which is tilted by 5° from the Ecliptic, and the angle between the Earth rotational axis and the direction perpendicular to the Ecliptic is about 24°. As a consequence, a large variation of the elevation of the Moon over the horizon can be observed. For a latitude of 40°, the minimum elevation of the Moon over the horizon is $50 - 24 - 5 = 21$ degrees, whereas the maximum elevation is $50 + 24 + 5 = 79$ degrees, with an excursion of more than 50 degrees, limiting the implementation of one day ineterferometry.

The Earth rotates with a period T_E of 1 day at an angular velocity of $\Omega_E = 2\pi/T_E = 7.292 \cdot 10^{-5}$ rad/s. $\Omega_E \gg \Omega_M$, so, in the following, for sake of simplicity, we assume that the Moon is fixed and the Earth is rotating; and we neglect higher order motions associated with librations (also causing a variation of the angular velocity very low when compared to Ω_E). Obviously, such effects must be considered for data processing in order to achieve fully focused images.

Table 1: Orbital and physical parameters of the Moon.

Description	Value	Symbol
Semi-major axis	384,748 km	
Mean eccentricity	0.0549006	
Average distance from the Earth	377,700 km	D_M
Sidereal orbital period	27.3 days	T_M
Average angular velocity around the Earth	2.664 10^{-6} rad/s	Ω_M
Average orbital speed	1.04 km/s	V_M
Inclination to ecliptic	5.145°	
Inclination to Earth's equator plane	18.29° ÷ 28.58°	
Mean radius	1,738 km	R_M

3. QUALITATIVE ANALYSIS

In the following, we briefly describe the main characteristics of a Moon based SAR system. For sake of simplicity, we refer to the geometry sketched in Figure 1, neglecting the inclination of the

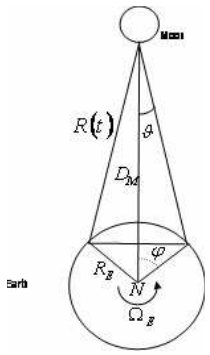

Figure 1: Moon-Earth reference geometry in the equatorial plane used for the calculation of the azimuth resolution.

Earth and the inclination of the axis connecting the Moon center to the Earth center. The Moon is still assumed to be fixed whereas the Earth is rotating along an axis orthogonal to the Ecliptic.

3.1. Resolution

Range resolution is governed by the transmitted pulse bandwidth B. It depends also on the elevation angle that, for the Moon-borne SAR case, can vary considerably in the sidereal month.

To evaluate the azimuth resolution, let Lbe the size of the SAR antenna. The 3-dB antenna aperture is $2\vartheta = \lambda/L$, where λ is the radiation wavelength. With simple geometrical considerations, we have:

$$\varphi \approx \frac{D_M}{R_E}\vartheta, \tag{1}$$

showing that the Earth angular semi aperture φ is amplified by a factor D_M/R_E with respect to the antenna aperture ϑ. Denoting with v_E the scatterer velocity vector and with $\hat{\mathbf{r}}$ the scatterer l.o.s., the Doppler Bandwidth (B_D) is given by:

$$B_D = 2\frac{2}{\lambda}(v_E \cdot \hat{\mathbf{r}})_{\max} = \frac{4}{\lambda}v_E \sin(\varphi_M + \vartheta_M) \approx \frac{4}{\lambda}v_E \sin\varphi_M \approx \frac{4}{\lambda}v_E\frac{D_M}{R_E}\vartheta_M = \frac{2v_E}{L}\frac{D_M}{R_E}, \tag{2}$$

assuming $\varphi \ll 1$. The azimuth resolution Δ_y for the Moon-borne case is then given by:

$$\Delta_y = \frac{v_E}{B_D} = \frac{L}{2}\frac{R_E}{D_M}, \tag{3}$$

and thus it is $D_M/R_E \approx 60$ times better than that of the LEO space-borne case ($L/2$). This resolution gain effect has been also highlighted in the study of Medium Earth Orbit SAR systems [7].

3.2. Ambiguity and Power Constraints

In any SAR system the Pulse Repetition Frequency (PRF) f_p is down- and up-bounded. The first limitation is related to the sampling of the azimuth bandwidth: for a correct sampling of the scene

$$f_p \geq \frac{2v_E}{L}\frac{D_M}{R_E} \approx \frac{2v_{Ma}}{L}, \tag{4}$$

where v_{Ma} is the equivalent Moon velocity with respect to a fixed Earth (almost D_M/R_E higher than the velocity of the scatterers on the ground). The second limitation is associated with the necessity to avoid that echoes backscattered by successive pulses are received simultaneously. We must ensure that [1] $f_p \leq c/2W$, where $W = (\lambda/L_r)D_M \cot\vartheta_{el}$ is the swath extension in the slant range direction, and L_R is the antenna size in the direction orthogonal to the azimuth and slant range. It follows that

$$LL_r \geq 4\frac{v_{Ma}}{c}D_M\lambda \cot\vartheta_{el} = 4\frac{v_E}{c}\frac{D_M^2}{R_E}\lambda \cot\vartheta_{el}, \tag{5}$$

showing that the minimum antenna area of a lunar SAR increases with respect to standard satellite systems for an increase of the distance and a scaling of the velocity (v_{Ma} in place of v_E).

Table 2: Parameters of three selected Moon-borne SAR systems compared to the Envisat ASAR system.

	L-band	C-band	X-band	ASAR
Azimuth Footprint [km]	378	252	189	5
Integration time [s]	823	549	411	0.7
Az. resolution [m]	1.5	0.7	0.5	5
Doppler Bandwidth [Hz]	306	656	889	1,400
Min antenna area [m^2]	20,987	6,529	3,614	2
Max ground range swath [km]	762	356	262	96
Min average power [kW]	42	26	27	0.1
Coverage rate [km^2/day]	$30{\cdot}10^6$	$14{\cdot}10^6$	$10{\cdot}10^6$	$58{\cdot}10^6$

With the same notation of [1], the basic constraint on the achievable SNR for lunar SAR system satisfying the constraint on the antenna minimum effective area is:

$$SNR \geq \frac{P_T}{KT^0FB}\frac{\lambda}{\pi D_M}\sigma^0\frac{v_{Ma}}{c}\frac{\cos\vartheta_{el}}{\sin^2\vartheta_{el}} \approx \frac{P_T}{KT^0FB}\frac{\lambda}{\pi R_E}\sigma^0\frac{v_E}{c}\frac{\cos\vartheta_{el}}{\sin^2\vartheta_{el}}. \quad (6)$$

On the basis of the previous analysis, Table 2 provides the quantitative parameters of the three lunar system configurations with reference to an average value of the elevation of 50 degree at 40° latitude; the Envisat ASAR satellite of the European Space Agency is reported for comparison. The transmitted power budget has been also evaluated accordingly to (6) by assuming: $T^0 = 290\,\mathrm{K}$, $SNR = 13\,\mathrm{dB}$, $F = 3\,\mathrm{dB}$ at L-Band, $F = 4\,\mathrm{dB}$ at C-Band and $F = 5\,\mathrm{dB}$ at X-Band. Moreover we considered $\sigma_0 = -15\,\mathrm{dB}$ at L-Band, $\sigma_0 = -9\,\mathrm{dB}$ at C-Band, and $\sigma_0 = -6\,\mathrm{dB}$ at X-Band corresponding to average values of agricultural fields.

3.3. Integration Time

The three example systems of Table 2 exhibits a long integration time. As a consequence, it greatly enlarges the well-known imaging artefacts of non stationary or partially coherent scatterers. For a scatterer having a line of sight motion with a velocity of v_t, the azimuth position in the final image is misplaced by $\Delta_{ey} = v_t D_M / v_{Ma}$. For $v_t = 1\,\mathrm{m/s}$ the scatterer would be misplaced of about 14 km. If τ_c is the coherence time of a scatterer, the effective azimuth resolution Δ_{ye} is degraded by a factor which is approximately the ratio of the integration time T over the coherence time: $\Delta_{ye} = \Delta_y T/\tau_c$. For instance, in case of a forest canopy, the azimuth resolution will degrade up to several kilometers.

The blurring effects from non stationary and partially coherent scatterers can also cause clutter power problems, due to the energy spreading over adjacent areas of stable scatterers. Analyzing the possible sources of clutter, the water can be considered to be not of great concern, unless for very windy days, being the scattering level significantly less (at least, a few dB less) than other area, e.g., urban or agricultural fields. Clutter from strong windblown forest might exhibit higher power. Except high wind velocity, it can be estimated that even the forest clutter would not constitute a significant limitation. However, to reduce the possible criticalities in the vicinity of non fully coherent areas, a synthetic aperture processing robust to energy leakage may be achieved by resorting to presumming, as hinted in [8].

3.4. Cross-track Interferometry

With respect to existing LEO satellites a main peculiarity of Moon-borne SAR imaging is related to the one day site accessibility. The elevation angle has a large excursion in the sidereal month, and the acquisitions useful for one day repeat pass interferometry could be quite limited. However, the Moon surface offers the possibility to install different antennas allowing collection of simultaneous radar images from different elevation angles, single pass cross-track interferometry, and even 3D tomographic imaging [5, 6].

ACKNOWLEDGMENT

The authors are grateful to Giovanni Vulpetti, of the Galileian Plus Italy for providing the Moon orbits via the computer program S.M.A.C. (Copyright, G. Vulpetti 1983, 2007). This work has been partially financed by the Italian Space Agency under the contract "Italian Vision for Moon Exploration Earth observation from the Moon" (n.I/042/06/0).

REFERENCES

1. Franceschetti, G. and R. Lanari, *Synthetic Aperture Radar Processing*, CRC Press, 1999.
2. Curlander, J. C. and R. N. McDonough, *Synthetic Aperture Radar: Systems and Signal Processing*, John Wiley & Sons, New York, 1991.
3. Dias, J. M. B. and P. A. C. Marques, "Multiple moving target detection and trajectory estimation using a single SAR sensor," *IEEE Trans. Aerosp. Electron. Sys.*, Vol. 39, No. 2, 604–624, April 2003.
4. Rosen, P. A., S. Hensley, I. R. Joughin, F. K. Li, S. N. Madsen, E. Rodriguez, and R. M. Goldstein, "Synthetic aperture radar interferometry," *Proc. IEEE*, Vol. 88, No. 3, 333–382, March 2000.
5. Reigber, A. and A. Moreira, "First demonstration of airborne SAR tomography using multibaseline L-band data," *IEEE Trans. Geosci. Remote Sens.*, Vol. 38, No. 5, 2142–2152, September 2000.

6. Fornaro, G., F. Lombardini, and F. Serafino, "Three-dimensional multipass SAR focusing: Experiments with long-term spaceborne data," *IEEE Trans. Geosci. Remote Sens.*, Vol. 43, No. 4, 702–714, April 2005.
7. Raney, K., "Consideration for SAR image quantification unique to orbital systems," *IEEE Trans. Geosci. Remote Sens.*, Vol. 29, No. 5, 754–760, September 1991.
8. Prati, F., F. Rocca, D. Giancola, and A. Monti Guarnieri, "Passive geosynchronous SAR system reusing backscattered digital audio broadcasting signals," *IEEE Trans. Geosci. Remote Sens.*, Vol. 36, No. 6, 1973–1976, November 1998.

Plane Wave Scattering by a Coated Thin Wire

A. Ike Mowete[1] and A. Ogunsola[1, 2]

[1]Department of Electrical and Electronics Engineering
Faculty of Engineering, University of Lagos, Lagos, Nigeria
[2]Parsons Group International, Rail Transit Division, London, United Kingdom

Abstract— This paper addresses the problem of scattering by an insulated perfectly conducting thin-wire, illuminated by a uniform, plane electromagnetic wave. The conductor is modeled by the usual 'thin-wire approximation', and the dielectric insulation, by a Schelkunuff's volume polarization current, defined in terms of a quasi-static electric field, which derives from the distribution of current along the axis of the bare-wire scatterer through the equation of continuity; so that a model for the composite structure then emerges as the sum of two axially directed currents radiating in free-space. In the moment-method technique subsequently utilized for the solution of the problem, testing functions, which are critical to specification of the voltage excitation matrix, are taken as having the two component parts indicated by the choice of model for the coated scatterer. Computational results obtained for the selected examples of two straight wires and a crossed-wire suggest that this analytical approach is valid, as the results reveal that the influence of the coating on the wires' broadside and bi-static radar cross-sections is consistent with those described in the open literature.

1. INTRODUCTION

Interest in the problem of scattering by structures coated with dielectric materials has been sustained by applications extending from dielectric lenses at frequencies in the microwave and optical regimes through ionospheric reflection by meteor trails, ablating and camouflaging applications [1], to the determination of equivalent cylindrical radii for scaterrers of non-cylindrical cross-sections [2, 5], to mention a few. A number of the associated investigations focused on the effects of different coating types on the fields scattered by perfectly conducting bodies of revolution, coated with thin layers of dielectric materials, and developed analytical models that provided significant insight. Huddleston et al. [3], for example, using a generalization of the combined field integral equation (CFIE) approach, developed explicit moment-method solutions for perfectly conducting bodies of revolution coated with insulating materials. In their own contributions, Sebak and his associates [4], examined the nature of the fields scattered by coated prolate (and oblate) spheroids illuminated by plane electromagnetic waves and obtained results that suggested that the magnitude and phase of the coating's dielectric constant has modifying effects on scattering cross section.

The scattering characteristics of thin, perfectly conducting wires coated with layers of dielectric materials have also engaged the attention of several analytical and experimental research investigations. These include the analysis reported by Bretones et al. [5], who extended the DOTIG3 tool for use in the time-domain investigation of the transient response coated thin-wire scatterers. Their quasi-static model for the dielectric layer consists of two layers of polarization charges of equal magnitudes and opposite signs, residing on the cylindrical surfaces that define the thickness of the insulating layer; and is limited in applicability [5], coating thickness that do not exceed three times the wire radius and permittivity of magnitude not greater than 10. A frequency domain equivalent of this approach was developed by Moore and West [6], whose simplified analysis also involved a quasi-static approximation through which a model for the dielectric layer emerged as a distributed reactive load on the bare scatterer. Earlier, Richmond and Newman [7], described a sinusoidal reaction integral approach to the solution of the coated thin-wire problem using a model that has been shown by Adekola et al. [8], to implicitly involve a quasi-static approximation. Variations of this approach have been developed by Li, Drissi, and Paladian [9], and Lee and Balmain [10].

Using a physical basis model characterized by three weighted travelling-wave functions as approximation for current distribution, Chatterjee, Volakis and Kent [11], provided another frequency-domain analysis technique for the solution of the problem of scattering by a thin, perfectly conducting and dielectrically coated wire. It is shown in this paper that when specialized for the $e^{-j\omega t}$ time-harmonic case, the model adopted by [11] for the dielectric coat is the same as that utilized in [7, 9] and [10]. And as pointed out elsewhere [8], the said model has the inherent assumption that the bare conductor is of infinite extent. In addition, the referenced models all have as an

important basis, the further assumption that the electric field in the dielectric coating has only a radial component, which assumption, as noted by Bretones et al. [5], ignores the fact that this field has an axial component whose strength increases with distance away from the conductor/dielectric interface. The quasi-static moment method approach presented in this paper removes these restrictions, and the computational results obtained for broadside radar cross-section and bi-static radar-cross-section for selected examples exhibit characteristics consistent with those reported in literature [5, 6], to indicate that the approach is valid.

2. THEORITICAL ANALYSIS

When a coated thin, perfectly conducting wire of the type illustrated by Fig. 1, is illuminated by a plane electromagnetic wave, its response may be modeled by a conduction current $\mathbf{J}_s$ and a volume polarization current $\mathbf{J}_V$, which then represents two sources radiating in free space to define the scattered field [9].

In the case of the conduction current, the usual thin-wire approximation [9, 12], applies, and the volume equivalence principle specifies the polarization current as

$$\mathbf{J}_V = j\omega\left(\varepsilon_d - \varepsilon_0\right)\mathbf{E}_d, \tag{1}$$

in which $\mathbf{E}_d$ stands for the electric field in the dielectric coating region, and where ε_d denotes the permittivity of the dielectric material. Because $\mathbf{E}_d$ is unknown, so is $\mathbf{J}_V$, and towards providing an approximation for $\mathbf{E}_d$, Chatterjee et al. [11] considered the form of (1) given as:

$$\mathbf{J}_V = \hat{\mathbf{a}}_\rho j k_0 Y_0\left(\varepsilon_r - 1\right)\mathbf{E}_d, \tag{2a}$$

which, for the $e^{-j\omega t}$ time-harmonic variation ($k_0 = \omega\sqrt{\mu_0\varepsilon_0}$; $Y_0 = \sqrt{\varepsilon_0/\mu_0}$), reduces to

$$\mathbf{J}_V = \hat{\mathbf{a}}_\rho j\omega\left(\varepsilon_d - \varepsilon_0\right)\mathbf{E}_\rho; \tag{2b}$$

with the inherent *ab-initio* assumption, that $\mathbf{E}$ has only a radial component. By invoking Mayes' source equivalence principle [11, 15] suggested that the field generated by $\mathbf{J}$ of (2b) is the same as that due to the equivalent magnetic source $\mathbf{M}$, which is given by:

$$\mathbf{M} = \hat{\mathbf{a}}_\phi\left(\varepsilon_r - 1\right)\frac{\partial E_\rho}{\partial z}, \tag{2c}$$

so that from Maxwell's equation (i.e., $E_\rho = -\frac{1}{j\omega\varepsilon_d}\frac{\partial H_\varphi}{\partial z}$), (2c) modifies to

$$\mathbf{M} = -\left(\frac{\varepsilon_r - 1}{j\omega\varepsilon_d}\right)\frac{\partial^2 H_\varphi}{\partial z^2}, \tag{2d}$$

Finally, the polarization current of (1) then admits expression in terms of the filamentary current carried by the bare conductor, when Ampere's circuital law, which states that

$$H_\varphi = \frac{I\left(z\right)}{2\pi\rho}, \tag{3}$$

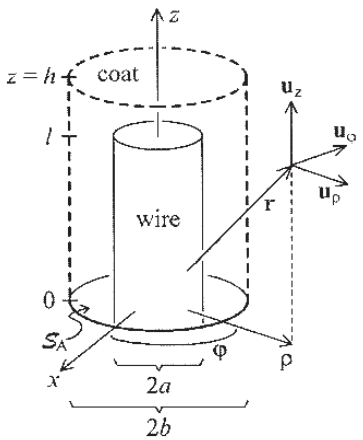

Figure 1: Dielectric coated thin wire.

is introduced in (2d), which then becomes [11],

$$\mathbf{M} = -\left(\frac{\varepsilon_r - 1}{j\omega\varepsilon_d}\right)\frac{1}{2\pi\rho}\frac{\partial^2 I(z)}{\partial z^2} \tag{4}$$

Equation (3) is the same solution provided by Lee and Balmain [10], who then invoked Maxwell's equation to show that the **E** field in (1) is given by:

$$E_\rho = \frac{\left(-\frac{1}{j\omega}\frac{\partial I(z)}{\partial z}\right)}{2\pi\varepsilon_d\rho}, \tag{5}$$

a solution earlier proposed by Richmond and Newman [7]. Adekola et al. [8] pointed out that (3) describes the field of the steady uniformly distributed current $I(z)$ carried by a straight conductor of infinite extent; and that the associated (5) is the field of a uniform line charge ($\sigma(z) = -\frac{1}{j\omega}\nabla\cdot I(z) = -\frac{1}{j\omega}\frac{\partial I(z)}{\partial z}$), also of infinite extent. In order to remove the restrictions inherent in (3) and (5) [8] proposed that a better approximation for **E** of (1) should be

$$\mathbf{E} = \frac{1}{4\pi\varepsilon_d}\int\limits_{wire}\left(\hat{\mathbf{a}}_\rho\frac{\rho\sigma(z')}{(z'^2+\rho^2)^{3/2}} - \hat{\mathbf{a}}_z\frac{z'\sigma(z')}{(z'^2+\rho^2)^{3/2}}\right)dz', \tag{6}$$

where the charge density is of the same finite extent as the thin-wire, and now derives from the conduction current carried by the wire through the equation of continuity. With (6), **J** of (1) becomes a known quantity, provided that $I(z)$ is known. Towards providing a method of moment solution for the problem so posed, it is convenient to replace **J** with the filamentary distribution of current defined as:

$$I_d = \iint\limits_s \mathbf{J}\cdot ds = \iint\limits_s \mathbf{J}\cdot\hat{\mathbf{a}}_\rho\rho d\phi dz + \iint\limits_s \mathbf{J}\cdot\hat{\mathbf{a}}_z\rho d\rho dz \;\hat{=}\; I_{d\rho}(\rho) + I_{ds}(z) \tag{7}$$

so that the model for the coated wire becomes:

$$I_{cw} = (I_{bw}(z) + I_{ds}(z)) + I_{d\rho}(z) \tag{8}$$

and it is the current specified by (8) that is responsible for the scattered field, whose tangential component on the perfectly conducting surface of the bare wire is given by [12],

$$\begin{aligned} -E_z^{sca} &= \frac{j\omega\mu_0}{4\pi}\int\limits_{wire}\left[\left(\hat{\mathbf{a}}_z\cdot\left(\hat{\mathbf{a}}_s'\left(I_{bw}(z') + I_{ds}(z') + \hat{\mathbf{a}}_\rho I_{d\rho}(\rho')\right)\right)\right)\frac{e^{-jkR}}{R}\right] \\ &\quad - \int\limits_{wire}\left(\frac{1}{j4\pi\omega\varepsilon_s}\frac{\partial I_{cw}}{\partial z'}\frac{\partial I_{cw}}{\partial z}\right)\frac{e^{-jkR}}{R}dz' \end{aligned} \tag{9}$$

Next, the conduction current carried by the bare wire is expanded in a series of known functions $T_n(z)$ and unknown coefficients, α_n according to

$$I_{bw} = \sum_{n=1}^{N}\alpha_n T_n(z) \tag{10a}$$

and for each expansion function T_n, we define a corresponding expansion function T_{nd}, as model for the dielectric through the expression given as [8],

$$T_{nd} = \frac{\varepsilon_0 - \varepsilon_d}{2\varepsilon_d}\left(\begin{array}{l} \xi_n\left\{\begin{array}{l}\left(b^2+z_{2n+1}^2\right)^{1/2} - \left(a^2+z_{2n+1}^2\right)^{1/2} \\ -\left(b^2+z_{2n+1}^2\right)^{1/2} - \left(a^2+z_{2n+1}^2\right)^{1/2}\end{array}\right\} \\ + \\ \xi_{n+1}\left\{\begin{array}{l}\left(b^2+z_{2n+3}^2\right)^{1/2} - \left(a^2+z_{2n+3}^2\right)^{1/2} \\ -\left(b^2+z_{2n+1}^2\right)^{1/2} - \left(a^2+z_{2n+1}^2\right)^{1/2}\end{array}\right\}\end{array}\right)\frac{\partial T_n(z)}{\partial z} \tag{10b}$$

with all symbols as defined in [8]. The boundary conditions at the perfectly conducting surface of the bare wire demand that

$$-E_z^{sca} = E_z^{inc} \tag{11}$$

in which E_z^{inc} represents the tangential component of the incident plane electromagnetic wave. By noting that the foregoing analysis indicate that for the coated wire, the choice of expansion functions is such that

$$I_{cwn} = \sum_{n=1}^{N} \alpha_n \left(T_n + T_{nd}\right) \tag{12}$$

we make the choice $T_m + T_{md}$ for the testing (or weighting) functions. Accordingly, the moment method solution [12, 14] for the problem then emerges as the matrix equation given as;

$$(\alpha_n) = \left[Z_{nm} + \Delta Z_{nm}\right]^{-1} (V_n) \tag{13}$$

where ΔZ_{nm} remains as defined in [8], and in which

$$(V_n) = \left\langle E_z^{inc},\ \left(T_n + T_{nd}\right)\right\rangle \tag{14}$$

provided that $\langle\, , \rangle$ denotes inner product as defined elsewhere [9, 12, 14].

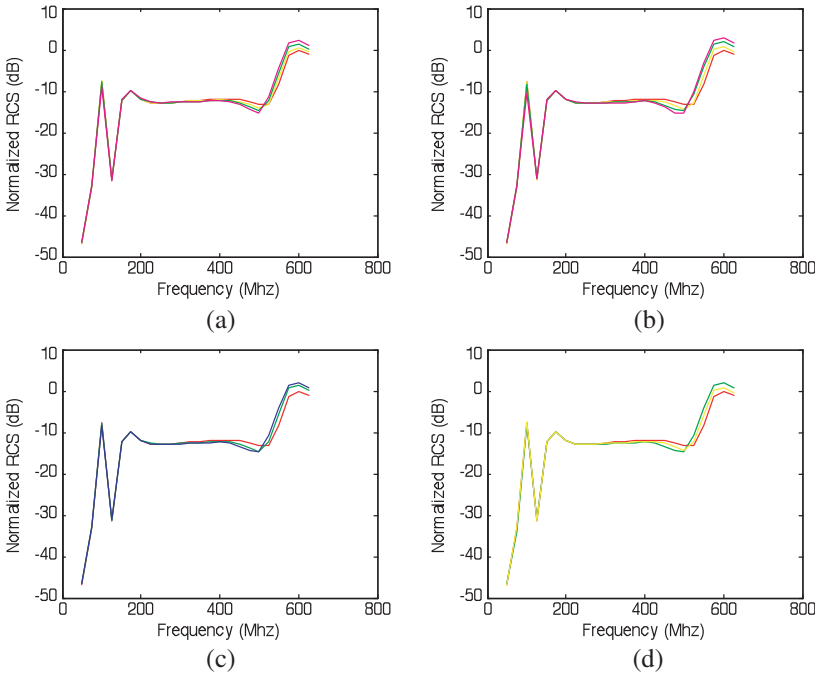

Figure 2: Normalised broadside radar cross-section vs. frequency for a coated thin wire. (a) $\varepsilon_r = 2$; (b) $\varepsilon_r = 5.3$; (c) $b = 2.1$ cm (green $\varepsilon_r = 2$; blue $\varepsilon_r = 5.3$); (d) $b = 2.8$ cm.

3. RESULTS

The FORTRAN computer program developed by Kuo and Strait [14] for use with bare wire scatterers was adapted for the representative computational results described in the ensuing discussions concerning three examples of coated thin-wire scatterers. The first example is the coated thin-wire problem addressed by Bretones et al., who investigated the coated thin-wire's transient response, using a time-domain analysis for a Gaussian travelling wave incidence. Fig. 2 below describes the broadside Radar Cross Section (RCS) for a coated wire of length 1 m and radius 6.67 mm, for various sizes of coating thickness and different values of permittivity, over a frequency range extending from 50 MHz to 600 MHz. And as can be seen from the illustrations, the curves exhibit the increasing shift to the left, with increase in permittivity, described in [5]. In addition, Figs. 2(a) and 2(b) suggest that the same shift to the left increases with increasing coating thickness. In Fig. 2,

red indentifies the curve for the bare wire; and yellow, green and magenta, those for the dielectric coating for coating thicknesses of 1.4 cm, 2.1 cm and 2.8 cm, respectively.

The second example concerns another straight 0.25 m long scatterer, whose radius is 3.175 mm, and for which broadside radar cross-section was computed for values of normalized length in the range $0.4 \leq l/\lambda \leq 0.6$.

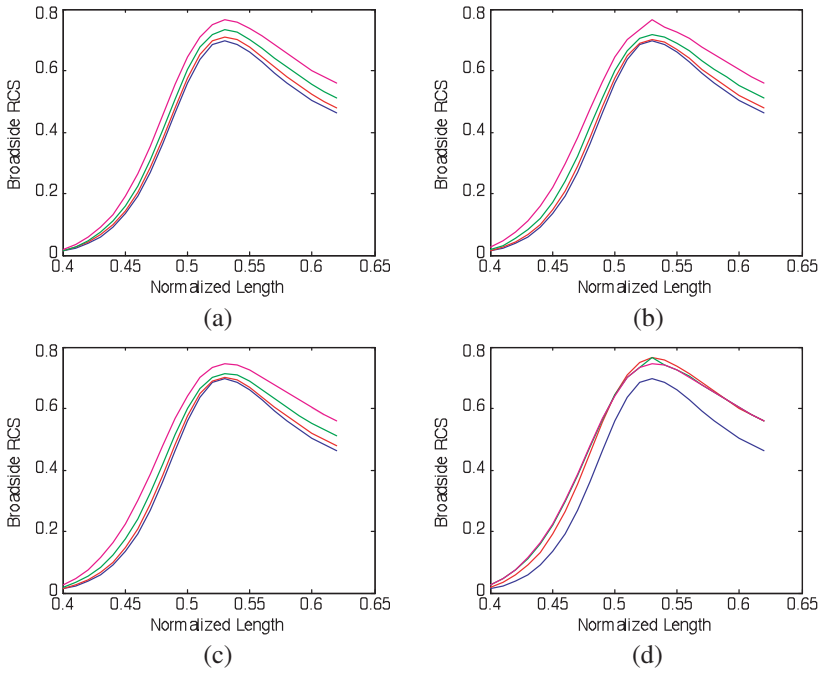

Figure 3: Broadside radar cross-section vs. normalized wire length for a coated thin wire. (a) $\varepsilon_r = 2$; (b) $\varepsilon_r = 5.3$; (c) $\varepsilon_r = 7.2$; (d) $b = 4a$ (red $\varepsilon_r = 2$; green $\varepsilon_r = 5.3$; magenta $\varepsilon_r = 7.2$).

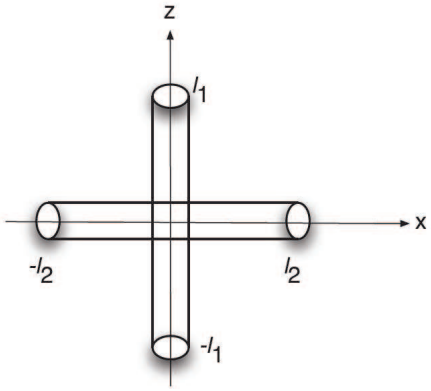

Figure 4: Dielectric coated cross wire scatterer.

The results of the computation are displayed in Fig. 3, from which we find again, that there is an increasing shift of broad-side radar cross-section (BRCS) to the left, as permittivity and thickness of coating increases. In Fig. 3, the blue coloured curves represent the bare wire; and red, green and magenta, curves for the dielectric coating, for thicknesses corresponding to $2a$, $3a$ and $4a$, (a denotes bare wire radius) respectively. One difference between these results and those obtained by Moore and West [6], who addressed a similar problem using a distributed reactive load as model for the coating, is that the curve for the bare wire is tracked by those for the coated wire, as indicated by the curves of Fig. 2, as being the case.

In the third example, computational data were obtained for a dielectric-coated version of the crossed-wire scatterer of Fig. 4, whose scattering characteristics have been described by Taylor et al. [13], and Kuo and Strait [14]. The vertical wire has a total length of 0.33 m (0.75λ) and

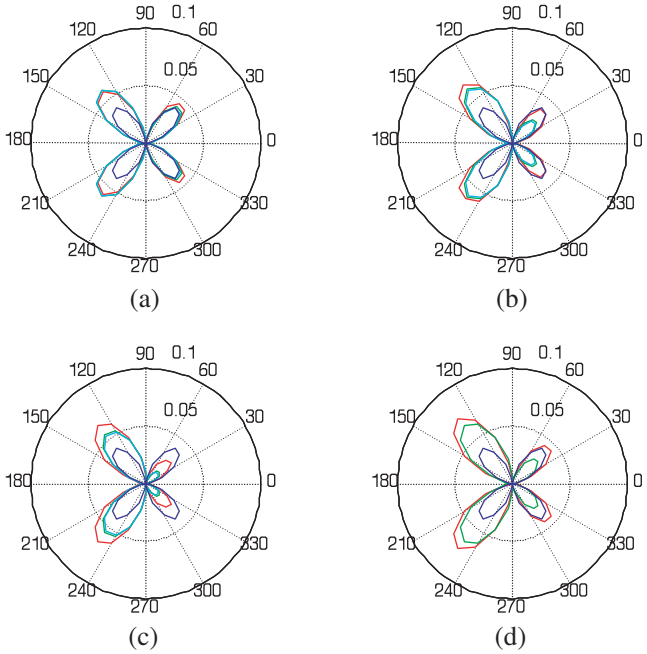

Figure 5: Bi-static radar cross-section, in the $\theta - 90°$ plane for the cross wire. (a) $b = 2a$; (b) $b = 3a$; (c) $b = 4a$; (d) $b = 3a$.

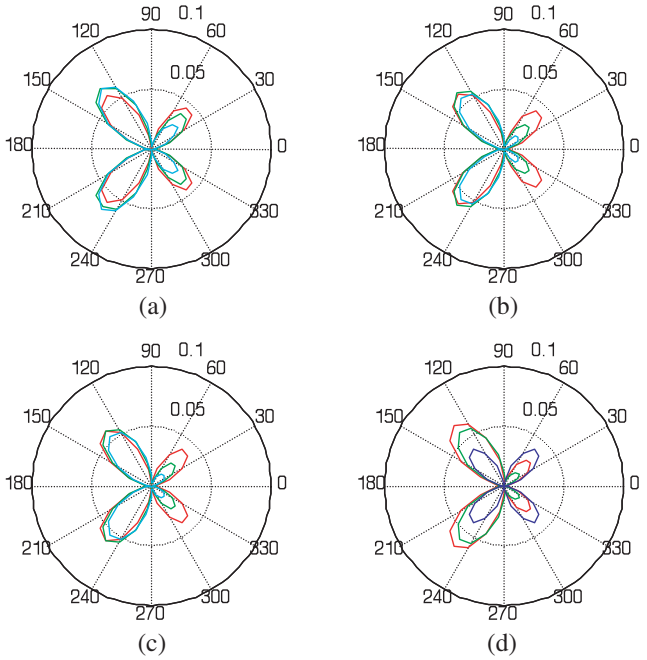

Figure 6: Bi-static radar cross-section in the $\theta - 90°$ plane for the cross wire. (a) $\varepsilon_r = 2.3$; (b) $\varepsilon_r = 5.3$; (c) $\varepsilon_r = 7$; (d) $\varepsilon_r = 5.3 - j0.35$.

a radius of 2.22 mm, and the corresponding values for the horizontal wire are 0.22 m (0.5λ) and 1.11 mm, respectively. The results are displayed in Figs. 5 and 6 for plane wave incidence at $(\theta, \varphi) = (90°, 90°)$, and various sizes of coating thickness and values of permittivity. In Figs. 5(a)–(c) blue represents the bare wire with red, green and cyan representing a dielectric coating having a relative permittivity of 2.3, 5.3 and 7 respectively. In Fig. 5(d), the relative permittivity of the dielectric coating is $2.3 - j0.35$ and $5.3 - j0.35$ respectively shown as red and green in the figure.

It can be seen from Fig. 5, that bistatic radar cross section in the back-scatter direction decreases with increasing values of permittivity, for fixed values of coating thickness; and that in general, the reverse is the case in the forward scatter direction. In the case of Fig. 6, it is readily observed that bistatic radar cross section in the back-scatter also decreases with increasing coating thickness, for

fixed values of permittivity. In Figs. 6(a)–(c), the dielectric coating has a radius of $2a$, $3a$ and $4a$ respectively shown as red, green and cyan. In Fig. 6(d), blue represents the bare wire, while red and green represents the dielectric coating having a radius of $3a$ and $4a$ respectively.

4. CONCLUSION

This concludes our analysis of scattering by perfectly conducting thin-wires, coated with thin layers of dielectric materials. First, the paper established the equivalence between four different approaches earlier reported in literature [7, 9–11], and identified certain restrictions inherently associated with them. In particular, this presentation suggest that the electric field in the dielectric shell has both a radial and an axial component, and then using a quasi-static moment-method approach, eliminated the radial component in subsequent analysis. Computational results obtained for two scattering geometries (a straight thin-wire and crossed thin-wire) very clearly reveal the influence of coating size and dielectric constant, to support claims of validity by the approach.

REFERENCES

1. Uslenghi, P. L. E., "Electromagnetic scattering from radially inhomogeneous media," Technical Report, Prepared for Division of Engineering, National Science Foundation, NSF Grant GK-1408, The University of Michigan, Washington DC, July 1967.
2. Hertel, T. W. and G. S. Smith, "The insulated linear antenna-revisited," *IEEE Transactions on Antennas and Propagation*, Vol. 48, No. 6, 914–920, June 2000.
3. Huddleston, P. L., L. N. Medgyesi-Mitschang, and J. M. Putnam, "Combined field integral equation formulation for scattering by dielectrically coated conducting bodies," *IEEE Transactions on Antennas and Propagation*, Vol. 34, No. 4, 510–520, April 1986.
4. Sebak, A. R. and B. P. Sinha, "Scattering by a conducting spheroidal object with dielectric coating at axial incidence," *IEEE Transactions on Antennas and Propagation*, Vol. 40, No. 3, 268–274, 1992.
5. Bretones, R. A., A. Salinas, M. R. Gomez, and G. I. Sanchez, "Time domain analysis of dielectric coated wire antennas and scatterers," *IEEE Transactions on Antennas Propagation*, Vol. 42, No. 6, 815–819, June 1994.
6. More, J. and M. A. West, "Simplified analysis of coated wire antennas and scatterers," *Proceedings of IEE Microwaves, Antennas and Propagation*, Vol. 142, No. 1, 14–18, 1995.
7. Richmond, J. H. and Ed. H. Newman, "Dielectric coated wire antennas," *Radio Science*, Vol. 11, No. 1, 13–20, 1976.
8. Adekola, A. A., A. I. Mowete, and A. Ogunsola, "On the problem of dielectric coated thin wire antenna," *PIERS Proceedings*, 431–437, Moscow, Russia, August 18–21, 2009.
9. Li, X., K. E. K. Drissi, and F. Paladian, "A Galerkin moment-method for the analysis of insulated wires above a lossy half-space," *Annales des Telecommunications*, Vol. 58, No. 7/8, 1157–1177, 2003.
10. Lee, J. P. Y. and K. G. Balmain, "Wire antennas coated with magnetically and electrically lossy material," *Radio Science*, Vol. 14, No. 3, 437–445, May–June, 1979.
11. Chatterjee, A., J. L. Volakis, and W. J. Kent, "Scattering by a perfectly conducting and a coated thin wire using a physical basis model," *IEEE Transactions on Antenna and Propagation*, Vol. 40, No. 7, 761–769, July 1992.
12. Harrington, R. F., "Matrix methods for field problems," *Proceedings of the IEEE*, Vol. 55, No. 2, 136–149, February 1967.
13. Taylor, C. D., S.-M. Lin, and H. V. McAdams, "Scattering from crossed wires," *IEEE Transactions on Antennas and Propagation*, Vol. 20, No. 6, 133–136, 1970.
14. Kuo, D.-C. and B. J. Strait, "Improved programs for analysis of radiation and scattering by configurations of arbitrarily bent thin wires," *Interaction Notes*, Notes 191, Electrical Engineering Department, Syracuse University, New York, 1970.
15. Mayes, P. E., "The equivalence of electric and magnetic sources," *IEEE Transactions on Antennas and Propagation*, Vol. 6, 295–297, July 1953.

Experimental Investigation on a Radio-on-free-space Optical System Suitable for Provision of Ubiquitous Wireless Services

Mitsuji Matsumoto[1], **Kamugisha Kazaura**[2], **Kazuhiko Wakamori**[3], **Takeshi Higashino**[4], **Kastutoshi Tsukamoto**[4], **and Shozo Komaki**[4]

[1]Graduate School of Global Information and Telecommunication Studies (GITS), Waseda University, Japan
[2]Research Institute for Science and Engineering (RISE), Waseda University, Japan
[3]Global Information and Telecommunication Institute (GITI), Waseda University, Japan
[4]Department of Electrical, Electronic and Information Engineering
Graduate School of Engineering, Osaka University, Japan

Abstract— Recent advancements in microwave and terahertz photonics technologies has led to development of innovative advanced wireless communications systems. One of the emerging promising technologies is Radio-on-Free-Space Optical (RoFSO) system described in this paper. RoFSO is achieved by combining Radio-over-Fiber (RoF) technique and free-space optical (FSO) communication technology using seamless connection of free-space and optical fiber. With this system it is possible to transmit simultaneously multiple RF signals representing different wireless services through free-space using WDM technique. In this paper we describe the design concept of the RoFSO system and highlight the performance evaluation based on the transmission of the various wireless services signals transmitted over it. The results obtained show satisfactory performance and demonstrate potential of the RoFSO system as a suitable platform for provision of ubiquitous wireless services. Moreover the link design of the RoFSO system and application scenario as an ubiquitous network are considered based on the experimental result.

1. INTRODUCTION

Free-space optics (FSO) systems are increasingly being considered as suitable alternative for transmission of optical and RF signals in situation where optical fiber deployment is not feasible. This can made possible by utilizing FSO links designed by taking advantage of the emerging new generation FSO systems [1] and advanced microwave and photonics technologies. We have developed and demonstrated a new Radio on Free-Space Optics (RoFSO) system, capable of simultaneous transmission of multiple RF signals. The RoFSO system is realized by combining new generation FSO system with Radio over Fiber (RoF) technique [2].

In this paper we present an experimental investigation on a RoFSO system suitable for provision of ubiquitous wireless services. The design concept and example of experimental results and analysis of performance evaluation of the RoFSO system when simultaneous transmitting multiple RF signals is given. Based on the system design specifications and operating environment the link margin and applicable operating range is theoretically derived and shown.

2. OUTLINE RoFSO SYSTEM

In recent years, new generation of FSO systems operating in the 1550 nm wavelength band have been developed and demonstrated [1]. In these systems for transmission or reception through free-space no optical-to-electrical or electrical-to-optical (OE/EO) conversions is necessary, unlike conventional systems operating in the 800 nm wavelength band. The optical beam is emitted directly to free-space from the fiber termination point using the FSO transceiver and at the receiving end it is focused directly to the single mode fiber (SMF) core. This configuration, i.e., direct emission and reception of optical signal through the atmosphere, achieves a bandwidth and protocol transparent communication system. It eliminates the necessity of reconfiguring the FSO transceiver even when the nature of the transmitted signals changes [3] therefore making them an attractive candidate for implementing the proposed RoFSO system discussed in this paper.

The RoFSO system is implemented by simply combining a new generation FSO system described above with Radio-over-Fiber (RoF) technology. RoF is a technique of modulating RF subcarriers onto an optical carrier for distribution over fiber network. For transmission through the atmosphere in the RoFSO system configuration direct optical amplification and emission of RoF signal into free-space is utilized [2] realizing a flexible wireless system capable of simultaneous transmitting multiple RF signals representing various wireless services.

However, RoFSO technology has several demerits which include high dependence on weather conditions (rain, snow, fog, dust particles etc) which can severely affect the performance of the links. They are also susceptible to atmospheric effects like scintillation and beam wander. Research on FSO systems is focused on developing robust techniques for atmospheric turbulence suppression especially in new generation FSO systems in which the optical signal is transparently transmitted and received through free-space without undergoing any opto/electical conversion in the transceivers.

3. EXPERIMENTAL RESULTS

Figure 1 shows a schematic of the experimental setup to evaluate the performance of the RoFSO system when simultaneously transmitting multiple RF signals consisting of ISDB-T, W-CDMA and WLAN signals. In the experimental setup, at one site (Site A) signal generators for producing the various RF based wireless service signals under investigation are placed and at a second site (Site B) signal analyzers and other measurement devices and equipment are situated. The RoFSO system consists of an optical interface unit (Optical IF unit) and a RF interface unit (RF IF unit). The optical interface unit consists of a wavelength multiplex and de-multiplex device, boost and post amplifier and an optical circulator to separate transmit and receive signals. The RF interface unit consists of RoF modules responsible for electro/optical signal conversion corresponding to each wireless service RF signal under investigation. The system specifications are given in Table 1.

The RF test signals (ISDB-T, W-CDMA and WLAN) are independently produced using signal generators (SG). The signals are generated at −20 dBm fed into designated RoF modules in the RF IF unit which have an optical modulation index (OMI) of 10%. The optical signals from the RoF

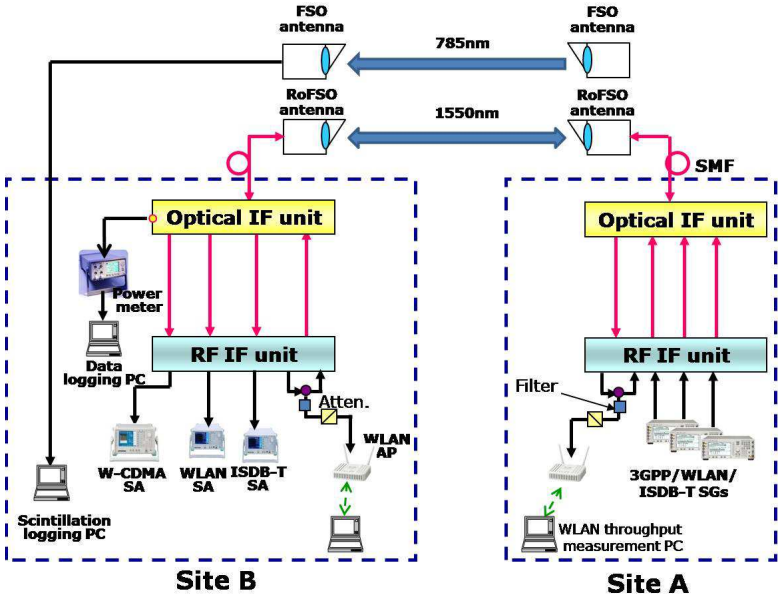

Figure 1: Experimental system setup.

Table 1: Specification of the RoFSO antenna.

Parameter	Specification
Operating wavelength	1550 nm
Transmit power	100 mW(20 dBm)
Antenna aperture	80 mm
Coupling losses	5 dB
Beam divergence	±47.3 µrad
Fiber coupling technique	Direct coupling using FPM
Frequency range of operation	more than 5 GHz
Tracking method	Automatic using QPD (Rough: 850 nm beacon, Fine: 1550 nm)

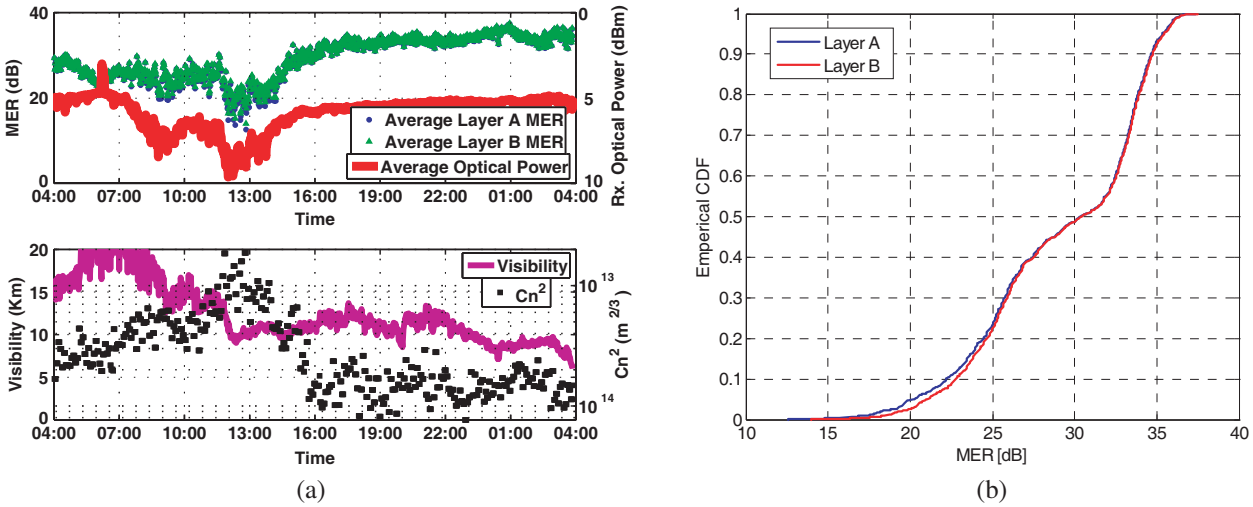

Figure 2: ISDB-T signal transmission (a) MER and received optical power and (b) CDF of ISDB-T(MER).

modules are then fed to the Optical IF unit, multiplexed then boosted by a 100 mW EDFA and subsequently sent to the rooftop via optical fiber cables for transmission through free-space using the RoFSO antenna. At the receiver side corresponding signal analyzers (SA) are used to measure the quality of the different RF signals.

3.1. ISDB-T signal Transmission

To evaluate the transmission characteristics of the ISDB-T signal transmission using the RoFSO system a modulation error ratio (MER) quality metric parameter is used. Figure 2 shows the measured ISDB-T MER characteristics. Figure 2(a) top shows the MER for both Layer A and Layer B together with the mean received optical power for a continuous 24 hour period. The measured MER and received optical power can be correlated with the atmospheric turbulence strength characterized by C_n^2 shown in Figure 2(a) below.

The ARIB STD-B21 standard specifies the minimum required CNR for Layer A and Layer B at the receiver should be 11.5 dB and 22 dB respectively. Ideally, the MER and CNR values should be roughly equivalent but in normal systems, MER is slightly lower than CNR. The MER values for Layer A and Layer B in Figure 2(a) top are consistently above 25 dB which shows good performance for the system. The MER values fall below this value around midday, a time characterized with increased atmospheric turbulence as shown in Figure 2(a) below. Figure 2(b) shows the CDF of the mean MER accumulated over a 24 hour period. From the CDF figure, for the case of Layer A 100% of the values are above the specified threshold of 11.5 dB and for the case of Layer B at least 95% of the measured values are above the required threshold of 22 dB. These results demonstrate consistent performance of the system.

3.2. W-CDMA Signal Transmission

In W-CDMA system, the downlink signal transmitted by the base station is designed to fulfill the specifications defined in the 3GPP standard. The spectral properties of the signal are measured by the Adjacent Channel Leakage Power Ratio (ACLR). The standard requires the ACLR to be better than 45 dB at 5 MHz offset and 50 dB at 10 MHz offset. Figure 3(a) shows an example of the received W-CDMA signal ACLR measurement made over a continuous 24 hour period. A stable optical received power consistently above −10 dBm is recorded and the measured ACLR variation can be closely correlated with the variations of the optical received power. The recorded values for ACLR at the −5 MHz offset satisfy the specification provided in the 3GPP standard i.e., better that 45 dB. Unfortunately, at the −10 MHz offset the ACLR values are below the required 50 dB threshold. This is due to the background noise caused by the boost amplifier resulting in inadequate degree of modulation of the 2 GHz W-CDMA RoF module currently used leading to insufficient SNR. This can be corrected by using an appropriately designed 2 GHz W-CDMA RoF module with optimum input power level and less background noise. Figure 3(b) shows the CDF of the mean ACLR at the −5 MHz offset accumulated over a 1 month period. More than 94% of the values are above the specified threshold of 45 dB.

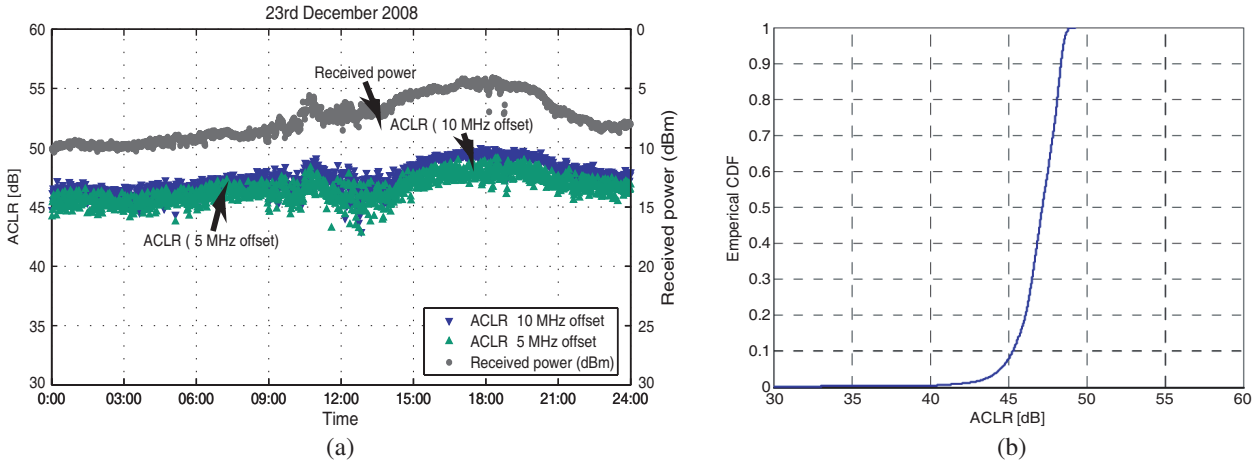

Figure 3: W-CDMA signal transmission (a) ACLR and received optical power and (b) CDF of ACLR at −5 MHz offset.

4. RoFSO LINK DESIGN ANALYSIS

The RoFSO system should be designed to operate in an environment characterized with atmospheric turbulence effects. Therefore a power margin is necessary to compensate for the following losses: (a) fading loss as a result of power fluctuations at the receiver due to random change of refractive index on the transmission path; (b) coupling loss at the receiver terminal when the receiving light is coupled directly into a SMF; (c) geometrical loss due to broadening of the laser beam when propagating in free-space and (d) the attenuation loss in the atmosphere.

The fading loss is due to the fluctuations of received optical power because of random change of refractive index on the transmission path and calculated by [4],

$$a_{scin} = 4.343 \left\{ erf^{-1}\left(2p_{thr} - 1\right) \cdot \left[2\ln\left(\sigma_p^2 + 1\right)\right]^{1/2} - \frac{1}{2}\ln\left(\sigma_p^2 + 1\right) \right\} \tag{1}$$

with p_{thr} is the probability of outage time, erf^{-1} is inverse error function and σ_p^2 is power scintillation index and calculated by [5],

$$\sigma_p^2\left(D_{RX}, L\right) = \exp\left[\frac{0.49\sigma_R^2}{\left(1 + 0.65d^2 + 1.11\sigma_R^{12/5}\right)^{7/6}} + \frac{0.51\sigma_R^2\left(1 + 0.69\sigma_R^{12/5}\right)^{-5/6}}{\left(1 + 0.9d^2 + 0.62d^2\sigma_R^{12/5}\right)^{7/6}} \right] - 1 \tag{2}$$

where $\sigma_R^2 = 1.23k^{7/6}L^{11/6}C_n^2$ is the Rytov variance parameter and $d = (kD_{RX}^2/4L)^{1/2}$ is the ratio of the aperture radius to the Fresnel zone size, D_{RX} is receiver aperture diameter, and L is link distance.

In the RoFSO system the received optical beam is focused directly into a SMF. However, the propagation through atmospheric turbulence degrades significantly the spatial coherence of a laser beam and limits the fiber-coupling efficiency. The coupling efficiency for a laser light distorted by atmospheric turbulence in a system without using any fine tracking scheme can be estimated by [6],

$$\eta = 8a^2 \int_0^1 \int_0^1 \exp\left[-\left(a^2 + \frac{A_R}{A_C}\right)\left(x_1^2 + x_2^2\right)\right] I_0\left(2\frac{A_R}{A_C}x_1x_2\right) x_1x_2dx_1dx_2 \tag{3}$$

where a and A_R/A_C represent the coupling geometry and number of speckles respectively, $A_R = \pi D2/4$, $A_C = \pi\rho_c^2$ is the spatial coherence area of the incident plane wave also called its speckle size with $\rho_c = \left(1.46C_n^2k^2L\right)^{-3/5}$ is spatial coherence diameter. I_0 is the modified Bessel function of the first kind and zero order.

In practice, the efficiency or compensation gain factor of the tracking system is significantly dependent on the tracking technology. The tracking scheme utilizing a fine pointing mirror (FPM)

and quadrant detectors (QDs) for the RoFSO system we have developed has demonstrated stable connection over 1-km transmission with a compensation gain of about 10 dB under moderate to strong turbulence condition.

The geometrical loss depends on the transmission distance, beam divergence angle and the diameters of the transmitter and receiver optics and is given as,

$$L_{geo} = 10 \log 10 \left(\frac{D_{RX}}{D_{TX} + L \cdot \theta} \right) \tag{4}$$

The link margin is also to compensate for the attenuation loss when the laser beam propagates over the in the atmosphere. Since it produces according to various factors, such as dispersion and absorption, generally attenuation, τ, is expressed using visibility as [7],

$$\tau(L) = \frac{P(L)}{P(0)} e^{-\alpha L} \tag{5}$$

$$\alpha = \frac{3.91}{V} \left(\frac{\lambda}{550\,\text{nm}} \right)^{-q} \tag{6}$$

We can derive this attenuation into decibels (dB) as,

$$Att_v = -10 \cdot \log 10 \left(e^{-\alpha L} \right) = 17 \frac{L}{V} \left(\frac{550}{\lambda} \right)^{q} \tag{7}$$

where V is visibility (km) and q is the size distribution of the scattering particles described by, q = (1.6 for $V > 50$, 1.3 for $6 < V < 50$, $V0.16 + 0.34$ for $1 < V < 6$, $V - 0.5$ for $0.5 < V < 1$, 0 for $V < 0.5$). The average value of visibility in clear weather in presence of atmospheric turbulence can be can be assumed to be 10 km.

The relation of link margin and applicable link range for a RoFSO system to operate in a strong turbulence characterized with C_n^2 of 2×10^{-13} ($\text{m}^{-2/3}$) derived using the above mathematical expressions is depicted in Figure 4. The link margin is considered as a sum of atmospheric scintillation loss Eq. (2), coupling loss Eq. (3), geometrical loss Eq. (4), the attenuation loss Eq. (7) and considering a coupling compensation gain of 10 dB. The basic parameters used in numerical analysis are shown in Table I and a probability of outage time p_{thr} of 1e-5 is considered. A value of 0.1% or less is used in Eq. (7) reflecting the cumulative distribution probability of visibility in the Tokyo area.

It can be observed that for the system to operate over a distance of 1 km under strong atmospheric turbulence, the necessary link margin should be more than 21 dB. For shorter distance communication there shall be no coupling loss because of the 10 dB coupling compensation gain the RoFSO system has.

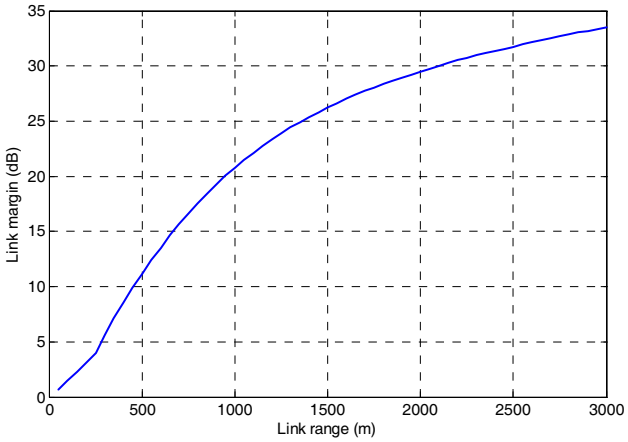

Figure 4: Applicable link range and link margin.

5. CONCLUSION

The design concept and performance characteristics of a RoFSO system capable of simultaneous transmission of multiple RF signals using WDM technology has been demonstrated. Example of transmission of ISDB-T and W-CDMA signals using the RoFSO system has been presented and satisfactory performance demonstrated. From numerical analysis the theoretical link margin of the system has been derived. For the system to operate for a distance beyond 1 km, a link margin of 21 dB will be required. The results obtained show satisfactory performance and demonstrate potential of the RoFSO system as a suitable platform for provision of ubiquitous wireless services.

This work was supported by a grant from the National Institute of Information and Communications Technology (NICT) of Japan.

REFERENCES

1. Kazaura, K., et al., "Performance evaluation of next generation free-space optical communication system," *IEICE Transactions on Electronics*, Vol. E90-C, 381–388, February 2007.
2. Tsukamoto, K., et al., "Development of DWDM radio on free space optic link system for ubiquitous wireless," *Proceedings of Asia-Pacific Microwave Photonics Conference*, April 2007.
3. Aburakawa, Y. and T. Otsu, "Dense wavelength division multiplexed optical wireless link towards terabit transmission," *Proceedings of Microwave Photonics 2003*, 135–138, September 2003.
4. Giggenbach, D. and H. Henniger, "Fading-loss assessment in atmospheric free-space optical communication links with on-off keying," *Optical Engineering*, Vol. 47, 046001, April 2008.
5. Andrews, L. C. and R. L. Phillips, *Laser Beam Propagation through Random Media*, 1st Edition, SPIE-International Society for Optical Engineering, 1998.
6. Dikmelik, Y. and F.M. Davidson, "Fiber-coupling efficiency for free-space optical communication through atmospheric turbulence," *Applied Optics*, Vol. 44, 4946–4952, 2005.
7. Kim, I. I., et al., "Wireless optical transmission of fast ethernet, FDDI, ATM, and ESCON protocol data using the TerraLink laser communication system," *Optical Engineering*, Vol. 37, 3143–3155, December 1998.

Stimulated Terahertz Emission from Optically Pumped Epitaxial Graphene-on-Si Heterostructures

T. Otsuji[1,3], **H. Karasawa**[1], **T. Komori**[1], **T. Watanabe**[1],
M. Suemitsu[1,3], **A. Satou**[2,3], **and V. Ryzhii**[2,3]

[1]Research Institute of Electrical Communication, Tohoku University, Sendai 9808577, Japan
[2]Computational Nano-Electronics Laboratory, University of Aizu, Japan
[3]JST-CREST, Tokyo 1020075, Japan

Abstract— We experimentally observed the fast relaxation and relatively slow recombination dynamics of photogenerated electrons/holes in an epitaxial graphene heterostructure. The result is interpreted as an amplified stimulated THz emission and well supports the occurrence of negative dynamic conductivity in far-infrared and terahertz spectral ranges.

1. INTRODUCTION

Graphene is a single-layer carbon-atomic honeycomb lattice crystal. Electrons and holes in graphene hold a linear dispersion relation with zero bandgap, resulting in peculiar features like negative-dynamic conductivity in far infrared and terahertz (THz) spectral ranges in optical pumping [1, 2]. Considering the negative-dynamic conductivity, a very fast relaxation of the optical phonon emission and relatively slow recombination, the population inversion can be achieved. This effect can be used the graphene-based coherent source of THz radiation. In this paper, we'll show the theory and experimental results of THz coherent emission from optically pumped epitaxial graphene heterostructures.

2. THEORITICAL MODEL

When graphene is pumped with the photon energy $\hbar\Omega$, electrons and holes are photogenerated via interband transitions. Due to a very short time of the optical phonon emission $\tau_0 \approx 10^{-12}$ s, the photogeneration of electrons and holes leads to the emission of a cascade of optical phonons, so that the photoelectrons and photoholes occupy the state with the energies close to $\varepsilon_N \approx \hbar(\Omega/2 - N\omega_0) < \hbar\omega_0$, where $\hbar\omega_0$ the optical phonon energy and N the number of emitted optical phonons. As a consequence, photoelectrons/holes recombine to radiate THz photons with the energy $\hbar\omega \approx 2\varepsilon_N$ as shown in Fig. 1 [2]. The incident photon spectra will reflect on the THz photoemission spectra as a proof of occurrence of such a process.

The electron and hole distribution functions at the Dirac point $f_e(0) = f_h(0) = 1/2$. This implies that at even weak photoexcitation, the values of the distribution functions at low energies ε can be $f_e(\varepsilon) = f_h(\varepsilon) > 1/2$, that corresponds to the population inversion [2]. Such a population inversion might lead to the negative *ac* conductivity at relatively low frequencies of THz associated with the interband transitions. However, the interband processes determined the Drude conductivity provide the positive contribution to the *ac* conductivity. One might expect that under sufficiently strong optical excitation resulting in photogeneration of electron-hole pairs, total *ac* conductivity becomes "*negative*".

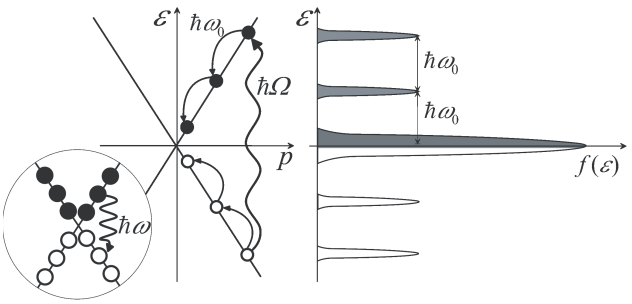

Figure 1: Schematics of carrier relaxation/recombination processes (left) and carrier distributions (right) under pumping with photon energy $\hbar\Omega$. $\hbar\omega_0$: optical phonon energy, $\hbar\omega$: radiative recombination energy [2].

The real part of the net *ac* conductivity $\mathrm{Re}\sigma_\omega$ is proportional to the absorption of photons with frequency ω and comprises the contributions of both interband and intraband transitions [2],

$$\mathrm{Re}\sigma_\omega = \mathrm{Re}\sigma_\omega^{inter} + \mathrm{Re}\sigma_\omega^{intra}. \tag{1}$$

Let us assume a relatively weak optical excitation: $\varepsilon_F < k_BT$, where ε_F the non-equilibrium quasi-Fermi energy and k_BT the thermal energy. In this case, for the THz frequencies $\omega < 2k_BT/\hbar$, $\mathrm{Re}\sigma_\omega^{inter}$ can be presented as

$$\mathrm{Re}\sigma_\omega^{inter} = \frac{e^2}{4\hbar}\left[1 - f_e\left(\frac{\hbar\omega}{2}\right) - f_h\left(\frac{\hbar\omega}{2}\right)\right] \simeq \frac{e^2}{8\hbar}\left(\frac{\hbar\omega}{2k_BT} - \eta_F\right), \tag{2}$$

where e the elementary charge, $\eta_F \equiv \varepsilon_F/k_BT$ the normalized quasi-Fermi energy [2]. On the other hand, $\mathrm{Re}\sigma_\omega^{intra}$ can be presented as

$$\mathrm{Re}\sigma_\omega^{intra} \simeq \frac{(\ln 2 + \eta_F/2)e^2}{\pi\hbar}\frac{T\tau}{\hbar(1+\omega^2\tau^2)}, \tag{3}$$

where τ the momentum relaxation time of electrons/holes [2]. Since η_F corresponds to the ratio of the excess electron/hole concentration δn (equivalent to photoelectron/photohole concentration) to the thermally equilibrium electron/hole concentration n_0, η_F is given by

$$\eta_F = \frac{\delta n}{n_0} = \frac{\tau_R\alpha_\Omega I_\Omega}{n_0} \approx \frac{12e^2}{\hbar c}\left(\frac{\hbar v_F}{k_BT}\right)^2\frac{\tau_R I_\Omega}{\hbar\Omega}, \tag{4}$$

where τ_R electron/hole recombination time, α_Ω the interband absorption coefficient, I_Ω the pumping intensity, c the speed of light, v_F the Fermi velocity [2]. As a consequence, $\mathrm{Re}\sigma_\omega$ becomes

$$\begin{aligned}\mathrm{Re}\sigma_\omega &\simeq \frac{e^2}{8\hbar}\left[\frac{\hbar\omega}{2k_BT} + \frac{8\ln 2}{\pi}\frac{k_BT\tau}{\hbar(1+\omega^2\tau^2)} - \frac{12e^2}{\hbar c}\left(\frac{\hbar v_F}{k_BT}\right)^2\frac{\tau_R I_\Omega}{\hbar\Omega}\right] \\ &\simeq \frac{e^2\bar{g}}{8\hbar}\left[1 + \frac{3}{2}\left(\frac{\omega-\bar{\omega}}{\bar{\omega}}\right)^2 - \frac{I_\Omega}{\overline{I_\Omega}}\right],\end{aligned} \tag{5}$$

where

$$\bar{\omega} \simeq \left(\frac{k_BT\tau}{\hbar}\right)^{2/3}\frac{1.5}{\tau}, \quad \overline{I_\Omega} \simeq 11\left(\frac{\hbar}{k_BT\tau}\right)^{1/3}\left(\frac{k_BT}{\hbar v_F}\right)^2\frac{\hbar\Omega}{\tau_R}. \tag{6}$$

When the pumping intensity exceeds the threshold: $I_\Omega > \overline{I_\Omega}$, $\mathrm{Re}\sigma_\omega$ becomes negative in a certain range around $\bar{\omega}$. When $T = 300\,\mathrm{K}$, $\tau = 10^{-12}\,\mathrm{s}, \tau_R = 10^{-11} \sim 10^{-9}\,\mathrm{s}$, $\bar{I}_\Omega \approx 6000 \sim 60\,\mathrm{W/cm^2}$. Assuming the device size of $(100\times100)\,\mu\mathrm{m}^2$, we find that the required pumping intensity, which provides the negative dynamic conductivity, $\bar{I}_\Omega \approx 600 \sim 6\,\mathrm{mW}$.

Figure 2 plots the calculated $\mathrm{Re}\sigma_\omega$ for various pumping intensities when $T = 300\,\mathrm{K}$, $\tau = 10^{-12}\,\mathrm{s}$, and $\tau_R = 10^{-9}\mathrm{s}$. The vertical scale is normalized to the characteristic conductivity $e^2/2\hbar$. It is clearly seen that the frequency range where the conductivity becomes negative widens with pumping intensity.

3. EXPERIMENTAL

We observed the carrier relaxation and recombination dynamics in optically pumped epitaxial graphene hetero-structures using THz emission spectroscopy [3]. An ultra-thin graphene layer was grown by the thermal decomposition of an 80-nm-thick 3C-SiC film heteroepitaxially grown on a B-doped Si(110) substrate [4]. Its 2D-band Raman spectra, as shown in Fig. 3, proven the existence of monolayer and bilayer of graphene, and the G-band spectra at $1595\,\mathrm{cm^{-1}}$ corresponds to the optical phonon energy of 198 meV [5].

The experimental setup and the scheme of coherent emission from the GOS sample by an optical-pump/THz-probe technique is shown in Fig. 4. A 1550-nm, 20-MHz, 80-fs pulsed fiber laser beam (Fig. 5) was impinged to the sample (normal to the surface). Its frequency spectra exhibit non-exponentially bumped big side-lobes apart from the main-lobe (Fig. 5). The pumping

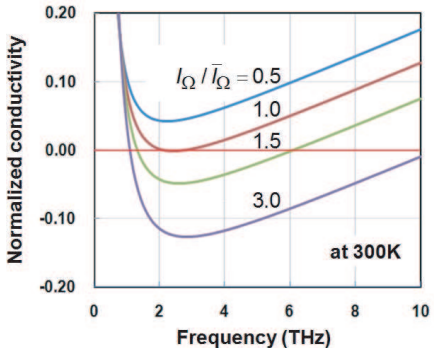

Figure 2: Calculated *ac* conductivity for various pumping intensities at 300 K. The vertical scale is normalized to the characteristic conductivity $e^2/2\hbar$.

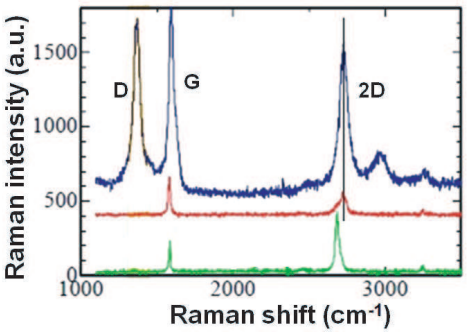

Figure 3: Raman spectra from our sample (top), graphite (middle), and mechanically exfoliated few-layer graphene (bottom).

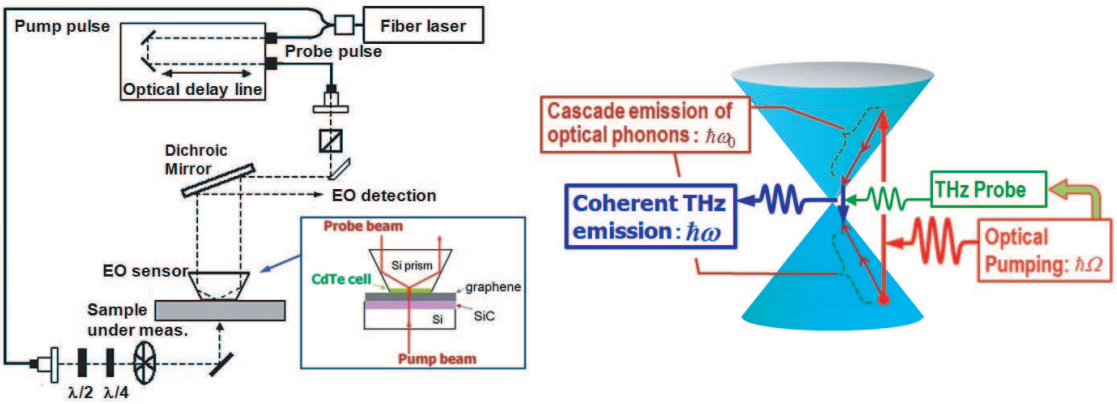

Figure 4: Experimental setup (left) and the scheme of coherent emission from graphene by an optical-pump/THz-probe technique (right). Time-resolved electric field intensity is electroopticaly sampled by the probe beam throughout the CdTe sensor crystal in total reflection geometry. The CdTe also works as a THz probe beam source.

intensity was optimized to satisfy the above-mentioned weak-excitation condition by defocusing the beam. Time-resolved electric-field intensity originated from the THz photon emission was electroopticaly sampled by a CdTe crystal placed on the sample in total-reflection geometry as shown in Fig. 4 [6]. Measured temporal profile (inset in Fig. 6) exhibited frequency-up/down chirped relaxation oscillation, and was damped in an exponential decay on the order of $\lesssim 10$ ps corresponding to the relaxation of radiative electron-hole recombination. Its Fourier spectrum roughly traces the pumping photon spectrum (Fig. 6) [3]. The spectral drop below 2 THz in the lower side-lobe might be caused by the band-gap opening due to existing bilayer graphene with the built-in vertical potential slope arisen at the heterointerface.

The coherent THz emission obtained in this experiment is expected as a result of stimulated THz emission due to the negative dynamic conductivity caused by the pumping photon radiation. The question arisen at this moment is "what stimulates the emission?" Since the phase information of pumping photons cannot be preserved throughout the photocarrier relaxation/recombination processes, it is interpreted that the THz emission from graphene is stimulated by the coherent THz probe radiation originated from the phonon-polariton and/or optical rectification in CdTe excited by the pump laser beam as shown in Fig. 4 (left). Further investigation is needed to obtain a clear evidence of the amplified stimulated THz emission from graphene. Nevertheless, graphene is a unique, potential material that can realize a new type of THz lasers. Study on the real laser cavity structures and lasing conditions has also been progressed [7, 8].

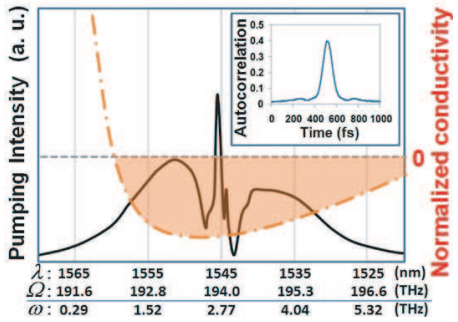

Figure 5: Profile of the pumping laser beam and possible conductivity.

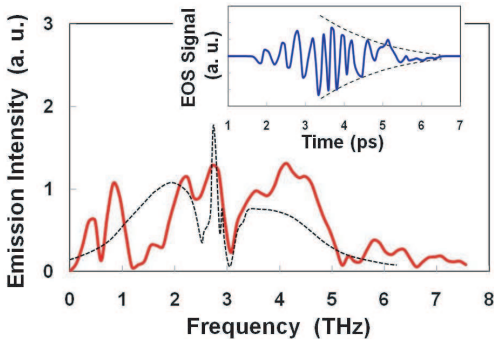

Figure 6: Observed temporal response (inset) and its Fourier spectrum.

4. CONCLUSIONS

We experimentally observed the coherent THz emission reflecting the fast relaxation and relatively slow recombination dynamics of photogenerated electrons/holes in an epitaxial graphene heterostructure. The result supports the occurrence of negative dynamic conductivity leading to the population inversion for a new type of THz lasers.

ACKNOWLEDGMENT

This work is financially supported in part by JST-CREST, Japan, and JSPS-BR(S), Japan.

REFERENCES

1. Geim, A. K. and K. S. Novoselov, "The rise of graphene," *Nat. Mat.*, Vol. 6, 183191, 2007.
2. Ryzhii, V., M. Ryzhii, and T. Otsuji, "Negative dynamic conductivity of graphene with optical pumping," *J. Appl. Phys.*, Vol. 101, No. 7, 083114-1-4, 2007.
3. Karasawa, H., T. Komori, T. Watanabe, M. Suemitsu, V. Ryzhii, and T. Otsuji, "Observation of carrier relaxation and recombination dynamics in optically pumped epitaxial graphene heterostructures using terahertz emission spectroscopy," *Tech. Dig. CLEO-Europe*, Munich, Germany, CF8.3, June 19, 2009.
4. Suemitsu, M., Y. Miyamoto, H. Handa, and A. Konno, "Graphene formation on a 3C-SiC(111) thin film grown on Si(110) substrate," *e-J. Surface Sci. Nanotech.*, Vol. 7, 311–313, 2009.
5. Miyamoto, Y., H. Handa, E. Saito, A. Konno, Y. Narita, M. Suemitsu, H. Fukidome, T. Ito, K. Yasui, H. Nakazawa, and T. Endo, "Raman-scattering spectroscopy of epitaxial graphene formed on SiC film on Si substrate," *e-J. Surface Sci. Nanotech.*, Vol. 7, 107–109, 2009.
6. Otsuji, T., Y. M. Meziani, M. Hanabe, T. Nishimura, and E. Sano, "Emission of terahertz radiation from InGaP/InGaAs/GaAs grating-bicoupled plasmon-resonant emitter," *Solid State Electron.*, Vol. 51, No. 10, 1319–1327, 2007.
7. Dubinov, A. A., V. Y. Aleshkin, M. Ryzhii, T. Otsuji, and V. Ryzhii, "Terahertz laser with optically pumped graphene layers and Fabri-Perot resonator," *Appl. Phys. Express*, Vol. 2, No. 9, 092301-1-3, 2009.
8. Ryzhii, V., M. Ryzhii, A. Satou, T. Otsuji, A. A. Dubinov, and V. Y. Aleshkin, "Feasibility of terahertz lasing in optically pumped epitaxial multiple graphene layer structures," *J. Appl. Phys.*, Vol. 106, No. 8, 084507-1-6, 2009.

Analysis of Optical Coupling for SOI Waveguides

Hirohito Yamada
Department of Electrical and Communication Engineering
Graduate School of Engineering, Tohoku University, Japan

Abstract— Optical coupling loss and alignment tolerance between SOI waveguides and laser diodes were investigated. It was found that the minimum optical coupling loss was about 1.6 dB and alignment tolerance was about ±0.7 μm. An optical input/output interface for optical fibers was also proposed and investigated the coupling loss characteristics.

1. INTRODUCTION

Photonic integrated circuits (ICs) based on silicon-on-insulator (SOI) waveguides are attractive for applying future ultra-high speed optical networks or ultra-high speed data communications in clustering computers. Thus far, various optical device functions have been demonstrated on the SOI waveguides [1–6]. Those devices can be extremely small compared with silica based waveguide devices because sharp bend is possible for the SOI waveguides [7, 8] and the crosssection of the waveguide is extremely small. Furthermore, integration with electronic circuits is also possible because those optical devices are fabricated with conventional CMOS fabrication process which makes electronic circuits. Monolithic integration of photonic circuits and electronic circuits eliminates wiring between photonic IC chips and electronic IC chips, and it makes possible ultra-high speed signal processing.

However, there are few reports for integrating light sources on the SOI waveguides. Integration of laser diodes (LDs) or photo diodes (PDs) with passive optical components on the same chip is essential for realizing compact and low-cost photonic ICs. LDs or PDs are made of compound semiconductors, and it makes difficult to integrate them with SOI waveguide devices on the same chip.

There are several approaches to integrate light sources on the SOI wafer. As practical methods, thermal bonding [9] or BenzoCycloButene (BCB) bonding [10] of compound semiconductor wafers and Si substrates with optical waveguides is studied. However, sufficient operation properties for practical use in actual systems have not yet been obtained.

Optical input/output (I/O) interface for optical fiber or external optical components is also required for the photonic ICs. Thus far, in-plane coupling type I/O with beam spot-size-converters (SSC) [11] and vertical coupling type I/O with grating coupler [12] were demonstrated for the SOI waveguides However, there are still difficulties to practical use of them. For example, optical fibers must be tilted to obtain high optical coupling efficiency for the grating coupler type interfaces, and it makes complex for the structure of optical connectors.

Based on these backgrounds, we studied a method for integrating LD chips on the waveguides and analyze optical coupling loss between the waveguides and LDs. We also proposed an optical I/O interface for single mode optical fibers (SMFs), and investigated the coupling efficiency.

2. INTEGRATION OF LDS ON SOI WAVEGUIDES

Our studied method is mounting LDs with flip-chip bonding on the SOI substrate as shown in Fig. 1. Light output from LDs is butt-joint coupled to the optical waveguides with spot-size converters. The alignment accuracy of commercially available flip-chip bonders is about ±1 μm. Therefore, more than 1 μm of alignment tolerance for optical coupling is required. We investigated the alignment tolerance for the optical coupling between conventional LDs and Si photonic-wire waveguides with horizontal taper type beam SSCs.

Figure 2 shows a schematic view of the SSC. BPM method was used for calculating the coupling loss for the SSC. In the analysis, total coupling loss is comprised of three loss factors; i.e., mode conversion loss in SSC, mode-mismatch between beam spot-size of LD light output and mode profile in the SSC, and reflection loss at the end facet of the SSC. Taking into account these loss factors, we calculated the coupling loss.

Figure 3 shows calculated coupling loss as a function of misalignment in x-direction (a) and y-direction (b). The coupling losses were calculated for the different W values from 2 μm to 5 μm. It is found that minimum 1.6 dB of coupling loss can be achieved provided that both end facets

of LD and SSC contact each other without air gap. We also found that the alignment tolerance for maintaining less than 3 dB optical coupling loss is about ± 0.7 μm when the SiO_x layer width is around $2 \sim 3$ μm.

We measured optical coupling loss between Si photonic-wire waveguides and LDs to verify the analytical results. First, we put an LD chip on an x-y-z moving stage in order to measure the optical coupling loss and the alignment tolerance for x and y directions. Fig. 4 shows measured coupling losses normalized at just aligned position for x-direction (a) and y-direction (b). If we assume the distance between the end facet of LD chip and the SSC was $10 \sim 15$ μm, the measurement results is in good agreement with the calculation.

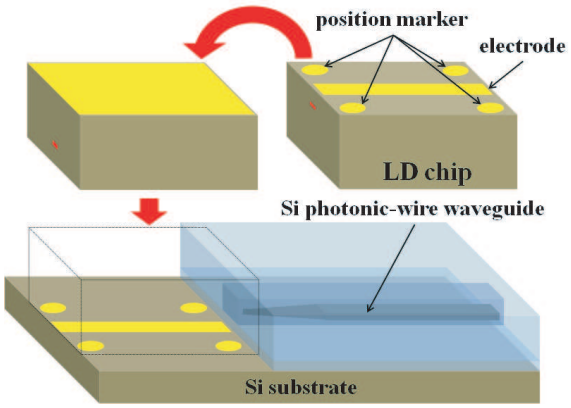

Figure 1: Flip-chip bonding of LD on SOI substrate.

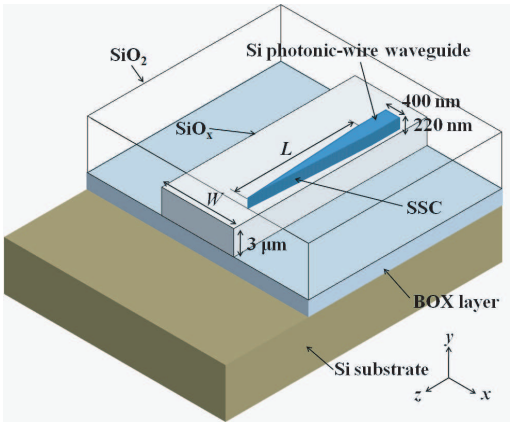

Figure 2: Schematic view of spot-size-converter.

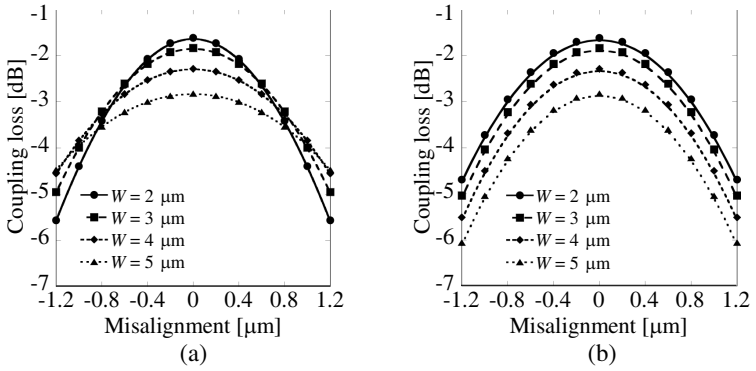

Figure 3: Calculated coupling loss as a function of misalignment in (a) x-direction and (b) y-direction.

3. OPTICAL I/O INTERFACE FOR EXTERNAL OPTICAL COMPONENTS

An optical input/output (I/O) interface for external optical components was also proposed. The interface consisting of a grating coupler can introduce light signal from vertical direction to the substrate although grating couplers reported so far must be used for tilting optical fibers from the vertical direction in order to obtain high coupling efficiency [12].

Figure 5 illustrates the structure. Light input signal irradiated from vertical direction to the substrate is diffracted for both right and left directions by the grating, and the diffracted light signals are combined with 3 dB coupler. We calculated coupling loss for SMFs with 3D FDTD method. Fig. 6 shows calculated optical coupling efficiency as a function of wavelength. It is found that about maximum 50% of coupling efficiency can be obtained with the interface and enough wide bandwidth for operating wavelength can be expected. We also investigated misalignment tolerance of input light beam, and found that the interface have enough tolerance for misalignment and tilt of input beam.

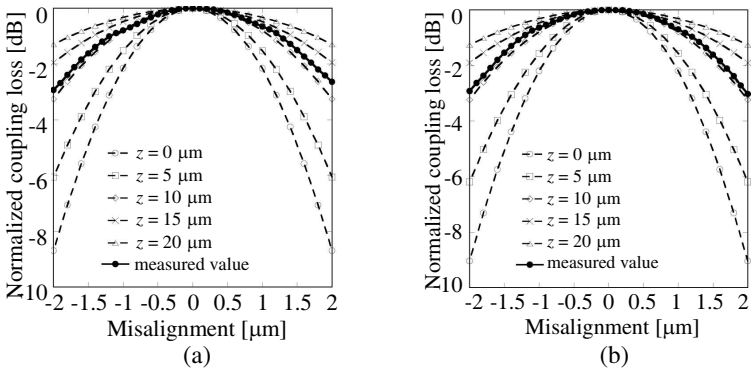

Figure 4: Measured coupling loss as a function of misalignment in (a) x-direction and (b) y-direction.

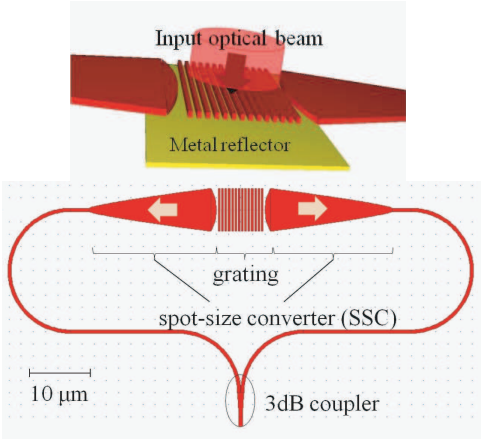

Figure 5: Proposed optical I/O structure for vertical coupling.

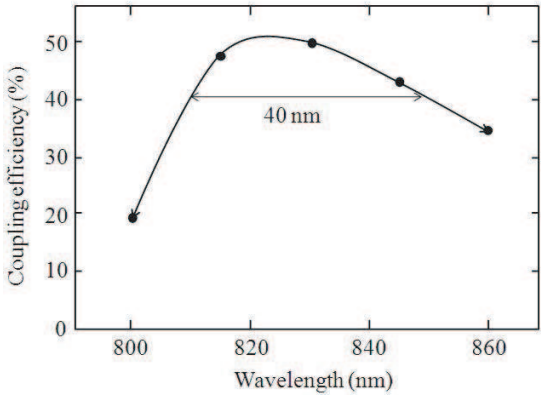

Figure 6: Calculated coupling efficiency.

4. CONCLUSION

We investigated optical coupling loss between LDs and SOI waveguides with BPM method, and found that about 2 dB of minimum coupling loss can be attained. Enough alignment tolerance was also confirmed for the flip-chip mounting of LD chips on the SOI waveguide substrates. Optical I/O interface for vertical coupling was also proposed and investigated the optical coupling efficiency with 3D FDTD method. It was found that maximum 50% of coupling efficiency can be obtained.

ACKNOWLEDGMENT

I would like to thank M. Abe, M. Nozawa, T. Kita and Y. Ohtera of Tohoku Univ. for useful discussions. The study of optical coupling for LDs was supported by KAKANHI (19201025) of the MEXT, and the study of optical I/O was supported by MIRAI Project of the Selete

REFERENCES

1. Dumon, P., W. Bogaerts, V. Wiaux, J. Wouters, S. Beckx, J. V. Campenhout, D. Taillaert, B. Luyssaert, P. Bienstman, D. V. Thourhout, and R. Baets, "Low-loss SOI photonic wires and ring resonators fabricated with deep UV lithography," *IEEE Photon. Technol. Lett.*, Vol. 16, No. 5, 1328–1330, 2004.
2. Tsuchizawa, T., K. Yamada, H. Fukuda, T. Watanabe, J. Takahashi, M. Takahashi, T. Shoji, E. Tamechika, S. Itabashi, and H. Morita, "Microphotonics devices based on silicon microfabrication technology," *IEEE J. Sel. Top. Quantum Electron.*, Vol. 11, No. 1, 232–240, 2005.
3. Chu, T., H. Yamada, S. Ishida, and Y. Arakawa, "Compact $1 \times N$ thermooptic switches based on silicon photonic wire waveguides," *Opt. Express*, Vol. 13, No. 25, 10109–10114, 2005.
4. Ohno, F., K. Sasaki, A. Motegi, and T. Baba, "Reduction in sidelobe level in ultracompact arrayed waveguide grating demultiplexer based on Si wire waveguide," *Jpn. J. Appl. Phys.*, Vol. 45, No. 8A, 6126–6131, 2006.

5. Yamada, H., T. Chu, S. Ishida, and Y. Arakawa, "Si photonic wire waveguide devices," *IEEE J. Sel. Top. Quantum Electron.*, Vol. 12, No. 6, 1371–1379, 2006.
6. Chu, T., H. Yamada, S. Nakamura, M. Ishizaka, M. Tokushima, Y. Urino, S. Ishida, and Y. Arakawa, "Ultra-small silicon photonic wire waveguide devices," *IEICE Trans.on Electron.*, Vol. E92-C, No. 2, 217–223, 2009.
7. Sakai, A., G. Hara, and T. Baba, "Propagation characteristics of ultrahigh-Δ optical waveguide on silicon-on-insulator substrate," *Jpn. J. Appl. Phys.*, Vol. 40, Part 2, No. 4B, L383–L385, 2001.
8. Vlasov, Y. A. and S. J. McNab, "Losses in single-mode silicon-on-insulator strip waveguides and bends," *Opt. Express*, Vol. 12, No. 8, 1622–1631, 2004.
9. Fang, A. W., H. Park, O. Cohen, R, Jones, M. J. Paniccia, and J. E. Bowers, "Electrically pumped hybrid AlGaInAs-silicon evanescent laser," *Opt. Express*, Vol. 14, No. 20, 9203–9210, 2006.
10. Roelkens, G., D. V. Thourhout, R. Baets, R. Notzel, and M. Smit, "Laser emission and photodetection in an InP/InGaAsP layer integrated on and coupled to a silicon-on-insulator waveguide circuit," *Opt. Express*, Vol. 14, No. 18, 8154–8159, 2006.
11. Shoji, T., T. Tsuchizawa, T. Watanabe, K. Yamada and H. Morita, "Low loss mode size converter from 0.3 μm square Si wire waveguides to singlemode fibers," *Electron. Lett.*, Vol. 38, No. 25, 1669–1670, 2002.
12. Laere, F. V., G. Roelkens, M. Ayre, J. Schrauwen, D. Taillaert, D. V. Thourhout, T. F. Krauss, and R. Baets, "Compact and highly efficient grating couplers between optical fiber and nanophotonic waveguides," *IEEE J. lightwave Technol.*, Vol. 25, No. 1, 151–156, 2007.

Continuous-wave Terahertz Spectroscopy System Based on Photodiodes

Tadao Nagatsuma[1, 2], Akira Kaino[1], Shintaro Hisatake[1], Katsuhiro Ajito[2], Ho-Jin Song[2], Atsushi Wakatsuki[3], Yoshifumi Muramoto[3], Naoya Kukutsu[2], and Yuichi Kado[2]

[1]Graduate School of Engineering Science, Osaka University
1-3 Machikaneyama, Toyonaka, Osaka 560-8531, Japan
[2]NTT Microsystem Integration Laboratories, NTT Corporation
3-1 Morinosato Wakamiya, Atsugi, Kanagawa 243-0198, Japan
[3]NTT Photonics Laboratories, NTT Corporation
3-1 Morinosato Wakamiya, Atsugi, Kanagawa 243-0198, Japan

Abstract— Photodiodes have been commonly used for generation of continuous terahertz (THz) waves. In this paper, we proposed the use of photodiodes also for detection of THz waves in order to realize CW THz spectroscopy system based on 1.55-μm fiber-optics. We experimentally demonstrated two detection schemes based on the square-law detection and downconversion, and compared them with respect to sensitivity and dynamic range at 260–420 GHz.

1. INTRODUCTION

Terahertz (THz) waves, which cover the frequency range from 100 GHz to 10 THz, have been actively applied to sensing, radars, spectroscopy, measurement and communications. THz pulses based on femto-second pulse lasers have proven to be useful for imaging of objects, and spectroscopy of gas, liquid and solid materials [1, 2]. In particular, the time-domain spectroscopy (TDS) system based on THz pulses has been established as a laboratory standard for the THz spectroscopy, and is commercially available. In the THz-TDS system, frequency characteristics are obtained by Fourier transforming the time-domain data as shown in Fig. 1.

Recently, spectroscopy systems based on continuous wave (CW) technology (Fig. 2), which uses monochromatic sources, have attracted great interest [3]. The CW source-based system provides a higher signal-to-noise ratio (SNR) and spectral resolution. When the frequency band of interest is targeted for the specific absorption line of the objects being tested, the CW system with the selected frequency-scan length and resolution is more practical in terms of data acquisition time as well as system cost.

1.55-μm telecom-wavelength technology is essential in universal instrumentation of CW systems, since low-loss/low-dispersion optical fiber cables can be employed similar to the use of coaxial

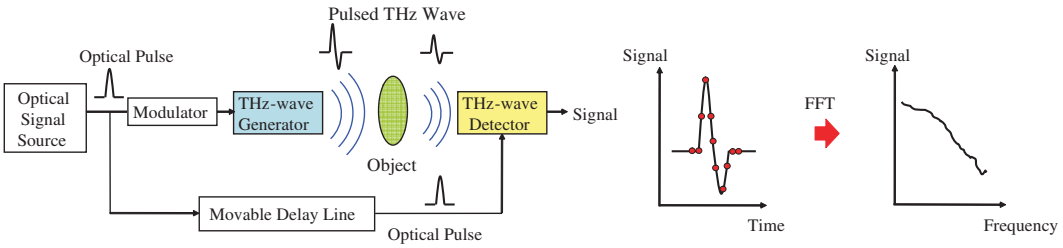

Figure 1: Block diagram of THz time-domain spectroscopy system.

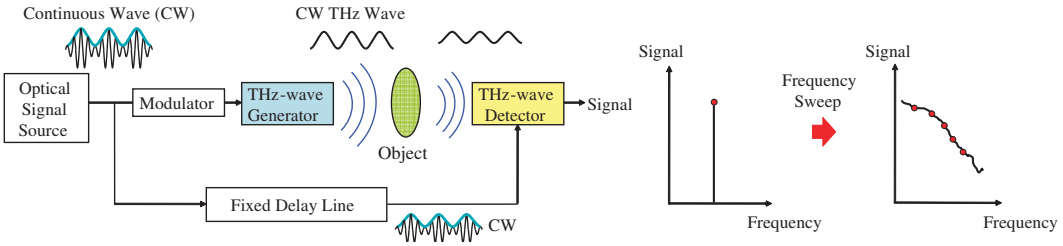

Figure 2: Block diagram of THz frequency-domain spectroscopy system, based on homodyne detection.

cables in the conventional RF systems, and optical components are highly reliable and matured. At 1.55 μm, high-power THz photodiodes such as uni-traveling-carrier-photodiodes (UTC-PDs) [4] are superior to photoconductors based on, for example, low-temperature grown InGaAs in terms of output power as THz signal generators or emitters, while only photoconductors have been used as THz detectors in the CW spectroscopy system [5, 6].

In this paper, we propose and demonstrate the use of photodiodes for "both" generation and detection in the CW spectroscopy system. First, we experimentally show two kinds of operation modes in photodiodes at 260–420 GHz; one is a square-law detector under forward bias, and the other is a down converter under reverse bias. Then, we compare them with respect to sensitivity and dynamic range.

2. THz PHOTODIODE TECHNOLOGIES

Figure 3(a) shows the band diagram of the photodiode optimized for the operation at 300–400 GHz [7]. This structure is a modification of the uni-traveling-carrier photodiode (UTC-PD). The UTC-PD has a feature of both high-speed and high-output power operation owing to its unique carrier transport mechanism [8].

The photodiode chip was packaged into the module with a rectangular waveguide (WR-3) output port [7]. The frequency dependence of the output power was evaluated by heterodyning the two wavelengths of light from the wavelength-tunable light sources at around 1.55 μm. The THz output power was measured by thermo-coupled power meter. Fig. 3(b) shows the frequency dependence of the output power generated from the module. The 3-dB bandwidth is 140 GHz (from 270 to 410 GHz). The peak output power was 110 μW at 380 GHz for a photocurrent of 10 mA with a bias voltage of 1.1 V. The output power could be further increased to over 400 μW (−4 dBm) with increasing the photocurrent up to 20 mA.

3. PRINCIPLE OF THz-WAVE DETECTION WITH PHOTODIODE

Figure 4(a) shows the operation principle of the photodiodes as THz-wave detectors. There are two operation modes with different voltage-bias conditions; one is a square-law detector under the forward bias condition, and the other is a downconverter under the reverse bias. In case of down-conversion (Fig. 4(b)), the origin of the nonlinearity of the UTC-PD can be explained by the dynamic capacitance associated with charge storage in the photo-absorption layer [9]. Mixing between the input THz wave, f_{RF}, and the local oscillator (LO) signal, f_{LO}, photonically generated

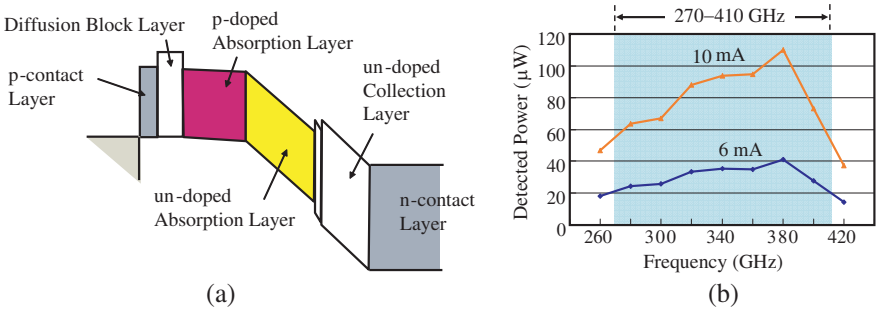

Figure 3: (a) Band diagram of the photodiode. (b) Frequency dependence of output power from the photodiode module for photocurrents of 6 mA and 10 mA.

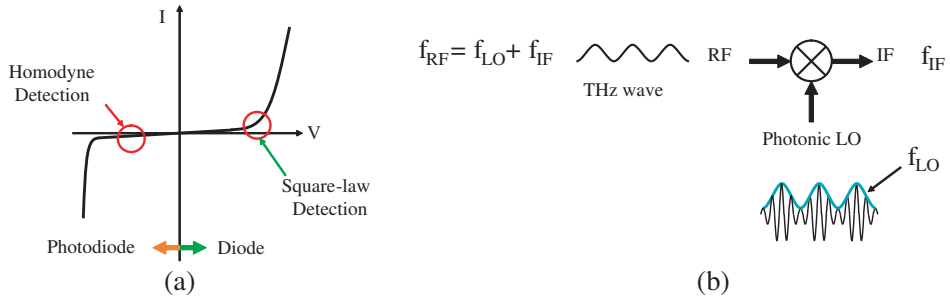

Figure 4: (a) Operation points of photodiode as a THz detector. (b) Schematic representation of photodiode as a down-converter.

in the photodiode leads to the intermediate frequency, f_{IF}.

4. EXPERIMENTS AND DISCUSSION

Figure 5 shows a block diagram of the CW THz spectrometer consisting of the transmitter (Tx) and the receiver (Rx) based on the square-law detection. Frequency can be changed by tuning a difference in the wavelengths of two frequency (wavelength)-tunable lasers. The RF frequency was modulated at an intermediate frequency (10 kHz) using an optical chopper, and the output signal from the Rx UTC-PD at 10 kHz was measured by the spectrum analyzer.

Figure 6 plots the relationship between the input THz power and the detected (IF) power at 350 GHz. Bias voltages were −1 V and 0.68 V for Tx UTC-PD and Rx UTC-PD, respectively, which were chosen to make the Tx output power and the Rx sensitivity maximum. In the experiment, Tx and Rx were directly connected by the rectangular waveguide. As shown in Fig. 6, the slope almost fits to the square-law relationship.

Figure 7 shows a block diagram of the CW THz spectrometer consisting of the transmitter and the receiver based on the down-conversion. This coherent system is often referred to as "homodyne" detection system [5]. Optical delay line was used to maximize the intermediate frequency signal at 10 kHz.

Figure 8(a) plots the relationship between the detected (IF) power and the optical delay length at 350 GHz. Bias voltages were −1 V and −1 V for Tx UTC-PD and Rx UTC-PD, respectively. In the experiment, Tx and Rx were directly connected by the rectangular waveguide. Two periods corresponds to the wavelength of 0.86 mm at 350 GHz, which confirms the proper homodyne detection. By changing the wavelength difference between two wavelength-tunable lasers, frequency dependence of the IF power was measured as shown in Fig. 8(b). 6-dB bandwidth ranges from 280 GHz to 410 GHz, which corresponds to 3-dB bandwidth of the output power of the UTC-PD (Fig. 3(b)).

Figure 9 shows the dependence of the IF power on the photocurrent, which corresponds to the optical LO power, at 350 GHz. As is the case of usual electrical mixers, the IF power increases with

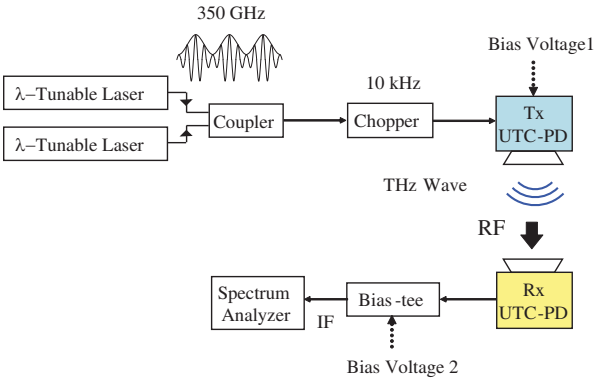

Figure 5: Block diagram of CW THz spectrometer using the receiver based on the square-law detection.

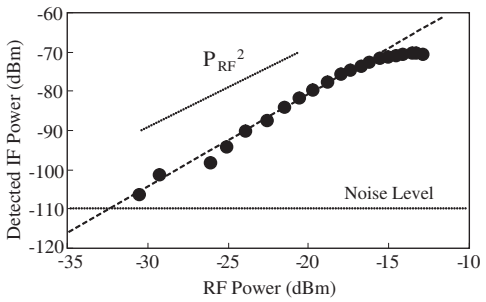

Figure 6: Relationship between input THz (RF) power and the detected (IF) power measured at 350 GHz.

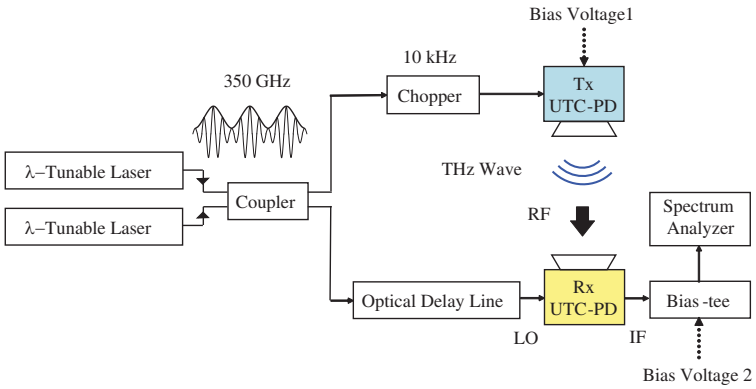

Figure 7: Block diagram of CW THz spectrometer using the receiver based on the down-conversion.

the LO power, and saturates at certain LO level, or the photocurrent of 4–5 mA.

Finally, dependence of the IF power on the input PF power was compared between the homodyne detection and the square-law detection as shown in Fig. 10. For the homodyne detection, the photocurrent was set to 4 mA, which is an optimum condition experimentally confirmed (Fig. 9). Maximum S/N (ratio of IF power to noise level) is 39 dB for the square-law detection, while it is 58 dB for the homodyne detection. This corresponds to the difference in the maximum conversion efficiency is 19 dB. Since the available output power from the UTC-PD is more than −4 dBm, about 20-dB loss in the transmission between transmitter and receiver and as well as in the object under test is still allowable for the actual spectroscopy. In addition, since the slope in the relationship between the RF power and the IF power is smaller for the homodyne detection, loss caused in the object and transmission has less effect, which may be a merit of the homodyne detection scheme.

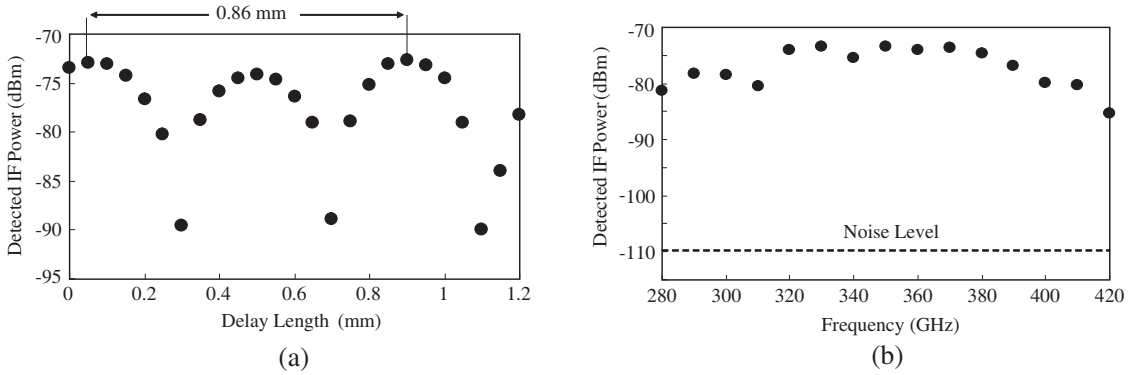

Figure 8: (a) Dependence of IF power on delay length. (b) Frequency characteristics of the homodyne system.

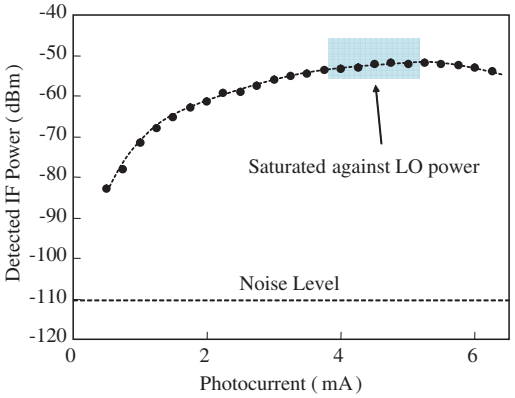

Figure 9: Relationship between the photocurrent and the detected (IF) power measured at 350 GHz.

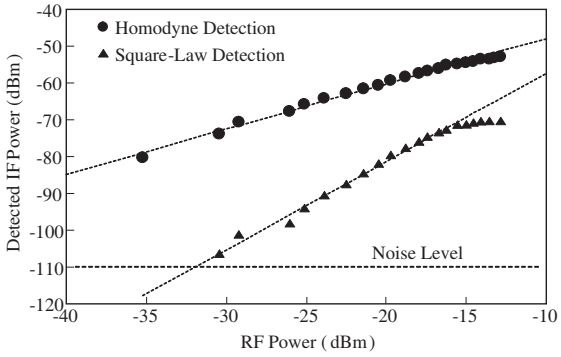

Figure 10: Comparison of receiver performance between down-conversion and square-law detection.

5. CONCLUSION

In the conventional CW THz spectroscopy system, photoconductor and/or photodiode have been used for the transmitter, while only photoconductors have been employed for the receiver. In this paper, we proposed the use of photodiode as the receiver for the CW terahertz spectroscopy system in addition to the transmitter, and conducted proof-of-concept experiments at 300–400 GHz. We compared two detection schemes; square-law detection with forward diode bias, and down-conversion with reverse bias. The conversion efficiency of the down-conversion was 19 dB higher than that of the square-law detection, and was comparable to those of InGaAs photoconductors. The components used are all 1.55-μm telecom-fiber-optic ones, which may lead to the cost-effective and versatile spectroscopy system. Currently, the bandwidth is limited by waveguide-structure of the transmitter and receiver modules, and it can be enhanced by using a broadband antenna integrated with the photodiode. Use of the same photodiodes for both transmitter and receiver will also promising for integrated spectrometer chip in bio-sensor applications [10].

ACKNOWLEDGMENT

The authors wish to thank Drs. K. Iwatsuki, N. Shigekawa, T. Enoki, and M. Kitamura for their support and encouragement.

REFERENCES

1. Cooke, M., "Filling the THz gap with new applications," *Semiconductor Today*, Vol. 2, No. 1, 39–43, 2007.
2. Zhang, X.-C. and J. Xu, *Introduction to THz Wave Photonics*, Springer, 2009.
3. Deninger, A., A. Roggenbuck, S. I. Schindler, C. Mayorga, H. Schmitz, J. Hemberger, R. Güsten, and M. Grüninge, "CW THz spectrometer with 90 dB SNR and MHz frequency resolution," *Proc. 2009 Infrared, Millimeter and Terahertz Waves (IRMMW-THz 2009)*, T4A03.0193, September 2009.
4. Nagatsuma, T., "Generating millimeter and terahertz waves," *IEEE Microwave Magazine*, Vol. 10, No. 4, 64–74, 2009.
5. Ducournau, G., A. Beck, K. Blary, E. Peytavit, M. Zaknoune, T. Akalin, J.-F.Lampin, M. Martin, and J. Mangeney, "All-fiber continuous wave coherent homodyne terahertz spectrometer operating at 1.55 µm wavelengths," *Proc. 2009 Infrared, Millimeter and Terahertz Waves (IRMMW-THz 2009)*, T4A02.0362, September 2009.
6. Stanze, D., H.-G. Bach, R. Kunkel, D. Schmidt, H. Roehle, M. Schlak, M. Schell, and B. Sartorius, "Coherent CW terahertz systems employing photodiode emitters," *Proc. 2009 Infrared, Millimeter and Terahertz Waves (IRMMW-THz 2009)*, T4A01.0176, September 2009.
7. Wakatsuki, A., T. Furuta, Y. Muramoto, T. Yoshimatsua, and H. Ito, "High-power and broadband sub-terahertz wave generation using a J-band photomixer module with rectangular-waveguide output port," *Proc. 2008 Infrared, Millimeter and Terahertz Waves (IRMMW-THz 2008)*, M4K2.1199, September 2008.
8. Nagatsuma, T., H. Ito, and T. Ishibashi, "High-power RF photodiodes and their applications," *Laser & Photonics Review*, Vol. 3, No. 1–2, 123–137, January 2009.
9. Fushimi, H., T. Furuta, T. Ishibashi, and H. Ito, "Photoresponse nonlinearity of a uni-traveling-carrier photodiode and its application to optoelectronic millimeter-wave mixing in 60 GHz band," *Jap. J. Appl. Phys.*, Vol. 43, No. 7B, L966–968, 2004.
10. Nagel, M., P. H. Bolivar, M. Brucherseifer, and H. Kurz, "Integrated THz technology for label-free genetic diagnostics," *Appl. Phys. Lett.*, Vol. 80, No. 1, 154–156, 2002.

Image Observations and Analyses of RF Wave Propagations on the Basis of LEI Camera

T. Shiozawa[1, 2], **A. Kanno**[2], **K. Sasagawa**[3], **and M. Tsuchiya**[2]

[1]Kagawa National College of Technology, Japan
[2]National Institute of Information and Communications Technology, Japan
[3]Nara Institute of Science and Technology, Japan

Abstract— We overview the recent progress of the novel experimental imaging scheme to intuitively analyze RF signal wave propagations. The scheme is based on a live-electrooptic-imaging camera (LEI camera; http://lei-camera.nict.go.jp/), which was invented and originally prototyped by NICT, and it involves the real-time visualization of phase evolution in RF wave electric fields. The scheme was demonstrated to be effective for determining the immediate essence of RF wave propagations.

1. INTRODUCTION

One of the most attractive RF tools to implement is an experimental gear for visualizing the propagation of electromagnetic waves in a real-time manner. The scheme of live electrooptic imaging (LEI) camera [1, 2], which was originally developed by the authors group, meets the demand. Alternatively, the well-established numerical simulation methods that are based on the electromagnetic wave theory are powerful for the same purpose, i.e., to provide one intuition to propagation characteristics of unseen electromagnetic waves. However, such a highly prompt experimental method for the RF-wave visualization method using the LEI camera is considerably attractive since it gives rise to the possible creation of new paradigms for RF-wave analyses in the real world, especially for novel high speed and high frequency circuits with sophisticated patterns.

2. PRINCIPLE AND CONFIGURATIONS OF LEI-CAMERA

The present LEI camera scheme provides a 10,000-parallel RF measurement, which leads to the real-time electric field image acquisition of 100×100 pixels at a frame rate of ordinary movies; 1,000 frames per second is the highest. The high degree of parallelism in the RF measurement is brought about by the photonic technology. It intuitively presents features of RF-wave propagations via its real-time motion pictures with sufficiently slowed phase evolution. The ultimate bandwidth of the system has reached the W-band range owing to the ultrafast nature of photonics [3]. Thus, the implementation of the LEI camera is based on the fusion of ultrafast and ultra-parallel properties of photonics, which are matched on the basis of the photonic frequency conversion technique.

Most of the results described in the present paper are derived with the latest prototype, which is shown in Figure 1(a). Figure 1(b) shows the basic optical and RF configurations of a LEI camera. One of the key components in the system is the electrooptic (EO) crystal plate, which is usually placed in the vicinity of device-under-test (DUT) surface and gives rise to distribution conversion from its evanescent electrical fields to local optical indices of the plate. The optical indices distribution thus generated is transformed to an in-plane distribution of optical intensity modulation by means of the irradiation of laterally expanded 780 nm laser beam and its propagation through polarimetric optics, and the modulation distribution pattern is finally detected by a 100×100 CMOS image sensor. The frequency relationship for the LEI camera is given by the following equations.

$$|f_{\mathrm{RF}} - f_{\mathrm{LO}}| = f_{\mathrm{IF}} \approx f_{\mathrm{IS}}/n \tag{1}$$

$$\delta f = |f_{\mathrm{IF}} - f_{\mathrm{IS}}/n| \tag{2}$$

Here, f_{RF}, f_{LO}, f_{IF}, and f_{IS} are the frequency of DUT, the frequency of optical LO signal, the difference frequency of f_{RF} and f_{LO}, and the sampling frequency of the image sensor. n is an integer for the sampling of a single period of IF wave. The slight difference δf between f_{IF} and f_{IS}/n corresponds to the frequency of the slowed phase evolution in a LEI movie.

Figure 2 shows a schematic cross-section of view window of the present LEI camera and a picture of the EO crystal plate (ZnTe). A sapphire substrate is inserted between the EO crystal plate and

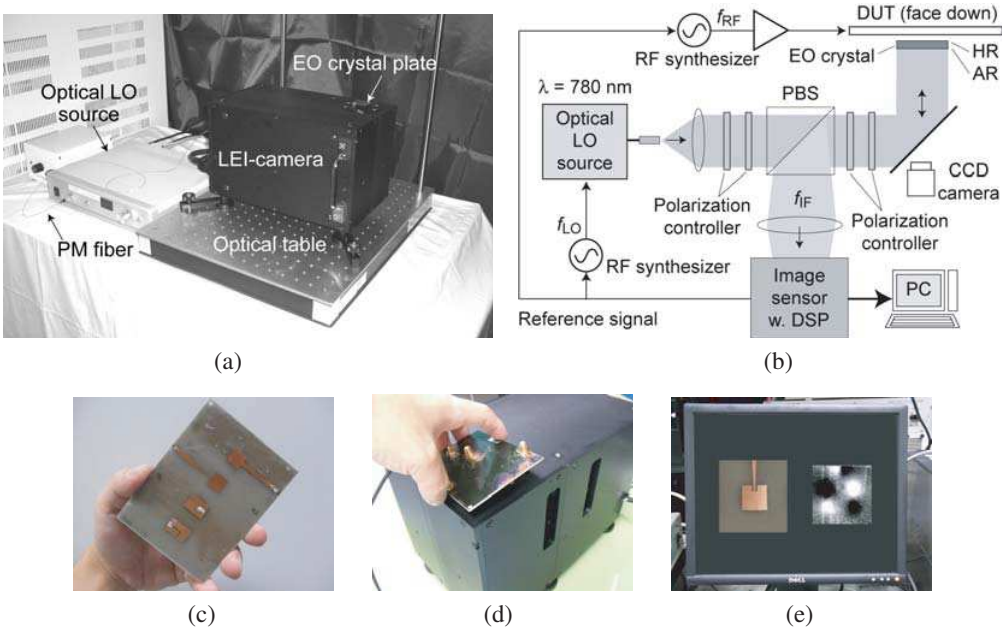

Figure 1: (a) Photograph of the LEI camera system: a main body and an optical LO source. (b) Schematically shown system configuration of LEI camera. (c)–(e) A typical procedure to observe a real-time LEI movie is shown by three sequential pictures.

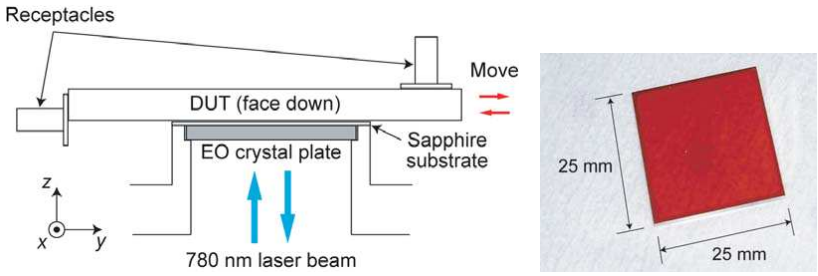

Figure 2: (a) Schematic cross section of the view window of the LEI camera prototype and a DUT on it. (b) Photograph of ZnTe crystal plate.

DUT so as to prevent unnecessary damages to the EO crystal surface when the DUT is moved back and forth quickly, which gives rise to the easy and prompt observation procedure of the LEI camera.

3. LEI OBSERVATIONS AND ANALYSES

Here, three examples for LEI observation results and relevant analytical results are presented. It is to be noted that all the images in this paper show the instantaneous distribution of electrical field E_z, where z is the direction perpendicular to the image plane. The gray scale shown in Fig. 3(b) is also common in all the LEI images in this paper.

Figure 3 shows two series of stroboscopic images for a 90-degree hybrid circuit designed for S_{21} minimum operation at around 7 GHz. The upper series is generated by numerical simulation while the lower one is taken by LEI camera. It is to be noted that the qualities of images in both series are almost the same whereas their acquisition times are quite different from each other. The LEI images clearly indicate the basic features of the circuit function: a signal comes in from the upper right port (port 1) into the circular portion in the middle, scarce reflection occurs to the upper left port (port 2), and two output signals with nearly equal power goes out through the two lower ports with a phase difference of 90 degrees (ports 3 and 4).

Figure 4 shows another example of stroboscopic image series, which exhibits a 5-GHz signal behavior around an outlet part of a meander microstrip line. Around this particular frequency, the standing wave nature, in other words, the trapped wave nature, was observed within the meander

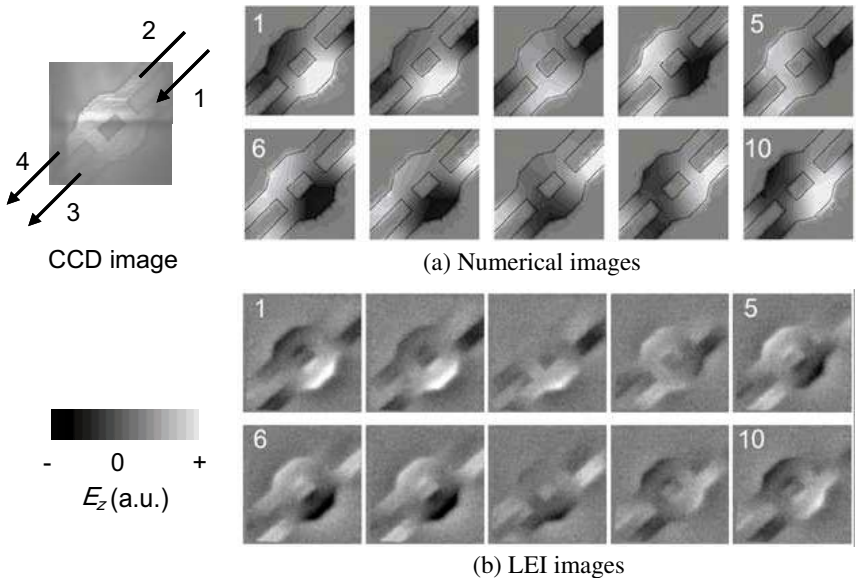

Figure 3: Stroboscopic LEI images for an operation of 90-degree hybrid circuit at the S_{21} minimum frequency. Phase difference between each two adjacent images is $\pi/5$. (a) Numerical simulation results and (b) LEI images. The field perpendicular to the images E_z is visualized. The photograph of the circuit patter in the above was taken during the LEI observation.

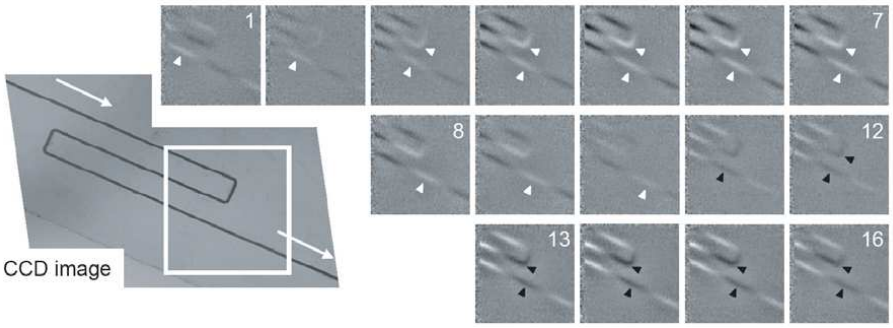

Figure 4: Stroboscopic LEI images for signal propagation at 5 GHz around the outlet part of a meander line. Phase evolution step is $\pi/8$.

structure [4] and can be seen again within the meander structure shown in Figure 4. No special movements of peaks and valleys of the wave are detected. However, another type of wave property can be seen at the outlet line, which partially contains the property of a traveling wave although more detailed image analyses are required. As indicated in this example, it is possible to clarify the local nature of waves in a "place by place" manner by means of LEI camera observation.

Figure 5 shows an example of LEI camera observation for a W-band traveling wave in a semiconductor slab waveguide. Here, the role of the EO crystal plate is two-fold: one is the usual field distribution sensor in the LEI camera system and the other is the semiconductor slab waveguide for W-band waves injected from the WR-10 waveguide flange (Figure 5(a)). Figure 5(b) shows a W-band wave propagating from left to right with some divergence in its lateral spread [5]. The pattern of the W-band wave divergence does not coincide with the simple diffraction theory

$$\theta = 1.22\lambda/a\sqrt{\varepsilon_r} \tag{3}$$

where θ, λ, a, and ε_r are the divergence angle, wavelength, aperture size, and relative permittivity of the waveguide material, respectively. However, it suggests an important parameter for the W-band wave propagation: loss tangent. Figures 5(c) and (d) indicate numerically simulated results with two loss tangent values of 0.00071 and 0.0018, respectively. On the basis of the coincidence in the wave divergence patterns between the experiments and the calculations, the loss tangent of the present ZnTe crystal plate can be reasonably determined to be around those values. Its validity is indicated by their comparison with the loss tangent values of similar semi-insulating GaAs and

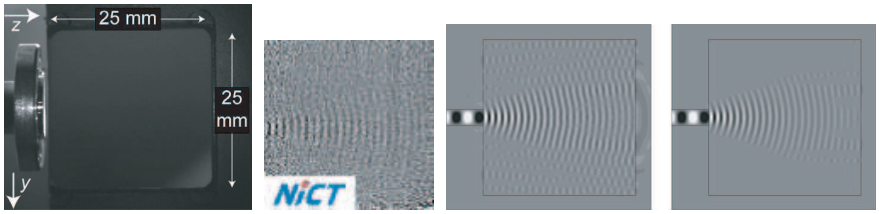

(a) (b) (c) (d)

Figure 5: Photograph of experimental setup for the W-band traveling wave observation. (b) The corresponding field image to the W-band traveling wave. (c)(d) Numerically simulated results with loss tangent values of 0.00071 and 0.0018.

InP substrates [6, 7] and of similar Zn-based II-VI compound semiconductor plates [8]. It is thus concluded that the LEI image can provide an image method to determine a semiconductor material parameter.

4. CONCLUSIONS

Three typical examples of LEI camera observations and wave analyses have been shown in this paper. The observation and analyses results in those examples clearly indicate that the following fairly attractive functionality are provided by the LEI camera system: (a) LEI camera observation provides through its images (movies) an intuition for the basic operation concept of an existing RF circuit, (b) LEI camera provides local wave properties by images, and (c) LEI camera analyses leads to the determination of a material parameter. For further developments of LEI camera functionality and usefulness, it is necessary to extend the list of observation recipes. Such trials are now underway in the authors group and extended collaboration schemes with other research groups will be effective for the purpose.

ACKNOWLEDGMENT

The authors would like to thank Dr. Y. Matsushima of NICT and Prof. T. Morimoto of KNCT.

REFERENCES

1. Sasagawa, K. and M. Tsuchiya, "Real-time monitoring system of RF near-field distribution images on the basis of 64-channel parallel electro-optic data acquisition," *IEICE Electronics Express*, Vol. 2, No. 24, 600–606, 2005.
2. Sasagawa, K., A. Kanno, T. Kawanishi, and M. Tsuchiya, "Live electro-optic imaging system based on ultra-parallel photonic heterodyne for microwave near-fields," *IEEE Trans. Microwave Theory and Tech.*, Vol. 55, 2782–2791, 2007.
3. Tsuchiya, M., A. Kanno, K. Sasagawa, and T. Shiozawa, "Image and/or movie analyses of 100-GHz traveling waves on the basis of real-time observation with live electrooptic imaging camera," to be published in *IEEE Trans. Microwave Theory and Tech.*.
4. Tsuchiya, M., K. Sasagawa, and T. Shiozawa, "Real-time observations and analyses of RF wave propagations by live electrooptic imaging camera," *Conference Proceedings of European Microwave Conference, Roma, EuMC42-1*, 787–790, September 2009.
5. Corresponding movie is available at http://ieeexplore.ieee.org.
6. Private communication from ZnTe substrate benders.
7. Available at http://home.arcor.de/frank.vongratowski/Lowlos.htm.
8. Asfer, M. N. and K. J. Button, "Millimeter-wave dielectric measurement of materials," *Proceedings of IEEE*, Vol. 73, 131–153, Jan. 1985.

Radio on LCX as Universal Radio Platform and Its Application

T. Higashino, K. Tsukamoto, and S. Komaki
Division of Electric, Electronic and Information Engineering, Graduate School of Engineering
Osaka University, Japan

Abstract— In the next generation wireless system, different kind of radio service coexists. To provide a common entrance network of those radio wireless services, broadband transparent network is required. In addition to radio frequency/radio service independent entrance networking such as Radio on Fiber (RoF)/Radio on Free Space Optics (RoFSO), broadband common remote antenna elements are required. One of the candidates of common antenna element, the Radio on leaky coaxial cable (RoLCX) system and its applications are introduced. Main aiming of remote LCX fed by radio on fiber is to make arbitrary coverage area compared to omni-antenna element.

In this paper, WiFi service fed by LCX are experimentally evaluated. In the experiment, received RF power in the coverage and the voice quality in voice over wireless LAN are provided.

1. INTRODUCTION

In the next generation wireless network, different kind of wireless access technologies and their services are integrated on the IP-based network.

Especially in Japan, microwave-band is a suitable for terrestrial mobile radio personal communication. They are extremely limited by the radio regulation (RR). As for the center frequency of the 4-th generation cell phone service, it will be allocated at 3 or 4 GHz RF band or above, which have higher path loss feature than current cell phone system on the 2-GHz band. Thus the coverage area must be smaller than current one. In these back-ground, to enhance the spatial frequency utilization efficiency, the micro-cell and pico-cell configuration would be a favorable solution, because these configurations allow us to repeatedly use one RF resource at the neighbor cell. Fig. 1 shows the configuration of radio services on leaky coaxial cable (RoLCX) system. In the figure, mobile IP phone and mobile IP video phone services are mutually connected under the Session Initiation Protocol (SIP) control. In addition to RF transmission is passively extended by using the RoF link, their coverage could be configured.

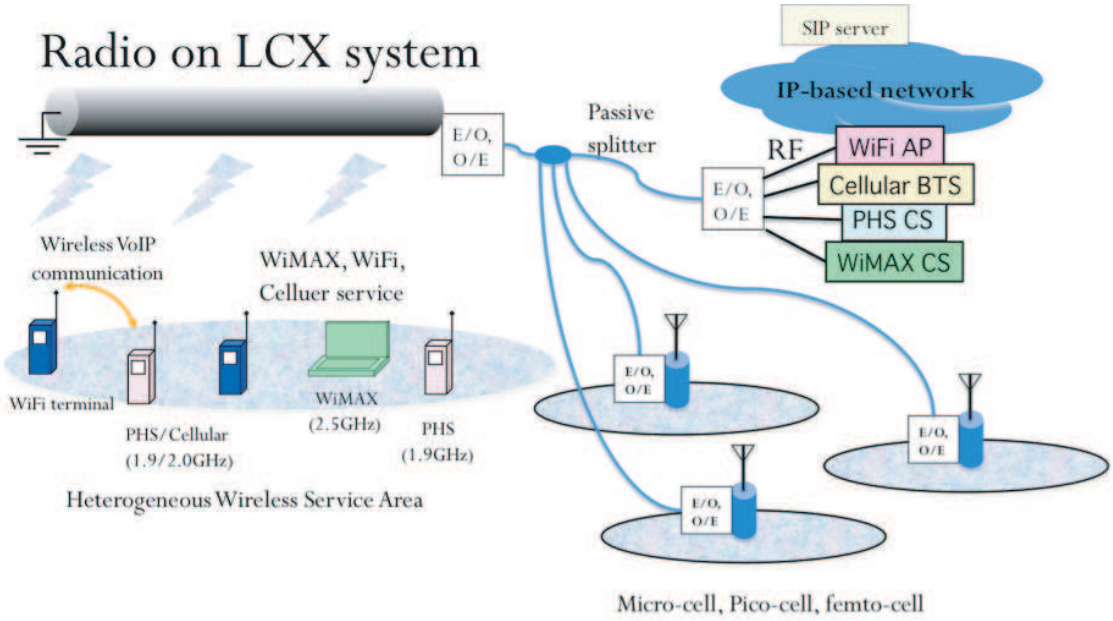

Figure 1: Radio service on leaky coaxial cable system.

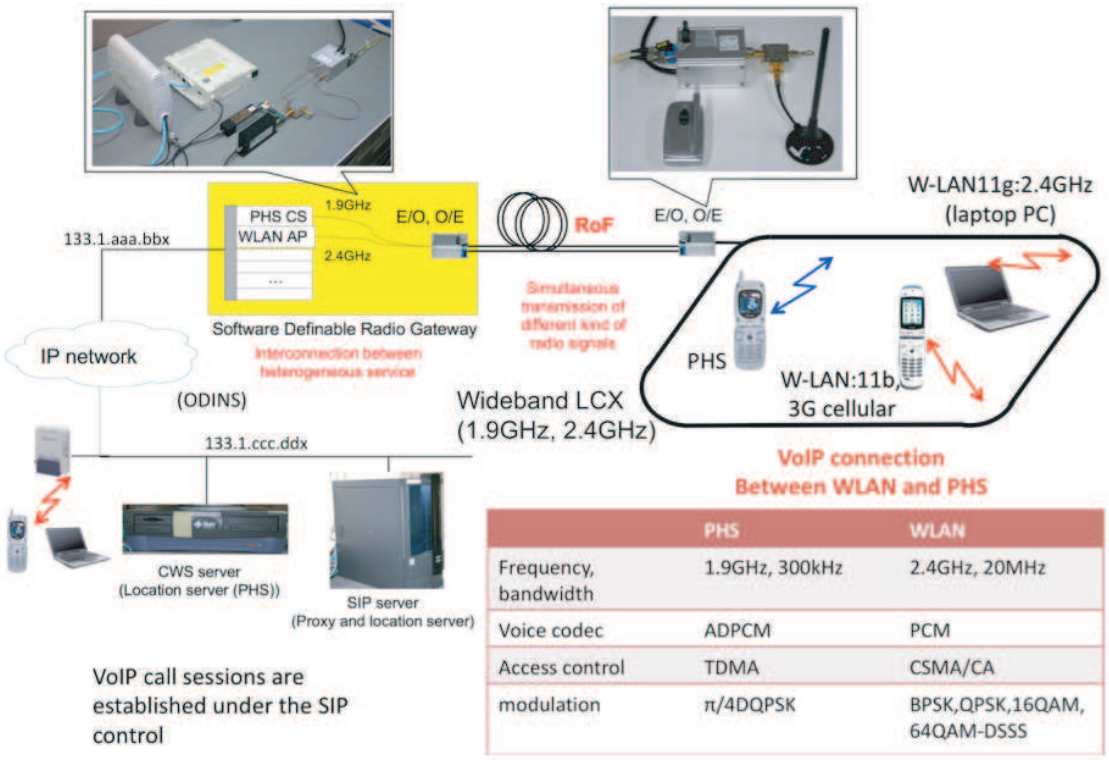

	PHS	WLAN
Frequency, bandwidth	1.9GHz, 300kHz	2.4GHz, 20MHz
Voice codec	ADPCM	PCM
Access control	TDMA	CSMA/CA
modulation	π/4DQPSK	BPSK,QPSK,16QAM, 64QAM-DSSS

Figure 2: VoIP service over LCX system.

2. WIRELESS SERVICES OVER IP SYSTEM

Figure 2 shows the configuration of the VoIP (Voice over Internet Protocol) service [1–3] over LCX [4] system. In the IP-based network, the SIP (Session Initiation Protocol) server and location server are located in the IP-based network. The 3G cellular terminal and any kinds of laptop PCs are able to access to the IP-based network via WiFi access point (AP). In this figure, Software Definable Radio Gateway (SDRGW) [5] plays a role of Interface (I/F) between different kind of air-interface and IP network which have multiple modulators and demodulators of RF signals. Their RF signals (in the figure, WiFi and Personal Handyphone System (PHS) are indicated) are simultaneously converted to the optical signal by using electrical-to-optical (E/O) and optical-to-electrical (O/E) converters. Multiple RF signals simultaneously modulate a Laser Diode (LD) whose modulation format is often used subcarrier multiplexing (SCM)/Intensity Modulation (IM) scheme. In the SDRGW, these RF services are easily discriminated by using the bandpass filter (BPF). At the remote site, SCM/IM signals are detected by using photodetector, then RF signals are regenerated. Since the typical SCM/IM/DD link have several GHz [6], broadband RF channel can be established by utilizing optical bandwidth. The Radio on Fiber link [6] does not require any change of physical configuration such as O/E and E/O devices even if the format of radio signals in physical layer is upgraded. Finally, different kind of radio signals are radiated from broadband LCX antenna. Thus, heterogeneous radio access network and radio service area are configured. In the area, VoIP session between PHS and WiFi terminals can establish under the SIP control.

3. OUTDOOR EXPERIMENT

We experimentally measured the received power of WiFi signal at 2.4 GHz, and also measured voice quality in MOS score, and compared them with conventional omni-antenna system. Outdoor experiments were conducted in the setup shown in Fig. 3. The LCX is cyclically set up at the area with its total length of 160 m in the Osaka university. Specifications of LCX are presented in Table 1. The coupling loss is defined as the received RF power by using standard omni-directional antenna separated from z-axis of LCX by 1.5 m. As for the outdoor experiment site, there are some trees and metallic BBSs in the open space. For comparison, we also measured the received power in the same area covered by a conventional omni-antenna, which was set at the location shown in the figure. Therefore, the omni-antenna covers both of indoor and outdoor area close to the building.

LCX	name	NH-WBLCX-20D-SSD
	Coupling loss	64.6 dB @ 2.4 GHz
	Transmission loss	7.8 dB/100 m
	length	160 m
Omni ant.	name	AT-CL011
	Antenna gain	2.2dBi @ 2.4 GHz vertical
	VSWR	1.3009 @ 2.4 GHz

Table 1: Specification.

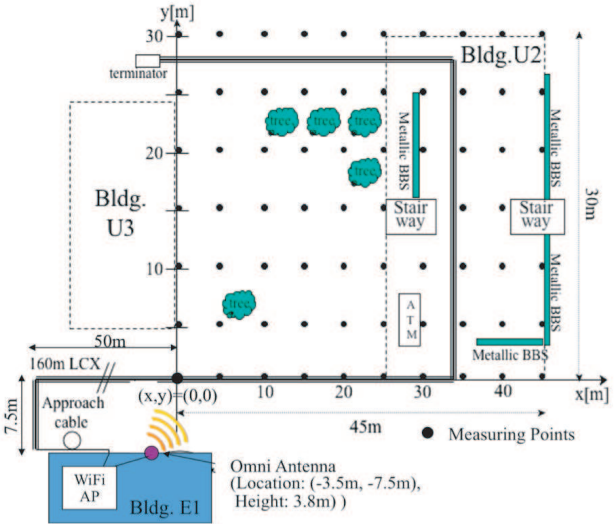

Figure 3: Outside experimental site.

This mean that this experiment exam the area extension capability of LCX. The measuring points are denoted as black circles shown in Fig. 3. The height of omni-antenna, LCX, and a receiver are 3.8 m, 2.5 m and 1.1 m, respectively. The shadowing reduction effect is expected in LCX system compared with omni-antenna system, because line-of-site path is always kept wherever the wireless terminals are distributed in the area.

Figures 4(a) and (b) show the measured results of average loss in LCX and omni-antenna systems, respectively. Under the regulation, each of total transmitted power from LCX or an omni-antenna was 10 mW. It is seen from Figs. 4(a) and (b) that at almost all positions, measured loss of LCX system is lower than those of omni antenna system. LCX system is effective in service area extension. In order to cover a square area, LCX is bent and set in this experiment. Therefore, multipath environment will be more emphasized than single omni-antenna system. As a result of investigation on fading level in the received power, the difference of maximum loss and minimum loss are reduced in LCX system compared with omni-antenna although a receiver directly receives some LOS signals.

These loss improvement results in improvement of voice quality of WiFi VoIP phone [5]. Figs. 5(a) and (b) shows the MOS values in the experimental area for omni antenna and LCX systems, respectively. We measured the MOS (Mean Opinion Score) values for voice quality by subjective evaluations based on "E-model" which was standardized as ITU-R G.107 [7].

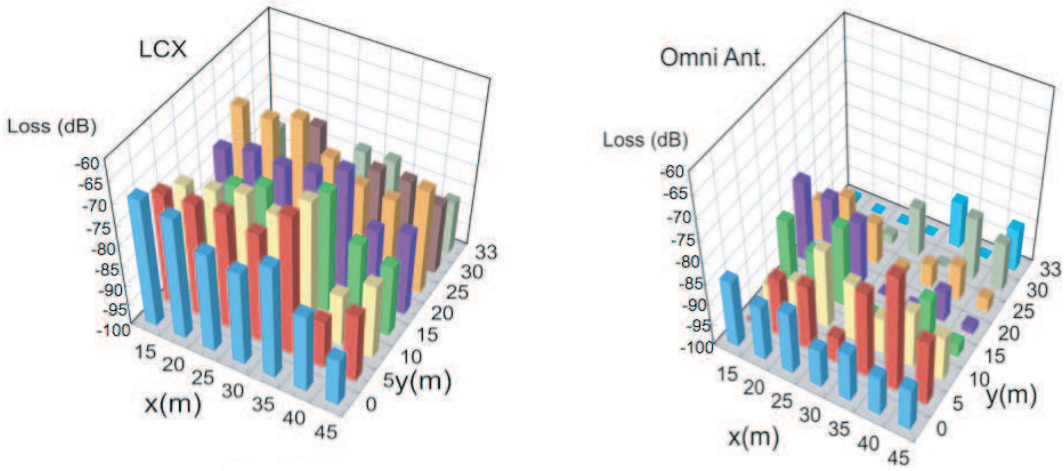

(a) LCX (b) Omni antenna

Figure 4: Propagation loss performance. (a) LCX. (b) Omni antenna.

(a) 802.11g VoIP

Voice Quality	5	4	3	2	1	0
(a) LCX	43	35	15	3	3	1
(b) Omni ant.	24	25	24	7	10	10

(b) 802.11b VoIP

Voice Quality	5	4	3	2	1	0
(a) LCX	65	28	6	1	0	0
(b) Omni ant.	4	4	18	7	3	63

Table 2: Percentage of voice quality.

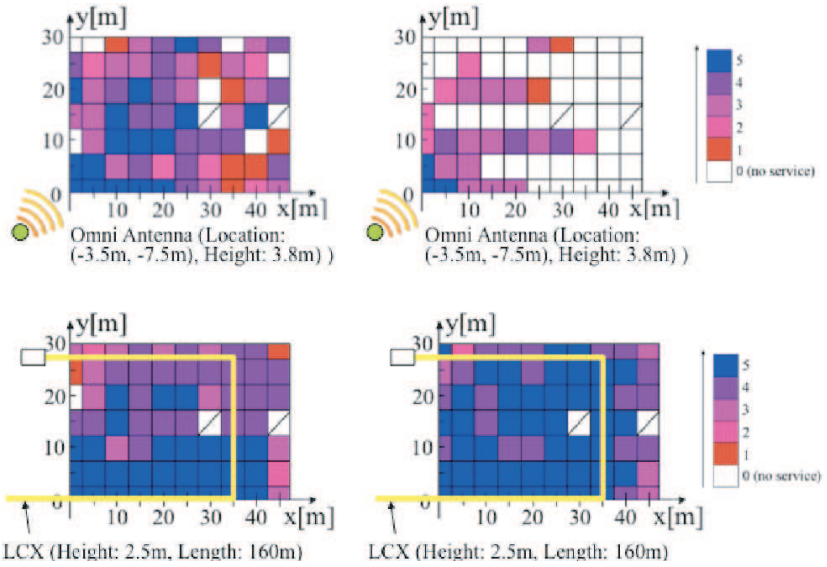

Figure 5: MOS values in the experimental are for omni-antenna (upper) and LCX (lower).

Table 2 summarizes the percentage of the area of positions achieving each MOS score for omni antenna and LCX systems, respectively. We can observe a difference in improvement between 802.11g and 11b. For Omni antenna system, the percentage of effective area achieving MOS score of more than 3 for 802.11g and 11b were 73% and 26%, respectively. For LCX system, on the other hand, the percentage of effective area of more than 90% was obtained for both of 802.11g and 11b.

4. CONCLUSION

This paper proposes a new universal infrastructure which is constructed by RoF and LCX in order to converge various kind of wireless services. Proposed method provides heterogeneous VoIP system and position detection service of wireless terminal. Outdoor experiments show the area extending effects on their coverage of wireless services over IP system compared with systems using omni-directional antenna.

ACKNOWLEDGMENT

This paper is partially supported by Grant-in-Aid of Scientific Research (B), No. 193601740.

REFERENCES

1. Fujii, N., et al., "Wide area experiment of private PHS over IP networks," *Tech. Report of IEICE Workshop*, MoMuC2001-5, 25–28, April 2001.
2. Otsuki, H., et al., "Service area expansion using IP-VPN and wireless LAN for wireless over IP networks and experimental evaluation of its signal quality," *Tech. Report of IEICE Workshop*, MoMuC2002-5, 63–68, May 2002.
3. Komaki, S., K. Tsukamoto, T. Ishida, N. Fujii, T. Higashino, and A. Murakoshi, "Wireless over ip experiments in osaka university," *Proc. of Asia Pacific Microwave Conference*, Vol. 1, No. APMC/04/I/7/60, December 2004.
4. Takano, K., et al., "Wideband leaky coaxial cable (WBLCX) used in Gigahertz band," *Fujikura Technical Review*, No. 110, 9–15, April 2006.
5. Fujisawa, Y., T. Higashino, K. Tsukamoto, and S. Komaki, "Experimental evaluation of service area in wireless service over IP systems," *Proc. of Asia Pacific Microwave Conference*, Vol. 1, No. WEOF-37, 524–527, December 2006.
6. Komaki, S. and H. Al-Raweshidy, *Radio over Fiber Technologies for Mobile Communications Networks*, Artech House Publishers, London, 2002.
7. ITU-T Recommendation G.107, "The E-model, a computational model for use in transmission planning," July 2002.

Close Proximity Wireless Communication Technologies Using Shortwaves, Microwaves, and Sub-terahertz Waves

Yuichi Kado[1], **Mitsuru Shinagawa**[1], **Ho-Jin Song**[1], **and Tadao Nagatsuma**[1, 2]

[1]Smart Device Laboratory, NTT Microsystem Integration Laboratories
3-1 Morinosato Wakamiya, Atsugi, Kanagawa 243-0198, Japan
[2]Graduate School of Engineering Science, Osaka University
1-3 Machikaneyama, Toyonaka, Osaka 560-8531, Japan

Abstract— Close proximity wireless technology features a propagation distance through space of under 10 cm, which enables natural actions like touching or holding something to act as a trigger for initiating communications. This feature is expected to have a wide range of applications. In this paper, we describe the relationship between application scenarios and future needs focusing on the transmission speeds of various close proximity wireless systems and the volume of data that can be instantaneously transmitted using the shortwave band, microwave band, and sub-terahertz band. We also present experimental results on the possibility of near-body electric-field communications in the 5–10 MHz band and close-range wireless links in the sub-terahertz 300–400 GHz band.

1. INTRODUCTION

Historically speaking, the development of wireless communications technology can be traced to the convenience it offers in sending signals to distant locations. More recently, however, attention has come to focus on local-area wireless technologies for use within the office or home and human-area wireless communication technologies for use within the reach of human limbs. In particular, close proximity wireless technology, whose propagation distance through space is limited to less than 10 cm, reduces the risk of unauthorized signal reading compared to close range wireless technologies like Bluetooth and ZigBee whose propagation distance is greater than 10 m. The use of close proximity wireless communications also enables simple actions like touching or holding something to act as a trigger for initiating communications. Such a feature can be used to enable anyone to operate an information device or home appliance in an easy-to-understand, intuitive manner. The potential scale of this market is expected to be several times or more that of mobile terminals. The needs of close proximity wireless communication technologies classified according to the volume of data handled by one operation are summarized in Figure 1.

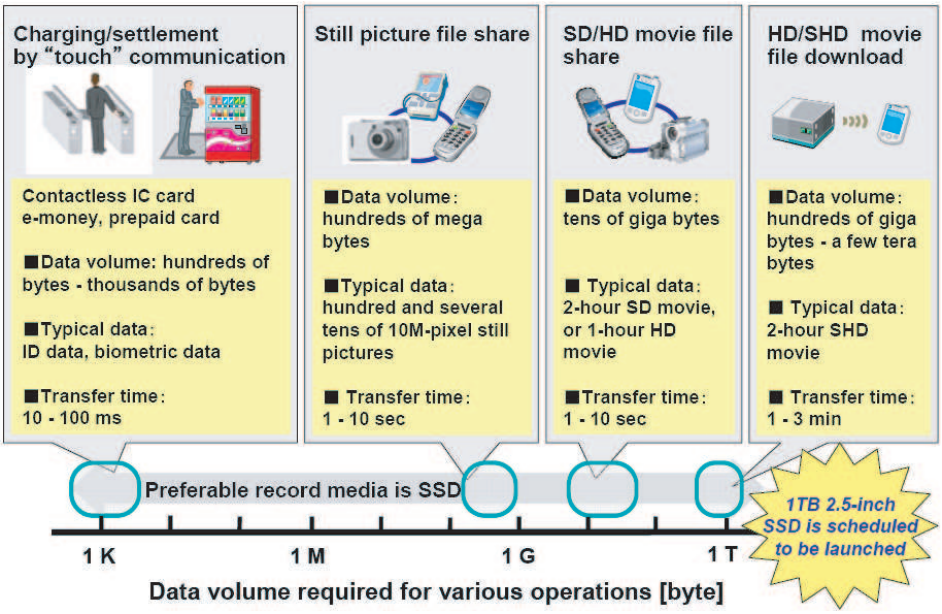

Figure 1: Needs of close proximity wireless communication classified by data volume.

In a data-volume range of hundreds of bytes to thousands of bytes, we have contactless IC cards using the shortwave band. Typical of these are IC cards conforming to the international standard referred to as Near Field Communication (NFC) using the 13.56-MHz band. This standard has been applied to e-money and prepaid cards. A key feature of the NFC card is the absence of batteries, but since it communicates by an electromagnetic induction method, it must be removed from a pocket, briefcase, etc. and held up to a card reader to operate (distance between reader and card: within 10 cm). In actuality, the IC card should touch the reader to ensure communication. At present, most commuters in Japan pay their train fare and pass through the ticket gate by a touch operation. In this type of touch communications, the time allowed for communications, authentication processing, and other processes is about 100 ms, while that for only communications is about 10 ms taking into account the margin needed for resending requests in the event of a communication error. As shown in Figure 2, a transmission speed of 200 kbit/sec enables the transfer of thousands of bytes of biometric data such as ID information, fingerprints, palm vein patterns, etc. in about 10 ms.

NTT has developed near-body electric-field communications technology having a transmission speed of 200 kbit/sec by applying an AC signal of 5–10 MHz to a parallel-plate electrode capacitively coupled to the human body and using the quasi-static electric field component propagating along the surface of the body as the primary communications medium [1, 2]. This technology is described in detail in Section 2.

Next, use of the microwave band enables close proximity wireless communications at transmission speeds on the order of 500 Mbit/sec. A key example is the TransferJet^{TM} wireless transfer technology that achieves a maximum data transfer speed of 560 Mbit/sec using the 4.48-GHz band [3]. In this technology, antennas are designed so as to suppress the emitted electric field while amplifying the induced electric field thereby limiting communication distance to within 3 cm. Today, as digital cameras, digital video recorders, and mobile terminals become smaller and less expensive, almost anyone can take and record pictures and video with ease. To share such content with friends or family and to play it back or store it, users desire a simplified way of transferring the content in a short time to other information devices like computers, televisions, game consoles, and printers. Considering indoor and outdoor application scenarios like the sharing of content between mobile terminals, we can assume an allowable transfer time of several seconds and 10 seconds at most. As shown in Figure 2, the volume of data that can be processed at TransferJet^{TM} transfer speeds is about 700 MB maximum given a transfer time of 10 seconds, which is equivalent to the amount of data that can be recorded on one CD-RW disc. This volume of data also corresponds to about 140 still pictures taken with a 10-million-pixel digital camera. In the case of video, however, no more than 10 minutes of recorded video (assuming a compression rate of 1/20) could be transferred at these speeds even for Standard Definition (SD) video. Considering that the resolution of video images will increase even further in the years to come, the need will arise for close proximity wireless links having extreme bandwidth.

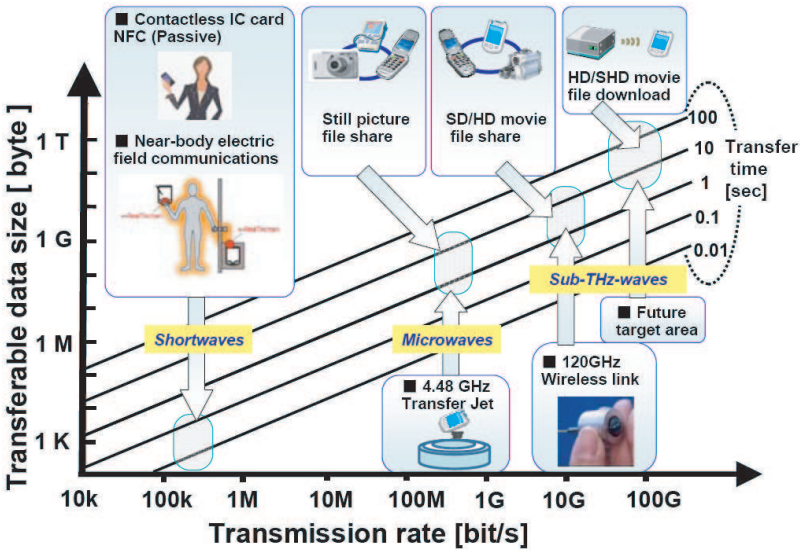

Figure 2: Transmission rate versus transferable data size for various close proximity wireless technologies.

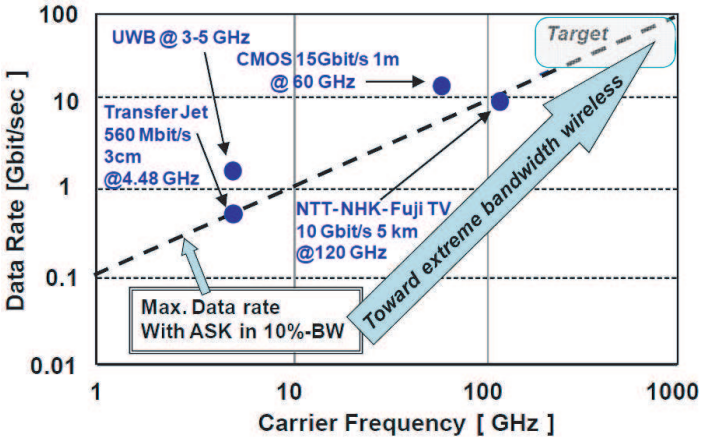

Figure 3: Relationship between carrier frequency and data rate in wireless links.

As can be seen by the trend in data rates for wireless links in Figure 3, increasing carrier frequency is an effective way of increasing data rate. The sub-terahertz-wave band, for example, can be used to achieve wireless communications having data rates in excess of 10 Gbit/sec. NTT has already developed 10-Gbit/sec wireless communications technology using the 120-GHz band [4]. At this data rate, a two-hour-long SD movie (assuming a compression rate of 1/20 and a data capacity of about 11 GB) could be transferred within 10 seconds, and the amount of data that can be recorded on one DVD disc (4.7 GB) could be transferred within 5 seconds. Likewise, a two-hour High Definition (HD) movie, which would come to about 63 GB (assuming a compression rate of 1/20), would require about 50 seconds to be transferred.

On the basis of the trend in wireless systems, we can expect to achieve a data rate of 100 Gbit/sec by either close-range wireless communications by QPSK modulation at a carrier frequency of 500 GHz or close-range wireless communications by ASK modulation at a carrier frequency of 1 THz. Close-range wireless communications on this level could transfer the above two-hour HD movie in about 5 seconds. We point out here that a two-hour Super High Definition (SHD) movie can be downloaded from a TB-class recording medium connected to optical fiber within three minutes. To verify the potential of the sub-THz band toward the realization of ultra-high-speed close-range wireless communications, we have begun transmission experiments on a close-range wireless link operating in the 300–400-GHz band. Details on this technology are given in Section 3.

2. NEAR-BODY ELECTRIC FIELD COMMUNICATIONS TECHNOLOGY

The near-body electric-field communication system described in this paper consists of a transmitter that emits an AC signal modulated by input data from an electrode, and a receiver which uses another electrode to read the weak AC electric field on the body induced by the signal, and demodulates it to recover the data from it (Figure 4) [1, 5]. Applying this technology to an entry system or ticket gate improves convenience considerably compared to conventional contactless cards, since the card does not even need to be removed from the user's pocket (Figure 5). A key aspect of the technology is the behavior of the AC electric field. Our near-body electric field communications technology uses the quasi-static electric field, which attenuates steeply with the distance from the body.

A prototype portable card transmitter and a receiver that can be built into environments such as doors or floors are shown in Figure 6. The system uses a carrier frequency of 5 MHz and Binary Phase Shift Keying (BPSK) modulation, and achieves transmission speeds of 200 kbit/s [2]. In order to highlight the fact that communication is only with the touched object, we give a comparison with other popular short-range wireless and contactless-card technologies in terms of transmission speed and propagation distance through space, in Figure 7. Our technology limits propagation through space to a range similar to contactless cards, and targets transmission speeds from 200 kbit/s to 10 Mbit/s. The start and end of communication is linked to the user's actions, which gives an intuitive sense of the connection to the network.

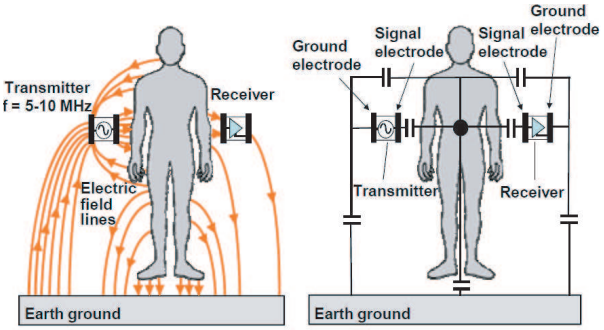

Figure 4: Electric field and capacitive coupling models for near-body electric-field communications.

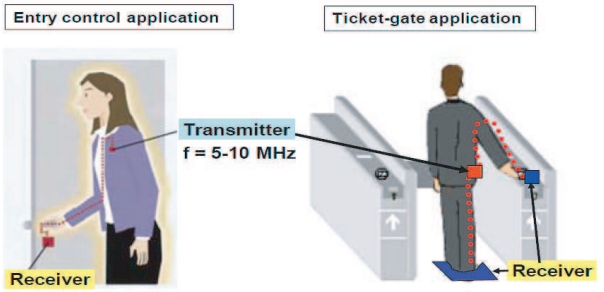

Figure 5: Typical application of near-body electric-field communication.

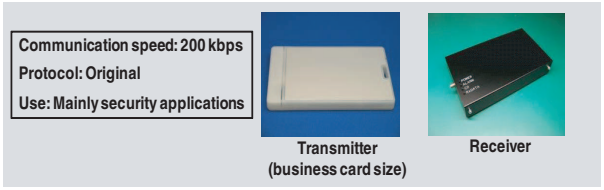

Figure 6: Transmitter and receiver prototypes.

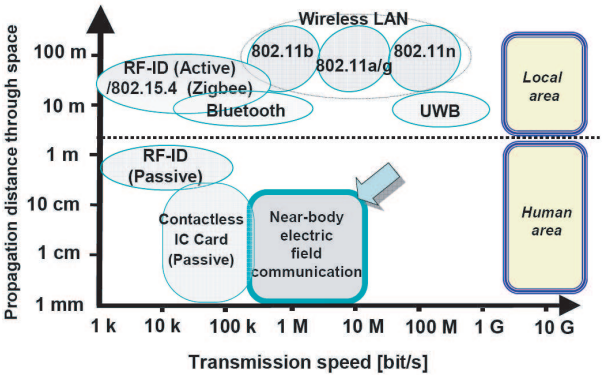

Figure 7: Comparison of short-range wireless technologies.

3. CLOSE-RANGE WIRELESS LINK USING 300–400 GHZ

One of the most direct and easiest ways to achieve a higher data rate of 10–100 Gbit/s is to increase carrier frequencies to terahertz regions of from 100 GHz to 500 GHz. Figure 8 shows the block diagram of the wireless link using photonics-based terahertz-wave transmitter [6]. First, an optical THz-wave signal is generated by heterodyning the two wavelengths of light from the wavelength-tunable light sources. The optical signal is digitally modulated by the optical intensity modulator driven by the pulse pattern generator. Finally, the optical signal is converted to an electrical signal by the uni-traveling-carrier photodiode (UTC-PD) module, and it is emitted to the free space via a horn antenna with a gain of 25 dBi. The emitted terahertz wave is well collimated by a 2-inch-diameter Teflon lens.

The receiver consists of the Schottky barrier diode (SBD) followed by a low-noise pre-amplifier and a limiting amplifier. The SBD module is a commercially available one (WR2.8ZBD) from Virginia Diode Inc. The specification of the operation frequency is 265–400 GHz. The video bandwidth of this SBD module is currently limited to about 300 MHz with the 50-ohm load.

Figure 9 shows transmission characteristics at a carrier frequency of 300 GHz. The transmission distance was 50 cm. Although the receiver bandwidth is limited to several hundreds of MHz, the maximum bit rate was 2 Gbit/s. Error-free transmission was obtained for the transmitter photocurrent of as low as 4 mA, or for the output power of about 10 μW. We also confirmed that error-free 1-Gbit/s transmission was possible over an ultra-wide carrier frequency range from 280 GHz to 400 GHz.

From the above results, an error-free transmission with a transmitter power of 10 μW/channel at 2 Gbit/s is encouraging for practical short-distance applications. For higher bit-rate transmission such as 43 Gbit/s, the video (baseband) bandwidth of the receiver should be increased by incorporating an appropriate intermediate frequency (IF) circuit as already demonstrated in our 120-GHz-band systems [7]. We have fabricated and tested an integrated receiver at 250 GHz, which has a video bandwidth of 4.5 GHz [8]. Maximum bit rate of 8 Gbit/s has been confirmed and further increase in the bit rate is now in progress.

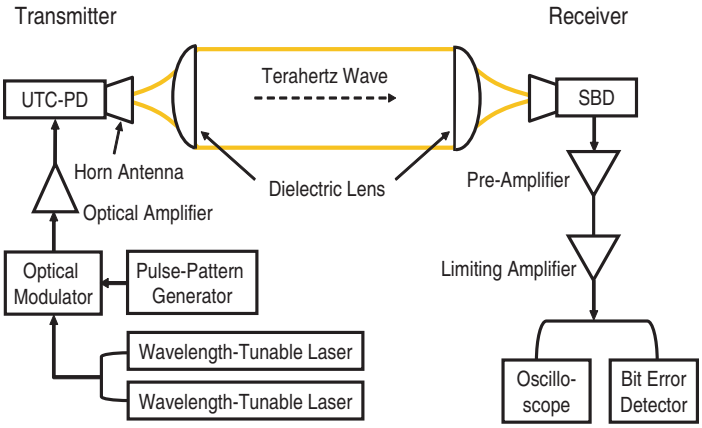

Figure 8: Block diagram of the wireless link using photonics-based terahertz-wave transmitter.

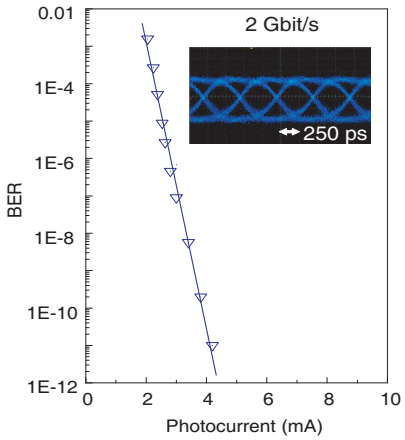

Figure 9: BER characteristics at 2 Gbit/s with a carrier frequency of 300 GHz. Horizontal axis is photocurrent of transmitter.

4. CONCLUSION

Close proximity wireless communication having a propagation distance through space of about 10 cm enables secure, instantaneous transfer of data. It can be used to initiate communications by simple and intuitive operations, which suggests a wide variety of applications. Transmission speeds of several 100 kbit/sec, several 100 Mbit/sec, and more than 10 Gbit/sec can be achieved for carrier frequencies in the shortwave band, microwave band, and 120 GHz band, respectively, and systems at some of these speeds have been commercialized. The volume of data that can be instantaneously transferred by using progressively higher carrier frequencies extends from several kB to 10 GB. Realizing the huge potential of this market, we have been focusing our research efforts on new close proximity wireless technology for use with contactless e-money cards and ultra-high-speed wireless technology that can instantaneously transfer video content between information devices. We reported our latest experimental results on these technologies in this paper.

We first described near-body electric-field communications technology in which the carrier frequency lies in the 5–10-MHz shortwave band. This technology suppresses the emitted electric field and uses the quasi-static electric field as the communication medium to propagate the data signal along the surface of the human body. Applying such a feature to the ticket gate at a train station can improve convenience considerably.

The volume of video data to be processed and transferred will increase dramatically as video shifts from a HD to a SHD format. A two-hour movie in HD format corresponds to a volume of data in excess of 50 GB. The transfer of such data between various kinds of information devices can create a bottleneck in the distribution of data from the production of high-definition video content to its sharing and playback. We confirmed that error-free transmission was possible at data rates of 1-Gbit/s and higher in the 300–400-GHz band. Looking forward, we aim to achieve extreme-bandwidth wireless transmission corresponding to 1/10 to 1/5 the carrier frequency within several years.

ACKNOWLEDGMENT

The authors wish to thank Drs. K. Iwatsuki, N. Kukutsu, T. Enoki, and M. Kitamura for their valuable discussions and supports.

REFERENCES

1. Shinagwa, M., M. Fukumoto, K. Ochiai, and H. Kyuragi, "A near-field-sensing transceiver for intra-body communication based on the electro-optic effect," *IEEE Trans. Instrum. Meas.*, Vol. 53, No. 6, 1533–1538, 2004.
2. Kado, Y., "A human-area networking technology as a universal interface," *Plenary Session, Keynote Speech, 2009 Symposium on VLSI Circuits, Digest of Technical Papers*, 102–105, Kyoto, Japan, June 15–18, 2009.
3. http://www.transferjet.org/tj/transferjet_whitepaper.pdf.

4. Hirata, A., R. Yamaguchi, T. Kosugi, H. Takahashi, K. Murata, T. Nagatsuma, N. Kukutsu, Y. Kado, N. Iai, S. Okabe, S. Kimura, H. Ikegawa, H. Nishikawa, T. Nakayama, and T. Inada, "10-Gbit/s wireless link using InP HEMT MMICs for generating 120-GHz-band millimeter-wave signal," *IEEE Trans. Microwave Theory Tech.*, Vol. 57, No. 5, 1102–1109, May 2009.
5. Zimmerman, T. G., "Personal area networks: Near-field intra-body communication," *IBM Systems Journal*, Vol. 35, No. 3&4, 609–617, 1996.
6. Nagatsuma, T., H.-J. Song, Y. Fujimoto, K. Miyake, A. Hirata, K. Ajito, A. Wakatsuki, T. Furuta, N. Kukutsu, and Y. Kado, "Giga-bit wireless link using 300–400 GHz bands," *Tech. Dig. IEEE International Topical Meeting on Microwave Photonics*, Th. 2.3, October 2009.
7. Hirata, A., T. Kosugi, H. Takahashi, R. Yamaguchi, F. Nakajima, T. Furuta, H. Ito, H. Sugahara, Y. Sato, and T. Nagatsuma, "120-GHz-band millimeter-wave photonic wireless link for 10-Gb/s data transmission," *IEEE Trans. Microwave Theory Tech.*, Vol. 54, No. 5, 1937–1944, May 2006.
8. Song, H.-J., K. Ajito, A. Hirata, A. Wakatsuki, Y. Muramoto, T. Furuta, N. Kukutsu, T. Nagatsuma, and Y. Kado, "8 Gbit/s wireless data transmission at 250 GHz," *IEE Electron. Lett.*, Vol. 45, No. 22, October 2009.

Convergence of WDM Access and Ubiquitous Antenna Architecture for Broadband Wireless Services

Katsutoshi Tsukamoto[1], **Tatsuya Nishiumi**[1], **Takuya Yamagami**[1], **Takeshi Higashino**[1], **Shozo Komaki**[1], **Ryogo Kubo**[2], **Tomohiro Taniguchi**[2], **Jun-Ichi Kani**[2], **Naoto Yoshimoto**[2], **Hideaki Kimura**[2], **and Katsumi Iwatsuki**[3]

[1]Graduate School of Engineering, Osaka University, Japan
[2]NTT Access Network Service Systems Laboratories, Japan
[3]NTT Service Integration Laboratories, Japan

Abstract— This paper proposes a novel network architecture for Giga-bit throughput in broadband ubiquitous networks. A convergence of WDM access and RoF ubiquitous antenna architecture can realize universality of remote base stations for various types of air interfaces and the scalabilities of WDM technologies are expected to improve the throughput in wireless service area covered by RoF-MIMO antenna. We discusse distribution of MIMO antenna, method of RoF MIMO signals over WDM PON, and configurations of center station and remote base stations.

1. INTRODUCTION

To comfortably connect various types of broadband wireless internet services at any places and any time, such as real time high definition videos and applications in cloud computing, an object of next generation wireless access is to realize higher bit-rate equivalent to that in current optical access. A strict limitation in radio frequency spectrum accelerates the reduction of cell size and the use of higher frequency band including microwave, millimeter-wave and terahertz band. Consequently, a huge number of radio access points (AP) will be required. The femtocell architecture, where broadband optical access network is used as entrance networks between core IP network and small APs, is expected as a attractive architecture to realize such a ubiquitous broadband wireless access, as shown in Fig. 1.

In this paper, we propose a novel architecture for broadband wireless services around gigabit/s as a convergence of WDM access [1] and ubiquitous antenna architecture with MIMO technologies [2]. Since the optical access has generally a star network topology, we employ a WDM-PON as the WDM access. The WDM-PON is a physically shared system, but a logically unshared system. This provides certain advantages as follows.

1) The bandwidth for each user can be easily upgraded.
2) Various services can be provided per wavelength.

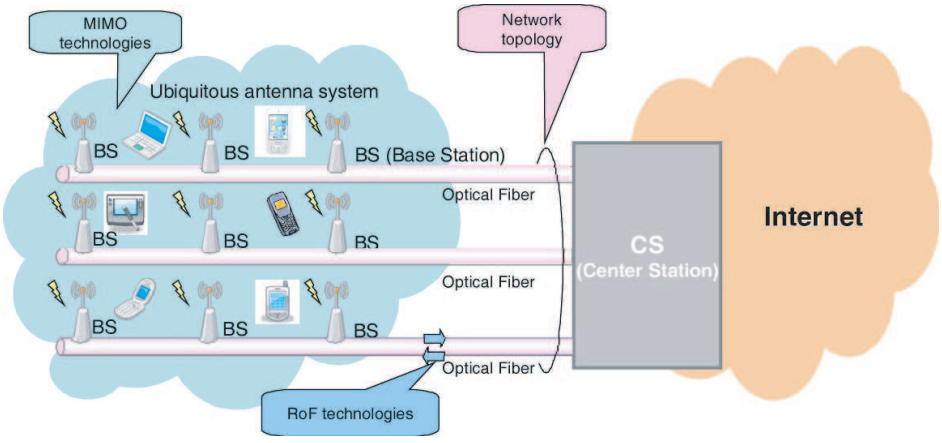

Figure 1: Concept of ubiquitous broadband wireless services over optical access.

From the viewpoint of advantage 2, we will flexibly provide broadband wireless services with the use of RoF technologies to achieve the universality for various types of air interfaces and to

increase the flexibility for non-uniform traffic distribution and users' mobility. Recent proposals establish to provide wireless and/or wired services over WDM-PON [3–5]. The proposed network architecture is expected to improve the throughput up to one Gbps in wireless service area provided by RoF-MIMO antenna system over WDM-PON.

In Section 2, the features of distributed and concentrated MIMO antenna systems over WDM-POM are discussed. Section 3 describes the accommodation of RoF-MIMO signal in WDM-PON, and configuration of center station (CS) and remote base stations (BSs) in the proposed network.

2. MIMO DISTRIBUTED ANTENNA SYSTEM

Figures 2(a) and (b) illustrates configurations of MIMO femtocell for wireless services provided and BS equipments which are accommodated over WDM-PON. We suppose a square cell provided by remote four MIMO antennas. There are following two kinds of cell configurations:

(1) Concentrated MIMO antenna system as shown in Fig. 2(a); Each BS is located at the center of a cell. Four MIMO antennas located in the same cell.
(2) Distributed MIMO antenna system as shown in Fig. 2(b); four MIMO antennas are around a cell. A BS equips four antennas each of which is used for each of four cells around a BS.

In the former system, four MIMO signals have equal delay over optical feeder, therefore, no delay compensations are needed. The latter system requires some delay compensations among four MIMO signals, and a little complicated configuration at CS to deliver each of MIMO signals to different BSs. However, distributed MIMO antenna can increase the throughput in cell because it emphasize rich scattering environment and reduce the correlation among four signals over wireless multipath channels [6]. In the next section, we discuss configurations of WDM-PON based on the distributed MIMO antenna system, wavelength allocations in WDM-PON, and configurations of CS and BS.

3. ROF-MIMO DISTRIBUTED ANTENNA SYSTEM OVER WDM-PON

Figure 3(a) illustrates a configuration of WDM-PON where different wavelengths are assigned to different BS. This configuration enable us to use a $2xN$ AWG as a wavelength router at wavelength demultiplexer. The use of $2xN$ AWG provide following advantages to WDM-PON:

- Easy design in optical loss budget
- Improvement of wavelength utilization efficiency by using cyclic property of AWG that can re-use a wavelength in up link as that for down link.

The configuration of WDM-PON shown in Fig. 3(a), therefore, has a large scalability in accommodating a large number of BS and femtocells.

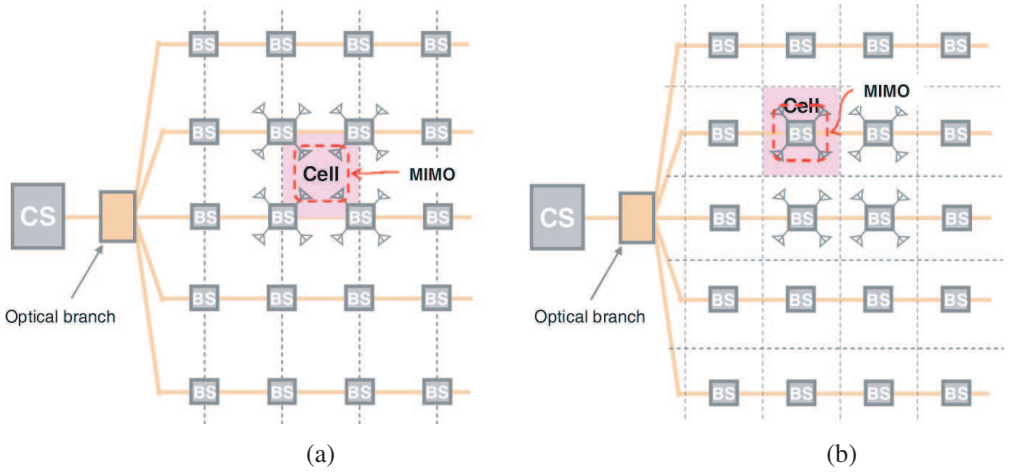

Figure 2: MIMO antenna system. (a) Distributed MIMO antenna system. (b) Concentrated MIMO antenna system.

At the CS in Fig. 3(a), a MIMO signal processing for RF signals is equipped, and four different RF signals for different four MIMO cells are multiplexed in electrical stage. Each BS employs

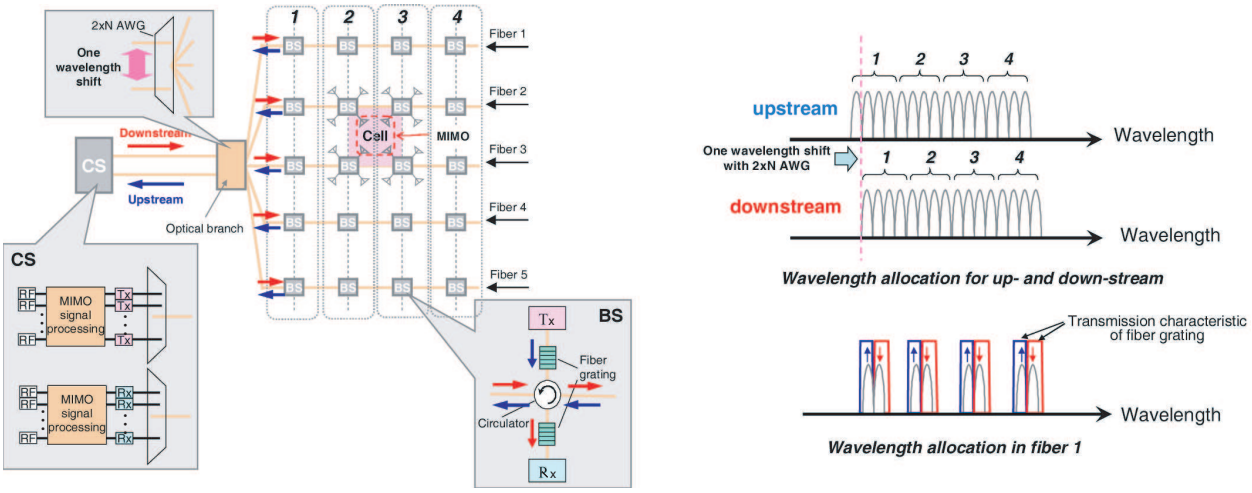

(a) (b)

Figure 3: Configuration of WDM-PON. (a) Configuration. (b) Wavelength allocation.

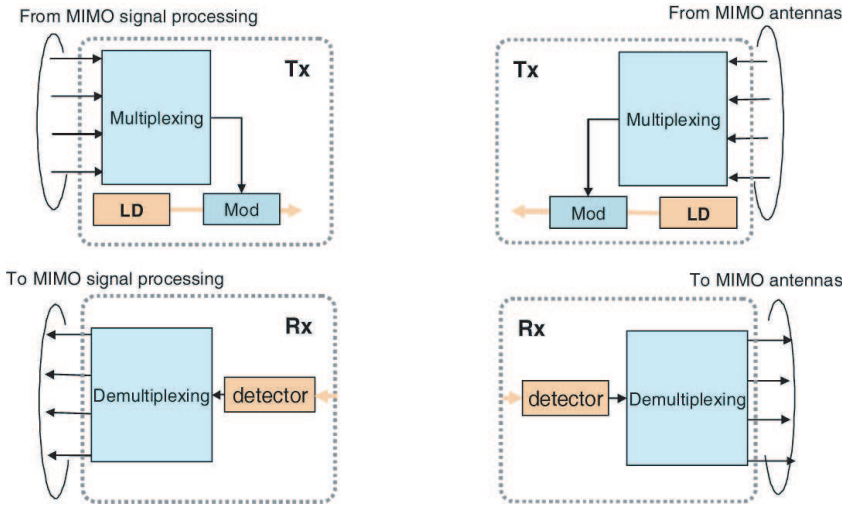

(a) (b)

Figure 4: Configuration of Tx and Rx. (a) Tx and Rx in CS. (b) Tx and Rx in BS.

optical circulator without any wavelength selectivity to easily add upstream signal and drop downstream signal. Optical filters; e.g., optical fiber gratings at the BS are used to select a wavelength assigned to the BS. This configuration achieves the transparency of transmission fiber through lack of optical filters, thus lead to increasing wavelength channels in future. To decrease the costs of operation, administration, and maintenance functions, as well as the production cost, we can introduce wavelength tunability in LDs and fiber gratings of BSs; that is colorless BS [1].

Figure 3(b) illustrates wavelength allocation for upstream and downstream. By using cyclic property of AWG, wavelength for upstream are shifted with one wavelength against those for downstream. We require $N + 1$ wavelengths to accommodate N BSs over the WDM-PON, thus lead to improving the wavelength utilization efficiency.

Figure 4 shows a configuration of transmitter (Tx) and receiver (Rx) at CS and BS. In the proposed distributed MIMO antenna architecture, each of four RF MIMO signals has to be transmitted to each of four BSs. We employ an electrical multiplexing technique to multiplex four RF signals each of which is transmitted to each cell around a BS as shown in Fig. 2(b). When each femtocell is operated with different radio frequency, four RF signals can be transmitted to the same BS by using subcarrier-multiplexing (SCM) method. However, recent wireless access tends toward one cell re-use of the same radio frequency to get higher radio-frequency utilization efficiency. To achieve this trend, some electrical multiplexing of four RF signals over a wavelength should be

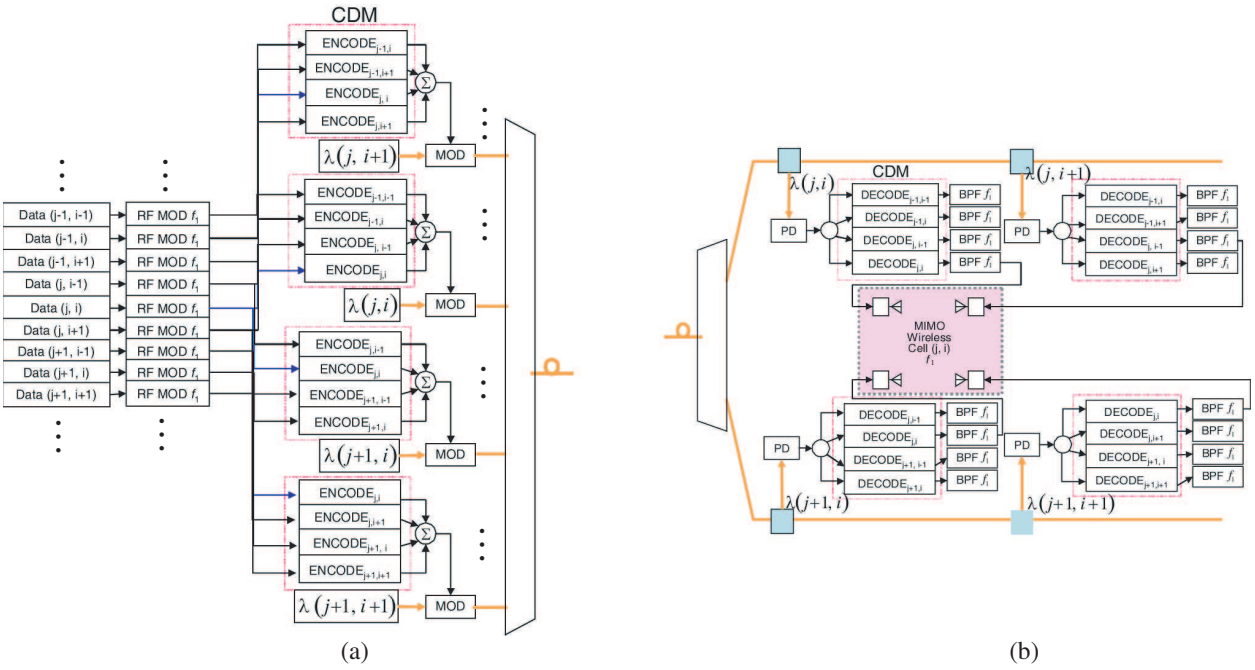

Figure 5: Configuration of electrical CDM-WDM-PON architecture. (a) CS. (b) BS.

considered in the proposed architecture. Not to degrade the transparence of radio air-interfaces, frequency conversions at CS and BS are not desirable.

Therefore, we propose TDM (time division multiplexing) or CDM (code division multiplexing) with bandpass sampling of RF signals to multiplex the four RF signals. As for the TDM, each of four RF signals is naturally sampled with two times faster than its signal bandwidth, and then the sampled four RF signals are multiplexed over one wavelength channel. Fig. 5 illustrates the example of proposed WDM-PON configuration with the use of CDM technique. Data (j, i) modulates RF carrier, f_1, and divided into four signals. Co-channel and independent four signals to BS (j, i) are electrically multiplexed at CDM encoder, and modulates optical carrier with its wavelength $\lambda(j, i)$. At BS (j, i), optical signal with $\lambda(j, i)$ is dropped and received at PD. The output of PD is demultiplexed with CDM decoder, and then four RF signals for different four cells are obtained.

As compared with TDM, CDM is complicated, and the sampling rate is higher than that of TDM. In Ref. [7], however, the CDM can improve the capacity of MIMO channel with controlling the correlation among spreading codes. The further study of spreading code for correlation control will be needed. When transmitting broadband wireless signals with larger bandwidth, the encoding/decoding of CDM can be realized by using a high-speed optical switch [8].

4. CONCLUSION

This paper proposed a novel network architecture for Giga-bit throughput in broadband ubiquitous networks. A convergence of WDM access and RoF ubiquitous antenna architecture can realize a large scalability of WDM and higher throughput in femtocell covered by RoF-MIMO antenna. We discussed the distribution of MIMO antenna, accommodation of RoF MIMO signals over WDM-PON, and configurations of center and base stations.

REFERENCES

1. Iwatsuki, K., J. Kani, H. Suzuki, and M. Fujiwara, "Access and metro networks based on WDM technologies," *IEEE J. Lightwave Technol.*, Vol. 22, No. 11, 2623–2630, 2004.
2. Okamura, S., M. Okada, K. Tsukamoto, S. Komaki, and Y. Heiichi, "Impact of successive interference canceler on the performance of ubiquitous antenna-based SDMA system," *Electronics and Communications in Japan, Part 3: Fundamental Electronic Science*, Vol. 1, No. 3, 10–24, December 2004.
3. Prince, K., J. B. Jensen, A. Caballero, X. Yu, T. B. Gibbon, D. Zibar, N. Guerrero, A. V. Osadchiy, and I. T. Monroy, "Converged wireline and wireless access over a 78-km deployed fiber long-reach WDM PON," *IEEE Photonics Technol. Lett.*, Vol. 21, No. 17, 1274–1276, 2009.

4. Shaw, W.-T., S.-W. Wong, S.-H. Yen, and L. G. Kazovsky, "An ultra-scalable broadband architecture for municipal hybrid wireless access using optical grid network," *Optical Fiber Communication Conference and Exposition and National Fiber Optic Engineers Conference (OFC/NFOEC)*, OThP2, 2009.
5. Jia, Z., J. Yu, G. Ellinas, and G. K. Chang, "Key enabling technologies for optical-wireless networks: Optical millimeter-wave generation, wavelength reuse, and architecture," *IEEE J. Lightwave Technol.*, Vol. 25, No. 11, 3452–3471, 2007.
6. Yamakami, T., T. Higashino, K. Tsukamoto, and S. Komaki, "An experimental investigation of applying MIMO to RoF ubiquitous antenna system," *Proc. of IEEE Topical Meeting on MWP/APMP*, 201–204, September 2008.
7. Nishiumi, T., T. Higashino, K. Tsukamoto, and S. Komaki, "A study of optimam optical code for maximizing throughput with optical CDM RoF-MIMO ubiquitous antenna system," Tech. Report of IEICE MWP, 11–15, November 2009.
8. Tsukamoto, K., T. Higashino, T. Nakanishi, and S. Komaki, "Direct optical switching code division multiple access system for fiber-optic radio highway networks," *IEEE J. Lightwave Technol.*, Vol. 21, No. 12, 3209–3220, December 2003.

Comparison of Microwave Links Prediction Methods: Barnett-Vigants vs. ITU Models

Basile L. Agba[1], **Robert Morin**[2], **and Germain Bergeron**[2]

[1]Institut de Recherche d'Hydro-Québec, 1800 Lionel-Boulet, Varennes, Québec, Canada
[2]Hydro-Québec, 1500 University, Montreal, Québec, Canada

Abstract— Hydro-Québec operates one of the widest electricity networks in the world. The microwave network infrastructure is essential to manage the power grid in Québec and therefore, it is important to meet the reliability criteria that are generally above those accepted by traditional communication operators. In addition, over one third of the existing links has lengths between 70 km and 90 km and operates in extreme weather conditions and all year long. To address these constraints, the microwave links design needs to be as much accurate as possible. The aim of the research presented in this paper is to make a comparative study between two commonly used prediction models for microwave links: Barnett-Vigants and ITU-R P. 530. The first part of this work considers each of the following aspects (unavailability, diversity gain and conversion methods). We analyse each aspect as a function of frequency, fading margin and link length. The two models led to significantly different results for the unavailability due to multipath as a function of the link length, and also for the space diversity as a function of the gain difference between the main antenna and the diversity antenna. Remarkable differences between the two models were also observed when studying the unavailability due to rain as a function of the frequency. The second part of this work compares the overall performance of both models in terms of the total outage probability over ten links with different lengths and different locations. The differences observed for some links are significant.

1. INTRODUCTION

The microwave links deployment, like any other wireless network, requires accurate prediction methods in order to minimize the discrepancies between simulation results and real system performance. Although numerous microwave links are deployed around the world, most of them can be considered as short-range or mean-range links for which the path length is less than 20 km. Hydro-Québec operates one of the widest electricity networks in the world. The microwave network infrastructure is essential to manage the power grid in Québec and therefore, it is important to meet the reliability criteria that are generally above those accepted by traditional communication operators. In addition, over one third of the existing links has lengths between 70 km and 90 km and operates in extreme weather conditions and all year long. To address these constraints, the microwave links design needs to be as much accurate as possible. The aim of the research presented in this paper is to make a comparative study between two commonly used prediction models for microwave links: Barnett-Vigants (B-V) and ITU-R P. 530 [1].

This paper is divided in two parts. The first part analyses some main aspects (such as unavailability, diversity methods and conversion methods) as a function of various parameters, frequency, fading margin and link length. The second part compares the overall performance of both models in terms of the total outage probability over some typical links. Due to space limitation and to reduce the number of figures, we will present only some figures which illustrated significant differences between B-V model and ITU model.

2. BARNETT-VIGANTS VS. ITU: STEP BY STEP COMPARISON

The two models are compared on a step by step basis to illustrate the effect of a given parameter or the combined effect of few parameters. Four main aspects will be analysed: unavailability due to multipath, diversity method with focus on space diversity, worst month to annual conversion methods, and unavailability due to rain.

2.1. Unavailability due to Multipath

The unavailability due to multipath is a key indicator in microwave links design. Indeed, it indicates the outage probability if any engineering techniques (diversity and other engineering techniques) is used to mitigate the propagation effects. The two options for calculating the unavailability in B-V model are respectively "Baseband switching systems" and "IF combining systems". The common

parameters of the two models are flat fade margin ($FFM = A$), frequency (f) and distance (d). One additional parameter is used in B-V model, C factor, while three additional parameters are used in ITU model, geoclimatic K factor, link inclination $|\varepsilon_p|$, and the lowest antenna altitude (above sea level) h_L. The outage probability is expressed in percentage (%) as follows [2, 3].

B-V model:

$$P_w = \left(\left[6 \cdot 10^{-7} C f d^{3.0} \right] 10^{-A/10} \right) \times 100 \tag{1}$$

ITU model:

$$P_w = K d^{3.0} \left(1 + |\varepsilon_p|\right)^{-1.2} \times 10^{0.033 f - 0.001 h_L - A/10} \tag{2}$$

For comparison purposes, real parameters of an existing link are used: $d = 70\,\text{km}$, $f = 7.425\,\text{GHz}$; $FFM = 37\,\text{dB}$; $C = 1$; $K = 1.84E-4$; $|\varepsilon_p| = 0.3\,\text{mrad}$ and $h_L = 150\,\text{m}$ [4]. Link length and frequency are the two parameters which led to significant difference on worst month unavailability due to multipath. In fact, it is obvious that the unavailability increases as the distance increases.

But using the above parameters which represent the real case configuration of a given link, B-V model overestimates worst month unavailability for link length greater than 25 km as illustrated on the Figure 1 (d varying from 5 km to 90 km).

The same observation is valid for any operating frequency used between 7 GHz and 12 GHz. The simulation of Figure 2 is done with $d = 70\,\text{km}$.

A major drawback of B-V model is the choice of C factor which is somewhat subjective. ITU-R P. 530 model is more appropriate to design detailed links. Indeed, there is flexibility to adjust optimally K factor value in contrast to C factor value which is solely based on generic tables or maps.

2.2. Diversity Methods

The frequency diversity calculation for the two models is significantly identical. Only the space diversity gain, I_{sd} is studied first as a function of the gain difference between main and diversity antennas in the receiver side, and second as a function of these two antennas separation. Figures 3 and 4 show that B-V model is also overestimated regardless the system used, "baseband switching" and "IF combining" [5].

B-V baseband switching systems

$$I_{sd} = 1.2 \cdot 10^{-3} \cdot \frac{f}{d} S^2 v^2 10^{A/10} \tag{3}$$

B-V IF combining systems

$$I_{sd} = 1.2 \cdot 10^{-3} \cdot \frac{f}{d} S^2 \frac{16 \cdot v^2}{(1+v)^4} 10^{A/10} \tag{4}$$

where, S is the main and diversity antennas separation; $v \leq 1$ and $v_{\text{dB}} \leq 0$.

Typically the gain difference is $v_{\text{dB}} = -|G_1 - G_2|$.

ITU-R P. 530-12

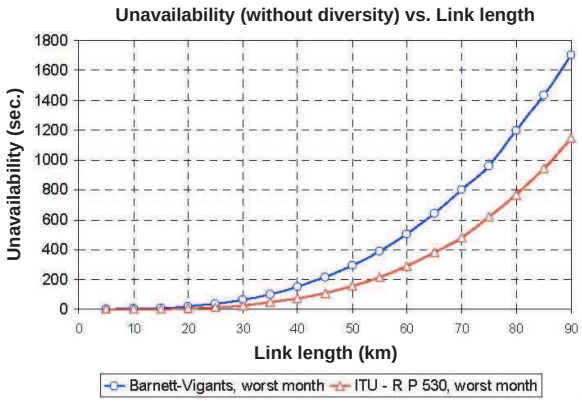

Figure 1: Worst month unavailability due to multipath as function of link length.

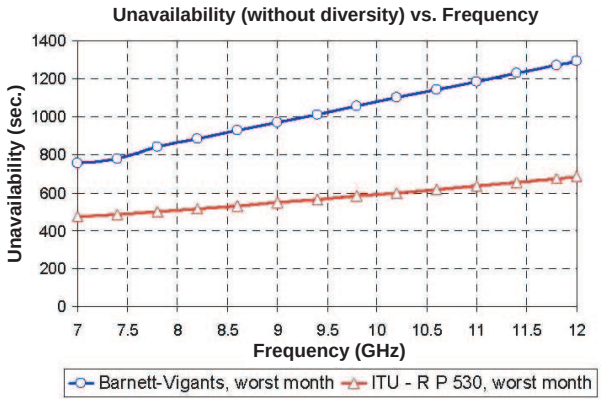

Figure 2: Worst month unavailability due to multipath as function of the operating frequency.

The diversity improvement is calculated differently for non selective and selective fading using radio signature method [2, 6]. The non selective outage probability with space diversity employs a basic formula given by $I_{sd} = I$:

$$I = \left[1 - \exp\left(-0.04 \times S^{0.87} f^{-0.12} d^{0.48} p_0^{-0.104}\right)\right] 10^{\left(\frac{A-|G_1-G_2|}{10}\right)} \quad (5)$$

where, p_0 is the occurrence factor of multipath propagation.

If there is no propagation problem along the diversity path, it is recommendable to ensure that the gain difference is as small as possible, ideally $|G_1 - G_2| = 0$ dB. Although the unavailability based on B-V model is higher compared to the ITU model, all the curves of Figures 3 and 4 follow the same trend. It is also noticeable that the space diversity gain increases very quickly in the B-V model while its variation is slow in the ITU model.

2.3. Conversion Methods for the Multipath Unavailability

For the unavailability due to multipath, the worst month value P_w is calculated first and then is converted to annual value P_{an} using one of the two following methods: mean annual temperature method (generally used in B-V model) and the conversion procedure described in ITU-R P. 530-12 [2, 7]. To show how the conversion method influences the annual value, we consider a typical link with the parameters defined previously. The following simulations are performed:

- Worst month unavailability is calculated by B-V model then converted to annual value using each of the two conversion methods.
- Worst month unavailability is calculated by the ITU model and converted into annual value also using each of the two conversion methods.

The simulation results are summarized in Table 1.

Depending on the conversion method, the annual unavailability values are completely different. But it seems to be more suitable to use ITU method because the formulation is only based on objective parameters such as length, inclination and latitude.

Table 1: Annual mean temperature method vs. ITU-R P. 530-12 method.

		Annual mean temperature	ITU-R P. 530 method
	Worst month unavailability	*Annual unavailability*	*Annual unavailability*
Barnett-Vigants	14.2 min.	30.7 min.	42.8 min.
ITU-R P. 530	13.9 min.	29.6 min.	42.07 min.

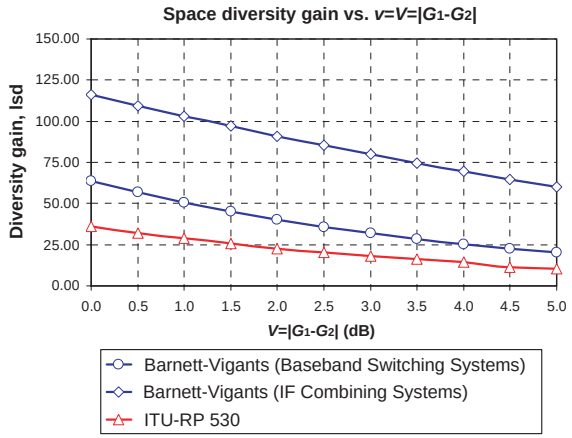

Figure 3: Space diversity gain as function of the gain difference between main and diversity antennas.

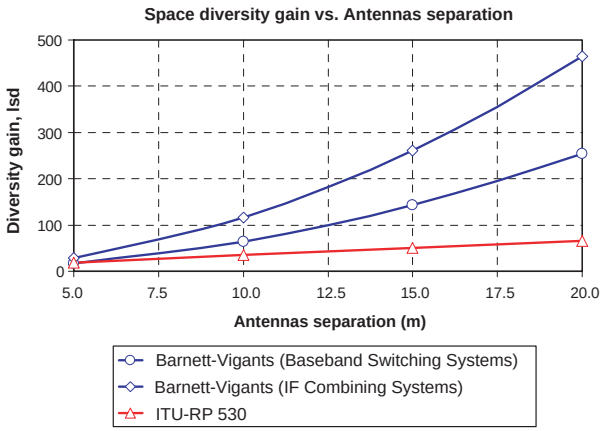

Figure 4: Space diversity gain as function of the main and diversity antennas separation.

2.4. Unavailability due to Rain

The commonly used method in B-V model to calculate the unavailability due to rain is the Crane method [8, 9]. The same calculation is made in ITU-R P. 530 model using the method described in ITU-R P. 838 recommendation [2, 10]. The rain regression coefficients (k and α defined as function of the frequency and the polarization) are essential. Although the two methods are different, the same coefficients are used.

For a given frequency (7.425 GHz), the annual unavailability due to rain increases with the link length. Figure 5 shows that:

- The vertical polarization is better than horizontal polarization for each method.
- For the link length more than 60 km, ITU method, especially in horizontal polarization will reduce the unavailability due to rain about ten seconds.

The unavailability due to rain is largely dependent on the operating frequency. Figure 6 shows that:

- The vertical polarization is better than the horizontal polarization for each method.
- Below 8 GHz and for horizontal polarization, the unavailability due to rain based on the ITU method is lower than the Crane method. Inversely, above 8 GHz, ITU method leads to much higher unavailability. Recall that this observation is valid for 50 km link length.

3. BARNETT-VIGANTS VS. ITU: OVERALL PERFORMANCE COMPARISON

We now present some main results using comparison table. Some main parameters used for simulation are summarized in Table 2. It is important to note that the ITU model includes radio signature method. In this case, we calculate separately the non-selective outage probability P_{ns}

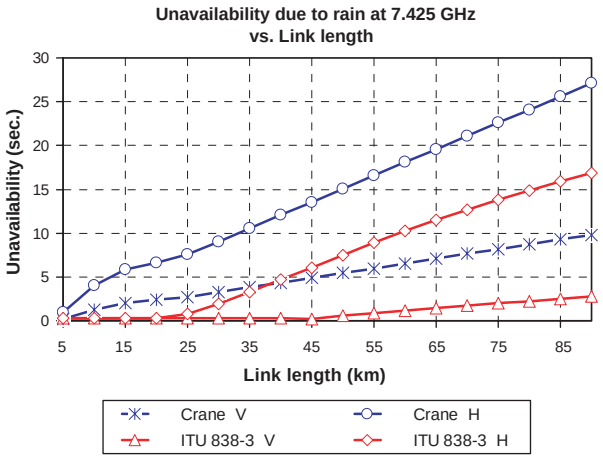

Figure 5: Annual unavailability due to rain as function of the link length.

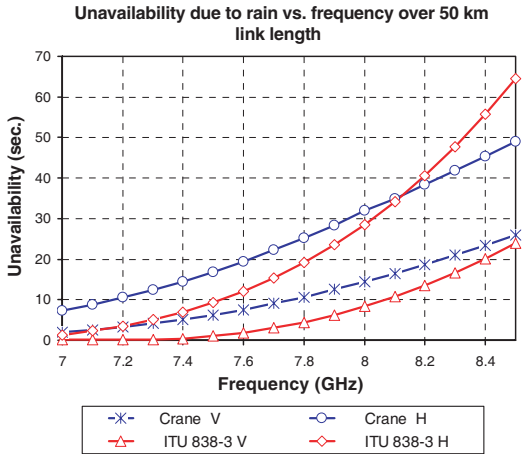

Figure 6: Annual unavailability due to rain as function of the operating frequency.

Table 2: Main parameters used for simulation.

Link	Link length (km)	Flat Fade Margin (dB)	Barnett-Vigants, C factor	ITU-R P. 530, K factor
1	70.00	41.52	0.25	1.24E-04
2	40.10	41.75	1.00	9.70E-05
3	22.30	40.66	3.29	1.55E-04
4	38.70	40.04	3.16	1.48E-04
5	60.30	43.63	0.25	1.11E-04
6	12.70	39.63	0.25	9.60E-05
7	82.30	45.93	0.52	1.41E-04
8	61.30	32.57	0.52	8.30E-05
9	70.10	41.19	0.25	1.06E-04

Table 3: Total bidirectional annual unavailability.

	Bidirectional annual unavailability with space and frequency diversity (sec.)		
Link	Barnett-Vigants, (Pathloss 4.0)	ITU-R P. 530-12 (MWLinkSim 1.0)	ITU improvement %
1	8.77	2.54	71.0%
2	5.15	0.81	84.3%
3*	6.42	6.64	−3.4%
4*	17.47	2.26	87.1%
5	2.20	0.57	74.1%
6	7.00	0.28	96.0%
7	1.28	3.12	−143.8%
8	352.39	43.58	87.6%
9	1.70	0.29	82.9%
The mean improvement % of ITU model over Barnett-Vigants model			48.4%

*ITU method is used without signature parameters

and the selective outage probability P_s. Then the two values are added together to obtain the total outage. The obtained results are also summarized in Table 3.

The analysis of overall performance in terms of worst month unavailability over the nine links shows clearly that the B-V model is oversized compared to the ITU model. This analysis confirms the results of step by step study made previously. The gain when the ITU model is used is rated at 50%.

4. CONCLUSION

The unavailability due to multipath and the unavailability due to rain are the two main phenomena we have studied in this paper. The results can be summarized as follows. The unavailability due to multipath is lower in the ITU model. In addition, the calculation procedure proposed by Recommendation ITU-R P. 530 provides extensive information on the criticality of the link and shows how some parameters affect microwave link design. For rain, the ITU model seems less severe for operating frequencies below 8 GHz while it is much more severe for frequencies above 8 GHz. In addition, the ITU model offers the possibility to take into account the combined effect of rain and wet snow (a phenomenon which may be interesting to consider in Quebec). The ongoing work is focused on in-situ measurements which will be compared to simulation results.

REFERENCES

1. Anderson, H. R., *Fixed Broadband Wireless System Design*, John Wiley & Sons, 2003.
2. International Telecommunication Union, "Propagation data and prediction methods required for the design of terrestrial line-of-sight systems," ITU-R P. 530-12, 2005.
3. Barnett, W. T., "Multipath propagation at 4, 6 and 11 GHz," *Bell System Technical Journal*, Vol. 51, No. 2, 311–361, Feb. 1972.
4. Agba, B. L., "Comparaison des modèles de propagation pour les liaisons hertziennes," IREQ-2008-0180 report, 2008.
5. Vigants, A., "Space-diversity engineering," *Bell System Technical Journal*, Vol. 54, No. 1, 103–142, Jan. 1975.
6. International Telecommunication Union, "Effects of multipath propagation on the design and operation of line-of-sight digital fixed wireless systems," ITU-R F-1093-2, 2006.
7. International Telecommunication Union, "Conversion of annual statistics to worst-month statistics," ITU-R P. 841-4, 2005.
8. Crane, R. K., "Prediction of attenuation by rain," *IEEE Transactions on Communications*, Vol. 28, No. 9, 1717–1732, Sep. 1980.
9. Crane, R. K., *Electromagnetic Wave Propagation through Rain*, John Wiley & Sons, New York, 1996.
10. International Telecommunication Union, "Specific attenuation model for rain for use in prediction methods," ITU-R P. 838-3, 2005.

Pecularities of the Total Electron Content and Their Reflections in the Ionospheric Model

O. A. Maltseva and T. Trinh Quang
Southern Federal University, Rostov-on-Don, Russia

Abstract— A number of wireless communication systems requires knowledge of real-time wave propagation conditions in the ionosphere. Widely used empirical ionospheric models provide median conditions and must be adapted to real-time parameters. One of the adaptation parameter is an experimental value of the critical frequency of the ionosphere foF2. It is shown that there are large discrepancies between model and experimental values of the total electron content in Chinese region after this adaptation. These discrepancies are due to differences between experimental and model values of τ where τ is an ionospheric slab thickness and can be determined by the correction factor $K(\tau)$. This factor is useful to get a global distribution of foF2 from TEC data and to fill gaps in foF2 data.

1. INTRODUCTION

The International Reference Ionosphere (IRI) model [1] is the most widely one. There are a number of modifications (e.g., IRI79, IRI90, IRI95, IRI2001, IRI2007) reflecting stages of its development. This model provides the global distribution of a number of parameters determining wave propagation conditions in the ionosphere: 1) the critical frequency foF2 (i.e., the maximum electron concentration NmF2), 2) the maximum height hmF2, 3) the propagation factor M3000F2, 4) N(h)-profile, 5) the total electron content (TEC). Four parameters are empirical. Parameter TEC is not empirical. It is calculated as an integral from the model N(h)-profile. In this case it is very important to compare model and experimental values of TEC. Earlier comprehensive comparisons of model and experimental TEC values were done by a lot of authors for the IRI2001 model. Essential differences were obtained. During last years the IRI2007 was developed. It includes two new options: IRI2007Bilitza, IRI2007NeQuick [2]. In the paper [3] the first option was called IRI-2007-cor, the second option — IRI-2007-NeQ. The given paper is devoted to comparison of experimental and model values of TEC. A specific attention is paid to comparison of TEC values adapted to real-time conditions with experimental data of foF2.

2. METHOD OF ANALYSES AND EXPERIMENTAL DATA

The total electron content is defined by $\mathrm{TEC} = \mathrm{NmF2} * \tau$ where NmF2 is the maximum electron density, $\tau = \mathrm{TEC/NmF2}$ is the ionospheric slab thickness. This definition indicates that discrepancies between experimental and model TEC values can be determined by means of $K(\mathrm{TEC}) = \mathrm{TEC(obs)/TEC(IRI2001)} = K(\mathrm{Nm}) * K(\tau)$, $K(\mathrm{Nm}) = \mathrm{NmF2(obs)/NmF2(IRI)}$, $K(\tau) = \tau(\mathrm{obs})/\tau(\mathrm{IRI2001})$. Correction factors of the IRI2007 model $K(\mathrm{cor}) = \mathrm{TECIRI2007(cor)/TEC(IRI2001)}$, $K(\mathrm{NeQ}) = \mathrm{TECIRI2007(NeQ)/TEC(IRI2001)}$ are used to compare results with experimental $K(\mathrm{TEC})$ values. The factor $K(\mathrm{TEC})$ estimates the difference between experimental and model TEC values. It is the experimental correction factor whose comparison with $K(\mathrm{cor})$ and $K(\mathrm{NeQ})$ allows to appreciate how these factors improve coincidence with experiment. The factor $K(\mathrm{Nm})$ is a contribution of discrepancies between experimental and model NmF2 values into $K(\mathrm{TEC})$. The factor $K(\tau)$ is a contribution of discrepancies between experimental and model τ. Parameter $\tau(\mathrm{obs})$ is the experimental value of τ. Adaptation of the model to experimental values of foF2 leads to $K(\mathrm{Nm}) = 1$. The residual difference is due to $K(\tau)$. Comparison was done for Chinese chain of stations: Beijing, Chongqing and Guangzhou. Data of foF2 were extracted from internet SPIDR system for January, April, October 2000 (data for July 2000 were absent) and October 2003. TEC data were extracted from global TEC maps provided by JPL (Jet Propulson Laboratory). Results are illustrated by diurnal, seasonal, latitudinal behavior of TEC and foF2. The attention was focused on real-time (RT) values. The factor $K(\tau)$ is used to get a global distribution of foF2 from TEC data and to fill gaps of foF2 data.

3. DIURNAL BEHAVIOR

Example of diurnal behavior differences is shown in Fig. 1. Left panels compare experimental and model TEC behavior for various stations and 3.04.2000. Curves "obs" belong to experimental

values. Curves "IRI" show model values. Curves "RT" give values adapted to experimental foF2 values that are presented in right panels (curves "obs") together with model values (curves "IRI"). Model values of foF2 preponderate experimental ones for Chongqing and experimental values preponderate model ones for Beijing. In any case discrepancies between RT and experimental TEC values remain large.

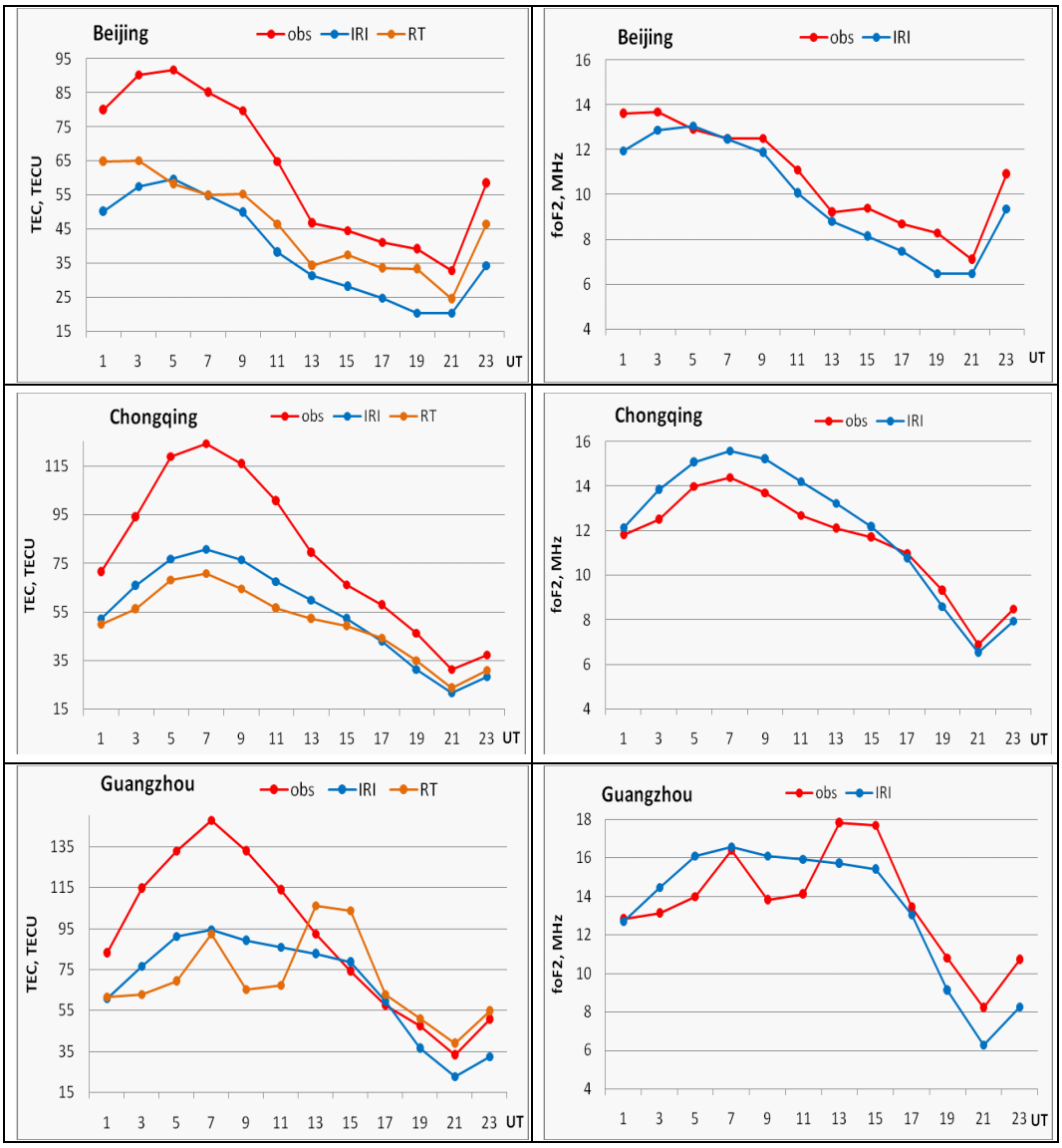

Figure 1: Diurnal behavior of TEC (left panels) and foF2 (right panel).

4. SEASONAL BEHAVIOR

Example of diurnal behavior differences is shown in Fig. 2. Left panels compare median diurnal dependencies for various months. Right panels present median correction factors. Factors $K(\mathrm{TEC})$, $K(\tau)$, $K(\mathrm{Nm})$ are larger than 1 and factors $K(\mathrm{cor})$, $K(\mathrm{NeQ})$ are lower than 1 for all months. Contribution of $K(\tau)$ into discrepancies of TEC are larger than contribution of $K(\mathrm{Nm})$ excluding the case when UT = 21 in January. Using experimental values of foF2 provides $K(\mathrm{Nm}) = 1$. If we knew $K(\tau)$ we could get values of foF2 close to experimental ones.

5. LATITUDINAL BEHAVIOR

Figure 3 gives an example of latitudinal dependencies for 3.04.2000, UT = 9. Left panel illustrates a large difference between experimental and model values of TEC. In Chinese area we had $K(\tau)$ for 3 stations and could get a regression equation with latitude φ. It was a linear equation ($K(\tau) = a*\varphi$).

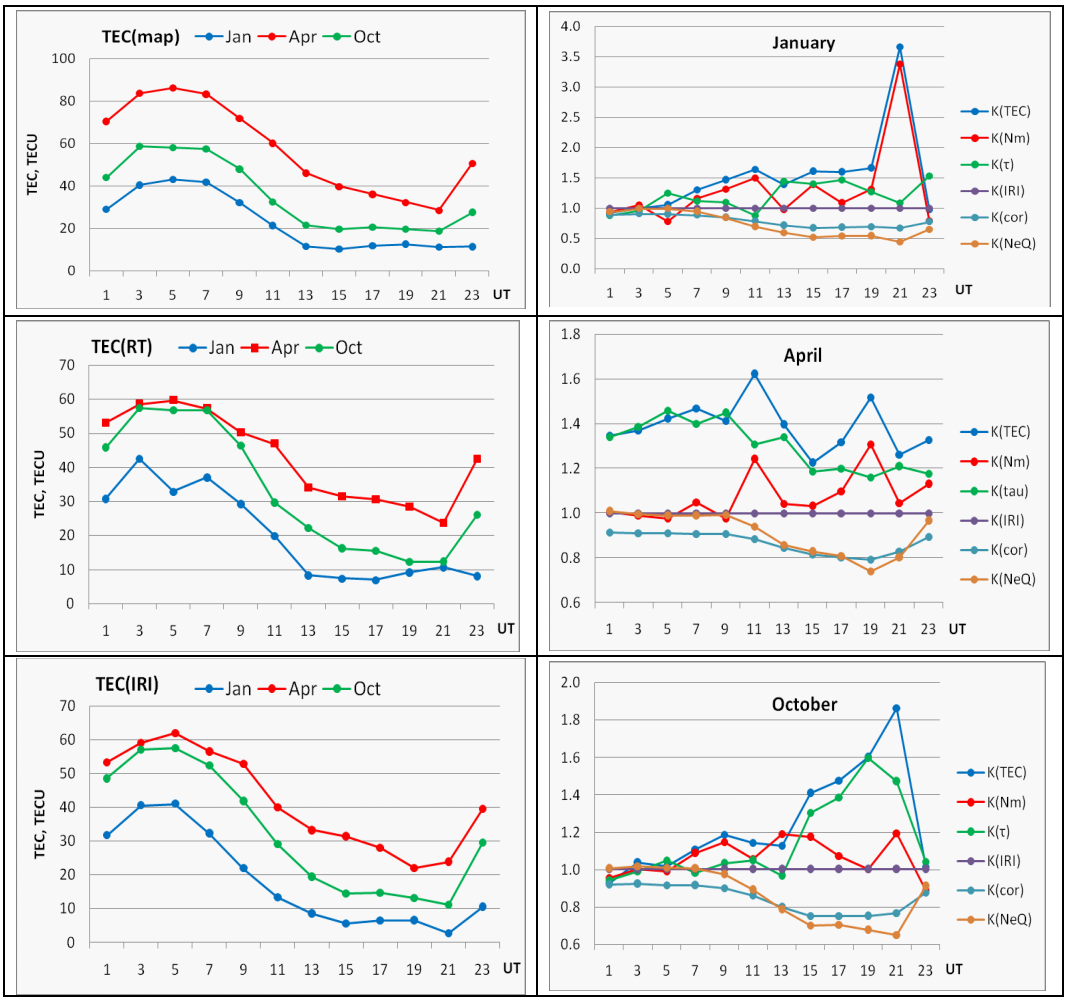

Figure 2: Seasonal behavior of median TEC (left panel) and correction factors (right panel) for various months.

This equation was used to get foF2(φ) behavior from TEC(φ) data. Model and calculated curves of foF2 are presented in right panel of Fig. 3. Adapted foF2 values can be lower than model ones despite large exceeding experimental TEC values over model ones.

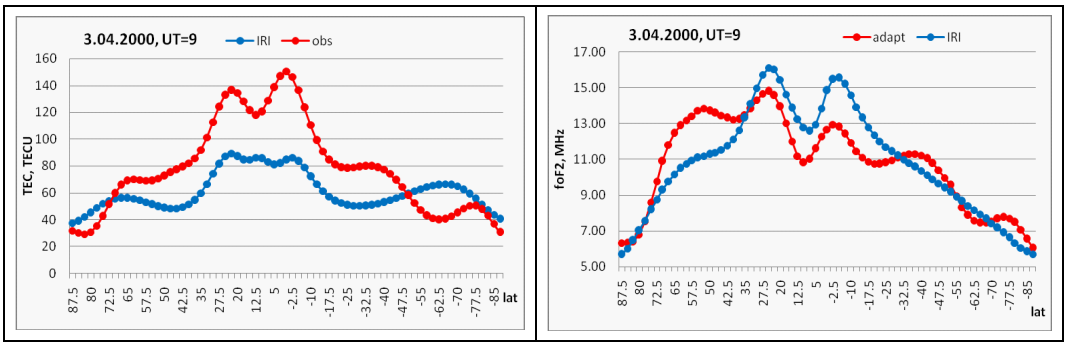

Figure 3: Latitudinal dependencies of TEC (left panel) and foF2 (right panel) for 3.04.2000, UT = 9.

6. USING THE FACTOR $K(\tau)$ FOR RECONSTRUCTION OF FOF2 DISTRIBUTION

This paragraph is devoted to using factor $K(\tau)$ to get foF2 values from TEC data. Sometimes continuous row of data can have gaps due to various reasons. It is shown that gaps can be filled using factor $K(\tau)$ and TEC data. This possibility is illustrated by Table 1 that shows average absolute

differences $|\Delta$foF2$|$ between experimental and model values of foF2. Column IRI2001 presents these differences for the IRI2001 model. Column $K(\tau)$ presents differences between experimental foF2 values and values calculated by using $K(\tau)$. Parameter N indicates number of available data.

The second example concerns reconstruction of foF2 distribution during period preceding the famous severe disturbance 31 October 2003. Data of foF2 of both stations are absent during 27 and 29 October. Fig. 4 shows experimental (28, 30, 31.10.2003) and adapted values (for 27, 29.10.2003). Full experimental data are presented for station Tashkent for comparison. Similar behavior is obvious.

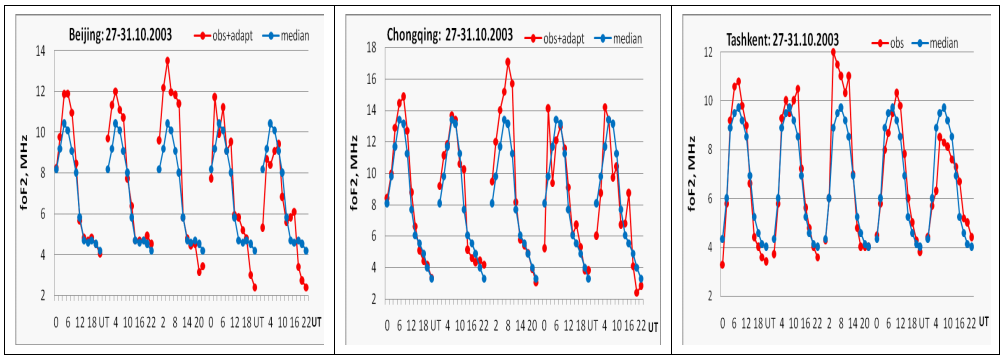

Figure 4: Illustration of reconstructed diurnal behavior for two stations Beijing and Chongqing during 27 and 29 October 2003. Full data for station Tashkent are given for comparison.

Table 1: Comparison of $|\Delta$foF2$|$ for the IRI2001 and using $K(\tau)$.

April 2000			$\|\Delta$foF2$\|$	
station	φ	N	IRI2001	$K(\tau)$
Beijing	40	13	0.58	0.34
Chongqing	29.5	9	0.86	0.63
Guangzhou	23.1	10	1.37	0.92

7. CONCLUSIONS

The IRI model plays a very important role providing long-term and operational (nearly RT) prediction of wave propagation conditions in the ionosphere. Using TEC data to get propagation conditions needs comparison of experimental and model values of TEC and methods to decrease discrepancies between them. Examples presented in this paper for Chinese region allows to do following conclusions. 1. Discrepancies between experimental and model values of TEC can be large. Using real time values of foF2 allows to decrease these discrepancies but residual differences remain large because the factor $K(\tau)$ is always larger than K(Nm). 2. Correction factors K(cor) and K(NeQ) of the IRI2007 model are always lower than 1. 3. Experimental values of $K(\tau)$ allows to get foF2 values from TEC data and fill gaps of data.

REFERENCES

1. Bilitza, D., "International reference ionosphere 2000," *Radio Sci.*, Vol. 36, No. 2, 261–275, 2001.
2. Bilitza, D., B. W. Reinisch, S. M. Radicella, S. Pulinets, T. Gulyaeva, and L. Triskova, "Improvements of the international reference ionosphere model for the topside electron density profile," *Radio Sci.*, Vol. 41, S5–S15, 2006.
3. Bilitza, D., "Evaluation of the IRI-2007 model options for topside electron density," *Adv. Space Res.*, Vol. 44, 701–706, 2009.

Research of the Effect of Electromagnetic Interference on Magnetic Sensors due to the Data Transmitting System of the Seismic Electromagnetic Satellite

Ye An[1], **Ping-Lian Wang**[1], **Ping Liu**[2], **Yu-Rong Liu**[1], **and Rui Yan**[3]

[1]Academy of Opto-Electronics, Chinese Academy of Sciences, Beijing 100190, China
[2]Dalian University of Technology, Dalian 116024, China
[3]Institute of Engineering Mechanics, China Earthquake Administration, Ha Erbin 150080, China

Abstract— This paper explores the effects of Electromagnetic Interference (EMI) on Magnetic Sensors due to The Data Transmitting System (DTS) in order to aid the system design of the Chinese first Seismic Electromagnetic Satellite. The research was focused by two ways including the EMC prediction between the DTS and the Magnetic sensors and the DTS's EMC test. The result of the research indicates that: the distance between the induction magnetometer and the power line of the DTS should be 1.2 m at least; and also the frequency flow and permanent magnetic materials should be designed properly in order to make the DTS and the sensors compatible.

1. INTRODUCTION

The main scientific objective of the Seismic Electromagnetic Satellite is to study the unusual perturbations about the space electric and magnetic field, which may be linked to seismic activity [1]. Some of the scientific payloads in the satellite, especially the Magnetic Sensors are very sensitive. Due to its high RF output power and high current characteristics, the DTS (The Data Transmitting System) radiates electromagnetic wave which is easy to result in the EMI (Electromagnetic Interference) effects on the Magnetic Sensors.

In this paper, according to the Chinese first Seismic Electromagnetic Satellite, we mainly focus on the possible effects of EMI on Magnetic Sensors due to the DTS. Additionally, the EMC test was performed on the DTS in order to validate the theoretic analysis. Finally some suggestions are given in order to make the DTS and the Magnetic sensors working compatibly.

2. THE DTS AND MAGNETIC SENSORS DESCRIPTION

At present, the Chinese first Seismic Electromagnetic Satellite is being designed but it has not been developed in project, so the specifications of the DTS and the sensors are not confirmed. In order to get the quantitative EMC prediction, the Magnetic Sensors characteristics referred to are mainly based on the Seismic Satellites that have been launched such as QUAKESAT and DEMETER. DTS consists of transmitter and the transmitting antenna. There are two main Magnetic Sensors: induction magnetometer and fluxgate magnetometer. Table 1 contains the key specifications of the DTS and the Magnetic Sensors.

3. EMC PREDICTION

The EMC prediction was focused by two ways including the interference from the DC power line of the DTS and the EM wave interference derived from the high RF output power.

There is the high current in-rush when the transmitter is turned on which may lead to radiant low frequency electromagnetic wave interference. In addition, there also exists conducted interference. The DC power supply block diagram of the satellite is shown in Fig. 1, which indicates the conducted interference path is that, it is transferred from the DTS's DC power line to the main bus, and then transferred to the Magnetic Sensors. But the EMC prediction about the conducted interference is based on the type of the DC/DC circuits, which is not confirmed yet, and so the conducted interference from the DC power line can not be analyzed here.

3.1. Radiation Interference from the DC Power Line

The power consumption of the DTS is 60 W and the power supply is +28 V, so the working current is 2.14 A. Generally speaking, the in-rush current when the DTS is powered on is about $5 \sim 10$ times more than the working current, and its duration is less than 2 ms. A function is used to

Table 1: Key specifications of the DTS and the Magnetic Sensors.

		Key Specifications
DTS	Transmitter	Frequency range: X-band; Output power: 20 W (continuous wave); Power consumption: 60 W; Power supply: +28 V; Symbol rate: 66 Mbps
	Transmitting Antenna	Frequency range: $f_0 \pm 60$ MHz; Gain: ≥ 6 dBi; Radiation pattern: earth-matched beam ($\pm 71^\circ$); Antenna polarization: right-hand polarized
Magnetic Sensors	Induction Magnetometer	Frequency range: 10 Hz $\sim$ 20 kHz; Sensitivity: 5×10^{-5} nT $\cdot$ Hz$^{-1/2}$ (2 kHz); Max. magnetic induction density at the sensor: 0.5 nT
	Fluxgate Magnetometer	Frequency range: DC $\sim$ 10 Hz; Range: $\pm$65000 nT; Resolution: 0.1 nT; Max. magnetic induction density at the sensor: 0.5 nT

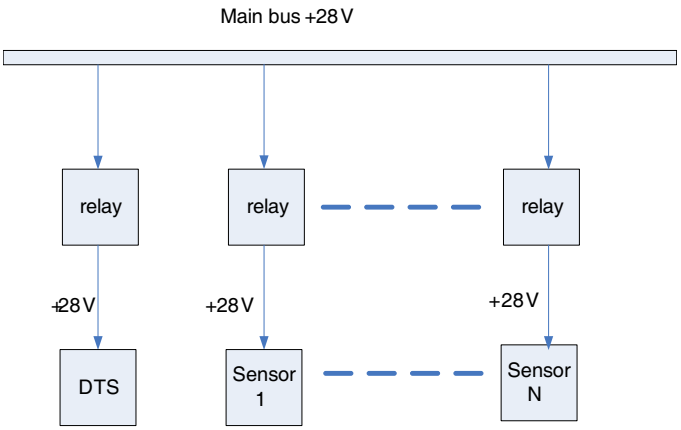

Figure 1: DC power supply block diagram.

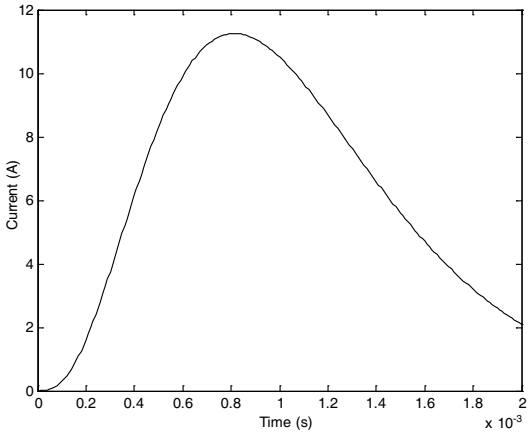

Figure 2: Simulated in-rush current curve.

simulate the in-rush current curve, with the duration time of 2 ms and the maximal in-rush current value of 10.71 A (5 times as much as the working current):

$$I(t) = At^3 \exp(-t/B) \tag{1}$$

where $A = 4.179711 \times 10^{11}$, $B = 2.7109 \times 10^{-4}$. The simulated in-rush current curve is shown is Fig. 2.

According to the simulation and calculation of electromagnetic emission of the DC power line when DTS is turned on, the EMC prediction results is outlined as follows:

1) Induction magnetometer: Based on the magnetic dipole model, during the frequency range 10 Hz $\sim$ 20 kHz, Fig. 3(a) shows the simulated magnetic induction density at the different distances of 0.4 m, 0.8 m, 1.2 m, 1.6 m and 2.0 m from the DTS DC power line respectively. From the simulation results, the distance must be more than 1.2 m between the induction magnetometer and the DC power line of the DTS in order to avoid the interference.

2) Fluxgate magnetometer: Magnetic dipole model is also available to calculate the magnetic induction density at different distances during the frequency rang DC $\sim$ 10 Hz. The simulation profile is shown in Fig. 3(b).

From the simulation results, the max magnetic induction density is 6.4×10^{-4} nT < 0.1 nT, so the fluxgate magnetometer can not be disturbed by the DC power line of the DTS with the distance more than 0.4 m.

3.2. Interference from the EM Wave Propagation

Based on the preliminary satellite configuration shown in Fig. 4, the induction magnetometer sensor and the fluxgate magnetometer sensor are located in the far field area of the transmitter antenna. The magnetic induction density distribution, which is brought by the transmitting antenna, at the location of the sensors can be calculated from the antenna radiation pattern and free space loss. At the location of the induction magnetometer sensor the magnetic induction density (B) is $0.1058\,\mathrm{nT} < 0.5\,\mathrm{nT}$; At the location of the fluxgate magnetometer sensor $B = 0.0798\,\mathrm{nT} < 0.5\,\mathrm{nT}$. Both of the magnetic sensors can not be interfered by the DTS Radiant EM wave.

3.3. Other Interferences

In addition to the interferences mentioned above, there are also the following interference possibilities:

1) The harmonic of the DTS base-band signals and crystal oscillators may bring interference due to the bad shielding. 2) Permanent magnetic materials within the DTS may result in permanent magnetic interference on the magnetic sensors. Both of the two possible factors should be considered by the designers to avoid the potential interferences.

4. DTS EMC TEST

The EMC test (Standard:GJB151A-97/GJB152A-97) was performed on a X-band Transmitter with the following items: CE101 (25 Hz ∼ 10 kHz conducted emissions, power leads), CE102 (10 kHz∼

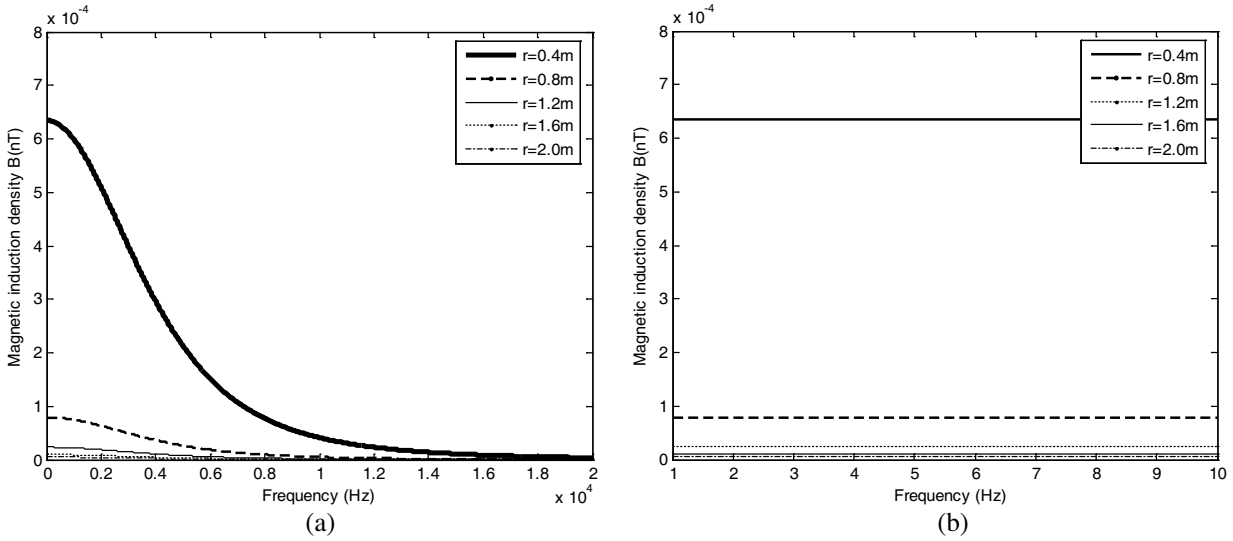

Figure 3: Simulated Magnetic induction density. (a) In the frequency range of Induction magnetometer. (b) In the frequency range of Fluxgate magnetometer.

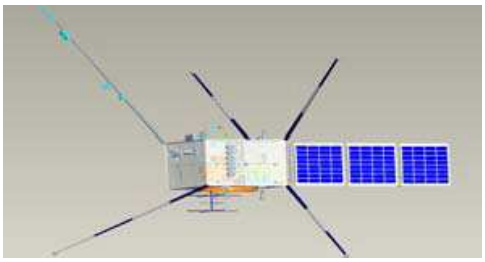

Figure 4: Satellite configuration.

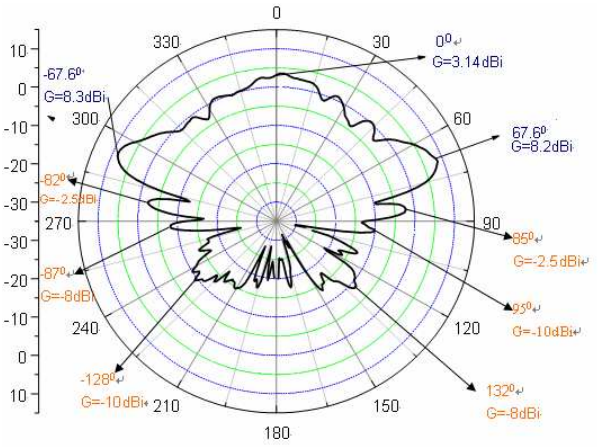

Figure 5: Transmitting antenna radiation pattern.

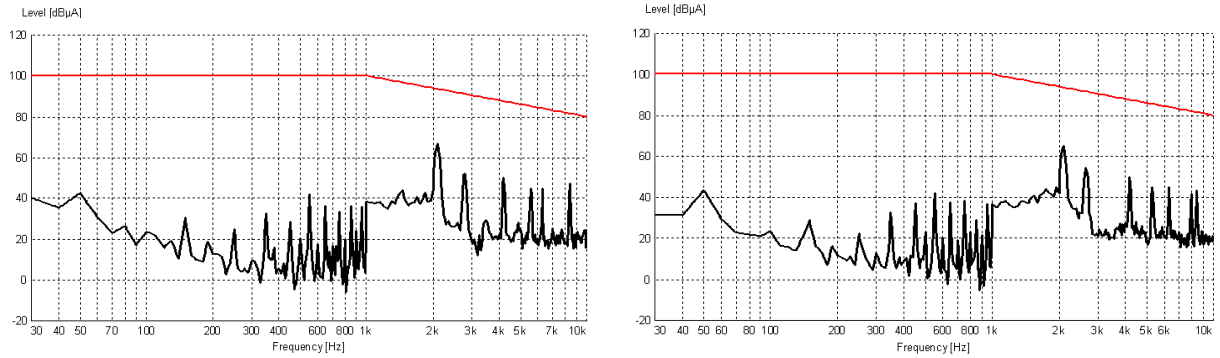

Figure 6: Measured CE101. (a) Main bus. (b) Return bus.

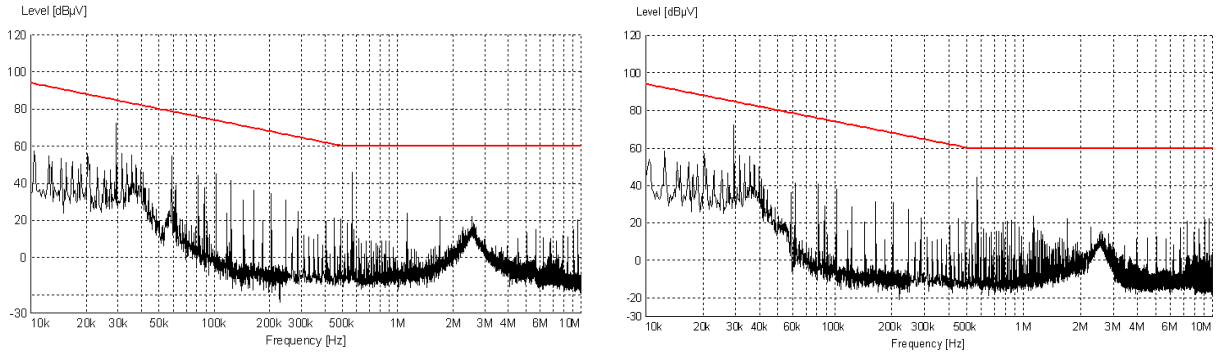

Figure 7: Measured CE102. (a) Main bus. (b) Return bus.

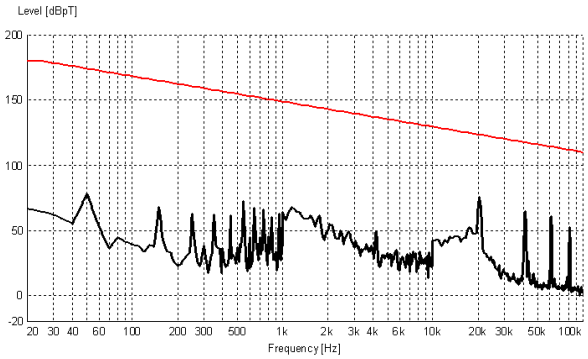

Figure 8: Measured RE101.

10 MHz conducted emissions, power leads), RE101 (25 Hz ∼ 100 kHz Radiated emissions, magnetic field) [2]. The tested profiles are showed in Fig. 6 ∼ Fig. 8 [3]. The measured results meet the requirements

5. CONCLUSIONS

Theoretical analysis and experiments tests have been presented for the effects of EMI on Magnetic Sensors due to the DTS. The main purpose of the research is to offer active suggestions for the system design of the Chinese first Seismic Electromagnetic Satellite.

ACKNOWLEDGMENT

The authors would like to thank the R&D Special Fund for Public Welfare Industry: 200808034, for sponsoring this work.

REFERENCES

1. Pulinets, S. and B. Kirill, *Ionospheric Precursors of Earthquakes*, Springer, Berlin, New York, 2003.
2. GJB151A, Electromagnetic emission and susceptibility requirements for military equipment and subsystems, 1997.
3. GJB152A, Measurement of electromagnetic emission and susceptibility for military equipment and subsystems, 1997.
4. Sarkar, S., A. K. Gwal, and M. Parrot, "Ionospheric variations observed by the DEMETER satellite in the mid-latitude region during strong earthquakes," *Journal of Atmospheric and Solar-terrestrial Physics*, Vol. 69, No. 13, 25–31, 2007.

Charge Continuity Equation in the Gravitational Field

Ying Weng[1] and Zi-Hua Weng[2]

[1]College of Chemistry & Chemical Engineering, Xiamen University, Xiamen 361005, China
[2]School of Physics and Mechanical & Electrical Engineering, Xiamen University, Xiamen 361005, China

Abstract— It is proposed a theoretical method with the quaternions to rephrase the charge continuity equation from the linear momentum, in the electromagnetic field with gravitational field. The paper claims that the gravitational strength and velocity both have an impact on the charge continuity equation. In the gravitational and electromagnetic fields, the charge continuity equation will change with the gravitational strength and linear momentum etc. The deduction can explain why the gravitational strength has an influence on the anomalous charge transport about the charge continuity equation in the crystal and electrolytes etc.

1. INTRODUCTION

The quaternion was first used by J. C. Maxwell in 1861 to describe the properties of electromagnetic field [1]. Similarly, the algebra of octonions [2] can be used to rephrase the features of gravitational field and electromagnetic field simultaneously, although these two kinds of fields are quite different. By means of the scalar invariant of octonions, we find that both of electromagnetic strength and gravitational strength have an influence on the charge continuity equation.

W. Watson in 1746 and B. Franklin in 1747 developed independently the conservation of charge and the charge continuity equation. The latter is similar to the mass continuity equation [3], and is quite significant in the physics [4], with numerous applications in the electromagnetic theory and the materials science [5] etc. Rephrasing with the algebra of octonions [6], we obtain the charge continuity equation in the case for coexistence of electromagnetic field and gravitational field.

The charge continuity equation was limited to a typical case of weak electromagnetic strength. In the octonion space, the definition of charge continuity equation can be extended through to the case for coexistence of electromagnetic field and gravitational field. With the features of the octonion [7], we study a few impact factors of the charge continuity equation in the electromagnetic field and gravitational field, including the velocity and field strengths.

The results state that either gravitational strength or electromagnetic strength has an influence on the charge continuity equation, although these impacts are usually tiny when the field strengths are weak. And then, the charge continuity equation is conserved in most cases. However, when the electromagnetic field and gravitational field are strong enough, the field strengths will affect the charge continuity equation obviously in the crystal and electrolytes etc.

2. OCTONION TRANSFORMATION

The physical quantities in the gravitational field and the electromagnetic field can be illustrated by the quaternions, although their definitions will be extended in some aspects.

In the quaternion space for gravitational field, the basis vector $\mathbb{E}_g = (i_0, i_1, i_2, i_3)$, with $i_0 = 1$. And that the radius vector $\mathbb{R}_g$ and velocity $\mathbb{V}_g$ are follows

$$\mathbb{R}_g = \Sigma(r_i i_i), \quad \mathbb{V}_g = \Sigma(v_i i_i), \tag{1}$$

where $r_0 = v_0 t$; v_0 is the speed of light; t denotes the time. $i = 0, 1, 2, 3$; $j = 1, 2, 3$.

In the quaternion space for electromagnetic field, the basis vector $\mathbb{E}_e = (I_0, I_1, I_2, I_3)$, with $\mathbb{E}_e = \mathbb{E}_g \circ I_0$. The radius vector $\mathbb{R}_e$ and velocity $\mathbb{V}_e$ are

$$\mathbb{R}_e = \Sigma(R_i I_i), \quad \mathbb{V}_e = \Sigma(V_i I_i), \tag{2}$$

where $R_0 = V_0 T$; V_0 is the speed of light-like; T is a time-like quantity. The symbol $\circ$ denotes the octonion multiplication.

Two quaternion spaces combine together to become one octonion space. In the octonion space, the radius vector $\mathbb{R}$ and velocity $\mathbb{V}$ are follows

$$\mathbb{R} = \Sigma(r_i i_i) + \Sigma(R_i I_i), \tag{3}$$
$$\mathbb{V} = \Sigma(v_i i_i) + \Sigma(V_i I_i), \tag{4}$$

meanwhile the basis vector $\mathbb{E}$ of octonion space is

$$\mathbb{E} = (1,\, i_1,\, i_2,\, i_3,\, I_0,\, I_1,\, I_2,\, I_3). \tag{5}$$

In some special cases, the electric charge is combined with the mass to become the electron or the proton etc. And then $R_iI_i = r_ii_i \circ I_0$ and $V_iI_i = v_ii_i \circ I_0$.

The octonion physical quantity $\mathbb{D}(d_0,\, d_1,\, d_2,\, d_3,\, D_0,\, D_1,\, D_2,\, D_3)$ is defined as follows

$$\mathbb{D} = \Sigma(d_ii_i) + \Sigma(D_iI_i), \tag{6}$$

where d_i and D_i are all real.

When the octonion coordinate system $\mathbb{O}(i_0,\, i_1,\, i_2,\, i_3,\, I_0,\, I_1,\, I_2,\, I_3)$ is transformed into one new coordinate system $\mathbb{O}'(i'_0,\, i'_1,\, i'_2,\, i'_3,\, I'_0,\, I'_1,\, I'_2,\, I'_3)$, the physical quantity $\mathbb{D}$ will be become one octonion physical quantity $\mathbb{D}'(d'_0,\, d'_1,\, d'_2,\, d'_3,\, D'_0,\, D'_1,\, D'_2,\, D'_3)$.

$$\mathbb{D}' = \mathbb{K}^* \circ \mathbb{D} \circ \mathbb{K}, \tag{7}$$

where $\mathbb{K}$ is the octonion, and $\mathbb{K}^* \circ \mathbb{K} = 1$; $*$ denotes the conjugate of octonion. $i'_0 = 1$.

Therefore, we obtain

$$d_0 = d'_0. \tag{8}$$

In the above equation, the scalar part is one and the same during the octonion coordinates are transforming. Some scalar invariants of electromagnetic field will be obtained from the features of octonion transformation.

Table 1: The octonion multiplication table.

	1	i_1	i_2	i_3	I_0	I_1	I_2	I_3
1	1	i_1	i_2	i_3	I_0	I_1	I_2	I_3
i_1	i_1	-1	i_3	$-i_2$	I_1	$-I_0$	$-I_3$	I_2
i_2	i_2	$-i_3$	-1	i_1	I_2	I_3	$-I_0$	$-I_1$
i_3	i_3	i_2	$-i_1$	-1	I_3	$-I_2$	I_1	$-I_0$
I_0	I_0	$-I_1$	$-I_2$	$-I_3$	-1	i_1	i_2	i_3
I_1	I_1	I_0	$-I_3$	I_2	$-i_1$	-1	$-i_3$	i_2
I_2	I_2	I_3	I_0	$-I_1$	$-i_2$	i_3	-1	$-i_1$
I_3	I_3	$-I_2$	I_1	I_0	$-i_3$	$-i_2$	i_1	-1

3. POTENTIAL AND STRENGTH

The gravitational potential is $\mathbb{A}_g = \Sigma(a_ii_i)$, and the electromagnetic potential is $\mathbb{A}_e = \Sigma(A_iI_i)$. In the octonion space, the gravitational potential and electromagnetic potential comprise the field potential $\mathbb{A}$, with k_{eg} being the coefficient,

$$\mathbb{A} = \mathbb{A}_g + k_{eg}\mathbb{A}_e. \tag{9}$$

When the coordinate system is transformed from the $\mathbb{O}$ to the $\mathbb{O}'$, we obtain the gravitational potential $\mathbb{A}'_g = \Sigma(a'_ii'_i)$, electromagnetic potential $\mathbb{A}'_e = \Sigma(A'_iI'_i)$, and the octonion field potential $\mathbb{A}' = \Sigma(a'_ii'_i) + k_{eg}\Sigma(A'_iI'_i)$. Therefore, we obtain an inference of the invariable scalar potential of gravitational field by Eq. (8),

$$a_0 = a'_0. \tag{10}$$

The field strength, $\mathbb{B} = \Sigma(b_ii_i) + k_{eg}\Sigma(B_iI_i)$, consists of the gravitational strength, $\mathbb{B}_g = \Sigma(b_ii_i)$, and the electromagnetic strength, $\mathbb{B}_e = \Sigma(B_iI_i)$.

$$\mathbb{B} = \Diamond \circ \mathbb{A} = \mathbb{B}_g + k_{eg}\mathbb{B}_e, \tag{11}$$

where the operator $\Diamond = \partial_0 + i_1\partial_1 + i_2\partial_2 + i_3\partial_3$.

In the above, we choose the following gauge conditions to simplify succeeding calculation,

$$b_0 = \partial_0 a_0 + \nabla \cdot a = 0, \tag{12}$$
$$B_0 = \partial_0 A_0 + \nabla \cdot A = 0, \tag{13}$$

where $a = \Sigma(a_j i_j)$; $A = \Sigma(A_j i_j)$; $\nabla = \Sigma(i_j \partial_j)$.

The gravitational strength $\mathbb{B}_g$ includes two parts,

$$g/c = \partial_0 a + \nabla a_0, \tag{14}$$
$$b = \nabla \times a, \tag{15}$$

meanwhile, the electromagnetic strength $\mathbb{B}_e$ involves two components,

$$E/c = (\partial_0 A + \nabla A_0) \circ I_0, \tag{16}$$
$$B = -(\nabla \times A) \circ I_0. \tag{17}$$

When the coordinate system $\mathbb{O}$ is transformed into the $\mathbb{O}'$, we have the octonion field strength $\mathbb{B}' = \Sigma(b'_i i'_i) + k_{eg}\Sigma(B'_i I'_i)$ from Eq. (7). And then, we have an inference of the invariable scalar strength of gravitational field by Eq. (8),

$$b_0 = b'_0. \tag{18}$$

The above means that the scalar potential and the scalar strength of gravitational field are the invariants in the octonion space, although the latter is equal to zero from Eq. (12).

4. SPEED OF LIGHT

In the octonion space, when the coordinate system $\mathbb{O}$ is transformed into the $\mathbb{O}'$, the new velocity $\mathbb{V}'$ from Eqs. (4) and (7) is,

$$\mathbb{V}' = \Sigma\left(v'_i i'_i\right) + \Sigma\left(V'_i I'_i\right). \tag{19}$$

From the above and Eq. (8), it concludes that the speed of light, v_0, will remain the same,

$$v_0 = v'_0. \tag{20}$$

The above states that the speed of light, v_0, keeps unchanged in the electromagnetic field and gravitational field during the octonion coordinate transformation.

In the octonion space, a new physical quantity $\mathbb{V}_q$ can be defined from Eq. (4),

$$\mathbb{V}_q = \mathbb{V} \circ I_0^* = \Sigma(V_i i_i) - \Sigma(v_i I_i). \tag{21}$$

By Eq. (7), we have the octonion physical quantity, $\mathbb{V}'_q = \Sigma(V'_i i'_i) - \Sigma(v'_i I'_i)$, when the coordinate system is transformed. Under the transformation, the scalar part of $\mathbb{V}_q$ keeps unchanged,

$$V_0 = V'_0. \tag{22}$$

The above means that the speed of light-like, V_0, will remain the same in the electromagnetic and gravitational fields during the octonion coordinate transformation.

Comparing Eq. (4) with Eq. (21), we find that the invariable speed of light equation Eq. (20) and invariable speed of light-like equation Eq. (22) can't be effective at the same time. This states that they will not be validated simultaneously.

5. CONSERVATION OF CHARGE

The linear momentum density $\mathbb{S}_g = m\mathbb{V}_g$ is the source for gravitational field, and the electric current density $\mathbb{S}_e = q\mathbb{V}_g \circ I_0$ is that for electromagnetic field. And they can be combined together to become the field source $\mathbb{S}$ as follows,

$$\mu\mathbb{S} = -(\mathbb{B}/v_0 + \Diamond)^* \circ \mathbb{B} = \mu_g \mathbb{S}_g + k_{eg}\mu_e \mathbb{S}_e - \mathbb{B}^* \circ \mathbb{B}/v_0, \tag{23}$$

where μ is the coefficient; μ_e is the electromagnetic constant; $\mu_g = 4\pi G/v_0^2$ is a coefficient, and G is the gravitational constant; $k_{eg}^2 = \mu_g/\mu_e$. And the field energy density is,

$$\mathbb{B}^* \circ \mathbb{B}/\mu_g = \mathbb{B}_g^* \circ \mathbb{B}_g/\mu_g + \mathbb{B}_e^* \circ \mathbb{B}_e/\mu_e. \tag{24}$$

In the octonion space, the linear momentum density $\mathbb{P}$ is,

$$\mathbb{P} = \mu\mathbb{S}/\mu_g = \widehat{m}v_0 + \Sigma(mv_j i_j) + \Sigma(MV_i I_i), \tag{25}$$

where the gravitational mass density $\widehat{m} = m + \triangle m$; $\triangle m = -(\mathbb{B}^* \circ \mathbb{B}/\mu_g)/v_0^2$; m is the inertial mass density. q is the electric charge density; $M = k_{eg}\mu_e q/\mu_g$.

A new physical quantity $\mathbb{P}_q$ can be defined from the above,

$$\mathbb{P}_q = \mathbb{P} \circ I_0^* = MV_0 + \Sigma(MV_j i_j) - \{\widehat{m}v_0 I_0 + \Sigma(mv_j I_j)\}. \tag{26}$$

When the octonion coordinate system $\mathbb{O}$ is transformed into one new coordinate system $\mathbb{O}'$, we have the linear momentum density, $\mathbb{P}'_q = M'V'_0 + \Sigma(M'V'_j i'_j) - \widehat{m}'v'_0 I'_0 - \Sigma(m'v'_j I'_j)$ from the $\mathbb{P}_q$ by Eq. (7). In the coordinate system $\mathbb{O}'$, the scalar quantity is $M' = k_{eg}\mu_e q'/\mu_g$, with q' being the electric charge density. Under the coordinate transformation, the scalar part, $P_0 = MV_0$, of linear momentum density $\mathbb{P}_q$ remains unchanged by Eq. (8),

$$MV_0 = M'V'_0. \tag{27}$$

With Eq. (22) and the above, the conservation of charge can be rewritten as follows,

$$M = M'. \tag{28}$$

Because the scalar parts, M and M', are in direct proportion to the electric charge density, q and q', respectively. Further the above can be reduced to,

$$q = q'. \tag{29}$$

The above states that the electric charge density keeps unchanged. The above also means that if we emphasize the definitions of velocity and of linear momentum, the electric charge density will keep the same, under the octonion coordinate transformation in the case for coexistence of electromagnetic field and gravitational field.

6. CHARGE CONTINUITY EQUATION

In the octonion space, the applied force density is,

$$\mathbb{F} = v_0(\mathbb{B}/v_0 + \Diamond)^* \circ \mathbb{P} = \Sigma(f_i i_i) + \Sigma(F_i I_i), \tag{30}$$

where $F_0 = v_0\partial P_0/\partial r_0 + v_0\Sigma(\partial P_j/\partial r_j) + \Sigma(b_j P_j - B_j p_j)$; $p_0 = \widehat{m}v_0$, $p_j = mv_j$; $P_i = MV_i$.

A new physical quantity $\mathbb{F}_q$ can be defined from the above,

$$\mathbb{F}_q = \mathbb{F} \circ I_0^* = F_0 + \Sigma(F_j i_j) - \Sigma(f_i I_i). \tag{31}$$

When the coordinate system $\mathbb{O}$ is transformed to $\mathbb{O}'$, we have some octonion physical quantities in $\mathbb{O}'$, such as the applied force density $\mathbb{F}' = \Sigma(f'_i i'_i) + \Sigma(F'_i I'_i)$, radius vector $\mathbb{R}' = \Sigma(r'_i i'_i) + \Sigma(R'_i I'_i)$, linear momentum density $\mathbb{P}' = \Sigma(p'_i i'_i) + \Sigma(P'_i I'_i)$, and field strength $\mathbb{B}' = \Sigma(b'_i i'_i) + \Sigma(B'_i I'_i)$, with the gauge equations $b'_0 = B'_0 = 0$. Under the octonion coordinate transformation, the scalar part F_0 of physical quantity $\mathbb{F}_q$ keeps unchanged by Eq. (8),

$$F_0 = F'_0. \tag{32}$$

When the right side is equal to zero in the above, we have the charge continuity equation in the case for coexistence of gravitational field and electromagnetic field,

$$\partial P_0/\partial r_0 + \Sigma(\partial P_j/\partial r_j) + \Sigma(b_j P_j - B_j p_j)/v_0 = 0. \tag{33}$$

When either the electromagnetic strength B_j or the linear momentum p_j can be neglect, the above can be reduced to,

$$\partial P_0/\partial r_0 + \Sigma(\partial P_j/\partial r_j) + \Sigma(b_j P_j)/v_0 = 0. \tag{34}$$

Further, if $\Sigma(b_j P_j - B_j p_j) = 0$ in Eq. (33), the equation will be reduced to,

$$\partial M/\partial t + \Sigma(\partial P_j/\partial r_j) = 0. \tag{35}$$

The above states that the gravitational strength and electromagnetic strength both have one small influence on the charge continuity equation, although the $\Sigma(b_j P_j - B_j p_j)/v_0$ is usually very tiny when the fields are weak. The charge continuity equation is the invariant under the octonion coordinate transformation etc, while the definition of linear momentum density has to be extended in the gravitational field and electromagnetic field.

Table 2: The definitions and related invariants of physical quantities in the octonion space.

definition	invariant	conservation
$\mathbb{V} \circ I_0^*$	$V_0 = V_0'$	invariable speed of light-like
$\mathbb{A} \circ I_0^*$	$A_0 = A_0'$	invariable electromagnetic scalar potential
$\mathbb{B} \circ I_0^*$	$B_0 = B_0'$	invariable electromagnetic gauge
$\mathbb{P} \circ I_0^*$	$P_0 = P_0'$	conservation of charge
$\mathbb{F} \circ I_0^*$	$F_0 = F_0'$	charge continuity equation

7. CONCLUSION

By means of the linear momentum, quaternion operator, and field strength, we have inferences about the charge continuity equation in the gravitational and electromagnetic fields. The charge continuity equation will vary in the strong gravitational field, and has a tiny deviation from the charge continuity equation described with vector terminology. In the gravitational and electromagnetic fields, this states that the charge continuity equation will change with the gravitational strength, electromagnetic strength, linear momentum, electric current, and the speed of light. The deduction can explain why the field strength has an impact on the anomalous charge transport about the charge continuity equation in the crystal and electrolytes etc.

It should be noted that the study for the charge continuity equation examined only one simple case of weak field strength under the octonion coordinate transformation. Despite its preliminary characteristics, this study can clearly indicate the charge continuity equation is an invariant and is only one simple inference due to the low velocity and weak strengths in the electromagnetic field and gravitational field. For the future studies, the paper will concentrate on only some predictions about the charge continuity equation in the high speed and strong gravitational strength.

ACKNOWLEDGMENT

This project was supported partially by the National Natural Science Foundation of China under grant number 60677039.

REFERENCES

1. Maxwell, J. C., *A Treatise on Electricity and Magnetism*, Dover Publications Inc., New York, 1954.
2. Cayley, A., *The Collected Mathematical Papers*, Johnson Reprint Co., New York, 1963.
3. Weng, Y. and Z.-H. Weng, "Mass continuity equation in the electromagnetic field," *PIERS Proceedings*, 900–903, Moscow, Russia, August 18–21, 2009.
4. Biel, B., X. Blase, F. Triozon, and S. Roche, "Anomalous doping effects on charge transport in graphene nanoribbons," *Physical Review Letters*, Vol. 102, No. 9, 096803, 2009.
5. Rosso, L. and M. E. Tuckerman, "Direct evidence of an anomalous charge transport mechanism in ammonium perchlorate crystal in an ammonia-rich atmosphere from first-principles molecular dynamics," *Solid State Ionics*, Vol. 161, No. 3, 219–229, 2003.
6. Cawagas, R. E., "Loops embedded in generalized Cayley algebras of dimension 2^r, $r \geq 2$," *International Journal of Mathematics and Mathematical Sciences*, Vol. 28, No. 3, 181–187, 2001.
7. Bisht, P. S., B. Pandey, and O. P. S. Negi, "Interpretations of octonion wave equations," *Fizika B*, Vol. 17, No. 1, 405–428, 2008.

Pyroelectric Properties of the Sr-doped Ferroelectric Barium Iron Niobate

S. B. Bajaj[1], **R. L. Raibagkar**[2], **and G. N. Shinde**[3]

[1]PG Department and Research Center in Physics and Electronics, JES College
Jalna 431203, India
[2]Department of Post Graduate Studies and Research in Materials Science, Gulbarga University
Gulbarga 585106, India
[3]Indira Gandhi College, CIDCO, Nanded 431603, India

Abstract— Ceramic material showing ferroelectric behaviour are being used in many optics and electro-optics application. A large number of applications of ferroelectric ceramics also exploit properties that are an indirect consequence of ferroelectricity, such as dielectric, piezoelectric and electro-optic properties. Ferroelectric relxors with high Curie temperature have been prepared by usual ceramic technique. All the samples of $(Ba_{1-x}Sr_x)(Fe_{0.5}Nb_{0.5})O_3$ [BSFN] were characterized at room temperature by X-Ray diffraction using Cu-Ka radiation and found to have single phase and cubic structure. Pyroelectric measurements were carried out in the temperature range 25°C to 400°C. The pyroelectric prperties of Sr-doped ferroelectric BSFN and their solid solutions were investigated in the temperature range covering their transition points. In these ceramics, a peak in pyroelectric currents and coefficients were observed at Curie temperatures. These Curie temperatures are consistent with that investigated in dielectric and hysteresis property. It is observed that the peak value of current and coefficient changes with Sr-concentration.

1. INTRODUCTION

In ferroelectric ceramics, a large number of pure and complex oxides having a perovskite structure were studied [1–4] due to their industrial and academic intrest. Moreover, ferroelectric materials whether they are single crystals or poled spontaneous polarization (P_s) of polar materials. Because P_s falls to zero at the Curie point, ferroelectric materials are likely to exhibit high pyroelectric coefficents just below their transition temperatures.

According to [5], the primary pyroelectric effect is the polarization of dielectrics as a function of temperature [6] devised a dynamic method for the study of pyroelectric effect insulator barium titanate [7] studied the temperature dependence of pyroelectriccurret insulator sodium nitret. A direct method for measuring pyroelectric coefficents and application to a nanosecond response time detector was reported by [8, 9] discussed the dielectricand pyroelectric properties of the single crystals of lead barium niobate at low temperature. the growing intrest insulator pyroelectric effect evidenced insulator recent years insulator connection with its use insulator the design of fast, sensetive thermal radiation detectors, which has stimulated research aimed at synthesis of new pyroelectric materials and study of their characteristics features. An attempt of this paper is to report the pyroelectric effect observed insulator Sr-doped barium iron niobate.

2. EXPERIMENTAL DETAILS

Perovskite compounds with the chemical formula $(Ba_{1-x}Sr_x)(Fe_{0.5}Nb_{0.5})O_3$ [BSFN] [$X = 0, 0.2, 0.4$, 0.5 and 0.8] were prepared from appropriate oxides namely, BaO, SrO, Fe_2O_3 and Nb_2O_5 by solid-state reaction thechnique [10]. They were heated insulator air for 12 hours at 950°C. this thermal cycle was repeated three times with intermediate grinding. The samples were then mounted between the rigid electrodes of the sample holder after coating with silver. The pyroelecrtic current (i) which results due to surface charge carries developed on constant heating (or cooling) of sample was recorded. The pyroelectric coefficient (p) was obtained using the relation [7],

$$p = i/a * T \tag{1}$$

where T is heating (or cooling) rate and a is the surface area of the pellet.

Spontaneous polarization Ps was estimated from the equation,

$$\mathrm{Ps} = p * dT \tag{2}$$

where dT is the change insulator temperature.

3. RESULT AND DISCUSSION

X-ray diffraction patterns of BSFN at room temperature showed that all the samples have single phase having cubic structure. The pyroelectricproperties of BSFN and their solid solution were investigated insulator the range 25°C to 400°C. The temperature dependance of pyroelecrtic current and pyroelectric coefficient for all the ferroelelcrtic ceramics materials are shown insulator Figures 1 and 2, respectively.

It is evident from Figures 1 and 2 that, the materials showed peak value insulator pyroelecrtic-current and pyroelectric coefficent at their Curie temperature. Figure 3 depicts the temperature depemdance of Ps obtaind from pyroelecrtic measurements. The ferroelecrtic Curie temperatures are good agreement with that investigated by hysteresis loop method and dielectric measurementes. The value of pyroelectric cureent and pyroelectric coefficent varies with Sr-doped concentration as seen from Figures 2 and 3.

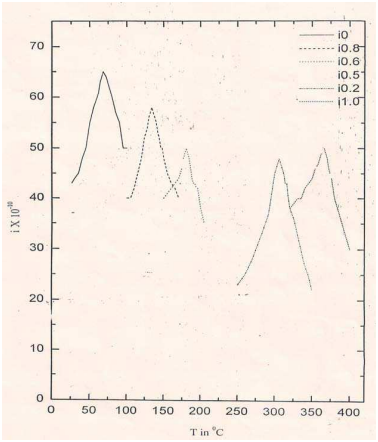

Figure 1: Temperature dependance of pyroelectric current of $(Ba_{1-x}Srx_x)$ $(Fe_{05}Nb_{0.5})O_3$.

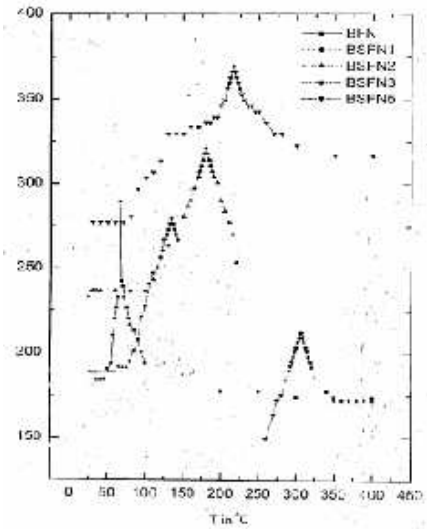

Figure 2: Temperature dependance of pyroelectric Coefficient of $(Ba_{1-x}Srx_x)$ $(Fe_{0.5}Nb_{0.5})O_3$.

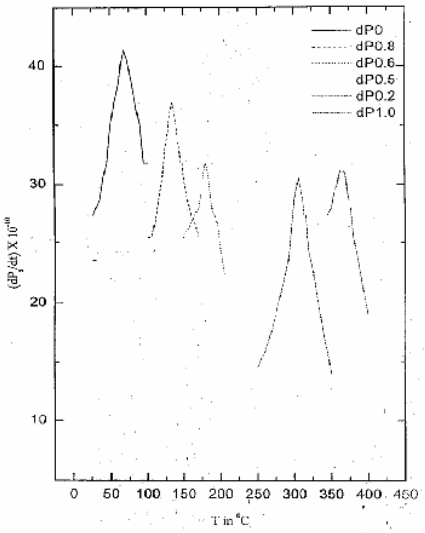

Figure 3: Temperature dependance of spontaneous polarization obtained from pyroelectric measurements for $(Ba_{1-x}Srx_x)$ $(Fe_{0.5}Nb_{0.5})O_3$.

REFERENCES

1. Kumar, P. M. and K. S. Rao, *Ferroelectrics*, Vol. 94, 299–303, 1989.
2. Senger, C. G. and A. J. Burgraf, *Phy. Stat. Sol. (a)*, Vol. 61, 275–285, 1980.
3. Yokomizo, Y. and T. Shoichiro, *J. Phy. Soc. Japan*, Vol. 28, No. 5, 1278–1284, 1970.

4. Ishii, Y. K. Nomura, et al., *Jpn. J. Appl. Phys.*, Vol. 34, Part 1, No. 9A, 4849-4853, September 1995.
5. Cady, W. G., *Piezoelectricity*, McGraw Hill, Ny, USA, 1946.
6. Chynoweth, A. G., *J. Appl. Phys.*, Vol. 27, 78–84, 1974.
7. Sawada, S., S. Nomura, and Y. Asao, *J. Phys. Soc. Japan*, Vol. 16, No. 11, 2207–2212, 1961.
8. Byer and Roundy, *Ferroelectrics*, Vol. 3, 333, 1972.
9. Guo, R., A. S. Bhalla, C. A. Randall, and L. E. Cross, *J. Appl. Phys.*, Vol. 679100, 6405–6410, 1990.
10. Raibagkar, L. J. and S. B. Bajaj, *Soild Staate Ionics*, Vol. 108, 105–108, 1999.

Study of EM Scattering from Electrically Large Objects in Planarly Multilayered Media with a Fast Algorithm

Lei Zhuang, **Si-Yuan He**, **Jing-Jing Yao**, **Ding-Feng Yu**, **and Guo-Qiang Zhu**
School of Electronic Information, Wuhan University, Wuhan 430079, China

Abstract— This paper studies electromagnetic (EM) scattering from electrically large objects buried in planarly multilayered media with a fast algorithm, which combines the stabilized biconjugate gradient fast Fourier transform (BCGS-FFT) method with an improved discrete complex image method (DCIM). Filling the table of Green's function and solving the matrix equation constitute two barriers for fast evaluation of EM scattering by buried objects. An improved DCIM is introduced to get a closed-form dyadic Green's function (DGF) in both lossless and lossy multilayered media for the volume electric field integral equation (EFIE), which is accurate both in the near- and far-field regions in layered media without any quasi-static and surface-wave extraction. In the simulation, a split scheme is adopted to avoid applying the improved DCIM repeatedly. By splitting spectral DGF before utilizing the improved DCIM, we need to apply the improved DCIM for only several times. Then, the iterative solver the BCGS-FFT method is combined with the improved DCIM for solving the matrix equation. Numerical results show that the improved DCIM can save tremendous CPU time in scattering problems involving buried objects. The fast algorithm proves effective for EM scattering from electrically large objects in both lossless and lossy multilayered media.

1. INTRODUCTION

EM scattering by dielectric and conducting objects buried in planarly layered media has drawn extensive attention from EM theory and applied electromagnetics. Since a planarly layered media is very important for various applications such as geophysical exploration, unexploded ordnance characterizing and microwave imaging, etc. Therefore, intensive investigations have been done during the past several decades.

Fast algorithms for electrically large objects buried in layered media are mainly hindered by two time-consuming processes. One is the table filling of Green's functions, and the other is solving of the impedance matrix equation. For the first, the dyadic Green's functions (DGFs) can be expressed as infinite integrals of spectral-domain Green's functions that are commonly known as Sommerfeld integrals (SIs). The calculation of SIs is time-consuming because of the slowly decaying and highly oscillating behavior of the integrands involved. Hence, in order to save CPU time in the table filling of Green's functions, several different techniques have been developed for this evaluation [1, 2]. One such technique that has reached a prominent position in the computation of Green's functions for layered media is the discrete complex image method (DCIM) [3–6]. This method circumvents the numerical computation of the SIs and yields the closed-form solution. Closed-form Green's functions not only save a large amount of time in filling the table of Green's functions but also make the "spherical-mean" Green's functions possible. In this paper, we introduce an improved DCIM [5] which does not share the drawback of the traditional DCIM [4]. It can work in both near- and far-field regions in layered media without quasi-static and surface-wave term extraction. Besides, the method can obtain the accurate simulation results of spatial-domain Green's functions in both lossless and lossy layered media.

For the second, because the scattering object has an arbitrary inhomogeneity, surface integral equation methods are in general not appropriate for this application. For general inhomogeneous objects, the volume integral equation methods are more suitable. To solve the electric field integral equation (EFIE) for electromagnetic scattering from inhomogeneous objects, the straightforward solution is the method of moments (MOM). However, for electrically large problems, gigantic CPU time and memory requirements make MOM impossible. In this paper, we choose the stabilized biconjugate gradient fast Fourier transform (BCGS-FFT) method combined with the improved DCIM for solving the matrix equation.

2. THEORY

In a planarly multilayered media, shown in Fig. 1, an arbitrary dielectric object is completely buried in the ith layer. The background media has N parallel layers with independent permittivity,

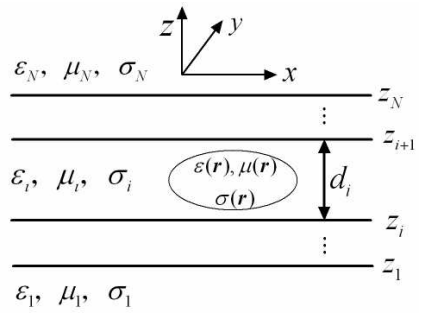

Figure 1: Typical configuration of an inhomogeneous object in a planarly layered media.

conductivity and permeability $(\varepsilon_i, \sigma_i, \mu_i, i = 1, \ldots, N)$. The complex permittivity is defined as $\tilde{\varepsilon}_i = \varepsilon_i - j\sigma_i/\omega$. The electromagnetic parameters of the inhomogeneous objects are $\varepsilon(r), \sigma(r)$ and $\mu(r)$. We assume that the object has the same permeability as layer i so that there is no contrast in μ between the object and layer i. Usually the upper region is free space. Our objective in this work is to calculate induced current density inside the object, then the scattering field everywhere can be computed by the Green's functions.

A discrete linear system can be obtained from EFIE by using Galerkin's method. In this work, both basis and testing functions are "rooftop" functions. Here we choose iterative solver BCGS combined FFT for solving the linear equation. And the computational complexity is $O(KN \log N)$, and K is the number of iterations. Although the similar method is presented in [6] by Zhang et al. to solve the EM scattering by objects in planarly layered media, it needs to extract the quasi-static and surface-wave terms first, and then approximate the remaining part by DCIM. The extraction of surface-wave components numerically is complicated in general multilayered media. The method proposed in this paper can handle the EM scattering problems in multilayered media.

3. NUMERICAL RESULTS

In example 1, the two-layer media is characterized by $\varepsilon_{r1} = 4$, $\sigma_{r1} = 0.002\,\mathrm{S/m}$, $\varepsilon_{r2} = 1$, $\sigma_{r2} = 0\,\mathrm{S/m}$. We consider an electrically large cuboid $6.4\lambda_0 \times 6.4\lambda_0 \times 0.05\lambda_0$ with the relative permittivity $\tilde{\varepsilon}(r) = 16 - j4$, and λ_0 is the wavelength in the free space. The distance from top of the electrically large object to the interface is $h = 1\lambda_0$. The source is an electric dipole given by $\hat{\alpha}_t\,(I\Delta l) = \hat{e}_z$. The dipole is located at (3.2 m, 3.2 m, 1 m). The scattering cuboid is divided into $256 \times 256 \times 2$ grids. We set the parameters of the sampling paths $\alpha = \beta = 0.4$, $N_1 = N_2 = 100$ in the improved DCIM. Fig. 2 shows the copolar electric currents on the bottom slice. Comparison with numerical integration of Sommerfeld integrals combined with BCGS-FFT is made and the excellent agreement is found. And the CPU time of the calculation of the reflected Green's functions by numerical integration is 28519 s separately, whereas the CPU time by improved DCIM is only 565.80 s on the same machine separately.

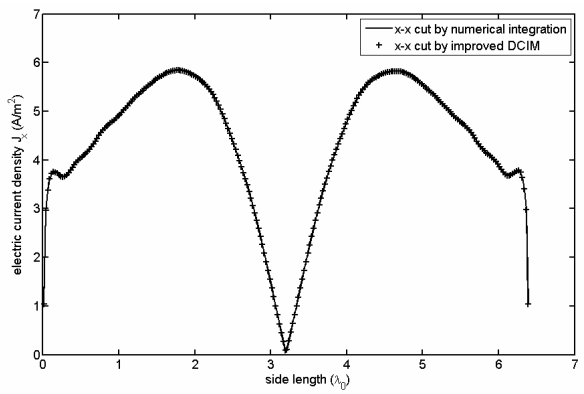

Figure 2: Copolar electric currents on the central x axis of the spheroid.

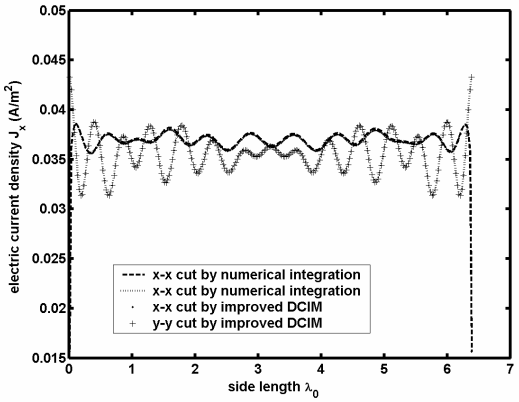

Figure 3: Copolar electric currents on the bottom slice of the dielectric cuboid.

In example 2, a plane wave with x polarization and normalized electric field normally is incident along the $\hat{z}$ direction. The operating frequency is 300 MHz. It simulates a dielectric cuboid $6.4\lambda_0 \times 6.4\lambda_0 \times 0.1\lambda_0$ with the relative permittivity $\tilde{\varepsilon}(r) = 8 - j2$ in the bottom layer of a three-layered media. The distance from top of the object to the first interface is $h = 0.5\lambda_0$. The three-layer media is characterized by $\varepsilon_{r1} = 4$, $\varepsilon_{r2} = 2$, $\varepsilon_{r3} = 1$, $\sigma_{r1} = \sigma_{r2} = \sigma_{r3} = 0\,\mathrm{S/m}$. The depth of the second layer is $2\lambda_0$. We set the parameters of the sampling paths $\alpha = \beta = 0.4$, $N_1 = N_2 = 100$ in the improved DCIM. When the cuboid is partitioned by $256 \times 256 \times 4$ grids, the results of the improved DCIM combined BCGS-FFT and the numerical integration of Sommerfeld integrals combined BCGS-FFT are illustrated in Fig. 3. Although the evaluation of the Green's functions in multilayered media is more complicated, the CPU time of the calculation of the reflected Green's functions by improved DCIM is only 1136.80 s. However, the numerical integration of the reflected Green's functions will cost 312510 s. So it indicates that the proposed method works well for the calculation of scatterers in multilayered media.

4. CONCLUSIONS

This paper presents an improved DCIM to accelerate the table-filling of Green's functions for buried objects in planar multilayered structures containing both lossless and lossy media. And the proposed method can evaluate Green's functions of electrically large objects in multilayered media. Hence, combined the method with fast algorithm BCGS-FFT makes it feasible to handle large-scale computing of buried scatterers.

ACKNOWLEDGMENT

This work is supported by the National Natural Science Foundation of China under Grant No. 60671-040 and the Chinese National High Technology Research Plan (863 Plan) under Grant No. 2007AA1-2Z172.

REFERENCES

1. Michalski, K. A. and J. R. Mosig, "Multilayered media Green's functions in integral equation formulations," *IEEE Trans. Antennas Propag.*, Vol. 45, No. 3, 508–519, Mar. 1997.
2. Cui, T. J. and W. C. Chew, "Fast evaluation of Sommerfeld integrals for EM scattering and radiation by three-dimensional buried objects," *IEEE Trans. Geosci. Remote Sens.*, Vol. 37, No. 2, 887–900, Mar. 1999.
3. Fang, D. G., J. J. Yang, and G. Y. Delisle, "Discrete image theory for horizontal electric dipoles in a multilayered medium," *Proc. Inst. Elect. Eng.*, Vol. 135, No. 5, 297–303, Oct. 1988.
4. Aksun, M. I., "A robust approach for the derivation of closed-form Green's functions," *IEEE Trans. Microw. Theory Tech.*, Vol. 44, No. 5, 651–658, May 1996.
5. Zhuang, L., G. Q. Zhu, Y. H. Zhang, and B. X. Xiao, "An improved discrete complex image method for Green's functions in multilayered mdia," *Microw. Opt. Technol. Lett.*, Vol. 49, No. 6, 1337–1340, Jun. 2007.
6. Zhang, Y. H., B. X. Xiao, and G. Q. Zhu, "An improved weak-form BCGS-FFT combined with DCIM for analyzing electromagnetic scattering by 3-D objects in planarly layered media," *IEEE Trans. Geosci. Remote Sens.*, Vol. 44, No. 12, 3540–3546, Dec. 2006.

Efficient Analysis of Electromagnetic Scattering Problem Using Proper Orthogonal Decomposition

Chao-Fu Wang
Temasek Laboratories, National University of Singapore, Singapore

Abstract— This paper describes a novel approach for efficiently solving electromagnetic (EM) scattering problems using proper orthogonal decomposition (POD). As a proof of concept and demonstration of how to use the POD to solve EM scattering problems, two ways of implementation of the POD procedure have been proposed and realized for calculating EM scattering from 2D PEC targets using electric field integral equation (EFIE) for TE polarization and magnetic field integral equation (MFIE) for TM polarization. Preliminary results obtained show that the POD is quite accurate for reconstructing backscatter patterns over wide range of frequencies and angles of interest based on the given snapshots.

1. INTRODUCTION

Practical requirement of the efficient modeling of electromagnetic (EM) scattering from large and complex targets requires the generation of wideband frequency and multiaspect responses, which is very expensive to compute using numerical methods. Several methods and algorithms have been proposed for speeding up the process of generating useful data of responses over wide range of frequencies and angles of interest. Of these, the asymptotic waveform evaluation (AWE) method has been successfully applied to analyze EM problems [1–9] and offers some feature of model-order-reduction (MOR) techniques.

One of the most popular MOR techniques in aerodynamics is the proper orthogonal decomposition (POD) [10–14]. In principle, POD exploits the correlations in the dynamics of the system states under different excitations to determine dominant modes (POD basis vectors), or coherent structures (eigenfunctions), governing the system behavior. It is essentially based on second-order statistical properties that result in a linear invertible transformation such that the eigenfunctions yielded would optimally represent the data, i.e., for any given orthonormal bases, the POD eigenfunction bases ensure it is the best bases and that the two-norm or L2-norm error between the original and reconstructed data is minimum. In addition to being optimal in a least square sense, POD has the property that it is completely data dependent and does not assume any prior knowledge of the process that generates the data. This property is advantageous in situations where *a priori* knowledge of the underlying process is insufficient to warrant a certain choice of basis [15, 16].

Recently, POD has been successfully applied to analyze some microwave problems [13, 14] and to obtain design parameters for multidisciplinary design of S-shaped intake [15–17]. In this paper, the POD method is used to the analysis of EM scattering problem over wide range of frequencies and angles of interest.

2. FUNDAMENTAL OF POD

The basic POD procedure for constructing the optimal POD basis vectors Φ to reconstruct a function $U(x,t)$ over some domains of interest based on its M given snapshots U_k can be briefly summarized as follows [10–15]:

1) Construct the correlation matrix R by computing the inner product between every pair of snapshots as shown in Eq. (1).

$$R_{ik} = \frac{1}{M}\left(U_i, U_k\right) \tag{1}$$

2) Solve the eigenvalue problem of Eq. (2) to get the eigenvectors of $\{\beta_{ij}\}$ corresponding to eigenvalues λ_i, $i = 1, \ldots, M$.

$$R\beta = \Lambda\beta \tag{2}$$

3) Construct the POD basis vector Φ^i using Eq. (3)

$$\Phi_i = \sum\nolimits_{j=1}^{M} \beta_{ij} U_j \tag{3}$$

4) Select the number of modes (POD basis vectors) (P) to be employed in the reconstruction by considering the relative "energy" (measured by the 2-norm) captured by the ith basis vector $\left(\lambda_i / \sum_{i=1}^{M} \lambda_i\right)$.

The approximate prediction of the function U is then given by a linear combination of the basis vectors using Eq. (4)

$$U \approx \sum_{i=1}^{P} \alpha_i \Phi_i \tag{4}$$

where $P \leq M$ is chosen to capture the desired level of energy.

3. IMPLEMENTATION OF POD FOR EM SCATTERING PROBLEM

For a given EM problem, its numerical analysis usually results in a matrix equation as follows:

$$Z(s)I(s) = V(s) \tag{5}$$

where Z denotes the impedance matrix, I is unknown vector, V is the known vector related to the source or excitation, and s is a modeling parameter related to frequency or angle. Let $I_k = I(s_k)$ be the solution of Eq. (5) for $V_k = V(s_k)$, $k = 1, \ldots, M$, and Φ_i, $i = 1, \ldots, P$ denote the POD modes constructed from these M solutions (snapshots). The unknown vector $I(s)$ can be expressed as a linear combination of the POD modes Φ_i

$$I(s) = \sum_{i=1}^{P} \alpha_i \Phi_i \tag{6}$$

Substituting (6) into (5) and applying testing procedure yields a matrix equation that can be used to determine coefficients α_i as follows

$$\begin{bmatrix} (Z(s)\Phi_1, Z(s)\Phi_1) & (Z(s)\Phi_1, Z(s)\Phi_2) & \ldots & (Z(s)\Phi_1, Z(s)\Phi_P) \\ (Z(s)\Phi_2, Z(s)\Phi_1) & (Z(s)\Phi_2, Z(s)\Phi_2) & \ldots & (Z(s)\Phi_2, Z(s)\Phi_P) \\ \vdots & \vdots & \vdots & \vdots \\ (Z(s)\Phi_P, Z(s)\Phi_1) & (Z(s)\Phi_P, Z(s)\Phi_2) & \ldots & (Z(s)\Phi_P, Z(s)\Phi_P) \end{bmatrix} \begin{bmatrix} \alpha_1 \\ \alpha_2 \\ \vdots \\ \alpha_P \end{bmatrix} = \begin{bmatrix} (Z(s)\Phi_1, V(s)) \\ (Z(s)\Phi_2, V(s)) \\ \vdots \\ (Z(s)\Phi_P, V(s)) \end{bmatrix} \tag{7}$$

If parameter s represents angle, the coefficients α_i can be simplified as

$$\alpha_i = (Z\Phi_i, V(s))/(Z\Phi_i, Z\Phi_i)$$

in which

$$Z\Phi_i = \sum_{j=1}^{M} \beta_{ij} V_j, \quad i = 1, \ldots, P.$$

It can be seen that if the impedance matrix Z is a function of parameter s, P matrix-vector multiplications are needed to set up the matrix Eq. (7) for solving α_i, which may be computationally expensive for modeling EM problem with electrically large and complex configuration. To reduce the computational cost for reconstructing $I(s)$ using POD basis vectors, $I(s)$ can be alternatively expressed as follows

$$I(s) = \sum_{i=1}^{P} \alpha_i(s) \Phi_i \tag{8}$$

$\alpha_i(s)$ can be expanded into a Taylor series or Padè approximation.

Let us expand $\alpha_i(s)$ into a Taylor series

$$\alpha_i(s) = \sum_{l=0}^{L} \alpha_{il} s^l, \quad i = 1, \ldots, P$$

Considering the orthonormality of the POD basis vectors Φ_i yields

$$\sum_{l=0}^{L} \alpha_{il} s^l = (I(s), \Phi_i), \quad i = 1, \ldots, P \tag{9}$$

Choosing $L+1$ different samples of parameter s, for example, s_{k_l}, $(l = 0, \ldots, L)$, and applying their corresponding snapshots $I_{k_l} = I(s_{k_l})$, $(l = 0, \ldots, L)$ to Eq. (9) results in

$$\begin{bmatrix} 1 & s_1 & \ldots & s_1^L \\ 1 & s_2 & \ldots & s_2^L \\ \vdots & \vdots & \vdots & \vdots \\ 1 & s_{L+1} & \ldots & s_{L+1}^L \end{bmatrix} \begin{bmatrix} \alpha_{i0} \\ \alpha_{i1} \\ \vdots \\ \alpha_{iL} \end{bmatrix} = \begin{bmatrix} (I_{k_0}, \Phi_i) \\ (I_{k_1}, \Phi_i) \\ \vdots \\ (I_{k_L}, \Phi_i) \end{bmatrix}, \quad i = 1, \ldots, P \tag{10}$$

Let us expand $\alpha_i(s)$ into a rational function or Padè approximation [1, 8, 9] as follows:

$$\alpha_i(s) = \sum_{l=0}^{L} \alpha_{il} s^l = \frac{\sum_{m=0}^{L_P} a_{im} s^m}{1 + \sum_{n=1}^{M_p} b_{in} s^n}, \quad i = 1, \ldots, P \tag{11}$$

where $L_p + M_p = L$. Following the standard procedure of the Padè approximation yields

$$\begin{bmatrix} \alpha_{iL_P} & \alpha_{iL_P-1} & \cdots & \alpha_{iL_P-M_P+1} \\ \alpha_{iL_P+1} & \alpha_{iL_P} & \cdots & \alpha_{iL_P-M_P+2} \\ \vdots & \vdots & \vdots & \vdots \\ \alpha_{iL_P+M_P-1} & \alpha_{iL_P+M_P-2} & \cdots & \alpha_{iL_P} \end{bmatrix} \cdot \begin{bmatrix} b_{i1} \\ b_{i2} \\ \vdots \\ b_{iM_P} \end{bmatrix} = - \begin{bmatrix} \alpha_{iL_P+1} \\ \alpha_{iL_P+2} \\ \vdots \\ \alpha_{iL_P+M_P} \end{bmatrix} \tag{12}$$

$$a_{im} = \sum_{n=0}^{m} b_{in} \alpha_{im-n}, \quad m = 0, 1, \ldots, L_P \tag{13}$$

Eqs. (7), (10), (11) and (12) can be easily solved to obtained reconstruction coefficients as both P and L are much smaller than the dimension of matrix Z.

4. DISCUSSION AND CONCLUSION

As a proof of concept and demonstration of how the POD works for EM modeling, the two ways of implementation of the POD procedure mentioned above have been realized for calculating EM scattering from 2D PEC targets using electric field integral equation (EFIE) for TE polarization and magnetic field integral equation (MFIE) for TM polarization [18]. Preliminary results obtained show that the POD is quite accurate for the reconstruction of backscatter patterns over wide range of frequencies and angles of interest based on the given snapshots. Further study on how to use POD to solve large and complex EM scattering problems is in progress. More discussion and numerical results to show the effectiveness of the POD will be presented at the conference.

REFERENCES

1. Jiao, D. and J. M. Jin, "Asymptotic waveform evaluation for broadband calculation," *Fast and Efficient Algorithms in Computational Electromagnetics*, edited by W. C. Chew, et al., Chapter 15, Artech House, 2001.
2. Pillage, L. T. and R. A. Rohrer, "Asymptotic waveform evaluation for timing analysis," *IEEE Trans. CAD*, Vol. 9, 352–366, April 1990.
3. Polstyanko, S. V., R. Dyczij-Edlinger, and J.-F. Lee, "Fast frequency sweep technique for the efficient analysis of dielectric waveguides," *IEEE Trans. Microwave Theory Tech.*, Vol. 45, 1118–1126, July 1997.
4. Erdemli, Y. E., J. Gong, C. J. Reddy, and J. L. Volakis, "Fast RCS pattern fill using AWE technique," *IEEE Trans. Antennas Propagat.*, Vol. 46, 1752–1753, November 1998.
5. Slone, R. D., R. Lee, and J. F. Lee, "Multipoint Galerkin asymptotic waveform evaluation for model order reduction of frequency domain FEM electromagnetic radiation problems," *IEEE Trans. Antennas Propagat.*, Vol. 49, 1504–1513, October 2001.
6. Wei, X. C., Y. J. Zhang, and E. P. Li, "The hybridization of fast multipole method with asymptotic waveform evaluation for the fast monostatic RCS computation," *IEEE Trans. Antennas Propagat.*, Vol. 52, No. 2, 605–607, February 2004.
7. Ngoly, A. and S. McFee, "An efficient high-order extrapolation procedure for multiaspect electromagnetic scattering analysis," *IEEE Trans. Magn.*, Vol. 44, No. 6, 750–753, June 2008.
8. Ling, F., D. Jiao, and J. M. Jin, "Efficient electromagnetic modeling of microstrip structures in multilayer media," *IEEE Trans. Microwave Theory Tech.*, Vol. 47, No. 9, 1810–1818, September 1999.
9. Nie, X. C., N. Yuan, L. W. Li, and Y. B. Gan, "Fast analysis of RCS over a frequency band using pre-corrected FFT/AIM and asymptotic waveform evaluation technique," *IEEE Trans. Antennas Propagat.*, Vol. 56, No. 11, 3526–3533, November 2008.
10. Sirovich, L., "Turbulence and the dynamics of coherent structures Part I–III," *Quart. App. Math.*, Vol. 45, 561–571, 573–582, 583–590, 1987.
11. Chatterjee, A., "An introduction to the proper orthogonal decomposition," *Current Science*, Vol. 78, No. 7, 808–817, 2000.

12. Bui-Thanh, T., M. Damodaran, and K. Willcox, "Aerodynamic data reconstruction and inverse design using proper orthogonal decomposition," *AIAA Journal*, Vol. 42, No. 8, 1505–1516, 2004.
13. Mijalkovic, S., "Using frequency response coherent structures for model-order reduction in microwave applications," *IEEE Trans. Microwave Theory Tech.*, Vol. 52, No. 9, 2292–2297, September 2004.
14. Lin, W. Z., Y. J. Zhang, and E. P. Li, "Proper orthogonal decomposition in reduced order model generation for microwave problem," *17th Int. Zurich Symp. on EMC*, 223–226, 2006.
15. Zhang, J. M., C. F. Wang, and K. Y. Lum, "Multidisciplinary design of S-shaped intake," *26th AIAA Appl. Aerodyn. Conf.*, 2008–7060, AIAA, 2008.
16. Zhang, J. M., C. F. Wang, and K. Y. Lum, "Joint aerodynamics and electromagnetics design of S-shaped intake using proper orthogonal decomposition method," *IEEE APS Int. Symp. Dig.*, s411.6, 2008.
17. Hu, F. G., C. F. Wang, and Y. B. Gan, "Efficient calculation of interior scattering from large three-dimensional PEC cavities," *IEEE Trans. Antennas Propagat.*, Vol. 55, No. 1, 167–177, January 2007.
18. Wang, C. F. and Y. B. Gan, "2D cavity modeling using method of moments and iterative solvers," *Journal of Electromagnetic Waves and Applications*, Vol. 17, No. 12, 1739–1740, 2003.

The Probability Distribution of the EM Fields in Single-cavity System and the Application of PWB Method

J. Liu, X. Zhao, and K. M. Huang
College of Electronics and Information Engineering, Sichuan University, Chengdu 610064, China

Abstract— Based on full-wave analysis method, the probability distribution curves of electromagnetic (EM) fields inside a single cavity with and without a mode stirrer are obtained, which obey a kind of unimodal functions. Although this unimodal function does not satisfy the assumption of power balance (PWB) method, the power losses of cavity wall at different frequencies evaluated by PWB method and those calculated by full-wave analysis method are comparable. The change trends of the power losses with frequency almost coincide with each other, and the difference is no more than an order of magnitude. It is remarkable that PWB method costs less than one minute while full-wave analysis method costs more than two hours, and PWB method saves almost 70% memory space. It means that PWB method can indeed give effective data that meet certain accuracy requirement with much smaller computational cost than full-wave analysis method. Finally, for further study of PWB method the inhomogeneous degree is defined to measure the inhomogeneity of EM field distribution inside the cavity.

1. INTRODUCTION

It is difficult to successfully resolve the response, especially, the high frequency response of large complex electronic system to the external EM environment by using traditional EM simulation methods. The main difficulties are the enormous computational cost of the traditional full-wave analysis and the uncertainty caused by the high sensitivity of the high-frequency response [1, 2]. Therefore, it is necessary to introduce some relatively simple estimation methods combined with "statistic language" to analyze the coupling and transmission processes of the external EM energy in electronic system. It has very important theoretical value and application perspective for EM compatibility and EM effects evaluation. The PWB method is a kind of estimation method, used to estimate the magnitude of EM energy in complex system under high-frequency interference. Flexibility and convenience are remarkable features of this method. Its effectiveness has been preliminarily confirmed, but it is still necessary to estimate its use range.

In order to compare full-wave analysis method and PWB method and to validate PWB method, the probability distributions of the EM fields and energy condition in a single-cavity system are attained by these two methods. Moreover, for further study of PWB method, the inhomogeneous degree V is defined to measure the inhomogeneity of the distribution of the EM fields inside the cavity.

2. PWB METHOD

The PWB method was first proposed by D. A. Hill in 1994, to solve the high-frequency response of a single cavity problem. It was developed as a kind of estimation method by I. Junqua etc., used to estimate the magnitude of EM energy in complex cavity system under high-frequency interference. PWB method is based on statistical concepts. The main assumption is that when the considered system is large enough compared with wavelength of EM interference, EM fields at any point inside the cavity are uniformly distributed random variables of the position. As a result, the mean EM environment can be viewed as pseudo-homogeneous [3, 4], and the cavity that behaves as a pseudo-mode stirred reverberation chamber (MSC) can be approximated.

For such a MSC under steady state condition, the mean power transmitted inside the cavity is equal to the mean power dissipated in different loss mechanisms. For example, for a single-cavity system shown in Fig. 1, it is required that [5],

$$P_t = P_d = P_W + P_{ap} + P_{ant} + P_{obj}, \tag{1}$$

where

P_t is the mean power transmitted inside the cavity,
P_d is the sum of various dissipated mechanisms inside the cavity,
P_W is the losses in the cavity walls,

P_{ap} is the re-radiation via POEs or generalized apertures,

P_{ant} is the power dissipated in antenna located inside the cavity,

P_{obj} is the absorption of inner objects in the cavity.

3. THE PROBABILITY DISTRIBUTIONS OF THE EM FIELDS IN A SINGLE-CAVITY SYSTEM

In order to verify the assumption of PWB method, the probability distribution that the EM field in a single cavity system obeys is studied. The considered model is constructed as shown in Fig. 2, and there is an ideal metal stirrer rotating different angles freely in the cavity. Based on full-wave analysis method FDTD, 60 situations of the stirrer are sampled, from which the probability distributions of the EM fields inside the cavity can be obtained statistically.

By using curve fitting, we find it satisfies the function: $y = y_0 + A \cdot e^{-e^{-z}-z+1}$, where $z = (x - x_c)/w$, y_0, x_c, w and A are all undetermined coefficients. This kind of probability density function is unimodal. The more intense the peak is the better uniformity is. As an example, Fig. 3(a) shows the statistical results of magnetic field, and Fig. 3(b) shows the curve fitting result at 3.5 GHz.

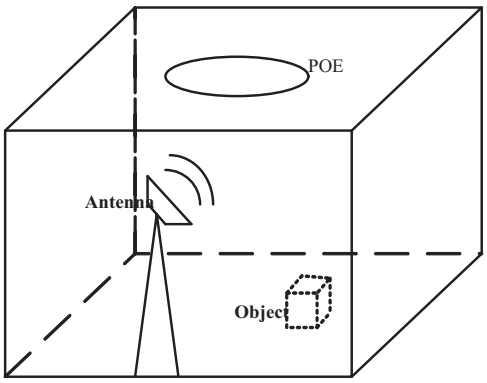

Figure 1: Various dissipated mechanisms inside the single-cavity.

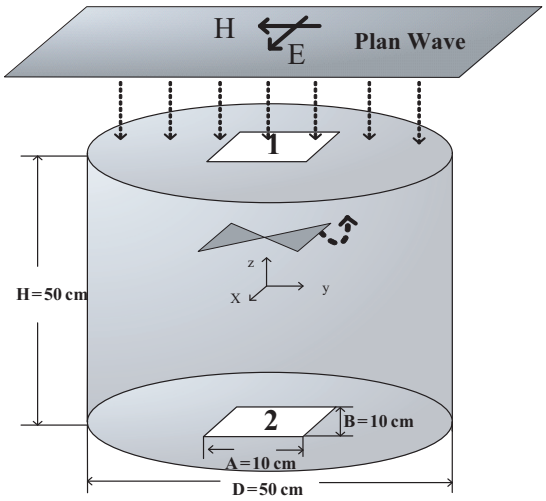

Figure 2: The single-cavity system under consideration.

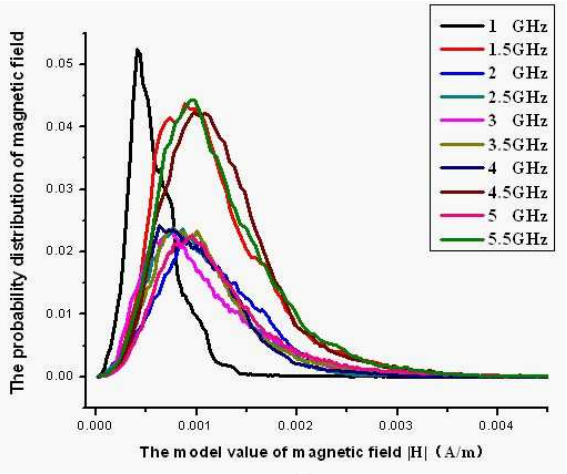

(a)

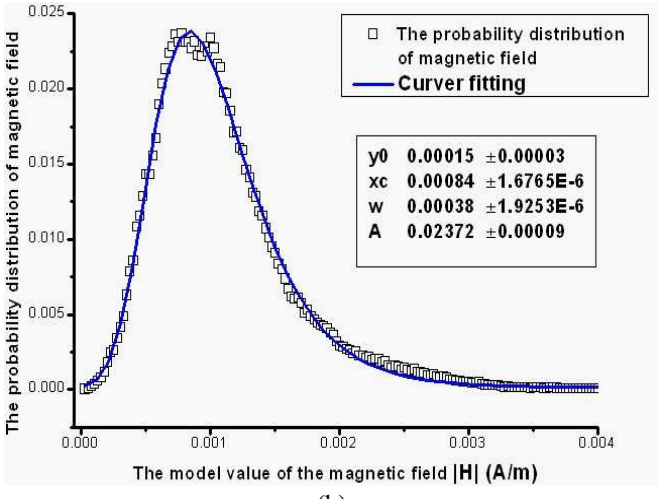

(b)

Figure 3: (a) The probability distribution curves of magnetic fields' model value. (b) Curve fitting at 3.5 GHz.

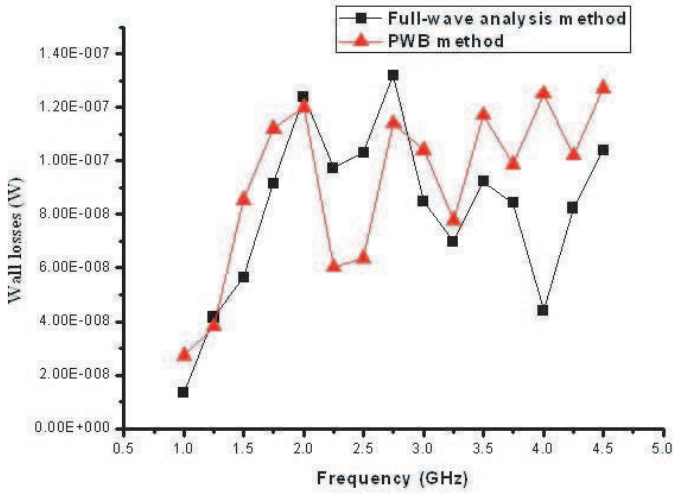

Figure 4: Comparison of PWB method and full-wave analysis method.

4. COMPARISON BETWEEN PWB METHOD AND FULL-WAVE ANALYSIS METHOD

To compare the PWB method and full-wave analysis method, the loss power in the cavity walls is considered as an example. For the cavity shown in Fig. 2, the mean power density S inside the cavity is gain by PWB method [5, 6],

$$S = \frac{\lambda}{2\pi V} \cdot \frac{P_{\text{inc}}}{\frac{1}{Q_1} + \frac{1}{Q_2} + \frac{1}{Q_{\text{wall}}}}, \tag{2}$$

where λ is the wavelength, V is the volume of the cavity, P_{inc} is the input power, Q_1, Q_2 and Q_{wall} are the elementary quality factors associated to the aperture 1, the aperture 2 and the cavity walls respectively. The elementary quality factors can be given by the mean coupling cross section $\langle\sigma\rangle$ [4, 5], for instance,

$$Q_{\text{wall}} = \frac{2\pi V}{\lambda \langle\sigma_{\text{wall}}\rangle}, \langle\sigma_{\text{wall}}\rangle = \frac{4S \cdot R_S}{3c \cdot \mu_0} = \frac{4\pi S}{3\lambda} \cdot \sqrt{\frac{\mu_r}{\pi f \mu_0 \sigma}}, \tag{3}$$

where S is the cavity surface area, μ_r is the relative wall permeability, σ is the wall conductivity, R_S is the wall surface impedance. Therefore the loss power in the cavity walls P_{wall} can be given by PWB method,

$$P_{\text{wall}} = \frac{2\pi V}{\lambda Q_{\text{wall}}} \cdot S \tag{4}$$

Meanwhile, the magnetic field inside the cavity can be obtained by full-wave analysis method, which can be used to calculate the loss power P_t in the cavity walls,

$$P_t = \frac{1}{2} |R_S| \oint_S |H_t|^2 ds, \tag{5}$$

where H_t is the tangential magnetic field component of the cavity inner surface.

The comparison of the loss power in the cavity walls gained by the two methods is shown in Fig. 4. It indicates that the change trends of the two curves with frequency almost coincide with each other, and the difference is no more than an order of magnitude. Moreover, it is remarkable that PWB method costs less than one minute while the full-wave analysis method costs about two hours, and PWB method saves almost 70% memory space. It means that PWB method can indeed give effective data that meet certain accuracy requirement with much smaller computational cost than the full-wave analysis method.

5. INHOMOGENEOUS DEGREE

According to MSC theory, the real and the imaginary parts of electric fields (and magnetic fields) are Gaussian random variables with a mean equal and the same variance. The mean EM environment

can be considered as pseudo-isotropic. In engineering practice, the chamber with a stir inside it is modeled as a MSC. To measure the inhomogeneity of the EM fields within the chamber, the inhomogeneous degree V is defined, in terms of the variance D and the mean E of the EM fields,

$$V = \frac{\sqrt{D}}{E} \tag{6}$$

The calculated results by using (6) show that the relationship of the Inhomogeneous Degree between with and without stir, $V2_i$ and $V1_i$, always meets (7),

$$V1_i \leq V2_i \quad (i = x, y, z) \tag{7}$$

which just meet our supposition.

6. CONCLUSIONS

In this paper, the probability distributions of the EM fields in a single-cavity system with or without a stirrer are studied, which obey a kind of unimodal function. Although they are not very satisfied with the assumption of PWB method, the power losses of cavity wall at different frequencies evaluated by PWB and the ones calculated by full-wave analysis are comparable. The comparison of the results shows that PWB method can indeed give effective data that meet certain accuracy requirement with much smaller computational cost than full-wave analysis method. What's more, the definition of the inhomogeneous degree is the preparation for further research of PWB method. Although only single-cavity system is considered, the above conclusions can be easily extended to the case of multi-cavity system through PWB network formula.

ACKNOWLEDGMENT

This work was supported in part by the National Science Foundation of China under Grant 60801035.

REFERENCES

1. Huang, K. M. and X. Zhao, *The Inverse Problems in Electromagnetic Field and Its Applications*, Science Press, Beijing, 2005.
2. Holland, R. and H. S. J. Richard, *Statistical Electromagnetics*, Taylor & Francis, New York, 1999.
3. Hill, D. A., "Plane wave integral representation for fields in reverberation chambers," *IEEE Trans. Electromagn. Compat.*, Vol. 40, No. 3, 209–217, 1998.
4. Hill, D. A., M. T. Ma, A. R. Ondrejka, B. Riddle, M. L. Crawford, and R. T. Jonk, "Aperture excitation of electrically large lossy cavities," *IEEE Trans. Electromagn. Compat.*, Vol. 36, No. 3, 169–179, 1994.
5. Junqua, I., J. P. Parmantier, and F. Issac, "A network formulation of the power balance method for high-frequency coupling," *Electromagnetics*, Vol. 25, 603–622, 2005.
6. Kirawanich, P., J. Wilson, and N. E. Islam, "Electromagnetic topology: A modular junction approach for a system level interaction problem," *IEEE Trans. Electromagn. Compat.*, Vol. 25, 7–8, 2005.

Design and Simulation of Planar Archimedean Spiral Antenna

Changjie Sun, **Guobin Wan**, **Zhang Hu**, **and Xin Ma**
School of Electronic and Information, Northwestern Polytechnical University, Xi'an 710129, China

Abstract— Planar Archimedean spiral antenna is widely used with its low profile, light weight, high efficiency, circular polarization and broad bandwidth. In this paper, the effects on the electromagnetic characteristics of the planar Archimedean spiral antenna, which are owing to the changes of the diameter and the heights of the transmutative cavity and the width of the spiral, are investigated respectively. Results show that the changes of the diameter and the heights of the transmutative cavity have much influence on the input impedance and the gain of the Archimedean spiral antenna, while the changes of the width of the spiral have much influence on the input impedance of the Archimedean spiral antenna.

1. INTRODUCTION

Archimedean spiral antennas have received increased interest due to their wide bandwidth [1], high efficiency, low profile, stable impedance characteristic and circular polarization over the last two decades. Archimedean spiral antennas have been widely used for airborne applications [2], satellite communications, wireless communications [3], UWB communications [4], radio navigations, biological medicine [5], radar and electronic counter measurements and so on.

The Archimedean spiral antenna isolated in free space radiates a circularly polarized wave in two directions normal to the antenna plane. But in most applications, the unidirectional beam is needed in stead of bidirectional beam. Unidirectional beam can be obtained by backing the Archimedean spiral antenna with a conducting plane [6], a conducting cavity or an absorbing cavity [7]. In this paper, the effects on the electromagnetic characteristics of the planar Archimedean spiral antenna operating at 5 GHz–7 GHz due to the changes of the diameter and the heights of the transmutative cavity [8] and the width of the spiral arm are investigated respectively. Section 1 descripts the background of the Archimedean spiral antenna and the main contents of the paper. Section 2 presents the models of the spiral radiator and the transmutative cavity, the parameters of the antenna is stated in detail. Simulation results and discussions are given in Section 3. Conclusions obtained in this paper are summarized in Section 4.

2. THE ANTENNA STRUCTURE

The spiral radiator is shown in Fig. 1, composing of two spiral arms. The spiral arm is characterized by Archimedean spiral function $r = r_0 + a\varphi$. The transmutative cavity is adopted to obtain the

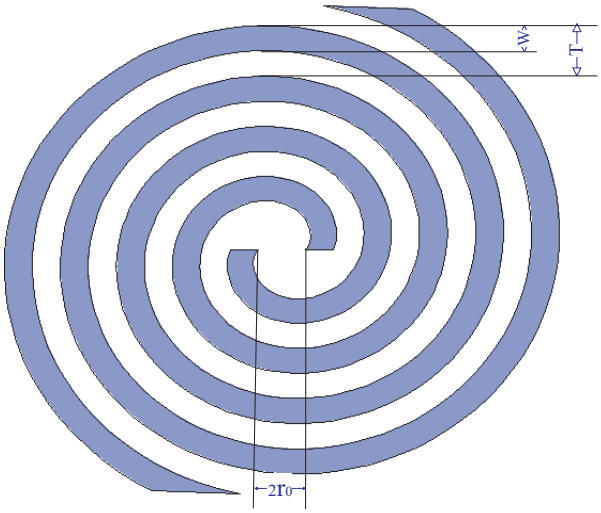

Figure 1: Spiral radiator.

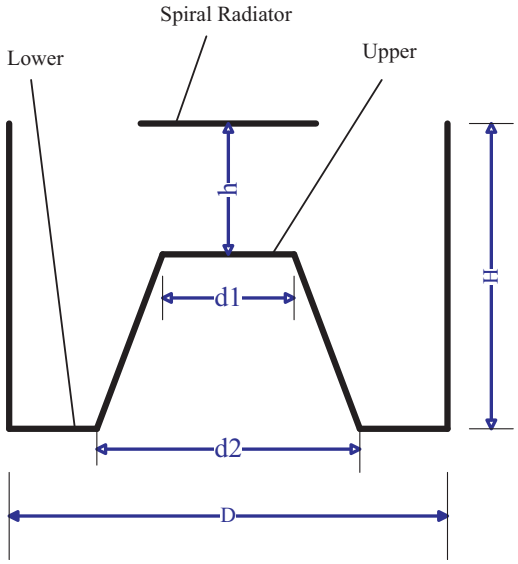

Figure 2: Transmutative cavity.

unidirectional beam, which is shown in Fig. 2. The parameters $d_1 = \lambda_H/\pi$ and $d_2 = \lambda_L/\pi \cdot \lambda_H$ is the wavelength of the maximum operating frequency f_H, λ_L is the wavelength of the minimum operating frequency f_L.

In this paper, we choose $r_0 = 1$ mm, $a = 0.764$, 0 rad$\leq \varphi \leq$14 rad. In order to make the antenna operate at 5–7 GHz, $H = 0.25\lambda_L$, $h = 0.25\lambda_H$, $D = 1.1\lambda_L$, $T = 2.4$ mm, $W = 1.2$ mm. Effects of changing one specific parameter of H, h, D and W on electromagnetic characteristics of the Archimedean spiral antenna are investigated thoroughly with keeping other parameters constant.

3. SIMULATION RESULTS AND DISCUSSIONS

Effects of changing D on the electromagnetic characteristics of the antenna are depicted in Fig. 3. It is seen that the magnitude of input impedance changes dramatically as D increases from $0.4\lambda_L$ to $0.6\lambda_L$, but keeps nearly constant about 180 Ω as D increases from $0.6\lambda_L$ to $1.2\lambda_L$. The gaintotal at 6 GHz increases linearly to the maximum value as D increases from $0.4\lambda_L$ to $1.1\lambda_L$, but drops dramatically as D changes from $1.1\lambda_L$ to $1.2\lambda_L$.

Figure 4 illustrate the effects of changing h on the electromagnetic characteristics of the antenna. The figures indicate that the magnitude of input impedance changes greatly as h increases from $0.05\lambda_H$ to $0.15\lambda_H$, while keeps fairly stable about 180 Ω as h increases from $0.15\lambda_H$ to $0.35\lambda_H$. The gaintotal at 7 GHz increases wavily as h changes from $0.05\lambda_H$ to $0.35\lambda_H$.

Effects of changing H on the electromagnetic characteristics are given in Fig. 5. It is seen that the magnitude of input impedance keeps nearly constant about 180 Ω with small fluctuation as H increases from $0.20\lambda_L$ to $0.30\lambda_L$, while changes greatly as H increases from $0.30\lambda_L$ to $0.45\lambda_L$. The gaintotal at 5 GHz keeps nearly constant as H increases from $0.20\lambda_L$ to $0.30\lambda_L$, rises greatly at first

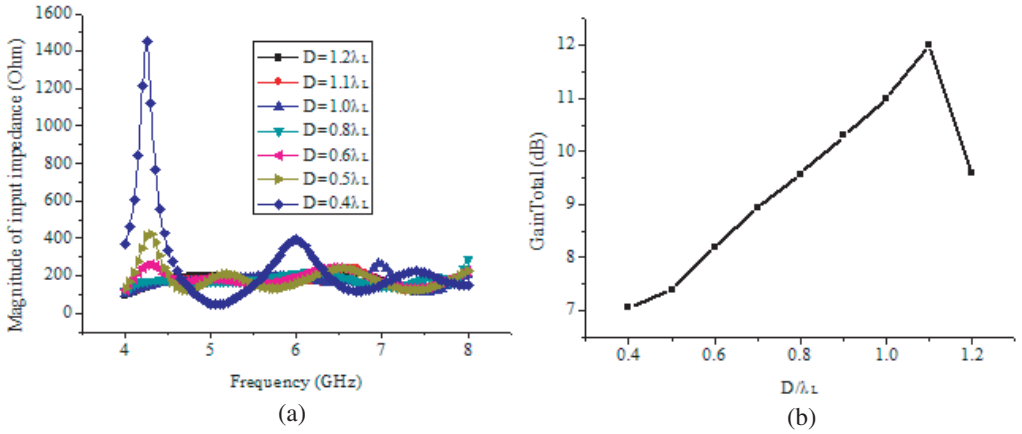

Figure 3: Effects of changing D on the electromagnetic characteristics. (a) Magnitude of input impedance curves. (b) Gaintotal curve.

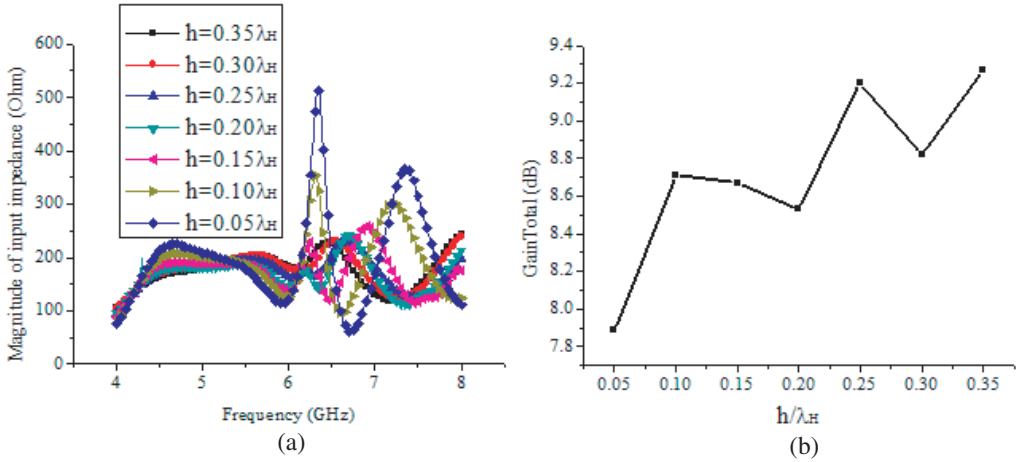

Figure 4: Effects of changing h on the electromagnetic characteristics. (a) Magnitude of input impedance curves. (b) Gaintotal curve.

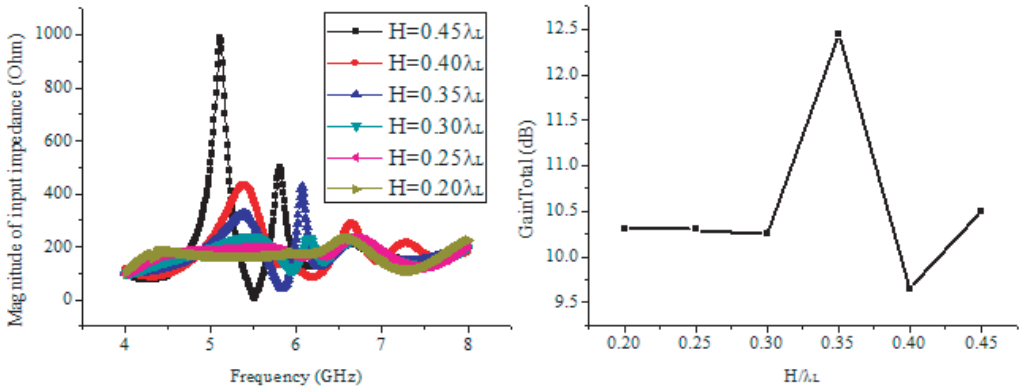

Figure 5: Effects of changing H on the electromagnetic characteristics. (a) Magnitude of input impedance curves. (b) Gaintotal curve.

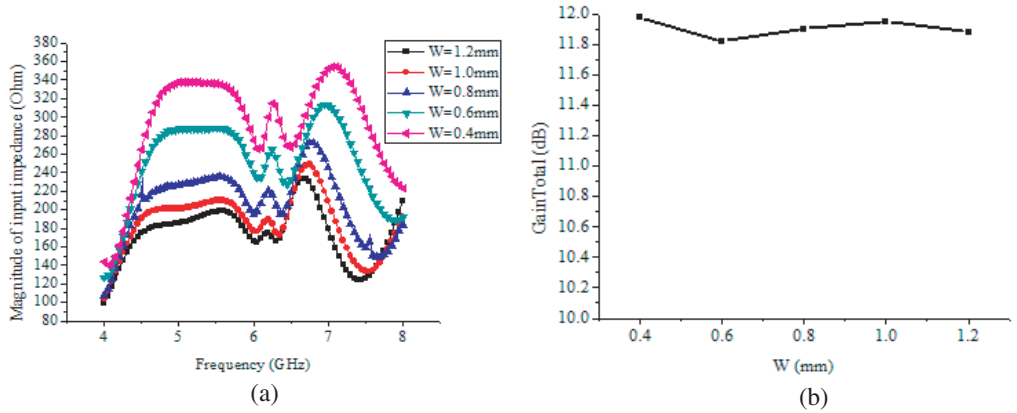

Figure 6: Effects of changing W on the electromagnetic characteristics. (a) Magnitude of input impedance curves. (b) Gaintotal curve.

and then drops dramatically as H increases from $0.30\lambda_L$ to $0.45\lambda_L$.

Figure 6 illustrate the effects of changing W on the electromagnetic characteristics of the antenna. It is seen clearly that the magnitude of input impedance increases as W decreases from 1.2 mm to 0.4 mm, while the gaintotal at 6 GHz keeps nearly constant as W changes from 1.2 mm to 0.4 mm.

4. CONCLUSIONS

The effects on the electromagnetic characteristics of the Archimedean spiral antenna operating at 5 GHz–7 GHz due to the changes of the diameter and the heights of the transmutative cavity and the width of the spiral arm are investigated respectively. The simulation results show that input impedance is fairly influenced by the diameter and the heights of the transmutative as well as the width of the spiral arm respectively. The gaintotal is affected by the parameters above all except the width of the spiral arm.

REFERENCES

1. Kaiser, J. A., "The Archimedean two-wire spiral antenna," *IRE Trans. Antennas and Propagation*, Vol. 8, No. 3, 312–323, 1986.
2. Schreider, L., X. Begaud, M. Soiron, and B. Perpere, "Design of a broadband Archimedean spiral antenna above a thin modified Electromagnetic Band Gap substrate," *Antennas and Propagation of First European Conference*, 1–4, Paris, France, November 2006.
3. Abdul Khalid, M. F., M. A. Haron, A.Baharudin, and A. A. Sulaiman, "Design of a spiral antenna for Wi-Fi applications," *2008 IEEE International RF and Microwave Conference Proceedings*, 431–435, Kuala Lumpur, Malaysia, December 2–4, 2008.

4. Powell, J. and A. Chandrakasan, "Spiral slot patch antenna and circular disc monopole antenna for 3.1–10.6 GHz ultra wideband communication," *Int. Symp. Antennas and Propagation*, August 2004.
5. Kwak, S. L., K. Chang, and Y. J. Yoon, "Small spiral antenna for wideband capsule endoscope," *Electronics Letters*, Vol. 42, No. 23, 9, November 2006.
6. Nakano, H., K. Nogami, S. Arai, H. Mimaki, and J. Yamauchi, "A spiral antenna backed by a conducting plane reflector," *IEEE Trans. Antennas Propag.*, Vol. 34, No. 6, 725–796, June 1986.
7. Corzine, R. G. and J. A. Moskl, *Four-arm Spiral Antennas*, Norwood, MA, Artech House, 1990.
8. Tang, W., "Study and design of UWB planar spiral antenna," Masetr's thesis of Xidian University, March 2007.

Study on Optimize Efficiency of Particle Swarm Optimization for the Synthesis of Subarrayed Arrays

Ning Ren, Guobin Wan, and Xin Ma
School of Electronic and Information, Northwestern Polytechnical University, Xi'an 710129, China

Abstract— Antenna arrays have received significant attention of the researchers, since they find a wide-range of application in microwave technology such as communication and radar. In the past years, there has been a great interest in the design of antenna arrays using optimization algorithms, particularly derivative-free, evolutionary algorithms such as ant colony algorithm, particle swarm optimization (PSO), and genetic algorithms. However, the optimization efficiency of large antenna arrays and two-dimension antenna arrays is low. In this paper, subarrayed array antennas with the definition of the elements clustering into spatially contiguous subarrays and the corresponding weights to obtain the same sidelobe level pattern with the unsubarrayed antenna array are optimized via the modern heuristic particle swarm optimization technique. The problem is discussed through comparing the efficiency of PSO in the subarrayed array antennas with that in unsubarrayed antenna array. A set of representative results concerned with difference subarray element numbers and amplitude distributions are shown to compare the performance of PSO. Also, the PSO method for subarrayed array can be extended to two-dimension antenna arrays.

1. INTRODUCTION

The definition of suitable tradeoff solutions between antenna performance and costs is a problem still actual and of interest in the scientific community involved in array antenna synthesis. To satisfy the need of design radiating systems with low sidelobe level patterns and achieve available low cost at the same time is become more and more popular. As a result, large antenna arrays are partitioned into subarrays in order to reduce cost through common use of components or mass production of identical subarrays in this paper. Typically, placing amplitude weights at the subarray ports rather than the elements creates grating lobes that are predicted using analytical expressions [1]. To properly address these issues, different approaches have been proposed to design efficient and cheaper antenna systems, such as using intelligent optimization algorithms.

Particle swarm optimization (PSO) is a population-based, self-adaptive search optimization technique first introduced by Kennedy and Eberthart in 1995 [2]. Because of its simplicity of implementation and computational effectiveness, it's been widely used in different areas including identification of nonlinear system [3]. However, the standard PSO has some defects such as prematurity, low convergent speed and poor robustness, and then many modified methods have been proposed [4–6]. In this paper, we propose another improved PSO with the idea of subarray.

The outline of this paper is as follows. The subarraying problem is mathematically formulated in Section 2 where the pattern functions and group method are described. Section 3 shows the comparative study of the efficiency of PSO in the subarrayed array antennas and in unsubarrayed antenna array with the uniform distribution amplitude, demonstrated the performances of PSO in the subarrayed array antennas when amplitude is uniform distribution, linear distribution or cosine distribution, as well. Ultimately, some conclusions are drawn.

2. OPTIMIZATION METHOD

The synthesis of the weights of linear arrays to meet certain requirements, such as high directivity, low sidelobe level, narrow beamwidth, high efficiency and nulls in specific directionshas been considered as the reference application to illustrate and analyse the usefulness and limitations of the PSO algorithm.

The far-field radiation pattern of a z-directed linear array at a direction given by the angle θ, neglecting mutual coupling effects, is given by

$$F(\theta) = F_1(\theta) \cdot F_2(\theta) \tag{1}$$

where $F_2(\theta)$ represents the element pattern and takes into account the type of radiator used and $F_1(\theta)$ is the array factor. Furthermore, the array factor for a linear array consisting of N elements

uniformly spaced a distance d on the z-axis is given by

$$F_1(\theta) = \sum_{n=1}^{N} I_n \cdot e^{jk(n-1)d\cos\theta} \tag{2}$$

in which $k = 2\pi/\lambda$ is the background wave-number, λ is the wavelength, and d is the element spacing.

In the network which is made of Q contiguous subarrays with different real weights at their input ports, the far field expression of the array factor is given by [7]

$$F_1(\theta) = \sum_{q=1}^{Q} \omega_q \sum_{n=1}^{N_q} \delta_{nq} I_n e^{jk(n-1)d\cos\theta} \tag{3}$$

where ω_q and I_n denote the weight of the subarray and the excitation amplitude weights of the nth radiating element, depending on amplitude-only is considered. Moreover, $\delta_{nq} = 1$ when the nth element belongs to the nth subarray and $\delta_{nq} = 0$ otherwise. N_q denote the element number of qth subarray while it could be different in every subarray, and $N = \sum_{q=1}^{Q} N_q$.

Starting from these analyses, the issue of optimal design of antenna arrays in this paper turns out to seek to the number Q of contiguous subarrays and their corresponding weights ω_q with the same N_q in every subarray to obtain a pattern with the lowest relative SLL. Moreover, the optimize efficiency and performance of PSO are compared through the issue.

Considering the certain design problem above, the issue is further transformed into doing multiple iterations to generate individual extremes p_{best} and global extremes g_{best} of the particle's velocity and position every generation, and the position of a particle just corresponds to one possible solution of the weights in the issue above. In PSO, the particle's velocity and position update equations as given by [8]

$$V_k^{i+1} = wV_k^i + c_1 r_1 (p_{\text{best}} - X_k^i) + c_2 r_2 (g_{\text{best}} - X_k^i) \tag{4}$$

$$X_k^{i+1} = X_k^i + V_k^{i+1} \cdot \Delta t \tag{5}$$

3. SIMULATION RESULTS

Aiming at comparing the optimize efficiency of PSO using in the subarrayed and unsubarrayed antenna array, first let us consider a linear array with 128 half-wavelength spaced isotropic radiators as the canonical problem to illustrate the study, and a mask showing a broadside pattern with 2° elevation beamwidth and −20 dB sidelobe level as the design goal.

The first experiment is carried out between the unsubarrayed antenna array and the subarrayed antenna array in which the antennas are divided into 4, 8, 16 and 32 groups respectively, with the

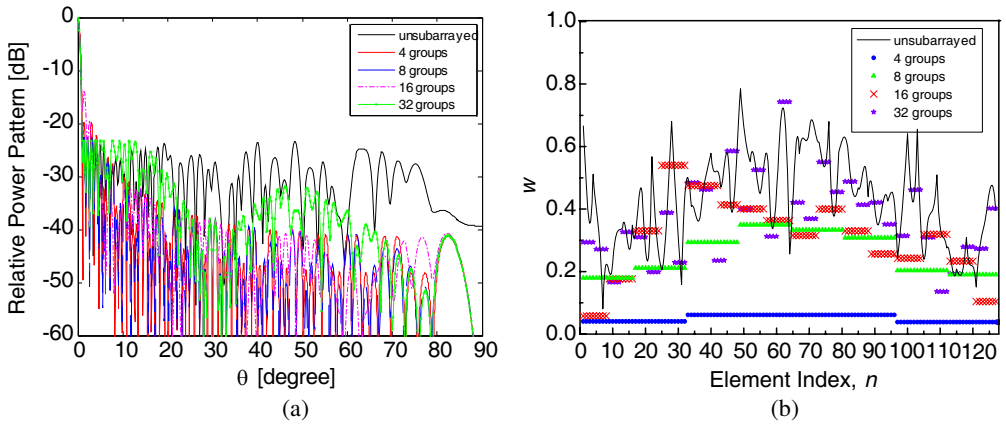

Figure 1: (a) Uniform subarraying optimized power patterns. $N = 128$. $Q = 128$ (unsubarrayed), 32, 16, 8, 4. (b) Optimized amplitude weights.

uniform and unitary set of excitations is considered. The optimized power patterns are shown in Fig. 1(a), and the optimized amplitude weights of these arrays are shown in Fig. 1(b). It is worth notice that since the antenna arrays subarrayed, the SLL is reduced by more than 2 dB and the pattern declined faster and become more smoothing. The time costs of PSO are shown in Table 1. As expected, the time costs are more or less reduced by subarrayed and it would be much more with Q raised. When $Q = 4$, the time cost is reduced to one third of in unsubarrayed array.

Table 1: Uniform subarrying ($N = 128$, $Q = 128$ (unsubarrayed), $32, 16, 8, 4$)-time cost of the PSO.

Q	128 (Unsubarrayed)	32	16	8	4
Time (s)	2979	2517	2454	1308	993

The second experiment considers the uniform and nonuniform subarraying cases in which the amplitude is uniform distribution, linear distribution or cosine distribution, respectively, and four tests are taken into account to compare the performance of PSO in subarrayed array antennas. In particular, each subarray has a number of elements equal to $N_q = 32$, $N_q = 16$, $N_q = 8$ and $N_q = 4$, respectively, while the total number of elements is kept equal to 128 as in the first experiment.

For comparison purposes, Table 2 summarizes the time costs of PSO while the amplitude according to these three kinds of distribution, whereas Fig. 2 shows the optimized power patterns based these assumptions all above.

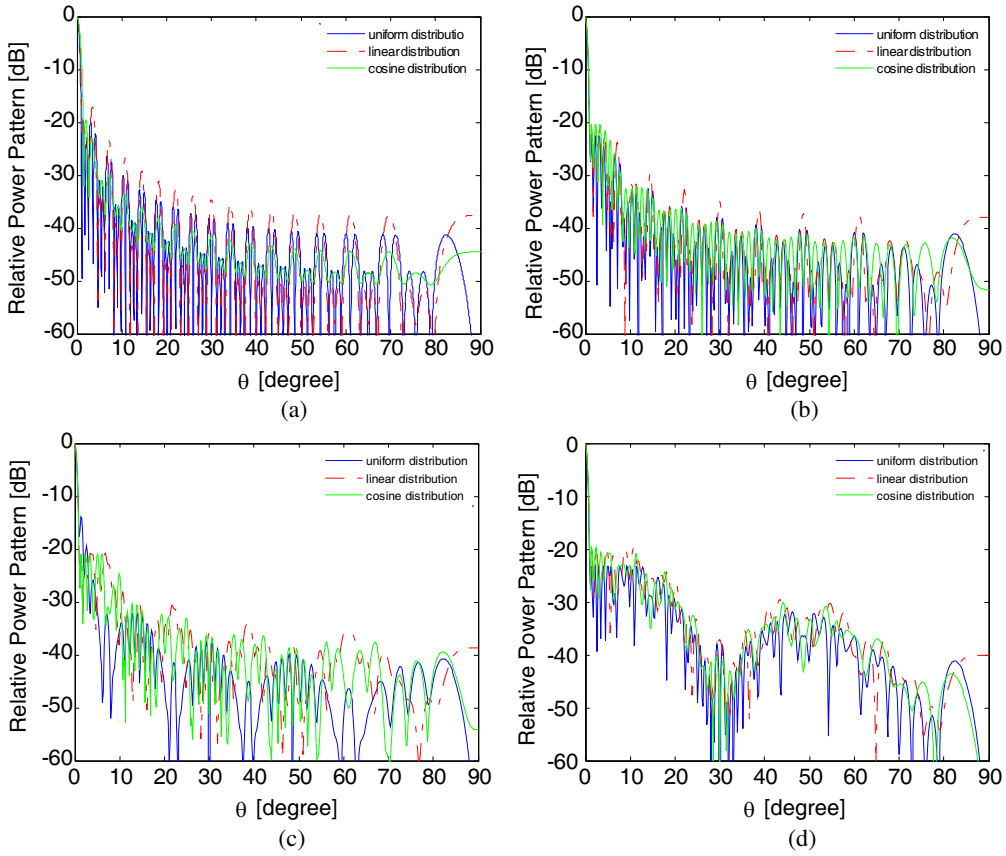

Figure 2: Uniform, linear and cosine subarrying optimized power patterns. $N = 128$. (a) $Q = 4$. (b) $Q = 8$. (c) $Q = 16$. (d) $Q = 32$.

Table 2: Uniform, linear and cosine subarrying ($N = 128$, $Q = 4, 8, 16, 32$)-time cost of the PSO.

Q	4	8	16	32
uniform distribution	993.0135	1307.9429	1454.8	2517.4161
linear distribution	150.2288	1440.6855	1726.6462	2904.6824
cosine distribution	1107.3152	1492.4216	1760.6243	2832.2174

It is worth notice that during the three kinds of amplitude distribution, the time cost in the uniform distribution is the least while the SLL in the cosine distribution is the lowest and declined fastest.

4. CONCLUSIONS

In this paper, the modern heuristic particle swarm optimization technique has been successfully applied to large linear array synthesis with the idea of subarray. Different procedures for the design of subarrayed antennas characterized by subarrays of unequal sizes and amplitude distributions have been presented. The grouping of the array elements into contiguous subarrays and the computation of the subarray weights have been simultaneously performed to compare the optimize efficiency of PSO using in the subarrayed and unsubarrayed antenna array firstly. Besides these, representative results have been reported to analyse the performance of PSO with different kinds of amplitude distributions and unequal size. Results demonstrate that the efficiency of PSO in subarrayed array antennas is much better than in unsubarrayed array antennas for the time cost is lower and the pattern is more smoothing. Moreover, the number of subarray fewer, the efficiency better. The results further suggest that different amplitude distributions also could affect the performance of PSO. The method also can be used to solve two-dimension antenna array synthesis problems.

REFERENCES

1. Mailloux, R. J., *Phased Array Antenna Handbook*, Artech House, Boston, MA, 2005.
2. Kennedy, J. and R. Eberhart, "Particle swarm optimization," *Proceeding of IEEE International Conference on Neural Networks*, 1942–1948, Perth, Australia, 1995.
3. Araujo, E., S. Dos, and L. Coelho, "Fuzzy model and particle swarm optimization for nonlinear identification of a Chua's oscillator," *Proceeding of IEEE International Conference on Fuzzy Systems*, 1–6, London, England, July 2007.
4. Li, M., C. Yang, and C. W. Yang, "An improved two particles PSO algorithm," *Proceedings of the World Congress on Intelligent Control and Automation*, 8743–8748, Chongqing, China, June 2008.
5. Wang, H., C. Li, Y. Liu, and S. Zeng, "A hybrid particle swarm algorithm with Cauchy mutation," *Proceedings of the 2007 IEEE Swarm Intelligence Symposium*, 356–360, Honolulu, USA, April 2007.
6. Tasgetiren, M. F., Y. C. Liang, M. Sevikli, and G. Gencyilmaz, "A particle swarm optimization algorithm for makespan and total fowtime minimization in the permutation flowshop sequencing problem," *European Journal of Operational Research*, Vol. 177, No. 3, 1930–1947, 2007.
7. Manica, L., P. Rocca, and A. Massa, "Design of subarrayed linear and planar array antennas with SLL control based on an excitation matching approach," *IEEE Transactions on Antennas and Propagation*, Vol. 57, No. 6, 1684–1691, June 2009.
8. Lopez, P., J. R. Basterrechea, and J. Verdeja, "Synthesis of linear arrays using particle swarm optimisation," *First European Conference on Antennas and Propagation, EuCAP 2006*, 1–6, November 6–10, 2006.

Directive Surface Wave Excitation Using Yagi-Uda Slots

Jinsheng Dong, **Liping Yan**, **and Kama Huang**
School of Electronics and Information Engineering, Sichuan University, Chengdu 610064, China

Abstract— A 5-slot Yagi-Uda surface-wave launcher operating at 20 GHz is proposed in this paper. The launcher, which is composed of a driven slot, a reflector slot and three director slots, fed by a spoon shaped microstrip line, and manufactured on a 0.6 mm thick substrate with $\varepsilon_r = 2.65$, is used to excite surface wave in a grounded teflon slab, whose thickness is optimized as 5 mm for maximum surface-wave power excitation. The Numerical results show that the relative bandwidth in terms of −10 dB return loss is increased from 11.4% to 13.85%, and the maximum forward/backward directivity ratio is increased from 16.7 dB to 24.7 dB, when compared to those of a three-slot launcher with only one director.

1. INTRODUCTION

Surface wave is usually suppressed in many applications, especially in patch antennas design and planar integrated microwave circuits, in that surface wave will lead to the diminution of the available radiated power and may cause unexpected coupling and interference. When frequency reaches the millimeter-wave region, the leakage will become much severe, even may exceed the radiated power. However, this also has opened a door for applying the surface wave in millimeter-wave region. During the past decade, several new applications whose objective is to efficiently excite the surface wave have emerged. One such application is the quasi-optical slab beam power combiners [1], which have attracted much attention in recent years because it can provide power combination by coupling rather than via transmission lines. One type of quasi-optical structure is the dielectric slab-beam waveguide (DSBW). With a directive launcher the surface wave power can be combined efficiently in electrically thick dielectric slab waveguide by using its dominant mode [2].

Although several planar antennas can be used for quasi-optical application, the slot antenna is the favorite candidate for TM_0 excitation. Yagi-Uda launcher with two and three slots fed by either microstrip lines [3] or coplanar-waveguide (CPW) [4] has been investigated to achieve directional excitation. In order to enhance the directivity further, in this paper we proposed a 5-slot Yagi-Uda launcher operating at 20 GHz. The launcher fed by a spoon shaped microstrip line composes of a driven slot, a reflector slot and three director slots instead of one. The structure of the launcher and optimized slab parameters are described in Section 2. The simulation results and discussion are shown in Section 3, and we summarize our conclusions in Section 4.

2. STRUCTURE OF THE LAUNCHER

A well-designed surface-wave launcher satisfies not only the maximum excitation of the dominant mode, but also the mode purity (dominant TE or TM mode) to ensure that only the dominant mode propagates inside the slab. The dominant mode of the slab is the TM_0, which exists at a certain frequency range. The total number of TM surface wave modes which may exist in a slab with known permittivity and thickness is equal to the largest integer N satisfying the condition [5],

$$\mathrm{N} < \frac{k_0 h}{\pi}\sqrt{\varepsilon_r - 1} \tag{1}$$

where h is the dielectric thickness, ε_r is the substrate permittivity, and $k_0 = 2\pi/\lambda_0$, λ_0 is the free space wavelength. N should be less than one if only TM_0 mode is expected. In this paper, the substrate permittivity ε_r is 2.1 and the operating frequency is 20 GHz. Substituting those parameters into Equation (1) we can obtain that h is about 7 mm.

Hammad etc. investigated the percentage of surface-wave power launched by a slot on a grounded dielectric slab versus normalized frequency defined as the following [4]

$$V = k_0 h\sqrt{\varepsilon_r - 1} \tag{2}$$

For a slab with permittivity around 3, the maximum-percentage surface-wave power occurs at $V \approx 2.2$. Then we obtained that the optimization of the slab thickness is approximately 5 mm for operating frequency 20 GHz.

The structure of the proposed five-slot Yagi-Uda launcher is shown in Fig. 1. It contains two dielectric layers separated by the slotted ground plane, as shown in Fig. 1(a). A microstrip feed line is on the top layer with thickness of 0.6 mm and permittivity $\varepsilon_r = 2.65$. The geometry of the feed line is shown in Fig. 1(b). It composes of a $\lambda/2$ 50 Ω microstrip line (L_1), a $\lambda/2$ exponential tapered line (L_2) which is used to match the 50 Ω microstrip line and the microstrip line L_3, the narrower microstrip line (L_3) and a spoon shaped microstrip feed line. The launcher, which is composed of a driven slot, a reflector slot and three director slots, is used to excite surface wave in the grounded Teflon slab with optimized thickness of 5 mm as mentioned above. The optimal dimensions are obtained as follows: Feed line offset d=0.58 mm, $L_1 = 0.49$ cm, $L_2 = 0.46$ cm, $L_3 = 1.22$ cm, $L_{dr} = 0.42$ cm, and $L_r : L_{dr} : L_{di1} : L_{di2} : L_{di3} = 1.05 : 1 : 0.9 : 0.882 : 0.864$.

3. SIMULATION RESULTS AND DISCUSSION

The directivity of the 5-slot surface-wave launcher is investigated using simulation model described in Fig. 2. Three same launchers are used in the simulation, the one with port 1 is used to radiate power, and the other two are used to couple the power propagating forward and backward. The difference between forward coupling S_{21} and backward coupling S_{31} (in decibels) yields the forward/backward directivity ratio (FBR).

Figure 3(a) shows the input return loss of a single launcher with 3 slots and 5 slots respectively. It can be found that the relative bandwidth in terms of −10 dB return loss is increased from 11.4% to 13.85%. Fig. 1(b) shows the FBR calculated using the model shown in Fig. 2. We can find that the FBR is increased by 2.6 dB at 20 GHz when adding two additional director slots, Moreover the maximum FBR is 24.7 dB at 21 GHz compared with 16.7 dB at the same frequency for the 3-slot launcher.

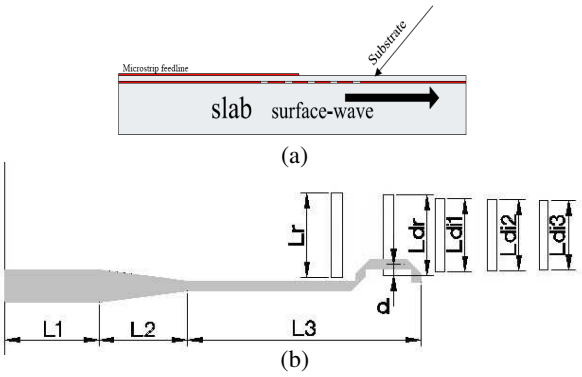

Figure 1: (a) Side view and (b) top view of the 5-slot Yagi-Uda launcher in a dielectric slab.

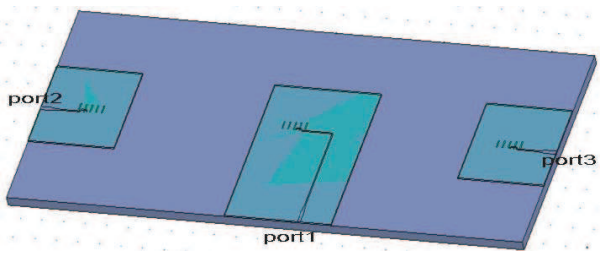

Figure 2: Simulation model for testing the launchers directivities.

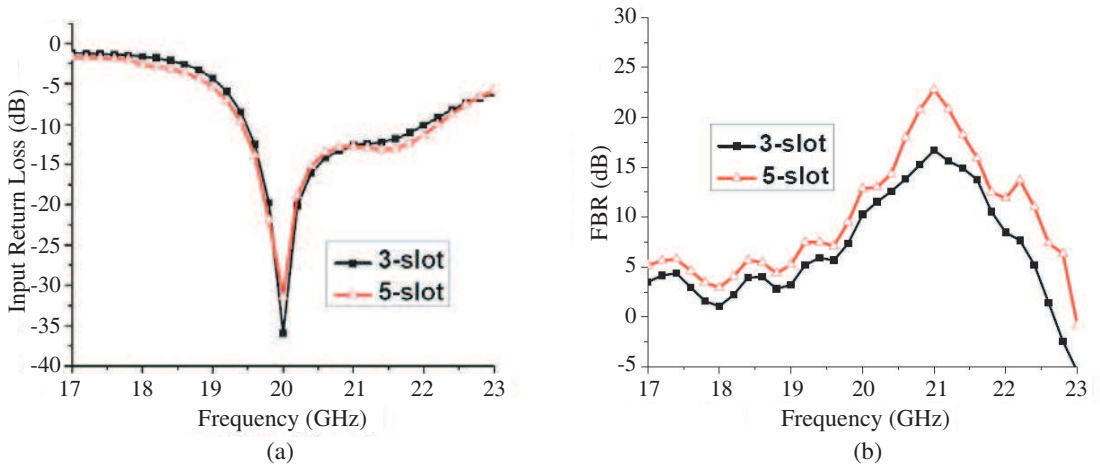

Figure 3: The comparisons of (a) input return loss and (b) the FBR between 3-slot and 5-slot Launcher.

4. CONCLUSION

A 5-slot Yagi-Uda surface-wave launcher operating at 20 GHz is proposed. Numerical results show that both the relative frequency and forward/backward directivity ratios are enhanced by adding additional two directors, which is expected in some practice use.

REFERENCES

1. Mink, J. W. and F. K. Schwering, "A hybrid dielectric slab-beam wave-guide for the sub-millimeter wave region," *IEEE Trans. Microw. Theory Tech.*, Vol. 46, 775–783, 1993.
2. Hwang, H., G. P. Monahan, M. B. Steer, J. W. Mink, J. Harvey, A. Paollea, and F. K. Sherting, "A dielectric slab waveguide with four planar power amplifiers," *IEEE MIT-S Microw. Symp. Dig.*, 921–924, 1995.
3. Perkons, A. R., Y. Qian, and T. Itoh, "TM surface-wave power combining by a planar active-lens amplifier," *IEEE Trans. Microw. Theory Tech.*, Vol. 46, 775–783, 1998.
4. Hammad, H. F., Y. M. M. Antar, A. P. Freundorfer, and S. F. Mahmoud, "Uni-planar CPW-fed slot launchers for efficient TM_0 surface-wave excitation," *IEEE Trans. Microw. Theory Tech.*, Vol. 51, 1234–1240, 2003.
5. Mahmoud, S. F., Y. M. M. Antar, H. F. Hammad, and A. P. Freundorfer, "Theoretical consideration in the optimization of surface waves on a planar structure," *IEEE Trans. Antennas Propagat.*, Vol. 52, 2057–2063, 2004.

Wideband Slot Antenna by Controlling Resonances

Hyengcheul Choi, **Sinhyung Jeon**, **Oul Cho**, **Seungwoo Kim**, **and Hyeongdong Kim**
Department of Electrical and Computer Engineering, Hanyang University
Haengdang-dong, Seongdong-gu, Seoul, Korea

Abstract— This paper proposes novel method to widen bandwidth of a slot antenna for mobile handset. The proposed method is adding rectangular loop and high dielectric material to a simple slot antenna for controlling resonances. Fundamental and two harmonic resonances can be converged within operation bands because the proposed method provides non-uniform resonance shifts. The bandwidth remarkably enhances from 320 MHz (1900–2220 MHz) to 880 MHz (1750–2630 MHz) by using the proposed method.

1. INTRODUCTION

The growth of world-wide mobile communications increases the number of operation frequency bands supported by a mobile handset [1], and it makes that small wideband antenna is important for mobile wireless communications. Branched antenna using EM coupling is studied for obtaining wide bandwidth at [2], but this multiple radiating structure has relatively large volume as compared with single radiating structure inevitably. Reference [3] presented single radiating structure having wideband characteristic by inserting reactive components to a loop antenna for controlling resonances. The proposed method in this paper is adding rectangular loop and high dielectric material ($\varepsilon_r = 30$) to a simple slot antenna for controlling resonance frequencies. The wideband

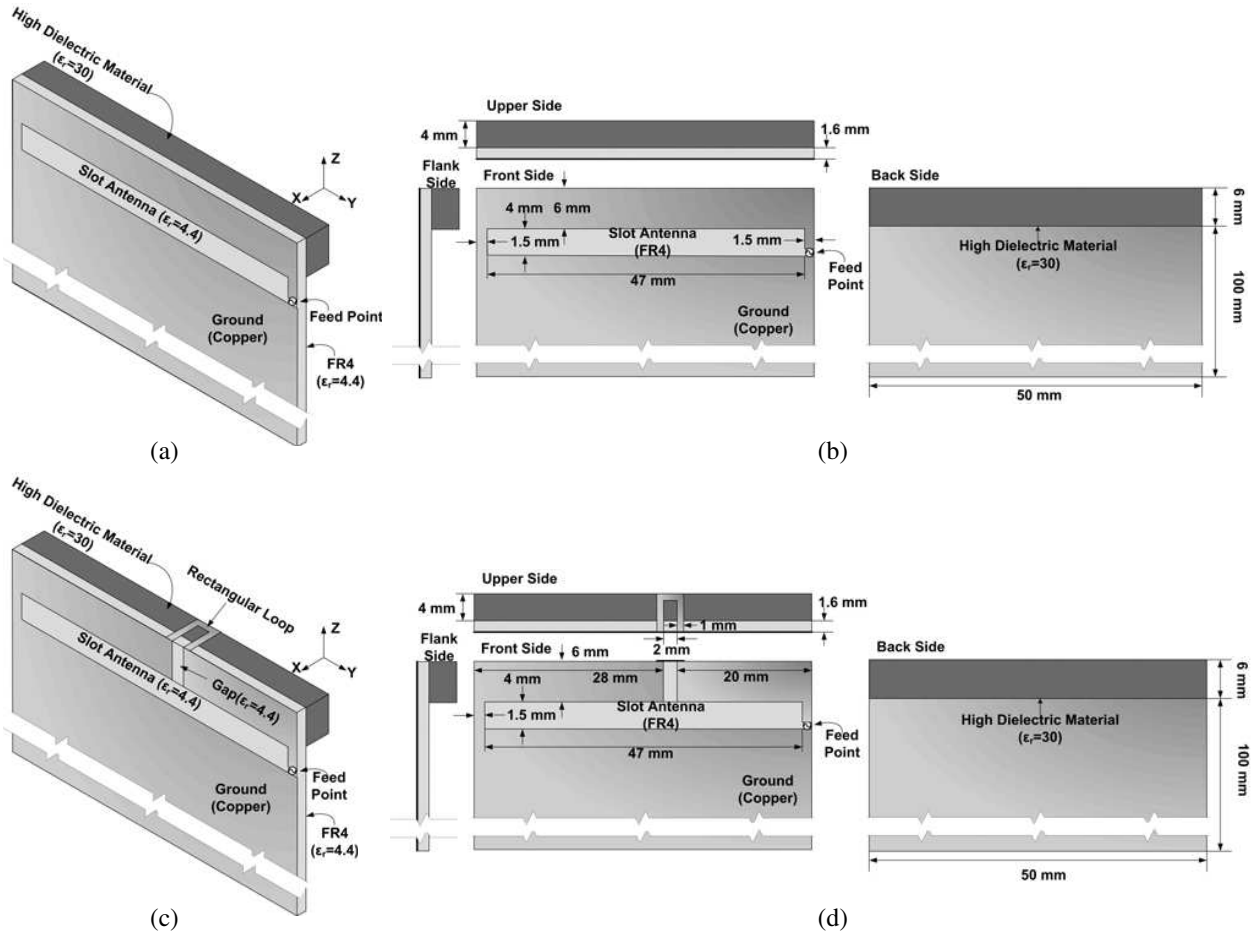

Figure 1: (a) Three-dimensional geometry and (b) two-dimensional geometry of reference antenna, and (c) three-dimensional geometry and (d) two-dimensional geometry of proposed antenna.

slot antenna can be designed when multiple resonances of the slot antenna are closed to each other due to non-uniform resonance shifts.

2. ANTENNA DESIGN AND RESULTS

Figure 1 shows the simple slot antenna (reference antenna) and the proposed antenna for a mobile handset. The slot antenna is placed on ground plane of 50 mm × 100 mm which is general size of bar type handsets. A fundamental resonance occurs when the electrical length of slot antenna is half-wavelength ($\lambda/2$) [4], and harmonic resonances additionally appear at $3\lambda/4$ and λ, respectively. Because of dielectric material (FR4 $\varepsilon_r = 4.4$) of PCB, wavelength (λ) in mobile handset is shorter than that in free space. The rectangular loop and the high dielectric material ($\varepsilon_r = 30$) is utilized to shift resonance frequencies of the slot antenna in this paper. To observe resonance shifts by the loop and the high dielectric material, we illustrate input reactances and VSWRs in Fig. 2 and Fig. 3, respectively. It is shown in these data that rectangular loop does not affect the fundamental resonance but decreases harmonic resonances, and then high dielectric material makes a large shift at the harmonic resonances but a small shift at the fundamental resonance. In other words, adding the rectangular loop and the high dielectric material to the reference antenna generates non-uniform resonance shifts. As a result, the fundamental resonance and two harmonic resonances are closed, which helps to obtain wide operation bandwidth. Note that the proposed method widens bandwidth from 320 MHz (1900–2220 MHz) to 880 MHz (1750–2630 MHz).

As shown in Fig. 4, simulated and measured VSWRs coincide with each other. Measured bandwidth under VSWR = 3 is 900 MHz (1750–2650 MHz) and it can sufficiently cover DCS/PCS/WCDMA/Bluetooth as considering resonance frequency decreases by a handset case [5]. In this paper,

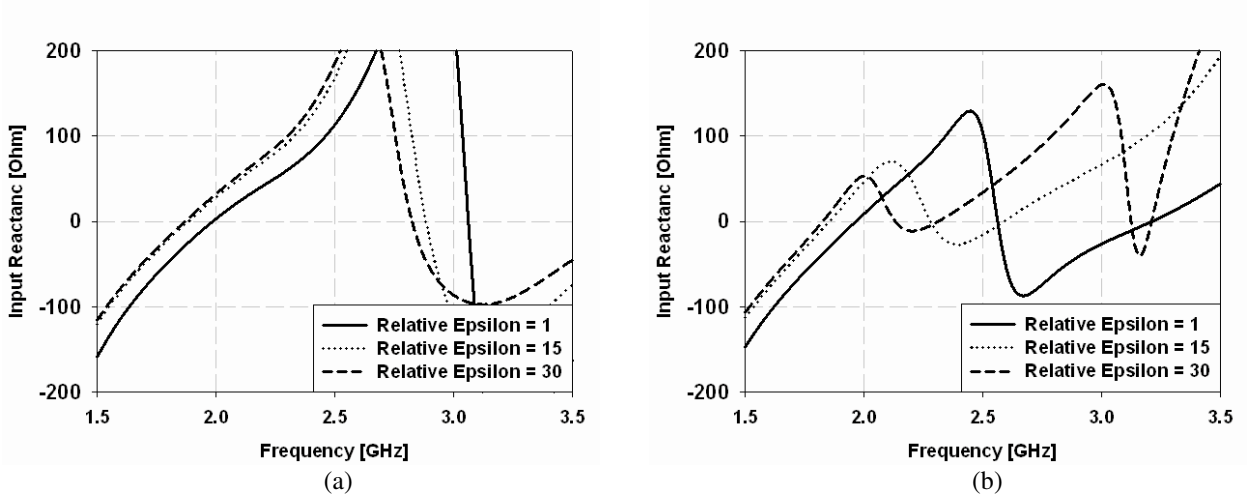

Figure 2: Input reactances of (a) without and (b) with rectangular loop.

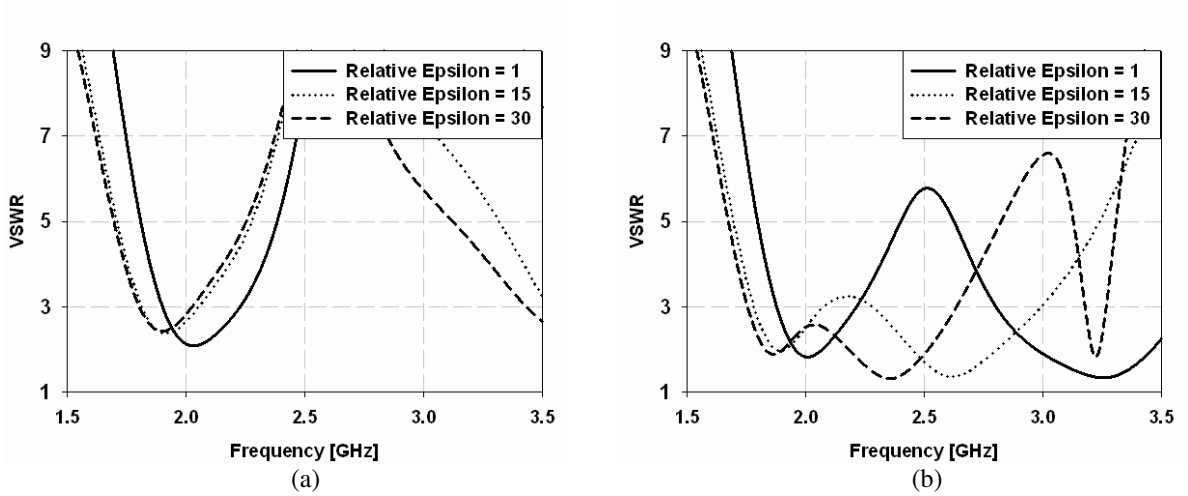

Figure 3: VSWRs of (a) without and (b) with rectangular loop.

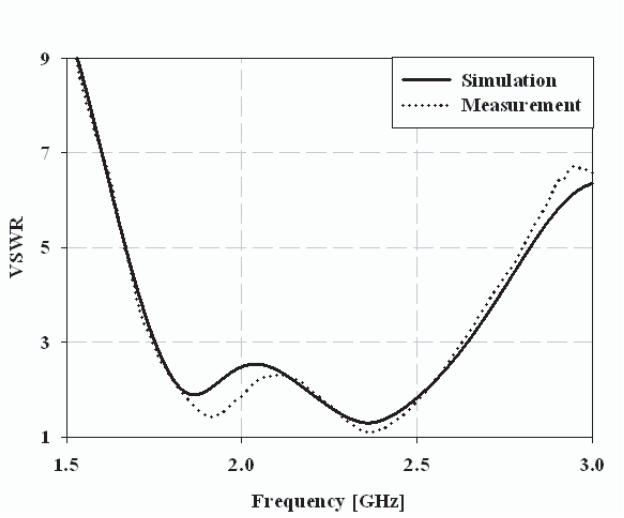

Figure 4: Simulation and measurement VSWRs.

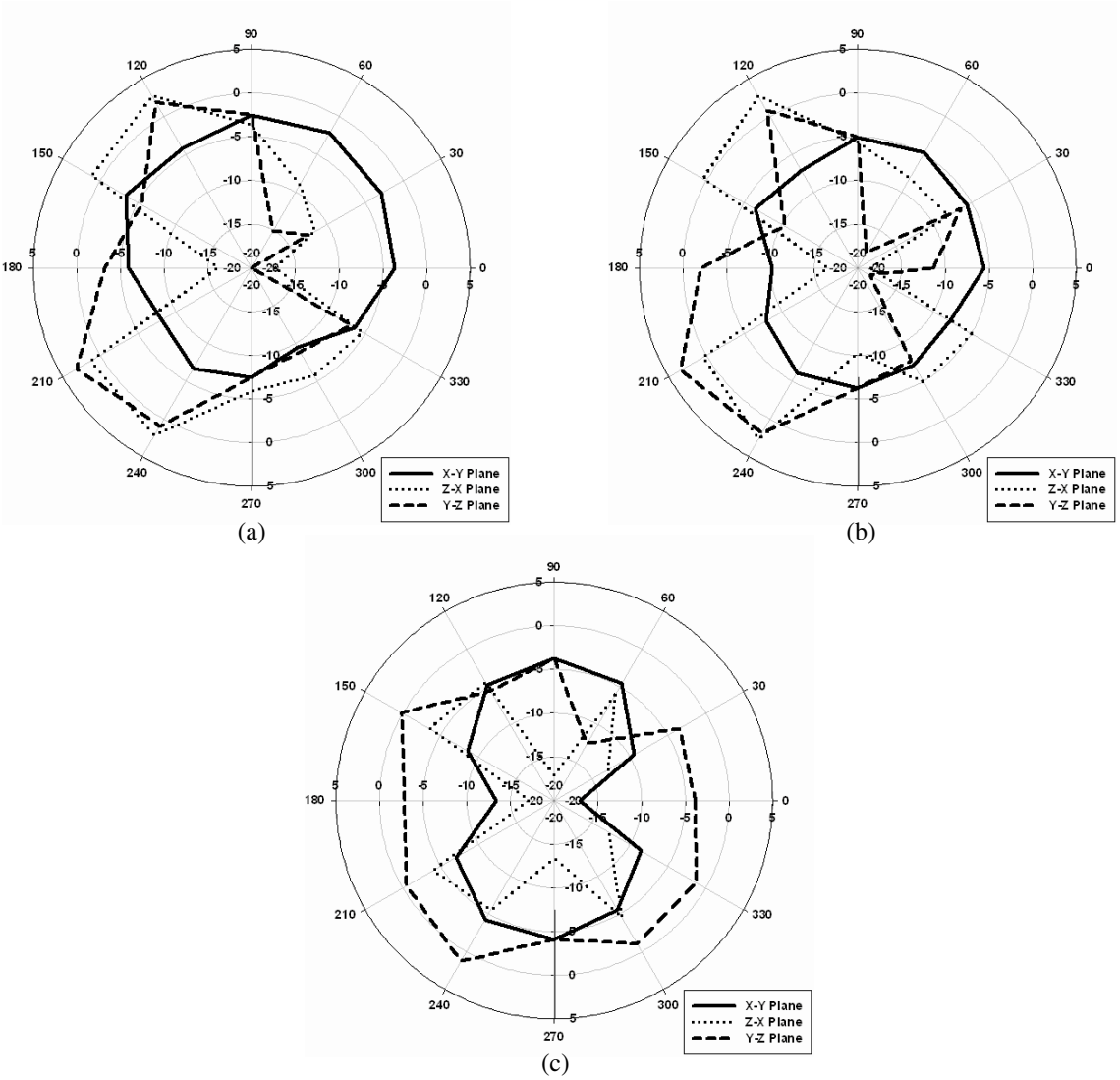

Figure 5: Measured radiation patterns at (a) 1.85 GHz, (b) 2.10G Hz, and (c) 2.35 GHz.

absolute gain patterns of the proposed antenna have been measured in x-y plane (azimuthal plane), z-x plane (elevation plane 1), and y-z plane (elevation plane 2) at three resonances (1.85 GHz,

2.1 GHz, and 2.35 GHz) as shown in Fig. 5. It is seen that the omnidirectional radiation pattern in the elevation plane disappears as increasing frequency because ground effect becomes small and harmonic resonance modes are excited when wavelength is short. Measured peak gains were 4.61 dBi, 4.59 dBi, and 3.72 dBi at three resonances, respectively. From VSWR and radiation patterns, it is found that the proposed antenna in this paper can be used for a mobile handset.

3. CONCLUSION

This paper proposes a novel method to design wideband slot antenna by using non-uniform resonance shifts. Adding rectangular loop and high dielectric material decreases two harmonic resonance frequencies while the fundamental resonance is almost fixed. As a result, input reactance curve between resonances becomes very smooth and this characteristic makes wideband slot antenna. Bandwidth of simple slot antenna (reference antenna) is enhanced form 320 MHz (1900–2220 MHz) to 880 MHz (1750–2630 MHz) by using the proposed method. In measurement, the proposed antenna has 900 MHz (1750–2650 MHz) bandwidth under VSWR = 3 and high gains at resonances within bandwidth. Based on measured data, we expect that the proposed antenna can be effectively used for DCS/PCS/WCDMA/Bluetooth.

ACKNOWLEDGMENT

This research was supported by the MKE (The Ministry of Knowledge Economy), Korea, under the ITRC (Information Technology Research Center) support program supervised by the IITA (Institute for Information Technology Advancement) (IITA-2009-C1090-0902-0003).

REFERENCES

1. Chen, Z. N., *Antennas for Portable Devices*, John Wiley & Sons, Chichester, 2007.
2. Yarman, B. S., *Design of Ultra Wideband Antenna Matching Networks: Via Simplified Real Frequency Technique*, Springer, New York, 2008.
3. Choi, H., S. Jeon, S. Kim, and H. Kim, "Controlling resonance frequencies in antennas to achieve wideband operation," *Electronics Letters*, Vol. 45, No. 14, 716–717, 2009.
4. Jeon, S., H. Choi, and H. Kim, "Hybrid planar inverted-f antenna with a t-shaped slot on the ground plane," *ETRI Journal*, Vol. 31, No. 5, 616–618, 2009.
5. Sim, D.-U. and S.-O. Park, "A triple-band internal antenna: Design and performance in presence of the handset case, battery, and human head," *IEEE Transactions on Electromagnetic Compatibility*, Vol. 47, No. 3, 658–666, 2005.

Design of a Gaussian Backscatter Antenna with Ring Focus Feed

W. Thaiwirot[1, 2], **R. Wongsan**[1, 2], **and M. Krairiksh**[3]

[1]School of Telecommunication Engineering, Institute of Engineering, Thailand
[2]Suranaree University of Technology, Nakhon Ratchasima, Thailand
[3]Faculty of Engineering, King Mongkut's Institute of Technology Ladkrabang, Bangkok, Thailand

Abstract— This paper presents a design of a Gaussian backscatter antenna with ring focus feed. The curvature of main reflector is Gaussian, and the subreflector is a portion of an ellipse. The antenna has axial symmetry. A backscattering technique is used with the main reflector to achieve wide beamwidth. The input parameters of the proposed antenna are derived in closed form. For analysis and design physical theory of diffraction (PTD) is utilized. The proposed antenna can produce high gain (maximum gain = 11.8 dB), wide beamwidth (coverage angle $\theta = \pm 65^\circ$) and small diffraction effects. This antenna can be used for realizing earth coverage beam in LEO satellite or indoor wireless LAN applications.

1. INTRODUCTION

Low Earth Orbit Satellite (LEO Satellite) communication systems are one of the new and exciting developments in providing global communication services. The satellites contain sophisticated equipment for processing, transmitting through antennas that communicate from and to hand-held user terminals on the ground. Since satellites in low earth orbit change their positions relative to the ground positions quickly, therefore, time required for ground station-satellite communications is limited. Hence, wide beam antennas are needed. At present, the antenna can be used for realizing earth coverage beam in LEO satellite such as shaped reflector antennas. The highly shaped-beam antenna was first developed to give approximately uniform coverage of the earth from satellite antenna [1]. Recently, the similar requirement but different application, the indoor high speed data transmission: wireless LAN operating in the millimeter wave, attracts considerable attentions [2]. A shaped reflector antenna for 60-GHz indoor wireless LAN access point was developed [3]. However, shaping the reflector to obtain shaped beam becomes complicated. This yields a discontinuous surface and more complicated manufacturing process. Thaivirot et al. [4] presented the synthesis of radiation pattern of variety of the shaped backscatters antenna. It was found that, the Gaussian backscatter will provide the appropriate characteristics. Therefore, it is suitable for using as an antenna for realizing earth coverage beam in LEO satellite application as shown in Fig. 1. To improve gain and efficiency of reflector antenna, the displaced-axis dual reflector antenna was discussed. It was found that the axially displaced ellipse (ADE antenna) provides an excellent choice for compact high-gain spacecraft antenna applications. As a result, this paper presents the axially displaced ellipse antenna. The proposed antenna is a centrally fed displaced axis Gaussian backscatter antenna with a ring focus feed. A backscattering technique is used with the main reflector to achieve wide beamwidth for earth coverage in LEO satellite. Moreover, this approach is fruitful for high-gain antenna applications, especially for Wireless Local Area Network (WLAN) large-scale indoor base station. The proposed antenna will be installed on the centre point of ceiling in the large hall and can illuminate a predefined circular area for all users without substantial spatial variation as shown in Fig. 2. Physical theory of diffraction (PTD) is utilized for analysis and design. The input parameters of the proposed antenna are derived in closed form.

2. ANTENNA GEOMETRY AND DESIGN PARAMETER

The cross section of the axially displaced ellipse antenna system is shown Fig. 3. The antenna has axial symmetry. The curvature of main reflector is Gaussian, and the subreflector is a portion of an ellipse. The two foci of the ellipse are located at the phase-center of the feed. The design procedure in this section is based on [5, 6]. The main reflector and subreflector are defined in their own coordinate system (O_{MR}, X_{MR}, Y_{MR}, Z_{MR}) and (O_{SR}, X_{SR}, Y_{SR}, Z_{SR}), respectively, and to have a general antenna coordinate system (O, X, Y, Z) in which the main reflector and subreflector are finally expressed. Note that the antenna arrangements we are proposing, is $O_{MR} \equiv O_{SR} \equiv O$.

For the classical symmetric Cassegrain or Gregorian reflector antenna, we are dealing with a system of nine parameters defining the overall geometry of the antenna. D_m, L, A, D_s, θ_e, L_m, L_s, a, and f (see Figs. 3–5). However, these parameters can not be specified arbitrarily. Therefore, we

choose five input parameters, i.e., D_m, A, D_s, L and θ_e to define the antenna, and then calculate from these the other design parameters in closed form.

For the definition of the main reflector geometry, we consider only the upper part of the (O_{MR}, X_{MR}, Z_{MR}) plane. The main-reflector profile, $z_{mr}(x_{mr})$, depends on the two real parameters A and L. The equation of a Gaussian backscatter is of the form

$$z_{mr}(x_{mr}) = Ae^{-\left(\frac{2}{D_m}x_{mr}\right)^2} - L, \tag{1}$$

with

$$0 \le x_{mr} \le \frac{D_m - D_s}{2}.$$

The elliptical subreflector profile, $z_{sr}(x_{sr})$, is defined in the (O_{SR}, X_{SR}, Z_{SR}) plane, and depends on the two real parameters a and f. It is of the form

$$z_{sr}(x_{sr}) = a\sqrt{1 + \frac{(x_{sr})^2}{f^2 - a^2}} - f. \tag{2}$$

Note: In the case an ellipsoid, $a > f > 0$.

The points defining the subreflector are such that when x_{sr} is expressed in the main-reflector coordinate system,

$$-\frac{D_s}{2} \le [x_{sr}]_{\text{Expressed in the MR coordinate system}} \le 0.$$

To design the antenna, we use the distance relationship in an ellipse [6] (see Figs. 3–5).

$$\|F_0P\| + \|OP\| = 2a \tag{3}$$

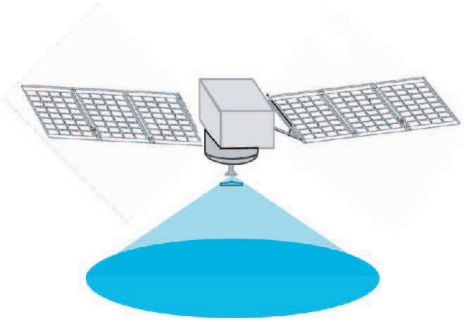

Figure 1: Application of shaped backscatter antenna for LEO satellite communication.

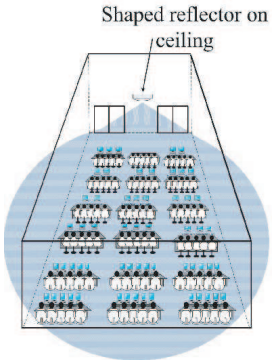

Figure 2: Application of shaped backscatter antenna for indoor WLAN in the large hall.

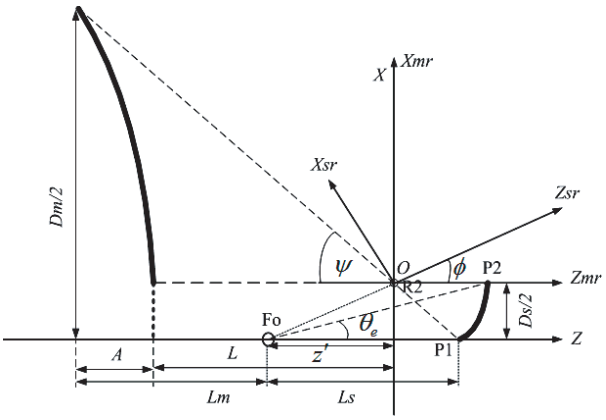

Figure 3: Cross-sectional view of the axially displaced ellipse antenna system.

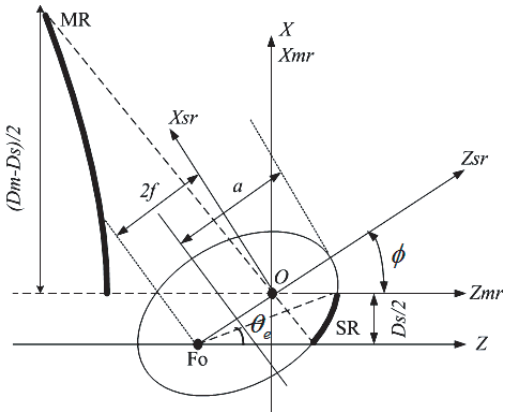

Figure 4: Cross-sectional view of the elliptical-subreflector coordinate system with its parameters.

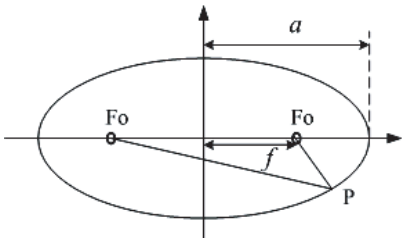

Figure 5: Distance relationship in an ellipse.

From the five input parameters D_m, A, D_s, L and θ_e, and using the distance relationship in an ellipse, we find that

$$\tan(\psi) = \frac{(D_m - D_s)e}{2(eL - A)}, \tag{4}$$

$$\tan(\phi) = \frac{2}{\left[\dfrac{\cos(\theta_e)+1}{\sin(\theta_e)} - \dfrac{\cos(\psi)+1}{\sin(\psi)}\right]}, \tag{5}$$

$$f = \frac{D_s}{4\sin(\phi)}, \tag{6}$$

$$a = \frac{D_s}{8}\left[\frac{\cos(\theta_e)+1}{\sin(\theta_e)} + \frac{\cos(\psi)+1}{\sin(\psi)}\right], \tag{7}$$

$$Ls = 2f\cos(\phi) + \frac{D_s}{2\tan(\psi)}, \tag{8}$$

$$L_m = L - \frac{D_s}{4}\left[\frac{\cos(\theta_e)+1}{\sin(\theta_e)} - \frac{\cos(\psi)+1}{\sin(\psi)}\right] + A. \tag{9}$$

The parameters necessary to represent the axially displaced ellipse reflector antenna system are defined.

3. RADIATION PATTERN

The antenna was designed using the input parameters, i.e., $D_m = 30\,\text{cm}$, $L = 32\,\text{cm}$, $D_s = 5.6\,\text{cm}$, $A = 8.2\,\text{cm}$ and $\theta_e = 25°$. These parameters can provide optimum characteristics. The main reflector edge illumination is taken at a level of $-15\,\text{dB}$. The antenna is fed by a corrugated conical horn, operating at 18.75 GHz. The antenna impedance of about $50\,\Omega$. The designed antenna is presented in Fig. 6. The radiation pattern of the antenna is analyzed by using physical theory of

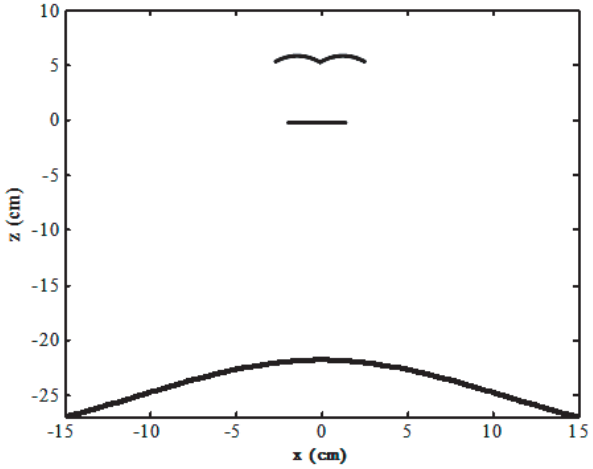

Figure 6: Antenna geometry.

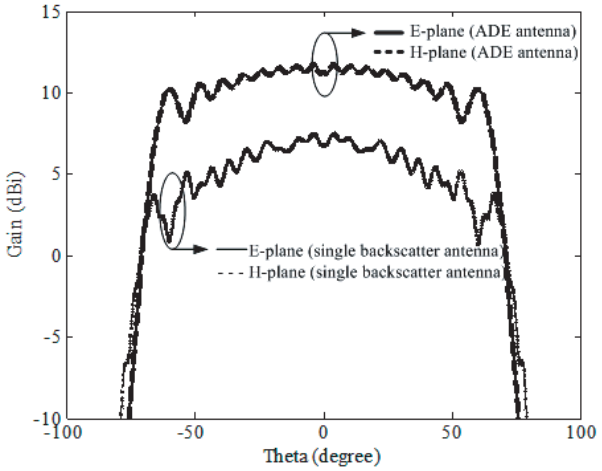

Figure 7: Radiation pattern at 18.75 GHz.

diffraction (see Fig. 7) [4, 7]. First of all, one observes that the radiation patterns are symmetry in both the E-plane and H-plane. The maximum gain of the ADE antenna is 11.8 dBi. The gain at $\theta = \pm 65^\circ$ is 7.5 dBi. There is not severe effect of edge effect. In the case of a single Gaussian backscatter antenna, the maximum gain is 7.5 dBi and gain at $\theta = \pm 65^\circ$ is 3.5 dBi. The main conclusion of this brief analysis is that Gaussian backscatter antenna with ring focus feeding produces higher gain and smaller diffraction effects than a single Gaussian backscatter antenna.

4. CONCLUSION

The design of Gaussian backscatter antenna with ring focus feed (ADE antenna) was presented. The antenna was analyzed by using the PTD technique. The radiation pattern in E-plane and H-plane can provide gain of 7.5 dBi at $\theta = \pm 65^\circ$ and maximum gain is 11.8 dBi. From these results we can conclude that Gaussian reflector antenna with ring focus feed produces higher gain and smaller diffraction effects than a single Gaussian reflector antenna.

ACKNOWLEDGMENT

I would like to thank the Office of the Higher Education Commission, Thailand for supporting grant under the program Strategic Scholarships for Frontier Research Network, the National Research Council of Thailand and Suranaree University of Technology for research grant.

REFERENCES

1. Hay, S. G., D. G. Bateman, T. S. Bird, and F. R. Cooray, "Simple ka-band earth coverage antennas for LEO satellites," *IEEE Antennas Propag. Soc. Int. Symp.*, Vol. 1, 11–16, 1999.
2. Bird, T. S., J. S. Kot, N. Nikolic, G. L. James, and S. J. Barke, "Millimeter-wave antenna and propagation studies for indoor wireless LANs," *IEEE Antennas Propag. Soc. Int. Symp.*, Vol. 1, 336–339, 1994.
3. Smulders, P. F. M., S. Khusial, and M. H. A. J. Herben, "A shaped reflector antenna for 60-GHz Indoor wireless LAN access points," *IEEE Trans. on Vehicular Technology*, Vol. 50, 584–591, 2001.
4. Thaivirot, V., P. Krachodnok, and R. Wongsan, "Radiation pattern synthesis from various shaped reflectors base on PO and PTD methods for point-to-multipoint applications," *WSEAS Transactions on Communications*, Vol. 7, 531–540, 2008.
5. Popov, A. P. and T. Milligan, "Amplitude aperture-distribution control in displaced-axis two reflector antenna," *IEEE Antennas and Propag. Magazine*, Vol. 39, No. 6, 58–63, 1997.
6. Granet, C., "A simple procedure for the design of classical displaced-axis dual-reflector antennas using a set of geometric parameters," *IEEE Antennas and Propag. Magazine*, Vol. 41, No. 6, 64–71, 1999.
7. Michaeli, A., "Elimination of infinities in equivalent edge currents, part I: Fringe current components," *IEEE Trans. Antennas Propag.*, Vol. 34, 912–918, 1986.

High Directive Gain Antenna Using Shorted-end Curved Strip Dipole on Electromagnetic Band Gap

N. Fhafhiem, P. Krachodnok, and R. Wongsan
School of Telecommunication Engineering, Institute of Engineering
Suranaree University of Technology, Nakhon Ratchasima, Thailand

Abstract— This paper presents a curved strip dipole constructed of a metallic sheet that is bended to a half annular and the both ends are short circuited on electromagnetic band gap (EBG) ground plane. The EBG surface is capable of providing a constructive image current within a certain frequency band, resulting in good radiation efficiency. The proposed antenna is suitable to apply for wireless communications at 2.45 GHz and it will be usually placed at the wall and ceiling of large rooms or buildings. The maximum gain occurs in the normal direction to a reflector plane that direct to service area. The numerical results are given by Computer Simulation Technology (CST) software. From the numerical results, the frequency response of return loss and radiation patterns can be investigated. The simulation results show a maximum gain of 9.7 dB, it has maximum gain higher than a curved strip dipole which is mounted over a conductor plane.

1. INTRODUCTION

With the rapid development of the wireless communications and the communication industry, the antenna is important to develop wireless local area network (WLAN) and worldwide interoperability for microwave access (WiMAX), it is applied for high frequency 2.45 GHz. In addition, the antenna has been sufficient gain and it required either unidirectional or omnidirectional beam, coverage abroad area, and high power handing. Moreover, the antenna is relatively simple in concept, structure easy, and inexpensive. The dipole antenna has some qualifications that are prominent point, its shape could be change easy and variety. However, the dipole antenna has low gain and the half power beamwidth (HPBW) in the E-plane is about 78 degree. This argues, if we can design antenna to illuminate a predefined wide coverage area, it will have more efficiency for field radiating. The related literatures to the shape or curved dipole structure have been reported by several authors. Krishnan et al. [1] presented a V-shape wire loop that structure like butterfly. Dubost [2] presented the antenna which short circuited dipole parallel on perfect conductor plane. Tumvichit et al. [3] presented a half-wave dipole with a conductor plane at a distance smaller than a quarter wavelengths. Pimpol and Wongsan [4] presented the impedance analysis of a shorted-end curved dipole on reflector plane. Fhafhiem et al. [5] presented shorted-end curved strip dipole antenna on conductor plane for 2.45 GHz. In this paper, shorted-end curved strip dipole antenna on EBG designed form extremely attractive solutions for wireless communication are presented. A strip dipole is bended to curve for wider HPBW and it is mounted over a curve dielectric for durable of the antenna. In recent years, the EBG structures have been developed in fields of antenna, and it is exhibit high impedance characteristic on a certain frequency range and in-phase reflection characteristics for the incident wave [6]. Therefore, the EBG surface is capable of providing a constructive image current within a certain frequency band, resulting in good radiation efficiency. For this reason, we are attractive solutions about EBG for the ground plane of curved strip dipole antenna. This antenna has achieved the maximum gain more than the antenna on conductor plane. In the same time, it could be cover bandwidth of IEEE standard (802.11 b/g).

2. ANTENNA DESCRIPTION AND DESIGN GEOMETRY

The geometry of the curved strip dipole antenna short circuited both ends on EBG ground plane with detailed dimensions is shown in Fig. 1. The antenna is constructed of a metal plate (a 1 mm thick perfect conductor plate), it is mounted over an inexpensive curve polyvinyl chloride (PVC) with the dielectric constant of 3.4. The thickness and wide of dielectric are 1 mm and 30 mm, respectively. The parameters of antenna consist of the total length and wide of curved strip dipole expressed by L_d and w_1, respectively, and the radius a is aligned along ϕ-direction. The feed center of this antenna is connected at $\phi = \pi/2$. In addition, the analysis models of EBG reflector plane consist of square metal patches on ground plane. The EBG structure, has 5×5 unit cell and an overall dimensions of 142.68 mm $\times$ 142.68 mm, uses a 1.6 mm thick FR4 substrate with a

permittivity of 4.5. The patch width (W) is 25.88 mm. The radius of the vias (r) is 1.48 mm and the gap width is 3.32 mm.

3. NUMERICAL SIMULATIONS RESULTS

3.1. The Curved Strip Dipole Antenna

The objective of this paper is increased directive gain of simple dipole to application in the WLAN and WiMAX environment. The curved strip dipole antenna is designed for 2.45 GHz ($\lambda g = 82.55$ mm) as shown in Fig. 2, it is curved strip dipole antenna without reflector plane. The half-wavelength of curve strip dipole is $Ld = \pi a$ and it is mounted on dielectric. The data of the curved strip dipole antenna geometry is summarized in Table 1. In the computations, L_d and w_1 are varied. From optimized analysis, the good matching of this antenna could be obtained, the input impedance is matched to a 50 Ohms transmission line [5]. From the resulting, the antenna has a low gain of 1.5 dB and return loss is illustrated in Fig. 2(b). The HPBW in E-plane is 95.3°. The curved strip dipole antenna will be usually placed at the center of large rooms but it has omnidirectional radiation pattern. The power may be loss to unnecessary place.

3.2. The Curved Strip Dipole Antenna Separated by 1/4 Wavelength from the Conductor Plane

From our objective, the antenna could be unidirectional antenna. The curved strip dipole antenna is located on the perfect electric conductor (PEC) as shown in Fig. 3(a). The present of a reflector redirects half of the radiation into the opposite direction, improving the antenna gain, and partially shielding objects on the other side. Unfortunately, if the antenna is too close to the conductive

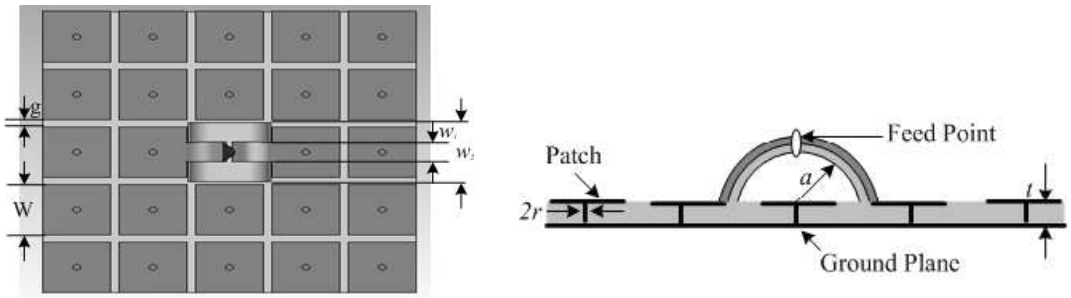

(a) (b)

Figure 1: Configulation of the propose antenna, (a) front view and (b) side view.

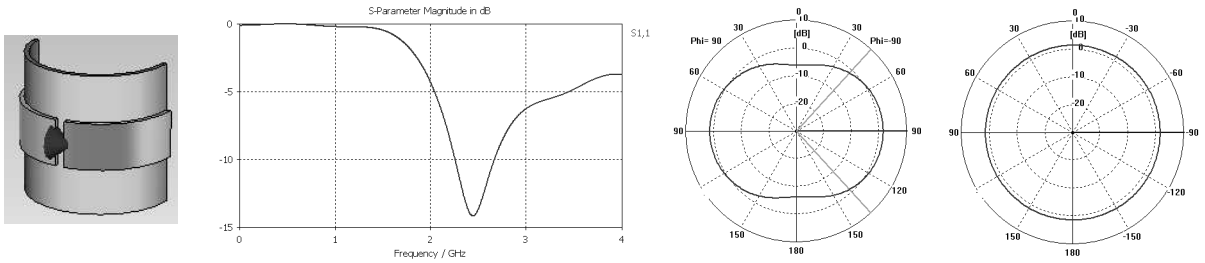

(a) structure (b) return loss (c) E-plane (d) H-plane

Figure 2: Curved strip dipole antenna without reflector plane.

Table 1: The data of the curved strip dipole.

Parameter	Size
w_1	10 mm
w_2	30 mm
L_d	52.77 mm
a	16.8 mm

surface, the face of the impinging wave is reversed upon reflection, resulting in destructive interference with the wave emitted in the other direction. Also, the image currents in the conductive sheet cancel the current in the antenna and the surface wave in electric and magnetic field of conductor plane is not suppressed. To solve this problem, the radiating element is separated from the reflector $\lambda_0/4$. The total round trip phase shift from the curved strip dipole, to the surface, and back to the antenna, equals one complete cycle, and the waves add constructively as shown in Fig. 3(b). The return loss of the curved strip dipole is -11 dB. The HPBW E- and H-plane are 73.1° and 99°, respectively, and directive gain is 7.52 dB. The antenna radiates efficiently, but the entire structure requires a minimum thickness of $\lambda_0/4$. In this case, the antenna is not durable for applications.

3.3. The Curved Strip Dipole Antenna Separated by 1/4 Wavelength from the EBG Ground Plane

A line of thought, the EBG structure presented in Fig. 4 is in-phase reflection characteristic, it is placed far from feed point of curved strip dipole $\lambda 0/4$. It is suitable to ground plane of curved strip dipole because the existence of the EBG structure can suppress the propagation of surface waves as shown in Fig. 4(b). The high-impedance surface reflects all of the power just like a metal sheet, but it reflects in-phase, rather than out-of-phase, allowing the radiating element to be directly adjacent to the surface. In the other hand, the direction of the image currents results in constructive interference, allowing the antenna to radiate efficiently. The simulation results have gain of 7.3 dB and return loss of -23.3 dB. The HPBW in E- and H-plane are 58° and 123.3°, respectively. However, the structure of antenna is not strong. For this purpose, curved strip dipole will be short circuited both ends on EBG ground plane for a durable of structure. The data of the EBG ground plane geometry is summarized in Table 2.

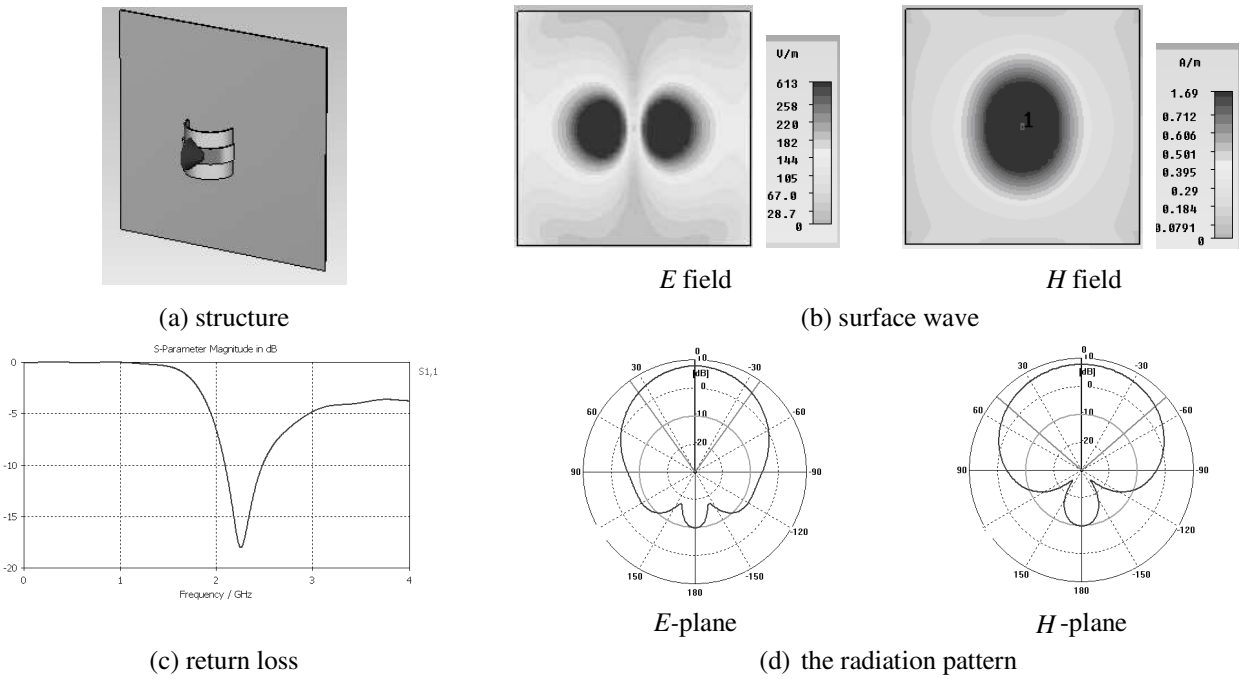

Figure 3: Curved strip dipole on conductor plane.

Table 2: The data of the EBG ground plane.

Parameter	Size
W	25.88 mm
g	3.32 mm
r	1.48 mm
t	1.6 mm

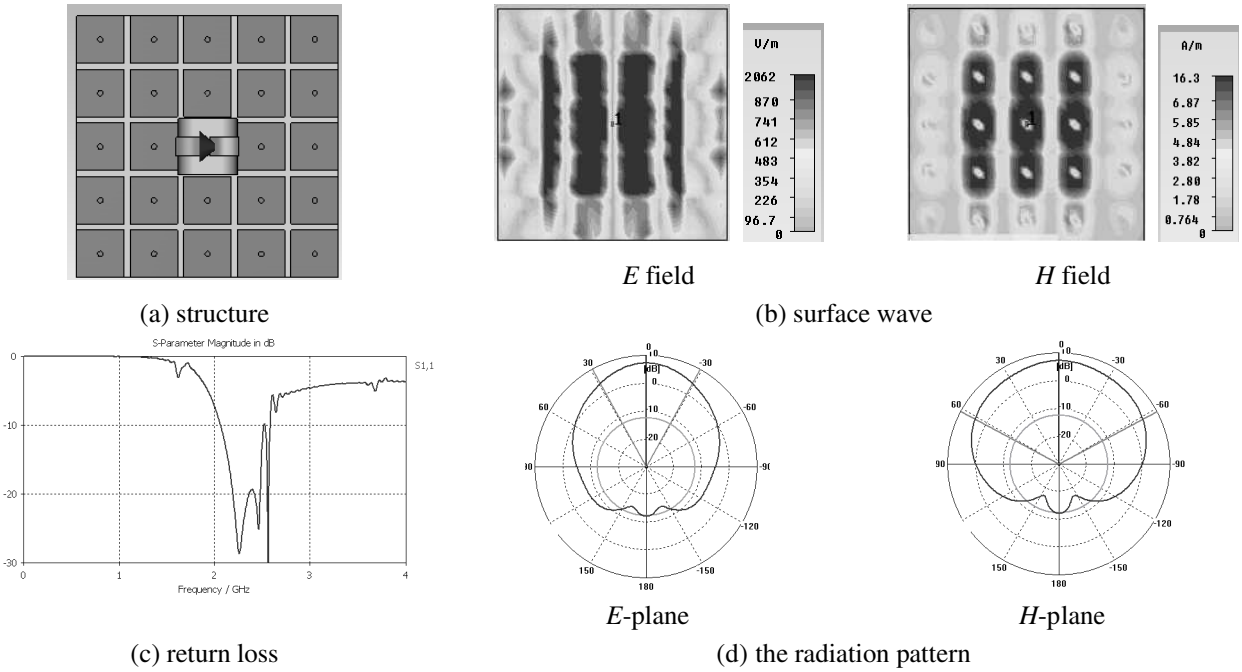

Figure 4: Curved strip dipole antenna separated by 1/4 wavelength from the EBG ground plane.

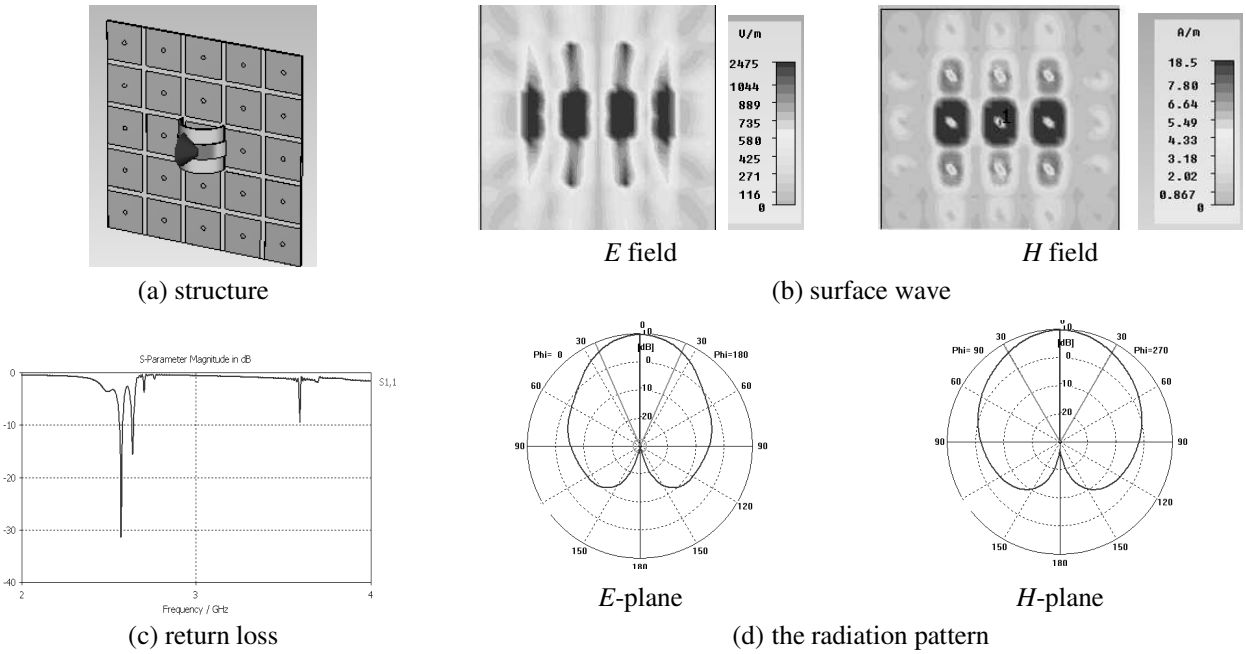

Figure 5: The short-circuited end curved strip dipole on EBG ground plane.

4. THE SHORT-CIRCUITED END CURVED STRIP DIPOLE ON EBG GROUND PLANE

From overall solutions, the short-circuited end curved strip dipole on EBG ground plane is illustrated in Fig. 5. It found that the excellent gain of proposed antenna is 9.6 dB and the return loss is -25.68 dB. The E- and H-plane radiation patterns are shown in Fig. 5(d). The maximum radiation occurs in the normal direction to ground plane. We have achieved a maximum gain which is higher than that of a radiating element on conductor plane and on EBG ground plane. Moreover, its HPBW in E- and H-plane are 47.3° and 60.4°, respectively. For the illustrated in Fig. 5(b), the surface waves in electric and magnetic field could be isolated. It is performed that the EBG structure has qualification to improve gain of antenna and to reduce the back lobe. The results of gain, HPBW, and patterns are well agreement of the antenna for WLAN and WiMAX

applications that wanted unidirectional beam and high gain. In addition, the 0-dB beamwidth in E- and H-plane are 96° and 150°, respectively.

5. CONCLUSIONS

This paper proposes a shorted-end curved strip dipole on EBG ground plane antenna which is utilized usually to place at the wall and ceiling for wireless communication system at 2.45 GHz. The antenna is designed by using Computer Simulation Technology (CST) software, it has successfully improved the gain of 9.7 dB because of the qualifications of EBG structure. The surface wave could be suppressed from EBG ground plane, therefore, the back lobe are obviated. Moreover, it has been structure uncomplicated and inexpensive that demand on equipment for communication system. The band of frequency can be improved furthermore.

REFERENCES

1. Krishnan, L.-W. and M.-S. Leong, "A V-shaped structure for improving the directional properties of the loop antenna," *IEEE Trans. Antenna Propag.*, Vol. 53, 2114–2117, 2005.
2. Dudost, G., *Flat Radiating Dipole and Applications to Arrays*, Wiley-Interscience, New York, 1981.
3. Thumvichit, A., T. Takano, and Y. Kamata, "Ultra low profile dipole antenna with a simplified feeding structure and a parasitic elelment ," *IEICE Trans. Commun.*, Vol. E89-B, No. 2, 576–580, 2006.
4. Pimpol, S. and R. Wongsan, "Impedance analysis of a shorted-end curved strip dipole on reflector plane using method of moment," *Proceedings of the ECTI International Conference*, 667–670, Chang Rai, Thailand, May 2007.
5. Fhafhiem, N., P. Krachodnok, and R. Wongsan, "A shorted-end curved strip dipole on dielectric and conducting plane for wireless LANs," *The 2009 International Symposium on Antenna and Propagation*, 835–838, Bangkok, Thailand, October 2009.
6. Sievenpiper, D., L. Zhang, R. F. J. Broas, N. G. Alexopolus, and E. Yablonovitch, "High impedance electromagnetic surface with a for-bidden frequency band," *IEEE Trans. Microw. Theory Tech.*, Vol. 47, No. 11, 2059–2074, 1999.

Printed Temperature Sensors for Passive RFID Tags

Jinlan Gao[1], **Johan Sidén**[1, 2], **and Hans-Erik Nilsson**[1, 2]

[1]Mid Sweden University, Sweden
[2]Sensible Solutions AB, Sweden

Abstract— A concept is presented where a temperature sensitive printed nano structure is integrated into a UHF RFID tag antenna. The printed structure acts as a WORM memory (Write Once Read Many) allowing telling whether a tag has been exposed to excessive temperature since the last read. The 1-bit WORM used in experiments is defined through its resistance where a logical zero equals a high resistance over 2 kΩ and a logical one equals a lower resistance, typically less than 50 Ω. Setting the bit can be achieved through sintering, which is a process to enhance junctions among nano-particle silver and reduce resistivity by heating. The WORM is designed to modulate the impedance of a passive RFID tag antenna, aiming to change the tag from readable to unreadable or the other way around. The simplest way of modulation is to set the WORM to be parallel with the silicon chip. The tag then works well with the high WORM resistance apparent before sintering and poorly or preferably not working at all after sintered because the chip is short-circuited by the low WORM resistance. A variant of the half wavelength dipole has been used to demonstrate this concept and it should also work with other antenna patterns. Both the WORM memory and the tag antenna are printed on photo paper by an Inkjet printer and the silicon chip is connected to the antenna using the electrically conductive ink.

Compared to the sensor solutions that integrate the normal battery supported sensors into silicon chips with the aid of A/D converters, the sensor tag presented in this paper is much simpler and allowing easy fabrication. It has long lifetime, a smaller size as well as a lower cost. Since the WORM memory by definition stores the state and can be read out long time after it's been programmed this tag can tell about past events. Potential use include all applications where one wants to detect if a high temperature has occurred since the last time of read and where normal sensors either have too short lifetime or are too expensive.

1. INTRODUCTION

With the technology maturity of sensors and Radio Frequency Identification (RFID), the complement of their functions has attracted more and more attention on the combination of them in recent years. The RFID with sensing function is expected as one of the important products of next generation. Now there are two architectures of RFID sensor tag [1]. The first one is an RFID tag which integrates the traditional battery supported sensor into silicon chip with the aid of A/D converter [1, 2]. This tag framework suits for many kinds of sensors. However, the additional sensor component enlarges the tag size and cost. Besides, its lifetime is limited by the battery capacity. In the second one, the sensor is integrated into the tag antenna [1, 3, 4]. This provides a smaller size and lower cost. But the tough problem is how to design a proper sensor component. There have been research efforts to realize this kind of sensing RFID system. Chang et al. [1] present a sensor tag with RH (relative humidity) sensing function using a patch antenna covered with polyimide film. Sidén et al. [3] demonstrate a moisture RFID sensor solution with antenna covered by moisture absorbing material. Bhattacharyya et al. [4] propose a displacement sensor utilizing the effect of the metal on the antenna. In this paper, we present a concept of the temperature sensing tag which integrates a printed nano sensor structure into a UHF RFID tag antenna. The printed structure acts as a WORM memory allowing telling whether a tag has been exposed to excessive temperature since the last read. The temperature sensor switch (WORM) works utilizing the technique of sintering widely used in printed electronics, which is a process to enhance junctions among nano-particle silver and reduce resistivity by heating because the high temperature can melt encapsulating polymer and cause neck formation and particle growth [5]. This temperature sensing tag has long lifetime, a smaller size as well as a lower cost. Since the WORM memory by definition stores the state and can be read out long time after it's been programmed this tag can tell about past events. Potential use include all applications where one wants to detect if a high temperature has occurred since the last time of read and where normal sensors either have too short lifetime or are too expensive.

2. WORM MEMORY

WORM [5] in this paper is a 1 bit write-once-read-many memory printed using nano conductive ink. It has two stages, on and off (WORM-bit = 1 and 0) but not like a perfect electrical switch. Printed WORM memory is defined through its resistance where a logical zero equals a high resistance and a logical one equals a lower resistance. Depending on applications this transition of resistance can be in different ranges.

A WORM is a segment of printed narrow line between two pads (shown in Figure 1). The WORM resistance mainly depends on the narrow junction line and two pads are designed to be easy to contact with other printed structures. Setting the bit value can be achieved through sintering, WORM-bit = 0 (high resistance) before sintering and WORM-bit = 1 (lower resistance) after sintered. Just like the normal metal wire, the WORM resistance is decided by the line length, width and thickness, but with lower conductivity than metal. The conductivity of the ink can have a great change with heating. This property makes the WORM memory acting as a temperature sensor switch.

Since the WORM memory can record the event by changing its stage and its value can be read out at a later occasion in time, the WORM is bridging the gap of time and suits for watch-dog applications.

3. SENSOR TAG

The WORM is designed to modulate the impedance of a passive UHF RFID tag antenna, aiming to change the tag from readable to unreadable or the other way around. The simplest way of modulation is to set the WORM to be in parallel with the silicon chip (shown in Figure 2). The sensor tag then works well with the high WORM resistance apparent before sintering and poorly or preferably not working at all after sintered because the chip is short-circuited by the low WORM resistance.

From the view point of impedance modulation, we get the voltage reflection coefficient Γ without WORM (Equation (1)) and that with WORM (Equation (2)).

$$\Gamma = \frac{Z_A - Z_C^*}{Z_A + Z_C} \tag{1}$$

$$\Gamma = \frac{Z_A - (Z_W \,\|Z_C\,)^*}{Z_A + (Z_W \,\|Z_C\,)} = \frac{Z_A - \left(\frac{Z_W Z_C}{Z_W + Z_C}\right)^*}{Z_A + \left(\frac{Z_W Z_C}{Z_W + Z_C}\right)} \tag{2}$$

The antenna and chip are supposed to be well matched without WORM, $Z_A = Z_C^*$. For the ideal situations, Γ equals zero which means there is no power reflection when the WORM resistance is infinite and Γ equals one which means the power is totally reflected when the WORM resistance is zero. The antenna shifts working state from well matching with chip to totally mismatching due to the WORM resistance transition. From the simulation we knew that the performance of the antenna reduced rapidly from 95% to less than 50% with a WORM resistance from 2 kΩ to 50 Ω.

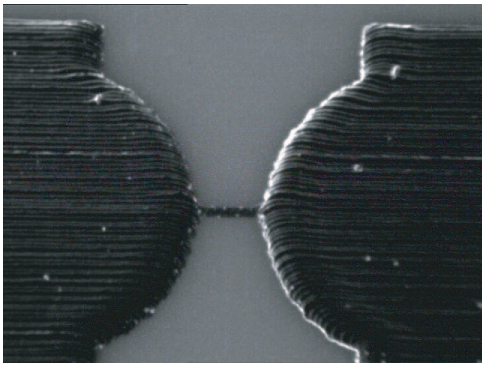

Figure 1: Photo of WORM captured from Printer.

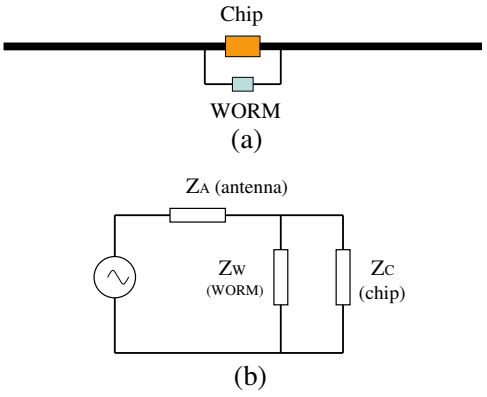

Figure 2: The schematic of the impedance modulation (a) and its electrical equivalent (b).

4. EXPERIMENTS AND RESULTS

Both the WORM memories and the RFID tag antennas were printed on photo paper by an inkjet printer from FUJIFILM Dimatix Inc. named Dimatix Material Printer DMP-2800. The ink was nano silver jet ink DGP-40LT-15C, from Advanced Nano Products Co. Ltd.

In order to increase the sensitivity, the WORMs were improved to have five parallel junction lines between two pads. The WORMs were printed with silver ink from two different batches, where batch number two had its temperature curing properties slightly improved. The printed junction line was approximately $200 * 30\,\mu m$. Figure 3 shows how the WORM resistance varies with time at different temperatures. The WORM printed with the ink from batch one had an initial resistance about 0.3–4 MΩ at room temperature and only could be sintered by the temperature higher than 80°C. The WORM with the ink from batch two had an initial resistance of 0.1–0.9 MΩ and could be sintered even at just 40°C.

The passive UHF RFID chips used in this paper were Alien Gen-2 Monza RFID chips which had impedance of approximately $30 - j130$ ohm at 868 MHz. A dipole antenna with an inductive loop in Figure 4 was designed to match with the chip. The tag antennas were printed with the silver ink from batch one and put in oven to cure at 120°C for 30 minutes since the ink from batch one also provided better printing quality for large structures. To get lower sheet resistance, the antennas were printed with two layers which gave a sheet resistance of 80 mΩ after curing. The silicon chip and WORM were connected to the antenna at 1 mm gaps shown in Figure 4 using the conductive silver ink.

The passive sensor tag was positioned right ahead of the patch antenna of a SAMSys RFID reader working at 868 MHz. The results were observed in two ways. One was to sweep the required minimum output power at a fixed reading distance and the other was to measure the maximum reading distance with a fixed output power. Figure 5, taking the WORM with ink from batch two at 60°C as an example, shows the resulting graphs of how much output power that was required to read the sensor tag at 2.0 m, 1.5 m and 1.0 m respectively and how long the reading distance could reach if the output power was set at 28.0 dBm. One can see that the sensor tag can shift its working state from readable to unreadable within two hours at 60°C if it is further than 1 meter away from reader and the response time is longer with shorter distance between the tag and the reader. Assisting with Figure 3(b), one can also see that both the required output power and reading distance change a little when the WORM resistance is higher than several kΩ and they change a lot when the resistance of the WORM is reduced from kΩ to 100 Ω. This is tallied with simulation of impedance modulation.

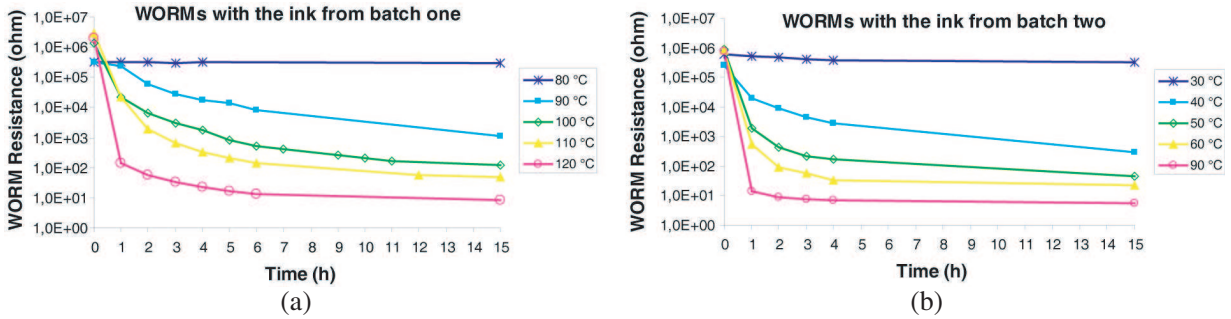

Figure 3: Performance of the WORMs Vs. temperature (a) with the ink from batch one and (b) with the ink from batch two.

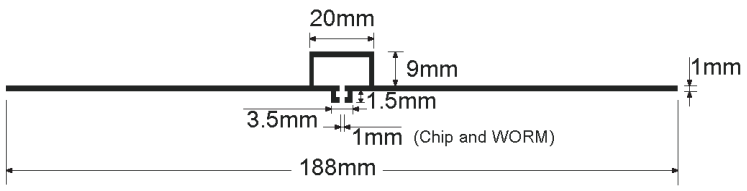

Figure 4: The RFID tag antenna used to demonstrate this concept of temperature sensor tag. (Two gaps are left for connecting the silicon chip and the WORM respectively.).

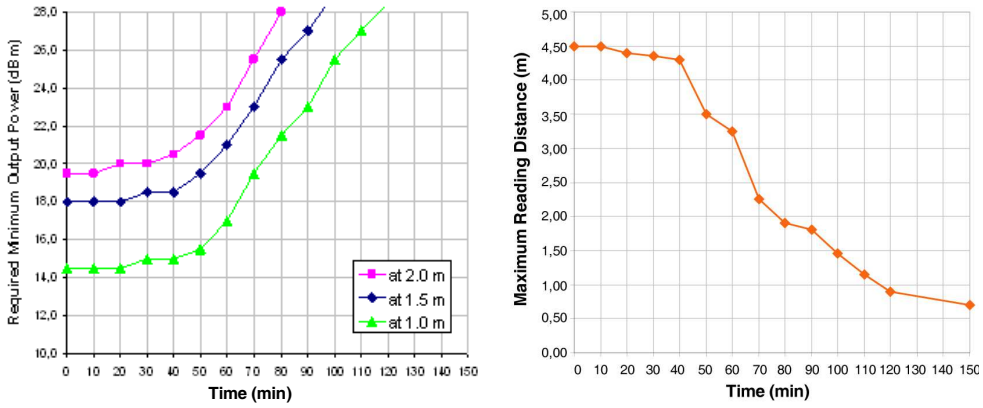

(a) (b)

Figure 5: Results of the sensor tag with the WORM which is printed with the ink from batch two at 60°C. Graph (a) shows the required minimum output power increasing with time at reading distance of 2.0 m, 1.5 m and 1.0 m respectively. Graph (b) shows the measured maximum reading distance with fixed output power of 28.0 dBm.

5. CONCLUSION

In this paper, we propose a concept of the temperature sensor tag which integrates the printed sensor switch into a tag antenna so as to realize the antenna impedance modulation. The sensor, called WORM, utilize the technique of sintering to work as a non-perfect switch and the WORM with different ink shows different sensitivity to the temperature. A printed inductive dipole antenna has been used to demonstrate this concept of sensor tag and it should also work with other antenna patterns. The performance of the sensor tag was observed in two ways. When the sensor tag was exposed to excessive temperature, the required minimum output power increased if the reading distance was fixed and the maximum reading distance decreased if the output power was fixed. In view of above mentioned fact that the change of the WORM resistance from MΩ to kΩ does not make obvious changes in the observed values, a pre-sintering process can be considered to make the WORM have an initial resistance about several kΩ so as to reduce the response time and increase the sensitivity of the WORM. Besides the parallel structure in Figure 2, the WORM can also be put in serial with the antenna next to the chip. It works in the opposite way of the parallel structure since the antenna is cut off by the high WORM resistance and turned on with the low WORM resistance. The ink is the key point for this sensor tag and its curing temperature decides the scope that the sensor tag suits for. Future work includes more research about the character of the ink so as to fabricate more WORMs which suit for different temperature applications.

ACKNOWLEDGMENT

The research leading to these results has received funding from the Swedish KK Foundation and European Community's Seventh Framework Programme (FP7/2007-2013) under grant agreement No. 215132.

REFERENCES

1. Chang, K., Y.-H. Kim, Y.-J. Kim, and Y. J. Yoon, "Patch antenna using synthesized polyimide for RFID sensing," *Proceedings of the 9th European Conference on Wireless Technology*, 83–86, Manchester, UK, September 2006.
2. Tentzeris, M. M., "Novel paper-based inkjet-printed antennas and wireless sensor modules," *IEEE International Conference on Microwaves, Communications, Antennas and Electronic Systems*, 1–8, Tel-Aviv, Israel, May 2008.
3. Sidén, J., X. Zeng, T. Unander, and H.-E. Nilsson, "Remote moisture sensing utilizing ordinary RFID tags," *2007 IEEE Sensors*, 308–311, Atlanta, USA, October 2007.
4. Bhattacharyya, R., C. Floerkemeier, and S. Sarma, "Towards tag antenna based sensing — An RFID displacement sensor," *IEEE RFID 2009 Conference*, 95–102, Orlando, USA, April 2009.
5. Allen, M. L., M. Aronniemi, T. Mattila, A. Alastalo, K. Ojanperä, M. Suhonen, and H. Seppä, "Electrical sintering of nanoparticle structures," *Journal Nanotechnology 2008*, Vol. 19, No. 175201, 4, 2008.

Outline of Noise Spectroscopy Potentialities

R. Kubásek[1], **P. Drexler**[1], **P. Fiala**[1], **and K. Bartušek**[2]

[1]Department of Theoretical and Experimental Electrical Engineering
Brno University of Technology, Kolejní 2906/4, Brno 612 00, Czech Republic
[2]Institute of Scientific Instruments, Academy of Sciences of the Czech Republic
Královopolská 147, Brno 612 64, Czech Republic

Abstract— The article describes basic study of broadband noise signal application in the investigation of materials. The aim is find a metrology method utilizable for the research on metamaterials in the frequency range of about 100 MHz to 10 GHz. The instrumental equipment and other requirements are presented. This research report provides an overview of the current potentialities in the described field and summarizes the aspects necessary for noise spectroscopy.

1. INTRODUCTION

In the complex investigation of material structures for the micro-wave application (tensor and composite character), the properties of materials are studied by means of the classic single-frequency methods, which bring about certain difficulties in the process [1]. In boundary changes with a size close to the wave-length there can occur wrong information concerning the examined objects [2, 3]. One of the possible ways of suppressing the negative sources of signals consists in the use of wide-band signals like white noise, and in researching into the problem of absorption in the examined material [4]. These methods require a source of noise, a receiving and a transmitting antenna, and A/D conversion featuring a large bandwidth; for our puproses, the bandwidth ranged between 0 Hz and 10 GHz. Until recently it had not been possible to realize an A/D converter of the described speed, or devices with the above-mentioned bandwidth. Currently, high-end oscilloscopes are available with a sampling frequency of tens of Gsa/s.

2. NOISE SOURCE

For UWB systems, several methods of the generation of short pulses with large bandwidth have been developed to date [5]. However, these singly-iterative processes are not applicable for noise spectroscopy; in this respect, there is a need of a continuous source of noise signal (ideally of white noise) with the given bandwidth. The type of source referred to is currently being produced by certain manufacturers specialized in this field. Importantly, for the noise spectroscopy application we require a comparatively large output power of up to 0 dB/mW; the assumed bandwidth characteristics range up to 10 GHz. Nevertheless, at this point it is appropriate to mention the fact that there occurs the fundamental problem of finding active devices capable of performing signal amplification at this kind of high frequencies. As a matter of fact, our requirements are thus limited by the current status of technology used in the production of commercially available devices; the highest-ranking solution for the bandwidth of up to 10 GHz can be found only up to the maximum of 0 dB/mW.

Our response to the above-discussed problem consisted in an attempt to produce a noise generator in laboratory conditions as, in principle, this type of generator can be considered as sufficient for testing and basic measurement. In view of the price and availability of noise diodes we decided to apply thermal noise on electrical resistance as the basic source of noise. The specific connection is shown in Fig. 1. The first transistor is in the CC configuration, where we require mainly a high input impedance of the amplifier. The thermal noise at the input is given by its input parameters. The generator could operate even without a resistor at the transistor input, yet the unconnected input would cause a substantial deterioration of the stability. The second and the third transistors form a cascade voltage amplifier in the CE configuration. The output impedance of the third amplifier is 50 Ω for its matching to coaxial line.

Figure 2 shows the realization of the tested noise generator; the BFP620 vf transistors were applied. This type of transistor features the characteristic of $f_t = 65$ GHz and the maximum stable amplification of 11 dB at the frequency of 6 GHz. The overall amplification of the two CE amplifiers in cascade for the output power of 0 dB/mW would have to approximate the value of 10000, and there is no hf transistor available for this kind of stable amplification. Therefore, for the stable noise generator we have to accept a lower output power.

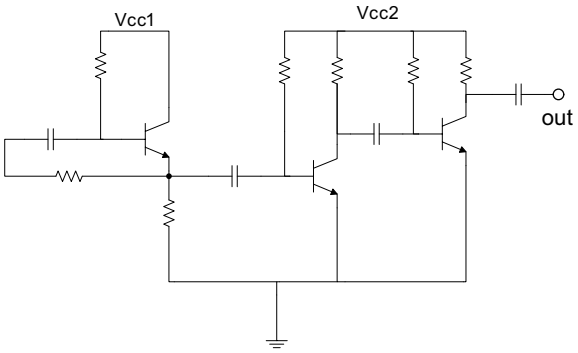

Figure 1: The noise generator configuration diagram.

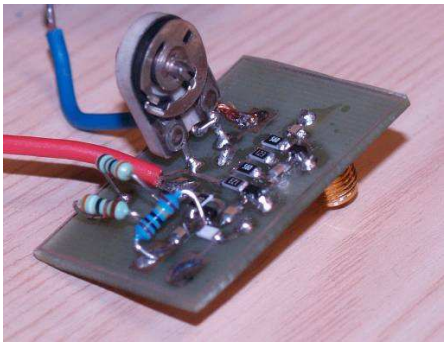

Figure 2: The noise generator realization.

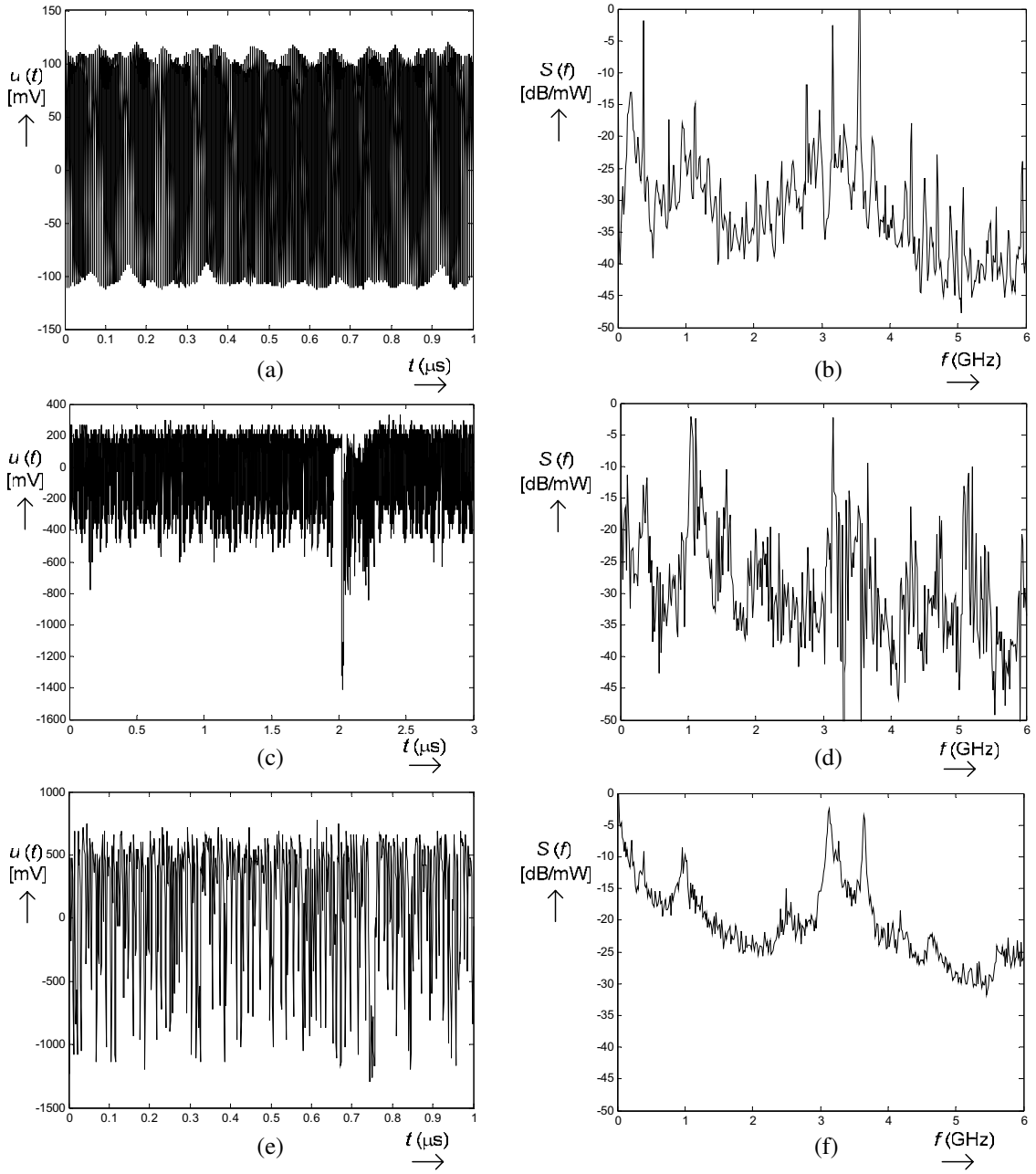

Figure 3: The waveform and spectrum of the noise generator output for three different working points.

Figure 3 shows the waveforms and the output voltage spectrum of the noise generator for three different working points. Figs. 3(a) and 3(b) display the generator output voltage waveform and spectrum for the situation when no large oscillations are yet measurable that normally cause the transistor closing and the subsequent transient process. There occur moderate oscillations, which are visible in the spectrum; their amplitude and frequency are subject to chaotic shifting and the output voltage can be considered as stochastic. However, we can not label this as white noise. Figs. 3(c) and 3(d) show a situation when, owing to large amplification, there already occur oscillations causing the transistor closing that is well noticeable in the waveform in the time of 2 µs. This type of pulses are randomly repeated within the time range of 10 to 30 µs. In the spectrum, they will upgrade the frequency range in the field of 20 MHz. In applying the low-pass filter we would obtain a signal that could be regarded as stochastic.

The last one of the described situations is given in Figs. 3(e) and 3(f); this situation is related to the operating field with the maximum amplification adjustable for the transistor safe operation region. The third transistor already randomly passes between the conditions of "closed" and "open" and the linear operating region. The closing interval ranges from units of ns to several tens of ns. No matter how stochastic this type of signal may be, still it rather models extreme shot noise combined with coloured noise. Its spectrum is the densest and importantly, the most stable of all the situations. For all measurement, spectrum analyzers noise background was −60 dB/mW.

3. ANTENNA

The purpose of the transmitting antenna connected to the noise generator output is to form an electromagnetic wave. As a matter of fact, in the field of noise we indeed have to consider a whole spectrum of electromagnetic waves, and it is not possible to define the antenna proximity area. In addition to this, most principles or rules related to the configuration of antennas have to be regarded as void here. The electromagnetic wave is let to impinge on the investigated material and the reflected or partially absorbed wave is then received through the receiving antenna, to the output of which an oscilloscope has been connected. This type of measurement configuration can be seen in Fig. 4(a).

Both antennas ought to feature a large bandwidth with, if possible, constant amplitude and defined radiaton pattern. In this respect, let us mention the fact that there exist approaches to the design of antennas that come close to the broadband requirements of noise spectroscopy. Suitable solutions include, for example, the spiral fractal antenna or the planar log-periodic antenna. The designed planar log-periodic antenna is applicable for transmission within the frequency range of between 100 MHz and 10 GHz; its real characteristics or qualities depend heavily on the quality of the design practical implementation. Fig. 4(b) shows the realization of a planar log-periodic antenna. The numerical design was performed for currently available materials and its evaluation exhibited the undulating module frequency characteristics. The antenna realization experiments using the PCB showed, above all, troubled transmission at higher frequencies from 2 GHz and problematic modification of the feeder. Other antenna designs are directed towards applying the fractal spiral version on Fig. 4(c).

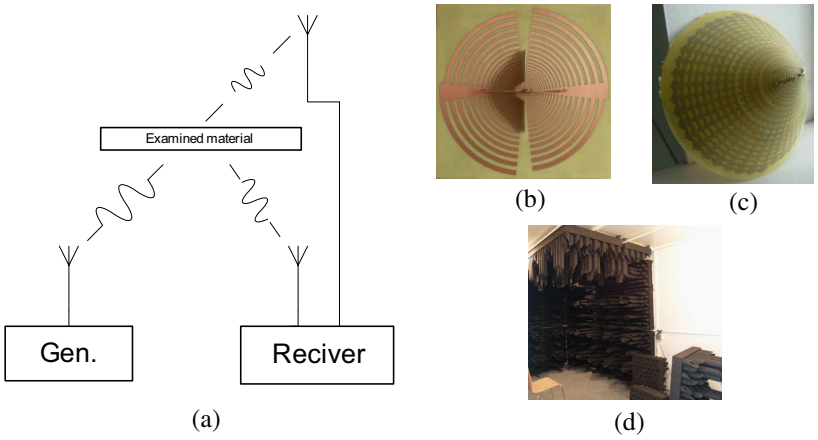

Figure 4: (a) The experiment configuration, (b) planar log-periodic antenna, (c) spiral fractal antenna, (d) Faraday cage.

The experiments and spectroscopy tests will be performed in an anechoic laboratory. We have selected a system of compelementing the Faraday cage shielding with absorbers of electromagnetic waves. The absorbers were designed for the range of 100 MHz–10 GHz with dampening below 35 dB. Thanks to the shielded and separated chamber, the external environment should not affect the internal part of measurement, and the complemented absorbers will enable us to lower foreign signals to a level of below −60 dB/mW. Thus, the measurement will not be affected by the outside environment of external electromagnetic sources like mobile phone and Wifi network signals or stationary waves and reflection within the Faraday cage.

4. DIGITAL RECEIVER

The process of sensing (scanning) has to be necessarily supported by a costly high-end digital oscilloscope featuring a bandwidth of around 10 GHz. Here, the limiting factor is clearly represented by the final price, unfortunately, it is not possible to realize this type of fast A/D converter using the researchers' own means and facilities. In the assessment of spectral properties of materials, the use of a spectral analyzer is normally a fully sufficient and financially effective method. This method, however, can not be utilized for the assessment of a system via the input-output technique, for the correlation analysis, or for other techniques utilizing the measured signal waveform.

5. CONCLUSION

The research paper provides an elementary overview and description of laboratory equipment for the realization of noise spectroscopy measurement. In the text, it is generally noted that the search of an applicable source of noise will be markedly problematic in terms of the output power, which is normally low for broadband applications. Yet it is also noted that, for the laboratory tasks, considerably lower values of transmission power are sufficient for broadband systems in comparison with their "narrowband" counterparts. The designing of a broadband antenna is, to a great extent, an uneasy-to-solve problem, and the requirements placed on the width of the antenna transmitted band are very intensive. Another parameter to be mentioned in this respect is the linear transmission characteristics depending on the frequency. Noise spectroscopy for the frequency band of between 100 MHz and 10 GHz is realizable using the current means of technology.

ACKNOWLEDGMENT

This work was supported by/within the project of the Grant Agency of the Czech Republic No. 102/09/0314 and ELCOM, No. MSM 0021630516.

REFERENCES

1. Maslovski, S., S. Tretyakov, and P. Alitalo, "Near-field enhancement and imaging in double planar polariton-resonant structures," *J. Appl. Phys.*, Vol. 96, 1293, 2004.
2. Freire, M. and R. Marques, "Near-field imaging in the megahertz range by strongly coupled magnetoinductive surfaces: Experiment and ab initio analysis," *J. Appl. Phys.*, Vol. 100, 063105, 2006.
3. Machac, J., P. Protiva, and J. Zehentner, "Isotropic epsilon-negative particles," *2007 IEEE MTT-S Int. Microwave Symp. Dig.*, TH4D-03, Honolulu, USA, June 2007.
4. Fiala, P., E. Gescheidtova, and T. Jirků, "Tuned structures for special THz applications," *PIERS Proceedings*, 151–155, Beijing, China, March 23–27, 2009.
5. Protiva, P., J. Mrkvica, and J. Machác, "Universal generator of ultra-wideband pulses," *Radioengineering*, Vol. 17, No. 4, 74–79, 2008.

Analysis of the RCS and Radiation Pattern of a Planar Array Antenna Integrated with Dielectric and FSS

Wenming Tian and Xinyu Hou
State Key Laboratory of Electronic Thin Films and Integrated Devices
School of Microelectronics and Solid-State Electronics
University of Electronic Science and Technology of China, Chengdu, China

Abstract— This paper investigates the effect of a planar array antenna integrated with dielectric and FSS to its backward RCS and radiation pattern. The results shows that dielectric layer can optimize radiation pattern of antenna when it is integrated on the surface of antenna, while rarely influence radiation pattern when dielectric layer have some distance from antenna surface. And, dielectric layer influences the RCS of antenna very little. One-layer FSS makes radiation pattern of antenna significantly bad when it be integrated on the surface of antenna, while when it is put some distance above the surface of antenna, it's influence to radiation pattern of antenna get very little. However one-layer FSS could dramatically optimize antenna's RCS at out of band.

1. INTRODUCTION

Frequency selective surface (FSS) structures have been extensively explored in recent decades. In order to obtain special center frequency and bandwidth, FSS unit is often designed to different figure to ensure electromagnetic wave can fully pass or be fully reflected at the resonance frequency. Although bandwidth of FSS is not only determined by single unit, resonance characteristics of different units can supply us a good start in FSS design by choosing proper unit [1, 2]. Frequency characteristics of FSS are not only influenced by the style of unit, but also the dielectric layer playing the supporting role in structure. When the dielectric thickness reaches some value, resonance frequency of FSS embed between dielectric layers will be stable by [3]. The transmission coefficient of two-layer periodical array structure using symmetrical and asymmetrical source has been analyzed [4].

Radar cross section (RCS) is one of the most important characteristics of an antenna. Reduction of an antenna has been a topic of immense strategic interest. For out-of-band frequencies, FSS can be employed to reduce the RCS of the array. Planar slotted array antennas are widely used in radar systems, but it is easy to be detected due to its large backward RCS. [5] shows the RCS of a planar slotted waveguide array antenna at different frequencies and mode numbers. In this paper, we concentrate on reducing the out-of-band RCS of planar slotted antenna array using FSS, and to find how FSS and only dielectric influence the RCS and radiation pattern of planar array antenna.

2. MODELING

Consider the planar slotted array antenna depicted in Figure 1. The waveguide have a width 21.3 mm and height 6.65 mm. Each waveguide may have a different length and may be divided in several sections. In order to calculate fast, the antenna waveguides are designed the same length 131.08 mm. The total number of slots is 100. In order to obtain the best performance, the slots are designed to different size. All the radiating slots are longitudinal and the length is 13 mm approximately. And the slots have two widths 1.2 mm and 2 mm. They have a different offset with respect to the center-line of the waveguides. The distance of adjacent slots is about 0.3 mm along y axis and 8.7 mm along y axis.

Figure 6 shows the periodic unit of one-layer FSS. The designed parameters are $P = 20$ mm, $L = 3.7$ mm, $w = 2$ mm. Dielectric substrate chooses Rogers 5880, and its dielectric constant $\varepsilon = 2.2$. Thickness of Rogers material is designed $h = 0.99$ mm. Its center frequency is designed very agree with the working frequency of planar array antenna. Figure 7 gives its transmission and reflection curves. From the curves we can find that, although one-layer FSS only have one resonant frequency point, it also has about 150 MHz bandwidth at -20 dB. This can satisfy the required working bandwidth around center frequency of planar array antenna.

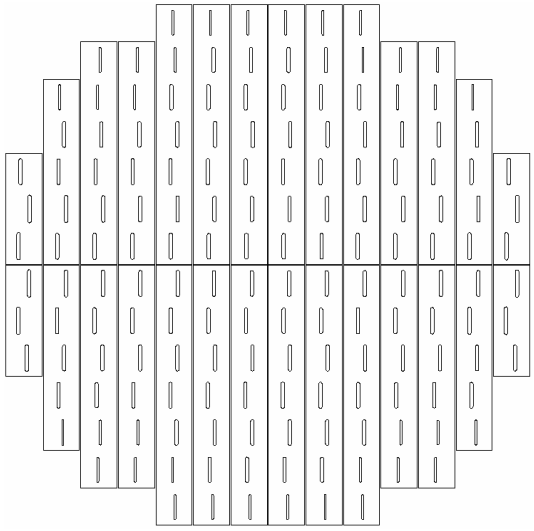

Figure 1: Geometry of a designed planar array antenna.

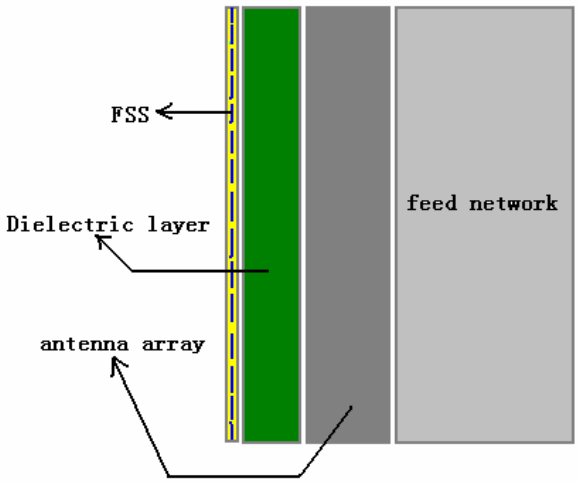

Figure 2: Planar array antenna integrated with single-layer FSS.

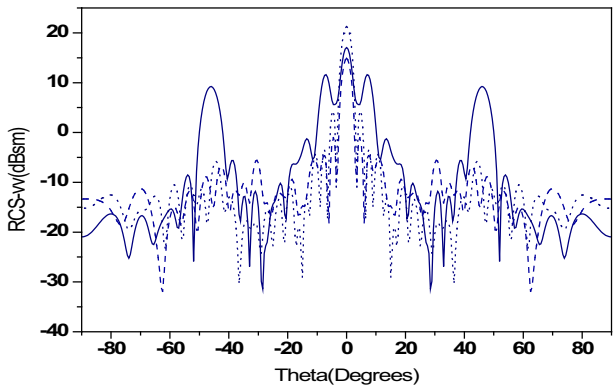

(a) Polarization-V-V

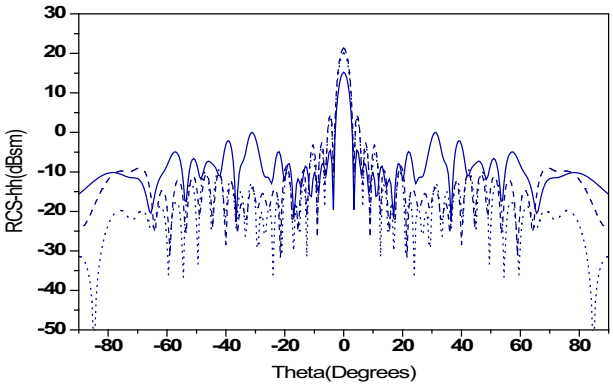

(b) Polarization -H-H

Figure 3: RCS of planar antenna at 9.5 GHz: (1) solid line: antenna, (2) dash line: antenna integrated with FSS on the surface, (3) dot line: antenna integrated with FSS above surface some distance.

3. NUMERICAL RESULTS

In Figure 3(a) for the E-plane case, the polarization of the incident wave is vertical to x-direction. It can be seen that there is evident RCS reduction of slot antenna array integrated with FSS for both an the surface and above surface in the angular region $-50^\circ \leq \theta \leq 50^\circ$ and the peak RCS in front direction has 2 dBsm reduction. Figure 3(b) gives the comparisons of the simulated two antennas for the H-polarized case. The polarization of the incident wave is along the x direction. RCS reduction is obtained in the full angular region. The peak RCS in front direction has 5 dB reduction. The simulated results show that FSS, whenever it is integrated with antenna or above some distance from antenna surface, can reduce the RCS of the antenna effectively in the angular region $-50^\circ \leq \theta \leq 50^\circ$ and makes the antenna has low RCS characteristics. Similar characteristics can be seen in Figure 4 when frequency of incident wave is 12 GHz.

Figure 5 illustrates the radiation pattern of antenna, antenna integrated with dielectric and FSS. The results show that dielectric integrated on antenna can optimize radiation pattern for both E-plane and H-plane, while it rarely influences the RCS of antenna. When FSS is put some distance above antenna surface, it rarely reduces radiation pattern of antenna. However, when FSS is integrated on the surface of antenna, it dramatically reduces the direction of antenna, and makes antenna can't work for both E-plane and H-plane.

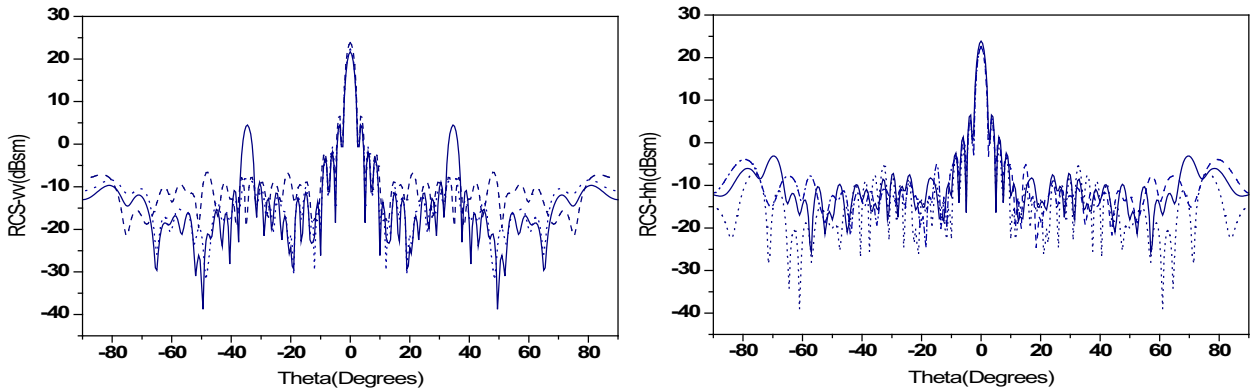

(a) Polarization-V-V (b) Polarization-H-H

Figure 4: RCS of planar antenna at 12 GHz: (1) solid line: antenna, (2) dash line: antenna integrated with FSS on the surface, (3) dot line: antenna integrated with FSS above surface some distance.

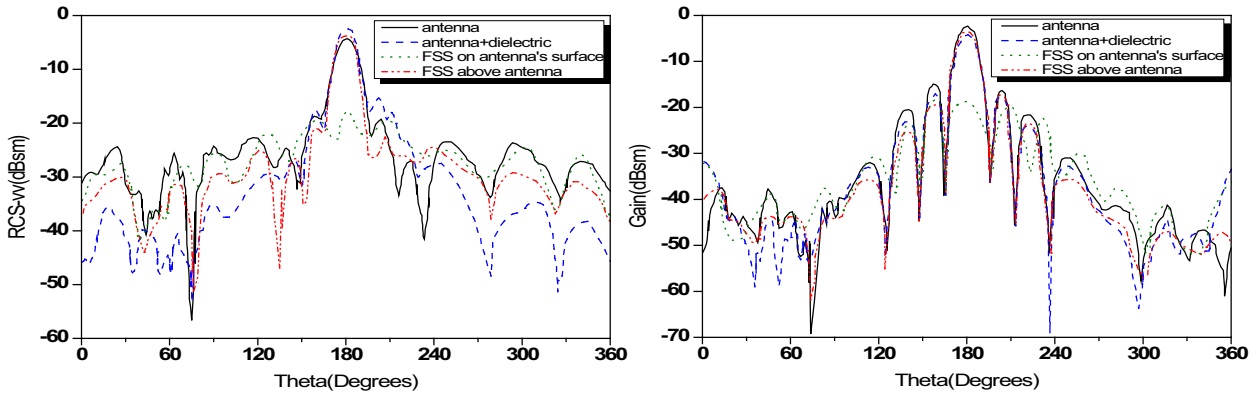

(a) *E*-plane (b) *H*-plane

Figure 5: Comparison of radiation patterns of four structures.

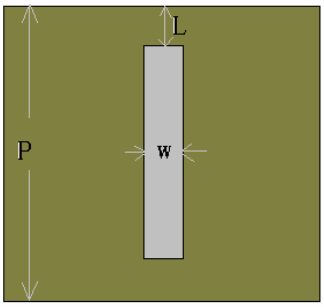

Figure 6: Structure of FSS unit.

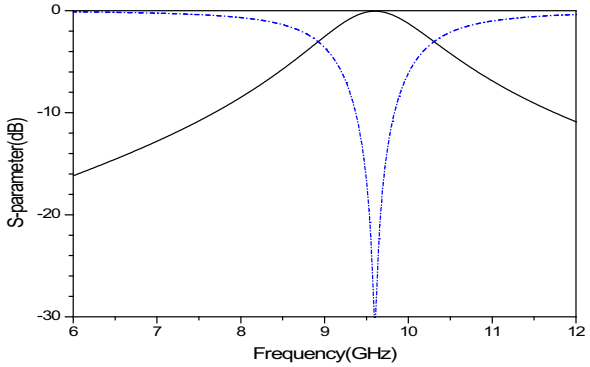

Figure 7: *S*-parameter of one-layer FSS.

4. CONCLUSION

This paper investigates the backward RCS and radiation pattern of a planar array antenna integrated with dielectric and FSS. From the results, we find that thin dielectric layer could optimize the radiation pattern of planar array antenna when it is integrated on the surface of antenna, while it rarely influence the radiation pattern of antenna when it have some distance from antenna's surface. And, it rarely affects the RCS of antenna for both structures. However one-layer FSS could dramatically optimize the RCS of antenna at out of band for two situations. But, One-layer FSS makes radiation pattern of antenna significantly bad when it is integrated on the surface of antenna, while when it be put some distance from the surface of antenna, it's influence to radiation pattern of antenna get very little.

REFERENCES

1. Munk, B. A., *Frequency Selective Surfaces: Theory and Design*, John Wiley & Sons Inc., New York, 2000.
2. Mittra, R., "A look at some challenging problems in computational electromagnetic," *IEEE Antennas and Propagation Magazine*, Vol. 45, No. 5, 18–32, 2004.
3. Luebbers, R. J. and B. A. Munk, "Some effects of dielectric loading on periodic slot arrays," *IEEE Trans. on Antennas Propagation*, Vol. 26, No. 4, 536–542, 1990.
4. Hou, X., W. Wan, and M. Tong, "Characteristic analysis of symmetrical two-layer FSSs," *Electronic Science Journal*, Vol. 21, No. 4, 569–572, 1999.
5. Zhang, L., N. Yuan, M. Zhang, L.-W. Li, and Y.-B. Gan, "RSC computation for a large array of waveguide slots with finite wall thickness using the MoM accelerated by P-FFT algorithm," *IEEE Trans. on Antena Propagation*, Vol. 53, No. 9, 3101–3105, Sep. 2005.

Wide-Angle Transmision Wave Polarizers Using Dielectric Layers

Mohammad Khalaj-Amirhosseini
College of Electrical Engineering, Iran University of Science and Technology, Tehran, Iran

Abstract— In this paper, several high permittivity dielectric layers are used as a wide-angle wave polarizer for the transmission waves to suppress the TE mode in the transmission wave. To design the polarizer, it is analyzed for a wide range of parameters and then the optimum values of the parameters are found out. The usefulness of the proposed structure is verified using a comprehensive example and the main principles for optimally design of polarizers is extracted.

1. INTRODUCTION

Wave polarizers have found some applications in microwave and optical systems such as free-space optical switching networks, read-write magneto-optic data storage systems and polarization-based imaging systems [1–14]. In a wave polarizer only one of two possible modes (TE or TM) can be appeared in the transmission or reflection waves. One can classifies the into the following types [9, 14]: dichroic polarizers, anisotropic crystal polarizers, Brewster angle polarizers, wire-grid polarizers and gyrotropic slab polarizers. The most straightforward idea to design a wave polarizer is using the Brewster's angle to eliminate the TM mode in the reflection wave [8, 9]. The Brewster's polarizers firstly operate for the reflection wave and secondly work only at a narrow angle of incidence. In this manuscript we use several dielectric layers as a wide-angle wave polarizer for the transmission waves to suppress the TE mode in the transmission wave. The introduced wave polarizer consists of several similar dielectric layers with high electric permittivity. Using a proposed method we analyze a polarizer for a wide range of parameters and then find out the optimum values of its parameters. The usefulness of the proposed structure is verified using a comprehensive example and the main principles for optimally design of polarizers is extracted.

2. INTRODUCING THE POLARIZER

Figure 1 shows the introduced wave polarizer consisting of N similar dielectric layers of thickness d_1 with electric permittivity ε_{r1}, while $N-1$ similar dielectric layers of thickness d_2 with electric permittivity ε_{r2} are being between them, alternately. The left and right mediums of the polarizer are assumed to be the free space. It is assumed that the incidence plane wave propagates obliquely towards positive x and z direction with an angle of incidence θ_i and electric filed strength E^i and with one of two possible polarizations TM or TE. We desire to design the introduced polarizer so that only TM mode is transmitted in the output medium, i.e., $z > d$, and TE mode can't be transmitted.

The characteristic matrix of an N period structure is given by [7] and [15, 16] but in here a simple approach is presented for the $ABCD$ matrix of an Nperiod dielectric layers using its transmission line equivalent circuit shown in Figure 1. The transverse electric and magnetic fields $[E_t,\ H_t]$ on the surfaces $z = 0$ and $z = d$ can be related to each other by the $ABCD$ matrix, which can be obtained as follows

$$\begin{bmatrix} A & B \\ C & D \end{bmatrix} = \begin{bmatrix} A_1 & B_1 \\ C_1 & D_1 \end{bmatrix} \left(\begin{bmatrix} A_2 & B_2 \\ C_2 & D_2 \end{bmatrix} \begin{bmatrix} A_1 & B_1 \\ C_1 & D_1 \end{bmatrix} \right)^{N-1} \tag{1}$$

in which

$$A_k = D_k = \cos(\beta_k d_k) \tag{2}$$

$$B_k = \eta_{t,k}^2 C_k = j\eta_{t,k} \sin(\beta_k d_k) \tag{3}$$

where $k = 1$ or 2. Moreover, β and η_t are the transverse propagation and characteristic impedance, respectively, given by

$$\beta_k = \frac{\omega}{c}\sqrt{\varepsilon_{r,k} - \sin^2(\theta_i)} \tag{4}$$

$$\eta_{t,k} = \begin{cases} \dfrac{\eta_0}{\sqrt{\varepsilon_{r,k} - \sin^2(\theta_i)}}, & \text{TE} \\ \dfrac{\eta_0}{\varepsilon_{r,k}}\sqrt{\varepsilon_{r,k} - \sin^2(\theta_i)}, & \text{TM} \end{cases} \tag{5}$$

where $\eta_0 = \sqrt{\mu_0/\varepsilon_0}$ is the characteristic impedance of the free space. Furthermore, the boundary conditions on the first and last surfaces are given by

$$E_t(0) + \eta_{0t} H_t(0) = \begin{cases} 2E^i, & \text{TE} \\ 2E^i \cos(\theta_i), & \text{TM} \end{cases} \tag{6}$$

$$E_t(d) = \eta_{0t} H_t(d) \tag{7}$$

where

$$\eta_{0t} = \begin{cases} \eta_0 / \cos(\theta_i), & \text{TE} \\ \eta_0 \cos(\theta_i), & \text{TM} \end{cases} \tag{8}$$

The transmission coefficient will be determined using (1), (6) and (7) as follows

$$T = \frac{E_t(d)}{E_t(0)} = \frac{2\eta_{0t}}{(A + \eta_{0t} C)\eta_{0t} + (B + \eta_{0t} D)} \tag{9}$$

To show the performance of a polarizer, we define the parameter R as the ratio of transmission coefficient of TE mode to that of TM mode, as follows

$$R \triangleq \frac{T_{\text{TE}}}{T_{\text{TM}}} \tag{10}$$

It is evident that as R approaches to zero the performance of polarizer become better.

3. DESIGN EXAMPLE

In this section we propose a general method to optimally design the introduced polarizer. In the proposed method we analyze the polarizer and find the optimum values of its parameters. Without loss of generality, assume that we wish to design a polarizer at frequency $f = 10\,\text{GHz}$ and at incidence angle $\theta_i = 60°$. Figures 2–4 illustrate the absolute value of the ratio R versus d_1 and d_2 for $N = 1$, 2 and 3 dielectric layers, respectively. We see that R varies periodically with respect to d_1 and d_2 and has some minimums. The minimum values of $|R|$ for $N = 1$ or 2 dielectric layers occur when the thicknesses d_1 and d_2 are an odd multiple of a quarter wavelengths λ_1 and λ_2, respectively, where

$$\lambda_k = \frac{2\pi}{\beta_k} = \frac{\lambda_0}{\sqrt{\varepsilon_{r,k} - \sin^2(\theta_i)}} \tag{11}$$

in which $k = 1$ or 2 and λ_0 is the wavelength in the free space. Also, Figures 5–7 illustrate the minimum of $|R|$ versus ε_{r1}, ε_{r2} and θ_i respectively for $N = 1$, 2, 3 and 4. We see that $|R|_{\min}$ decreases as ε_{r1}, θ_i and N are increased and as ε_{r2} is decreased. According to the above results, one may conclude the following steps to optimally design the polarizer to work at frequency f and at incidence angle θ_i:

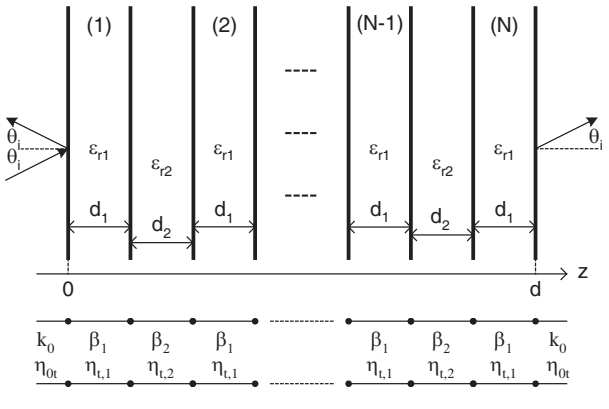

Figure 1: Several dielectric layers as a wave polarizer and its equivalent circuit.

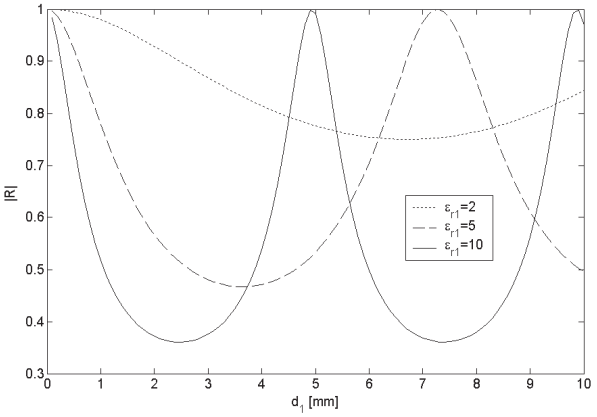

Figure 2: The absolute value of R for $N = 1$ dielectric layer.

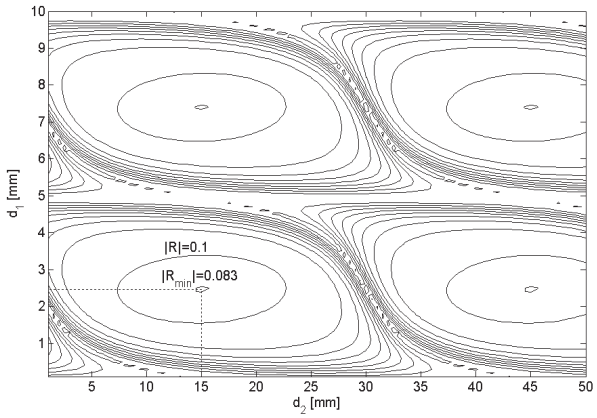

Figure 3: Contour of $|R|$ for $N = 2$ dielectric layers with $\varepsilon_{r1} = 10$ and $\varepsilon_{r2} = 1$.

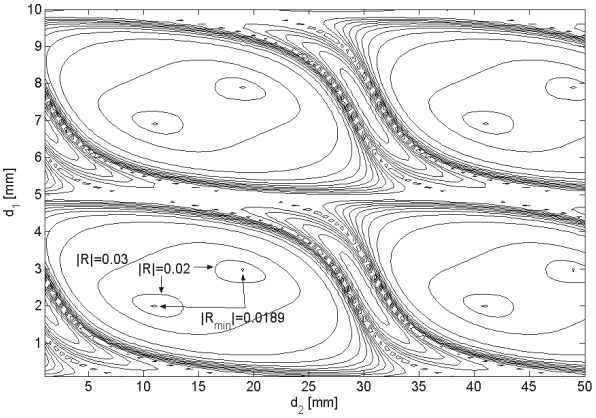

Figure 4: The contour of $|R|$ for $N = 3$ dielectric layers with $\varepsilon_{r1} = 10$ and $\varepsilon_{r2} = 1$.

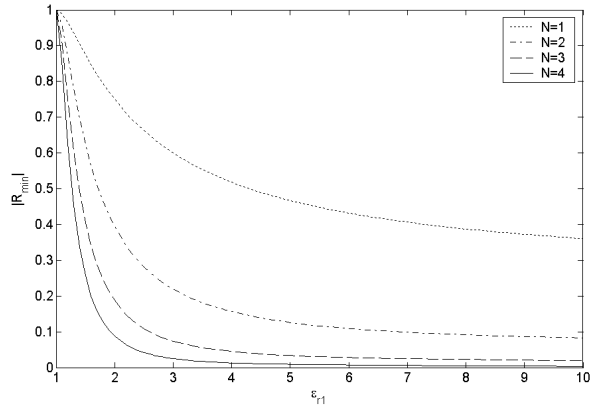

Figure 5: The minimum of $|R|$ versus ε_{r1} when $\varepsilon_{r2} = 1$ and $\theta_i = 60°$.

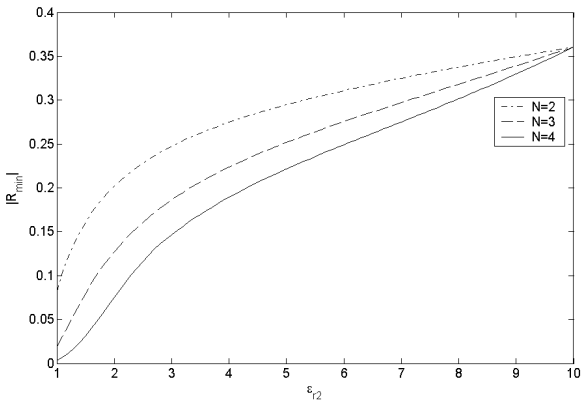

Figure 6: The minimum of $|R|$ versus ε_{r2} when $\varepsilon_{r1} = 10$ and $\theta_i = 60°$.

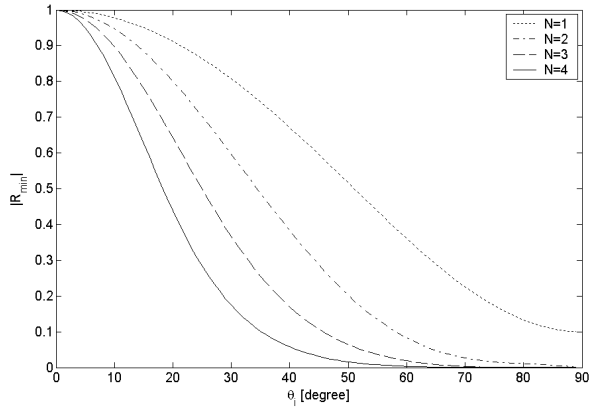

Figure 7: The minimum of $|R|$ versus θ_i when $\varepsilon_{r1} = 10$ and $\varepsilon_{r2} = 1$.

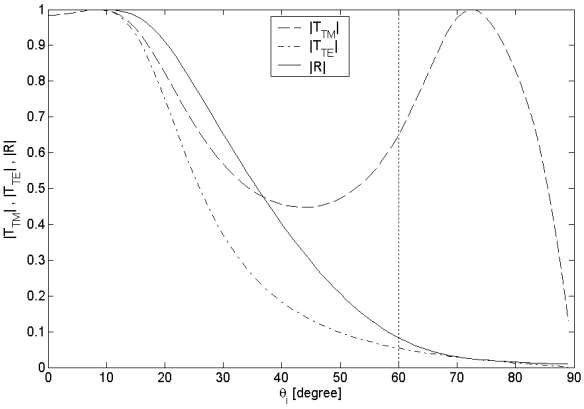

Figure 8: The $|R|$ as well as $|T_{TM}|$ and $|T_{TE}|$ of designed polarizer versus θ_i.

1. Select ε_{r1} as high as possible.
2. Select ε_{r2} as low as possible (the air).
3. Find $|R|$ versus d_1 and d_2 for some Ns to obtain minimum of $|R|$ for each N and then select N.
4. Select optimum values of d_1 and d_2 ($\lambda_1/4$ and $\lambda_2/4$ for $N = 1$ or 2).

To design a polarizer at frequency $f = 10\,\text{GHz}$ and at incidence angle $\theta_i = 60°$, consider

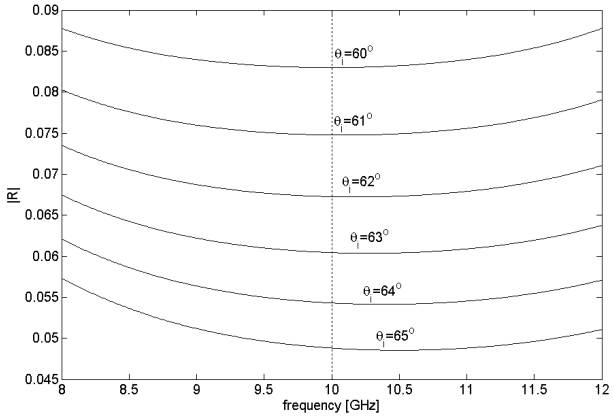

Figure 9: The $|R|$ of designed polarizer versus f.

$\varepsilon_{r1} = 10$, $\varepsilon_{r2} = 1$ and $N = 2$. The optimum values of d_1 and d_2 are obtained 2.466 mm and 15 mm, respectively ($d = 19.932$ mm). Figures 8–9 show $|R|$ of designed polarizer versus θ_i and f, respectively. It is seen that as θ_i increases $|R|$ decreases but either decreasing or increasing the frequency increases $|R|$. Thus the proposed polarizers operate well not at a narrow angle of incidence but at all angles greater than the optimum designed angle. Of course, the transmission coefficient of TE mode, T_{TE}, becomes one only at the brewster's angle (in here 72.45°), at which the transverse characteristic impedance of the high permittivity dielectric layers becomes equal to that of the air (as well as the low permittivity dielectric layers).

4. CONCLUSION

Several high permittivity dielectric layers were used as a wide-angle wave polarizer for the transmission waves to suppress the TE mode in the transmission wave. To design a polarizer, it is analyzed for a wide range of parameters and then the optimum values of the parameters are found out. The usefulness of the proposed structure was verified using a comprehensive example and the main principles for optimally design of polarizers was extracted. It was seen that to have a high performance polarizer the electric permittivity and the number of the dielectric layers have to be increased. Also, there are some optimum values for the thickness of dielectric layers, which are odd multiples of a quarter wavelengths for polarizers with one or two dielectric layers. Moreover, it was seen that the proposed polarizers are wide-angle ones because they operate well at all angles greater than the optimum designed angle.

REFERENCES

1. MacNeille, S. M., "Beam splitter," U. S. patent 2, 403, 731, July 9, 1946.
2. Mouchart, J., J. Begel, and E. Duda, "Modified MacNeille cube polarizer for a wide angular field," *Appl. Opt.*, Vol. 28, 2847–2853, 1989.
3. Monga, J. C., "Multilayer thin-film polarizers with reduced electric-field intensity," *J. Mod. Opt.*, Vol. 36, 769–784, 1989.
4. Li, L. and J. A. Dobrowolski, "Visible broadband, wide-angle, thin-film multilayer polarizing beam splitter," *Appl. Opt.*, Vol. 35, 2221–2225, 1996.
5. Thomsen, M. and Z. L. Wu, "Polarizing and reflective coatings based on half-wave layer pairs," *Appl. Opt.*, Vol. 36, 307–313, 1997.
6. Li, L. and J. A. Dobrowolski, "High-performance thin-film polarizing beam splitter operating at angles greater than the critical angle," *Appl. Opt.*, Vol. 39, 2754–2771, 2000.
7. Awasthi, S. K. and S. P. Ojha, "Wide-angle, broadband plate polarizer with 1D photonic crystal," *Progress In Electromagnetics Research*, PIER 88, 321–335, 2008.
8. Hecht, E., *Optics*, 4th Edition, 349, Addison Wesley, 2002.
9. Dummer, D. J., S. G. Kaplan, L. M. Hanssen, A. S. Pine, and Y. Zong, "High-quality Brewster's angle polarizer for broadband infrared application," *Appl. Opt.*, Vol. 37, 1194–1204, 1998.

10. McCormick, F. B., F. A. P. Tooley, T. J. Cloonan, J. L. Brubaker, A. L. Lentine, R. L. Morrison, S. J. Hinterlong, M. J. Herron, S. L. Walker, and J. M. Sasian, "Experimental investigation of a free-space optical switching network by using symmetric selfelectro-optic-effect devices," *Appl. Opt.*, Vol. 31, 5431–5446, 1992.
11. Ojima, M., A. Saito, T. Kaku, M. Ito, Y. Tsunoda, S. Takayama, and Y. Sugita, "Compact magnetooptical disk for coded data storage," *Appl. Opt.*, Vol. 25, 483–489, 1986.
12. Kunstmann, P. and H. J. Spitschan, "General complex amplitude addition in a polarization interferometer in the detection of pattern differences," *Opt. Commun.*, Vol. 4, 166–168, 1971.
13. Zhang, J.-C., Y.-Z. Yin, and J.-P. Ma, "Mulifunctional meander line polarizer," *Progress In Electromagnetics Research Letters*, Vol. 6, 55–60, 2009.
14. Huang, H., Y. Fan, B.-I. Wu, and J. A. Kong, "Tunable TE/TM wave splitter using a gyrotropic slab," *Progress In Electromagnetics Research*, PIER 85, 367–380, 2008.
15. Awasthi, S. K., U. Malaviya, and S. P. Ojha, "Design of a tunable polarizer using a one-dimensional nano sized photonic bandgap structure," *Progress In Electromagnetics Research B*, Vol. 5, 133–152, 2008.
16. Born, M. and E. Wolf, "Basic properties of the electromagnetic field," *Principles of Optics*, 1–70, Cambridge University Press, UK, 1980.

A Broadband Shorted-patch Antenna for DCS/PCS/UMTS Application

Dongya Shen[1, 2], **Jie Xu**[1], **Yanni Cui**[1], **Xiupu Zhang**[3], **and Ke Wu**[4]

[1]School of Information Science and Engineering, Yunnan University, Kunming, China
[2]State Key Lab of Millimeter Waves, Nanjing, China
[3]Department of Electrical Engineering, Concordia University, Canada
[4]Department of Electrical Engineering, Montreal University, Canada

Abstract— A broadband shorted-patch antenna suitable for DCS (1710–1880 MHz), PCS (1850–1990 MHz) and UMTS (1920–2170 MHz) application is presented. The antenna was fed by an aperture-coupled feed with an H-shaped coupling slot on the ground. The antenna has an impedance bandwidth (VSWR < 2) from 1700 MHz to 2200 MHz. Good broadside radiation characteristics of the proposed antenna at 1800 MHz, 1900 MHz and 2050 MHz have been observed.

1. INTRODUCTION

Broadband probe feed antennas with a thick air substrate could have a wider impedance bandwidth. In order to reduce the size of broadband antennas, several designs of shorted-patch antennas with an air or foam substrate excited by a probe feed, an L-probe proximity feed, a coplanar waveguide feed, have been demonstrated [1–3]. These shorted-patch antennas could operate at quarter-wavelength resonant, and thus have a smaller size compared with conventional half-wavelength antennas. In [4], an aperture coupled shorted-patch antenna suitable for DCS/PCS application has been presented by Wong, and broadband operation has been achieved by cutting an H-shaped slot on the ground. In this paper a broadband shorted-patch antenna with an H-shaped aperture coupling feed has been presented. The width, length and height of the antenna is 40 mm, 23.5 mm and 10 mm respectively. The proposed antenna could well cover the frequency band from 1700 MHz to 2200 MHz and is suitable for DCS, PCS and UMTS application. This antenna has a relatively small size, and is suitable for practical application.

2. ANTENNA CONFIGURATION AND DESIGN

The geometry of the proposed antenna is shown in Fig. 1(a), and all the variables are illustrated in Figs. 1(b) and 1(c). The radiation patch is a rectangular patch with length L and width W, and it is shorted to the ground by a pair of shorting plates. Thus, this antenna works as a quarter-wave antenna. The width of the shorting plates is W_s, which is important in achieving good impedance matching. The substrate of the patch is air, so the cost and weight is reduced. An H-shaped aperture is cut on the ground in order to strengthen the coupling of the patch and the microstrip feed line. Also, an H-shaped aperture could greatly broaden the impedance bandwidth. On the other side of the ground, a 50 Ω microstrip feed line with FR4 substrate is used to feed the antenna. The thickness and permittivity of the substrate are 0.8 mm and 4.4 respectively. The H-shaped aperture was cut centered below the patch. The center arm of the H-shaped slot has a width Wa_2 and a length W1. The upper (closer to the shorting plates) and lower sections of the two side arms have lengths S_1 and S_2 respectively, and the two side arms have the same width Wa_1. The energy from the microstrip feed line on the other side of the ground could efficiently coupled to the patch through the H-shaped slot. By tuning Wa_1, Wa_2, S_1, S_2 and W_1, good impedance matching could be achieved. W_s and h are also important in achieving good impedance matching. The value of the variables are optimized using HFSS and CST. And they are given below:

$L = 23.5$ mm, $W = 40$ mm, $W_1 = 20$ mm, $Wa_1 = 1$ mm, $Wa_2 = 2$ mm, $W_s = 11$ mm, $S_1 = 10$ mm, $S_2 = 8.1$ mm, $T = 5.8$ mm, $h = 10$ mm.

3. RETURN LOSS

The proposed antenna has been simulated and optimized using HFSS and CST, and the results agree well. The return loss is shown in Fig. 2. This antenna could well cover a wide frequency bandwidth from 1700 MHz to 2200 MHz (VSWR < 2), covering some frequency bands used most frequently, such as DCS (1710 MHz–1880 MHz), PCS (1850–1990 MHz) and UMTS (1920–2170 MHz). So it

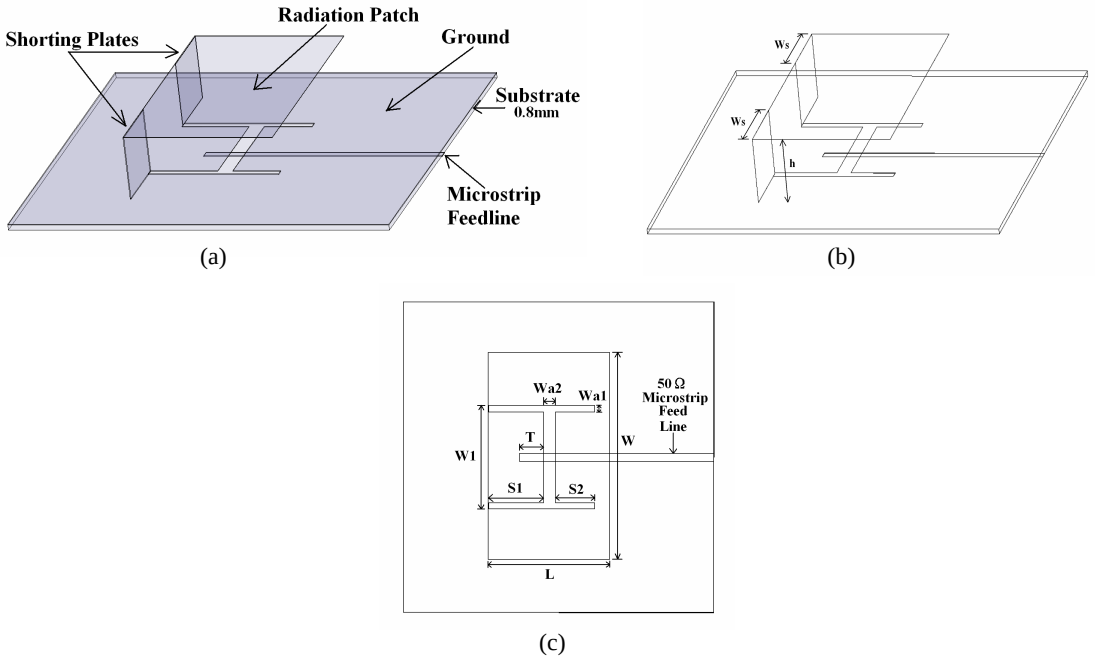

Figure 1: Geometry of the proposed antenna. (a) Three dimensional view. (b) Three dimensional view with variables. (c) Top view with variables.

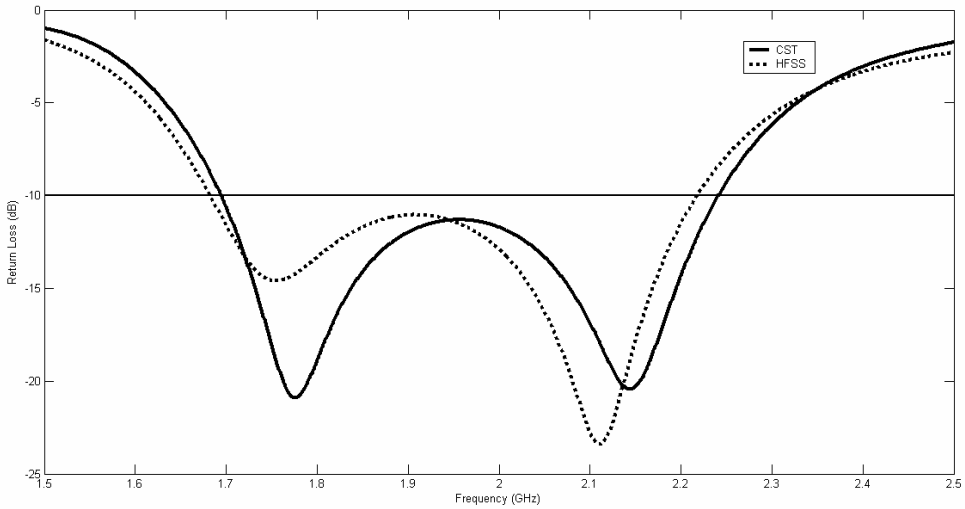

Figure 2: Simulated return loss of the proposed antenna.

could be used in 2G and 3G mobile communication networks. Because of the use of an H-shaped coupling slot, two resonant modes could be excited to broaden the impedance bandwidth, which is 25.6% compared with the center frequency 1950 MHz.

4. RADIATION PATTERNS

The three dimensional radiation patterns of the proposed antenna at 1795 MHz, 1920 MHz and 2045 MHz are illustrated in Fig. 3.

The two dimensional radiation patterns at 1795 MHz, 1920 MHz and 2045 MHz are illustrated in Fig. 4.

It is observed in Fig. 3 and Fig. 4 that the radiation patterns remain stable at 1795 MHz, 1920 MHz and 2045 MHz. And broadside radiation patterns could be observed.

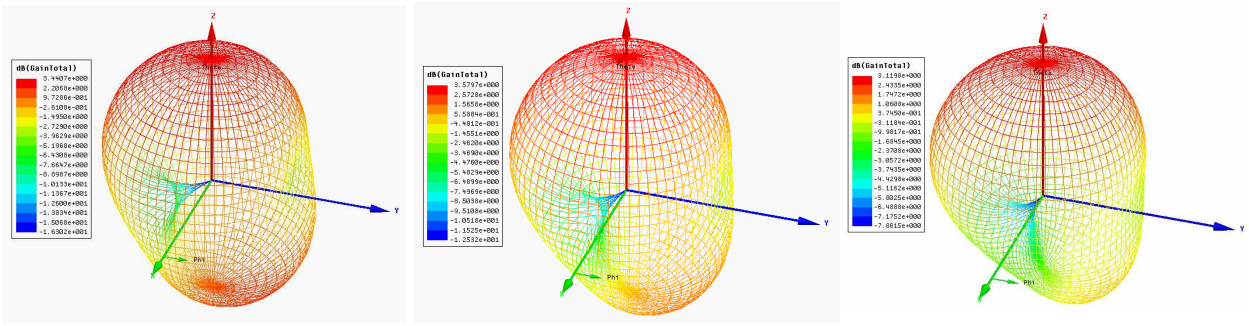

(a) (b) (c)

Figure 3: Three dimensional polar plot of the radiation patterns. (a) 1795 MHz. (b) 1920 MHz. (c) 2045 MHz.

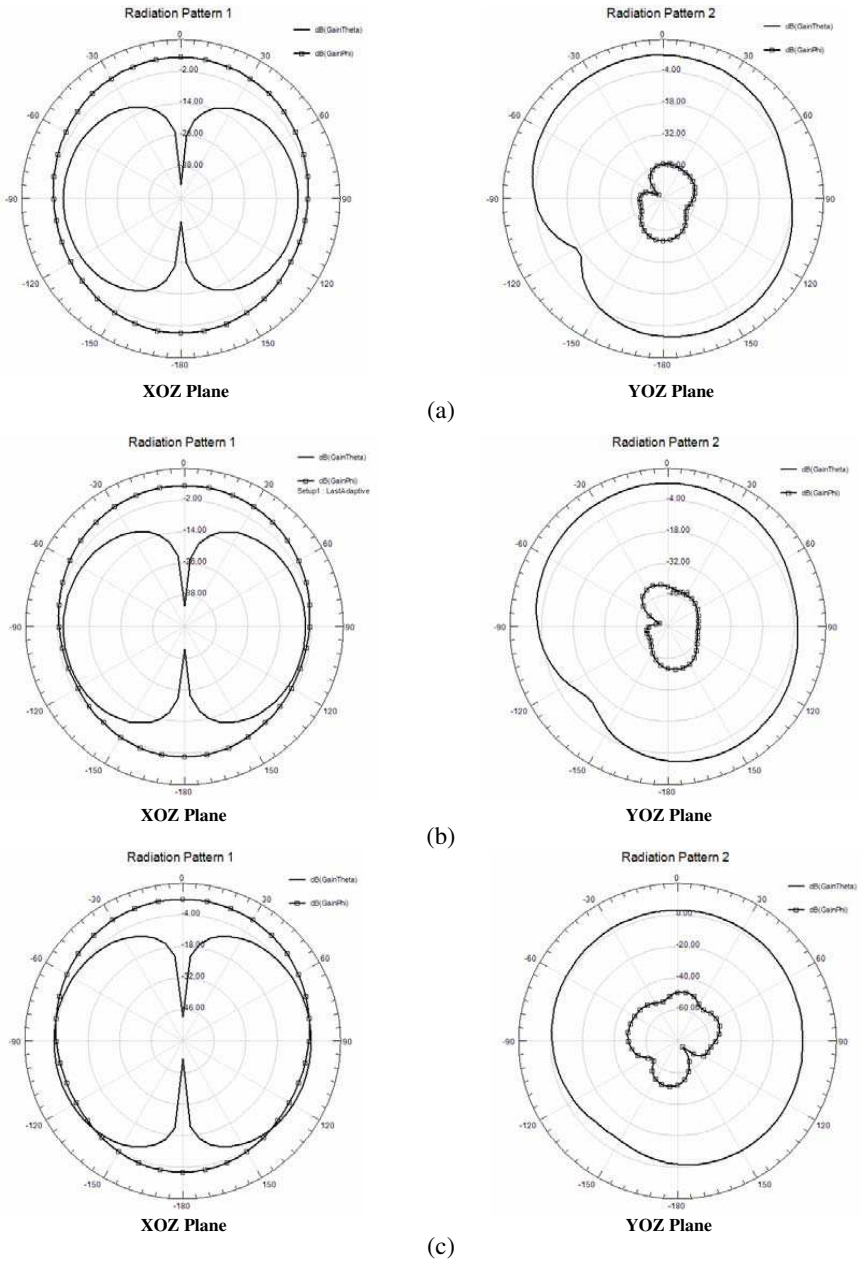

Figure 4: Radiation patterns of the proposed antenna at different frequencies. (a) 1795 MHz. (b) 1920 MHz. (c) 2045 MHz.

5. CONCLUSIONS

A broadband aperture coupled shorted-patch antenna has been presented. It well covers the frequency band from 1700 MHz to 2200 MHz with VSWR < 2. It could work at DCS, PCS and UMTS frequency bands, and is suitable for 2G and 3G mobile communication application.

ACKNOWLEDGMENT

This paper is supported by National Natural Science Foundation of China (No. 60662004), National 863 Project (2007AA01Z2B4), State Key Lab of Millimeter Waves Foundation (No. K200814) and Key Project of International Scientific and Technical Cooperation of Yunnan Province (No. 2009AC-010).

REFERENCES

1. Lee, K. F., K. M. Luk, K. F. Tong, S. M. Shum, T. Huynh, and R. Q. Lee, "Experimental and simulation studies of the coaxially fed U-slot rectangular patch antenna," *Proc. Inst. Elect. Eng.*, Vol. 144, 354–358, 1997.
2. Yang, F. and Y. Rahmat-Samii, "Wideband dual parallel slot patch antenna (DPSPA) for wireless communications," *2000 IEEE Antennas Propagat Soc. Int. Symp. Dig.*, 1650–1653, 2000.
3. Wong, K. L. and W. H. Hsu, "A broadband rectangular patch antenna with a pair of wide slits," *IEEE Trans. Antennas Propagat.*, Vol. 48, 2001.
4. Hsu, W. H. and K. L. Wong, "Broadband aperture-coupled shorted patch antenna," *Microwave Opt. Technol. Lett.*, Vol. 28, 306–307, March 5, 2001.
5. Kuo, J. S. and K. L. Wong, "A low-cost microstrip-line-fed shorted patch antenna for PCS base station," *Microwave Opt. Technol. Lett.*, Vol. 29, 146–148, May 5, 2001.
6. Huynh, T. and K. F. Lee, "Single-layer single-patch wideband microstrip antenna," *Electron. Lett.*, Vol. 31, 1310–1311, August 3, 1995.
7. Wong, K. L. and W. H. Hsu, "A broadband rectangular patch antenna with a pair of wide slits," *IEEE Trans. Antennas Propagat.*, Vol. 49, 1345–1347, September 2001.
8. Herscovici, N., "A wide-band single-layer patch antenna," *IEEE Trans. Antennas Propagat.*, Vol. 46, 471–473, April 1998.
9. Xu, J., D. Shen, B. Huang, and J. Yang, "A low-cost shorted-patch antenna for GSM 900/1800 application," *Proceedings of the Third IEEE International Symposium on Microwave, Antenna, Propagation and EMC Technologies for Wireless Communications*, Beijing, China, October 27–29, 2009.
10. Chen, Z. N. and M. Y. W. Chia, "A feeding scheme for enhancing the impedance bandwidth of a suspended plate antenna," *Microwave Opt. Technol. Lett.*, Vol. 38, 21–25, July 5, 2003.
11. Chen, Z. N., M. Y. W. Chia, and C. L. Lim, "A stacked suspended plate antenna," *Microwave Opt. Technol. Lett.* Vol. 37, 337–339, June 5, 2003.
12. Chang, F.-S. and K.-L. Wong, "Broadband patch antenna edge-fed by a coplanar probe feed," *Microwave Opt. Technol. Lett.*, Vol. 31, 287–289, November 20, 2001.
13. Chen, Z. N. and J. H. Ng, "Probe-fed center-slotted suspended plate antennas with resistive and capacitive loadings," *Microwave Opt. Technol. Lett.*, Vol. 45, 355–360, May 20, 2005.

Design of Planar Monopole Antenna with Annulus Shape for Ultra-wideband Applications

Fangfang Yan and Jiadong Xu
School of Electronics and Information, Northwestern Polytechnical University
Xi'an 710129, China

Abstract— A novel planar antenna with annulus shape for ultra-wideband (UWB) applications is presented in this paper. The element fed by microstrip line consists of an annulus patch and a truncated ground plane which is used to achieve good impedance match over a broad bandwidth. The performance of the antenna is analyzed and optimized with by software Ansoft HFSS. The proposed antenna is much smaller than the conventional antenna, it has been fabricated by etching copper on the FR4 substrate. The simulated and measured results have shown that the designed antenna covers the 3.1–10.6 GHz band allocated to UWB systems. The radiation pattern and gain characteristics are given.

1. INTRODUCTION

Since the allocation of 3.1–10.6 GHz frequency spectrum by the Federal Communications Commission (FCC) for the UWB radio applications, the UWB technology has attracted more and more attention from both academic and industry due to its amazing advantages in recent years [1]. The UWB antennas play a crucial role in the UWB systems. However, there are more challenges in designing a UWB antenna than a narrow band one [2]. Many wideband antenas have been developed during these years including bow-tie, log-periodic, spiral, and TEM horn antennas, but they are difficultly integrated to the printed circuit board. For these applications, printed UWB antennas like monopole antennas and slot antennas are very popular due to their merits such as low profile, low cost, lightweight, easy fabrication and compatibility to the printed circuit board [3]. In the past two years, printed monopole antennas fed by microstrip line or coplanar waveguide (CPW) have been proposed for UWB applications. Recently, several monopoles [4–7] have been proposed for various UWB applications. These antennas make use of different structures to meet the requirements of return loss and radiation patterns, including circular disc monopole, Elliptical Shape, Butterfly-Shaped Monopole and the planar inverted cone antenna.

In this paper, a planar antenna with annulus shape for ultra-wideband application is investigated both numerically and experimentally. The compact antenna with annulus shape radiator and a square ground is about $30 \times 30\,\text{mm}^2$. The simulated and measured results show good impedance matching over UWB band. The radiation patterns and gain characteristics are given as well.

2. ANTENNA DESIGN

The proposed antenna consists of that includes annulus radiator and truncated square ground printed on both sides of FR4 dielectric substrate with the relative permittivity $\varepsilon_r = 4.4$ and thickness $t = 1.6\,\text{mm}$, and its size is $30 \times 30\,\text{mm}^2$. Fig. 1 shows the geometry and dimension of the proposed antenna. In Fig. 1(a), the antenna is fed by a 50 ohm microstrip line whose width is 2.4 mm and length is 9 mm respectively. The radiator is an annulus patch consisting of an inner circle subtracted from an outer one and the distance between centers of the circles is 0.5 mm. The radius of the outer circle is 10 mm, and that of the inner circle is 5 mm. The ground is a rectangular patch whose width is 24 mm and length is 8.8 mm, as shown in Fig. 1(b).

3. SIMULATION AND MEASUREMENT

The HFSS software based on Finite Element Method is applied to investigate the proposed UWB antenna. The Agilent E8363B Vector Network Analyzer is used to measure the return loss. The simulated and measured VSWR results of the proposed antenna is shown in Fig. 2. The simulated bandwidth of VSWR ≤ 2 is from 3.06 GHz to 15.4 GHz and the measured one is from 3.02 GHz to 15 GHz. Both of them cover the UWB of 3.1–10.6 GHz for short wireless communications. The simulated patterns of E- and H-plane at 4, 7 and 10 GHz are shown in Figs. 3 and 4, respectively. It shows that the E- and H-plane patterns at 4 and 7 GHz are approximately omni-directional while those at 10 GHz do not meet the omnidirectional requirement.

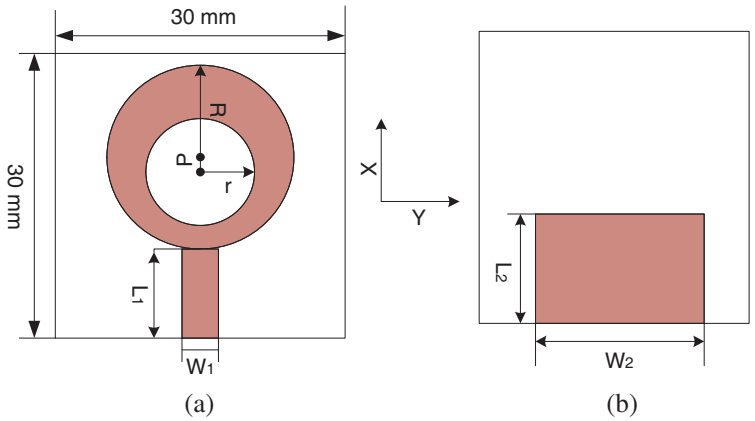

Figure 1: Geometry and configuration of proposed antenna. (a) Front view. (b) Back view.

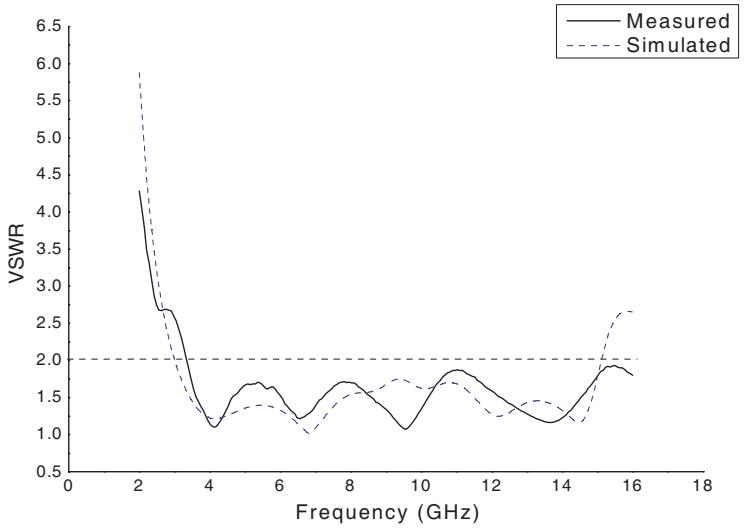

Figure 2: Measured and simulated VSWR of the proposed antenna.

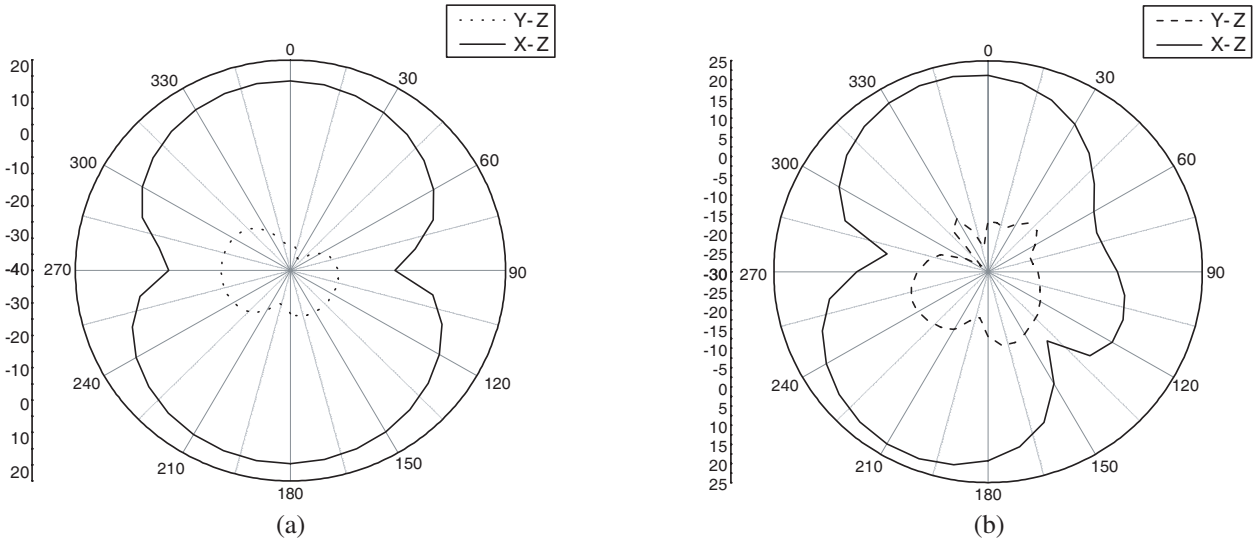

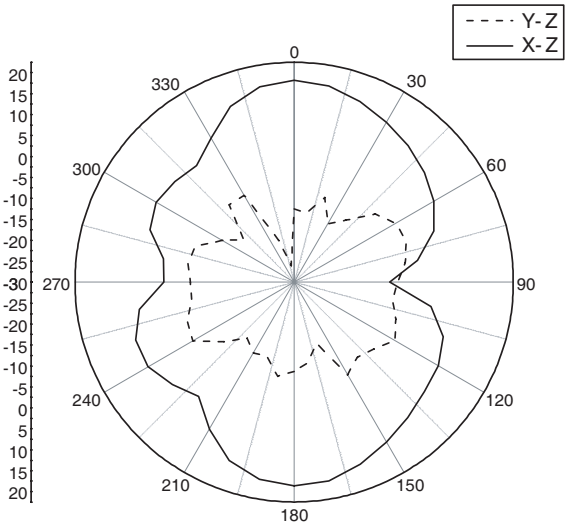

(c)

Figure 3: (a) E-plane pattern at 4 GHz. (b) E-plane pattern at 7 GHz. (c) E-plane pattern at 10 GHz.

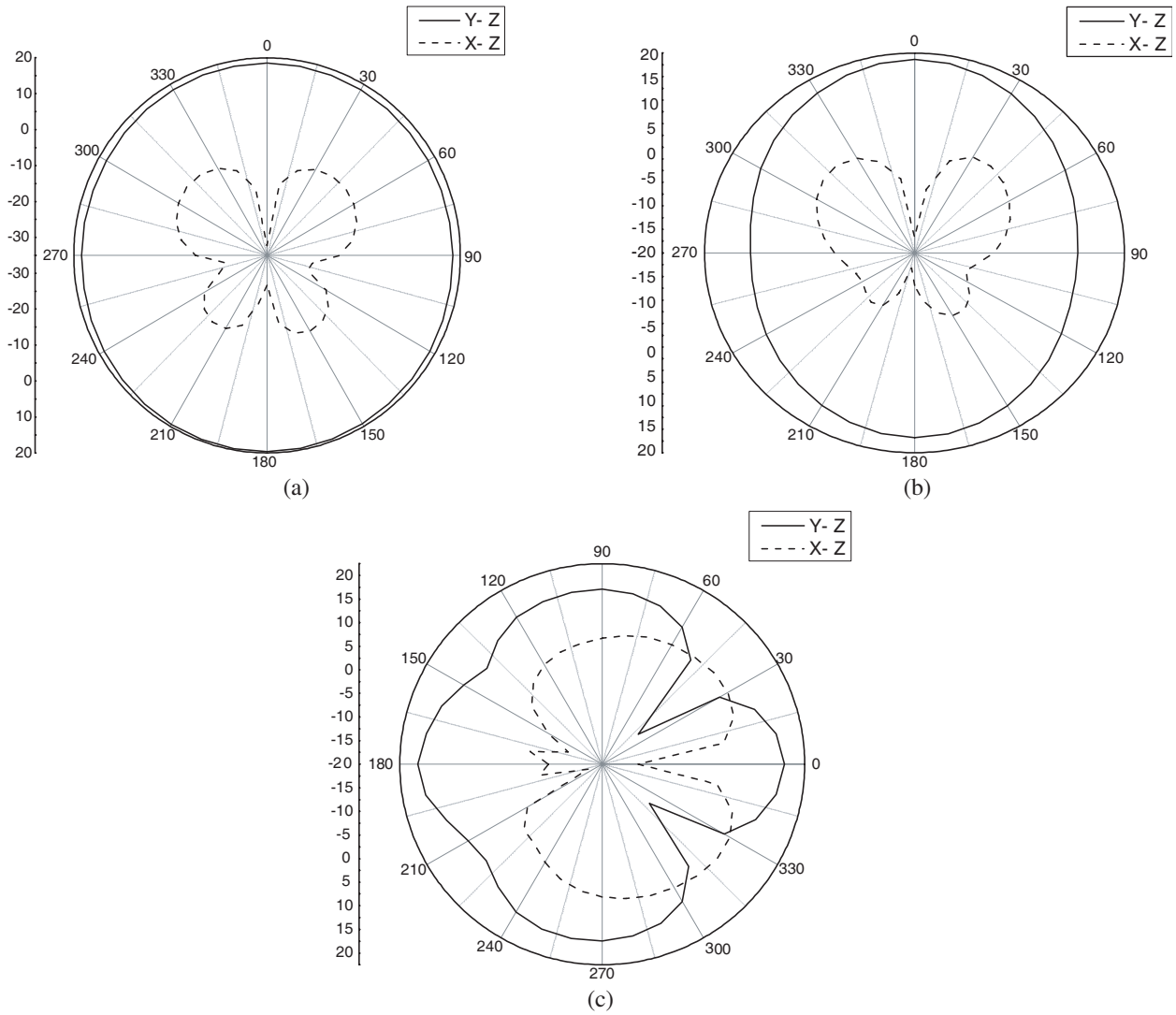

(a) (b) (c)

Figure 4: (a) H-plane pattern at 4 GHz. (b) H-plane pattern at 7 GHz. (c) H-plane pattern at 10 GHz.

4. CONCLUSION

In this paper, a compact UWB planar monopole antenna with annulus shape has been proposed and investigated. The proposed antenna has been manufactured using RF4 substrate. The simulations and measurements have shown that the proposed antenna provided good impedance matching covering UWB frequency range very well. The radiation patterns for the proposed antenna have been studied in details including co-and cross-polarization performances for x-z and y-z planes. The design has been validated by both simulation and measurement.

REFERENCES

1. "New public safety applications and broadband internet accessamong uses envisioned by FCC authorization of ultra-wideband technology," FCC News Release, Feb. 14, 2002.
2. Yazdandoost, K. Y. and R. Kohno, "Ultra wideband antenna," *IEEE Communication Magazine*, Vol. 42, No. 6, 29–32, 2004.
3. Zhong, S.-S. and X.-L. Liang, "Progress in ultra-wideband planar antennas," *Journal of Shanghai University*, English Edition, Vol. 11, No. 2, 95–101, 2007.
4. Qiu, J., J. Qi, and W. Li, "A circular monopole ulatr-wideband antena," *IEEE-Russia Conference: MEMIA*, 2005.
5. Abbosh, A. M. and M. E. Bioalkowski, "Design of ultrawideband palnar monopole antennas of circular and elliptical shape," *IEEE Transactions on Antennas and Propagation*, Vol. 56, No. 1, Jan. 2008.
6. Ye, Q. and Z. N. Chen, "A novel butterfly-shaped monopole UWB antenna," *Antenna Technology Small and Smart Antennas Metamaterials and VSWR Applications*, 2007.
7. Suh, S.-Y., W. L. Stutzman, and W. A. Davis, "A new ultrawideband pinted monopole antenna: The planar inverted cone antenna (PICA)," *IEEE Transactions on Antennas and Propagation*, Vol. 52, No. 5, 1361–1365, 2004.

Universal UHF RFID Rose Reader Antenna

T. G. Abo-Elnaga[1], **E. A. F. Abdallah**[1], **and H. El-Hennawy**[2]

[1]Electronics Research Institute, Cairo, Egypt
[2]Faculty of Engineering, Ain Shams University, Cairo, Egypt

Abstract— Two meandered UHF RFID reader antennas are proposed. Both antenna structures are composed of a single loop on the top of FR4 substrate, which is meandered in the form of a rose to obtain compact size. The rose antenna is fed directly through microstrip line connecting the rose with the RF input. Down the microstrip feeding line a finite ground line placed on the bottom of the substrate. The antenna input impedance is controlled by adjusting the offset length of the ground line. Both antennas occupy areas of radius 25 mm and 21 mm, respectively compared to 72.5 mm for the conventional printed loop one. The measured bandwidths of the designed antennas cover the universal UHF frequency band of 840–960 MHz. Other radiation properties are found to be acceptable for both proposed antennas. Therefore, the proposed fabricated antennas are cheap, compact and universal for UHF RFID applications reader worldwide.

1. INTRODUCTION

RFID system has been developed for several years owing to its wide range of possible application fields. RFID system operating at UHF frequencies has received considerable interests for various commercial applications, such as supply chain management or inventory control. In this regard, a great demand of UHF RFID system is expected to replace the current position of barcode system. Reader antenna is one of the important components in RFID systems, which is used to transmit or receive signal from a tag. Most RFID systems operate at ISM frequencies, such as 13.56 MHz, 2.45 GHz and 5.8 GHz, some work at UHF frequencies such as 840.5–844.5 and 920.5–924.5 MHz in China, 920–926 MHz in Australia, 866–869 and 920–925 MHz in Singapore, 952–955 MHz in Japan and 902–928 MHz in USA, Canada, Mexico, Puerto Rica, Costa Rica, Latin America, and so on. So, the UHF RFID frequency ranges from 840.5 to 955 MHz [1]. Therefore, a universal reader antenna across the entire UHF RFID band with desired performance would be beneficial for RFID system implementation and configuration, as well as cost reduction. In order to communicate in the UHF frequency band the antenna size will be larger relative to the wavelength. In this paper, two meandered UHF RFID reader antennas are proposed in order to communicate with the tags working at UHF band where tag orientation is known and fixed and low power consumption is required in the reader system. Both antenna structures are composed of a single loop on the top of the substrate, which is meandered to obtain compact size, fed directly through microstrip line connecting the rose with the RF input. Down the microstrip line, a finite ground line placed on the bottom of the substrate. The antenna input impedance can be controlled by adjusting the offset length of the ground line. Both antennas occupy areas of radius 25 mm and 21 mm, respectively compared to 72.5 mm for the conventional printed loop one or other complicated designs with circular polarization, which may occupy areas of 155 mm × 230 mm [2] or 250 mm × 250 mm [3]. The measured bandwidths of the designed antennas cover the universal UHF frequency band, which agree well with the computed results. Other radiation properties are found to be acceptable for both proposed antennas.

2. ANTENNA DESIGN

The Fourier series analysis for the thin-wire circular loop or its image equivalent half-loop antenna excited with a transverse electromagnetic (TEM) mode assumed in the aperture of the coaxial line is used for the prototype circular antenna radius prediction in free space. The antenna has radius R, resonant wavelength λ_o, constructed from a perfectly conducting wire of radius a_i, $a_i \ll R$, $\beta_o a_i \ll 1$ and $\beta_o = 2\pi/\lambda_o$. MATLAB code based on Equations (1)–(5) [5], was built to calculate

the input admittance using this theoretical model

$$Y = G + jB = I(0)/V_o) = \left(I_o + 2\sum_{n=1}^{\infty} I_n \right) \Big/ V_o \tag{1}$$

$$I_n = \frac{-jV_o}{\xi_o \pi} \frac{b_n}{a_n} \qquad n = 0, 1, 2, \ldots \tag{2}$$

$$a_n = \frac{\beta_o R}{2} \left(K_{n+1} + K_{n-1} \right) - \frac{n^2}{\beta_o R} K_n \tag{3}$$

$$K_n = \frac{1}{\pi} B_0 \left[\frac{a_i}{R} \sqrt{n^2 - (\beta_o R)^2} \right] H_0 \left[\frac{a_i}{R} \sqrt{n^2 - (\beta_o R)^2} \right] + \frac{1}{\pi} \left\{ \gamma + \ln \left[4 \left(n^2 - \beta_o^2 R^2 \right)^{0.5} \right] \right\} - \frac{2}{\pi} \sum_{m=0}^{n-1} \frac{1}{2m+1} - \frac{1}{2} \int_0^{2\beta_o R} \left[\Omega_{2n}(x) + j J_{2n}(x) \right] dx \tag{4}$$

$$b_n = \frac{1}{\ln (a_o/a_i)} \left(B_0 \left[\frac{a_i}{R} \sqrt{(n+1)^2 - (\beta_o R)^2} \right] \cdot \left\{ H_0 \left[\frac{a_i}{R} \sqrt{(n+1)^2 - (\beta_o R)^2} \right] - H_0 \left[\frac{a_o}{R} \sqrt{(n+1)^2 - (\beta_o R)^2} \right] \right\} + B_0 \left[\frac{a_i}{R} \sqrt{(n-1)^2 - (\beta_o R)^2} \right] \cdot \left\{ H_0 \left[\frac{a_i}{R} \sqrt{(n-1)^2 - (\beta_o R)^2} \right] - H_0 \left[\frac{a_o}{R} \sqrt{(n-1)^2 - (\beta_o R)^2} \right] \right\} \right) \tag{5}$$

In Equations (1)–(5), G and B are the input conductance and susceptance respectively, B_0 and H_0 are the modified Bessel functions of the first and second kinds and order zero, Ω_{2n} is the Lommel-Weber function of order $2n$, J_{2n} is the Bessel function of the first kind and order $2n$, Euler's

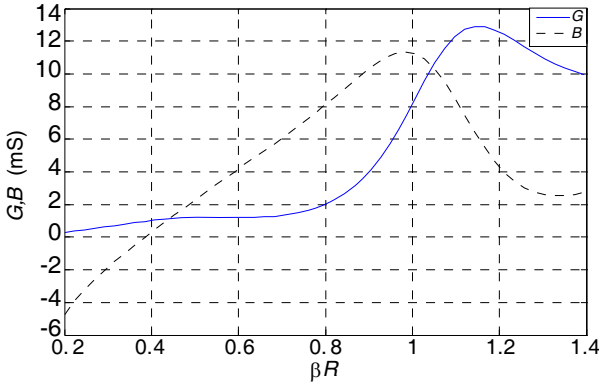

Figure 1: Input admittance of loop antenna versus βR.

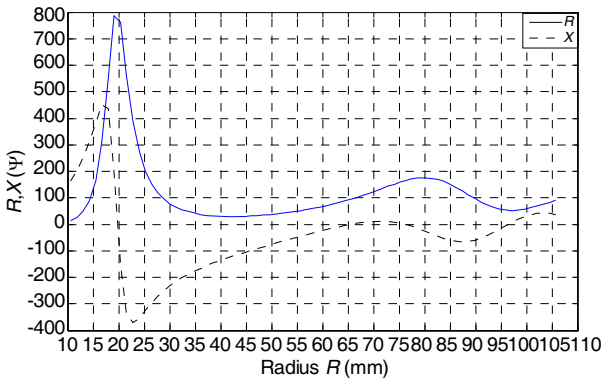

Figure 2: Input impedance of loop antenna versus R at $F = 900$ MHz.

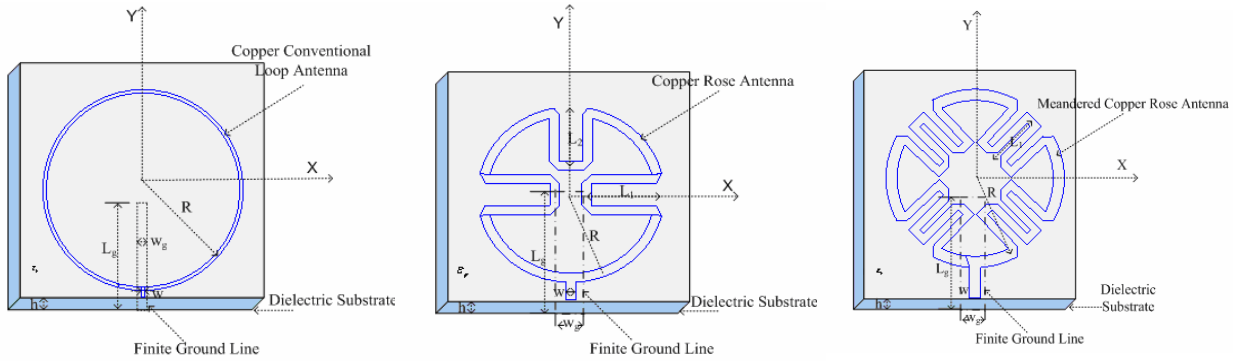

Figure 3: (a) Conventional printed loop antenna. (b) Rose printed loop antenna. (c) Meandered rose printed loop antenna.

constant $\gamma = 0.57722$ and $\xi_o = \sqrt{\mu_o/\varepsilon_o} = 120\pi\,\Omega$ with μ_o and ε_o are free space permeability and permittivity, respectively. The input admittance of an antenna has $R = 40.36\,\text{mm}$, $2a_i = 3.25\,\text{mm}$ and outer to inner coaxial line feed radius ratio $a_o/a_i = 2.174$ was calculated with the MATLAB code. The result in Figure 1 agreed well with the results published in [4]. The code was modified to calculate different radii with different input impedances at the same frequency which is chosen to be 900 MHz as shown in Figure 2, with $a_o = 3.5\,\text{mm}$ and $a_i = 1.52\,\text{mm}$ for coaxial line characteristic impedance $Z_c = 50\,\Omega$. The thin-wire circular loop with $R = 96.09\,\text{mm}$ and input impedance $Z = R + jX = 52.96 - j3.73\,\Omega$ (R and X are the input resistance and reactance, respectively) is transformed to a printed circular loop with width $w = 4a_i$ [5]. FR4 material with relative dielectric constant $\varepsilon_r = 4.65$ and thickness $h = 1.5\,\text{mm}$ is used as substrate. Microstrip line on a finite ground line is used for feeding purpose. The whole structure was optimized using the method of moments based IE3D Zeland software. Figure 3 shows the proposed RFID reader antennas which uses the same feeding scheme in which a microstrip feeding line connected directly with the radiating element on the top, beneath lied a finite ground line. Figure 3(a) shows an optimized Conventional Printed Loop Antenna with width $w = 2.73\,\text{mm}$, ground line with width $w_g = 1.46w$ is chosen, $L_g = 75\,\text{mm}$ and radius $R = 72.5\,\text{mm}$. Figure 3(b) shows the Rose Antenna (RA) in which the radiating loop element is meandered to a rose figure with $L_1 = 19.66\,\text{mm}$, $L_2 = 16.94\,\text{mm}$, $R = 25\,\text{mm}$, and $Lg = 27.5\,\text{mm}$. Figure 3(c) shows the Meandered Rose Antenna (MRA) with $L_1 = 12.09\,\text{mm}$, $R = 21\,\text{mm}$, and $L_g = 26.86\,\text{mm}$.

3. SIMULATED AND MEASURED RESULTS

The fabricated Rose Antenna (RA) and Meandered Rose Antenna (MRA) are shown in Figures 4 and 5, respectively. At the beginning, we design RA and MRA with radii 29 mm and 25 mm, respectively. Figure 6 shows that the measured antenna return loss departs the interested bandwidth, again RA and MRA designed with radii 25 mm and 21 mm, respectively with other dimensions as given in the previous section. The measured impedance bandwidth of the RA at the UHF band reaches 22.47% (0.78437–0.970 GHz) at resonant frequency of 0.82625 GHz, which is broader than

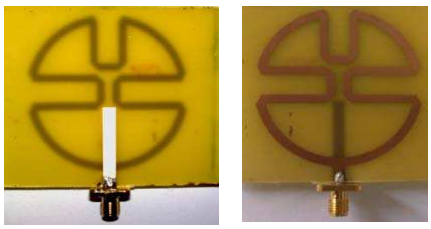

(a) (b)

Figure 4: RA (a) Bottom view. (b) Top view.

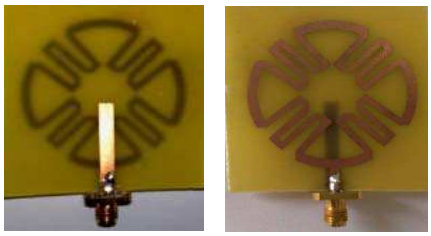

(a) (b)

Figure 5: MRA (a) Bottom view. (b) Top view.

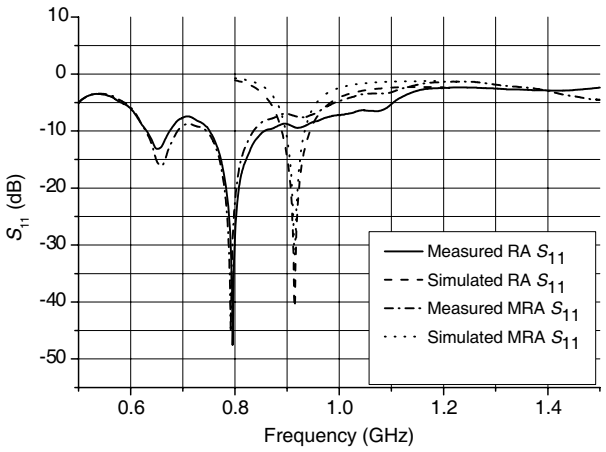

Figure 6: Reflection coefficient S_{11} versus frequency for both RA and MRA with radii 29 mm and 25 mm, respectively.

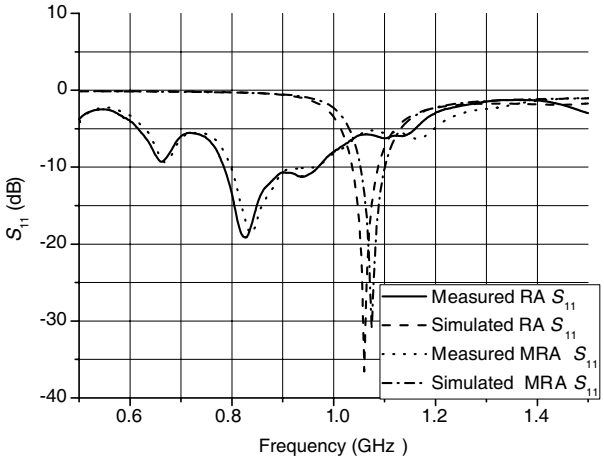

Figure 7: Reflection coefficient S_{11} versus frequency for both RA and MRA with radii 25 mm and 21 mm, respectively.

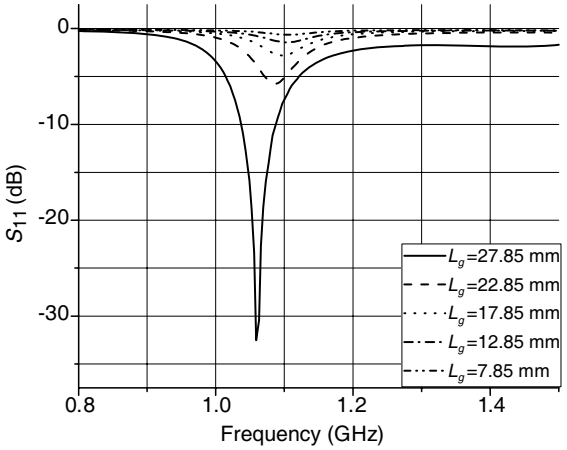

Figure 8: RA offset ground line effect.

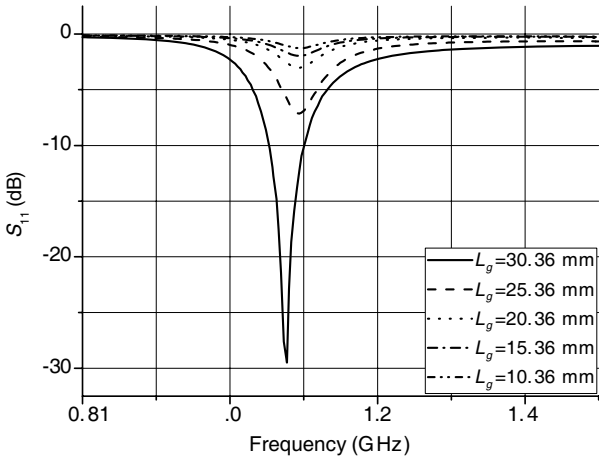

Figure 9: MRA offset ground line effect.

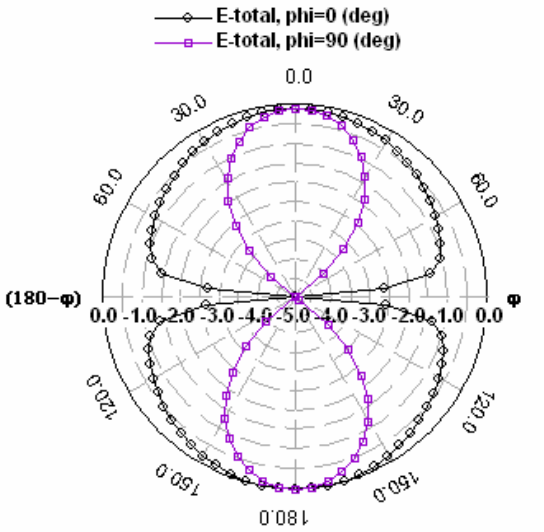

Figure 10: RA radiation pattern.

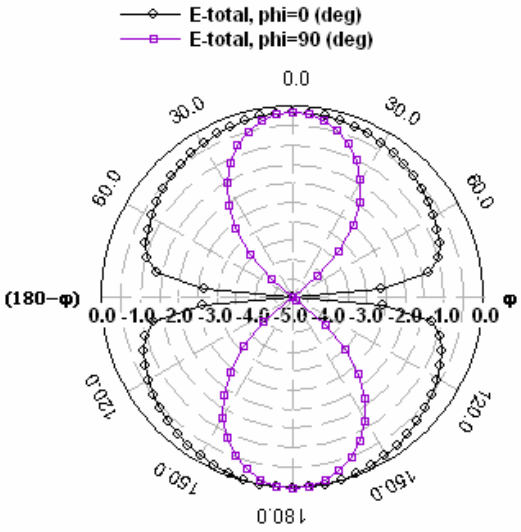

Figure 11: MRA radiation pattern.

the 5.35% (1.077–1.136 GHz) predicted during simulation at 1.06 GHz and cover the universal UHF RFID band. For the MRA, the measured bandwidth reaches 25.25% (0.7981 GHz–0.9675 GHz) at resonant frequency of 0.83625 GHz, which is broader than the 4.47% (1.052–1.1 GHz) predicted during simulation at 1.074 GHz and cover also the universal UHF RFID band as shown in Figure 7. The discrepancies are mainly because of the fabrication difficulty in precise alignment between the finite ground line and the radiated element and the SMA connector soldering before measurement. Figures 8 and 9 show the effect of ground line on the tuning of the input impedance for both RA and MRA, respectively. The MRA radiation efficiency was found to be 73.6% with gain of 1.21 dBi and directivity of 2.54 dBi. For the RA, radiation efficiency was found to be 74.1% with gain of 1.136 dBi and directivity of 2.5527 dBi. RA and MRA radiation patterns are shown in Figures 10 and 11, respectively.

4. CONCLUSIONS

A Rose Antenna (RA) and Meandered Rose Antenna (MRA) for UHF RFID reader are designed and fabricated. The measured input impedances could be controlled by the ground line length. The measured bandwidths cover the universal UHF frequency band of 840–960 MHz. Therefore, the proposed fabricated antennas are simple, cheap, compact and suitable for the universal UHF RFID applications.

REFERENCES

1. Barthel, H., "Regulatory status for RFID in the UHF Spectrum," *EPC Global*, Brussels, Belgium, March 2009.

2. Xu, Z. and X. Li, "Aperture coupling two-layered dual-band RFID reader antenna design," *Proceedings of Microwave and Millimeter Wave Technology ICMMT*, 1218–1221, Nanjing, China, April 2008.
3. Chen, Z. N. and H. L. Chung, "A universal UHF RFID reader antenna," *IEEE Transactions on Microwave Theory and Techniques*, Vol. 57, No. 5, 1275–1282, 2009.
4. Guangping, Z. and S. S. Glenn, "An accurate theoretical model for the thin-wire circular half-loop antenna," *IEEE Transactions on Antennas and Propagation*, Vol. 39, No. 8, 1167–1177, 1991.
5. Hejase, H. N., "Analysis of a printed wire loop antenna," *IEEE Transactions on Microwave Theory and Techniques*, Vol. 42, No. 2, 227–233, 1994.

Antenna Radome Using Split Ring Resonator

The-Nan Chang[1], **Jyun-Ming Lin**[1], **and Min-Chi Wu**[2]

[1]Tatung University, Taipei, Taiwan
[2]WHA YU Industrial Corporation, Hshin Chu, Taiwan

Abstract— In this paper, application of coupled square shaped split ring resonators (CSSSRR) is extended to enhance gain of a circularly polarized (CP) microstrip patch antenna. We etch coupled CSSSRR on both sides of a superstrate which is separated from the patch by an air layer. Open gaps of each CSSSRR on opposite side of the superstrate are orthogonally oriented to each other. This unique orientation allows the radome not only enhance gain but also maintain good CP performance for the patch antenna.

1. INTRODUCTION

Extensive researches have been investigated to increase gain of a microstrip patch antenna. Methods of using periodic metal elements printed on one or two sides of a dielectric substrate in a multi-layer structure are commonly used. Most of them are focused on linearly polarized antenna. In [1], optimized metal element patterns were etched on both sides of an FR4 material in a three layer structure.

In this paper, we etch coupled square-shape split ring resonators (CSSSRR) on both sides of an FR4 material also in a three-layer structure. The CSSSRR are much simpler than those proposed in [1]. The coupling is now between the patch and those square rings. The patch is designed as a circularly polarized antenna. Therefore, we are concerned about enhancement of a circularly polarized antenna gain. We also care about its axial ratio performance.

In the literature, CSSSRR has been widely used to mimic negative permeability materials. However, it is also a periodic structure which can potentially be considered as an energy bad gapped (EBG) material. A similar unit denoted by gapped ring pair element has also been studied in [2]. In [2], we have studied that gap in an open loop may block current flow in a specified direction. This property was employed to reduce cross polarization gain of a linearly polarized reflect array. The CSSSRR unit contains two coupled open loops; therefore, it also owns two gaps. It causes our interest to investigate effect of these gaps on gain enhancement for a circularly polarized wave antenna.

2. ANTENNA STRUCTURE

The proposed structure is shown in Fig. 1. There are 25 CSSSRR with five in row and five in column respectively on both sides of an FR4 material. The CP antenna is a truncated square patch on a grounded substrate. FR4 materials are used for both dielectric layers with a thickness of $h = 0.8\,\text{mm}$ and $H = 1.6\,\text{mm}$. Geometrical parameters of the CSSSRR unit are shown in Fig. 2 where two gaps are said to be lined in y-direction. Two gaps can be arranged to line in x-direction by rotating 90 degrees counter clockwise with respect to its geometrical center. In Fig. 1, "gaps" on upper surface of the superstrate are all lined in x-direction and those on lower surface are all lined in y-direction. We shall denote it as radome A. Alternatively; radome B and C are referred

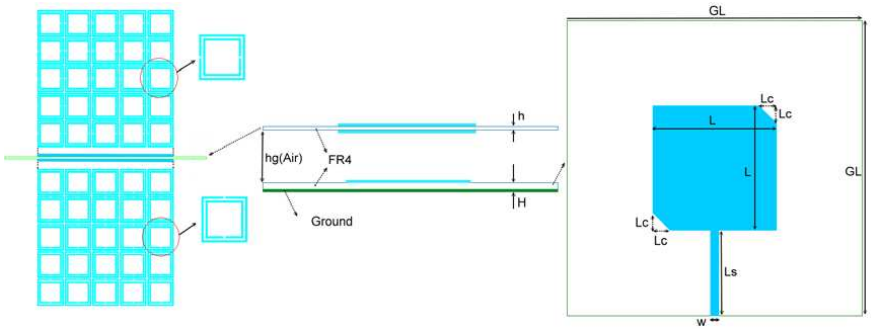

Figure 1: The proposed structure used to enhance gain of a CP antenna.

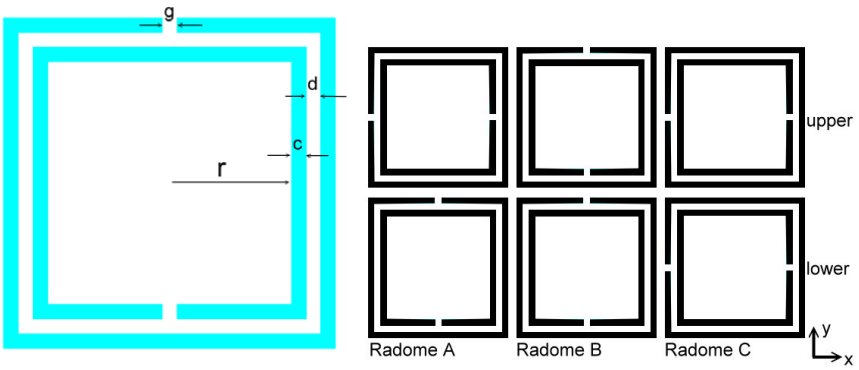

Figure 2: Geometry of a CSSSRR unit (left hand side) and patterns of CSSSRR on upper and lower layers of a superstrate for radome A, B, and C (right hand side).

Table 1

L (mm)	GL (mm)	Ls (mm)	w (mm)	Lc (mm)	r (mm)	c (mm)	d (mm)	g (mm)	s (mm)	hg (mm)	h (mm)	H (mm)
29	69	20	2	4	3.1	0.4	0.4	0.2	'0.4	13	'0.8	1.6

to configurations having all "gaps" on both upper and lower surfaces lined respectively in y- and x- directions.

Table 1 lists parameters of the patch and the CSSSRR unit of a designed example, where r, c, d, g, and s are for the CSSSRR unit and others are for the patch. S is the spacing between two adjacent CSSSRR units.

3. ANALYSIS AND MEASUREMENT

With the radome removed, it results in an isolated patch. It is simulated that it resonates at around 2.495 GHz with an overlapped 10 dB return loss and 3 dB axial ratio bandwidths of around 1.2%. The antenna has a flat gain of 2.8 dBic within 2.47–2.52 GHz.

Figure 3 shows transmission responses of three infinite arrays under normal incident plane waves. All arrays are assumed incident by a y-polarized plane wave at normal direction. Array A, B, and C is infinitely extended from radome A, B, and C in both column and row directions. We found that array B, having y-directed cuts, is easier to be blocked by a y-polarized wave within 2.0 to 2.7 GHz than array C, having x-polarized cuts. We also found that array C has two transmission zeros (stop bands centered at around 1.7 and 4.5 GHz). Although not presented here, it was investigated that the two zeros vary as the circumference lengths of the inner and outer open-cut rings changes.

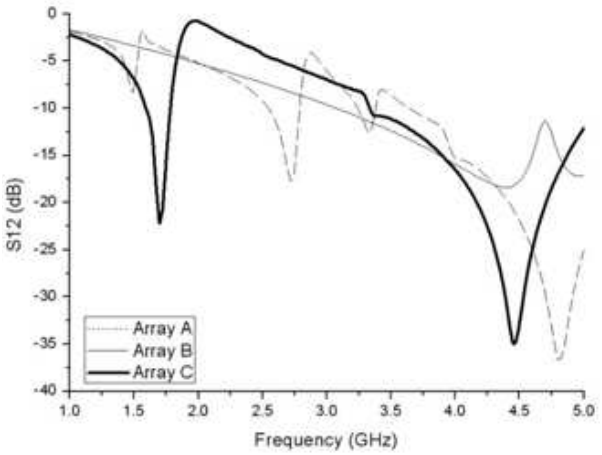

Figure 3: Transmission coefficients of three infinite arrays.

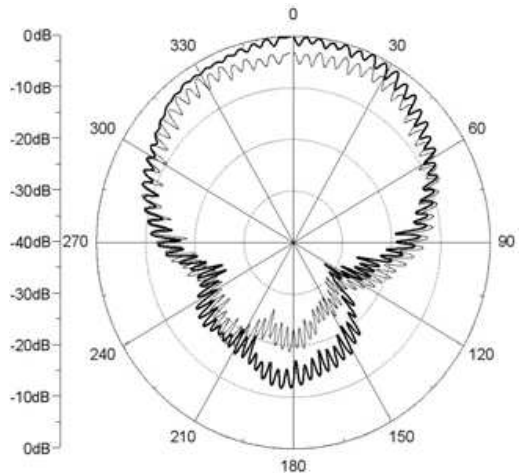

Figure 4: Measured H-plane pattern of the patch with and without radome A.

Apparently, a CSSSRR unit will exhibit polarization-dependent stop bands. Stop bands can also be found for array A. In comparison array A with C and B, there is an extra stop band centered at 2.6 GHz. Array A has the lowest transmission coefficient at 2.45 GHz among the three arrays and array C is the least reflective at 2.45 GHz among the three arrays. To say in another word, array A or B is more reflective than C if all are operated at 2.45 GHz. As our antenna is operated at 2.45 GHz, radome A or B is expected to potentially behave like a partially reflector and could possibly increase y-polarized gain for a y-polarized patch due to a cavity resonant effect. For a CP wave, radome A is better than B as induced current in A will not be blocked in either x or y-direction. The gain enhancement with and without using radome A of the patch antenna is demonstrated in Fig. 4 by showing the associated H-plane patterns. It is shown axial ratio of the patch after putting on the radome can still be maintained in low value.

4. CONCLUSION

Conventionally, we can use stacked dielectric covers or various EBG structures as radome to increase gain of an antenna. For such a radome, it seems of no meaning to distinguish whether the antenna is a linearly or a circularly polarized one. In this paper, a radome is formed by etching CSSSRR on both sides of a superstrate. If all "gaps" of the CSSSRR lie in the same direction, the radome is viewed differently from two orthogonal directions.

Hence, it brings a question whether it is suitable to increase gain for a circularly polarized antenna. After study of three different configurations, we find that "gaps" on opposite side of the superstrate should be orthogonally oriented. By this unique arrangement, not only the gain of a CP antenna can be increased but also good CP performance can be kept.

There leaves one issue that may need further thorough investigation. We found that the gain enhancement of the proposed structure seems largely dependent on the air thickness. The gain reaches a maximum value when the thickness is 0.1 wave length. As information provided in Fig. 3 can only be applied to the case when the radome is far away from the patch, more near field investigation is required.

REFERENCES

1. Ge, Y. and K. P. Esselle, "High-gain, low-profile EBG resonator antennas with very thin metamaterial superstrates," *Antennas and Propagation Society International Symposium*, Jul. 2008.
2. Chang, T. N. and C.-S. Chu, "Cross polarization level of reflectarray with gapped ring elements," *Electronics Letters*, Vol. 43, No. 5, 255–256, Mar. 2007.

Design of the Novel Band Notched UWB Antenna with the Spiral Loop Resonators

Dang-Oh Kim, **Nam-I Jo**, **Dong-Muk Choi**, **and Che-Young Kim**
School of Electrical Engineering and Computer Science, Kyungpook National University
Sankyuk-dong, Puk-gu, Daegu 702-701, South Korea

Abstract— In this paper, a novel configuration of circular ultra-wideband (UWB) antenna with band rejection characteristic is presented. In order to obtain this characteristic, the spiral loop resonators resonating at the rejection frequency are located in both sides of the circular radiating patch. This novel structure provides the band-notched characteristic without the degradation of the UWB antenna performance itself. Furthermore, the notched band can be easily tuned by adjustment of resonator dimension because the size of the spiral loop resonators controls the corresponding resonance frequency. This prototype antenna has been fabricated on a substrate, Rogers 4003, with the thickness of 0.8 mm and relative permittivity of 3.38. The fabricated UWB antenna covers the frequency band from 3.1 to 11.23 GHz ($S_{11} \leq -10$ dB), and the band rejection characteristic appears near at 5.8 GHz band to which the wireless LAN service is assigned. And the far-field radiation patterns of the proposed antenna show omnidirectional and stable over the whole frequency band, which prospects the deployment in the UWB system. The measured results agree well with the simulation by the Microwave Studio of CST. This novel technique utilizing the spiral loop resonators might be useful to the planar antennas requiring the band rejection characteristics.

1. INTRODUCTION

The ultra-wideband (UWB) antennas have been widely adopted in communication systems of commercial and military domains. Because of its attractive features, such as low cost, small size, and easy fabrication, the printed ultra-wideband antenna has been a topic of intense research over the last ten years. The UWB communication uses the spectrum from 3.1 GHz to 10.6 GHz, unfortunately, WLAN 802.11a/n also uses the collision spectrum from 5.15 GHz to 5.825 GHz. Thus, there should be a way of avoidance to get out of interference between UWB and WLAN communication systems. For many years, various UWB antennas with a notch function have been developed to overcome this annoying mutual interference problem by resorting to a various shape slot patch and slot ground [1–4]. Recently, several research groups have attempted to reject the unwanted WLAN frequency bands using the metamaterial resonator such as the SRR (split ring resonator) or the CSRR (the negative image of SRR) structure [5–7]. Because the metamaterial resonator can be considered as an electronically small resonator with a very high Q, it has been used to be respective structure in constructing filters requiring a sharp notch or pass of a certain frequency band. In this paper, the spiral loop resonator (SLR) different in structure from the SRR and CSRR has been utilized, although the basic mechanism is the same to both type.

The characteristics of the SLR for the size reduction of antenna and metamaterial insulator have been already studied by several groups [8–10]. They have established the major theory and illustrated a large portion of experimental results on the SLR as a metamaterial resonator. However, there are few investigations on the interference protection method based on the SLR. Due to lack on these studies, our presentations are likely to be focused to this topic in terms of the known SLR principle.

In this article, a novel design method of the printed ultra-wideband antenna with unwanted band notched characteristics is proposed. By adjusting and tuning on the length of SLR, the desired band rejection performance can be obtained.

2. ANTENNA DESIGN

The geometry of the proposed unit cell of the SLR is shown in Figure 1. The spiral loop acts as an inductor, coupling energy from an incident time-varying magnetic field to produce a current loop in the spiral. There is a distributed capacitance and inductance between the loops of the spiral, and the interaction between the spiral inductance and spiral capacitance causes the resonant behavior. So, the design method of the SLR is similar to the design of SRR and CSRR. According to the published literature on the CSRR analysis, S-parameter of basic resonator cell on 50 Ω microstrip

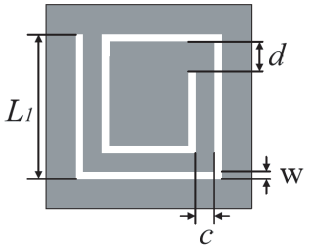

Figure 1: Unit cell of the complementary SLR.

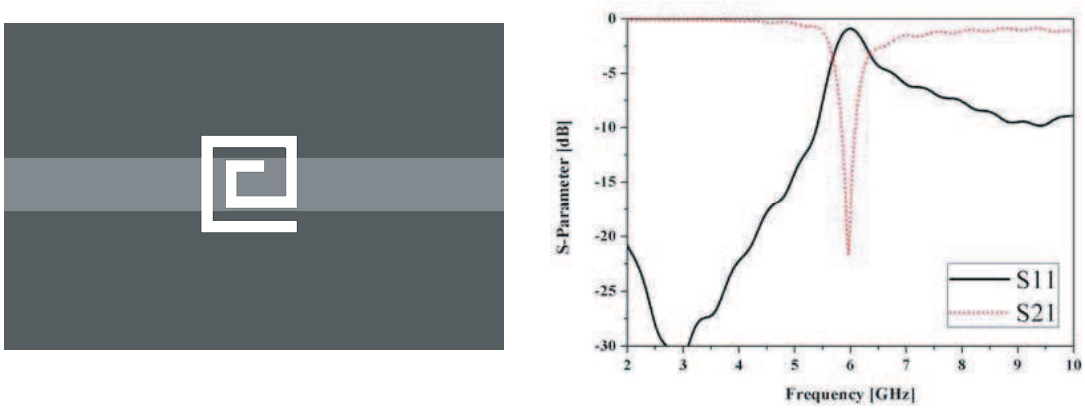

Figure 2: Basic cell of the complementary SLR. (a) Basic cell, (b) S-parameter on the basic cell.

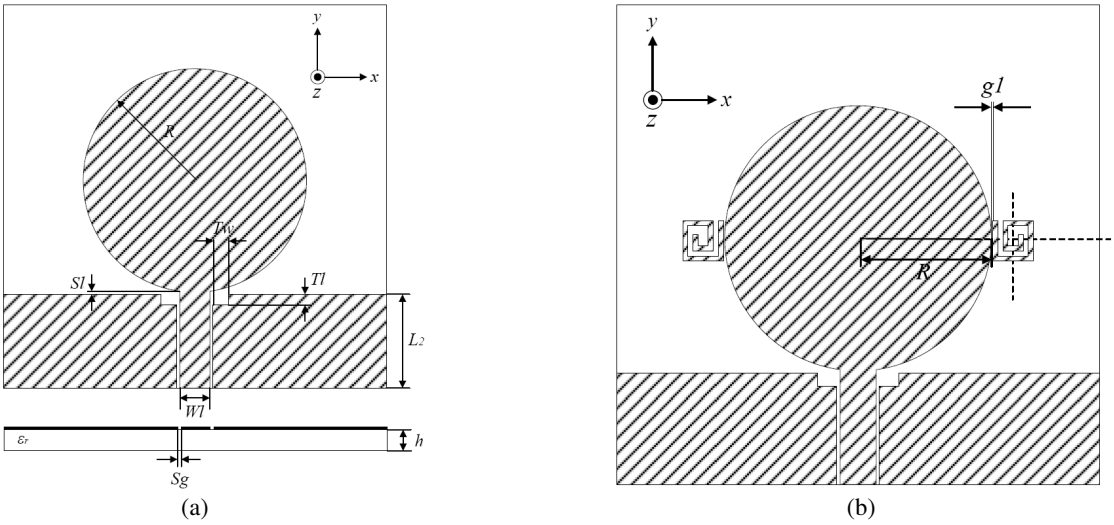

Figure 3: Geometry of the UWB antenna. (a) Prototype UWB antenna, (b) Band notched UWB antenna proposed.

transmission line are simulated by the electromagnetic simulator firstly, which allows to decide the size of resonator by observing the stop band frequencies [11–13]. To apply the same method to SLR, a model of complementary SLR loaded on the microstrip transmission line and the resultant S-parameter are shown in Figures 2(a) and (b), respectively. Figure 2(a) is mounted on RO4003 (thickness $h = 0.812\,\text{mm}$, $\varepsilon_r = 3.38$ and $\tan\delta = 0.0027$) substrate, and optimized by using the CST Microwave Studio (MWS) simulation software. To the unit cell of resonator, the outer length of resonator is $L_1 = 3.3\,\text{mm}$, spiral loop has a constant line width $w = 0.4\,\text{mm}$, and the rest of values are $c = 0.4\,\text{mm}$, $d = 0.7\,\text{mm}$. These physical parameters of the simulated resonator on microstrip transmission line have the band stop characteristic at the attenuation pole of 6 GHz in rejection band. As a simulation finding, many resonance frequencies are observed when the length of the

SLR is adjusted. A series of this step is useful to the design of the proposed antenna. Figures 3(a) and (b) show the geometry of the prototype UWB antenna without the SLR and the proposed band notched UWB antenna, respectively. As shown in Figure 3(a), two sets of the SLRs are stuck on both sides of circular radiating patch. And design of the proposed antenna is based on a traditional UWB antenna with the circular shape patch and the CPW fed as shown in Figure 3(b), and two antennas have the same size and same shape except for resonator of band notched UWB antenna. These UWB antennas have a size of $38 \times 38\,\text{mm}^2$ and are fed by a microstrip line of length $(L_2 + Sl)$ 9.1 mm, and width $Wl = 2.84\,\text{mm}$, which is connected with an SMA connector. And two feed lines with a gap $Sg = 0.27\,\text{mm}$ on each side form a coplanar waveguide (CPW) fed transmission line of the characteristic impedance $Z_0 = 50\,\Omega$. A circular radiating patch has a radius $R = 10.5\,\text{mm}$, and the distances of gap between other elements (the ground plane and SLRs) are $Sl = 0.3\,\text{mm}$, $gl = 0.1\,\text{mm}$. On the same side of the dielectric substrate (Rogers RO 4003, $h = 0.812\,\text{mm}$), the ground plane with two rectangular notches ($Tl = 1\,\text{mm}$, $Tw = 1.5\,\text{mm}$) are used. These antennas are simulated by the same simulation software of the Microwave Studio.

3. RESULT AND DISCUSSION

Figure 4 shows the photographs of the fabricated band notched UWB antenna. Its performance is measured by the Anritsu 38397C network analyzer. The simulated result and measured results are shown in Figure 5, and are in good agreement between them. According to the measured return loss curves on the general UWB antenna and the proposed band notched UWB antenna, it covers the band (3.1 GHz ~ 10.6 GHz) assigned for the UWB communication applications. And measured notched bands (reference level $S_{11} = -10\,\text{dB}$) are 5.91 GHz ~ 6.15 GHz and 240 MHz bandwidth.

Figure 4: The fabricated band notched UWB antenna.

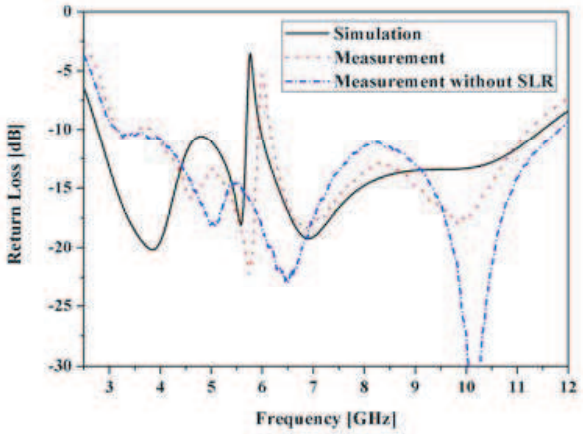

Figure 5: Comparison of simulated results and measured results.

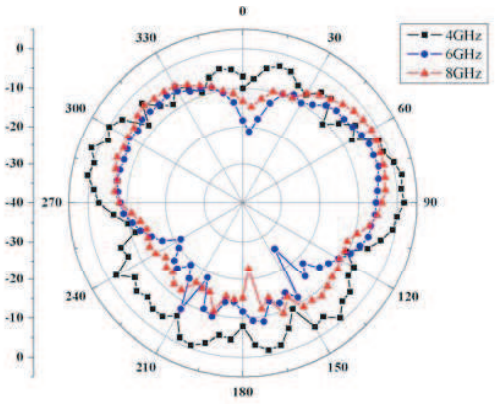

(a)

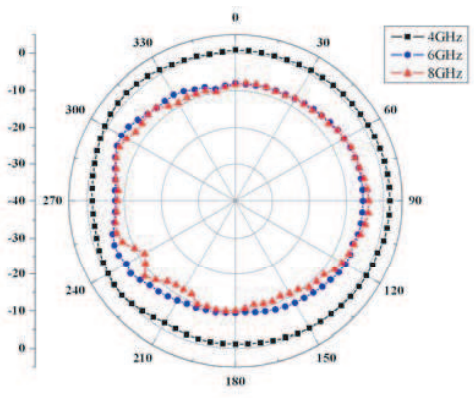

(b)

Figure 6: Measured radiation patterns for the proposed band notched UWB antenna. (a) E-plane, (b) H-plane.

The return loss plotted in Figure 5 indicates that the SLR is operated only at the notched band, and it ensures that adjustment of the outer length of SLRs can tune a notched band to the goal. Figure 6 represents the radiation patterns of E-plane and H-plane at 4 GHz, 6 GHz and 8 GHz. The pattern seen in Figure 6 reveals that the receiving power level is relatively low at notched band 6 GHz and the pattern of the other bands is omnidirectional and remains stable. And furthermore, it says that the application of SLRs can eliminate the 6 GHz frequency band involved in the original UWB antenna structure.

4. CONCLUSION

This paper presents a new technique on how to impose the band rejection property to the prototype UWB antenna. To this end, the SLRs were inserted into the both sides of the radiating patch of the UWB antenna. Especially, the synthesis approach on a traditional UWB antenna to add the complementary SLR has been attempted to achieve the band rejecting property. This technique shows an easy fabrication, cost down merit, and attractive means for the UWB antenna oriented applications.

REFERENCES

1. Song, Y., Y. C. Jiao, T. L. Zhang, J. B. Jiang, X. Zhang, and F. S. Zhang, "Frequency notched UWB slot antenna with a fractal-shaped slot," *Journal of Electromagnetic Waves and Applications*, Vol. 23, No. 2–3, 321–327, 2009.
2. Yuan, T., C. W. Qiu, L. W. Li, M. S. Leong, and Q. Zhang, "Elliptically shaped ultra-wideband patch antenna with band-notched features," *Microwave and Optical Technology Letters*, Vol. 50, No. 3, 736–738, 2008.
3. Wong, K. L., Y. W. Chi, C. M. Su, and F. S. Chang, "Band-notched ultra-wideband circular-disk monopole antenna with an arc-shaped slot," *Microwave and Optical Technology Letters*, Vol. 45, No. 3, 188–191, 2005.
4. Fallahi, R., A. A. Kalteh, and M. G. Roozbahani, "A novel UWB elliptical slot antenna with band-notched characteristics," *Progress In Electromagnetics Research*, PIER 82, 127136, 2008.
5. Kim, J., C. S. Cho, and J. W. Lee, "5.2 GHz notched ultra-wideband antenna using slot-type SRR," *Electronics Letters*, Vol. 42, No. 6, 315–316, 2006.
6. Liu, J., S. Gong, Y. Xu, X. Zhang, C. Feng, and N. Qi, "Compact printed ultra-wideband monopole antenna with dual band-notched characteristics," *Electronics Letters*, Vol. 44, No. 12, 710–711, 2008.
7. Liu, L., Y. Z. Yin, C. Jie, J. P. Xiong, and Z. Cui, "A compact printed antenna using slot-type CSRR for 5.2 GHz/5.8 GHz band-notched UWB application," *Microwave and Optical Technology Letters*, Vol. 50, No. 12, 3239–3242, 2008.
8. Buell, K., H. Mosallaei, and K. Sarabandi, "A substrate for small patch antennas providing tunable miniaturization factors," *IEEE Trans. Microwave Theory Tech.*, Vol. 54, No. 1, 135–146, Jan. 2006.
9. Buell, K., H. Mosallaei, and K. Sarabandi, "Metamaterial insulator enabled superdirective array," *IEEE Trans. Antennas Propag.*, Vol. 55, No. 4, 1074–1085, Apr. 2007.
10. Yousefi, L. and O. M. Ramahi, "New artificial magnetic materials based on fractal hillbert curves," *International Workshop on Antenna Technology, IWAT'07*, 237–240, Mar. 2007.
11. Wu, H. W., M. H. Weng, Y. K. Su, R. Y. Yang, and C. Y. Hung, "Propagation characteristics of complementary split-ring resonator for wide bandgap enhancement in microstrip bandpass filter," *Microwave and Optical Technology Letters*, Vol. 49, No. 2, 292–295, 2007.
12. Lee, Y. J. and Y. Hao, "Characterization of microstrip patch antennas on metamaterial substrates loaded with complementary split-ring resonators," *Microwave and Optical Technology Letters*, Vol. 50, No. 8, 2131–2135, 2008.
13. Zhang, S. and F. L. Liu, "The studies on coupling characteristics of microstrip complementary split ring resonators (CSRRs)," *International Conference on Microwave and Millimeter Wave Technology ICMMT 2008*, 287–290, Apr. 2008.

UWB Circular Polarization RFID Reader Antenna for 2.4 GHz Band

T. G. Abo-Elnaga[1], **E. A. F. Abdallah**[1], **and H. El-Hennawy**[2]

[1]Electronics Research Institute, Cairo, Egypt
[2]Faculty of Engineering, Ain Shams University, Cairo, Egypt

Abstract— Ultra Wide Band (UWB) left hand, right hand circularly polarized antenna is proposed for the supper high frequency (SHF) 2.4–2.483 GHz Radio Frequency Identification (RFID) applications. The antenna is composed of three layers, upper FR4 layer with circular slotted patch antenna on the top, middle foam layer, bottom FR4 layer with modified branch line coupler on the top and ground plane on the bottom of this layer. The slotted circular patch is fed by two posts connecting the circular patch through the foam layer with the branch line coupler. The antenna achieves impedance bandwidth of 1.66 GHz from 2.34–4 GHz for both left hand and right hand circular polarization operation which agree well with the computed results. The proposed antenna has 3 dB axial ratio bandwidth of 488 MHz for the left hand circular polarization covering the range 2.37299–2.86174 GHz and 591 MHz for the right hand circular polarization covering the range 232154–2.91318 GHz. The proposed antenna offers an acceptable gain and other antenna parameters within its bandwidth.

1. INTRODUCTION

Radio Frequency Identification (RFID), which was developed around World War II, is a technology that provides wireless identification and tracking capability. In recent years, RFID technology has been rapidly developed and applied to many service industries, distribution logistics, manufacturing companies, and goods flow systems. In RFID system, the role of antennas (for reader and tag) is very important. The reader antenna should have circular polarization (CP) characteristic since the tag antenna can be arbitrarily positioned on the target. Such CP antennas have been reported in literatures [1, 2]. When an RFID tag comprising an antenna and an application-specific integrated circuit (ASIC) is located in the reading zone of the reader antenna, the tag is activated and interrogated for its content information by the reader. Most RFID systems operate at ISM frequencies, such as 13.56 MHz, 2.45 GHz and 5.8 GHz, some operate at UHF frequencies such as 840∼845 MHz, 920∼925 MHz (China), 952∼954 MHz (Japan), 868∼870 MHz (Europe) and 902∼928 MHz (USA) [3], etc. The proposed antenna is designed to cover the Supper High Frequency (SHF) Radio Frequency Identification (RFID) band of 2.4–2.483 GHz with acceptable performance in terms of gain, AR, and impedance matching. The antenna achieves −10 dB impedance bandwidth of 1.66 GHz from 2.34–4 GHz for both left hand and right hand circular polarization operation which agree well with the computed results. The proposed antenna has 3 dB axial ratio bandwidth of 488 MHz for the left hand circular polarization covering the range 2.37299–2.86174 GHz and 591 MHz for the right hand circular polarization covering the range 232154–2.91318 GHz. The proposed antenna offers an acceptable gain and other antenna parameters within its bandwidth. The antenna configure is simple and easy for fabrication.

2. ANTENNA DESIGN

Figure 1 shows the proposed three-layered circularly polarized RFID reader antenna where the proposed antenna flipped down to see clearly the ground plane, modified branch-line coupler, posts and finally, the T-slotted circular patch. Figure 2 shows the four T-slots which are etched on the circular patch of the top layer with radius $R_1 = 15.6$ mm and width $w = 1$ mm and occupy a circular sector with central angle of 80° positioned at 45° from the center of the circular patch with radius $R = 16.5$ mm calculated from Eq. (1) and Eq. (2) [4], with resonance frequency $f_r = 2.4$ GHz. The slot has a radial length $L = 5$ mm. The circular patch is fabricated on FR4 substrate with thickness $h_1 = 1.5$ mm and permittivity $\varepsilon_r = 4.65$. The radius R is optimized to be 19.5 mm. The middle layer consists of foam layer with thickness $h_2 = 4.8$ mm acts as air layer. The branch-line coupler is designed according to [5]. Two stubs added axially with length of 5.63 mm and width of 2.75 mm for matching and bandwidth enhancement purpose. The modified branchline coupler is fabricated on FR4 substrate with thickness $h_1 = 1.5$ mm and permittivity $\varepsilon_r = 4.65$. Finally two copper posts with radius 0.25 mm and height of 6.3 mm are used to connect the modified branch line coupler

with circular patch through the foam layer with distant 11 mm away from the center of the patch in x and y direction. Noted that LHCP and RHCP could be achieved by alternately feeding one input of modified branchline coupler and matching the other input. The whole structure is analyzed using IE3D Zeland Method of Moments based software.

$$R = \frac{A}{\left\{1 + \frac{2h_1}{\pi\varepsilon_r A}\left[\ln\left(\frac{\pi A}{2h_1}\right)\right] + 1.7726\right\}^{1/2}} \tag{1}$$

where

$$A = \frac{8.791 \times 10^9}{f_r\sqrt{\varepsilon_r}} \tag{2}$$

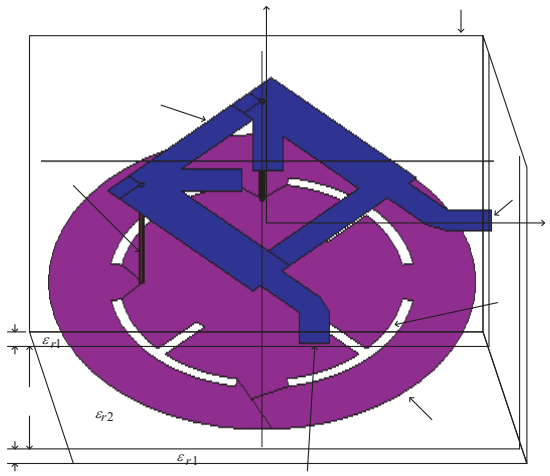

Figure 1: CP RFID reader antenna.

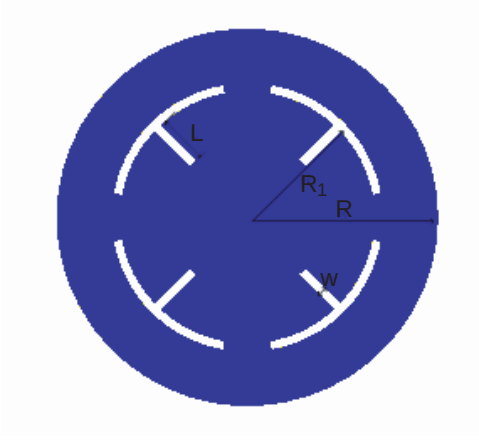

Figure 2: Circular patch with four T slots.

(a) (b)

Figure 3: (a) Fabricated RHCP antenna top view. (b) Fabricated RHCP antenna bottom view.

(a) (b)

Figure 4: (a) Fabricated LHCP antenna side view. (b) Fabricated LHCP antenna bottom view.

3. SIMULATED AND MEASURED RESULTS

The fabricated antenna is shown in Figure 3 and Figure 4, and its dimensions are given in the previous section. Figure 5 shows the simulated and measured return loss characteristics of the fabricated antenna shown in Figure 3 for right hand circular polarization operation. The measured impedance bandwidth reaches 58.5% (from 2.34–4 GHz) with resonant frequency of 2.837 GHz which is broader than 37.45% (2.33–3.36 GHz) predicted during simulation at resonant frequency of 2.75 GHz. The 3 dB axial ratio (AR) bandwidth reaches 20.8%. The measured impedance bandwidth for the left hand circular polarization reaches 67.76% (from 2.34–4 GHz) at resonant frequency of 2.535 GHz, which is narrower than the simulated result 39.95% (from 2.32–3.29 GHz) with resonance at 2.45 GHz as shown in Figure 5 and Figure 6 respectively. The 3 dB axial ratio (AR) bandwidth reaches 19.95% (from 2.37299–2.86174 GHz). Figures 7–12 show the other antenna parameters. The discrepancies are mainly attributed to fabrication tolerance, using three layers of foam to reach the required thickness, SMA soldering, imperfect matched loads for the branch-line coupler, etc.

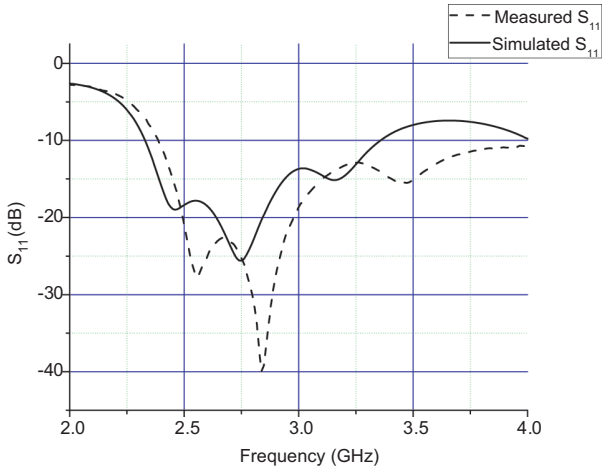

Figure 5: RHCP S_{11} versus frequency.

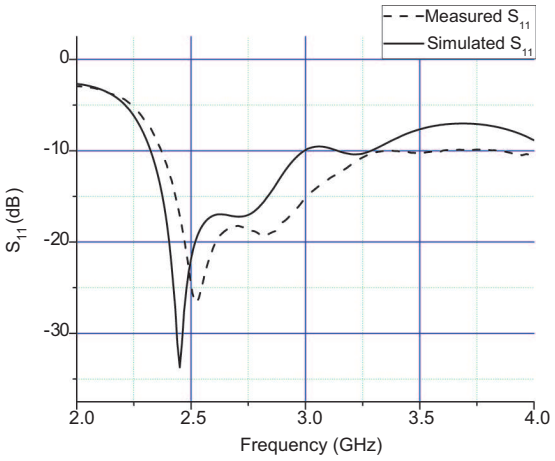

Figure 6: LHCP S_{11} versus frequency.

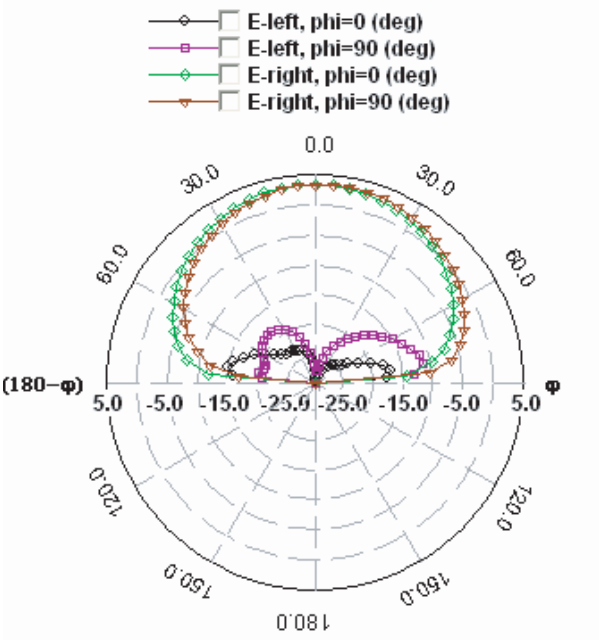

Figure 7: RHCP elevation pattern gain.

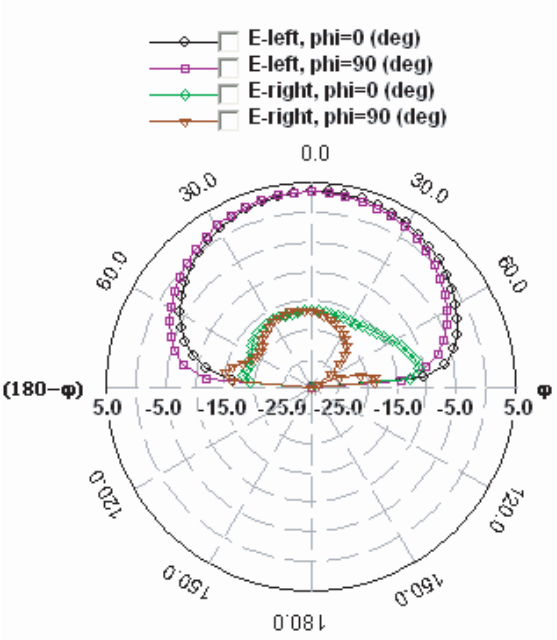

Figure 8: LHCP elevation pattern gain.

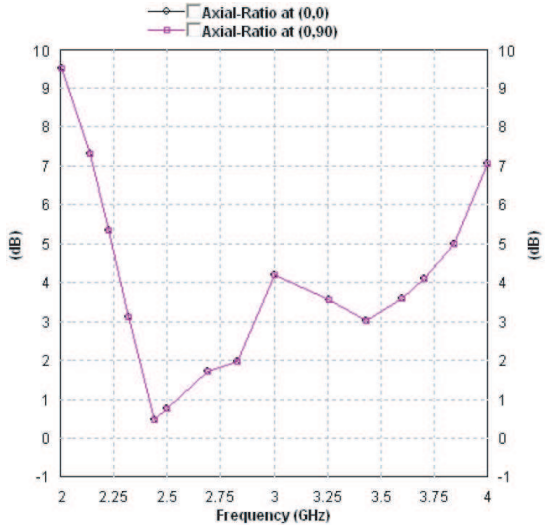

Figure 9: RHCP axial ratio versus frequency.

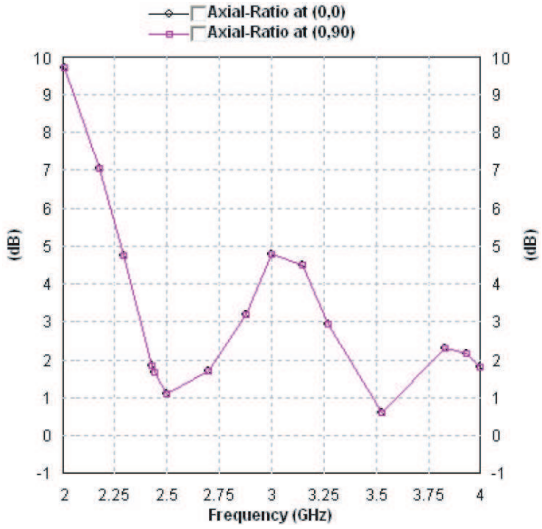

Figure 10: LHCP axial ratio versus frequency.

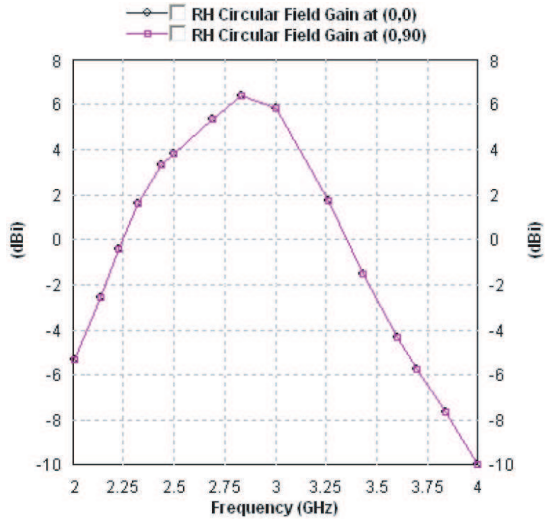

Figure 11: RHCP gain versus frequency.

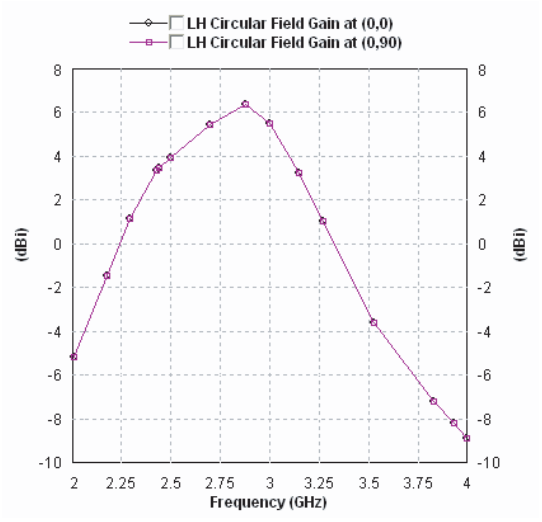

Figure 12: LHCP gain versus frequency.

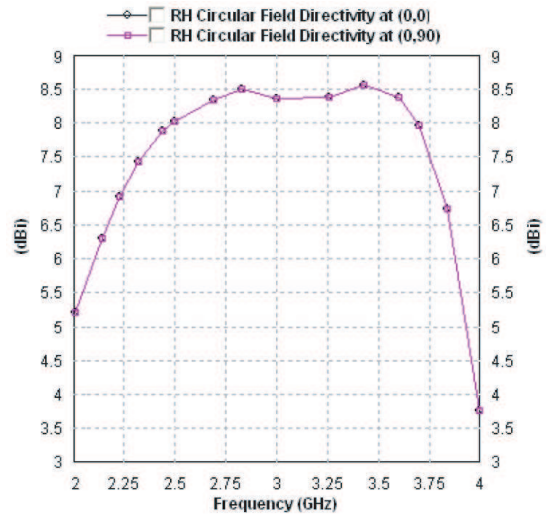

Figure 13: RHCP directivity versus frequency.

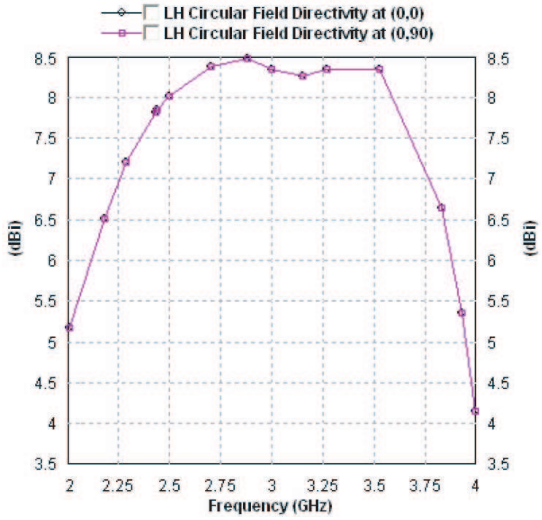

Figure 14: LHCP directivity versus frequency.

4. SIMULATED AND MEASURED RESULTS

LHCP, RHCP three-layered circular T-slotted patch antenna for 2.4 GHz RFID readers applications is presented. The proposed antenna is optimized using method of moments based IE3D Zeland software. By optimal design for both circular T slotted circular patch and modified branchline coupler inner arms, the measured −10 dB input impedance bandwidth reaches 58.5% for the right hand circular polarization and 67.76% for the left hand circular polarization. The 3 dB axial ratio (AR) bandwidth reaches 20.8% for the right hand circular polarization and 19.95% for the left hand circular polarization The proposed antenna presents an UWB performance with an acceptable 3 dB axial ratio bandwidth and all other antenna parameters.

REFERENCES

1. Chen, W., C. Wu, and K. Wong, "Novel compact circularly polarized square microstrip antenna," *IEEE Trans. AP*, Vol. 49, No. 3, 340–342, Mar. 2001.
2. Paulson, M., S. Kundukulam, C. Aanandan, P. Mohanan, and K. Kasudevan, "Circularly polarized compact microstrip antenna," *Microwave Optical Technology Letters*, Vol. 26, No. 5, 308–309, Sep. 2005.
3. Barthel, H., "Regulatory status for RFID in the UHF spectrum," *EPC Global*, Brussels, Belgium, Mar. 2009.
4. Shen, L., S. Long, M. Allerding, and M. Walton, "Resonant frequency of a circular disc, printed-circuit antenna," *APS*, Vol. 25, No. 4, 595–596, Jul. 1977.
5. Wen, C. and M. Chen, "Design of multipassband microstrip branch-line couplers with open stubs," *IEEE Trans. MTT*, Vol. 57, No. 1, 196–204, Jan. 2009.

A Compact UWB Antenna Design for Breast Cancer Detection

S. Adnan, **R. A. Abd-Alhameed**, **C. H. See**, **H. I. Hraga**, **I. T. E. Elfergani**, **and D. Zhou**
Mobile and Satellite Communications Research Centre, University of Bradford
Bradford, West Yorkshire, BD7 1DP, UK

Abstract— Near field imaging using microwave in medical applications has gain much attention recently as various researchers show its high ability and accuracy in illuminating object compares to well known screening tools. This paper documents the development of new compact ultra wide bandwidth antenna designed primarily for microwave imaging application such as breast cancer detection. A parametric study is carried out using two well known softwares packages to achieve optimum antenna performances. The performance of the Prototype antenna is tested and analyzed experimentally and exhibit reasonable agreement with the simulations.

1. INTRODUCTION

Breast cancer is the most common non-skin related malignancy and the second leading cause of cancer death among women in the world [1]. Every year thousand of women die from the disease. Early detection will be look upon as the best hope for reducing the serious toll of this disease until research uncovers a way to prevent breast cancer or to cure all women. The early detection of cancer by screening reduces mortality from cancer.

Fifty years ago there was no establish method for detection of breast cancer at an early stage but advance in technology and legal mandates have thoroughly changed the situation. The use of X-ray imaging for detection of breast was first suggested, Mammography was not an acceptable technology until the 1960s. Over the past decade the investment in breast cancer research including early detection has increased significantly. New or improved technologies are rapidly emerging and providing hope of early detection.

The X-ray mammography is proved to be the most effective tool and play an important role in the early breast cancer detection. Despite showing high percentage of successful detection compare to other screening tools, X-ray mammography also has its limitations. The uncomfortable breast compression associated with this diagnose method prevents patients to undergo early stage examination and both false positive and negative rate have been reported which subsequently introduces to alternative screening. Another issue that raises the concern by using X-ray mammography is the radiation level from ionizing X-ray.

All these imperfection factors have motivated and encouraged to search for the better solution. One of the alternatives under investigation is microwave imaging. The applications of microwave technology were increasing in the field of biomedical engineering for diagnostic purposes. Based on the variations of the dielectric properties this technique promises non destructive evaluation of the biological tissue, which creates the images related to the electrical properties of the breast tissue. This will identify that the tissue with malignant tumor has higher water content than the normal breast tissue, hence they have higher dielectric properties than the normal tissue which have low water content, therefore strong scattering take place when the microwave hit the tissue with malignant tumor. Several applications of microwave imaging in the medical field were recorded and implemented for breast cancer detection [2].

Antenna is the key element of the microwave imaging system that radiates and receives signals to or from nearby scatterer objects. The application is similar to the GPR but operating at high frequencies. Various wideband (WB) and ultra wideband (UWB) antennas have been proposed for microwave imaging. Most of the antennas present in the literature show omni-directional radiation pattern with low gain [3–5]. These type of antenna are suitable for short range indoor and outdoor communication. However, for a microwave imaging system that is used to operate and detect the breast tumor might preferable to have a directive antenna with high gain [2, 6–8]. This paper presents a planar metal plat antenna in terms of circular disc mounted on the two vertical rectangular plates. The antenna is designed using Ansoft High Frequency Structure Software (HFSS). The results of two softwares including the measured one show good agreement.

The layout of the paper is as follow. Section 2 presents the geometry, the antenna model and the parametric study of various antenna dimensions; Section 3 discusses the simulated and the experimental results performed and Section 4 is summarized the final conclusions of this study.

2. ANTENNA DESIGN AND FABRICATION

Figure 1 shows the geometry of the antenna. The antenna is placed on the ground plane of dimension $L = W = 40$ mm and thickness 0.5 mm. The antenna is fed by vertical plate of maximum height 5 mm and width of 15 mm, in which it is connected to the feeding probe through the slot of 4 mm diameter in the ground plane. The antenna is modelled and optimised using high frequency structure simulator (HFSS).

The parametric simulation is carried out with HFSS in which the numerical analysis is based on the Finite Element Method (FEM). The parametric study helps to optimise the antenna performance before the antenna is manufactured and tested experimentally. Different antenna parameters are considered for optimisation the operated bandwidth subject to suitable radiated power gain. Some of these parameters are the total size of the ground, feed length, diameter of the circular disc

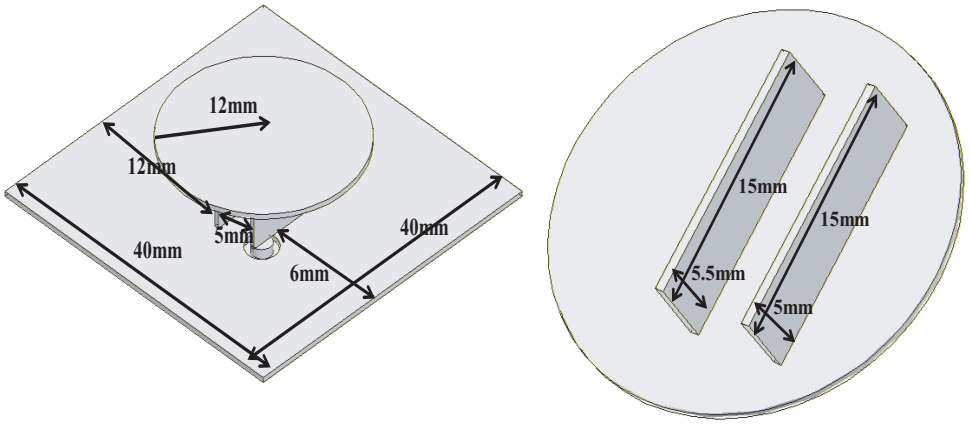

(a) Top View (b) Bottom view

Figure 1: Geometry of proposed antenna.

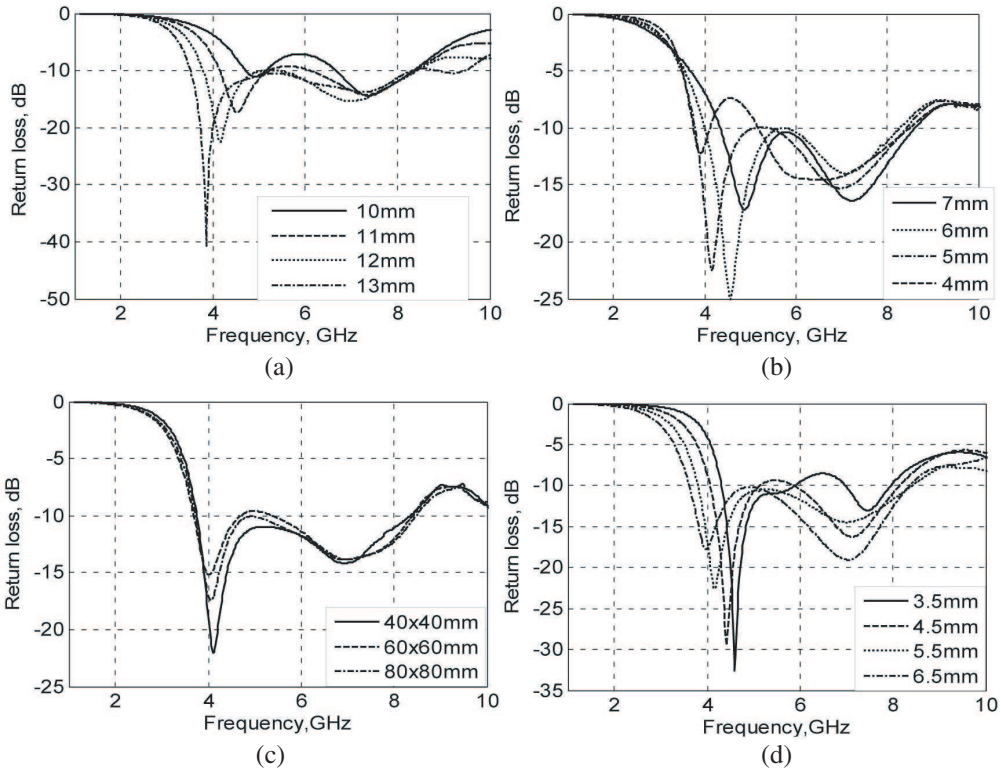

Figure 2: Parametric study. (a) Radius of the circular disc, (b) Gap between the vertical plates, (c) Ground size, (d) Height of the antenna from ground.

and gap between the vertical plates. To check the influence of these parameters on the impedance bandwidth, one parameter is varied and the remaining parameters remain fixed. Simulation result shows that the affect of changing these dimensions of antenna have appreciable change in the resonant frequency and return loss as shown in Figure 2.

3. RESULTS AND DISCUSSION

The antenna is also modelled using CST software package for comparison. Figure 3 shows the simulated return loss computed from HFSS and CST softwares, the result show good agreement. The gain of the antenna was found slightly more than 8 dBi at central frequency 6 GHz as shown in Figure 4. In addition, a directional radiation pattern was detected as preferred for imaging application as shown in Figure 5. A prototype of the antenna is fabricated from a copper sheet of thickness 0.5 mm for the practical realization. The HP 8510C network analyser was used for measurements. The experimental result shows reasonable agreement with the simulated one as illustrated in Figure 6. The slight differences in the return loss curves can be attributed to the fabrication inaccuracies.

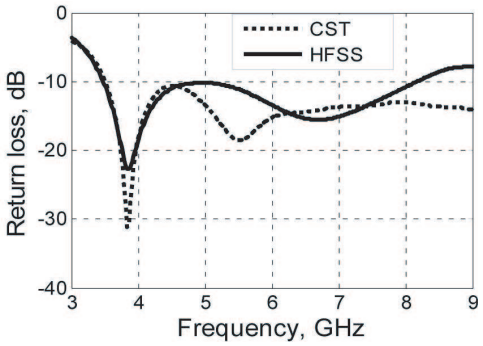

Figure 3: Simulated return loss.

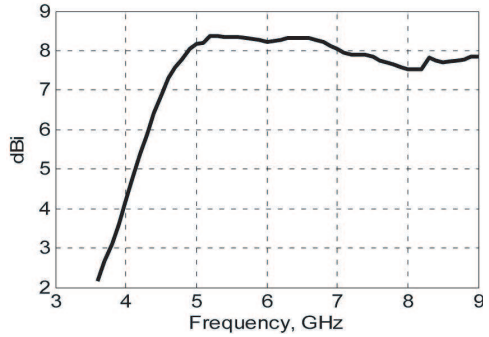

Figure 4: Gain of the antenna.

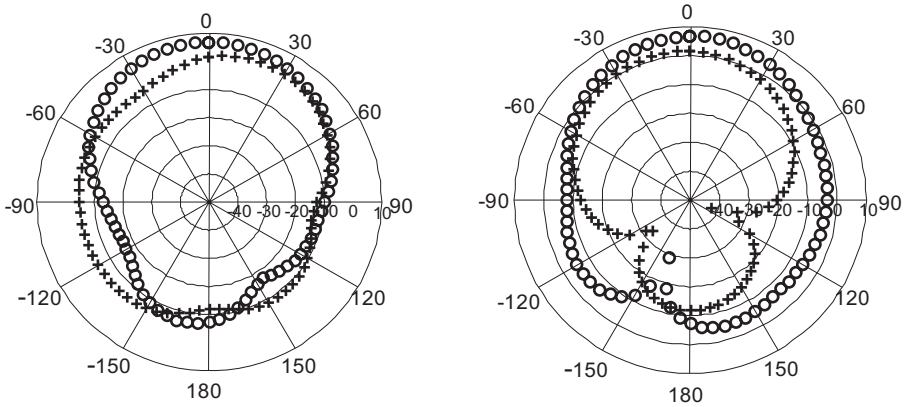

Figure 5: Radiation patterns for the proposed antenna at 6 GHz in dBi at z-x plane (left) and z-y plane (right) ('+++' E_θ and 'o o o' E_φ).

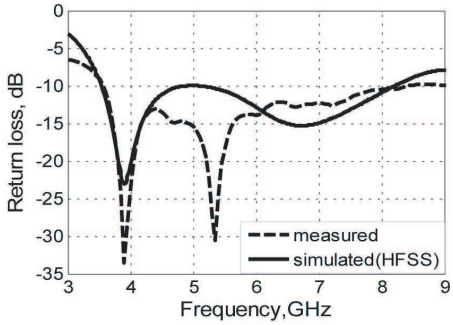

Figure 6: Input return loss of the proposed antenna.

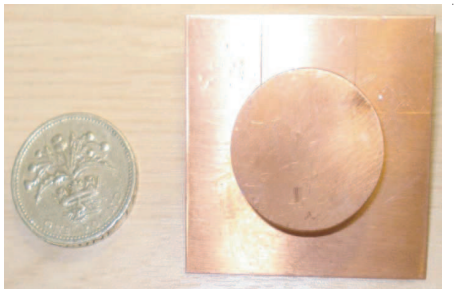

Figure 7: Photograph of the prototype antenna.

4. CONCLUSION

In this paper a new compact UWB antenna design has been presented. The affect of the various antenna parameters on the bandwidth and the resonance characteristic were discussed. The operating bandwidth of the antenna at a minimum workable return loss of 10 dB achieved was 3.5 GHz to 8 GHz. The measurement results show a good agreement with the simulated one. The antenna exhibited good directional radiation pattern with acceptable gain of 8 dBi over most of the UWB considered as preferred for imaging application.

ACKNOWLEDGMENT

The authors would like to thanks Mr. Dhirajlal Chavda for his help in the fabrication and measurement of the antenna.

REFERENCES

1. Blanks, R. G., S. M. Moss, C. E. McGahan, M. J. Quinn, and P. J. Babb, "Effect of NHS breast screening programme on mortality from breast cancer in England and Wales, 1990-8: Comparison of observed with predicted mortality," 665–669, 2000.
2. Yun, X., E. C. Fear, and R. H. Johnston, "Compact antenna for radar-based breast cancer detection," *IEEE Trans. Antenna Propagat.*, Vol. 53, 2374–2380, Aug. 2005.
3. Ngah, R., Y. Rahayu, T. Prakoso, and M. S. Othman, "Printed square UWB antenna," *International Conference on Electrical Engineering and Informatics*, 972–975, Institut Teknologi Bandung, Indonesia, 2007.
4. Yin, X.-C., C.-L. Ruan, C.-Y. Ding, and J.-H. Chu, "A planar U type monopole antenna for UWB applications," *Progress In Electromagnetics Research Letters*, Vol. 2, 1–10, 2008.
5. Shlager, K. L., G. S. SMith, and J. G. Maloney, "Optimization of bow-tie antennas for pulse radiation," *IEEE Trans. Antennas Propagat.*, Vol. 42, 975–982, July 1994.
6. Lestari, A. A., D. Yulian, L. A. B. Suksmono, E. Bharata, A. G. Yarovoy, and L. P. Ligthart, "Improved bow-tie antenna for pulse radiation and its implementation in a GPR survey," *2007 4th International Workshop on Advanced Ground Penetrating Radar*, 197–202, June 2007.
7. Shannon, C. J., "A dielectric filled slotline bowtie antenna for breast cancer detection," M. Sc. Thesis, The University of Calgary, Alberta, Canada, September 2004.
8. Hossain, I., S. Noghanian, and S. Pistorius, "A diamond shaped small planar ultra wide band (UWB) antenna for microwave imaging purpose," *2007 IEEE Antennas and Propagation Society International Symposium*, 5713–5716, 2007.

An 8-element Tapered Slot Antenna Array with a Bandwidth in Excess of 16.5:1

Yue Song, **Yong-Chang Jiao**, **Nai-Biao Wang**, **Tian-Ling Zhang**, **and Fu-Shun Zhang**
National Laboratory of Antennas and Microwave Technology, Xidian University
Xi'an, ShaanXi 710071, China

Abstract— A one-dimension single-polarized tapered slot antenna array fed by microstrip line is proposed. A modified transformer is used to obtain the impedance matching from microstrip line to slot line in the operating band. A 1 : 8 microstrip line power divider is designed to feed the 8-element array. The experimental results also show that the proposed antenna array achieves a ratio impedance bandwidth of 16.5 : 1 for VSWR ≤ 2 from 0.8 to 13.2 GHz, and exhibits good radiation patterns over the operating band that the cross polarized levels are better than 15 dB.

1. INTRODUCTION

The modern radar, communication and radio astronomy system require wideband antenna systems. The tapered slot antenna (TSA) is one good candidate to meet this demand, which is an endfire travelling antenna and features low profile, light weight, easy fabrication and compatibility with microwave integrated circuits (MIC).

This antenna proposed by Lewis [1] firstly in 1974 has been studied many years. An exponent tapered slot antenna called Vivaldi antenna is reported by Gibson in 1979, which fed by microstrip line can cover a bandwidth of 8–40 GHz [2]. An antipodal tapered slot antenna, allowing to directly be fed by a microstrip line to overcome the restriction of impedance matching, was introduced in [3]. Later, a balanced antipodal Vivaldi consisting three metallization layers was proposed which shows -15 dB lower cross-polarization across a 18 : 1 band [4]. Over these years, TSA arrays have also been studied in the literature. By using full-wave numerical methods, the characteristics of the array operating over multiple octaves of bandwidth have been analyzed based on the results of infinite array analyses [5]. Both single- and dual-polarized finite tapered-slot arrays have been built [6–11]. However, compared to microstrip line structure, the stripline-fed one in many TSA's designs is not easy to been installed, which may introduce some errors at the port.

In this paper, a one-dimension microstrip-fed tapered slot antenna array covering 0.8–13.2 GHz band for VSWR ≤ 2 is proposed. Modified microstrip-to-slotline transformers and a 1 : 8 microstrip line power divider composed of T-junctions are used to feed this array. In measurement, radiation patterns in the entire operation band are stable, the cross-polarized ratios are lower than -15 dB and the front-to-back ratio are better than 15 dB.

2. ANTENNA DESIGN

The performance of TSA is sensitive to the thickness and dielectric constant of the substrate. The acceptable range of the effective thickness $t_{eff} = t(\sqrt{\varepsilon_r} - 1)$ determined experimentally for the good operation of a TSA is confined in $0.005 \leq t_{eff}/\lambda_o \leq 0.03$ which was presented in [12].

A wideband T-junction power divider is needed to feed this tapered slot antenna array. According to the position of the array element's port and the operation bandwidth of the antenna array, a 3-section T-junction power divider, which provides signals with balanced amplitudes and phases from the output ports, is used to design the 8-way feed network. The total section number of impedance transformer from Rin to Rout is 14 according to the theory of the quarter-wave transformer [12]. The length of each section of impedance transformers is set approximately $\lambda g/4$, where λg the guided wavelength at center frequency. The widths are firstly optimized by Microwave office of AWR Design Environment^{TM} suite 2007. Optimal parameters are set as follow: $R_1 = 91.7\,\Omega$, $R_2 = 87.5\,\Omega$, $R_3 = 76.9\,\Omega$, $R_4 = 65.9\,\Omega$, $R_5 = 59.4\,\Omega$, $R_6 = 50.3\,\Omega$, $R_7 = 40.9\,\Omega$, $R_8 = 34.3\,\Omega$, $R_9 = 59.7\,\Omega$, $R_{10} = 53.0\,\Omega$, $R_{11} = 45.2\,\Omega$, $R_{12} = 36.8\,\Omega$, $R_{13} = 62.9\,\Omega$, $R_{14} = 56.8\,\Omega$. The simulated results of return loss S_{11} obtained by the help of IE3D which can consider the mutual coupling effect are also shown in Figure 2. It can be seen that the return loss is lower than -13.7 dB from 1.0 to 12.8 GHz.

The modified Marchand balun is designed to provide the transition between the antenna slotline and the microstrip line. The dimension of this balun is shown in the Figure 3. The microstrip stub contains three parts: a quarter of circle with the radius of 4.4 mm, a quarter of ellipse with a

length of long axis 8.8 mm and short axis 6.8 mm, respectively, and a polygon connected the radial part to microstrip line nearby the slotline. The radius microstrip stub of the slotline cavity and the total length of microstrip stub are both set about $\lambda g/4$. A 3-section impedance transformer is used to connect the power divider to Marchand balun according to the operating band. The optimal dimension and the simulated results of this balun are given in the Figure 3 and Figure 4, respectively. Figure 4 shows the simulated S-parameter results of a pair of back-to-back Marchand balun by IE3D. It demonstrates a broadband characteristics (175 % for VSWR < 2) achieved.

The geometry of microstrip-fed tapered slot antenna along the sides is shown in Figure 5. The antenna array with a dimension of $250 \times 230\,\text{mm}^2$ was fabricated on a 0.6 mm thick substrate with the dielectric constant $\varepsilon_r = 2.65$. In order to avoid sharp resonance related to the finite size of elements, the antenna is electrically connected to each other. The slot flare is tapered exponentially

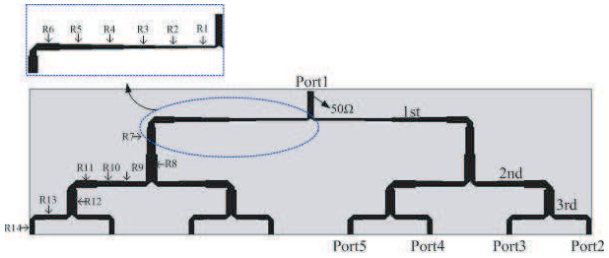

Figure 1: Geometry of 8-way T-junction power divider.

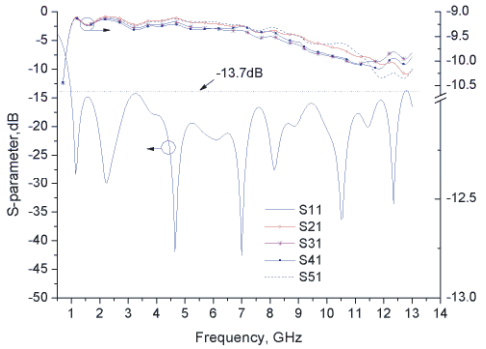

Figure 2: Simulated performance of 8-way T-junction power.

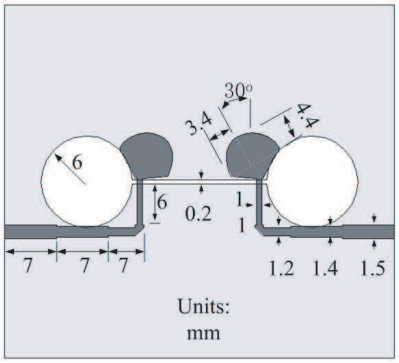

Figure 3: Geometry of Marchand transformer.

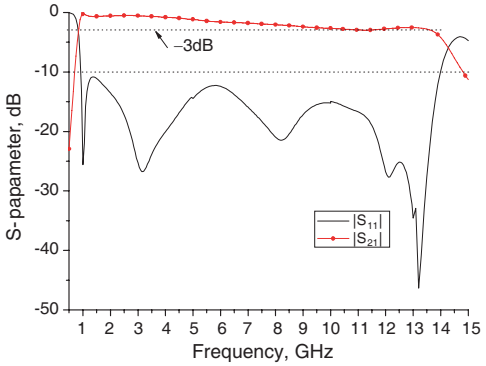

Figure 4: Simulated performance of a pair of Marchand transformer.

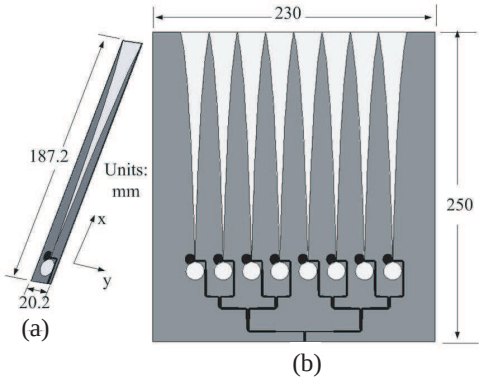

Figure 5: Schematic and photographs of 8-element microstrip TSA array.

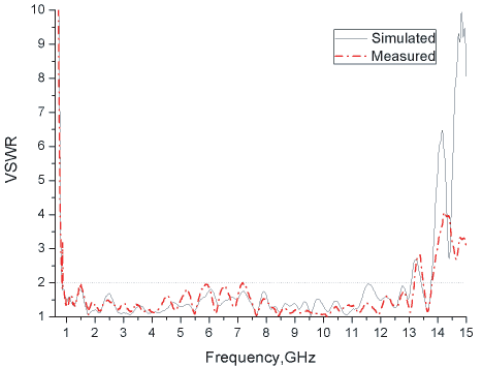

Figure 6: Simulated and measured VSWR results of the proposed TSA array.

which is determined by the following equation:

$$y = C_1 \cdot e^{R \cdot x} + C_2 \tag{1}$$

$$C_1 = \frac{y_1 - y_2}{e^{R \cdot x_1} - e^{R \cdot x_2}} \tag{2}$$

$$C_2 = \frac{y_1 e^{R \cdot x_2} - y_2 e^{R \cdot x_1}}{e^{R \cdot x_2} - e^{R \cdot x_1}} \tag{3}$$

where (x_1, y_1), (x_2, y_2) are the end points of the flare, $x \in [0\,\text{mm}, 160\,\text{mm}]$, $y \in [0.1\,\text{mm}, 10.1\,\text{mm}]$ and R are parameters to be determined by the desire patterns. The length of the tapered flare is set about $\lambda g/2$. For an array with uniform grid, the element spacing d should be satisfied by the follow Equation (4) to ensure no grating lobes [13]:

$$d \leq \frac{\lambda}{1 + |\cos \phi_o|} \tag{4}$$

where d is the element spacing, λ is the wavelength at the highest operating frequency, and ϕ_o is the main beam angle. For this 8-element array, only the broadside needs to be considered. At $\phi_o = -90$ degree, the equation can reduce the easier condition d$\leq \lambda$.

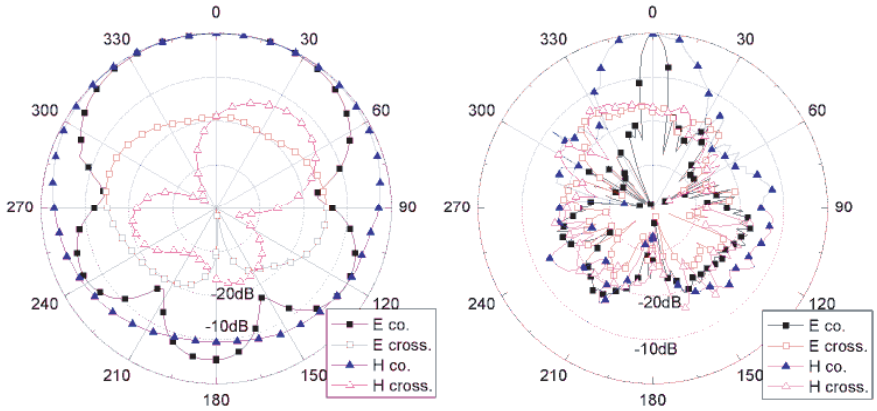

Figure 7: Measured radiation patterns of the proposed TSA array at: (a) 1 GHz, (b) 13 GHz.

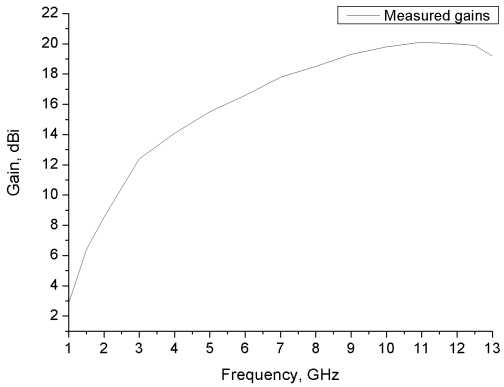

Figure 8: Measured gains of the proposed TSA array.

3. RESULTS AND DISCUSSION

Figure 7 shows the simulated and measured VSWR of the proposed antenna obtained using CST and WILTRON37269A vector network analyzer. It can be seen that a VSWR ≤ 2 frequency range of the proposed wideband TSA with an exponential flare slot from 0.8 to 13.2 GHz have been

achieved which is about a ratio bandwidth of 16.5 : 1. The measured radiation patterns at two sample frequencies (1 and 13 GHz) are shown in Figure 8. It can be observed that good direction of the proposed antenna in the radiation patterns by the use of the logarithmic flare slotline, and cross polarization in the operating band are less than −17 dB. The measured gain values of the proposed antenna array have been obtained between 0.8 and 13 GHz as shown in Figure 9. It can be seen that the proposed antenna array's gains are increasing from 2.9 to 20.1 dBi between 0.8 and 11 GHz, and decline to 18.8 dBi in the frequency range from 11 GHZ to 13 GHz. According to the electric length of the TSA array at the lower band is about $\lambda g/2$, the gains of the proposed TSA array in the lower band are comparative smaller than those in the higher band.

4. CONCLUSION

An 8-element tapered slot antenna array with a bandwidth in excess of 16.5 : 1 is proposed. The experimental results also show that this tapered slot antenna array is good candidate for wideband applications.

ACKNOWLEDGMENT

This work is supported by the RIM Wireless Research Scholarship Program.

REFERENCES

1. Lewis, L. R., M. Fassett, and J. Hunt, "A broadband stripline array element," *IEEE Antennas and Propagation Society International Symposium*, Vol. 12, 335–337, Atlanta, GA, June 1974.
2. Gibson, P. J., "The vivaldi aerial," *9th European Microwave Conf.*, 101–105, Brighton, England, 1979.
3. Gazit, E., "Improved design of the vivaldi antenna," *IEE Proc.*, Part H, Vol. 135, No. 2, 89–92, 1988.
4. Langley, J. D. S., P. S. Hall, and P. Newham, "Balanced antipodal vivaldi antenna for wide bandwidth phased arrays," *IEE Proc. Antennas Propag.*, Vol. 143, No. 2, 97–102, April 1996.
5. Shin, J. and D. H. Schaubert, "A parameter study of stripline-fed vivaldi notch antenna arrays," *IEEE Trans. Antennas Propagat.*, Vol. 47, 879–886, 1999.
6. Holter, H., T. H. Chio, and D. H. Schaubert, "Experimental results of 144-element dual-polarized endfire tapered-slot phased arrays," *IEEE Trans. Antennas Propagat.*, Vol. 48, No. 11, 1707–1718, 2000.
7. Hemmi, C., T. Dover, F. German, and A. Vespa, "Multifunction wide-band array design," *IEEE Trans. Antennas Propagat.*, Vol. 47, 425–431, March 1999.
8. Povinelli, M. J., "Wideband dual polarized apertures utilizing closely spaced printed circuit flared slot antenna elements for active transmit and receive phased array demonstration," *Proc. Antenna Applicat. Symp.*, Allerton Park, IL, 1989.
9. Povinelli, M. J. and J. D. Angelo, "Design, performance characterization and hybrid finite element boundary element analysis of a linearly polarized printed circuit tapered notch array," *Proc. Antenna Applicat. Symp.*, Allerton Park, IL, 1989.
10. Povinelli, M. J., "Experimental design and performance of endfire and conformal flared slot (notch) antennas and application to phased arrays: An overview of development," *Proc. Antenna Applicat. Symp.*, Allerton Park, IL, 1988.
11. Yang, L., N. Ito, C. W. Domier, N. C. Luhmann, and A. Mase, "18–40-GHz beam-shaping/steering phased antenna array system using fermi antenna," *IEEE Trans. Microw. Theory Tech.*, Vol. 56, No. 4, 767–773, April 2008.
12. Young, L., "Stepped-impedance transformers and filter prototypes," *IEEE Trans. Microw. Theory Tech.*, 339–359, Sep. 1962.
13. Orfanidis, S. J., *Electromagnetic Waves and Antennas*, Rutgers University, February 2008.

Short Range Propagation Characteristics of UHF Frequency Band for Moving Vehicles RFID

Deock-Ho Ha[1] and Yeon-Wook Choe[2]

[1]Department of Telecommunication Engineering, Pukyong National University, Busan, Korea
[2]Department of Control and Measurement Engineering, Pukyong National University, Busan, Korea

Abstract— In this paper, we describe the short range propagation characteristic of UHF RFID frequency band used for moving vehicles. To analyze the propagation characteristic of UHF RFID radio signals in short range radio propagation environment, we transmitted 910 MHz and 2.45 GHz continuous wave carrier signals using by several polarized antenna combinations. From the measurement analysis, it can be clearly seen that the UHF RFID signal can be encountered to multipath interference rays due to ground plane and the reader/antenna equipment booth. In addition, it was found that the multipath interference signals can be effectively removed by using a circularly polarized antenna. Especially, in case of NLOS environment, it was also found that circular polarization diversity method using the two branches of vertical and horizontal receiving antenna shows better fading reduction effect.

1. INTRODUCTION

In this paper, we analyzed the propagation characteristic for the UHF RFID frequency band. With the aim of reducing the multipath fading in short range wireless environments, we used a multi-polarized antenna system. To obtain maximum power transfer between two antennas the combinational polarized waves can be used. Assuming that the reception model of circular polarization diversity, we calculated a correlation coefficient (ρ) considering XPD (cross polarization discriminator). In this model, a transmitting antenna emits circularly polarized signal while the receiving end uses two-branch polarized diversity antenna. It is also assumed that the transmitter and receiver unit are located in the wireless environment, and they are sufficiently far away to produce a Rayleigh distributed signal at the receiver.

2. DIVERSITY RECEPTION MODEL

To analyze the theoretical correlation coefficient for the received signals between the two branches, we used a spherical coordinate model for the circularly polarized waves. Fig. 1 shows the model of circularly polarized diversity. In this model, a transmitting antenna emits circularly polarized signal while the receiving end uses two-branch polarized diversity antenna.

Let the receiving antenna system be positioned at the origin, and the angular location of the transmitter is given by ϕ and θ from the origin, both of which are oriented at an angle α from the positive z-axis. It is also assumed that the transmitting and receiving ends are located in a short range radio wave environment and they are sufficiently far away to produce a Rayleigh-distributed signal at the receiver. Generally, the circular polarization is expressed as follows;

$$E_{RC} = E_H + jE_V, \quad E_{LC} = E_H - jE_V \tag{1}$$

Here, E_{RC} is the electric field of right-handed circular polarization and E_{LC} is the electric field of left-handed circular polarization. Also, the signal arriving at the receiving end consists of vertical and horizontal polarized components (E_V, E_H) and the two polarized components are expressed as follows;

$$E_H = r_1 \cos(\omega t + \phi_1), \quad E_V = r_2 \cos(\omega t + \phi_2) \tag{2}$$

Here, it is assumed that r_1 and r_2 are Rayleigh-distributed and the phase ϕ_1 and ϕ_2 are random, uniformly distributed, and uncorrelated. The vector form of Equation (1) can be represented as follows;

$$\begin{aligned} \tilde{E}_{RC} &= e_R \cos(\omega t + \phi_R)\, \tilde{u}_1 + e_R \cos\left(\omega t + \phi_R + \frac{\pi}{2}\right) \tilde{u}_2, \\ \tilde{E}_{LC} &= e_L \cos(\omega t + \phi_L)\, \tilde{u}_1 + e_L \cos\left(\omega t + \phi_L + \frac{\pi}{2}\right) \tilde{u}_2 \end{aligned} \tag{3}$$

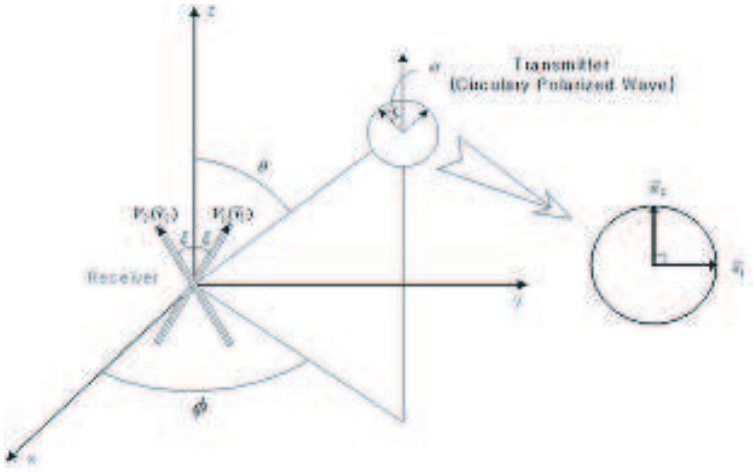

Figure 1: A reception model of circular polarization diversity.

Here, the unit vector $\tilde{u}_1$ and $\tilde{u}_2$ are perpendicular to the direction of propagation. The unit vector $\tilde{u}_1$ lies in the horizontal plane and $\tilde{u}_2$ is non-horizontal and tilted from the vertical axis by the elevation angle, $\alpha(\alpha = \frac{\pi}{2} - \theta)$ And e_R and e_L are Rayleigh-distributed random variables of right-handed and left-handed circularly polarized signals, respectively. The unit vector $\tilde{u}_1$ and $\tilde{u}_2$ in Fig. 1 are represented as follows;

$$\tilde{u}_1 = -\sin\phi\,\tilde{x} + \cos\phi\,y, \quad \tilde{u}_2 = -\sin\alpha\cos\phi\,\tilde{x} - \sin\alpha\sin\phi\,\tilde{y} + \cos\alpha\,\tilde{z} \tag{4}$$

Also, from the Fig. 1, when the expression of each unit vector of two-branch received diversity branches is the same as Equation (5). In this case, the diversity branches, V_1 and V_2 are tilted from the z-axis by the angle, ξ. The unit vector $\tilde{v}_1$ and $\tilde{v}_2$ are represented as follows;

$$\tilde{v}_1 = \sin\xi\,\tilde{y} + \cos\xi\,\tilde{z}, \quad \tilde{v}_2 = -\sin\xi\,\tilde{y} + \cos\xi\,\tilde{z} \tag{5}$$

Using the Equations (1)–(5), the received electric field to each branch is represented as Equation (6). The equation (6) indicates the received signal by antenna V_1 (branch 1) and antenna V_2 (branch 2).

$$V_1 = E_{RC}\tilde{u}_1 \cdot \tilde{v}_1 + E_{LC}\tilde{u}_2 \cdot \tilde{v}_1, \quad V_2 = E_{RC}\tilde{u}_1 \cdot \tilde{v}_2 + E_{LC}\tilde{u}_2 \cdot \tilde{v}_2 \tag{6}$$

Therefore, the amplitudes (A_1 and A_2) of the received signals by antenna V_1 and V_2 can be described as following Equation (7):

$$\begin{aligned} A_1 &= \left\{\left(a^2+b^2\right)\left(e_R^2+e_L^2\right) + 2e_Re_L\left(\left(a^2-b^2\right)\cos\left(\phi_R-\phi_L\right) + 2ab\sin\left(\phi_R-\phi_L\right)\right)\right\}^{1/2} \\ A_2 &= \left\{\left(a^2+c^2\right)\left(e_R^2+e_L^2\right) + 2e_Re_L\left(\left(a^2-c^2\right)\cos\left(\phi_R-\phi_L\right) + 2ab\sin\left(\phi_R-\phi_L\right)\right)\right\}^{1/2} \end{aligned} \tag{7}$$

$$\text{where, } a = \sin\xi\cos\phi, \quad b = \cos\alpha\cos\xi - \sin\alpha\sin\phi\sin\xi, \quad c = \cos\alpha\cos\xi + \sin\alpha\sin\phi\sin\xi. \tag{8}$$

Meanwhile, the general equation of correlation coefficient (ρ) is represented as Equation (9).

$$\rho = \frac{\left\langle A_1^2 \cdot A_2^2\right\rangle - \left\langle A_1^2\right\rangle\left\langle A_2^2\right\rangle}{\left[\left(\left\langle A_1^4\right\rangle - \left\langle A_1^2\right\rangle^2\right)\left(\left\langle A_2^4\right\rangle - \left\langle A_2^2\right\rangle^2\right)\right]^{1/2}} \tag{9}$$

Therefore, by substituting Equations (7) and (8) into Equation (9) the correlation coefficient is given by Equation (10).

$$\rho = \frac{\left(a^2+b^2\right)\left(a^2+c^2\right)\left(1+\Gamma^2\right) + 2\Gamma\left(a^2-b^2\right)\left(a^2-c^2\right) - 8\Gamma a^2bc}{\left[\left(a^2+b^2\right)^2\left(a^2+c^2\right)^2\left(1+\Gamma\right)^4\right]^{1/2}} \tag{10}$$

$$\text{where, } XPD = \frac{\left\langle e_R^2\right\rangle}{\left\langle e_L^2\right\rangle} \cong \Gamma$$

Assuming the reception model of circular polarization diversity, we calculated a correlation coefficient (ρ) considering XPD.

3. MEASUREMENT RESULTS

From the measured data analysis, it was found that the C-C (circular-circular antenna) combination shows better fading reduction result than the cases of V-V (vertical-vertical antenna) and H-H (horizontal-horizontal antenna) combination in LOS environment, respectively. On the other hand, in the case of NLOS environment, it was also found that the polarization diversity effect using the two branches of C-V (circular-vertical) and C-H (circular-horizontal) branches shows better fading reduction effect than the cases of C-C, C-X (right handed polarized circular-left handed polarized circular), V-V and H-H. Fig. 2 shows a correlation coefficient in 3-D diagram when the linearly polarized antenna and circularly polarized antenna were used at the transmitting end in NLOS environment, respectively. As shown in Fig. 2, the correlation coefficient value of circular polarization diversity (CV-CH branches) was much lower than that of conventional linear polarization diversity (VV-VH branches) because in this case where the circular polarized wave was applied. Furthermore, as shown in Fig. 3, in the case where the circular polarized wave was applied (CX), the XPD value also was much lower than that of the linear polarized wave (VH). So it can be predicted that circular polarization diversity is a more effective diversity technique to reduce the multi-path fading in NLOS short range radio propagation environments.

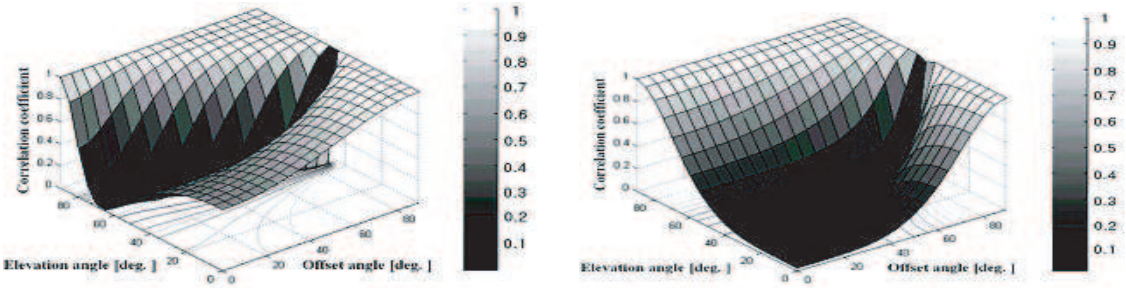

(a) VV-VH diversity branches (b) CV-CH diversity branches

Figure 2: Correlation coefficients of the two models.

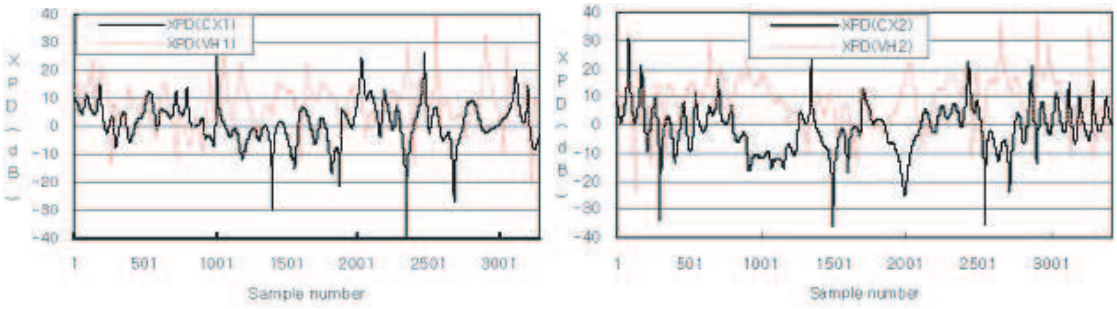

(a) XPD for path 1 (b) XPD for path 2

Figure 3: Comparisons of XPD for the CX and VH branches in each NLOS radio paths.

4. CONCLUSION

We found that the correlation coefficient value of the proposed circular polarization diversity system show lower value than that of conventional linear polarization diversity In the case where the circular polarized wave was applied, the XPD value also was much lower than that of the linear polarized wave. So it can be predicted that circular polarization diversity is a more effective diversity technique to reduce the multipath fading in NLOS short range radio propagation environments. To estimate proposed system performance, we also measured the propagation characteristic with a vehicle in motion using the implemented circular and conventional polarization diversity systems in indoor NLOS environments. From the measurement results, we was also found that the proposed circular polarization diversity scheme had better diversity gain than that of the conventional linear polarization diversity in short range radio propagation environment.

ACKNOWLEDGMENT

Following are results of a study on the "Human Resource Development Center for Economic Region Leading Industry" Project, supported by the Ministry of Education, Science & Technology (MEST) and the National Research Foundation of Korea (NRF).

REFERENCES

1. Ha, D. H., et al., "A study on optimum condition of polarization diversity in indoor mobile radio propagation environments," *Proceedings of 3rd Asia-Pacific Conference on Communications*, Sydney, Australia, Dec. 7–10, 1997.
2. Lee, J.-H., "A study on the fabrication and performance estimation of a circularly polarized diversity system for multipath fading reduction in mobile wireless environments," Ph.D. Dissertation, Pukyong Natonal University, Busan, Korea, Aug. 2003.
3. Lee, W. and Y. Yu, "Polarization diversity system for mobile radio," *IEEE Trans. on Communications*, Vol. 20, No. 5, 912–923, Oct. 1972.
4. Rappaport, T. S. and D. A. Hawbaker, "Effects of circular and linear polarized antenna on wideband propagation parameters in indoor radio channels," *Proceedings of the Globecom'91*, 1287–1291, 1991.

A 1.2 V Low-power Receiver for Short Range Applications

Wei-Hsiang Hung, **Kuan-Ting Lin**, **and Shey-Shi Lu**
Graduate Institute of Electronics Engineering, National Taiwan University, Taiwan, R.O.C.

Abstract— In this paper, a 1.2-V 2.4 GHz low power receiver front-end for wireless sensor node is demonstrated in standard 0.18 µm CMOS technology, which consists of an LNA, an active balun, and a sub-harmonic passive mixer. The measurement results of the proposed circuit show a low power consumption of 8.7 mw, 8 dB noise figure, 18 dB conversion gain and a third-order intercept point (IIP3) of −15 dBm. In this design, a common-source (CS) staged LNA is adopted to achieve high gain as well as low noise figure. A balun is connected successively to provide a single-to-differential transformation which enhances the immunity to the noise from the power supply. A sub-harmonic mixer is used to minimize the dc-offset issue, which also results in a less required LO power and the DC power consumed by the LO buffers in the mean time. The active part of this circuit only occupies 0.71 mm × 0.37 mm of chip area. The measurement results exhibit that this sub-harmonic receiver front-end is promising for short range wireless sensor network application.

1. INTRODUCTION

Recently, the research of wireless sensor network for heart monitoring, biological detection or pollution sensing has gained a lot of attention. A wireless sensor node consists of many distributed system blocks that need to operate continuously over a long time with only a single battery [1]. Therefore, the need of a highly integrated, low-cost and low-power single chip transceiver is indispensable. In this context, direct conversion transceiver architecture has the advantages of high level of integration with reasonable performance and low-cost [2]. Nevertheless, design tradeoffs between power, dc offset, linearity and noise figure (NF) still need to be considered seriously.

Many low power receivers have been presented recently [3, 4], but still face the dc-offset and large LO power which consumed by the LO buffers. To conquer these disadvantages, a 1.2-V 2.4 GHz low power receiver front-end system for short range communication is demonstrated. The system consists of a common source (CS) LNA, an active balun and a sub-harmonic passive mixer, leading to not only low power consumption but also solid performance. The CS LNA is chosen for achieving high gain and low noise performance simultaneously under properly designed. The following active balun not only provides a single-to-differential transformation but also keeps desired signals immune from noise. Moreover, subharmonic conversion is selected for two main considerations. First, it minimizes the effect of self-mixing dc-offset generated from the local oscillator. The LO signals fed-back to LNA will be amplified if they fall within the LNA passband [5]. Consequently, a large dc offset is thus generated. Secondly, the LO buffers consume less power due to the fact that LO frequency is reduced to half of the targeted frequency. In other words, the receiver saves both dynamic and biasing power. With these design techniques, a 1.2-V 2.4 GHz low power receiver is implemented by a standard 0.18-µm CMOS technology. It achieves high power gain, low noise performance under a small area and reasonable power consumption.

2. RECEIVER ARCHITECTURE AND CIRCUIT TOPOLOGY

2.1. Receiver Architecture

Figure 1 shows the block diagram of the proposed 1.2 V low power receiver consisting of a CS-LNA, an active balun (single to differential conversion), and a passive subharmonic mixer. While the desired signal is first amplified by the CS-LNA, the following active balun performs a single to differential conversion which can provide noise immunity. After two stages of amplification, the desired signal enters the double balanced passive SHMs, these differential signals are multiplied with the subharmonic LOs to accomplish signal down conversion. This work provides a low voltage operation and a technique which offers extra LO-to-RF isolation and LO rejection (LOR).

2.2. CS-LNA and Active Balun

Figure 2 shows the topologies of both CS-LNA and Active Balun. In the first stage, the CS-LNA adopts the cascade configuration which offers good isolation and frequency response [3]. Besides, the bond-wire design is chosen to minimize chip area. The input matching network can be considered as Equation (1). With proper device selection [4] for input transistor and matching elements, input

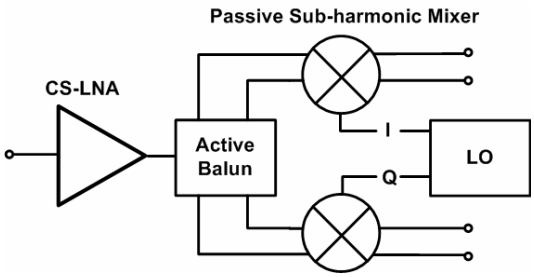

Figure 1: The block diagram of the low power receiver.

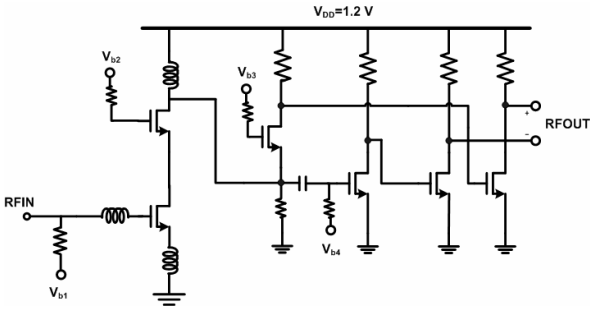

Figure 2: LNA and active balun.

impedance matching, low noise response, and high gain can achieve simultaneously under 1.2 V supply voltage.

$$Z_{in} = R_g + R_{\lg} + R_{lf} + R_f + \frac{g_m L_S}{C_{gs}} + \frac{1 + g_m R_f}{j\omega C_{gs}} + j\omega(L_g + L_S) \tag{1}$$

The second stage is an active balun which consists of a common gate and a common source stages. Two benefits can be obtained here; first, the maximum power transfer can be acquired because the input matching can be provided by the CG stage. Moreover, the CS stage realizes an anti-phase output signal. Unfortunately, the output gain of two stages is not equal due to the unbalanced trans-conductance and loading resistor. In order to solve this problem, additional CS buffer is carefully design to compensate the gain error.

2.3. Subharmonic Mixer

Figure 3 shows how sub-harmonic mixing is derived from conventional mixing. As we known, Gilbert-cell mixer has lots of advantages over both single balance mixer and un-balanced mixer due to its immunity of LO-IF feedthrough and RF-IF feedthrough. Based on these advantages, we transformed the conventional Gilbert cell mixer into a SHM by altering the configuration of the switching quads [5]. Each single-transistor switches in Gilbert cell is replaced by a dual-transistor switch where the two transistors are connected in parallel. As illustration in Fig. 3, if we apply two mutually out-of phase signals to the dual-transistor switch is equivalent to that of turning on a single-transistor switch with twice of the frequency. Thus, with these switches, we can perform sub-harmonic mixing.Under communication system consideration, the direct down-conversion in the sub-harmonic mixer can be achieved with LO signals operating at 1/2 RF frequency. This can alleviate DC-offset problem due to LO self-mixing in direct-conversion receiver. Moreover, the linearity of the system can be increased by using passive mixer. After careful consideration, the passive subharmonic mixer is chosen for this design.

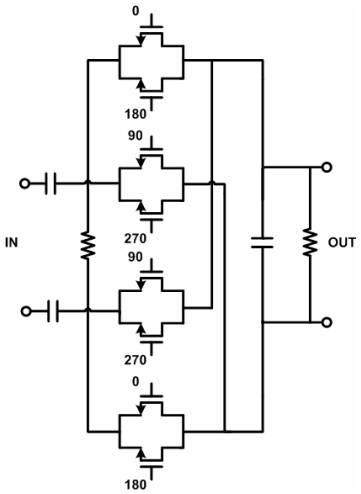

Figure 3: Sub-harmonic passive mixer.

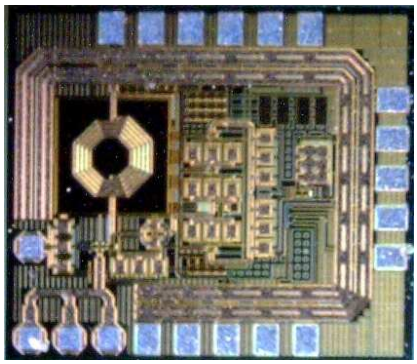

Figure 4: Die photograph.

3. MEASUREMENT RESULTS

The proposed low power receiver was implemented in standard 0.18 µm CMOS technology. The die photograph is shown in Fig. 4. The active area only occupies $0.71\,\mathrm{mm}^2 \times 0.37\,\mathrm{mm}^2$. The circuit was tested on board for RF characterization. The receiver draws 7.3 mA from a 1.2-V supply.

Figre 5 shows both simulated and measured results of the input return loss of the broadband LNA. Fig. 6 shows that the conversion gain is over 18 dB while LO is sweeping from 100 K to 10 MHz. The noise performance is both simulated and measured. The receiver has excellent low noise performance of 8 dB at 2.4 GHz. In Fig. 7, to characterize the nonlinear behavior, two-tone signals with equal power levels at 2.41 and 2.411 GHz were applied to the proposed low power receiver. The measured results indicate that this receiver has an IIP3 of −15 dBm. Measurement results indicate that this subharmonic receiver front-end is suitable for short range applications.

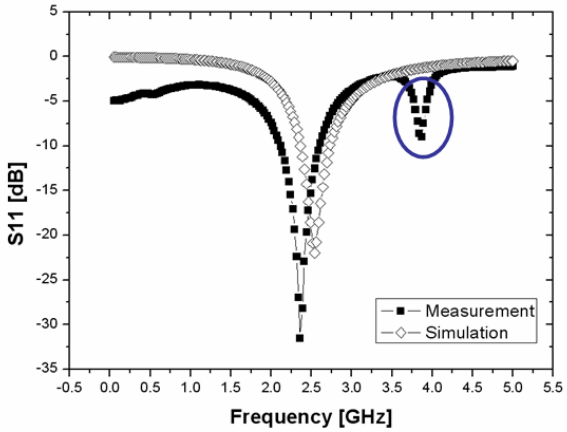

Figure 5: Input return loss.

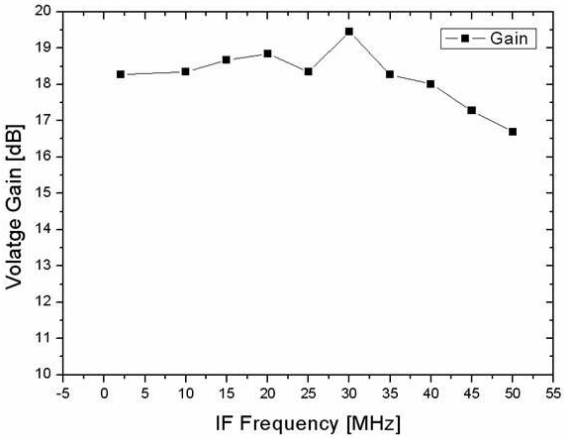

Figure 6: Conversion gain.

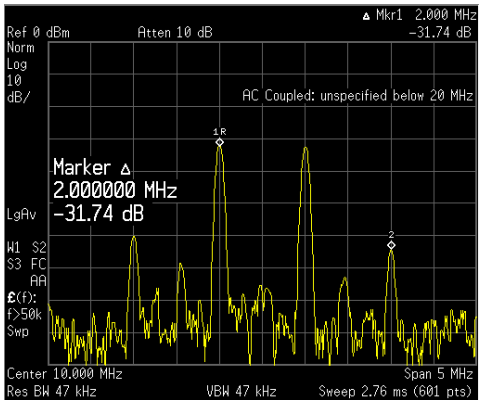

Figure 7: Spectrum of two-tone test.

4. CONCLUSIONS

A 1.2 V 2.4 GHz receiver front-end has been implemented in standard 0.18 µm CMOS technology. The receiver which composed of traditional CS-LNA, active balun and passive subharmonic mixer provides a method for low supply voltage and DC-offset-free. The receiver not only achieves 50 ohm matching at 2.4 GHz, but also achieves 18 dB of conversion gain, 8-dB of noise figure and −15 dBm of IIP3. Both simulation and measurement results exhibit that this subhamonic receiver front-end is promising for short range wireless sensor network application.

REFERENCES

1. Teo, T. H. and W. G. Yeoh, "Low-power short-range radio CMOS subharmonic RF front-end using CG-CS LNA," *IEEE Trans. Circuits Syst. II, Exp. Brifes*, Vol. 55, No. 7, 658–662, Jul. 2008.
2. Namgoong, W. and T. H. Meng, "Direct-conversion RF receiver design," *IEEE Trans. Commun.*, Vol. 49, No. 3, 518–529, Mar. 2001.
3. Wong, A. C. W., G. Kathiresan, C. K. T. Chan, O. Eljamaly, O. Omeni, D. McDonagh, A. J. Burdett, and C. Toumazou, "A 1 V wireless transceiver for an ultra-low-power SoC for biotelemetry applications," *IEEE J. Solid-State Circuits*, Vol. 43, No. 7, 1511–1521, Jul. 2008.
4. Song, T., H. S. Oh, E. Yoon, and S. Hong, "A low-power 2.4-GHz current-reused receiver front-end and frequency source for wireless sensor network," *IEEE J. Solid-State Circuits*, Vol. 42, No. 5, 1012–1022, May 2007.
5. Chen, H. C., T. Wang, S. S. Lu, and G. W. Huang, "A monolithic 5.9-GHz CMOS I/Q direct-down converter utilizing a quadrature coupler and transformer-coupled subharmonic mixers," *IEEE Microw. Wireless Compon. Lett.*, Vol. 16, No. 4, 197–199, Apr. 2006.

Design of a Novel Three-way Tri-band Power Divider

Xin Huai Wang, **Yan Fu Bai**, **Dong Zhou Chen**, **Xiao Wei Shi**, **and Xin Li**
National Key Laboratory of Science and Technology on Antennas and Microwaves
Xidian University, Xi'an 710071, China

Abstract— A three-way triple-band equal-split power divider is analyzed and designed in this paper. The topology of the circuit is six sections of three transmission lines and planar isolation resistors, which provides high isolation and good amplitude balance simultaneously at three arbitrary frequencies. The structure of the power divider and the formulas used to determine design parameters are presented. To demonstrate the design methodology, a 900/1800/2400 MHz power divider is realized. Good performances of the proposed power divider at three frequencies are obtained.

1. INTRODUCTION

Power dividers are fundamental components of many microwave circuits and subsystems. Conventional power dividers have been designed for two or even-number of outputs [1–3]. However, when it comes to three or an odd-numbered output, 3-D resistors are required and are difficult to realize in a planar form in monolithic microwave integrated circuits (MMIC) or hybrid microwave integrated circuits (HMIC). Therefore, many new three-way power dividers have been proposed [4]. These three-way power dividers operate only at one design frequency or dual-band frequencies. However, multi-standard operation of wireless transceivers is of increasing importance in practical applications and so components that work at three or more frequencies are of interest. Therefore, these are not suitable for some multi-band operations. In 2005, a three-section transmission-line transformer was introduced by M. Chongcheawchamnan [5], which can operate at any three arbitrary frequencies f_1, f_2, and f_3. A two-way tri-band Wilkinson power divider with this transformer section has been reported in [6]. This paper presents the technique to design a three-way tri-band power divider with 50 Ω impedance terminations based on a three-section transmission-line impedance transformer. The proposed power divider operates at three arbitrary frequencies of interest f_1, f_2, and f_3. The formulas, which used to determine design parameters of the three-way tri-band power divider, are presented. The technique is validated by experimental results on a 900/1800/2400 MHz power divider, which can be applied in the present global system for mobile communication (GSM), the personal communication system (PCS), and wireless local-area network (WLAN).

2. THEROY AND DESIGN EQUATIONS

Figure 1 shows the configuration of the conventional three-way power divider [1]. Assuming all input and output ports impedance to be 50 Ω, the characteristic impedances Z_{11} and Z_{22} are selected as $Z_{11} = 65.8\,\Omega$ and $Z_{22} = 114\,\Omega$, the length of each section is quarter-wavelength, and the resistances R_1 and R_2 of the planar isolation resistors are selected as $R_1 = 200\,\Omega$ and $R_2 = 64.95\,\Omega$, respectively. Appling M. Chongcheawchamnan's theory in the design of a three-way tri-band power divider, each quarter-wavelength section of the conventional three-way power divider is substituted by three sections of transmission-line with the characteristic impedance of Z_1, Z_2, and Z_3 and the electrical length θ_1, θ_2, and θ_3 at frequency f_1 with the condition that $f_3 > f_2 > f_1$, respectively. To

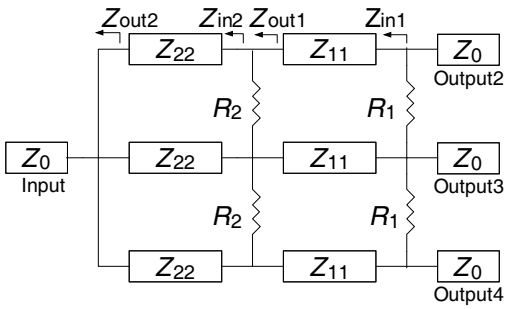

Figure 1: Circuit of conventional three-way power divider.

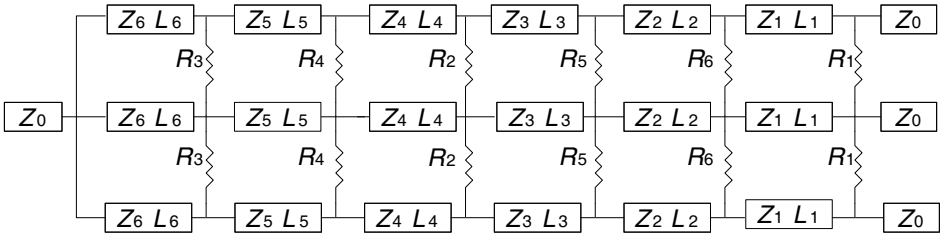

Figure 2: Circuit of three-way tri-band power divider.

improve the isolation of the power divider, except for R_1 and R_2, the more isolation resistances R_3, R_4, R_5 and R_6 are added. A schematic diagram of the proposed three-way tri-band power divider, which operates at three arbitrary frequencies, is shown in Fig. 2. When M. Chongcheawchamnan's theory is applied, it is necessary to determine the input and output impedances of each section of the conventional three-way power divider. Because each section is a quarter-wavelength transformer in this power divider, assuming the characteristic impedance of each section is Z_{kk}, we can determine $Z_{\text{in}k}$ and $Z_{\text{out}k}$ using:

$$Z_{\text{out}k} = \frac{(Z_{kk})^2}{Z_{\text{in}k}} \tag{1}$$

where k is either 1 or 2. Let Z_0 be 50 Ω. We want $Z_{\text{out2}} = 3Z_0$, $Z_{\text{in1}} = Z_0$, $Z_{\text{in2}} = (Z_{22})^2/3Z_0$, $Z_{\text{out1}} = (Z_{11})^2/Z_0$. We have known $Z_{11} = 65.8\,\Omega$ and $Z_{22} = 114\,\Omega$, then Z_{out1} and Z_{in2} can be obtained as $Z_{\text{out1}} = 86.59\,\Omega$ and $Z_{\text{in2}} = 86.64\,\Omega$. With Z_{in2} and Z_{out1} known, the parameters of the three-way tri-band power divider can be determined by M. Chongcheawchamnan's theory (here, we assume $f_3 > f_2 > f_1$):

$$k = Z_{\text{out}}/Z_{\text{in}} \tag{2}$$

$$u_1 = f_2/f_1, \quad u_2 = f_3/f_1, \quad (1 < u_1 < u_2 < 3) \tag{3}$$

$$a = \sqrt{k}\left(\frac{Z_{\text{in}}}{Z_1} - \frac{Z_1}{Z_{\text{in}}}\right), \quad b = \frac{Z_{\text{in}}^2}{Z_1^2}k - \frac{Z_1^2}{Z_{\text{in}}^2} \tag{4}$$

$$u_1 = \frac{\arctan\left(\frac{(1-k)\cot(u_1\theta_1) - b\tan(u_1\theta_1)}{2a}\right) + q\pi}{\arctan\left(\frac{(1-k)\cot\theta_1 - b\tan\theta_1}{2a}\right)} \tag{5}$$

$$u_2 = \frac{\arctan\left(\frac{(1-k)\cot(u_2\theta_1) - b\tan(u_2\theta_1)}{2a}\right) + r\pi}{\arctan\left(\frac{(1-k)\cot\theta_1 - b\tan\theta_1}{2a}\right)} \tag{6}$$

$$Z_2 = \sqrt{k}Z_{\text{in}}, \quad Z_3 = \frac{Z_2^2}{Z_1} \tag{7}$$

$$\theta_2 = \arctan\left(\frac{(1-k)\cot\theta_1 - b\tan\theta_1}{2a}\right) \pm p\pi, \quad \theta_3 = \theta_1 \tag{8}$$

where p, q, and r are integer numbers and p, q, $r \geq 0$.

The electrical length θ_1 and Z_1 (Z_1 is embedded in variable a, and b) can be determined by solving these two nonlinear equations (Equations (5) and (6)) simultaneously via an optimization process. During the optimization process, q and r in (5) and (6) will be set to 1 if the inverse tangent term in the nominator of (5) or (6) is negative to prevent and from being negative. After obtaining θ_1 and Z_1, all unknown design parameters (Z_2, Z_3, θ_2, and θ_3) can be simple obtained from (7) and (8). In the design of the three-way tri-band 900/1800/2400 MHz power divider, the condition ($q = r = 1$, $p = 0$) must be satisfied.

3. EXPERIMENT

The three-way tri-band power divider design has been performed using a PTFE substrate ($\varepsilon_r = 2.65$, $h = 1$ mm) based on 50 Ω port characteristic impedance. The power divider is designed for $f_1 = 0.9$ GHz, $f_2 = 1.8$ GHz, and $f_3 = 2.4$ GHz. Simulation with models of a real lumped component

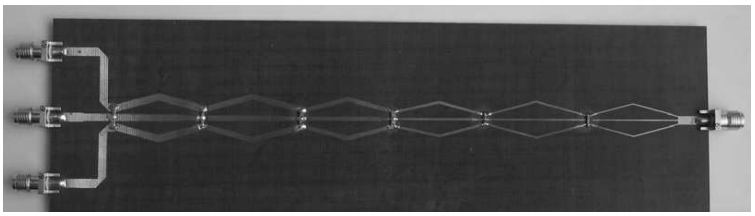

Figure 3: Photograph of the proposed three-way tri-band power divider.

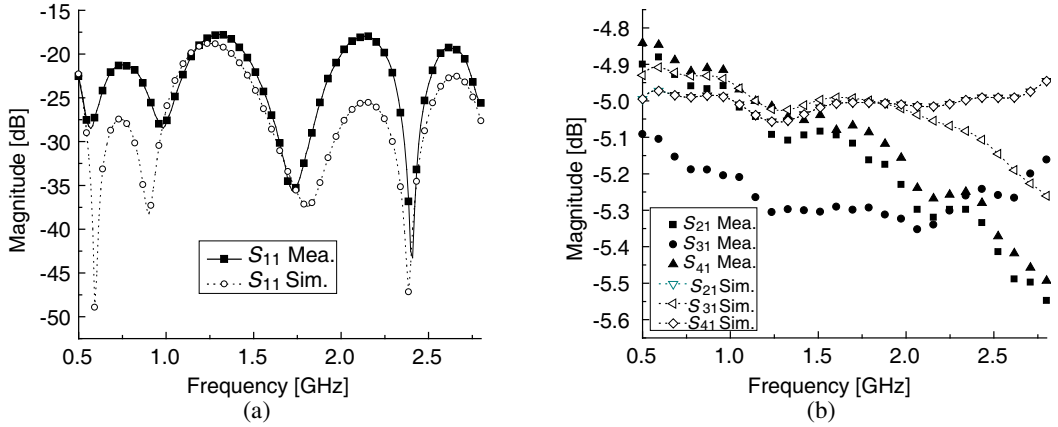

Figure 4: Simulation and measurement results of S-parameters for 0.9 GHz, 1.8 GHz, and 2.4 GHz: (a) Magnitude of S_{11}. (b) Magnitude of S_{21}, S_{31}, S_{41}.

and the real substrate is done applying the software Microwave Office 2004, and measured data is collected from an Agilent N5230A network analyzer.

The design parameters of the power divider are given below. The electrical length of each transformer section are $\theta_1 = 0.8$, $\theta_2 = 0.66$, $\theta_3 = 0.8$, $\theta_4 = 0.8$, $\theta_5 = 0.9$, and $\theta_6 = 0.8$, respectively. The corresponding length of each transformer section is $L_1 = 28.86\,\text{mm}$, $L_2 = 32.3\,\text{mm}$, $L_3 = 29.38\,\text{mm}$, $L_4 = 29.8\,\text{mm}$, $L_5 = 33.62\,\text{mm}$, and $L_6 = 30.29\,\text{mm}$, respectively. The characteristic impedances Z_1, Z_2, Z_3, Z_4, Z_5, and Z_6 of the six transformer sections can be determined as $Z_1 = 56.5\,\Omega$, $Z_2 = 65.8\,\Omega$, $Z_3 = 76.6\,\Omega$, $Z_4 = 97.8\,\Omega$, $Z_5 = 114\,\Omega$, $Z_6 = 132.88\,\Omega$, respectively. The resistances R_1, R_2, R_3, R_4,R_5, and R_6 of the planar isolation resistors are selected as $R_1 = 200\,\Omega$, $R_2 = 64.95\,\Omega$, $R_3 = 10\,\Omega$, $R_4 = 24\,\Omega$, $R_5 = 75\,\Omega$, and $R_6 = 150\,\Omega$, respectively. The overall dimension of the circuit is about $60 \times 204\,\text{mm}^2$, as shown in Fig. 3. The simulated and measured results are presented in Fig. 4. The insertion loss of the three output ports, as shown in Fig. 4, is about 5.08 ± 0.1 dB at 0.9 GHz, 5.20 ± 0.06 dB at 1.8 GHz, and 5.26 ± 0.03 dB at 2.4 GHz, respectively. These indicate that the designed power divider can successfully separate an incoming signal into three parts with equivalent amplitudes of output. The measured isolation between port2 and port3 or between port3 and port4 are close, which are better than 21 dB at 0.9 GHz, 24 dB at 1.8 GHz, and 25 dB at 2.4 GHz. The measured isolation between port2 and port4 is also better than 37 dB at 0.9 GHz, 36 dB at 1.8 GHz, and 28 dB at 2.4 GHz.

4. CONCLUSION

A novel three-way tri-band equal-split power divider based on a three-section transmission line transformer, which operates at any three arbitrary frequencies, is proposed. The structure of this power divider and the formulas used to determine its parameters are presented. Good agreement between simulation and measurement is achieved. Measured results show that all the features of the proposed power divider, such as an equal power split, impedance matching at all ports, and a good isolation between the two arbitrary output ports can be fulfilled at three arbitrary given frequencies simultaneously.

REFERENCES

1. Nagai, N., E. Maekawa, and K. Ono, "New n-way hybrid power dividers," *IEEE Trans. Microw. Theory Tech.*, Vol. 25, 1008–1012, 1977.

2. Wu, Y., Y. Liu, et al., "Dual-frequency power divider with isolation stubs," *Electronics Letters*, Vol. 44, No. 24, 1407–1408, 2008.
3. Wu, Y., Y. Liu, et al., "A new dual-frequency wilkinson power divider," *Journal of Electromagnetic Waves and Applications*, Vol. 23, No. 4, 83–492, 2009.
4. Feng, C. and G. Zhao, "Planar three-way dual-frequency power divide," *Electronics Letters*, Vol. 44, No. 2, 133–134, Jan. 2008.
5. Chongcheawchamnan, M. and S. Patisang, "Analysis and design of a three-section transmission-line transformer," *IEEE Trans. Microw. Theory Tech.*, Vol. 53, No. 7, 2458–2462, Jul. 2005.
6. Chongcheawchamnan, M. and S. Patisang, "Tri-band wilkinson power divider using a three-section transmission-line transformer," *IEEE Microw. Wirel. Compon. Lett.*, Vol. 16, No. 8, 452–454, Aug. 2006.

Bit Error Rate Reduction of Multi-user by UWB Antennas

Chien-Hung Chen[1], **Shu-Han Liao**[2], **Min-Hui Ho**[2], **and Chien-Ching Chiu**[2]

[1]Department of Computer and Communication Engineering, Taipei College of Maritime Technology
Shilin, Taipei, Taiwan, R.O.C.

[2]Department of Electrical Engineering, Tamkang University, Tamsui, Taipei, Taiwan, R.O.C.

Abstract— In this paper, a new ultra wideband circular antenna array (UCAA) combining genetic algorithm to minimize the bit error rate (BER) is proposed. Based on the topography of the antenna and the BER formula, the array pattern synthesis problem can be reformulated into an optimization problem and solved by the genetic algorithm. Simulation results show that the synthesized antenna array pattern is effective to focus maximum gain to the multi-user which scales as the number of array elements. In other words, the receiver can increase the received signal energy to noise ratio. The synthesized array pattern also can mitigate severe multipath fading in complex propagation environment. As a result, the BER can be reduced substantially in indoor UWB communication system.

1. INTRODUCTION

Ultra wideband (UWB) technology is an ideal candidate for a low power, low cost, high data rate, and short rang wireless communication systems. According to the Federal Communication Commission (FCC), UWB signal is defined as a signal having fractional bandwidth greater than 20% of the center frequency [1]. Ultra wide bandwidth of the system causes antenna design to be a new challenge [2].

Smart antennas employ arrays of antenna elements and can integrate multiple antenna elements with a signal processing. These smart antennas combine the signals from multiple antennas in a way that mitigates multipath fading and maximize the output signal-to-noise ratio. It can dramatically increase the performance of a communication system. The smart antenna technology in wireless communication can apply to the receiver [3] and the transmitter [4].

In this paper, the genetic algorithm is used to regulate the antenna feed length of each array element to minimize the BER performance of the communication system. The remaining sections of this paper are organized as follows: Section 2 briefly explains the formulation of the problem about channel modeling. Section 3 describes the genetic algorithm. The propagation modeling and numerical results are then presented in Section 4 and conclusion is made in Section 5.

2. SYSTEM DESCRIPTION

2.1. UWB Channel Modeling

Because the UWB communication span a wide bandwidth in the frequency domain, the channel impulse response variations are significant for different type antennas [5]. As a result, we do not only describe the antenna radiation pattern which varies with different frequencies but also use the SBR/Image technique to calculate the channel impulse response which includes angular characteristics of radiation patterns and the variation between different frequencies of wave propagation.

SBR/Image techniques are good techniques to calculate channel frequency response for wireless communication [6]. In this paper, we develop SBR/Image techniques including antenna pattern to model our simulation channel. It can perform the identification of major scattering objects causing reflection, diffraction and penetration in our simulation environment. The SBR/Image technique conceptually assumes that many triangular ray tubes (not rays) are shot from a transmitter. The triangular ray tubes whose vertexes are on a sphere are determined by the following method. First, we construct an icosahedron which is made of 20 identical equilateral triangles. Then, each triangle of the icosahedrons is tessellated into a lot of smaller equilateral triangles. Finally, these small triangles projected on to the sphere and each ray tube whose vertexes determined by the small equilateral triangle are constructed. Then each ray tube will bounce and penetrate in the simulate environments. If the receiver falls within the reflected ray tube, the contribution of the ray tube to the receiver can be attributed to an equivalent source (image). Using these images and received fields, the channel frequency response can be obtained as following

$$H(f) = \sum_{i=1}^{N_i} |a_i(f)|\, e^{j\,\theta_i(f)} \tag{1}$$

where f is the frequency of sinusoidal wave, i is the path index, θ_i is the i-th phase shift, $|a_i|$ is the i-th receiving magnitude which depend on the radiation vector of the transmitting and receiving antenna in. Note that the receiving antenna in our simulation is only one omnidirectional UWB dipole antenna and the transmitter is the UWB circular antenna array (UCAA) which has been described in above section. The channel frequency response of UWB can be calculated by Equation (1) in the frequency range of UWB.

The frequency is response are transformed to the time domain by using the inverse fast Fourier transform with the Hermitian signal processing [7]. Therefore, the time domain impulse response of the equivalent baseband can be written as follows

$$h_b(t) = \sum_{m=1}^{M} \alpha_m \delta(t - \tau_m) \tag{2}$$

where M is the number of paths observed at time. α_m and τ_m are the channel gain and time delay for the n-th path respectively.

2.2. Formulation of BER

As shown in Fig. 1, $\{a\}$ is the input binary data stream and $\{\widehat{a}\}$ is the output binary data stream after demodulator and decision device. When $\{a\}$ passing through the B-PAM modulator, the transmitted UWB pulse stream is expressed as follows:

$$x(t) = \sqrt{E_t} \sum_{n=0}^{\infty} \mathrm{p}(t - nT_d) d_n \tag{3}$$

The average BER for B-PAM IR UWB system can be expressed as

$$\mathrm{BER} = \sum_{n=0}^{N} P(\vec{d}_n) \cdot \frac{1}{2} erfc \left[\frac{V(t = nT_d)}{\sqrt{2}\sigma} \cdot (d_N) \right] \tag{4}$$

3. GENETIC ALGORITHM

Genetic algorithms are the global numerical optimization methods based on genetic recombination and evaluation in nature [8]. They use the iterative optimization procedures, which start with a randomly selected population of potential solutions. Then gradually evolve toward a better solution through the application of the genetic operators. Genetic algorithms typically operate on a discretized and coded representation of the parameters rather than on the parameters themselves. These representations are often considered to be "chromosomes", while the individual element, which constitutes chromosomes, is the "gene". Simple but often very effective chromosome representations for optimization problem involving several continuous parameters can be obtained through the juxtaposition of discretized binary representations of the individual parameter.

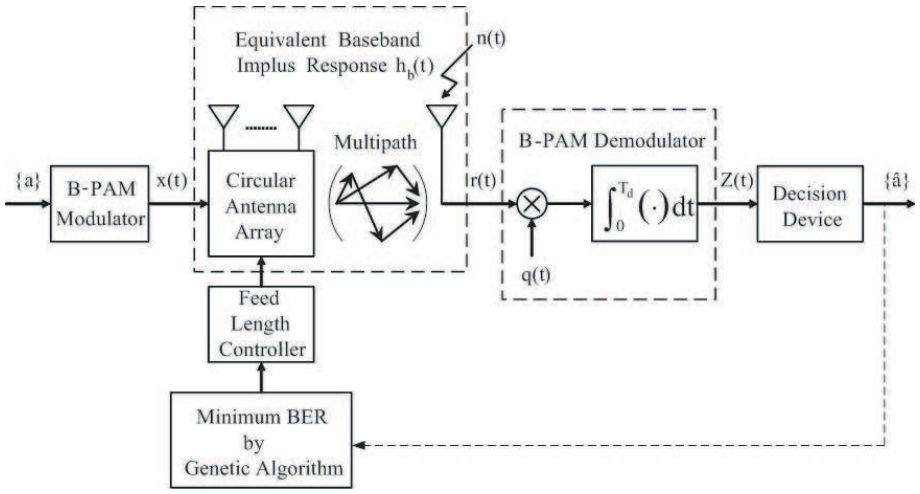

Figure 1. Block diagram of the simulated system.

When analyzing the circular antenna array, the feed length of each array element provides the phase delay of excitation current which varies with different frequencies.

4. NUMERICAL RESULTS

A realistic environment was investigated. It consists of a living room with dimensions 10 m × 10 m × 3 m, housing one metallic cupboard and three wooden bookcases. Both of the cupboard and

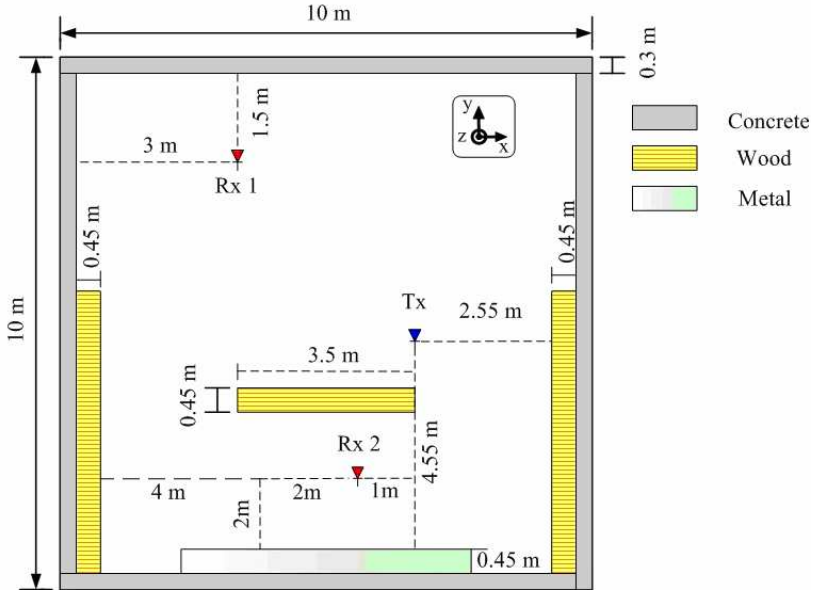

Figure 2. Block diagram of the simulated system.

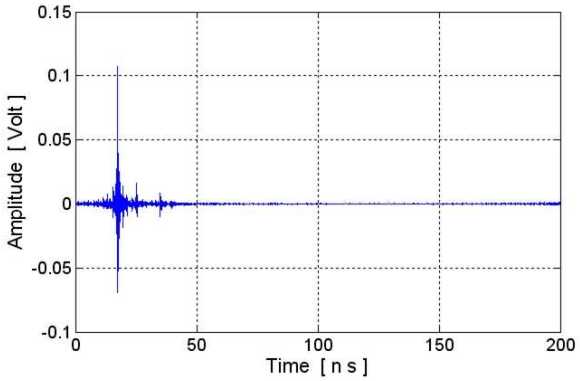

Figure 3. The channel impulse response of Tx-$Rx1$ using GA-UCAA as transmitting antenna.

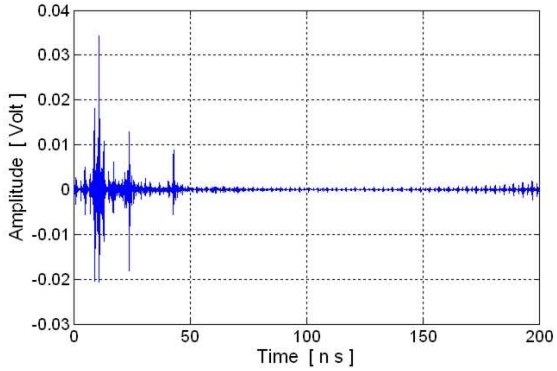

Figure 4. The channel impulse response of Tx-$Rx2$ using GA-UCAA as transmitting antenna.

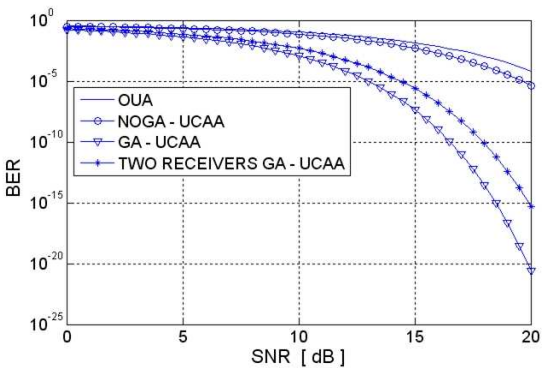

Figure 5. BER V.S. SNR over Scenario for kinds of transmitter.

bookcase are 2 meter in height. The radio wave can penetrate through the wooden bookcase and totally reflect by the metallic cupboard. The plan view of the simulated environment is shown in Fig. 2. Tx and $Rx1$, $Rx2$ antennas were all mounted 1 meter above the floor. The transmitter Tx position is (7 m, 5 m, 1 m). We simulated scenarios with different Rx positions. Scenario has two receivers: one is a line-of-sight path to the $Rx1$ (3 m, 8.5 m, 1 m) and the other is no line-of-sight path to the $Rx2$ (6 m, 2 m, 1 m). Tx and $Rx1$ are at a distance of approximately 5.315 meter. Tx and $Rx3$ are at a distance of approximately 3.2 meter. The height of the wooden bookcase was higher than that of the Tx, $Rx2$. A three-dimensional SBR/Image technique combined antenna radiation pattern has been presented in this paper. This technique is used to calculate the UWB channel impulse response for each location of the receiver.

Three kinds of transmitting antennas were used in this simulation scenario: (a) Only one UWB printed antenna (OUA). (b) A circular array of eight UWB printed Dipole antenna, each element antenna has the same feed Length without GA regulating (NOGA-UCAA). (c) A circular array of eight UWB printed dipole antenna , each element antenna feed length was regulated by GA (GA-UCAA).

Channel impulse response of Tx-$Rx1$ was shown in Fig. 3. In this scenario, GA-UCAA was used as the transmitting antenna. Channel impulse response of Tx-$Rx2$ was presented in Fig. 4. Similar to Fig. 3, the transmitting antenna was GA-UCAA.

Figure 5 shows the BER V.S. SNR for Tx-$Rx1$, which is a line-of-sight path, using three kinds of transmitters. Fig. 5 also shows the BER V. S. SNR for Tx-$Rx1$-$Rx2$, whose transmitter is GA-UCAA. Here SNR is defined as the ratio of the average transmitting power to the noise power. The results show that the BER curve decrease greatly when using the GA-UCAA to be transmitter. It is due to the fact that the GA-UCAA can minimize the fading and reduce the mulitpath effects. It also can focus the synthesized antenna array pattern to optimize available processing gain to the receiver.

5. CONCLUSION

Using the smart UWB circular antenna array to minimize the BER performance in indoor wireless local loop is presented. The impulse response of the channel is computed by SBR/Image techniques, inverse fast Fourier transform and Hermitian processing. By using the impulse response of the multipath channel and the genetic algorithm synthesizing optimal antenna radiation pattern, the BER performance of B-PAM IR UWB communication system is investigated. Base on the BER formulation, the synthesis problem can be reformulated into an optimization problem. In this paper, the fitness function is defined as the reciprocal of BER of the system. The genetic algorithm maximizes the fitness function by adjust the feed length of each antenna. Numerical results show that the BER can be reduced substantially in indoor UWB communication system.

ACKNOWLEDGMENT

This work was supported by National to Science Council, Republic of China, under Grant NSC-96-2221-E-229-001.

REFERENCES

1. Federal Communications Commission, "Revision of Part 15 of the commission's rules regarding ultra-wideband transmission system, FIRST REPORT AND ORDER," 1–118, FCC, ET Docket, Feb. 14, 2002.
2. Colak, S., T. F. Wong, and A. H. Serbest, "UWB dipole array with equally spaced elements of different lengths," *2007 IEEE International Conference on Ultra-wideband*, 789–793, 2007.
3. Ghavami, M., "Wideband smart antenna theory using rectangular array structures," *IEEE Trans. Signal Processing*, Vol. 50, No. 9, 2143–2151, Sep. 2002.
4. Chen, C.-H. and C. C. Chiu, "Novel optimum radiation pattern by genetic algorithms in indoor wireless local loop, " *Proc. IST Mobile Summit 2000*, 391–399, Galway, Ireland, Oct. 2000.
5. Manteuffel, D., "Radio link characterization using real antenna integration scenarios for UWB consumer electronic applications," *Ultra Wideband Systems, Technologies and Applications, 2006*, 123–130, The Institution of Engineering and Technology Seminar, Apr. 2006.
6. Malik, W. Q., D. J. Edwards, Y. Zhang, and A. K. Brown, "Three-dimensional equalization of ultrawideband antenna distortion," *Proc. Int. Conf. Electromagn. Adv. Apps. (ICEAA)*, Torino, Italy, Sept. 2007.

7. Oppermann, I., M. Hamalainen, and J. Iinatti, *UWB Theory and Applications*, John Wiley & Sons, 2004.
8. Goldberg, D. E., *Genetic Algorithm in Search, Optimization and Machine Learning*, Addison Wesley, 1989.